

C55.612:1976/v.1



# Collected Reprints

# 1976

Atlantic Oceanographic and Meteorological Laboratories

## Volume I

April 1977



**U.S. DEPARTMENT OF COMMERCE**  
National Oceanic and Atmospheric  
Administration





# Collected Reprints

# 1976

Atlantic Oceanographic and Meteorological Laboratories  
Miami, Florida 33149

Volume I

April 1977

Boulder, Colorado

**U.S. DEPARTMENT OF COMMERCE**

Juanita M. Kreps, Secretary

National Oceanic and Atmospheric Administration  
Robert M. White, Administrator

Environmental Research Laboratories  
Wilmot Hess, Director



## FORWARD

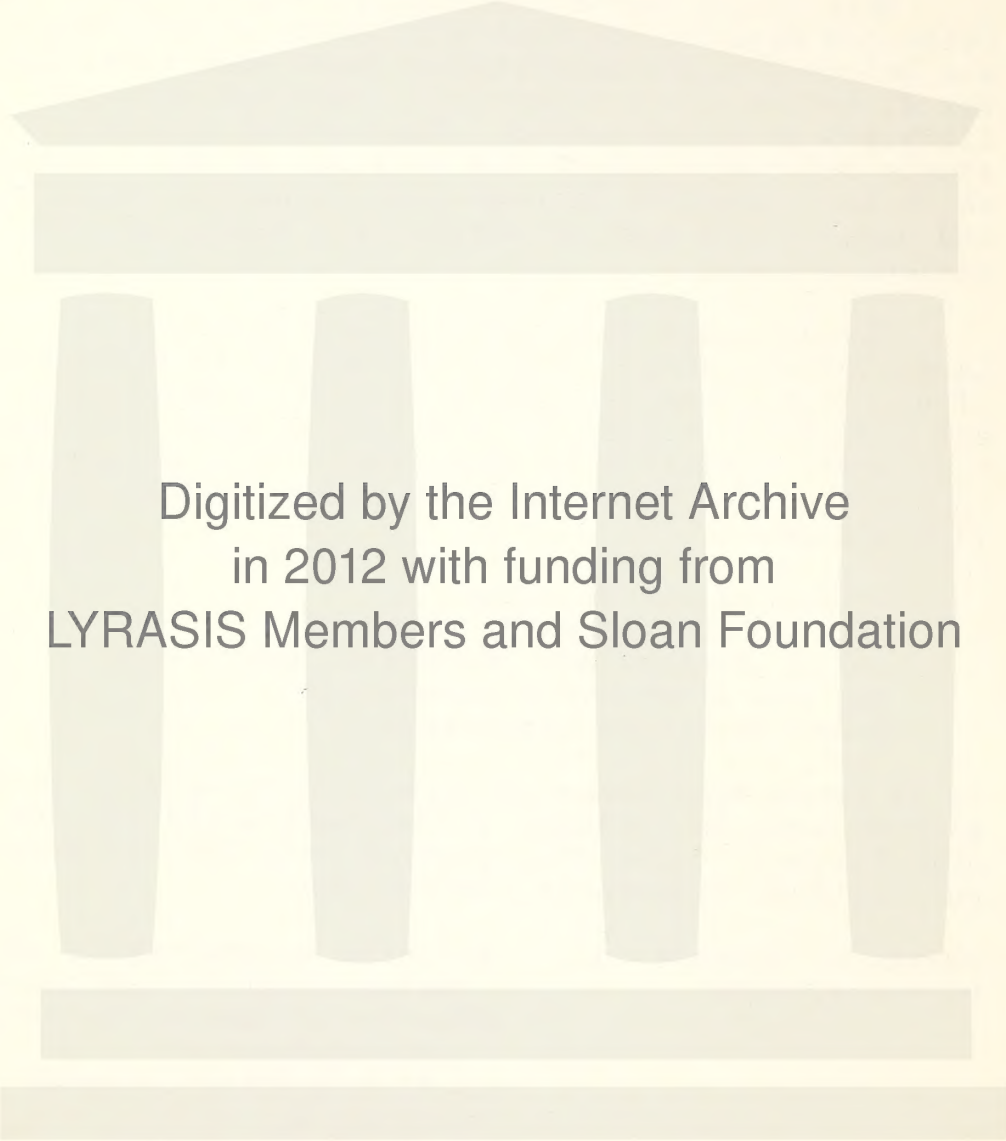
This is the tenth consecutive year in which the Collected Reprints of NOAA's Atlantic Oceanographic and Meteorological Laboratories have been published for distribution to scientists, institutions, and libraries here and abroad. This series provides a single reference source for articles by AOML personnel which have appeared in numerous scientific journals and various internal scientific and technical publications.

The Atlantic Oceanographic and Meteorological Laboratories conduct research programs in the areas of physical, chemical, and geological oceanography and air-sea interaction. The 1976 edition presents the papers published in that year. They are arranged in alphabetical order by first author within each of five groups:

Office of the Director  
Physical Oceanography Laboratory  
Marine Geology and Geophysics Laboratory  
Sea Air Interaction Laboratory  
Ocean Chemistry Laboratory

It is hoped that those recipients with whom we do not already have an exchange arrangement would add the AOML Library to the distribution list for any relevant publications from their institution.

Harris B. Stewart, Jr.     Atlantic Oceanographic and  
Director, AOML             Meteorological Laboratories  
                                 NOAA/Environmental Research  
                                 Laboratories  
                                 15 Rickenbacker Causeway  
                                 Virginia Key  
                                 Miami, Florida 33149



Digitized by the Internet Archive  
in 2012 with funding from  
LYRASIS Members and Sloan Foundation

<http://archive.org/details/collectedreprin1976v1atla>

CONTENTS

VOLUME I

General

	Page
1. Apel, J. P. Ocean Science from Space. <i>EOS</i> , Vol. 57, No. 9, 612-624.	1
2. Sawyer, C. B. High-Speed Streams and Sector Boundaries. <i>Journal of Geophysical Research</i> , Vol. 81, No. 13, 2437-2441.	14
3. Sawyer, C. B. and M. Haurwitz. Geomagnetic Activity at the Passage of High-Speed Stream in the Solar Wind. <i>Journal of Geophysical Research</i> , Vol. 81, No. 13, 2435-2436.	19
4. Stewart, H. B., Jr. Introduction. Proc. of CICAR-II Symposium: Progress in Marine Research in the Caribbean and Adjacent Regions, Caracas, Venezuela, July 12-16, 1976, p. 126.	21
5. Stewart, H. B., Jr. Introduction to the CICAR-II Symposium. Proc. of CICAR-II Symposium: Progress in Marine Research in the Caribbean and Adjacent Regions, Caracas, Venezuela, July 12-16, 1976, p. 241.	22
6. Stewart, H. B., Jr. Preliminary Bibliography of Published Results of Marine Research by U.S. Scientists in the CICAR Area, 1968- 1975: Introduction. U.S. Department of Commerce, NOAA/ERL/AOML-National Oceanographic Data Center Publication, Washington, D.C., 50 p.*	23
7. Stewart, H. B., Jr. Where the Sea and Man Meet: The Coastal Zone. <i>Museum</i> , Vol. 7, No. 11, 19-25, 44-48.	24

\* Introduction only.

PHYSICAL OCEANOGRAPHY LABORATORY

	Page
8. Beardsley, R. C., W. C. Boicourt, and D. V. Hansen.	
Physical Oceanography of the Middle Atlantic Bight. Middle Atlantic Continental Shelf and the New York Bight. ASLO Special Symposia, Volume 2, 20-34.	34
9. Charnell, R. L., M. E. Darnell, G. A. Berberian, B. L. Kolitz, and J. B. Hazelworth.	
New York Bight Project, Water Column Characterization Cruises 1 and 2 of the NOAA Ship <i>Researcher</i> , 4-15 March, 5-14 May 1974. <i>NOAA Data Report ERL MESA-18</i> , 220 p.*	49
10. Festa, J. F., and D. V. Hansen.	
A Two-Dimensional Numerical Model of Estuarine Cir- culation: The Effects of Altering Depth and River Discharge. <i>Estuarine and Coastal Marine Science</i> , Vol. 4, 309-323.	50
11. Gordon, H. R.	
Radiative Transfer: A Technique for Simulating the Ocean in Satellite Remote Sensing Calculations. <i>Applied Optics</i> , Vol. 15, No. 8, 1974-1979.	65
12. Hansen, D. V.	
A Lagrangian Buoy Experiment in the Sargasso Sea. Proc. AIAA Drift Symposium, Hampton, Va., May 22-23, 1974, NASA CP-2003, 175-192.	71
13. Herman, A.	
Automated Contouring of Vertical Oceanographic Sections Using an Objective Analysis. Proc. of the Third Annual Conference on Computer Graphics, Interactive Techniques, and Image Processing, University of Pennsylvania, Computer Graphics 10, No. 2, 218-223.	89

---

\* Abstract only;  
Complete text available on microfiche.



	Page
14. Herman, A. and A. C. Campbell.	
An Automated Solution for Omega Navigation. Proc. of the Fourteenth Annual Southeast Regional ACM Conference, University of Alabama, Birmingham, Alabama, 305-308.	95
15. Leetmaa, A.	
Some Simple Mechanism for Steady Shelf Circulation. <i>Marine Sediment Transport and Environmental Management</i> , D. J. Stanley and D. J. P. Swift, editors, John Wiley and Son, Inc., Chapter 3, 23-28.	99
16. Leetmaa, A. and M. Cestari.	
A Comparison of Satellite-Observed Sea Surface Temperatures with Ground Truth in the Indian Ocean. <i>NOAA Technical Report ERL 376-AOML 22</i> , 10 p.	105
17. Maul, G. A.	
The Study of Ocean Circulation from Space. Proc. of the Thirteenth Space Congress: Technology for the New Horizon, 3-27--3-36.	118
18. Maul, G. A., H. R. Gordon, S. R. Baig, M. McCaslin, and R. DeVivo.	
An Experiment to Evaluate SKYLAB Earth Resources Sensors for Detection of the Gulf Stream. <i>NOAA Technical Report ERL 378-AOML 23</i> , 69 p.	128
19. Mofjeld, H. O.	
Tidal Currents. <i>Marine Sediment Transport and Environmental Management</i> , D. J. Stanley and D. J. P. Swift, editors, John Wiley and Sons, Inc., Chapter 5, 53-64.	201
20. Molinari, R. L.	
The Formation of the Yucatan Current Based on Observations of Summer 1971. <i>Journal of Physical Oceanography</i> , Vol. 6, No. 4, 596-602.	213

	Page
21. Molinari, R. and A. D. Kirwan.	
Calculations of Differential Kinematic Properties from Lagrangian Observations. Proc. AIAA Drift Buoy Symposium, Hampton, Va., May 22-23, 1974, NASA CP-2003, 193-209.	220
22. Starr, R. B., G. A. Berberian, and M. A. Weiselberg.	
MESA New York Bight Project, Expanded Water Column Characterization Cruise XWCC-1 of the <i>R/V ADVANCE</i> II. NOAA Data Report ERL MESA-22, 43 p.*	237
23. Voorhis, A. D., E. H. Schroeder, and A. Leetmaa.	
The Influence of Deep Mesoscale Eddies on Sea Surface Temperature in the North Atlantic Sub- tropical Convergence. <i>Journal of Physical</i> <i>Oceanography</i> , Vol. 6, No. 6, 953-961.	238
MARINE GEOLOGY AND GEOPHYSICS LABORATORY	
24. Bennett, R. H., W. R. Bryant, W. A. Dunlap, and G. H. Keller.	
Initial Results and Progress of the Mississippi Delta Sediment Pore Water Pressure Experiment. <i>Marine Geotechnology</i> , Vol. 1, No. 4, 327-335.	247
25. Dash, B. P., M. M. Ball, G. A. King, L. W. Butler, and P. A. Rona.	
Geophysical Investigation of the Cape Verde Archipelago. <i>Journal of Geophysical Research</i> , Vol. 81, No. 29, 5249-5259.	256
26. Dietz, R. S.	
Iceland: Where the Mid-Ocean Ridge Bares Its Back. <i>Sea Frontiers</i> , Vol. 22, No. 1, 9-15.	267
27. Dietz, R. S. and K. O. Emery.	
Early Days of Marine Geology. <i>Oceanus</i> , Vol. 19, No. 4, 19-22.	274

---

\* Abstract only;  
complete text available on microfiche.

	Page
28. Dietz, R. S. and J. F. McHone.	
El'gygtgyn: Probably World's Largest Meteorite Crater. <i>Geology</i> , Vol. 4, No. 7, 391-392.	278
29. Freeland, G. L. and G. F. Merrill.	
Deposition and Erosion in the Dredge Spoil and Other New York Bight Dumping Areas. Proc. American Society of Civil Engineers Specialty Conference on Dredging and Its Environmental Effects, Mobile, Al., 26-28 January 1976, 936-946.	280
30. Freeland, G. L., D. J. P. Swift, W. L. Stubblefield, and A. E. Cok.	
Surficial Sediments of the NOAA-MESA Study Areas in the New York Bight. Middle Atlantic Shelf and the New York Bight, ASLO Special Symposia, Volume 2, 90-101.	291
31. Lavelle, J. W., P. E. Gadd, G. C. Han, D. A. Mayer, W. L. Stubblefield, D. J. P. Swift, R. L. Charnell, H. R. Brashear, F. N. Case, K. W. Haff, and C. W. Kunselman.	
Preliminary Results of Coincident Current Meter and Sediment Transport Observations for Wintertime Conditions on the Long Island Inner Shelf. <i>Geophysical Research Letters</i> , Vol. 3, No. 2, 97-100.	303
32. Lowell, R. P. and P. A. Rona.	
On the Interpretation of Near Bottom Water Temperature Anomalies. <i>Earth and Planetary Science Letters</i> , Vol. 32, No. 1, 18-24.	307
33. Nelsen, T. A.	
An Automated Rapid Sediment Analyser (ARSA). <i>Sedimentology</i> , Vol. 23, No. 6, 867-872.	314
34. Peter, G. and G. K. Westbrook.	
Tectonics of Southwestern North Atlantic and Barbados Ridge Complex. <i>American Association of Petroleum Geologists Bulletin</i> , Vol. 60, No. 7, 1078-1106.	320

	Page
35. Richardson, E. and C. G. A. Harrison.	
Opening of the Red Sea With Two Poles of Rotation. <i>Earth and Planetary Science Letters</i> , Vol. 30, No. 1, 135-142.	349
36. Richardson, E. and C. G. A. Harrison.	
Reply: Opening of the Red Sea With Two Poles of Rotation. <i>Earth and Planetary Science Letters</i> , Vol. 30, No. 2, 173-175.	357
37. Rona, P. A.	
Asymmetric Fracture Zones and Sea-Floor Spreading. <i>Earth and Planetary Science     Letters</i> , Vol. 30, No. 1, 109-116.	360
38. Rona, P. A.	
Book Review: Plate Tectonics and Oil. <i>Earth Science Reviews</i> , Vol. 12, No. 1, 74-75.	368
39. Rona, P. A., Editor.	
Mid-Atlantic Ridge. <i>Geological Society of     America, Microform Publication</i> , Vol. 5, 490 p.*	369
40. Rona, P. A.	
Pattern of Hydrothermal Mineral Deposition: Mid- Atlantic Ridge Crest at Latitude 26° N. <i>Marine     Geology</i> , Vol. 21, No. 4, M59-M66.	371
41. Rona, P. A.	
Resource Research and Assessment of Marine Phosphorite and Hard Rock Minerals. Proc. of NOAA Marine Minerals Workshop, March 1976, 111-119.	379

\* Abstract only;  
complete text on microform.

	Page
42. Rona, P. A.	
Salt Deposits of the Atlantic. <i>Special Volume of 'Annals of the Brazilian Academy of Sciences. Anais Acad. Brasil Ciencias (Suplemento)</i> , Vol. 48, 265-274.	388
43. Rona, P. A. and L. D. Neuman.	
Energy and Mineral Resources of the Pacific Region in Light of Plate Tectonics. <i>Journal of Ocean Management</i> , Vol. 3, 57-78.	398
44. Rona, P. A. and L. D. Neuman.	
Plate Tectonics and Mineral Resources of Circum-Pacific Region. Papers from Circum-Pacific Energy and Mineral Resources Conference, Honolulu, Hawaii, August 26-30, 1974, publ. by Amer. Assoc. of Petroleum Geologists, Memoir 25, 48-57.	420
45. Rona, P. A., R. N. Harbison, B. G. Bassinger, R. B. Scott, and A. J. Nalwalk.	
Tectonic Fabric and Hydrothermal Activity of Mid-Atlantic Ridge Crest (lat 26° N). <i>Geological Society of America Bulletin</i> , Vol. 87, 661-674.	430
46. Scott, R. B., J. Malpas, P. A. Rona and G. Udintsev.	
Duration of Hydrothermal Activity at an Oceanic Spreading Center, Mid-Atlantic Ridge (lat 26° N). <i>Geology</i> , Vol. 4, No. 4, 233-236.	444
47. Stubblefield, W. L. and D. J. P. Swift.	
Ridge Development as Revealed by Sub-Bottom Profiles on the Central New Jersey Shelf. <i>Marine Geology</i> , Vol. 20, No. 4, 315-334.	448
48. Swift, D. J. P.	
Coastal Sedimentation. <i>Marine Sediment Transport and Environmental Management</i> , D. J. Stanley and D. J. P. Swift, editors, John Wiley and Sons, Inc., Chapter 14, 255-310.	468

	Page
49. Swift, D. J. P.	
Continental Shelf Sedimentation. <i>Marine Sediment Transport and Environmental Management</i> , D. J. Stanley and D. J. P. Swift, editors, John Wiley and Sons, Inc., Chapter 15, 311-350.	524
50. Swift, D. J. P. and J. C. Ludwick.	
Substrate Response to Hydraulic Process: Grain-Size Frequency Distributions and Bed Forms. <i>Marine Sediment Transport and Environmental Management</i> , D. J. Stanley and D. J. P. Swift, editors, John Wiley and Sons, Inc., Chapter 10, 159-196.	564
51. Swift, D. J. P., G. L. Freeland, P. E. Gadd, G. Han, J. W. Lavelle, and W. L. Stubblefield.	
Morphologic Evolution and Coastal Sand Transport, New York-New Jersey Shelf. Middle Atlantic Shelf and the New York Bight, ASLO Special Symposia, Volume 2, 69-89.	602

## VOLUME II

### SEA-AIR INTERACTION LABORATORY

52. Apel, J. R., H. M. Byrne, J. R. Proni, R. Sellers.	
A Study of Oceanic Internal Waves Using Satellite Imagery and Ship Data. <i>Remote Sensing of Environment</i> 5, No. 2, 125-135. Also appeared in Proc. Thirteenth Space Congress, Technology for the New Horizon, Cocoa Beach, Florida, April 7, 8, 9, 1976, 3-21--3-25.	623
53. Hanson, K. J.	
A New Estimate of Solar Irradiance at the Earth's Surface on Zonal and Global Scales. <i>Journal of Geophysical Research</i> , Vol. 81, No. 24, 4435-4443.	634

	Page
54. Hasselmann, K., D. B. Ross, P. Muller, and W. Sell. A Parametric Wave Prediction Model. <i>Journal of Physical Oceanography</i> , Vol. 6, No. 2, 200-228.	643
55. McLeish, W. and S. M. Minton. STD Observations From the R/V COLUMBUS ISELIN During Phase III of GATE. <i>NOAA Technical Report ERL 379-AOML 24</i> . 101 p.	672
56. Newman, F. C. Temperature Steps in Lake Kivu: A Bottom Heated Saline Lake. <i>Journal of Physical Oceanography</i> , Vol. 6, No. 2, 157-163.	776
57. Proni, J. R., F. C. Newman, D. C. Rona, D. E. Drake, G. A. Berberian, C. A. Lauter, Jr., and R. L. Sellers. On the Use of Acoustics for Studying Suspended Oceanic Sediment and for Determining the Onset of the Shallow Thermocline. <i>Deep-Sea Research</i> , Vol. 23, No. 9, 831-837.	783
58. Proni, J. R., F. C. Newman, R. L. Sellers, and C. Parker. Acoustic Tracking of Ocean-Dumped Sewage Sludge. <i>Science</i> , Vol. 193, 1005-1007.	794
59. Thacker, W. C. A Solvable Model of "Shear Dispersion." <i>Journal of Physical Oceanography</i> , Vol. 6, No. 1, 66-75.	797
60. Thacker, W. C. Spatial Growth of Gulf Stream Meanders. <i>Geophysical Fluid Dynamics</i> , Vol. 7, 271-295.	807
61. Webster, W. J., Jr., T. T. Wilheit, D. B. Ross, and P. Gloersen. Spectral Characteristics of the Microwave Emission From A Wind-Driven Foam-Covered Sea. <i>Journal of Geophysical Research</i> , Vol. 81, No. 18, 3095-3099.	832

62. Atwood, D. K.  
Regional Oceanography as it Relates to Present and Future Pollution Problems and Living Resources-Caribbean. IOC/FAO/UNEP International Workshop on Marine Pollution in the Caribbean and Adjacent Regions, Port of Spain, Trinidad, IOC/FAO/UNEP/IWMPCAR/8, 40 p. 837
63. Gilio, J. L. and D. A. Segar.  
Biogeochemistry of Trace Elements in Card Sound, Florida Inventory and Annual Turnover. Proc. of the Sea Grant Symposium on Biscayne Bay, April 2-3, 1976, 17 p. 879
64. Hatcher, P. G. and L. E. Keister.  
Carbohydrates and Organic Carbon in New York Bight Sediments as Possible Indicators of Sewage Contamination. Middle Atlantic Continental Shelf and the New York Bight, ASLO Special Symposia, Volume 2, 240-248. 896
65. Hatcher, P. G. and D. A. Segar.  
Chemistry and Continental Margin Sedimentation. *Marine Transport and Environmental Management*, D. J. Stanley and D. J. P. Swift, editors, Chapter 19, 461-477. 905
66. Segar, D. A. and G. A. Berberian.  
Oxygen Depletion in the New York Bight Apex: Causes and Consequences. Middle Atlantic Continental Shelf and the New York Bight, ASLO Special Symposia, Volume 2, 220-239. 922
67. Segar, D. A. and A. Y. Cantillo.  
Some Considerations on Monitoring of Trace Metals in Estuaries and Oceans. Proc. of the International Conference on Environmental Sensing and Assessment, IEEE Annuals No. 75CH004-1, 6-5, 1-5. 942



68. Segar, D. A. and A. Y. Cantillo.  
Trace Metals in the New York Bight. Middle  
Atlantic Continental Shelf and the New York  
Bight, ASLO Special Symposia, Volume 2,  
171-198. 947
69. Tosteson, T. R., D. K. Atwood, and R. S. Tsai.  
Surface Active Organics in the Caribbean Sea.  
MTS-IEEE Oceans '76, 13C-1-13C-7. 975



# Ocean Science From Space

John R. Apel

## Introduction

The ocean plays as fundamental a role in the natural scheme of things as does the atmosphere, although its functions, being considerably more varied and diffuse, are probably neither as well appreciated nor as well understood. The sea profoundly affects the weather and climate and in turn is affected by the atmosphere, acting as both a heat reservoir for storing, distributing, and releasing solar energy and as the source for most atmospheric moisture. It interacts with the bounding land and air over times ranging from minutes to millennia. Geological activity on all time and space scales takes place in and under the seas, which serve as the repository for the detritus of man and nature and, just as important, as practicable sources of petroleum and a few useful minerals. Its currents and dilutant powers are called upon to disperse sewage, poisonous and nonpoisonous wastes, solid trash, and excess heat, while it maintains a role as the aqua viva for an extremely complicated and

commercially important food chain and a role as a means of recreation and refreshment for people. In the estuaries and the coastal zones these conflicting demands are especially severe.

This article attempts a rather limited review of the types of oceanic information that current experimental results and planning indicate should be available from spacecraft in the near future. To the author's knowledge, plans exist to orbit sensors that will yield measurements or observations of all of the parameters discussed here, albeit often only on an experimental basis.

Questions on the usefulness of satellites for ocean science have been raised by oceanographers since the first space-derived imagery was returned to earth. It was not at all obvious what relationships such data might have to the physical oceanographer's usual repertory of salinity, temperature, and depth measurements, the biologist's concerns with flora or fauna, or the geologist's interests in rocks or sediments.

After nearly two decades of activity in space it is becoming obvious that for several limited but nevertheless important classes of phenomena it is possible to make observations and measurements from spacecraft of considerable usefulness to oceanographers. In a few isolated instances it even appears one may do so with a breadth and accuracy exceeding anything attainable from ships or buoys. For these types of observations, the satellite represents a new tool of great power, and the information on physical and biological processes obtained from it will be worthy of inclusion in the data banks and in the minds of researchers.

However, for a sizable percentage of physical and biological ocean scientists, much of these data may fall far afield or might be too indirect or perhaps even too esoteric for their tastes. The value of the data to these workers will chiefly be in the concomitant enlargement of the general fund of oceanic knowledge.

By and large, satellite oceanography is confined to surface and near-surface phenomena. This constraint

is not as severe as it appears at first glance, because data taken from spacecraft will be appended to other, conventionally derived surface and subsurface measurements of parameters such as vertical current or temperature profiles in order to construct a more nearly three-dimensional view of the ocean. In addition, near-surface data are useful in their own right, since the coupled nonlinear interactions between ocean and atmosphere largely take place in the few tens of meters above and below the sea-air interface, at least for shorter time scales. Man's marine activities are mostly confined to near that surface as well, so that the kind of two-dimensional oceanography that one can pursue from spacecraft is often highly relevant.

#### Uses of Spacecraft Data

The answer as to who needs what information from spacecraft obviously depends on the type of information that is obtainable. In research areas the disciplines served with some degree of usefulness are marine geodesy and gravity; physical, geological, and biological oceanography; glaciology; boundary layer meteorology; and climatology. Various maritime operations, shipping, offshore mining, oil drilling, and fishing, all require an improved and expanded data base and more accurate marine forecasts. The ever-increasing fraction of the population living along the seacoasts needs improved forecasting and warning services for protection of life and property. However, because of the great length and breadth of the sea the difficulties in obtaining timely detailed information of sufficient observational density across its expanse have prevented an effective monitoring and forecasting system for the oceans.

#### Satellites of Utility to Oceanography

The number of satellites carrying sensors that yield data useful to ocean science is large, and the value of the data from them variable. Ta-

ble 1 is a listing [LaViolette, 1974; Apel and Siry, 1974; NASA, 1975; Koffler, 1975] of the spacecraft that have been or will be sources of data having oceanographic significance. Of the several listed, the most useful are probably NOAA 3 and 4, ERTS 1/Landsat 2, Geos 3, the SMS/GOES quintuplets, Tiros-N, Seasat-A, and Nimbus-G. The data types are diverse, as is discussed below. The last three satellites, which are to be launched in 1978, are of much interest to oceanography. Tiros-N is the first of a new generation of operational meteorological and environmental polar-orbiting satellites. Seasat-A is dedicated to oceanography, geodesy, meteorology, and climatology [Apel and Siry, 1974]. Nimbus-G is designed to serve experimental ends for both pollution monitoring and oceanography [NASA, 1975].

#### Data Available From Satellites

Spacecraft data presently available on any basis other than a primarily experimental one are quite limited and are effectively confined to low- and medium-resolution visible and infrared imagery (NOAA, GOES), from which sea surface temperatures having accuracies of order  $\pm 1.5^{\circ}$ - $2.0^{\circ}$ C may be derived, and small amounts of high-resolution Landsat images. However, the near future promises a large increase in the quantity, quality, and coverage of oceanic data.

The estimates of data accuracy and coverage cited below are thought to be valid for the general 1978-1982 era, when Tiros-N, Seasat-A, Nimbus-G, Landsat 3, and the GOES system are all to be active. In each case the dominant instruments contributing to the



Fig. 1. Surface isotherms in degrees centigrade of Lake Huron derived from the VHR sensor on the NOAA 4 environmental satellite, August 7, 1975. Relative accuracy is approximately  $\pm 1^{\circ}$ C (NOAA, National Environmental Satellite Service).

TABLE 1. U.S. Satellites of Utility in Oceanography

Satellite	Launch Date	Orbit	Utility of Data	Character	Sensors	Oceanic Parameters
Mercury Gemini Apollo Apollo-Soyuz	1962- 1975	Variable	Low to medium	Exploratory	Cameras	Imagery
Nimbus 4 Nimbus 5 Nimbus 6 Nimbus-G	1970 1973 1975 1978	Polar	Medium progressing to high	Experimental	IR and MW radiometers and bolometer; color scanner	Temperature, ice cover, radiation budget, wind, color
ITOS 1-4 ESSA 1-9 NOAA 1-4	1966- 1975	Polar	Medium and high	Operational	Visible vidicon; IR scanner	Imagery, temperature
ATS 1-3	1966 1967	Synchronous	Medium	Prototype	Visible, IR scanners; data channel	Imagery, temperature, data relay
SMS/GOES 1-5	1974- 1978	Synchronous	High	Operational	Visible, IR scanners; data channel	Imagery, temperature, data relay
Geos 1-3	1965 1975	Variable	High	Experimental	Laser reflectors; altimeter	Geoid, ocean geoid
ERTS 1 Landsat 2 Landsat 3	1972 1974 1978	Polar	Medium progressing to high	Prototype	Visible, near-IR scanner; thermal IR scanner	Imagery, temperature
Skylab	1973		Medium progressing to high	Experimental	Cameras; visible, IR scanner; spectro radi- ometer; MW radiom- eters; altimeter; scatter- ometer	Imagery, temperature, wave height, wind speed, geoid
Shuttle	1983	Varied	Medium to high	Varied	Varied	Unknown
Tiros-N	1978	Polar	High	Operational	Visible, IR scanners	Imagery, temperature
Seasat-A Seasat-B	1978- 1983	Near Polar	High	Experimental	Altimeter; imaging radar; scatterometer; MW radiometer; visible/IR scanner	Geoid, wave spectra, wind speed, ice, temperature

From *LaViolette* [1974], *Apel and Stry* [1974], and *NASA* [1975].

TABLE 2. Sensors of Oceanographic Interest

Short Form	Sensor Name	Wavelength or Frequency	Spacecraft	Spatial Resolution
SR	Scanning radiometer	Visible and thermal IR	NOAA 1-4	7 km
VHRR	Very high resolution radiometer	Visible and thermal IR	NOAA 1-4	1 km
VISSR	Visible and infrared spin scan radiometer	Visible and thermal IR	GOES	1-7 km
AVHRR	Advanced very high resolution radiometer	Visible and thermal IR	Tiros-N	1 km
MSS	Multispectral scanner	Four channels, visible and reflected IR;	ERTS/Landsat 1 and 2	70 km
CZCS	Thematic mapper	Thermal IR	Landsat 3, Landsat 4	25 m, 100 m (IR)
	Coastal zone color scanner	Six channels, visible, reflected and thermal IR	Nimbus-G	800 m
ESMR	Electronically scanned microwave radiometer	19 GHz	Nimbus 5	15 km
SMMR	Scanning multichannel microwave radiometer	Five channels: 6.6, 10, 18, 21, 35 GHz	Nimbus-G, Seasat-A	15-140 km
Alt	Short pulse altimeter	13.9 GHz	Skylab, Geos 3, Seasat-A	2 km
Scatt	Radar wind scatterometer	13.4 GHz	Skylab, Seasat-A	25 km
SAR	Synthetic aperture radar	1.4 GHz	Seasat-A	25 m

measurement are listed, although to achieve the precision or accuracy cited, ancillary data will usually be required. There is every reason to blend surface and satellite data together, so that the space-derived information can be calibrated and verified by point surface measurements and thus can often extend the surface observations to near-planetary scales. The sensors of prime interest are also cited and with their shortened forms are listed in Table 2.

One finds a diverse list of features, or observables, that enter into oceanic processes. In listing these parameters it is convenient to begin at the level of the action of the atmosphere upon the sea; then follow the ocean's response, waves and currents, and its effects upon the shore. Other land-sea interactions are then listed. Identification of water mass properties established by natural and man-made influences is discussed next. Finally, some estimates of the role of the ocean in establishing climatology are given.

In many of the parameter values and ranges given below the lack of experimental verification requires that the data be regarded as preliminary estimates only, and the reader is cautioned to remain skeptical. In most cases they represent compromises between requirements leveled by the ocean scientists and the attempts of the instrument designers to meet those requirements via remote sensing.

#### Air-Sea Interaction

The transport of matter, momentum, and energy across the air-sea interface is chiefly due to solar radiation and atmospheric stress. Such parameters as the air-sea temperature difference, exchange of latent and sensible heat, and the vector surface wind field are important observables for climatological, meteorological, and oceanic purposes. For spacecraft the following estimates appear reasonable.

*Sea surface temperature.* For the estimated capability, in cloud-free areas it should be possible to determine absolute temperature ac-

curacy to order  $1^{\circ}\text{C}$  and precision or relative accuracy to approximately  $\pm 0.5^{\circ}\text{C}$ . Over coastal waters and lakes, space-time averaging of order 4 km and 1 day is needed [Koffler, 1975]; for regional ocean areas, 10-km and few-day averages are required; in the open ocean, 50-km and several-day averages should suffice [Bromer et al., 1976]. The sensors to be used are VHRR, VISSR, and AVHRR (Table 2). In cloudy areas or in light rain a temperature precision of  $\pm 1.5^{\circ}\text{--}2.0^{\circ}\text{C}$  should obtain with 100-km and few-day averages away from coasts by using SMMR. To the satellite-derived temperatures should be appended ship surface and vertical temperature profiles to the maximum extent possible.

Figure 1 shows isotherms for Great Lakes surface temperatures as an example of the current high-resolution thermal mapping in a limited region, derived from the VHRR sensor on the NOAA 4 satellite [Koffler, 1975].

*Surface vector wind field.* As

referenced to a 20-m height, the scatterometer may measure surface wind speed from a very few to perhaps 20 m/s, with a precision of about  $\pm 2$  m/s or 25% of the actual value (whichever is larger) and wind direction to  $\pm 20^{\circ}$  through clouds and light rainfall; 25-km resolution over a several hundred kilometer swath width will be the case [Grantham et al., 1975]. For higher winds, attempts will be made to determine speed from 5 to perhaps 35 m/s within  $\pm 25\%$  of actual speed over a several hundred kilometer swath through clouds and light rain by using the SMMR [Apel and Siry, 1974, p. 14; NASA, 1975; Barath and Gloersen, 1975].

Figure 2 shows radar backscatter cross section of the ocean  $\sigma^{\circ}$  as a function of wind speed at 20 m, with angle of illumination (measured from nadir) as a parameter. This effect forms the basis for the wind speed measurement with the radar wind scatterometer [Grantham et al., 1975].

*Radiation budget.* Precision

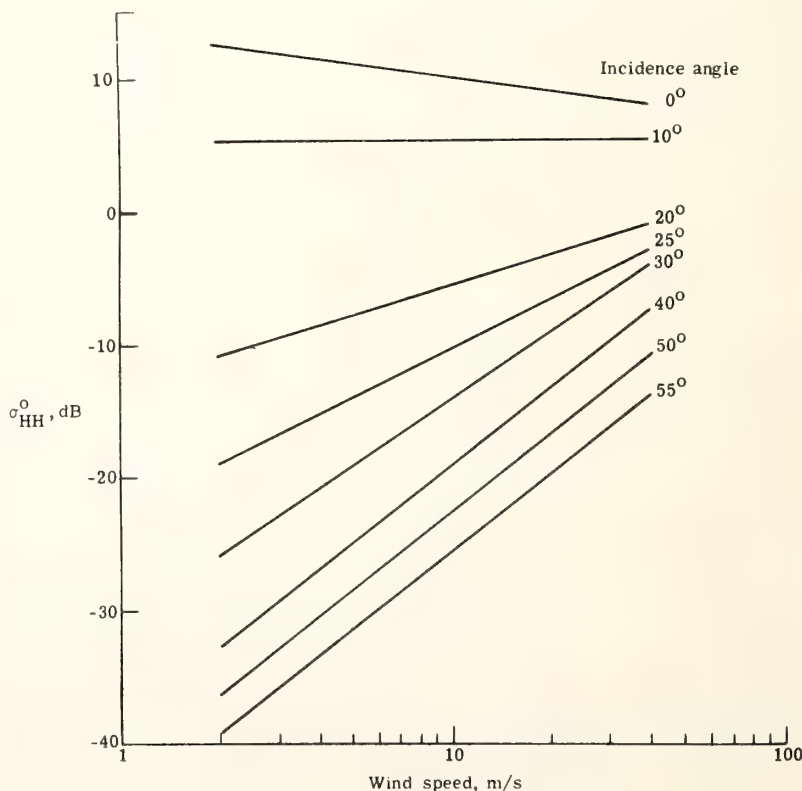


Fig. 2. Radar cross section  $\sigma_{HH}^{\circ}$  of ocean surface at 13 GHz versus surface wind speed measured at 20-m height. Angle off nadir is the parameter. Horizontal polarization, cross-wind illumination (NASA Langley Research Center).

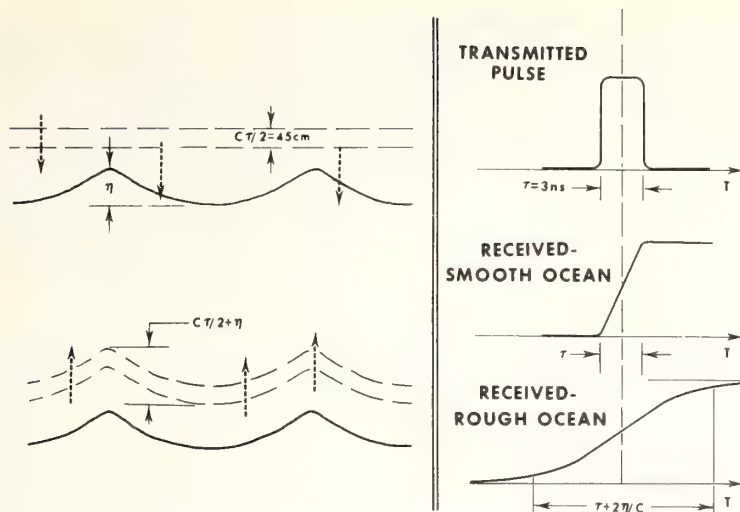


Fig. 3. Short-pulse method for determining significant wave height with a 3-ns radar altimeter.

radiometers are estimated to be able to determine spectrally integrated solar radiation absorbed in and reflected by the global ocean, with a precision of approximately  $\pm 5$  Ly/day, with various spatial resolutions [NASA, 1975].

#### Surface Wave Field

There is obviously a strong coupling between the surface wind field

and ocean waves, with the wind initially generating short-length capillary waves which then cascade toward longer wavelengths and larger amplitudes, dependent upon the strength, direction, duration, and fetch of the wind. While significant wave height  $H_{1/3}$  is a one-parameter specification of sea state, the proper description of a homogeneous surface wave field is more detailed, e.g., the two-dimen-

sional power spectral density as a function of surface wave vector. A reasonably complete determination of this function near storms, when used as input data to numerical models, would allow wave forecasts to be made at a distance of several hundred kilometers from the high wind regions. Where the field is nonhomogeneous, as near shorelines, near intense low pressure systems, or in shoaling water, an image of the surface field is more appropriate than a spectrum.

*Significant wave height.* For the estimated capability, it appears possible to measure significant wave height  $H_{1/3}$  with a precision of  $\pm 1$  m or  $\pm 25\%$  of the actual height over a range of 1–20 m along the subsatellite track on a near-all-weather basis by using the short-pulse altimeter [Walsh, 1974]. Figure 3 illustrates the effect of a rough ocean in broadening a 3-ns radar altimeter pulse, the measurement of which forms the basis for the determination of  $H_{1/3}$ .

*Surface wave spectrum.* For the surface wave power spectrum the synthetic aperture radar (SAR) may yield square amplitude measurements consistent with the precision for  $H_{1/3}$  (above) for all wavelengths between 50 m and the largest observable length, measured at  $10^\circ$  intervals for all angles of propagation; the spatial and temporal resolution is limited to small samples taken near the United States or to more intensive spectra in selected regions. The instrument appears to have an all-weather capability [Brown et al., 1976].

*Wave refraction patterns.* Surface waves reflect, refract, and diffract under the influence of shoal water and may converge or diverge, depending on bottom topography. Heavy wave action moves shoals and channels about and damages ocean structures such as jetties and offshore platforms. Wave refraction studies for a given region assist in shoreline protection, channel maintenance, and understanding of wave-driven circulation. Under these conditions, images rather than spectra are required. The SAR should image wave refrac-

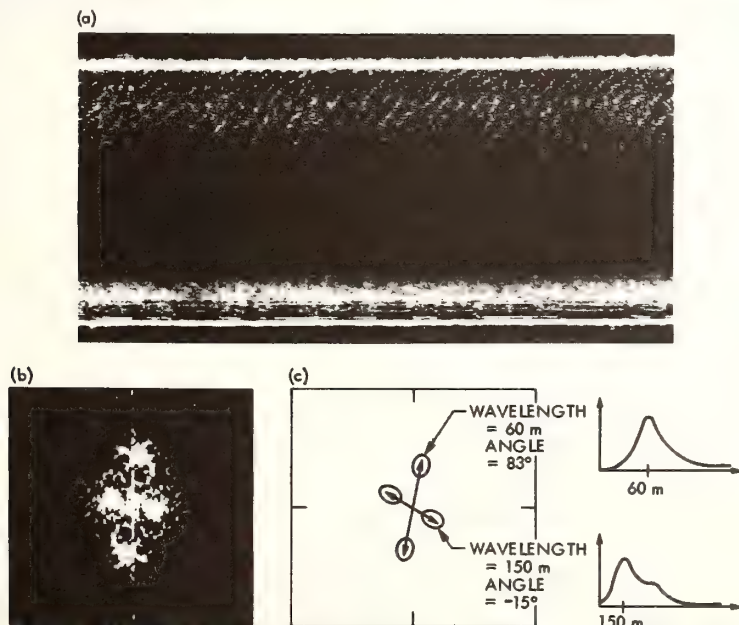


Fig. 4. (a) band synthetic aperture radar image of 60-m and 150-m ocean waves off Alaska; (b) two-dimensional Fourier transform of part a showing wave energy concentrations as bright spots; (c) interpretation of part b in terms of two dominant wave trains, with densitometer traces of the figure taken at  $83^\circ$  and  $-15^\circ$  (Jet Propulsion Laboratory).

tion patterns for wavelengths greater than 50 m over swath widths of up to 100 km on a selected basis; it does so with a near-all-weather capability [Brown *et al.*, 1976].

Figure 4 shows a surface wave field as obtained from the synthetic aperture imaging radar and a digital Fourier transform, which appears to yield a wave slope spectrum [Brown *et al.*, 1976].

#### Currents and Vertical Motions

Ocean currents are driven by wind stress, by tidal forces, and by uneven temperature and salinity distributions in the body of the sea. On the rotating earth a moving fluid tilts its surface relative to the geoid with a slope proportional to the fluid velocity; this is called geostrophic flow. In the case of western boundary currents, e.g., the Gulf Stream, the slopes are of order  $10^{-5}$  or less; the resultant topographic elevations across the stream, measured with respect to the geoid, are about 1 m or less.

Upwellings and downwellings are slow vertical flows usually brought about by wind stress and coastal topography. Upwellings in particular are of interest because the cold subsurface water often has a high nutrient level that may lead to a plankton bloom and ultimately an enhanced fish population. From the standpoint of spacecraft data the speed of the current in an upwelling is not observable, but rather the timely identification and location of the event are possible.

In order to determine the complete dynamical current velocity field, one must measure speed and direction as a function of position and time. In addition, the vertical distribution of current velocity throughout the water column is needed for measuring total transports of water, dissolved chemicals, nutrients, etc. This is obviously impossible from satellites, and therefore to any surface current measurements made from spacecraft must be appended subsurface current profiles taken by conventional means.

Present estimates [Kaula, 1970;

Apel, 1972; Apel and Byrne, 1974] give roughly  $\pm 20$  cm/s as the ultimate achievable precision in the determination of surface geostrophic speeds from spacecraft by way of surface slope measurements using a radar altimeter and perhaps several kilometers as the time-averaged error in the position of the current measurements along the subsatellite track only. Nevertheless, surface current speeds considerably below 20 cm/s are found in the ocean and are of interest. No apparent means exist for remotely determining such low speeds from spacecraft. However, drifting Lagrangian buoys may act as near-surface water movement tracers for these lower speeds

[Molinari, 1974]. When the drifting buoys are equipped with satellite positioning devices and data collection systems, they become extremely valuable adjuncts to the remote sensors on board the spacecraft.

However, it should be emphasized again that spacecraft remote sensors alone can by no means deliver all of the required information.

Figure 5, taken from Defant [1961], shows the long-time mean surface topography of the western North Atlantic as calculated assuming that geostrophy obtains, with elevations above and below an equipotential surface close to the geoid given in centimeters. The time-averaged Gulf Stream is

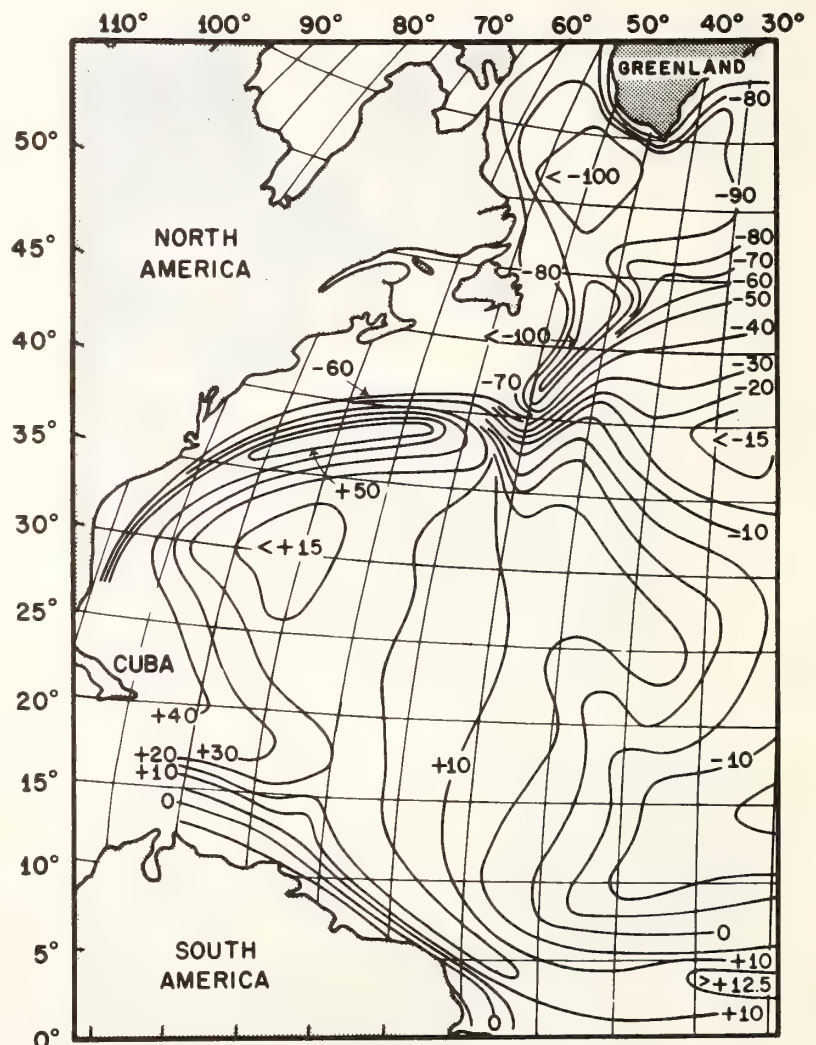


Fig. 5. Long-term topographic setup of western North Atlantic as calculated from oceanic density anomalies; elevations are given in centimeters relative to the geoid [Defant, 1961].



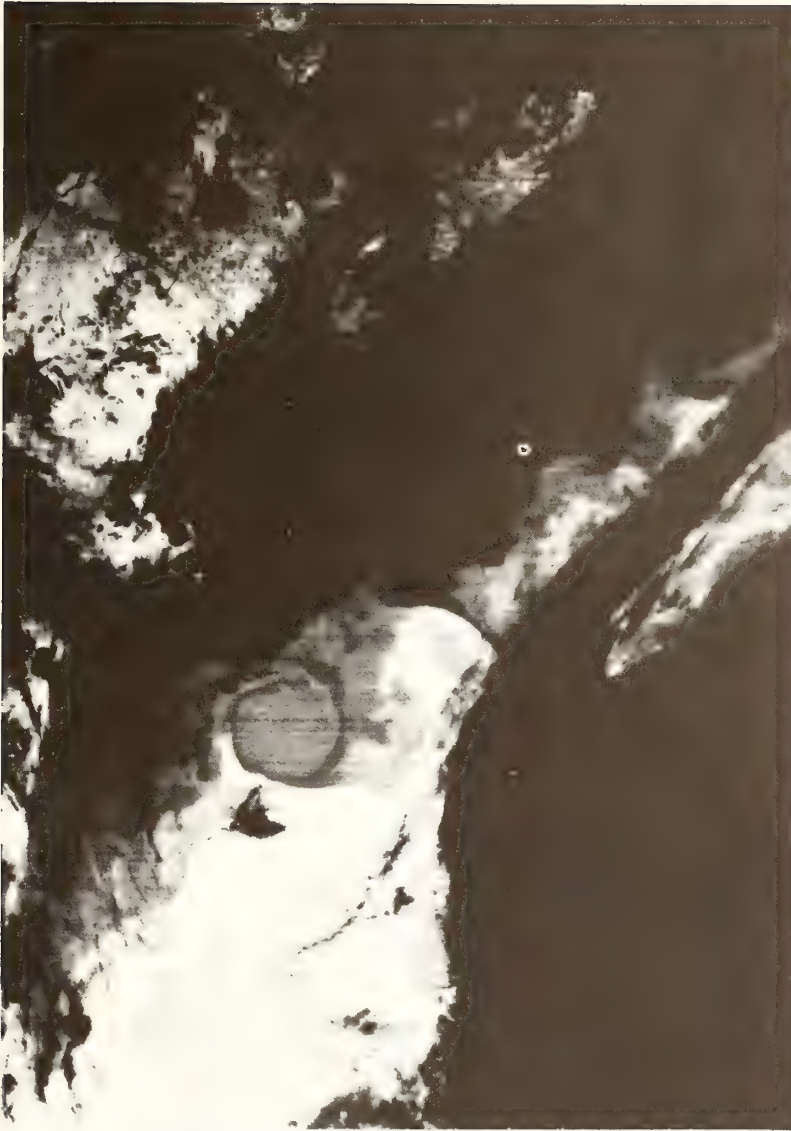


Fig. 6. Thermal infrared image made off U.S. East Coast on May 12, 1975, showing Gulf Stream, meanders, and eddies in lighter shades; dark areas are cold clouds (NOAA, National Environmental Satellite Service).

clearly visible; its instantaneous position may depart from the horizontal mean axis by amounts approaching 200 km, moving slowly (5- to 40-day periods) in comparison with the time (a few days) required to map the area with a satellite. The hope is that satellite altimetry will become sufficiently precise so that this dynamic topography, and hence surface current speed, can be determined by using it [Kaula, 1970; Apel, 1972; Apel and Byrne, 1974]. This requires that both the background geoid and the topographic departures from it be determined with precisions approaching  $\pm 10$

cm in the vertical. The requirement inextricably links dynamical oceanography and marine geodesy if such schemes are to be pursued.

Figure 6 illustrates a NOAA 4 thermal infrared image off the northeastern U.S. coast with the warm water of the Gulf Stream in lighter shades [Koffler, 1975]. Such imagery can be used to interpolate between the altimetry traces in order to obtain a more complete mapping of the Gulf Stream or similar intense flows in regard to surface position and current speed.

For upwellings it appears feasible to determine position, temperature,

and areal extent of an upwelling event to 5 km within 1 to 2 days of its onset and to obtain estimates of the near-surface chlorophyll concentration by using combined temperature and color imaging devices such as CZCS [NASA, 1975].

#### *Tides: Open Ocean and Shelf*

Deep-sea tides, being largely astronomically driven by the moon and sun, occur at precise frequencies, some five of which contain about 95% of the tidal energy. Their amplitudes in the open ocean are typically 0-1 m. Open ocean and shelf tides are difficult and time-consuming to measure, and their relationships to coastal tides are hard to establish. Worldwide deep-sea tidal measurements would aid in the theoretical understanding and prediction of tides at arbitrary locations along the coastlines.

By using precision altimetry in the way described earlier, it appears that one may determine tidal range to  $\pm 25$  cm (relative to mean sea level) and phase to  $\pm 20^\circ$  for diurnal and semidiurnal periods [Hendershott et al., 1974]. The required spacings are 25 km on continental shelves and 100 km globally. Approximately 1 year of data is needed for the solution.

#### *Sea-Earth Interactions*

In the category of interactions between the ocean and the solid earth is found such a wide diversity of features that no general discussion will suffice. Instead, each observable will be taken up individually.

*Storm surge and wind setup along a coast.* Storm systems pile up water ahead of them as they approach a coastline from seaward. In the case of hurricanes this surge is often directly responsible for more damage and loss of life than the wind is. Hurricane surges are confined to a few tens of kilometers and a few hours of time during the landfall; amplitudes can exceed 9 m. Wind setup is the accumulation of water along a coast due to long-term stresses such as trade winds; a typical elevation is about 1 m.

By altimetric means it should be possible to measure storm surge elevations to  $\pm 1$  m in a storm system on a target-of-opportunity basis, along a single subsatellite track [Apel and Siry, 1974]. It should be recognized that the space-time coincidence of storm and satellite is a low probability event, however.

*Tsunamis.* Tsunamis are seismically excited long-length ocean waves capable of great damage. Their peak-to-trough amplitudes in midocean have never been measured but theoretically should be of order  $1/2$  m; wavelengths are a few hundred kilometers, and the disturbance ultimately fills an entire ocean basin. As they approach shore, the amplitude may increase to tens of meters. Assessing the energy content of a tsunami is a difficult task, and thus much overwarning results. In principle, altimetric measurements could yield a tsunami amplitude to  $\pm 25$  cm and a wavelength to  $\pm 20\%$  in the open ocean on a target-of-opportunity basis along a subsatellite track. This is again a low-probability observation [Apel and Siry, 1974].

*Beach and shoal dynamics.* Waves and currents erode and build shorelines and shallow water features. Base line data on shoreline and shoal configurations allow assessment of changes due to wave action. By using an imaging radar it should be possible under storm conditions to image shorelines and shoal waters with resolutions down to 25 m with image centers located to  $\pm 500$  m over swath widths of up to 100 km on a selected basis near the continental United States. High-resolution optical and near-infrared imagery taken at several wavelengths (such as will be available from the Landsat 4 thematic mapper) can yield data on subsurface conditions as well under clear skies.

*Shallow-water charting and bathymetry.* The positioning of newly formed or poorly charted shoals and some assessment of their topography can be obtained by using multispectral optical imagers such as MSS or CZCS. It is possible

to image shoals of depths less than 10-15 m where the water is clear enough, with vertical resolutions of 2-5 m and horizontal resolutions of order 70 m, with image centers located to  $\pm 500$  m, on a selected basis [Polcyn and Lyzenga, 1974].

*Near-surface sediment transport.* Wave action, river discharges, tidal flushing, and advection by current systems result in transport of sediments and sands throughout the ocean. Surface sediment patterns and particulate concentrations are indicators of transport of material, which can be viewed at several optical wavelengths with 800-m resolution over swath widths of up to 700 km (MSS, CZCS). By designing algorithms that use image brightnesses at these wavelength bands it may be possible to determine concentrations from approximately 0.2 to 100 mg/m<sup>3</sup> on a selected basis [Pirie and Steller, 1974].

*Ice cover, dynamics, and icebergs.* Ice cover and ice movements vary greatly with the time of year and surface wind conditions. The percentage of ice cover in polar regions governs much of the

weather there, owing to the large exchange of heat between air and water occurring through open water areas, especially in narrow leads and openings. In coastal areas and lakes, shipping depends upon an accurate assessment of ice conditions throughout the navigable waters. Iceberg tracking and forecasting are vital for protection and navigation of shipping. The observation of ice from satellites is greatly compounded by the persistent cloud cover found in polar and subpolar regions. Thus the synthetic aperture radar will be very useful for imaging ice cover and perhaps very large icebergs, with a resolution of 25 m and with image centers located to  $\pm 500$  m, over swath widths of up to 100 km, on a near-all-weather but very selected basis. With the SMMR it is possible to image ice cover with low resolution, 20 km, over the entire polar caps with swaths of 1000 km on a near-all-weather basis [Gloersen and Salomonson, 1975].

Figure 7 is a brightness map of the Antarctic continent as obtained from the 19-GHz microwave radiometer on Nimbus 5 and gathered in the course of approx-



Fig. 7. Microwave image of the Antarctic continent with brightness scales affixed made from the ESMR on Nimbus 5 during January 1973 (NASA Goddard Space Flight Center).

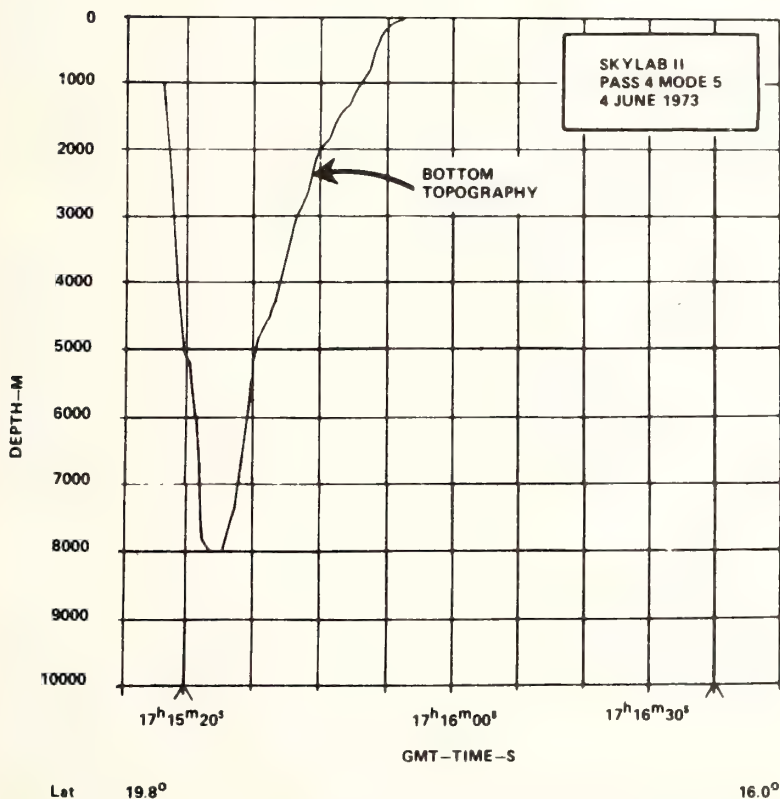
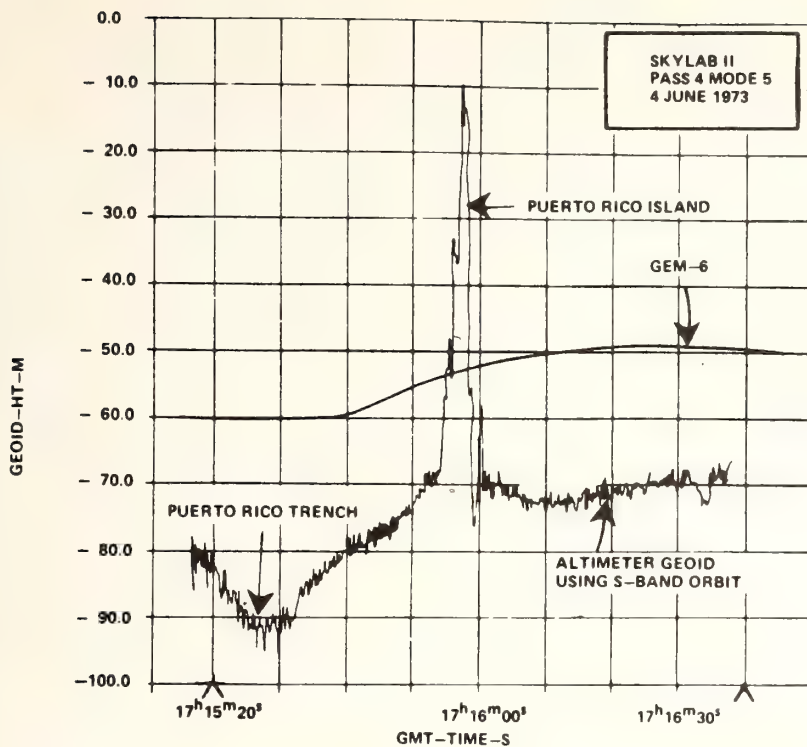


Fig. 8. (Top) Altimeter geoid heights referenced to a spheroid, as measured across western Puerto Rico by the Skylab S-193 altimeter; precision is about  $\pm 1$  m. (Bottom) Bottom topography over a portion of the subsatellite track (NASA Wallops Flight Center).

imately 5 days; the resolution is approximately 15 km [Gloersen and Salomonson, 1975].

*Marine geoid.* In a quite separate category from the previous observables is the marine or ocean geoid, defined as the surface assumed by a motionless uniform ocean under the influence of gravitational and rotational forces only. Geostrophic currents, tides, storm surges, setup, and waves lead to an ocean surface that departs from the geoid; the latter must then be known on a spatial grid with precision at least as fine as that with which the observable is to be determined. Although only preliminary data have been published, it appears altogether possible to measure relative short-scale vertical variations in the marine geoid to  $\pm 20$  cm and long-scale to perhaps  $\pm 100$  cm along the subsatellite track over a grid spacing of order 25 km over all open ocean areas by using the altimeter and precise orbit determination [Apel and Siry, 1974; Kaula, 1970; Apel, 1972; Apel and Byrne, 1974; McGoogan *et al.*, 1975]. Data from Skylab [McGoogan *et al.*, 1975] and Geos 3 (H. R. Stanley, private communication, 1975) support this view. Some of the data from Skylab are illustrated in Figure 8, which shows the variation in relative geoid height and water depth along the subsatellite track across Puerto Rico. By using the altimeter, whose noise figure was approximately  $\pm 1$  m, the gravity anomaly associated with the Puerto Rico trench is clearly seen as a geoidal depression of order 15–20 m [McGoogan *et al.*, 1975]. Such short wavelength data, taken globally, can be combined with long wavelength geoidal models obtained via satellite tracking and orbit analysis to obtain a precision geoid over the ocean. While this has not yet been done, attempts have been made to combine marine gravimetric measurements with satellite geoids to produce a geoidal map such as is shown in Figure 9 for the western Atlantic [Vincent *et al.*, 1972; Marsh *et al.*, 1973]. Here heights are given in meters relative to the reference ellipsoid. The problem of measuring geostrophic

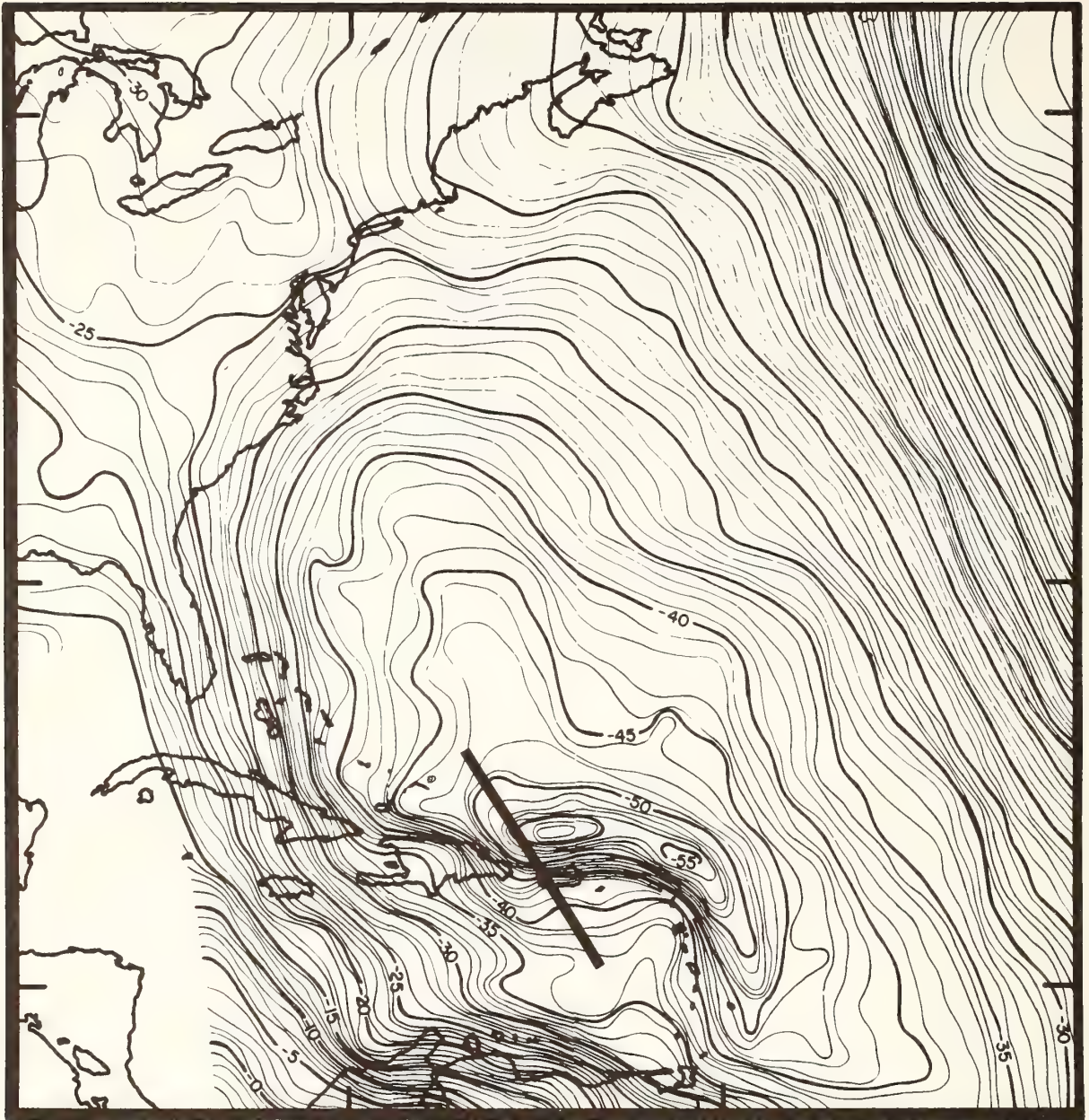


Fig. 9. Geoid calculated in the western Atlantic from satellite orbit perturbations and marine gravity measurements; elevations are in meters relative to the reference ellipsoid. The track of Skylab while taking the data of Figure 8 is shown as a stripe off Puerto Rico (NASA Goddard Space Flight Center).

currents is equivalent to discerning the 100-cm setup due to current shown in Figure 5 against the background of 100-m geoidal undulations illustrated in Figure 9 [Kaula, 1970; Apel, 1972; Apel and Byrne, 1974].

#### *Climatology*

The role of the ocean in climatic change is not completely under-

stood, but it is clear that the transformation of absorbed sunlight into thermal energy in the upper layers of the sea is an important one, as is the poleward transport of this heat by western boundary currents. Variations in the positions of major ocean currents in part appear to be induced by changing wind stress, which apparently lead to the El Niño phenomenon, for example. The appearance of anomalous large

areas of warm water in the Pacific has been hypothesized as the origin of warm winters in the eastern United States through poorly understood processes involving motions of the upper atmosphere [Gates and Mintz, 1975].

The contributions which spacecraft can make to ocean climatology therefore appear to be mainly related to the global determination of sea surface tem-

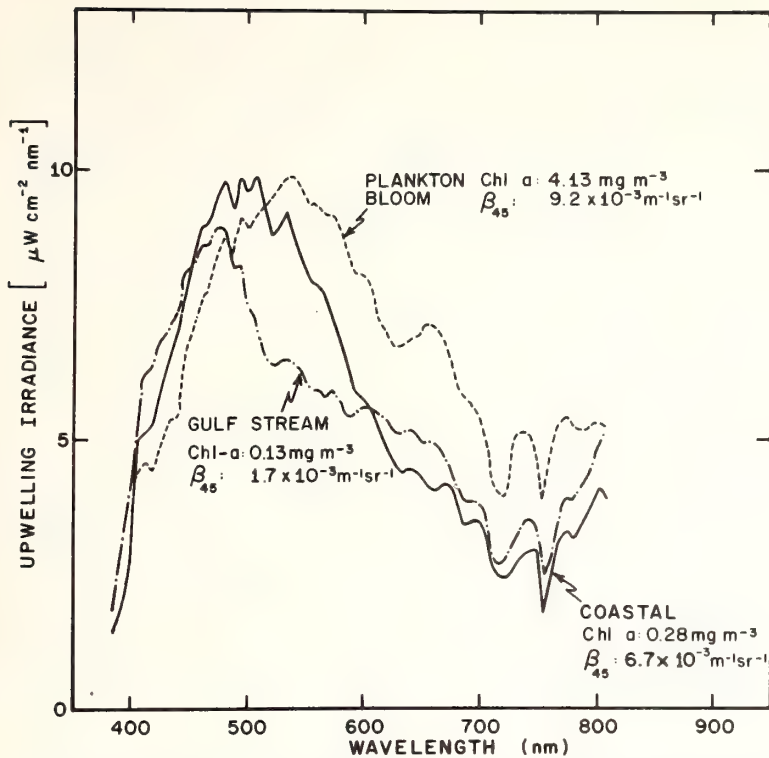


Fig. 10. Upwelling spectral irradiance as measured in three types of water masses in the Gulf of Mexico; the shift toward the red end of the spectrum is due to increased surface chlorophyll *a* (NOAA Environmental Research Laboratories).

perature and heat transport [Gates and Mintz, 1975; Stommel, 1974; NACOA, 1974]. The five GOES-type synchronous satellites appear capable of delivering the temperature data over mid-latitude regions with the required accuracy of  $\pm 0.5^\circ\text{C}$  relative, if special processing is undertaken. Over polar regions the Tiroson series is more suitable. Programs for optimal extraction of the global temperature fields, averaged over approximately  $100 \times 100 \text{ km}^2$  areas and several days, are in the embryonic stages.

#### Water Mass Properties

Variations in the physical or chemical composition of a water mass lead to variations in its color or reflectivity, for example. These changes can be natural or man-made; in either case they tend to be more pronounced near continents. The color is determined primarily by molecular scattering and secondarily by nutrients, chlorophyll *a* in plankton and algae, suspended sediment load, pollutants, and,

TABLE 3. Summary of Sensors and Observables

Observables	Imaging Radiometers			Short Pulse Altimeter	Imaging Radar	Scatterometer
	Visible	Thermal IR	Microwave			
Chlorophyll and algae	1	-	-	-	-	-
Current position	2	1	1	1	1	-
Current speed	-	-	-	1	3	3
Estuarine circulation	1	1	-	-	-	-
Fog	1	1	-	-	-	-
Ice cover	1	2	1	1	1	-
Icebergs	-	-	-	-	1	-
Internal waves	1	-	-	-	1	-
Marine geoid	-	-	-	1	-	-
Oil spills	1	-	-	-	1	-
Pollutant identification	1	-	-	-	-	-
Salinity	-	-	3	-	-	-
Sea state and swell	2	-	2	1	1	2
Sediment transport	1	-	-	-	-	-
Setup	-	-	-	1	-	-
Shallow water bathymetry	1	-	-	-	-	-
Storm surges	3	3	3	1	3	3
Surface winds	-	-	1	2	2	1
Temperature	-	1	1	-	-	-
Tides	-	-	-	1	-	-
Tsunamis	-	-	-	1	-	-
Upwellings	2	1	2	-	-	-
Water vapor	-	1	1	-	-	-
Wave refraction	1	-	-	-	1	-
Wave spectrum	2	-	-	-	1	-

Numbers indicate order or importance in determining the observable with 1 for primary, 2 for secondary, and 3 for tertiary. Hyphens indicate no utility.

where water is sufficiently shallow, water depth and bottom type. Other environmental factors such as atmospheric conditions, sun and viewing angles, surface winds, and waves also influence the measurement of ocean color.

Figure 10 shows surface measurements of upwelling spectra from three types of water masses and illustrates the increase in energy in the green and red regimes of the spectrum as the transition from Gulf Stream to estuarine water is made [Maul and Gordon, 1975].

Figure 11 is a computer-enhanced Landsat image of a  $140 \times 140 \text{ km}^2$  sector of the New York Bight, showing suspended sediments from the Hudson River, acid-dumping events, water mass variations, and internal waves, the last being visible because of the sun glint [Apel *et al.*, 1975].

*Ocean color.* The CZCS on Nimbus-G will image the ocean surface and near-surface in multiple wavelengths of visible light and reflected and thermal infrared radiation with 800-m spatial resolution over swath widths of 700 km under controlled illumination conditions; the observation interval will be 1-6 days. The choice of wavelength bands was dictated by the requirement for making quantitative measurements relating to chlorophyll and sediment concentrations (W. Hovis, private communication, 1976).

Measurement of ocean color from radiometric quality imagery of the desired area in several spectral intervals will perhaps allow measurement, at least under certain limited conditions, of the following features: suspended near-surface sediment distribution and concentration; chlorophyll distribution and concentration between perhaps 0.1 and 20  $\text{mg/m}^3$  (W. Hovis, private communication, 1976); fish stock location via relationship to biosignificant observables [Stevenson *et al.*, 1973]; and pollutant distribution and concentration [Wezernak and

Thomson, 1972]. The CZCS sensor may be used to make most of the measurements [NASA, 1975].

*Surface reflectivity.* By viewing toward rather than away from the sun it is possible to observe surface features in the sun glitter owing to the changes in surface reflectivity. A variable viewing angle is required to measure either color or reflected sunlight; viewing upsun allows determination of oil spills, internal waves via surface slicks, and variations in surface roughness (Figure 11).

Table 3 summarizes the various parameters discussed above and lists the sensors and instruments contributing to their determination. The estimates of their usefulness are given by primary (1), secondary (2), and tertiary (3) designations.

#### Surface Data Collection From Spacecraft

The United States and France have programs in data collection from unmanned automatic buoys,

both anchored and drifting, with methods for data transmission through such satellites as SMS/GOES and Tiros-N. In addition, the United States maintains large archives for surface-derived oceanographic and meteorological data. It is felt that presently planned systems are sufficient to meet the buoy data collection and positioning requirements in the next 5 years.

#### Integrated Global Ocean Station System (IGOSS)

A system called IGOSS is an evolving cooperative services system for international exchange of ocean data proceeding under the auspices of the Intergovernmental Oceanographic Commission of Unesco [Junghans and Zachariason, 1974]. The coordination activities needed to amalgamate the quite disparate oceanic data sources, including some of the data coming from the spacecraft systems discussed here, will be undertaken by IGOSS



Fig. 11. Image of the New York Bight made with Landsat 1 on July 24, 1973. The 'marbling' effect is due to light winds; internal waves are visible in the southeast section (NOAA Environmental Research Laboratories).

if present plans materialize. However, much of the spacecraft data are experimental, and their reliability and accuracy not yet established, and it is not clear how the archiving will be accomplished. The presently recommended method of utilizing satellite-derived data is to become involved with the ongoing programs as a scientific investigator or similar role.

## Summary

It has almost invariably been the case that the introduction of a significant new instrument technology has yielded for the science to which it was applied a number of unsuspected and often highly significant results. Such serendipitous discoveries can surely be expected from instruments as advanced as those being orbited on ocean-looking satellites. Oceanographers have been hard put to gain the overview of their domain required to understand synoptic or planetary scale events in the sea; for a limited but important group of phenomena, satellites promise to provide the vantage point for this vision.

## References

Apel, J. R., Ed., Sea Surface Topography From Space, vol. 1 and 2, *Tech. Rep. ERL 228*, Nat. Oceanic and Atmos. Admin., Boulder, Colo., May 1972.

Apel, J. R., and H. M. Byrne, Oceanography and the marine geoid, in *Applications of Marine Geodesy*, p. 59, Marine Technology Society, Washington, D. C., 1974.

Apel, J. R., and J. W. Siry, A synopsis of Seasat-A scientific contributions, in *Seasat-A Scientific Contributions*, NASA, Washington, D. C., July 1974.

Apel, J. R., H. M. Byrne, J. R. Proni, and R. L. Charnell, Observations of oceanic internal and surface waves from the Earth Resources Technology satellite, *J. Geophys. Res.*, **80**, 865, 1975.

Barath, F. T., and P. Gloersen, The scanning multichannel microwave radiometer, paper presented at U.S. Annual Meeting, Int. Union of Radio Sci., Boulder, Colo., 1975.

Bromer, R. L., W. G. Pichel, T. L. Segnore, C. C. Walton, and H. S. Gohrband, \*Satellite-derived sea-surface temperatures from NOAA spacecraft, *NOAA/NESS Tech. Memo.*, in press, 1976.

Brown, W. E., Jr., C. Elachi, and T. W.

Thompson, Radar imaging of ocean surface patterns, *J. Geophys. Res.*, **81**, 2657, 1976.

Defant, A., *Physical Oceanography*, vol. 1, Pergamon, New York, 1961.

Gates, W. L., and Y. Mintz, *Understanding Climatic Change: A Program for Action*, National Academy of Sciences, Washington, D. C., 1975.

Gloersen, P., and V. V. Salomonson, Satellites: New global observing techniques for ice and snow, *J. Glaciol.*, **15**, 373, 1975.

Grantham, W. L., E. M. Bracalente, W. L. Jones, J. H. Schrader, L. C. Schroeder, and J. L. Mitchell, An operational satellite scatterometer for wind vector measurements over the ocean, *NASA Tech. Memo. X-72672*, 1975.

Hendershott, M. C., W. H. Munk, and B. D. Zetler, Ocean tides from Seasat-A, in *Seasat-A Scientific Contributions*, p. 54, NASA, Washington, D. C., July 1974.

Junghans, R., and R. Zachariason, The integrated global ocean station system (IGOSS), in *Environmental Data Service*, National Oceanic and Atmospheric Administration, Government Printing Office, Washington, D. C., July 1974.

Kaula, W. M. (Ed.), *The Terrestrial Environment: Solid Earth and Ocean Physics*, MIT Press, Cambridge, Mass., April 1970.

Koffler, R., Uses of NOAA environmental satellites to remotely sense ocean phenomena, in *Ocean '75 Conference Record*, Institute of Electrical and Electronics Engineers and Marine Technology Society, Washington, D. C., 1975.

LaViolette, P. E., Remote optical sensing in oceanography utilizing satellite sensors, in *Optical Aspects of Oceanography*, edited by N. G. Jerlov and E. S. Nielsen, Academic, New York, 1974.

Marsh, J. G., F. J. Lerch, and S. F. Vincent, The geoid and free air gravity anomalies corresponding to the Gem-4 earth gravitational model, *NASA/GSFC X-592-73-58*, Feb. 1973.

Maul, G. A., and H. R. Gordon, On the use of the Earth Resources Technology satellite (Landsat-1) in optical oceanography, in *Remote Sensing of the Environment*, p. 95, Elsevier, New York, 1975.

McGoogan, J. T., C. D. Leitao, and W. T. Wells, Summary of Skylab S-193 altimeter altitude results, *NASA Tech. Memo. X-69355*, Feb. 1975.

Molinari, R. L., Buoy tracking of ocean currents, *Advan. Astronaut. Sci.*, **30**, 431, 1974.

NACOA, Third annual report to the President and Congress, Government Printing Office, Washington, D. C., 1974.

NASA, Announcement of opportunity Science support for the Nimbus-G sensors, *NASA A.O. OA-75-1*, Washington, D. C., 1975.

Pirie, D. M., and D. D. Steller, California coastal processes study, Third ERTS-1 Symposium I, *NASA Spec. Publ. 351*, 1413, 1974.

Polcyn, F. C., and D. R. Lyzenga, Updating coastal and navigational charts using ERTS-1 data, Third ERTS-1 Symposium I, *NASA Spec. Publ. 351*, 1333, 1974.

NASA, Announcement of opportunity: Science support for the Nimbus-G sensors, *NASA A.O. OA-75-1*, Washington, D. C., 1975.

Stevenson, W. H., A. J. Kemmerer, B. H. Atwell, and P. M. Maughan, A review of initial investigations to utilize ERTS-1 data in determining the availability and distribution of living marine resources, in Third ERTS-1 Symposium I, *NASA Spec. Publ. 351*, 1317, 1973.

Stommel, H., *The Ocean's Role in Climate Prediction*, National Academy of Sciences, Washington, D. C., 1974.

Vincent, S., W. E. Strange, and J. G. Marsh, A detailed gravimetric geoid of North America, the North Atlantic, Eurasia, and Australia, *NASA/GSFC X-553-72-331*, September 1972.

Walsh, E. J., Analysis of experimental NRL radar altimeter data, *Radio Sci.*, **9**, 711, 1974.

Wezernak, C. T., and F. J. Thomson, Barge dumping of wastes in the New York Bight, ERTS-1 Symposium Proceedings, *NASA Doc. X-650-73-10*, 142, 1972.



John R. Apel is a supervisory oceanographer and Director of Pacific Marine Environmental Laboratory in Seattle, Washington, a component of the NOAA Environmental Research Laboratories. He holds B.S. and M.S. degrees in theoretical physics from the University of Maryland and a Ph.D. in applied physics from Johns Hopkins University. His specialties are in the physics of fluids and in remote sensing. Apel is a consultant to numerous government organizations, and has played a leading role in the development of satellites for oceanography.

## High-Speed Streams and Sector Boundaries

C. SAWYER

*Ocean Remote Sensing Laboratory, Atlantic Oceanographic and Meteorological Laboratories  
Environmental Research Laboratories, NOAA, Miami, Florida 33149*

High-speed streams in the solar wind are located with respect to interplanetary magnetic sectors, and their location in the sector is analyzed. The relation to the sector taken as a whole is clearer than the relation to sector boundaries. The streams occur preferentially near the center of the sector. Although high-speed streams, as do sector boundaries, show a clear pattern of recurrence with solar rotation and although they are about equally frequent in the period studied (1965-1971), there is no one-to-one relation between them; sectors with no stream or with more than one stream are common. Longer sectors contain more streams, showing that streams occur at a certain rate per unit time rather than at a constant number per sector.

### INTRODUCTION

This paper describes an investigation of the relation of high-speed streams in the solar wind to interplanetary magnetic sectors. Earlier studies showed that the average solar wind velocity rises after passage of a sector boundary [Wilcox and Ness, 1965; Ness *et al.*, 1971]. Here we find high-speed streams to occur most frequently near the middle of a sector. This is true for sectors of either polarity, although the frequency of streams organized about sector boundaries may depend on the sense of the boundary.

### DATA ON HIGH-SPEED STREAMS AND ON MAGNETIC SECTORS

*Intriligator* [1973, 1974] presents and discusses a compilation of data on high-speed streams in the solar wind based on measurements of velocity made at earth-orbiting Vela and sun-orbiting Pioneer spacecraft. The times of peak speed at the spacecraft are given, along with the corotation delay time appropriate to the beginning of the stream. These delay times were used to estimate the times of both beginning and maximum at earth passage of the stream. In the appendix the error in applying to the maximum the delay time appropriate to the beginning is shown to be relatively small. Times of maximum were used to identify observations of the same stream at different spacecraft. Grouping of these observations reduced the 349 entries in *Intriligator's* list to descriptions of 235 separate streams, for 215 of which interplanetary magnetic data are available.

A list of 'observed and well-defined' sector boundaries given by *Wilcox* [1973] includes 51 sector boundaries in the period July 1965 to November 1970. These are supplemented by data from charts presented by *Wilcox and Colburn* [1969, 1970, 1972]. Except for one period of missing data, April to August 1967, a plausible map of the sector structure from July 1965 through 1970 can be completed. This defines 195 sectors, of which 44 are 'well-defined' in the sense that both boundaries appear on the *Wilcox* list, while the remainder fit into an evolving recurrent pattern that includes all of the well-defined boundaries. Sectors shorter than 4 days are included only when they belong to a recurrent sequence.

### RECURRENCE OF SECTORS AND HIGH-SPEED STREAMS

Both sector boundaries and maxima of high-speed streams are plotted in *Bartel's* 27-day recurrence scheme in Figure 1.

Copyright © 1976 by the American Geophysical Union.

This plot is strongly compressed in the vertical direction, and departures of recurrence period from 27 days are thus exaggerated. Shading connects velocity maxima considered to be members of a sequence of rotational recurrences. Open circles have been added to emphasize gaps in these sequences, i.e., when an expected stream does not appear on the list. *Intriligator* points out that gaps exist in the data when there was no ground tracking of the spacecraft. These data gaps are not seriously detrimental to our purpose. Even if all the gaps in sequences represent data gaps, no more than 10% of the streams were missed. In any case, missing streams are expected to have no systematic effect on the main conclusions of this study.

The identification of sequences is of course not certain, and the reader will have to judge to what extent a different identification of sequences is possible and how it might affect the derived recurrence period, noting that this value is unaffected by wiggles but is determined by the mean slope.

While one can pick out streams with recurrence patterns that match a nearby sector boundary, there are also many stream sequences that cross from one sector to another, seeming to develop quite independently of the sector pattern. Figure 2 shows the distribution of values of recurrence period for the sector boundaries and high-speed streams shown in Figure 1. Sector boundary recurrence periods are distributed more broadly than those of stream maxima, no doubt because boundaries run behind or ahead of the sector center when the sector is waxing or waning. The mean recurrence period of high-speed streams is shorter than that of sector boundaries in the same epoch by 0.45 day, which is more than 4 times the variance of the mean.

*Gosling* [1971] compared daily velocity measurements from close and from distant spacecraft and found that solar wind speeds at one location are almost uncorrelated with speeds measured at another location when the separation corresponds to a rotation delay time of more than 4 days. He concluded that solar wind speed cannot be successfully predicted over a span of more than 4 days. In contrast, the recurrence of high-speed streams in Figure 1 is remarkably stable and would permit accurate advance prediction of the occurrence and time of passage of a high-speed stream, though perhaps not of the peak velocity. The difference between the two conclusions lies in the fact that here we consider the high velocities, forming the top tenth of all the days. *Gosling's* results, which show a high mean predicted speed for the highest category of observed speeds, are not in conflict with the present conclusion.



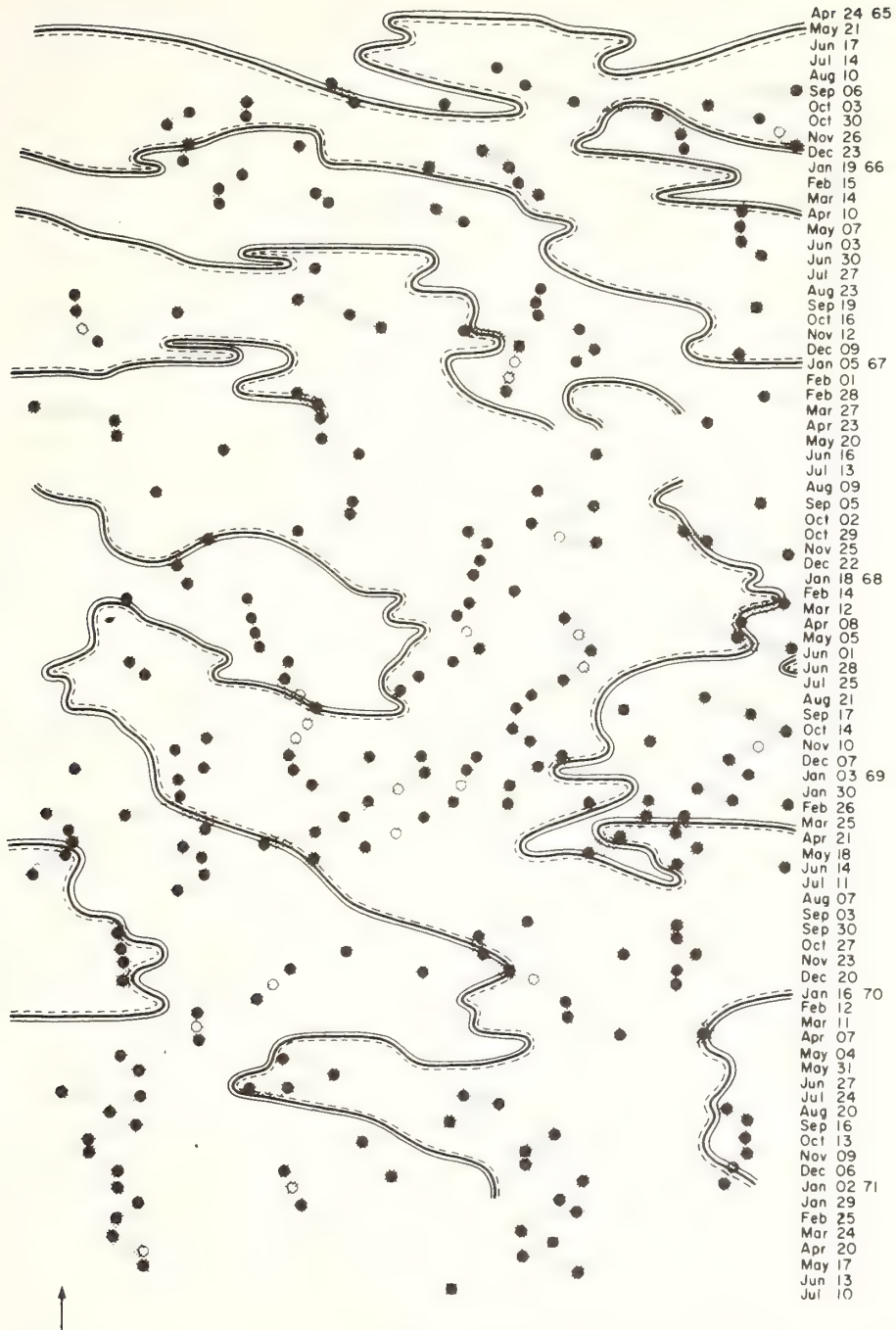


Fig. 1. Twenty-seven-day recurrence diagram of interplanetary magnetic sectors and high-speed streams in the solar wind. Bartel's day zero is listed at the right and is located at the arrow, shown on the left. Dashed lines are in the toward sector; continuous lines are in the away sector. Time of earth passage of the peak of a high-speed stream is indicated by solid circles, and absence of a listed stream in a sequence is indicated by open circles. Note that the strong vertical compression of the chart exaggerates drifts due to periods longer or shorter than 27 days.

LOCATION OF STREAM IN SECTOR

In order to make a more quantitative investigation of the location of streams in magnetic sectors, I classified each stream according to the day in its sector that peak speed occurred,

noting also the field direction in the sector and the duration of the sector in days. Then I counted the number of streams in each category; e.g., there are two streams with maxima on day zero (same day as boundary) of 6-day sectors of away (away from sun) polarity.

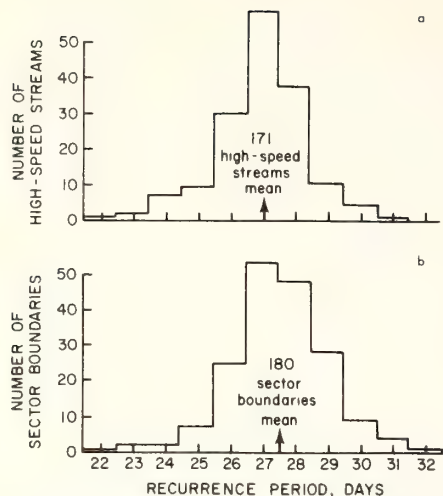


Fig. 2. Frequency distribution of recurrence period values for (a) high-speed streams and (b) sector boundaries, in sequences indicated in Figure 1.

**Number of streams in sectors of different duration.** First, let us examine the density of high-speed streams as a function of sector length. The data for away and toward sectors both show the same trend and are combined in Figure 3, where the quantity (number of high-speed streams in sectors of length  $l$ )/(number of sectors of length  $l$ ) is plotted against  $l$ . If high-speed streams were closely associated with sector boundaries, we should expect to see one stream in each sector, since the total number of streams and sectors is approximately equal. In fact, the number of streams per sector increases with sector length, in agreement with the hypothesis that streams occur at a constant rate of 3.1 per rotation regardless of sector length.

**Occurrence frequency of streams at each sector day.** From the results of Wilcox and Ness [1965] and Ness et al. [1971] we expect the maximum of a high-speed stream to tend to fall 2-4 days after passage of a sector boundary. Figure 4 shows the number of maxima occurring in each day of a sector, summed over all away sectors and separately over all toward sectors. Because a day 0 occurs in every sector but later sector days are less frequent (day 20 occurs only in sectors of a duration of at least 21 days), the number of maxima decreases away from the beginning of the sector. In order to interpret the distribution of stream maxima among sector days we need to know the expected frequency, given the distribution of sector lengths. The smooth continuous curves in Figures 4a and 4b show the

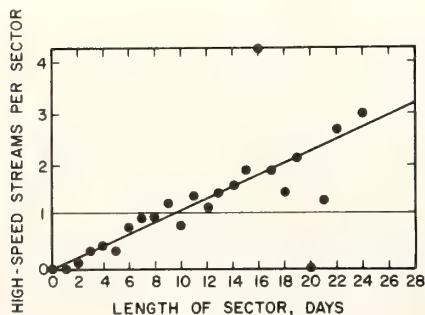


Fig. 3. Number of high-speed streams per sector as a function of sector length. Streams occur at the rate of about three per rotation regardless of sector length.

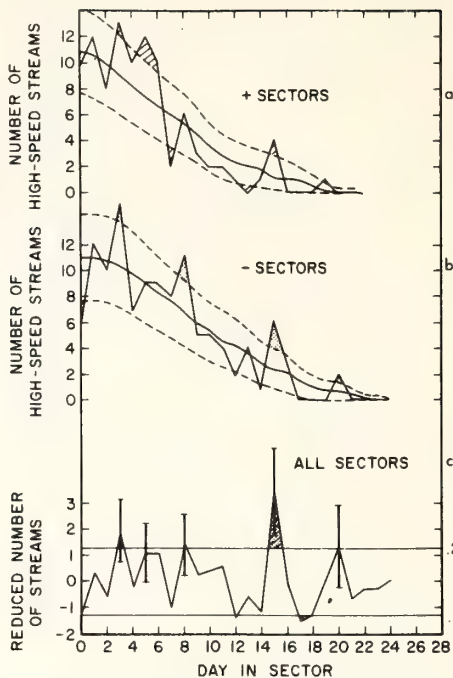


Fig. 4. (a) The number of high-speed streams occurring on each day of a sector for away (plus) sectors. (b) The number of high-speed streams occurring on each day of a sector for toward (minus) sectors. The continuous curve shows the expected number (see text) with dashed curves at one standard deviation (square root of counted number). (c) All data are combined, and the quantity plotted is the reduced number, the difference between the observed and expected numbers, divided by the variance. Error bars show the square root of the observed number for the peak values. Eighty percent of the points are expected to lie between the dashed horizontal lines.

expected number as a function of sector length  $l$ : (total number of high-speed streams/total number of sector days)  $\times$  number of sectors with duration greater than  $l$ . The general tendency for the frequency of high-velocity streams to fall as distance

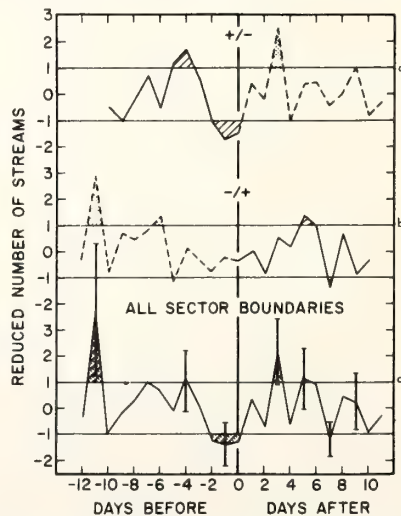


Fig. 5. The reduced number of high-velocity streams is plotted (a) for away/toward (plus/minus) sector boundaries, (b) for toward/away (minus/plus) boundaries, and (c) for all boundaries. One third of the points are expected to lie beyond the horizontal dashed lines.

from sector beginning increases follows the expected trend. The dashed curves differ from the expected number by plus or minus the square root of the expected number, which we take as an estimate of the variance. In a normal error distribution we expect a proportion of 0.32, or about one third of the values, to differ by this amount or more from the mean or expected value. Of the 21 points of Figure 4a or the 22 points of Figure 4b we expect 7 to fall beyond the dashed curves and observe 7 and 5. In Figure 4c, data from away and toward sectors have been combined. The plotted quantity is the reduced number:

$$\frac{\text{observed number of high-speed streams} - \text{expected number}}{(\text{expected number})^{1/2}}$$

Again, deviant points are scattered across the sector, the total number deviating beyond the expected variance about as expected. From this analysis the high-speed streams seem to be randomly located with respect to the leading boundary of the sector, though we shall find a relation to the sector itself.

**Location of stream with respect to sector boundary.** Next, let us designate the last day of a sector as day -1, the day before as day -2, etc., so that we can examine the stream frequency on either side of a sector boundary. In Figures 5a and 5b is plotted the reduced number, i.e., (observed number - expected number)/expected variance, for away/toward and for toward/away sector boundaries, and in Figure 5c it is plotted for all sector boundaries. The difference between this organization and that of the preceding section and Figure 4 can be shown by an example. A stream that falls on day 8 of a 10-day sector appears at day 8 in Figure 4 and at day -2 in Figure 5. Again, difference from a random distribution is difficult to demonstrate. Of interest, however, is the minimum at day -1, which corresponds to a minimum in geomagnetic index  $K_p$  found by Shapiro [1974] to precede away/toward sector boundaries and to be the outstanding feature of his analysis.

**Stream location as fraction of sector.** Finally, each stream maximum was characterized as being in the first tenth, second tenth, . . . ,  $n$ th tenth of its sector. Figure 6 shows the plots for

away sectors, for toward sectors, and for all sectors. Although deviations from expected values are not large, these plots show a consistent trend through the sector, with below-average occurrence frequency near the beginning and end of the sector and above-average occurrence frequency in the center of the sector for both away and toward sectors. In the combined data we find 6 of 10 points falling beyond the expected variance where 3 are expected. Although high-speed streams may fall anywhere in a sector, they fall more frequently near the center of the sector and least frequently near the sector boundary. Thus we see that a clearer relation to high-speed streams emerges when we consider the sector as a whole rather than sector boundaries. The majority of sectors do not fit the simple picture of a stream in midsector, however. Of 195 sectors, only 91 (47%) contain a single stream, 56 (29%) have no stream, and 48 (24%) have more than one stream.

**Conclusion.** Although earlier studies showed the average solar wind speed to be organized around sector boundaries, specific high-speed streams are nearly randomly distributed with respect to sector boundaries, with a more obvious pattern of occurrence with respect to the whole sector. The total number of streams is similar to the total number of sectors, but fewer than half the sectors have just one stream. Longer sectors have more streams, so that the occurrence rate of streams is nearly constant instead of the number of streams per sector. Individual high-speed streams show a stable and predictable pattern of recurrence, in contrast to Gosling's conclusion about the unpredictability of solar wind speeds in general.

#### APPENDIX: EFFECT OF APPLYING DELAY TIME APPROPRIATE TO BEGINNING VELOCITY TO LOCATE MAXIMUM OF STREAM

The delay from observation of the beginning of the stream at the spacecraft to observation at the earth, given by *Intriligator* [1973], is

$$\tau = \frac{\phi}{\Omega} - \frac{\Delta r}{U}$$

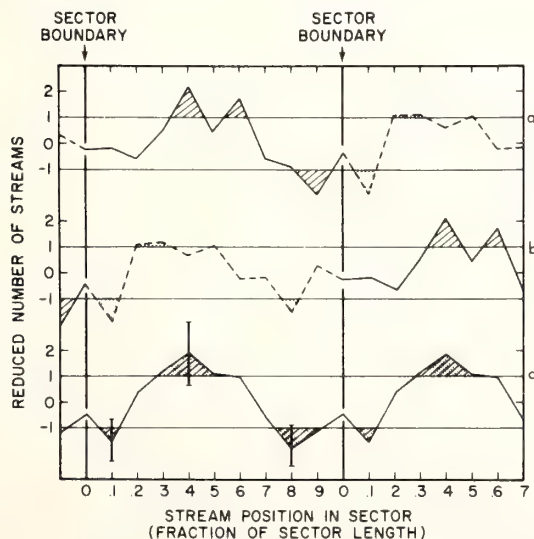


Fig. 6. The reduced number of high-velocity streams is plotted for each tenth of a sector, (a) Plot for away sectors, (b) Plot for toward sectors, (c) Plot for all sectors. One third of the points are expected to fall beyond the horizontal lines.

where  $\phi$  is the longitudinal displacement of the spacecraft from the earth and  $\Delta r$  is the radial displacement. The angular velocity of rotation of the stream is taken as  $2.6934 \cdot 10^{-6}$  rad  $s^{-1}$ , corresponding to a synodic rotation period of 27 days.  $U$  is the velocity at the beginning of the stream. The mean peak velocity for all measurements is  $577$  km  $s^{-1}$ . The mean number of  $50$  km  $s^{-1}$  steps of velocity increase is  $3.77$ , giving a mean velocity increase of  $189$  km  $s^{-1}$  and mean beginning velocity of  $388$  km  $s^{-1}$ . Taking a typical value of  $0.1$  Au for  $\Delta r$ , we find the error from using beginning rather than peak velocity to be between 3 and 4 hours. In Figure 2, showing the distribution of recurrence period values, the full width at half maximum is 3.0 days, so 1.5 days is an estimate of the uncertainty in the value of the period. This leads to an uncertainty in  $\tau$  of 9 hours when  $\phi = 90^\circ$ . The median difference in time of earth passage of streams observed at different spacecraft but deemed to be the same stream is 0.9 day. The difference from the mean is half this value, or about 11 hours. We conclude that the error due to using beginning velocity rather than peak velocity is small relative to the errors due to uncertainty in the time of maximum and in the appropriate rotation period.

**Acknowledgments.** The Editor thanks D. S. Colburn and R. Shapiro for their assistance in evaluating this report.

## REFERENCES

- Gosling, J. T., Variations in the solar wind speed along the earth's orbit, *Solar Phys.*, **17**, 499, 1971.
- Intriligator, D., High speed streams in the solar wind, *Rep. UAG-27*, World Data Center A for Solar Terr. Phys., Boulder, Colo., 1973.
- Intriligator, D., Evidence of solar-cycle variations in the solar wind, *Astrophys. J. Lett.*, **188**, L23-L26, 1974.
- Ness, N., A. Hundhausen, and S. Bame, Observations of the interplanetary medium Vela 3 and Imp 3, 1965-1967, *J. Geophys. Res.*, **76**, 6643, 1971.
- Shapiro, R., Geomagnetic activity in the vicinity of sector boundaries, *J. Geophys. Res.*, **79**, 289, 1974.
- Wilcox, J., Solar activity and weather, *Rep. 544*, Inst. for Plasma Res., Stanford Univ., Stanford, Calif., 1973.
- Wilcox, J., and D. Colburn, Interplanetary sector structure in the rising portion of the sunspot cycle, *J. Geophys. Res.*, **74**, 2388, 1969.
- Wilcox, J., and D. Colburn, Interplanetary sector structure near the maximum of the solar cycle, *J. Geophys. Res.*, **75**, 6366, 1970.
- Wilcox, J., and D. Colburn, Interplanetary sector structure at solar maximum, *J. Geophys. Res.*, **77**, 751, 1972.
- Wilcox, J., and N. Ness, Quasi-stationary corotating structure in the interplanetary medium, *J. Geophys. Res.*, **70**, 5793, 1965.

(Received October 6, 1975;  
accepted January 13, 1976.)

## Geomagnetic Activity at the Passage of High-Speed Streams in the Solar Wind

C. SAWYER

*Ocean Remote Sensing Laboratory, Atlantic Oceanographic and Meteorological Laboratories  
 Environmental Research Laboratories, NOAA, Miami, Florida 33149*

M. HAURWITZ

*Fort Collins, Colorado 80521*

The times of maximum velocity of high-speed streams in the solar wind are used to organize the analysis of planetary geomagnetic activity index  $A_p$ , and this organization of the data is shown to give a clearer pattern than the organization of the data around sector boundaries. Geomagnetic activity is highest on the day preceding peak velocity in the high-speed stream. The sector boundary analysis confirms the minimum in geomagnetic activity preceding sector boundary crossing found by Shapiro (1974) but shows little dependence on the sense of the boundary.

Hirshberg and Colburn [1973] discussed the mechanism of geomagnetic disturbance that involves merging of southward-directed interplanetary field with earth's field. They showed that the presence of southward-directed field tends to be short-lived, lasting only about 6 hours before the vertical component of the interplanetary field returns to normal. On the other hand, geomagnetic indices  $K_p$  (planetary index) and  $AE$  (auroral zone substorm index) remain elevated for a day or longer. They suggested that the disturbance-prolonging factor may be a high-speed stream in the solar wind and showed for the period 1965-1967 that the disturbance index  $AE$  increased as clearly following passage of a high-speed stream as it did following passage of an interplanetary magnetic sector boundary.

Patterson [1973] found geomagnetic activity to be markedly higher in away sectors, where the magnetic field is directed predominantly outward from the sun, than in toward sectors, when the sectors are defined by geomagnetic diurnal variation at high latitude, although the difference disappears in space-observed sectors. Shapiro [1974] analyzed  $K_p$  about sector boundaries (space-observed) and concluded that the salient feature is a  $K_p$  minimum preceding passage of a toward/away boundary. He emphasized the difference between away/toward and toward away boundaries, suggesting that it tends to confirm the Hirshberg-Colburn model of disturbance initiated by field line merging and prolonged by a high-speed stream.

A list of such high-speed streams measured from earth-orbiting Vela and sun-orbiting Pioneer satellites has been published and discussed by Intriligator [1973, 1974]. The data presented there allow determination of the time of earth passage of each observed stream and matching of observations at various satellites to obtain a single description of each of 235 high-speed streams in the period July 1965 through June 1971. The distribution of the observed streams in a recurrent pattern indicates that no more than 10% of the streams were missed through lack of ground tracking of the satellites. The times of earth passage of peak speed in these streams are used as zero days in a superposed epoch analysis of the geomagnetic index  $A_p$ , and this analysis is compared to similar analyses in which  $A_p$  is organized around magnetic sector boundaries. These

include the 'well-defined' sector boundaries determined by Wilcox [1973] as well as less certain boundaries found from charts published by Wilcox and Colburn [1969, 1970, 1972]. The 'well-defined' boundaries are preceded and followed by at least 4 days of consistent polarity. Additional sector boundaries that do not meet this criterion are included only if they are members of a 27-day recurrent series. In Figure 1 the average  $A_p$  at away/toward sector boundaries is compared to that at toward/away boundaries. The bold lines show mean  $A_p$  values for all boundaries, and the light lines show those for well-defined boundaries. In order to estimate the significance of departures from the mean value we need an estimate of the variance of the distribution of values of  $A_p$ . For each of 20 months in 1972 and 1973 the variance  $\sigma$  was computed according to the definition

$$\sigma^2 = \frac{\sum_1^n A_p^2 - n\bar{A}_p^2}{n - 1}$$

where  $n$  is the number of days in the month and  $\bar{A}_p$  is the mean for the month. A plot of  $\sigma$  versus  $\bar{A}_p$  showed that  $\sigma$  increases as  $\bar{A}_p$  increases and allowed determination of values of  $\sigma(\bar{A}_p)$  given below:

$\bar{A}_p$	$\sigma$
5	3.8
10	7.5
15	12.6
20	18.6
25	24.5

It also allowed determination of the 1% and 5% confidence levels indicated at the right side of the figure. Shaded portions of the curves fall beyond the 1% confidence level. These values, computed on the assumption that the daily  $A_p$  values are mutually independent, are not to be interpreted literally but serve as a basis for comparing one curve to another.

None of the features in the sector boundary analysis are very convincing in themselves, but the two most significant features correspond to those found by Shapiro in his analysis of  $K_p$ : a minimum in geomagnetic activity preceding entry into a toward sector and a maximum at the beginning of an away

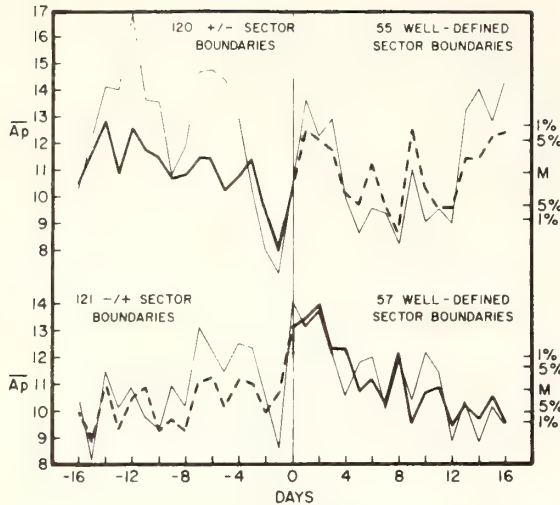


Fig. 1. Superposed epoch analysis of geomagnetic planetary index  $A_p$  around magnetic sector boundaries with (top) away toward (plus-minus) polarity and (bottom) toward/away (minus-plus) polarity. The light curve is for a smaller sample of well-defined boundaries. Shaded portions deviate from the mean value by more than the deviation corresponding to the 1% confidence level; we expect no more than one point in 100 to deviate this much by chance (see text).

sector. These two features are echoed in the analysis of the small and relatively noisy sample of well-defined sector boundaries. Because the similarity of the sector boundary analyses seems more impressive than any difference, the two sector boundary analyses are combined to give the comparison curve in the bottom part of Figure 2. The curve in the top part of Figure 2 shows mean  $A_p$  when organized about high-speed streams, an organization that is obviously cleaner than that around sector boundaries. The two analyses cover the same period of time, with a similar number of zero days. The median value of beginning-to-maximum time for the high-speed streams is 36 hours and that of the duration of the streams is 4 to 5 days. The  $A_p$  peak accompanies the beginning of the high-speed stream, and  $A_p$  is decreasing by the time maximum velocity is reached, the suggestion being that the beginning of the high-speed stream would have been a wiser choice for zero day of the analysis than the time of peak velocity. In any case, the result is consistent with Hirshberg and Colburn's suggestion that high-speed streams are important in the production of geomagnetic variation. If we identify the  $A_p$  maximum with that in the sector boundary analysis, supposing that geomagnetic disturbance, high-speed solar wind stream, and sector boundary each form a part of a single pattern, the high-speed stream must fall 2 or 3 days after the boundary crossing.

To summarize, geomagnetic activity maximizes early in the passage of a high-speed stream, on the day before peak speed at the earth. The average geomagnetic response to earth cross-

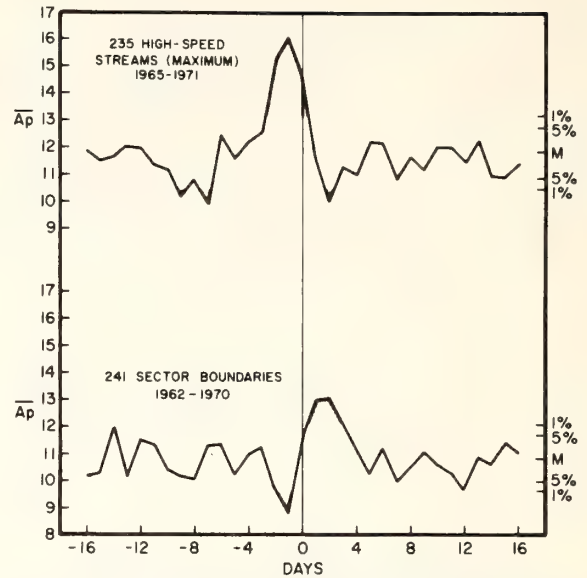


Fig. 2. The pattern of  $A_p$  superposed about high-velocity streams is stronger than the pattern about a similar number of sector boundaries in the same period of time. The sector boundary precedes the  $A_p$  maximum, and the high-speed stream maximum follows it.

ing of a sector boundary is weaker but is similar to that found previously by Shapiro.

*Acknowledgments.* We are grateful to Catherine Candalera for carrying out part of the analysis by computer.

The Editor thanks D. S. Colburn and R. Shapiro for their assistance in evaluating this report.

#### REFERENCES

- Hirshberg, J., and D. Colburn, Geomagnetic activity at sector boundaries, *J. Geophys. Res.*, **78**, 3952, 1973.
- Intriligator, D., High-speed streams in the solar wind, *Rep. UAG-27*, World Data Center A for Solar Terr. Phys., Boulder, Colo., 1973.
- Intriligator, D., Evidence of solar-cycle variations in the solar wind, *Astrophys. J. Lett.*, **188**, L23-L26, 1974.
- Patterson, V., Forty years of implied interplanetary magnetic field data related to the geomagnetic index  $A_p$  (abstract), *Eos Trans. AGU*, **54**, 447, 1973.
- Shapiro, R., Geomagnetic activity in the vicinity of sector boundaries, *J. Geophys. Res.*, **79**, 289, 1974.
- Wilcox, J., Solar activity and the weather, *Rep. 544*, Inst. for Plasma Res., Stanford Univ., Stanford, Calif., 1973.
- Wilcox, J., and D. Colburn, Interplanetary sector structure in the rising portion of the sunspot cycle, *J. Geophys. Res.*, **74**, 2388, 1969.
- Wilcox, J., and D. Colburn, Interplanetary sector structure near the maximum of the sunspot cycle, *J. Geophys. Res.*, **75**, 6366, 1970.
- Wilcox, J., and D. Colburn, Interplanetary sector structure at solar maximum, *J. Geophys. Res.*, **77**, 751, 1972.

(Received October 6, 1975;  
accepted January 13, 1976.)

Reprinted from: Proc. of CICAR-II Symposium: Progress in Marine Research in the Caribbean and Adjacent Resions, Caracas, Venezuela, July 12-16, 1976, p. 126.

-126-

INTRODUCTION

This volume contains more than one hundred abstracts submitted to the CICAR-II Symposium Steering Committee for consideration for oral presentation at the CICAR-II Symposium held in Caracas, Venezuela, 12-16 July, 1976. In addition to the abstracts of the invited papers and of those contributed papers that were accepted, we have also included the abstracts of those contributed papers which could not be accommodated in the limited time available for actual oral presentations. It was the consensus of the Steering Committee that all submitted abstracts be included and that all be presented in both Spanish and English. Although providing translations in the second language created some problems for both authors and editors, it was felt that the need to make the information available to as many Caribbean scientists and students as possible justified the extra effort.

The abstracts are arranged in eight separate groups corresponding to the eight Sessions of the Symposium (Marine Biology, Marine Geology and Geophysics, etc.), and within each group they are arranged alphabetically by the last name of the first author of each paper.

The volume was printed at the University of Miami's Rosenstiel School of Marine and Atmospheric Science with financial support provided by the Intergovernmental Oceanographic Commission. Carol Wolverton, Rosemary Gutierrez, and Becky Newell of NOAA's Atlantic Oceanographic and Meteorological Laboratories in Miami, Florida, put in long hours typing correspondence, preparing the abstracts in final form for the printer, and in proof reading. Their contribution is gratefully acknowledged.

Harris B. Stewart, Jr., Chairman  
CICAR-II Symposium Steering  
Committee, Editor

Reprinted from: Proc. of CICAR-II Symposium: Progress in Marine Research in the Caribbean and Adjacent Regions, Caracas, Venezuela, July 12-16, 1976, p. 241.

-241-

## INTRODUCTION TO THE CICAR-II SYMPOSIUM

Harris B. Stewart, Jr.  
National Oceanic and Atmospheric Administration  
Atlantic Oceanographic and Meteorological Laboratories  
Miami, Florida, U.S.A.

The first CICAR Symposium was held in Curacao in 1968. That meeting provided a summary of the status of our knowledge of the Caribbean and adjacent regions at that time, but more importantly it pointed out the areas where additional knowledge was required. Now, some eight years later, we are starting five days of presentations of the results of our efforts to provide some of that knowledge. But during these five days we will also be considering what still needs to be done, and how we can best accomplish this through the continuation of the fine regional scientific cooperation we have developed during the CICAR Program.

The eight separate Sessions of the Symposium will be described briefly with special attention paid to the Friday afternoon Summary Session at which each of the Conveners will summarize the results presented in his Session and what the scientists involved feel are the directions future marine scientific work in the area should take.

In addition to adding to our scientific knowledge of the area, CICAR has established the basic mechanism for continued cooperation in marine science among the many nations within the region. The effectiveness of this mechanism has been recognized by the Intergovernmental Oceanographic Commission which is in the process of establishing the first IOC Regional Association, and the Caribbean is the region selected for this experiment. The degree to which such an Association is effective will depend heavily on you, the involved scientists, and you are encouraged to put forth your ideas during the rest of this week.



Reprinted from: U.S. Department of Commerce, NOAA/ERL/AOML-National  
Oceanographic Data Center Publication, Washington, D.C. 50 p.

## INTRODUCTION

The U.S. National Oceanographic Data Center as the CICAR Regional Data Center published a series of CICAR bibliographies in 1972. These were of great utility to the scientists of many countries then involved in the Cooperative Investigation of the Caribbean and Adjacent Regions (CICAR) being sponsored by the Intergovernmental Oceanographic Commission. However, these volumes could not include references to papers published subsequently which presented the results of work on the CICAR Program itself, the field phase of which terminated in December of 1975.

This present preliminary bibliography is an attempt to provide in one place a listing of the references to published papers documenting the results of marine research by scientists, mainly from the United States, working in the Caribbean and adjacent regions during the 1969-1975 CICAR period. Only those references provided by the cooperating USA institutions or taken directly from the literature by the staff of NOAA's Atlantic Oceanographic and Meteorological Laboratories are included. Furthermore, only those references are included which could be verified by the Environmental Science Information Center of NOAA's Environmental Data Service. Therefore, the listing is not complete, but it should prove useful to Caribbean marine researchers, and it does document a portion of the extensive contributions of the United States in the CICAR Program.

The final text of this bibliography has been prepared for distribution at the CICAR-II Symposium, July 12-16, 1976, in Caracas, Venezuela by the U.S. National Oceanographic Data Center using a computerized text editing/formatting system. It is hoped that it will stimulate the other cooperating CICAR nations to prepare similar bibliographies and that United States marine scientists will provide references to their published papers that have not been included in this preliminary listing.

Harris B. Stewart, Jr.  
U.S. National Coordinator for CICAR  
NOAA Atlantic Oceanographic and  
Meteorological Laboratories  
Virginia Key, Miami, Florida 33149  
U.S.A.

*Where the Sea and Man Meet***THE COASTAL ZONE****Fishing, Recreation, Commerce, Energy,  
Esthetics Must Be Considered in Plans  
To Use Southeast Florida's Coastal Zone**

By HARRIS B. STEWART JR., Ph.D.

The coastal zone has been described as the zone where the sea and the land meet, but I submit that the problems come not because it is where the sea and the land meet, but because it is where the sea and man meet. It is the injection of man himself into the coastal system that creates very real problems.

Let's look briefly at some of the economic aspects of the wet side of the Florida coastal zone.

Look, for example, at the value of the fish landings in the South Florida area. The actual value has gone up even though the total volume of landings has in fact gone down. This is related, as one might suspect, to the increased price for fisheries products.

Remember that a portion of the life cycle of nearly all of both the commercial and sport fish which contribute so largely to the South Florida economy is spent in the shallow mangrove fringes. These shallow coastal mangrove areas are areas of extremely high productivity and areas where man also has made very heavy incursions. Once an area is dredged and bulkheaded, there

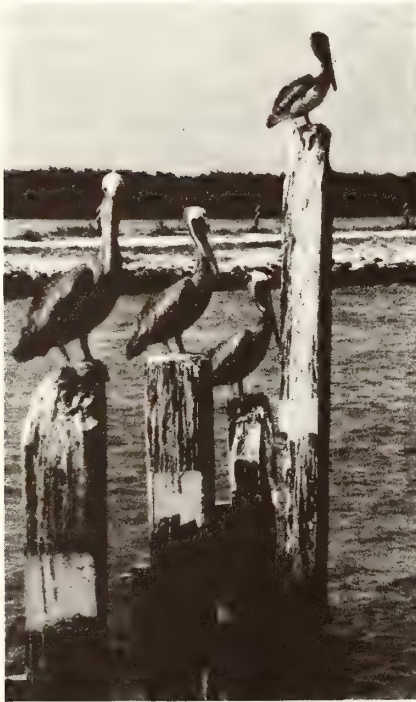


Photo by Dr. Donald P. deSylva

Dr. Stewart is director of the Atlantic Oceanographic and Meteorological Laboratories, NOAA, on Virginia Key. The accompanying article is a condensation of an address he made last fall to the Workshop on Coastal Zone Economics.

April 1976

is no chance for the fish to spend that critical part of their life cycle in the area anymore.

#### **Boating More Popular**

The recreational aspects of the wet side of the coastal zone certainly should not be neglected. Recreational boating is on the rise. Between 1970 and 1973, boating registrations<sup>o</sup> in the South Florida area rose 15.3 per cent. A recent poll taken of tourists coming into the south Florida area indicated that a significantly large percentage of tourists were attracted to the area by the water sports available here. In 1974, the tourist industry in southeast Florida amounted to some two billion dollars. Therefore, one must

keep in mind the fact that the maintenance of good recreational facilities within the southeast Florida coastal zone is an important aspect of the economic development of this zone.

Commerce is a large portion of the industrial economic activity of southeast Florida. Check the numbers of passengers, the volume of freight and the total monies coming into the area as a result of our major port areas – the Port of Miami at Dodge Island, Port Everglades at Ft. Lauderdale and Port St. Lucie.

In addition to fishing, recreation and commerce, I submit that the esthetic value of the coastal zone is one that should

not be overlooked. It may be difficult to put cost figures on it, but certainly an attractive coastal area cannot be underrated for its economic value to the south Florida coastal zone. Industries and people come to south Florida to work and to live because it is a pleasant place to work and live. In addition to our pleasant climate, the major attractive force for these people is our ocean.

#### Energy Problems

But we do other things with our ocean that have economic import. Let's take a look briefly at energy. The minute you say "energy" and "coastal zone" in the same breath in south Florida, people immediately say "Turkey Point," the major power plant of Florida Power & Light. It has had lots of problems, but these problems have been brought about primarily because we are now living in an era of eco-hysteria. Because so much furor was raised over the apparent destruction of approximately 60 acres of turtle grass on the bottom of Biscayne Bay, the company was forced to go to some other technique for cooling the waters used to cool the power plant. As a result, they constructed a "radiator" of 200-foot wide cooling canals through the mangroves south and west of the plant. I would rather not get embroiled in a controversy on the relative merits of 60

**"The major problem in the coastal zone arises because it is a resource held in common and a resource for which many of the uses are in mutual conflict."**

acres of bay bottom versus something over 600 acres of mangroves.

So, the problems of the coastal zone are not only economic ones. They are environmental ones; they are legal ones; they are social ones; they are political ones. This must be kept in mind.

There is another facet of the energy aspect of the coastal zone. This is the possibility that the ocean side of the coastal zone will in time be utilized for the development of energy for supplying, at least in part, the needs of the growing southeast Florida area. There are two systems that appear to be particularly attractive at this point.

The first one is the one known in the business as Delta-T. That is, it is the system which utilizes the temperature difference between the warm surface waters and the cooler waters at depth to run a closed-cycle Rankin-type heat engine. The other is the possible utilization of the Florida current portion of the Gulf Stream system as an energy source. In addition there is the possibility that offshore reactors — nuclear reactors or possibly fossil fueled

power plants — could be sited in the waters off Florida where the problems with cooling water would be vastly reduced.

### Offshore Wells

As long as we are talking about energy, I feel I must say that for the immediate future the major energy source from the ocean will be oil and gas from wells drilled offshore. To date, the northeast Gulf of Mexico areas for which the oil companies had such great hopes just have not proved out. The oil does not appear to be there. We will worry about that one when the possibilities look a little brighter.

Another possible use of the wet side of the coastal zone in relation to the energy problem is the potential development of deep water ports. This involves the establishment of what is called a mono-buoy offshore — pipelines running from the mono-buoy up into the dry side of the coastal zone to refineries well inward from the coastal area. To the mono-buoy would come large tankers that could not possibly negotiate the narrow channels and shallow areas nearer to shore.

The major problem in the coastal zone arises because it is a resource held in common and a resource for which many of the uses are in mutual conflict. Perhaps the best enunciation of this problem is provided by Garrett Hardin in an article written for

**“If you want to use bays like Biscayne Bay as disposal sites for sewage, fine. They are good ones; they flush themselves twice a day and are relatively effective disposal mechanisms. But if you want to use them for that, don’t plan to use them for much else.”**

Science magazine several years ago.

In the last century in Europe it was a normal practice to have a central common within a community. The idea here is that the common could support a certain number of cattle. Let us say that the maximum sustainable yield was 100 head of cattle on the common. Any more than 100 cattle would mean a deterioration of the resource.

Let us now assume that there were ten herdsmen in the town, each of whom had ten cattle. This meant that grass was growing just as fast as the cows could eat it, and everything was just fine; the common was able to support the animals that were feeding on it. Then one of the herdsmen began to realize that if he added one cow to his herd, they would be then 1 per cent over what the common could maintain, but the deleterious effect would be shared by all ten of them, and his share of this would be only 0.1 per cent. However, the worth of his own herd would be extended by 10 per cent.



Photo by Dr. Donald P. deSylva

*A Mangrove Thicket*

Thus, even though he would share in the depletion of the resource, his own net gain would be some 9.9 per cent. So by adding one cow to his herd, he would gain nearly a 10 per cent increase; so he added his one cow. Other herdsmen saw what he had done, and each of them added one cow, and very soon the grass was not able to keep up with the munching, the whole common disappeared, and none of them was able to benefit from what originally had been a very fine resource.

There is a lesson to be learned from this analogy insofar as the Florida coastal zone is concerned. When there were 200 people living on Biscayne Bay, they could dump all of their sewage directly into the bay and the bay could accommodate it. But

now with several million people living on the same bay, the problem has become acute: if you want to have boats tied up at your marinas with no system for taking care of their sewage, then you can not expect to swim in the boat slips with impunity—at least esthetic impunity.

If you build causeways, you cannot sail through them.

If you bulkhead your mangrove areas to put up condominiums, you can not expect to have your sport and commercial fisheries as productive as they have been in the past.

If you want to use bays like Biscayne Bay as disposal sites for sewage, fine. They are good ones; they flush themselves twice a day and are relatively effective disposal mechanisms. But if you want to use them for



Photo by Dr. Donald P. deSylva

### *A Bay Squatter*

that, don't plan to use them for much else.

#### **Coastal Zone Program**

The question then is: how do you avoid totally destroying your "common" and still maintain viable uses for many of those who would use it even though the uses are in conflict? Its solution will, I suspect, be in large measure a political solution. This bothers me a little bit as a scientist who is in love with the ocean on the wet side of the coastal zone, but again we have come to learn to live with life as it really is.

Through the Coastal Zone Management Act and the interaction between the federal government and the states there has developed a really fine program whereby the federal government will provide funds for the development of individual state plans for management of the coastal zone.

There is one other aspect: the need for new ideas, particularly exciting new concepts. Somehow, though, "the system" just does not seem ready for new ideas. There seems to be an allegiance to the *status quo* which I find quite disconcerting. But let me give you an example of what I mean.

I can think of five specific south Florida coastal zone problems which could be solved with one solution: the problem of our incredible beach erosion; the problem related to storm surge associated with hurricanes; the problem of inadequate beach frontage; the problem of providing adequate offshore sport fishing areas; and the esthetic problem or the environmental enhancement problem.

My contention is that all five of these could very neatly be solved by the establishment of offshore islands. My proposal is

that the southeast Florida area look into the engineering and economic feasibility of developing offshore islands. These islands would be man-made islands situated in 50-60 feet of water.

Off Miami Beach, for example, this would probably be in the order of a mile or a mile and a half offshore. These would be linear islands, maybe a mile to a mile and a half long, maybe a hundred yards wide. They would be built up from the sea floor, and once they broke the surface they would be covered with top soil, and one would plant sea grapes and palms that can survive in that fairly rugged coastal zone environment.

But how would these solve the problems? Let me take the points I made in reverse order. First, the esthetics. As you look out of a Miami Beach hotel instead of seeing an empty expanse of ocean, beautiful though I consider that happens to be, you would see a series of palm-covered islands parallel to the shore, which would help to erase our image as spoilers of the environment and switch it to one of improvers of the environment.

### **Sport Fishing**

What about the sport fishing? It is well known that the development of offshore reefs, particularly artificial reefs whether they be made up of rocks or old automobile tires or sunken

**“My proposal is that the southeast Florida area look into the engineering and economic feasibility of developing offshore islands . . . These would be linear islands, maybe a mile to a mile and a half long, maybe a hundred yards wide.”**

vessels or serpulid worms, provides an ecological niche where fish gradually congregate in increasing numbers until you have developed a very good sport fishery. So, my offshore islands would also do this.

Within the south Florida area we have relatively few beaches which are open to the public. With the increasing population, there is increasing pressure for recreational use of beaches, and these islands would in fact provide additional frontage for swimming, sunning, surfing and all the other things that people do on beaches.

These offshore islands would also reduce the waves and it is on that aspect that my last two benefits from these offshore islands rest. With an approaching hurricane, there is a build-up of sea level because of the waters being pushed shoreward by the strong winds. The rising water is bad enough, but the real problem comes from the strong storm waves on the surface of these rising waters.

(Continued on Page 44)



## *Coastal Zone*

(Continued from Page 25)

Waves in a storm surge begin to attack areas where normally waves do not cause problems. I am thinking in terms of the upper berm on beaches, hotel lobbies, the living rooms of beach homes. The development of these offshore islands would very definitely reduce the amount of wave action and thus would reduce the damage resulting from these hazardous waves riding on top of a hurricane storm surge.

### **Politically Controversial**

Perhaps the most politically controversial aspect of these islands relates to beach erosion. The erosion of south Florida's beaches results from two phe-

nomena. The first of these is the longshore current which moves sediment in suspension generally on this coast from north to south. The second is the waves themselves. As waves break on the beach, they throw sand grains into suspension. The sand grains then start to fall back down to the bottom, but the place where they fall is somewhat to the south of the place where they were picked up because of the longshore current. Therefore, if you can reduce the wave action at the beach, you will then reduce the southerly movement of sand; that is, the sand grains can not be thrown into suspension by the smaller

(Continued on Page 46)

---

## *Coastal Zone*

(Continued From Page 44)

waves in the lee of these offshore islands. What this means is that sand migrating down the coast with the longshore current, once coming in the "shadow" of these islands, will then be deposited. Gradually you will have a buildup of sand on the beach in the lee of the islands.

For something over five years I have been trying to get the federal government, the state government, the Miami Tourist Development Authority, anyone, to sponsor a relatively inexpensive engineering study of the feasibility of offshore islands for the south Florida area.

Maybe the idea is no good; if

so, it should be discarded. On the other hand it may be a good idea, and I would hope that someday some group could say this is in fact worth investigating.

### **Limit Acreage**

One possibility that should be considered is the limiting of actual ocean front acreage to those industries or other uses which require their being right on the water. If an activity can be located equally well in West Palm Beach or in west Dade County or in the western part of Broward County rather than on the waterfront, it should be denied access to the waterfront.

Virginia Key is an island between Key Biscayne and the mainland connected to both of

them by causeways and bridges. Several years ago the Miami City Commission and the Dade County Commission were convinced that with a heavily tourist-dependent economy, it was important to develop other activities within the area which could lure new industry and new dollars into the county. Thus we were able to convince both Metro Dade County and the City of Miami to zone 162 acres specifically for marine research work.

Presently the complex has the Miami Seaquarium, Planet Ocean of the International Oceanographic Foundation, the world-renowned Rosenstiel School of Marine and Atmo-

spheric Science of the University of Miami, and two NOAA Laboratories: the Southeast Fisheries Center of NOAA's National Marine Fisheries Service, and my own Atlantic Oceanographic and Meteorological Laboratories.

Over the past year, we have worked with Dade County, and three acres of county land have just been transferred to Miami-Dade Community College for its marine technician training program, and five acres have gone to a group from industry known as Palisades Geophysical Institute which does primarily underwater acoustic research work for the navy.

In ten years I can see Vir-

ginia Key being the major marine research area in the United States, if not the entire world. Today one thinks of the Scripps Institution of Oceanography in California and the Woods Hole Oceanographic Institution in Massachusetts as the major oceanographic research places in the United States. But neither group had enough foresight to provide space for long term development. If you wanted to locate near the Scripps Institution of Oceanography today, you could get probably no more closer than eight or ten miles and be way back on the mesa. If you wanted to be at Woods Hole, there would be no chance. Even Woods Hole Oceanographic In-

stitution itself has had to build a second campus several miles away and inland from their main coastal lab and ship facility.

The sort of thing that is happening with the growing marine science complex on Virginia Key is not something that happens by itself. It takes concerned and dedicated citizens willing to approach their local governments and to lobby, if you will, to see that the things that have to be done are in fact accomplished.

In conclusion, I would like to be sure that I leave with you only really one major point. That is in consideration of the economics of the Southeast Florida Coastal Zone, you can not afford to neglect the ocean. We must consider it; we must take care of it; we must utilize it effectively. But in order to do this and to assure the continuing economic growth of the Southeast Florida Coastal Zone, we must continue to consider the ocean as the major aspect that makes our coastal zone and its economic and industrial development problems considerably different from those of Saint Louis, Kansas City, or Cedar Rapids, Iowa.

Section 2

Physical processes

Physical oceanography of the Middle Atlantic Bight<sup>1,2</sup>

*R. C. Beardsley*

Woods Hole Oceanographic Institution, Woods Hole, Massachusetts 02543

*W. C. Boicourt*

Chesapeake Bay Institute, The Johns Hopkins University, Baltimore, Maryland 21218

*D. V. Hansen*

Atlantic Oceanographic and Meteorological Laboratories, NOAA, Miami, Florida 33419

*Abstract*

Kinetic energy spectra from moored current meters in the mid-Atlantic Bight reveal marked differences in current variability between the inner shelf and the outer shelf and slope regions. The nearshore subtidal current variability appears to be dominated by meteorological forcing. The amplitude of the semidiurnal and diurnal tidal peaks decreases in the offshore direction. Shallow water records show little or no inertial energy, while at the shelf break and over the slope, inertial motion contributes significantly to the current variance. A simple conceptual model is presented to explain how intense winter low pressure systems ("northeasters") drive strong alongshore currents which are coherent over much of the bight. A map of "mean" currents measured in recent moored array experiments demonstrates subsurface water flow along the shore toward the southwest. The average currents generally increase in magnitude offshore and decrease with closeness to bottom. At most sites, the mean current veers toward shore with increasing depth. The alongshore volume transport measured at three transects across the bight shows surprising uniformity, considering the possible sources for discrepancy. This transport (order  $2.0 \times 10^5 \text{m}^3 \text{s}^{-1}$ ) of water within the 100-m isobath implies a mean residence time of the order  $\frac{3}{4}$  year. Much of the shelf water observed flowing westward south of New England must originate in the Gulf of Maine-Georges Bank area.

Before 1970, information on the circulation of the mid-Atlantic Bight came mostly from temperature and salinity measurements and from drift bottles and seabed drifters. Bigelow (1933) and Bigelow and Sears (1935) first described seasonal tem-

perature and salinity changes on the continental shelf, where vernal warming and freshwater runoff build a strong stratification which is subsequently destroyed in the fall by storms and cooling. Iselin (1939, 1955) postulated an offshore motion in the

<sup>1</sup> Contribution 3701 of the Woods Hole Oceanographic Institution and 228 of the Chesapeake Bay Institute.

<sup>2</sup> The collection of these data has been supported by the NOAA-MESA New York Bight project, the National Science Foundation, and the Office of Naval Research. The New Jersey Public Service

Electric and Gas Company and B. Magnell (EG&G) contributed ideas and data. Preparation of this report has been supported by the National Science Foundation under grants DES-74-03001 (R.C.B.) and DES-74-03913-A02 (W.C.B.) and the MESA project (D.V.H.).

upper layers of the shelf water and corresponding shoreward flow in the lower layers because salinity generally increases with depth. He also noted that the circulation obeys the "rule of coastal circulation," whereby the average flow is parallel to the coast with land on the right-hand side of an observer facing downstream. Bumpus (1973) in his summary of a 10-year program of drift-bottle and seabed drifter releases and occasional drogue and drift-pole measurements, concluded that "a mean alongshore flow of order  $5 \text{ cm s}^{-1}$  occurs from Cape Cod to Cape Hatteras, except during periods of strong southerly winds and low runoff (Bumpus 1969). Nantucket Shoals and Diamond Shoals appear to be oceanographic "barriers" which limit the alongshore flow. At the Cape Hatteras end, the alongshore flow turns seaward and becomes entrained in the Gulf Stream. Occasionally strong northeast winds drive a small amount of mid-Atlantic Bight water southward around Cape Hatteras (Bumpus and Pierce 1955).

The transition zone between shelf water and warmer, saltier slope water often occurs during winter as a sharp inclined front located near the shelf break. In summer, the front is less distinct but large temperature and salinity gradients still occur in the offshore direction below the seasonal thermocline. These gradients are due to a band of cold, low-salinity water located near the bottom on the outer shelf. Described by Bigelow (1933) as a remnant from the previous winter's cooling, these waters can have temperatures of  $6\text{--}8^\circ\text{C}$  in August. Temperatures are around  $16^\circ\text{C}$  only 20 km offshore of the "cold pool." The mechanisms governing the movement of this frontal zone and exchanges of heat, salt, water, and

momentum across it are not well understood.

#### *Current variability, circulation, and water structure*

Self-contained current meters, temperature and pressure gauges, and other instruments deployed in moored arrays in the mid-Atlantic Bight are now beginning to provide records of sufficient length to characterize the variability of the subsurface current field in this region. We will present here some preliminary results of these field programs with an emphasis on describing the "mean" circulation and subtidal current variability.

We begin by examining in Fig. 1 several kinetic energy spectra computed from 1-month or longer current records obtained at several different sites on the middle Atlantic continental shelf and rise. The four sites, labeled "A" through "D," and the location, water depth, depth at which the current record was taken, and other pertinent information for each site are given in Table 1. (Sites A through D correspond respectively to stations 18, 1, 4, and 11 shown in Fig. 2.)

The site A data has been taken and reported by EG&G (1975) under contract to the Public Service Electric and Gas Company of New Jersey. Flagg et al. (1976) obtained the site B and C data. The low-frequency cutoff for each estimated spectrum is inversely proportional to the length of the particular current record analyzed. The Woods Hole Oceanographic Institution has maintained moored arrays at site D for almost a decade and the very long current records obtained there allowed Webster (1969) and Thompson (1971) to make a reliable estimate of the kinetic energy spec-

Table 1. Location and other pertinent information for the current and wind spectra shown in Fig. 1.

Site	Sta. No. (Fig. 2)	Location	Time	Water depth (m)	Instr. depth (m)	Data source
A	18	$39^\circ 28' \text{N}, 75^\circ 15' \text{W}$	Dec 73–Feb 74	12	5	EG&G (1975)
B	1	$40^\circ 54' \text{N}, 71^\circ 04' \text{W}$	Mar 74	58	28	Flagg et al. (1976)
C	4	$40^\circ 18' \text{N}, 75^\circ 51' \text{W}$	Mar 74	112	30	Flagg et al. (1976)
D	11	$39^\circ 20' \text{N}, 70^\circ 00' \text{W}$	Several years	2,640	100	Webster (1969); Thompson (1971)

trum in the slope water over a seven-decade range frequency. The power density of the wind stress observed at site A is also shown in Fig. 1. Wind stress has been computed using the quadratic drag law  $\tau = C_D |W_{10}| W_{10}$  where  $W_{10}$  is the observed

wind vector at 10-m height and the assumed constant drag coefficient is  $C_D = 3.2 \times 10^{-7}$  in c.g.s. units.

The spectra have been visually smoothed within the estimated uncertainties to simplify graphical presentation and our spec-

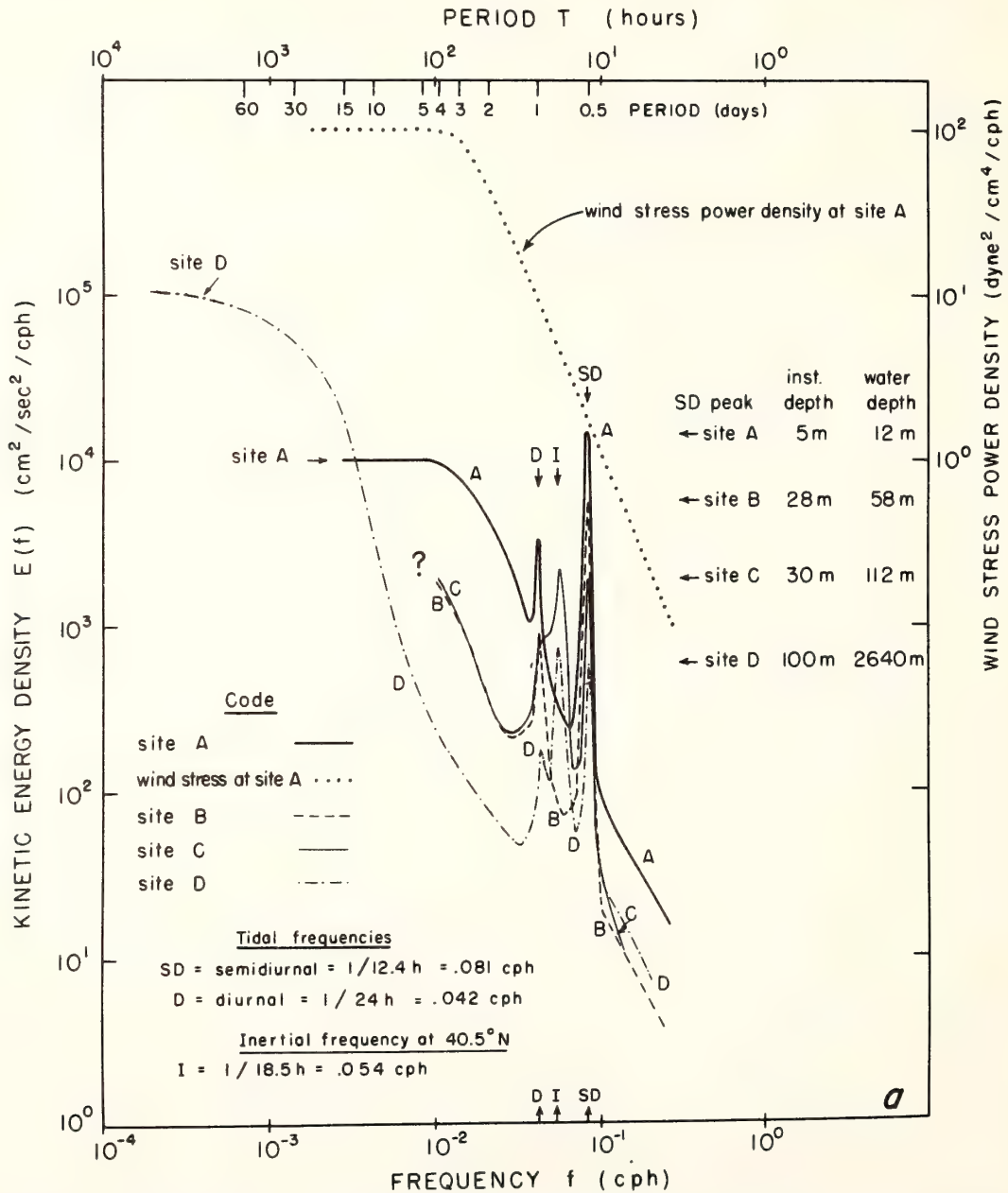


Fig. 1. Spectra of currents and wind in the Middle Atlantic Bight. Locations of current meter moorings are listed in Table 1. (See text for explanation of different formats.)

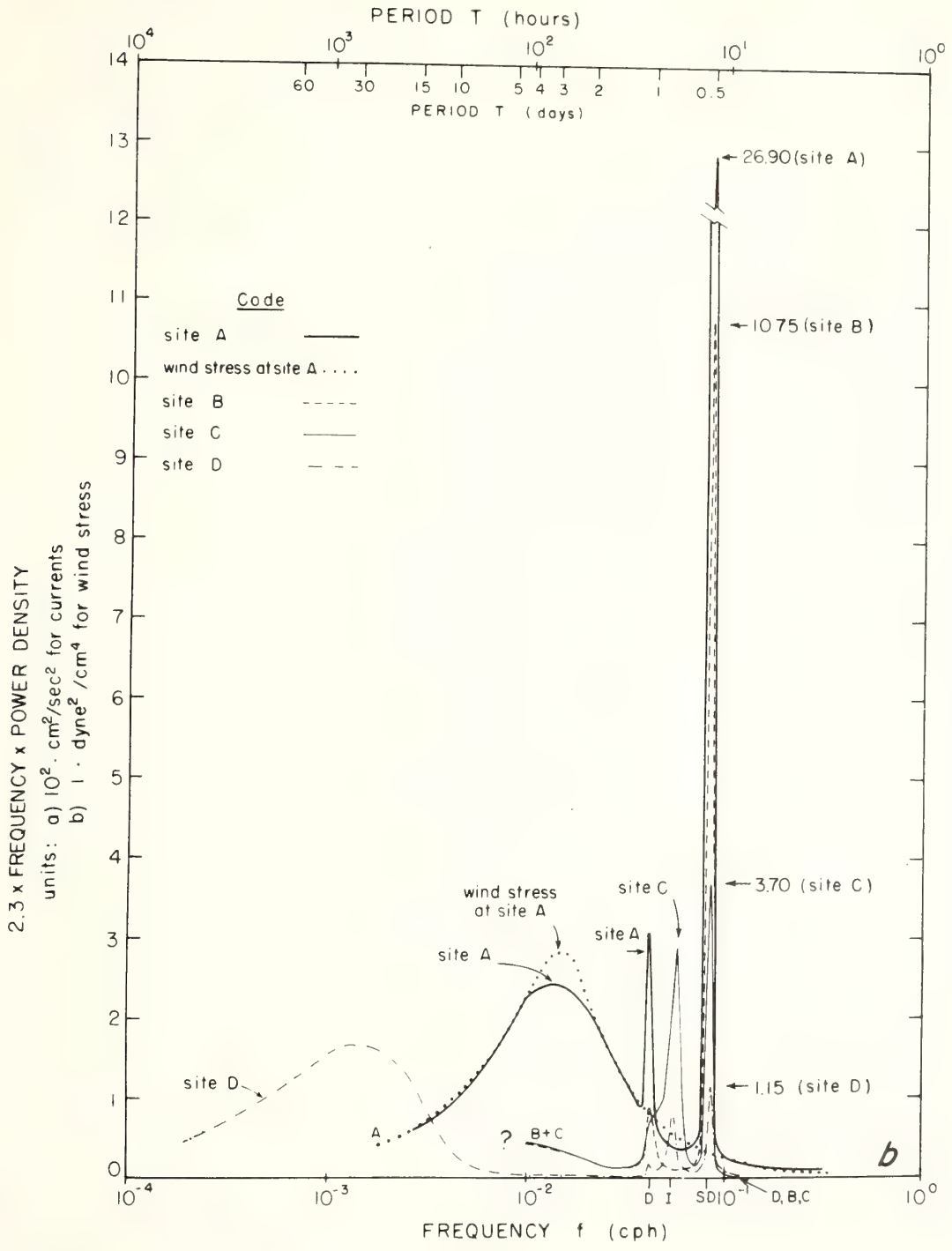


Fig. 1. Continued

tral characterization of wind and current variability over the continental shelf. The reader should remember that spectra obtained from *much longer* records will presumably show more structure than the smoothed *estimates* shown in Fig. 1. The spectra have been plotted in both the  $\log E(f)$  versus  $\log f$  format (Fig. 1a) and the area-preserving linear  $2.3 \times f \times E(f)$  versus  $\log f$  format (Fig. 1b). The first format best displays the functional form of the energy density  $E$  as a function of frequency, e.g.  $E(f) \propto 1/f^m$  corresponds to a straight line plotted in Fig. 1a with a slope of  $-m$ . The second format in Fig. 1b is used to illustrate how much different frequency bands contribute to the total variance of the current record. The total area under the  $2.3 \times f \times E(f)$  curve is equal to the variance, and the area under the curve between two specific frequencies is the contribution from that frequency range to the variance.

The spectra shown in Fig. 1 illustrate several fundamental features of wind and current variability on and near the mid-Atlantic continental shelf. Wind stress and current spectra are inherently "red," with the power or kinetic energy density generally decreasing with increasing frequency. Wind stress power density at site A is approximately constant at lower frequencies with a transition occurring at periods between 2 and 4 days and a higher frequency falloff of about  $f^{-5/2}$ .

Most of the fluctuation in the wind stress at site A is caused by rather wideband meteorological transients which have characteristic periods between 1 and 8 days. The intense low pressure disturbances or cyclones which generally form over the southeast United States and intensify while propagating up along the eastern seaboard have characteristic periods of 2 to 4 days and cause the peak in the site A wind stress power density curve shown in Fig. 1b.

In addition to being red at lower frequencies, the four current spectra exhibit relatively sharp peaks at the semidiurnal (SD) and diurnal (D) frequencies. Amplitude of the semidiurnal peaks generally increases across the shelf toward shallower water; at sites B and C, the kinetic energy

density at the semidiurnal frequency crudely follows the relationship  $E \propto h^{-3/2}$  as predicted by shallow-water wave theory. The large semidiurnal peak observed at site A is probably caused by the proximity of Little Egg Inlet which can channel and intensify local tidal currents. Semidiurnal and diurnal tidal currents are weakest at site D on the continental rise. While the kinetic energy density at the diurnal frequency shows a general increase with decreasing depth across the shelf, the spatial structure of the diurnal tidal currents is not yet understood.

It is important here to note, however, that semidiurnal and diurnal tidal currents on the continental shelf are in part predictable since the astronomical forcing is deterministic and periodic. The accuracy of this prediction depends on the basic accuracy of the initial calibration of local tidal currents with the astronomical forcing, the degree of local nonlinearity (e.g. the phase shifting of the surface tide by strong storms), and the relative importance of baroclinic or "internal" tides, i.e. internal waves of tidal frequency. We expect baroclinic effects to be important perhaps all the time in the deeper water near the shelf break and over most of the shelf during the warmer months when a strong seasonal pycnocline has formed. Wunsch and Hendry (1972) observed bottom-intensified semidiurnal tidal currents in about 850 m of water on the New England continental slope. They described these observations as a train of internal waves of semidiurnal frequency generated at greater depth on the slope and propagating up the slope toward the shelf. How far these internal tides penetrate onto the shelf and how much mixing is caused by their dissipation is as yet unknown.

Tidal flow over topographic features can also generate higher frequency internal waves via nonlinear mechanisms. For example, trains of large-amplitude internal waves have been observed by remote sensing to propagate almost across the shelf during summer stratified conditions. Apel et al. (1975) believed such wave trains are formed near the shelf break by diurnal and semidiurnal tidal currents. The question of



how much energy is really drained from the barotropic tides via topographic generation of internal waves remains unanswered.

Current spectra at sites C and D show an additional kinetic energy density peak near the local inertial frequency. The contribution of the near-inertial frequency band to the current variance is considerable at these two sites and especially so at site C near the shelf break (Fig. 1). The local generation of near-inertial currents by meteorological transients has been well documented at site D by Pollard and Millard (1970): fast moving fronts or strong veering winds which rotate clockwise with near-inertial frequency clearly excite nearly vertically propagating internal waves. The *absence* of near-inertial peaks in the kinetic energy spectra at sites A and B nearer shore is probably due to the existence of other "natural" modes like edge and shelf waves (*see* Reid 1958) which are preferentially excited during any transient adjustment period. The observed lack of strong near-inertial energy in shallow nearshore water should simplify the local current prediction problem.

We now turn to the lower frequency end of the current spectra. Long records at site D show that much of the current variance at 100 m in slope water is caused by low frequency motion with characteristic periods centered at about 30 days. Propagation of topographic Rossby waves up the continental rise (perhaps generated by the Gulf Stream), meandering of the Gulf Stream itself, and formation of anticyclonic (warm core) eddies can all generate strong low frequency currents at site D which cause the spectral shape shown. In contrast with site D, kinetic density spectrum at site A (Fig. 1b) shows that subtidal frequency currents in nearshore *shallow water* are strongly *wind driven* and cause most of the total current variance (*see* EG&G 1975). We thus suggest that the current prediction problem in shallow nearshore water further simplifies to the development of a model which relates the subtidal current to measurable meteorological forcings.

Current records obtained at sites B and C are too short for the computed spectra to indicate locations and magnitudes of lower

frequency peaks; hence the large question mark shown in Fig. 1. It is *not* known at this time how much of the lower frequency end of the spectra is caused by local or regional meteorological forcing or by the transmission (or leakage) of lower frequency energy onto the continental shelf from the deeper ocean. We have used the model of Nüiler and Kroll (in prep.) to estimate the possible transmission of topographic Rossby wave energy from the rise onto the shelf and find that this flux of energy across the shelf break is comparable with the direct kinetic energy input due to a surface wind stress of 1 dyne/cm<sup>2</sup> acting over the width of the continental shelf. Based on this and other preliminary observations, we suggest that the open ocean causes energetic low frequency motion on the outer continental shelf of the mid-Atlantic Bight. Longer current records (8 months or longer) are needed to quantify accurately the importance of low frequency energy transmission onto the shelf.

Having shown that much of the current variability in the shallower section of the bight is directly wind driven, we now describe a simple conceptual model for the dynamics of the response of this region to strong wind events. This model, suggested by Beardsley and Butman (1974), has been supported by other observations (Boicourt and Hacker 1976; Beardsley et al. in prep.). Intense winter lows, the "northeasters" which pass to the east of the mid-Atlantic Bight, produce strong wind stress fields toward the south and west over the shelf, generally paralleling the coast from Cape Cod to Cape Hatteras. The transient mass flux in the surface Ekman layer has a component to the right of the wind stress vector and a component parallel to the wind stress. During northeasters, the Ekman component directed to the right of the wind stress is onshore, causing sea level to rise along the coast. Wunsch (1972) and Brown et al. (1975) have shown that sea level over the deep ocean (and presumably the outer slope) is nearly constant over time scales of several days, so that the coastal rise in sea level creates a large onshore pressure gradient that is roughly in geostrophic balance

with the strong alongshore flow. Since the wind stress field tends to parallel the coastline, the intense northeaster generates strong alongshore currents and cross-shelf pressure gradients which appear to be coherent over the entire shelf from Cape Cod to Cape Hatteras. Boicourt and Hacker (1976) observed that the more energetic subtidal current fluctuations (especially those associated with northeasters) oriented along the 35-m isobath off Maryland and Delaware are coherent and approximately in phase over distances of 230 km. They report typical maximum daily mean speeds of 40 cm/s at depths of 10 and 20 m, which can produce alongshore fluid particle excursions of 40–80 km during the several days of the storm. Beardsley et al. (in prep.) found that subsurface pressure gradients caused by sea level changes are coherent over the mid-Atlantic shelf from Cape May to Cape Cod. These observations suggest that the wind-driven component of the alongshore flow may be predicted from the more easily measured wind-stress and pressure fields and coastal sea level fluctuations.

We will now focus on the “mean” or very low frequency current field on the mid-Atlantic Bight. We have plotted in Fig. 2 the average currents which have been measured in recent moored array experiments. Only records of 1 month or longer duration have been used and information on the individual measurements (e.g. local water depth, instrument depth, time of measurement, current values, source of data, etc.) is given in Table 2. The mean currents are plotted as vectors with the magnitude equal to the average speed. The same current meter stations are numbered in Fig. 2 sequentially starting from the north and the same key is used in Table 2. The depth (in meters) of an individual measurement is indicated in Fig. 2 by a small number located near the head of the current vector. We have separated the measurements into winter (unstratified) measurements (denoted by solid vectors) and summer (stratified) measurements (dashed vectors). Measurements from several sites (5–11) on the continental rise and outer slope are in-

cluded to show the mean westward flow of slope water. The mean position of the northern edge of the Gulf Stream is also shown, with the reminder that the actual position of the Gulf Stream in this region is highly variable (Hansen 1970).

These direct measurements of the mean current field on the shelf *demonstrate* subsurface water flow along the shore toward the southwest. The mean currents generally increase in magnitude offshore and decrease with closeness to the bottom. At most sites, the mean current veers toward shore with increasing depth. With the exception of station 21, a net southwestward transport is observed at all sites.

Measurements made along the three transects labeled I (New England), II (New York), and III (Norfolk) in Fig. 2 have been used to *estimate* mean alongshore volume transport. The transects cover the bulk of the continental shelf out to the 100-m isobath. Calculated transport values, cross-sectional area, and mean speeds for each transect are listed in Table 3. Although Wright and Parker (1976) estimated that roughly half of the volume of the shelf water from Cape Cod to Cape Hatteras lies in a thin surface wedge outside the 100-m isobath, there are essentially no direct measurements of mean current in the shelf water wedge beyond the 100-m isobath.

The estimated volume transports for the three transects are surprisingly consistent, considering that the northern transects (I and II) are early spring measurements in two different years, while the southern transect (III) value represents summer measurements. In addition, the transects were made at different depths, with different instruments, and with varying spatial resolutions. For these reasons, we hesitate to speculate about exchange of shelf water and slope water based on continuity arguments and assumed stationary flow through the transects. We are uncertain, for example, whether the higher mean alongshore speed shown in transect III is due to a continuity of transport within the 100-m isobath which forces the mean speed to increase through the smaller cross-sectional

area, or whether it is due to a more consistent southward flow in summertime (for which there is some evidence). The con-

sistency of the transports lead us to speculate that there may be little significant seasonal change in alongshore transport. Only

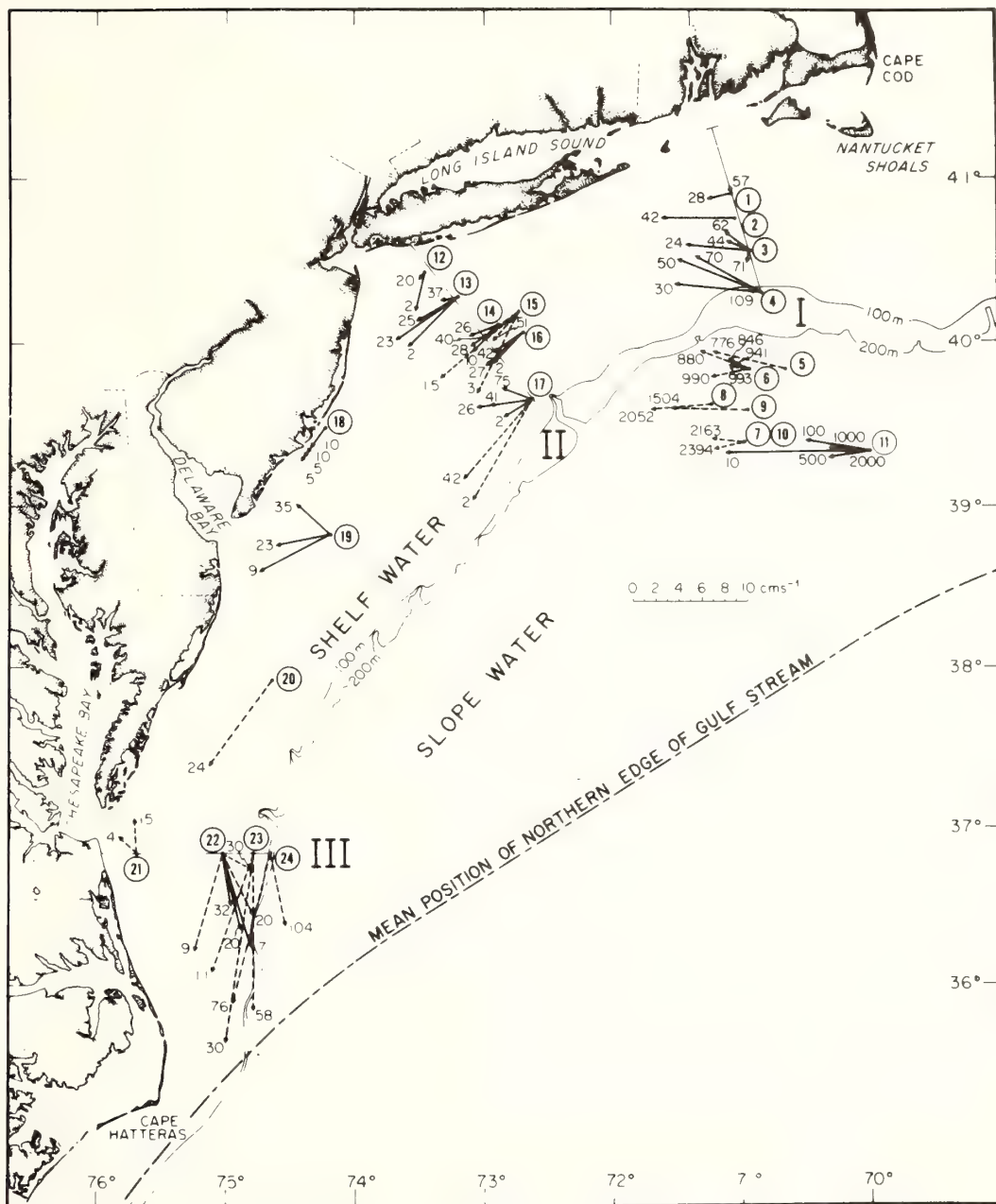


Fig. 2. Mean velocities as measured by moored current meters in the Middle Atlantic Bight region. Winter measurements are indicated by solid arrows, summer velocities by dashed arrows. Individual stations are numbered according to Table 2; station numbers are circled. Measurement depths (in meters) are shown near the head of the arrows.

Table 2. Tabulation of the recent direct measurements of sub- and near-surface mean currents shown in Fig. 2. (NA = not applicable.)

Sta. No.	Location	Start time	Record length (days)	Water depth (m)	Instr. depth (m)	E (cm/s)	N (cm/s)	Data source*
1	40°54N,71°04W	28 Feb 74	35	58	28	-2.1	-0.5	A
					57	-0.2	0.8	
3	40°33N,70°56W	28 Feb 74	35	72	24	-5.7	0.5	A
					44	-2.2	1.0	
					62	-2.2	1.8	
					71	-0.1	-0.5	
4	40°18N,70°51W	28 Feb 74	35	110	30	-7.8	0.7	A
					50	-7.4	3.0	
					70	-5.9	3.3	
					109	-0.8	0.0	
7	39°23N,70°59W	20 Aug 70	46	2,527	1,504	-2.8	0.3	B
9	39°35N,70°58W	20 Aug 70	111	2,263	2,163	-6.4	0.2	B
5	39°50N,70°40W	20 Aug 70	104	876	776	-6.4	1.6	B
6a	39°50N,70°56W	20 Aug 70	45	943	846	-2.0	1.0	B
			45		933	-2.0	0.4	
			45		941	-1.5	0.4	
b	39°50N,70°56W	20 Aug 70	451	993	880	-4.6	1.8	
			86		990	-3.6	-0.7	
8	39°37N,71°15W	20 Aug 70	111	2,150	2,052	-5.1	-0.4	B
10	39°23N,71°01W	20 Aug 70	56	2,509	2,394	-2.4	-0.5	B
2	40°45N,71°03W	8 Mar 73	33	60	42	-6.4	0.0	C
11	39°20N,70°00W	NA	NA	2,640	10	-13.0	-0.6	D
					100	-5.7	1.1	
					500	-3.7	-0.6	
					1,000	-3.5	0.3	
					2,000	-1.6	-0.1	
12	40°25N,73°28W	22 Mar 74	59	23	2	-0.7	-3.5	E
			89		20	-0.6	-0.7	
13	40°16N,73°13W	25 Feb 75	111	38	2	-4.7	-4.8	E
		25 Feb 75	37		25	-3.6	-2.2	
		29 Apr 75	48		23	-5.5	-3.9	
		25 Feb 75	111		37	-1.5	-0.3	
14	40°06N,72°54W	25 Feb 75	112	48	10	-2.4	-2.6	E
		25 Feb 75	62		26	-2.8	-1.1	
		25 Feb 75	112		40	-1.6	-1.3	
16	40°03N,72°42W	1 Mar 75	59	59	2	-2.8	-2.8	E
		1 Mar 75	59		27	-3.1	-2.8	
		1 Mar 75	108		42	-2.9	-1.9	
17	39°39N,72°38W	24 Feb 75	64	76	2	-2.6	-1.7	E
		23 May 75	25		2	-5.4	-9.1	
		24 Feb 75	64		26	-4.9	-0.7	
		24 Feb 75	64		41	-4.0	-0.6	
		30 Apr 75	42		42	-6.2	-7.4	
		24 Feb 75	64		75	-2.6	1.0	
18	39°28N,74°15W	1 Jul 72,73,74	60	12	5	-2.1	-2.9	F
		1 Dec 73,74	60		5	-2.0	-2.8	
		1 Jul 72,73,74	60		10	-1.7	-2.3	
		1 Dec 73,74	60		10	-1.3	-1.8	
15	40°07N,72°51W	18 Jun 74	35	50	2	-3.8	-6.9	E
		18 Jun 74			13	-6.8	-5.5	
		18 Jun 74			26	-4.1	-3.0	
		18 Jun 74			46	-1.7	-1.8	

Table 2. Continued

Sta. No.	Location	Start time	Record length (days)	Water depth (m)	Instr. depth (m)	E (cm/s)	N (cm/s)	Data source*
19	38°49N,74°12W	29 Oct 74	36	43	9	-6.2	-3.2	G
		29 Oct 74			23	-4.9	-1.0	
		29 Oct 74			35	-3.0	2.8	
20	37°55N,74°39W	26 Jun 74	22	35	24	-5.7	-7.5	H
21	36°50N,75°42W	21 Jul 74	29	16	4	-1.7	1.5	H
					15	-0.2	3.1	
22a	36°50N,75°02W	21 Jul 74	37	36	9	-2.4	-8.4	H
		21 Jul 74			20	2.6	-5.5	
		21 Jul 74			30	2.4	-1.3	
b	36°50N,75°02W	15 Jan 74	29	36	7	2.6	-8.6	
		15 Jan 74			20	1.6	-6.9	
		15 Jan 74			32	0.7	-4.7	
23	36°50N,74°48W	21 Jul 74	26	70	11	-3.7	-10.7	H
		21 Jul 74			30	-2.3	-16.6	
		21 Jul 74			58	0	-13.8	
24	36°50N,74°40W	21 Jul 74	18	70	76	-3.1	-12.6	H
		21 Jul 74			104	1.4	-6.6	

\* A-Beardsley and Flagg (1976); B-Schmitz (1974); C-Beardsley and Butman (1974); D-Webster (1969); E-NOAA-MESA (in prep.); F-EG&G (in prep.); G-Boicourt (personal communication); H-Boicourt and Hacker (1976).

simultaneous measurements will provide conclusive evidence.

If the fluxes through the three transects are approximately the same, we postulate that there is little *net* flow between the shelf and slope regions; Wright (1976) estimated that as much as 2,000 km<sup>3</sup>/yr might leave the shelf region off New England via the "calving" process. This number, however, was determined on the basis of a much larger alongshore gradient in transport than we observed.

The various volume fluxes for the mid-Atlantic Bight are shown schematically in Fig. 3. For comparison, note that the alongshore transport of shelf water within the

100-m isobath, while 60 times the river runoff, is only about 0.3% of the northward transport of the Gulf Stream. The volume of the shelf water within the 100-m isobath is estimated to be  $V_{sh} = 6,000 \text{ km}^3$  (Ketchum and Keen 1955; Wright and Parker 1976) and the estimated alongshore mean flux of shelf water within the 100-m isobath is  $T_{sh} = 8,000 \text{ km}^3/\text{yr}$ . The mean residence time is then  $\tau = V_{sh}/T_{sh} = 3/4 \text{ yr}$ . This implies that the shelf water between Cape Hatteras and Cape Cod is removed from the shelf and entrained into the Gulf Stream in less than a year. This estimate is slightly less than the 1.3 years estimated by Ketchum and Keen (1955) who knew the freshwater inflow and the salinity distribution on the shelf and who assumed no flow entering or leaving the bight via the Nantucket Shoals and Cape Hatteras.

The Gulf of Maine and Georges Bank region must supply the low salinity water observed flowing westward through transect I, i.e.  $T_{sh} = T_{GM} + T_{GB}$  following the notation in Fig. 3. This conclusion is implicit in the hydrographic structure of the shelf water in this region, namely that the shelf-slope water salinity front is a persistent and continuous feature from New York to the southern flank of Georges Bank and

Table 3. Alongshore transport to the 100-m isobath estimated through three transects across mid-Atlantic Bight. Position of individual transects shown in Fig. 2.

Transect	Cross-sectional area to 100-m isobath A (km <sup>2</sup> )	Transport to 100-m isobath T (km <sup>3</sup> /yr)	Mean speed $u = T/A$ (cm/s)	Period
I	6.4	5,300	2.7	Mar 74
II	7.6	8,800	3.7	Mar-Apr 75
III	3.6	8,200	7.2	Jul-Aug 74

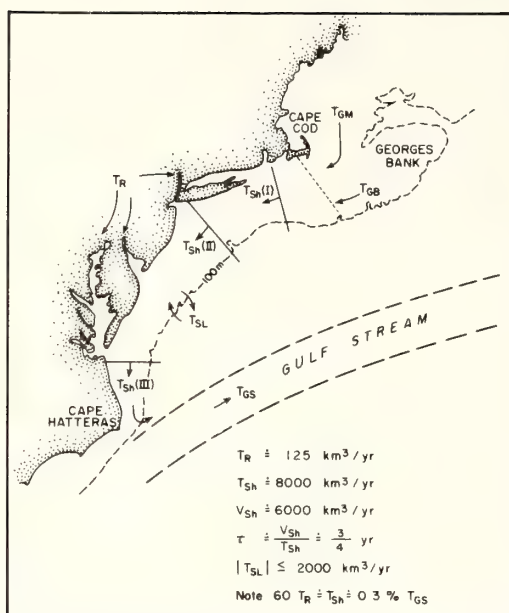


Fig. 3. Schematic diagram of the important volume transports for the Middle Atlantic Bight.  $T_R$  is the total annual freshwater runoff (of which over 50% occurs via the Chesapeake Bay),  $T_{Sh}$  is the alongshore transport over the shelf out to the 100-m isobath,  $T_{SL}$  is the net flux of slope water into the shelf water,  $T_{GS}$  is the transport of the Gulf Stream, and  $T_{GM}$  and  $T_{GB}$  are the unknown fluxes of shelf water from the Gulf of Maine and southern flank of Georges Bank. The volume of the shelf water mass out to the 100-m isobath is  $V_{Sh}$ , and the average residence time  $\tau$  is simply  $V_{Sh}/T_{Sh}$ .

the "cold pool" is also continuous during spring and summer along this same section of the shelf (*see* Bumpus 1976). Any substantial flux of more saline slope water occurring across the 100-m isobath must be balanced by an increased flux of low salinity water (above  $T_{Sh}$ ) from the Gulf of Maine and Georges Bank to maintain a steady salt balance. This conclusion is also dictated by simple continuity arguments which require a northern source region to maintain the observed westward flux of shelf water shown in Fig. 2.

The summer current measurements in transects II and III show that the alongshore currents in the cold pool water equals or exceeds the mean southward current of the surrounding warmer water. These measurements counteract the traditional im-

pression that the cold pool, formed by winter cooling, remains stationary throughout the spring and summer seasons (Ketchum and Corwin 1964). There is good evidence (Ford et al. 1952; Boicourt 1973) that the cold pool moves southward and is entrained by the Gulf Stream. High alongshore velocities of the cold water, as measured in transects II and III, imply that the cold water found near Cape Hatteras in August must have formed by winter cooling near Cape Cod or perhaps in the Gulf of Maine.

Two large unknowns in the calculation of water and salt budgets in the mid-Atlantic Bight are fluxes of water and salt into the region from the north and amounts of water and salt exchanged across the shelf-slope boundary. Although we cannot yet quantify shelf-slope exchanges, we can describe some processes involved. In summer and winter, much exchange appears to be wind controlled, with onshore-offshore flows in the upper Ekman layer compensated by opposite flows in the lower layer (Boicourt and Hacker 1976). In winter the cross-shelf flows driven by northeast winds enhance the thermal front at the shelf break and vertically mix the midshelf region. Winds from the south and southwest, on the other hand, cause offshore flows in the upper Ekman layer and intrusions of warm salty slope water along the bottom, thereby tending to stratify the outer shelf region.

Summertime cross-shelf circulation is larger and has a more complex vertical structure. Boicourt (1973) and Boicourt and Hacker (1976) found that southerly winds can drive an intrusion of high salinity slope water onto the shelf at middepths in the southern mid-Atlantic Bight. Because these intrusions have been commonly observed on the outer shelf, they may be an important process in shelf water-slope water exchange. Gordon et al. (1976) observed a high salinity layer at middepth in the New York Bight, indicating that such intrusions may occur widely in the bight. The cold pool and strong thermocline are evident in the water temperatures in the southern mid-Atlantic Bight (Fig. 4). The salinity distribution shows an intrusion of high salinity slope waters in the upper ther-

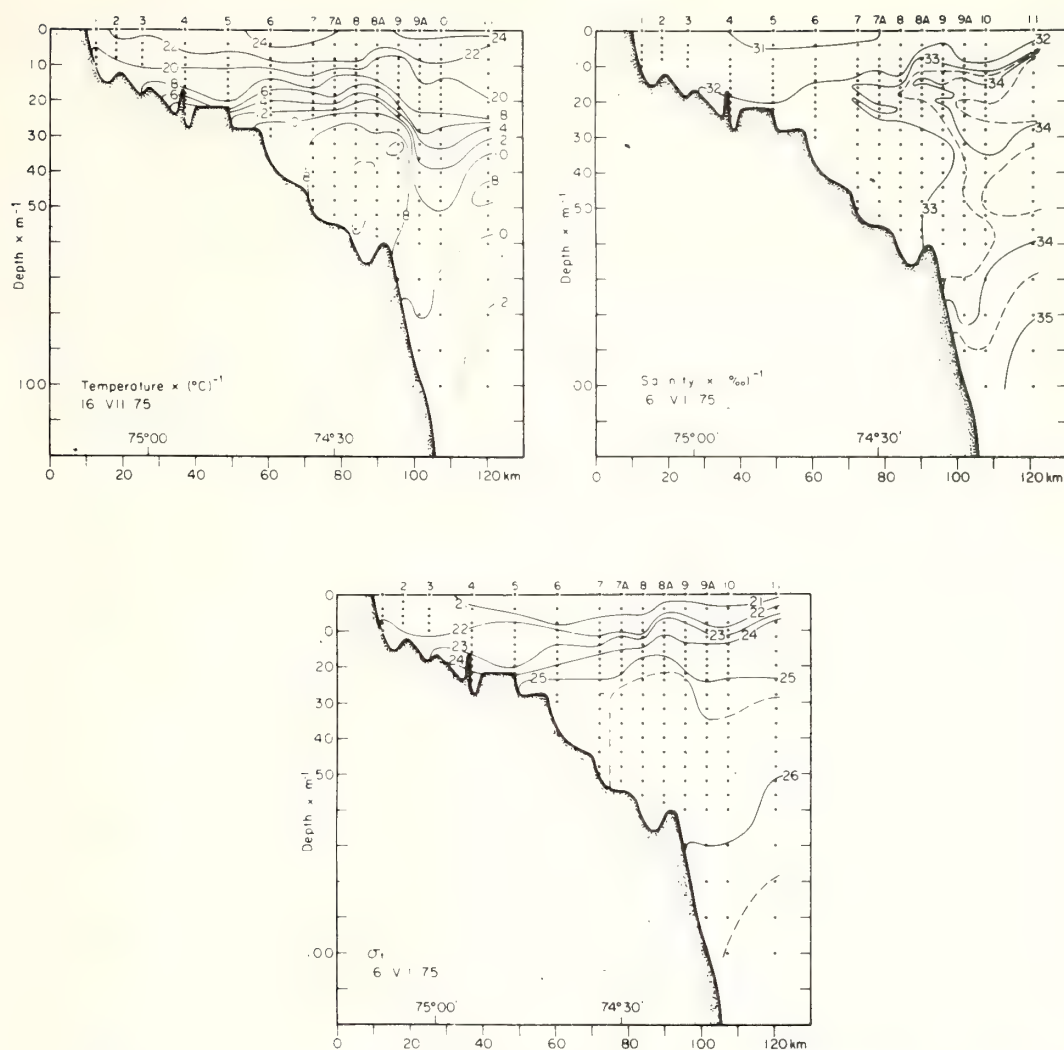


Fig. 4. Distributions of temperature, salinity, and  $\sigma_t$  in a cross-shelf vertical section off Ocean City, Maryland, July 1975.

mocline. This intrusion extends about 30 km inshore of the shelf break, apparently driven by southerly winds. A small parcel of cold ( $<8^{\circ}\text{C}$ ), low salinity water may have been detached from the cold pool and moved offshore. Because such parcels are commonly found in this position, however, the amount of water actually detaching is uncertain.

South of New England, Bigelow (1933) and Cresswell (1967) described calving of the cold pool with parcels or bubbles of shelf water moving into slope water. Wright (1976) suggested that significant inter-

change of shelf and slope water may occur via this mechanism. This process may be related to the formation of anticyclonic Gulf Stream eddies and their subsequent south-west drift along the edge of the slope. Satellite infrared photographs (e.g. Hughes 1975) suggest some exchange of shallow surface water, and Saunders' (1971) aerial temperature survey of one warm-core eddy suggests that some deep shelf water is pulled off the shelf and entrained into the trailing side of the eddy. How much shelf water is exchanged via these processes and

with what frequency (i.e. the intermittency of these processes) is not known.

We conclude this section with a brief discussion of the physical processes that govern the mean circulation in the mid-Atlantic Bight. Stommel and Leetmaa (1972) have constructed a theoretical model (with linear dynamics) for the winter shelf circulation driven by a mean wind stress and a distributed freshwater source at the coast. They then applied this model to the bight and concluded that an alongshore sea level slope of about 10 cm drop from Cape Cod to Cape Hatteras must exist to drive the mean flow toward the southwest (as observed!) *against* the mean eastward wind stress. This same basic conclusion was also reached by Csanady (in prep.) who examined the influence of wind stress variability on the Stommel and Leetmaa model. This inferred alongshore pressure gradient can be either created by a succession of long, shore-trapped waves as suggested by Csanady (in prep.), who showed evidence for this process in Lake Ontario, or maintained by an upstream source of fresh shelf water, presumably here the St. Lawrence system and inshore Labrador Current. Sutcliffe et al. (1976) reported evidence that fluctuations in the transport of the St. Lawrence system can be traced down the Scotian Shelf and into the Gulf of Maine. This, together with our early point that most of the fresh shelf water observed flowing westward through transect I (Fig. 2) must be supplied by the Gulf of Maine and outer Georges Bank regions, suggests a continuous freshwater pathway from the St. Lawrence to Cape Hatteras. The alongshore pressure gradient inferred to occur over the mid-Atlantic Bight may be partially supported by a northward rise in sea level found by oceanic leveling in the slope water by Sturges (1974).

#### *Special features of the New York Bight and adjacent nearshore zone*

The New York Bight contains several features of general interest that have been intensely studied. Special topographic features of this region include a relatively deeply incised inner shelf region into which

enters one of the major river systems of the region and the Hudson Shelf Valley and Hudson Canyon.

The Hudson-Raritan estuary has a characteristic circulation consisting of a seaward flow of relatively brackish estuarine water in the near-surface water, and a shoreward flow of more saline water near the bottom. The relatively great width and complicated channel system in the Sandy Hook-Rockaway transect allows inertial and Coriolis effects to further modify currents such that seaward flow tends toward the southern side of the entrance, and the inflow occurs mainly in the navigation channels and along the northern side of the entrance (*see* Parker et al. 1976). This mean flow of a few centimeters per second is a weak residual superimposed on stronger tidal flow but causes most of the material exchange between the estuary and shelf regions.

The Hudson Shelf Valley is the offshore expression of the Hudson estuary. Current measurements in this valley (30 km off the New Jersey shore) indicate that the average flow in the valley over intervals as long as a month can be shoreward with an average speed of a few kilometers per day. Such flows are more than ample, if coherent in space, to return suspended materials to the harbor entrance from far out on the continental shelf.

The combination of the Hudson estuary, the complex bottom topography, and the nearly right-angle bend in the shoreline produces quite complicated flow patterns over the inner shelf. There is evidence in the water properties that the near-surface flow from the estuary tends to move southward along the New Jersey shoreline. Recovery of seabed drifters suggests the statistical occurrence of a mean clockwise circulation within the inner bight, counter to the flow over the shelf farther offshore. This circulation is sometimes reflected in current measurements (Charnell and Mayer 1975), but the current regime is best described as more dispersive than advective, especially during spring and summer, the seasons of maximum stratification.



An interesting and significant aspect of the flow in the inner bight is a shoreward velocity component in the bottom boundary layer. Numerous current measurements have been made for the NOAA-MESA project at distances of 1–5 m above the bottom. Averages of such measurements over any significant time frequently show a distinctly shoreward component. In 19 out of 21 cases examined in which a clear distinction could be made, there was a shoreward component in the bottom boundary layer. Furthermore, subdividing the data into sets in which the flow is east or west along Long Island, for instance, yields the same result: flow in the bottom boundary layer is shoreward in both cases. It is not yet ascertained whether this shoreward veering is a result of surface winds or whether it may be a manifestation of estuarine circulation generally over the shelf, but in any case it suggests a tendency for near-bottom materials to be carried inshore. Such a process is a plausible explanation for the relatively high and constant rate of return of seabed drifters from bight waters (Charnell and Hansen 1974) and supports previous reports (Bumpus 1973).

#### *Some remaining problems*

Although progress has been made in determining the current variability and circulation pattern over the mid-Atlantic shelf, we are still unable to provide unambiguous answers to many questions of a basic engineering sort posed by environmental managers. Only a general estimate of the flushing rate of the shelf is available, and critical evaluation of the importance of the shelf-break exchange is not yet possible. Although a first-order description of flow to be expected can now be given for many parts of the bight, our ability to predict details and events remains poor. The dominant forces controlling the circulation are believed known but their relative importance and region of influence are not. Neither conceptual nor observational tools are adequate to the task of modeling of other than tides and tidal currents. Local models have useful applications but must be posed very carefully (especially boundary conditions) in the context of what is

and what is not known about the physics of water movement over the shelf. It cannot be safely assumed that the way to solve a given management problem will be pointed by a mathematical model in any straightforward sense. Finally, there remain fundamental questions related to smaller scale phenomena, especially mixing and other dissipative processes. Smaller scale topographic features like the inner New York Bight embayment, the ridge and swale areas, and the shelf valleys and submarine canyons must exert some steering influences on the local flow. Some of these smaller scale problems will be immediately addressable when the physics of shelf circulation are better known; others must await improvement of observational instruments and techniques.

#### *References*

- APEL, J. R., H. M. BYRNE, J. R. PRONI, AND R. L. CHARNELL. 1975. Observations of oceanic internal and surface waves from the Earth Resources Technology Satellite. *J. Geophys. Res.* **80**: 865–881.
- BEARDSLEY, R. C., AND B. BUTMAN. 1974. Circulation on the New England continental shelf: Response to strong winter storm. *Geophys. Res. Lett.* **1**: 181–184.
- , AND C. FLAGG. 1976. The water structure, mean currents, and shelf water/slope water front on the New England continental shelf. *Proc. 1975 Liege Colloq. Ocean Hydrodynam.*, in press.
- BIGELOW, H. B. 1933. Studies of the waters on the continental shelf, Cape Cod to Chesapeake Bay. 1. The cycle of temperature. *Pap. Phys. Oceanogr. Meteorol.* **2**(4): 135 p.
- , AND M. SEARS. 1935. Studies of the waters on the continental shelf, Cape Cod to Chesapeake Bay. 2. Salinity. *Pap. Phys. Oceanogr. Meteorol.* **4**(1): 94 p.
- BOICOURT, W. 1973. The circulation of water on the continental shelf from Chesapeake Bay to Cape Hatteras. Ph.D. thesis, The Johns Hopkins Univ., Baltimore, 183 p.
- , AND P. HACKER. 1976. Circulation on the Atlantic continental shelf of the United States, Cape May to Cape Hatteras. *Mem. Soc. R. Sci. Liege Ser. 6* **10**: 187–200.
- BROWN, W., W. MUNK, F. SNODGRASS, H. MOFJELD, AND B. ZETLER. 1975. MODE bottom experiment. *J. Phys. Oceanogr.* **5**: 75–85.
- BUMPUS, D. F. 1969. Reversals in the surface drift in the Middle Atlantic Bight area. *Deep-Sea Res.* **16**(suppl.): 17–23.

- . 1973. A description of the circulation on the continental shelf of the east coast of the United States. *Prog. Oceanogr.* 6: 111-157.
- . 1976. Review of the physical oceanography of George's Bank. *Int. Comm. N. Atl. Fish. Res. Bull.* In press.
- , AND E. L. PIERCE. 1955. The hydrography and the distribution of chaetognaths over the continental shelf off North Carolina. *Deep-Sea Res.* 3(suppl.): 92-109.
- CHARNELL, R. L., AND D. V. HANSEN. 1974. Summary and analyses of physical oceanographic data collected in the New York Bight apex during 1969 and 1970. MESA Rep. 74-3. NOAA-ERL. 44 p.
- , AND D. A. MAYER. 1975. Water movement within the apex of the New York Bight during summer and fall of 1973. NOAA Tech. Memo. ERL MESA-3. 29 p.
- CRESSWELL, G. M. 1967. Quasi-synoptic monthly hydrography of the transition region between coastal and slope water south of Cape Cod, Massachusetts. Woods Hole Oceanogr. Inst. Tech. Rep. Ref. 67-35. 114 p.
- EG&G. 1975. Summary of oceanographic observations in New Jersey coastal waters near 39°28'N latitude and 74°15'W longitude during the period May 1973 through April 1974. Rep. B4424, EG&G Environ. Consultants, Waltham, Mass.
- FLAGG, C., J. VERMERSCH, AND R. BEARDSLEY. 1976. Report on the 1974 MIT New England shelf dynamics experiment, Part 2; the moored array. Dep. Meteorol. Mass. Inst. Technol., Lab. Rep. (Unpublished.)
- FORD, W. L., J. R. LONGARD, AND R. E. BANKS. 1952. On the nature, occurrence and origin of cold low salinity water along the edge of the Gulf Stream. *J. Mar. Res.* 11: 281-293.
- GORDON, A. L., A. F. AMOS, AND R. D. GERARD. 1976. New York Bight water stratification—October 1974. *Am. Soc. Limnol. Oceanogr. Spec. Symp.* 2: 45-57.
- HANSEN, D. V. 1970. Gulf Stream meanders between Cape Hatteras and the Grand Banks. *Deep-Sea Res.* 17: 495-511.
- HUGHES, P. 1975. The view from space. Environmental Data Service, January Bull., NOAA.
- ISELIN, C. O'D. 1939. Some physical factors which may influence the productivity of New England's coastal waters. *J. Mar. Res.* 2: 74-85.
- . 1955. Coastal currents and the fisheries. *Deep-Sea Res.* 3(suppl.): 474-478.
- KETCHUM, B. H., AND N. CORWIN. 1964. The persistence of "winter" water on the continental shelf south of Long Island, New York. *Limnol. Oceanogr.* 9: 467-475.
- , AND D. J. KEEN. 1955. The accumulation of river water over the continental shelf between Cape Cod and Chesapeake Bay. *Deep-Sea Res.* 3(suppl.): 346-357.
- PARKER, J. H., I. W. DUEDALL, H. B. O'CONNORS, JR., AND R. E. WILSON. 1976. Raritan Bay as a source of ammonium and chlorophyll *a* for the New York Bight apex. *Am. Soc. Limnol. Oceanogr. Spec. Symp.* 2: 212-219.
- POLLARD, R. T., AND R. C. MILLARD, JR. 1970. Comparison between observed and simulated wind-generated inertial oscillations. *Deep-Sea Res.* 17: 813-821.
- REID, R. O. 1958. Effect of Coriolis force on edge waves (I) investigation of the normal modes. *J. Mar. Res.* 16: 109-141.
- SAUNDERS, P. M. 1971. Anticyclonic eddies formed from shoreward meanders of Gulf Stream. *Deep-Sea Res.* 18: 1207-1219.
- SCHMITZ, W. J. 1974. Observations of low-frequency current fluctuations on the continental slope and rise near site D. *J. Mar. Res.* 32: 233-251.
- STOMMEL, H., AND A. LEETMAA. 1972. Circulation on the continental shelf. *Proc. Natl. Acad. Sci.* 69: 3380-3384.
- STURGES, W. 1974. Sea level slope along continental boundaries. *J. Geophys. Res.* 79: 825-830.
- SUTCLIFFE, W. H., R. LOUCKS, AND K. DRINKWATER. 1976. Considerations of ocean circulation and fish production on the Scotian Shelf and in the Gulf of Maine, Pt. 1. Ocean circulation and physical oceanography. *J. Fish. Res. Bd. Can.*, in press.
- THOMPSON, R. 1971. Topographic Rossby waves at a site north of the Gulf Stream. *Deep-Sea Res.* 18: 1-19.
- WEBSTER, F. 1969. Vertical profiles of horizontal ocean currents. *Deep-Sea Res.* 16: 85-98.
- WRIGHT, W. R. 1976. The limits of shelf water south of Cape Cod, 1941 to 1972. *J. Mar. Res.* 34: 1-14.
- , AND R. HENDRY. 1972. Array measurements of the bottom boundary layer and the internal wave field on the continental slope. *Geophys. Fluid Dynam.* 4: 101-145.
- , AND C. E. PARKER. 1976. A volumetric temperature/salinity census for the Middle Atlantic Bight. *Limnol. Oceanogr.* 21: 563-571.
- WUNSCH, C. 1972. Bermuda sea level in relation to tides, weather, and baroclinic fluctuations. *Rev. Geophys. Space Phys.* 10(1): 1-49.

Reprinted from: *NOAA Data Report ERL MESA-18*, 220 p.

#### ABSTRACT

During April 1974, two oceanographic cruises were made by the NOAA Ship *Researcher* in the New York Bight. The cruises were used for deployment and recovery of three bottom-mounted pressure gauges and to collect physical and chemical oceanographic data from the water column. Thirty-one oceanographic stations were occupied on a segment of the continental shelf bounded on the east by Block Island, on the south by Cape May, and extending outward to the edge of the continental shelf. This report presents the corrected water column data from these two cruises and describes the measurement methods and corrections applied to the data.

## A Two-dimensional Numerical Model of Estuarine Circulation: The Effects of Altering Depth and River Discharge

**John F. Festa and Donald V. Hansen**

*Atlantic Oceanographic and Meteorological Laboratories,  
15 Rickenbacker Causeway, Virginia Key, Miami, Fla 33149, U.S.A.  
Received 22 December 1974 and in revised form 25 June 1975*

---

Steady-state numerical solutions are obtained for a two-dimensional, vertically stratified model of a partially mixed estuary. The boundary at the seaward end of the estuary is considered to be open, with the profiles of salinity, vorticity and streamfunction obtained by extrapolating interior dynamics out to the boundary. A salinity source is maintained at the bottom at the mouth. Zero salt flux is required at a free-slip top and no-slip bottom boundary. Zero salinity and a parabolic velocity profile are maintained at the head of the estuary.

A number of cases are run for various estuarine parameters; the river transport and Rayleigh number being the two parameters that have the most pronounced effect. The river transport is varied by adjusting the mean freshwater velocity,  $U_f$ . Decreasing  $U_f$  allows salt as well as the stagnation or null point to penetrate upstream. The estuarine circulation weakens, but expands over a larger portion of the estuary. The position of the stagnation point, with respect to the seaward boundary, varies as  $U_f^{-5/8}$  for  $U_f > 1$  cm/s and as  $U_f^{-5/6}$  for  $U_f < 1$  cm/s. Increasing the Rayleigh number, by deepening the estuarine channel,  $H$ , results in an increased circulation as well as strong intrusion of salinity and inward migration of the stagnation point. The horizontal location of the stagnation point is found to be proportional to  $Ra$  and therefore, varies as  $H^3$ .

### Introduction

Estuaries are the part of the ocean most subject to modification, sometimes to enhance their commercial utility, sometimes as an unanticipated side effect of engineering works elsewhere in their watershed. One of the earliest, and still most common, modifications stems from the attractiveness of estuaries as sites for coastal cities and seaports. Most of the major seaports of the world consist of estuaries improved for large vessel navigation by dredging of entrance bars and channel deepening; however, undesired side effects have sometimes accompanied these improvements. Freshwater supplies on the Delaware River estuary are periodically threatened. Marine borers have invaded previously inhospitable regions in San Francisco Bay. Both of these have resulted from alteration of the salinity distribution as a consequence of channel deepening. The growth of urban areas on estuaries sometimes has more subtle effects. Filling bay marshes for development results in a reduction of the tidal prism, thus inhibiting natural water exchange and flushing processes. River flow modifications for agriculture, flood control or hydroelectric power generation have also had unpredicted

adverse downstream consequences due to alteration of the salinity distribution and circulation in the river estuary. The classic example of this type of misadventure was the diversion of Santee River water into the Cooper River in South Carolina. Readjustment of the estuarine circulation to the new dynamic regime resulted almost immediately in severe shoaling problems in Charleston Harbor. More subtle effects, such as the reduction of water exchange within estuarine embayments because of the regulation of seasonal peaks of river discharge, probably occur, but we know of no clear documentation of this effect.

Mathematical models have come into frequent use in estuaries, especially in application to problems of distribution of heat, salinity and solutes. Nearly all of these models are of the barotropic or vertically integrated numerical type. These are very useful for wave phenomena such as tides and tidal currents, or transports of solutes for which effective dispersion coefficients can be determined empirically. They are not well suited for predicting responses of circulation and salinity distributions to engineering modifications, because estuarine dynamics depend strongly upon the vertical structure of the circulation and stratification and their interaction. Baroclinic models in which vertical variations are retained have been presented by Rattray & Hansen (1962) and Hansen & Rattray (1965) by the method of similarity solutions. Although instructive as to the interpretation and generalization of physical processes observed in estuaries, these models are of limited utility in predicting responses to alterations. A characteristic feature of estuarine flows, the transition from estuarine to riverine dynamics is precluded by the mathematical constraints of the similarity approach.

In this paper we present some results from a two-dimensional, numerical model of the gravitational circulation within estuaries. The model is used to investigate effects of channel deepening and variation of stationary river discharge volumes on the circulation and salinity distribution in estuaries. Turbulent transports of salt and momentum are expressed by Fickian type diffusion coefficients. The vertical structure of circulation and stratification, and their interaction, are retained, in contrast to the model of Harleman *et al.* (1974) which has inconsistent modeling of density advection. A time-dependent version of the problem has been modeled by Hamilton (1975), but he seems not to have run the model long enough to ascertain that the circulation had come to equilibrium with the density field.

### Governing equations

The problem considered is that of a steady state, two-dimensional, laterally homogeneous estuary (Pritchard, 1956). The co-ordinate system is Cartesian in  $x$  and  $z$ , where  $z$  is positive upward and  $x$  increases toward the river. A linear equation of state,  $\rho = \rho_0(1 + \beta S)$ , is assumed and the Boussinesq approximation (Spiegel & Veronis, 1960) is employed.

The horizontal and vertical momentum balances, continuity of flow and conservation of salinity are:

$$u_t + uu_x + wu_z = -\rho_0^{-1}P_x + (A_h u_x)_x + (A_v u_z)_z, \quad (1a)$$

$$w_t + uw_x + ww_z = -\rho_0^{-1}P_z + (A_h w_x)_x + (A_v w_z)_z - \beta g S, \quad (1b)$$

$$u_x + w_z = 0, \quad (1c)$$

$$S_t + uS_x + wS_z = (K_h S_x)_x + (K_v S_z)_z. \quad (1d)$$

where  $u$  and  $w$  are the horizontal and vertical components of velocity respectively,  $P$  is the hydrostatically reduced pressure,  $S$  is the salinity field,  $\beta$  is the coefficient of 'salt contraction',  $\rho_0$  is the density of fresh water,  $A_h$ ,  $A_v$ , and  $K_h$ ,  $K_v$  are the horizontal and vertical exchange coefficients of momentum and salt, respectively, and  $g$  is the gravitational acceleration.

Tidal fluctuations have been averaged out; however, the tides are considered to be the primary source of energy for turbulent mixing. The exchange coefficients therefore represent a measure of the strength of tidal mixing. For simplicity, these coefficients are chosen to be constant.

The vorticity and salt equations corresponding to (1) are:

$$\eta_t = -\tilde{J}(\psi, \eta) + A_h \eta_{xx} + A_v \eta_{zz} - \beta g S_x, \quad (2a)$$

$$S_t = -\tilde{J}(\psi, S) + K_h S_{xx} + K_v S_{zz}. \quad (2b)$$

where  $\psi$  is a streamfunction with  $\vec{u} = \vec{i}\psi_x \hat{j}$  ( $\hat{j}$  being a unit vector in the  $+y$  direction),  $\eta = \Delta_2^2 \psi$  is the vorticity,  $\tilde{J}$  is the Jacobian and  $\Delta_2^2$  is the two-dimensional Laplacian operator.

Non-dimensional equations, corresponding to equation (2), are obtained by scaling  $t$  and  $\eta$  by  $\tau_d = H^2/K_v$  and  $\tau_d^{-1}$ , respectively,  $x$  and  $z$  by  $H$ ,  $\psi$  by  $K_v$  and  $S$  by  $\Delta S_h$ .  $\tau_d$  is the vertical diffusive time scale,  $H$  is the depth of the estuary, and  $\Delta S_h$  is the horizontal salinity difference between the river and mouth of the estuary. In non-dimensional form the vorticity and salt equations are:

$$\eta_t = -\tilde{J}(\psi, \eta) + \sigma(A\eta_{xx} + \eta_{zz} - RaS_x), \quad (3a)$$

$$S_t = -\tilde{J}(\psi, S) + KS_{xx} + S_{zz}, \quad (3b)$$

where  $\eta = \Delta^2 \psi = \psi_{xx} + \psi_{zz}$ ,  $Ra = \beta g \Delta S_h H^3 / (A_v K_v)$  is the estuarine Rayleigh number,  $\sigma = A_v / K_v$  is the Prandtl number,  $A = A_h / A_v$  and  $K = K_h / K_v$ . Non-dimensionalizing both horizontal and vertical distances by the estuarine depth,  $H$ , while arbitrary, forces an aspect ratio,  $\varepsilon = H/L$ , to enter only through the boundary conditions. Here,  $L$  is defined as the computational length of the model estuary, that is, the location of the upstream boundary. This length should not be confused with the dynamical length of the estuary,  $L_d$ , roughly equivalent to the extent of salinity intrusion. The determination of the dynamical length is a major object of analysis.

### Boundary conditions

The boundary conditions to be satisfied at the river end are zero salinity and a parabolic velocity profile (consistent with constant density and viscosity) having a transport per unit width  $T_r = U_f H$ , where  $U_f$  is the vertically averaged river flow per unit width. At the bottom boundary, a no-slip condition and zero vertical flux of salt are specified. At the top boundary, a free-slip condition and zero vertical flux of salt are specified. These are expressed by:

$$\begin{aligned} S = 0, \psi(z) = 1.5R(z^2 - z^3/3), \text{ and } \eta(z) = 3R(1-z) \text{ at } x = \varepsilon^{-1} \\ S_z = 0, \psi = 0 \text{ and } \psi_z = 0 \text{ at } z = 0, \\ S_z = 0, \psi = R \text{ and } \eta = 0 \text{ at } z = 1, \end{aligned} \quad (4)$$

where  $R = T_r / K_v$  is the non-dimensional river transport. Inclusion of non-zero wind stress at the surface is an easy modification to the model, but is not pursued herein. The remaining boundary conditions to be considered are those at the mouth of the estuary,  $x = 0$ . These are perhaps the most difficult part of the model and will be discussed at some length.

Estuaries empty either into a larger bay or directly onto a continental shelf (see Figure 1). They usually widen abruptly, allowing geometrical and rotational effects to become important. A two-dimensional model is no longer appropriate. To investigate estuarine dynamics in its simplest form, attention must be focussed landward of this outer region. The inshore limit of this region is herein considered to be the mouth of the estuary.

Salinity and velocity distributions at the mouth are functionally dependent upon river flow, depth, horizontal density difference and other parameters. The surface layers become

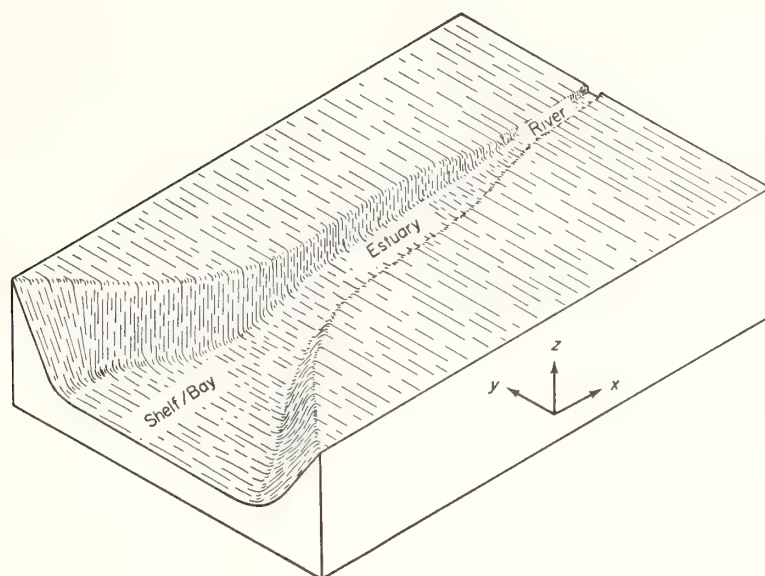


Figure 1. An idealized estuarine system.

fresher as the river transport increases. The estuarine circulation becomes stronger for increasing Rayleigh numbers. Consequently internal dynamics determine seaward boundary profiles as well as those within the estuary. The boundary conditions given at the seaward end of the model must be consistent with these internal dynamics. Thus, salinity and velocity profiles cannot be specified as boundary conditions. Preliminary numerical experiments support this result, since unrealistic seaward boundary layers occur where salinity and velocity profiles are specified as seaward boundary conditions. Experimentation also showed that unless a source of salt in the form of a definite salinity value is specified somewhere in the region, the solution  $S = 0$  is obtained. Observations suggest that, although the salinity distribution everywhere within estuarine regions is strongly influenced by variation of river discharge and other parameters, the salinity of the deep water near the seaward boundary is least influenced. We have therefore made salinity at the bottom of the seaward boundary invariant,  $S_{(0,0)} = 1$ , to assure estuarine behavior. In order to obtain the seaward boundary conditions, attention is focused on the dynamics near the estuarine mouth.

In the vicinity of the seaward boundary for the model it is expected that the estuarine circulation is relatively well developed. Pritchard (1954, 1956) has shown that in this situation the salt balance is maintained primarily by a dynamic balance between horizontal advection and vertical diffusion of salt and a vorticity balance is maintained primarily by a balance between buoyancy forces due to horizontal density gradients and vertical diffusion of vorticity. Horizontal diffusion of salt, especially, while shown by Hansen & Rattray (1965) to be essential to the overall estuarine regime, does not appear to be locally important where the gravitational circulation is well developed. In addition, horizontal diffusion of vorticity and horizontal shear in the vertical velocity field are also assumed to be locally unimportant. These conditions are:

$$\begin{aligned} S_{xx} &\doteq 0, \\ \eta_{xx} &\doteq 0, \text{ at } x = 0 \\ \psi_{xx} &\doteq 0. \end{aligned} \tag{5}$$

and

Thus, horizontal diffusive fluxes of salt and vorticity are required to be constant, but unspecified, at the open boundary. Although we are unable to provide a completely rigorous justification of these conditions, they do provide a means of completing the mathematical specification of the problem, without inducing boundary layer behavior near the seaward boundary.

### Numerical formulation and procedures

A finite-difference grid is chosen to be uniform in  $x$  and  $z$ , such that

$$\left. \begin{aligned} x_i &= i\Delta x, & i &= 0, 1, \dots, I \\ z_j &= j\Delta z, & j &= 0, 1, \dots, J \\ t^n &= n\Delta t, & n &= 0, 1, \dots \end{aligned} \right\} \quad (6)$$

where  $\Delta x = (\varepsilon I)^{-1}$ ,  $\Delta z = J^{-1}$  and  $\Delta t$  is the time step whose magnitude depends upon the stability of the differencing scheme that is chosen. The Laplacian operator is approximated by the usual five-point difference scheme. The advection of salt and vorticity, expressed in terms of the Jacobian,  $\tilde{y}$ , is approximated by using the  $\tilde{y}_2$  and  $\tilde{y}_3$  forms of Arakawa (1966), respectively. These conserve salinity and salinity squared and vorticity and kinetic energy. Diffusion is approximated by the time-centered scheme of DuFort-Frankel (1953). The resulting finite difference analogs to (3) are:

$$\begin{aligned} (\eta_{ij}^{n+1} - \eta_{ij}^{n-1})/(2\Delta t) &= -\tilde{y}_3^n(\psi, \eta)/(4\Delta x \Delta z) + \sigma \Delta x^{-2}(\eta_{i+1j}^n + \eta_{i-1j}^n - \eta_{ij}^{n+1} - \eta_{ij}^{n-1}) \\ &\quad + \sigma \Delta z^{-2}(\eta_{ij+1}^n + \eta_{ij-1}^n - \eta_{ij}^{n+1} - \eta_{ij}^{n-1}) \\ &\quad - \sigma Ra(S_{i+1i}^n - S_{i-1j}^n)/(2\Delta x), \end{aligned} \quad (7)$$

$$\begin{aligned} (S_{ij}^{n+1} - S_{ij}^{n-1})/(2\Delta t) &= -\tilde{y}_2^n(\psi, S)/(4\Delta x \Delta z) + K \Delta x^{-2}(S_{i+1j}^n + S_{i-1j}^n - S_{ij}^{n+1} - S_{ij}^{n-1}) \\ &\quad + \Delta z^{-2}(S_{ij+1}^n + S_{ij-1}^n - S_{ij}^{n+1} - S_{ij}^{n-1}). \end{aligned} \quad (8)$$

The streamfunction at the latest time step,  $\psi_{ij}^{n+1}$ , is calculated by means of a direct solution (Buzbee *et al.*, 1970) to the finite difference Poisson equation,

$$\eta_{ij}^{n+1} = \Delta x^{-2}(\psi_{i+1j}^{n+1} + \psi_{i-1j}^{n+1} - 2\psi_{ij}^{n+1}) + \Delta z^{-2}(\psi_{ij+1}^{n+1} + \psi_{ij-1}^{n+1} - 2\psi_{ij}^{n+1}). \quad (9)$$

In finite difference schemes, the size of the time increment,  $\Delta t$ , is often limited by two stability requirements. The first of these is the advective stability condition, the Courant-Freidricks-Lewy criterion, which requires that for a given grid spacing,  $\delta$ ,  $\Delta t V_m / \delta \leq 1$ , where  $V_m$  represents the maximum velocity of the fluid. The other condition, the diffusive stability criterion, requires  $\Delta t \leq \delta^2 / 8k$ , where  $k$  is a diffusion coefficient. This condition associated with most explicit difference schemes (Richtmyer & Morton, 1967), which would greatly limit the size of the time step in this particular model, is eliminated by using the DuFort-Frankel scheme. This scheme may produce spurious transient results if the time increment is much larger than the diffusive requirements; however, transient fluctuations are unimportant when steady-state solutions are desired. Comparisons between the DuFort-Frankel and the usual leapfrog (time and spatially centered) difference approximations indicate that the DuFort-Frankel scheme does produce similar steady-state solutions.

The salinity, streamfunction and vorticity fields are averaged periodically over adjacent time steps to hasten convergence and maintain computational stability. The fields are considered to represent steady-state solutions when the difference between the kinetic



energy, salinity and streamfunction fields at two adjacent time steps are less than 1% of the average kinetic energy, salinity and streamfunctions, respectively.

In all of the computations, the choice of a value for the model estuary length,  $L$ , or equivalently the aspect ratio,  $\varepsilon$ , depends upon the estuarine dynamics. The dynamical length of the estuary,  $L_d$  is parameter dependent, with  $L_d < L$ . For large river flows, as in the Columbia River, the dynamical length is small compared to the geomorphic length classically associated with this estuary, while for low river flows, such as that of the Delaware Estuary, they are likely to be of the same order. The location of the seaward boundary,  $x = 0$ , is fixed by assigning a bottom salinity value and thus determining  $\Delta S_b$ . The location of the river boundary,  $x = \varepsilon^{-1}$  and  $S = 0$ , is then adjusted for each experiment to effectively resolve the gravitational circulation, salinity intrusion and stagnation point. Thus,  $L$  is optimized to provide efficient use of the horizontal grid points. If  $L$  is too small, a smooth transition to the freshwater of the river will be prevented, since the upstream boundary will be too close to the mouth. If  $L$  is too large, there will be too few grid points to resolve the dynamics close to the estuary mouth. Initially,  $L$  is estimated at the beginning of a calculation and then is adjusted after a small number of iterations, if necessary.

### Initial conditions

Optimum initial fields are desired to shorten the time needed to reach a steady-state solution. In most cases the initial conditions were adapted from the similarity solution of Hansen & Rattray (1965)

$$\left. \begin{aligned} \psi_{ij} &= \psi_g(1 - \varepsilon x_i) + \psi_r, \\ \eta_{ij} &= \eta_g(1 - \varepsilon x_i) + \eta_r, \\ S_{ij} &= S_g(1 - \sin \frac{\pi \varepsilon x_i}{2}), \end{aligned} \right\} \quad (10)$$

where

$$\left. \begin{aligned} \psi_r &= 1.5R(z_j^2 - z_j^3/3), \\ \psi_g &= \nu Ra(-2z_j^4 + 5z_j^3 - 3z_j^2)/48, \\ \eta_r &= 3R(1 - z_j), \\ \eta_g &= \nu Ra(-4z_j^2 + 5z_j - 1)/8, \\ S_g &= 1 + \nu \left[ \frac{\nu Ra(-2z_j^5 + 6z_j^4 - 5z_j^3)/240}{+R(-z_j^4 + 4z_j^3 - z_j^2)/8} \right]. \end{aligned} \right\} \quad (11)$$

and where  $\nu$  is a function of  $Ra$ ,  $R$  and  $K$ .

### Finite difference boundary conditions

The computational grid is extended one grid point beyond the bottom, top and mouth of the estuary. This allows the finite difference representation of derivatives at the boundary to be consistent with interior computations. Values of  $S$ ,  $\psi$  and  $\eta$  outside the boundaries are defined as

$$\left. \begin{aligned} (1) \text{ Bottom } (j = 0) \\ S_{ij-1}^n &= S_{ij+1}^n; (S_z = 0), \\ \psi_{ij-1}^n &= \psi_{ij+1}^n; (u = 0). \\ (2) \text{ Top } (j = \mathcal{J}) \\ S_{ij+1}^n &= S_{ij-1}^n; (S_z = 0), \\ \psi_{ij+1}^n &= 2\psi_{ij}^n - \psi_{ij-1}^n; (u_z = 0). \\ (3) \text{ Mouth } (i = 0) \\ S_{i-1j}^n &= 2S_{ij}^n - S_{i+1j}^n; (S_{xx} = 0), \\ \psi_{i-1j}^n &= 2\psi_{ij}^n - \psi_{i+1j}^n; (\psi_{xx} = 0), \\ \eta_{i-1j}^n &= 2\eta_{ij}^n - \eta_{i+1j}^n; (\eta_{xx} = 0). \end{aligned} \right\} \quad (12)$$

Solutions at the boundaries are obtained by substituting these values into the difference equations, (7), (8) and (9). The bottom vorticity is evaluated using the first order Taylor series approximation developed by Bryan (1963):

$$\eta_{i0}^{n+1} = 2\psi_{i1}^{n+1}/\Delta z^2. \quad (13)$$

At the mouth of the estuary, a three point forward difference scheme for the salinity gradient,

$$S_x^n|_{i=0} \doteq (2\Delta x)^{-1}(-3S_{0j}^n + 4S_{1j}^n - S_{2j}^n), \quad (14)$$

is used in equation (7) to calculate vorticity boundary values. We double integrate the boundary vorticity field by means of a Gaussian-elimination procedure to calculate  $\psi$  at the seaward end of the estuary. Given  $\psi$  on all boundaries, we invert Poisson's equation to obtain the interior streamfunctions. Salinity and velocity profiles obtained by this method are slightly closer to the similarity solution than are those obtained by using the central difference representation of the salinity gradient. A third method, in which the boundary vorticity is simply extrapolated out from the interior,

$$\eta_{0j}^{n+1} = 2\eta_{1j}^{n+1} - \eta_{2j}^{n+1}, \quad (15)$$

also produces acceptable solutions.

Simple extrapolation, however, does not work well when calculating the salinity distribution at the mouth. We have found that simple smoothing produces significantly lower values for the salinity throughout the estuary. Smaller horizontal salinity gradients occur and as a consequence lower values of the streamfunction and velocity fields result throughout the interior. The full salinity equation (8) must therefore be used for the calculation at the open boundary.

### Discussion of results

Steady-state solutions to the model equation were obtained using a  $33 \times 33$ -point finite difference grid. Initially, a 17-point vertical resolution seemed adequate; however, tests with similarity solutions indicated that truncation errors may produce significant differences between analytical and numerical values of  $\psi$  and  $\eta$ .

Results of computations not included here showed that variations of  $A$  between 1 and  $10^6$ , and  $\sigma$  from 1 to  $10^2$  have a negligible effect upon the results. Prandtl number independence is common in thermal convection problems (Beardsley & Festa, 1972). Variation of  $K$  from 1 to  $10^7$  does produce significant change in the solutions, but this effect will not be fully explored here.

The model was run for a range of parameters characteristic of, or centered on, nominal values typical of coastal plain estuaries for which data have been published. These nominal values are  $\Delta S_h = 30\text{‰}$ ,  $K = 10^6$  ( $K_v = 1 \text{ cm}^2/\text{s}$ ),  $Ra = 3 \times 10^9$  ( $H = 10 \text{ m}$ ), and  $R = 2 \times 10^3$  ( $U_f = 2 \text{ cm/s}$ ).

Contours of the streamfunction and salinity distribution obtained are presented in Figures 3 and 8. The salinity distribution shows a stratified intrusion into the estuary, and the streamfunction shows the typically estuarine pattern of seaward flow of near surface water and a landward flow of deeper water.

The vertical component of flow is of considerable interest in connection with estuarine problems, but is not directly, or in many cases indirectly, measurable. It is of interest therefore, to explore the magnitude and structure of the vertical flow associated with the

conditions and parameter ranges of the model. The longitudinal variation of vertical velocity at three levels for  $H = 10$  m and  $U_t = 2$  cm/s is shown in Figure 2. The boundary conditions require the vertical flow to be identically zero on the top and bottom boundaries. Both the order of magnitude and the vertical structure of the vertical flow are consistent with the determination of vertical velocity in the James River estuary made by Pritchard (1954). The principal feature of this longitudinal variation is that at all levels a maximum occurs somewhat seaward of the stagnation point (intersection of the internal zero of the streamfunction with the bottom) and a rapid falloff across the position of the stagnation point.

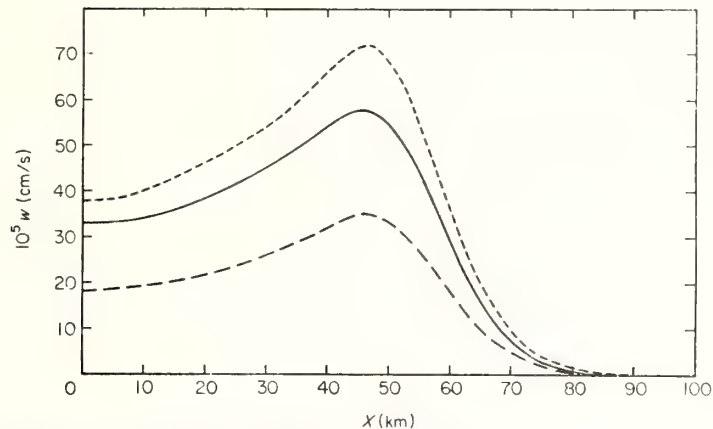


Figure 2. Longitudinal variations of the vertical velocity field at  $z = 0.25, 0.5$  and  $0.75$  for  $U_t = 2$  cm/s.  $Ra = 3 \times 10^9$  ( $H = 10$  m),  $\sigma = 10$ ,  $K = 10^6$ . Stagnation point is at  $x = 60$  km. ---,  $z = 0.50$ ; —,  $z = 0.75$ ; - · - ·,  $z = 0.25$ .

The model provides a mutually consistent system of salinity, advection and diffusion fields which can be used for investigation of a variety of kinematic problems of biological or geological origin in estuaries. Such applications will require (empirical) determination of the model parameters required to represent a particular estuary, and provide a vehicle for modelling biological or geochemical processes. Our focus here, however, is on the interactions of purely physical processes in estuaries.

#### *Influence of river discharge*

Effects of river discharge on the estuarine circulation and the salinity distribution are presented for  $Ra = 3 \times 10^9$  ( $H = 10$  m). The river transport parameter,  $R$ , is varied between  $5 \times 10^2$  and  $6 \times 10^3$ , corresponding to a range in  $U_t$  of  $0.5$  to  $6.0$  cm/s. Streamfunction and salinity distributions from this series of numerical experiments are shown in Figure 3. Both the stratification and the strength of the estuarine circulation increase with increased freshwater discharge. Vertical profiles of salinity and horizontal velocity, at the seaward end of the modelled region (Figure 4), where the estuarine circulation is well developed, are very similar to the solutions obtained by Hansen & Rattray (1965). The principal response to changes in volume of freshwater discharge occurs in the upper half of the water column. Velocity profiles contain a more or less invariant region near  $z = 0.4$ , below which velocity profiles differ little. Current measurements at this level, or elsewhere in the bottom half of the estuary, would be unable to discriminate between these profiles;

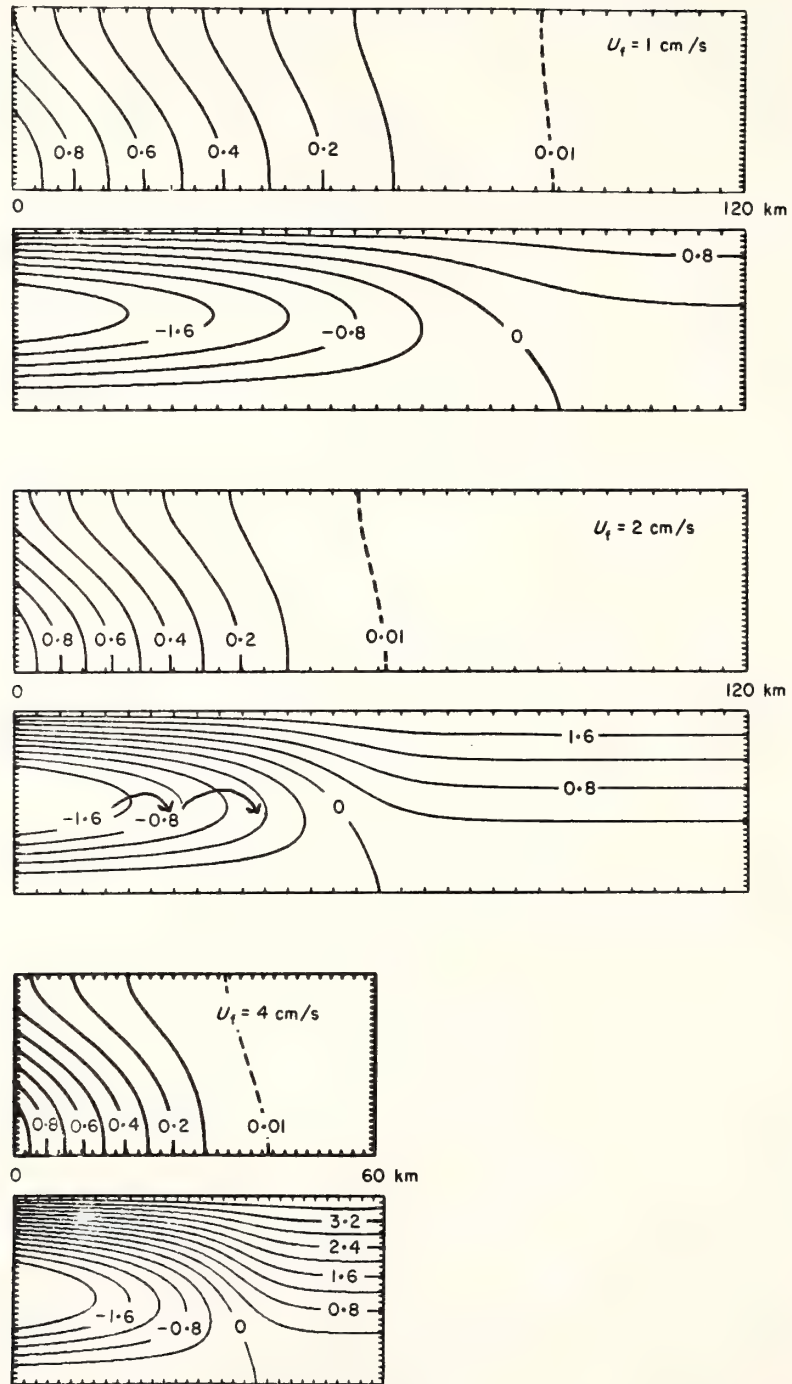


Figure 3. Salinity and streamfunction fields as a function of river flow,  $U_r$ . Salinity fields are contoured from 0 to 1 in intervals of 0.1. The streamfunction fields are scaled by  $10^3$  and contoured from 0 in intervals of 0.4.  $Ra = 3 \times 10^9$  ( $H = 10$  m),  $\sigma = 10$ ,  $K = 10^6$  ( $K_v = 1$  cm<sup>2</sup>/s).

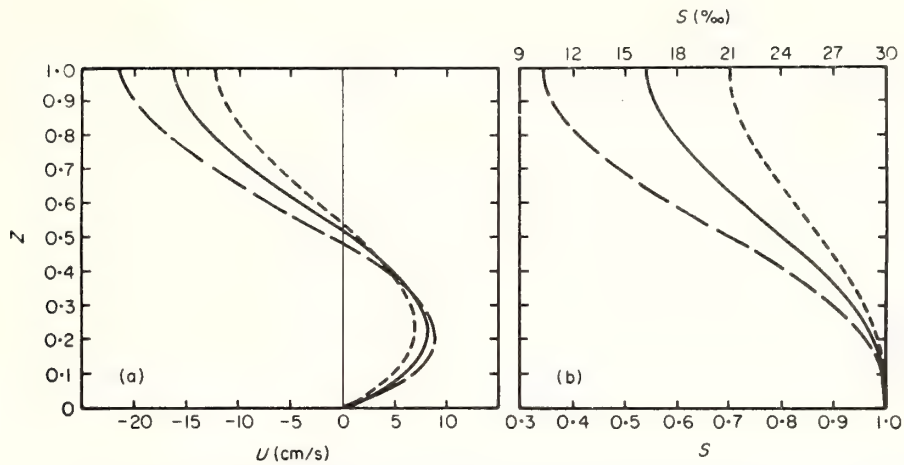


Figure 4. Variations of (a) velocity and (b) salinity profiles at the seaward boundary,  $x = 0$ , with river flow,  $U_r$ .  $U_r$  (cm/s): - - -, 1; —, 2; — · —, 4.

nevertheless, they are quite different overall. The total landward transport into the lower layer is almost independent of the amount of freshwater discharged. This is a somewhat surprising result, but may be due in part to making the bottom salinity at the seaward entrance independent of river flow. Upstream attenuation of the landward flow is considerably more rapid for larger river flows.

This model varies qualitatively from the similarity solutions in that the vertical profiles are not constrained to be similar throughout the estuary. Two features of particular interest are the length of the salinity intrusion into the estuary and the position of the stagnation point. The horizontal variations of salinity at the surface and at the bottom are shown in Figure 5. The longitudinal patterns are similar to the exponential forms given by Hansen & Rattray (1965), except that here we obtain what is not available as an analytic similarity solution: a complete transition to zero salinity. The length of the salinity intrusion, defined by the

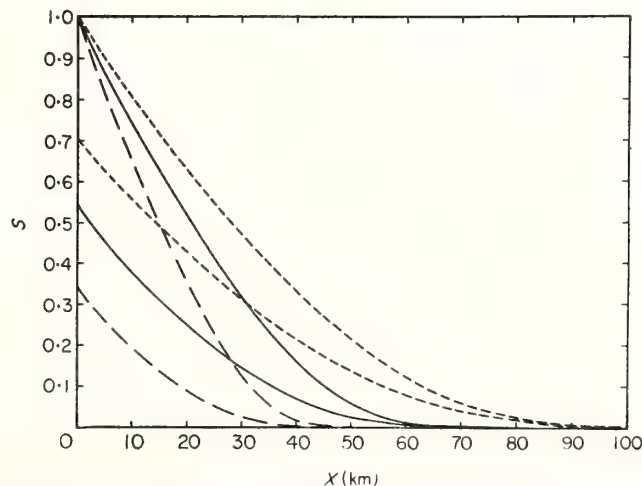


Figure 5. Longitudinal variations of surface and bottom salinity as a function of river flow,  $U_r$ .  $U_r$  (cm/s): - - -, 1; —, 2; — · —, 4.

distance over which  $S \geq 0.15\%$  at the bottom of the estuary, is a strong function of freshwater discharge. It increases from 44 km for  $U_f = 4$  cm/s to 170 km for  $U_f = 0.5$  cm/s as shown in Figures 5 and 6. This behavior has been empirically, if qualitatively, known to hydraulic engineers for many years. The functional form of the dependence of salinity intrusion upon freshwater discharge is of special interest because a characteristic value of  $U_f$  in coastal plain estuaries is approximately 1 cm/s. It is apparent from Figure 6 that for the values of other parameters used, the length of salinity intrusion changes behavior in the

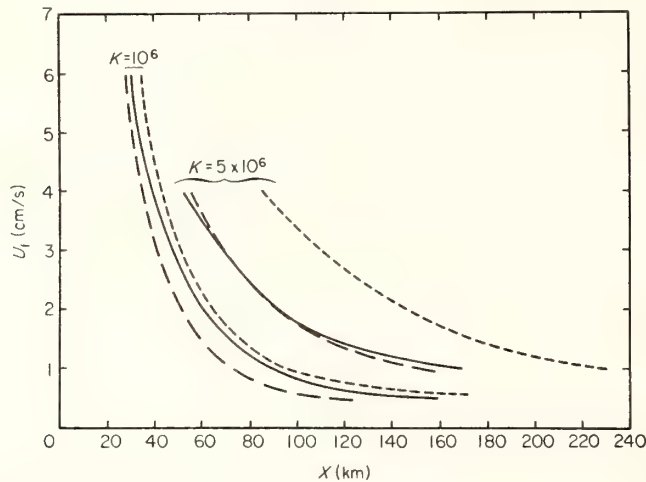


Figure 6. Influence of river runoff on salinity intrusion and stagnation point location. —,  $S = 0.05$ ; — —, stagnation point; - - -,  $S = 0.005$ .

vicinity of  $U_f = 1$  cm/s. Increases of  $U_f$  from 1 cm/s lead to modest retreat of salinity intrusion, but reductions of  $U_f$  result in greatly increased salinity intrusion. The implication of this non-linear relationship for reduction of freshwater discharge into already critical estuaries is fairly obvious. Within the range of values explored, the salinity intrusion varies approximately as  $U_f^{-4/7}$  for  $U_f > 1$  cm/s and as  $U_f^{-5/6}$  for  $U_f < 1$  cm/s.

The location of the stagnation point is closely related to the extent of salinity intrusion as may be seen from Figure 3. For  $U_f > 1$  cm/s, the position of the stagnation point varies approximately as  $U_f^{-5/8}$ , and as  $U_f^{-5/6}$  for  $U_f < 1$  cm/s. Its position is shown in Figure 5 to be bracketed by the (dimensional) salinity values 1.5‰ and 0.15‰ at the bottom. This result could be of great value to engineers, but it must be understood that the particular values obtained here are a function of the parameters used for these model runs. This fact is demonstrated also in Figure 6 by means of results from model runs using the same set of parameters except for  $K$ , which was increased by a factor of 5. Establishment of a criterion for the location of the stagnation point based on salinity intrusion, for particular estuaries in which good estimates of the exchange coefficients are obtainable, seems possible in principle. The exchange coefficients of course cannot be those inferred from application of a one-dimensional model to data.

Figure 7 shows contours of the vertical velocity field at mid-depth,  $z = 0.5$ , as a function of  $x$ , and  $U_f$ , for the range of parameters explored. Increasing river discharge results in an increase in the magnitude of the vertical velocity as well as a seaward displacement of its spatial maximum.

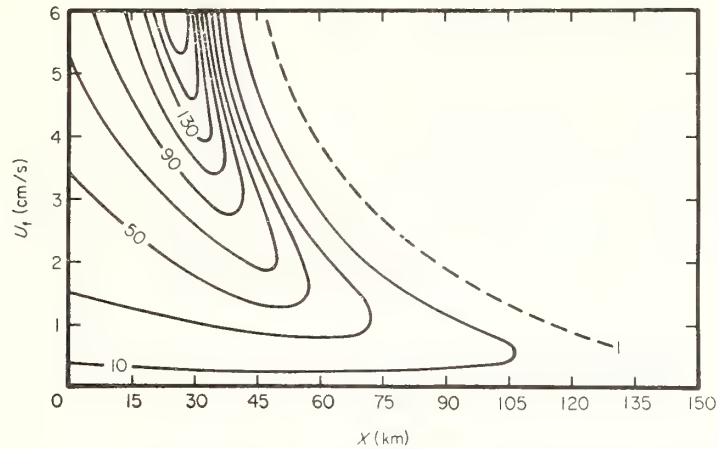


Figure 7. Vertical velocity contours at  $z = 0.5$  as a function of river discharge,  $U_r$ . Vertical velocity contours are scaled by  $10^{-6}$  cm/s with a contour interval of 20.

#### *Influence of depth*

Effects of the depth of an estuary on the estuarine circulation and salinity distribution are presented for a non-dimensional river discharge,  $R$ , of  $2 \times 10^3$ . The depth is varied from 7.5 to 12.5 m by varying the Rayleigh number,  $Ra$ , from  $1.3 \times 10^9$  to  $5.9 \times 10^9$  (this of course results in a variation of  $U_r$  inversely as the depth). Streamfunctions and salinity distributions are shown in Figure 8. Increasing the depth increases the strength of the gravitational circulation and results in greater salt penetration. The landward and seaward flow both increase with increasing depth, but their integral transport is constant and equal to the river discharge. Vertical profiles of salinity and horizontal velocity at the seaward boundary are shown in Figure 9. At the mouth, the speed of the seaward flow near the upper surface is a weak function of the depth of the estuary, but the landward flow is increased except very near the bottom. A current measurement within a meter of the top or the bottom would not discriminate between these profiles, although, to be sure, boundary layer phenomena are not well resolved here. In general, there is a striking difference between the responses of the vertical profiles, at the mouth, to depth and to freshwater discharge. Whereas changes in river discharge affect the horizontal velocity primarily in the top half of the water column, depth changes influence primarily the landward transport in the bottom half of the estuary.

The salinity stratification decreases with increasing depth. This result is attributable to the tendency for the greater horizontal current shear found in the shallower estuary to increase stratification as described by Hansen (1964).

The general effect of changing depth on the extent of salinity intrusion is inverse to that of river discharge. Salinity intrusion increases from 34 km for a depth of 7.5 m to 118 km for a depth of 12.5 m, as shown by Figures 8, 10 and 11. The position of the stagnation point in the circulation also has a similar behavior, as shown by Figures 8 and 11. As might be expected, the position of the stagnation point shows strong Rayleigh number dependence, varying very closely as  $H^3$ . Diffusive processes weaken the dependence of the salinity intrusion on Rayleigh number however, causing the length of salinity intrusion to vary approximately as  $H^{5/2}$ .

Figure 12 shows contours of the vertical velocity field at  $z = 0.5$  as a function of  $x$  and  $H$  for the range of parameters explored. Decreasing the depth of an estuary results in an

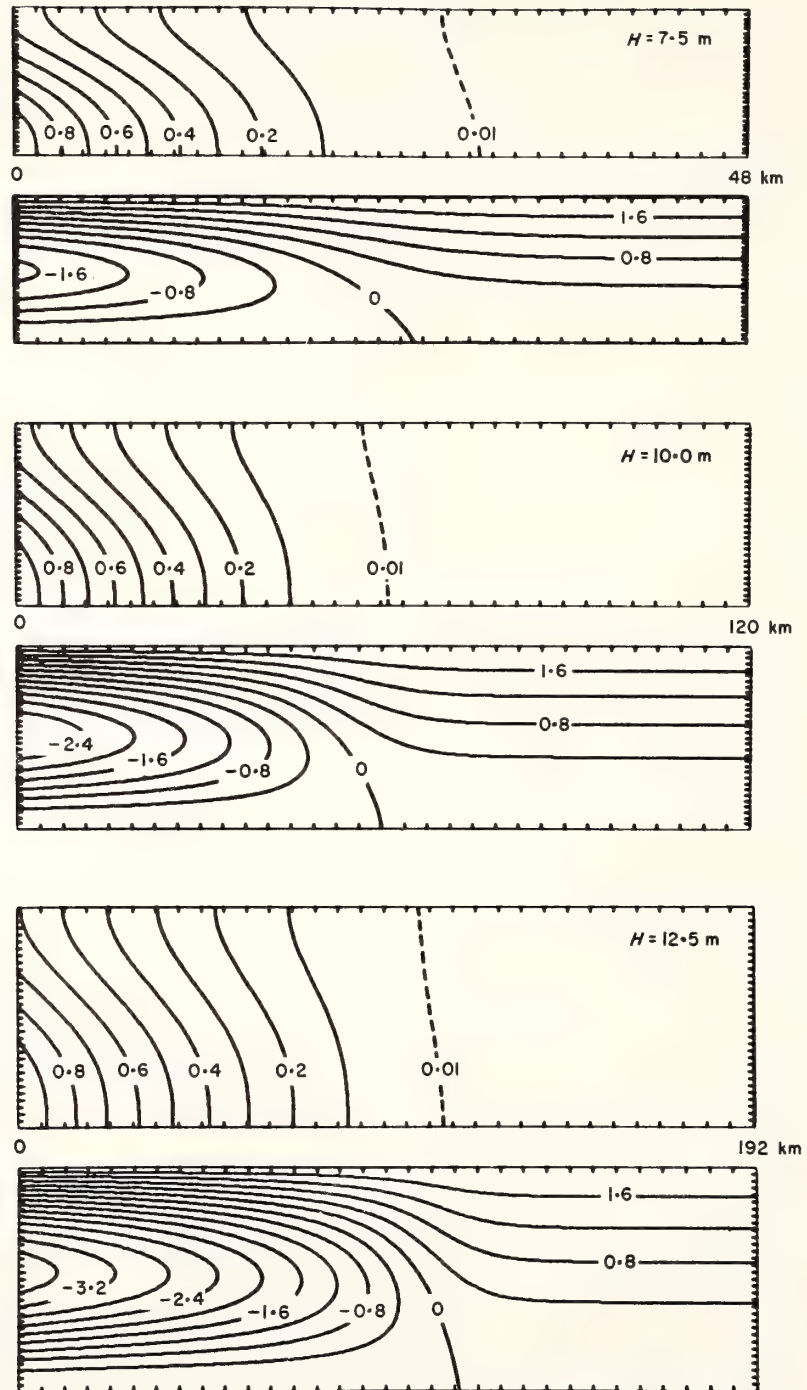


Figure 8. Salinity and streamfunction fields as a function of estuarine depth,  $H$ . Salinity fields are contoured from 0 to 1 in intervals of 0.1. The streamfunction fields are scaled by  $10^3$  and contoured from 0 in intervals of 0.4.  $R = 2 \times 10^3$ ,  $\sigma = 10$ ,  $K = 10^6$  ( $K_v = 1$  cm<sup>2</sup>/s).



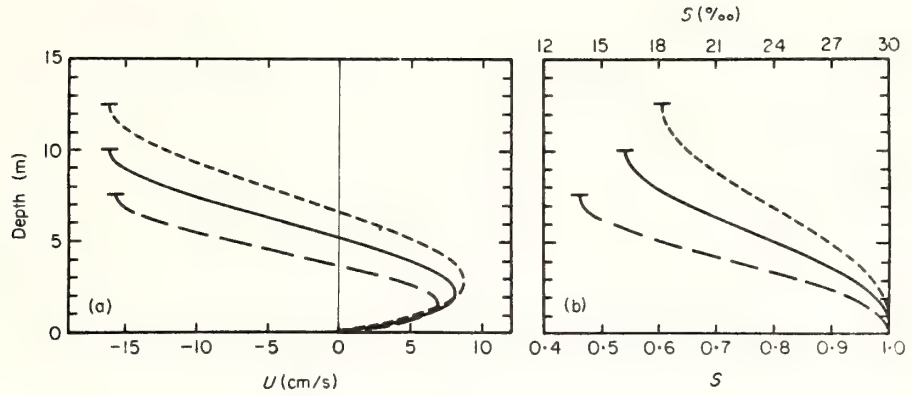


Figure 9. Variations of (a) velocity and (b) salinity profiles at the seaward boundary,  $x = 0$ , with depth,  $H$ .  $H$ : ---, 12.5 m; —, 10 m; — · —, 7.5 m.

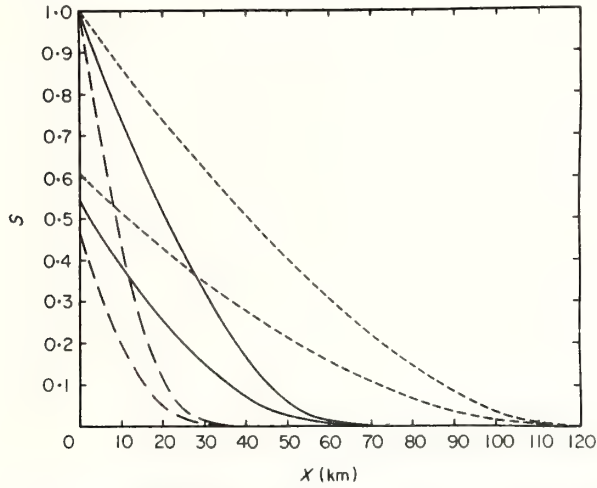


Figure 10. Longitudinal variations of surface and bottom salinity as a function of depth,  $H$ .  $H$ : — · —, 7.5 m; —, 10 m; ---, 12.5.

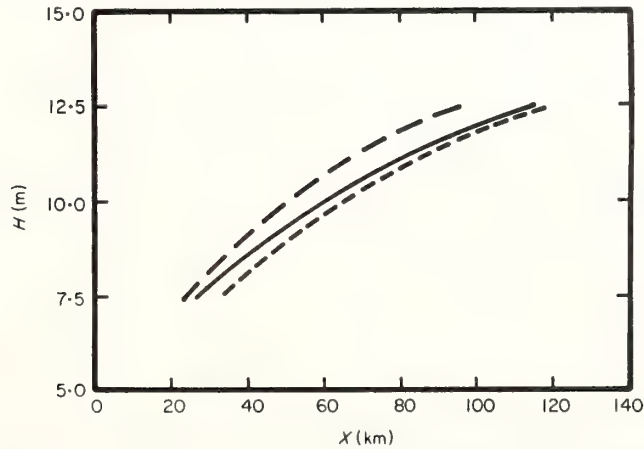


Figure 11. Influence of estuarine depth on salinity intrusion and stagnation point location. —,  $S = 0.05$ ; —, stagnation point; ---,  $S = 0.005$ .

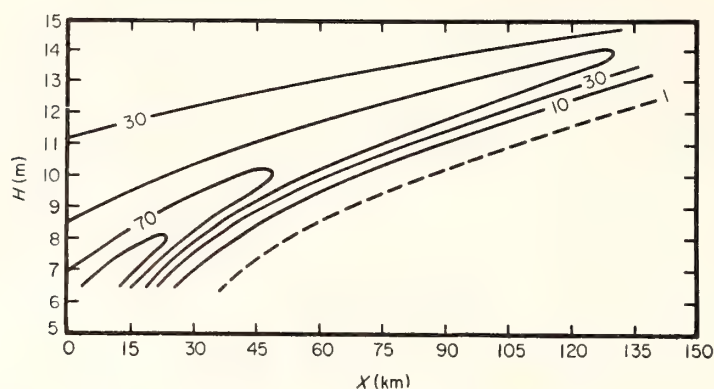


Figure 12. Vertical velocity contours at  $z = 0.5$  as a function of estuary depth,  $H$ . Vertical velocity contours are scaled by  $10^{-5}$  cm/s with a contour interval of 20.

increase in the magnitude of the vertical velocity as well as a seaward displacement of its spatial maximum.

The caveat regarding dependence of particular values upon the choice of values for the exchange coefficients used in the model must also be accepted here, but the general behavior will be unchanged.

### Acknowledgements

The progress of this research has benefitted from numerous discussions and criticism of the manuscript by Drs H. Mofjeld, A. Leetmaa and C. Thacker. The manuscript was prepared by Ms K. Philips.

### References

- Arakawa, A. 1966 Computational design for long-term numerical integration of the equations of fluid motion. Two-dimensional incompressible flow. Part 1. *Journal of Computational Physics* **1**, 119-143.
- Beardsley, R. C. & Festa, J. F. 1972 A numerical model of convection driven by a surface stress and non-uniform horizontal heating. *Journal of Physical Oceanography* **2**, 444-455.
- Bryan, K. 1963 A numerical investigation of a non-linear model of a wind-driven ocean. *Journal of Atmospheric Science* **20**, 594-606.
- Buzbee, B. L., Golub, G. H. & Nielson, C. W. 1970 On direct methods for solving Poisson's equations. SIAM. *Journal of Numerical Analysis* **7**, 627-656.
- DuFort, E. C. & Frankel, S. P. 1953 Stability conditions in the numerical treatment of parabolic differential equations. *Mathematical Tables and other Aids to Computation* **7**, 135.
- Hamilton, P. 1975 A numerical model of the vertical circulation of tidal estuaries and its application to the Rotterdam Waterway. *Geophysical Journal of the Royal Astronomical Society* **40**, 1-22.
- Hansen, D. V. 1964 Salt balance and circulation in partially mixed estuaries. *Proceedings from the Conference on Estuaries, Jekyll Island*.
- Hansen, D. V. & Rattray, M. Jr 1965 Gravitational circulation in straits and estuaries. *Journal of Marine Research* **23**, 104-122.
- Harleman, D. R. F., Fisher, J. S. & Thatcher, M. L. 1974 Unsteady salinity intrusion in estuaries. *Technical Bulletin No. 20*, U.S. Army Corps of Engineers.
- Pritchard, D. W. 1954 A study of the salt balance in a coastal plain estuary. *Journal of Marine Research* **13**, 133-144.
- Pritchard, D. W. 1956 The dynamic structure of a coastal plain estuary. *Journal of Marine Research* **15**, 33-42.
- Rattray, M. Jr & Hansen, D. V. 1962 A similarity solution for circulation in an estuary. *Journal of Marine Research* **20**, 121-123.
- Richtmyer, R. D. & Morton, K. W. 1967 *Difference Methods for Initial-value Problems*. 405 pp. Interscience, New York.
- Spiegel, E. A. & Veronis, G. 1960 On the Boussinesq approximation for a compressible fluid. *Astrophysics Journal* **131**, 442-447.

## Radiative transfer: a technique for simulating the ocean in satellite remote sensing calculations

Howard R. Gordon

A method is presented for computing the radiative transfer in the ocean-atmosphere system which does not require detailed knowledge of the optical properties of the ocean. The calculation scheme is based on the observation that the upwelling radiance just beneath the sea surface is approximately uniform, which implies that the effect of the ocean can be simulated by a lambertian reflector just beneath the sea surface. It is further shown that for aerosol concentrations up to ten times the normal concentration, the radiative transfer in homogeneous and vertically stratified atmospheres (of the same optical thickness) is nearly identical. Examples indicating the applicability of these results to the remote sensing of ocean color from space are discussed in detail.

### Introduction

It is now well established that the upwelling light field above the oceans can contain significant information concerning the oceanic concentration of sediments and organic material. However, when the oceans are viewed from satellite altitudes, the increased radiance due to the intervening atmosphere has made quantitative interpretation (in terms of oceanic properties) of the radiance observed by the satellite difficult. We can realize the full potential of oceanic remote sensing from space in the visible portions of the spectrum only if we can learn to relate the radiance which reaches the top of the atmosphere to the optical properties of the ocean. To effect this, the radiative transfer equation must be solved for the ocean-atmosphere system with collimated flux incident at the top of the atmosphere. In such calculations, the optical properties of the ocean which must be varied are the scattering phase function  $P_0(\theta)$  and the single scattering albedo  $\omega_0$  (defined as the ratio of the scattering coefficient to the total attenuation coefficient). Furthermore, unless the ocean is assumed to be homogeneous, the influence of vertical structure in these properties must be considered. To describe the cloud-free atmosphere, we must know the optical properties of the aerosols and their variation with wavelength and altitude as well as the ozone concentration. Considering the ocean for the present to be homogeneous, we can relate the radiance

at the satellite to the ocean's properties by choosing an atmospheric model and solving the transfer equation for several oceanic phase functions and  $\omega_0$ 's at each wavelength of interest. The number of separate computational cases required is then the product of the number of phase functions, the number of values of  $\omega_0$ , and the number of wavelengths. Even if the multiphase Monte Carlo method (MPMC)<sup>1</sup> is used, the  $\omega_0$  resolution of Gordon and Brown<sup>2</sup> would require a number of simulations equal to ten times the number of wavelengths for each atmospheric model considered. In this paper an alternate method of computation that does not require detailed knowledge of the ocean's optical properties is presented.

### Calculations

From the work of Plass and Kattawar<sup>3,4</sup> on radiative transfer in the ocean atmosphere system, it is seen that when the solar zenith angle is small, the upwelling radiance just beneath the sea surface is approximately uniform (i.e., not strongly dependent on viewing angle) and hence determined by the upwelling irradiance. It is possible for remote sensing purposes to utilize this observation in simulations of the transfer of radiation in the ocean-atmosphere by assuming that a fraction  $R$  of the downwelling photons just beneath the sea surface are reflected back toward the surface with a uniform radiance distribution, while the rest of the downwelling photons are absorbed. The ocean is then treated as if there were a lambertian reflecting surface of albedo  $R$  just beneath the sea surface. In this case, Gordon and Brown<sup>5</sup> have shown that any radiometric quantity  $Q$  can be written

$$Q = Q_1 + [Q_2 R / (1 - rR)], \quad (1)$$

where  $Q_1$  is the contribution to  $Q$  from photons that

The author is with University of Miami, Physics Department, and Rosenstiel School of Marine & Atmospheric Sciences, Coral Gables, Florida 33124.

Received 20 December 1975.

Table I. Three Ocean Scattering Phase Functions

$\theta$ (deg)	KA ( $\times 10^2$ )	KB ( $\times 10^3$ )	KC ( $\times 10^2$ )
0	10924	10171	9521
1	4916	4577	4285
5	573.5	534.0	499.9
10	169.3	157.7	147.6
20	29.5	29.39	29.31
30	12.56	11.95	11.42
45	3.059	3.661	4.189
60	1.092	1.577	1.999
75	0.546	0.915	1.190
90	0.341	0.661	0.952
105	0.311	0.641	0.928
120	0.317	0.732	1.094
135	0.410	0.829	1.309
150	0.492	1.017	1.618
165	0.579	1.261	1.856
180	0.617	1.357	1.999

never penetrate the sea surface (but may be specularly reflected from the surface),  $Q_2$  is the contribution to  $Q$  from photons that interact with the hypothetical lambertian surface once for the case  $R = 1$ , and  $r$  is the ratio of the number of photons interacting with the lambertian surface twice to the number of interacting once, again for  $R = 1$ . Using Eq. (1) any radiometric quantity can then be computed as a function of  $R$ . Physically the quantity  $R$  is the ratio of upwelling to downwelling irradiance just beneath the sea surface and is known as the reflectance function<sup>6</sup> [ $R(0,-)$ ] in the ocean optics literature. Spectral measurements of the reflectance function  $R(\lambda)$  have been presented for various oceanic areas by Tyler and Smith.<sup>7</sup> Henceforth in this paper  $R(\lambda)$  will be referred to as the ocean color spectrum.

A series of Monte Carlo computations has been carried out to see if an approximate simulation (AS1) using this assumption of uniform upwelling radiance beneath the sea surface yields results that agree with computations carried out using an exact simulation (ES) in which the photons are accurately followed in the ocean as well as the atmosphere. The Monte Carlo codes used in Refs. 2 and 5 were modified by the addition of an atmosphere. The atmosphere consisted of fifty layers and included the effects of aerosols, ozone, and Rayleigh scattering, using data taken from the work of Elterman.<sup>8</sup> The aerosol scattering phase functions were computed by Fraser<sup>9</sup> from Mie theory assuming an index of refraction of 1.5 and Deirmendjian's<sup>10</sup> haze  $C$  size distribution. Also, to determine the extent to which the vertical structure of the atmosphere influences the approximate simulation, a second approximate simulation (AS2) was carried out in which the atmosphere was considered to be homogeneous, i.e., the aerosol scattering, Rayleigh scattering, and ozone absorption were independent of altitude. The oceanic phase functions in the ES are based on Kullenberg's<sup>11</sup> observations in the Sargasso Sea and are given in Table I.  $KA$  is roughly an average of Kullenberg's phase function at 632.8 nm and 655 nm, and  $KC$  is his phase function at 460 nm.  $KB$  is an average of  $KA$  and  $KC$ . These phase functions show considerably less scattering at very small

angles  $\theta < 1^\circ$  than observed by Petzold<sup>12</sup> in other clear water areas; however, the exact form of the oceanic phase function is not very important, since it has been shown<sup>13</sup> to influence the diffuse reflectance and  $R(0,-)$  only through the backscattering probability ( $B$ )

$$B = 2\pi \int_{\pi/2}^{\pi} P_0(\theta) \sin\theta d\theta.$$

In all the computations reported here, the solar beam is incident on the top of the atmosphere from the zenith with unit flux. At visible wavelengths, the variable atmospheric constituent that will most strongly influence the radiance at the top of the atmosphere is the aerosol concentration. (Plass and Kattawar<sup>14</sup> have shown that for the range of expected variation of the ozone concentration, the radiance at 700 nm is essentially independent of the concentration.) Thus, we have carried out computations for aerosol concentrations in each layer of one, three, and ten times the normal concentration given by Elterman. These aerosol models are henceforth labeled  $N$ ,  $3 \times N$  and  $10 \times N$ . All computations presented here are carried out at 400 nm, the wavelength in the visible portion of the spectrum where the atmospheric effects are expected to be most severe.

Results

A sample of the results is given in Table II where the upward flux at the top of the atmosphere for the AS cases is compared with the ES case for oceanic phase function  $KC$  and  $\omega_0 = 0.8$ . The values of  $R$  used to effect the AC computations were taken from the EC computation of this quantity; however, if  $R$  is taken from

$$R = 0.0001 + 0.3244x + 0.1425x^2 + 0.1308x^3, \quad (2)$$

where  $x = \omega_0 B / [1 - \omega_0(1 - B)]$  which, according to Gordon *et al.*,<sup>15</sup> reproduces the in-water reflection function for the corresponding case, but with no atmosphere present, the results of the AS computations agree with those listed to within 0.2%. The numbers in the parenthesis next to each flux value represent the statistical error in the flux based on the actual number of photons collected in each case. It is seen that ES and AS simulations generally agree to within the accuracy of the computations. Notice also the excellent agreement between the AS1 and AS2 fluxes.

In Fig. 1 the comparison between the ES, AS1, and AS2 upward radiances at the top of the atmosphere is presented for the three aerosol models. The steplike curve in the figure is for ES, the solid circles for AS1, and the open circles for AS2, and  $\mu$  is the cosine of the

Table II. Comparison of the Flux at the Top of the Atmosphere for the ES, AS1, and AS2 Simulations

Aerosol concentration	Model		
	ES	AS1	AS2
$N$	0.222 (+0.002)	0.224 (+0.001)	0.226 (+0.001)
$3 \times N$	0.274 (+0.003)	0.273 (+0.001)	0.275 (+0.001)
$10 \times N$	0.423 (+0.004)	0.426 (+0.002)	0.425 (+0.002)

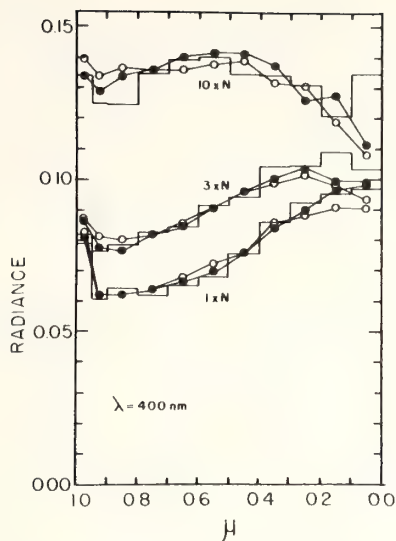


Fig. 1. Comparison between ES (steplike curve), AS1 (solid circles), and AS2 (open circles) upward radiances at the top of the atmosphere for an ocean with  $\omega_0 = 0.8$  and phase function  $KC$  and an atmosphere with a normal ( $1 \times N$ ), three times normal ( $3 \times N$ ), and ten times normal ( $10 \times N$ ) aerosol concentration.

angle between the nadir and the direction toward which the sensor is viewing. The radiances in Fig. 1 for the ES cases are accurate to about 3% in the  $\mu = 1$  to about 0.4 range, while for the AS cases the accuracy is about 1%. It is seen that again, to within the accuracy of the computations, the three simulations agree for all the aerosol concentrations except within the  $\mu = 0$  to about 0.3 range, i.e., viewing near the horizon. It is felt that these computations demonstrate that the transfer of the ocean color spectrum through the atmosphere can be studied with either the AS1 or AS2 model as long as radiances close to the horizon are not of interest. Furthermore, from the reciprocity principle,<sup>16</sup> the nadir radiance, when the solar beam makes an angle  $\theta_0$  with the zenith, can be found by multiplying the radiance  $I(\mu)$  in Fig. 1 by  $\mu$  where  $\mu$  is taken to be  $\cos\theta_0$ . This implies that as long as the sun is not too near the horizon, the AS1 and AS2 methods of computation can be used to determine the nadir radiance at the top of the atmosphere as a function of the ocean's properties through Eq. (2). The fact that the AS2 model (homogeneous atmosphere) yields accurate radiances is very important in remote sensing since it implies that only the total concentration (or equivalently the total optical thickness) of the aerosol need be determined to recover the ocean color spectrum from satellite spectral radiometric data. In principle, as suggested by Curran,<sup>17</sup> this can be accomplished by observing the ocean (assumed free of white caps) in the near ir where  $R(\lambda) \cong 0$ .

It should be pointed out that these results also strongly suggest that  $R(\lambda)$  is the quantity relating the subsurface conditions that can be quantitatively determined from space and hence is the most natural definition of the ocean color spectrum. Moreover, it has

been shown<sup>15</sup> that  $R(\lambda)$  is not a strong function of the solar zenith angle [the maximum variation in  $R(0,-)$  with  $\theta_0$  is of the order of 15% for  $0 < \theta_0 \leq 60^\circ$ ] in contrast with other definitions.<sup>17,18</sup> Of course any attempt to relate satellite measurements to subsurface conditions must be through an understanding of how the concentrations of suspended material, dissolved organic material, chlorophyll, etc. influence  $R(\lambda)$  or more fundamentally influence  $\omega_0(\lambda)$  and  $B(\lambda)$ .

#### Application: Minimum Detectable Change in $R$

As an example of the application of AS1 to oceanic remote sensing, we compute the minimum change  $\Delta R$  in  $R$  at 400 nm, which can be detected with a sensor of given sensitivity, or conversely specify the sensor sensitivity required to detect a given change in  $R$ . Applying Eq. (1) to the radiance  $I(\mu)$  at the top of the atmosphere with the sun at the zenith, we have

$$I(\mu) = I_1(\mu) + \{[RI_2(\mu)]/(1 - rR)\}. \quad (3)$$

$I_1(\mu)$  and  $I_2(\mu)$  are presented in Figs. 2 and 3, respectively, for the three aerosol models discussed above as well as an aerosol-free model ( $0 \times N$ ) and a model with seven times the normal aerosol concentration ( $7 \times N$ ). Now  $I_1(\mu)$  and  $I_2(\mu)$  depend only on the direction of the incident solar beam, the properties of the atmosphere, and ocean surface, but not on  $R$ , so if we assume these latter properties remain essentially constant over horizontal distances large compared to those over which  $R$  changes significantly, we can directly relate changes in  $I(\mu)$  to changes in  $R$ . Noting that in general  $R \leq 0.1$ , we have

$$[\partial I(\mu)]/(\partial R) \approx I_2(\mu). \quad (4)$$

Figure 3 shows that  $\partial I/\partial R$  is not an extremely strong function of the aerosol concentration for concentrations

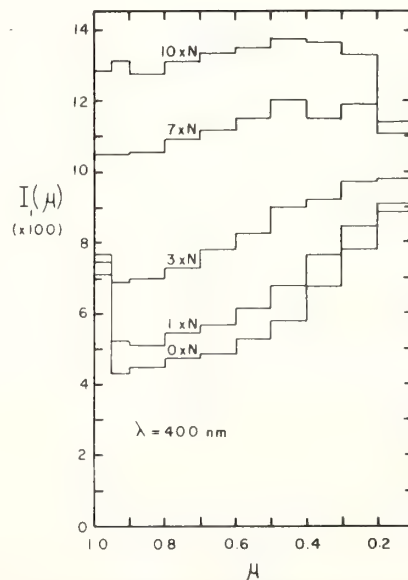


Fig. 2.  $I_1(\mu)$  as a function of  $\mu$  for various aerosol concentrations.

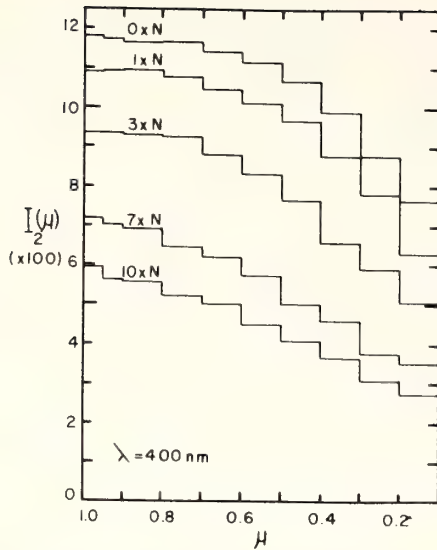


Fig. 3.  $I_2(\mu)$  as a function of  $\mu$  for various aerosol concentrations.

up to three times normal and viewing angles up to  $35^\circ$  from nadir. This suggests that horizontal gradients in  $R$  can be estimated without knowing the aerosol optical thickness with great accuracy.

We can now use Eq. (4) to relate changes in radiance  $\Delta I(\mu)$  to changes in  $R(\Delta R)$ , i.e.,

$$\Delta I(\mu) = [-I(\mu)/R]\Delta R \approx I_2(\mu)\Delta R \quad (5a)$$

Equation (5a) enables one to determine the minimum radiance change the sensor must be able to detect for a given  $\Delta R$ . For example, suppose that observing at  $\mu = 0.85$  it is desired to detect a 5% change in  $R$  for clear ocean water at 400 nm ( $R \approx 0.1$ ) through an atmosphere with three times the normal aerosol concentration. Figure 3 shows that  $I_2(0.85)$  is about 0.092, and noting that the extra terrestrial flux at 400 nm is about  $140 \mu\text{W}/\text{cm}^2 \text{ nm}$ , we find from Eq. (4) that  $\Delta I(0.85)$  is  $0.064 \mu\text{W}/\text{cm}^2 \text{ nm sr}$ . In a similar way we can relate radiance changes to  $\Delta R$  for a nadir viewing sensor and any solar zenith angle. As mentioned previously from the reciprocity principle,  $I_{\text{nadir}} = I(\mu_0)\mu_0$ , where  $\mu_0 = \cos\theta_0$ ,  $\theta_0$  is the solar zenith angle, and  $I(\mu_0)$  is the radiance at the top of the atmosphere seen by a sensor viewing at  $\mu_0$  when the sun is at the zenith. Following through with the same arguments that led to Eq. (5a), we find

$$\Delta I_{\text{nadir}} = \mu_0[-I(\mu_0)/R]\Delta R \approx \mu_0 I_2(\mu_0)\Delta R \quad (5b)$$

Clearly, for a given  $\Delta R$ ,  $\Delta I_{\text{nadir}}$  decreases substantially with increasing solar zenith angle due to the presence of the  $\mu_0$  factor in Eq. (5b). For example, with a three times normal aerosol concentration, a nadir viewing sensor would have to have about 2.5 times more sensitivity at  $\theta_0 = 60^\circ$  as compared to  $\theta_0 \approx 0$  to detect the same  $\Delta R$ .

The above examples indicate how ASI can be used in the design of a satellite sensor system for estimating some ocean property such as the concentration of sus-

pended sediments or organic material. Specifically, one must first determine the effect of the property to be investigated on  $R$ , then, based on the sensitivity desired, find  $\Delta R$ , and, finally, use Eqs. (5a) or (5b) to find the minimum radiance change the sensor must be capable of detecting. If the sensor has a limited dynamic range, Eq. (3) can be used with Eqs. (5a) or (5b) to aid in the sensor performance design tradeoffs. Unfortunately at this time relationships between  $R(\lambda)$  and sea water constituents are not well established.

## Conclusions

It has been shown that the upward radiance at the top of the atmosphere can be accurately computed by assuming the radiation entering the ocean is diffusely reflected from a hypothetical lambertian surface (beneath the ocean surface) of albedo  $R(0,-)$ . This leads to the natural definition of  $R(\lambda)$  [ $R(0,-)$  as a function of wavelength] as the ocean color spectrum. The determination of subsurface oceanic properties from space can thus be divided into two problems: (1) the determination of  $R(\lambda)$  from satellite radiance measurements and (2) the establishment of relationships between  $R(\lambda)$  and the desired ocean properties. Since the method of computation conveniently separates the radiance into a component that interacts with the ocean ( $I_2$ ) and a component due to reflection from the atmosphere and sea surface ( $I_1$ ), it is easy to relate changes in radiance to changes in  $R(\lambda)$ . It was found that for viewing angles up to  $35^\circ$  from nadir,  $I_2$  is a relatively weak function of the aerosol concentration for concentrations up to three times normal. This suggests that spatial gradients of  $R(\lambda)$  can be determined with only a rough estimate of the aerosol concentration.

Presently, computations are being extended to several wavelengths in the visible and near ir portions of the spectrum. When these are complete, it will be possible to determine the radiance for any  $R(\lambda)$  and perhaps point the way toward recovering  $R(\lambda)$  from satellite radiances.

The author is also affiliated with NOAA Atlantic Oceanographic and Meteorological Laboratories, Physical Oceanography Laboratory, Miami, Florida 33149.

## Appendix: Influence of Aerosol Phase Function on $I_1$ and $I_2$

It is natural to inquire how strongly the computations of  $I_1(\mu)$  and  $I_2(\mu)$  presented in Figs. 2 and 3 depend on the shape of the aerosol phase function. To effect a qualitative understanding of the influence of the aerosol phase function, computations of  $I_1$  and  $I_2$  have been carried out using the well known Henyey-Greenstein (HG) phase function,

$$P_{\text{HG}}(\theta) = \frac{(1-g^2)/4\pi}{(1+g^2-2g\cos\theta)^{3/2}}$$

where the asymmetry parameter  $g$  is defined according to

$$g = 2\pi \int_0^\pi P(\theta) \cos\theta \sin\theta d\theta,$$

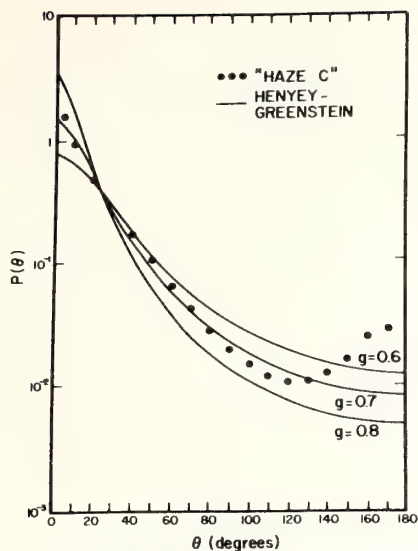


Fig. 4. Comparison between the haze C and various Henyey-Greenstein phase functions characterized by asymmetry parameters 0.6, 0.7, and 0.8.

and  $\theta$  is the scattering angle. Since  $g$  for the haze C phase function used in the computations described in the text is 0.690, computations have been made with  $P_{HG}(\theta)$  for  $g$  values of 0.6, 0.7, and 0.8. Figure 4 compares these  $P_{HG}(\theta)$ 's with the haze C phase function. The HG phase function for  $g = 0.7$  clearly fits the haze C phase function quite well in the range of  $5^\circ \leq \theta \leq 140^\circ$ ; however, as is well known, the HG formula is incapable of reproducing phase functions computed from Mie theory in the extreme forward and backward directions. The HG phase functions with asymmetry parameter 0.6 and 0.8 are seen to be substantially different from the haze C distribution at nearly all scattering angles. On the basis of Fig. 4, it should be expected that  $I_1$  and  $I_2$  computed with  $P_{HG}(\theta)$  will be in close agreement with the haze C computations only for  $g$  close to 0.7. Figures 5 and 6, which compare the results of computations of  $I_1$  and  $I_2$ , respectively, for  $P_{HG}(\theta)$  with  $g = 0.6, 0.7, 0.8$  (steplike lines) and the haze C phase function (solid circles) for the normal aerosol concentration, show that this is indeed the case. It is seen that except for apparent statistical fluctuations, the HG phase function for  $g = 0.7$  yields values of  $I_1$  and  $I_2$  in good agreement with the haze C computations. This suggests that the detailed structure of the phase function is not of primary importance in determining  $I_1$  and  $I_2$ , and it may be sufficient for remote sensing purposes to parameterize the phase function by  $g$ .

To get a feeling for the importance of variations in the phase function in the remote sensing of ocean color, consider the effect of changing the aerosol phase function from a HG with  $g = 0.6$  to  $g = 0.8$  over an ocean with  $R = 0.1$ . From Figs. 5 and 6, it is found that the normalized radiance at  $\mu = 0.85$  (the assumed observation angle) decreases by  $4.9 \times 10^{-3}$ ; this decrease in

radiance would be interpreted under the assumption of no atmospheric change as a decrease in  $R$  from 0.10 to 0.056. This clearly indicates then that variations in the aerosol phase function in the horizontal direction could be erroneously interpreted as horizontal variations in the optical properties of the ocean. It is, however, probably unlikely that, except in extreme cases, the clear atmosphere oceanic aerosol phase function will exhibit variations as large as considered in this example.

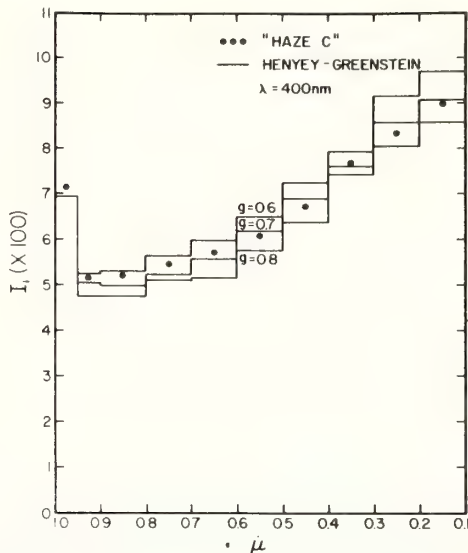


Fig. 5. Comparison between  $I_1(\mu)$  computed for the haze C and Henyey-Greenstein phase functions for an atmosphere with a normal aerosol concentration.

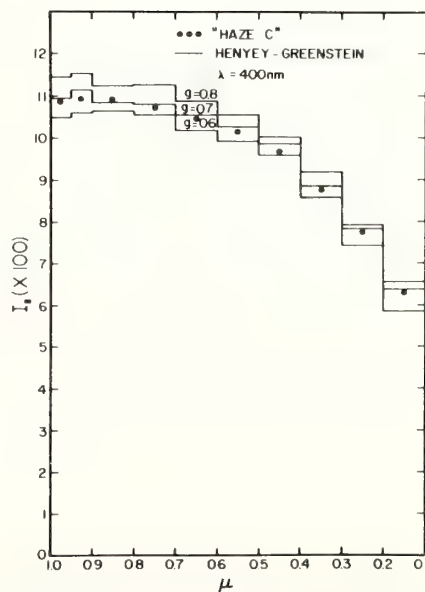


Fig. 6. Comparison between  $I_2(\mu)$  computed for the haze C and Henyey-Greenstein phase functions for an atmosphere with a normal aerosol concentration.

Assuming that the aerosol concentration of the atmosphere can be determined, the uncertainty in the aerosol phase function will still of course provide a limit to the accuracy with which the ocean color spectrum can be retrieved from satellite radiance measurements.

### References

1. H. R. Gordon and O. B. Brown, *J. Quant. Spectrosc. Radiat. Transfer* **15**, 419 (1975).
2. H. R. Gordon and O. B. Brown, *Appl. Opt.* **12**, 1544 (1973).
3. G. N. Plass and G. W. Kattawar, *Appl. Opt.* **8**, 455 (1969).
4. G. W. Kattawar and G. N. Plass, *J. Phys. Ocean* **2**, 146 (1972).
5. H. R. Gordon and O. B. Brown, *Appl. Opt.* **13**, 2153 (1974).
6. R. W. Preisendorfer, *U.G.G.I. Monogr.* **10**, 11 (1961).
7. J. E. Tyler and R. C. Smith, *Measurements of Spectral Irradiance Underwater* (Gordon and Breach, New York, 1970).
8. L. Elterman, *UV, Visible, and IR Attenuation for Altitudes to 50 km, 1968*, Air Force Cambridge Research Laboratories, Report AFCRL-68-0153 (1968).
9. R. S. Fraser, Goddard Space Flight Center, Greenbelt, Md., Personal Communication.
10. D. Diermendjian, *Appl. Opt.* **3**, 187 (1964).
11. G. Kullonberg, *Deep Sea Res.* **15**, 423 (1968). Note that all the phase functions in the present paper are normalized according to

$$2\pi \int_0^\pi P(\theta) \sin\theta d\theta = 1.$$

12. T. J. Petzold, *Volume Scattering Functions for Selected Waters* (Scripps Institution of Oceanography, University of California at San Diego, 1972), SIO Ref. 72-78.
13. H. R. Gordon, *Appl. Opt.* **12**, 2803 (1973).
14. G. N. Plass and G. W. Kattawar, *Appl. Opt.* **11**, 1598 (1972).
15. H. R. Gordon, O. B. Brown, and M. M. Jacobs, *Appl. Opt.* **14**, 417 (1975).
16. S. Chandrasekhar, *Radiative Transfer* (Clarendon, Oxford, 1950).
17. R. Curran, *Appl. Opt.* **11**, 1857 (1972).
18. J. L. Mueller, "The Influence of Phytoplankton on Ocean Color Spectra," Ph.D. Thesis, Oregon State University (1973).



Reprinted from: Proc. AIAA Drift Symposium, Hampton, Va., May 22-23, 1974,  
NASA CP-2003, 175-192.

A LAGRANGIAN BUOY EXPERIMENT IN THE  
SARGASSO SEA

by

Dr. Donald V. Hansen  
Atlantic Oceanographic and Meteorological Laboratories  
Environmental Research Laboratories  
National Oceanic and Atmospheric Administration  
Miami, Florida

As indicated, we'll hear from a group of distinguished drifters this morning. In order to be sure we don't run out of time for me, I'll say my piece first. I can make mine a little bit shorter than I'd planned because a number of comments that have already been given set the stage for it. The genesis of my story begins back about 1970 when a number of people in the physical oceanographic community in this country and abroad began thinking and talking about a project to be called the Mid-Ocean Dynamics Experiment (MODE). It was referred to yesterday by Doug Webb and others as the MODE-1 Project. About that time, I began talking to Sam Stevens about the possibility of hitching a free ride, or at least an inexpensive ride, on the French EOLE satellite system, and through the very good offices of Sam and his crack team, we were indeed able to do that. The engineering for the project was done by the Miami Branch of the Engineering Development

The Author: Dr. Hansen received his Ph.D. in Oceanography from the University of Washington in 1964. He worked as a Research Assistant Professor at the University for 1 year before becoming a Research Oceanographer with the Department of Commerce in 1965. He is presently Director, Physical Oceanography Laboratory, Atlantic Oceanographic and Meteorological Laboratories, NOAA, Miami, Florida.

Laboratory of NOAA's National Ocean Survey in Miami. Charlie Kearsse described yesterday some of the shipboard procedures and arrangements that were developed by them for us to get these buoys in the water, but what he did not mention was that they also were entirely in charge of the engineering and fitting out of these buoys, and in getting them into the water on what turned out to be extremely short notice. As the project developed, it really didn't go quite as we had planned to have it go, because, due to changes in the scheduling of the MODE Project and of the EOLE Satellite Project, it appeared at a critical time that the two after all were not going to be coincident in time. The EOLE Project was to terminate before the MODE Project went to sea. However, it seemed an interesting and important enough experiment to do in its own right, so we pressed on and did it anyway, almost totally independent of MODE. There was about a 1 month overlap between the termination of this project and the initiation of MODE and, in fact, the buoy that we initially had deployed farthest from the MODE area passed within 30 miles of the central mooring of MODE during the second month of that project.

I want to show you a few slides first to indicate some of the motivation for having done the experiment in the way we did it, and to set the stage to address the question of interpretation which Dean Bumpus raised yesterday with some vigor. If I can see the first slide now, please.

This is an example of a publication that is put out by the Navy. They're called Pilot Charts and show currents and wind to be expected in this region of the Sargasso Sea, what mariners and, in fact, what the rest of us know about surface currents in the Sargasso Sea. I might mention in passing, that all of the data that you can find anywhere on such atlases or charts are, in fact, derived by Lagrangian means. These currents summarized in atlases are about 99 44/100% pure ship drift calculation. They're currents inferred from the deviation of ships from their navigational calculations. The major feature I want to point out here is the fact that all of these current vectors show a very smooth steady flow to the west at

speeds ranging from about a knot to speeds on the order of 1/2 a knot. The MODE Project which you saw illustrated in one of Doug Webb's slides; I believe, was conducted in a circle of about 200 kilometer radius. Figure 2 is a copy of a slide taken from some Soviet work in this region. The Soviets have an active interest in the oceanography of the low latitude Atlantic because they conduct vigorous fisheries activities out there and they have conducted intensive research cruises in this region in 1969 and again in 1971. Figure 2 shows their interpretation of those observations. They're a rather intensive set of observations. Soviet literature is a bit hard to interpret as many of you know, in that they don't document their conclusions by Western standards, but as best one can determine, the observations themselves are good. The interpretation is that the solid dark vectors represent the conventional wisdom about the Antilles Current - the northward and westward flow. Imbedded within them are open vectors which are directed to the southeast, which they interpret as a major countercurrent within the Antilles Current and flowing from someplace just off Florida, all the way down, as a continuous feature, joining the complicated equatorial current system and then flowing off to the east. The light lines you see are where they have intensive sets of observations. The observations consist of moored current meter measurements and shipboard measurements of temperature and salinity, from which are computed the velocity field by classical methods. This is the interpretation of what looks like a rather good set of conventional measurements in the region. When I first saw it, I was a little skeptical to say the least - if it's true, it certainly is rather exciting news to the oceanographic community in general and, in fact, rather embarrassing news to the American oceanographic community: that the Soviets should discover right on our doorstep a very major oceanographic feature about which we have no knowledge. This is a very major current. It is a surface current which, however, extends to about a kilometer deep in the ocean and it has a volume transport approximately equivalent to that of the Gulf Stream or Florida Current as it issues from the Florida Strait and heads up the east coast, which all of you are aware, I am sure, is the major oceanographic feature off the U.S. east coast.

So to try to serve two purposes here--one, we recognized before we went to sea that we would not be able to conduct an experiment in close coordination with the rest of the MODE operations; nonetheless, it seemed worthwhile to try to obtain a direct measure of the near surface current structure and its variability in the MODE region. Hence we deployed our buoys along 67°W, immediately to the east of the MODE area, presuming that with the northward and westward drift they would sweep through the MODE area and probably be gone, along the lines of the rather imaginative sketch that Vukovich showed us yesterday, before MODE-I operations began. That was my preliminary guess as to what we might expect in the way of a trajectory development of these buoys when they were deployed, but as you will see, it didn't go quite that way. The idea then was to deploy the buoys so that they would sweep through the surface water in the MODE area before MODE ships came out for that project, except for the southernmost buoy. We learned of the Russian work fairly late in the game and modified the plan to some extent. The buoys were deployed 1° of latitude, 60 miles apart, between 28 north and 25 north. We placed the last one an additional 30 miles south, to place it in the middle of the region where the Soviets claimed to have discovered the countercurrent, to test that particular hypothesis.

Figure 3 shows one of our buoys in the water, using the EOLE satellite tracking system which is exhibited in the side room.

The next slide is of some interest because I think there probably will be additional discussion of this EOLE system today. Figure 4 shows the distribution of position fixes in time for the No. 5 buoy. It shows the hour of the day from midnight to midnight versus day of drift, so the points show the hour and day from time 0 that positions were obtained through the satellite system. They have a quasi-random pattern providing generally 2 - 5 fixes per day which round the clock slowly. The satellite "day" turns out to be something on the order of 23 1/2 hours. This is not a particularly good data distribution for most kinds of analysis we anticipated doing. Once we saw how the data were evolving, we did polynomial fitting

to the X and Y coordinates of the position to provide some smoothing, then we interpolated positions on these polynomial fits at 1-day intervals so we could deal in terms of a fixed time interval. I have a film animation, which we will see, that is the same sort of thing that Doug Webb showed yesterday. It runs rather rapidly so I want to take just a moment to tell you what it contains.

EDITOR'S NOTE: At this point, an animated film sequence showing the drift history of all five buoys was shown.

Figure 5 shows the complete trajectory for the buoy, No. 4, that survived longest. It was retrieved and returned to the laboratory in April 1973.

To speak very briefly about interpretations now, I think that even from this fairly simple experiment, one must begin to make some interpretations and begin to think seriously about how to interpret such data. Some things come fairly immediately to mind--in particular the region where we were exploring the possibility of a major countercurrent. Three of the buoys moved into the region of the supposed countercurrent and pretty much negate the possibility of there being any such countercurrent, and in fact, identified the source of confusion about a countercurrent. It's a sampling problem. The Soviet observations I think are good observations. Their current observations are usually good ones and their shipboard observations are good also. However, they have sampled at fairly widely spaced sections, as one must by traditional methods, and in each of these sections they have found some sort of eddy motion. The error is not in the observation, but in interpretation, in assuming continuity between these various sections. A Lagrangian technique appears to offer much potential for exploring spatial structure in the flow, and offers a fairly economic means for exploring or answering questions about spatial distributions or the existence of particular phenomena.

Another thing that we are working on now--I just have a bare beginning of some things to say about it, another kind of application that has been of interest in oceanography for many decades now is an interest in trying to

predict in a semiquantitative sense the transport or the distribution or dispersion of things dissolved or fine objects scattered in the sea, etc. As an example, the interest is in being able to predict the concentration or the probability of a particular object being in a particular place by an equation in the form:

$$\frac{\partial P}{\partial t} = K_{ij} \frac{\partial^2}{\partial x_i \partial x_j} P$$

In this formulation,  $K_{ij}$  is a dispersion coefficient relating the concentration change to the spatial gradient in two dimensions, essentially saying the time change is a diffusion type process related to the gradient, but with a tensor diffusion coefficient. In some classic work by G. I. Taylor dating back to 1921, it's shown that the kind of information that is needed to approach this kind of a problem is, in fact, the Lagrangian information--not Eulerian information, and is laboratory and wind tunnel dynamics, a lot of work over several decades has gone into the problem of trying to establish a relation between Lagrangian and Eulerian statistics. The Eulerian statistics are easier to measure, but for certain problems the Lagrangian statistics are the ones that you really want.

Given a particular particle or particular buoy that has a particular path, one can consider the mean path and the deviations from it, and compute the time lagged autocorrelation. That's what we have done but only for the diagonal components to date.

What we did was to take position data, differentiate it to obtain velocity data, and then compute a statistical function.

The autocorrelation, call it  $R$ , is the ensemble average  $\overline{V_i(t)V_j(t+\tau)}$ .

$V_i(t)$  denotes east or north component of velocity at some time  $t$ , and  $\tau$  a time lag interval.

This is averaged over the ensemble or averaged over all time for the buoy motion. It's a measure of how rapidly the motion loses similarity with itself. At no lag at all the velocity looks exactly like itself so the autocorrelation is equal to the variance. The correlation decays with some structure as time runs on. Figure 6 shows the nature of the autocorrelation function for buoy 4.

The major features of the curve show that the correlation drops to zero on a time scale of about a week or 10 days. That is the Lagrangian time scale for motion in the Sargasso Sea. It also has an oscillatory structure that damps out with increasing lag. It really has validity only out to about 120 days. After that there are too few data points, to draw even tentative conclusions. There are roughly 200 observations going to make up each data point in the beginning of the curve. I don't believe anything out in the tail end of the curve, so basically what is revealed at least during this set of observations is a periodic variability in current having a time scale of about a month--peak to peak here is a lag time of about a month.

The next step to apply this to the dispersion problem is to relate the  $K_{ij}$  to the autocorrelation function using logic of G. I. Taylor and others. The result is that the  $K_{ij}$  is obtained from the integral of the autocorrelation over time. From a quick calculator integration of the function for buoy 4, I obtained a value  $10^7 \text{ cm}^2/\text{s}$ , which turns out to be a number popular among oceanographers. If one had to guess without knowing anything else it probably would be slightly higher than this, perhaps by a factor of 5 or so.

The other thing you can do--this is a thing that I think Lagrangian techniques are in fact more appropriate for, relative to other kinds of observation and fixed moorings, etc., is to explore not the time correlation behavior but the thing that's really hard to get from moored current meters, the space correlation behavior, because it's really an expensive undertaking to put down a lot of moorings with fixed current meters to explore how currents vary on a time scale of 1 mile - 10 miles - a hundred miles, etc.

By deploying an array of drifters such as we've been discussing here, one can set the initial scale, but as the pattern evolves, it covers quite efficiently a considerable band of space scale. We tried doing that with the buoy data we have here using the buoys in pairs, and in order to get the bulk of data up to some usable level it turns out we don't really have very much data at all yet. In order to try to get the statistics as well behaved as possible, we borrowed a ploy from the field of homogeneous turbulence and worked with buoys in pairs which are separated by a vector having some direction and some length  $L$  and decomposed them, presuming that the flow field is isotropic. I really don't have any very good argument to defend that except that the r.m.s. speed in the east directions are approximately the same at about 15 cm/sec, so with a little bit of hand waving we must pass over that question. Then we decomposed the velocity components at buoy pairs into components parallel to and orthogonal to the separation vector between them and computed spatial correlations at fixed times for the parallel and perpendicular components so defined. It turns out, however, that for the space scales covered by this data set, 100-400 km, the correlations are evidently so low that they cannot be distinguished from zero in the quantity of data available. Indications are that probably the spatial correlation is lowest someplace here in the first 100 kilometers or so which is essentially the same sort of thing that was found before and during the MODE experiment for the deep water circulation--deep currents in this same area. I think I've taken about as much time as I ought to. Thank you for your attention. If anyone has any comments, I'll try to respond.



## QUESTIONS

JIM RUSSELL -- U. S. Naval Avionics Facility:

When you assume your isotropy in your turbulence, what kind of scales are you really looking at in your measurements? Are they fairly large?

Answer -- DR. HANSEN:

Right, the scales we're looking at here are roughly in the 100-500 kilometer range for enough data to be of any significance at all.

JIM RUSSELL -- U. S. Naval Avionics Facility:

And it's also in the surface water rather in the deeper water that we're talking about?

Answer -- DR. HANSEN:

This is strictly the surface water. This was using the buoy that Charlie Kearse showed some slides of yesterday. We had a parachute drogue on them which was at 30 meters depth, so it's really very much in the upper layers of the ocean. The thermocline there is 800 meters deep or so.

JIM RUSSELL -- U. S. Naval Avionics Facility:

Something does bother me about assuming isotropy there. Did the results you got indicate that assumption may have been o.k.?

Answer -- DR. HANSEN:

I really don't think I can address that. I haven't looked at it carefully. The only think I can say in justification is that the variance in the north-south and in the east-west direction is approximately equal, about 13 and 15 centimeters per second for the r.m.s. speed. There is some indication that in deeper water there probably is some anistropy, higher energy levels in the north-south direction as compared to the east-west, but it does not show up in this surface data set.

BOB HEINMILLER -- Woods Hole:

There is a little event on your film that caught my eye. There were two buoys--looked like they were very close together--just estimating from the scale 5 and 10 miles--the tail of one about 10 times the tail of the other, both going in the same direction which implies that the speeds for one were considerably, an order of magnitude, higher than the other. I didn't notice that that occurred any other time during the film. Have you seen any sort of that? That seems like an awfully high differential.

Answer -- DR. HANSEN:

It does happen other times. You have to see the film several times to detect more of these events, but when we first deployed the buoys I thought we had discovered the center of the ocean circulation because for a period of about 10 days the No. 4 didn't move within the resolution of the satellite, which is about a kilometer there, while buoys north and south of it, particularly one of them north of it, turned and moved toward it and came by at a good rate of speed within about 30 miles, yet the one that was initially deployed there hardly moved for about 10 days. After 10 days it suddenly took off and moved to the south as rapidly as any of them. I interpret that as being indicative of large lateral shears in the flow. In the movies that Doug showed yesterday, you see very much the same sort of thing in the SOFAR float measurements. It looks there as if there are jets imbedded in the flow. They seem to be north-south oriented there but didn't show up quite so much here perhaps because a lot of the statistics may be biased by the fact that the buoys spent a fraction of their time fairly near the Bahama Banks where presumably north-south motion is strongly inhibited and east-west motion parallel to the banks is favored.

CHRIS WELSH -- Virginia Institute of Marine Science(VIMS):

It occurs to me that if you were to put a current meter section out where the Russians did for a long length of time and average over the time to get a climatological circulation, you would still see the countercurrent structure

that they apparently saw simply because when the currents going south, the western boundary, if you want to call it that, structure is apparently more intense from the little worms you have than when they go off to the north.

Answer -- DR HANSEN:

I think that's probably true - if you'd observe just those sections, you likely would see what you interpret as a countercurrent migrating onshore and offshore and north and south or something. I suspect different eddies or different waves or whatever they are occur there at various times. You're probably right. You'd really have to have a very dense set of current meter moorings to be able to resolve the spatial structure in the flow to disabuse yourself of that idea.

PETER HACKER -- JOHN HOPKINS:

I'm worried a little bit about the slippage of the drogues in regions where you do have high lateral shear from the currents you observed and from the winds that are typical in that area. Do you have any kind of a percentage estimate of slippage of the drogue with respect to a water mass?

Answer -- DR. HANSEN:

I haven't put a number on it. We're investigating. We just got all the tropical weather information. We will correlate the local winds with the buoy movements; however, I haven't put a number on it. Maybe Charlie has, I don't know. I think the wind drift for this particular buoy is probably negligible in terms of the currents and the things we see for two reasons: one, the dominant periodicities in the major flow features have a time scale of about a month and you just don't see things like that down there in the weather pattern. You don't expect major wind events in a time scale of a month. Strictly from the engineering point of view, this buoy was about 40-41' long with the major portion of the cross section submerged and, in addition, it has a parachute drogue on it. All indications are that the parachute drogues did indeed survive for a time scale of 6 months or better. Bob Heinmiller was one of the last people, I think, to see buoy No. 5 and the reports I have from the appearance of the buoy in the water, the way accessory

floats were arrayed and so on, indicate that the parachute drogue hardware apparently was still on at that time. We recovered one in December after 3 months at sea, and the whole subsurface hardware was essentially in perfect condition then. The one we recovered after 8 months outside the Bahamas had lost its parachute. I don't think it's a serious problem. Did you ever put a number on the windage Charlie?

CHARLIE KEARSE:

I guess I'm just worried. You know, even if it's just 5 or 10 percent--if a flow drifts 100 kilometers downstream or something, at the same time it can be going cross stream 5 or 10 kilometers in a region where you do have intense shear, it may in fact drift from a countercurrent into the other part of the countercurrent if you do have closely spaced currents.

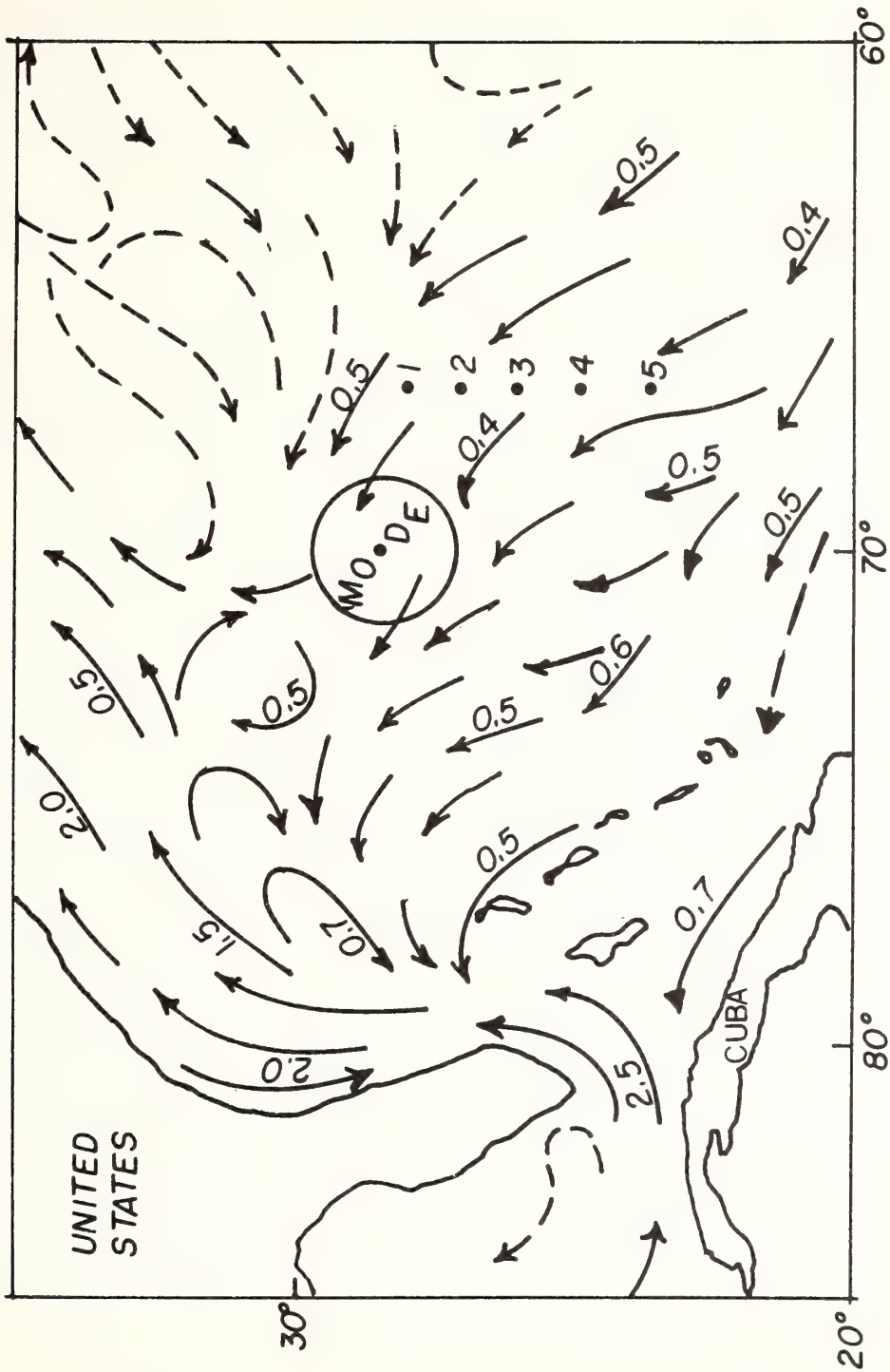


Figure 1. SURFACE CURRENTS IN THE SARGASSO SEA AS TYPICALLY SHOWN IN ATLASES (The MODE-1 region and deployment positions of 5 drifting buoys using the EOLE position locating system are also indicated.

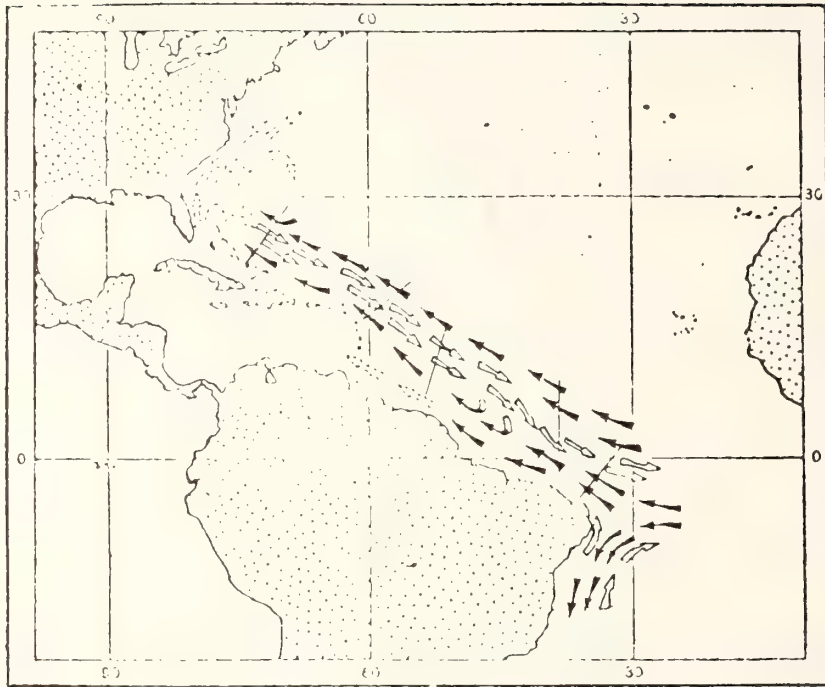


Figure 2 THE ANTILLES COUNTERCURRENT AS HYPOTHESIZED BY V.G. KORT



Figure 3 DRIFTING BUOY USING EOLE TRANSPONDER DEPLOYED AT SEA

BUOY #5

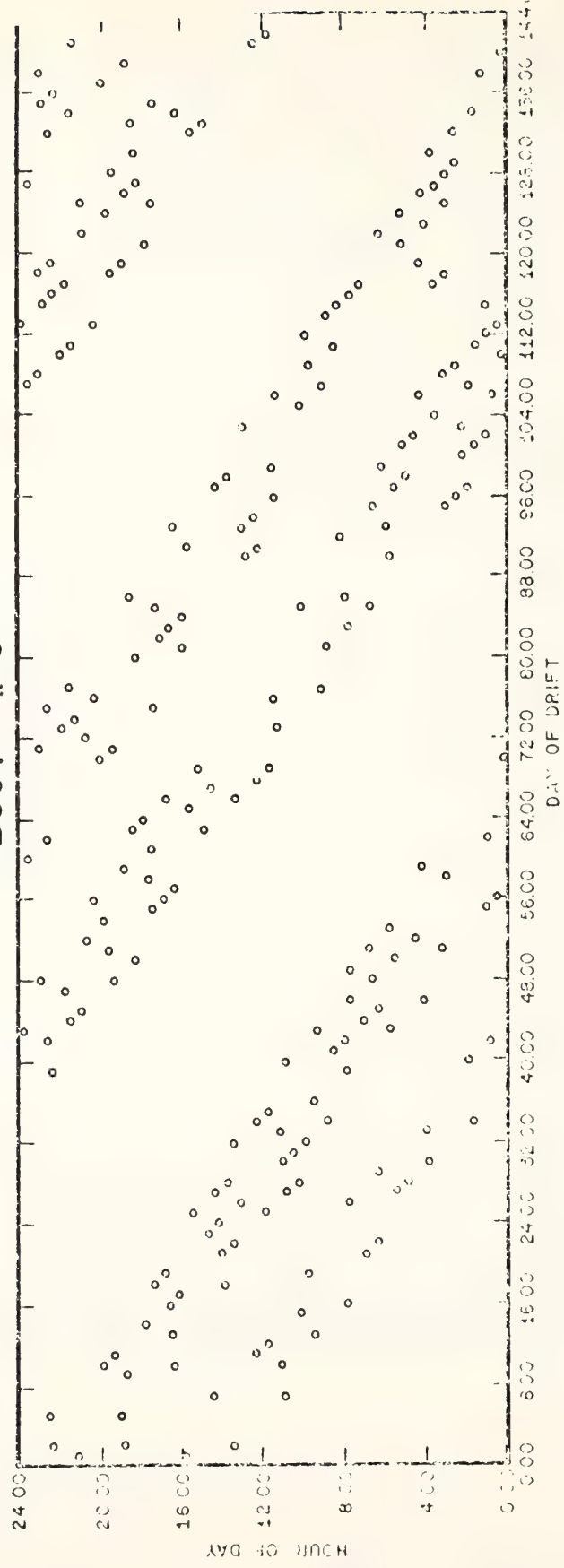


Figure 4 DISTRIBUTION OF EOLE POSITION FIXES IN TIME FOR A DRIFTING BUOY



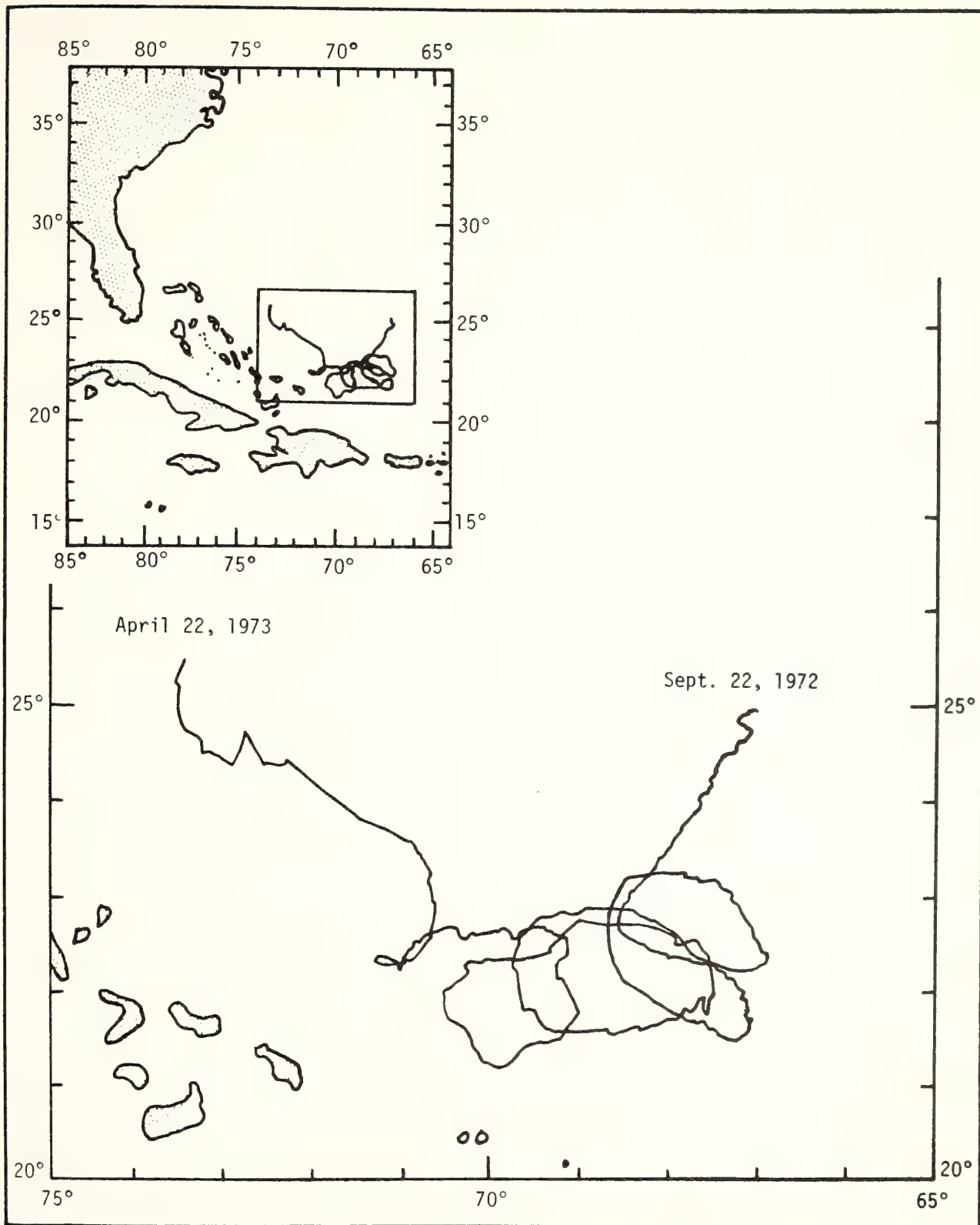


Figure 5 DRIFT TRAJECTORY FOR BUOY No. 4

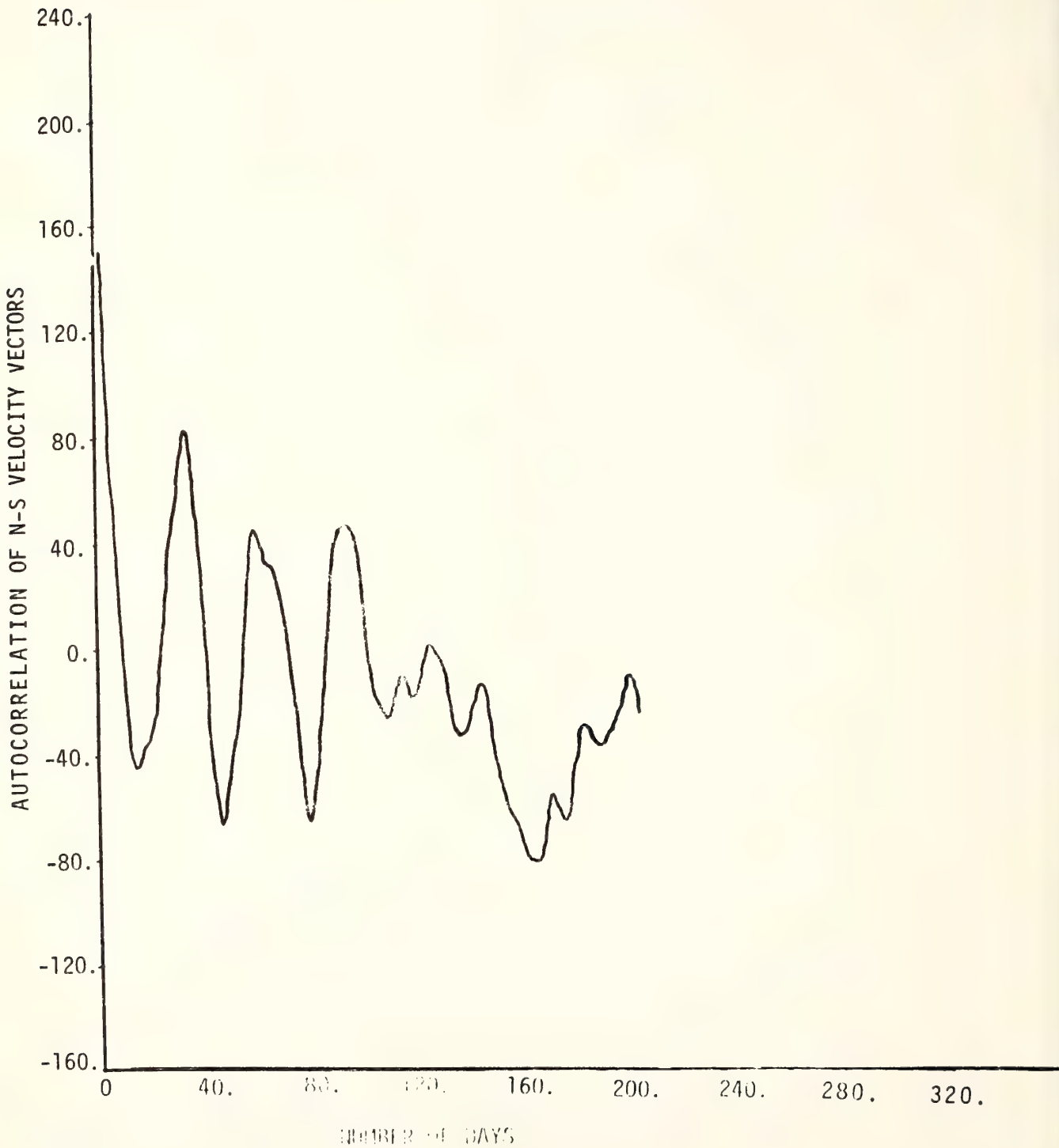


Figure 6. LAGRANGIAN TIME CORRELATION FUNCTION FOR BUOY No. 4

Reprinted from: Proc. of the Third Annual Conference on Computer Graphics, Interactive Techniques, and Image Processing, University of Pennsylvania, Computer Graphics 10, No. 2, 218-223.

AUTOMATED CONTOURING OF VERTICAL OCEANOGRAPHIC  
SECTIONS USING AN OBJECTIVE ANALYSIS

A. HERMAN

National Oceanic and Atmospheric Administration  
Atlantic Oceanographic and Meteorological Laboratories  
15 Rickenbacker Causeway  
Miami, Florida

This paper describes a group of computer programs developed for contouring vertical sections of oceanographic parameters. The vertical profiles can be constructed from data collected in a variety of ways. The input data for the driver subroutine need not be equally spaced horizontally or vertically. The routines are written in Fortran for a UNIVAC 1108 with an offline Gould Plotter, but can easily be adapted to any computer with a Fortran compiler and a plotter which accepts Calcomp-like commands. The routines are of modular construction.

## 1. INTRODUCTION

This paper describes an automated technique for producing vertical profiles of oceanographic data using quasi-objective analysis. The computer program based on the method is also described. Though objective analysis is well established in meteorology, it has seldom been used in oceanography, and when used, it has been restricted to a specific geographical area [Bretherton (2)]. This program is not restricted to a specific geographical area and is currently being used by oceanographers at the Atlantic Oceanographic and Meteorological Laboratories (AOML) of the National Oceanic and Atmospheric Administration (NOAA) for studying profiles and creating contour maps in the Gulf of Mexico and the New York Bight areas. The advantages of this technique over others generally available to oceanographers are:

1. The sampling points for the input data need not be uniformly spaced in either the vertical or the horizontal direction.
2. Contours are not extrapolated beyond the input data.
3. Interpolation of data is done using statistically based correlation coefficients.

The program is based on the assumptions that all stations in a single profile lie close enough to a straight line connecting the two farthest stations that no significant errors will be introduced by assuming all stations to be on that line, and that time differences in the collection of data points may be ignored. These assumptions are needed when data do not exist for accurate spatial and time

corrections. When studies are made with adequate resolution in time and space to make such corrections the program can be modified to include them.

## 2. PROGRAM FLOW PLAN

The driver subroutine Versex, calls many subroutines which together accomplish the following:

1. The conversion of latitude and longitude to rectangular coordinates on a Mercator projection.
2. The projection perpendicularly of all stations onto a line connecting the end stations, and the computation of the distance of each station from an end of the line. The distances are in inches at a scale of four inches equal to one degree of longitude (Figures 1 and 3).
3. The determination of the depth scaling is such that the deepest depth is equivalent to the distance between the farthest stations. This will produce a square chart with a fixed horizontal scale and the vertical scale being a function of depth and horizontal size.
4. The fitting of data to a matrix with user controlled smoothing with matrix values below deepest depths being logged.
5. The construction of a contour matrix such that a chart is left blank below deepest data, all data points are marked, and the vertical scale is labeled (Figures 2 and 4).

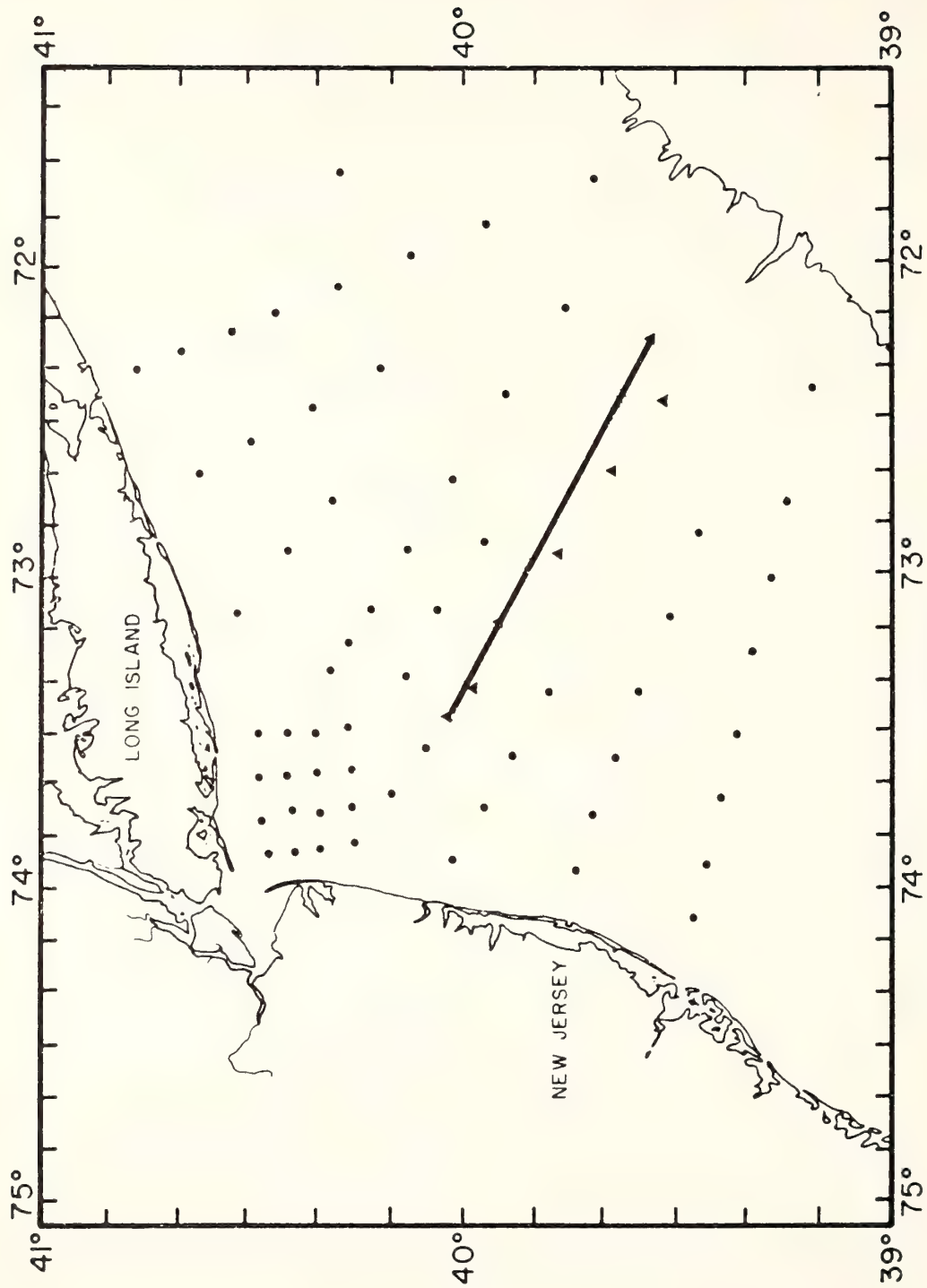


FIGURE 1

Figure 1. Profile Locations in New York Bight.

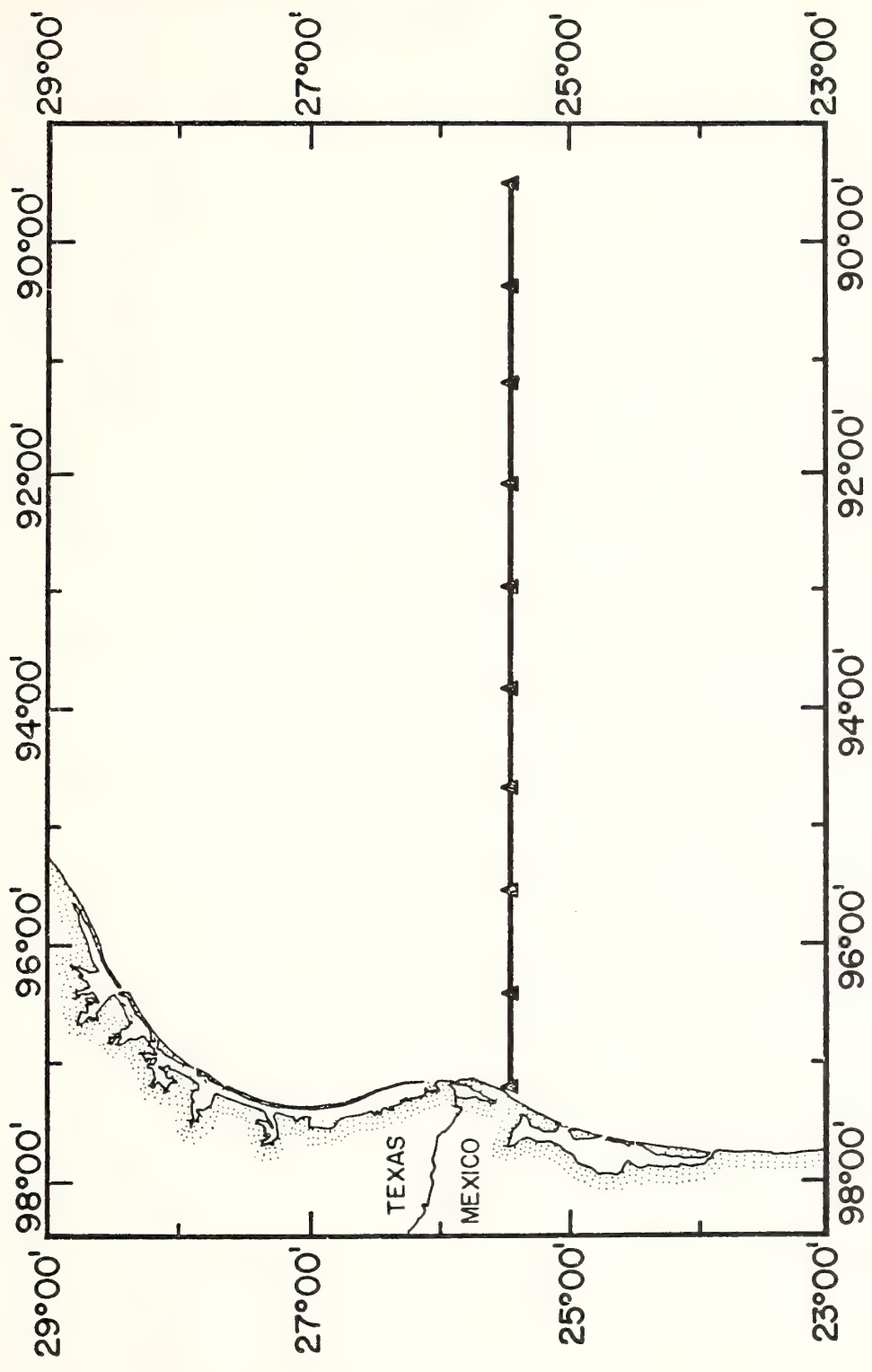


FIGURE 3

Figure 3. Profile locations in Gulf of Mexico.

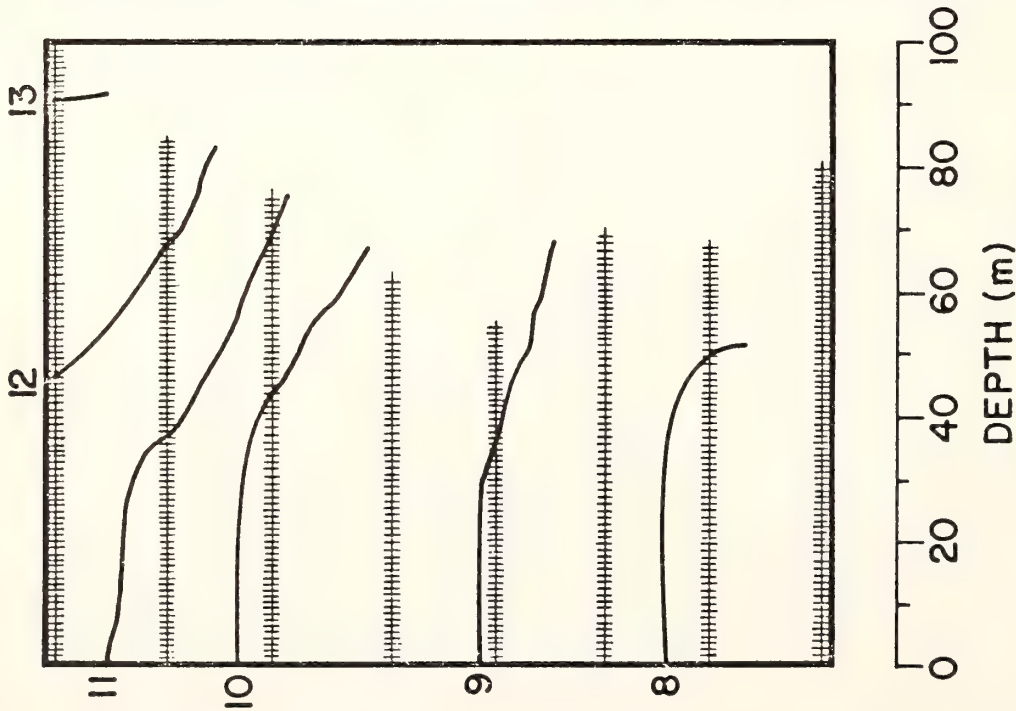


Figure 2. Temperature ( $^{\circ}\text{C}$ ) contour output based on New York Bight Data.

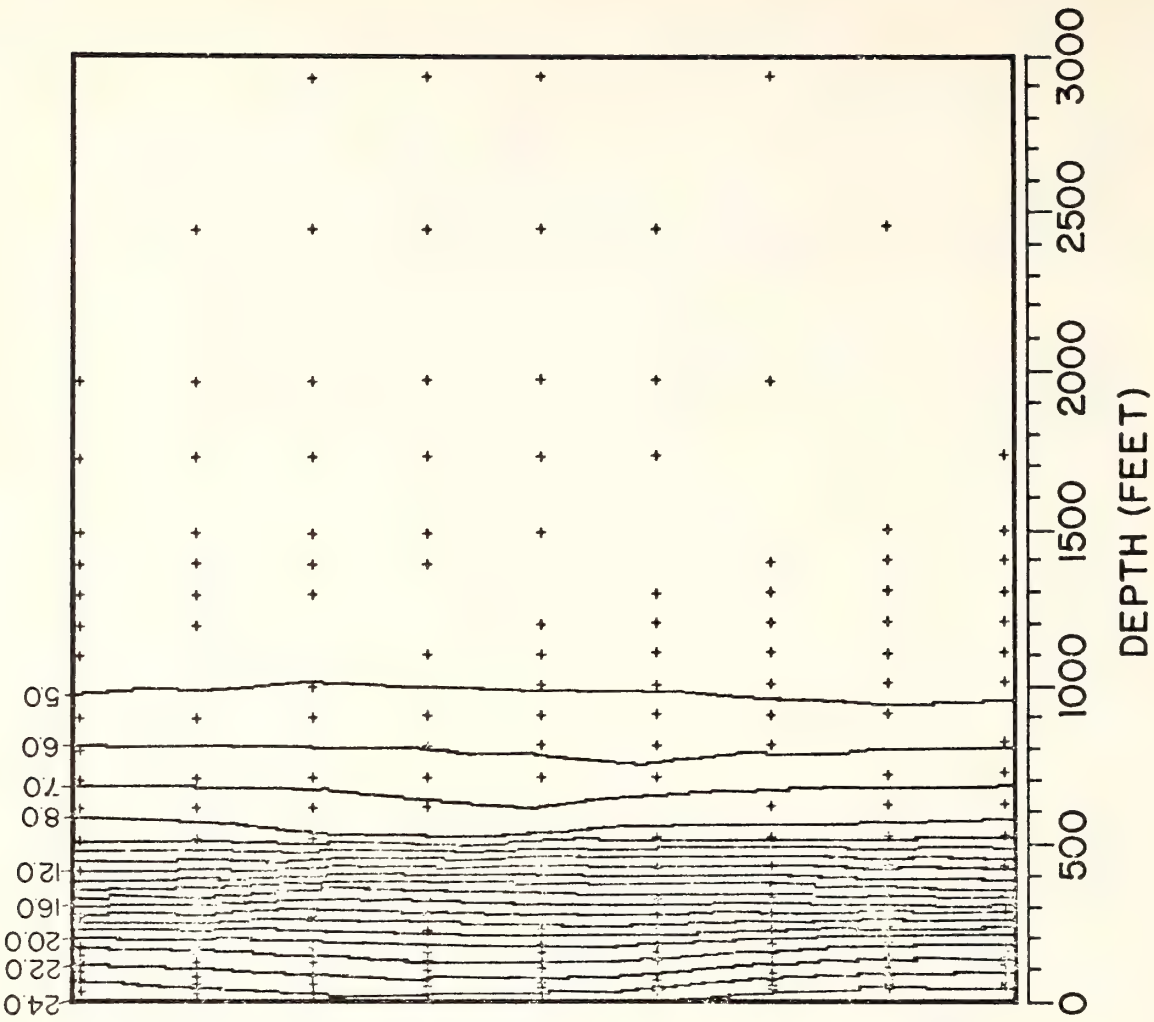


FIGURE 4

Figure 4. Temperature ( $^{\circ}\text{C}$ ) contour output based on Gulf of Mexico Data.

### 3. CONVERSION OF LATITUDE AND LONGITUDE TO CARTESIAN COORDINATES

Subroutine Merc converts latitude and longitude to cartesian coordinates on a Mercator projection chart at a scale of four inches equal to one degree of longitude. The chart has its origin at 80° S and the Greenwich meridian. Chart values increase to the east and the north. Formulae for the Mercator projection can be found in Bomford(1).

### 4. CREATING THE DATA MATRIX

The interpolation of data onto a grid is normally subjective. Thus the quality of the result depends on the skill of the analyst. In order to obtain a more uniform quality, subroutine WMAT performs the interpolation in a quasi-objective manner. First an array of correlation functions is established, and then the interpolation is done based on the correlation function. The method of objective analysis is described in Gandin (3). The equations are of the following form:

The autocorrelation function for the field  $f(r)$  is:

$$M_f(\vec{r}_1, \vec{r}_2) = \overline{f(\vec{r}_1)f(\vec{r}_2)} \quad (1)$$

where  $\vec{r}_1$  and  $\vec{r}_2$  are two points in the vertical plane of interest. Instead of using  $f$ , it is convenient to use  $f' = f - \bar{f}$ , the statistical deviation from the norm.

$$M_{f'}(\vec{r}_1, \vec{r}_2) = \overline{f'(\vec{r}_1)f'(\vec{r}_2)} \quad (2)$$

Because of assumptions of homogeneity and isotropy [Gandin (3)], the correlation function is expressed in terms of separation distance.

$$\rho = \vec{r}_2 - \vec{r}_1 \quad (3)$$

Both noisy data and wave data will have a correlation function which crosses zero more than once. To reduce the effects of noise, the correlation function,  $M_f$ , is taken to be zero past the first zero crossing. The effect of the presence of waves on the data will not be smoothed out if the interpolation grid is fine enough (grid size is a user option in VERSEX).

The correlation coefficient is a normalized correlation function:

$$U_{f'}(\rho) = \frac{M_{f'}(\rho)}{M_{f'}(0)} \quad (4)$$

$U_{f'}(\rho)$  represents a correlation coefficient between the values of  $f'$  at two points apart and is a function of distance.

\* A  $\bar{\phantom{x}}$  denotes an average and an arrow a vector.

The interpolation is done using the following equation:

$$f_o = \frac{\sum_{i=1}^n U(r_i)f_i}{\sum_{i=1}^n U(r_i)}$$

where  $f_o$  = deviation of value from known position.

$f_i$  = values at known distances  $r_i$ .

$n$  = number of observation points.

The actual contouring is done on a Gould electrostatic plotter using a Fortran program with Calcomp type plot instructions. The contouring algorithm involves only linear interpolation between grid points. This method was chosen for simplicity.

### 6. INSTRUCTIONS FOR USE OF SUBROUTINE VERSEX

VERSEX is the only routine that must be called by the user as illustrated in Appendix A. The calling statement is as follows:

Call VERSEX (N, M, XLAT, XLON, DAT, DEP, CI, DTMIN, DTMAX, DPMIN, DPMAX, NROWS)

where N = number profiles to be input

M = maximum number of data points in a profile.

XLAT = array of latitudes in degrees

XLON = array of longitudes in degrees

DAT = a two-dimensional array (N,M) of data values (empty locations should be set to a negative number.)

DEP = a two-dimensional array (N,M) of depths corresponding to data points.

CI = contour interval (if zero or negative, CI is set = maximum data value - minimum data values divided by 10).

DTMIN = minimum data value to be considered. If it is negative, then it is reset to the lowest value in DAT.

DTMAX = maximum data value to be considered. If it is negative, then it is reset to the largest data value in DAT.

DPMIN = minimum depth. If it is negative, then it is reset to the least depth value at which there is a data value.

DPMAX = maximum depth. If it is negative or zero, then it is reset to the greatest depth at which there is a data value.

NROWS (if greater than zero) is the number of rows you want in the matrix to be computed if you wish to control the amount of smoothing. The fewer the number of rows the greater the smoothing. Minimum

smoothing occurs when  $NROWS = M-1$ .

#### REFERENCES

- (1) Bomford, G., "GEODESY", Oxford, Clarendon Press, 1971.
- (2) Bretherton, F.P., "A Technique for objective Analysis and Design of Oceanographic Experiments", to be published in Deep Sea Research.
- (3) Gandin, L.S., "Objective Analysis of Meteorological Fields", Gimiz, Leningrad, 1965.



Reprinted from: Proc. of the Fourteenth Annual Southeast Regional ACM Conference, University of Alabama, Birmingham, Alabama, 305-308.

## AN AUTOMATED SOLUTION FOR OMEGA NAVIGATION

A. Herman, NOAA/AOML  
A. C. Campbell, U.S. Naval Oceanographic Office

### ABSTRACT

Omega is a commercially available, electronic, world wide navigation system. Navigators and other Omega users generally determine geographic positions from Omega lane counts either by scaling charts and tabulated corrections or by a programmed iterative technique. This paper describes an algorithm which determines position directly.

### INTRODUCTION

Omega is a worldwide navigation system usable anywhere and at any time. Other navigation systems have the limitation of being available only locally or at certain times of day. Electronic navigation systems can be classified by the kind of line of position they generate. These include hyperbolic, concentric circles, radials or any combination. Omega is a hyperbolic system. A hyperbola is defined as the locus of a point moving such that the difference in distances from two fixed points to the moving point remains a constant. Thus, a hyperbolic navigation system is one in which a mobile user measures the difference in transmission time between signals from two shore stations. This difference, as can be seen from figure 1, determines one line of position. Two lines of position are required for a fix. Omega is a pulsed hyperbolic system. A master station transmits an encoded series of pulses at short intervals; these pulses are retransmitted each time they are received by a slave station. The system has fixed time delays such that the mobile user always receives first the master pulse, then the slave. The receiver measures the time difference between master and slave signals, removes the time delays, and displays the resulting time differences in lane counts. Two time differences (lane counts) define two hyperbolic lines of position. The signals are affected by: (1) The conductivity of the surface over which the signal propagates and (2) refractivity of the atmosphere through which the signal propagates.

This paper introduces a new method for calculating the point of intersection of two hyperbolic lines of position. The computation differs from the usual method in that it is a noniterative solution. The method is an application of the solution for hyperbolic systems described in Campbell (1965). The Defense Mapping Agency of the Department of Defense publishes the data necessary to make calculations including station locations, datum, spheroid specifications, and transmission frequencies. The program described in this report is for 10.2 KHz with a phase velocity of 300574 Km/sec. (Omega lane widths are equal to 1/2 wave length along the base line, which is equal to velocity/2x frequency or 14734.02 meters.) The time delay mentioned above is such that the base line bisector is 900 lines. Therefore, the length of the baseline in wavelength plus coding delay = 900.

### MATHEMATICAL METHOD

The method requires an approximate initial position from which  $x$  and  $y$  distances from the approximate position,  $P^1$ , to the true position,  $P$ , are computed. The geometry of the problem is displayed in figure 2. Four normal equations of the form:

$$x \sin \alpha + y \cos \alpha_i + a_i' - a_i = 0 \quad (1)$$

$$i = 1, 2, 3, 4,$$

are utilized to obtain  $x$  and  $y$ . As is shown in Figure 2,  $x$ ,  $y$ , and the four  $a_i$  are the unknowns. Lane counts must be translated into distances along the baseline.

$$K_j = c_j - b_j \text{ where } j = 1, 2. \quad (2)$$

$$K_j = H_j \times 147342.02 \text{ meters.} \quad (3)$$

The differences  $a_i' - a_i$  can be written as:

$$\begin{aligned} a_1' - a_1 &= a_1' - (a_2 + k_1) = (a_1' - k_1) - a_2 \\ a_2' - a_2 &= a_2' - a_2 \end{aligned} \quad (4)$$

$$a_3' - a_3 = a_3' - (a_4 + k_2) = (a_3' - k_2) - a_4$$

$$a_4' - a_4 = a_4' - a_4$$

Then the 4 observational equations (1) become

$$\begin{aligned} x \sin \alpha_1 + y \cos \alpha_1 - a_2 + (a_1' - k_1) &= 0 \\ x \sin \alpha_2 + y \cos \alpha_2 - a_2 + a_2' &= 0 \\ x \sin \alpha_3 + y \cos \alpha_3 - a_4 + (a_3' - k_2) &= 0 \\ x \sin \alpha_4 + y \cos \alpha_4 - a_4 + a_4' &= 0 \end{aligned} \quad (5)$$

A simplified notation for (5) is:

$$\begin{aligned} Ax + By + a_2 + C &= 0 \\ Dx + Ey + a_2 + F &= 0 \\ Gx + Hy + a_4 + J &= 0 \\ Kx + Ly + a_4 + M &= 0 \end{aligned} \quad (6)$$

This according to Cramer's Rule reduces to:

$$y = \frac{(A-D) \begin{vmatrix} J-M \\ L-H \end{vmatrix} + (C-F) \begin{vmatrix} K-G \\ G-K \end{vmatrix}}{(A-D) \begin{vmatrix} J-M \\ L-H \end{vmatrix} + (B-E) \begin{vmatrix} K-G \\ G-K \end{vmatrix}}$$

$x$  and  $y$  are then used in a forward geodetic position computation as described in Bomford (1971) to determine the latitude and longitude of the actual position.

Implementation Procedure: A fortran program has been written which accomplishes the following.

1. Transfers DMA Omega correction tables from DMA supplied tape to a high speed drum.

2. Interpolates a correction to the hyperbolic rate based on month, day, time of day, and approximate position.
3. Applies the outlined mathematical methods to determine latitude and longitude.
4. Uses the position in 3 as an approximate position to compute a new approximate position for the next point, then goes to 2, and continues until all positions have been computed.

#### RECOMMENDATIONS FOR BEST RESULTS

Assuming all Omega stations that can be received are broadcasting with the same reliability\*, the accuracy of a fix is a function of the network geometry. According to Bigelow (1963) the accuracy of a fix is determined by the angle of intersection of the lines of position. Bigelow says "those lines intersecting with the smaller angle between  $60^{\circ}$  and  $90^{\circ}$  give strong fixes," and "a net should not be used where the smaller angle of intersection is less than  $15^{\circ}$ ". Thus if one utilizes station monitoring information, DMA corrections, and network geometry considerations, he can decide on the best networks to use.

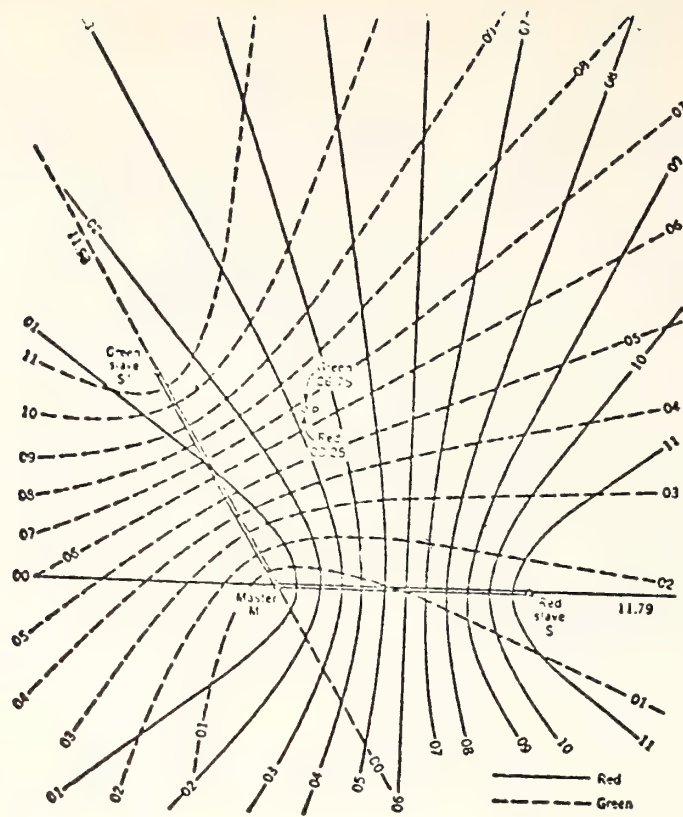
#### GENERAL COMPUTER PROGRAM DESCRIPTION

The Atlantic Oceanographic and Meteorological Laboratories, Physical Oceanography Laboratory program uses correction tables for time and location that are made available by the Defense Mapping Agency on magnetic tape. The program works as follows: A position is computed based on the hyperbolic rates. This position is then used as input to an interpolation routine along the time information which utilizes the DMA tape to derive a correction to the hyperbolic rates. These rates are used to recompute the position. When there are many fixes to be computed, the prior point to the one being computed is used as an approximate position for the next calculation.

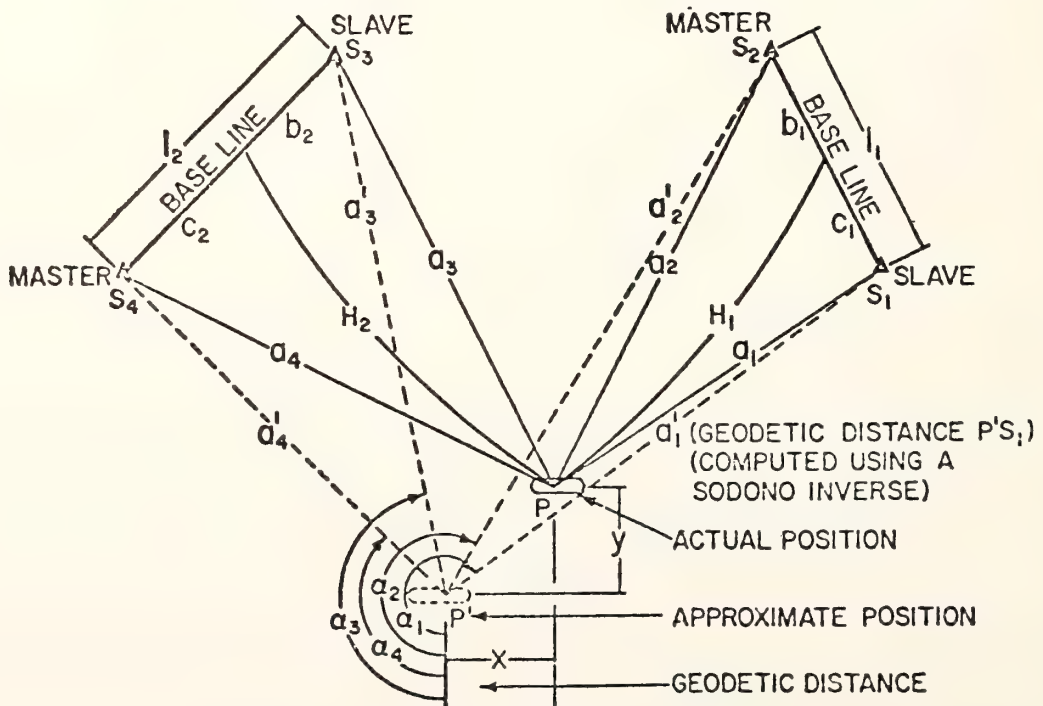
\*Reliability here means transmitters are functioning properly.

#### REFERENCES

1. Bigelow, Henry W., "Electronic Surveying: Accuracy of Electronic Positioning Systems", Journal of the Surveying and Mapping Division, Proceedings of the American Society of Civil Engineers, October 1963.
2. Bomford, G., "Geodesy", Oxford, Clarendon Press, 1971.
3. Campbell, Andrew C., "Geodesy at Sea", an unpublished masters thesis, the Ohio State University Press, 1965.
4. Sodano, Emmanuel M., "General Non-iterative Solution of the Inverse and Direct Geodetic Problems." Proceedings of the XIII I.U.G.G. General Assembly at Berkley, Calif., 1963.
5. Defense Mapping Agency "Specifications for Omega", revised 9 January 1973.



HYPERBOLIC TRIAD  
FIGURE 1



MATH MODEL GEOMETRY  
FIGURE 2

Reprinted from: *Marine Sediment Transport and Environmental Management*,  
D. J. Stanley and D. J. P. Swift, editors, John Wiley and Son, Inc.,  
Chapter 3, 23-28.

## Some Simple Mechanisms for Steady Shelf Circulation

ANTS LEETMAA

*Atlantic Oceanographic and Meteorological Laboratories, Miami, Florida*

An understanding of the mechanisms of sediment transport on the continental margins depends on a knowledge of the oceanic shelf circulations. This, in itself, is a complex phenomenon, and its study has just begun. Ideally, the geologist is generally not interested in the totality of the circulation pattern. Although sediment transport can occur at all levels, the primary interest of the geologist is in knowing the magnitude and direction of the flow close to the bottom; this can be obtained either from observations or theory. However, there is little of either. Bumpus (1973) describes what is known about the circulation on the continental shelf off the east coast of the United States. There is little theory to describe these observations. The motions appear to be complex and highly variable. Factors that determine the circulation on one shelf likely are not as important on another. Seasonal effects are dominant.

Some of the simplest models for shelf circulation are examined in this chapter. With these models, various concepts about forcing mechanisms and the nature of the dynamics can be explored. The relevance of the model for the real world depends on how well its results compare with observations. More complex models can be developed by using the simpler models whose dynamics are well understood and hopefully verified by observations, as building blocks. Realistic models ultimately permit calculating the nature of the flow close to the bottom, and determining which types of forcing are of importance for sediment transport.

The simplest models to treat theoretically are steady state ones. In this chapter attention is confined to these. Following chapters discuss wave effects, tidal flows, and other time-dependent phenomena. We start by exploring several models that differ only in their forcing mechanisms. The forces that are most important for steady motions on the shelf are thermohaline effects and wind stress. The former are caused by spatial differences in the temperature and/or salinity distributions. These produce pressure differences that drive water motions.

Results will depend strongly on the value of the frictional coefficients chosen. For very "viscous" models, the flows are little influenced by the rotation of the earth. However, for small values of viscosity, the solutions are strongly influenced by the earth's rotation. The magnitude of the viscosity is observationally extremely difficult to measure, and perhaps is best estimated from theoretical models.

### THERMOHALINE FORCING

One example of thermohaline forcing is freshwater runoff from land. This produces fresher and consequently lighter water close to the coast than further offshore. This also is the dominant driving force in estuaries. To understand the general type of motion this creates, consider the following problem. We assume that the dynamics are governed by the following set of equations:

$$-f \frac{\partial v}{\partial z} = -g\beta \frac{\partial s}{\partial x} + A_v \frac{\partial^3 u}{\partial z^3} \quad (1)$$

$$f \frac{\partial u}{\partial z} = A_v \frac{\partial^3 v}{\partial z^3} \tag{2}$$

$$0 = \frac{\partial u}{\partial x} + \frac{\partial w}{\partial z} \tag{3}$$

$$u \frac{\partial s}{\partial x} + w \frac{\partial s}{\partial z} = K_v \frac{\partial^2 s}{\partial z^2} \tag{4}$$

For this right-handed coordinate system,  $x$  is perpendicular to the coast,  $y$  is parallel to it, and  $z$  is vertically upward;  $u, v, w$  are the  $x, y, z$  components of velocity, respectively;  $A_v$  and  $K_v$  are the vertical eddy mixing coefficients for momentum and salt;  $s$  is the salinity; and  $\beta$  is the coefficient of contraction for salt. The effects of the earth's rotation are contained in the terms  $fv_z$  and  $fu_x$ , where  $f$  is known as the Coriolis parameter and  $f = 2\Omega \sin \theta$  where  $\Omega$  is the angular velocity of the earth and  $\theta$  is the latitude.

To arrive at these equations it is assumed that the effects of lateral mixing are small, and that the motions are slow and steady so that nonlinear effects and time dependence can be neglected. To simplify the problem further it is assumed that the motion does not vary in the direction parallel to the coast, i.e.,  $\partial(\ )/\partial y = 0$ . The geometry is shown in Fig. 1.

At the coast there is a laterally distributed transport of fresh water (river runoff) denoted by  $T_R$ . This sets up a salinity gradient normal to the coast. What are the implications of this gradient? Equation 1 is

$$-fv_z = -g\beta s_x + A_v u_{zz}$$

where

$$(\ )_z = \frac{\partial}{\partial z} (\ ), \quad (\ )_{zz} = \frac{\partial^2}{\partial z^2} (\ ), \quad \dots$$

In an estuary where there are lateral side walls,  $v$  is either very small or absent. Similarly, on the shelf it can be shown that in shallow water, or for large values of  $A_v$  and  $K_v$ , this is also true. In such situations the term  $fv_z$  can be neglected and

$$vu_{zzz} = g\beta s_x$$

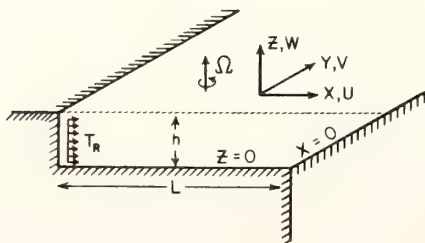


FIGURE 1. Geometry for shelf models.

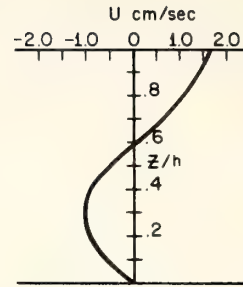


FIGURE 2. Vertical profile of the offshore velocity for the following parameters:  $A_v = 10^2 \text{ sec}^{-1}$ ;  $g\beta s_x = 6.25 \times 10^{-8}$ ;  $H = 5 \times 10 \text{ cm}$ ;  $T_R = 50 \text{ cm}^2/\text{sec}$ .

Situations exist on the shelf or in estuaries in which  $s_x$  is essentially independent of  $z$ . In these cases the solution for  $u$  is given by

$$u = -\frac{g\beta s_x h^3}{A_v} \left[ \frac{1}{6} \left(\frac{z}{h}\right)^3 - \frac{5}{16} \left(\frac{z}{h}\right)^2 + \frac{1}{8} \left(\frac{z}{h}\right) \right] + 3 \left[ \frac{1}{2} \left(\frac{z}{h}\right)^2 - \frac{z}{h} \right]$$

As boundary conditions we have assumed that the stress is zero at the sea surface ( $u_z = 0$  at  $z = h$ ), the velocity is zero at the bottom ( $u = 0$  at  $z = 0$ ), and the net transport of water offshore is given by  $\int_0^h u dz = T_R$ . This solution is illustrated in Fig. 2. Although there is a net offshore transport of water,  $T_R$ , the magnitude of the flow toward the source of the river transport is much larger than  $T_R$ .

This perhaps is of importance for sediment or sewage transport onshore. Similar velocity profiles are obtained for more general and difficult problems. The circulations in estuaries are of this type. It should also be noted that the inflow velocity is at least an order of magnitude larger than the river outflow velocity  $T_R/h$ , 0.01 cm/sec. This type of problem becomes considerably more difficult when the distribution of  $s$  in  $x$  and  $z$  is solved for simultaneously.

The earth's rotation can play an important role in determining the nature of the flow. In the preceding example by the choice of geometry (in the case of estuaries) or by the assumption that the flow was very viscous, this effect was not present. If the value of the eddy coefficient is decreased or the water depth is increased, rotational effects become important. Then the solution, over most of the water column, becomes

$$u = 0, \quad v = \left( \frac{g}{f} \beta \frac{\partial s}{\partial x} \right) z$$

Close to the surface and the bottom this solution is modified by friction. Note the differences between this solution and the preceding one. The primary flow is now parallel to the coast and northward. Only in thin regions close to the top and bottom is there on- or offshore transport (it is in these "boundary layers" that the offshore transport of fresh water occurs). The most likely direction for sediment transport is now parallel to the coast. The primary factor that determines whether this solution or the previous one applies is the value of  $A_v$ . Unfortunately this parameter is extremely difficult to measure directly, and within the range of physically possible  $A_v$  either solution can occur.

## WIND FORCING

Consider a situation where a wind stress is applied at the surface, and  $T_R = 0$  ( $s_x = 0$ ). The governing equations are

$$-fv = -\frac{1}{\rho_0} p_x + A_v u_{zz}$$

$$fu = A_v v_{zz}$$

$$0 = -p_z - \rho_0 g$$

$$0 = u_x + w_z$$

where  $p$  is the pressure. At the sea surface we apply a stress  $\rho_0 A_v (\partial v / \partial z) = \tau_y$ . The boundary conditions are

$$\text{at } z = h, \quad \rho_0 A_v \frac{\partial v}{\partial z} = \tau_y; \quad \frac{\partial u}{\partial z} = 0; \quad w = 0$$

$$\text{at } z = 0, \quad u = v = w = 0$$

For small values of  $A_v$  the solution consists of two parts. In the interior of the fluid there is a "geostrophic" part where

$$u = 0, \quad v = \frac{1}{\rho_0 f}, \quad p_x = \frac{\tau_y}{\rho_0} \left( \frac{2}{A_v f} \right)^{1/2}$$

In addition, there are contributions that die away exponentially from the surface and bottom that match the interior solution to the boundary conditions. These are called Ekman layers. They have the property that the net transport in each layer is given by  $T_{EL} = \tau_y f$ , which is independent of the eddy coefficient. The velocities are of the order of a few centimeters per second for reasonable values of the wind stress.

The transport in the surface layer is to the right of the wind stress, or offshore in this example. The transport

in the lower layer is equal to that in the upper layer, but onshore. The detailed solutions for these layers are given in textbooks on dynamical oceanography.

We can understand this system of currents in the following way. When the wind begins to blow, the upper Ekman layer starts to transport water away from the coast. This lowers the sea surface next to the coast and creates a pressure gradient perpendicular to the coast. This is balanced by a flow parallel to the coast [ $fv = (1/\rho_0)p_x$ ]. Close to the bottom, friction acting on this flow causes another Ekman layer to form with onshore transport. The pressure gradient continues to build until the transports in the upper and lower Ekman layers balance. A steady state is then obtained. This is the solution that was presented earlier.

In this problem the transports close to the bottom are again directed onshore and would support sediment transport in that direction.

The thickness ( $D_{EL}$ ) of each Ekman layer is proportional to  $(A_v f)^{1/2}$ , and this depends on the square root of the eddy coefficient. As the flow becomes more viscous (i.e.,  $A_v$  increasing)  $D_{EL}$  increases, and the upper and lower Ekman layers merge.

When this happens the solution becomes (in the limit of  $D_{EL} > h$ )

$$u = 0, \quad v = \left( \frac{\tau_y}{h} \right) z$$

This is known as Couette flow. Rotational effects are no longer important and all the flow is parallel to the coast in the direction of the stress. The velocities close to the bottom are small.

In the examples presented so far, the magnitude of the eddy coefficient plays an important role in determining the nature of the solution. This is another reason for difficulty in formulating satisfactory models of shelf circulations. The criterion which determines the nature of the solution is the ratio of  $D_{EL}$ , the Ekman depth, to  $h$ , the depth of water. When  $D_{EL}$  is less than  $h$  the flows tend to be rotationally dominated. When  $D_{EL}$  is comparable to or larger than  $h$ , the effects of rotation diminish or disappear. Consequently, the nature of the solutions for a given value of  $A_v$  can depend also on the depth of the water. In deep water offshore, the solutions may be rotationally dominated, whereas inshore, where the water is shallower, they might become more Couette or estuarine in nature.

The simplest possible effects of two types of forcing in a simple model have now been briefly examined. As should be obvious the problems can become extremely complex even for this simple model, when the depth varies, when  $s_x$  is to be determined, and when rotational and viscous effects are equally important.

A MODEL OF CONTINENTAL SHELF CIRCULATION

The ideas explored in the preceding sections can be used to form a model of shelf circulations driven by freshwater runoff from land and by wind stress (Stommel and Leetmaa, 1972). As before a shelf of infinite length ( $y$  direction) and a semiinfinite width (extending from the deep ocean at  $x = 0$  to negative  $x$ -infinity) is considered. The depth of the shelf is  $h$ . A mean flux of freshwater,  $T_R$  per unit length of coastline, flows toward the sea, due to the cumulative effects of river discharge along the coast. The steady wind stress components at the surface  $z = h$  are  $\tau_x$  and  $\tau_y$ . The salinity and density are related by  $\rho = \rho_0(1 + \beta s)$ . Assume linear dynamics:

$$\begin{aligned} A_v \psi_{zzzz} - \beta g s_x - f v_z &= 0 \\ A_v V_{zz} + f \psi_z &= 0 \\ K_v s_{zz} + \psi_z s_x - \psi_x s_z &= 0 \end{aligned}$$

where the motion is independent of  $y$ ;  $x$  derivatives of diffusion terms are neglected because of the large ratio of horizontal to vertical scales; and the stream function  $\psi$  defines the velocity components  $u = -\psi_z$ ,  $v = \psi_x$ . The boundary conditions in  $z$  are that

$$\begin{aligned} \text{at } z = 0, \quad \psi &= \psi_z = s_z = v = 0 \\ \text{at } z = h, \quad \psi &= -T_R; \quad -\rho_0 A_v \psi_{zz} = \tau_x; \\ &\quad \rho_0 A_v V_z = \tau_y; \quad s_z = 0 \end{aligned}$$

This problem models wintertime conditions on the east coast continental shelf of North America. Winter is attractive because (1) density is primarily controlled by the salinity distribution and (2) the weak vertical density gradient in winter permits a simplification in the treatment of the third equation above, which is nonlinear. Even for this simple model, a complete solution is difficult. Instead the model is used to estimate the natural horizontal scale length  $L = s_0 \nabla_x \nabla_s$  where  $\nabla_x$  is the observed width of the shelf and  $\nabla_s$  is the decrease in salinity over that distance from the ocean value,  $s_0$ . The details of the solution are given by Stommel and Leetmaa (1972). The solution for  $L$  for various values of the wind stress and the eddy coefficient  $A_v$  is shown in Fig. 3, where  $E$  (the Ekman number) is equal to  $A_v f h^2$ .

For these solutions, values of the parameters which are appropriate for the eastern U.S. continental shelf from Nantucket Shoals to Cape Hatteras have been chosen:  $f = 0.7 \times 10^{-4} \text{ sec}^{-1}$ ,  $h = 5 \times 10^3 \text{ cm}$ ,  $\beta g s_0 = 30 \text{ cm}^2/\text{sec}^2$ ,  $T_R = 50 \text{ cm}^2 \text{ sec}$ ,  $A_v K_v = 1$ .

The upper curves of the diagram correspond to the purely wind-driven regime. The lowest curve, which is convex upward, is the pure density-driven model. For

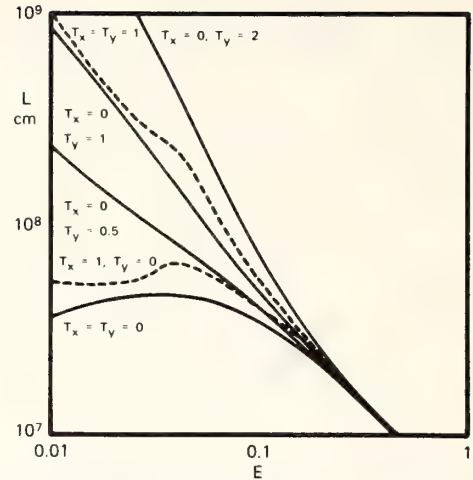


FIGURE 3. Solutions for  $L$  for different values of the wind stress and the Ekman number ( $E = A_v f h^2$ ).

large values of the mixing coefficient all curves coalesce and the motion is basically density driven and of the estuarine nature that was described earlier.

For small values of the vertical mixing coefficient, with  $y$  stress predominant, the Ekman transports which convect salt onshore and offshore are independent of  $A_v$  (as was pointed out earlier). However, vertical mixing,  $K_v$ , "short-circuits" these transports. This is proportional to  $A_v$  since we assumed that the Prandtl number,  $A_v K_v$ , was unity. Thus small values of  $A_v$  correspond to small mixing between the upper and lower Ekman layers and large penetration of salt occurs (i.e., large  $L$ ). When there is no applied wind stress, the Ekman transports are driven by stress associated with the shear produced by the horizontal salinity gradient, i.e.,  $A_v v_z = (A_v g \beta f) s_x$ . This diminishes as  $A_v$  becomes smaller, and despite a partial compensation because  $k$  is also smaller, the salt penetration diminishes. This accounts for the different behavior for  $L$  ( $A_v$ ) for density as compared to wind forcing.

For large values of mixing, as pointed out earlier, the dynamics of the flow become nonrotational and also vertical mixing is enhanced. Thus all the curves coalesce in the purely salinity-driven case.

Attempts to compare this theory with the observations are difficult because a priori the appropriate values of  $A_v$  and  $k$  are unknown. It is assumed that  $A_v/K_v = 1$ . The observations in this area indicate that  $L$  is about  $3.2 \times 10^8 \text{ cm}$ . Wintertime mean wind stress in this area can be estimated from Hellermann's (1967) world charts. These indicate that the magnitude of the  $x$  and  $y$  components of stress is about  $1 \text{ dyne cm}^2$ . Thus with  $\tau_x = \tau_y = 1$  and  $L = 3.2 \times 10^8$ , Fig. 3 indicates that  $A_v$  is about  $37 \text{ cm}^2/\text{sec}$ . This is consistent with the observations. It



should also be noted that values of  $L$  as large as those observed imply that the shelf circulation, at least for this model, is basically wind-driven. As another test of the model the difference between the salinity at the top and bottom can be computed. This turns out to be 0.14‰. Again this is of the right order of magnitude according to the observations.

Despite these limited successes of the model, there is a serious discrepancy between the predicted  $v$  component of velocity and the observed value. All the observations indicate a negative  $v$  velocity of an order of 5 cm sec. The theoretical  $v$  component is positive, about 20 cm sec. If the observations are correct, this indicates that this simple model is not adequate to describe the observed shelf circulation.

There is some observational evidence to indicate that there is a northward rise in sea level along the coast (Sturges, 1974). If this feature is introduced into the model, the discrepancy in the direction of flow parallel to the coast can be resolved (Stommel and Lectma, 1972). However, the observations are not conclusive on this point. The theoretical flow close to the bottom then is in the right direction and is on the order of a centimeter or two per second.

## CONCLUSIONS

As contradictions occur between model results and observations, more details can be added to the models. At some point, however, the question has to be asked as to how applicable steady state models are to shelf circulations and in particular to sediment transport. Examination of daily wind records at Nantucket Shoals light vessel shows that the wintertime root-mean-square wind stress is 5 to 10 times larger than the mean. Thus the transient fluxes are possibly an order of magnitude larger than the mean ones. For sediment transport this could be the dominant factor since the steady models give rather low near-bottom velocities.

Better observations are needed to indicate the direction that modeling should go. Long-term series of current and density measurements are needed to obtain an observational verification of the mean fields and their vertical structure. Time series of currents and density as functions of depth are needed; without these the more complex transient theories of shelf circulations cannot be adequately attained. Finally, for the results of the physical oceanographer to be of relevance to those interested in sediment transport we need to know whether the means or the transients are important in sediment transport.

In this chapter the reader is introduced to some of the problems facing a shelf modeler. Other more compli-

cated models exist that were not examined. Two of these are the models by Csanady (1974) and Pietrafesa (1973). Csanady discussed the barotropic (depth independent) response of a shelf to an imposed wind stress or external pressure gradient. Pietrafesa considers a steady state, nonlinear, wind-driven model of an eastern meridional coastal circulation. Both are considerably more complex analyses than the one presented here. A more extensive list of references can also be found in them.

## SUMMARY

This chapter provides an introduction to steady state models of the oceanic circulation on the continental margin. Horizontal salinity gradients comprise a major forcing mechanism for shelf circulation. A gradient of seaward-increasing salinity will result in a seaward net transport of surface water and a larger landward net transport of bottom water, if the flow is relatively viscous (low values for the eddy coefficient and depth). With decreasing viscosity, the earth's rotation plays an increasingly important role in determining the nature of the flow. The primary flow tends to parallel the coast, while onshore and offshore transport is confined to the surface and bottom layers.

Wind forcing is effected by the application of wind stress to the sea surface. For small values of the eddy coefficient, the solution for the horizontal components of motion occurs in two parts. There is a coast-parallel "geostrophic" component of flow in the interior of the fluid. Additional flow components are experienced at the upper and lower boundaries, which die away exponentially toward the interior of the flow. Net transport in these *Ekman layers* is given by  $T_{EL} = \tau_y f$ , where  $\tau_y$  is the component of shear stress parallel to the coast and  $f$  is the Coriolis parameter. Net transport is independent of the eddy coefficient. The thickness of each Ekman layer is proportional to the square root of the eddy coefficient.

As wind-driven flow becomes more viscous (because of increasing eddy coefficient or decreasing depth), the upper and lower Ekman layers merge and the vertical velocity gradient becomes linear in nature (Couette flow). Rotational effects are no longer important, and all flow is parallel to the coast in the direction of stress.

These relationships may be combined into a single steady state model for shelf circulation. When applied to the Middle Atlantic Bight of North America, the model predicts an eddy coefficient of 37 cm<sup>2</sup>/sec, and for the observed horizontal length scale, a primarily wind-driven circulation. However, it is necessary to postulate a northward rise in sea level along the coast, in order for the model to predict net flow to the south, as observed.

## SYMBOLS

$A_v$	vertical eddy mixing coefficient for momentum
$D_{EL}$	thickness of the Ekman layer
$E$	Ekman number
$f$	Coriolis parameter: $f = 2\Omega \sin \theta$
$h$	depth of water
$K_v$	vertical eddy mixing coefficient for salt
$L$	natural horizontal length scale
$p$	pressure
$s$	salinity
$T_R$	river transport
$u$	$x$ component of velocity
$v$	$y$ component of velocity
$w$	$z$ component of velocity
$x$	horizontal distance from origin perpendicular to coast
$y$	horizontal distance from origin parallel to coast
$z$	vertical distance upward from origin
$\beta$	coefficient of contraction for salt

$\theta$	latitude
$\tau$	shear stress
$\rho$	density
$\psi$	stream function
$\Omega$	angular velocity of the earth

## REFERENCES

- Bumpus, D. F. (1973). A description of the circulation on the continental shelf of the East Coast of the United States. *Prog. Oceanogr.*, **6**: 111-158.
- Csanady, G. T. (1974). Barotropic currents over the continental shelf. *J. Phys. Oceanogr.* **4**(3): 357-371.
- Hellermann, S. (1967). An update estimate of the wind stress on the world ocean. *Mon. Weather Rev.*, **95**: 607-626.
- Pietrafesa, L. J. (1973). Steady baroclinic circulation on a continental shelf. Ph.D. Dissertation, Dept. of Oceanography and Geophysics Group, University of Washington, Seattle.
- Stommel, H. and A. Lectmaa (1972). Circulation on the continental shelf. *Proc. Natl. Acad. Sci. U.S.A.*, **69**(11): 3380-3384.
- Sturges, W. (1974). Sea level slope along continental boundaries. *J. Geophys. Res.*, **79**(6): 825-830.

Reprinted from: *NOAA Technical Report ERL 376-AOML 22*, 10 p.

**NOAA Technical Report ERL 376-AOML 22**

# **A Comparison of Satellite-Observed Sea-Surface Temperatures With Ground Truth in the Indian Ocean**



**Ants Leetmaa  
Matthew Cestari**

**Atlantic Oceanographic and Meteorological Laboratories  
Miami, Florida**

**August 1976**

**U.S. DEPARTMENT OF COMMERCE**

Elliot Richardson, Secretary

**National Oceanic and Atmospheric Administration**

Robert M. White, Administrator

**Environmental Research Laboratories**

Wilmot Hess, Director



Boulder, Colorado

## NOTICE

The Environmental Research Laboratories do not approve, recommend, or endorse any proprietary product or proprietary material mentioned in this publication. No reference shall be made to the Environmental Research Laboratories or to this publication furnished by the Environmental Research Laboratories in any advertising or sales promotion which would indicate or imply that the Environmental Research Laboratories approve, recommend, or endorse any proprietary product or proprietary material mentioned herein, or which has as its purpose an intent to cause directly or indirectly the advertised product to be used or purchased because of this Environmental Research Laboratories publication.

## CONTENTS

	Page
1. INTRODUCTION	1
2. THE SATELLITE-OBSERVED SEA-SURFACE TEMPERATURE MAPS	2
3. SEA-SURFACE TEMPERATURE VARIATIONS ACCORDING TO SATELLITE DATA	3
4. COMPARISON OF SATELLITE DATA WITH SHIP REPORTS	5
5. COMPARISON OF SATELLITE DATA WITH 1963 SURFACE OBSERVATIONS	8
6. SUMMARY	10
7. REFERENCES	10

# A COMPARISON OF SATELLITE-OBSERVED SEA-SURFACE TEMPERATURES WITH GROUND TRUTH IN THE INDIAN OCEAN

Ants Leetmaa  
Matthew Cestari

Daily worldwide sea-surface temperature maps are produced by the National Environmental Satellite Service. For the first half of 1975, sea-surface temperatures recorded on these maps were compared with concurrent ship observations in the Indian Ocean. Additional comparisons were made with historical data. These show systematic differences between the satellite and sea-surface observations. The satellite-derived temperatures appear to be too low along the equator and along the East African coast in the vicinity of the equator. Furthermore, in April, May, and June the areas off the equator (and not along the coast) appear to have temperatures that are too high. Although the mean differences are not large ( $1^{\circ}$ - $2^{\circ}$ C), the fact that the errors vary in time and space made it difficult to apply the satellite data for oceanographic interpretations.

## 1. INTRODUCTION

Numerical experimentation has shown that the tropics are an important area for interactions and feedbacks between the ocean and the atmosphere. From present planning, it is clear that during the First GARP Global Experiment (FGGE) equatorial regions will receive special attention in the ocean as well as in the atmosphere. The Indian Ocean, because of the monsoons, will also have a special observing period during FGGE, the Monsoon Experiment (MONEX).

Because of the importance of equatorial regions to climatic studies, and because FGGE will provide relatively complete meteorological coverage, a group of oceanographers has started planning an Indian Ocean Experiment (INDEX). The primary goal of INDEX will be to study the transient response of a low latitude ocean to a strong regular forcing by the atmosphere. Pilot experiments, whose results will aid in the design of the final experiment, are now taking place. Sea-surface temperature maps from satellite data could be a valuable tool to study the onset of the Somali Current, upwelling along the Arabian coast, and heat budgets in the Arabian Sea. At the present time such maps are available from the National Environmental Satellite Service. However, as with every new product or technique, they have to be examined carefully to ascertain their limits of accuracy and applicability. This study reports on a number of intercomparisons between the satellite-observed sea-surface temperatures and "ground truth" in the Indian Ocean during the first half of 1975. The results suggest that more work has to be done before reliable sea-surface temperatures can be obtained from satellites.

## 2. THE SATELLITE-OBSERVED SEA-SURFACE TEMPERATURE MAPS

The National Environmental Satellite Service provides daily worldwide satellite sea-surface temperature (SSST) maps. This product is known as the Global Sea-Surface Temperature Computation (GOSSTCOMP). One form of this is an uncontroled computer printout with sea-surface temperature values for each one-half degree of latitude and longitude. With each numerical value for temperature is a code that indicates the estimated reliability of the data. If the code is "+4", then the last reading had been taken four days before the date of the map, etc. If the number of days exceeds nine, the code space is blank, and the temperature value given is from historical data. If data are available for the day of the map, a letter appears in the code space. An "+A" indicates that the temperature listed is an average of five readings. A "+B" indicates an average of five to eight values and so on up to "+H" which indicates that over 25 values were averaged. The better maps in our analysis had mostly D's through H's associated with the temperature readings.

For this study, the daily map with the highest code letter was selected to represent an entire week. One day was chosen to be representative of a whole week because changes from day to day were observed to be small, and weekly representations were more readily compared than daily maps. They start with the week of January 3-9 and end with June 1-7, 1975. Each map selected was contoured in the area of the Indian Ocean off the coast of Africa from 6°S to 15°N and 35°W to 65°E in latitude and longitude. From the collection of maps, one was selected from the early portion of each month to illustrate any monthly differences (Figs. 1-3).

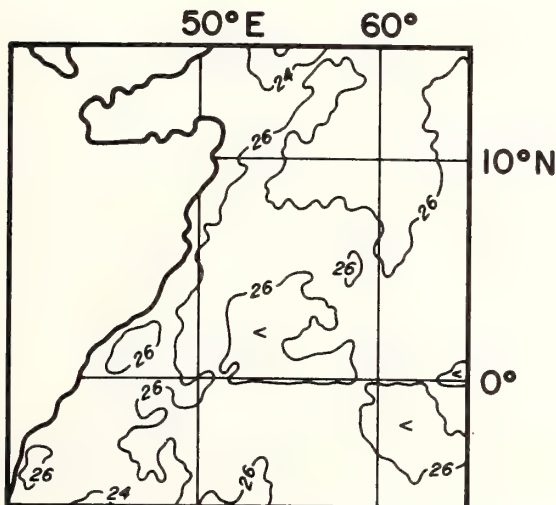


Figure 1. Satellite sea-surface temperature data for January 1975.

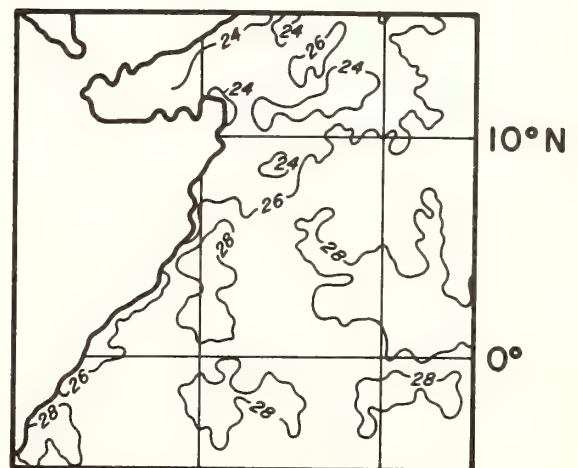


Figure 2. Satellite sea-surface temperature data for February 1975.

### 3. SEA-SURFACE TEMPERATURE VARIATIONS ACCORDING TO SATELLITE DATA

The seasonal variations of sea-surface temperatures in the Indian Ocean is strongly related to the NE and SW monsoons, the transition periods between them, and the ocean current systems established by the winds. The features observed on the maps must be interpreted in the context of these phenomena. Figure 1 shows that there was not a wide range of temperatures in January. Most of the readings were either slightly greater or less than 26°C. On either side of the equator the temperatures are somewhat warmer than at the equator. During February (fig. 2), the sea surface immediately north and south of the equator warms, while temperatures at the equator remain cool, as in January. North of approximately 8°N the temperatures begin to decline with areas containing temperatures lower than 24°C. This is colder than in January. In March (fig 3) the same pattern persists, but a warming trend is evident. The area of the equator continues to remain cool, and the areas immediately north and south of the equator (5°S-8°N) are warmer. Larger areas of 28°C and higher temperatures are visible, with 30°C temperatures reported for some locations. Temperatures for April (fig. 4) show an increased warming trend, with many areas containing temperatures of 30°C and higher.

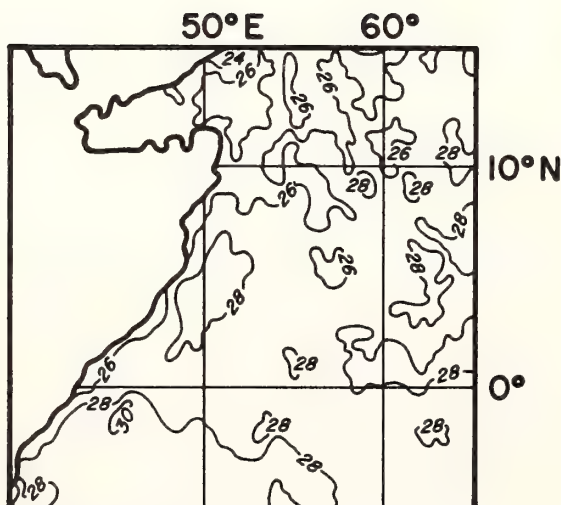


Figure 3. Satellite sea-surface temperature data for March 1975.

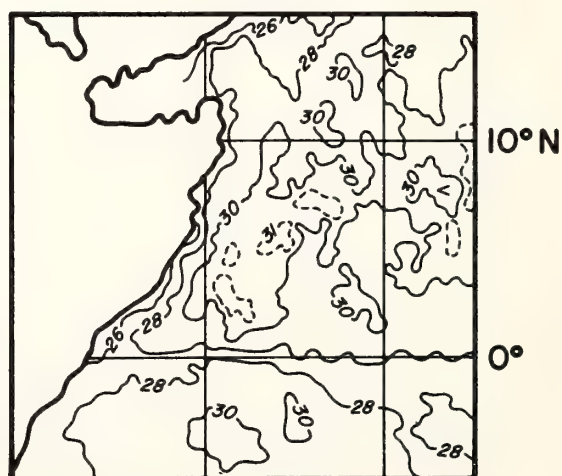


Figure 4. Satellite sea-surface temperature data for April 1975.



Temperatures in the area of the equator, as noted in all previous months, remain between 26°C and 28°C. Areas immediately north and south of the equator have become considerably warmer. In the north there are isolated areas with temperatures higher than 31°C. The warmest month from January to June, 1975, is May (fig. 5). Again the area at the equator remains cool. Large areas of 30°C and higher temperatures are visible north and south of the equator. The north exhibits a slight cooling trend in June (fig. 6). The equatorial band remains cool, and areas to the north and south become cooler. Fewer and smaller areas of 30°C and higher temperatures are still present, and the major portion of the entire region contains temperatures of 28°C or slightly higher. The areas of 30°C and higher temperatures seem to have moved toward the north and south, away from the area immediately north and south of the equator. In all months, temperatures along the East African coast were cooler than those offshore.

On first glance the seasonal variation in the sea-surface temperature pattern as seen from these maps appears to be reasonable. The transition period between the northeast and the southwest monsoon occurs during March, April, and through the middle of May. A major factor in the heat budget of the surface layers is evaporation, which is proportional to wind speed. During the transition, the evaporation decreases and the sea-surface temperature increases. The cooler coastal areas could be related to upwelling or to north-south transport of cooler water by the Somali Current along the coast. A feature that is anomalous, however, is the cool band of water along the equator. In the Pacific and Atlantic Oceans, such a cool band is indicative of equatorial upwelling. However, in the Indian Ocean the winds are not favorable for upwelling, and this feature is rarely present. To examine the validity of this indication and others in more detail, a comparison was made of these satellite data with data from a number of other sources.

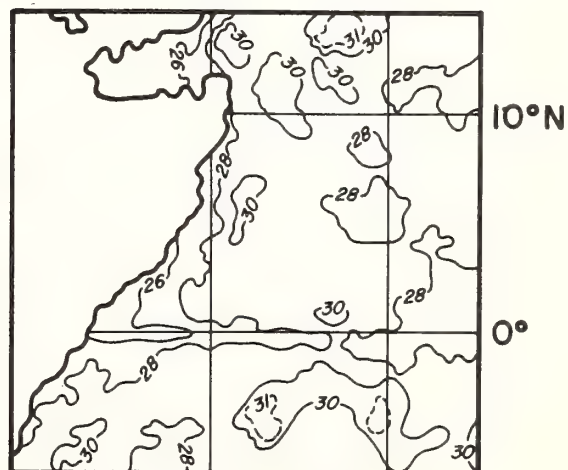
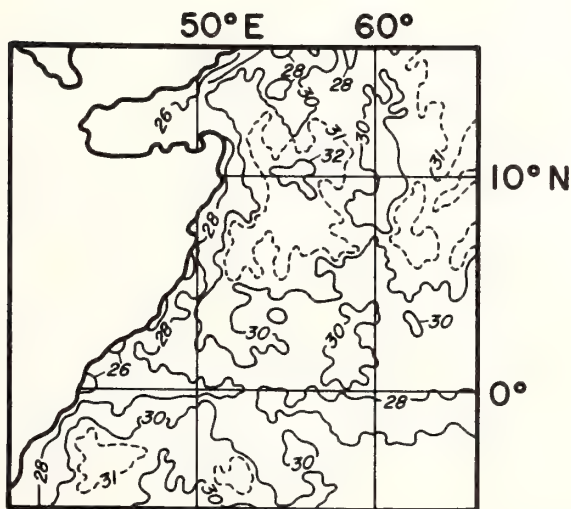


Figure 5. Satellite sea-surface temperature data for May 1975.

Figure 6. Satellite sea-surface temperature data for June 1975.

#### 4. COMPARISON OF SATELLITE DATA WITH SHIP REPORTS

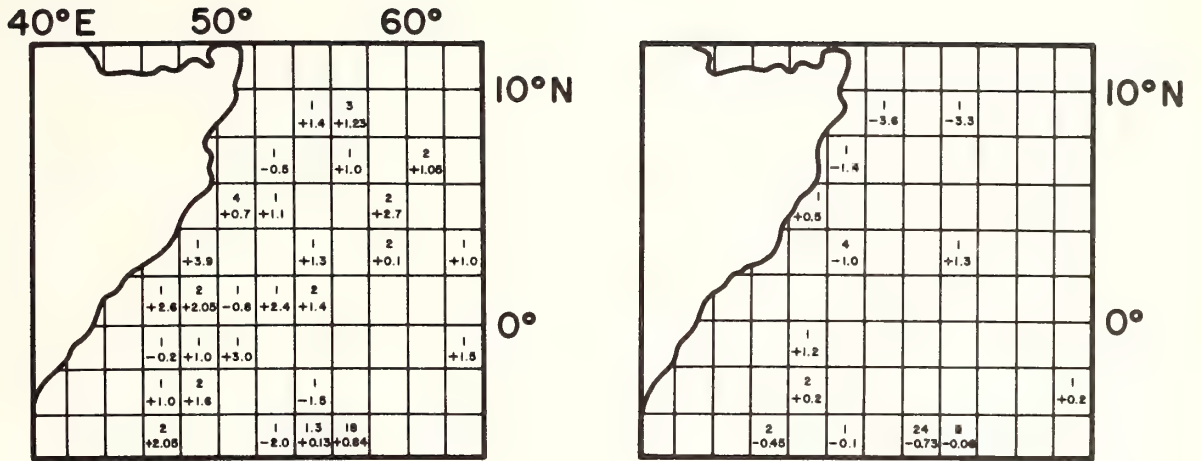
We can compare the satellite data with actual ship observations obtained at the same time in the same area. For February through May 1975 data are available from a chartered research vessel, *La Curieuse*, in the vicinity of the equator. Bucket thermometer readings (estimated accuracy  $\pm 0.2^{\circ}\text{C}$ ) were taken periodically along  $55^{\circ}40'\text{E}$  from  $3^{\circ}\text{S}$  to  $2^{\circ}\text{N}$ . The National Weather Service also provides information on air temperature, dew point, and sea surface temperature at ship positions through its twice-daily surface-weather maps.

There were 106 cases in which bucket thermometer readings from *La Curieuse* could be compared with data from the satellite. The mean difference for the whole data set was  $+0.4^{\circ}\text{C}$ . Temperatures recorded from the ships were, on the average, higher. The standard deviation was  $0.9^{\circ}\text{C}$ . This indicates that the scatter was quite large. The mean difference actually is rather small. However, if the data are studied in more detail, it becomes clear that there are obvious trends. The satellite temperature data for the equator are always lower than the surface observations and the difference becomes greater as time goes on. For example, for all intercomparisons (32) in the region from  $0.5^{\circ}\text{S}$  to  $0.5^{\circ}\text{N}$  the mean difference is  $+0.9^{\circ}\text{C}$ . The standard deviation is  $0.7^{\circ}\text{C}$ . Clearly the equator is systematically colder in the satellite data. This conclusion supports our previous speculations.

The satellite data were also compared with merchant ship reports. Unfortunately, there is a very limited amount of ship data available in real time. Also, frequently only the air temperatures are available rather than the sea-surface temperatures. In the tropics this is not a serious problem because the differences between these are usually small. Thus, to maximize the data set, the ship reports were compared three ways. First the Satellite Sea Surface Temperatures (SSSTs) were compared with the reported air temperatures. The SSSTs were then compared with the sea-surface temperatures, and finally with air and sea temperatures that were within one degree of each other. Approximately 270 ship reports were available in the period from January to June 1975.

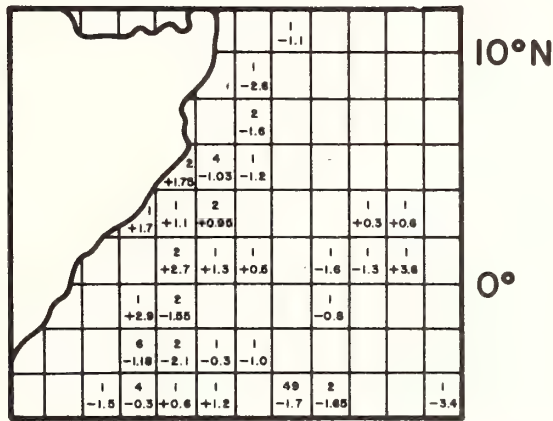
The difference between air temperature from ship reports and satellite sea-surface temperature was determined from three 2-month groups. For January-February, the mean difference was  $+0.85$ . For March-April it was  $-0.59$ , and for May-June it was  $-0.97$ . This indicates that the satellite temperatures are lower than actual temperature measurements for January and February, but higher than actual for March-April and May-June. These differences also appear to have a geographic dependence. Figure 7 shows the geographical distribution of these differences. For May-June the satellite reads low in the vicinity of the equator and along the Somali coast, and high elsewhere. March-April shows the same trend. In January-February the satellite reads systematically low almost everywhere.

The difference between sea-surface temperatures from merchant vessels and SSST was investigated for only May-June because not enough data were available for other months. The geographic distribution of the differences is shown in figure 8. Again the satellite appears to read low in the vicinity of the coast and the equator and high elsewhere.



January-February

March-April



May-June

Figure 7. Geographic distribution of differences between air temperatures and satellite sea-surface temperatures. The upper number in each square indicates the number of comparisons.

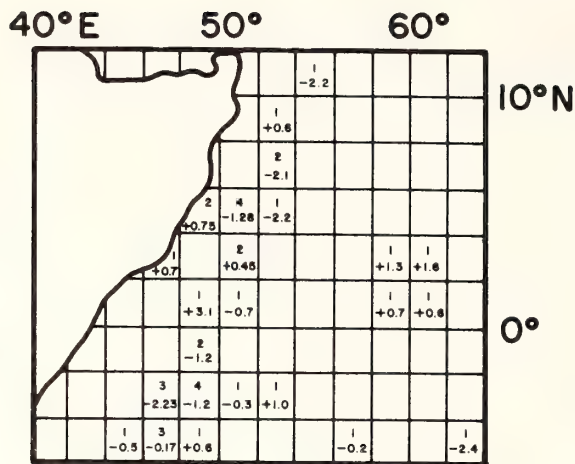


Figure 8. Geographic distribution of differences between sea-surface temperatures from merchant ships and satellite sea-surface temperatures for May-June 1975.

For a final intercomparison, we computed the monthly mean (SSST) for April, May and June, 1975 for the areas: REGION I - 12°-13°N, 54°-56°E; REGION II - 11°-12°N, 54°-55°E; REGION III - 10°-11°N, 53°-55°E (fig. 9). We compared these with the 21-year mean temperatures in these regions as derived from all ship reports on file at the National Climatic Center. These were computed by Fieux and Stommel (1975). The results are presented in Table 1.

It should be noted that the satellite data, except for one comparison always give higher temperatures than the historical data do in this region. In April and June the satellite temperatures are nearly always two standard deviations away from the historical temperatures.

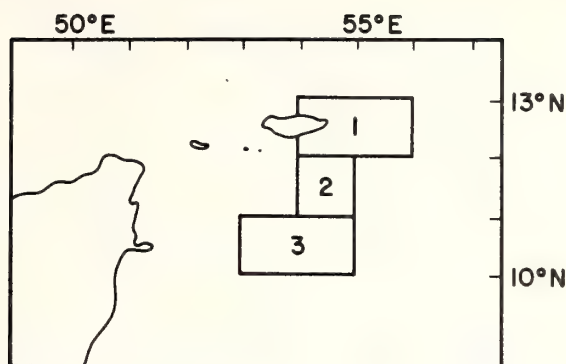


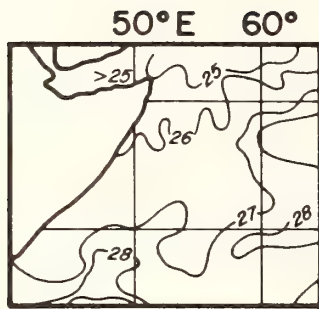
Figure 9. Regions for which comparisons were made between satellite sea-surface temperature data and historical ship data.

Table 1. Comparison of Average SSST's with Historical Ship Data.

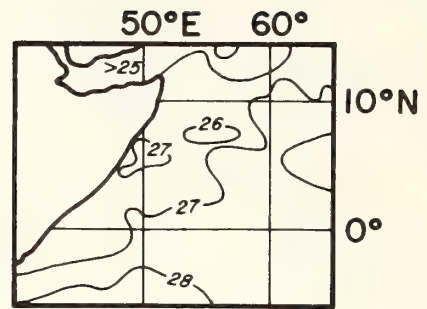
	SSST	SHIPS	SSST	SHIPS	SSST	SHIPS	
	April		May		June		
REGION I	28.49	28.52	29.64	29.51	29.32	27.90	Mean Temp.
		0.48		0.66		0.86	Standard Deviation
REGION II	29.25	28.38	30.34	29.50	29.74	27.17	Mean Temp.
		0.60		0.78		0.90	Standard Deviation
REGION III	29.93	28.84	30.82	29.43	29.49	26.65	Mean Temp.
		0.56		1.06		1.20	Standard Deviation

##### 5. COMPARISON OF SATELLITE DATA WITH 1963 SURFACE OBSERVATIONS

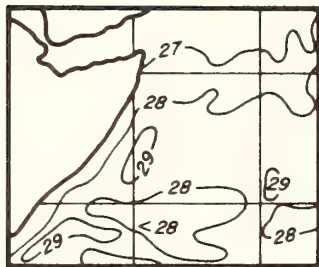
From the International Indian Ocean Expedition, data are available on sea-surface temperature for 1963 (Wyrski, 1973). These were accumulated from surface observations from ships. Maps for January through June 1963 (see fig. 10) may be compared with satellite temperature maps from 1975. One obvious difference is that in January-June, 1963, there was no equatorial temperature minimum. Also in the 1963 data, there is no indication that along the coast sea-surface temperatures are lower for January-April as they are in the satellite data. Another difference between the two data sets is that the International Indian Ocean Expedition maps for April and May contain



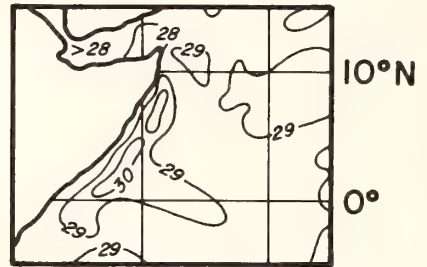
January



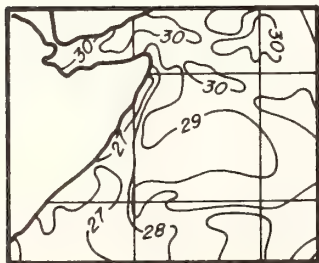
February



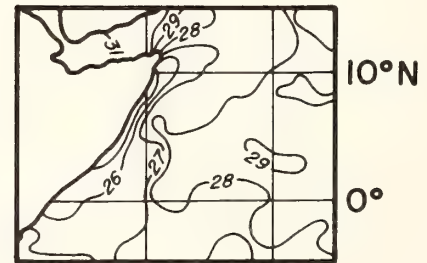
March



April



May



June

Figure 10. Sea-surface temperature data for 1963 obtained from the International Indian Ocean Expedition.

temperatures of 30°C and slightly above as maximum temperatures for the area being studied, while the satellite maps contain areas with temperatures above 31°C for April and above 32°C for May. The maximum temperatures are therefore higher in the satellite readings than in the 1963 International Indian Ocean Expedition data. This, of course, might be related to year-to-year variations.

The final major difference between 1963 and 1975 data is the north-south temperature gradient for May. The satellite temperatures range from 27°C at the equator to greater than 32°C at about 10°N along 55°E, while the International Indian Ocean Expedition data range from 29°C to between 30°C and 31°C in the same area. Clearly the satellite temperature data have a wider range. Satellite-measured temperatures are higher in warm areas and lower in cool ones than temperatures measured at sea-surface.

## 6. SUMMARY

It is difficult to obtain reliable sea-surface temperature data for the Indian Ocean. Potentially, satellite IR data could satisfy this need. However, the quality of these data has to be assessed before extensive use can be made of them. Since ground truth is difficult to obtain in this region, we tried to evaluate the SSST's by comparing them with data from a number of independent sources. In each case, the intercomparisons showed serious discrepancies between the satellite data and the ground truth. Although any one result might be suspect, a clear trend emerged from the analyses. The SSST's appear to be too low along the equator and along the East African coast in the vicinity of the equator for the time period examined. Furthermore, in April, May, and June in the areas off the equator and not along the coast, they appear to be too high.

On the basis of this study, one would have to conclude that the SSST's, at least for the Indian Ocean, are suspect. The errors appear to vary geographically in time and more work must be done if SSST's are to be of great usefulness to oceanography. Meteorologically, improved SSST's are very important because during FGGE, SSST's will be used in the numerical models. An enhanced north-south temperature gradient in the models will probably create unrealistic atmospheric circulation patterns in the tropics.

## 7. REFERENCES

- Fioux, M. L. and H. Stommel, 1975: Personal communication. M.I.T., Cambridge, Mass. 02139.
- Wyrtki, K. 1973: Oceanographic Atlas of the International Indian Ocean Expedition. NSF-IOE-1, Washington, D.C. 531 pp.

## THE STUDY OF OCEAN CIRCULATION FROM SPACE

George A. Maul  
National Oceanic and Atmospheric Administration  
Atlantic Oceanographic and Meteorological Laboratories  
15 Rickenbacker Causeway  
Miami, Florida 33149

## ABSTRACT

Major ocean currents have surface manifestations that make them observable by spacecraft sensors. Under certain conditions, any one or a combination of the following may be used to identify the current's boundary: changes in sea surface temperature, salinity, color (diffuse), sea state (specular), sea surface topography, wave refraction patterns, and modifications to the lower atmosphere. Infrared sensors have been used most extensively to study ocean circulation; however, new instruments such as passive and active microwave sensors can sense temperature, salinity, sea state, and surface topography, and multispectral visible scanners and spectroradiometers are providing new information on ocean color and sea state. Man's role as an observer and photographer provides the highest spatial resolution to date for describing visible changes across boundaries as well as sea and swell patterns.

## INTRODUCTION

Ocean currents have several sea surface manifestations that can be used singularly or in concert, to locate their boundaries. Coastal currents typically have significant energy at the tidal (1-2 cycles per day; cpd) or local inertial frequencies (0.5 - 1.5 cpd for mid-latitudes). These frequencies are too high for the ocean's density field to adjust to the motion. Adjustment of the density field provides the conditions by which many satellite sensing techniques can be employed in studying the ocean.

The Gulf Stream off the east coast of North America is an example of a quasi-stationary current system that is well described by its density field alone. The density distribution defines that portion of the pressure field which is used to measure the flow called a geostrophic current. Frequencies associated with the boundary of this current are approximately 0.25-0.1 cpd in the Straits of Florida (1) and 0.03 - 0.01 cpd in the meander region off New England (2). Geostrophic adjustment associated with low frequencies requires that the density surfaces are inclined with respect

to level surfaces (surfaces of equal geopotential). The intersection of these density surfaces with the sea surface marks the so-called cyclonic boundary of the current, which is the left-hand side facing downstream in the northern hemisphere.

Figure 1 schematically represents a cross-section of a geostrophically adjusted current. The view is downstream in the northern hemisphere. Several important features should be noted: The mean density ( $\rho$ ) in the current is slightly less than in the juxtaposed water to left. Typically the surface temperature ( $T_s$ ) in the current ranges from 20°C to 10°C warmer and salinity ( $S$  ‰) is usually 1‰ to 2‰ higher; this is due to high insolation and evaporation in the tropical source region of the Stream. In terms of density, thermal expansion is larger than saline effects, and the average density of Gulf Stream waters is less than the slope waters along the left-hand side looking north. From the hydrostatic equation,

$$H = \int_p^0 \frac{dp}{\rho g} \quad (1)$$

where  $g$  is gravity and  $p$  is pressure, it is seen that the height of the sea surface ( $H$ ) is larger in the current when the integration is to some deep base pressure, say  $p=2000$  db (i.e. approximately 2000 m). That is, there is a physical rise in the sea surface of the order of 1 m when crossing into the Gulf Stream. The last feature on this figure to be noticed is the horizontal velocity profile drawn at the top. In a geostrophically balanced system, the surface velocity ( $V_s$ ) is given by

$$V_s = \frac{g}{f} \frac{\partial H}{\partial x} \quad (2)$$

where  $f$  is the Coriolis parameter, and  $x$  is the cross-stream horizontal dimension. The horizontal velocity shear,  $\partial V_s / \partial x$ , becomes a valuable feature in the study of ocean circulation from space, because it has surface manifestations. More importantly, there is some prospect of determining  $V_s$  directly from remote sensing;



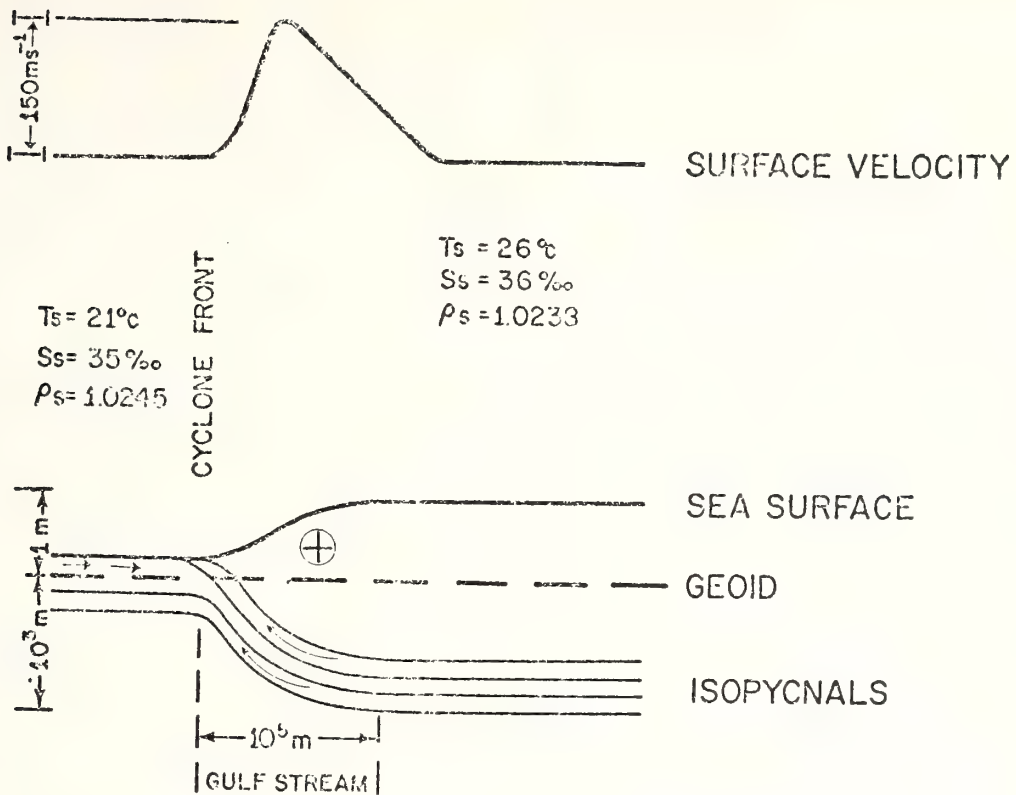


Figure 1. Schematic cross-section of a western boundary current in the northern hemisphere. Note the exaggeration of the sea surface as compared to the subsurface features, where a  $10^3$  scale change is used for clarity.

one example of that will be discussed later.

Associated with the horizontal motion, there appears to be a vertical circulation, which is also sketched on Figure 1.<sup>(3)</sup> Details of this upwelling motion are not fully understood; however, the effect is to continuously bring nutrients into the euphotic zone along the cyclonic edge. These nutrients are utilized by photosynthetic organisms which are chlorophyll-bearing plants. Pigmented molecules absorb blue light, and when in sufficient concentration, shift the color of the sea towards the green. The phytoplankton and other associated organisms change the optical properties of the water by increased scattering of light. Frequently, entrained sediments from the coastal regions can be detected along the current boundaries, which also modify the optical properties of the water.<sup>(4)</sup>

When wind and waves run in opposition to the current, the local sea builds higher

than when they run in the same direction. Thus the sea may be higher or lower in the current depending on the relative wind/current directions. The latter feature often translates into changes in white cap and foam distributions, changes in glitter patterns, and changes in surface wave refraction patterns.

To reiterate, when crossing into the Gulf Stream from the west, one typically encounters an increase in temperature, salinity, and perhaps sea state; the color shifts from the green to deep blue, and the particulate scattering decreases; there is a rise in sea level due to steric conditions, and a sudden increase in horizontal velocity. The detection of these features of the edge of the currents from spacecraft is discussed in the following sections.

#### INFRARED SENSING

The ocean surface acts very nearly as a blackbody. Its radiative behavior closely

follows Planck's Law with emissivities ( $\epsilon$ ) greater than 0.99. As a consequence of Kirchoff's Law, this requires that the source of the radiation be from the upper millimeter. Evaporation and condensation can thus play a role in the radiative temperature of water which is frequently 0.5°C or so less than its thermodynamic temperature.<sup>(9)</sup> This is of fundamental importance in determining  $T_s$  from space, but for ocean current boundary determination, the observer is looking for thermal gradients rather than absolute temperatures.

Thermal radiation leaving the earth is modified by atmospheric absorption and emission. Clouds are opaque to the earth's radiation, which peaks at about 10 $\mu$ m. The radiative transfer equation for spectral thermal radiation is

$$N_0 = N_s \tau_0 + \int_0^s N_G \frac{\partial \tau_0}{\partial p} dp \quad (3)$$

For this formulation,  $N$  is radiance,  $\tau$  is transmittance,  $p$  is pressure, and the subscripts  $s$  and  $a$  are surface and atmosphere, respectively. The radiance at the top of the atmosphere ( $N_0$ ) is the sum of the loss of surface radiance due to atmospheric transmittance ( $N_s \tau_0$ ) plus the integral term which formulates the contribution of the atmosphere. Scattering is neglected in this formulation, because it is very small at these wavelengths ( $\lambda$ ).

One consequence of atmospheric transmission is that ocean surface thermal gradients are lessened at satellite altitudes. For a very moist atmosphere in the 10.5-12.5 $\mu$ m water vapor absorption window, an 8°C difference in  $T_s$  can be reduced to 3°C in  $T_0$ .<sup>(7)</sup> This is a fundamental restriction in infrared remote sensing of ocean current boundaries. In low latitudes where the thermal differences across oceanic fronts are small and the atmospheric moisture is high, the infrared techniques are limited.

When radiation from the surface passes through a cloud,  $\tau_a \rightarrow 0$ , and the spacecraft views cloud-top temperatures. This is due to the fact that clouds are made up of liquid water, and as noted earlier, infrared photons are emitted from a very shallow depth. Low clouds often have temperatures close to the oceanic values and hence are a hindrance to proper interpretation of satellite data. Similarly, low lying coastal lands can have near-oceanic radiances. However, in the longer visible wavelengths ( $>0.6\mu$ m) the reflectance of the ocean is an order of magnitude less than that of clouds and land. If both visible and infrared data are acquired simultaneously, then the picture elements which are cloud-free can be identified. Dual channel

visible and infrared scanners aboard spacecraft are providing the data for such interpretation; an example is given in Figure 2.

(8)

The left-hand panel of Figure 2 is an infrared (10.5 - 12.5 $\mu$ m) image of the Mid-Atlantic Bight showing the coastline from Cape Hatteras to Nova Scotia. The right-hand panel is the simultaneously scanned visible (0.6-0.7 $\mu$ m) image taken on 11 May 1975, at 1450 GMT. The visible image is a positive print, that is, higher radiances are lighter; the infrared is a negative print with lower radiances (i. e. cloud tops) lighter. The large feature off Nova Scotia is seen in the visible panel to be cloud, but in the infrared alone it is not clear where the cloud-sea boundary is. By comparing the images, radiance patterns are seen to be cloud-free expressions of Gulf Stream meanders, rings, eddies, and other surface thermal features. There are some hints of these patterns in the visible image as well. This will be discussed in the section on visible imagery. The cloud discrimination would be improved if the visible channel were in the near infrared (approximately 1 $\mu$ m) where the water is more highly absorbing. An alternate method of cloud determination involves use of the synchronous satellites that observe the earth in the same infrared band, but every 30 minutes instead of several times a day.<sup>(9,10)</sup> Using only infrared data, the 30-minute images are made into time-lapse motion pictures. Clouds have advection rates several orders of magnitude faster than ocean features, and therefore they can be readily identified against the ocean thermal background. Since the sample interval is 30 minutes, ocean features of all frequencies down to the Nyquist of 24 cpd can be studied if detectable. The spatial resolution of approximately 10 km, and the mid-latitude limits of the viewing geometry are the limiting features of this sampling system.

Infrared satellite data are processed primarily for meteorological purposes. Many ocean features are not emphasized due to the match in the gray scale range of the film and the radiance range of the sea, land, and clouds. Improved ocean radiance resolution can be obtained by specially processing the data such that only the oceanic range is matched to the gray scale range. When this type of processing is done, most clouds saturate the film and appear white, and, as in the case of Figure 2, the land and very warm water appear black. A specially designed device for the synchronous satellites to accomplish this is being constructed, so film loop products for the ocean community will become available.

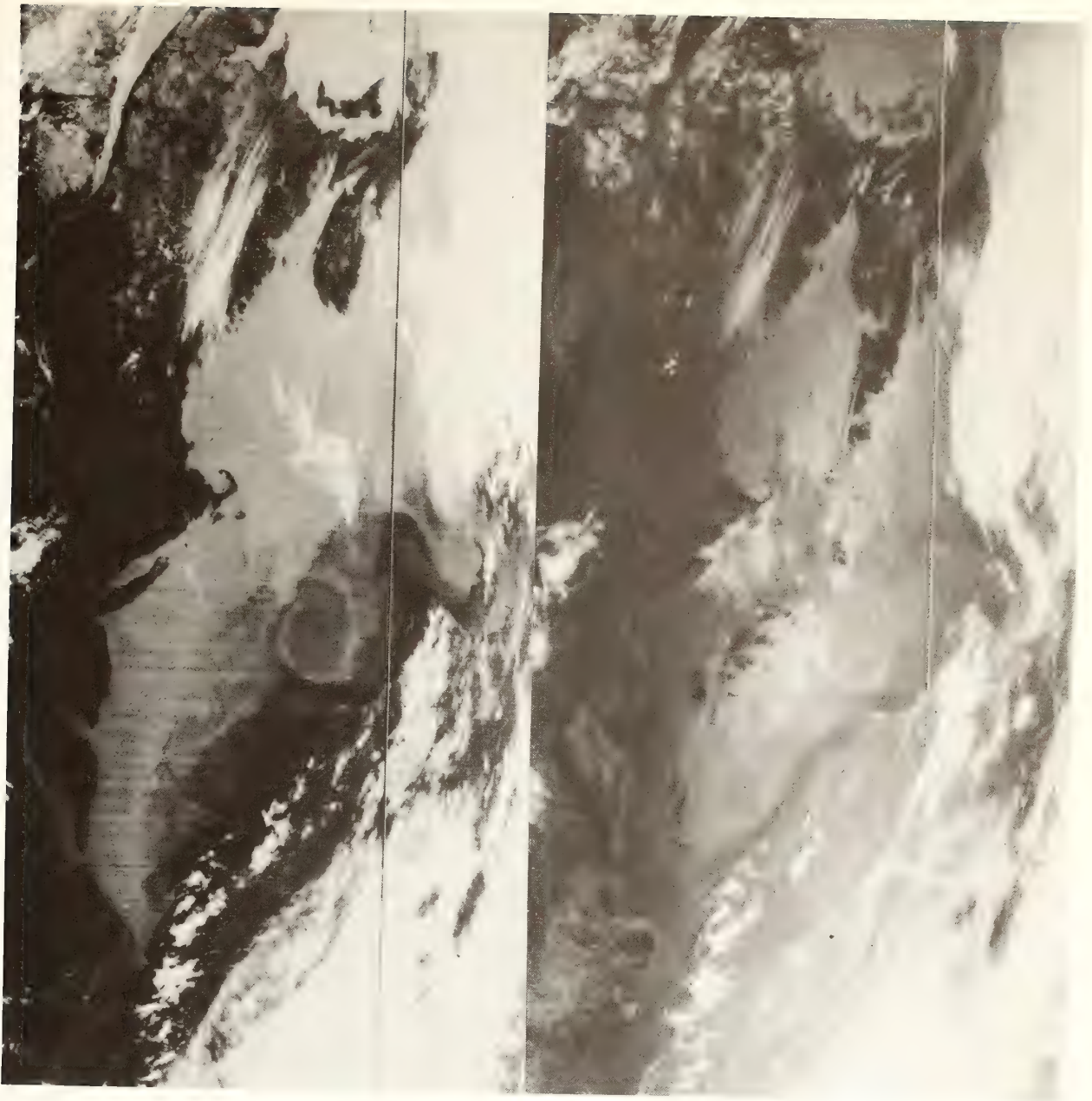


Figure 2. Infrared (left-panel) and visible (right panel) image pair of the Gulf Stream off New England. These data are from the very high resolution scanning radiometer of the NOAA polar orbiting satellite (8).

$$N_0 = N_a + \gamma N_s + \alpha N_d \quad (4)$$

#### VISIBLE SENSING

Detection of ocean currents in the visible wavelengths (0.4-0.7 $\mu$ m) depends on the change of ocean color and the change of sea state associated with the boundary. The spectral radiance at the top of the atmosphere in the visible region ( $N_0$ ) is given by

where  $N_a$  is the contribution of the atmosphere alone (mostly Rayleigh scattering),  $N_s$  is the contribution at the surface due to reflection from the surface,  $N_d$  is the diffuse radiance at the surface due to photons that have penetrated the surface;  $\gamma$  and  $\alpha$  are atmospheric transmittance factors

for  $N_s$  and  $N_i$  respectively. Changes in sea state, by which is meant changes in white caps, foam, glitter, etc., enter the equation only through the  $N_s$  term. Similarly changes in the optical properties of the water itself, which is information on the absorption and scattering of light by particles in the water, is represented by  $N_d$ . (4)

The spectrum of diffuse radiation is a complex function of scattering and absorption. In a simple single-scattering model, the independent variables were shown to be the total attenuation coefficient, the total scattering coefficient, and the fraction of backscattered light. (11) Each variable is also wavelength dependent, so that an infinite variety of optical conditions can combine to produce the same  $N_d$ . In the case of current boundary determinations, the highly productive water along-side the Gulf Stream cyclonic front is high in pigmented molecules as well as in particulate matter. The net result is to shift the peak of the upwelling radiance spectrum toward longer wavelengths, that is towards green colors. At the same time, the optical intensity increases due to increased scattering. When these conditions hold, the water along the cyclonic side of the stream will have a higher radiance in a multispectral image such as on the NOAA polar orbiting satellite. In Figure 2 the edge of the current can be seen in the visible imagery as well as the infrared. The Gulf Stream appears to have lower radiance than the slope waters in agreement with the above explanation.

However, the  $N_s$  term also contributes to  $N_0$ , and its behavior requires discussion. Reflection from the surface at these wavelengths changes the radiance spectrum in a wavelength dependent fashion. In the 0.6-0.7  $\mu\text{m}$  interval of Figure 2, a higher sea state in the Gulf Stream could raise the radiance to the same level as the  $N_d$  influence on the slope water (and thus there would be no visible signature), or it could exceed the radiance and once again a signature would exist. Winds for this day were from the southwest at less than  $2 \text{ m s}^{-1}$  due to a high-pressure ridge lying parallel to the east coast. Under conditions of such weak and variable winds, no foam or white caps are anticipated (12), and the contribution to  $N_0$  is dominated by  $N_d$ , with  $N_s$  contribution at a uniform value over the whole image.

Some effects of what is a probable lack of specular return can be seen in Long Island Sound and south of Nova Scotia. These dark areas are interpreted to be zones of calm seas where glitter does not reflect the morning sun (0930 EST). The major features of the Gulf Stream front, the large eddy-like structure south of Cape Cod, and the

complex patterns in the slope water off New York, are observable in both the visible and infrared images. In the visible they are regions of higher radiance embedded in a zone of low and probably uniform specular return. This suggests that what is seen is due to patterns in the diffuse radiance. Thus the interpretation is that these circulation features are being detected due to variations in the optical properties of the water and are variations in biochromes and particulate scatterers. (13)

The interpretation is difficult here because only two channels of data are available. The 0.6-0.7  $\mu\text{m}$  channel is a good choice for visible radiance and was the most useful in applying LANDSAT (Earth Resources Technology Satellite) data to the marine environment. (4) However, since it is a valuable channel in the study of optical oceanography, it is not the best spectral interval for cloud and sea state discrimination. Experience with LANDSAT and the experimental scanner on SKYLAB have shown that 0.95-1.05  $\mu\text{m}$  is the optimum band for this purpose. Incorporation of this wavelength interval in future multispectral images is strongly recommended in order to overcome the ambiguities of oceanic interpretation in the present system.

#### MICROWAVE SENSING

Microwave sensing may be considered in two ways: Active systems, by which is meant radar type devices such as altimeters, scatterometers, and imaging radars; and passive or radiometer-type devices that sense the emitted microwave energy in the same sense as infrared or visible radiometers do. Many features of the edge of a current (see Figure 1) can be identified in microwave data, including sea state changes, temperature and salinity changes, the physical shape of the sea surface, and actual current speeds. (14)

Passive microwave energy is sensitive to changes in surface temperature, salinity, roughness, and foam coverage, and to the presence of sea ice. (15) The transfer of radiation follows Equation 3, except that the  $N_s$  term is a function of polarization as well as nadir angle and wavelength. Since foam transmits energy from below, transmission ( $\tau$ ), emissivity ( $\epsilon$ ) and reflectivity ( $\rho$ ) all contribute to  $N_s$  as follows:

$$N_s = \tau_\lambda N_i + \epsilon_\lambda N_{BB} + \rho_\lambda N_0 \quad (5)$$

The subscripts in this expression denote the blackbody radiance (BB), the incident

radiation from the atmosphere (a), and the incident radiation from the ocean (i) on the foam. The atmosphere is opaque to microwave energy at wavelengths below 1 cm due to water vapor, but between 1 cm and 100 cm (30-0.5 GHz) the atmospheric transmissivity is very close to 1.0.

Measurements of thermodynamic temperature relate to  $N_{\text{dB}}$  by Planck's law.  $N_{\text{dB}}$  can be approximated by the Rayleigh-Jeans Law at microwave wavelengths, and this is proportional to  $T \lambda^4$ . This simplifies the calculations in that the radiance is directly proportional to the first power of the temperature. Salinity affects  $\epsilon$ , and absolute measurements by aircraft of the order of 1°/00-2°/00 are being reported. (16) Salinity determining techniques measure

emissivity at 21 cm and require the ancillary measurement of temperature. Salinity effects on the dielectric constant of sea water are small at 8 cm. Thus a two-channel microwave sensor can provide salinity and temperature measurements in the absence of foam coverage ( $\rho=0$ ).

Sea state effects on an imaging radar are shown in Figure 3. These data from a side-looking airborne radar (17) show two narrow lineations which were shown by simultaneous infrared thermometers to be associated with a large temperature gradient in the Gulf Stream front region off Cape Hatteras. These lineations are changes in the radar backscattering cross-section which suggest changes in sea state associated with the thermal change. This is

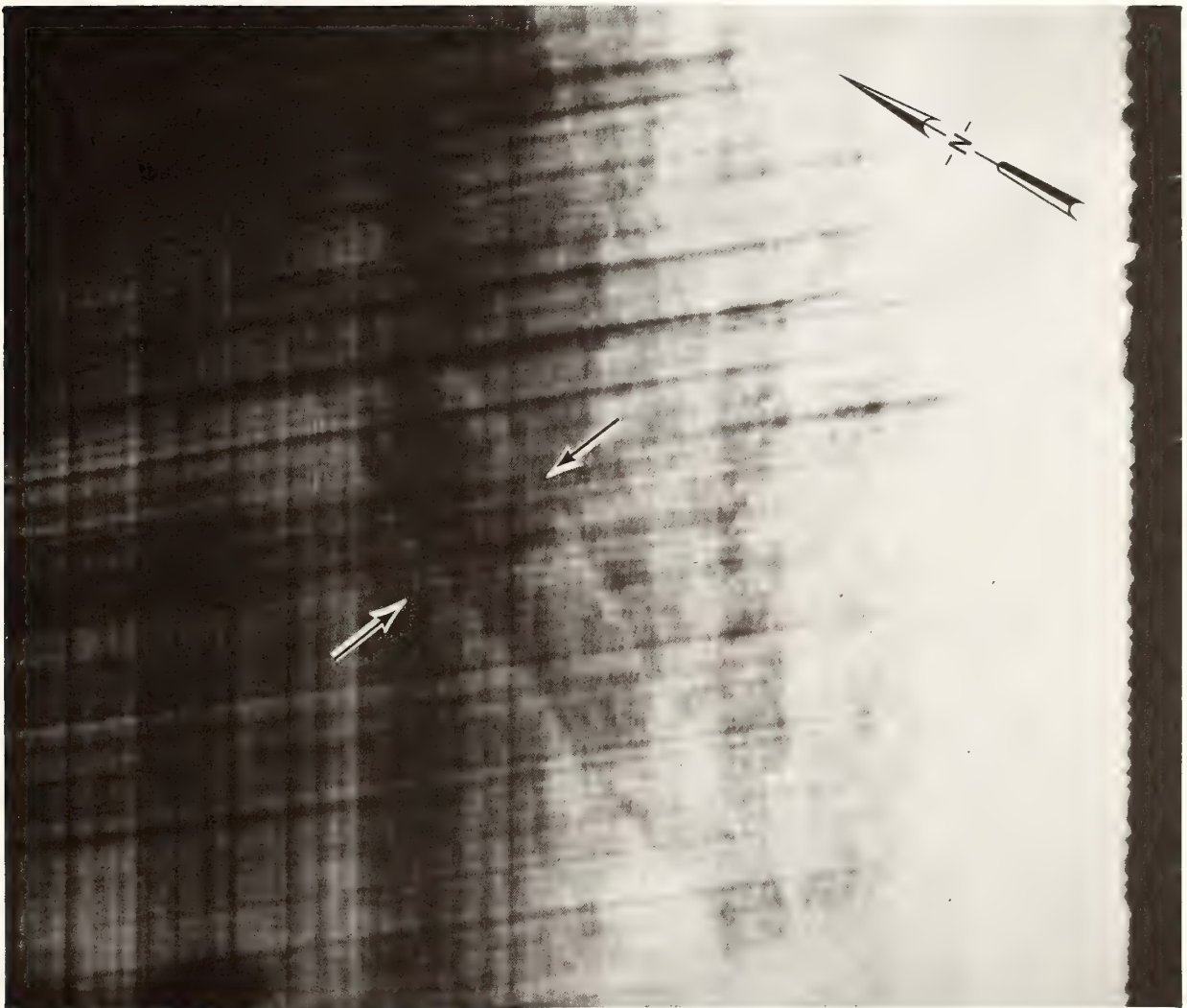


Fig. 3. Side-looking microwave image of breaklines in the vicinity of the Gulf Stream front off Cape Hatteras (17). Refraction in surface waves can be seen in the original data.

one application of active radar in locating boundaries.

Another active radar system is the precision altimeter. It provides a suborbital (only) measure of the topography of the sea surface. If the geoid is known in the area of interest, and tidal effects are eliminated, the surface topography can be used to estimate the absolute pressure gradients at the sea surface (see again Figure 1). Absolute pressure gradients will provide the oceanographer with a measure of surface currents (only) which can be inferred from Equation 2. A note of caution must be mentioned here concerning the  $\pm 10$  cm accuracy of a radar altimeter (i.e. SEASAT). Using Equation 2 and assuming that  $H = +10$  cm,  $x = 10^7$  cm (i.e. the width of the Gulf Stream), the following errors in  $V_S$  are calculated for several latitudes ( $\phi$ ):

$\phi$	$V_S$
$50^\circ$	$\pm 8.8$ cm sec
$40^\circ$	$\pm 10.5$ cm sec
$30^\circ$	$\pm 13.5$ cm sec
$20^\circ$	$\pm 19.7$ cm sec
$10^\circ$	$\pm 38.8$ cm sec

As can be seen, at the Gulf Stream latitudes ( $\phi = 40^\circ$ ) the error is 10% of the flow; this is not an improvement over conventional measurements. At lower latitudes the error approaches values of the order of 50% or higher. Other ocean currents have typical speeds of 15-20 cm sec<sup>-1</sup>, and the error can be greater than a factor of 2. One may argue that if a large number of observations were taken,  $\pm 10$  cm would lead to a good absolute determination. This is only valid for a static system, which the ocean is not. Barotropic motions in the Gulf Stream at inertial and tidal frequencies (1) would require many radar altimeters in orbit at the same time to begin getting the coverage needed for such averaging. This somewhat diminishes the enthusiasm for a  $\pm 10$  cm altimeter for strictly ocean current determination.

Studies of the backscattering from radars show promise for application to many problems in radio oceanography (18). A particularly interesting application is that of current speed determination (14). Figure 4 is a plot of current speed ( $V_S$ ) as a function of radar backscattering cross-section per unit area for several wind speeds ( $W$ ). If the wind speed can be determined through one or several independent techniques (9,10), then  $V_S$  can be inferred. Alternatively, if  $V_S$  can be determined by an altimeter or a Lagrangian drifter (19), a refinement on  $W$  is possible. These and other microwave techniques are a new and exciting horizon for remote sensing.

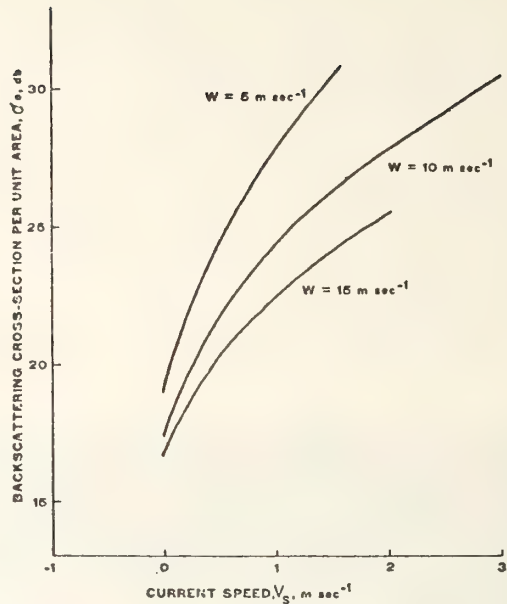


Figure 4. Plot of current speed versus radar backscattering as a function of different wind speeds (12). Gulf Stream current speeds are typically 1-2-meters per second.

#### Photographic Sensing

Man's role as an observer in space was appreciated from the earlier missions, but none so fully as SKYLAB. Astronauts were for the first time given training in observing and photographing ocean features from space. This program was carried on to the recent Apollo-Soyuz test project and hopefully will be strengthened in the future. Many ocean circulation features such as confluences, upwelling, eddies, and other patterns that reflect currents were observed and photographed from space (20). These data are providing new insight into the details of the ocean at a spatial resolution unavailable by other imaging systems.

An example of such detail is given in Figure 5 which is a hand-held photograph of turbulent mixing in the confluence region of the Falkland and Brazil currents off South America (21). These currents are a southern hemisphere analog of the Labrador Current/Gulf Stream system in the North Atlantic. The confluence was first seen by the astronauts near the Brazil/Uruguay border and was followed for over 1000 km to sea. The color boundary showed very little mixing across the front, unlike the eddies



*Figure 5. Hand-held 16 mm photograph of eddies and other circular expressions of the boundary of the Falkland Current taken from SKYLAB 11. Details have been photogrammetrically enhanced by laboratory techniques. The eddy is estimated to be 20 km in diameter.*

shown in Figure 2. The eddy in figure 5 can be seen because plankton or suspended materials cause color variations in the sea. The eddy appears to be anticyclonic and is possibly caused by the velocity shear along the Falkland current.

Photographic details like this are usually chance happenings. In the case of SKYLAB however, the spacecraft transited the area several times on several consecutive days, and features such as those in figure 5 were not only viewed several times, but they were studied with the many devices in the Earth Resources Experiment Package.

An important reason for the successful observations was the real-time communications between the crew and oceanographers at mission control. Future manned earth observing missions must exploit this communications feed-back even further, so that ships and aircraft can conduct detailed studies into these interesting new-found features of the ocean's circulation.

#### Conclusions

Several techniques have been described that offer useful application to the study of ocean circulation from space. Each has

advantages and disadvantages. The very high spatial resolution of visible and infrared sensors is not practical at microwave frequencies because of limitations in antenna design. On the other hand, the microwave devices offer all-weather sensing capability but at reduced radiant resolution. The sensing of ocean currents should be approached with multispectral techniques using visible, infrared, and microwave observations. This will not only provide the best opportunity to observe the feature, but will also increase the degrees-of-freedom in an automated identification scheme which is an important goal for studying ocean physics from space

Acknowledgement: The author wishes to express his appreciation to his colleagues at AOML for assistance in preparing this manuscript, and particularly to D.V. Hansen with whom there have been many fruitful discussions.

#### References

- (1) Duing, W. (1975). Synoptic Studies of Transients in the Florida Current, J. Mar. Res., 33(1), pp. 53-73.
- (2) Hansen, D.V. (1970). Gulf Stream Meanders between Cape Hatteras and the Grand Banks. Deep Sea Res., 17, pp. 495-511.
- (3) Neumann, G. and W.J. Pierson, Jr. (1966). Principles of Physical Oceanography, Prentice-Hall, Englewood Cliffs, N.J., pp. 224-228.
- (4) Maul, G.A. and H.R. Gordon (1975). On the Use of the Earth Resources Technology Satellite (LANDSAT-1) in Optical Oceanography, Remote Sensing of Environ., 4, pp. 95-128.
- (5) Teague, W.J. (1974). Refraction of Surface Gravity Waves in an Eddy. Scientific Report, U. of Miami, Coral Gables, Fla., UM-RSMAS-No. 74034, 94 pgs.
- (6) Ewing, G. and E.D. McArister (1960). On the thermal Boundary Layer of the Ocean, Science, 131, pp. 1374-1376.
- (7) Maul, G.A. and M. Sidran (1973). Atmospheric Effects on Ocean Surface Temperature Sensing from the NOAA Satellite Scanning Radiometer, J. Geophys. Res., 78(12), pp. 1909-1916.
- (8) Data from the NOAA-4 meteorological satellite provided by H.M. Byrne (NOAA-AOML).
- (9) Maul, G.A. and S.R. Baig (1975). A New Technique for Observing Mid-latitude Ocean Currents from Space, Proceedings, Amer. Soc. Photogram., Wash. D.C., pp. 713-716.
- (10) Legeckis, R. (1975). Application of Synchronous Meteorological Satellite Data to the Study of Time Dependent Sea Surface Temperature Changes Along the Boundary of the Gulf Stream, Geophys. Res. Ltrs., 2(10), pp. 435 - 438.
- (11) Gordon, H.R. (1973). A Simple Calculation of the Diffuse Reflectance of the Ocean., Appl. Opt., 12, pp. 2804 - 2805.
- (12) Ross, D.B. and V. Cordone (1974). Observations of Oceanic Whitecaps and their Relation to Remote Measurements of Surface Wind Speed., J. Geophys. Res., 79(5), pp. 444-452.
- (13) Compare with the interpretation under different wind conditions given by Strong, A.E. and R.J. DeRycke, Ocean Current Monitoring Employing a New Satellite Sensing Technique, Science, 181, pp. 482-484.
- (14) Parsons, C. and G.S. Brown (1976). Remote Sensing of Currents Using Backscattering Cross-Section Measurements by a Satellite Altimeter. (Submitted to J. Geophys. Res.)
- (15) Hanson, K.J. (1972). Remote Sensing of the Ocean. In: Remote Sensing of the Troposphere, V.E. Derr, ed., U.S. Gov't. Printing Office, Washington, D.C., pp. 22-1 to 22-56.
- (16) Thomann, C.G. (1975). Remote Sensing of Salinity. Proceedings of the NASA Earth Resources Survey Symposium, NASA TM X-58168, pp. 2099-2126.
- (17) Data provided by D.B. Ross, NOAA-AOML.
- (18) Eisenberg, R.P. (1974). Practical Considerations to the Use of Microwave Sensing from Space Platforms. In: Remote Sensing Applied to Energy-Related Problems, T.N. Veziroglu, ed., U. of Miami, Coral Gables, Fla., pp. S3-29 to S3-41.
- (19) Molinari, R.L. (1973). Buoy Tracking of Ocean Currents. In: Advances in the Astronautical Sciences, F.S. Johnson, ed., Amer. Astron. Soc., Tarzana Calif., pp. 431-444.
- (20) Kaltenbach, J.L., W.B. Lenoir, M.C. McEwen, R.A. Weitenhagen, and V.R. Wilmarth, eds. (1974). SKYLAB-4 Visual Observations Project Report, NASA, JSC-09053, TM X-58142, Houston, Texas, 250 pgs.



(21) Johnson, W.R. and D.R. Norris (1976).  
A Multispectral Analysis of the Interface  
between the Brazil and Falkland Currents  
from SKYLAB. Submitted to Remote Sensing  
of Environ.

Reprinted from: *NOAA Technical Report ERL 378-AOML 23*, 69 p.

**NOAA Technical Report ERL 378-AOML 23**



# **An Experiment to Evaluate SKYLAB Earth Resources Sensors for Detection of the Gulf Stream**

**George A. Maul  
Howard R. Gordon  
Stephen R. Baig  
Michael McCaslin  
Roger DeVivo**

**Atlantic Oceanographic and Meteorological Laboratories  
Miami, Florida**

**August 1976**

**U.S. DEPARTMENT OF COMMERCE**

Elliot Richardson, Secretary

National Oceanic and Atmospheric Administration

Robert M. White, Administrator

Environmental Research Laboratories

Wilmot Hess, Director



Boulder, Colorado

## NOTICE

The Environmental Research Laboratories do not approve, recommend, or endorse any proprietary product or proprietary material mentioned in this publication. No reference shall be made to the Environmental Research Laboratories or to this publication furnished by the Environmental Research Laboratories in any advertising or sales promotion which would indicate or imply that the Environmental Research Laboratories approve, recommend, or endorse any proprietary product or proprietary material mentioned herein, or which has as its purpose an intent to cause directly or indirectly the advertised product to be used or purchased because of this Environmental Research Laboratories publication.

## CONTENTS

	Page
ABSTRACT	
1. INTRODUCTION	1
1.1 Background & Purpose	2
1.2 Test Site	2
1.3 Prior Investigations	3
2. SURFACE TRUTH DATA	3
2.1 Cruise Report	4
2.2 Trackline Profile Data	4
2.3 Spectrometer Data	8
3. PHOTOGRAPHIC EXPERIMENT	11
3.1 Measurements	11
3.2 Data Analysis	12
3.3 Discussion	16
4. SPECTROMETER EXPERIMENT	17
4.1 Tracking Data	17
4.2 Infrared Radiance	18
4.2.1 Theoretical calculations	19
4.2.2 Comparisons of S-191 and models	21
4.3 Visible Radiance	23
4.3.1 Theoretical calculations	23
4.3.2 Technique for atmospheric correction	35
4.3.3 Recovery of $R(\lambda)$ from the S-191 data	36

	Page
5. MULTISPECTRAL SCANNER EXPERIMENT	37
5.1 S-192 Data	38
5.2 Computer Enhancement	39
5.3 Discussion	44
6. SUMMARY	46
7. ACKNOWLEDGMENTS	48
8. REFERENCES	48

AN EXPERIMENT TO EVALUATE SKYLAB EARTH RESOURCES  
SENSORS FOR DETECTION OF THE GULF STREAM

George A. Maul  
Howard R. Gordon  
Stephen R. Baig  
Michael McCaslin  
Roger DeVivo

An experiment to evaluate the SKYLAB Earth Resources Package for observing ocean currents was performed in the Straits of Florida in January 1974. Data from the S-190 photographic facility, S-191 spectroradiometer, and the S-192 multispectral scanner were compared with surface observations made simultaneously by the R/V VIRGINIA KEY and the NASA C-130 aircraft. The anticyclonic edge of the Gulf Stream could be identified in the SKYLAB S-190 A and B photographs, but the cyclonic edge was obscured by clouds. The aircraft photographs were judged not useful for spectral analysis because vignetting caused the blue/green ratios of selected areas to be dependent on their position in the photograph. The spectral measurement technique could not identify the anticyclonic front, but a mass of Florida Bay water, which was in the process of flowing into the Straits could be identified and classified. No calibration was available for the S-191 infrared detector, so the goal of comparing the measurements with theoretical calculations was not accomplished. Monte Carlo simulations of the visible spectrum showed that the aerosol concentration could be estimated and a correction technique was devised. The S-192 scanner was not useful for detecting the anticyclonic front because the radiance resolution was inadequate. An objective cloud discrimination technique was developed; the results were applied to the several useful oceanographic channels to specify the radiance ranges required for an ocean tuned visible multispectral scanner.

## 1. INTRODUCTION

An important problem in physical oceanography is determining the boundaries of surface currents. Many techniques have been proposed to study such boundaries from space, but the actual process of extracting the correct information from satellite data is in the early stages of development. SKYLAB, with its several types of sensors (NASA, 1975), afforded the means of testing three techniques simultaneously: photography, spectroscopy, and multispectral imagery.

## 1.1 Background and Purpose

Major ocean currents are known to have several observable surface features that make them distinguishable from the surrounding waters. The Gulf Stream system is used as an example to typify these changes because it is one of the most important ocean currents, and because understanding of its features can be applied to the study of other current systems.

Because of its subtropical origin, the Gulf Stream is typically warmer than surrounding waters and thus has a surface thermal signature that often can be detected in infrared (IR) imagery. The waters of the current are also much lower in biological productivity and hence there are fewer particles and biological pigment molecules in the Stream; this translates to a deep blue color of water. Conversely, the juxtaposed water masses are frequently higher in biological productivity, and this can cause that water to be greener. Another feature of the current that makes it visibly distinguishable is caused by the large horizontal velocity shear. Frequently the faster moving water in the current has a different sea state than surrounding waters. Just as common are the many slick lines associated with the shear. Finally, modifications of the atmosphere above the Gulf Stream, under certain conditions, can also give an indication of the current's location.

Several other features of the Gulf Stream, potentially detectable by satellite altimetry and other microwave techniques, will not be discussed in this report. The approach here is confined to visible and infrared wavelengths. The goal of this experiment was to contribute to the determination of the location of the Gulf Stream by visible and infrared measurements of radiance.

## 1.2 Test Site

The site chosen for the experiment was in the Straits of Florida along a suborbital track in the vicinity of Key West, Florida. In this channel, the Gulf Stream runs approximately perpendicular to the satellite ground track. This track would maximize the changes in oceanic variables while minimizing the impact on the data acquisition facility onboard SKYLAB. Furthermore, the logistics of obtaining the surface-truth data from a 65-foot vessel in January weather made the choice of a semi-protected body of water mandatory.

Hydrographic conditions in the test site are controlled by the location and intensity of the Gulf Stream (also called the Florida Current in this vicinity). The cyclonic edge, defined as the left hand edge facing downstream, has horizontal excursions of approximately 50 km; that is, at some times of the year the current's edge may be found 20 km south of Key West and at other times 70 km to the south (Maul, 1975). The location

of the cyclonic front determines the location of the major hydrographic features of the Straits. Materials from Florida Bay are also known to flow into the Straits and at times become entrained in the current. Occurrences involving mixing of Gulf Stream and Florida Bay waters are of fundamental importance to the understanding of the dispersal of natural and man-introduced materials.

### 1.3 Prior Investigations

A general review of remote sensing of ocean color was given by Hanson (1972); Maul (1975) discussed the application of visible spectroscopy to locating ocean current boundaries. Gordon, in a series of papers (e.g. Gordon, 1973; Gordon and Brown, 1973; Maul and Gordon, 1975) discussed the spectra of upwelling irradiance as a function of the optical properties of the water as calculated by Monte Carlo simulations; those studies are directly related to the current boundary location problem because the spectrum of light changes from Gulf Stream water to coastal water. Techniques for determining ocean chlorophyll (e.g. Baig and Yentsch, 1969; Mueller, 1973; Duntley et al., 1974) are also related to current boundary determination because pigment-forming molecules, along with suspended materials, affect the light spectrum.

Remote sensing of ocean currents in the infrared region of the electromagnetic spectrum has been attempted for many years (e.g.: Warnecke, et al., 1971; Hanson, 1972; Richardson, et al., 1973). However, there have been questions concerning the radiative transfer model dependency of the atmospheric correction (Maul and Sidran, 1972; Anding and Kauth, 1972) that have awaited SKYLAB to be addressed. Adequate atmospheric correction techniques are required for ocean current boundary determination using once-or twice-daily observations because compositing of images is required in order to fill in the areas covered by clouds; composites must be based on a common measurement, that of the sea surface temperature itself.

SKYLAB provided the first opportunity to evaluate photographic, spectrometric, and multispectral imagery in a specific experiment designed for current boundary location. It will be seen that each instrument has unique advantages, disadvantages, and limitations. It is the intent of this report to objectively evaluate each technique and to provide recommendations for future equipment and measurements.

## 2. SURFACE-TRUTH DATA

This section gives the details of how the ocean surface data were obtained, calibrated, and analyzed. In many cases surface optical measurements are useful indicators of the properties of the water that need to be measured. This is because the theory is well ahead of the measurements, and adequate



instruments are not yet designed or built. In the case of spectrometer measurements, the ideal observations are in fact physically impossible.

## 2.1 Cruise Report

The at-sea observations were designed to provide simultaneous measurements of the ocean while the aircraft and satellite transited the area. Since the speeds of the three vehicles are mismatched, the assumption must be made that the oceanic conditions are a steady-state for 12 hours or so. While it is recognized that this is not strictly true, it is a necessary assumption in view of resources available.

Underway operations on the Virginia Key included gathering data on ocean salinity, chlorophyll-a concentration, surface nutrients, seawater scattering properties, sea surface temperature by bucket and by a continuous radiometric profile, and ocean temperature down to 450 m with expendable bathythermographs; ship was hove-to for these spectrometry observations. Collection of data started at  $24^{\circ} 39'.1$  N,  $81^{\circ} 08.1$  W at 1253 GMT, 8 January 1974. This point is about 7 km SSE of Marathon in the Florida Keys. The track was directed SW and ended at  $23^{\circ} 33'.2$  N,  $81^{\circ} 55'.5$  W at 0150 GMT 9 January. This was 41 km off the north coast of Cuba on the evening of the same day.

Weather conditions for the experiment were not ideal, with partly cloudy skies and moderate seas. Wind was from  $045^{\circ}$  at  $4 \text{ ms}^{-1}$  and remained steady most of the day. Air temperature ranged from  $23.8^{\circ}$  to  $26.1^{\circ}\text{C}$ . Wet bulb values were  $23.0^{\circ}\text{C}$  most of the day. Visibility was 20 km except in a rain shower at 1700 GMT when it dropped to less than 5 km. Barometer was steady at 1025 mb until 1900 GMT when it abruptly dropped to 1023 mb and remained so thereafter. Wave height was one-fourth meter until 2100 GMT when it abruptly increased to one-half meter; wave period remained 4 seconds throughout the day.

The Virginia Key traveled at 8 knots while on track. The boat stopped only for spectrometry stations; all the trackline profile data were collected while making speed.

## 2.2 Trackline Profile Data

Figure 2.1 is a plot of the trackline data, after reduction. The stippled profile below the  $22^{\circ}\text{C}$  isotherm shows the bottom profile along the track. The arrow shows where the  $22^{\circ}\text{C}$  isotherm crosses a depth of 100m, a point interpreted to be approximately 15 km south of the boundary of the Gulf Stream (Maul, 1975). The  $\beta(45)$  curves show the volume scattering function at  $45^{\circ}$ , and are in units of  $\text{meter}^{-1} \text{steradian}^{-1} (\text{m}^{-1} \text{sr}^{-1})$ .

A detailed discussion of the data collection, reduction, and interpretation follows.

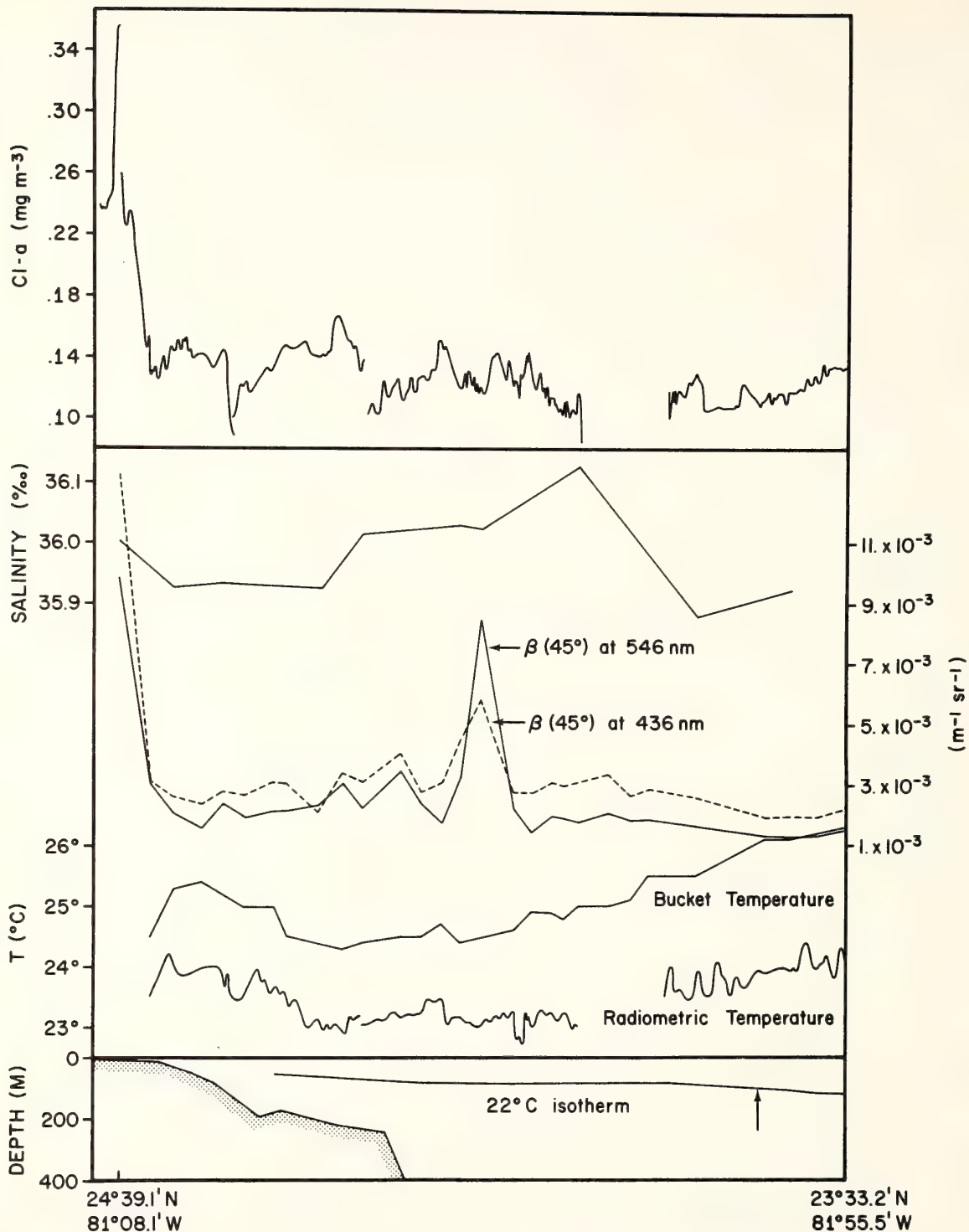


Figure 2.1 Surface truth profiles across the Straits of Florida on 8 January 1974. The profiles, from top to bottom are: Continuous chlorophyll-a ( $\text{mg m}^{-3}$ ); discrete salinity ( $\text{‰}$ ); discrete volume scattering function at  $45^\circ$  ( $\text{m}^{-1}\text{sr}^{-1}$ ); discrete thermometric temperature ( $^\circ\text{C}$ ); continuous radiometric temperature in  $10.5 - 12.5 \mu\text{m}$  band ( $^\circ\text{C}$ ) discrete depth of  $22^\circ\text{C}$  isotherm.

a) Chlorophyll-a (CL-a)

Cl-a concentrations were obtained continuously by measuring the fluorescence when Cl-a was exposed to blue light. The data are reported as if all the pigment-forming molecules (including pheophytins) were chlorophylls. The continuous record was obtained by using a Turner fluorometer, Model 111, which measured the fluorescence of surface water drawn through a continuous-flow intake system. This method is as described in Strickland and Parsons (1968), with the addition of a bubble trap. In order to calibrate the continuous record, three discrete samples were obtained by filtration and measured against a known standard after the cruise. This also is as described by Strickland and Parsons (1968), and uses the SCOR/UNESCO equation. Table A.1 in Appendix A shows the times and positions of the three samples.

The large gap in the Cl-a curve on Fig. 2.1 is due to a combination of drift on a particularly long spectrometry observation and a delay in turning on the fluorometer after leaving the station. The three other breaks in the record represent a change in fluorescence during stops for short spectrometry observations. The degree of variability in Cl-a concentration over the short distances indicated in the record shows the desirability of a continuous record instead of discrete samples as a source of the profile. The high values at the northern (left hand) end of the line occur over the reefs of the Florida Keys.

In addition to the three discrete surface samples, discrete samples at various depths were obtained during stops at two of the spectrometer stations. This was achieved by acquiring water at the various depths for filtration and measurement later with the surface samples. Times, depths, and positions are given in Table A.1.

b) Salinity (S ‰)

Ten salinity samples were obtained on the trackline. These were surface water samples which were bottled for measurement after the cruise. The times and positions of the salinity samples are given in Table A.2. The salinity profile in Fig. 2.1, which starts at 1200 GMT, is a straight-line plot of the ten values obtained.

c) Volume scattering ( $\beta$ )

The volume scattering function is a measure of the amount of scattering at various angles by a sample of seawater irradiated by a beam of light. In this case a single angle of  $45^\circ$  was measured, for a beam with a blue filter (436 nm) and a beam with

a green filter (546 nm), with a Brice-Phoenix light-scattering photometer.  $\beta(45)$  was calculated by using:

$$\beta(45^\circ) = \frac{a}{\pi} \frac{TD}{h} \frac{D(45^\circ)}{D(0^\circ)} \tau \sin 45^\circ$$

where  $a$  is the ratio of the working standard diffuser to the reference standard diffuser,  $TD$  is the transmittance of the reference standard diffuser,  $h$  is the dimension of the irradiated element,  $D$  is the deflection of the galvanometer, and  $\tau$  is the transmittance of the neutral density filters.

Measurements were obtained by collecting water samples with PVC sampler bottles. Thirty surface samples were measured, and at five stations samples were collected at various depths. Values, times, and positions appear in Table A.3. The curve in Fig. 2.1, which starts at 1200 GMT, is a straight-line plot of the surface values.

#### d) Bucket Temperatures ( $T_s$ )

As is customary, bucket temperatures were acquired at each XBT cast. Additional bucket temperatures were acquired at spectrometry stations and at samplings for scattering measurements. The curve in Fig. 2.1, which starts at 1215 GMT, is a straight-line plot of the 28 total temperatures obtained. See Table A.4 for values, times, and positions.

#### e) Radiometric Temperature

A continuous sea-surface temperature profile was obtained by using a Barnes, Model PRT-5, precision radiometric thermometer. This radiometer has a special 10.5-12.5  $\mu\text{m}$  filter that approximates those in the SKYLAB multispectral scanner. The instrument's voltage output was converted to temperature based on a calibration performed in March 1974. The profile in Fig. 2.1 begins at 1215 GMT. The large gap in the temperature profile matches the gap in the Cl-a profile and exists for the same reasons.

#### f) Expendable Bathythermograph (XBT)

The 23 XBT casts used the Sippican XBT system with 450-m probes. These casts provided the information to plot the depth of the 22°C isotherm. The point where the 22°C isotherm crosses the 100-m depth (arrow in Fig. 2.1) is taken to mark the zone of maximum horizontal velocity shear of the Gulf Stream. This crossing happened at 23° 40.9' N, 81° 51.0' W, about 57 km north of the coast of Cuba. See Table A.4 for times and positions of casts.

## 2.3 SPECTROMETER DATA

The spectral signature of the ocean and the sky at various points along the trackline was measured in the visible range of light. The vessel was stopped for the spectrometry observations; six observations were made to obtain a total of 25 spectra. Table 2.1 shows the times and positions of these stations. A detailed discussion of the instrument, data reduction and wavelength calibration follows.

TABLE 2.1  
Spectrometry Observations

<u>Time (GMT)</u>	<u>Position</u>	<u>Solar Zenith angle</u>	<u>No. of ocean spectra</u>	<u>No. of sky spectra</u>
1406	24° 38.9 N 81° 08.0 W	64°	3	1
1603	24° 30.7 N 81° 16.3 W	51°	3	2
1815	24° 19.1 N 81° 27.3 W	47°	3	2
1956	24° 08.1 N 81° 34.6 W	56°	4	1
2100	24° 04.0 N 81° 37.0 W	65°	2	0
2210	23° 58.8 N 81° 40.4 W	76°	3	1

### a) Instrument

The instrument was a Gamma Scientific, Model 2400 SR, spectroradiometer in a special water tight case. The Model 2400 SR scans in a wavelength range of 350 to 750 nm by rotating a high efficiency diffraction grating that faces a narrow aperture slit. It has a wavelength accuracy of  $\pm 2.5$  nm. For this experiment the instrument was set to scan from 370 to 725 nm with a Wratten 2b filter installed over the entry slit. This filter effectively cuts transmission below 400 nm, insuring that the results will not contain secondary diffraction return. An opal glass diffuser plate was used as a cosine (Lambertian) collector; all measurements are irradiances. The data were recorded on a dual-channel strip chart recorder.

### b) Data Reduction

Fig. 2.2 is a typical spectral scan. It is a scan of ocean upwelling light from the station at 2210 GMT (see Table 2.1). The dashed curve with the many peaks is the original unsmoothed data. The peaks are due to changes in the angle of the water surface relative to the instrument as waves pass underneath. These changes impose a fairly regular periodic variation over the general trend of the spectral return; all of the spectra acquired on the cruise showed this variation to some extent. It is necessary to remove the peaks if the data are to be useful.

Digital low-pass time series filtering techniques were used to produce the smooth curve in Fig. 2.2. These techniques, to be explained in some detail below, permit an objective filtering of the unwanted periodicities with a minimum loss of significant data trends. The filtering was performed on a UNIVAC 1108 using a FESTSA (Herman and Jacobson, 1975) software system at the Atlantic Oceanographic and Meteorological Laboratories.

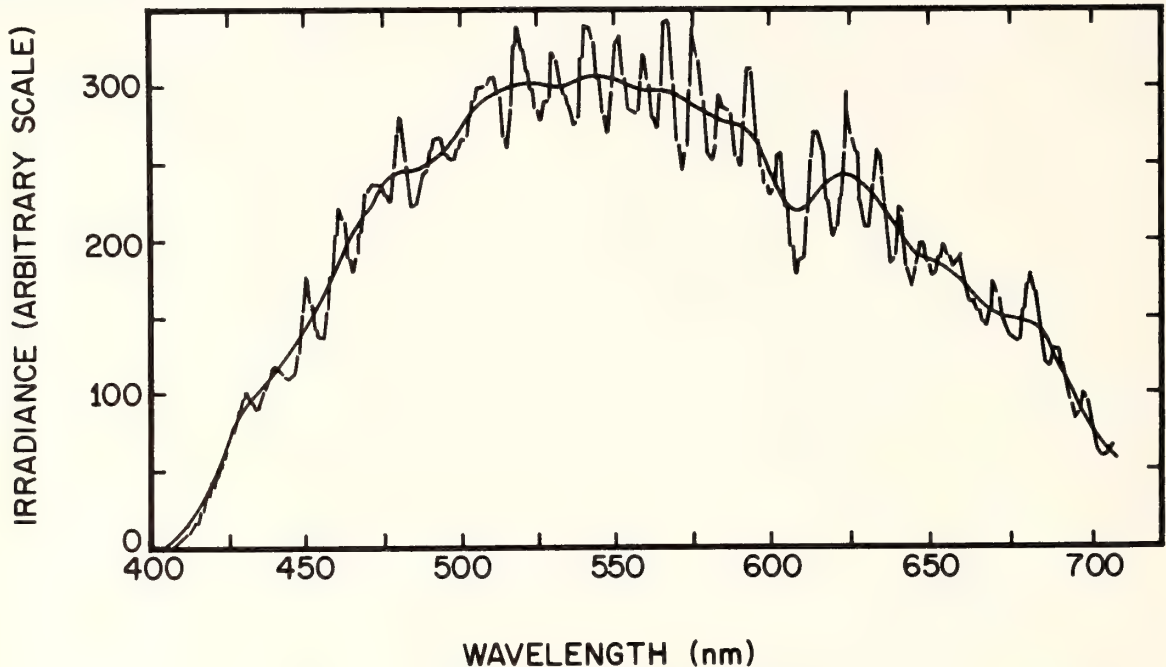


*Figure 2.2 Example of upwelling spectral irradiance before (broken line) and after (solid line) filtering to eliminate the effect of ocean surface glitter variations due to surface waves.*

The spectra were digitized off the strip chart at intervals of 20 points per inch; the points were sufficiently close to retain the shape of the original traces. The trace in Fig. 2.2, provided 248 data points. As different wavelength drive speeds were used on different stations, this number varied from scan to scan.

In order to choose a filter that successfully removes high frequency energy with a minimum loss of significant trends, it is important to identify the periods of the high frequency signals. Fig. 2.3 contains a plot (light, broken line) of the relative strengths of various periodicities of the spectrometry scan shown in Fig. 2.2. This is a power spectrum of the spectrometry scan using Tukey's method (see Herman and Jacobson, 1975). One can see strong periodicities at approximately 6,7,9,20, and 30 data points per cycle. These are the dominant high frequency signals that give the original scan in Fig. 2.2 its sawtooth appearance.

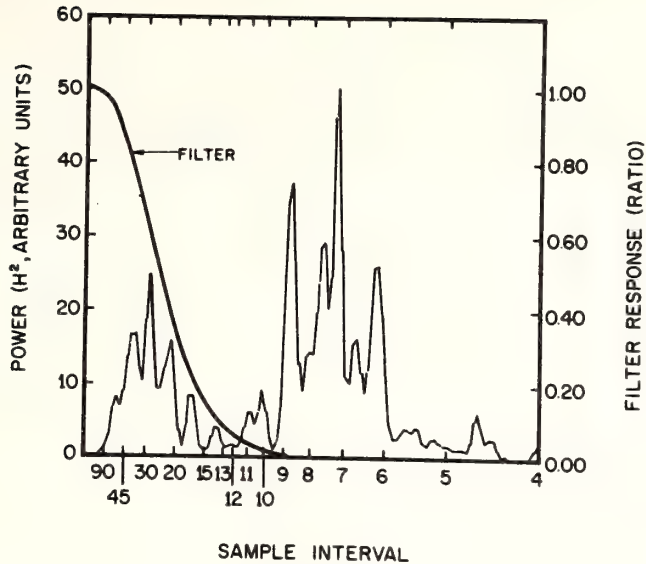


Figure 2.3 Power spectrum of upwelling spectral irradiance shown in Figure 2.2 The narrow line is the high frequency motion caused by surface waves reflecting specularly; the heavy line is the response of the Fourier filter to low-pass the data.

The response of the filter chosen to remove these high frequency signals is shown by the heavy, solid curve in Fig. 2.3. This response is in terms of a ratio of the contribution various frequencies make to the form of the original trace, to the contribution the same frequencies are allowed to make to the form of the filtered result. Thus in the example chosen, no contribution is allowed for periods smaller than about 9 data points per cycle (10 nm); full contribution is allowed for periods greater than about 90 points per cycle (100 nm), and half contributions are allowed at about 25 points per cycle (30 nm), which was the longest period of the major peak in Fig. 2.3.

In general, all filters were chosen to remove the short period (high frequency) signals in the same way. Power spectra of different spectrometry scans did not always closely resemble each other however, and each filter had to be chosen on the basis of an individual inspection of each scan.

### c) Wavelength Calibration

Irradiance and wavelength are indicated by separate voltage outputs. The wavelength voltage is produced by a potentiometer directly connected to the diffraction grating, voltage varying with angle. In addition, an inscribed wavelength scale is connected directly to the potentiometer. Thus it is possible to compare the voltage of the wavelength output as recorded by whatever strip chart recorder is used with the wavelength indicated by the scale. Such a comparison was performed on the strip chart recorder used during the cruise, and is the basis of

the wavelength calibration employed for these data. The drift-free nature of the grating-scale design permits this type of calibration.

Recorder outputs were compared with scale readings at 5 nm intervals over the entire wavelength range used in this experiment. A third-order polynomial was fitted to the resulting numbers to obtain an equation giving wavelength in terms of the position within the spectra on the time axis of the strip chart. This form of equation was chosen because it does not require a fixed number of data points for all spectra; the only requirement is that the digitizing interval remain constant.

Comparison of this calibration with known spectral lines indicates that the calibration is within 3 nm of true wavelength over the whole range of visible light.

### 3. PHOTOGRAPHY

The use of color photographs to measure phytoplankton concentrations in natural waters is based on the argument that the photographic material responds in a quantitative, reproducible manner to the variance in the light field of the water. The variance is associated in a fixed manner with the concentration of the phytoplankton, its distribution with depth, and its species and nutritive history. For a number of years there have been applications of these variance techniques to remote sensing of the ocean (e.g. Baig and Yentsch, 1969; Mueller, 1973). The SKYLAB experiments provided the opportunity to extend some of the techniques developed from laboratory tanks and low-level aircraft flights to synoptic mesoscale coverage. The field program (section 2.1) was to provide surface truth for the variance analysis; the SKYLAB photography was to provide the photographic products.

#### 3.1 Measurements

A photograph is merely the record of the integral of the intensity of the illuminant falling on a subject and the reflectivity of the subject. In a color photograph a third variable is introduced in the spectral properties of both the illuminant and the subject. A color photograph is satisfactory if it produces, in a viewer's eye, a response similar to that produced by the actual subject. The satisfactory spectral response brought about by the color photograph is a result of the eye's inability to distinguish between a pure spectral source of light and a mixture of such sources. A color photograph does not produce in each pixel (picture element) the exact spectral reflectivity of the corresponding spot of the subject (with the exception of a subject that is itself a color photograph). Instead the photograph produces in each pixel a mixture of three colors which the eye perceives as a single color, and it produces only these three colors; this is called a "metameric" match.



A color can be thought of as a vector in n-space, with pure light as the origin. An infinity of coordinate systems may be created around this vector, but once one of the coordinate axes is fixed the others also become fixed. Common varieties of color films need only three colors to reproduce the variety of colors seen in the real world. To the eye these colors look like yellow, magenta, and cyan (blue-green). These colors are the coordinate axes of the color space. Every other color is a unique combination of these three primary colors. If the subject is composed of two different colors then the eye will perceive it as if it were a single color. The eye in this case performs the metameric match. A color photograph will do the same. If the color of a subject is changing then the change may be noted as differing quantities of the three dyes in a color photograph of the subject.

The utility of monitoring the changes in dye concentration of a color photograph can be carried a step further. It has been shown that provided the continuous spectrum of the subject has previously been measured, the dye concentrations can be used to generate a new spectrum--- without re-measuring the spectrum (Baig and Yentsch, 1969). The new spectrum must have been part of a "training set" of spectra for which the color photographs exist, or must be any combination of the original training set spectra. Then, through a multivariate analysis and regression technique, a synthetic spectrum can be generated using only the dye concentrations. The technique is especially useful when the concentration of one of the components of a mixture is changing. Tank (Baig and Atwell 1975) and low-level aircraft flights (Baig, 1973) have amply demonstrated that phytoplankton concentration in natural waters can be easily and accurately measured with the technique. If the spectra of the phytoplankton are not of immediate interest, then the multivariate reduction is not necessary. The problem then reduces to a correlation between the concentration of phytoplankton in a training sample and the variation in the dye concentrations in the color photograph.

### 3.2 Data Analysis

The first photographs to be analysed were the 9-inch color transparencies from the aircraft aerial cameras. On a number of frames there were subjective color differences. However, similar differences were noted on frames in which the color of the subject area would have been expected to be uniform. A densitometric analysis of one of these frames revealed a variable blue/green ratio as a function of radial distance from the principal point. These data are presented graphically in Fig. 3.1. Attempts to use these data to "correct" data from other frames of aircraft transparencies were not successful. This vignetting problem was so severe that the images were displayed on the non-linear portion of the film's D-log e curve. This introduced an unknown non-linear error which could not be

corrected without an in-flight calibration with targets of known spectral response.

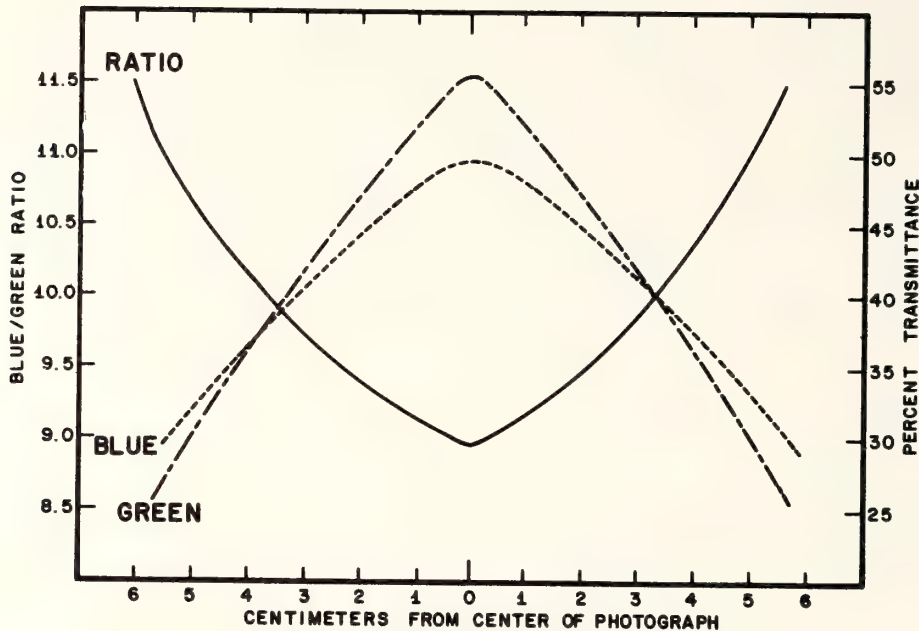
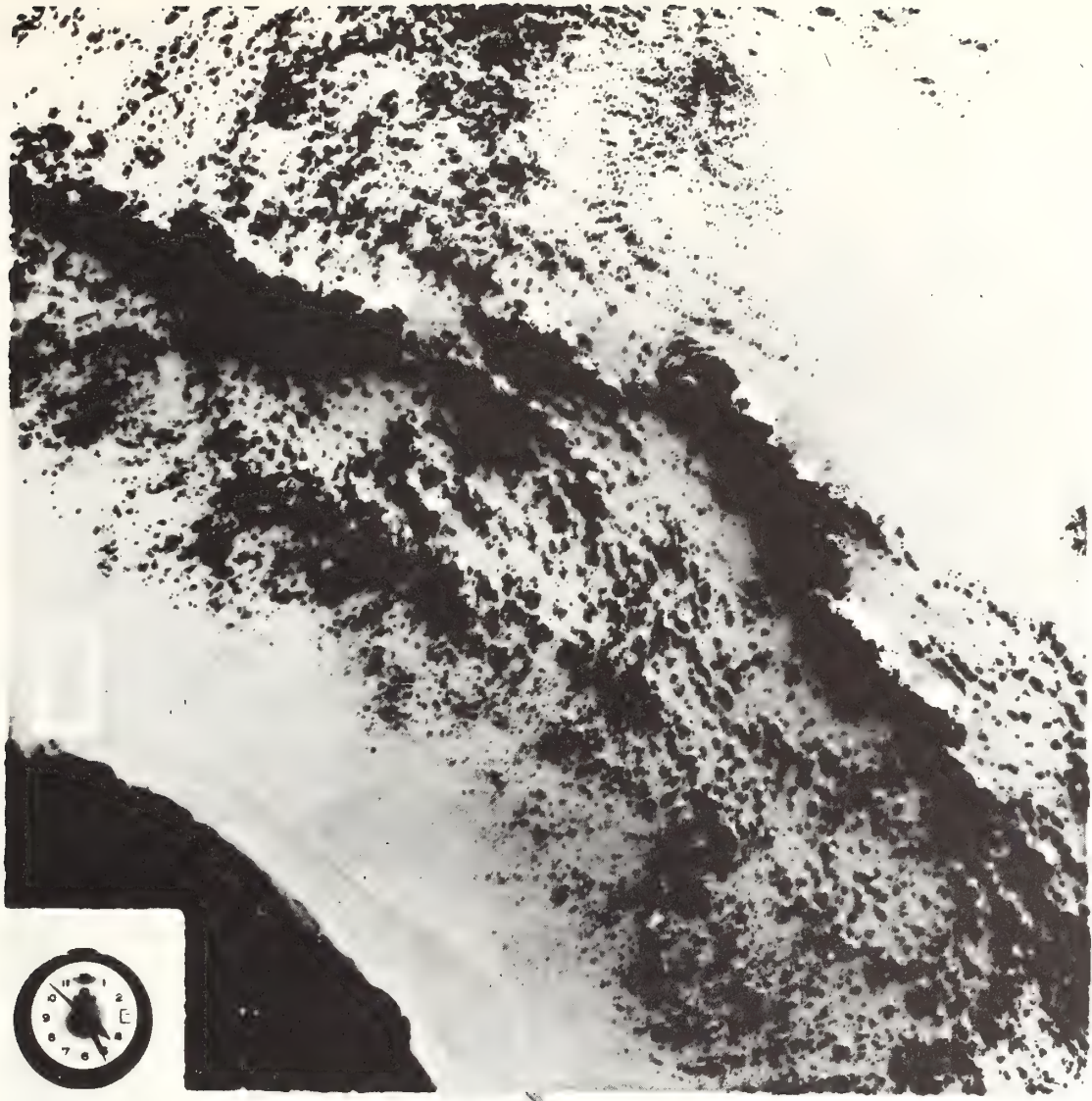


Figure 3.1 Example of the effect of vignetting in aircraft film data on the percent transmittance of blue (450nm) and green (550 nm) light, and on the blue/green ratio. Aerial color-positive film was used in the RC-8 camera.

Because the scale of the satellite photos is so much smaller than that of the aircraft photos, discontinuities such as fronts and eddies are recorded in only a small area of the photo. By comparison, similar elements have to be recorded over large areas of single aircraft photos, or even in a sequence of such aircraft photos. The practical effect of this scale difference is that variations in film density related to position on the photo can be ignored where the area of interest covers only a small area of the photo. Of course comparisons between areas widely scattered over the photo are still subject to the problem of spatial density in the photo.

All of the pertinent SL-4 duplicate films were analysed on a hybrid transmissometer. The light table and associated apertures, filters, and diffuse acceptor are from a Welch Densichron densitometer. The light sensor and associated electronics are a Gamma Digital Photometer. The transmission of each of the three color filters and of the white light setting was calibrated with a non-silver standard step wedge which is traceable to N.B.S. standards. Such a step-wedge is a better approximation to the actual attenuation characteristics of color film than the usual silver grain step wedges. This is because color films do not have any silver in the final image, depending instead on dye



NASA JSC SL4 FEB 74

89-312

*Figure 3.2 S-190B panchromatic (SO-022) photograph of the Straits of Florida and the northern coast of Cuba. The box in the lower left brackets the anticyclonic front of the Gulf Stream, and defines the area where densitometric measurements were made.*



*Figure 3.3 S-190B panchromatic (S)-022) photographs of the Straits of Florida and the western Florida Keys. The box in the lower left brackets a plume of water from Florida Bay, and defines the area where densitometric measurements were made.*

densities for attenuation of the illuminant. Data in the following paragraph are reported as the percent fraction of transmitted light rather than as density, since transmission ratios will have more meaningful interpretation than density ratios. Standard deviations ( $\sigma$ ) follow each ratio.

The first area analysed was a plume of water off the coast of Cuba, in frame 97, roll 64 SL-4, near reseau #8 (Fig. 3.2). The average Blue/Green transmission (B/G) ratio is 5.9,  $\sigma + 0.1$ . Just to the left of the interface of this plume with the Gulf Stream, the B/G ratio changes to 7.0,  $\sigma + 0.1$  in Gulf Stream water. In frame 98 a similar plume on the Florida Keys side of the Gulf Stream has a B/G ratio of 6.0,  $\sigma + 0.1$ , while the Gulf Stream water immediately to the right of the plume has a B/G ratio of 6.8,  $\sigma + 0.1$  (Fig. 3.3). This particular plume shows in frames 97, 98, and 99. The B/G ratios for the plume are 5.5, 6.0, and 6.2, respectively; the B/G ratios for the Gulf Stream water adjacent to the plume are 6.3, 6.8, and 7.1, respectively. Thus, while the absolute values of the ratio are changing, the difference between the plume ratio and the Gulf Stream water ratio is nearly constant from frame to frame.

Both filtered panchromatic films SO-022 showed some apparent density changes in the same areas as those in roll 64. Roll 65, filtered to pass 0.6 to 0.7 micron light showed a transmission change from  $40.0 \times 10^{-1}$  to  $34.0 \times 10^{-1}$  on going from the plume off Cuba to adjacent Gulf Stream water. Roll 66, filtered for 0.5 to 0.6 micron light showed no transmission change between these two areas, both noted as  $34 \times 10^{-1}$ .

Neither of the two b/w IR films showed any transmission differences among the areas analyzed. The color IR film did show some differences that are considered to be statistically significant. The plume off of Cuba showed a B/G ratio of 7.0, while adjacent Gulf Stream water showed a ratio of 7.5. The plume off the Florida Keys showed a B/G ratio of 8.5, while across the interface of the Gulf Stream the water showed a ratio of 7.2. It should be noted that the B/G ratio of the color infrared film is really a ratio of the green to the visible red radiation.

The conclusions that can be drawn from this limited data set are that a significant variation in ocean color can be observed by changes in dye concentrations in color photographs of the scene. When the surface truth is considered the evidence tends to favor the variation in suspended chlorophyll as the most probable cause of the color variation.

### 3.3 Discussion

It is immediately apparent from the data that the transmission ratio technique is a useful means of analyzing variations in color of satellite-derived photography. At the same time the data

might have been more useful had certain precautions been taken. Reference is specifically made to the aircraft-derived photography. To achieve a flat spectral response across the film the associated optics should have been fitted with anti-vignetting filters. The space craft cameras suffered to a lesser extent with the same problem. In the latter case each of the associated optics had been calibrated so that the error in transmission was known. There is however, no indication that such care was taken in preparation of the subsequent duplicate images. While care was taken to ensure that duplicate grey scales were reproduced at the same levels as those on the on-board films, apparently no account was taken of the variation in illumination across the print head of the printer. All of these problems taken together substantially reduce the possible intercomparisons that might have been attempted.

The photographs in Figs. 3.2 and 3.3 are both S-190B products that have been enhanced by printing on high-contrast film. Exposure levels were set to saturate the details in the non-oceanic features. This is a trial and error technique that extracts markedly more low radiance level information. The change in texture marking differing sea states in Fig. 3.2 is not measurable by the densitometer technique, but it is clearly noticeable to the eye. The boundary between the two levels of radiance is probably the anticyclonic edge of the Florida Current. The detection of the features in Figs. 3.2 and 3.3 by the S-192 scanner is discussed in section 5.

#### 4. SPECTROMETER EXPERIMENT

The SKYLAB S-191 steerable spectroradiometer was to be used in this experiment to study changes in the visible (0.4-0.7 $\mu$ m) and infrared (7.0-14.0  $\mu$ m) spectra of the ocean across the current's cyclonic boundary. The plan was for the crew to acquire a cloud-free oceanic area with the S-191 looking 45° forward of nadir, and to track that site until 0°. Thereafter, the spectroradiometer was to be locked into nadir viewing across the cyclonic front and up into the waters of Florida Bay.

The experiment proved to be not very successful for several reasons: although the crew did as the plan said, the data acquisition camera (DAC) was turned off and the exact tracking data (angles, times, locations) were never recorded; the calibration of the S-191 infrared detectors is not known; the visible region data radiance values do not agree with theoretical or observed values reported by other investigators.

##### 4.1 Tracking Data

Location of the data was made difficult by the lack of DAC output. The voice log was the best clue to what actually was done by the crew. According to the transcript of the voice tape, at

16:29:33 GMT the pilot had the S-191 set at  $35^{\circ}$  looking forward along the track, although all crew instructions were to set the S-191 target acquisition at  $45^{\circ}$ . The word "thirty-five" was not clearly audible however, and the pilot may have followed the instructions sent up to SKYLAB just prior to the pass. At 16:29:35 GMT, the pilot reported tracking a clear area of water; the assigned start time was 16:29:33. The exact time of reaching nadir is difficult to tell from the voice log however, 16:30:45 is the approximate time.

The location and time of the nadir point were calculated from geometrical considerations assuming a spherical Earth with a radius of 6378 km and a satellite altitude of 443 km. If the nadir angle was  $45^{\circ}$  at 16:29:33 GMT, the position of the point tracked was  $23^{\circ}53'.4$  N,  $81^{\circ}58'.0$  W; the time of arrival of the spacecraft over this point from the best available positioning data was 16:30:41.1 GMT, which is in good agreement with the voice log estimate. The message sent up to the crew had the finish of the tracking at 16:31:05.

The S-192 line-straightened data show that the position given above was in the middle of a clear ocean area and it appears reasonable to have tracked this as the site. The vehicle was over Florida Bay at 16:30:55 according to the S-192, but the pilot commented at 16:31:10 that they were going across the Keys. This discrepancy cannot be accounted for unless the Florida Keys were observed well after the spacecraft transit.

If the above analysis is correct, then according to the surface truth data in Fig. 2.1, the S-191 probably never acquired data from the Gulf Stream. The position of the  $22^{\circ}\text{C}$  isotherm at 100 meters depth indicator was 25 km SW of the point where the pilot tracked a clear area. Although the exact location of the front cannot be identified in the ship track data it appears that it was also SW of the nadir tracking point. Maul (1975) reported the mean separation between the indicator isotherm and the front to be 11 km in this area, and that further supports the contention that the S-191 did not obtain spectra in the Gulf Stream. The objective of analyzing the change in spectra across the front cannot be accomplished with these data.

#### 4.2 Infrared Radiance

The infrared experiment was designed to study the accuracy of atmospheric transmission models. This objective could not be accomplished because the calibration of the infrared detector is an unknown function of wavelength (Barnett, NASA-JSC personal communication; Anding, and Walker, 1976). Several relative tests were made however, which provide some information on the atmospheric transmission model dependency, and these will be discussed below.

#### 4.2.1 Theoretical calculations

Emitted infrared radiation ( $7 \mu\text{m} < \lambda < 14 \mu\text{m}$ ) leaving the Earth passes through the atmosphere before detection at the S-191 sensor. The atmosphere modifies the infrared radiation by absorption and, to a very minor degree, by scattering. Details of the theory are given by Chandrasekar (1960) and recent reviews on its application to oceanography are given by Hansen (1972) and Maul (1973). The radiative transfer equation through an absorbing but non-scattering atmosphere is:

$$\begin{aligned}
 N(\theta, \lambda) = & \epsilon(\theta', \lambda) L(T, \lambda) \tau(\theta, \lambda) \\
 & + \int_0^S L(T_a, P, \lambda) \frac{\partial \tau(p, \theta, \lambda)}{\partial p} p \\
 & + \rho(\theta', \lambda) N_{as}(\theta'', \lambda) \tau(\theta, \lambda)
 \end{aligned} \quad (4.1)$$

where  $\theta, \theta', \lambda''$  are the nadir angle, angle of reflectance, and angle of incidence, respectively. Radiance ( $N$ ) at the satellite is wavelength-dependent, and is a function of the surface blackbody radiance ( $L$ ), the emissivity of the surface ( $\epsilon$ ) and the transmittance of the atmosphere ( $\tau$ ); these three parameters describe the absorption of emitted blackbody radiation by the atmosphere. The second term in the equation, the integral term, describes the atmospheric (a) modification of the radiance as a function of pressure ( $P$ ). The third term describes the contribution of the reflected ( $\rho$ ) atmospheric radiance at the surface ( $N_{as}$ ), again as modified by transmittance.

The theoretical calculations discussed herein are an extension of the model used by Maul and Sidran (1973) which uses the transmissivity data of Davis and Viezee (1964). The area of interest is the  $10.5 - 12.5 \mu\text{m}$  band that is used on many spacecraft including the SKYLAB S-192 multispectral imager. In this spectral interval  $\epsilon > 0.99$  at low nadir angles; hence  $\rho (= 1 - \epsilon)$  is very small and equation (4.1) may be written

$$\begin{aligned}
 N(\theta) = & \int_0^S \int_0^{\infty} \phi(\lambda) L(T_s, \lambda) \tau(\theta, \lambda) d\lambda \\
 & + \int_0^S \int_0^{\infty} \phi(\lambda) L(T_a, p, \lambda) \frac{\partial \tau(p, \theta, \lambda)}{\partial p} dp d\lambda
 \end{aligned} \quad (4.2)$$

The filter function ( $\phi$ ) is zero outside the interval discussed above. The radiance may be converted to equivalent blackbody temperature by inverting the Planck equation ( $L$ ) which has been integrated over the same  $10.5 < \lambda < 12.5$  interval.

The calculations were carried out on the AOML computer. A special radiosonde was released by the Key West office of the



National Weather Service at the time of SKYLAB transit (see Fig. 4.1). Before the radiative transfer from a radiosonde is computed the data must be inspected to insure that no clouds are in the path of ascent, in order to compute a cloud-free radiance. Clouds are readily identified by their characteristically high relative humidity and isothermal temperature. There is evidence of clouds in the data in Fig. 4.1, so calculations were made to test the effect of clouds.

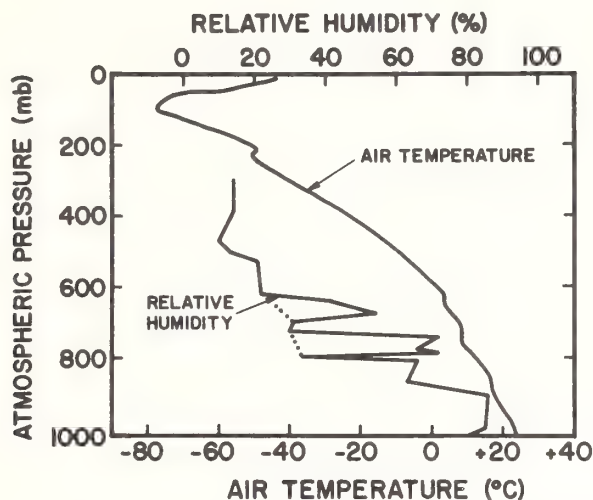


Figure 4.1 Vertical profiles of atmospheric pressure and relative humidity taken at the times of SKYLAB transit. The dotted lines on the relative humidity profile are the cloud-free estimate of atmospheric moisture.

Two cloud layers are in evidence, one centered at 744 mb and one centered at 671 mb. Clouds are characterized by a sudden increase in relative humidity and a small (near zero) lapse rate. An equivalent clear sky estimate is made by assuming the clouds are absent; the estimated relative humidity profile in the clouds region is given by the dotted curve. The calculated equivalent blackbody temperatures for  $T_s$  298.15°C are:

Wavelength	Observed (Appendix B)	Cloud-free Equivalent
11 $\mu$ m	293.22° K	293.85° K
12.5 $\mu$ m	290.46° K	291.28° K

The differences in this case are small, 0.63°K at 11 $\mu$ m, and 0.82°K integrated over the 10.5-12.5 $\mu$ m region where the S-192, NOAA-4/5, and SMS-1/2 observe. Other experience with this type of cloud-free equivalence has been as high as 5°K over the Gulf of Mexico.

#### 4.2.2 Comparison of S-191 and models

As stated in section 1.3, the wavelengths chosen for the two-channel technique, (Anding and Kauth, 1970) of atmospheric correction depend on the radiative transfer model. SKYLAB was to be used to study that question but since the calibration of the S-191 infrared detector is unknown, the problem cannot be investigated.

The mean sea surface temperature along the trackline was  $25.0^{\circ}\text{C}$ . This value has been used in the calculations shown in Fig. 4.2. The Davis and Vizee (1964) model does not include absorption due to the ozone molecules which show up as a maximum at  $9.6\mu\text{m}$  in the S-191 observation. The comparison shows that ozone does not affect the  $10.5\text{-}12.5\mu\text{m}$  window and hence is not a factor in the S-192 infrared scanner data. At  $11.0\mu\text{m}$ , the apparent difference between the observed and calculated equivalent blackbody temperature ( $T_{\text{BB}}$ ) is  $3.5^{\circ}\text{C}$ . This seems to be the approximate error estimate of other SKYLAB investigators (personal communications), but no conclusions can be drawn.

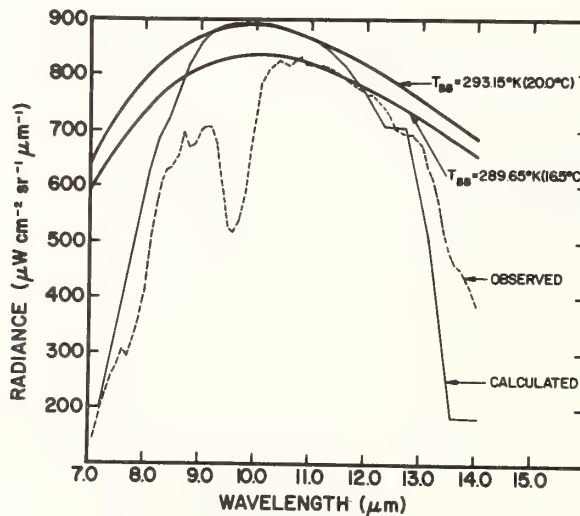
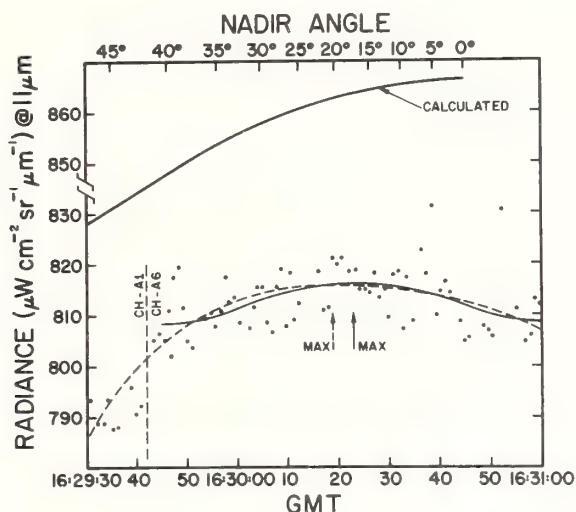


Figure 4.2 Spectral infrared radiance observed by the S-191 spectroradiometer (dashed line), and calculated by the ozone excluding model of Davis and Vizee (fine solid line). Heavy solid lines are blackbody curves.

Since the calibration uncertainty is wavelength-dependent the data at  $11\mu\text{m}$  were studied to determine the shape of the nadir angle dependence curve. In the lower half of Fig. 4.3 is a least squares fourth-order polynomial fit to all the observed radiances as a function of time (dashed line). Since the same ocean spot was to be tracked, radiance should be a function of nadir angle up to 16:30:45 GMT. The maximum on this curve (arrow) is at

16:30:19. The upper curve is the theoretical calculation using equation 4.2 for the same atmosphere in Fig. 4.1 and for  $T=25^{\circ}\text{C}$ . Nadir angles were computed using a start time of 16:29:35 GMT ( $45^{\circ}$ ) and a stop time of 16:30:45 GMT ( $0^{\circ}$ ) following the discussion in section 4.0. The match in the curves maxima would be approximately coincident if the tracking started with a  $37^{\circ}$  nadir angle, which is in agreement with the voice tape transcript.



*Figure 4.3 Radiance at 11  $\mu\text{m}$  as a function of nadir angle of the same ocean spot as that tracked on the S-191 (dots). The dashed vertical line separates channel A1 and channel A6 data. Dashed curve is fourth-order polynomial fit to all data; fine solid line is fourth-order polynomial fit to A6 data only. Heavy solid line is the calculated nadir angle dependence.*

The S-191 spectroradiometer uses a series of detectors that cover a segment of the spectrum. In some regions these overlap and ambiguity often exists as to which detector to use. In the sections to follow, those detectors (channels) chosen were as recommended in the NASA reports on instrument performance. It is suggested that only those data that are well calibrated be reported to non-instrument engineering investigators in the future.

Barnett (personal communication) cautioned against the use of radiometer channel A1 in the S-191 (see again Fig. 4.3). Accordingly a second fourth-order polynomial (solid line) was fitted to the channel A6 data only. The rms spread of the radiance about this polynomial is  $4.48\mu\text{W cm}^{-2}\text{ sr}^{-1}$ . This corresponds to a noise-equivalent temperature difference (NEAT) of  $+0.3^{\circ}\text{K}$  at  $289.65^{\circ}\text{K}$ . Since the atmospheric attenuation tends to diminish surface gradients, this results in a calculated NEAT of

approximately  $+0.6^{\circ}\text{C}$  in  $T$  for this model at  $11\mu\text{m}$  on this day. The equivalent blackbody temperature at the maximum in the polynomial is  $16.5^{\circ}\text{C}$  at the top of the atmosphere. This implies a temperature correction of  $8.5^{\circ}\text{C}$  which is not unreasonable for a tropical winter atmosphere whose precipitable water vapor is 3.6 cm (cf. Maul and Sidran, 1973).

#### 4.3 VISIBLE RADIANCE

The visible radiance experiment was designed to study the accuracy with which spectral changes across oceanic fronts can be observed and interpreted from satellite altitudes. Unfortunately, the strongest front expected in the experiment area was missed by the S-191 so this objective, as discussed before, could not be accomplished. However, during the course of this work, a theoretical technique for recovering the "ocean color spectrum" through the atmosphere was developed. This is discussed in detail below and an attempt is made to compare the predictions of the theory with the S-191 data and the associated ground truth.

##### 4.3.1 Theoretical calculations

It is clear that the full potential of oceanic remote sensing from space in the visible portions of the spectrum can be realized only if the radiance that reaches the top of the atmosphere can be related to the optical properties of the ocean. To effect this, the radiative transfer equation must be solved for the ocean-atmosphere system with collimated flux incident at the top of the atmosphere. In such calculations the optical properties of the ocean that must be varied are the scattering phase function ( $P_0(\theta)$ ) and the single scattering albedo ( $\omega_0$ ; defined as the ratio of the scattering coefficient to the total attenuation coefficient). Furthermore, unless the ocean is assumed to be homogeneous, the influence of vertical structure in these properties must be considered. To describe the cloud-free atmosphere, the optical properties of the aerosols and their variation with wavelength and altitude as well as the ozone concentration must be known. Considering the ocean for the present to be homogeneous, the radiance at the satellite can be related to the ocean's properties by choosing an atmospheric model and solving the transfer equation for several oceanic phase functions and  $\omega_0$ 's at each wavelength of interest. The number of separate computational cases required is then the product of the number of phase functions, the number of values of  $\omega_0$ , and the number of wavelengths. Even if the multi-phase Monte Carlo method (MPMC) (Gordon and Brown, 1975) is used, the  $\omega_0$  resolution of Gordon and Brown (1973) would require a number of simulations equal to ten times the number of wavelengths for each atmospheric model considered. It is possible, however, to obtain the necessary information without modeling the ocean's optical properties in such detail.

The model is based on an observation evident in results of computations given by Plass and Kattawar (1969) and by Kattawar and Plass (1972) on radiative transfer in the ocean-atmosphere system, namely, that when the solar zenith angle is small, the upwelling radiance just beneath the sea surface is approximately uniform, (i.e., not strongly dependent on viewing angle) and hence determined by the upwelling irradiance. This observation is utilized in simulations of oceanic remote sensing situations by assuming that a fraction  $R$  of the downwelling photons are absorbed. The ocean is then treated as if there is a Lambertian reflecting surface of albedo  $R$  just beneath the sea surface. In this case Gordon and Brown (1974) have shown that any radiometric quantity  $Q_1$  can be written.

$$Q = Q_1 + \frac{Q_2 R}{1-rR} \quad (4.3)$$

$Q_1$  is the contribution to  $Q$  from photons that never penetrate the sea surface (but may be specularly reflected from the surface).  $Q_2$  is the contribution to  $Q$  from photons that interact with the hypothetical "Lambertian surface" once for the case  $R=1$ .  $r$  is the ratio of the number of photons interacting with the "Lambertian surface" twice, to the number of photons interacting once, again for  $R=1$ .

By use of equation 4.3, any radiometric quantity can then be computed as a function of  $R$ . Physically the quantity  $R$  is the ratio of upwelling to downwelling irradiance just beneath the sea surface and is known as the reflectance function  $[R(0,-)]$  in the ocean optics literature (Preisendorfer, 1961). Spectral measurements of the reflectance function  $R(\lambda)$  have been presented for various oceanic areas by Tyler and Smith (1970). Henceforth,  $R(\lambda)$  will be referred to as the "ocean color spectrum"

A series of Monte Carlo computations have been carried out to see if an approximate simulation (AS1), using this assumption of uniform upwelling radiance beneath the sea surface, yields results that agree with computations carried out using an exact simulation (ES), in which the photons are accurately followed in the ocean as well as the atmosphere. The Monte Carlo codes used in Gordon and Brown (1973, 1974) were modified by the addition of an atmosphere. The atmosphere consisted of 50 layers and includes the effects of aerosols, ozone, and Rayleigh scattering, using data taken from the work of Elterman (1968). The aerosol scattering phase functions were computed by Fraser (NASA-GSFC, personal communication) from Mie theory assuming an index of refraction of 1.5 and Deirmendjian's (1964) "haze-C" size distribution. Also, to determine the extent to which the vertical structure of the atmosphere influences the approximate simulation, a second approximate simulation (AS2) was carried out in which the atmosphere was considered to be homogeneous; i.e., the aerosol scattering, Rayleigh scattering, and ozone absorption were independent of altitude. The oceanic phase functions in the ES

are based on Kullenberg's (1968) observations in the Sargasso Sea, and are given in Table 4.1 (Note that all the phase functions in the present paper are normalized according to  $2\pi \int_0^\pi P(\theta) \sin \theta d\theta = 1$ ).

Table 4.1 The Three Ocean Scattering Phase Functions

$\theta$ (deg)	KA ( $\times 10^2$ )	KB ( $\times 10^2$ )	KC ( $\times 10^2$ )
0	10924	10171	9521
1	4916	4577	4285
5	573.5	534.0	499.9
10	169.3	157.7	147.6
20	29.5	29.39	29.31
30	12.56	11.95	11.42
45	3.059	3.661	4.189
60	1.092	1.577	1.999
75	0.546	0.915	1.190
90	0.344	0.661	0.952
105	0.311	0.641	0.928
120	0.317	0.732	1.094
135	0.410	0.829	1.309
150	0.492	1.017	1.618
165	0.579	1.261	1.856
180	0.617	1.357	1.999

KA is roughly an average of Kullenberg's phase function at 632.8 nm and 655 nm, and KC is his phase function at 460 nm. KB is an average of KA and KC. These phase functions show considerably less scattering at very small angles ( $\theta < 1^\circ$ ) than was observed by Petzold (1972) in other clear-water areas; however, the exact form of the oceanic phase function is not very important, since it has been shown (Gordon, 1973) to influence the diffuse reflectance and  $R(0,-)$  only through the back-scattering probability (B)

$$B = 2\pi \int_{\pi/2}^{\pi} P_o(\theta) \sin \theta d\theta.$$

In all of the computations reported here the solar beam incident on the top of the atmosphere is from the zenith, and with unit flux. At visible wavelengths the variable atmospheric constituent that will most strongly influence the radiance at the top of the atmosphere is the aerosol concentration, so the computations have all been carried out as a function of the aerosol computation.

Table 4.2 gives a sample comparison of upward fluxes at the top of the atmosphere at 400 nm in the three simulation models (ES, AS1, and AS2) as a function of the aerosol concentration. N, 3xN, and 10xN refer to aerosol concentrations in each layer

of 1, 3, and 10 times the normal concentration given by Elterman. 400 nm is chosen because in the visible portion of the spectrum it is the wavelength at which the atmospheric effects are expected to be most severe. The ES case uses  $\omega_0 = 0.8$  and phase function KC. The values of R used to effect the AC computations were taken from the EC computation of this quantity. However, if R is taken from

$$R = 0.0001 + 0.3244x + 0.1425x^2 + 0.1308x^3 \quad (4.4)$$

where  $x = \omega B / (1 - \omega_0(1 - B))$  which, according to Gordon, Brown and Jacobs (1975), reproduces the in-water reflection function for the corresponding case but with no atmosphere present, the results of the AS model computations agree with those listed to within 0.2%. The numbers in the parenthesis next to each flux value represent the statistical error in the flux based on the actual number of photons collected in each case. It is seen that ES and AS simulations generally agree to within the accuracy of the computations. Notice also the excellent agreement between the AS1 and AS2 fluxes.

Table 4.2: Comparison of the flux at the top of the atmosphere for the ES, AS1, and AS2 simulations.

Aerosol Concentration	ES	AS1	AS2
N	0.222 (+.002)	0.224 (+.001)	0.226 (+.001)
3xN	0.274 (+.003)	0.273 (+.001)	0.275 (+.001)
10xN	-.423 (+.004)	-.426 (+.002)	0.425 (+.002)

Fig. 4A presents a comparison between the ES, AS1, and AS2 upward radiances at the top of the atmosphere. The step-like curve in the figure is for ES, the solid circles for AS1, and the open circles for AS2, and  $\mu_0$  is the cosine of the angle between the nadir and the direction toward which the sensor is viewing. The radiances in Fig. 4.4 for the ES cases are accurate to about 3% in the range  $\mu=1$  to about 0.4, while for the AS cases the accuracy is about 1%. To within the accuracy of the computations, the three simulations again agree for all the aerosol concentrations except within the range  $\mu=0$  to about 0.3; i.e. viewing near the horizon. These computations appear to demonstrate that the transfer of the ocean color spectrum through the atmosphere can be studied with either the AS1 or AS2 model as long as radiances close to the horizon are not of interest. Furthermore, from the reciprocity principle (Chandrasekhar, 1960)

the nadir radiance, when the solar beam makes an angle  $\theta_0$  with the zenith, can be found by multiplying the radiance  $I(\mu)$  in Fig. 4.4 by  $\mu$  where  $\mu$  is taken to be  $\cos \theta_0$ . This implies that as long as the Sun is not too near the horizon, the AS1 and AS2 methods of computation can be used to determine the nadir radiance at the tip of the atmosphere as a function of the ocean's properties through equation 4.4. The fact that the AS2 model (homogeneous atmosphere) yields accurate radiances is very important in remote sensing since it implies that only the total concentration (or equivalently the total optical thickness) of the aerosol need be determined to recover the ocean color spectrum from satellite spectral radiometric data.

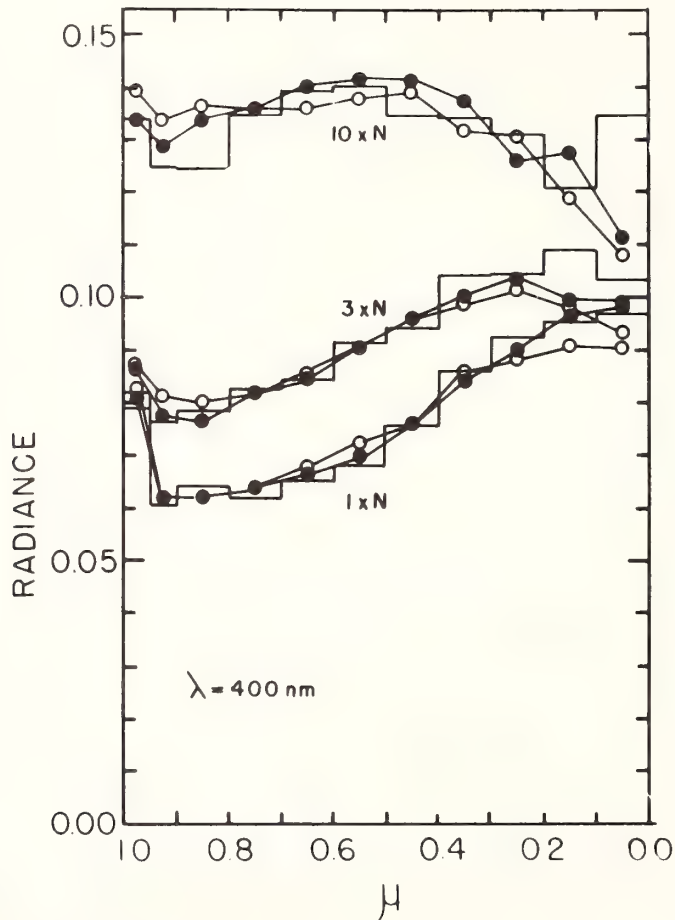


Figure 4.4 Comparison between ES (step-like curve) AS1 (solid circles) and AS2 (open circles) upward radiances at the top of the atmosphere for an ocean with  $\omega_0 = 0.8$  and phase function KC and an atmosphere with a normal (1xN), three times normal (3xN) and ten times normal (10xN) aerosol concentration.



It should be noted that these results also strongly suggest that  $R(\lambda)$  is the quantity relating to the subsurface conditions that can be determined from space, and hence, is the most natural definition of the "ocean color spectrum". Moreover, it has been shown (Gordon, Brown, and Jacobs, 1975) that  $R(\lambda)$  is not a strong function of the solar zenith angle (the maximum variation in  $R(0,-)$  with  $\theta_0$  is of the order of 15% for  $0 < \theta_0 < 60^\circ$ ), in contrast with other definitions (Curran, 1972; Mueller, 1973).

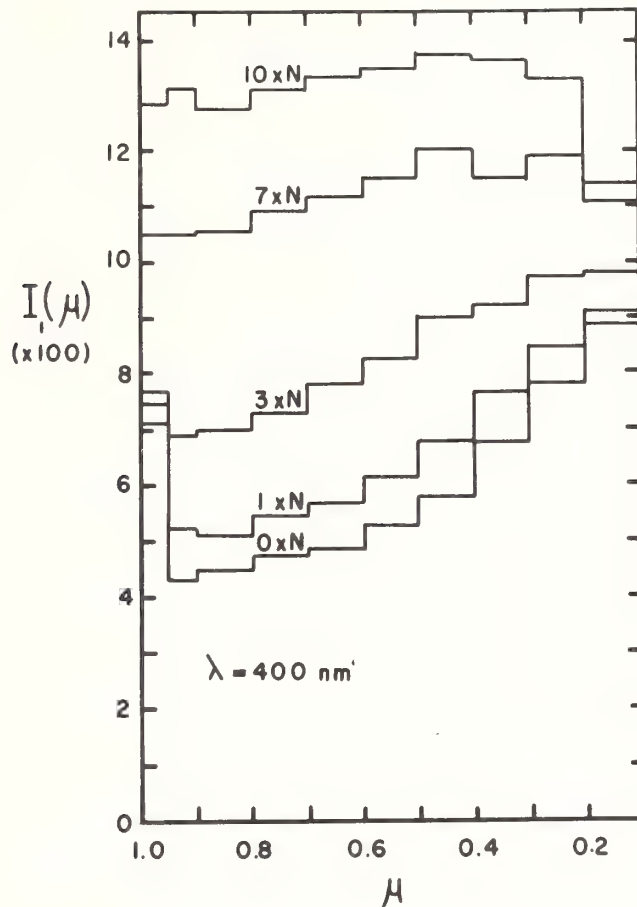


Figure 4.5  $I_1(\mu)$  as a function of  $\mu$  for various aerosol concentrations; wavelength of calculations is 400 nanometers.

The only way spacecraft data can be used to obtain information concerning subsurface conditions (such as concentrations of chlorophyll, suspended sediments, etc.) is through determination of  $R(\lambda)$ . [It is assumed here that the relationship between  $R(\lambda)$  and the ocean constituents is well known, whereas in fact much work still remains to be carried out before such a relationship can be established]. This can be effected by applying equation (4.3) to radiance  $I(\mu)$  at the top of the atmosphere with the Sun at the zenith, which yields,

$$I(\mu) = I_1(\mu) + \frac{R I(\mu)}{1 - rR}$$

$I_1(\mu)$  and  $I_2(\mu)$  are presented in Figs. 4.5 and 4.6 for the three aerosol models discussed above as well as for an aerosol free model (0xN) and a model with seven times the normal aerosol concentration (7xN).

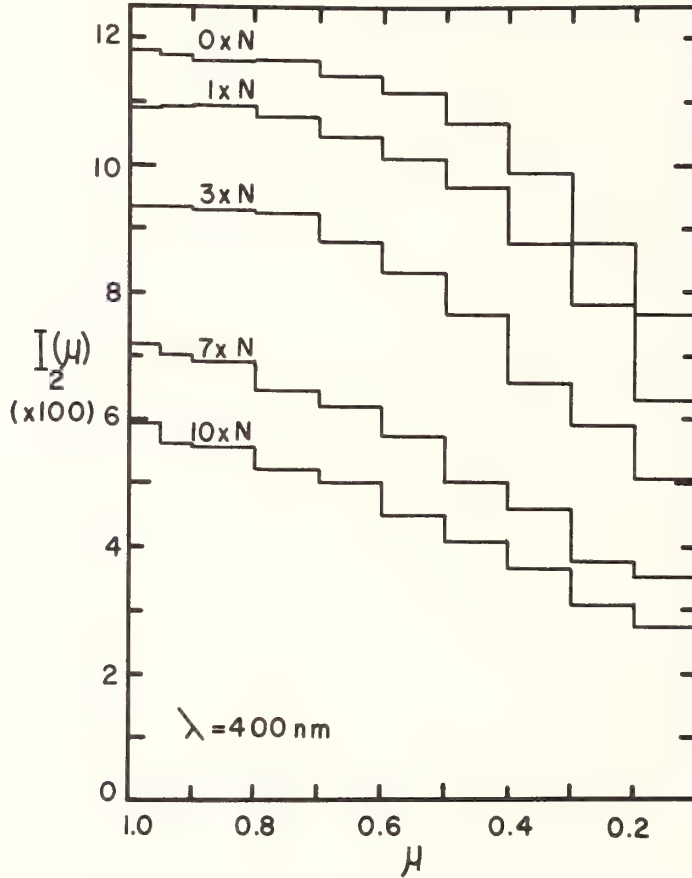


Figure 4.6  $I_2(\mu)$  as a function of  $\mu$  for various aerosol concentrations; wavelength of calculations is 400 nanometers.

For the cases considered,  $R \approx 0.5$ , and since  $R$  is usually about 0.03 to 0.10 at this wavelength we can rewrite equation (4.5) approximately as

$$I(\mu) = I_1(\mu) + RI_2'(\mu) \tag{4.5}$$

so

$$R \approx \frac{I(\mu) - I_1(\mu)}{I_2(\mu)}$$

Applying the reciprocity theorem to equation 4.6 it is found for nadir viewing that

$$R \cong \frac{I_{\text{nadir}} - \mu_0 I_1(\mu_0)}{\mu_0 I_2(\mu_0)} \quad (4.7)$$

where  $\mu_0$  is the cosine of the solar zenith angle. Noting again that  $R$  is 0.10 it is seen that the difference between  $I_{\text{nadir}}$  and  $\mu_0 I_1(\mu_0)$  must be small, which implies that the accuracy in  $R$  will be limited by knowledge of  $I_1(\mu_0)$ . Since  $I_1(\mu_0)$  depends strongly on the aerosol concentration, it is absolutely necessary to be able to determine the aerosol concentration if an accurate value of  $R$  is desired. Curran (1972) has suggested that this can be accomplished by observing the ocean (assumed free of white caps) in the near infrared where  $R(\lambda) \approx 0$ . In section 4.3.2 of this report, Curran's suggestion is utilized to find the aerosol concentration from the S-191 data.

Before trying to apply the relationships developed here to the S-191 spectra, there are several important implications of the theory to be discussed. Noting that  $I_1(\mu)$  and  $I_2(\mu)$  depend only on the direction of the incident solar beam, the properties of the atmosphere and ocean surface, but not  $R$  (if it is assumed these latter properties remain essentially constant over horizontal distances large compared with those over which  $R$  changes significantly), one can directly relate changes in  $I(\mu)$  to changes in  $R$ . From equation 4.5

$$\frac{\partial I(\mu)}{\partial R} \cong I_2(\mu).$$

Figure 4.6 shows that  $\partial I/\partial R$  is not an extremely strong function of the aerosol concentration for concentrations up to three times normal and viewing angles up to  $35^\circ$  from nadir. This suggests that horizontal gradients in  $R$  can be estimated without an accurate aerosol optical thickness.

When equation 4.5 is used to relate changes in radiance ( $\Delta I(\mu)$ ) to changes in  $R(\Delta R)$ ,

$$I(\mu) = [\partial I(\mu)/\partial R] \Delta R \cong I_2(\mu) \Delta R. \quad (4.8a)$$

Equation (4.8a) makes possible a determination of minimum radiance change the sensor must be able to detect for a given  $\Delta R$ . For example, suppose that observing at  $\mu=0.85$  it is desired to detect a 5% change in  $R$  for clear ocean water at 400 nm ( $R \approx 0.1$ ) through an atmosphere with three times the normal aerosol concentration. Figure 4.6 shows that  $I_2(0.85)$  is about 0.11 and noting that the extraterrestrial flux 400nm is about  $140 \text{ W cm}^{-2} \text{ nm}^{-1}$ , we find from equation (4.6) that  $\Delta I(0.85)$  is

0.077 Wcm<sup>-2</sup> nm<sup>-1</sup>sr<sup>-1</sup>. In a similar way radiance changes can be related to ΔR for a nadir-viewing sensor and any solar zenith angle. As mentioned previously from the reciprocity principle,

$$I_{\text{nadir}} = I(\mu_0)\mu_0$$

where  $\mu_0 = \cos \theta_0$ ,  $\theta_0$  is the solar zenith angle and  $I(\mu_0)$  is the radiance at the top of the atmosphere seen by a sensor viewing at  $\theta_0$  when the Sun is at the zenith. Following through with the same arguments that led to equation (4.8a) it is found that

$$\Delta I_{\text{nadir}} = \mu_0 [\partial I(\mu_0) / \partial R], R \cong \mu_0 I_2(\mu_0) \Delta R. \quad (4.8b)$$

Clearly, for a given ΔR,  $I_{\text{nadir}}$  decreases substantially with increasing solar zenith angle because of the presence of the  $\mu_0$  factor in equation (4.8b). For example, with a three-times normal aerosol concentration, a nadir-viewing sensor would need about 2.5 times more sensitivity at  $\theta_0 = 60^\circ$  as compared with  $\theta_0 \approx 0$  to detect the same R.

The above examples indicate how the theory (AS1) can be used in the design of a satellite sensor system for estimating some ocean property such as the concentration of suspended sediments or organic material. Specifically, one must first determine the effect of the property on R. Then, on the basis of the sensitivity desired, find ΔR, and finally, use equation (4.8a) or (4.8b) to find the minimum radiance change the sensor must be capable of detecting. If the sensor has a limited dynamic range, then equation (4.5) can be used with equation (4.8a) or (4.8b) to aid in the sensor performance design trade-offs. [Unfortunately at this time, relationships between  $R(\lambda)$  and seawater constituents are not well established.]

Considering the fact that we have used only the "haze-C" aerosol phase function (which is clearly only approximately characteristic of the actual aerosol scattering) it is natural to inquire how strongly the computations of  $I_1(\mu)$  and  $I_2(\mu)$  presented in Figs. 4.5 and 4.6 depend on the shape of the aerosol phase function. To effect a qualitative understanding of the influence of the aerosol phase function, computations of  $I_1$  and  $I_2$  have been carried out using the well known Henyey-Greenstein (HG) phase function

$$P_{\text{HG}}(\theta) = \frac{(1-g^2)/4\pi}{(1+g^2-2g \cos \theta)^{3/2}},$$

where the asymmetry parameter g is defined according to

$$g = 2\pi \int_0^\pi P(\theta) \cos \theta \sin \theta d\theta,$$

and  $\theta$  is the scattering angle. Since g for the haze-C phase

function is 0.690, computations have been made with  $P_{HG}(\theta)$  for  $g$  values of 0.6, 0.7, and 0.8. Figure 4.7 compares these  $P_{HG}(\theta)$ 's with the haze-C phase function. The HG phase function for  $g=0.7$  clearly fits the haze-C phase function quite well in the range  $5^\circ < \theta < 140^\circ$ ; however, as is well known, the HG formula is incapable

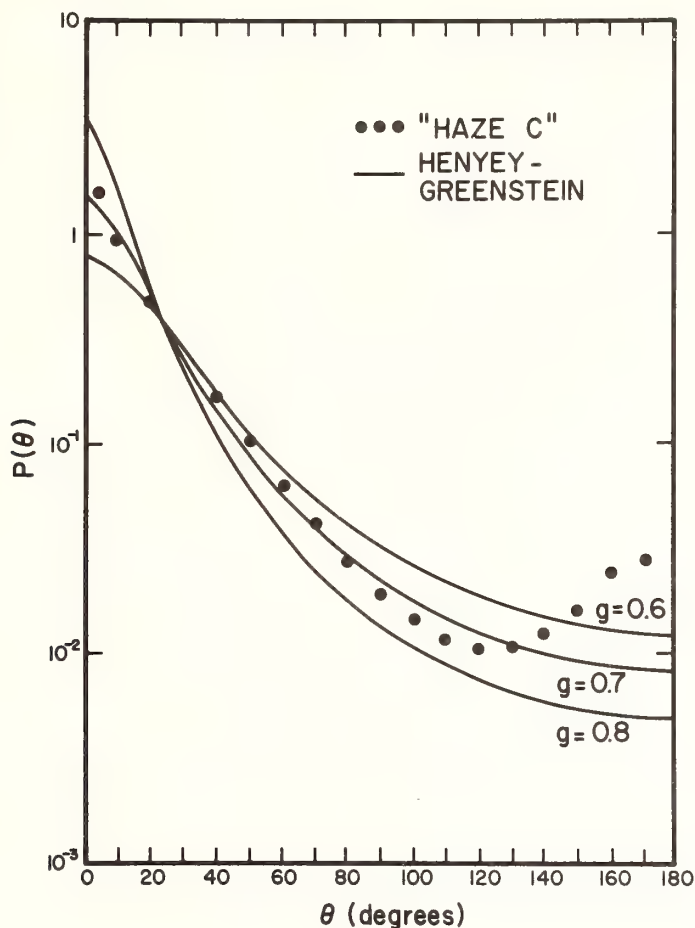


Figure 4.7 Comparison between the "haze-C" and various Henyey-Greenstein phase functions characterized by asymmetry parameters 0.6, 0.7, and 0.8, as a function of scattering angle ( $\theta$ ).

of reproducing phase functions computed from Mie theory in the extreme forward and backward directions. The HG phase functions with asymmetry parameter 0.6 and 0.8 are seen to be substantially different from the haze-C distribution at nearly all scattering angles. On the basis of Fig. 4.7 it should be expected that  $I_1$  and  $I_2$  computed with  $P_{HG}(\theta)$  will be in close agreement with the haze-C computations only for  $g$  close to 0.7. Figures 4.8 and 4.9, which compare the results of computations of  $I_1$  and  $I_2$  for  $P_{HG}(\theta)$  for the normal aerosol concentration, show that this is indeed the case. It is seen that except for apparent statistical fluctuations, the HG phase function for  $g=0.7$  yields values of

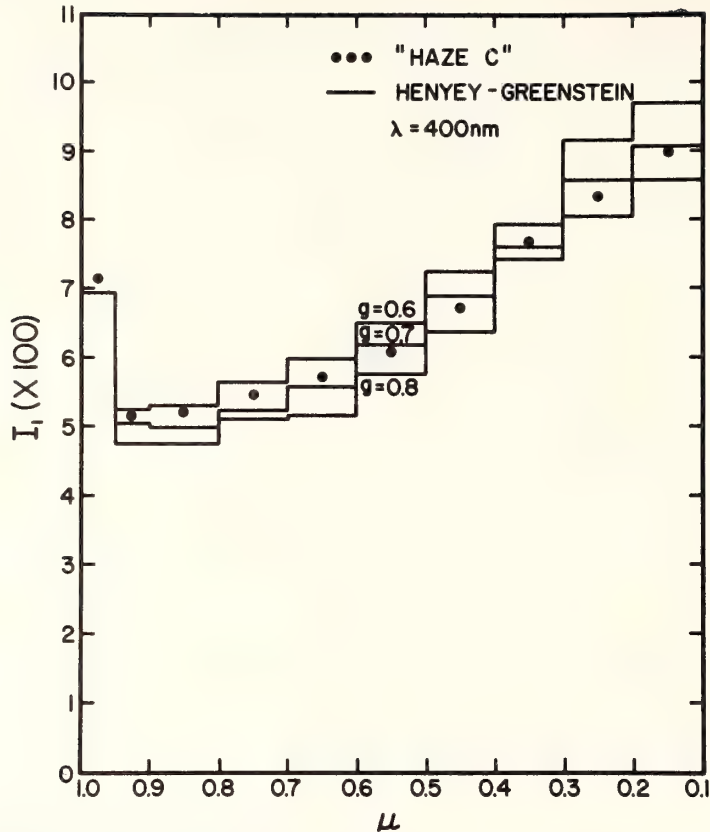


Figure 4.8 Comparison between  $I_1(\mu)$  computed for the "haze-C" and Henyey-Greenstein phase functions for an atmosphere with a normal aerosol concentration, as a function of cosine  $\theta(\mu)$ : wavelength of calculations is 400 nanometers.

$I_1$  and  $I_2$  in good agreement with the haze-C computations. This suggests that the detailed structure of the phase function is not of primary importance in determining  $I_1$  and  $I_2$ , and it may be sufficient for remote sensing purposes to parameterize the phase function by  $g$ .

To get a feeling for the importance of variations in the phase function in the remote sensing of ocean color, consider the effect of changing the aerosol phase function from an HG with  $g = 0.6$  to one with  $g = 0.8$  over an ocean with  $R = 0.1$ . From Figs. 4.8 and 4.9 it is found that the normalized radiance at  $\mu = 0.85$  (the assumed observation angle) decreases by  $4.9 \times 10^3$ . This decrease in radiance would be interpreted under the assumption of no atmospheric change as a decrease in  $R$  from 0.10 to 0.056. This clearly indicates then that variations in the aerosol phase function in the horizontal direction could be erroneously interpreted as horizontal variations in the optical properties of the ocean. However, it is probably unlikely that the clear

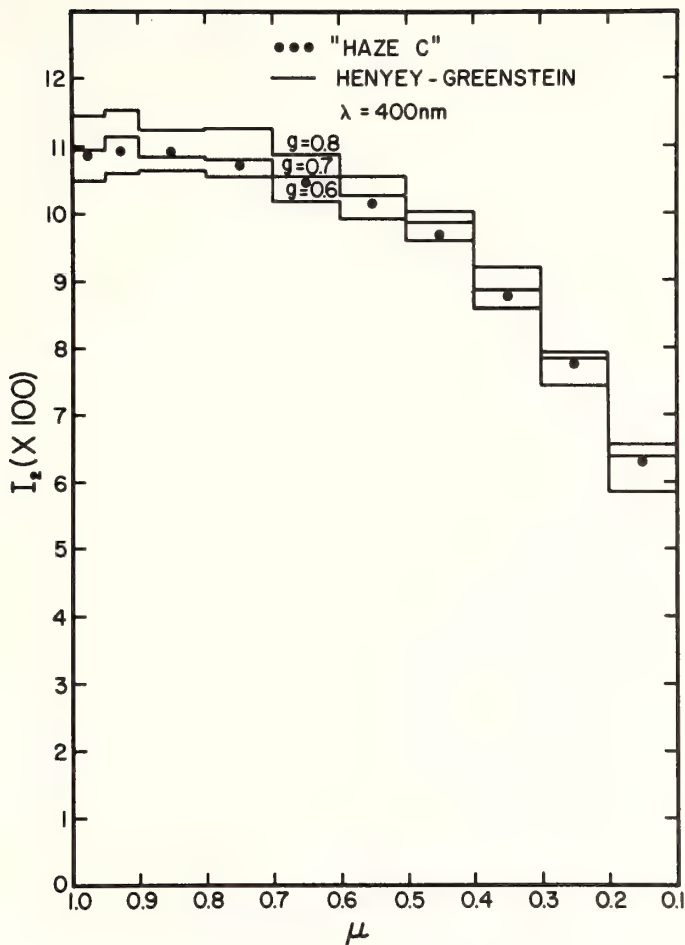


Figure 4.9 Comparison between  $I_2(\mu)$  computed for the "haze-C" Henyey-Greenstein phase functions for an atmosphere with a normal aerosol concentration, as a function of cosine  $\theta$  ( $\mu$ ); wavelength of calculations is 400 nanometers.

atmospheric oceanic aerosol phase function will exhibit variations as large as that considered in this example, except in extreme cases. Assuming that the aerosol concentration of the atmosphere can be determined, the uncertainty in the aerosol phase function will still of course provide a limit to the accuracy with which the ocean color-spectrum can be retrieved from satellite radiance measurements.

In summary then, the theory (AS1) leads to the natural definition of  $R(\lambda)$  [ $R(0,-)$ ] as a function of wavelength] as the "ocean color-spectrum". The determination of subsurface oceanic properties from space can thus be divided into two problems:

1) the determination of  $R(\lambda)$  from satellite radiance measurements, and 2) the establishment of relationships between  $R(\lambda)$  and the desired ocean properties. Since the method of computation conveniently separates the radiance into a component that interacts with the ocean ( $I_2$ ) and a component due to reflection from the atmosphere and sea surface ( $I_1$ ), it is easy to relate changes in radiance to changes in  $R(\lambda)$ . It is found that for viewing angles up to  $35^\circ$  from nadir,  $I_2$  is a relatively weak function of the aerosol concentration for concentrations up to three times normal. This suggests that spatial gradients of  $R(\lambda)$  can be determined with only a rough estimate of the aerosol concentration. It is further found that variations in the aerosol phase function can strongly influence the interpretation of the radiance at the satellite. Clearly then, it is vital to understand the magnitude of aerosol phase function variations.

#### 4.3.2 Technique for Atmospheric Correction

As discussed in section 4.3.1 it is necessary to know the aerosol concentration in order to recover the ocean color-spectrum  $R(\lambda)$  from the nadir radiance spectrum observed at the satellite. In this section a method based on Curran's suggestion of using the near-infrared radiance to determine the concentration is developed and applied to the S-191 data.

The method involves finding a band of wavelengths in the near infrared for which the absorption by ozone and water vapor is negligible. Since the Rayleigh scattering by air is very small in the near-infrared, the greatest contributor to the optical thickness at the wavelength in question is the aerosol. It is found that at 780 nm ozone and water vapor do not absorb significantly, and the Rayleigh scattering contributes only about 0.023 to the total optical thickness of the atmosphere. This implies that aerosols play the dominant role in the radiative transfer here with the normal aerosol concentration yielding an optical thickness of about 0.2. Also since  $R(0,-)$  for wavelengths greater than about 700 nm is essentially zero, the upward radiance at the top of the atmosphere at 780 nm simply becomes

$$\frac{I(\mu)}{F_0} = I_1(\mu)$$

where  $F_0$  is the solar irradiance ( $\text{mW cm}^{-2}\mu\text{m}^{-1}$ ) at the top of the atmosphere (Kondrat'ev 1973). By use of the reciprocity principle for nadir viewing and any solar zenith angle ( $\theta_0$ ),  $I_{\text{nadir}}$  can be written

$$I_{\text{nadir}} = \mu_0 F I_1(\mu_0).$$

$I_1(\mu)$  and  $I_2(\mu)$  have been computed for aerosol concentrations  $0\times N$ ,  $1\times N$ ,  $2\times N$ , and  $3\times N$  at 400 nm, 500 nm, 600 nm, and 780 nm.



The results for the  $0xN$  and  $1xN$  computations are presented in Appendix C.

Using  $I_1(\mu)$  for 780 nm and noting that the S-191 nadir radiance was recorded with  $\theta_0$   $40^\circ$  the upward radiance at the top of the atmosphere for nadir viewing is found to be 0.323 and 0.938  $mWcm^{-2} sr^{-1}\mu m^{-1}$  for aerosol concentrations of  $0xN$  and  $1xN$  respectively. Using the S-191 radiances at 780 nm for the nadir viewing spectra taken on Jan. 8, 1975 at 16:30:45.75 GMT (spectrum A) and 16:30:52.2 GMT (spectrum B) which respectively were 0.64 and 0.72  $mW cm^{-2} sr^{-1}$ , it is found that the theory suggests the aerosol concentration was  $0.51xN$  for spectrum A and  $0.64xN$  for spectrum B. In order to compute  $R(\lambda)$  from the S-191 data the assumption is made that the variation of the aerosol extinction coefficient with wavelength is exactly as given by Elterman.

#### 4.3.3 Recovery of $R(\lambda)$ from the S-191 data

As mentioned above, in order to recover  $R(\lambda)$  from the S-191 data it is necessary to assume that the variation of the aerosol extinction coefficient with wavelength is identical to that given by Elterman. Also, since  $I_1(\mu)$  and  $I_2(\mu)$  at 780 nm were derived using the haze-C phase function for the aerosols, the assumption is implicit that this phase function is correct. With these assumptions the nadir radiance at the top of the atmosphere has been computed at 400, 500, 600, and 780 nm for aerosol concentrations  $0xN$  and  $1xN$ , assuming that  $R(\lambda)$  is zero. These radiances are presented in Table 4.3 along with those from spectra A and B.

Since the actual aerosol concentration is known to be between  $0xN$  and  $1xN$ , it appears that the S-191 data at 400 nm are in error. It is virtually impossible for the nadir radiance to be less than that for a  $0xN$  atmosphere. (It should be noted that the discrepancy here is great, i.e., the S-191 radiances at 400 nm appear to be too small by more than a factor of 2.) The radiances at the other wavelengths listed in Table 4.3 seem to be reasonable and were used in equation (4.7) to estimate  $R(\lambda)$ . The results are shown in Table 4.4.

It is seen that  $R(\lambda)$  is negative except in the spectral region 500-550 nm where the values shown compare well with the Tyler and Smith Gulf Stream data for  $R(0,-)$ . As discussed above, the 400 nm data are apparently in error. However, the data at other wavelengths appear realistic, so the negative  $R(0,-)$  values are probably due to the assumptions that the haze-C phase function characterizes the aerosol, and that the spectral variation of the aerosol scattering coefficient is correctly described by Elterman's data. It is clear that considerably more experimental work is needed to test the ability of the theory discussed in 4.3.1 to obtain an accurate  $R(\lambda)$  from the satellite radiance.

Table 4.3

Wavelength (nm)	F <sub>0</sub> lmW cm <sup>-2</sup> μm <sup>-1</sup>	I <sub>nadir</sub> (R=0)			
		0xN	1xN	Spect A	Spect B
400	157	5.61	6.58	2.30	2.50
500	201	2.93	4.10	4.13	4.39
600	184	1.25	2.13	1.55	1.67
780	125	0.323	0.938	0.64	0.72

Table 4.4

Wavelength (nm)	R(0,-)	
	Spectrum A	Spectrum B
400	-0.274	-0.268
450	-0.0242	-0.0235
500	0.0318	0.0370
550	0.0295	0.0303
600	-0.00715	-0.00547
780	0	0

## 5. MULTISPECTRAL SCANNER EXPERIMENT

SKYLAB's multispectral scanner was a unique design that had 13 spectral channels of data spread over the visible and infrared bands. The system used a conical scan which had the advantage of keeping the atmospheric path length the same at all times. The visible region of the spectrum (0.4 - 0.75 μm) was divided into 6 channels, each about 0.05 μm wide. Two reflected infrared (0.75 - 1.0 μm) channels and one in the emitted infrared (10.2 - 12.5 μm) were also provided. The channels useful to Table 5.1.

LANDSAT-1 has been shown to have several useful applications of visible region imagery to marine science (Maul, 1974). The much finer spectral resolution of the S-192 provided an opportunity to expand those results to ocean current boundary determination and to test if the lower wavelength (0.05 μm) intervals were useful through the intervening atmosphere.

Table 5.1

## Spectral Channels Useful for Oceanography

BAND	DESCRIPTION	RANGE ( $\mu\text{m}$ )
1	Violet	0.41 - 0.46
2	Violet-Blue	0.46 - 0.51
3	Blue-Green	0.52 - 0.56
4	Green-Yellow	0.56 - 0.61
5	Orange-Red	0.62 - 0.67
6	Red	0.68 - 0.76
7	Reflected Infrared	0.78 - 0.88
8	Reflected Infrared	0.98 - 1.03
13	Thermal Infrared	10.2 - 12.5

## 5.1 S-192 Data

S-192 data were collected from 16:29:22 GMT (over the open sea just north of the Cuban coastline) to 16:31:04 GMT (over the mainland Florida coast north of Florida Bay). All channels listed in Table 5.2 were carefully examined in the analog format provided by NASA to the principal investigator. The data in the images were compared with the S-190A and S-190B photographs to see if what is interpreted in section 3.2 as the anticyclonic edge of the current could be detected. This feature was not observable in the standard data product.

The cyclonic edge of the stream appears to be obscured by clouds. This is often a useful means of locating the edge of the current but unfortunately made the objective of directly sensing the edge an impossibility.

However, an unexpected opportunity to evaluate the S-192 developed by the photographic detection (section 3) of a mass of water from Florida Bay flowing south into the Straits of Florida just west of Key West. This water is milky in appearance and somewhat greener in color. No ocean surface spectra were observed inside or outside of the plume of Florida Bay water, although it could have been easily accomplished if the SKYLAB crew had observed the feature and notified the ship of its presence. Upwelling spectral irradiance reported by Maul and Gordon (1975) probably describes the essential features of the plume and water in the straits.

An intensive effort was made by Norris (NASA-JSC), Johnson (Lockheed-JSC), and Maul (NOAA-AOML) to identify from S-192 data the plume and the anticyclonic edge, using the computer enhancement facilities at NASA-JSC. After approximately 10 hours of

machine time on both conical and line straightened data, the feature described as the anticyclonic edge could not be identified, although it is clearly brought out in the photographic enhancements (see Fig. 3.2). Further effort to bring out the anticyclonic edge was judged to be unwarranted and attention was turned to the plume feature which is visible in Fig. 3.3, and which preliminary computer enhancement showed to be a useful area in which to work.

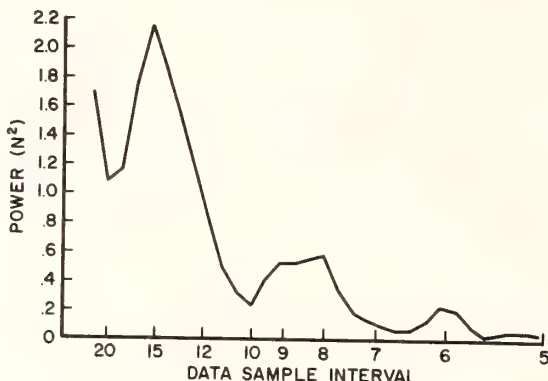


Figure 5.1 Power spectrum of the radiance in the unfiltered S-192 conical format. Significant noise is noted every 15, 8-9, and 6 data points.

Before a general computer enhancement technique was developed, the data were examined for periodic features in a spectrum. Figure 5.1 is a spectrum of data specially provided for this experiment that was to be high-pass filtered only; the calibration of the S-192 data is considered a high-pass filter. Significant periods at about 15 data sample intervals are noted in these conical data as has been reported (Schell, Philco-JSC, personal communication, 1975). The line-straightened data (see Figure 5.2) have been band-pass filtered to remove this 15-data-sample periodicity. The wavy patterns near the edge of clouds are the result of filter ringing.

## 5.2 Computer Enhancement

Computer enhancement of S-192 data was an objective of the experiment. The technique described below is a step toward automatic detection of clouds in multispectral data. The goal is to use a near infrared channel (channel 8 in this case) to specify where cloud-free areas are, for analysis of sea surface temperature or ocean color.

Channel 8 (0.98 -1.03  $\mu\text{m}$ ) is selected as the cloud discrimination channel because there is a maximum in the atmospheric transmissivity at this wavelength, and a maximum in the



Figure 5.2 S-192 Line-straightened, filtered, scanner data over the Straits of Florida near the western Florida Keys. The appropriate S-192 channel number is at the top of each panel.

absorption coefficient of water. The high absorption coefficient of water at 1  $\mu\text{m}$  causes the ocean surface to have a very low radiance when compared with land or clouds. Thus there should be two modes in the frequency distribution of radiance: one mode for the clear ocean and another mode for land and/or clouds. An example of such a bimodal distribution is given by the histogram in Fig. 5.3.

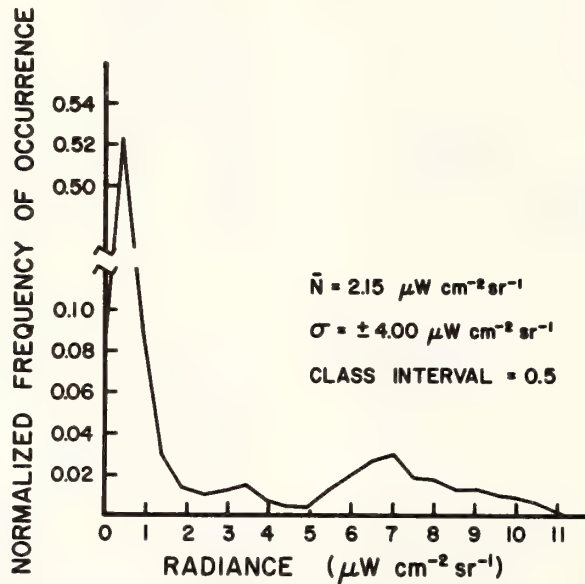


Figure 5.3 Histogram (normalized to unity) of the radiance over the area shown for channel 8 in figure 5.2. The primary peak at the left is clear ocean; the broad peak centered at  $7 \mu\text{W cm}^{-2}\text{sr}^{-1}$  is due to clouds and land.

In this figure, the low ocean radiances are clustered at the mode centered at  $N = 0.2 \mu\text{W cm}^{-2} \text{sr}^{-1}$ . The other mode, centered at  $N = 5.7 \mu\text{W cm}^{-2} \text{sr}^{-1}$  is a contribution of the clouds. (There is no land in this example.) If these modes can be identified and separated, a statistical identification of cloud-free ocean pixels can be made.

Cox and Munk (1954) observed that the radiance reflected from the ocean is essentially Gaussian in character. The problem then is to fit a curve of the form

$$y = \frac{ni}{\sigma \sqrt{2\pi}} \exp \left[ -\frac{(N - \bar{N})^2}{s\sigma^2} \right] \quad (5.1)$$

to the data at the lower valued mode. In this equation, the normal frequency curve ( $y$ ) is a function of the total number of observations ( $n$ ), the class interval ( $i$ ), and the standard deviation ( $\sigma$ ); the overbar on the dependent variable ( $N$ ) denotes ensemble average. Fitting equation (5.1) to the data is done in an iteration scheme that uses the lower valued mode as a first estimate of  $N$ . (Only the values  $N \pm 2\sigma$  from the original ensemble are used in this first iteration; this eliminates many of the cloud contaminated data.) After the first fit using a prescribed  $\bar{N}$ , the scheme is to iterate the data using only  $\pm 2\sigma$  of each new fit. When  $\sigma$  (or  $\bar{N}$ ) changes less than 0.1% between iterations, the fit is considered acceptable and the cloud-free pixels are defined as those between  $0 < y < y + 3$ . This guarantees that 99% of the values around the lower mode are accepted and included in the ocean data. Experience with this algorithm suggests that only five or six iterations are usually necessary for the scheme to converge.

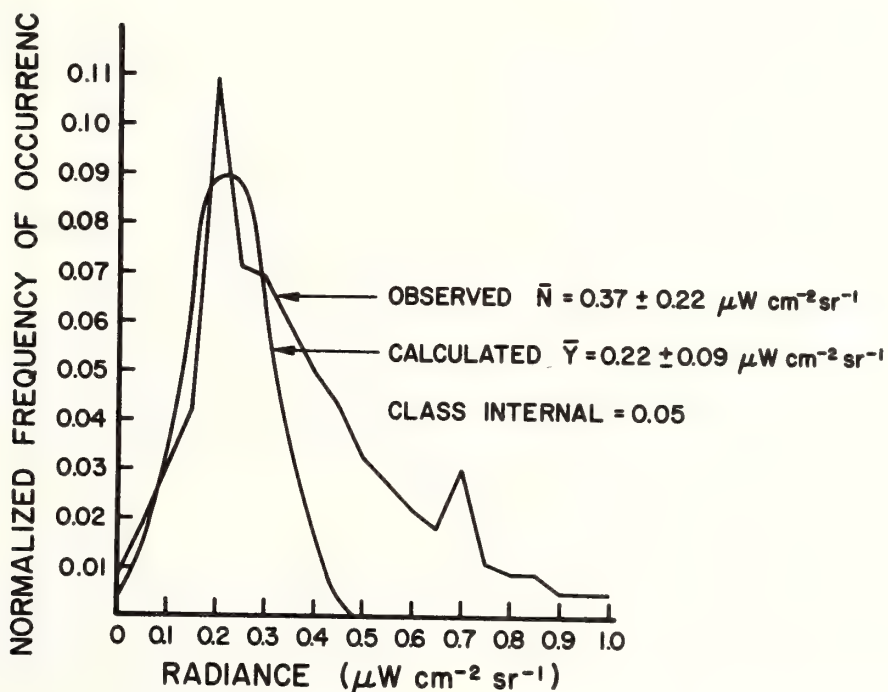


Figure 5.4 Expansion of low radiance portion of the histogram in Figure 5.3. The smooth curve is the fitted Gaussian approximation to the observed radiance distribution.

In Fig. 5.4, the data from the left hand portion of Fig. 5.3 are plotted along with the fitted frequency distribution given by equation (5.1). This fit required five iterations. Cloud-free data are conservatively identified as all those whose

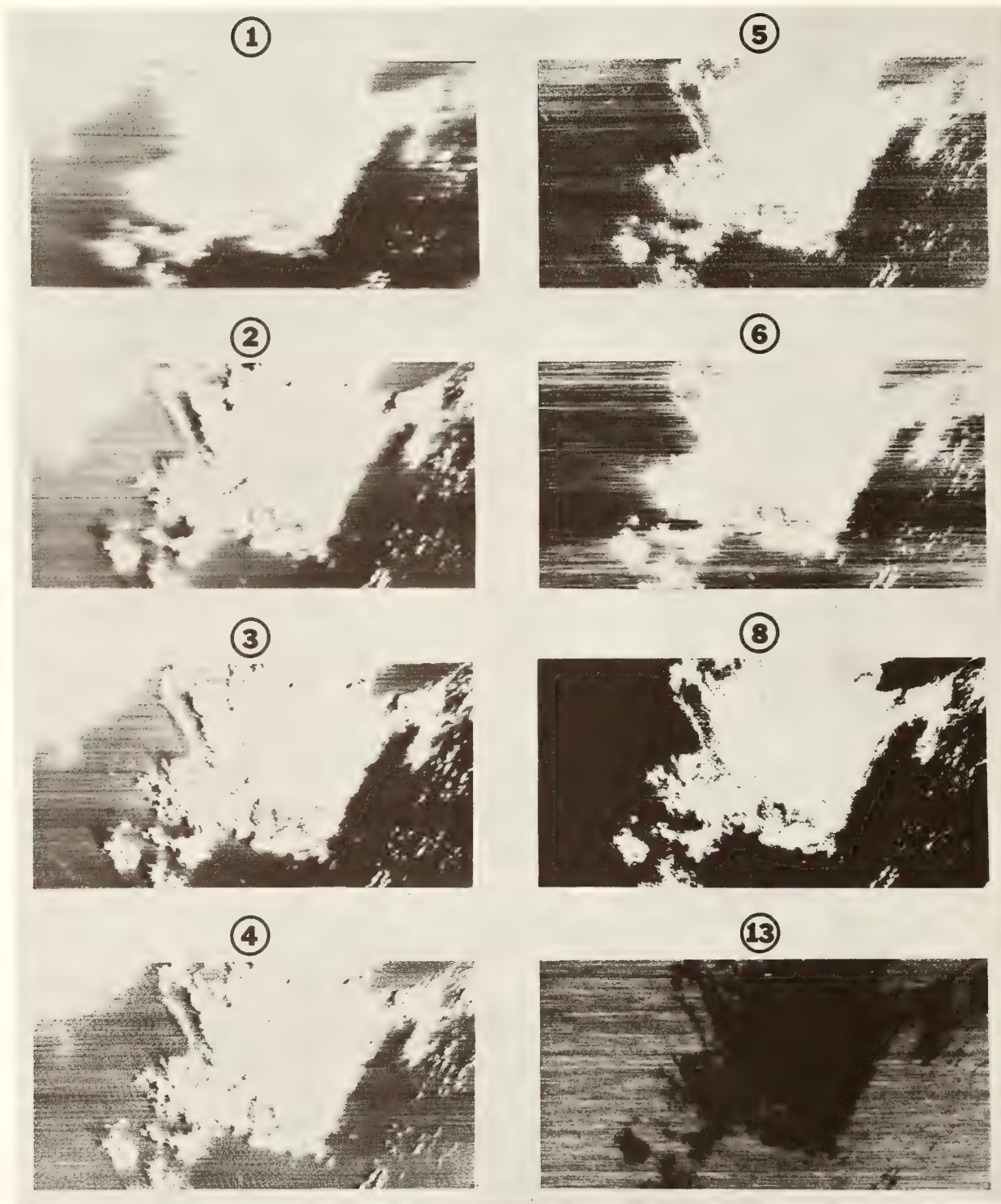


Figure 5.5 Conical S-192 imagery of the area shown in figure 5.2. Channel 8 in this figure is a binary mask with clear ocean black, and clouds, land, and other unwanted pixels are white.



$N < 0.5 W \text{ cm}^{-2} \text{ sr}^{-1} (\bar{N} + 3\sigma)$ . Data from any other channel can be statistically examined on a pixel-by-pixel comparison with channel 8; only "cloud-free" values go into the statistics.

Cloud-free data from any other channel are analyzed for their mean and standard deviations. These calculations automatically provide the limits over which the ocean data are to be stretched. Following the technique suggested by Maul, Charnell, and Qualset (1974), the formulation used by Maul (1975) is used here. The stretch variable ( $\zeta$ ) for a negative image is defined by:

$$\zeta = 0 \text{ for } N > \bar{N} + \kappa\sigma$$

$$\zeta = \frac{M [(\bar{N} + \kappa\sigma) - N]}{2\kappa\sigma} \text{ for } (\bar{N} - \kappa\sigma) \leq N \leq (\bar{N} + \kappa\sigma)$$

$$\zeta = M \text{ for } N < \bar{N} - \kappa\sigma$$

In this formulation  $M$  is the maximum value allowed by the digital-to-analog (D/A) output device;  $\bar{N}$  is the mean radiance of the cloud-free data, and is a constant. Considering  $N$  a continuous variable, setting  $\kappa=2$  would stretch 95% of the cloud-free data over the full range of the photographic enhancement device.

The technique described above allows an objective specification of both the range of settings for an optimum enhancement of an ocean scene, and a statement of the radiance range required of an ocean color sensor under these conditions. In Fig. 5.5, the data from the sediment plume flowing through the Florida Keys are presented for channels 1-6, 8, and 13. These data are not line-straightened and they are only high-pass filtered. Although the data are distorted geographically, they represent the best radiometric information from the S-192.

### 5.3 Discussion

Without actual spectra as surface truth it is not possible to interpret the scanner data in the vicinity of the plume. Other spectral data (see Section 4.2 and Maul, 1975) suggest that there should be a detectable difference in the data from channels 1 through 5. Little information, let alone information difference, is contained in channel 1 (see Figs. 5.2 & 5.5). These findings are in agreement with Hovis (NASA-GSFC, personal communication, 1975) who found that little or no information is detectable through the atmosphere for wavelengths much shorter than 0.45  $\mu\text{m}$ . The Rayleigh scattering at shorter wavelengths is so intense that multispectral scanners such as the S-192 or the coastal zone color scanner destined for NIMBUS-G should not have a violet (0.41 - 0.46  $\mu\text{m}$ ) channel. This means that the wavelengths that contain much of the oceanographic information are of little

value at orbital altitudes.

Analysis of the conical data used in Fig. 5.5 allows a specification of the radiance range encountered. Since an ocean color sensor should be allowed to saturate over land or clouds, the range appears narrow. The range is based on  $+3\sigma$ , which describes 99% of the data encountered herein. Saturation at higher signal levels is recommended in order to expand the quantization commensurate with an acceptable data flow rate. Table 5.2 lists the radiance ranges.

Table 5.2

Radiance Ranges of Infrared Channels

Channel	Mean $\pm$ $\sigma$	Oceanic Radiance Range mW cm <sup>-2</sup> sr <sup>-1</sup> $\mu$ m <sup>-1</sup>
1	3.56 $\pm$ 0.45	2.21-4.91
2	4.71 $\pm$ 0.97	1.80-7.62
3	4.07 $\pm$ 1.33	0.08-8.06
4	2.83 $\pm$ 1.46	0.00-7.21
5	1.73 $\pm$ 0.92	0.00-4.49
6	0.93 $\pm$ 0.43	0.00-2.22
7	0.57 $\pm$ 0.29	0.00-1.46
8	0.37 $\pm$ 0.22	0.00-1.03
13	0.80 $\pm$ 0.03	0.71-0.89

This range of values applies only to this data set, which represents low latitude, winter conditions. A similar analysis of S-192 data from other areas of the oceans and at other times could lead to an objective statement of the radiance range specification for an oceanic color sensor. Note that the lower value on the shorter wavelength channels is non-zero. This reflects the radiance of the atmosphere only.

Neither the line-straightened (Fig. 5.2) nor the conical (Fig. 5.5) imagery was capable of detecting any ocean thermal variations. The thermal data (channel 13) were processed in both negative and positive format in an attempt to show some of the 2°C range recorded in the surface observations (Fig. 2.1). In comparing the data, note that the area covered is not identical because of geographical distortion in the line-straightened processing.

The actual mask generated from using equation 5.1 is illustrated in the channel 8 data in Fig. 5.2. Here the values 0 or 3 are assigned for contaminated or ocean (respectively) radiances.

The channel 8 data in Fig. 5.5 were simply stretched over the  $+2\sigma$  range by equation (5.2). A significant error in the automatic stretch units of other channels would occur if the extra step of 0 or 1 assignment were not made, because of the exclusion of some ocean radiances. Note also that the effect of filter ringing is eliminated in the Fig. 5.2 masking; this can also lead to wrong stretch limits if care is not exercised in application of the technique. Filtering should always be done after the data are masked.

The conical scan technique is an unusual approach to multispectral scanning. Quality of the S-192 data is judged to be poorer than the quality of data from LANDSAT MSS which uses a linear scan. If poorer data quality is inherent in the design of all conical scanners then the conical scan technique cannot be recommended for the NIMBUS-G coastal zone color scanner. If this is not the case there is no reason based on this investigation to not consider such a future design.

## 6. SUMMARY

The objectives of this experiment were to obtain simultaneous ship, aircraft, and spacecraft data across the Gulf Stream in the Straits of Florida in order to evaluate several techniques for remote sensing of this ocean current. Calibration of the S-191 infrared detectors was not known; this precluded comparing the atmospheric transmission models, which was an objective. Detection of the current with the photographs was possible but the S-192 scanner was not useful in this respect because the gain settings were not adequate for ocean radiances. A technique to determine atmospheric corrections for visible radiometers based on theoretical considerations was shown to be promising. Details of those results are enumerated below:

1. Observation and data reduction techniques for obtaining surface truth data included measurement of ocean color spectra from 3 meters above the surface. Objective filtering techniques were developed to remove periodic specular return caused by wave facets. (section 2.3)

2. The limited photographic (S-190) data set in this experiment provides a baseline against which satellite photos of more biologically productive waters may be compared. Inter-comparisons with aircraft derived photography may be more difficult. This problem was not resolved in this experiment because of unforeseen variation in the exposure level of these photos. (section 3.)

Non-uniformity in the satellite space-derived photography is probably most due to the effects of variable lens transmission. It is recommended that the production of multiple generation photos ("dupes") be documented in a manner similar to that of the

original films. This should include some documentation on the printer light variation across the platen, suspected to be a major source of the variability measured in the dupes used in this experiment. (section 3.2)

3. The data acquisition camera on SKYLAB was not turned on during the experiment; this made any quantitative comparisons with spectra impossible. There should be a positive interlock on all future missions to prevent a recurrence. Spectra were not obtained across the Gulf Stream front because a) no data just prior to the mission were obtained, and b) no direct communication link from the ship to the spacecraft could be set up. Future experiments must include a mechanism to communicate to surface-truth investigators the position of variable features such as ocean currents. (section 4.1)

4. Unfortunately the S-191 visible near-IR data could not be used to study the observability of oceanic fronts from satellite altitudes because the Gulf Stream front was missed. However, a theoretical method for recovering the ocean color spectrum through the atmosphere was developed. This was used to try and retrieve the ocean color spectrum from the nadir-viewing S-191 data, with limited success. The results agreed well with measurements (Tyler and Smith, 1970) for wavelengths greater than 500 nm, but in the blue the S-191 radiance was substantially smaller than previous aircraft observations, and even a factor of 2 less than theoretical predictions for an aerosol-free atmosphere. This is either due to a malfunction of the sensor in the blue or to the presence of a very strongly absorbing aerosol. Our present knowledge of the optical properties of marine aerosols does not appear to be sufficiently complete to effect a quantitative retrieval of ocean color spectrum from spacecraft data. Clearly further research on this problem is indicated. (section 4.3)

5. Ocean features that were visible in photographs (section 3.2) were not visible in the S-192 multispectral scanner data because of the lack of radiance resolution. The range of radiances needed to observe ocean features adequately is presented in table 5.2. These data support the view that an ocean color multispectral sensor can do without a channel equivalent to channel 1 (0.41 - 0.46  $\mu\text{m}$ ) of the S-192, as no information on a very strong color boundary was contained in those data (section 5.3).

An objective S-192 cloud detection technique was developed that uses Gaussian statistics to identify cloud-free areas in channel 8 (0.98 - 1.03  $\mu\text{m}$ ). Cloud-free pixels are then analyzed in other channels so that contrast stretching based on the same statistics is automatically accomplished (section 5.2).

## 7. ACKNOWLEDGMENTS

This research was supported in part by the National Aeronautics and Space Administration under the SKYLAB Earth Resources Experiment Program. The authors wish to express their appreciation to the crews of the SKYLAB, the R/V VIRGINIA KEY, and the NASA C-130 without whose enthusiastic support the experiment could not have been accomplished. Specifically we would like to acknowledge the assistance of A. Yanaway for computer programming, D. Norris and W. Johnson for image enhancement experiments, N. Larsen, S. O'Brien, and A. Ramsey for secretarial, drafting, and photographic contributions. The special radiosonde was taken by the Key West office of the National Weather Service; helpful arrangements by P. Connors of AOML are also gratefully acknowledged.

## 8. REFERENCES

1. Anding, D. and J. Walker (1976): Use of SKYLAB EREP data in a Sea-Surface Temperature Experiment, NASA CR-144479, NITS Report E 76-10217, 54 pgs.
2. Anding, D. and R. Kauth (1970): Estimation of sea surface temperature from space, Remote Sensing of Environ., 1(4), pp. 217-220.
3. Anding, D. and Kauth, R. (1972): Reply to comment by G. Maul and M. Sidran, Remote Sensing of Environ., 2(3), pp.171-173.
4. Baig, S.R. (1973): Spectral properties of some marine phytoplankters, J. Soc. of Mot. Pict. & T.V. Engrs., 82, pp. 1007-1012.
5. Baig, S.R. and Atwell, B.H., (1975): Spectra of Phytoplankters in Aqueous Suspension, (in preparation).
6. Baig, S.R. and Yentsch, C.S., (1969): A photographic means of obtaining monochromatic spectra of marine algae, Appl. Opt. 8(12), pp. 2566-2568.
7. Chandrasekhar, S. (1960): Radiative Transfer, Dover Press, N.Y., 393 p.
8. Cox and W. Munk (1954). Measurements of the roughness of the sea surface from photographs of the Sun's glitter. J. Opt. Soc. Am., 44(11), pp. 838-850.
9. Curran, R. (1972): Ocean color determination through a scattering atmosphere, Appl. Opt., 11, pp. 1857-1866.

10. Davis, P.A., and Viezee, W. (1964): A Model for computing infrared transmission through atmospheric water vapor and carbon dioxide, J. Geophys. Res., 69, pp. 3785-3794.
11. Deirmendjian, D. (1964): Scattering and polarization properties of water clouds and hazes in the visible and infrared, Appl. Opt., 3, pp. 187-96.
12. Duntley, S.Q., Austin, R.W. Wilson, W.H., Edgerton, S.F. and S.E. Moran, (1974): Ocean Color Analysis, Scripps Institution of Oceanography, San Diego, Calif., Ref. 74-10, 72 p.
13. Elterman, L., (1968): UV, Visible, and IR Attenuation for Altitudes to 50 km., Air Force Cambridge Research Laboratories Report AFCRL-68-0153.
14. Gordon, H.R. (1973): Sample calculation of diffuse reflectance of the ocean, Appl. Opt. 12, pp. 2803-2804.
15. Gordon, H.R. and Brown, O.B., (1973): Irradiance reflectivity of a flat ocean as a function of its optical properties: Appl. Opt. 12, pp. 1549-1551.
16. Gordon, H.R. and Brown, O.B., (1974): Influence of bottom depth and albedo on the diffuse reflectance of a flat homogenous ocean, Appl. Opt. 13, pp. 2153-2159.
17. Gordon, H.R., and Brown, O.B., (1975): A multiphase Monte Carlo technique for simulation of radiative transfer, J. Quant. Spectrosc. Radiat. Transfer, 15, pp. 419-422.
18. Gordon, H.R., Brown, O.B., and M.M. Jacobs, (1975): Computed relationships between inherent and apparent optical properties of a flat homogenous ocean, Appl. Opt. 14, pp. 417-427.
19. Hanson, K.J. (1972): Remote sensing of the troposphere IV. Derr, Ed.), U.S. Government Printing Office, Washington, D.C. 22-1 to 22-56.
20. Herman, A. and Jacobson, S.R., (1975). FESTA: A System for Time Series Analysis, NOAA/AOML, Miami, Fla., Unpublished manuscript.
21. Kattawar, C.W., and Plass, G.N., (1972): Radiative transfer in the Earth's atmosphere ocean system: II Radiance in atmosphere and ocean, J. Phys. Ocean. 2, pp. 146-156.
22. Kondrat'ev, K.Y., (Ed). (1973: Radiation Characteristics of the Atmosphere on the Earth's Surface, Amerind. Pub. Co. Pvt. Ltd., New Delhi.

23. Kullenberg, G., (1968): Scattering of light by Sargasso Sea water, Deep Sea Res., 15, pp. 423-32.
24. Maul, G.A., (1975): An Evaluation of the use of the Earth Resources Technology Satellite for observing ocean current boundaries in the Gulf Stream system, NOAA Technical Report ERL 335-AOML 18, Boulder, Colorado, 125 pp.
25. Maul, G.A. (1974): Applications of ERTS data to oceanography and the marine environment, COSPAR: Approaches to techniques, Akademie-Verlag, Berlin, pp. 335-347.
26. Maul, G.A. (1973): Infrared Sensing of Ocean Surface Temperature, In: The Second Fifteen Years in Space, A.A.S., 31, pp. 451-464.
27. Maul, G.A., and Gordon, H.R., (1975), On the Use of the Earth Resources Technology Satellite (LANDSAT-1) in Optical Oceanography, Remote Sensing of Environment, 4(2), pp. 95-128.
28. Maul, G.A. and Sidran, M., (1973): Atmospheric effects of ocean surface temperature sensing from the NOAA satellite scanning radiometer, J. Geophys. Res., 78(12), pp. 1908-1916.
29. Maul, G.A. and Sidran, M. (1972): Comment on "Estimation of Sea Surface Temperature from Space" by D. Anding and R. Kauth, Remote Sensing of Environment, 2(3), pp.165-169.
30. Maul, G.A., Charnell, R.L., and Qualset R.H. (1974). Computer Enhancement of ERTS-1 Images for ocean radiances Remote Sensing of Environ., 3, pp. 237-253.
31. Mueller, J.L., (1973): The influence of Photoplankton on Ocean Color Spectra, PhD. Dissertation, Oregon State University, Corvallis, Oregon, 237 p.
32. NASA (1975): Report on Active and Planned Spacecraft and Experiments, NS SDC1 WDC-A-R&S, 7501, Goddard Spaceflight Center, Greenbelt, Maryland, 303 p.
33. Petzold, T.J. (1972): Volume Scattering Functions for Selected Waters, Scripps Institution of Oceanography, Univ. of California at San Diego, SIO Ref. 72-78.
34. Plass, G.N. and Kattawar, G.W., (1969): Radiative Transfer in an atmosphere ocean system, Appl. Opt., 8, pp. 455-466.

35. Preisendorfer, R.W., (1961): Application of Radiative Transfer Theory to Light Measurements in Sea, U.G.G.I., Monogr. 10, pp. 11-30.
36. Richardson, P.L., Strong, A.E., and J.A. Knaus, (1973): Gulf Stream Eddies: recent observations in the western Sargasso Sea, J. Phys. Ocean., 3(3), pp. 297-301.
37. Strickland, J.D.H. and Parsons, R.R. (1968): A Practical Handbook of Seawater Analysis, Fisheries Research Board of Canada, Ottawa, 311 p.
38. Tyler, J.E., and Smith, R.C., (1970): Measurements of Spectral Irradiance Underwater, Gordon and Breach, N.Y. 103 p.



## Appendix A

### Surface Data Obtained During Cruises of R/V Virginia Key

This appendix lists the surface data obtained during the 8-9 January 1974 (GMT) cruises of R/V VIRGINIA KEY. The geographic positions were determined after the control data were carefully replotted and a best fit of the vessel's location made. Values reported were determined by using standard oceanographic techniques unless modified as explained in section 2.2 of the text.

TABLE A.1  
Cl-a  
SURFACE SAMPLES

Cl-a (mg/m <sup>3</sup> )	TIME (GMT)	<u>Position</u>
0.15	1957	24° 08.1 N, 81° 34.6 W
0.09	2200	23° 58.8 N, 81° 40.4 W
0.11	2400	23° 47.5 N, 81° 47.2 W

SAMPLES at depth at 1957 GMT at 24° 08.1 N, 81°34.6 W

<u>Depth</u>	<u>Cl-a (mg/m<sup>3</sup>)</u>
10 m	0.79
20 m	0.21
30 m	0.25
40 m	0.42
50 m	0.30

SAMPLES at depth at 2200 GMT at 23° 58.8 N, 81° 40.4 W

<u>Depth</u>	<u>Cl-a (mg/m<sup>3</sup>)</u>
10 m	0.10
20 m	0.20
30 m	0.35
40 m	0.31
50 m	0.30

TABLE A.2  
SALINITY SURFACE SAMPLES

Sal(‰)	Time (GMT)	Position
35.996	1314	24° 38.9 N, 81° 08.0 W
35.924	1449	24° 34.5 N, 81° 12.2 W
35.929	1515	24° 30.7 N, 81° 16.3 W
35.921	1719	24° 23.3 N, 81° 21.8 W
36.009	1806	24° 19.1 N, 81° 27.3 W
36.023	1940	24° 10.2 N, 81° 33.7 W
36.017	1958	24° 08.1 N, 81° 34.6 W
36.119	2200	23° 58.8 N, 81° 40.4 W
35.874	2400	23° 47.5 N, 81° 47.2 W
35.918	0110	23° 38.2 N, 81° 52.6 W

Table A.3

Volume Scattering  $\beta$  (45)

## Surface Samples

Blue ( $\text{m}^{-1}\text{sr}^{-1} \times 10^{-3}$ )	Green ( $\text{m}^{-1}\text{sr}^{-1} \times 10^{-3}$ )	GMT Time	Position
17.3	13.5	1300	24° 40.2 N 81° 07.3 W
13.2	9.9	1314	24° 38.9 N 81° 08.0 W
3.03	3.02	1434	24° 36.5 N 81° 10.6 W
2.61	2.08	1449	24° 34.5 N 81° 12.2 W
2.40	1.60	1504	24° 32.2 N 81° 14.7 W
2.82	2.37	1515	24° 30.7 N 81° 16.3 W
2.69	1.95	1630	24° 27.7 N 81° 16.3 W
3.07	2.15	1645	24° 26.1 N 81° 18.1 W
3.06	2.16	1700	24° 24.6 N 81° 20.2 W
2.16	2.31	1715	24° 23.3 N 81° 21.8 W
3.42	3.09	1750	24° 20.5 N 81° 25.4 W
3.10	2.24	1802	24° 19.1 N 81° 27.3 W
4.02	3.49	1855	24° 16.3 N 81° 31.0 W
2.74	2.49	1910	24° 14.6 N 81° 32.5 W
3.08	1.75	1925	24° 12.4 N 81° 33.5 W
4.54	3.29	1940	24° 10.2 N 81° 33.7 W
5.82	8.44	1957	24° 08.1 N 81° 34.6 W
2.76	2.20	2040	24° 04.5 N 81° 35.6 W
2.73	1.45	2115	24° 03.2 N 81° 37.7 W
3.08	1.98	2130	24° 01.5 N 81° 39.0 W
2.99	1.90	2145	24° 00.5 N 81° 39.8 W
1.65	1.77	2200	23° 58.8 N 81° 40.4 W

Table A.3 (cont'd)

Volume Scattering  $\beta$  (45)

Blue ( $\text{m}^{-1}\text{sr}^{-1} \times 10^{-3}$ )	Green ( $\text{m}^{-1}\text{sr}^{-1} \times 10^{-3}$ )	GMT Time	Position
3.35	2.04	2255	23° 55.8 N 81° 42.0 W
2.63	1.85	2310	23° 53.8 N 81° 43.5 W
2.85	1.83	2325	23° 51.9 N 81° 44.6 W
2.58	1.67	2400	23° 47.5 N 81° 47.2 W
1.92	1.30	0050	23° 40.9 N 81° 51.1 W
1.93	1.28	0110	23° 38.2 N 81° 52.6 W
1.96	1.35	0130	23° 35.7 N 81° 54.1 W
2.19	1.50	0150	23° 33.2 N 81° 55.6 W

Volume Scattering  $\beta$  (45)

Samples at depth at 1314 GMT at 24° 38.9 N, 81° 08.0 W

<u>depth</u>	<u>Blue (<math>\text{m}^{-1}\text{sr}^{-1} \times 10^{-3}</math>)</u>	<u>Green (<math>\text{m}^{-1}\text{sr}^{-1} \times 10^{-3}</math>)</u>
10 m	2.11	1.83

Samples at depth at 1600 GMT at 24° 29.3 N, 81° 15.5 W

<u>depth</u>	<u>Blue (<math>\text{m}^{-1}\text{sr}^{-1} \times 10^{-3}</math>)</u>	<u>Green (<math>\text{m}^{-1}\text{sr}^{-1} \times 10^{-3}</math>)</u>
10 m	13.4	11.1
20 m	2.39	1.77
30 m	2.88	2.80
40 m	2.27	1.86
50 m	1.46	1.42

Table A.3 (cont'd)

Volume Scattering  $\beta(45)$ 

Samples at depth at 1806 GMT at 24° 19.1 N, 81° 27.3 W

<u>depth</u>	<u>Blue (<math>m^{-1}sr^{-1} \times 10^{-3}</math>)</u>	<u>Green (<math>m^{-1}sr^{-1} \times 10^{-3}</math>)</u>
10 m	8.07	8.43
20 m	2.57	2.19
30 m	4.37	3.37
40 m	3.34	2.46
50 m	6.87	5.05

Samples at depth at 1957 GMT at 24° 08.1 N, 81° 34.6 W

<u>depth</u>	<u>Blue (<math>m^{-1}sr^{-1} \times 10^{-3}</math>)</u>	<u>Green (<math>m^{-1}sr^{-1} \times 10^{-3}</math>)</u>
10 m	5.68	3.78
20 m	4.26	3.66
30 m	4.61	3.73
40 m	3.87	3.26
50 m	4.41	3.55

Samples at depth at 2200 GMT at 23° 58.8 N, 81° 40.4 W

<u>depth</u>	<u>Blue (<math>m^{-1}sr^{-1} \times 10^{-3}</math>)</u>	<u>Green (<math>m^{-1}sr^{-1} \times 10^{-3}</math>)</u>
10 m	4.12	2.99
20 m	2.60	1.94
30 m	5.70	4.06
40 m	3.98	3.42
50 m	3.28	2.60

Table A.4  
Bucket Temperatures

<u>Temp. (°C)</u>	<u>TIME GMT</u>	<u>Position</u>
24.5	1315	24° 38.9 N, 81° 08.0 W
* 24.8	1434	24° 36.5 N, 81° 10.6 W
* 25.3	1449	24° 34.5 N, 81° 12.2 W
* 25.4	1504	24° 32.2 N, 81° 14.7 W
* 25.0	1630	24° 27.7 N, 81° 16.3 W
25.0	1645	24° 26.1 N, 81° 18.1 W
* 24.5	1700	24° 24.6 N, 81° 20.2 W
* 24.3	1750	24° 20.5 N, 81° 25.4 W
* 24.4	1805	24° 19.1 N, 81° 27.3 W
* 24.5	1855	24° 16.3 N, 81° 31.0 W
* 24.5	1910	24° 14.6 N, 81° 32.5 W
* 24.7	1925	24° 12.4 N, 81° 33.5 W
* 24.4	1940	24° 10.2 N, 81° 33.7 W
24.4	2010	24° 07.0 N, 81° 34.6 W
* 24.6	2040	24° 04.5 N, 81° 35.6 W
* 24.9	2115	24° 03.2 N, 81° 37.7 W
* 24.9	2130	24° 01.5 N, 81° 39.0 W
* 24.8	2145	24° 00.5 N, 81° 39.8 W
25.0	2200	23° 58.8 N, 81° 40.4 W
* 25.0	2255	23° 55.8 N, 81° 42.0 W
* 25.1	2310	23° 53.8 N, 81° 43.5 W
* 25.5	2325	23° 51.9 N, 81° 44.6 W
* 25.5	2340	23° 49.9 N, 81° 45.8 W
25.5	2400	23° 47.5 N, 81° 47.2 W

Table A.4 (cont.)  
Bucket Temperatures

<u>Temp. (°C)</u>	<u>TIME GMT</u>	<u>Position</u>
* 26.1	0050	23° 40.9 N, 81° 51.1 W
* 26.1	0110	23° 38.2 N, 81° 52.6 W
* 26.2	0130	23° 35.7 N, 81° 54.1 W
* 26.3	0150	23° 33.2 N, 81° 55.6 W

\* Denotes XBT casts.



APPENDIX B

Radiosonde data      Key West      1600 GMT,      8 January 1974

Pressure (mb)	Temp.(°C)	R.H. (%)	
			Surface
1021	024.8	79	
1011	023.5	82	Dry Bulb: 24.09C
1000	023.0	85	Wet Bulb: 22.02C
902	017.1	86	RH: 79%
869	015.9	63	Wind Dir: 050°T
850	015.1	64	Wind Spd: 5 mps
808	012.8	66	Clouds 1/10 cu
799	012.2	34	φ 24°35'N
788	011.2	72	λ 81°42'W
744	009.9	66	
740	008.3	72	
722	008.5	30	
700	007.8	31	
671	005.2	55	
640	003.3	42	
621	003.1	22	
530	-06.3	21	
500	-09.4	13	
470	-12.4	10	
384	-24.9	14	
300	-39.1	14	
250	-48.9		
224	-50.3		
212	-48.9		
200	-50.3		
150	-62.6		
100	-77.1		
070	-75.7		
066	-75.2		
061	-71.5		
058	-72.7		
054	-67.6		
050	-67.8		
045	-64.7		
043	-58.1		
030	-51.2		
023	-46.3		
020	-47.4		
017	-48.0		
016	-48.2		
13.5	-43.9		

## APPENDIX C - Monte Carlo Simulations

This appendix lists the Monte Carlo simulations of radiances  $I_1$  and  $I_2$  as described in Section 4.3.2. Wavelengths at which the  $O_xN$  and  $I_xN$  atmospheric aerosol concentrations were computed are 400, 500, 600, and 780 nm. The cosines of ten zenith angles ( $\mu$ ) were the independent variables.  $I_1$  and  $I_2$  are normalized to unit solar flux on a surface normal to the solar beam.

Wavelength = 400 nm

Aerosol = OxN

$\mu$	$I_1(\mu)$	$I_2(\mu)$
0.00	.10089+00	.53255-01
0.10	.88850-01	.72697-01
0.20	.78011-01	.87278-01
0.30	.67433-01	.98883-01
0.40	.57839-01	.10661+00
0.50	.52975-01	.11159+00
0.60	.48109-01	.11406+00
0.70	.46607-01	.11634+00
0.80	.44244-01	.11615+00
0.90	.42872-01	.11701+00
0.95	.75049-01	.11782+00
1.00		

Wavelength = 400 nm

Aerosol = 1xN

$\mu$	$I_1(\mu)$	$I_2(\mu)$
0.00	.93753-01	.51310-01
0.10	.90653-01	.63140-01
0.20	.83232-01	.77826-01
0.30	.76449-01	.87640-01
0.40	.67122-01	.96479-01
0.50	.61046-01	.10118+00
0.60	.57118-01	.10457+00
0.70	.54662-01	.10757+00
0.80	.52434-01	.10919+00
0.90	.52278-01	.10916+00
0.95	.71513-01	.10906+00
1.00		

Wavelength = 500 nm

Aerosol = 0xN

$\mu$	$I_1(\mu)$	$I_2(\mu)$
0.00	.63253-01	.59700-01
0.10	.52971-01	.91621-01
0.20	.37429-01	.10902+00
0.30	.29710-01	.12474+00
0.40	.24246-01	.13138+00
0.50	.22112-01	.13641+00
0.60	.19925-01	.13898+00
0.70	.19015-01	.14171+00
0.80	.18002-01	.14225+00
0.90	.17044-01	.14326+00
0.95	.17044-01	.14326+00
1.00	.67308-01	.14203+00

Wavelength = 500 nm

Aerosol = 1xN

$\mu$	$I_1(\mu)$	$I_2(\mu)$
0.00	.62318-01	.56038-01
0.10	.59056-01	.75227-01
0.20	.49220-01	.96058-01
0.30	.41716-01	.11022+00
0.40	.35218-01	.11781+00
0.50	.31928-01	.12576+00
0.60	.27678-01	.12875+00
0.70	.26638-01	.13063+00
0.80	.25573-01	.13228+00
0.90	.26419-01	.13315+00
0.95	.57385-01	.13155+00
1.00		

Wavelength = 600 nm

Aerosol = 1xN

$\mu$	$I_1(\mu)$	$I_2(\mu)$
0.00	.27632-01	.36991-01
0.10	.36531-01	.67189-01
0.20	.29628-01	.92357-01
0.30	.25526-01	.10823+00
0.40	.21423-01	.11883+00
0.50	.17841-01	.12614+00
0.60	.16190-01	.13059+00
0.70	.15107-01	.13303+00
0.80	.14509-01	.13448+00
0.90	.16199-01	.13524+00
0.95	.52310-01	.13560+00
1.00		

Wavelength = 600 nm

Aerosol = 0xN

$\mu$	$I_1(\mu)$	$I_2(\mu)$
0.00	.30110-01	.42002-01
0.10	.24508-01	.80947-01
0.20	.17292-01	.10497+00
0.30	.13224-01	.12254+00
0.40	.10725-01	.13037+00
0.50	.98865-02	.13672+00
0.60	.90777-02	.14052+00
0.70	.88360-02	.14304+00
0.80	.80934-02	.14358+00
0.90	.77006-02	.14664+00
0.95	.61865-01	.14694+00
1.00		



Wavelength = 780 nm

Aerosol = 0xN

$\mu$	$I_1(\mu)$	$I_2(\mu)$
0.00	.27838-01	.69923-01
0.10	.13026-01	.10854+00
0.20	.76052-02	.13086+00
0.30	.51505-02	.14849+00
0.40	.42167-02	.15502+00
0.50	.37095-02	.16096+00
0.60	.34865-02	.16342+00
0.70	.33889-02	.16269+00
0.80	.30901-02	.16464+00
0.90	.30811-02	.16649+00
0.95	.65909-01	.16607+00
1.00		

Wavelength = 780 nm

Aerosol = 1xN

$\mu$	$I_1(\mu)$	$I_2(\mu)$
0.00	.40506-01	.67910-01
0.10	.33748-01	.95346-01
0.20	.24905-01	.11832+00
0.30	.18224-01	.13459+00
0.40	.14512-01	.14180+00
0.50	.11931-01	.14856+00
0.60	.10491-01	.15236+00
0.70	.98166-02	.15399+00
0.80	.98476-02	.15395+00
0.90	.11295-01	.15613+00
0.95	.57149-01	.15511+00
1.00		

Reprinted from: *Marine Sediment Transport and Environmental Management*, D. J. Stanley and D. J. P. Swift, editors, John Wiley and Sons, Inc., Chapter 5, 53-64.

## Tidal Currents

HAROLD O. MOFJELD

*Atlantic Oceanographic and Meteorological Laboratories, Miami, Florida*

In regions where they are sufficiently strong, tidal currents constantly rework bottom sediment. Weaker currents combine with storm-generated wave motion and currents to move sediment both at the water-bottom interface and in suspension. Tidal currents are especially effective agents of sediment transport because they persist throughout the year, whereas other types of water motion, particularly storm events, tend to be seasonal. They are the background upon which are superimposed other kinds of currents causing sediment transport.

The tides typically rise and fall twice a day (semidaily tides), once a day (daily tides), or occur as a combination of daily and semidaily components. Figure 1 illustrates tides at different locations along the east coast of the United States and in the Gulf of Mexico. The tide is semidaily along the eastern seaboard and dominantly daily in the Gulf of Mexico (Pensacola and Galveston).

As the earth rotates about its axis, the forces producing the tides move across the earth's surface from east to west. The motion of the moon around the earth and the earth-moon system around the sun produce variations of the tides and tidal currents with periods of about two weeks, a month, six months, a year, and longer.

Approximately twice monthly the range of the tide is a maximum; that is, the difference in sea level between successive high tide and low tide is largest. These *spring tides* occur for both the daily and semidaily tides, although not necessarily on the same day. The term *neap tides* refers to the tides with minimum range.

If the ocean covered the entire earth to a constant depth, the pattern of sea-level changes caused by the tides would be simple. However, since the oceans have complicated shapes, these patterns in the real oceans are also complicated. The global distributions of the daily and semidaily tides are given in Figs. 2 and 3. The numbers in small type along the coast and at islands in Figs. 2 and 3 are the spring ranges averaged over a year.

The lines traversing the oceans in these figures give a general idea of the stage of the tide, i.e., when high, mean, and low water occur. For example, assume that in a particular region of the North Atlantic the semidaily high water is occurring along the cotidal line marked 0 hour. Then along the 3 and 9 hour lines, the semidaily tide is passing through mean sea level; and along the 6 hour line, the tide has reached low water. About 3 hours later, high water for the semidaily tide will occur along the 3 hour line, low water along the 9 hour line, and so forth. The pattern rotates counterclockwise around a point in the North Atlantic where the range of the semidaily tide is zero. Such a rotating pattern is called an amphidromic system, and the point is called an amphidromic point. Amphidromic systems are a general feature of both the daily and semidaily tides in the deep ocean. Amphidromic systems also occur in shallow seas, such as the North Sea, as shown in Fig. 4.

The tides and tidal currents on the continental shelves and seas bordering the open seas are propagated as waves from the open oceans. These waves are partially

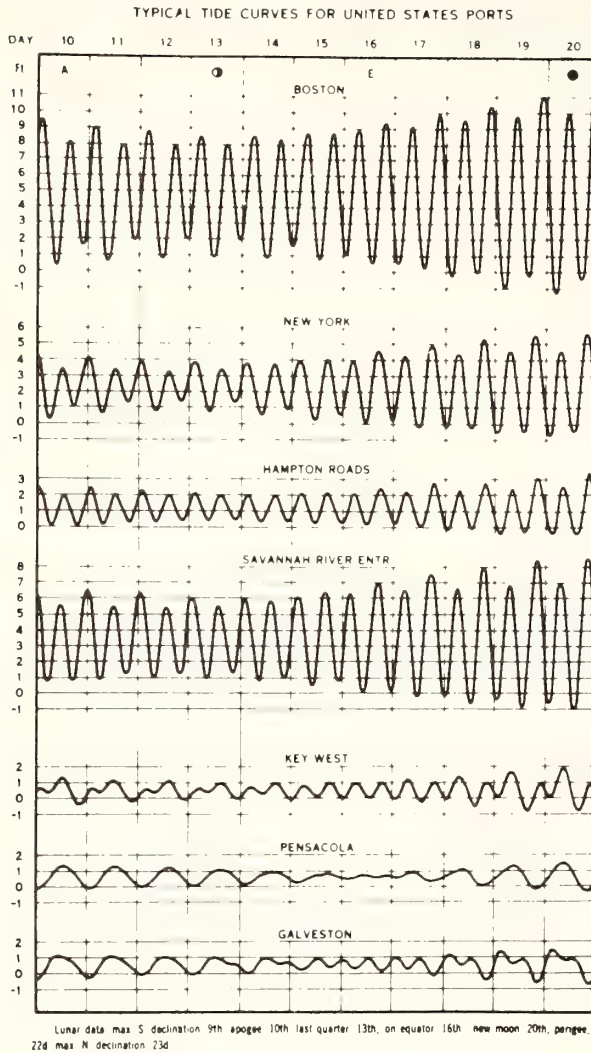


FIGURE 1. Predicted tides at selected ports along the U.S. east coast and in the Gulf of Mexico. The range and character of tides differ significantly along coasts and between distinct regions. From the U.S. Department of Commerce Tide Tables (1974).

reflected back out to sea by the shoaling bottom which rises toward the beach. The combination of the incoming, or incident, wave and the reflected wave is called a standing tide; the semidaily tide on the continental shelf between Cape Hatteras and Long Island is an example of a standing tide. The wave may also propagate along the coast, in which case it is called a progressive tide; that is, the stages of the tide progress down the coastline. An example of a progressive tide is the daily tide along the U.S. east coast. Both of these examples can be seen in Figs. 2 and 3. The technical term for a tide that is generated elsewhere and propa-

gates into a given region is cooscillation. The water on the continental shelf off the U.S. east coast cooscillates with the North Atlantic.

Coastal lagoons, bays, and estuaries cooscillate with the water on the continental shelves. The tides often enter these coastal bodies of water through inlets and over bars, both of which can significantly attenuate the tides so that the tides inside the embayment are smaller than the tides along the open coast.

## EQUATIONS OF MOTION

To compute the tides and tidal currents within a region having a complicated shape and realistic bathymetry, computer programs have been developed which use information at a number of points to compute the motion at those or other points. How well the results of the calculations describe the motion depends on the spacing between points (how well the grid of points resolves depth variations), approximations to the fundamental equations, knowledge of the motions at the boundaries of the region, and estimates of the bottom stress coefficient determining the drag of the sediment on the water.

When idealized depth variations are assumed and when less significant forces are neglected, the tides and tidal currents can sometimes be described by simple formulas from which considerable insight can be gained into tidal phenomena. Historically, intensive research was done on the behavior of tides in channels having constant depth and vertical side boundaries. The channel theory of tides is used in the present discussion and then extended to open regions such as the continental shelves.

In a channel where bottom stress and the Coriolis effect due to the earth's rotation can be neglected, a tide causes the water to accelerate through the downchannel slope of the sea surface. Horizontal differences in the resulting tidal currents in turn cause sea level to change. The interplay between these two effects produces a wave that propagates down the channel, away from the source of the tide. A general theory of waves has been presented by Mooers in Chapter 2; tides are waves whose wavelengths are long compared with the water depth but whose amplitudes are small compared with the depth. With these assumptions, the tidal motion in a channel is described by the pair of equations

$$\frac{\partial u}{\partial t} = -g \frac{\partial \eta}{\partial x} \quad (1)$$

$$\frac{\partial \eta}{\partial t} = -h \frac{\partial u}{\partial x} \quad (2)$$

CHART 6  
Semi-diurnal Tides and Tidal Forms in  
The World Ocean

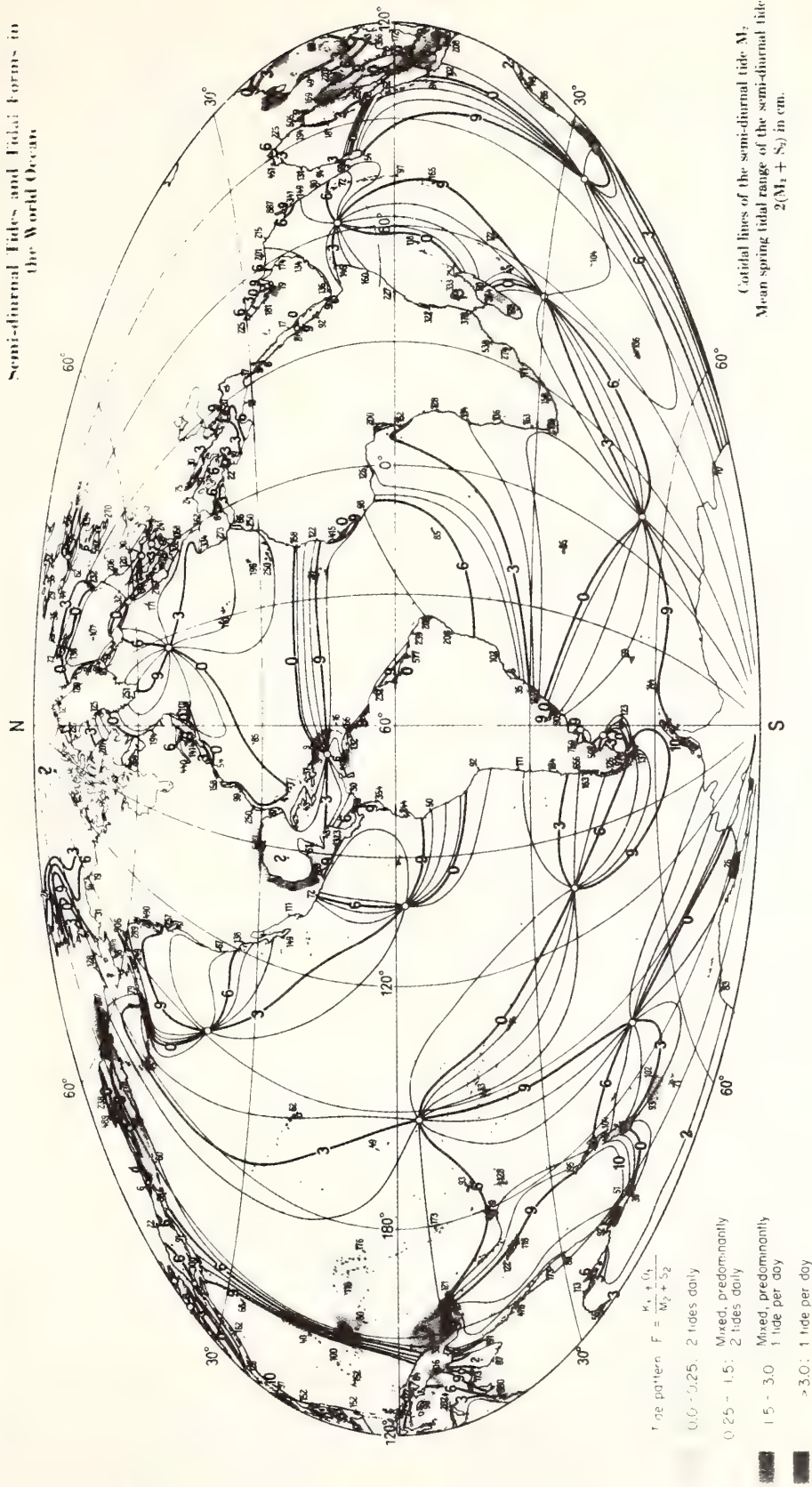
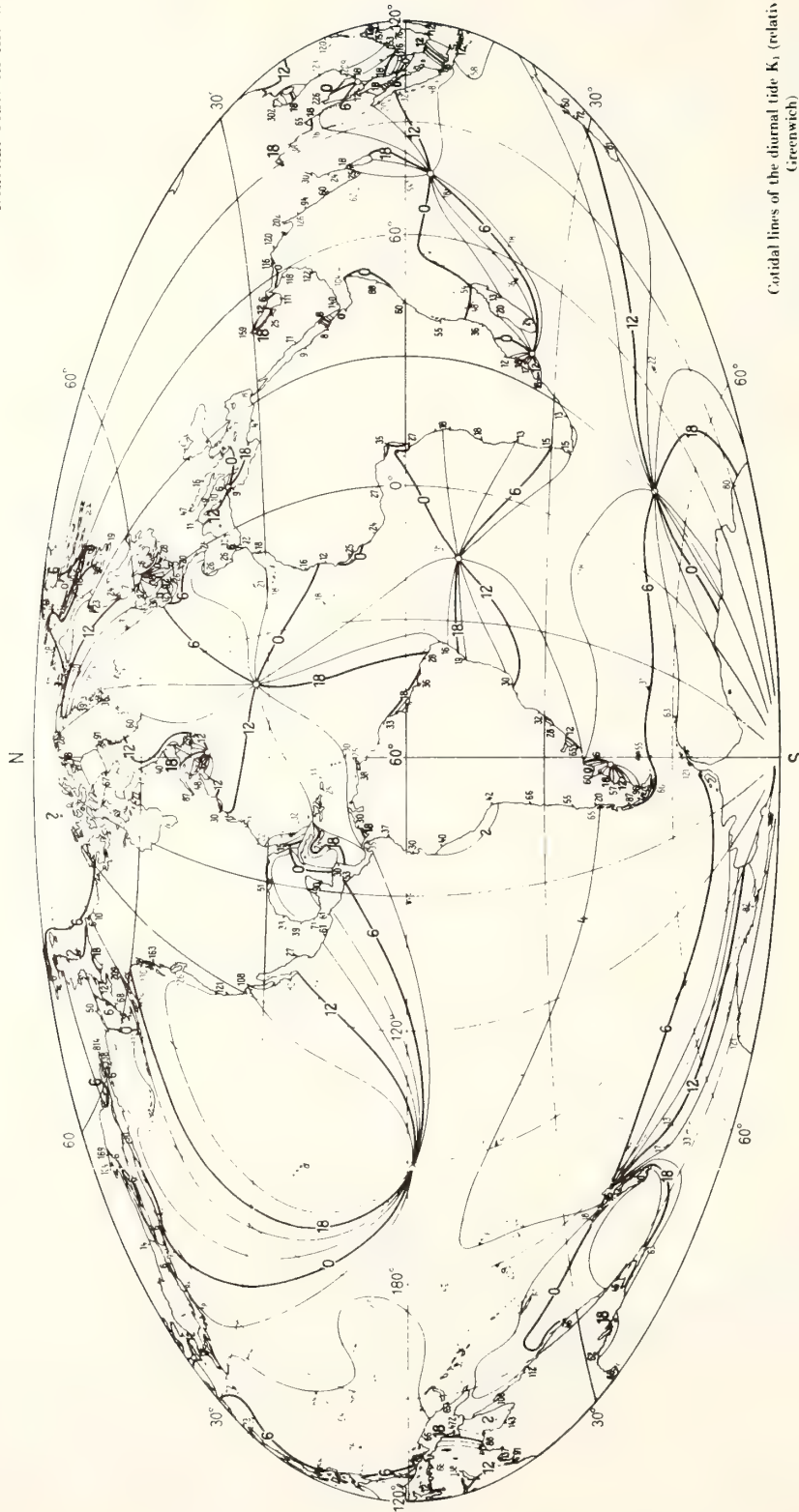


FIGURE 2. Global distribution of semidiurnal tides obtained from a theoretical model using coastal and island tide data as boundary conditions. The numbers in small type along the coasts and at islands are spring ranges in centimeters; the contour lines in the oceans are successive loci of high water as seen in hourly intervals. From Dietrich (1963).



Contour lines of the diurnal tide  $K_1$  (relative to Greenwich)  
 Mean spring tidal range of the diurnal tide:  $2(K_1 + O_1)$   
 in cm.

FIGURE 3. Global distribution of daily tides. From Dietrich (1963).

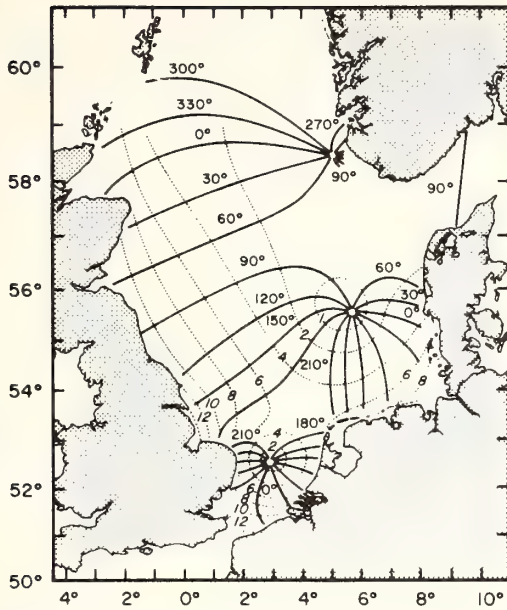


FIGURE 4. Amphidromic systems of the  $M_2$  tidal constituent (semidaily lunar tide) in the North Sea. The cotidal lines show the progress of the tide each constituent hour ( $30^\circ$  phase change), the dotted orange lines show the decrease in feet of the  $M_2$  tidal range away from the shore. From Doodson and Warburg (1941).

Equation 1 states that the time rate of change of the downchannel horizontal velocity  $u$  is equal to the acceleration of gravity  $g$  multiplied by the downchannel slope of the sea surface, whose displacement above mean water is  $\eta$ ;  $t$  is the time elapsed after high water at the source; and  $x$  is the distance away from the source of the tide as measured along the axis of the channel. Equation 2 states that the time rate of change of the sea surface displacement  $\eta$  is equal to the mean depth  $h$  multiplied

by the horizontal rate of change of the downchannel velocity  $u$ .

Assuming that the mean depth  $h$  is uniform throughout the channel, a tide with a period  $T$  and an amplitude  $a$  (one-half the range) would be described by

$$\eta = a \cos \left[ \frac{2\pi}{T} \left( t - \frac{x}{c} \right) \right] \quad (3)$$

$$u = a \left( \frac{g}{h} \right)^{1/2} \cos \left[ \frac{2\pi}{T} \left( t - \frac{x}{c} \right) \right] \quad (4)$$

where  $c = (gh)^{1/2}$  is the speed of propagation at which the shape of the sea surface moves down the channel. For oceanic and shelf depths  $c$  is 200 and 31 m/sec, respectively.

If the depth  $h$  were representative of the open ocean ( $h = 4000$  m) and the amplitude of the tide were  $a = 0.5$  m, the maximum tidal current according to (4) would be 2.5 cm/sec, a relatively small speed. On the other hand, if the depth were representative of the continental shelves ( $h = 100$  m), the corresponding current would be 15.8 cm/sec. For a given tidal amplitude, the maximum tidal currents are inversely proportional to the square root of depth. In very shallow water, where (4) would predict unrealistically large currents, the formula is not applicable since turbulent dissipation and bottom stress which would limit the currents have not been included.

In Fig. 5, the tide and tidal current are shown along a vertical section parallel to the channel axis; both are uniform across the channel. At any given time, the pattern repeats itself downchannel with a horizontal distance equal to the wavelength  $\lambda = cT$  of the wave. The water velocity  $u$  is the same at every depth because no bottom stress is allowed in this idealized model.

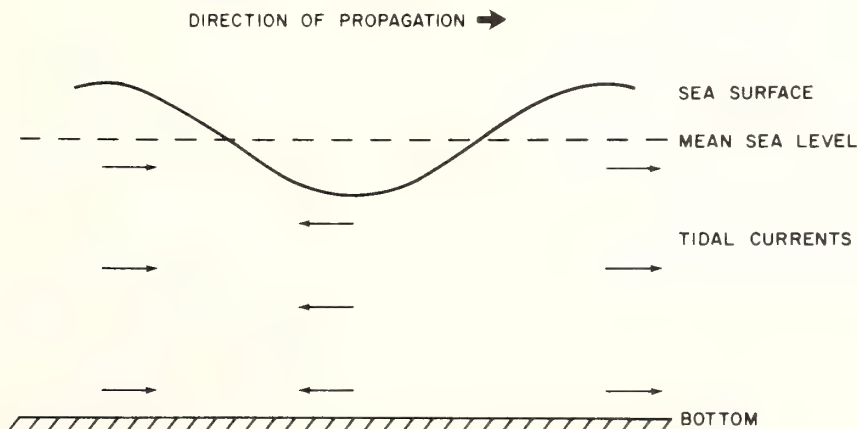


FIGURE 5. Idealized progressive tide propagating in a narrow channel in which bottom stress effects on the tidal currents are neglected. The vertical scale is greatly exaggerated.

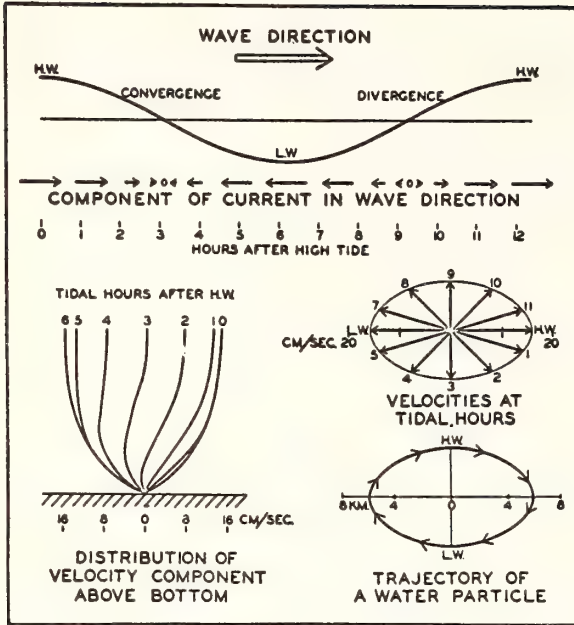


FIGURE 6. Typical tidal currents on a continental shelf where bottom stress forces the currents to zero speed at the bottom. From Fleming and Revelle (1939, p. 130); after Sverdrup (1927).

With turbulent stresses, a more realistic profile of  $u$  is shown in Fig. 6, in which  $u$  decreases within the bottom boundary layer to essentially zero at the water-sediment interface.

Since the tide propagates down the channel, it is a progressive tide. In this case, the maximum horizontal currents occur at high water and low water where the current is in the direction and opposite to the direction of propagation, respectively. As the sea level passes through mean sea level,  $\eta = 0$ , the current is momentarily zero.

As a water parcel moves in the channel, its position  $X$  is the integral in time of the horizontal velocity:

$$X = \int_0^t u dt + X_0 \quad (5)$$

where  $X_0$  is the position of the parcel at the initial time  $t = 0$ . Using (4), the horizontal displacement of the parcel is given by

$$X = \frac{a_0 T}{2\pi} \left(\frac{g}{h}\right)^{1/2} \sin \left[ \frac{2\pi}{T} \left( t - \frac{x}{c} \right) \right] + X_0 \quad (6)$$

Water subject to the tidal motion oscillates about an average position  $X_0$  with an amplitude equal to half the total excursion. For a semidaily tide ( $T = 12.5$  hours) and a tidal range  $2a = 1$  m, the excursion for open sea

depths ( $h = 4000$  m) is 0.35 km, whereas for shelf depths ( $h = 100$  m) it is 2.25 km.

In (6), tidal currents would produce no net displacement of water or suspended particles. That is, if a water parcel were tagged using dye and observed throughout a tidal cycle, the parcel would return to the same location at the end of each tidal cycle.

### STANDING TIDES

In bays and many estuaries, the incident progressive tide is reflected. The tide in this region is the combination of the incident and reflected tides. An analogous tide can be created in a channel by inserting a reflecting barrier. The sea surface displacement  $\eta$  above mean sea level and horizontal water parcel velocity for the standing tide are

$$\eta = a \cos\left(\frac{2\pi t}{T}\right) \cos\left(\frac{2\pi x}{\lambda}\right) \quad (7)$$

$$u = a \left(\frac{g}{h}\right)^{1/2} \sin\left(\frac{2\pi t}{T}\right) \sin\left(\frac{2\pi x}{\lambda}\right) \quad (8)$$

where  $a$  is the tidal amplitude at the reflecting barrier,  $x$  is the distance seaward from the barrier, and  $\lambda = (gh)^{1/2} T$  is the wavelength of the tide.

The tide and tidal currents are out of phase. At mean water, the strongest flood tide current occurs. It brings water into the embayment whose sea level must then rise. The incoming current finally ceases when the tide outside the embayment has reached high tide. As sea level begins to drop outside, an ebb current develops which continues until low tide outside the embayment. On the next rising tide, the flood tide again refills the embayment.

An important parameter determining the characters of tides in bays, sounds (large bays), and estuaries is the ratio  $R = L/\lambda$ , of the distance  $L$  between the reflecting barrier and the mouth of the embayment to the wavelength  $\lambda$  of the tide. Where the ratio is small, such as a deep bay or a small indentation in the coastline, the tide as expressed in (7) has the same range as the tide outside the embayment. This is because the factor  $\cos(2\pi x/\lambda)$  determining the variation of the sea surface displacement  $\eta$  over the embayment is equal to unity if  $2\pi x/\lambda$  is always much less than unity. The tidal currents are small since the factor  $\sin(2\pi x/\lambda)$  is equal to  $2\pi x/\lambda$ , a small number.

For example, a semidaily tide ( $T \approx 12.5$  hours) in a fjord with a depth  $h$  of 500 m and a length  $L$  of 100 km has a wavelength  $\lambda = (gh)^{1/2} T$  of 3180 km and hence a maximum tidal current of 2.8 cm/sec at the mouth of



the fjord ( $x = L$ ) if the amplitude  $a$  of the tide is 1 m. The current decreases linearly from the mouth to the head where the reflecting barrier forces the horizontal tidal current to be zero. Usually, fjords are separated from the outside by a shallow sill which can strongly inhibit the tidal penetration into the fjord. The tidal currents over sills can reach several meters per second. The example above treats currents inside the sill.

For large, shallow embayments, areal variations in tides can occur, if the length  $L$  is comparable to one-fourth of the semidaily or daily tidal wavelengths. One measure of this variation is the ratio between amplitudes of the tide at the head of the embayment and at the mouth:

$$\frac{\eta(x = 0)}{\eta(x = L)} = \frac{1}{\cos(2\pi L / \lambda)} \quad (9)$$

If  $L$  is close to  $\lambda/4$ , the ratio is large so that the tidal range inside the embayment is much larger than the tide outside. The embayment is near resonance with the tide.

The Gulf of Mexico is near resonance with the daily tides. In shallow bays, such as the Bay of Fundy, the Straits of Georgia, and Long Island Sound which are near resonance, bottom stress and other effects limit the motion. By assuming that the tides consist of progressive waves that diminish exponentially with the distance of propagation, Redfield (1950) has been able to reproduce most of the tidal characteristics in these bays. As the incident wave propagates up a bay, its amplitude diminishes; after reflection and return to the mouth of the bay, the wave is significantly smaller in amplitude than when it entered the bay. Near the mouth the tide is progressive, whereas near the closed end of the bay it is standing. The maximum amplification of the tide in naturally occurring bays is about four times the incident tide.

## TIDES IN SHALLOW WATER

Where the tidal range is a significant fraction of the depth, processes that cause the waveform to propagate act in the deeper water under the wave crest to move that part of the waveform more rapidly than the waveform near the trough. The tide becomes distorted, with the slope of the sea surface greater on the leading side of the crest. Where this distortion is large, there is significantly more landward water discharge associated with the crest of the tidal wave than there is seaward discharge associated with the trough of the tidal wave. This landward net transport of water is known as Stokes drift. The difference between the distorted and

undistorted tides is a shallow water tide. The flood tidal current is also greater than the ebbing current.

Ebb and flood channels occur in shallow water in which the tidal currents in one direction are largely confined to one set of channels and the currents in the opposite direction are confined to other channels. Ebb-flood channel systems are described in detail in Chapter 10.

A shallow bar separating the shelf from an embayment offers considerable resistance to tidal flow. Large differences in sea level develop during the tidal cycles, which generate strong tidal currents. While the velocity of the water is large across the bar, the total amount of water that can flow in and out of the embayment is severely limited by the constriction. As a result, the tide in the embayment is less than it would be without the bar.

In an embayment having a complicated bathymetry, a water parcel wanders into a variety of tidal regimes, such as tidal flats and channels, bars, and shoals; the simple theory predicting a return of the parcel to its original position at the end of each tidal cycle does not apply in this case. The Stokes drift induced by the distinct tidal regimes is a net drift of the parcel which may be thought of as a steady current.

Under some circumstances, tides should cause a net transport of sediment through the Stokes drift. However, this phenomenon has not been adequately documented by field study.

In the frictional boundary layer near the bottom where the horizontal tidal currents increase with height above the bottom, the increase in wave tidal momentum with height produces a steady current. This steady current, which can advect suspended sediment, is driven by variations in tidal momentum and is limited by turbulent friction.

## EFFECTS OF THE EARTH'S ROTATION

In larger bodies of water, the tides and tidal currents are subject to the Coriolis effect, caused by the earth's rotation. A moving water parcel experiences a force proportional to its speed which, looking down on the sea surface, is to the right in the northern hemisphere and to the left in the southern hemisphere. This Coriolis effect, when not counteracted by another force, drives the water in an elliptical path: the direction of the tidal current rotates clockwise in the northern hemisphere and counterclockwise in the southern hemisphere; the speed of the current is never zero. The semidaily tidal currents in the Middle Atlantic Bight are an example of this type of motion, shown schematically in

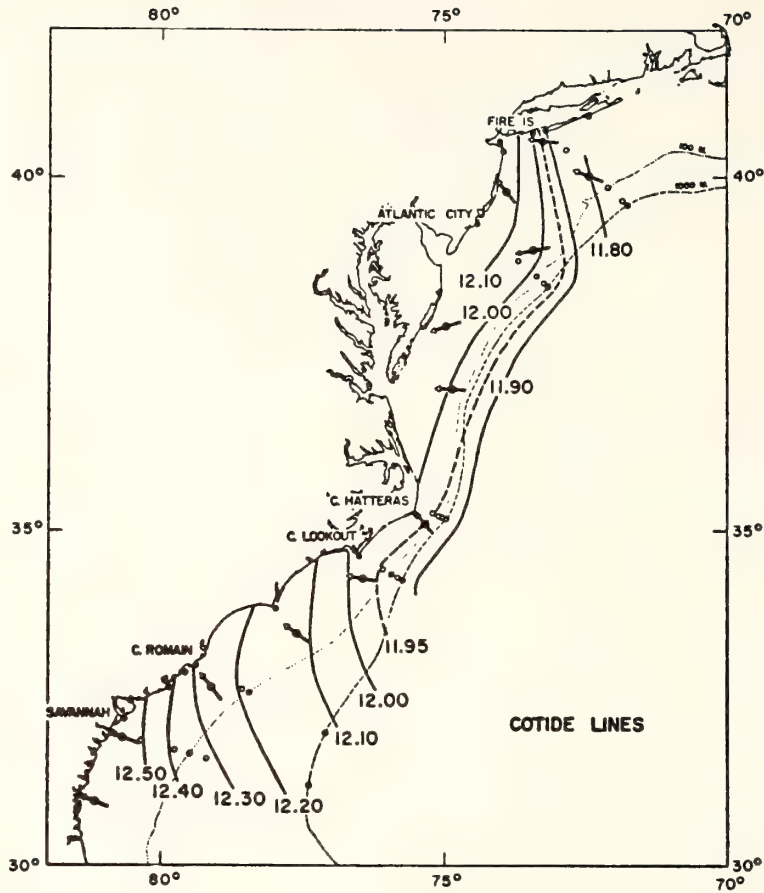


FIGURE 7. Theoretical corange chart for the  $M_2$  semidiaily tide off the U.S. east coast. Ranges are in feet. From Redfield (1958).

Fig. 6; the corange and cotidal charts are given in Figs. 7 and 8.

In regions where bottom stress can be neglected, the motion is determined approximately by the following equations:

$$\frac{\partial u}{\partial t} - fv = -g \frac{\partial \eta}{\partial x} \quad (10)$$

$$\frac{\partial v}{\partial t} + fu = -g \frac{\partial \eta}{\partial y} \quad (11)$$

$$\frac{\partial \eta}{\partial t} = -h \left( \frac{\partial u}{\partial x} + \frac{\partial v}{\partial y} \right) \quad (12)$$

The second terms,  $-fv$  and  $+fu$ , in (10) and (11) represent effects of the earth's rotation.

There are two ways in which the Coriolis effect can alter tides and tidal current. In the case of a Poincare wave, the water parcel trajectories are ellipses whose major (larger) axis is in the direction of propagation; the ratio of the major to minor axis is the inertial

period  $T_e$  divided by the period  $T$  of the tidal constituent. This type of tide can occur only where  $T_e > T$  and is generally found in exposed regions such as continental shelves. The semidiaily tide in the Middle Atlantic Bight (Fig. 7) is a standing Poincare wave (Redfield, 1958).

In restricted embayments such as the North Sea (Fig. 4) or on continental shelves where the direction of propagation of the tide is parallel to the coastline, a slope in the sea surface set up against the shore can balance the Coriolis effect. The result is a Kelvin wave. For a coastline parallel to the  $x$  direction and located at  $y = 0$ , a Kelvin wave has the form

$$\eta = ae^{-fy/c} \cos \left[ \frac{2\pi}{T} \left( t - \frac{x}{c} \right) \right] \quad (13)$$

$$u = a \left( \frac{g}{h} \right)^{1/2} e^{-fy/c} \cos \left[ \frac{2\pi}{T} \left( t - \frac{x}{c} \right) \right] \quad (14)$$

$$v = 0 \quad (15)$$

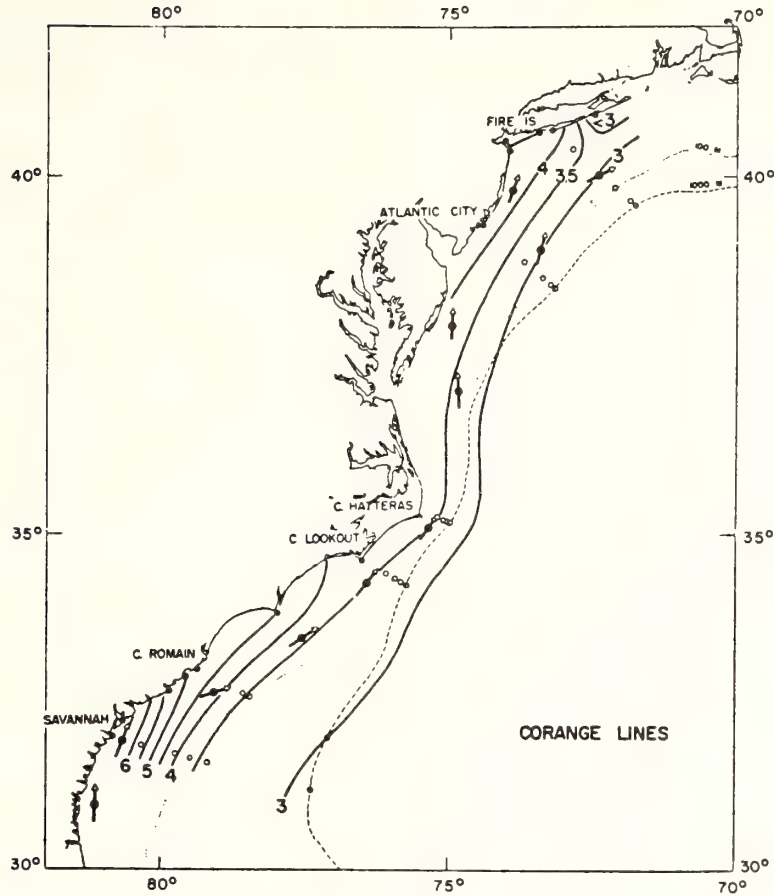


FIGURE 8. Theoretical cotidal chart for the  $M_2$  semidiurnal tide off the U.S. east coast. The cotidal lines are in hours after the Greenwich transit of the  $M_2$  moon. From Redfield (1958).

The tidal currents are parallel to shore ( $v = 0$ ). At a latitude of  $45^\circ$  and with a depth of 50 m, a Kelvin wave decays to  $e^{-1}$  (36.8%) of its magnitude at the coast in a distance  $y = c/f$  of 286 km. Conversely, a Kelvin wave propagating at  $45^\circ N$  along a continental shelf 150 km wide with a depth of 50 m has a tidal amplitude 59% of the amplitude at the coast.

A Kelvin wave propagating around a sea or ocean produces an amphidromic system. When a Kelvin wave enters an embayment in the northern hemisphere, such as the North Sea, it propagates counterclockwise around the embayment with the maximum tides and currents nearshore. Because the Kelvin waves do not decay rapidly away from their respective coasts, the motion at any given location is a combination of Kelvin waves. As a result, the tidal currents may not be colinear with the bathymetry. The sense of rotation of the tidal current direction is counterclockwise in this case, which is opposite to the direction for a Poincare wave on a continental shelf.

**BOTTOM STRESS**

Bottom stress modifies tides and tidal currents; its effect is greatest where strong tidal currents occur in shallow water. To model quantitatively the stress applied by the sediment on the water above, the flow is assumed to consist of a slowly varying tidal current superimposed on turbulence. The distribution of turbulent stress within the water determines the variation of tidal currents with distance above the bottom (velocity profile) and the dissipation of tidal energy. The details of flow near the bottom and estimates of bottom stress are central to the study of sediment transport.

The turbulent stress  $\tau$  is often modeled as proportional to the rate of change of the current with increasing distance  $z$  above the bottom:

$$\frac{\tau}{\rho} = A_v \frac{\partial u}{\partial z} \tag{16}$$

where the stress vector  $\tau$  is that part of the horizontal stress caused by vertical changes in the horizontal current  $\mathbf{u}$  and  $A_v$  is the vertical eddy or turbulent viscosity. There are other terms caused by horizontal variations in  $\mathbf{u}$  which could be added to the stress, but the term in (16) dominates turbulent processes in shallow water. A layer of water will produce a force opposite to the relative motion of the water just above the layer. The slower moving water near the bottom therefore acts as a drag on the water above. In general,  $A_v$  is determined by the spatial variations of currents, distance from boundaries, stratification of the water density, and the past history of the motion.

In turbulent boundary layers, a sublayer near the boundary layer exists where the stress is constant and the current speed increases logarithmically with distance from the boundary:

$$u = \frac{1}{k} \left( \frac{\tau_b}{\rho} \right)^{1/2} \ln \frac{30z}{z_0} \quad (17)$$

where  $z_0$  is the roughness length of the boundary which is determined by bottom irregularities,  $\tau_b$  is the magnitude of the bottom stress, and  $k$  is von Karman's constant ( $\approx 0.4$ ). The effects of turbulence generally diminish with height above the water; the inertia of the water and the Coriolis effect become more important in balancing the pressure force due to the sea surface slope. In an oscillating tidal flow, the water farther from the bottom is moving faster and therefore has more inertia than the water near the bottom. In Fig. 6 the water farther from the bottom takes longer to respond to the pressure force and lags in time the motion near the bottom.

To model the attenuation of progressive tides due to bottom stress, an empirical formula is often used which relates the bottom stress  $\tau_b/\rho$  to the vertically averaged tidal current  $U$ :

$$\tau_b = -C_f \rho U^2 \quad (18)$$

The bottom stress is proportional to the square of the tidal current and opposite in direction to the current. The stress depends on the depth  $h$  through the current  $U$ , which is inversely proportional to  $\sqrt{h}$ . The stress is inversely proportional to  $h$  and hence is greater in shallower regions. The constant of proportionality  $C_f$  has been found from field studies to be about 0.0025. A number of such studies are described in Proudman (1952) for shallow regions around England.

## INTERNAL TIDES

An internal tide is a wave with tidal period, associated with displacements within the water column and with very little displacement of the sea surface. Where there

are two layers, the currents are in opposite directions in the two layers. The speed of propagation in this case is

$$c = \left( g \frac{\Delta\rho}{\rho} \cdot \frac{h_1 h_2}{h_1 + h_2} \right)^{1/2} \quad (19)$$

where  $\Delta\rho/\rho$  is the fractional change in water density between the lower and upper layers,  $g$  is the acceleration of gravity, and  $h_1$  and  $h_2$  are the thicknesses of the upper and lower layers. On a typical shelf with  $\Delta\rho/\rho \approx 0.002$ ,  $g = 980 \text{ cm/sec}^2$ ,  $h_1 = 10 \text{ m}$ , and  $h_2 = 50 \text{ m}$ , an internal wave would propagate with a speed  $c$  of 40.4 cm/sec, which is about 60 times slower than the surface tide's speed of propagation.

On the continental slope and at the shelf break, tidal currents interact with bathymetry to produce vertical displacements of density layers within the water column. The resulting undulations propagate both shoreward and seaward as internal tides.

As internal tides propagate inshore, the shoaling bottom thins the lower layer and hence slows the wave. Since the wave energy then becomes more concentrated, the amplitude of the currents increases as does the dissipation into turbulence. Sufficiently strong currents produce an internal bore in analogy to tidal bores in rivers. The internal tide becomes a series of pulses of waves with periods of several minutes, the pulses separated in time by the tidal period. The formation of internal bores occurs when the internal tidal currents equal the speed of propagation of internal waves.

Internal waves in a two-layered fluid cannot propagate shoreward of the intersection of the density interface with the bottom. Any internal waves that have not dissipated will lose the remainder of their energy to turbulence at the location where the water becomes unstratified. On some narrow shelves with strong stratification intercepting sharply rising bottom topography, internal tides are reflected back to sea, producing an internal standing tide.

A more realistic description of internal tides requires a continuously stratified water column and the Coriolis effect. The tides then propagate in the vertical as well as the horizontal direction. Whether an internal wave as it reflects off the bottom continues to propagate shoreward, or whether it is reflected seaward, is determined by the slope of the bottom and the direction of wave energy propagation (slope of the wave characteristic). A bottom slope steeper than the wave characteristic produces reflection seaward. Smaller slopes allow the wave to continue in the incident direction. A discussion of the reflection process may be found in Cacchione and Wunsch (1974).

Since the water density structure depends on the time of year, the existence and behavior of internal waves are

also seasonal. In summer when the shelf water is stratified, internal waves can exist over most of the shelf regions; in winter, the lack of stratification precludes occurrence of internal waves.

### ADDITIONAL READING

This chapter was written to provide a qualitative introduction to the study of tidal currents. There is a large literature on tidal phenomena; as in any scientific field, the recent research is presented in succinct journal articles which presuppose a knowledge of the field.

There are a number of texts which treat tides and tidal currents in much more detail and more quantitatively than was possible in this chapter. The general texts by Sverdrup et al. (1942), Proudman (1952), and Dietrich (1963) provide such treatments. The text by Neumann and Pierson (1966) is more recent and more advanced.

### SUMMARY

Equations may be written to describe the propagation of an idealized tidal wave down a straight-walled channel. If bottom stress and the Coriolis effect are neglected, the wave is seen to propagate as a result of the interaction between water level displacement and the flow of water induced by this displacement. The speed of the tidal wave form ( $c$ ) is equal to  $(gh)^{1/2}$ , where  $g$  is the acceleration of gravity and  $h$  is water depth, while the speed of the associated current ( $u$ ) is proportional to this value. In very shallow water,  $u$  is reduced by turbulent dissipation of energy and frictional loss of energy to the bottom.

In nature, tides are propagated onto the continental margin as waves from the open ocean. Such marginal tides are said to cooscillate with the oceanic tide. Since the incoming wave is rarely parallel to the coast, it appears to propagate along the coast. Tidal waves behaving in this fashion are referred to as *progressive tidal waves*. The tidal wave may be partially reflected back out to sea by the shoaling bottom and interact with the next incoming wave so as to produce a *standing tidal wave*. In a progressive tidal wave, maximum flood velocity occurs at high water, while maximum ebb velocity occurs at low water; in a standing tidal wave the tide and tidal currents are out of phase, so that maximum flood velocity occurs during the rising tide, and maximum ebb velocity occurs during the falling tide.

An important parameter determining the character of tides in bays and estuaries is the ratio  $R = L/\lambda$ , where

$L$  is the distance between the reflecting barrier and the mouth of the embayment, and  $\lambda$  is the wavelength of the tide. When the ratio is small, the tide within the bay has the same range as outside, and tidal currents are small. However, if  $L$  is comparable to one-fourth of the semidaily or daily tidal wavelength, the embayment resonates with the outside tide. Ranges are up to four times higher, and currents are more intense.

When the tide range is a significant fraction of the depth, the wave form becomes distorted, with the slope of the sea surface becoming greater on the leading side of the crest. The difference between the time-water height curves of the undistorted and distorted tides is called a shallow water tide. Where this distortion is large, the velocity and discharge associated with the crest are greater than those associated with the trough. The resulting net transport of water is known as Stokes drift.

In larger bodies of water, the tides and tidal currents are subject to the Coriolis effect, caused by the earth's rotation. A moving parcel of water experiences a force proportional to its speed, which looking down at the sea surface, is to the right in the northern hemisphere, and to the left in the southern hemisphere. On open continental margins, the pressure force associated with the passage of the tidal wave, together with the apparent Coriolis force, results in a water parcel following an elliptical trajectory with right-hand sense of rotation. A tidal wave behaving in this fashion is a Poincaré wave. It occurs where the inertial period  $T_i$  is greater than the period  $T$  of the tidal constituent. In restricted embayments such as the North Sea, or on continental shelves where the tidal wave propagates parallel to the coastline, coastward water flow induced by the Coriolis effect is blocked by the coast, and there results a slope of the sea surface up toward the coast. A tidal wave thus modified is a Kelvin wave. A Kelvin wave propagating around a sea or ocean is known as an amphidromic system. The sense of rotation is counterclockwise.

The turbulent stress  $\tau$  is often modeled as proportional to the rate of change of the current with increasing distance above bottom. The proportionality constant  $A_v$  is the vertical eddy viscosity. It is determined by the spatial variation of the currents, distance from boundaries, stratification of the water density, and the past history of the motion. In turbulent boundary layers, a sublayer near the boundary exists where stress is constant and the current speed increases logarithmically with distance from the boundary. The slope of velocity profile is determined in part by the degree of roughness of the bottom, as measured by a bottom roughness length  $Z_0$ .

An internal tide is a wave with a tidal period, asso-

ciated with displacements within the water column, and with very little displacement of the sea surface. The wave may occur at the interface between fluids of two densities, or may occur in a continuously stratified fluid. On a typical shelf, an internal wave would propagate with a speed about 60 times slower than the surface tide's speed of propagation.

As the internal tide propagates inshore, the shoaling bottom thins the lower layer and hence slows the wave. Amplitude increases as does dissipation into turbulence; eventually the wave becomes a bore. Internal waves in a two-layered fluid cannot propagate shoreward of the intersection of the density interface with the bottom. At this point the waves lose their energy to turbulence, or if the bottom slope is steep enough, are reflected.

### SYMBOLS

$A_v$	vertical eddy coefficient
$a$	amplitude
$C_f$	drag coefficient
$c$	phase velocity of tidal wave
$g$	acceleration of gravity
$h$	water depth
$K$	a constant; von Karman's constant ( $\approx 0.4$ )
$L$	horizontal length scale
$T$	period of tidal wave
$t$	time
$\bar{U}$	vertically averaged tidal current
$u$	current velocity
$x$	horizontal distance

$Z_0$	roughness length
$z$	vertical distance
$\lambda$	wavelength
$\eta$	vertical displacement of sea surface with respect to mean water level
$\rho$	density

### REFERENCES

- Cacchione, D. and C. I. Wunsch (1974). Experimental study of internal waves over a slope. *J. Fluid Mech.*, **66**: 233-239.
- Dietrich, G. (1963). *General Oceanography*. New York: Wiley-Interscience, 588 pp.
- Doodson, A. T. and H. D. Warburg (1941). *Admiralty Manual of Tides*, London: HM Stationery Office, 270 pp.
- Fleming, R. H. and R. Revelle (1939). Physical processes in the ocean. In P. D. Trask, ed., *Recent Marine Sediments*. New York: Dover, pp. 48-141.
- Neumann, G. and W. J. Pierson (1966). *Principles of Physical Oceanography*. Englewood Cliffs, N.J.: Prentice-Hall, 545 pp.
- Proudman, J. (1952). *Dynamical Oceanography*. New York: Dover, 409 pp.
- Redfield, A. C. (1950). The analysis of tidal phenomena in narrow embayments. *Pap. Phys. Oceanogr. Meteorol.*, **11**(4): 1-36.
- Redfield, A. C. (1958). The influence of the continental shelf on the tides of the Atlantic coast of the United States. *J. Mar. Res.*, **17**: 432-448.
- Sverdrup, H. V. (1927). Dynamics of tides on the North Siberian shelf, results from the Maud Expedition. *Geophys. Publ.*, **4**: 5.
- Sverdrup, H. V., M. W. Johnson, and R. H. Fleming (1942). *The Oceans*. Englewood Cliffs, N.J.: Prentice-Hall, 1087 pp.
- U.S. Department of Commerce, National Oceanic and Atmospheric Administration, National Ocean Survey (1974). *Tide Tables, East Coast of North and South Americas, 1973*. National Ocean Survey, Rockville, Maryland, 288 pp.

## The Formation of the Yucatan Current Based on Observations of Summer 1971

ROBERT L. MOLINARI

*NOAA Atlantic Oceanographic and Meteorological Laboratories, Miami, Fla. 33149*

2 January 1975 and 15 January 1976

### ABSTRACT

Temperature, salinity and Lagrangian current data collected during the summer of 1971 in the western Caribbean Sea are employed to evaluate the ageostrophic components of the flow in the formation region of the Yucatan Current. The ratio of tangential and centripetal accelerations to Coriolis acceleration for data averaged over 24 h periods remain less than 10% except in two areas. An anticyclonic turn, centered at 19°30'N, 86°W, has the largest centripetal accelerations, and in the region of Cozumel Island significant tangential accelerations occur. The large-scale accelerations and additional evidence support the hypothesis that inertial effects dominate in the formation of the Yucatan Current.

### 1. Introduction

The Yucatan Current is considered the first segment of the Gulf Stream system, in the sense that current speeds similar to those measured further downstream

are first observed in this region. Recent studies by Molinari (1975) and Molinari and Kirwan (1975) suggest that inertial effects dominate in the formation of the Yucatan Current.

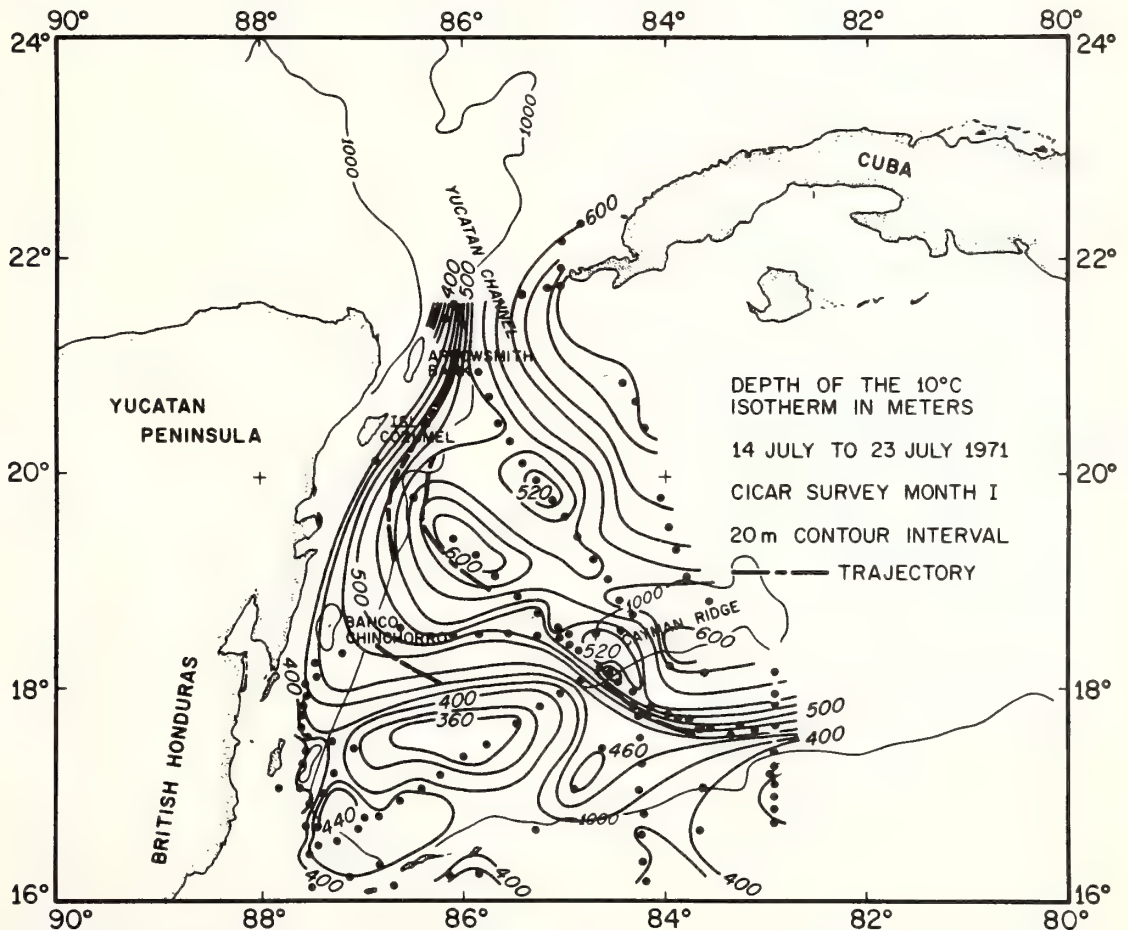


FIG. 1. The depth (m) of the 10°C isotherm, during the interval A, 14 to 23 July, 1971. The station locations are indicated by solid circles. Trajectories for the center of mass of buoy triads are also shown (see text).

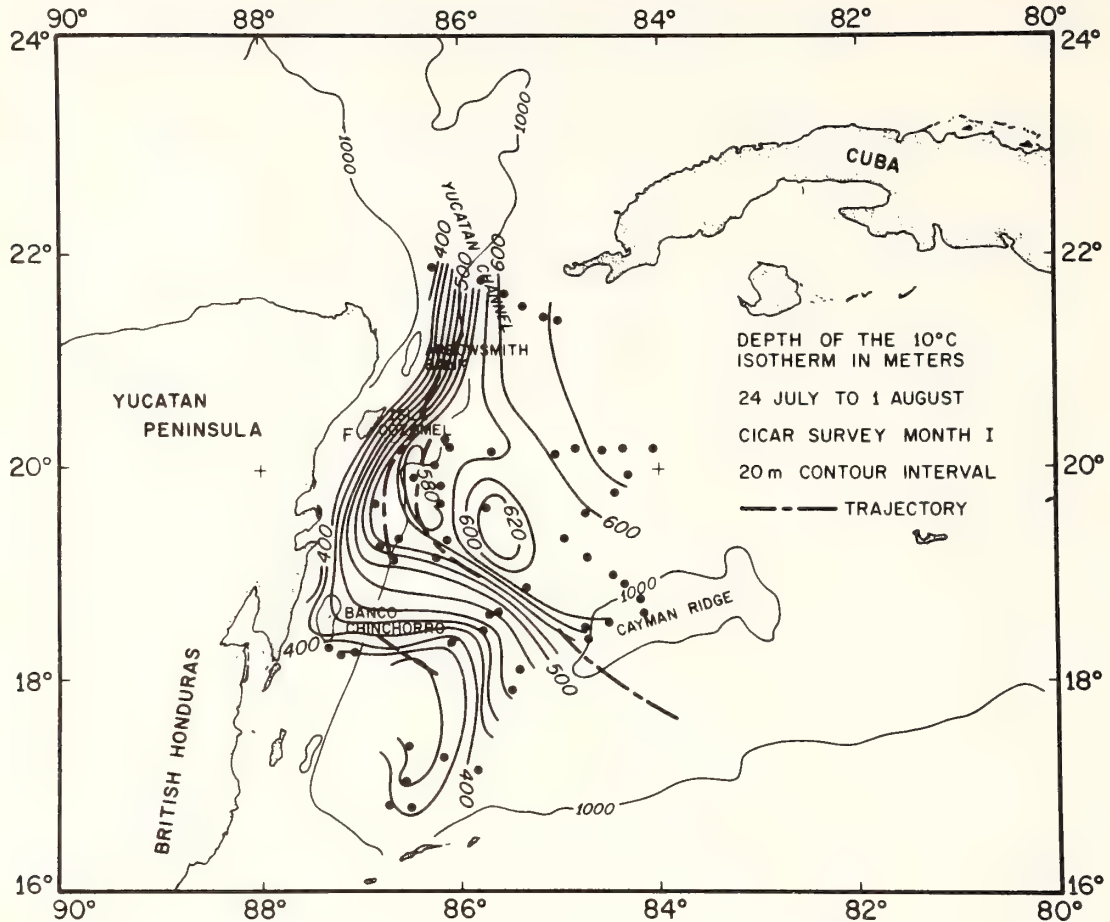


FIG. 2. As in Fig. 1, except for the interval B, 24 July to 1 August, 1971.

A two-ship operation was conducted in the summer of 1971 to investigate the formation of the Yucatan Current, and in particular to determine the nature and extent of the ageostrophic component in the western Caribbean Sea (Fig. 1) where the Current forms. In this field study, the ageostrophic component of the flow was determined by measuring the acceleration of water parcels tagged by drift buoys.

The surface buoy was described by Molinari (1973); nominally it senses the motion of the water at 40 m by a parachute drogue. Data reduction techniques, and the reduced surface drifter, temperature and salinity data collected by the NOAA ship *Researcher* were also discussed by Molinari (1973). These data, supplemented by additional temperature data collected by *Discoverer* (Hazelworth and Starr, 1975) are used in the following sections to describe the formation of the Yucatan Current in the summer of 1971.

**2. Temperature-salinity data**

Certain isotherm topographies are useful surrogates for the density distribution in this area. In particular,

Molinari (1975) found that the 10°C topography closely maps the geostrophic current regime in the western portion of the Caribbean Sea. The study period, 14 July to 22 August, 1971, is divided into three time intervals. The intervals are selected to provide spatial resolution of the temperature field over the shortest time span. Figs. 1-3 show the 10°C topographies during these intervals (identified as A, B, C).

The 10°C topography at 83°W (Fig. 1) has a slope at 18°N consistent with a narrow and fast geostrophic current. The maximum slope occurs along a band bounded by the 460 m and 520 m contours. The band extends continuously from 83°W, 18°N to the Yucatan Strait. The acceleration along this band is not monotonic. Rather, the direction of and gradients along the band vary, suggesting accelerations, decelerations and meanderings of the current.

The temperature structure indicates the presence of eddies on either side of the maximum slope. The flows around these eddies are both cyclonic and anticyclonic. Figs. 1 and 2 suggest that there is a south to north



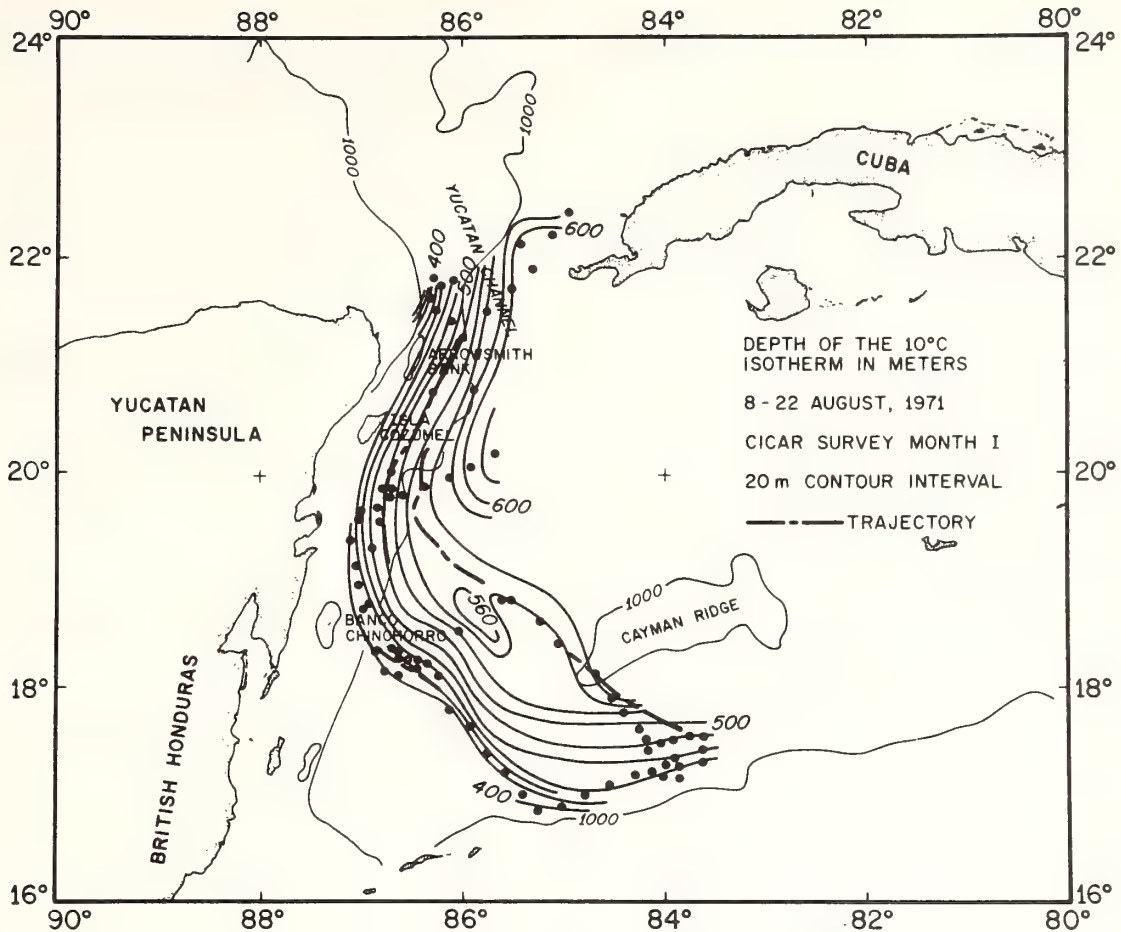


FIG. 3. As in Fig. 1, except for the interval C, 8 to 22 August, 1971.

decrease in eddy size, with no resolvable eddies found at the Yucatan Strait.

The migrations of the 460 to 520 m band show the temporal changes which occur in the main current. The only significant temporal variability occurs in the southern basin where the large eddy initially centered at 17°30'N, 86°W (Fig. 1) apparently drifts to the west. There is no significant movement of the band at the Yucatan Strait during the six-week time period.

### 3. Drifter data

The technique for reducing the drifter data was described by Molinari (1973) and Molinari and Kirwan (1975). This procedure provides geographic positions every 2h. The individual drogue trajectories are shown in Fig. 4.

Four sets of trajectories were obtained, and with at least three drifters being deployed in each set. Legs 1 and 2 employed the same buoys which drifted unattended from points 4 to 5 during an emergency port call. The buoys were retrieved at the end of leg 2, and redeployed in an unsuccessful attempt to sample the

cyclonic flank of the current (leg 3). After a scheduled port call leg 4 was initiated, and then prematurely terminated when a storm threatened the operations area.

The results of the drifter analysis are presented below in increasing order of the derivatives of the buoy coordinate-vs-time functions, i.e., trajectories, speeds and accelerations. Finally, the ageostrophic components of the flow, as evaluated from the drifter data, are discussed.

#### a. Trajectories

Trajectories are computed for the center of mass of the buoy triads, and are given in Figs. 1-3. The current fields inferred from these trajectories are very similar to the circulation fields inferred from the 10°C topographies. For instance, in the Yucatan Strait region the trajectories closely follow the depth contours of the 10°C isothermal surface during all three time intervals. However, in the southern basin the trajectories parallel only those contours obtained concurrently, i.e., the leg 1 trajectory parallels the phase 1 temperature field

(Fig. 1), and the leg 4 trajectory parallels the phase 3 temperature field (Fig. 3). This result is consistent with the temporal variability observed in the temperature field and discussed above.

Visual inspection of the trajectories in Fig. 4 indicates that large-amplitude meanders did not occur in the area. The largest curvature in the trajectories occurs in the anticyclonic turn indicated in the temperature fields at 19°30'N, 86°W (Figs. 1-3). The average anticyclonic radius of curvature from points 7 to 10 shown in Fig. 4 is 75 km.

*b. Speeds and accelerations*

Buoy speeds have been computed from the position data by using a centered difference approximation to the differential. The accelerations have been computed in natural coordinates, i.e., downstream  $s$ , crossstream  $n$  (positive to the left of the downstream axis), and vertical  $z$  (positive up). The accelerations are tangential ( $dV/dt$ ), centripetal ( $KV^2$ ) and Coriolis ( $fV$ ), where  $d(\ )/dt = \partial(\ )/\partial t + V\partial(\ )/\partial s$ ,  $V$  is the measured speed,  $K$  the horizontal curvature (positive for downstream cyclonic turning), and  $f$  the Coriolis parameter.

The trends in the individual buoy speeds have been

determined by fitting in a least-squares sense a cubic polynomial in time to the speed values. The fitted polynomial trend has been subtracted from the observed values to arrive at residual speed curves. The speed and residual speed curves for each drifter, and the polynomial fit curve for one drifter, are given in Fig. 5.

The large-scale accelerations inferred from the temperature data are apparent in the fitted polynomial curves. For instance, the temperature gradients of the anticyclonic turn centered at 19°30'N, 86°W suggest a deceleration in the flow. This deceleration occurs at 206/1930 (Fig. 5), as the drifters enter this turn. The temperature gradients increase as do the buoy speeds (leg 3, 210/0315 to 213/1315), as the drifters approach the Yucatan Strait. The largest average downstream accelerations occur in the vicinity of and north of Cozumel Island, where the speeds approach those observed in the Gulf Stream. These large-scale accelerations occur on time scales of days and/or space scales of hundreds of kilometers.

Smaller time and/or space scale disturbances are superimposed on these large-scale features. In Fig. 5, the speed curves with the trends removed show that the amplitude of these oscillations are relatively constant

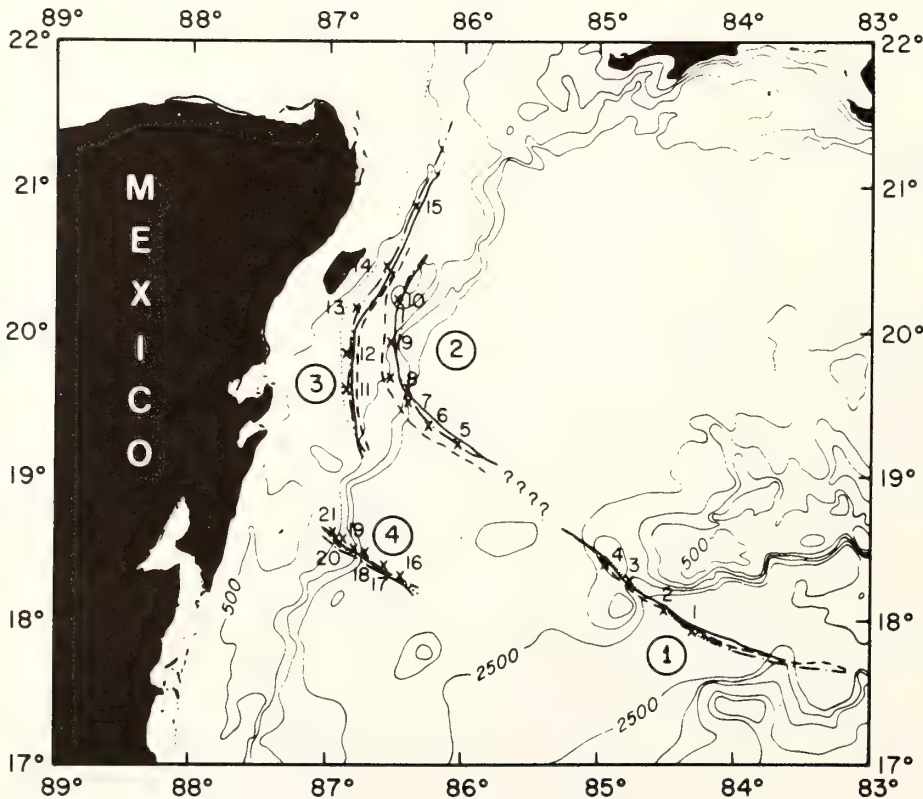


FIG. 4. Drogue trajectories as determined from 2 h positions. The trajectory of buoy 2 is continuous during legs 1 and 2 (identified by circled numbers), although the buoy was not continuously tracked from interval 4 to 5. The first and last position times (Julian day/hour) are: leg 1, 200/1830 to 204/1630; leg 2, 205/1930 to 209/0730; leg 3, 210/0315 to 213/1315; and leg 4, 228/1600 to 232/1000.

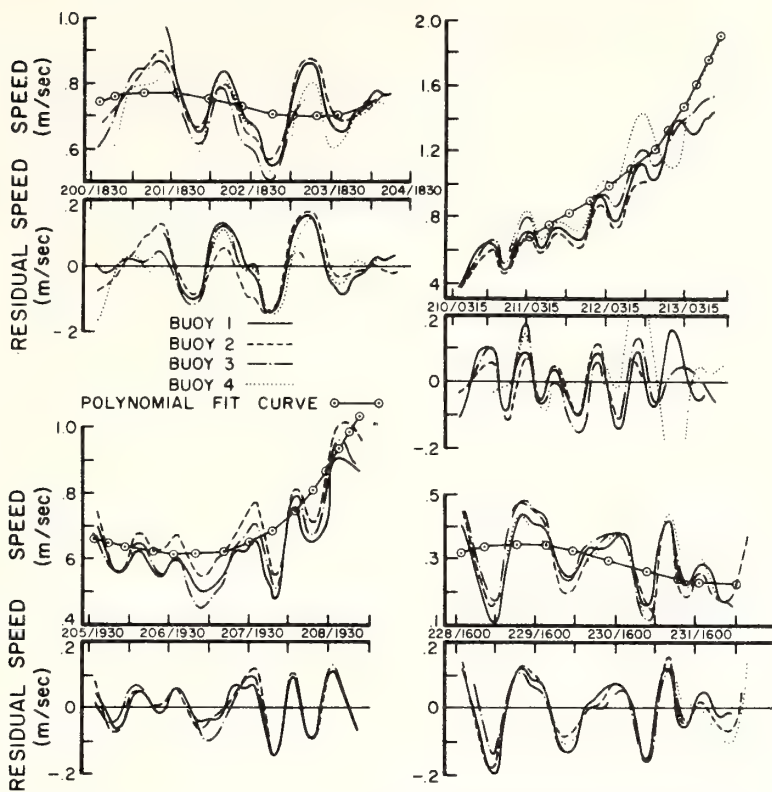


FIG. 5. The observed and residual speed curves for the trajectories of Fig. 4 as a function of time (Julian day/hour). The residual speeds are determined by subtracting the third-degree polynomial fit curve (a representative curve is shown in the upper panels of each time interval) from the observed curve.

throughout the basin, although their primary period appears to vary. A visual inspection of the records indicates that the principal period in the southern speed data is 24 h, and in the northern data, 12 h.

As indicated, no large-amplitude meanders, similar to Gulf Stream meanders, appear in the trajectory data (Fig. 4). Thus, the velocity oscillations discussed above occur along the axis of the flow, rather than normal to it. The downstream spatial extent of the oscillations vary from approximately 25 km in the low-speed regions to 75 km in the high-speed region of the basin.

### c. Ageostrophic components

The horizontal equations of motion can be written in natural coordinates as

$$\frac{dV}{dt} + \frac{\partial D}{\partial s} = R_1, \quad (1)$$

$$KV^2 + fV + \frac{\partial D}{\partial n} = R_2, \quad (2)$$

where  $D$  is the dynamic height relative to a level of no

motion, and  $R_1$  and  $R_2$  include all the forcing and retarding functions. In a frictionless system the ageostrophic components are the centripetal acceleration  $KV^2$  and the tangential acceleration  $dV/dt$ .

The terms on the left-hand side of (1) and (2) are evaluated for those portions of the trajectories where density data are available. Dynamic heights are computed relative to 600 m, since the majority of the hydrographic casts were to this depth. Accelerations for the center of mass trajectories and the density gradients are averaged over 24 h periods to eliminate the small-scale oscillations shown in Fig. 5. Table 1 lists these average properties at 12 h intervals.

If  $R_2 = 0$ , Eq. (2) becomes the gradient equation. The gradient balance expressed in percentages as  $[R_2 / (KV^2 + fV)] \times 100$  was maintained on the average to within 10% during legs 1, 2 and 3. The gradient balance computed relative to 600 m was not maintained during leg 4 for undetermined reasons (although internal wave aliasing of the density field may be a cause).

The terms in (1) are an order of magnitude less than the terms in (2) and therefore more difficult to evaluate realistically. However, the large-scale tangential accelerations are consistent with downstream pressure gradients observed during legs 2 and 3 (Fig. 4).

TABLE 1. Ageostrophic and geostrophic components averaged over 24 h periods.

Fig. 4 point	Time Julian day/hour	$V$ ( $\text{cm s}^{-1}$ )	$fV$ ( $\text{cm s}^{-2} \times 10^4$ )	$\partial D/\partial n$ ( $\text{cm s}^{-2} \times 10^4$ )	$ KV^2 /fV$ $\times 100$ (percent)	$ dV/dt /fV$ $\times 100$ (percent)
1	202/1330	0.69	0.31	0.27	8	2
2	203/0130	0.68	0.30	0.25	11	2
3	203/1330	0.71	0.32	0.31	6	4
4	204/0130	0.71	0.33	0.36	7	3
5	206/0830	0.61	0.28		10	4
6	206/2030	0.58	0.27		9	4
7	207/0830	0.58	0.28	0.20	12	3
8	207/2030	0.61	0.30	0.22	17	10
9	208/0830	0.69	0.34	0.28	12	8
10	208/2030	0.76	0.38		7	3
11	211/0215	0.66	0.32		4	3
12	211/1415	0.75	0.37	0.29	13	4
13	212/0215	0.94	0.47	0.34	8	13
14	212/1415	1.15	0.59	0.50	1	8
15	213/0215	1.49	0.70		1	7
16	229/0500	0.32	0.14		2	5
17	229/1700	0.33	0.15		9	4
18	230/0500	0.30	0.14		3	1
19	230/1700	0.29	0.13		7	3
20	231/0500	0.28	0.13		9	8
21	231/1700	0.26	0.12		0	6

The data listed in Table 1 verify the results described qualitatively in previous sections; that is, the large-scale flow undergoes little acceleration in the mid-basin (points 1–4, Fig. 4), the largest centripetal accelerations occur in the anticyclonic turn centered at  $19^{\circ}30'N$ ,  $86^{\circ}W$  (point 8, Fig. 4), and the largest accelerations occur in the vicinity of Cozumel Island (point 13, Fig. 4). If  $R_1=R_2=0$ , the large-scale flow is geostrophic to within 20%. In particular, although the average velocity more than doubles from points 11 to 15 (Fig. 4), the maximum value of the ratio  $[(dv/dt)/fV] \times 100$  is only 13%.

If the ageostrophic components are evaluated for intervals of monotonically accelerating or decelerating flow (Fig. 5), the ratios of ageostrophic to geostrophic terms are considerably higher than those listed in Table 1. For instance, over these shorter averaging intervals the centripetal acceleration is as large as one-third the Coriolis acceleration, and the tangential acceleration is as large as one-fourth the Coriolis acceleration.

#### 4. Discussion

For the average accelerations listed in Table 1, the balances expressed in (1) and (2) are confirmed qualitatively for (1), and quantitatively for (2). Molinari and Kirwan (1975) demonstrate qualitatively that potential vorticity is conserved for portions of legs 2 and 3 (points 5–9 and 11–15, Fig. 4). In addition, the absolute value of their relative vorticity is approximately 40% of the value of the planetary vorticity on the northern portion of these trajectories.

The 1971 measurements also suggest that if lateral friction plays a role in the formation process of the Yucatan Current it is limited to a narrow band along the Yucatan Peninsula. A frictional boundary layer can be characterized by a cyclonic shear zone, but the westernmost buoy of leg 3 (Fig. 4) exhibits the highest speeds measured (Fig. 5), indicating the buoys are in the anticyclonic zone of the current. The only indication that the buoys may be on the cyclonic flank of the current occur as this buoy drifts over Arrowsmith Bank. However, it is difficult to ascertain if the speed reduction is a local effect of the bank topography, or if the buoy has indeed crossed the speed axis. The preceding results provide additional support for the contention of Molinari (1975) that inertial effects dominate in the formation of the Yucatan Current.

The 24 h average ageostrophic components listed in Table 1 are seldom greater than 10% of the Coriolis accelerations. As discussed, if shorter averaging periods are used the ratio of ageostrophic to geostrophic components increases. The effect of these smaller scale features on the formation process are still matters for speculation. Plausible explanations are wind and/or tidal forcing of the upper layers. For instance, the dominant semi-diurnal and diurnal periods of the speed oscillations (Fig. 5), their constant amplitude throughout the basin, and the predominantly downstream orientation of these disturbances suggested a tidal modulation of the flow. However, the results of a tidal analysis performed on the data were inconclusive.

*Acknowledgments.* The invaluable assistance in the collection of data of the officers and crew of the *Researcher* is gratefully acknowledged.

The data analysis was facilitated by the programming of Mr. A. Herman, and the efforts of Mr. D. Tidwell. The figures were drafted by the publication and presentation group of Mr. R. L. Carrodus.

This work was supported in part by the National Science Foundation, under International Decade of Ocean Exploration Grant AG-253.

## REFERENCES

- Hazelworth, J., and R. B. Starr, 1975: Oceanographic conditions in the Caribbean Sea during the summer of 1971. NOAA Tech. Rep. ERL 344-AOML 20, 144 pp.
- Molinari, R. L., 1973: Data from the Lagrangian current measurement project conducted aboard the NOAA ship *Researcher* during CICAR Survey Month I. NOAA Tech. Memo. ERL-AOML-19, 81 pp.
- , 1975: A comparison of observed and numerically simulated circulation in the Cayman Sea. *J. Phys. Oceanogr.*, **5**, 51–62.
- , and A. D. Kirwan, 1975: Calculation of differential kinematic properties from Lagrangian observations in the western Caribbean Sea. *J. Phys. Oceanogr.*, **5**, 483–491.

CALCULATIONS OF DIFFERENTIAL KINEMATIC PROPERTIES  
FROM LAGRANGIAN OBSERVATIONS

by

Dr. R. Molinari  
Atlantic Oceanographic and Meteorological Laboratories

Dr. A. D. Kirwan, Jr.  
Texas A&M University, Department of Oceanography

INTRODUCTION

In the past oceanographers have used Lagrangian data, primarily to obtain elementary fluid properties such as trajectories, velocities, and accelerations. However, meteorologists have recognized the utility of Lagrangian data in determining estimates of the differential kinematic properties, divergence, vorticity, shearing deformation, and stretching deformation. These properties are important ingredients in any description and/or explanation of fluid motions. For instance, divergence is an important factor in determining vertical motion in the ocean, vorticity can be related to the field of force that drives ocean flows, and the two deformations are important in the formation and dissipation of fronts.

The Authors: Robert Molinari received his Ph.D. in Physical Oceanography from Texas A&M University in 1970. Since 1971 he has held the position of Research Oceanographer with NOAA/AOML. His work has centered on observational and theoretical study of the Cayman Sea and the Gulf of Mexico.

Dennis Kirwan, Jr. also received his Ph.D. from Texas A&M. He has been an associate Professor at New York University and worked as a Program Director with the Office of Naval Research. More recently, he has become Research Scientist at Texas A&M and has been involved in drift buoy studies.

Two methods are presented for the calculation of these properties. One method is more readily applicable to a large number of buoys. The other approach is given to provide estimates to verify the results of the more general technique. A short description of the experiment and data analysis is given.

## DATA COLLECTION AND ANALYSIS

Figure 1 is a schematic diagram of the ship-tracked buoy used in the experiment. The buoy nominally was tied to a water parcel at 40 m by a 35-ft diameter parachute.

The experiment was conducted in the western Caribbean Sea in the summer of 1971, aboard the NOAA ship RESEARCHER. The prime navigational control was supplied by a satellite positioning unit. In that region, satellite fixes can be obtained on the average every 1.5 hours. The satellite positions were supplemented by Omega fixes collected every 15 minutes. The buoys were positioned relative to the ship at each fix.

Errors are introduced into the buoy positions by the imprecision of the satellite, Omega, and radar systems. Assuming the satellite system to be the more precise of the two positioning techniques, an estimate of the Omega errors was made. An individual Omega position is accurate approximately to  $\pm 2$  km. Thus, there is a very small signal-to-noise ratio when considering the 15-minute fixes.

The following smoothing procedure was applied to the Omega fixes to eliminate some of the noise in the trajectory data. Hourly fixes were obtained by taking 5-point running averages of the 15-minute component coordinates. A second degree polynomial curve was then fitted to 13 consecutive hourly fixes to arrive at the data used in the analysis.

Kirwan, in a previous talk, indicated other possible sources of error when attempting to tag a particular water parcel. Using his analysis for the drifter configuration used in this experiment, it was found that a 10 m/sec

wind could cause a 5 percent error in the estimate of the true current. This effect was not considered in reducing the data from this experiment.

#### A. Least Square Method

Consider a small, but finite, parcel of water, and assume that within this parcel the velocity at any point is adequately represented by the linear terms in a Taylor's expansion about the center of mass of the parcel. For a cluster of  $N$  drifters located within the parcel, the expansion yields for the velocity components of the  $i^{\text{th}}$  drifter.

$$\begin{aligned}
 U_i &= U + g_i + \{(D + N) X_i\} / 2 + \{(S - \zeta) Y_i\} / 2 \\
 & \qquad \qquad \qquad i = 1, \dots, N \quad (1) \\
 V_i &= V + h_i + \{(S + \zeta) X_i\} / 2 + \{(D - N) Y_i\} / 2
 \end{aligned}$$

The  $U$  and  $V$  are the components of the velocity of the center of mass of the parcel. The coordinates with respect to the cluster center of mass of drifter  $i$  are  $X_i$  and  $Y_i$ . The  $g_i$  and  $h_i$  represent the sum of the higher order non-linear terms in the expansion.

The differential kinematic properties are:

$$\begin{aligned}
 D &= \partial U / \partial X + \partial V / \partial Y && \text{(Divergence)} \\
 \partial &= \partial V / \partial X - \partial U / \partial Y && \text{(Vorticity)} \\
 S &= \partial V / \partial X + \partial U / \partial Y && \text{(Shearing deformation rate)} \\
 N &= \partial U / \partial X - \partial V / \partial Y && \text{(Stretching deformation rate)}
 \end{aligned} \quad (2)$$

The divergence,  $D$ , is a measure of the parcel volume change without change of orientation or shape.  $\zeta$ , the vorticity, is a measure of the orientation change without volume or shape change of the parcel. Shape changes without change of volume or orientation are given by  $S$  and  $N$  respectively.

In equation (1),  $U_i$ ,  $V_i$ , and  $U$  and  $V$  are computed from the buoy coordinates. The  $g$  and  $h$  functions, and  $D$ ,  $N$ ,  $S$ , and  $\zeta$  can be computed by noting



that at each time the total kinetic energy density of the cluster due to small-scale turbulence is:

$$KE = \sum_{i=1}^N \frac{g_i^2 + h_i^2}{2} \quad (3)$$

Substituting (1) into (3) shows that the kinetic energy density depends on the kinematic properties. These four parameters can be estimated by selecting values which give a minimum for the kinetic energy density. The  $g$  and  $h$  functions can then be determined from (1).

The minimum number of drifters that can be used to determine  $D$ ,  $S$ ,  $N$ , and  $\zeta$  is three. However, this approach is readily extended to consider larger numbers of drifters. In addition, the approach generates time series of the turbulent velocities,  $g_i$  and  $h_i$ , from which direct estimates of turbulent stresses can be made.

#### B. Area Method

Horizontal divergence can be expressed as the fractional time rate of change of the horizontal area,  $A$ , of a parcel:

$$\frac{\partial U}{\partial X} + \frac{\partial V}{\partial Y} = \frac{1}{A} \frac{DA}{Dt} \quad (4)$$

For a triad of drifters,  $A$  is readily evaluated from the buoy positions. From the time series of  $A$ 's an appropriate numerical technique is used to estimate the time rate of change.

Vorticity, shearing and stretching deformation can be evaluated by selected rotations of the velocity vectors of the three drifters. Saucier (1955) describes this technique.

## RESULTS

Figure 2 is a schematic diagram of representative drogue trajectories and speeds. Four trajectories are shown. Beginning with the trajectory over the Cayman Ridge and preceeding counterclockwise around the basin, the trajectories will be numbered 1, 2, 3, and 4 for purposes of identification.

The area of figure 2 is the formation region of the Yucatan Current. The accelerations which occur during legs 2 and 3 are indicative of the formation processes occuring in the vicinity of the Yucatan Channel.

Figure 3 is a more detailed plot of the drogue trajectories of leg 1. A Universal Transverse Mercator projection is used, and the x and y coordinates are marked in kilometers. The apexes of the triangles represent drogue positions.

Also given on the figure are the velocity, acceleration, and radius of curvature of the triad center of mass. The last two curves indicate the difficulty of obtaining from these data smooth estimates for higher order derivative terms.

Figure 4 gives the divergence and vorticity as determined by the two methods. The solid lines connect the values computed by the least square approach, and the crosses represent the values computed by the area method. The triad areas (figure 4) are small and the estimates of the kinematic properties are very irregular with respect to time.

Figures 5 and 6 present the buoy trajectories and all the kinematic properties for leg 2. Again, the agreement between the two methods is good. The estimates of these parameters are smoother functions of time for this leg.

Figures 7 and 8, and 9 and 10 display the results for legs 3 and 4 respectively. The buoy speeds were lowest during leg 4, on the average 0.3 m/sec, and the triangle areas small. The kinematic property estimates given on figure 10 are very ragged, with frequent crossings of the axis. It is doubtful that these values are reliable estimates of the differential kinematic properties.

The value of the measurements is increased if the resulting data can be used to explain the dynamics of the circulation. An attempt to incorporate the data of leg 2 (figure 6) into a dynamic expression is made.

Figure 11 gives the conservation of potential vorticity relation, and the evaluation of the terms in this relation using the data of leg 2. This equation is derived by assuming no external forces (tides, winds) are acting on the flow. The terms in this expression are  $Z$ , the relative vorticity,  $f$ , the Coriolis parameter, and  $\nabla \cdot \bar{V}$ , the divergence. The qualitative balance of the terms for the first two days of the trajectories suggests a balance exists.

To summarize, it appears feasible to compute differential kinematic properties from drifting buoy data. In addition, if estimates are sufficiently well-behaved, some dynamical statements about the flow can be offered.

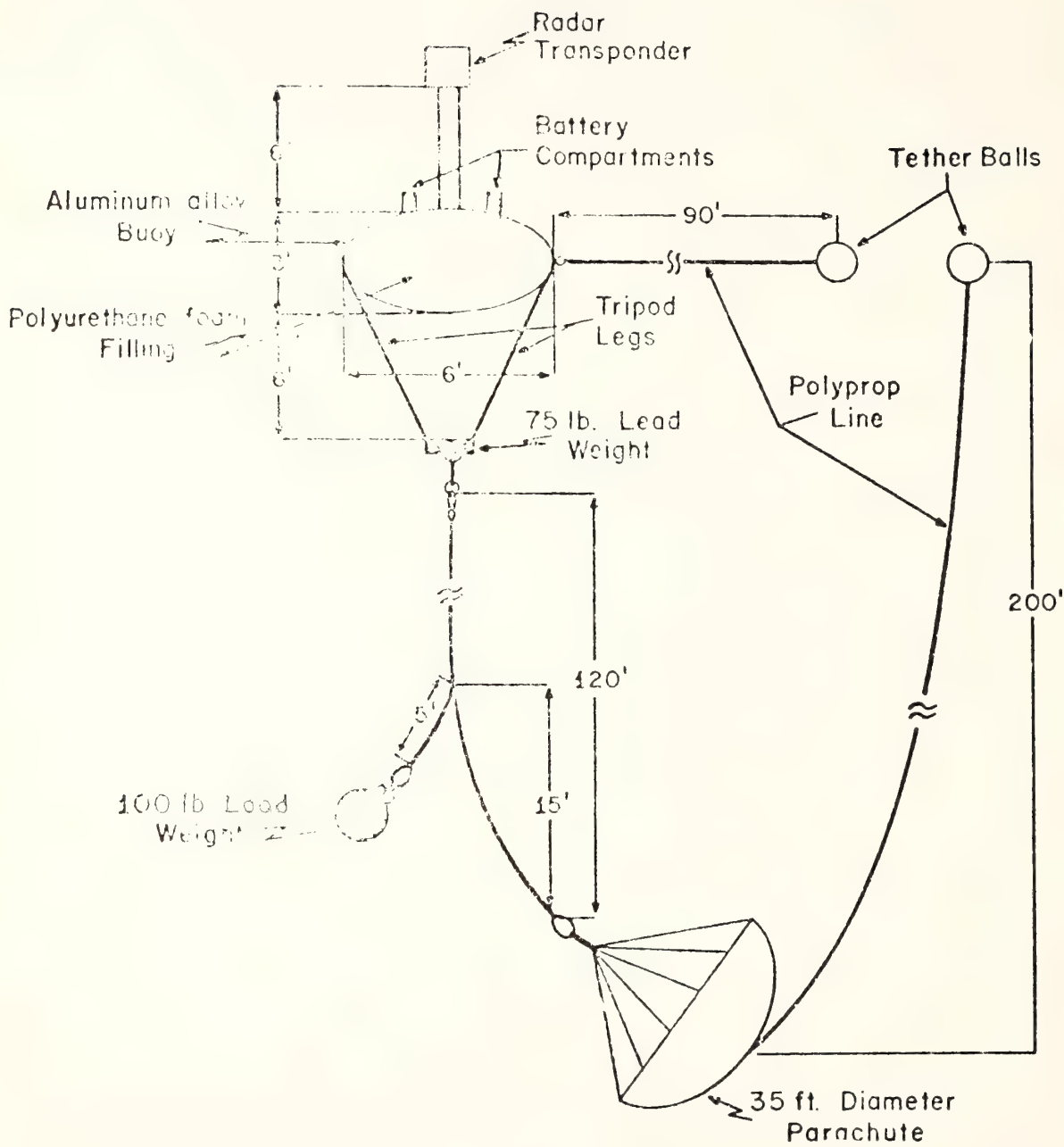


Figure 1.

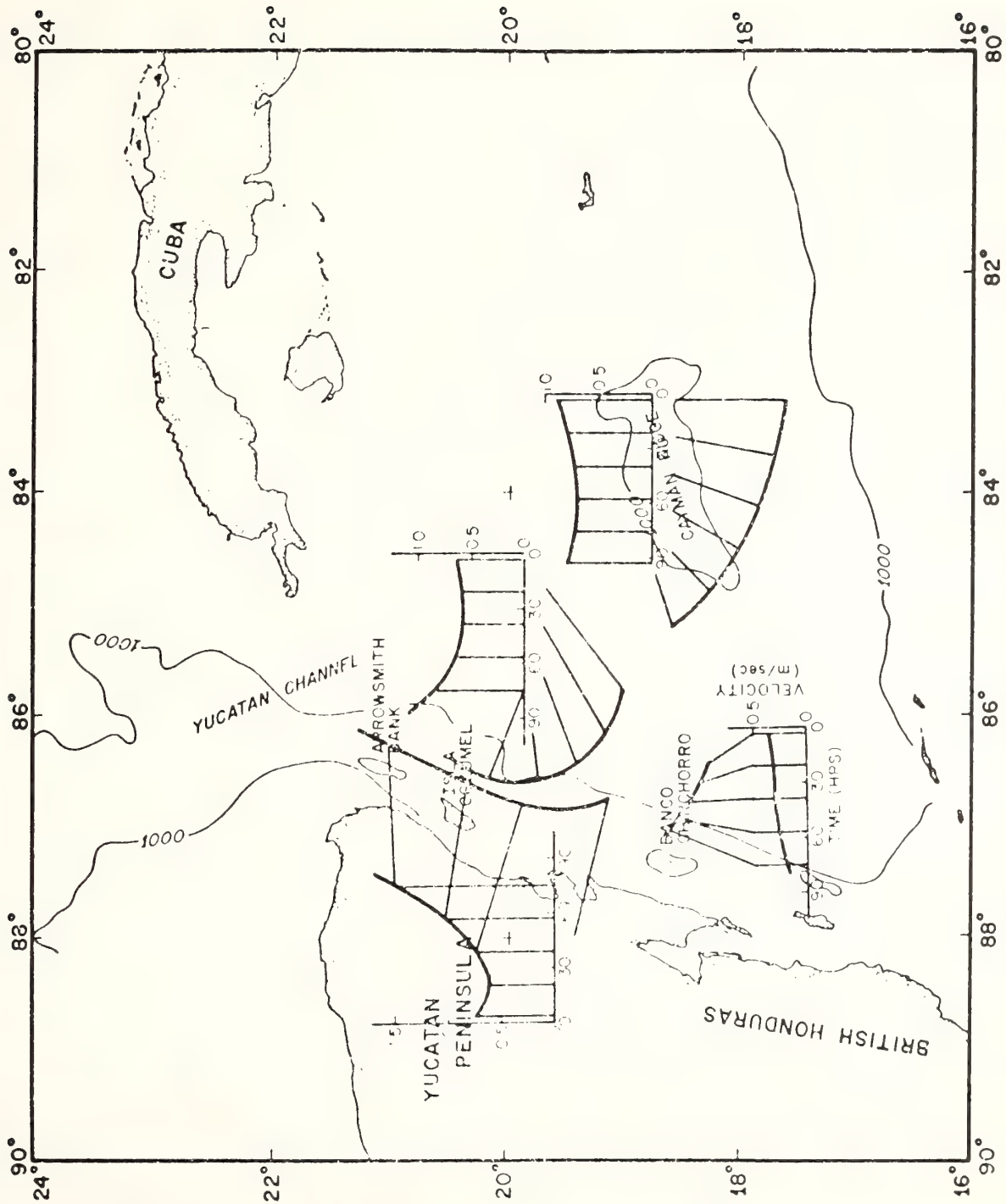


Figure 2.

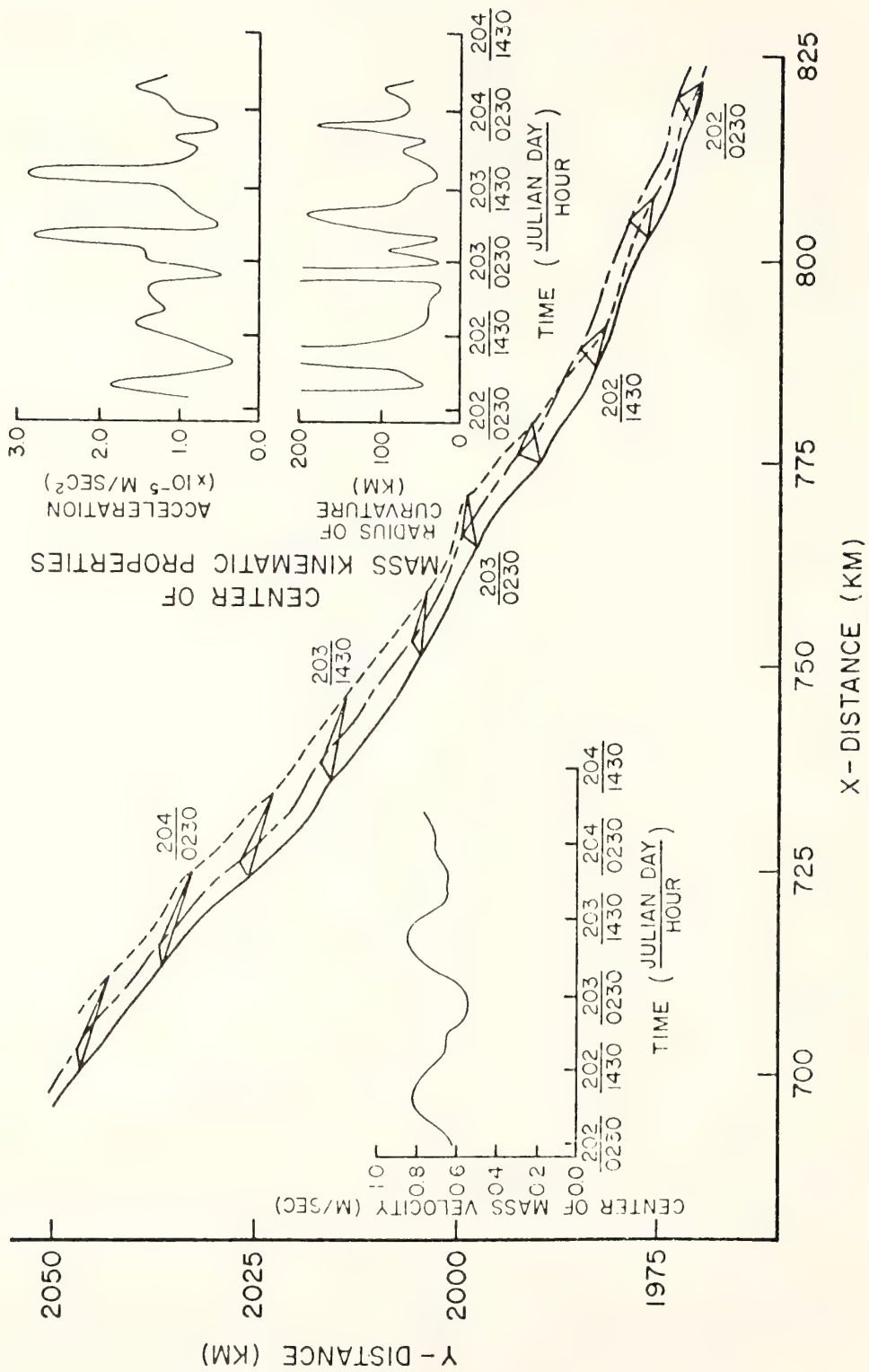


Figure 3.

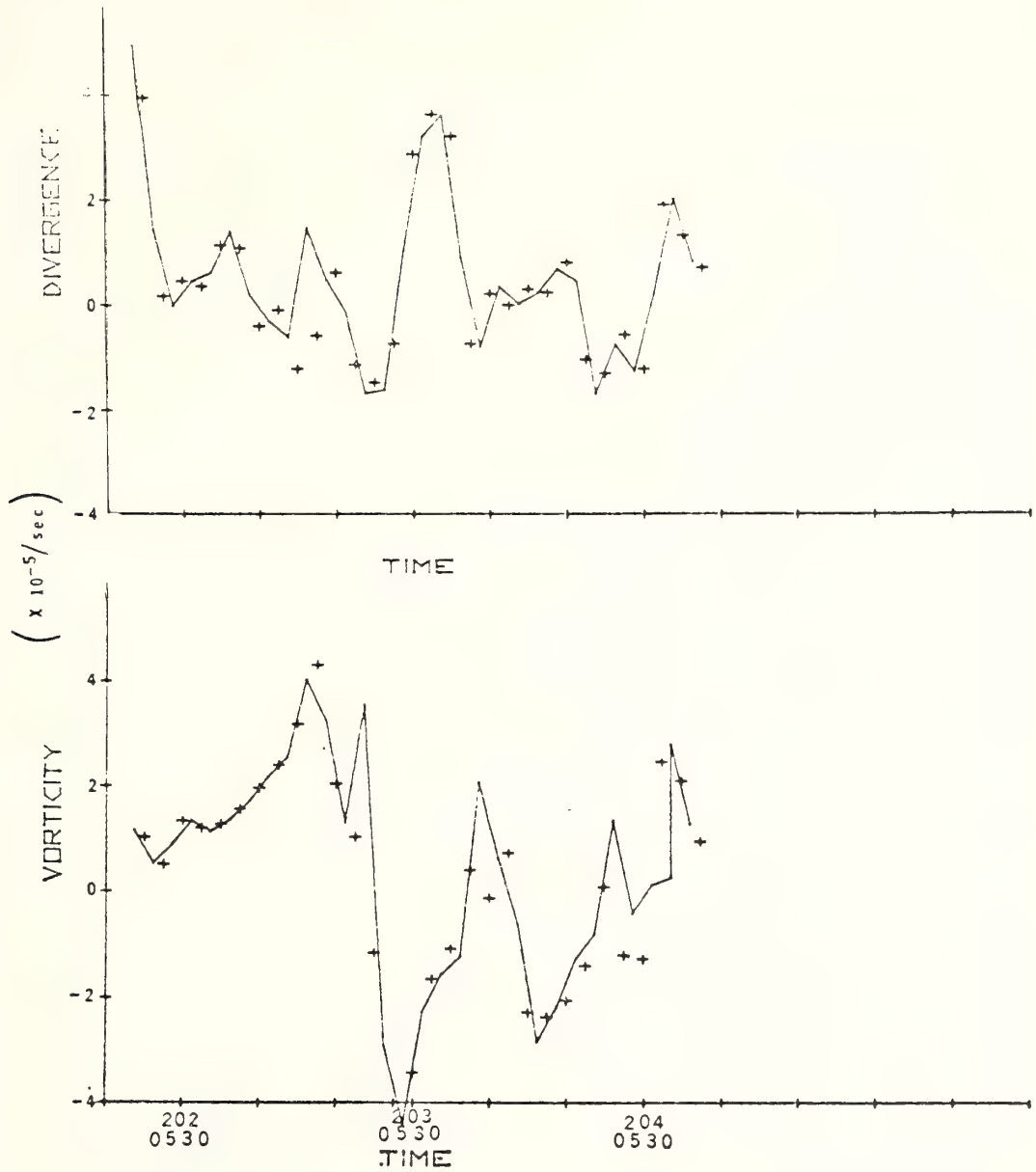


Figure 4.

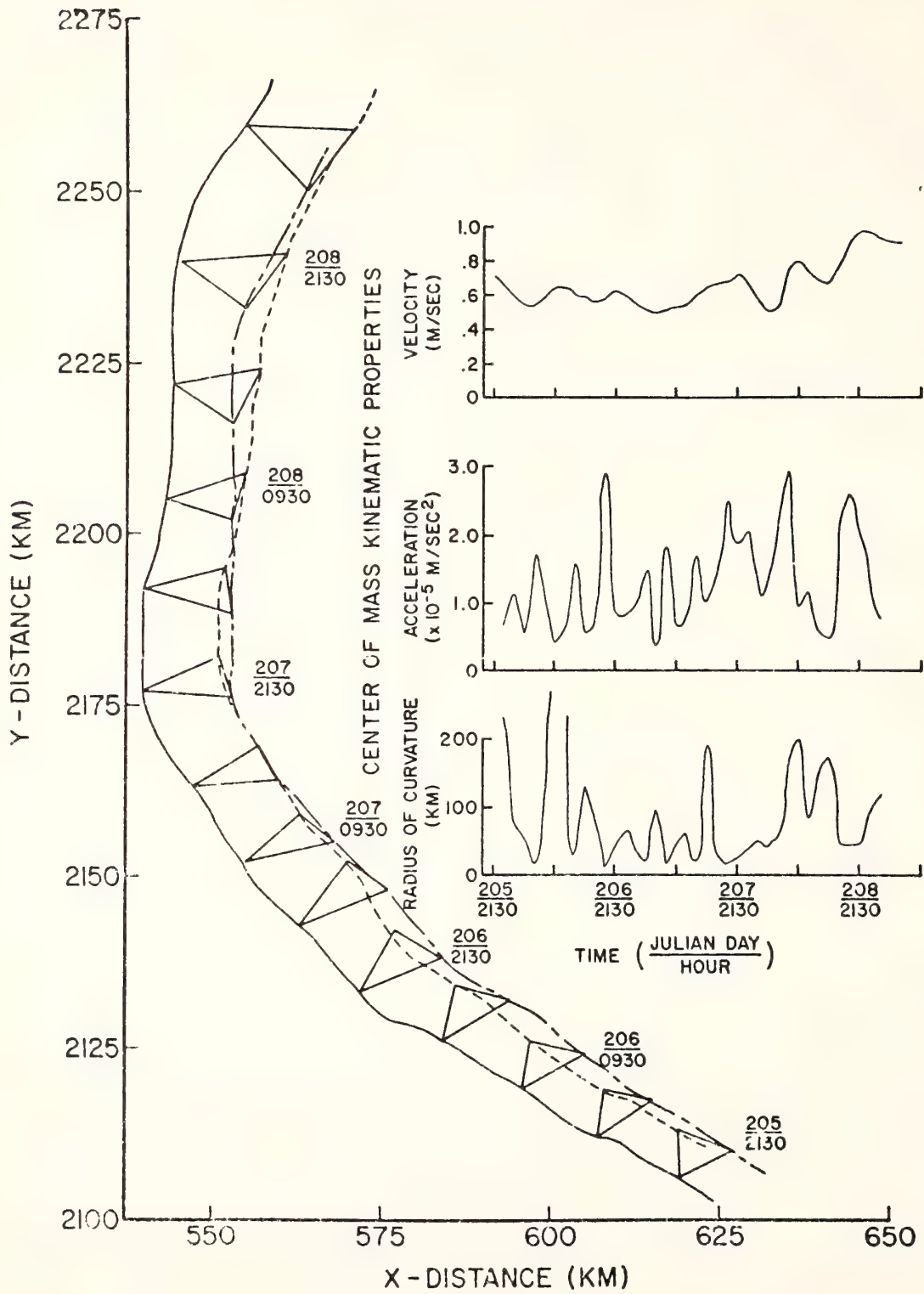


Figure 5.



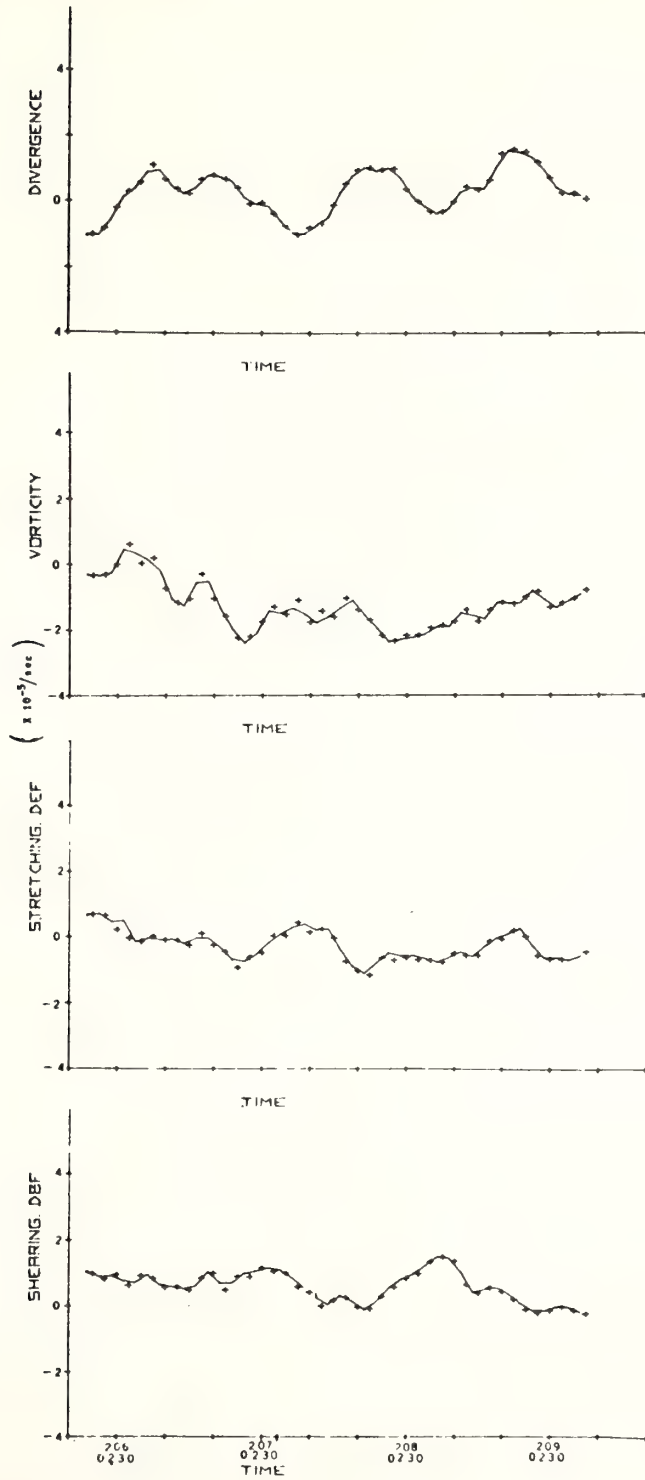


Figure 6.

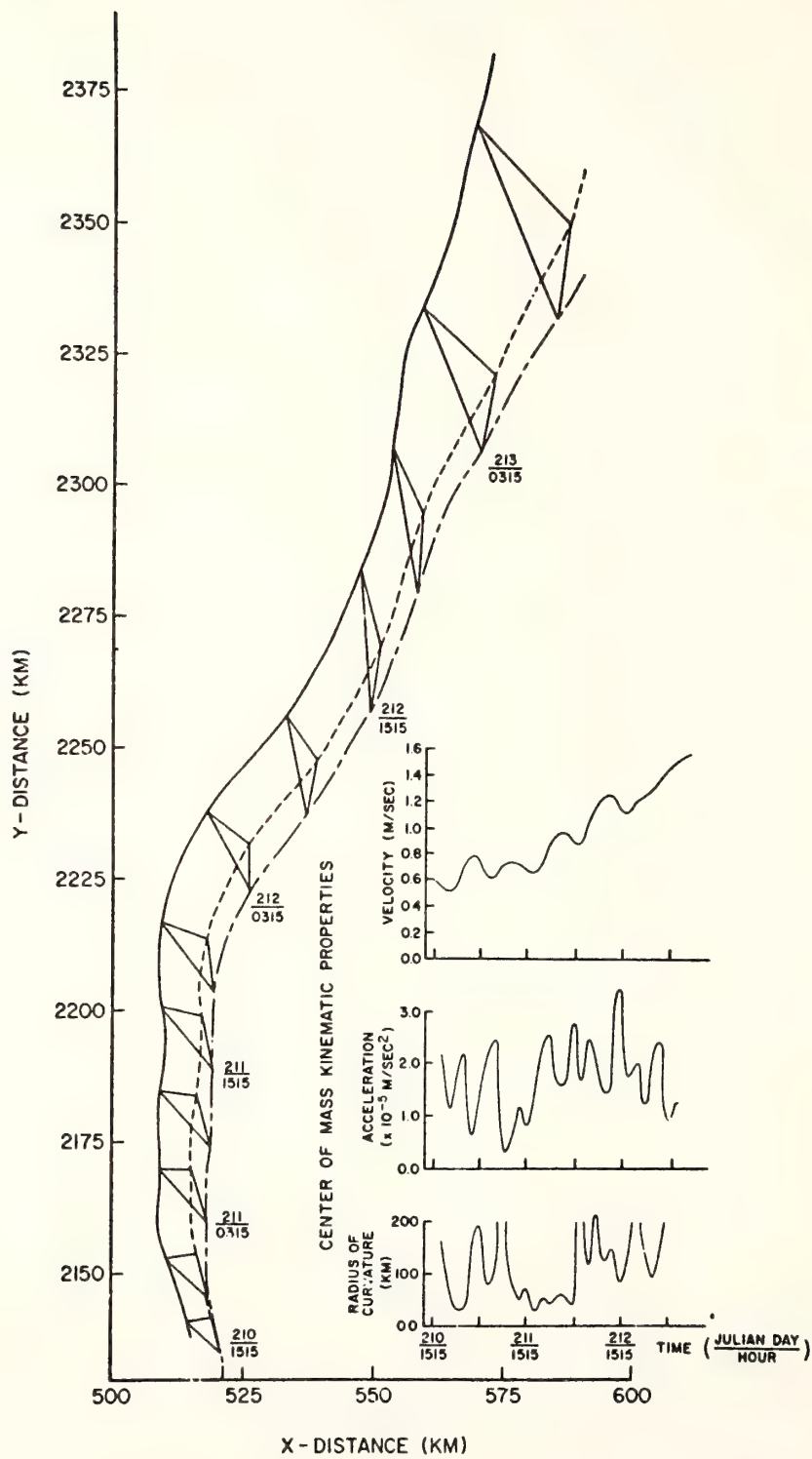


Figure 7.

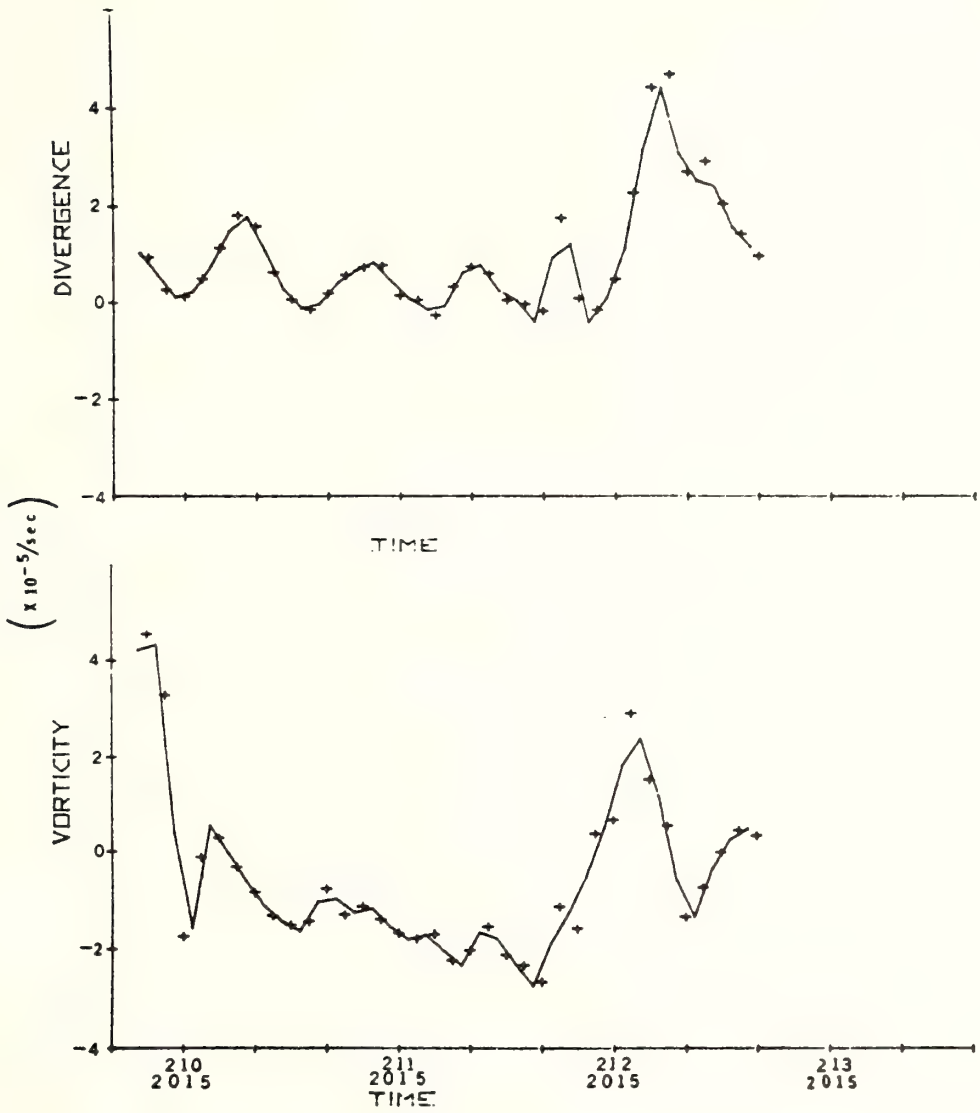


Figure 8.

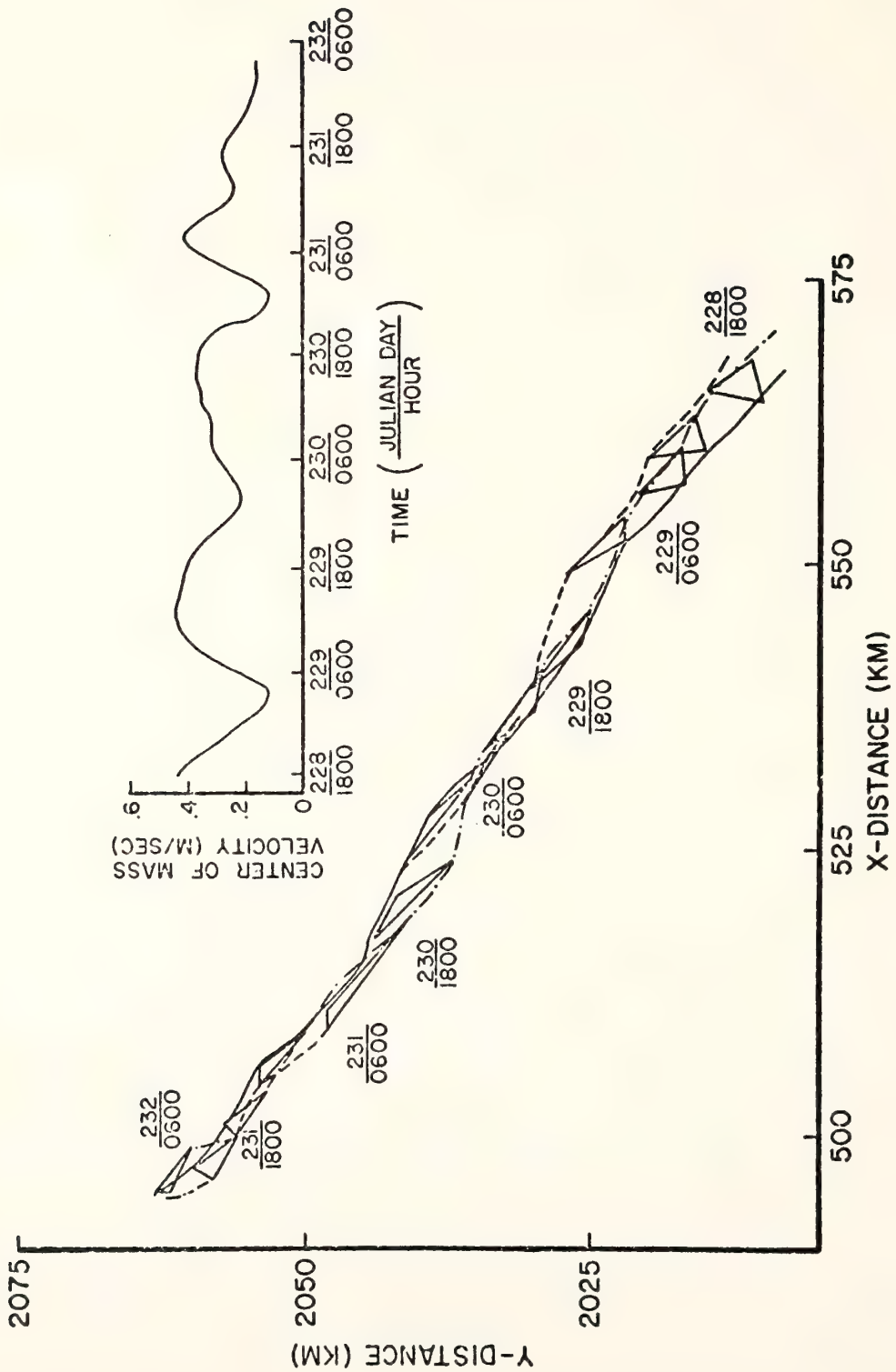


Figure 9.

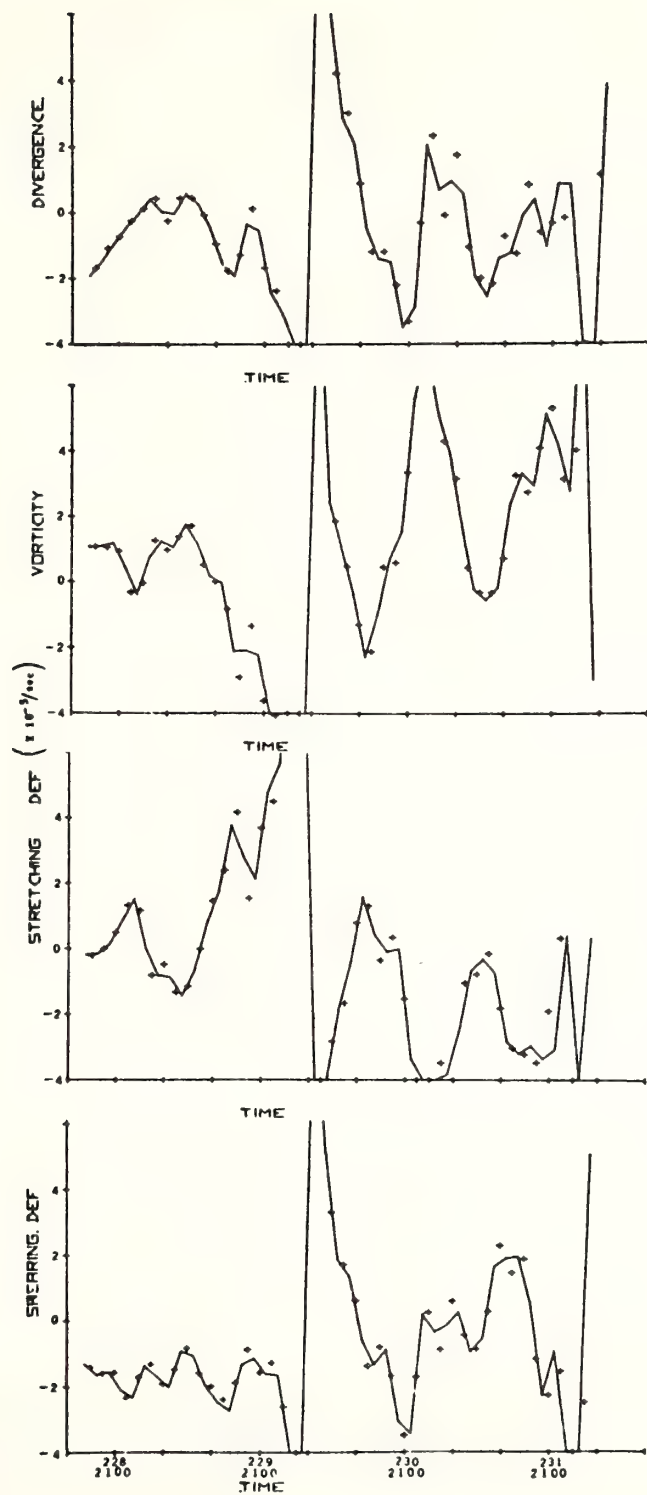


Figure 10.

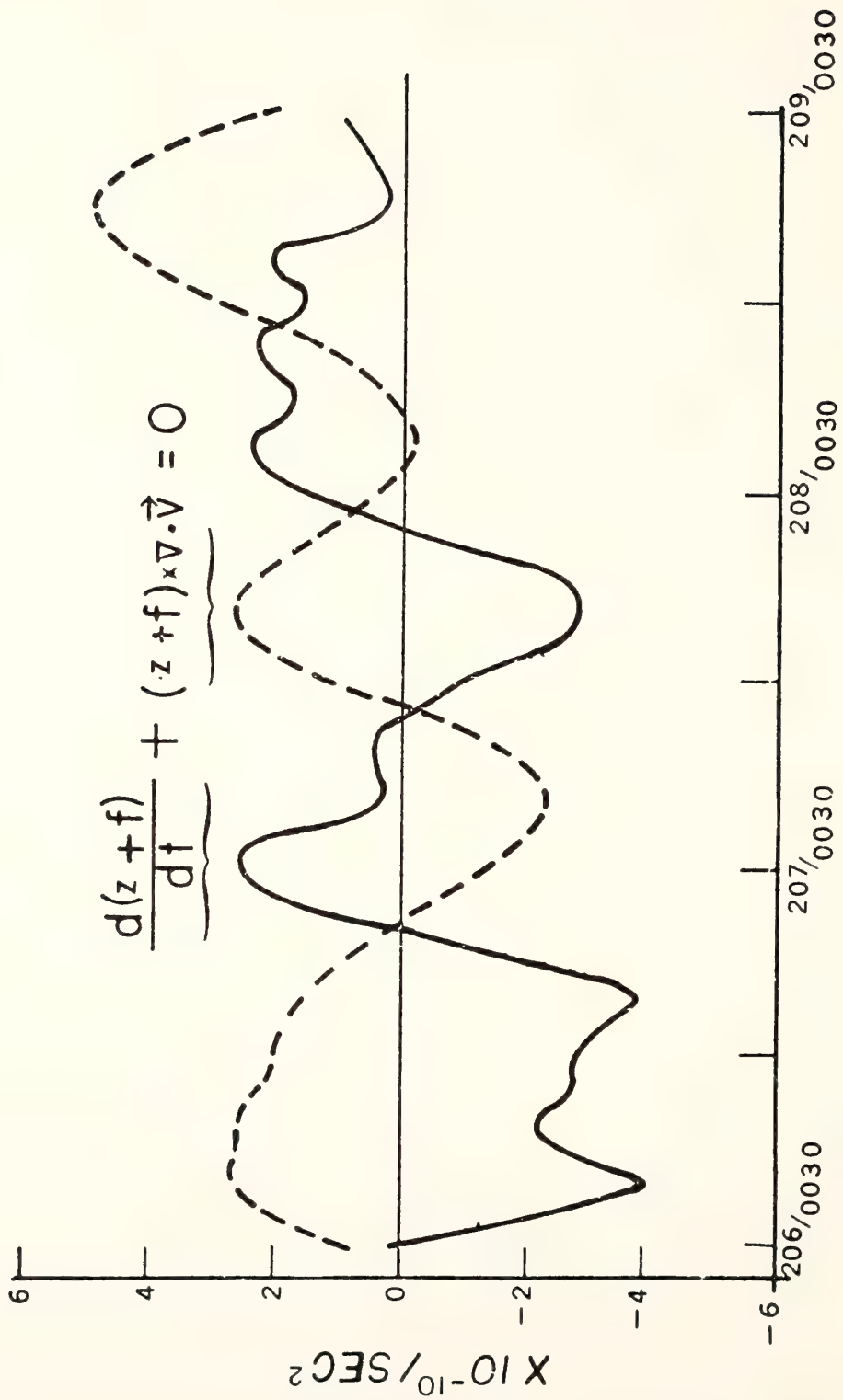


Figure 11.

Reprinted from: *NOAA Data Report ERL MESA-22*, 43 p.

#### ABSTRACT

During January 1975, an oceanographic cruise, denoted XWCC-1 was made by R/V *Advance II* in the New York Bight. The objective of the cruise was to supply data for analysis of the water characteristics in the New York Bight. This report presents the physical and chemical data from this cruise, and describes the parameters measured, the measurement methods, and the procedures for reducing the data.

Reprinted from JOURNAL OF PHYSICAL OCEANOGRAPHY, Vol. 6, No. 6, November 1976  
 American Meteorological Society  
 Printed in U. S. A.

## The Influence of Deep Mesoscale Eddies on Sea Surface Temperature in the North Atlantic Subtropical Convergence<sup>1</sup>

ARTHUR D. VOORHIS AND ELIZABETH H. SCHROEDER

*Woods Hole Oceanographic Institution, Woods Hole, Mass. 02543*

ANTS LEETMAA

*Atlantic Oceanographic and Meteorological Laboratory, NOAA, Miami, Fla. 33149*

(Manuscript received 24 February 1976, in revised form 8 July 1976)

### ABSTRACT

Maps of sea surface temperature in the North Atlantic subtropical convergence during the 1973 MODE field experiment (and recent satellite imagery) show large meridional and zonal features on a scale of 40–400 km which are superimposed on the seasonal meridional temperature gradient. After comparing these maps with dynamic topography relative to 1500 db it is argued that these features are mainly due to advective distortion by surface currents associated with the deep baroclinic mesoscale eddy field. Wind-induced surface currents appear to have a lesser effect in generating such structure. Surface frontogenesis observed during MODE and by earlier workers in the area suggests that jet-like shallow surface density currents may be also significant in advecting and distorting the surface temperature field on scales of 10 km and less. Finally, rough calculations indicate that these advective processes of the sea surface may supply annually an amount of heat to the surface water mass of the northern Sargasso Sea which is significant compared with that lost to the atmosphere.

### 1. Introduction

An important goal of contemporary oceanography is to understand the horizontal distributions of properties at the sea surface and the mechanisms that produce them. Major programs such as the North Pacific Experiment (NORPAX) in the United States and the Joint Air-Sea Interaction Experiment (JASIN) in the United Kingdom are actively working in this area. Although progress has been made in modeling the vertical structure of the upper ocean, much remains to be done in modeling its horizontal structure, particularly over intermediate oceanic scales of 100 to 500 km. Presented here are observations in the subtropical convergence of the western North Atlantic which provide a reasonably detailed look at one aspect of this problem.

The subtropical convergence is one of the classical transition zones (Wüst, 1928) separating two meteorological regimes. In the western North Atlantic it lies roughly between 22°N and 32°N latitude and separates the prevailing westerlies to the north from the easterly trades to the south. Maps of monthly mean sea surface temperature in this zone are relatively simple eastward of the Gulf Stream's influence. This can be seen in Fig. 1. In general, the temperature

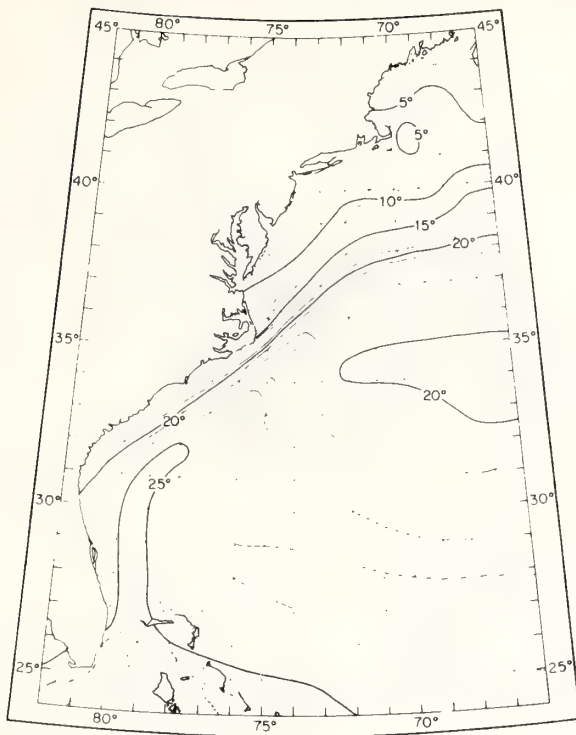
decreases northward at all times of the year by an amount which varies seasonally. The maximum meridional gradient occurs in late winter (approximately 0.5°C per degree of latitude) and the minimum in late summer (approximately 0.1°C per degree of latitude). The large-scale zonal temperature variation is small.

How does the synoptic temperature distribution, that is, the actual temperatures at any one time, differ from the above average picture? Surveys of thermal fronts in the area (Voorhis, 1969) suggested that major differences occurred on surprisingly large scales of hundreds of kilometers. More recent evidence comes from satellite infrared imagery of the sea surface, such as shown in Fig. 2. In this image the synoptic temperature is dominated by large meridional and zonal variations on the same scale. What is the reason for this large-scale structure?

Except for the *Aries* data (Crease, 1962) little was known about the sub-surface currents in this region until the Mid-Ocean Dynamics Experiment (MODE), which was conducted over a period of four months during the spring of 1973 in a 400 km square area centered at 28°09'N, 69°40'W. The principle finding from MODE was that subsurface currents were dominated by eddy-like motions, having spatial scales of several hundred kilometers and time scales (residence time) of two to three months, which were

<sup>1</sup> Contribution No. 3709 from the Woods Hole Oceanographic Institution.





APRIL 17,589 OBS  
AVERAGE SURFACE TEMPERATURES, °C

FIG. 1. Climatic mean April sea surface temperature in western North Atlantic after Schroeder (1966). MODE was conducted during March–April, 1963, in cross-hatched area.

nearly in geostrophic balance with vertical deformations of the main thermocline. We have collected all useful sea surface temperature measurements made during MODE and constructed maps which, in the following, are presented and compared with the surface geostrophic circulation. From this we argue that most of the large-scale synoptic surface temperature structure in the subtropical convergence is due directly to surface advection by the geostrophic eddy field.

## 2. The surface temperature field

MODE was designed to study deep currents and water structures and very little effort was expended in surface measurements. In addition, no adequate satellite thermal images of the surface were obtained during the experiment. Nevertheless, surface temperatures were recorded continuously from three ships<sup>2</sup> as they maneuvered about the area during the four months of the experiment. We have used these data plus that from CTD and STD casts to describe the large-scale evolution of the surface temperature field. In order to retain adequate spatial coverage, we chose

<sup>2</sup> R. V. *Chain* from the Woods Hole Oceanographic Institution, Woods Hole, Mass.; R. R. S. *Discovery* from the United Kingdom; and NOAA ship *Reseacher*.

to group the data in successive time periods of about 15 days. The spatial coverage during the period 31 March to 14 April, which was typical, is shown in the upper half of Fig. 5.

For each period the records of surface temperature were sub-sampled every 10 min to the nearest 0.2°C and plotted along the ship's tracks. These were combined with temperatures from the STD and CTD casts, which were also used to calibrate the surface temperature records. The total data set was then subjectively contoured by one of us (Schroeder) in half-degree intervals without any prior knowledge of the field of surface currents discussed in the next section. For the most part spurious spatial effects introduced by diurnal heating and cooling along the tracks of the moving ships could be recognized and eliminated in the contouring. Data were rejected, however, on about ten days when afternoon diurnal heating during calm weather exceeded 0.5°C. The resulting maps from 9 March through 13 July are shown in the upper part of each picture in Figs. 3 and 4.

The average surface temperature and its average meridional gradient over the MODE area were computed from each map and these are shown as a function of time in the lower half of Fig. 5. The spatially averaged temperature was close to its late winter minimum (approximately 22°C) at the start of the experiment. Thereafter it increased, due to surface heating, to almost 27°C at the end of the experiment. The average meridional gradient is, perhaps, not too meaningful because of the fluctuations introduced by eddy distortion in the MODE area. Nevertheless, it shows an overall decrease during the experiment from approximately 0.007 to 0.002°C km<sup>-1</sup>, with cooler water always to the north.

All of the temperature maps in Figs. 3 and 4 show a large, changing zonal and meridional structure superimposed on the mean meridional gradient. Usually, this structure is dominated by long intrusive features or tongues of alternate warm and cool water, 40–50 km wide, which can extend for distances of several hundred kilometers. The resemblance between the temperature pattern in most of these maps and that shown in the satellite image in Fig. 2 is remarkable.

## 3. Mesoscale eddy surface currents

The mesoscale eddy field found during MODE has been discussed by Robinson (1975), McWilliams (1976), and by other participants in the report of the MODE-I Dynamics Group (1975) cited in the references. The purpose here is to describe the motion of the sea surface in a way which allows one to see its effect on the distribution of surface temperature. Over 800 CTD, STD, and hydrographic lowerings were made during the experiment from the sea surface to depths greater than 2000 m. In addition, cur-

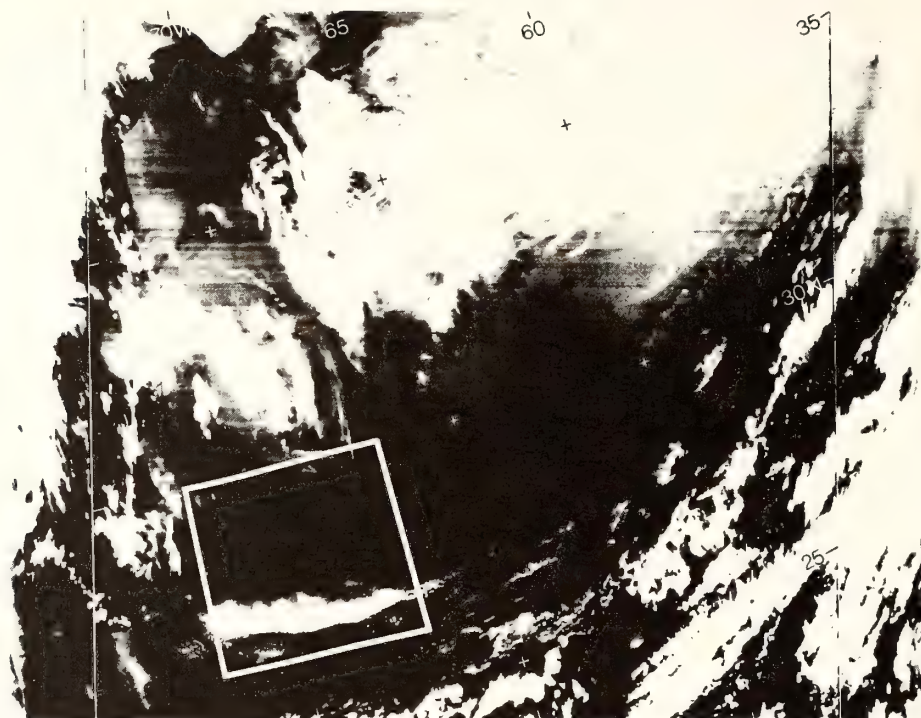


FIG. 2. Enhanced infrared satellite image of sea surface (courtesy of A. Strong and R. Legechis, NOAA/NESS, Suitland, Md.) showing large-scale advective patterns on 2 April 1974 along latitude 30°N in western North Atlantic. Dark areas are warm water, grey are cool water, and white are clouds. The warm water of the Gulf Stream appears all along the left on the image. MODE was conducted the previous year in the outlined quadrangle.

rents were measured extensively at depths below 400 m, primarily by moored current meters and by drifting neutral buoyant floats. These currents, when averaged over a period of several days, have been shown by Bryden (1974) to be in geostrophic equilibrium with the density field within the limits imposed by measurement noise. Furthermore, the vertical structure of these time-averaged currents is highly baroclinic, with most of the eddy energy confined to the main thermocline and above. One concludes, in fact, from the analysis of Schmitz *et al.* (1976) that about 80% of the geostrophic surface current is, on average, due to density structure above 1500 m. To describe the eddy surface motion, therefore, we computed the dynamic height of the sea surface relative to 1500 db from the CTD and STD data and constructed the maps of dynamic topography (in meters) shown by the solid contours in the lower portion of each picture in Figs. 3 and 4. The mapping time interval was chosen to be the same as that for the accompanying surface temperature maps. For each map the direction of geostrophic current is indicated by the arrows and the magnitude can be estimated from the geostrophic speed scale shown. The positions of the CTD and STD stations are given by small dots. The maps were contoured by computer in intervals of 4 dyn cm using an objective analysis program which smoothed

the dynamic heights over a space scale of 60 km and a time scale of 30 days. The ability of the contours to resolve the spatial structure of the field depends on the density of the station data. Near the map centers about 80% of the total dynamic height variance has been resolved. On the map periphery the resolution is much poorer, only 20 to 30% of the variance being resolved.

The sequence in Figs. 3 and 4 shows a slowly moving, close-packed array of cyclonic and anticyclonic surface pressure disturbances having a spatial periodicity of about 400 km (eddy diameter of 200 km) and an amplitude of about 0.1 dyn m. The field is clearly irregular and unsteady. Features on scales of several hundred kilometers tend to persist throughout the mapping sequence (4 months) while on the smallest scale (60 km) they cannot be traced from one map to another (15 days). In March the center of the MODE area appears to be in a saddle between two high pressure cells (anticyclonic eddies) to the east and west and two low pressure cells (cyclonic eddies) to the north and south. The eastern anticyclonic eddy moves into the center during the first half of April and then enlarges and dominates the MODE area until the end of June. During this period it slowly drifts westward, moving out of the area in the first half of July at the end of MODE.

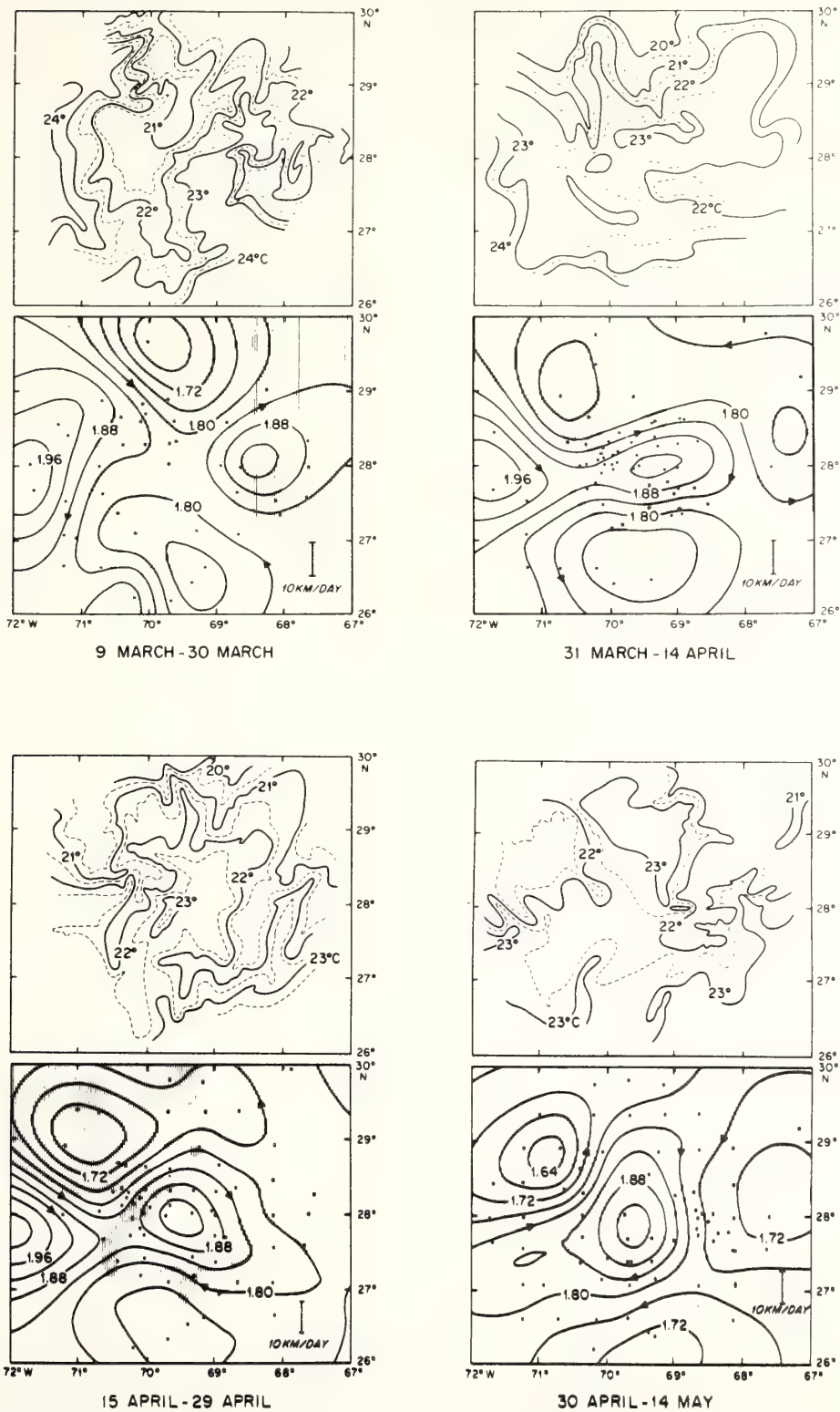


FIG. 3. Sea surface temperature maps (upper) and surface dynamic topography (lower), relative to 1500 db, of the MODE area for four successive periods in the first half of the experiment. The cross-hatched area on the maps of dynamic height show all surface water cooler than the mean for that period.

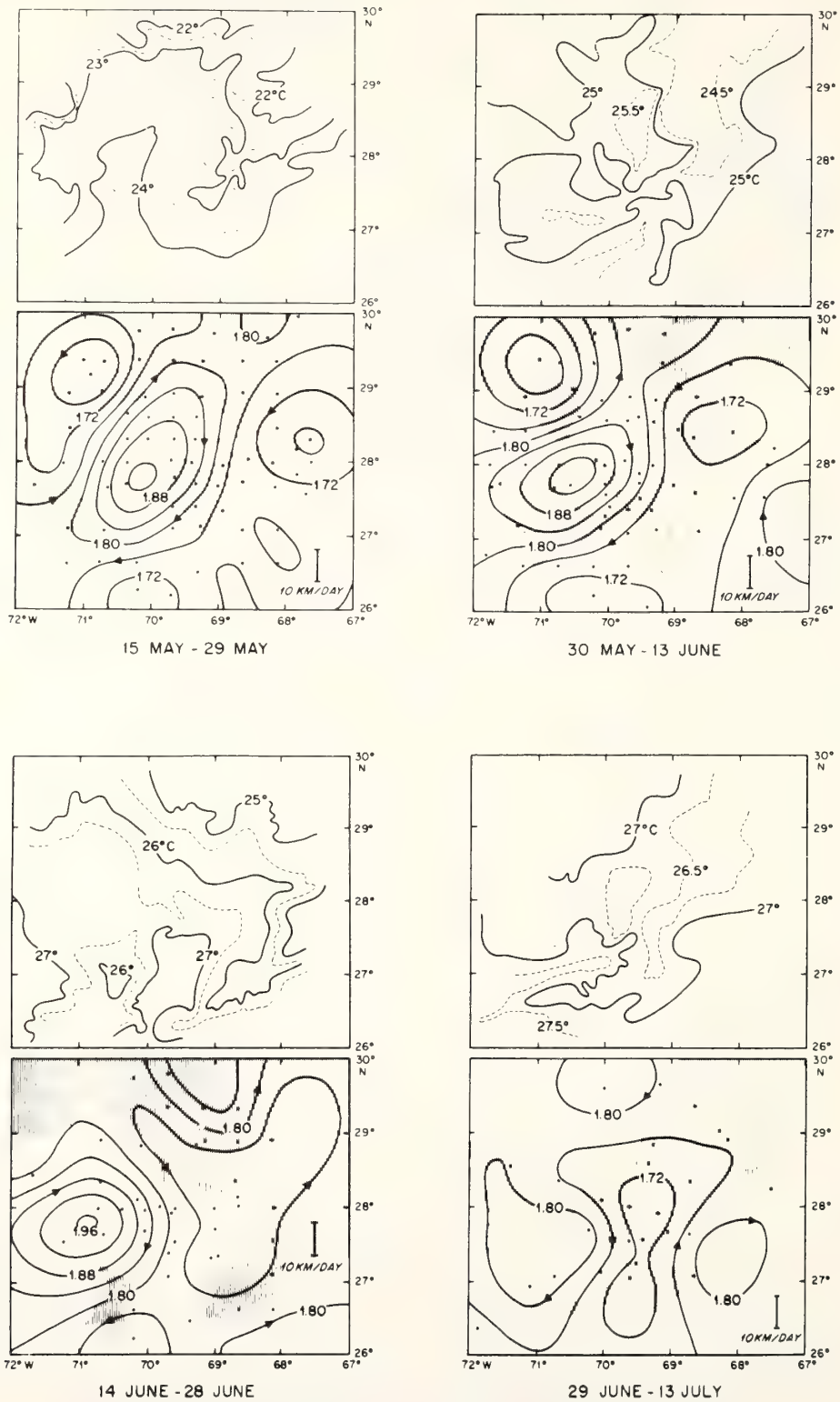


FIG. 4. As in Fig. 3 except for the second half of the experiment.

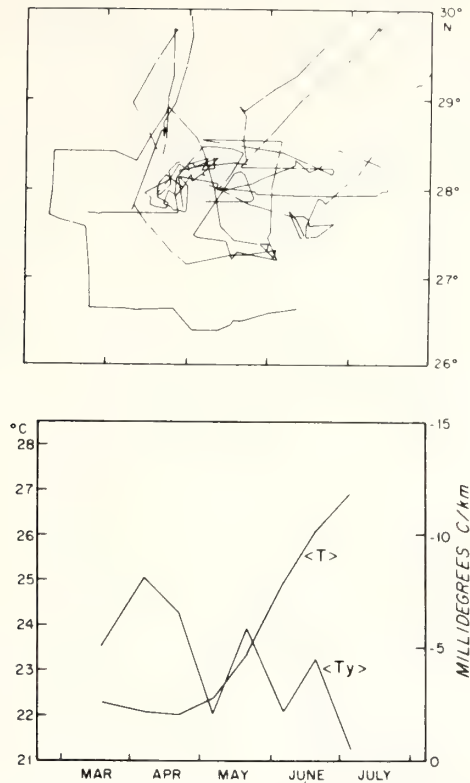


FIG. 5. (Upper) Ships tracks showing typical spatial coverage used to construct temperature maps in Figs. 3 and 4. (Lower) Mean temperature ( $T$ ) and mean meridional temperature gradient ( $T_y$ ) averaged over MODE area as a function of time during the experiment.

Geostrophic surface currents in the maps vary in speed from zero at the eddy centers to as high as  $30 \text{ km day}^{-1}$  in the high-gradient regions between the eddies. The latter is undoubtedly limited by resolution. The average speed around the periphery of an eddy is about  $20 \text{ km day}^{-1}$ . If an eddy were stationary it would take about one month for surface water to go around it once at this speed.

#### 4. Surface temperature advection

By comparing maps in Figs. 3 and 4 it becomes very clear that large-scale features in the surface temperature field are due primarily to eddy surface currents which advectively distort the mean meridional gradient.<sup>3</sup> To facilitate this comparison we have cross-hatched on the maps of dynamic topography all those areas of the sea surface which are cooler than the mean temperature of the corresponding temperature map. Note, in particular, the situation during the period 9–30 March in Fig. 3. Here, the interplay be-

<sup>3</sup> Ideally one would like to quantify this statement by numerical correlation between temperature and eddy fields. The density of our data set is not high enough, unfortunately, to make such a correlation statistically significant.

tween four apparent eddies advects southward a 200–300 km tongue of cool northern water along longitude  $70^{\circ}30'W$ , and advects northward a similar tongue of warm southern water along  $69^{\circ}00'W$ . Similar patterns occur in the other maps. At times, isolated pools of warm water (30 April–14 May) or cool water (14 June–28 June) are formed as a result of the eddy currents.

Important changes can occur within the mapping periods of Figs. 3 and 4. It is possible to examine some of this in more detail on a one-week time scale by examining selected STD data. These fields are shown for the weeks of 14 May and 21 May in Fig. 6. The temperature pattern at a depth of 50 m looks very similar to the surface pattern for the same time in Fig. 4. Two tongues of water are evident, a warm tongue extending to the north, and a developing cold tongue extending to the south. Even on a weekly time scale considerable changes occur (in both the depicted fields). It is interesting to note that the temperature field is asymmetric relative to the dynamic topography. The warm tongue sits over the eddy defined by closed contours of dynamic height, suggesting a recirculation of the warm waters within the tongue. The cold tongue, however, is situated over dynamic height contours that do not close.

In general, surface isotherms do not coincide on the large scale with contours of dynamic height. The pattern of the first is intrusive or finger-like while the second is circular or eddy-like. This is in direct contrast with the deep horizontal temperature structure in the main thermocline where the patterns were remarkably similar, with cyclonic eddies having cool centers and anticyclonic eddies warm centers.

The anomalous surface temperature structure in our maps extends at least over a decade of decreasing scales, from 400 km down to the order of 40 km. The former corresponds to the average wavelength between eddies and the latter is typical of the width of the long intrusions of warm and cool water. (Features on a smaller scale, although occasionally resolved, were likely to be advected and distorted beyond recognition in the mapping intervals.) Over this range it is reasonable to suppose that temperature variance is extracted from the mean meridional temperature gradient at the large scale and cascades to the small scales. The Lagrangian time for this cascade would depend on how quickly the surface currents can distort the temperature field. From the spatial structure on the maps of dynamic height one estimates that large temperature features are stretched and thinned by a factor of 2 in a period of 5 days to a week. Hence, one estimates that the long intrusions are formed in 15 to 30 days, that is, in the time required for surface water to move one-half to once around the periphery of a typical eddy.

The above cascade extends to much smaller scales than those resolved in our maps. The most obvious

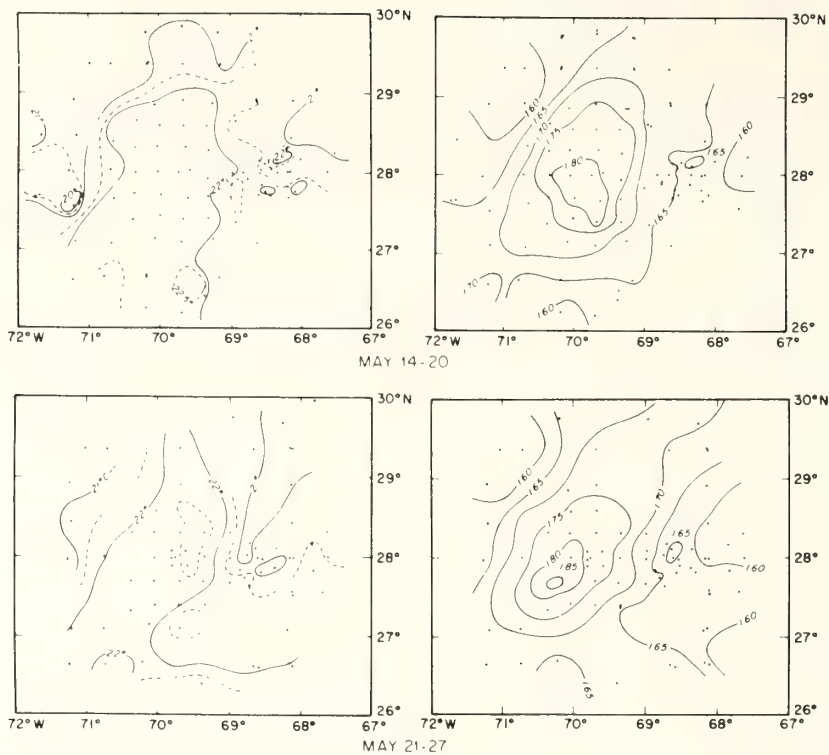


FIG. 6. Temperature maps at 50 m (left) and dynamic topography (right), relative to 1500 db, of the MODE area for two successive weekly periods.

of such features observed during MODE were those associated with surface frontogenesis. Voorhis and Hersey (1964), Voorhis (1969) and Katz (1969) had shown prior to MODE that these surface fronts are very narrow transition zones separating adjacent surface water masses of different temperatures, salinities and densities which can meander along the sea surface for distances of several hundred kilometers. Surface temperature changes of 1–2°C are frequently observed across a front in a distance of only 100 to 200 m. Beneath the surface a frontal pycnocline slopes downward beneath the lighter water and becomes level in a horizontal distance of the order of 10 km and at depths usually of the order of 100 to 200 m, although occasionally it is much deeper. Associated with the sloping pycnocline is a geostrophic current jet flowing along the front with surface speeds as large as 50 to 100  $\text{cm s}^{-1}$ .

The continuous shipboard records of surface temperature from MODE showed numerous frontal crossings along the boundaries of the long intrusive warm and cool tongues in Figs. 3 and 4, and fronts were frequently seen in these areas by the high concentrations of surface debris. The nature of the program and the haphazard sampling, however, made it impossible to map particular frontal features. It is significant, however, that a synoptic image of the surface temperature field from a satellite (Fig. 2)

usually shows the boundaries between the intrusive tongues to be much sharper (greater thermal gradients) than in our 7–15 day maps. We suggest that frontogenesis is common along these boundaries and that frontal currents may contribute an important near surface circulation *around* the boundaries of the long intrusive features which is superimposed on broader scale eddy surface currents along their axis.

### 5. Surface wind drift

We have so far neglected the advection and distortion of surface temperature structure by surface currents other than those due to mesoscale eddies or possible near surface geostrophic currents associated with frontogenesis. The most important of the former are the shallow surface currents driven by wind stress.

During MODE all ships routinely reported wind speed and direction once daily. The weather from March through mid-May was dominated by a succession of moderate high and low pressure disturbance every 5 to 10 days with mainly veering winds which varied in speed from less than 1  $\text{m s}^{-1}$  to no more than 15  $\text{m s}^{-1}$ . Conditions were somewhat steadier from mid-May onward with disturbance every 10 to 15 days. The wind backed and veered with maximum speeds less than 10  $\text{m s}^{-1}$ .

Surface drift current was computed using the model of Gonella (1971), which assumes an Ekman current

TABLE 1. Mean surface stress magnitude ( $\tau$ ) and direction ( $\phi$ ) computed from observed wind speed and direction, assuming a drag coefficient of  $1.2 \times 10^{-3}$ ; mean mixed layer depth ( $h$ ) from CTD observations; and mean surface wind drift speed ( $\Gamma$ ) and direction ( $\theta$ ) computed from Gonella (1971), assuming an eddy viscosity of  $10^2 \text{ cm}^2 \text{ s}^{-1}$ .

Period	$\tau$ ( $\text{dyn cm}^{-2}$ )*	$\phi$ ( $^{\circ}\text{T}$ )	$h$ (m)	$\Gamma$ ( $\text{km day}^{-1}$ )	$\theta$ ( $^{\circ}\text{T}$ )
9 Mar–30 Mar	0.16	68	38	1.7	115
31 Mar–14 Apr	0.30	37	34	3.1	81
15 Apr–29 Apr	0.82	260	48	8.5	305
30 Apr–14 May	0.40	260	28	4.1	305
15 May–29 May	0.26	353	11	3.2	68
30 May–13 June	0.50	261	13	6.1	335
14 Jun–28 Jun	0.21	329	12	3.1	36
29 Jun–13 Jul	0.20	323	11	3.0	33
Mode mean	0.20	293	25	2.2	356

\*  $1 \text{ dyn cm}^{-2} = 0.1 \text{ N m}^{-2}$ .

completely confined to the surface mixed layer (zero stress at the bottom of the layer). The surface stress was determined from the usual relation  $C\rho_A|\mathbf{V}_W|\mathbf{V}_W$ , where  $\mathbf{V}_W$  is the reported wind velocity,  $\rho_A$  is the standard air density ( $1.2 \times 10^{-3} \text{ g cm}^{-3}$ ), and  $C$  is a drag coefficient taken to be  $1.2 \times 10^{-3}$ . From Gonella (1971) we assumed a constant and conservative value of  $10^2 \text{ cm}^2 \text{ s}^{-1}$  for the eddy coefficient of viscosity in the layer. A larger viscosity will reduce the currents, but not less than about 25% of the values computed. A smaller value will increase the current (by a factor roughly proportional to the inverse square root of the viscosity).

In Table 1 we have listed the spatially averaged net vector wind stress and surface drift current for each of the mapping intervals in Figs. 3 and 4. Also shown is the average depth of the mixed layer, which clearly shows the effect of decreasing wind stress and increasing surface heating over the duration of MODE. The computed currents are all less than  $10 \text{ km day}^{-1}$  and except for the two periods 15 April–29 April and 30 May–13 June, when there were periods of persistent wind direction, less than  $5 \text{ km day}^{-1}$ . It is apparent, therefore, from the maps of dynamic height (Figs. 3 and 4) that advection by the eddy surface currents (of order  $20 \text{ km day}^{-1}$ ) around the periphery of the eddies dominates the surface wind drift. The latter, however, is significant over large areas where there is little relief in the dynamic topography. The average surface displacement due to the wind drift was approximately  $60 \text{ km}$  per mapping interval.

Also shown in Table 1 is the net vector wind stress and surface current over the entire 127 days of MODE. The stress is quite comparable in magnitude and direction to the typical long-term stress in the MODE area computed by Saunders (1976) for the years 1959–1971. The overall surface drift is predominantly northward and the total northward volume transport,

computed from the surface stress, is  $2.6 \times 10^3 \text{ m}^3 \text{ s}^{-1}$  across each kilometer in an east–west direction.

The spatial variation of surface wind drift contributes, of course, to the distortion of surface temperature structure. Superficially it appeared small because the reported daily wind speed and direction were remarkably similar from ship to ship. Nevertheless, there were differences. By comparing wind data from one ship to another we found over an average horizontal scale of  $100 \text{ km}$  that there were variations of net surface drift speed of about  $\frac{1}{3}$  the spatially averaged value in Table 1, and variations of drift direction of about  $\pm 20^{\circ}$ . The distortion of surface temperature features by such variations is an order of magnitude less important than that due to the spatial variations of the eddy surface currents. We tentatively conclude, therefore, that the dominant effect of the surface wind drift is to shift but not distort the temperature pattern shown in Figs. 3 and 4 according to the drift currents in Table 1.

## 6. Conclusions and discussion

In the MODE area we conclude that the surface temperature field, on time scales less than about one month and over space scales from  $400$  to about  $40 \text{ km}$ , tags primarily the surface currents associated with the baroclinic mesoscale eddy field of the main thermocline. Surface currents induced by wind stress appear to be of secondary importance in generating spatial structure in this scale range. Relatively little can be said about scales less than  $40 \text{ km}$ . However, there is some evidence from MODE but mostly from previous measurements in the same area that much of the spatial structure on scales less than about  $10 \text{ km}^2$  tags not only the mesoscale current field but also a relatively shallow field of currents which are in geostrophic equilibrium with horizontal density gradients in the near surface layers. This new field of currents is often jet-like and is associated with surface frontogenesis.

Mesoscale eddies appear to be an effective mechanism for stirring the large-scale thermal (and haline) field imposed on the near surface layers by the atmosphere. One can speculate that this surface process on an eddy time scale may generate a net meridional heat transport in the surface layer on a longer time scale. For example, if a single anticyclonic eddy develops in the convergence zone one would expect warm water to move initially northward on its western side and cool water southward on its eastern side. (The flows will change sides if the eddy is cyclonic.) In time both flows will simply circulate in a complex manner around the eddy with a great deal of stirring but no net heat transport if there is no heat exchange between the warm and cool water. However, if there

<sup>4</sup> It is significant that this scale is of the order of the internal radius of deformation of the near-surface pycnocline.

are many eddies, which are evolving, moving and decaying, it is highly likely that surface water is exchanged<sup>5</sup> from eddy to eddy and one might expect to observe at times long tongues of warm and cool surface water running north and south. This is very similar to what one sees in Fig. 2. The result would be a mean meridional heat transport northward in the MODE area of the order of  $VH$  per eddy, where  $V$  is the geostrophic advecting surface velocity, and  $H$  is the anomalous heat carried by each tongue. The latter can be approximated by  $\rho_w C_p D L \Delta T$ , where  $\Delta T$  is the temperature difference between north and south flowing tongues,  $L$  is the zonal width of the tongue, and  $D$  is the depth of the heat anomaly. Representative values for these parameters are  $V=20$  cm s<sup>-1</sup>,  $\rho_w=1$  g cm<sup>-3</sup>,  $C_p=4.18$  J g<sup>-1</sup> K<sup>-1</sup>,  $D=50$  m,  $L=100$  km,  $\Delta T=2^\circ\text{C}$ . Using these values one computes a transport of  $8.2 \times 10^{12}$  W per eddy. Taking 200 km as a mean zonal spacing between eddies one finds a northward eddy heat transport of  $4.2 \times 10^{10}$  W across each kilometer in an east-west direction. Assuming the northern Sargasso Sea to be bounded on the north and west by the Gulf Stream, on the east by 50°W longitude, and on the south by 30°N latitude, one computes an annual heat input of  $32 \times 10^{20}$  J across its southern boundary (length 2400 km) by the eddy mechanism. This is of the same order as the annual heat loss to the atmosphere across its surface area ( $2.2 \times 10^6$  km<sup>2</sup>) computed from Bunker and Worthington (1976), using an average net heat surface flux of  $66$  W m<sup>-2</sup> ( $50$  kcal cm<sup>-2</sup> year<sup>-1</sup>). Speculating on a still larger scale and assuming that the observed mesoscale eddy activity extends across both the northern Atlantic and Pacific Oceans at mid-latitudes, a total distance of the order of  $1.6 \times 10^4$  km, one finds an annual poleward heat transport by the eddies at these latitudes of the order of  $6.8 \times 10^{14}$  W. This can be compared with the annual oceanic poleward energy transport of about  $22.6 \times 10^{14}$  W ( $1.7 \times 10^{22}$  cal year<sup>-1</sup>) estimated by Vonder Haar and Oort (1973). Considering the uncertainties in all of these estimates one concludes that the mesoscale eddy heat transport may not be inconsequential.

Finally, our results can have important implications for oceanographers and meteorologists interested in annual or longer term changes in sea surface temperature and their effect on world climate. The fluctuating mesoscale temperature field is unwanted noise from their point of view and introduces an uncertainty to estimates of mean temperatures. For data collected from a fixed point (or within an eddy radius of this point) this uncertainty is of the order of  $\langle \Delta T_e \rangle / \sqrt{n}$ , where  $\langle \Delta T_e \rangle$  is the rms temperature change due to a typical eddy, and  $n$  is the number of eddy events

in the averaging time. Assuming  $\langle \Delta T_e \rangle \approx 0.5^\circ\text{C}$  and no other sources of noise, one would have to average over 25 eddy events in the MODE area in order to resolve a climatic  $0.1^\circ\text{C}$  change in mean surface temperature. If the eddy residence time is of the order of 2 months this would take 4 to 5 years.

*Acknowledgments.* This work was supported by the Office of Naval Research under Contract N00014-74-C-0262, NR 083-004 and by the Office of the International Decade for Ocean Exploration of the National Science Foundation under Funding Agreement AG-385.

The data used in this paper were collected and processed by many people in the MODE program and the authors wish to acknowledge all of this work and to express their gratitude. We would also like to thank N. Fofonoff of the Woods Hole Oceanographic Institution, Woods Hole, Mass., who programmed and computed the objective maps of dynamic height in Figs. 3 and 4.

#### REFERENCES

- Bryden, H. L., 1974: Geostrophic comparisons using moored measurements of current and temperature. *Nature*, **251**, 409-410.
- Bunker, A. F., and L. V. Worthington, 1976: Energy exchange charts of the North Atlantic Ocean. *Bull. Amer. Meteor. Soc.*, **57**, 670-678.
- Crease, J., 1962: Velocity measurements in the deep water of the western North Atlantic. *J. Geophys. Res.*, **67**, 3173-3176.
- Dynamics and the Analysis of MODE-1, March 1975: Report of the MODE-1 dynamics group (unpublished manuscript). [The MODE Executive Office, 54-1417, M.I.T., Cambridge, Mass. 02139.]
- Gonella, J., 1971: The drift current from observations made on the Bouée-Laboratoire. *Cah. Oceanogr.*, **23**, 1-15.
- Katz, E. J., 1969: Further study of a front in the Sargasso Sea. *Tellus*, **21**, 259-269.
- McWilliams, J. C., 1976: Maps from the Mid-Ocean Dynamics Experiment. I. Geostrophic streamfunction. *J. Phys. Oceanogr.* (accepted for publication).
- Robinson, A. R., 1975: The variability of ocean currents. *Rev. Geophys. Space Phys.*, **13**, 598-601.
- Saunders, P. M., 1976: On the uncertainty of wind stress curl calculations. *J. Mar. Res.* (submitted for publication).
- Schmitz, W. J., J. R. Luyten, R. E. Payne, R. H. Heinmiller, G. H. Volkmann, G. H. Tupper, J. P. Dean and R. G. Walden, 1976: A description of recent exploration of the eddy field in the western North Atlantic with a discussion of Knorr Cruise 49. WHOI Tech. Rep. (to be published).
- Schroeder, E. H., 1966: Average surface temperatures of the western North Atlantic. *Bull. Mar. Sci.*, **16**, 302-323.
- Vonder Haar, T. H., and A. H. Oort, 1973: New estimate of annual poleward energy transport by Northern Hemisphere oceans. *J. Phys. Oceanogr.*, **3**, 169-172.
- Voorhis, A. D., 1969: The horizontal extent and persistence of thermal fronts in the Sargasso Sea. *Deep-Sea Res.*, **16**, 331-337.
- and J. B. Hersey, 1964: Oceanic thermal fronts in the Sargasso Sea. *Deep-Sea Res.*, **69**, 3809-3814.
- Wüst, G., 1928: Der Ursprung der atlantischen Tiefenwasser. *Z. Ges. Erdk. Berl.*, Sonderband zur Hundertjahrfeier, 506-534.

<sup>5</sup> This may be greatly enhanced by the unusually strong surface currents associated with surface frontogenesis.



Reprinted from: *Marine Geotechnology*, Vol. 1, No. 4, 327-335.

## Initial Results and Progress of the Mississippi Delta Sediment Pore Water Pressure Experiment

RICHARD H. BENNETT,\* WILLIAM R. BRYANT,†  
WAYNE A. DUNLAP,† AND GEORGE H. KELLER††

*Abstract* This report describes the instrumentation, initial results, and progress of an experiment designed to measure and monitor submarine sediment pore water and hydrostatic pressures in a selected area of the Mississippi Delta. The experiment also is intended to monitor significant pressure perturbations during active storm periods. Initial analysis of the data revealed excess pore water pressures in the silty clay sediment at selected depths below the mudline. Continuous monitoring of the pore water and hydrostatic pressures was expected to reveal important information regarding sediment pore water pressure variations as a function of the geological processes active in the Mississippi Delta.

### Introduction

The NOAA-Atlantic Oceanographic and Meteorological Laboratories is presently engaged in a NOAA program directed toward the delineation and understanding of important processes and mechanisms related to submarine sediment stability. A unique situation arose to test some of the equipment and concepts being developed in this program on Project SEASWAB (*Shallow Experiment to Assess Storm Waves Affecting Bottom*), which is part of a larger study of the Mississippi Delta being conducted by the U.S. Geological Survey.

---

\*NOAA-Atlantic Oceanographic and Meteorological Laboratories, Miami, Florida.

†Texas A&M University, College Station, Texas.

††School of Oceanography, Oregon State University, Corvallis, Oregon.

(Received December 4, 1975; Revised February 13, 1976.)

*Marine Geotechnology*, Volume 1, Number 4

Copyright © 1976. Crane, Russak & Company, Inc.

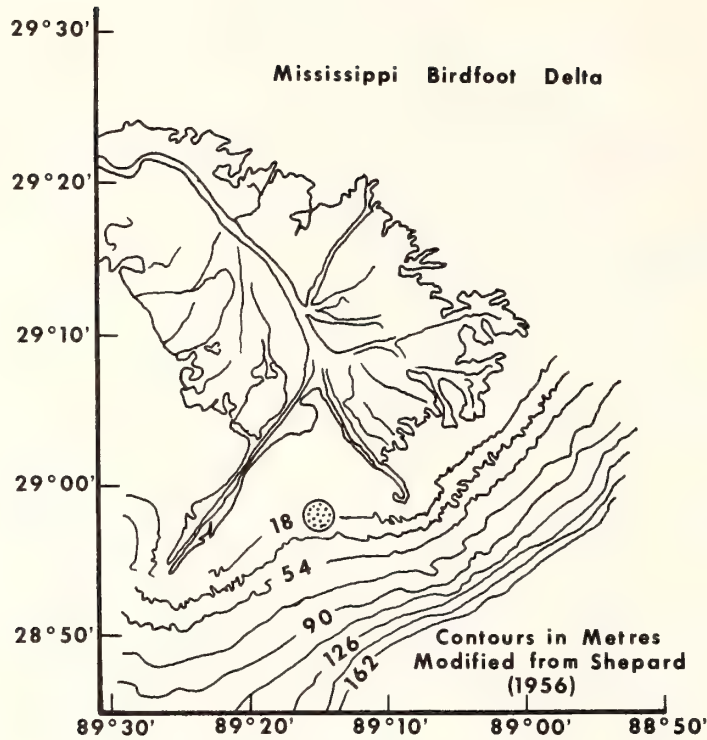


Figure 1. General study area.

The purpose here is to describe the instrumentation, progress, and initial results of an experiment designed to measure and continuously monitor, over a period of several months, submarine sediment pore water pressures in a selected area of the Mississippi Delta (Figure 1). Objectives of the experiment are to measure not only pore water and hydrostatic pressures at various depths below the mudline, but also to monitor significant pressure perturbations during active storm wave periods. It is interesting to note that while engineers have known for decades that pore water pressures are an important geotechnical consideration, the first reported attempt to measure pore water pressures in submarine sediments was made by Lai et al. (1968) and Richards et al. (1975).

The Mississippi Delta is well known for being a very dynamic region characterized by the interaction of riverine and marine processes and the large discharge of bedload and suspended sediment. Large plumes of sediment extend considerable distances beyond the subaerially exposed delta and deposit vast

quantities of silt and clay in the prodelta environment. This environment is characterized not only by the rapid deposition of fine-grained sediment having very high water contents, but also by the accumulation of organic material (Coleman et al., 1974). Methane and carbon dioxide gases, intimately related to decomposition of the organic material, influence substantial portions of the Mississippi Delta submarine sediments (Whelan et al., 1975). Knowledge of the sediment geotechnical properties in this complex and dynamic environment is of great importance to engineers faced with the design and construction of offshore structures, and to geologists investigating sedimentological processes relating to submarine diagenesis, environments of deposition, mass movement, and sediment stability (Morelock and Bryant, 1966; Keller and Bennett, 1968; Bennett and Bryant, 1973). Not only will the measurement of pore water pressures in the Mississippi Delta sediment aid in understanding and interpreting the sediment geotechnical properties, but it also should provide an insight into the behavior of these sediments in response to dynamic and static loads.

#### **Instrumentation**

The NOAA sediment pore water pressure probe (piezometer) system consists of the following components:

1. Probe and Sensing Units (Transducers)
2. Signal Conducting Cables
3. Signal Conditioner Units
4. Voltage and Frequency Regulator Units
5. Recording Unit.

The probe enclosing the pressure sensing devices is a 0.10-m O.D. steel pipe having a total length of 17.12 m. A weight stand mounts to the top of the probe on four steel gusset plates. The weight stand is fastened to the probe with two steel pins and the probe assembly is lowered into the seafloor by a steel cable fastened to the top of the weight stand. Four sensing units (variable reluctance pressure transducers) were placed in the probe at selected intervals; two sensors measured pore water pressure and two measured hydrostatic pressure (Figure 2). The pore water was transmitted through 0.05-m diameter porous corundum stones, which were inset in the pipe and ground to the pipe radius. Hydrostatic pressure was transmitted from the mudline through the seawater-filled steel pipe to the sensors installed inside the probe. Sensors were mounted inside oil-filled capsules in the probe and connected to the appropriate pressure ports with short tubing. Separate measurement of the pore water and hydrostatic pressures was necessary since one objective of the experiment was to determine the effect of

bottom pressures from storm waves on the pore water pressures. This approach, however, is feasible only in shallow water. A sensing unit which is robust enough for use in deeper water will generally not have sufficient resolution for the purposes desired. For measurement of static pressures, this limitation is largely overcome by a differential piezometer of the type described by Hirst and Richards (1976).

The signals from each transducer are transmitted through a conducting cable to signal conditioners and filtering systems before being recorded on a strip chart recorder. Electronic units and pressure transducers were tested and calibrated prior to the assembly of the probe. Calibration was carried out using a fused quartz Bourdon tube pressure gage having a sensitivity of 1 part in 200,000. The transducers have a maximum working range of 689.5 kPa (1 *psi* = 6.89 kPa) and a reproducibility of  $\pm 3.5$  kPa. The electronic units were checked frequently during various phases of the probe assembly.

#### **Installation of the Probe**

The probe and electronics system were assembled in the field aboard the Texas A&M University Ship R/V *Gyre* during 18–19 September, 1975. The total weight of the probe and weight stand loaded with four train wheels was 1.115 Mg in sea water; this weight having been calculated as adequate to implant the probe to the desired depth of penetration. On the afternoon of 19 September, 1975, the probe was lowered from the *Gyre* in the Mississippi Delta sediment (Block 28, South Pass Area, slightly south of 29°00'N, 89°15'W) at a preselected site 145 m from an offshore production platform where the recorder and signal conditioner units were installed later. The water depth was approximately 19 m at the site. After installation, divers removed the steel pins and made a general inspection of the exposed portion of the instrument. The weight stand and weights were returned to the ship.

Pore water and hydrostatic pressures were monitored from the ship during installation and for 40 min afterward. In the ensuing 4 h period, no readings were made while the electronic units were transferred to the platform. During this time divers installed the signal conducting cables along the sea floor to the platform. After reconnection, all systems appeared to be functioning properly. The probe was implanted only a few days before the passage of Hurricane Eloise near the site.

#### **Discussion**

Sediment pore water pressures,  $u_w$ , were measured at depths of approximately 8 and 15 m below the mudline. Hydrostatic pressures,  $u_s$ , were measured simultaneously at depths of approximately (actual mudline difficult to de-

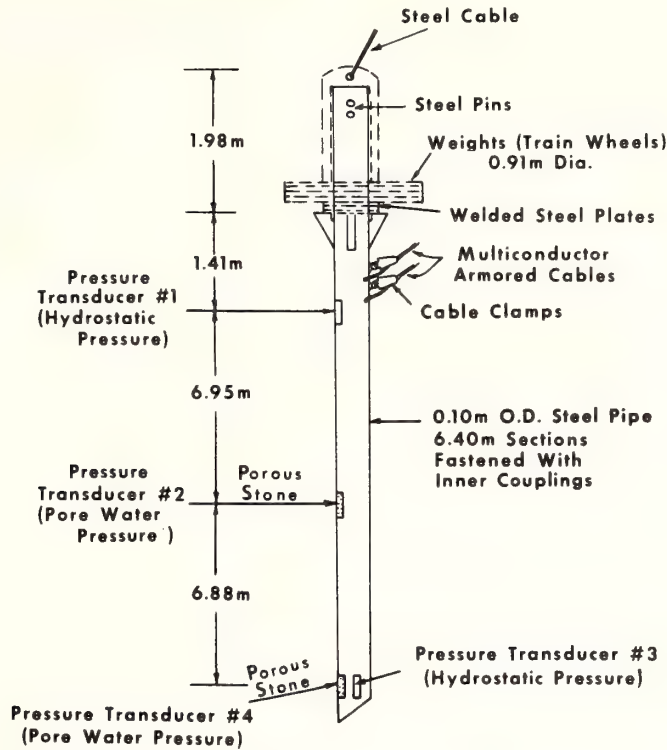


Figure 2. Sediment pore water pressure probe and weight stand. Drawing not to scale.

termine) 1 and 15 m below the mudline (Figure 2). A value of 68.9 kPa, equivalent to 7 m of sea water, has been added to Pressure Transducer 1 data for direct comparison with the sediment pore water pressures recorded by Transducer 2. Comparison of the hydrostatic pressure and sediment pore water pressure for a given depth below the mudline may reveal one of three possible conditions:

- Condition 1.* Sediment pore water pressure equals the hydrostatic pressure ( $u_w \approx u_s$ ).
- Condition 2.* Sediment pore water pressure exceeds the hydrostatic pressure ( $u_w > u_s$ ).
- Condition 3.* Hydrostatic pressure exceeds the sediment pore water pressure ( $u_w < u_s$ ).

Condition 1 is common for normally consolidated sediments assuming there has been no movement or shearing of the sediment. The pore water pressure is in equilibrium with the hydrostatic pressure. Condition 3 may occur with some overconsolidated sediments and possibly with other sediments while responding to complex dynamic conditions. This condition is not directly related to the results presented here and therefore will not be treated. When the sediment pore water pressure exceeds the hydrostatic pressure (Condition 2) the difference is termed excess pore water pressure,  $u_e$ . Thus,  $u_e = u_w - u_s$ . This condition is associated with underconsolidated sediments wherein very low sediment permeabilities hinder dissipation of the pore water pressure which builds up under rapid rates of deposition and loading (Bryant et al., 1975). Sediment movement and shearing may also contribute to the presence of excess pore water pressures, as may the undissolved gases present in some muds. Since the possible existence of excess pore pressures was the major reason for conducting the Mississippi Delta pore pressure experiment, the results reported here are expressed in terms of excess pore pressures,  $u_e$ .

The data reveal relatively high excess pore water pressures of 99.3 kPa at 15 m below the mudline and 49.6 kPa at a depth of 8 m below the mudline immediately following probe insertion (Figure 3). High excess pore water pressures were expected to occur due to implanting the probe and this condition also was observed by Richards et al. (1975). It was expected that these pore pressures would dissipate to the static condition following a typical log time consolidation relationship, and, in fact, this appeared to be the trend at the 8 m depth. However, little value can be given to these early readings owing to stabilization of the electronic system including temperature equilibration of the pressure transducers. Six hours after inserting the probe, excess pore water pressures were still relatively high at 81.4 kPa (15 m depth) and 37.2 kPa (8 m depth). They appeared to become relatively constant after approximately 7 h at the 8 m depth and 10–12 h at the 15 m depth, although at the latter depth, the excess pore pressures began to decline again just prior to the initial effects of Hurricane Eloise. Excess pore water pressures averaged approximately 72 kPa (15 m depth) and 32 kPa (8 m depth) after 7 h of initial stabilization of the system and prior to the storm. Clearly, significant sediment excess pore pressures were observed for a considerable period of time prior to the initial effects of the storm activity that began 21 September, 1975.

The records gathered during the passage of Hurricane Eloise indicate that the system was functioning satisfactorily. Pore water pressures appear to have varied significantly in response to the storm wave activity; however, these data require considerably more analysis for a complete assessment of the pore water condi-

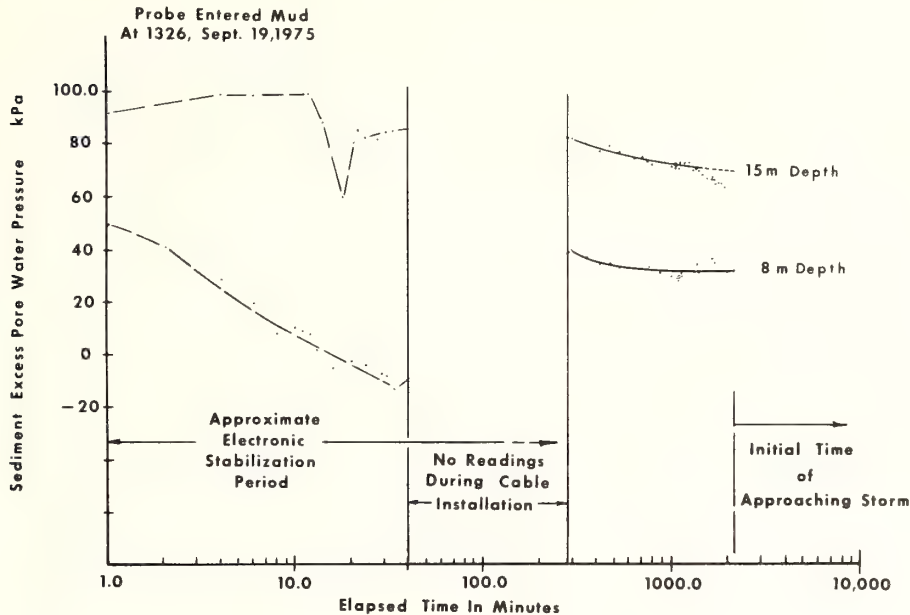


Figure 3. Sediment excess pore water pressures at approximate depths of 8 and 15 m below the mudline off the Mississippi Delta.

tions relating to the influence of the hurricane. Further data analysis for the period of time from 22–23 September, during which Hurricane Eloise passed in close proximity to the probe, is expected to reveal important information regarding pore water pressure fluctuations, particularly observed increases, and the degree of pore water pressure dissipation as recorded by the sensors implanted at various depths below the mudline. Poststorm data also are being collected in order to assess any possible long term changes in the pore water pressures of these prodelta muds.

A soil boring was completed in the immediate area approximately six weeks after the probe was installed. The sediment contained large amounts of gas as evidenced by the appearance of the recovered cores. It is not known whether undissolved gas was present in the area of the sensors. If this were the case, then the sensors may have responded to possible higher pore gas pressure rather than pore water pressures. Based on the success of this experiment, it is anticipated that future pore pressure probes will include high air entry ceramic stones to separate the water from the gas pressure.

### Summary

Significant excess pore water pressures have been observed in the submarine sediment of South Pass, Block 28, Mississippi Delta. Excess pressures averaging 72 and 32 kPa at depths of 15 and 8 m below the mudline respectively, appear to be characteristic of the general conditions prior to the passage of Hurricane Eloise. Further data analysis and study may result in a slight refinement of these initial observations and may also reveal important information regarding sediment pore water pressure variations during and after the passage of the storm. Initial evaluation of the data collected during Hurricane Eloise indicates that sediment pore water pressures varied significantly in response to the storm activity.

### Acknowledgments

The writers wish to express their appreciation for support given by NOAA Atlantic Oceanographic and Meteorological Laboratories (AOML). Considerable support for the Delta Project was given by the U.S.G.S. Marine Geology Branch, Corpus Christi, Texas, and the Conservation Division, New Orleans, Louisiana. From NOAA/AOML we thank John Burns for his assistance in assembling the electronics system, Frances Nastav for the drafting of the figures, and Thomas Clarke for the computer processing of the data. Calibration of the pressure transducers was made at the Naval Coastal Systems Laboratory, Panama City, Florida, through the consideration and help of G. W. Noble. The writers also appreciate the cooperation and assistance given by various members of the Shell Oil Company staff. Critical review of this paper was made by Drs. T. Hirst, A. Richards, B. McGregor, H. B. Stewart, Jr., L. Garrison, and Mr. R. Bea.

### References

- Bennett, R. H., and W. R. Bryant, 1973. Submarine sediment microstructure (abstracted). Clay and Clay Minerals Society 22nd Annual Clay Minerals Conference. Banff, Canada, Program Abstracts, p. 22.
- Bryant, W. R., W. Hottman, and P. Trabant, 1975. Permeability of unconsolidated and consolidated marine sediments, Gulf of Mexico. *Marine Geotechnology*, vol. 1, pp. 1-14.
- Coleman, J. M., J. N. Suhayda, T. Whelan, and L. D. Wright, 1974. Mass movement of Mississippi Delta sediments. *Transactions of the Gulf Coast Association of Geological Societies*, vol. 24, pp. 49-68.
- Hirst, T. J., and A. F. Richards, 1976. Excess pore pressure in Mississippi Delta front sediments: initial report. *Marine Geotechnology*, vol. 1, pp. 337-344.
- Keller, G. H., and R. H. Bennett, 1968. Mass physical properties of submarine sediments in the Atlantic and Pacific Basins. *Proceedings of the 23rd International Geological Congress, Prague*, vol. 8, pp. 33-50.
- Lai, J. Y., A. F. Richards, and G. H. Keller, 1968. In place measurement of excess pore water pressure of Gulf of Maine clays (abstract). *Transactions of the American Geophysical Union*, vol. 49, p. 221.
- Morelock, J., and W. R. Bryant, 1966. Physical properties and stability of continental slope



- deposits, northwest Gulf of Mexico. Transactions of the Gulf Coast Association of Geological Societies, vol. 16, pp. 279-295.
- Richards, A. F., K. Øien, G. H. Keller, and J. Y. Lai, 1975. Differential piezometer probe for an in situ measurement of sea-floor pore pressure. *Géotechnique*, vol. 25, pp. 229-238.
- Shepard, F. P., 1956. Marginal sediments of the Mississippi Delta. *American Association Petroleum Geologists Bulletin*, vol. 40, pp. 2537-2623.
- Whelan, T., J. M. Coleman, and J. N. Suhayda, 1975. The geochemistry of recent Mississippi River Delta sediment: gas concentration and sediment stability. Proceedings of the Offshore Technology Conference, vol. 3, pp. 71-84.

## GEOPHYSICAL INVESTIGATION OF THE CAPE VERDE ARCHIPELAGO

B. P. Dash,<sup>1</sup> M. M. Ball,<sup>2</sup> G. A. King,<sup>1</sup>L. W. Butler,<sup>3</sup> and P. A. Rona<sup>3</sup>

**Abstract.** The Cape Verde Islands are emerged portions of a Mesozoic-Cenozoic volcanic accretion in the form of a westward-opening horseshoe along fracture zones converging from the mid-Atlantic ridge toward Africa. An interior abyssal plain slopes westward, increasing in depth from 2.7 to 4.5 km. The plain is underlain by low relief on acoustic basement that is associated with a 300-gamma negative magnetic anomaly. The flanks of the Sal-Maio ridge appear bounded by large-displacement normal faults; superficial slumping is common. The trends of magnetic anomalies are linear N-S north of the islands and less linear within the islands and may change coincident with E-W bathymetric trends south of the islands. A triangular pattern of reversed refraction lines 200-250 km long along the north and east ridges and NW-SE across the interior abyssal plain indicated 2-3 km of semiconsolidated sediments underlain by 3-6 km of basalt and 6-8 km of plutonic rocks. The depth of the Moho is between 16 and 17 km. A deep NW-SE trending fault intersects the Sal-Maio ridge near Boa Vista. The consistent depth to Moho and the regional Bouguer anomaly indicate lack of local relief at the base of the crust. The crustal load of the entire archipelago is regionally adjusted.

## Introduction

The Cape Verde archipelago is situated on the continental rise about 500 km west of the north-west African continental shelf and 2000 km east of the mid-Atlantic ridge. The archipelago is encompassed by the 3700-m isobath which outlines the Cape Verde plateau extending seaward from northwest Africa [Rona, 1971; Egloff, 1972]. The islands are aligned along three bathymetric ridges which form a horseshoe opening westward (Figure 1). The segment of the mid-Atlantic ridge facing the Cape Verde archipelago exhibits a progressive change in trend of the ridge axis from NE-SW to N-S accompanied by an abrupt change in the displacement of the

fracture zones from right to left lateral at the Kane fracture zone [Heezen and Tharp, 1968]. It is problematic how the structure of the archipelago relates on the one hand to that of the continent and on the other to that of the ocean basin. Rock compositions on the islands exhibit both continental and oceanic affinities.

A geophysical investigation of the islands, including the adjacent sea floor, was undertaken to complement prior geological investigations in order to determine the structure of the Cape Verde archipelago. The Geophysics Department of Imperial College performed geophysical studies around the islands. The Rosenstiel School of Marine and Atmospheric Science of the University of Miami and the National Oceanic and Atmospheric Administration's (NOAA) Atlantic Oceanographic and Meteorological Laboratories, Miami, collaborated in the project, with the university research vessel John Elliott Pillsbury and the NOAA Ship Discoverer as part of the NOAA Trans-Atlantic Geotraverse (TAG) project.

## Lithology and Structure of the Islands

The oldest known rocks in the Cape Verde Islands are Lower Cretaceous (possibly Upper Jurassic) limestones exposed on Maio. An aptychus of *Lamellaptrychus angulocostatus atlanticus* occurring in the Lower Cretaceous limestones on Maio suggests an open marine origin for the limestone. Outcrops of questionable Mesozoic age are present on São Nicolau, Sal, and Boa Vista. Paleogene sediments and lavas are known on Maio, and Neogene rocks are present on most of the islands. Eruptions have occurred on Fogo as recently as 1951 [Machado, 1965].

Part [1950] cites early observations of structural trends in the island made by J. B. Bebiano of the Portuguese Geological Survey who noted (1) the marked linear distribution of Santo Antão, São Vicente, São Nicolau, and Boa Vista, marking a possible WNW-ESE fault trend; (2) NE-SW linear trends on the west side of Santo Antão within the island itself and between Santo Antão and neighboring São Vicente; (3) generally NW-SE structures running through São Nicolau, São Tiago, and Fogo; and (4) the N-S Sal-Maio ridge. Ballard and Hemler [1969] have reported an eastward-facing fault scarp on the east side of the Sal-Maio ridge. Of key importance in a structural analysis of the island group are

<sup>1</sup>Department of Geophysics, Imperial College of Science and Technology, London SW 7 2BP, England

<sup>2</sup>Rosenstiel School of Marine and Atmospheric Science, University of Miami, Miami, Florida 33149

<sup>3</sup>National Oceanic and Atmospheric Administration, Atlantic Oceanographic and Meteorological Laboratories, Miami, Florida 33149

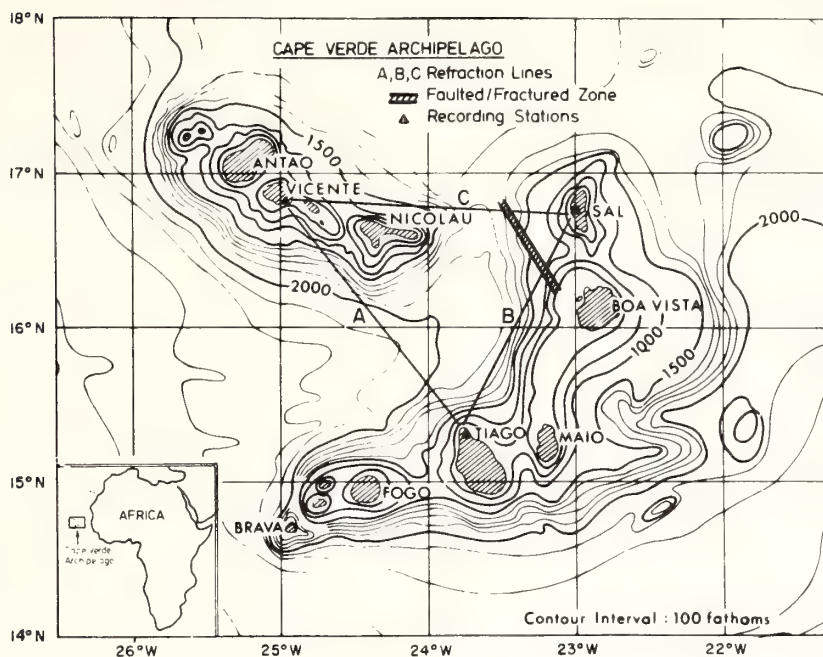


Fig. 1. The Cape Verde archipelago and its location with respect to the African continent. A, B, and C are the refraction profiles showing the recording stations on the islands of São Vicente, São Tiago, and Sal. The Sal-Maio fracture zone is indicated. Contours are at 100 fm (182.88m) intervals.

the recently recognized trends on the island of Maio [Serralheiro, 1970].

It appears that this Cretaceous sequence on Maio represents a section of marine limestones and shales invaded by highly undersaturated alkaline intrusive and extrusive rocks along a NNW-SSE zone of weakness in the North Atlantic sea floor. Carbonatites are present on Maio, Fogo, Brava, São Vicente, and possibly Sal [Assuncao et al., 1968]. On Brava the syenite-carbonatite series forms a ring complex intruded into a series of palagonitic basaltic pillow lavas of submarine origin and probable Cretaceous age [Machado et al., 1967].

Essexite-syenite-carbonatite associations commonly occur as a compound central plug enclosed in a ring complex, a structural pattern suggesting emplacement of the carbonate as well as the alkaline basic rocks by intrusion. This is the prevailing pattern in some of the east African rift valleys [Turner and Verhooogen, 1960]. Such intrusions are thought to be characteristic of a prerifting up-doming phase in continental areas [LeBas, 1971]

#### Area of Investigation and Data Collection

The first phase of the geophysical investigation carried out in 1969 consisted of refraction seismic work supplemented by magnetic profiling. Three seismic stations were established on the islands of Sal, São Tiago, and São Vicente, forming a triangle with sides of over 200 km (Figure 1). Shots ranging from 50 to 350 lb (23-159 kg) were fired on each line while all

three stations were recording. This system meant that for every shot fired, two stations were in line, whereas the third was 'broadside'. All the data collected were recorded on magnetic tape for subsequent digital processing.

#### Refraction Seismic Data Processing and Integration

**Digital processing.** The seismic data were digitized at a sampling interval of 10 ms, giving a maximum recoverable frequency for the digital data of 50Hz. The first stage of processing was to increase the signal to noise ratio. A number of methods were tried, including predictive deconvolution and band-pass frequency filtering. The latter was found to be the most effective as well as the most economical in terms of computer storage and operating time. Having obtained the filtered records, we applied stacking and correlation techniques. These methods were used in conjunction with routine operations such as correction of the data to a datum plane which allows for differences in water depths at shot points. These methods were applied to synthetic data as well as to the field data for purposes of comparison.

The best method for use on the field data was the stacking method in which several traces are added, or stacked, after being given time shifts defined as the ratio of the offset distance to the apparent velocity being examined ( $T = X/V$ ). The correlation technique was less successful, since it is heavily dependent on wave shape and is extremely suscep-

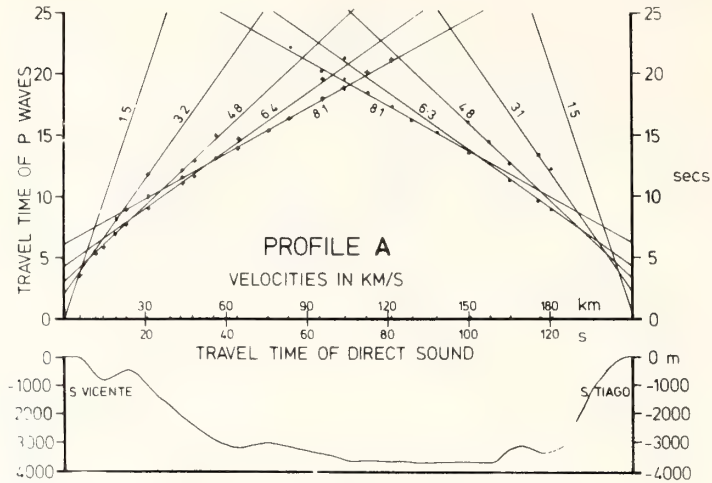


Fig. 2. Time-distance plot of profile A. Bathymetry along the profile is shown below the time-distance graph.

tible to noise.

**Synthetic seismograms.** Synthetic seismograms were produced for various crustal models inferred from the seismic and gravity data by an iterative program based on ray theory [Dash et al., 1970]. This approach assumes that the geological units constituting the model are isotropic, elastic, and homogeneous media with no attenuation of seismic energy and are two-dimensional with interfaces between the rock units normal to the plane of section.

Results

All the seismograms obtained were subjected to the processing techniques described above, and the results obtained for each profile are indicated below.

**Line A.** This line was shot between São Tiago on the south and São Vicente on the north with Sal as the broad side listening point (Figure 1). The lateral separation between São Tiago and São Vicente is about 200 km, and as can be seen from the time-distance plot (Figure 2), the two stations provide a reversed profile. The mean water depth along this line was about 3000 m. The observed times were corrected for shot and detector locations. The thickness and velocity of the various layers are shown in Table 1.

**Line B.** This line was shot between the islands of São Tiago and Sal. The station at São Vicente acted as the broadside listening point. The time-distance plot is shown in Figure 3. As Figure 3 shows, this line presented an interesting problem. The station at São Tiago registered the seismic arrivals from above the Moho up to a distance of about 100 km. However, the station at Sal failed to register any arrivals at all for shots fired beyond 30 km. Within 30 km the arrivals were strong and readily recognizable. The most plausible explanation for this loss of energy is that the shots were being fired beyond a heavily faulted or fractured zone where seismic energy was dissipated. Once past this zone there was no interference, and normal arrivals were registered at Sal.

Table 2 shows the velocities and thickness of various layers calculated from the data obtained from São Tiago. The low apparent velocity of 7.9 km/s would suggest a slight rise of the Moho toward Sal.

**Line C.** Line C was shot between the islands of Sal and São Vicente with São Tiago acting as the broadside recording station. The line was about 200 km long. The time-distance graph is shown in Figure 4. A situation similar to that along line B was encountered here. At Sal, arrivals were registered up to about 30 km west of the island. From then on for a further 30 km, no arrivals were registered at either Sal or São Vicente. From a point approximately 65 km away from Sal, São Vicente began to receive distinct arrivals from the Moho, while Sal recorded nothing. This anomalous behavior indicates that seismic energy was being dissipated by a near-surface fractured or faulted zone 39 km west of Sal. Once past this region the energy propagated in the usual

TABLE 1. P Wave Velocities and Thicknesses of Various Refractors Along Refraction Profile A

Horizon	Velocity km/s	Thickness km	Depth to Top of Layer km
São Vicente			
Water	1.5	3.4	0.0
1	3.2	1.9	3.4
2	4.8	3.6	5.3
3	6.4	7.2	8.9
4	8.1		16.1
São Tiago			
Water	1.5	3.4	0.0
1	3.1	2.1	3.4
2	4.8	2.9	5.5
3	6.3	8.0	8.4
4	8.1		16.4

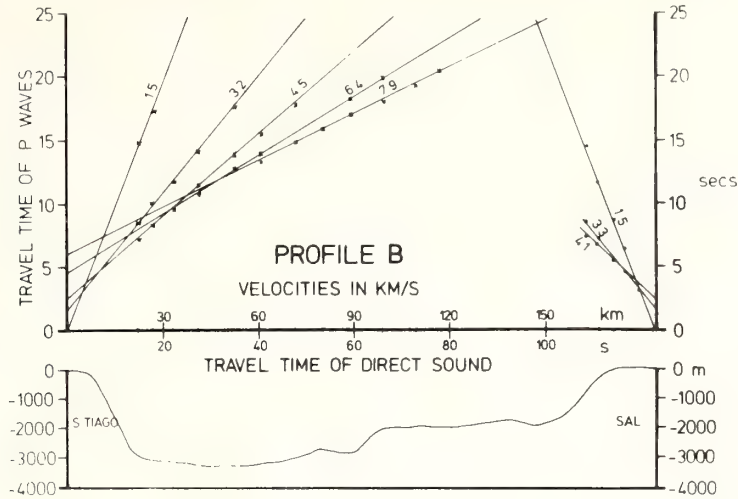


Fig. 3. Time-distance plot of profile B. Bathymetry along the profile is shown below the time-distance graph.

manner, and arrivals were registered at São Vicente. However, Sal remained in a shadow zone, and no deep seismic arrivals were registered on the island. Table 3 shows the velocities and thicknesses of several layers. For the purposes of calculation, profile C was considered a reversed line as far as the first two layers were concerned. The depths to the layers of velocities of 6.6 and 8.0 km/s were calculated from the data obtained on São Vicente.

Broadside at Sal and São Vicente. Analysis of the later arrivals of the broadside data suggested the existence of a fault zone with a throw of about 900-1000 m. The large shot point to detector distance, inadequate charge size, and associated noise in the seismograms prevented us from drawing a final conclusion. Nevertheless, from the results it was possible to postulate the general trend of the fault system, which is in the NW-SE direction.

Refraction Summary. Seismic velocities obtained in this survey, can be successfully correlated between profiles and are inferred to represent the following materials:

1. Surface velocity of 3.1-3.2 km/s consists of semiconsolidated sediments.
2. Layer with velocities ranging from 4.4 to 4.8 km/s may be basaltic pillow lava.
3. Velocities of 6.3 km/s are typically gabbroic rocks.
4. The velocity of 8.1 km/s signifies the Moho.

Extrapolation of the seismic results obtained at Sal and São Vicente suggests that the Moho rises toward the Sal-Maio ridge.

A wide faulted and fractured zone is associated with the Sal-Maio ridge (Figure 1). The attitude of the Moho in this area suggests that the western islands of the Cape Verde archipelago lie on a crust with a thickness of between 16 and 17 km. the implication thus being that the islands are structurally not part of the African continent.

#### Seismic Reflection Profiling

In 1968 the U.S. research vessel Kane carried out a reconnaissance reflection seismic, magnetic, and gravity survey from Dakar to the eastern Cape Verde Islands [Lowrie and Escowitz, 1969]. In 1970, NOAA participated in the present research project with their ship Discoverer. Their work was confined to reflection seismic, gravity, and magnetic profiling within the Cape Verde archipelago. The tracks of Discoverer and Kane are shown in Figure 5. For the sake of better understanding the reflection data obtained by Discoverer the results of the Kane survey are also presented here (Figures 6, 7, and 8). The following is a description of these records.

West of Dakar to the Sal-Maio ridge, line AA (Figure 6). In the east the Cape Verde block is bounded by a 1-s-thick stratified deposit incised by canyons and leveed channels. The present drainage system of Senegal and Mauritania is insufficient for considerable sediment accumulation, and the present stratified deposit can only be explained by deposition of sediments from the continent or by water flowing seaward across the shelf break. This thick sequence ends abruptly about 185 km from the Cape Verde block. A shallow opaque reflector blankets the

TABLE 2. P Wave Velocities and Thicknesses of Various Refractors Along Refraction Profile B as Recorded at São Tiago

Horizon	Velocity km/s	Thickness kms	Depth to Top of Layer km
Water	1.5	2.9	0.0
1	3.2	1.9	2.9
2	4.5	5.6	4.8
3	6.4	6.3	10.4
4	7.9		16.7

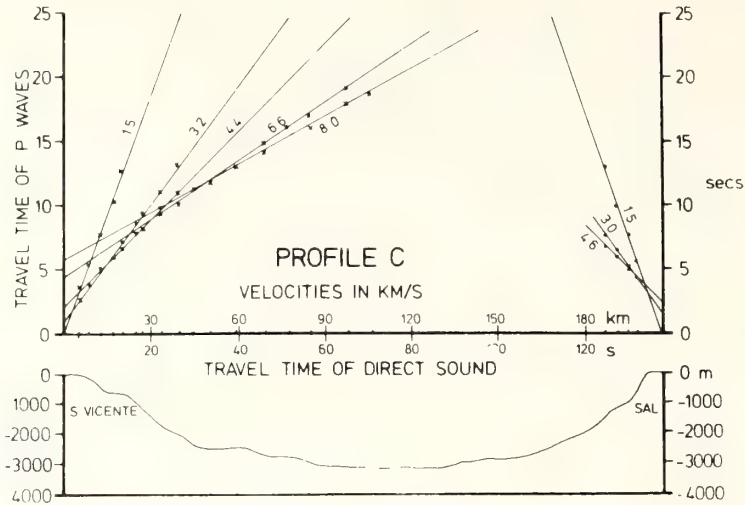


Fig. 4. Time-distance plot of profile C. Bathymetry along the profile is shown below the time-distance graph.

island block. The opaque reflector may be cherty, volcanic, or calcareous, or perhaps a combination of these lithologies. A seamount east of the Cape Verde block is easily recognizable. At the western end of line AA the Sal-Maio ridge is steep sided and flat topped. The basement beneath the ridge steps down to the east. A fault occurs at the first of these steps of the eastern slope. Ballard and Hemler [1969] have noted a N-S striking fault with a displacement of about 450 m at this location. Some indications of sediment infill, possibly due to sediments derived from the ridge and the seamount, are seen on the western side of the seamount.

Sal-Maio ridge to the abyssal plain, line BB (Figures 6 and 7). This section of the profile runs northwest through the Cape Verde 'horseshoe'. At the eastern end of this line (Figure 7), transparent poorly stratified presumably pelagic deposits cap a protruding and elongated hill. The opaque reflector, as was indicated earlier, can be found almost invariably on this profile. Two diapiric structures protruding through the seabed can be seen. At the extreme end of the profile a partly buried abyssal hill covered by 1-s-thick stratified sediments is apparent.

South of the Fogo-São Tiago ride to north of São Nicolau, lines DD and CC (Figure 8). The N-S profile across the Fogo-São Tiago ridge suggests some small displacements indicated by irregular topography and hyperbolic echoes. Although they are not very clearly defined, there are suggestions of the presence of several slumped blocks on the ridge. Numerous sediment masses have slid down the flanks of the ridge and are best seen on its south side. In the area north of the ridge and south of São Nicolau, stratified sediment partly covered by the dark reflector can be seen. The presence of hyperbolic echoes south of São Nicolau suggests a rough shallow basement. Seismic refraction data (line C, Figure 1) in the vicinity of this profile confirm the presence

of this layer at a depth of 1.9 to 2.1 km. This basement appears to rise stepwise toward São Nicolau from about 15 n. mi. (28 km) south of the island. Slumped blocks are evident at the base of the island rise. Farther north, beyond São Nicolau, thick deposits of sediments are noticeable. The basement in this area is rugged, with indication of faulting, consistent with the N-S fault lineation suggested by Ballard and Hemler [1969].

The seismic reflection records within the Cape Verde archipelago show several successive areas having well-defined to poorly defined stratified zones. The basement configuration is also ill defined except in certain areas. Wherever there are clear reflections, correlation with refraction seismic data is excellent. From the refraction data it is apparent that the average thickness of sediments varies from 1.9 to 2.4 km. This is in close agreement with the indications from the reflection results.

According to these observations the area inside the Cape Verde 'horseshoe' seems to be built up by sediments supplied from either the continent or the islands. Erosion seems to be of minor importance, while slumping was observed more frequently.

TABLE 3. P Wave Velocities and Thicknesses of Various Profile C as Recorded at São Vicente

Horizon	Velocity km/s	Thickness km	Depth to Top of Layer km
Water	1.5	2.4	0.0
1	3.2	2.4	2.4
2	4.4	5.8	4.8
3	6.6	5.6	10.6
4	8.0		16.2

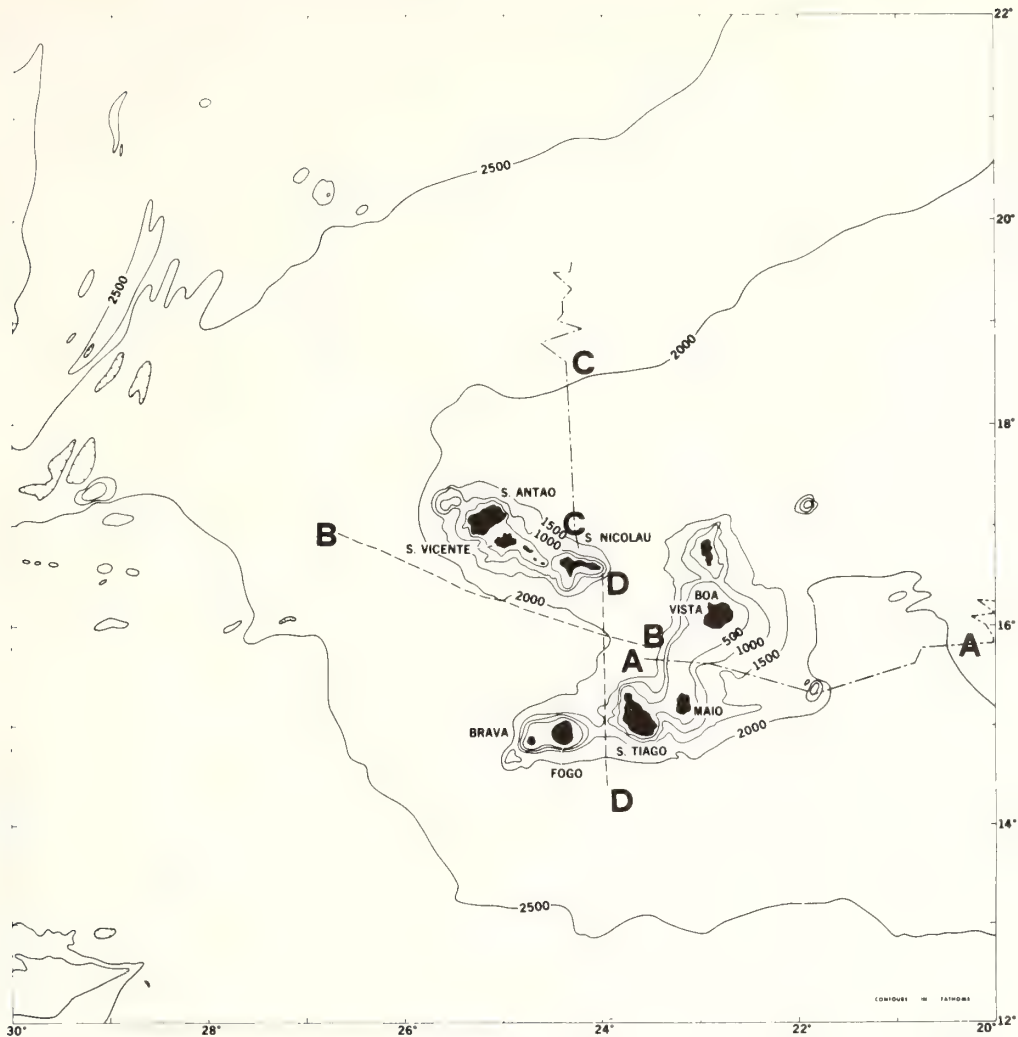


Fig. 5. Track chart of air gun reflection lines AA, BB, CC, and DD. Data on lines AA and CC were collected by Kane, the rest by Discoverer. The contours are in fathoms (1 fm = 1.8288m).

#### Gravity Investigation

The seismic data were supplemented by the measurements of the earth's gravitational field on and around the islands (Figure 9). The marine data were collected during two research cruises in the area. In 1970 the NOAA ship Discoverer carried out a limited survey (3500 km) around the islands. The ship's position was accurately known at all times by means of satellite and Omega navigation systems. The course, speed, and position of the ship and the bathymetry of the area were recorded along the profiles. All these data together with the gravity readings taken, on the average, every 5 to 6 km were fed into the on-board computer (Univac 1208) which applied latitude and Eotvos corrections to the data and thus yielded the free air anomaly value at each station. In 1972 the same ship recorded a

further 1350-km line of gravity profiles. This survey was conducted mainly within the island 'horseshoe' and provided a tight grid of data to the west of the Sal-Maio ridge. In addition to these marine data, gravity values at 168 land gravity stations (collected by Servico Meteorologico Nacional de Portugal and kindly made available to us) were used. The land data were corrected to a sea level datum, and all three surveys were combined. Since the gravity data were still influenced by variations in the ocean bottom topography and the subaerial topography of the islands, it was necessary to remove these effects in order to observe abnormalities in the structure of the crust. The method used was that proposed by Talwani and Ewing [1960] for a three-dimensional body. To this end a new bathymetric chart was contoured from the existing data together with those collected

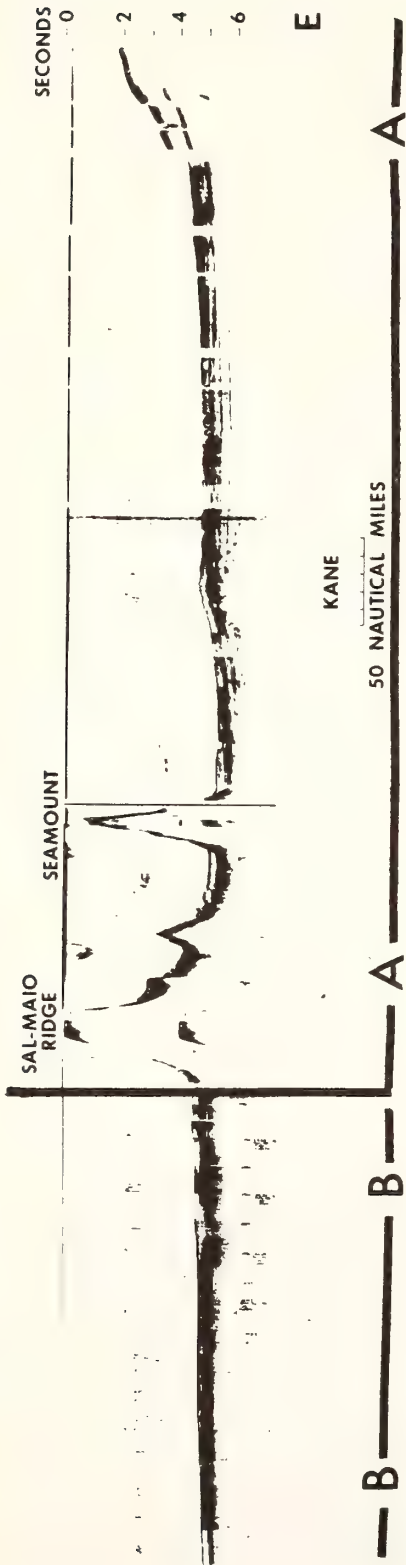


Fig. 6. Reflection seismic section of line AA and part of line BB, starting from west of Dakar to west of the Sal-Maio ridge and showing a seamount and the ridge.

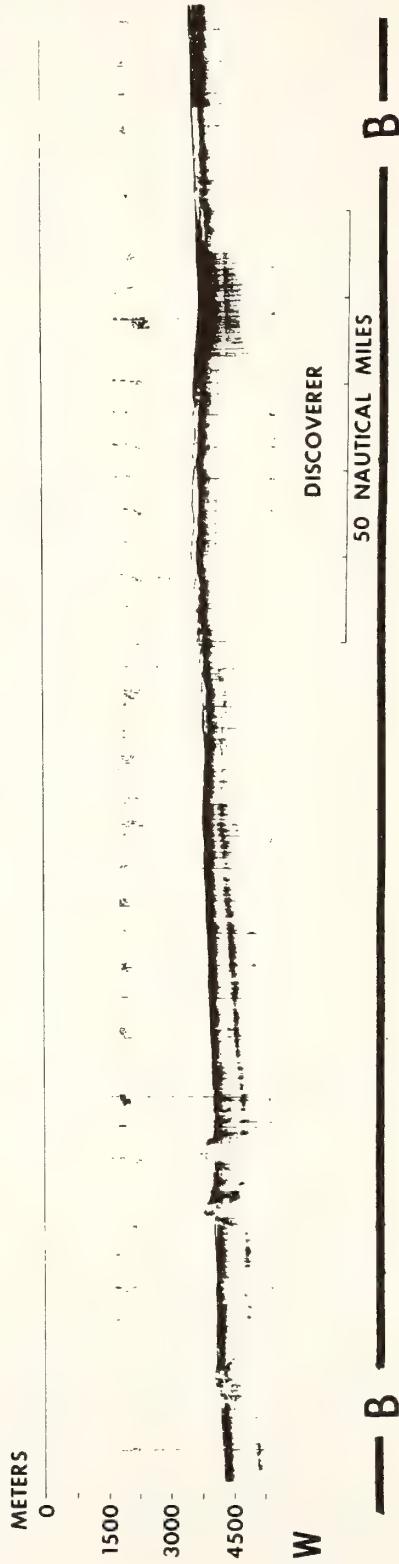


Fig. 7. Reflection section of line BB at the west of the Sal-Maio ridge extending to the abyssal plain. Two diapiric structures and an abyssal hill are clearly visible.



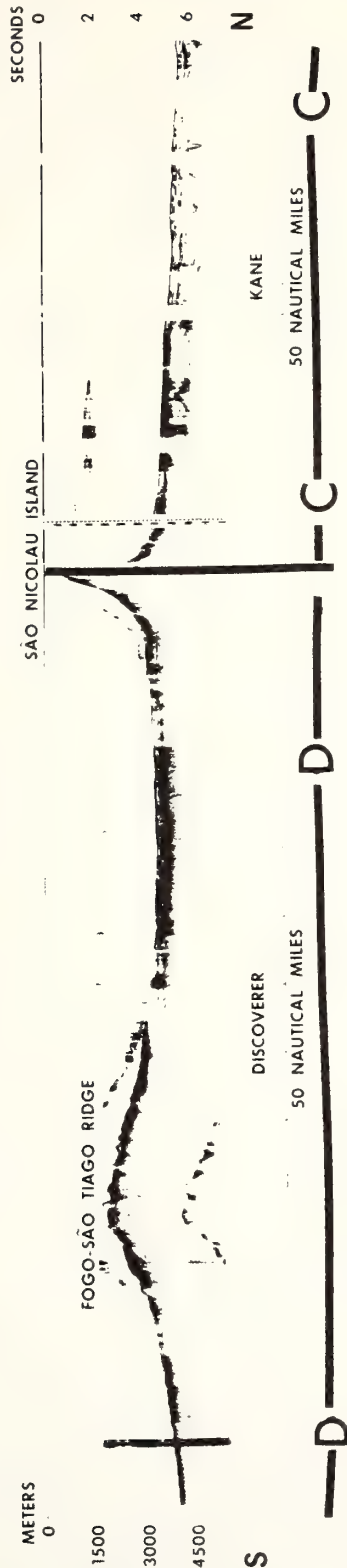


Fig. 8. Reflection sections of lines CC and DD. This N-S line extends from between the islands of Fogo and São Tiago in the south to the north of São Nicolau island.

by the Pillsbury and Discoverer (Figure 1).

In order to estimate the most likely replacement density the terrain-corrected Bouguer anomalies were computed for a range of reasonable density contrasts. If the gravity field varies smoothly, it can be represented by a low-order polynomial. Various low-order polynomials were calculated for each density contrast. The root mean square deviations between the predicated values of the field and the actual values were computed for each surface fitted. A fifth-order polynomial was accepted for which a least squares best fit was obtained. Comparison of the results of this polynomial fitting method with those of the density profiling method of Nettleton [1939] revealed that a value of  $2.3 \text{ g/cm}^3$  for the subaerial parts and  $2.4 \text{ g/cm}^3$  for the submarine portions should be accepted for the replacement bulk densities to be used for detailed investigations in the Cape Verde region. These values are all in accord with those predicted from the Nafe and Drake [1963] curve. The detailed terrain-corrected Bouguer anomaly map is shown in Figure 9. There are numerous positive anomaly closures which are assumed to be caused by high-density plutonic bodies. To the southeast of the island of Maio there occurs a sharply angled bend in the isogals coupled with extremely high gradients perpendicular to both arms of the bend. The northward continuation of the bend passes through major deviations in the isogals to the southeast of Boa Vista and emerges to the east of Sal, where another steep gradient is observed. A major roughly N-S fault is postulated to the east of the islands of Maio and Sal.

Bebiano [1932] postulated a major fault through the four northern islands extending to Boa Vista. There is no extreme anomaly gradient perpendicular to this proposed fault trace. It is possible that the observed minor and major deviations of the isogals could indicate a large tectonic feature whose field has been partially obscured by the interfering effects of extruded magma occupying a large area.

Analysis of the data corrected with the regional replacement density of  $2.58 \text{ g/cm}^3$  indicates that the Moho ranges between 16 and 18 km beneath the island block. These values are in excellent agreement with those inferred from the seismic refraction data.

#### Magnetic Anomalies

The magnetic quiet zone boundary in the eastern North Atlantic lies between the Cape Verde archipelago and the African continent and trends basically N-S [Heirtzler and Hayes, 1967; Rona et al., 1970]. A sequence of oceanic magnetic anomalies, the Keathley sequence or J anomalies, forms a 350-km-wide band seaward of the quiet zone boundary and extends up to the eastern margin of the Cape Verde archipelago (Figure 10). Vogt et al. [1970] along with Rona et al. [1970] have shown that this J anomaly band occurs with almost mirror image similarity on the east and west sides of the central North Atlantic.

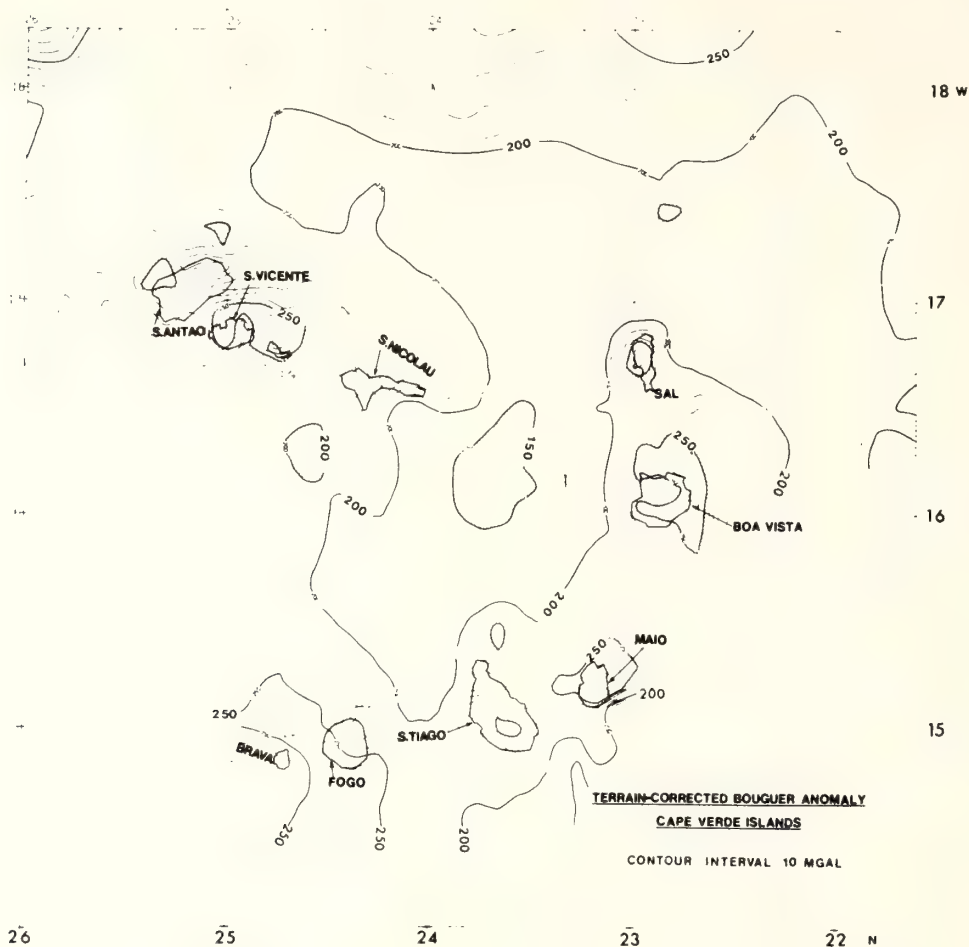


Fig. 9. Terrain-corrected Bouguer anomaly map around the Cape Verde archipelago with a contour interval of 10 mGal.

Tentative correlation of oceanic magnetic anomalies in the Cape Verde area based on our new data and added on to those published by Rona et al. [1970] substantially confirms the general N-S trends established by previous work. There is some indication of minor offsets of anomalies, although no fracture zones can be mapped except the possible eastern extension of the Kane fracture zone at about 21°N latitude. Where deviations from the general N-S anomaly trend occur, the preferred orientation is NNW-SSE, parallel with structural features and morphological lineations within the island group as well as with the postulated deep fault trends derived from the seismic and gravity data.

#### Conclusions

The present crustal structure beneath the Cape Verde archipelago determined by our seismic refraction and gravity measurements is transitional in that the Moho lies at a crustal depth between 16 and 17 km, midway between dimensions typical for continental and oceanic crust.

It is interesting to compare the crustal structure of the Canary Islands, lying off the coast of Spanish Sahara with that of the Cape Verde archipelago. Dash and Bosshard [1969] postulated that the five western islands of the Canaries group are not related structurally to the African continent. The crust is of oceanic thickness on the west. In the central part of the island group the thickness of the crust is transitional. The depth to Moho varies from 12 to 14 km. Roeser et al. [1971], from their refraction seismic and gravity studies of the area between Africa and Gran Canaria, suggest a Moho depth of 21 km with a crust originally of oceanic character having presumably been depressed to the depth of 21 km with 10 km of differentially metamorphosed sediments deposited on it. The transitional zone between the oceanic and continental crust is characterized by major faults of NE-SW strike.

The original composition of the crust underlying the Cape Verde archipelago was probably oceanic as is evidenced by (1) the

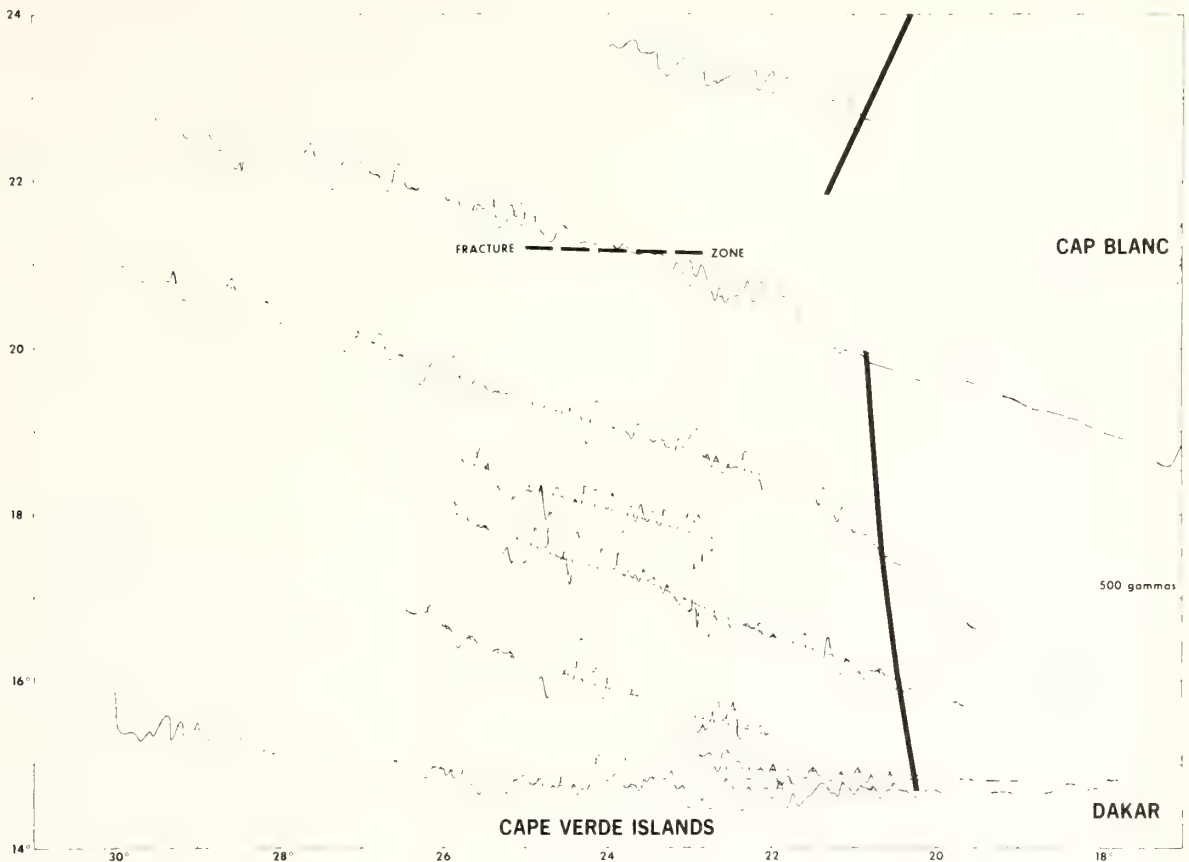


Fig. 10. Magnetic anomaly map around Cape Verde Islands and continental shelf of Africa to 24°N. The Keathley sequences, a possible fracture zone, and the magnetic quiet zone boundary are indicated. No major bottom topographic features occur along the magnetic track lines.

occurrence of a typically oceanic layer 3 with a velocity of 6.3 km/s; (2) the presence of the magnetic quiet zone boundary landward of the islands [Rona et al., 1970]; and (3) the presence of open water aptychus limestone (Upper Jurassic-Lower Cretaceous) exposed on Maio similar to limestones recovered from analogous locations of the western North Atlantic deep ocean basin [Hollister et al., 1972]. The origin of the Canaries is closely linked with the faults through the islands [Dash and Bosshard, 1969]. The Cape Verde archipelago also originated as igneous intrusions and extrusions along a fault system. The similarities between the Canary and Cape Verde islands end at the comparison of their crustal structures. Owing to a lack of any detailed seismic refraction data in the area between the two island groups it is not possible to draw any extension of similarities between them. The magnetic signature of each of the two island groups is singularly distinctive. The Cape Verde islands lie west of the magnetic quiet zone, whereas in the Canaries the magnetic quiet zone passes through the island

of Tenerife. The magnetic quiet zone almost follows the transitional crustal zone on the west coast of Africa.

To reconcile the present transitional thickness and the inferred former oceanic composition of the crust beneath the Cape Verde archipelago, we postulate that these islands originated as igneous intrusions and extrusions along the N-NW, NW, and W-SW trending fault systems. The Moho was depressed from oceanic to transitional depth as a result of the loading of accumulated materials of the islands. It is suggested that the building of the Cape Verde archipelago began at an early stage in the Mesozoic opening of the central North Atlantic and at no time did the islands belong to the African continent. The position of the archipelago was apparently controlled by the convergence of fracture zones as a consequence of the marked change in the trend of the adjacent mid-Atlantic ridge.

**Acknowledgements.** The authors wish to thank A. Richardson, F. Machado, P. Hubral, B. Buttkus, and C. J. M. Hewlett for their

help during the collection of the data. Thanks are also due to the officers and crew of the R/V John Elliot Pillsbury and the NOAA ship Discoverer. Financial support for the project was kindly made available by the Natural Environment Research Council of Great Britain, U.S. ONR grant N00014-67-A-0201-0013, NSF grants GA-39744, GA-19471, GB-27252, and GA-27465, and NOAA. The authors gratefully acknowledge this support.

## References

- Assuncao, C.F.T. de, F. Machado and A. Serralheiro, New investigations on the geology and volcanism of the Cape Verde Islands, Int. Geol. Congr. Rep. Sess. 23rd, 2, 9-16, 1968.
- Ballard, J.A., and L.G. Hemler, Structure of the Cape Verde rise (abstract), Eos Trans. AGU, 50, 210, 1969.
- Bebiano, J.B., A geologia do arquipelago de Cabo Verde, Comun. Serv. Geol. Port., 18, 1-275, 1932.
- Dash, B.P., and E. Bosshard, Seismic and gravity investigations around the western Canary Islands, Earth Plan et. Sci. Lett., 72, 169-177, 1969.
- Dash, B.P., K.O. Ahmed, and P. Hubral, Seismic investigation in the region of Poulo Panjang, offshore from southwestern Vietnam, ECAFF Tech. Bull., 3, pp. 37-54, 1970.
- Egloff, J., Morphology of the ocean basin seaward of northwest Africa: Canary Islands to Monrovia, Liberia, Amer. Ass. Petrol. Geol. Bull., 56, 694-706, 1972.
- Heezen, B.C., and M. Tharp, Physiographic diagram of the North Atlantic Ocean, Geol. Soc. Amer. Spec. Pap., 65, 1968.
- Heirtzler, J.R., and D.E. Hayes, Magnetic boundaries in the North Atlantic Ocean, Science, 157, 185-187, 1967.
- Hollister, C.D., et al., Initial Reports of the Deep Sea Drilling Project, vol. 11, p. 1077, U.S. Government Printing Office, Washington, D.C., 1972.
- LeBas, M.J., Per-alkaline volcanism, crustal swells and rifting, Nature Phys. Sci., 230, 1971.
- Lowrie, A., and E. Escowitz, Eds. Kane 9, in Global Ocean Floor Analysis and Research Data Series, 971 pp., U.S. Naval Oceanographic Office, Washington, D.C., 1969.
- Machado, F., Vulcanismo das Ilhas de Cabo Verde e das outras ilhas Atlântidas, Junta Invest. Ultramar Port., Estud. Ensaios Doc., 117, 1-83, 1965.
- Machado, F., J. Azeredo Leme, and J. Monjardino, O complexo sienitocarbonatítico dal Ilha Bravo, Cabo Verde, Garcia de Orta, 15, (1) 93-98, 1967.
- Nafe, J.E., and C.L. Drake, Physical properties of marine sediments, in The Sea, vol. 3, The Earth Beneath the Sea, edited by M.N. Hill, pp. 794-813, Interscience, New York, 1963.
- Nettleton, L.L., Gravity and magnetic calculation, Geophysics, 4, 176-185, 1939.
- Part, G.M., Volcanic rocks from the Cape Verde Islands, Bull. Brit. Mus. Natur. Hist. Geol., 1(2), 27, 1950.
- Roeser, H.A., K. Hinz, and S. Plaumann, Continental margin structure in the Canaries, The Geology of the East Atlantic Continental Margin, 2, Africa, edited by F.M. Delany, rep. 70/16, pp. 27-36, Inst. Geol. Sci.,
- Rona, P.A., Bathymetry off central northwest Africa, Deep Sea Res., 18, 321-327, 1971.
- Rona, P.A., J. Brakl, and J.R. Heirtzler, Magnetic anomalies in the northeast Atlantic between the Canary and Cape Verde islands, J. Geophys. Res., 75(35), 7412-7420, 1970.
- Serralheiro, A., Geologia da Ilha de Maio (Cabo Verde), Junta Invest. Ultramar Port., Estud. Ensaios Doc., 103, 1970.
- Talwani, M., and M. Ewing, Rapid computation of gravitational attraction of three-dimensional bodies of arbitrary shape, Geophysics, 25, 203-205, 1960.
- Turner, F.J., and J. Verhoogen, Igneous and Metamorphic Petrology, p. 694, McGraw-Hill, New York, 1960.
- Vogt, P.R., C.N. Anderson, D.R. Bracey, and E.D. Schneider, North Atlantic magnetic smooth zones, J. Geophys. Res., 75(20), 3955-3968, 1970.

(Received July 31, 1975;  
revised February 13, 1976;  
accepted February 29, 1976.)

Reprinted from: *Sea Frontiers*, Vol. 22, No. 1, 9-15.

# Iceland

## Where the Mid-Ocean Ridge Bares Its Back

By ROBERT S. DIETZ

*NOAA, Atlantic Oceanographic and Meteorological Laboratories  
Miami, Florida.*

*ONLY IN ICELAND can man walk on the Mid-Atlantic Ridge. This is the one place where part of the 45,000-kilometer-long ocean rift is exposed above sea level.*

Robert S. Dietz



ICELAND, a bleak, windswept island in the far North Atlantic, touching on the Arctic Circle, lies on rock hotter than lands at the equator. It is not entirely a foolish joke to say that an inhabitant of this island who runs short of hot water in his bathroom has only to drive a pipe down through the floor to get plenty for his hot bath. But the interest of geologists runs deeper and concerns more fundamental aspects of the earth's history than hot water.

#### A Grand Scheme

Only at Iceland does the 45,000-kilometer-long mid-ocean ridge, a rift marking the pulling apart of the earth's crustal plates, breach the surface of the ocean. This island is, there-

45,000 kilometers = 27,900 miles

LOOKING NORTH along Iceland's central rift, one can see where the earth's crust is slowly being pulled apart. To the left of the rift, the western Atlantic Ocean and North America to as far as the San Andreas Fault in California are drifting west at a rate of 1 centimeter each year. To the right of the rift, the eastern Atlantic Ocean and all of Eurasia are drifting eastward to as far as the Pacific trenches off Kamchatka and Japan. In Iceland, the rifting is strongly "overprinted" by companion effects—the formation of volcanoes and the effusion of lava above a vast ascending plume of magma, rising from deep within the earth's mantle.

10

fore, crucial to the revolutionary new concept of plate tectonics, or structural geology of the earth's crust. (Also see "A Magnificent Revolution," *Sea Frontiers*, Vol. 18, No. 6, November-December, 1972.)

According to plate tectonics, the earth's crust is a mosaic of about eight 100-kilometer-thick rigid plates, or shells, which slowly drifts over a

100 kilometers = 62 miles



plastic upper mantle. The plates do not collide with one another; instead, one edge subducts, or descends, into the earth's mantle while the opposite edge accretes new ocean floor to its margin. The latter process occurs at the mid-ocean ridge and is called sea-floor spreading. Along still other boundaries of a crustal plate are giant zones of shear, or transform faults, where a plate slides past its neighbor.

Geologists only recently have come to understand this grand scheme of earth tectonics because the evidence is largely not on land but out of sight beneath the sea. Tectonism, or permanent displacement of the earth's crust, is confined to the plate boundaries which, although over 100,000 kilometers in total length, are nearly all in oceanic crust. Major exceptions

100,000 kilometers = 62,000 miles

Robert S. Dietz



are California's San Andreas Fault (a transform fault); Africa's Afar triangle (a triple junction where three plates join) at the nexus of the Red Sea and Gulf of Aden; and Iceland, the only place on earth where the mid-ocean ridge is above sea level.

### Three Types of Volcanism

Geologists recognize three distinctly different types of volcanism, or lava production, on the earth. The first is subduction (calc-alkalic) volcanism associated with the oceanic trenches and island arcs. It is caused by the return of molten rock to the surface from crustal plates that are being subducted, or carried down, into the earth's mantle. The lavas are charged with steam and thus are highly explosive. They create the classic volcanoes around the Pacific "ring of fire" such as Mount Rainier in the United States and Mount Fuji in Japan.

The second type of volcanism (tholeiitic) is that which injects the dikes and pillow lavas that fill in the mid-ocean ridge as it spreads apart. This process, which generates new ocean floor by symmetrical accretion to the plates that are moving apart, is called sea-floor spreading. This volcanism is effusive and quiet, producing dikes and flows, but not a single volcanic cone. Although never directly observed, this type of volcanism adds more to the earth's crust than either of the others. It repaves the ocean floor along the mid-ocean ridges around the world at the rate of 2 square kilometers per year—enough to renew the entire ocean

floor in only 150 million years.

A third type of volcanism is plume (alkalic) volcanism, caused by lavas that rise as ascending columns from deep within the earth's mantle. Upon breaking through the earth's crust, they create volcanoes that may be compared to the thunderheads that form over ascending columns of air. Plume volcanoes usually form in a row as the magma rises from the fixed deep mantle over which the earth's outer crust is drifting. The Hawaiian Chain is a good example. The Pacific plate is moving northwest at about 10 centimeters each year so that, as the old volcanoes drift away, a new one is created over the fixed plume site. The only modern active volcanism is on the big island of Hawaii, at the southeast end of the chain.

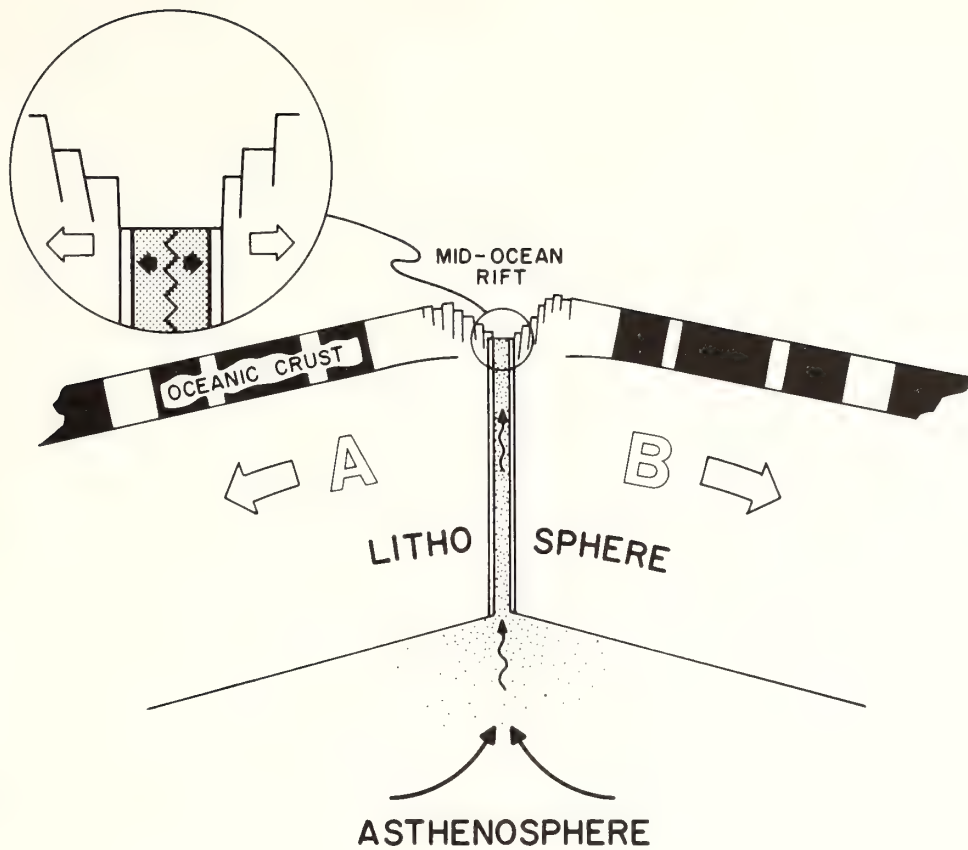
Iceland has been built by the last two named types of volcanism: tholeiitic (rift injection) lavas and plume lavas. Among the chief centers of plume volcanism on earth, Iceland probably ranks first, spewing out about 20 percent of all surface lavas. (Other major centers of plume volcanism are Hawaii, the Galápagos Islands, and the Azores.)

In Iceland, the rift lavas are abundantly augmented by plume lavas, which have built more than 200 volcanoes, many of them active. This volcanic pile that straddles the Mid-Atlantic Ridge is thus of a composite nature. The process of sea-floor spreading (rifting) observable in Iceland is strongly "overprinted" by plume lavas. Accordingly, the spreading process within Iceland is more complex than the beautiful simplicity

2 square kilometers = 0.77 square mile

10 centimeters = 3.9 inches

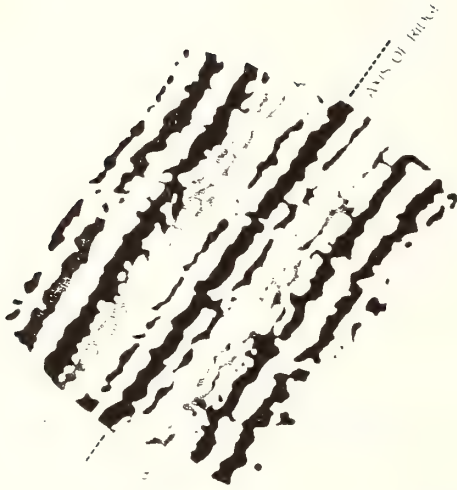
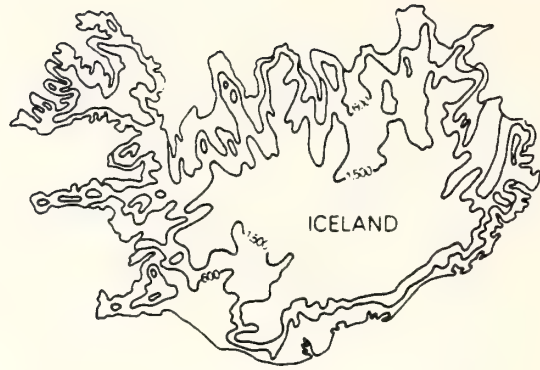




THIS HIGHLY SIMPLIFIED sketch illustrates the process of marginal plate accretion, or sea-floor spreading, which takes place at the mid-Atlantic rift. As the America plate (A) and the Eurasia plate (B) are pulled apart, a dike of hot lava is injected into the earth's lithosphere, or crust. Partial melting in the soft asthenosphere (the region below the crust) provides an ever-present source of new magma. The hot dike (speckled) cools (blue) against the adjacent plates. With renewed extension (inset), the dike breaks symmetrically along its warm and, hence, weak axis. Upon congealing and passing through the so-called Curie point at  $575^{\circ}\text{C}$ ., the upper portion of the dike takes on the ambient sense of the earth's magnetic field. The white bands are intervals when the earth's magnetic field has been normal; the black ones indicate intervals of reversed magnetic fields.

observed farther to the south along the Reykjanes Ridge, and along most other portions of the world-wide mid-ocean ridge system. While it is true that the mid-ocean ridge does bare its back at Iceland, this exposure is somewhat anomalous, complex, and atypical.

The geologic structure of Iceland is dominated by two giant rifts which trend, generally, north-south. These rifts are clearly discernible from the air. The eastern rift is now comparatively inactive, and it is believed that active rifting, or spreading apart, is largely confined to the western rift.



From *The Origin of the Oceanic Ridges*, by Egge Onizawa, 1969, by Scientific American, Inc. All rights reserved.

FLOWN BY NAVY AIRCRAFT over the crest of the *Reykjanes Ridge* south of Iceland, this magnetic survey shows, in red, the present period of normal magnetism (during which the north magnetic pole has been near the north geographic pole). This period extends back to 700,000 years ago, and it overlies and flanks the axis of the mid-ocean ridge. Other rainbow colors mark earlier periods of normal magnetism back to anomaly five which occurred about 10 million years ago. Intervening periods of reversed magnetism (when the north magnetic pole was near the south geographic pole) are shown in white. The anomaly patterns are symmetric, as each injected dike eventually split into two equal parts which accreted to opposite plates. This survey thus provides "back-to-back tape recorders" of ocean-floor growth. Each limb of anomaly patterns is 100 kilometers wide which means, since anomaly five is 10 million years old, a growth, or spreading, rate of 10 kilometers per million years or 1 centimeter per year. This is a separation rate for the two plates of 2 centimeters per year. The *Reykjanes Ridge* is, therefore, splitting apart at the rate at which a fingernail grows.

Down-dropped blocks of basalt, a dark lava rock, reveal that there has been extension within the earth's crust. The earth's outer crust, or lithosphere, is computed to be pulling apart at a rate of about 2 centimeters per year. Attempts have been made by scientists from Imperial College in London to actually measure this rifting, using a laser beam. The results, thus far, are not conclusive but are said to be consistent with the theoretically computed 2 centimeter-per-year spreading rate. No clear pattern of magnetic anomalies are observable along the Icelandic rift, but this seems certainly related to two factors: the confusion created by the plume lavas and the fact that strong magnetic imprinting occurs only in the quickly quenched pillow lavas, which must be erupted beneath water.

#### Magnetic Anomalies

Reference to the Reykjanes Ridge laying athwart the Mid-Atlantic Ridge, immediately to the south of Iceland, is convincing evidence that the Icelandic rift was created by sea-floor spreading. In fact, this process, although inferred earlier by geologic considerations, was first demonstrated by an aerial magnetic survey flown across this ridge. This survey revealed a succession of stripes or bands of strongly magnetized rock with their magnetic signal being alternated, i.e., normal and then reversed in sign. The banding, or stripes, of this survey quantitatively measured the growth of the ocean floor in a manner somewhat analogous to the growth of a tree by its annual rings. The anomalies

2 centimeters = 0.78 inches

revealed that the earth's magnetic field switches its polarity, so that the north pole becomes the south pole (and vice versa), about once every one half million years. The ambient direction of the earth's magnetic field is frozen into the mid-ocean ridge lavas as they pass through the so-called Curie point at 575°C, when solidifying.

A central band running along the axis of the mid-ocean rift was found to be normally magnetized. With respect to this central band, the others on either side of the ridge lay in mirror image, so that, if the survey map was folded into a V along the axis, the anomalies on opposite sides of the fold would be juxtaposed. Clearly these were vertical growth lines demonstrating that the ocean floor had grown by some process whereby new sea floor was being slowly accreted to crustal plates moving apart from the mid-ocean rift locus. Although these remarkable magnetic anomalies could not be traced through Iceland, lava ages showed that a similar pattern existed. The strips of lava are progressively older on both wings of Iceland as one moves away from the central rifts.

Iceland is thus not only a remote island of vivid contrasts in the far North Atlantic touching on the Arctic Circle. Its mountains, volcanoes, geysers, and thermal springs have a deeper significance. Its rugged youth, with no portion being older than 15 million years, can now be understood. It is the only place on earth where one can actually observe the earth's crust being pulled apart.

575°C = 1,035°F

# EARLY DAYS OF MARINE GEOLOGY

BY R. S. DIETZ AND K. O. EMERY

We hold no brief for the "good old days" but perhaps it adds to the perspective of marine sciences, and certainly to humor, to recall something of the beginnings of marine geology in the United States by citing some of our early experiences. This subdiscipline of geology commenced almost simultaneously in the mid-1930s on the East Coast at the Woods Hole Oceanographic Institution with the research of Henry C. Stetson and on the West Coast with the studies of Francis P. Shepard. Stetson died at sea aboard *Atlantis* off Chile in 1955, while Shepard is still actively working at the Scripps Institution of Oceanography in La Jolla, California.

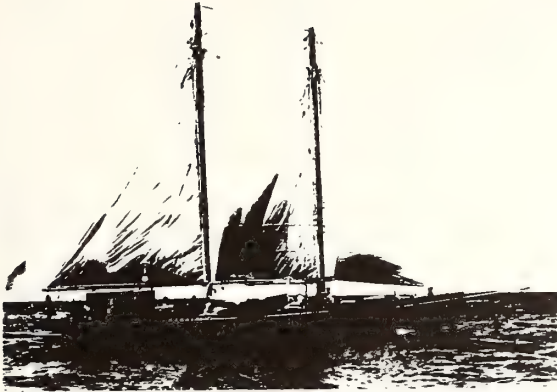
We were the first of Shepard's sixty or so marine geology students, shuttling with him between the University of Illinois and Scripps. We met at the University of Illinois, where we arrived via modes of transportation that were the norm for those Depression days. Dietz arrived by hitchhiking from the East Coast; Emery came by train, riding boxcars from San Diego.

In 1936 Shepard received a grant from the Penrose Fund of the Geological Society of America for studying submarine canyons and the sea floor generally off the coast of California. The amount was \$10,000, which was a handsome grant for those days—in fact, the largest ever given by the GSA in prewar years. With the money he was able to charter the 96-foot schooner *E. W. Scripps* of the Scripps Institution of Oceanography for six one-month cruises, build the necessary scientific equipment, employ us as his assistants at a salary of \$30 per month, and support the abortive development (to the tune of \$1,000) of the Varney-Redwine hydrostatic corer. It was hoped that this latter device would outperform the famous

C. S. Piggot gun corer, which shot the barrel into the ocean bottom. We should add "in principle," because the Piggot device, when used from *Atlantis*, seemed to obtain cores of equivalent length whether or not the gun actually fired. A subsequent grant provided for three more months in the Gulf of California during the fall of 1940. Since bed and board was provided aboard ship, we both signed on for \$1 for the three months to make us official expedition members (but Scripps never paid the \$1—perhaps fearing that we'd spend it unwisely). An interesting guideline also was that students should not receive any pay for research that pertained to their own thesis projects.

The low funding at least required us to develop some ingenuity in devising simple, inexpensive instrumentation. For example, we used the 2-meter-long Roger Revelle, later director of Scripps Institution of Oceanography, as a wave staff by having him stand at various distances from shore in the buffeting surf. This rather absent-minded wave staff also was noted for having stepped into a bucket while measuring cores aboard ship and wearing it for a couple of hours. As another example, we organized a rock preparation and sedimentation laboratory for which a budget of \$50 per year was arranged. This was considered a reasonable proportion of the Scripps' overall budget of \$125,000 per year.

Notably also, Woods Hole Oceanographic Institution was founded in 1930 with a gift of \$3,500,000 from the Rockefeller Foundation received over a period of several years; this was sufficient to construct the large brick Bigelow Building and the ketch *Atlantis*, and to cover all operations for ten years. The annual budgets for



*The 96-foot schooner E. W. Scripps, principle research vessel of the Scripps Institution of Oceanography from 1937 to 1950. (Courtesy of SIO)*

the two institutions have remained about equal, nowadays almost \$22 million for Scripps and \$20 million for Woods Hole.

Life aboard *E. W. Scripps* was somewhat different from shipboard duty today. The ship's crew consisted of only four persons—captain, engineer, deck hand, and cook; the scientific party was seven—the number of bunks available. We generally worked around the clock, six hours on and six off. The scientific party was expected to be sailors to run the ship and technicians to operate oceanographic winches, assemble and use the water and bottom samplers, and do various shipboard analyses for water chemistry. Among our duties while steering the ship was to tabulate by hand the water depth every two minutes. We did this with great enthusiasm since we had installed aboard the latest Submarine Signal Co. fathometer, which indicated the depth on a revolving red-flashing neon light. Graphic recorders had not yet been invented, so this instrument represented to us a remarkable advance over the sounding lead. And, in fact, we continued to use the hand-powered wire-and-lead sounding winch installed on a rowboat for making hydrographic surveys of the inner heads of several submarine canyons. Rather remarkably, it was possible to demonstrate that canyon heads were repeatedly filling with sediment and then emptying out.

Prior to the cruises we built dredges, grab samplers, sediment traps, and corers. The best corer that we constructed was a 600-pound open-barrel gravity model that increased the weight of such devices over earlier models by a factor of ten. We purchased junk lead at 3¢ per pound, used scrap 2½-inch pipe, and built two corers for about

\$50 each. It was not until after the war that we heard about Kullenberg's invention of the piston corer. Nevertheless, we commonly obtained cores 12 feet long, and in one instance, a diatomaceous ooze core in the Gulf of California 17 feet long for a new record. Of course, things were considerably cheaper in those times. By way of example, an apparently wealthy American tourist at the local swinging bistro named El Tecolote (The Owl) in Guaymas, Mexico, generously offered to buy beer for our ship's staff. When he discovered that the bartender could not change his U.S. \$10 bill, he gallantly said, "Set up the whole amount in beer." One hundred and twenty bottles of Carta Blanca were lined up along the bar, and as was customary then in Guaymas, bowls of unshelled shrimp were thrown in like the free peanuts of today. A side advantage was that the long row of beers immediately stopped the girls' pestering us for drinks.

After the cruises, when the ship was unloaded so that the biologists or physical oceanographers could take their turns, we were able to study the samples and other results. Since all was new, both to us and to others, we had no difficulty in finding problems. Our masters' theses were on mechanics of coring and on the extensive phosphorite deposits we discovered covering many of the offshore banks. Our doctoral dissertations were on clay minerals of the deep areas and on rocks of the shallow banks. We recognized that the offshore basement geology of the Southern California borderland belonged to the Franciscan province. Articles on terraces, currents, barite concretions, and transport of rocks by kelp and sea lions were by-products. The overall results were incorporated into Special Paper 31 of the Geological Society of America by Shepard and Emery, a monograph treating submarine canyons and the general bathymetry of the sea floor off California. These must have been our most productive years in terms of variety and number of investigations, because of newness of the field and, probably, the aid of funds too small to permit much diversion of time and energy.

Local transportation was provided by a succession of old cars, starting with a 1928 Chevy that Shepard bought for us for \$50. By the time we drove it 15 miles, cork in the transmission wore out and serious noises developed. Replacement by junk gears extended the life of the Chevy for a year or so. After tiring of having to tie a rope around the car to keep the doors closed, we swapped it for a 1928 Reo that had a good engine but bad tires. Eventually, this was swapped for Walter Munk's 1928 Buick (The Queen Mary). The state of the Reo's tires is illustrated by a blowout of the spare tire in the hot California sunshine when he drove northward too long. In time the differential of the Buick disintegrated, and a 1928 Ford was next. The total cost of these four cars was \$200—nothing



*Dietz with gravity coring device at rail of E. W. Scripps, about June 1938.*



*Emery with hollow giant worm or animal tube of enigmatic origin dredged from the wall of Dume Canyon off California, May 1938.*

compared to their present value as antiques if they had been stored until now.

The four years of cross-country commuting, cruising (at least 12 months aboard *E. W. Scripps*), and study came to an end in 1941. Just before receiving his doctorate, Emery wrote 135 individual letters, blanketing the entire country, seeking employment. Dietz, being congenitally lazier (or possibly more efficient), trusted that this blizzard of inquiries would produce several plums of which he might select one after Emery made his acceptance. But the market for marine geologists, like the job market for poets then and now, was bleak. Not a single position was tendered. As with many products, there is commonly no demand for the first ones off the line. Even the U.S. Navy saw no particular need to know anything about oceanography; in fact, its interest, when it did develop, probably stemmed from the initiative shown by the Army Air Corps in setting up a group of officers and civilians to predict the paths of downed airmen in their rubber life rafts carried by surface currents of the western Pacific.

In retrospect, the "good old days" were both the best of times and the worst of times. Happily, one tends to recall the ups rather than the downs—and there is no substitute for the buoyancy

of youth. Oceanography of today is, of course, much more sophisticated and the results ever more quantitative. But there was a certain enjoyable simplicity, and even beauty, in working with instruments that had less than one vacuum tube, let alone one transistor. The need to do all kinds of work gave us a broad view of the ocean such that we were oceanographers and not just marine geologists. We even thought we understood physical chemical, and biological oceanography. Working on the low-freeboard *E. W. Scripps* with decks awash gave an intimate feel for the oceans such as experienced today only by scuba divers.

As we write this note Charley Hollister is

putting out to sea with his "Super Straw," the giant 4½-inch coring device, and a new generation of marine sedimentologists. They will study complex seabed forms, subbottom acoustically reflecting layers, and mass physical properties of muds. In this work they will be guided by the multisensor MPL Deep-Tow, a real-life dream machine. All in all, a million-dollar effort. Yes, times have changed—and for the better.

*R. S. Dietz is a research oceanographer at the National Oceanographic and Atmospheric Administration, Miami, Florida. K. O. Emery is Henry Bryant Bigelow Oceanographer at Woods Hole Oceanographic Institution.*



*Dietz with sediment trap and Emery and Shepard with wire sounding machine setting one for the survey of La Jolla Submarine Canyon, November 1938.*

Reprinted from: *Geology*, Vol. 4, No. 7, 391-392.

## El'gygtyn: Probably world's largest meteorite crater

Robert S. Dietz

National Oceanic and Atmospheric Administration  
Miami, Florida 33149

John F. McHone

Department of Geology, University of Illinois  
Urbana, Illinois 61801

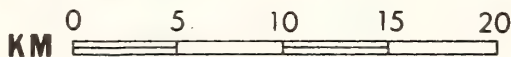
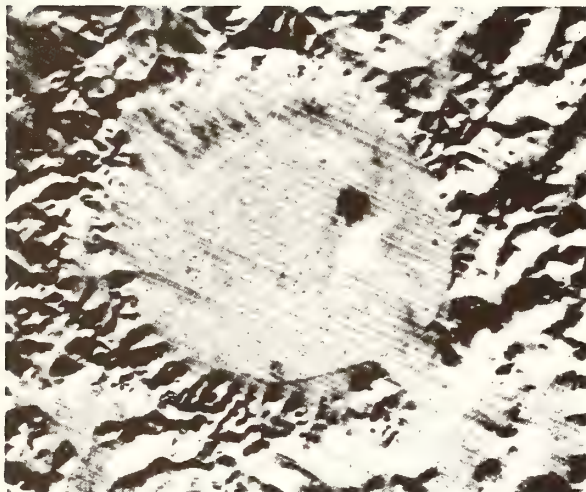


Figure 1. LANDSAT images of the Siberian meteorite crater El'gygtyn. Remarkable circularity of feature is revealed in upper snow-covered winter view (dark spot near center is cloud shadow, not island). Lower scene shows central lake in ice-free summer conditions.

### ABSTRACT

LANDSAT imagery indicates that El'gygtyn in northern Siberia is probably a giant meteorite crater, the largest Quaternary impact structure on Earth, and not a tectonic depression. This probability is supported by the remarkable circularity of the crater, as outlined by the ring-mountain rim, remoteness from modern volcanic sites, and lack of collapse scalloping of the margin.

Siberia appears to have an unusual attraction for cosmic bodies. The Tunguska comet head exploded above central Siberia in 1908, and the Sikhote-Alin nickel-iron meteorite struck eastern Siberia in 1947. A million or so years earlier, Siberia probably was the site of the largest crater-forming meteorite impact to strike the continents in modern times. We refer to the El'gygtyn crater (sometimes transliterated El'gytkhyn; lat 67°30'N, long 172°00'E), in the remote Anadyr Mountains of eastern Siberia; this crater, by morphologic criteria, appears to be a meteorite impact site. Its 18-km diameter would make it by far the largest meteorite crater on Earth, far exceeding both the Lake Bosumtwé crater in Ghana, 10.5 km across, and the New Quebec crater of Canada, 3.2 km across. There are, of course, larger ancient impact sites or astroblemes, but these are now so deeply eroded that they are the roots of craters that are no longer craterform.

El'gygtyn has been previously listed as a possible impact site by Dence (1972), citing Zotkin and Tsvetkov (1970), who listed the diameter as only 12 km, which is approximately that of the rudely circular lake occupying the center of this depression. LANDSAT imagery (Fig. 1) reveals the remarkable circularity, symmetry, and elevated rim of the overall crater, 18 km across. This circularity is easily overlooked on maps because of cartographic emphasis of the lake shoreline, as large sediment aprons have filled parts of the crater (Fig. 1, lower) and produced an irregular form.



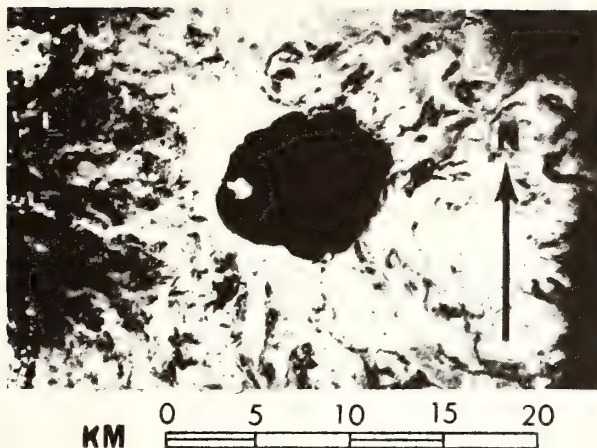


Figure 2. LANDSAT image of Crater Lake, Oregon, showing scalloped walls, central volcanic island, and asymmetric perimeter typical of calderas.

El'gygytyn is a unique feature of the maturely dissected and nonglaciated Anadyr mountainland. The nearest active volcanoes lie 600 km away on the Kamchatka Peninsula. This craterform depression is asymmetrically filled with a 170-m-deep lake about 12 km across and of squarish outline. The crater is outlined by a ring mountain that attains its greatest relief to the west. The rim is breached by a river in the southeast quadrant, the outflow of which eventually reaches the Belaya River of the Pacific watershed. The highest elevations along the rim are about 1,060 m, according to the U.S. Air Force operational navigational chart. This rim thus stands about 450 m above lake level, or 620 m above the lake bottom. Extensive talus aprons along the western half of the crater are now being entrenched, suggesting that the lake level was once higher than at present. The almost perfect circularity of the depression is enhanced in the winter LANDSAT image because snow masks the outline of the lake shore. The mature degree of erosion suggests that the crater was created one to a few million years ago.

El'gygytyn was discovered in 1933 by S. V. Obruchev from an aircraft, according to Nekrasov and Raudonis (1973). The lake-filled crater immediately attracted attention because of its unusual shape. Obruchev expressed the opinion that it was a volcanic crater or caldera of vast dimensions, yet there are no young volcanic rocks associated with the feature. Further negative evidence is provided by LANDSAT images of calderas that are quite unlike El'gygytyn. Figure 2, for example, is a LANDSAT image of Crater Lake, Oregon, one of the world's best examples of a caldera. Crater Lake is situated on top of a large volcanic dome, and although it is rudely round, its circularity is spoiled by its scalloped margin. This was created by land slippage, subsidence associated with magma withdrawal, and subsequent internal evisceration by ash eruptions. A caldera has been aptly described as "a volcanic crater whose head has fallen in when its insides were blown out." El'gygytyn does not have the geomorphic aspect of a caldera, which is invariably situated atop a large volcanic cone and which occurs in chains or groups and not as a solitary feature. El'gygytyn is also larger than most calderas and more symmetrical.

Nekrasov and Raudonis (1973) have described El'gygytyn as a collapse feature of unspecified origin. One must assume that a subsidence of this magnitude would necessarily be tectonic. Such an origin, however, would not account for the ring of mountains unless the structure underwent domal uplift by injection of magma prior to collapse. In this event, the remarkable circularity would remain unexplained. Nekrasov and Raudonis (1973) studied eight rock samples collected from the north and northeast parts of the ring mountain and found them to be an assortment of silicic, intermediate, and mafic igneous rocks, including both intrusive and extrusive types, of probable Mesozoic age. These specimens appear to be country rocks rather than products of the crater-forming event. Nekrasov and Raudonis concluded that the crater could not be an impact site because they detected no coesite in thin sections. This conclusion is unjustified, as coesite is virtually unrecognizable in thin section, and, in any event, shock overpressures at an impact-crater rim are already far below those needed to create this high-pressure silica polymorph. In general, shock metamorphism and shatter coning are never found in situ beyond one-half of the radius of an impact crater from ground zero.

We conclude that El'gygytyn is probably the world's largest modern impact crater.

#### REFERENCES CITED

- Dence, M., 1972, The nature and significances of terrestrial impact structures: Internat. Geol. Cong., 24th, Montreal 1972, Proc., sec. 15, Planetology, p. 77-89.  
 Nekrasov, I., and Raudonis, P., 1973, Meteorite craters (translation from Russian ms.): Ottawa, Canada, Canadian Translation Bureau.  
 Zotkin, I. T., and Tsvetkov, V. I., 1970, Searches for meteorite craters on earth: Astron. Vestnik, v. 4, p. 55-65.

#### ACKNOWLEDGMENTS

Reviewed by Peter Rona.  
 The work of John McHone was supported by a grant-in-aid for meteoritic research from the Barringer Crater Company.

MANUSCRIPT RECEIVED MARCH 22, 1976

MANUSCRIPT ACCEPTED APRIL 27, 1976

Reprinted from: *Proc. American Society of Civil Engineers Specialty Conference on Dredging and Its Environmental Effects, Mobile, Al., 26-28 January 1976, 936-946.*

DEPOSITION AND EROSION IN THE DREDGE SPOIL AND  
OTHER NEW YORK BIGHT DUMPING AREAS

By: George L. Freeland<sup>1</sup> and George F. Merrill<sup>1</sup>

INTRODUCTION

The disposal of solid wastes from the New York City metropolitan area is the cause of considerable environmental concern, as most of these wastes are dumped in marine waters outside of the harbor mouth (Table 1). Dredge spoil and sewage sludge constitute over 94% of the volume of material dumped containing solids.

In 1973 the National Oceanic and Atmospheric Administration (NOAA), under the Marine Eco Systems Analysis (MESA) Project, initiated research to determine the effect of dumping in the New York Bight. A new hydrographic survey of the Bight apex was immediately started to determine what changes had occurred in bottom topography since the last previous survey in 1936. Some results from this survey are presented here.

HYDROGRAPHIC SURVEYS

Hydrographic surveys have been made in the New York Bight since 1845 by the U.S. Coast and Geodetic Survey (now the National Ocean Survey, NOS, part of NOAA). The last U.S. C.&G.S. survey to cover the Bight apex, the area immediately adjacent to the harbor mouth where dumping is most intense, was in 1936. Comparison with the 1845 revealed the development of several knolls due to early dumping (4).

Our 1973 survey had depth sounding lines spaced 1000 ft (305 m) apart over an area approximately 15 nautical miles (28 km) square (Fig. 1). Data from this survey were then compared with data from the 1936 survey to produce a net-change map.

NET BATHYMETRIC CHANGE

Examination of the boat sheets (detailed maps showing final data plots) from the 1936 survey (NOS No. H-6190) revealed trackline spacing of approximately 0.5 nautical miles (900 m) versus 1000 ft (305 m) spacing for the 1973 survey, and divergence of trackline directions. In order to compare the two surveys, boat sheets from both surveys were contoured on a 3 ft. (0.92 m) contour interval (see Fig. 1 for the 1973 map). A 1000 ft. (305 m) grid was then prepared for the entire area and overlaid on both maps. From

<sup>1</sup>. National Oceanic and Atmospheric Administration, Atlantic Oceanographic and Meteorological Laboratories, 15 Rickenbacker Causeway, Miami, Florida 33149



Fig. 1. 1973 Bathymetric map of the New York Bight apex. From a NOAA survey. Contour interval one meter.

plotted data on the boat sheets and interpolations between contour lines, a value was picked for the center of each 1000 ft (305 m) square for each survey. These numbers were added algebraically to produce a positive or negative number for each square representing erosion or deposition in that square for the 37 years between surveys. The values were corrected for a sea level rise of 0.62 ft (0.189 m) from NOS mean monthly sea levels at Sandy Hook, N.J. They were then contoured to produce the net-change map (see Fig. 3).

Volumes of erosion and deposition were calculated by planimetry of all contours and multiplying these areas by the appropriate contour interval. Appropriate volumes were added for slope sediment between contours.

Areas, volumes of erosion and deposition, and net changes for Bight apex features are listed in Table 2.

#### DISCUSSION: ANTHROPOGENIC SEDIMENTS

Sediments are introduced into the Bight apex almost entirely in the form of fine-grained matter. Dredge spoil constitutes the most important source of solids brought in by man (anthropogenic sediment) (Table 1). Estimates of the total amounts of dredgings barged from 1936 to 1973 (records are unreliable prior to 1954) indicate that about  $186 \times 10^6$  cu. yd. ( $142 \times 10^6$  m<sup>3</sup>) were dumped, compared to  $162 \times 10^6$  cu. yd. ( $124 \times 10^6$  m<sup>3</sup>) calculated on the basis of net bathymetric change for the dredge spoil dumpsite and the dumping areas near Ambrose Channel and Sandy Hook Channel (Table 2). This indicates that approximately 87% of the material barged is still in place on the bottom.

Detailed mapping of the dredge spoil dumpsite shown that shoaling of up to 34 ft. (10.36 m) has occurred over an area of 11 square nautical miles (36. Km<sup>2</sup>) south of a knoll which itself was formed by earlier dumping (Figs. 4-6).

Sewage sludge, on the other hand, has a bulk density only slightly greater than that of sea water and contains mostly organic matter. It does not settle to the bottom as rapidly as dredge spoil. Once on the bottom at the designated site of the western edge of Cholera Bank, sludge is apparently easily resuspended and dispersed, as only traces of sludge can be found at the designated site. An unknown fraction settles in the Christiaensen Basin and the upper Hudson Shelf Valley where it mixes with natural muds, the remainder being dispersed by the water column. For this reason, the sludge dumpsite is not listed in Table 2. Differentiation of sludge from natural muds, mostly by chemical means, is currently undergoing intensive study by NOAA. Although the volume of sludge barged is considerable, and will increase in the future as more plants come on line in the New York area and percentage treatment improves, solids by weight do not constitute an important addition to sediment volume on the bottom (Table 1). Contamination of bottom sediment and sediment suspended in the water column by

NEW YORK BIGHT

939

TABLE 1  
Source of Solids Transported into Marine Waters  
of the New York Bight

SOURCE	VOLUME		WEIGHT		
	$10^6$ cu yd/yr ( $10^6$ m <sup>3</sup> )	% of barged	$10^6$ short tons/yr ( $10^6$ metric tons)	% of barged	% of total input
Dredge spoil	8.35 (6.38)	62.4	5.21 (4.73)	85.8	54
Sewage sludge	4.28 (3.27)	32	0.203 (0.184)	3.3	2.1
Cellar dirt	0.76 (0.58)	5.7	0.557 (0.51)	9.0	6.8
Total Barged	13.39 (10.24)	100.0	6.07 (5.51)	100.0	72.9
Atmospheric			0.45 (0.41)		3.1
Wastewater*					
Municipal			0.39 (0.35)		4.0
Industrial			0.2 (0.2)		0.2
Runoff*					
Gaged			1.5 (1.4)		16
Urban			1.2 (1.1)		12
Total input			9.60 (8.76)		100.2

From Ref. 3

\* 95% of these coastal zone inputs come through the Rockaway - Sandy Hook transect.  
Figures do not include shelf-derived sediment from outside the Bight.

TABLE 2  
Volumes of Erosion and Deposition in the New York Bight Apex  
between 1936 and 1973

	Area sq (km <sup>2</sup> )	Volume $10^6$ cu yd. ( $10^6$ m <sup>3</sup> )		
		Erosion	Deposition	Net Change
1. Entire Apex	209 (718)	182 (140)	212 (162)	29 D (22)
2. Dredge Spoil Dumpsite	11 (36)		122 (93)	122 D (93)
3. Cellar Dirt Dumpsite	2 (8)		6 (5)	6 D (5)
4. Ambrose & Sandy Hook Channels	25 (86)	63 (48)	40 (31)	23 E (17)
5. Anthropogenic	38 (130)	63 (48)	168 (129)	105 E (81)
6. Christiaensen Basin <sup>1</sup>	24 (83)	13 (10)	8 (6)	5 E (4)
7. Hudson Shelf Valley <sup>2</sup>	7 (23)	12 (10)	3 (2)	10 E (7)
8. Non-anthropogenic	171 (587)	120 (91)	43 (33)	76 E (58)

1. Area between 14 and 20 fathoms (26-37 m) north of 40°24'N.

2. Area deeper than 20 fathoms (37 m) north of 40°19.22'N.

3. Equal to a layer 0.106 in. (2.7 mm) thick per year.

Some figures may not agree due to rounding off.

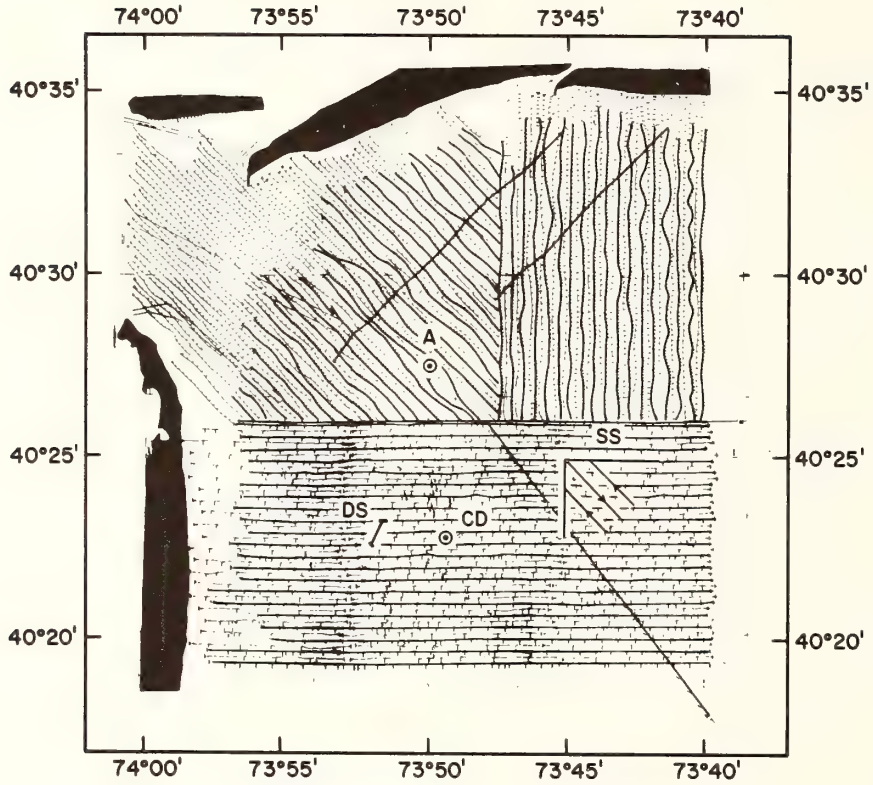


Fig. 2. Tracklines of the 1973 bathymetric survey. Light lines show tracklines for bathymetry only. On heavy lines both bathymetric and geophysical data were collected.

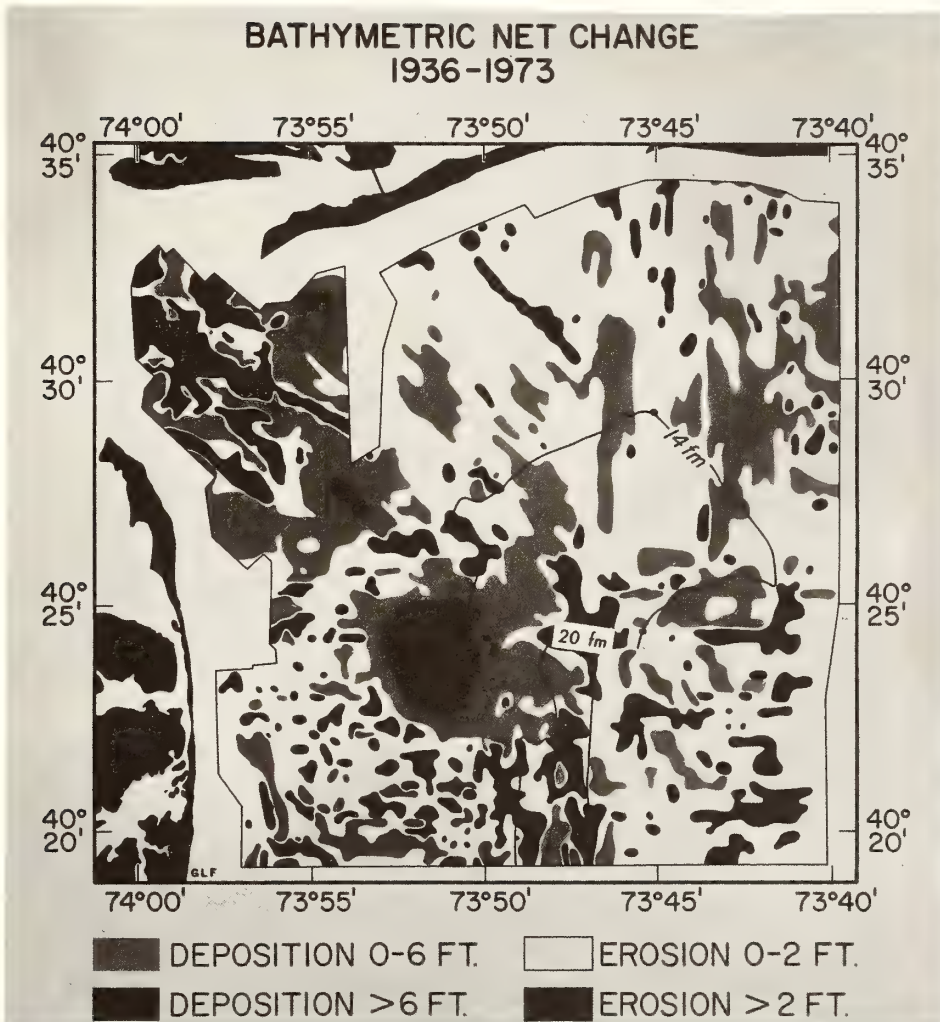


Fig. 3. Net bathymetric change, N.Y. Bight Apex, from 1936 to 1973.

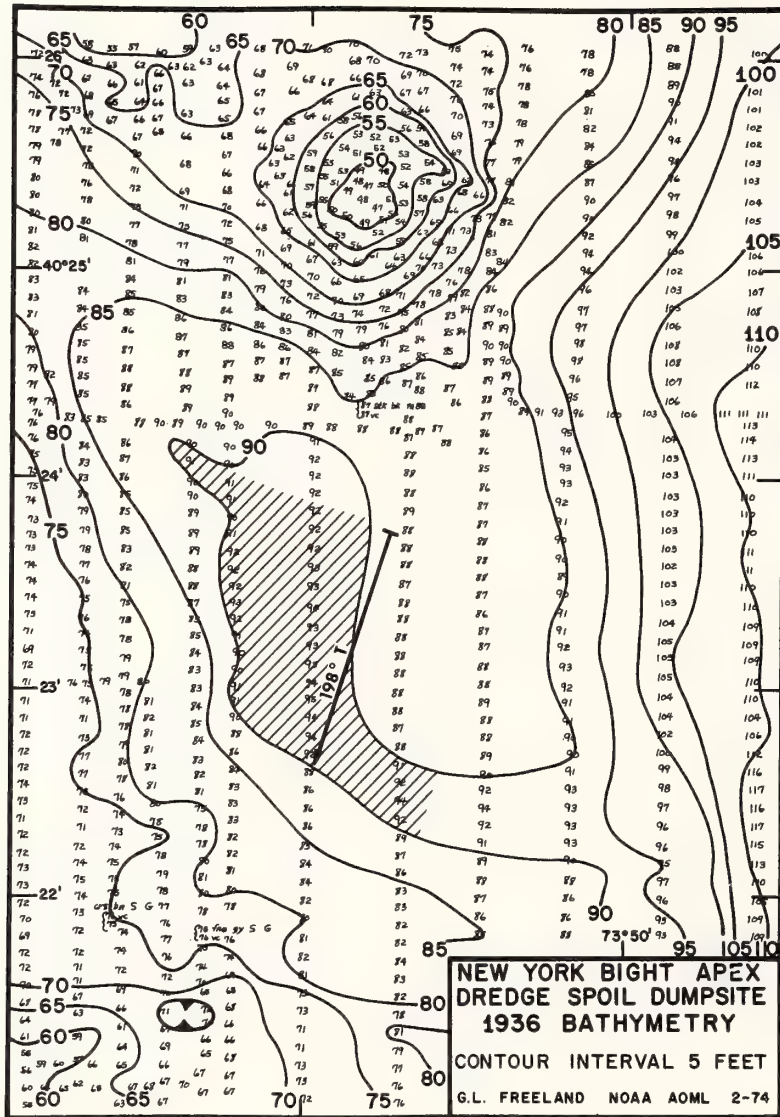


Fig. 4. N.Y. Bight dredge spoil dumpsite. 1936 Bathymetry. Line marked  $198^{\circ}$ T and hachured area show the designated dumpsite (Figures 4-6) based on 1936 soundings to lie within the 90 ft. isobath.



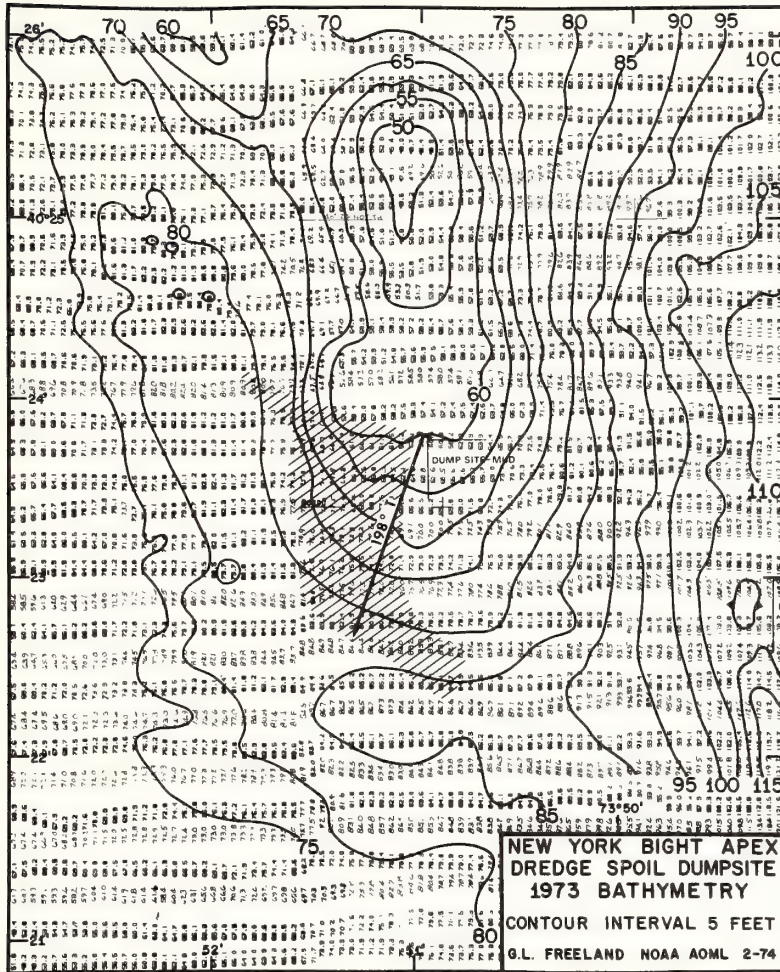
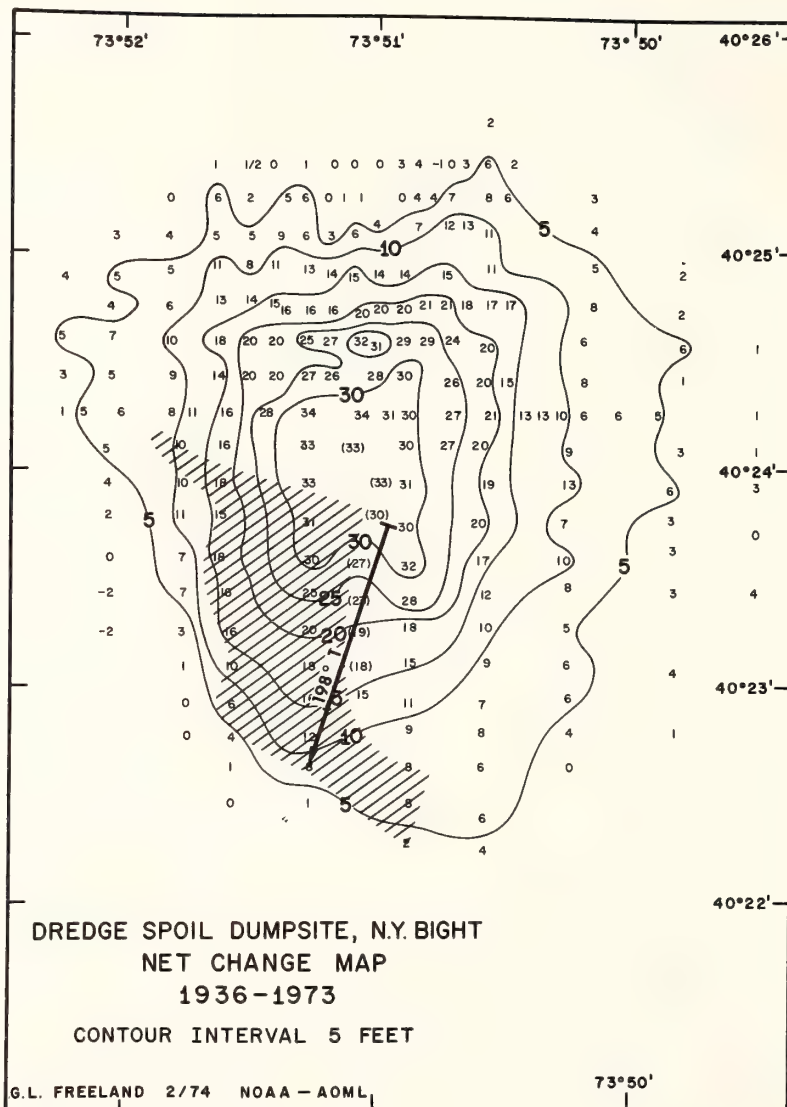


Fig. 5. N.Y. Bight dredge spoil dumpsite. 1973 Bathymetry.

DREDGING EFFECTS



organic pesticides and heavy metals in sludge is, however, a serious concern.

Cellar dirt, the third anthropogenic sediment, consists of demolition rubble from demolition, foundation rock and dirt, and slag. Brick, metamorphic rocks, and red sandstone are commonly recovered in grab samples. Cellar dirt, while making a recognizable spoil mound, is not considered an important pollutant because of low volumes and the absence of toxic chemicals.

#### NATURAL SEDIMENTS

Natural sediment input from land sources comes mainly from stream runoff from the Hudson River drainage basin and urban runoff from the New York metropolitan area (Table 1). These sources are relatively easy to measure compared to sediment transported from other areas of the shelf. Various estimates of sediment transport indicate that, for the eastern U.S. continental margin, a) 90% of the sediment from land sources is deposited in estuaries and wetlands; b) net suspended fine sediment transport on the shelf is probably landward, with possibly much of the material finally settling in estuaries; and c) recycling (resuspension and settling) of sediment on the shelf may transport orders of magnitude more sediment than either enters or leaves the shelf (1, 2).

From our net change map, we have calculated volumes of natural sediment eroded and deposited in the Bight apex (Table 2). After subtracting the anthropogenic material in the Ambrose - Sandy Hook Channels area and in the dredge spoil and cellar dirt dumpsites, the volume of material eroded exceeds deposition by  $76 \times 10^6$  cu yd ( $58 \times 10^6$  m<sup>3</sup>), equivalent to a layer 0.106 in. (2.7 mm) thick over the non-anthropogenic areas. From other ongoing studies, it appears that this erosion occurs primarily during storms which pass most frequently in winter months.

#### ERROR SOURCES

Tidal corrections from the Sandy Hook tidegage were made on all records and are not considered to be a significant error source.

Bar checks for fathometer error were made before and after daily operations at sea. Surveying was not done or was rerun if fathometer readings were incorrect.

After contouring was completed, data from some small areas in the northern Christjaensen Basin became suspect because of sinusoidal wiggles in contour lines which varied systematically with tracklines, amounting to a maximum of about 1.5 ft. (0.457 m) difference between adjacent tracklines. After reruns of bathymetry lines in an east and west direction (perpendicular to the original tracklines), it was determined that the "waves" originally mapped in the bottom were real, although of lower amplitude, in one area, and non-existent in other areas where the original waves were lower than maximum amplitude. Further analysis indicated the source of error to be "squat" of the

survey boat (level of ride of the boat in the water) on geophysical tracklines, in certain areas due to towed instruments. These errors were corrected in the final contour map and at least partially compensated for in the net change map. Maximum error is estimated to be  $\pm 0.5$  ft. (0.1524 m).

#### ACKNOWLEDGEMENTS

Grateful appreciation is given to the Corps of Engineers Operations Section of the New York District, contractor for the 1973 survey: Mr. Lewis Pinata, Acting Chief, Mr. Dennis Suszkowski, Oceanographer, Mr. Herbert K... and Mr. Bill Musak, Chief and Assistant Chief of the Survey Branch, and the crew of the survey vessel HATTON, which did the northern half of the survey. Thanks are also given to Mr. Robert Spies, and Mr. Robert Wagner, Chief and Assistant Chief of the Survey Branch of the Corps Philadelphia District, and to the crew of the survey vessel SHUMAN, which did the southern part of the survey. Mr. George Lapiene, electronic technician at AOML in 1973, was aboard both survey vessels during the three months of work on geophysical tracklines. Dr. Anthony E. Cok, Professor of Geology at Adelphi University, Garden City, New York, was aboard the HATTON during geophysical trackline work. Dr. John J. Dowling, Associate Professor, Marine Sciences Institute, University of Connecticut, Groton, Connecticut, made the net change calculations. The Tidal Datum Planes Section, Oceanographic Division, of the National Ocean Survey (NOAA), Rockville, Maryland, supplied monthly mean sea level data for the Sand Hook Station for 1936 and 1973. Cdr. R. L. Swanson, Project Manager, MESA New York Bight Project, Stony Brook, New York, provided additional tidal correction data. Finally, Drs. H. B. Stewart, Jr., and D. J. P. Swift of AOML reviewed the manuscript.

#### REFERENCES CITED

1. Meade, R.H., Sachs, P.L., Manheim, F.T., Hathaway, J.C., and Spencer, D.W., "Sources of Suspended Matter in Waters of the Middle Atlantic Bight", *Journal of Sedimentary Petrology*, Vol. 45, 1975, pp. 171-188.
2. Milliman, J.D., Pilkey, O.H., and Ross, D.A., "Sediments of the Continental Margin of the Eastern U.S.", *Bulletin of the Geological Society of America*, Vol. 83, 1972, pp. 1315-1334.
3. Mueller, J.A., Anderson, A.R., and Jeris, J.S., "Contaminants Entering the New York Bight - Sources, Mass Loads, Significance", Report sent to NOAA, MESA N.Y. Bight Project Office, Stony Brook, N.Y., 11794, 1975.
4. Williams, S.J., and Duane, D.B., "Geomorphology and Sediments of the Inner New York Bight Continental Shelf", *Technical Memorandum 45*, U.S. Army, Corps. of Engineers, Coastal Engineering Research Center, July, 1974.

Reprinted from: Middle Atlantic Shelf and the New York Bight, ASLO Special Symposia, Volume 2, 90-101.

## Surficial sediments of the NOAA-MESA study areas in the New York Bight

George L. Freeland, Donald J. P. Swift, and William L. Stubblefield

Atlantic Oceanographic and Meteorological Laboratories, NOAA, 15 Rickenbacker Causeway, Miami, Florida 33149

Anthony E. Cok

Department of Earth Sciences, Adelphi University, Garden City, New York 11530

### Abstract

In the New York Bight apex, extensive sedimentological studies and a 1973 bathymetric survey reveal that the only significant change in bottom topography since 1936 occurred at the dredge spoil dumpsite where the dumping of  $98 \times 10^6 \text{ m}^3$  of dredged material has caused up to 10 m of shoaling. The center of the Christiaensen Basin, a natural collecting area for fine-grained sediment, is no doubt contaminated with sludge but shows no apparent sediment buildup during the intervening 37 years. The apex outside of the Christiaensen Basin is floored primarily by sand ranging from silty fine to coarse, with small areas of sandy gravel, artifact (anthropogenic) gravel, and mud. Nearshore mud patches appear to be covered at times with sand and occasionally scoured out. Sidescan sonar records show linear bedforms, indicative of sand movement, over most of the apex area.

Two midshelf areas have been proposed as interim alternative dumping areas. The northern area is in a tributary valley of the ancestral Long Island river system. Fine sands cover the northeast part and medium sands predominate to the west and south. Bottom photographs show a smooth, slightly undulatory, mounded or rippled sea floor.

In the southern alternative dumping area coarse sand and gravel deposits lie on the crest and east flank of the Hudson divide, while medium and fine sand occurs in the ridge and swale topography to the west. These distributions suggest fine sediment is winnowed from the crest and east flank of the divide and deposited to the west. Veatch and Smith Trough contains a veneer of shelly, pebble sand with large, angular clay pebbles and occasional oyster shells derived from exposed early Holocene lagoonal clay. These studies suggest that if sewage sludge were dumped, widespread dispersion, mostly to the southwest, could be expected, with winter resuspension and transport of fine material on the bottom. Possible permanent buildup on the bottom could be expected if dredged material were dumped.

The nature of bottom sediments and sediment particles suspended in the water column becomes of interest to environmental managers when man's activities in the ocean disturb the sea floor or the near-bottom water column. In addition to the immediate results, one must also consider the effect on long term natural phenomena. How are these processes affected by what man has done, or perhaps more importantly, how do natural processes modify what man has done to disturb the natural environment?

Here we report work done at the Atlantic Oceanographic and Meteorological Laboratory as part of the NOAA-MESA New York Bight Project.

Hydrographic surveys of the New York Bight were initiated in 1936 by the Coast and Geodetic Survey (now the National Ocean Survey) in nearshore areas and have been repeated periodically. Bathymetric

maps at 1-fathom (Stearns and Garrison 1967) and 4-m intervals on the shelf and 200-m-intervals on the continental slope (Fig. 1; Uchupi 1970) were made from 1936 survey data. A new survey of the bight was made in 1975; results should be available in 1977.

Surficial morphology of the New York Bight, and sediment distribution across this surface, may be explained by sea level fluctuations caused by continental glaciation during the past several million years. The last glacial stage ended 15,000 years ago (Milliman and Emery 1968) when the eastern North American ice sheet extended as far as Long Island and northern New Jersey. During maximum glacial advance sea level was lowered about 160 m (Veatch and Smith 1939) so that the shoreline of the bight was in the vicinity of Hudson Canyon (see Fig. 1). Since the ice melted, the shore-

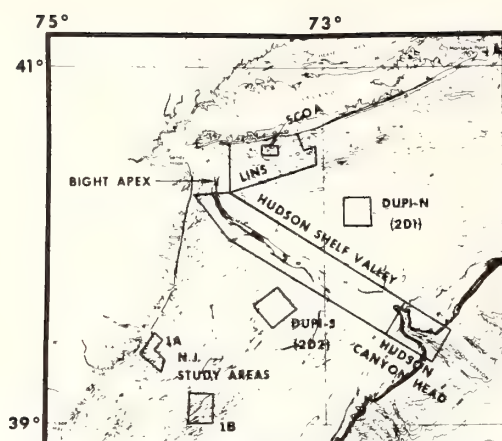


Fig. 1. Index to detailed study areas and topographic features in the New York Bight. (Bathymetry from Uchupi 1970.) Contour intervals 4 and 200 m. 1A—New Jersey nearshore ridge and swale study area and the Atlantic generating station site; 1B—New Jersey central shelf ridge and swale study area; LINS—Long Island nearshore study area; SCOA—Suffolk County outfall area; 2D1, 2D2—proposed interim alternative dumpsites.

line advanced to its present position; many features of the shelf are the result of several sea level fluctuations. Morphologic features are discussed in our companion paper in this volume (Swift et al. 1976) and elsewhere (e.g. McKinney and Friedman 1970; McKinney et al. 1974; Stubblefield et al. 1974, 1975; Knott and Hoskins 1968; Duane et al. 1972; Williams 1976).

#### Surficial sediments

A comprehensive sampling program for the outer shelf was conducted by the Woods Hole Oceanographic Institution and the U.S. Geological Survey, who sampled on an 18-km spacing. The Corps of Engineers Coastal Engineering Research Center has collected about 4,200 km of geophysical data and over 300 cores as a part of its studies on the inner shelf of the bight (Duane 1969; Williams and Duane 1974; Williams 1976). MESA work had been conducted primarily in New Jersey nearshore and central shelf areas, the bight apex, the nearshore of Long Island eastward to Fire Island, two central shelf alternative dumping areas, and the Hudson Shelf Valley (Fig.

1). Emphasis here is on the bight apex and the central shelf alternative dumping areas.

*Source and age of sediments*—Sediments covering the floor of the bight were mostly deposited during lowered sea level and were reworked during the landward-seaward migrations of the shoreline. As transgression progressed, fluvial and older sediments were covered by estuarine and lagoonal sediments behind barrier islands or directly reworked by littoral processes associated with the advancing shoreline. During a transgression, bottom currents of the inner shelf interact with the shelf floor to form a concave surface whose profile resembles an exponential curve, with the steep limb comprising the shoreface (Swift et al. 1972). With a loose, sandy substrate, the inner shelf shoreface tends to extend itself laterally across the mouths of bays, closing them, except for inlets, by the deposition of sand in the form of spits and barrier islands. Estuaries and lagoons behind these spits and islands then trap suspended fine sediment (mud), while the barrier islands are nourished by littoral drift from eroding headlands and by sand moving landward from the shelf.

As sea level rose during the Holocene transgression, the inner shelf profile moved shoreward by means of shoreface erosion. Some eroded sand was swept onto the barrier islands by storm overwash and buried, only to be re-exposed again at the eroding shoreface. Most material from shoreface erosion, has, however, been washed down-coast and seaward to form a discontinuous sand blanket 0 to 10 m thick (Stahl et al. 1974). Thus, the New York Bight shelf floor is dominantly sand-sized sediment (Schlee 1973). Fine-grained sediments are generally absent, having been transported either into the Hudson-Raritan estuary, behind barrier islands, or off the shelf edge. Locally, underlying strata of transgressed lagoonal and estuarine semiconsolidated mud deposits or resistant coastal plain strata are exposed on the sea floor (Swift et al. 1972; Stahl et al. 1974; Sheridan et al. 1974).

*Sediment types*—Sediment types have been mapped in the New York Bight primarily by dominant grain size (Fig. 2).

Generally, the shelf is covered by sand-sized sediment with isolated gravel patches (Schlee 1973, 1975; Williams and Duane 1974; Williams 1976). In deeper water, generally seaward of the 60-m isobath, in the Hudson Shelf Valley, and in lagoons and estuaries where wave action is less pronounced, silt is the dominant sediment (Freeland and Swift in press). In the Long Island nearshore zone west of Fire Island, small mud patches, some of which are seasonal, are of considerable environmental concern owing to contamination of the fines by pollutants.

*Suspended sediments*—Meade (1972a, b) noted the following: Pleistocene glaciations and sea level fluctuations drastically altered the composition and distribution of sediments on continental margins; it is not always immediately evident whether present shelf deposits reflect modern or Pleistocene conditions. Fine sediment transport studies are hindered by the fact that deposited sediments may reflect processes acting over thousands of years, whereas our

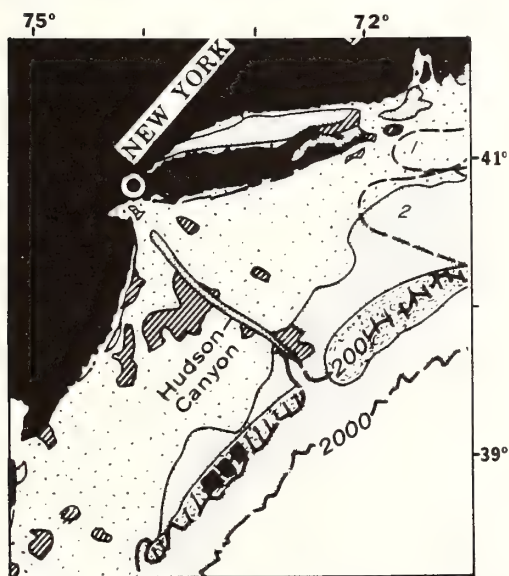


Fig. 2. Sediment types in the bight area (depth in meters). Hatching—gravel, sandy gravel, and gravelly sand; speckling—sand; stippling—silty sand, sandy silt, and clayey silt; dappling—glauconitic sand, silty sand, and sandy silt. ■■■—Pyrite-filled foraminiferal tests. 1—Zone of rounded quartz grains; 2—zone of limonitic pellets. (From Uchupi 1963.)

Table 1. Source of suspended solids in the New York Bight.\*

	×10 <sup>6</sup> tonnes/yr
Direct bight (68%)	
Dredged (54%)	4.73
Sludge (2.1%)	0.18
Cellar dirt (6.8%)	0.60
Total barged (62.9%)	5.51
Atmospheric (5%)	0.45
Coastal zone (32%)	
(98% of coastal zone input is through the Rockaway-Sandy Hook transect)	
Municipal wastewater (4%)	0.35
Industrial wastewater (0.2%)	0.02
Gauged runoff (16%)	1.4
Urban runoff (12%)	1.1
Total coastal zone	2.87
Total input	8.83

\* From Mueller et al. 1976.

studies of suspended sediment are commonly limited to a few days or months of observations. Natural processes may be impossible to separate from the changes produced by human activities, particularly in estuaries (and at the present dumpsites).

*Fine sediment sources to estuaries and the shelf*—Fine sediment discharged into the bight is shown in Table 1 (Mueller et al. 1976). Fluvial sediment is comprised of roughly 85% inorganic and 15% combustible organic material (Table 2). The fine inorganic fraction is mostly illite, chlorite, feldspar, and hornblende from the Hudson River (Hathaway 1972).

Shelf erosion and coast-parallel transport appear to be significant but unmeasured sources of suspended material and were probably major sources during the Holocene transgression. Hathaway (1972) showed that fine sediments near the mouths

Table 2. Composition of suspended matter.

Rivers	80–90% minerals	10–20% combustible organics
Estuaries	60–80% minerals + biogenic shells	20–40% combustible organics
Shelf	10–70% minerals + biogenic shells	30–90% combustible organics

of coastal plain estuaries differ significantly from the composition of riverborne sediments. It is probable that much estuary-mouth sediment is being eroded from shelf deposits and returned to and trapped in estuaries (Meade 1969). The fact that the sediments from modern rivers have not obscured this conclusion implies that either the modern sediment is bypassing the lower portions of the estuary, or it is trapped almost completely near the river mouths. Along the east coast, the heads of the Chesapeake and Delaware estuaries are far upstream from the estuary mouth, therefore, most river sediment is deposited far inland from the sea. Although saline tidal water is present in the Hudson River up to Albany, fine fluvial sediment is carried by low-salinity surface water to Upper and Lower New York Bays where some fines settle out (Folger 1972*b*) and the remainder is carried with estuarine sediment into the bight apex and mixed with recirculated shelf sediment. In the northeast United States, most of the fluvial suspended sediment is effectively trapped in estuaries and coastal wetlands (Milliman 1972).

At the present, the annual suspended sediment discharge of Atlantic coastal rivers is about equal to the annual deposition on marsh surfaces (Meade 1972*a*). However, much of the deposited material re-enters the shelf water column after the shoreline has passed over the marsh, through the process of shoreface erosion (Fischer 1961).

Particles derived from biologic processes are also a significant component of suspended matter in estuaries and on the shelf (Table 2), ranging from 20–90% in surface waters (Manheim et al. 1970). However, concentrations of combustible biogenic matter decrease rapidly with depth, and little of this material is preserved in sediment deposits (Folger 1972*a*; Gross 1972).

Atmospheric fallout over the New York Bight is small relative to other sediment sources (Table 1), but it may be a significant transport path for specific pollutants (e.g. lead from vehicular exhaust emissions).

Highest concentrations of organic and inorganic suspended materials in the water

occur within 10 km of the coastline and decrease nearly exponentially seaward (Manheim et al. 1970). Mineral grains larger than 4  $\mu\text{m}$  (silt-size) comprise 10–25% of nearshore suspended sediment and only 2–5% of offshore samples; the remainder is organic matter. The zone of strong terrigenous influence is restricted to nearshore waters and, specifically, to the inner shelf zone of turbid water drifting away from the estuary mouth. The coarser grains in this zone are effectively trapped in the “estuarine” circulation (which serves to reinforce the surface concentrations) and are transferred from one estuary to the next along the path of the longshore current.

Studies of other areas (Postma 1967) suggest that volumes of suspended sediment transported on the many feedback loops in the bight are probably orders of magnitude greater than both the net volume from the Hudson River that is transported across the shelf and the much larger amounts introduced by dumping.

Although the factors which influence suspended sediment dispersal can be readily defined, many large gaps in our knowledge must be closed before quantitative sediment transport budgets can be constructed on a regional scale. The most important of these are: shelf circulation patterns and mechanisms, particularly during storms; hydraulic properties of suspended sediments, particularly resuspension and settling properties; and the influence of flocculation and biologic aggregation on settling.

#### *Detailed studies in the New York Bight apex*

A 1973 bathymetric map (Fig. 3) of the bight apex was made as the result of a NOAA-Corps of Engineers survey. The principal topographic features are the northern end of the Hudson Shelf Valley, Cholera Bank, and the Christiaensen Basin, an amphitheaterlike feature terminating the Hudson Shelf Valley (Veatch and Smith 1939). Dumpsites for dredge spoils (the mud dump), cellar dirt, sewage sludge, and acid wastes are shown. Knolls immediately northwest of Ambrose Light and north and northwest of the dredge spoil dumpsite



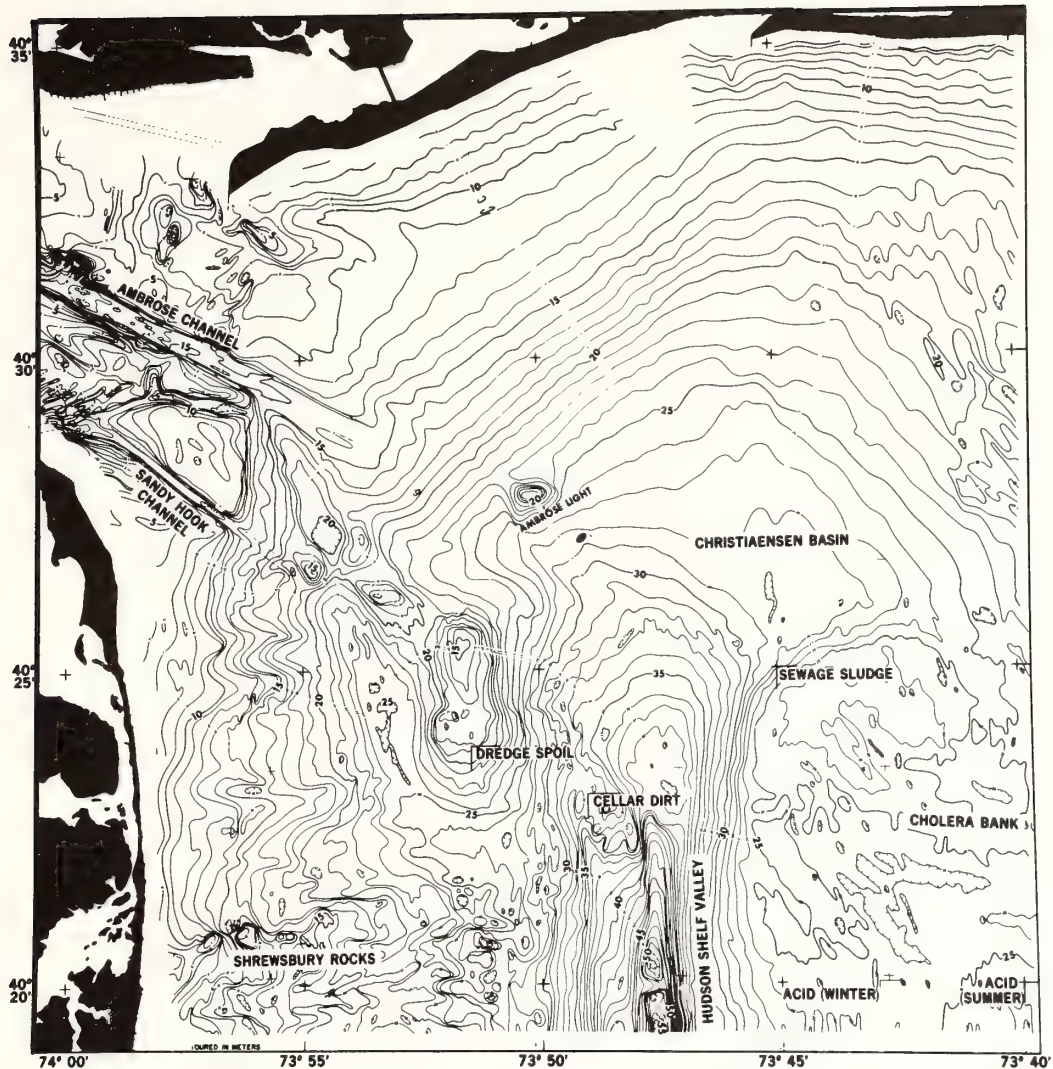


Fig. 3. Bathymetric map of the New York Bight apex. Contour interval, 1 m. Data (in meters) from 1973 NOAA-Corps of Engineers survey.

were formed from early 20th century dumping of assorted building excavation material and sand and gravel from the dredging of Ambrose and Sandy Hook Channels (Williams 1975).

Comparison of the 1973 bathymetric survey results with data from the 1936 survey reveals that only the anthropogenic areas have changed significantly. Figure 4 shows the 1973 and 1936 bathymetry of the dredge spoil site, as well as the net change between the two surveys. The 50-ft knoll on the 1936 map (relatively unchanged in 1973) is itself

the result of earlier dumping (Williams 1975). The amount of anthropogenic material accumulated during these years (1936–1973) has been calculated to be about  $124 \times 10^6 \text{ m}^3$ . This compares with about  $142 \times 10^6 \text{ m}^3$  dumped. The difference easily can be accounted for by settling alone.

Surficial sediments have been mapped by analyzing over 700 bottom grab samples collected at 1-km spacing (Fig. 5). The topographically low Hudson Shelf Valley and the Christiaensen Basin are floored

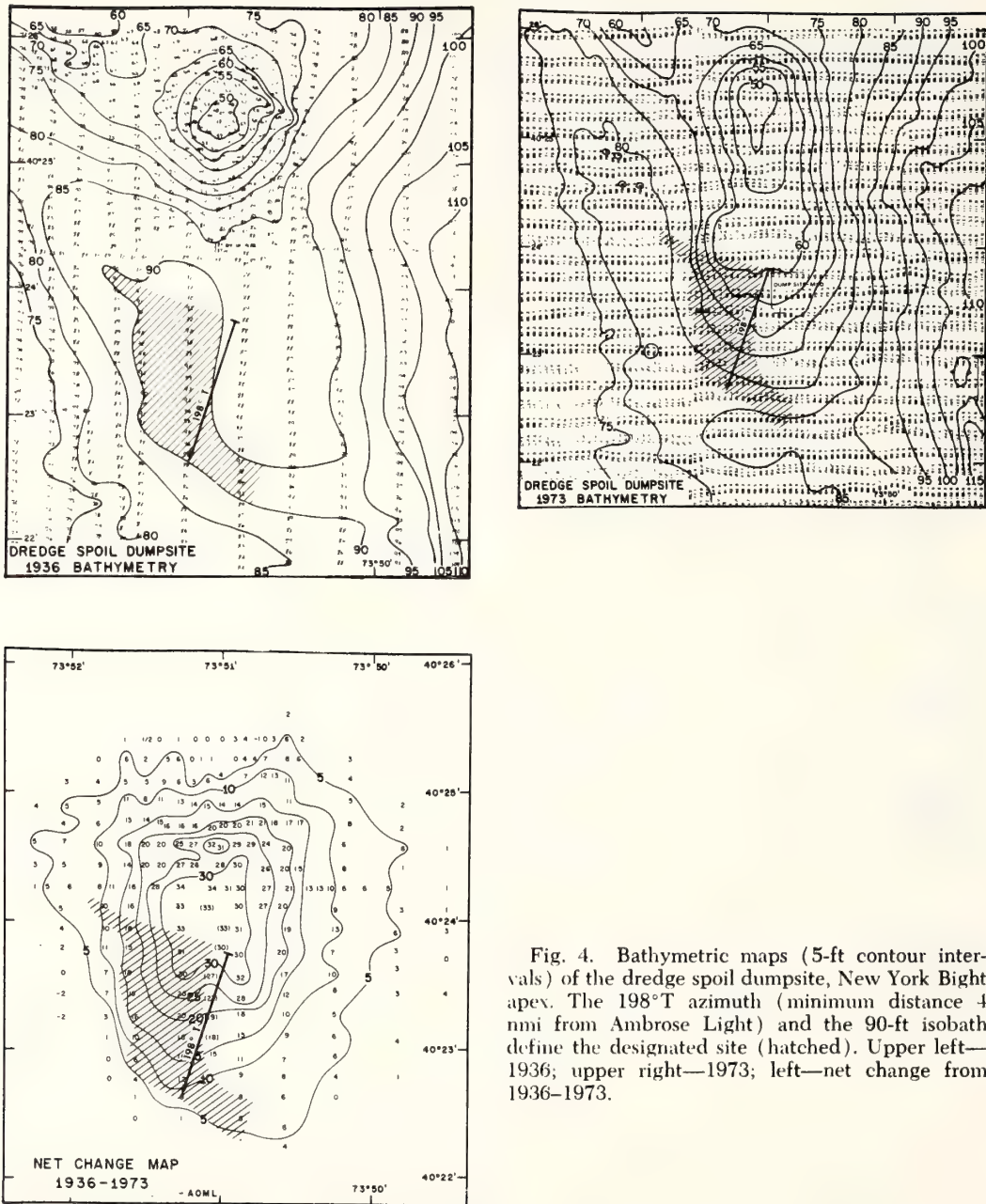


Fig. 4. Bathymetric maps (5-ft contour intervals) of the dredge spoil dumpsite, New York Bight apex. The 198°T azimuth (minimum distance 4 nmi from Ambrose Light) and the 90-ft isobath define the designated site (hatched). Upper left—1936; upper right—1973; left—net change from 1936–1973.

with fine-grained sediment, whereas the rest of the area contains assorted sizes of sand and both anthropogenic (artifact) and natural gravel deposits. Artifact gravels consist of recognizable construction rubble—brick, schist, concrete, etc.

Geophysical data taken during the 1973 survey consisted of 3.5-kHz shallow-penetration seismic reflection records and side-

scan sonar records with 150-m range on each side of 610-m-spaced tracklines. Although data interpretation is incomplete, bottom roughness patterns and trends of linear bedforms (sand ribbons and degraded sand waves) have been mapped from sidescan data (Fig. 6). These bedforms appear as alternating light and dark bands corresponding to fine- and coarse-

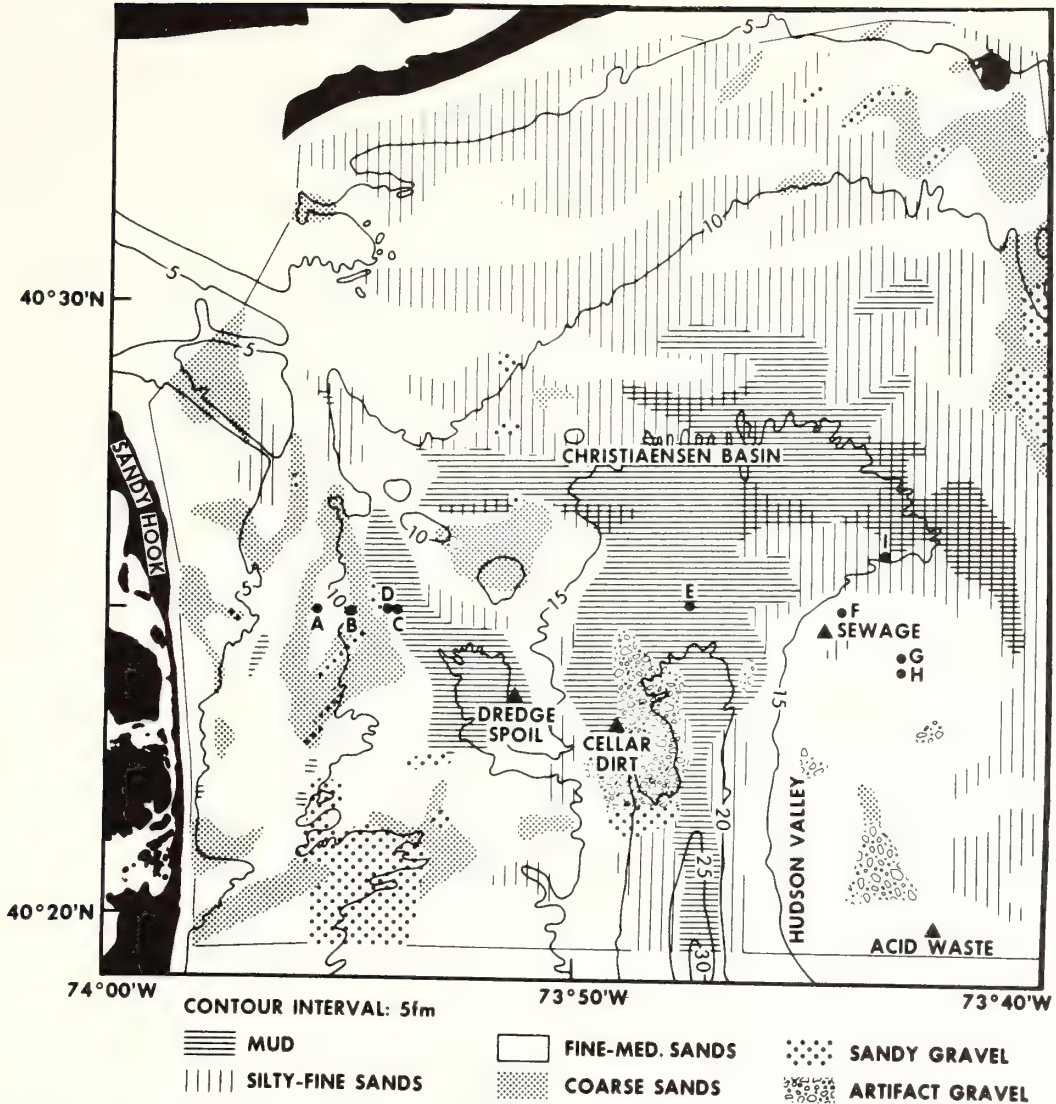


Fig. 5. Distribution of surficial sediment based on visual sample examination. Bathymetry from 1936 data.

grained sediment or as isolated dark bands. Streaky, patchy, and rough textures are associated with the dredge spoil and cellar dirt dumpsites and may be related to individual dumps.

Preliminary analysis of seismic data shows filling of the Hudson Shelf Valley from Cholesterol Bank.

Suspended sediment studies are particularly important in the bight apex because of the large amounts of fine particles dispersed in the water by waste disposal operations.

These particles are in addition to the fine sediments discharged from the Hudson River, other river mouths, and tidal inlets connected to coastal wetlands. Fine-grained sediment is also eroded from the sea floor during storms. Of immediate concern is sewage sludge which contains bacterial, viral, and heavy metal contaminants that adhere to fine sediment particles in the water column. The suspended fraction of dredge spoils is also probably similarly contaminated. All of these fines are largely re-

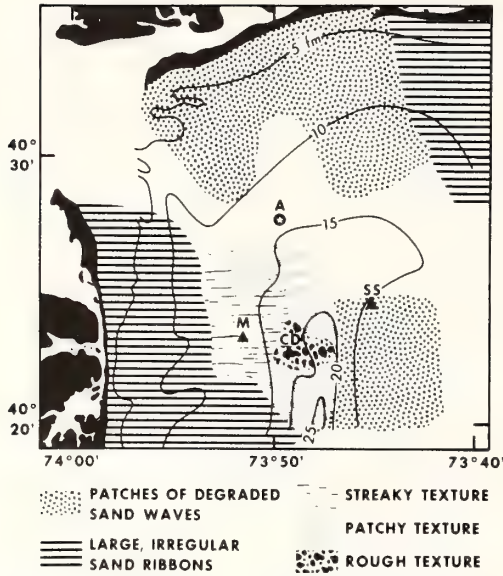


Fig. 6. Distribution of bottom roughness patterns from sidescan sonographs. Blank area NW and SE of Ambrose Light (A) shows no bedforms. M—Dredge spoil dumpsite; CD—cellar dirt site; SS—sewage sludge site.

tained in the nearshore water column as a consequence of the bight circulation pattern.

Suspended sediment studies were initiated in the bight apex during 1973 when sample stations were occupied to collect chemical and physical oceanographic data. Water samples were collected, filtered, and examined from the surface, 10-m depth, and the bottom at 25 stations. Preliminary

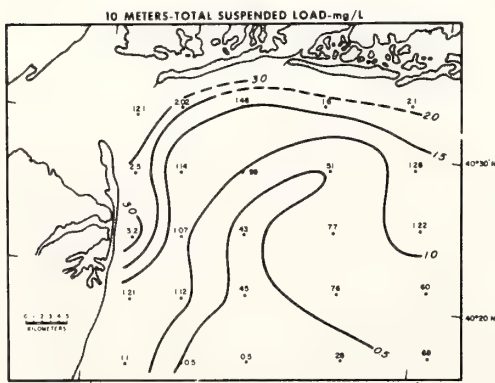


Fig. 7. Total suspended sediment load in waters at 10-m depth, late November 1973. (From Drake 1974.)

results for data taken in fall 1973 (Drake 1974; Figs. 7-10) indicate the existence of a fair-weather, clockwise current-circulation gyre, driven in part by the southwest drift of offshore shelf water. This has been verified by current meter studies in the

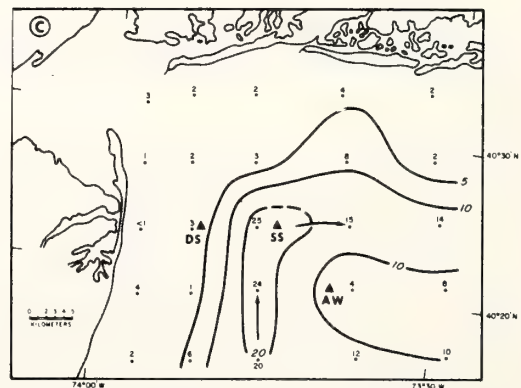
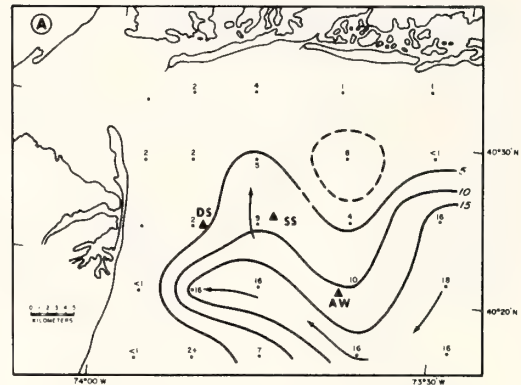


Fig. 8. Distribution of ferric hydroxide particles in the water column in late November 1973 (grains  $\times 10^3$ /liter). A—Surface; B—midwater; C—bottom water. (From Drake 1974.)

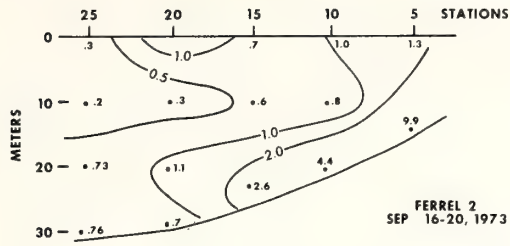


Fig. 9. Vertical distribution of total suspended load (in mg/liter) seaward of Long Beach, Long Island. (From D. E. Drake unpublished.)

apex (Charnell and Hansen 1974). Part of the total suspended load in the bight apex is easily identifiable, red-orange ferric hydroxide particles. These particles are formed by precipitation of iron in seawater as the result of acid waste dumping. They constitute an excellent tracer of suspended sediment circulation. The vertical distribution of suspended sediment shows high values (1.0 mg/liter) near the surface, and 2.0 mg/liter in the near-bottom "nepheloid" layer, typical of shelf areas (Fig. 9). It is expected that this layer will transport much of the suspended particulate matter and its associated contaminants.

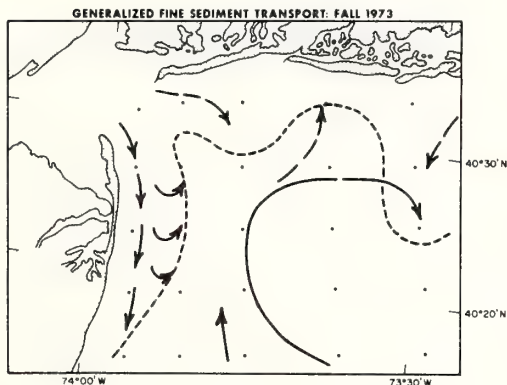


Fig. 10. Fine sediment transport system as inferred from distribution of suspended sediments during fall 1973. Dashed line is mean position of boundary between more turbid coastal water and less turbid offshore water. Clockwise gyre is apparently driven by southwesterly drift of offshore shelf water, and, on the bottom, by influx of saline water into New York Harbor. Regional currents which appear to be persistent are indicated by solid arrows. (From Drake 1974.)

Preliminary results show there is a concentration of fine-grained sediment in enclosed lows in the Hudson Valley axis, sandy mud in the remainder of the valley axis, and coarser sediment up the flanks of the valley and onto the shelf.

#### Alternative dumping area studies

Two midshelf areas have been designated as possible interim alternative dumping areas for sewage sludge and dredge spoils from the New York metropolitan area (see Fig. 1). The northern area is to be a minimum of 46 km from the Long Island shoreline, 18 km from the axis of the Hudson Shelf Valley, and 120 km from the entrance to New York Harbor. The southern area is seaward of the 36-m isobath and the same distances from the Hudson Valley axis and the New York Harbor entrance as the northern area (areas 2D1 and 2D2 on Fig. 1). Each area is 18.5×18.5 km.

*Northern area*—In the northern area (Fig. 1, 2D1), the sampling grid was placed seaward of the center of the location-criteria triangle to investigate, in part, a shallow tributary valley of the ancestral Long Island drainage system. The surficial sediments consist of sand with some areas of over 5% gravel (Fig. 11). Fine sands lie in the northeastern part of the area, medium sands cover the western and southern parts, with a gravel deposit ( $\leq 39\%$  gravel) at one station associated with an area of coarser medium sand in the southern part of the area. Only two stations contained  $>5\%$  mud. Bottom photographs indicate that the area is characterized by a smooth, slightly undulatory, mounded or rippled bottom. Side-scan sonar records reveal elongate dark areas which may be erosional windows in the Holocene sand sheet that expose the basal Holocene pebbly sand or may be areas of abundant large shell fragments. Grab samples were spaced too far apart to be definitive. Bottom photo and submersible-observation data support the existence of windrows of shell fragments.

*Southern area*—The southern study area in Fig. 1 (2D2) is centered over the broad, flat high of the Hudson divide (Fig. 12). To

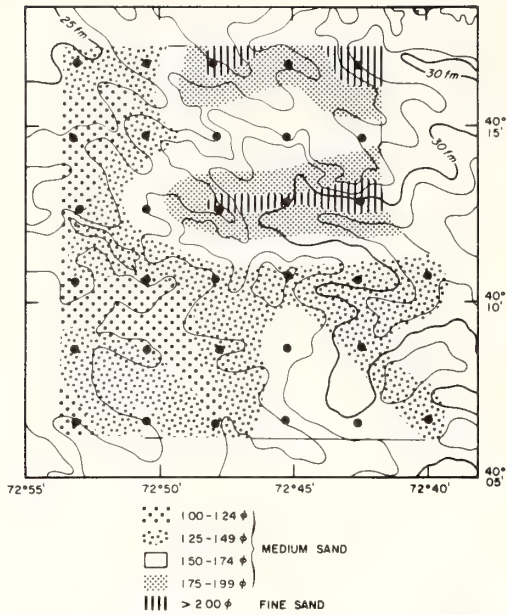


Fig. 11. Northern proposed interim alternative dumping area (2D1 on Fig. 1). Grain-size distribution of sand-sized fraction. Large dots—sample stations. (Bathymetry from Stearns and Garrison 1967; 1-fm contour intervals.)

the northeast the bottom grades gently into the Hudson Shelf Valley, while the western section is characterized by northeast-trend-

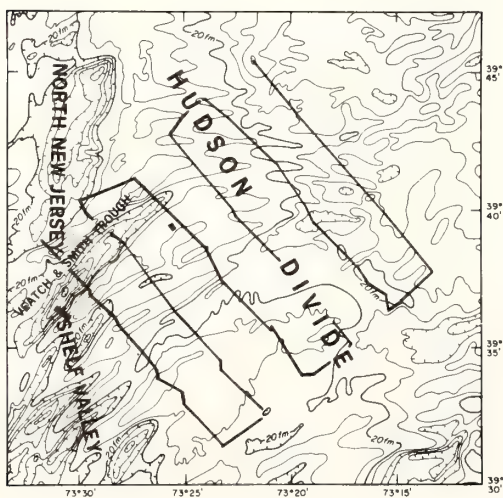


Fig. 12. Southern proposed interim alternative dumping area (2D2 on Fig. 1). (Bathymetry from Stearns and Garrison 1967, 1-fm contour intervals.) Solid lines—geophysical tracklines; bars—sites of dives by submersibles.

ing ridge and swale topography. Geophysical data, sediment samples, and two dives in submersibles showed that grain-size patterns appear to be related to bottom topography; coarser sand and gravel deposits lie on the crest and east flank of the Hudson divide, while medium- and fine-grained sand occur in the ridge and swale topography (Fig. 13). These distributions suggest that fine sediment is winnowed from the crest and east flank of the divide and deposited to the west. Observations from a submersible in Veatch and Smith Trough reveal a veneer of shelly, pebbly sand with large, angular clay pebbles and occasional oyster shells derived from the underlying early Holocene lagoonal clay. Seismic data also reveal that the reflector associated with this surface outcrops on the ridge flank. It appears that storm-generated currents from the northeast have winnowed the east flank of the Hudson divide and formed or maintained the ridge and swale topography on the west side of the divide.

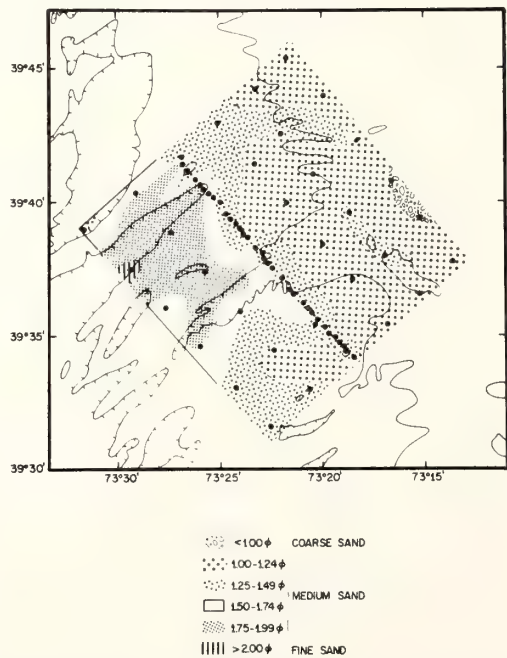


Fig. 13. Southern proposed interim alternative dumping area, (2D2 on Fig. 1). Grain-size distribution of sand-sized fraction. Large dots—sample stations. (Only the 20-fm isobath is shown.)

*Suspended sediment*—As previously mentioned, most fluvial suspended sediment is effectively trapped in estuaries and coastal wetlands. Consequently, the terrigenous fraction of the suspended matter decreases rapidly seaward. Suspended solids throughout the water column in the alternative dumping areas were predominately plankton and their noncombustible remains. Total suspended matter concentration in surface water is from 100–500  $\mu\text{g}/\text{liter}$ , comprised of 5% or less terrigenous matter, 80% combustible matter, and 15% siliceous and calcareous noncombustible planktonic remains (D. E. Drake personal communication). Subsurface water–suspended matter concentration is similar or somewhat less, except in the nepheloid layer 5–10 m above bottom. There, suspended matter concentrations are 500–2,000  $\mu\text{g}/\text{liter}$ , consisting of 30–60% combustible matter and 50–80% noncombustible matter which includes 10–20% terrigenous matter. Textural properties of sediment deposits in the alternative dumping areas show that very little sediment finer than 62 microns is present.

### References

- CHARNELL, R. L., AND D. V. HANSEN. 1974. Summary and analysis of physical oceanography data collected in the New York Bight apex during 1969–1970. NOAA-MESA Rep. 74-3. 74 p.
- DRAKE, D. E. 1974. Suspended particulate matter in the New York Bight apex: September–November 1973. NOAA Tech. Rep. ERL 318-MESA 1.
- DUANE, D. B. 1969. Sand inventory program. A study of New Jersey and northern New England coastal waters. Shore Beach **October**.
- , M. E. FIELD, E. P. MEISBURBER, D. J. SWIFT, AND S. J. WILLIAMS. 1972. Linear shoals on the Atlantic inner continental shelf, Florida to Long Island, p. 447–498. *In* D. J. Swift et al. [eds.], Shelf sediment transport: Process and pattern. Dowden, Hutchinson & Ross.
- FISCHER, A. G. 1961. Stratigraphic record of transgressing seas in light of sedimentation on Atlantic coast of New Jersey. *Bull. Am. Assoc. Pet. Geol.* **45**: 1656–1666.
- FOLGER, D. W. 1972a. Texture and organic carbon content of bottom sediment in some estuaries of the United States, p. 391–408. *In* B. W. Nelson [ed.], Environmental framework of coastal plain estuaries. *Geol. Soc. Am. Mem.* 133.
- . 1972b. Characteristics of estuarine sediments of the United States. *U.S. Geol. Surv. Prof. Pap.* 742. 94 p.
- FREELAND, C. L., AND D. J. SWIFT. In press. Surficial sediments. NOAA-MESA New York Bight Atlas Monogr. 10.
- GROSS, M. G. 1972. Geologic aspects of waste solids and marine waste deposits, New York metropolitan region. *Geol. Soc. Am. Bull.* **83**: 3163–3176.
- HATHAWAY, J. C. 1972. Regional clay mineral facies in estuaries and continental margin of the U.S. East Coast, p. 293–316. *In* B. W. Nelson [ed.], Environmental framework of coastal plain estuaries. *Geol. Soc. Am. Mem.* 133.
- KNOTT, S. T., AND H. HOSKINS. 1968. Evidence of Pleistocene events in the structure of the continental shelf of the northeastern U.S. *Mar. Geol.* **6**: 5–43.
- McKINNEY, T. F., AND G. M. FRIEDMAN. 1970. Continental shelf sediments of Long Island, N.Y. *J. Sediment. Petrol.* **40**: 213–218.
- , W. L. STUBBLEFIELD, AND D. J. SWIFT. 1974. Large-scale current lineations on the central New Jersey shelf: Investigations by side-scan sonar. *Mar. Geol.* **17**: 79–102.
- MANHEIM, F. T., R. H. MEADE, AND G. C. BOND. 1970. Suspended matter in surface waters of the Atlantic continental margin from Cape Cod to the Florida Keys. *Science* **167**: 371–376.
- MEADE, R. H. 1969. Landward transport of bottom sediments in estuaries of the Atlantic Coastal plain. *J. Sediment. Petrol.* **39**: 222–234.
- . 1972a. Transport and deposition of sediments in estuaries, p. 91–120. *In* B. W. Nelson [ed.], Environmental framework of coastal plain estuaries. *Geol. Soc. Am. Mem.* 133.
- . 1972b. Sources and sinks of suspended matter on continental shelves, p. 249–262. *In* D. J. Swift et al. [eds.], Shelf sediment transport: Process and pattern. Dowden, Hutchinson & Ross.
- MILLIMAN, J. D. 1972. Marine geology, p. 10-1 to 10-91. *In* Coastal and offshore environmental inventory, Cape Hatteras to Nantucket Shoals. *Mar. Publ. Ser. 6. Univ. R.I.*
- , AND K. O. EMERY. 1968. Sea levels during the past 35,000 years. *Science* **162**: 1121–1123.
- MUELLER, J. A., A. R. ANDERSON, AND J. S. JERIS. 1976. Contaminants entering the New York Bight: Sources, mass loads, significance. *Am. Soc. Limnol. Oceanogr. Spec. Symp.* **2**: 162–170.
- POSTMA, H. 1967. Sediment transport and sedimentation in the estuarine environment, p. 158–179. *In* G. H. Lauff [ed.], *Estuaries*. *Publ. Am. Assoc. Adv. Sci.* 83.
- SCHLEE, J. 1973. Atlantic continental shelf and slope of the U.S. Sediment texture of the

- northeast part. U.S. Geol. Surv. Prof. Pap. 529-L. 64 p.
- . 1975. Sand and gravel. MESA New York Bight Atlas Monogr. 21. 26 p.
- SHERIDAN, R. E., C. E. DILL, JR., AND J. C. KRAFT. 1974. Holocene sedimentary environment of the Atlantic inner shelf off Delaware. *Geol. Soc. Am. Bull.* **85**: 1319–1328.
- STAHL, L., J. KOCZAN, AND D. J. SWIFT. 1974. Anatomy of a shoreface-connected sand ridge on the New Jersey shelf: Implications for the genesis of the surficial sand sheet. *Geology* **2**: 117–120.
- STEARNS, F., AND L. E. GARRISON. 1967. Bathymetric maps, middle Atlantic U.S. continental shelf, 1:125,000. NOAA, Natl. Ocean Surv.
- STUBBLEFIELD, W. L., M. DICKEN, AND D. J. SWIFT. 1974. Reconnaissance of bottom sediment on the inner and central New Jersey shelf. NOAA-MESA Rep. 1.
- , J. W. LAVELLE, T. F. MCKINNEY, AND D. J. SWIFT. 1975. Sediment response to the present hydraulic regime on the central New Jersey shelf. *J. Sediment. Petrol.* **45**: 337–358.
- SWIFT, D. J., G. L. FREELAND, P. E. GADD, C. HAN, J. W. LAVELLE, AND W. L. STUBBLEFIELD. 1976. Morphologic evolution and coastal sand transport, New York–New Jersey shelf. *Am. Soc. Limnol. Oceanogr. Spec. Symp.* **2**: 69–89.
- , J. W. KOFOED, F. P. SAULSBURY, AND P. SEARS. 1972. Holocene evolution of the shelf surface, central and southern Atlantic shelf of North America, p. 499–574. *In* D. J. Swift et al. [eds.], *Shelf sediment transport: Process and pattern*. Dowden, Hutchinson & Ross.
- UCHUPI, E. 1963. Sediments on the continental margin off eastern U.S. U.S. Geol. Surv. Prof. Pap. 475-C, p. C132–C137.
- . 1970. Atlantic continental shelf and slope of the U.S.—shallow structure. U.S. Geol. Surv. Prof. Pap. 529-I.
- VEATCH, A. C., AND P. A. SMITH. 1939. Atlantic submarine valleys of the United States and the Congo Submarine Valley. *Geol. Soc. Am. Spec. Pap.* 7.
- WILLIAMS, S. J. 1975. Anthropogenic filling of the Hudson River shelf channel. *Geology* **10**: 597–600.
- . 1976. Geomorphology, shallow subbottom structure, and sediments of the Atlantic intercontinental shelf off Long Island, New York. U.S. Army Corps Eng. Coastal Eng. Res. Center Tech. Pap. 76–2. 123 p.
- , AND D. B. DUANE. 1974. Geomorphology and sediments of the inner New York Bight continental shelf. *Tech. Memo.* 45. U.S. Army Corps Eng. Coastal Eng. Res. Center. 81 p.



PRELIMINARY RESULTS OF COINCIDENT CURRENT METER AND SEDIMENT TRANSPORT OBSERVATIONS FOR WINTERTIME CONDITIONS ON THE LONG ISLAND INNER SHELF

J.W. Lavelle, P.E. Gadd, G.C. Han, D.A. Mayer, W.L. Stubblefield, and D.J.P. Swift

NOAA/Atlantic Oceanographic and Meteorological Laboratories,  
15 Rickenbacker Causeway, Miami, Florida 33149

R.L. Charnell

NOAA/Pacific Marine Environmental Laboratory, 3711 15th Avenue N.E.,  
Seattle, Washington 98105

H.R. Brashear, F.N. Case, K.W. Haff, and C.W. Kunselman

Oak Ridge National Laboratory, P.O. Box X, Oak Ridge, Tennessee 37830

**Abstract.** We have observed late fall and winter bedload sediment transport and the overlying current field in ridge and swale topography on the inner continental shelf south of Long Island, and can report movement of bed material at a water depth of 20 m to a distance of approximately 1500 m after several storm events. Movement over an 11-week observation period was longshore and oblique to the ridge crest at the experimental site. Currents were also predominately longshore, but long term averages demonstrate that a vertical shear existed in the fluid motion. Although the number of sediment transport "events" suggested by the current meter data is nearly balanced in eastward and westward directions, both estimates of transport from current speeds and sand tracer dispersion patterns show that several westward flowing events dominated the transport during a two and one-half month period. A quantitative upper bound of 31 cm/sec on the threshold velocity for sediment movement in this size range is also set by the data.

hensionless sediment movement and its immediate forcing mechanism, the overlying water velocity field.

The Long Island Near-Shore (LINS) Study (Figure 1) was centered at 40°33'N and 73°25'W, halfway between Jones and Fire Island Inlets, Long Island, New York, some 9 km offshore. The study area, an 8 x 10 km rectangle, was located in an area of undulating morphological features described in Duane et al. (1972) as ridge and swale topography. Bedforms at the study site have wavelengths of approximately 1 km with wave heights of 4-7 m, intersect the shoreline obliquely, and are composed of relatively clean, medium to fine sands; the ridges are asymmetrical with steeper southwest facing flanks. The experimental design was twofold: to gather sediment dispersion and current meter data which could be used to aid in quantifying sediment transport; and to gather qualitative data on the construction and/or the maintenance mechanism of ridge and swale features which are widespread on the Atlantic continental

Introduction

Increasingly widespread interest in the characterization and quantification of shelf sediment transport stems from the requirements of the growing number of shelf and nearshore users to understand the dynamics of an area on which they may have potential impact. The uses and interests are myriad, but more common expressions of concern are phrased in terms of recovery rates of contaminated sediments by replacement, the stability of the substrate for offshore structures, the influence of offshore work on beach and nearshore features, and the temporal variability of sediment transport as an influence on faunal habitats. While considerable efforts have been made in observing and describing water-sediment coupling in the laboratory, under riverine flow, and in the nearshore area, few direct measurements of offshore sediment movement and the associated near-bottom water velocity field have been made. For these reasons, we are reporting preliminary results of an experiment recently completed in the New York Bight to directly measure offshore co-

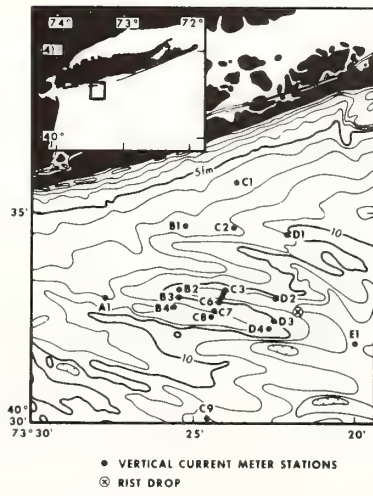


Fig. 1. Bathymetry and current meter station locations for the Long Island Nearshore Study (LINS). Stations C1, C6, C7, and C8 returned no usable data.

shelf (Swift et al., 1973). Field work was divided into two concurrent operations: a sediment tracer experiment and a current meter array of high spatial resolution. We present here a qualitative, preliminary view of the data collected in those efforts.

#### Current Meter Observations

During the first six weeks of the current meter operation (October 16 to December 4, 1974), nineteen stations (Figure 1) were occupied. A single current meter string was retained in the area during the remainder of the experiment. Aandaraa RCM-4 Savonius rotor current meters which record instantaneous direction and integrated average speed at 10-minute intervals were used throughout. Measurement emphasis was placed on a well-defined ridge and trough; meters were located on a crest, flank, and trough on each of three transects (B, C, and D of Figure 1) as well as the adjacent flank of transect C. Additional meters were set outside the central study area to measure far-field velocities.

Flow during the observation period trended both east and west, parallel to the coast. Figure 2 is a vector time series of velocities at station 2C (1.5 m above the bottom) and is representative of near-bottom water movement during one of the most active periods of flow. The data presented here have been subjected to a 40-hr low pass filter and then resampled at hourly intervals. Although east is the dominant flow direction during this sampling interval, the most intense flow was westward during a three day period near the end of this period.

Predominance of eastward flow is consistent with

the observation of Charnell and Mayer (1975) who reported the existence, in the statistical sense, of a clockwise gyre in the long term mean flow within the New York Bight apex during the fall and winter of 1973. The strong westward flow (Figure 2A) occurred during the storm of December 1 - December 4, 1974, an event which was reported to have been the most damaging northeaster since the Ash Wednesday storm of 1962 (C. Galvin, Coastal Engineering Research Center, personal communication). Winds from the east-northeast up to 16 m/s were recorded at John F. Kennedy International Airport during the initial 36 hrs of this period; winds from the northwest at an average speed of 10 m/s followed on December 3 and 4. The second most important flow during the observation period, that which began during December 16, also followed east winds. Periods of high speed winds from the west and northwest cause less intense near-bottom water movement. The asymmetry of the fluid response to easterly and westerly winds in this area has been noted by Beardsley and Butman (1974).

Vertical shear in current velocities was unmasked in the data (Figures 2B and 2C) when long term velocity averages were made on data from meters grouped by position in the water column. Flow recorded by meters 1.5 to 4 m from the bottom (B), 5 and 6 m from the bottom (M), and 6 to 11 m from the surface (S), were averaged separately in time over periods when flow had eastward and westward components. Water depths at the stations varied from 15 to 22 m. These data show that near surface water flow had an offshore component for both eastward and westward flow, while bottom flow tended to be more inshore, parallel to the isobaths during westward flows and more strongly inshore during eastward flows. Speeds decreased in a relatively uniform fashion from the upper to the bottom meters. Wind records document a northerly wind component throughout much of the observation period; the observed shore-normal components may be an indication of upwelling contributions to fluid motion.

#### Sand Tracer Measurements

In order to directly assess the flow response of the sediment to the observed water movement, we employed the Radioisotope Sand Tracer (RIST) system developed at Oak Ridge National Laboratory (Duane, 1970; Case et al., 1971). Indigenous sand was sorted to produce a fraction whose size distribution was roughly Gaussian, with a mean diameter of .15 mm (fine to very fine sand), a standard deviation of .03 mm, and no material larger than .25 mm or smaller than .06 mm. Approximately 500 cm<sup>3</sup> of this material was surface coated with 10 Curies of the isotope <sup>103</sup>Ru (T<sub>1/2</sub> = 39.6 days). On November 12, equal portions of the tagged sand in water soluble bags were released at three points at the east end of the main trough (Figures 1 and 3). The injection points formed an equilateral triangle with sides roughly 100 m in length. The ensuing dispersal pattern of labeled sand was surveyed at intervals by scintillation detectors mounted in a cylindrical vehicle which was towed across the bottom. Raydist precision navigation with 10 m resolution was used. Four post-injection surveys were made during the 11-week tracer experiment.

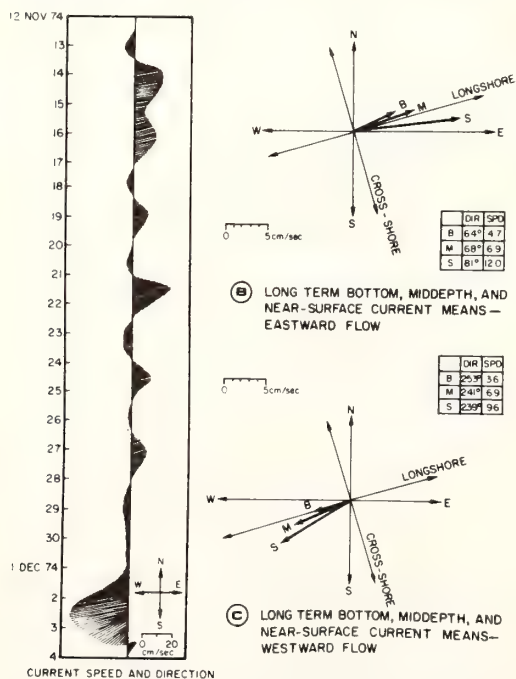


Fig. 2. Near bottom current vector time series and velocity averages. Shoreline direction represents the trend of the 5 fathom isobath between Jones and Fire Island Inlets.

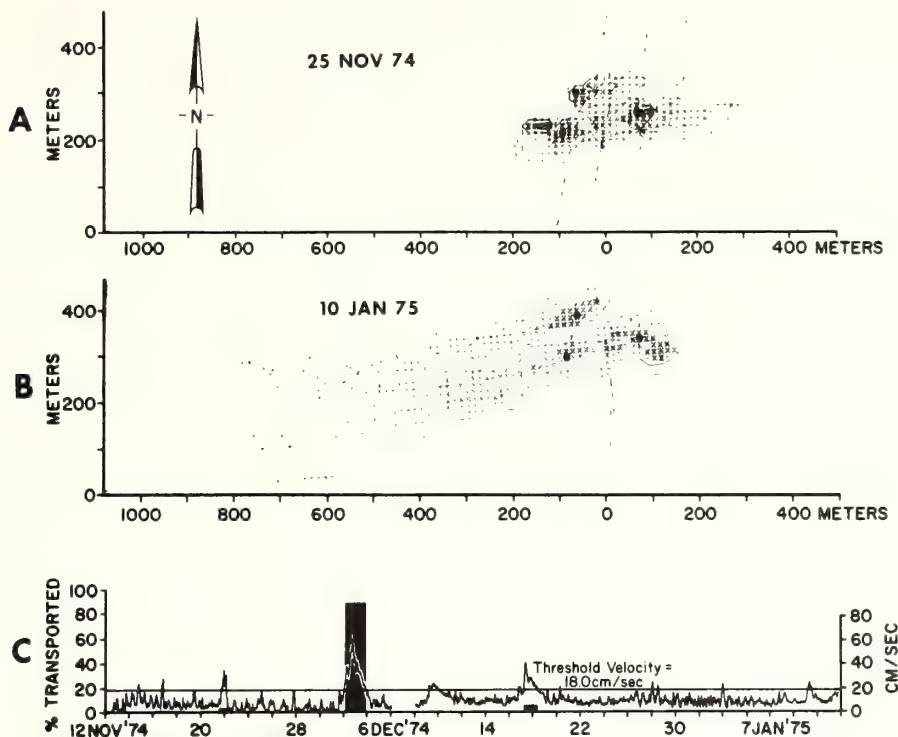


Fig. 3. a and b) Dispersion patterns measured 13 and 59 days after injection of tagged sand. Point sources are represented by dots. Broken line is the survey trackline; stippling represents radiation intensity. c) Near bottom current speed record over the length of the experiment, and calculated sediment transport information (see text).

Dispersion patterns mapped two and eight weeks after injection are shown in Figure 3; each has been corrected for background radiation and decay. After two weeks (November 25) roughly ellipsoidal smears trended east from each of the three injection points (Figure 3a). Each smear could be traced for about 200 m before the signal was lost in the background radiation. After eight weeks (January 10), the three eastward smears had been replaced by a single, more extensive pattern extending 700 m to the west (Figure 3b). The reversal of the patterns from east to west was more markedly demonstrated by preliminary data from a survey made during mid-December (December 17-19). Although those data have not yet satisfactorily been processed, the data at the time of that survey were sufficient to indicate that the reversal of the dispersion pattern of Figure 3a had already occurred, and in fact extended approximately 1,500 m to the west. We should point out that the patterns of Figure 3 must be regarded as minimum transport patterns, in the sense that tagged material which has been buried or has diffused downward into the bed is attenuated in signal strength by the overburden. For this reason, the signal measured is an underestimate of the true signal and the observations must be regarded as a lower bound to the true transport.

The temporal pattern of sediment transport over a 60-day period may be inferred from Figure 3c. The basic record is current speed, measured 1.5 m from the bed, versus time. The horizontal line at 18 cm/sec is an estimated threshold, based on the

work of Shields and subsequent workers for shear velocity (Graf, 1971) and a choice of  $3.0 \times 10^{-3}$  for the drag coefficient (Sternberg, 1972). We believe that this choice of threshold velocity is in part verified by empirical evidence obtained during the course of the experiment (see below). We have made estimates of the relative role each transport event played in the overall transport record, based on the concept of the proportionality of frictional energy expenditure to the transport volume (Bagnold, 1963). For each event where velocities exceeding threshold were recorded, we have calculated a transport volume:

$$Q_i = \frac{\alpha}{T_i} \int_i (|V| - |V_{TH}|)^3 dt \quad (1)$$

where  $|V|$  is measured current speed,  $|V_{TH}|$  is threshold speed,  $\alpha$  is a constant of proportionality, and  $T_i$  is the duration of the transport event. Expression of sediment transport as a power of the difference of measured and threshold velocity is supported by analysis of stream transport data (Kennedy, 1969). Without assigning a value to  $\alpha$ , one may calculate relative rates of transport, one event to the next, or one event to the total transport evidenced by the current meter record. We have taken the second of these options, and have represented relative sand transport by solid bars superimposed on the current record (Figure 3c). Despite the exceedence of the sediment transport threshold at many points in the record, only the solid bars centered on December 2 and December 16-

17 arc visible in the figure, bearing witness to the dominance of the calculated transport by these two events. Furthermore, the figure also shows that most of the calculated transport occurred during the early December storm. While this calculated transport index may be biased by the choice of threshold speed as well as the functional dependence on velocity, we believe any other reasonable parameterization is likely to lead to the same general conclusion: the storm event of December 1 - December 4 moved more sand at 20 m water depth than the combination of all other transport events.

The reversing nature of sediment flow during the observation period provides a constraint on the entrainment velocity. A threshold speed greater than approximately 31 cm/sec at 150 cm off the bottom would eliminate transport during the first 14 days of the record, in contradiction to the observation of eastward transport (Figure 3a). Setting the threshold much below 12 cm/sec would result in more eastward transport during the entire tracer experiment than was the case. Based on the relative extent of the dispersion patterns in Figures 3a and 3b, we believe that the calculated threshold velocity of 18 cm/sec is realistic.

#### Summary

Water movement on the Long Island Inner Shelf at depths of 10 to 20 m and at frequencies below  $1/40 \text{ hr}^{-1}$  was predominately alongshore with a net flow over the observation period to the east. The non-tidal flow reversals at these depths suggest domination by winds associated with frontal passages; the net eastward flow likely reflects the average winds from the north and west through the fall and winter months. Vertical shear of the flow is observable in long term averages of the current records; small offshore mid-depth flows and some onshore bottom flow may reflect as an upwelling circulation the net offshore component of the wind. The most intense water movements recorded during the experimental period followed high northeasterly and easterly winds.

Sediment is transported both eastward and westward parallel to the shoreline, and oblique to the ridge and trough system. Current speeds recorded 150 cm from the bed show that the sediment entrainment threshold is exceeded only intermittently; sand transport occurs only during storm events, separated by periods of quiescence. Mean water movement was to the east over the observation period in sharp contrast to the observed mean westward sediment transport. Some eastward sediment transport was observed, but the most intense water movement and resultant sand movement were associated with several "northeaster" storm events. Asymmetry of the ridges (steeper southwest facing flanks) suggests that westward flows associated with such storms constitute the primary sediment flow mechanism in this ridge and swale topography.

#### Acknowledgements.

Support for this work has come from NOAA's New York Bight Marine Ecosystems Analysis (MESA) Project, NOAA's Environmental Research Laboratories, and ERDA's Division of Biomedical and Environmental Research. Oak Ridge National Laboratory is operated by Union Carbide Corporation for the U.S. Energy Research and Development Administration.

#### References

- Bagnold, R.A., Beach and near-shore processes, part I, mechanics of marine sedimentation, In: The Sea, vol. 3, pp. 507-528, Interscience Pub., New York, 1963.
- Beardsley, R., and B. Butman, Conditions on the New England continental shelf: response to strong winter storms, Geophys. Res. Letters, 1, 181-184, 1974.
- Case, F.N., E.H. Acree, and H.R. Brashear, Detection system for tracing radionuclide-labeled sediment in the marine environment, Isotopes and Radiation Technology, 8, 412-414, 1971.
- Charnell, R.L., and D.A. Mayer, Water movement within the apex of the New York Bight during summer and fall of 1973, Tech. Memo., National Oceanic and Atmospheric Administration, Boulder, Co. (in press).
- Duane, D.B., Tracing sand movement in the littoral zone: progress in the Radio Isotopic Sand Tracers (RIST) study, July 1968-February 1969, Coastal Eng. Res. Center Misc. Paper, Washington, D.C., 1970.
- Duane, D.B., M.E. Field, E.P. Meisburger, D.J.P. Swift, and S.J. Williams, Linear shoal on the Atlantic inner continental shelf, Florida to Long Island, In: Shelf Sediment Transport: Process and Pattern, pp. 447-498, Dowden, Hutchinson and Ross, Stroudsburg, Pa., 1972.
- Graf, W.H., Hydraulics of Sediment Transport, p. 96, McGraw Hill, New York, 1971.
- Kennedy, J.F., The formation of sediment ripples, dunes, and antidunes, In: Annual Review of Fluid Mechanics, vol. 1, pp. 147-168, Annual Reviews, Inc., Palo Alto, Calif., 1969.
- Sternberg, R.W., Predicting initial motion and bedload transport of sediment particles in the shallow marine environment, In: Shelf Sediment Transport: Process and Pattern, pp. 61-82, Dowden, Hutchinson and Ross, Stroudsburg, Pa., 1972.
- Swift, D.J.P., D.B. Duane, and T.F. McKinney, Ridge and swale topography of the Middle Atlantic Bight, North America: secular response to the Holocene hydraulic regime, Mar. Geol., 15, 227-247, 1973.

(Received October 14, 1975;  
accepted November 21, 1975.)

## ON THE INTERPRETATION OF NEAR-BOTTOM WATER TEMPERATURE ANOMALIES

R.P. LOWELL

*School of Geophysical Sciences, Georgia Institute of Technology, Atlanta, Ga. 30332 (USA)*

and

P.A. RONA

*National Oceanic and Atmospheric Administration, Atlantic Oceanographic and  
Meteorological Laboratories, Miami, Fla. 33149 (USA)*

Received November 16, 1975

Final revised version received June 21, 1976

A positive water temperature anomaly of  $0.11^{\circ}\text{C}$  and an inverse gradient of potential temperature of  $1.5 \times 10^{-2}^{\circ}\text{C}/\text{m}$  has been measured at the TAG hydrothermal field in the rift valley of the Mid-Atlantic Ridge at latitude  $26^{\circ}\text{N}$  by means of a thermistor array towed between 2 and 20 m above the seafloor. This anomaly appears to be associated with hydrothermal discharge from the oceanic crust. The temperature data are interpreted in terms of (1) a steady, turbulent thermal plume rising in a homogeneous, neutrally buoyant medium, and (2) turbulent diffusion in the ocean-bottom boundary layer. The calculations indicate that the thermal output of the TAG anomaly area is of the order of several megawatts, which is of the same order of magnitude as some continental geothermal systems. The thermal output from the TAG anomaly area represents a significant fraction of the total heat loss resulting from the generation of new lithosphere at the Mid-Atlantic Ridge at  $26^{\circ}\text{N}$ .

### 1. Introduction

Conductive heat flow measurements in the crestral zone of various sections of the ocean ridge system exhibit a high degree of scatter [1,2], in a manner opposite to that expected from heat flow refraction effects [3]. Moreover, the mean conductive heat flow in the crestral zone is frequently less than the conductive heat flow from a uniformly spreading lithospheric plate generated at the ridge axis [4,5]. This discrepancy between the observed heat flow and conductive heat flow models based on a uniformly spreading lithosphere is usually attributed to convective heat losses due to hydrothermal circulation in the newly created oceanic crustal rocks. Additional evidence for hydrothermal circulation comes from the occurrence of hydrothermally altered rocks [6] and deposits of hydrothermal origin [7,8]. Lastly, thermistor probes

towed over segments of the axial zone within 10–20 m of the seafloor have measured temperature anomalies which appear to be associated with hydrothermal discharge [2,9,10].

Theoretical models for hydrothermal circulation in the oceanic crust have been based both on models of convection in porous rock [3,11], as well as on models of convection in fractured rock [12,13]. Ocean ridge hydrothermal systems are exceptionally complicated and the theoretical modelling is still in its initial stages of development. Near-bottom water temperature data, however, may provide useful, quantitative information with regard to the thermal regime in the oceanic crust. Such information may, for example, give estimates of the heat flux through the ocean floor and place some constraints on acceptable hydrothermal convection models. This is of particular importance in regions of young crust, where the sedi-

ment layer is too thin for standard conductive heat flow measurements to be made.

The purpose of this paper is to examine the implications of near-bottom temperature anomalies measured with towed thermistors. Since the crestral zone of the Mid-Atlantic Ridge at 26°N has been studied in some detail [8–10,14–16], the data from this area will be used in discussing the theoretical results.

## 2. The TAG hydrothermal field

During the 1972 and succeeding cruises of the NOAA Trans-Atlantic Geotraverse (TAG) project, anomalously thick manganese oxide crusts were repeatedly dredged from the southeast wall of the rift valley at 26°N (Fig. 1). Radiogenic dating of the manganese crusts, which attain thickness of 42 mm only 5 km from the axis of the rift valley, show them to be accumulating at about 200 mm per 10<sup>6</sup> years, about two orders of magnitude faster than hydrogenous ferromanganese [8]. The crusts are almost pure manganese (40%), with only trace quantities of Fe, Cu, Ni, and Co [8]. The rapid accumulation rate and pure composition evidence a hydrothermal origin for crusts.

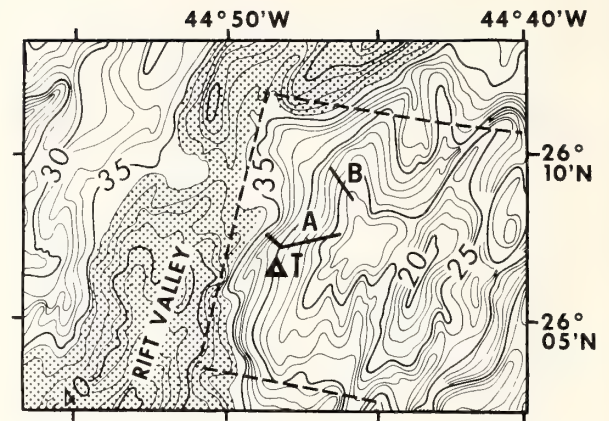


Fig. 1. Bathymetric map contoured in hundreds of meters [16] showing locations of profiles A and B, along which water temperature measurements and bottom photographs were concurrently made at the southeast wall of the rift valley of the Mid-Atlantic Ridge at 26°N. A water temperature anomaly ( $\Delta T$ ) was measured between 2950 and 3000 m along profile A [10]. No water temperature anomaly was present along profile B. The floor of the rift valley is shaded. The TAG hydrothermal field is outlined (dashed lines).

TABLE 1

Temperature profiles at the TAG hydrothermal field (Fig. 2) \*

Temperature profile (number)	Cumulative distance along ocean bottom (m)	Depth (m)	Potential temperature (°C). Thermistor position in vertical array (m above lowermost thermistor)			Vertical gradient (°C/m)
			4	3	0	
1	0– 115	3080–3068	2.461	2.449	2.434	+0.007
2	115– 230	3068–3055	2.460	2.454	2.433	+0.007
3	230– 345	3055–3043	2.464	2.453	2.434	+0.008
4	345– 460	3043–3030	2.464	2.455	2.440	+0.006
5	460– 575	3030–3015	2.491	2.482	2.462	+0.007
6	575– 690	3015–2997	2.484	2.470	2.464	+0.005
7	690– 805	2997–2990	2.529	2.518	2.561	–0.014
8	805– 920	2990–2975	2.542	2.510	2.559	–0.016
9	920–1035	2975–2965	2.603	2.599	2.574	+0.007
10	1035–1150	2965–2950	2.617	2.610	2.598	+0.005
11	1150–1265	2950–2935	2.615	2.599	2.469	+0.037
12	1265–1380	2935–2915	2.482	2.481	2.470	+0.003
13	1380–1495	2915–2910	2.508	2.499	2.476	+0.008
14	1495–1610	2910–2905	2.514	2.501	2.482	+0.008

\* Based on Rona et al. [10].

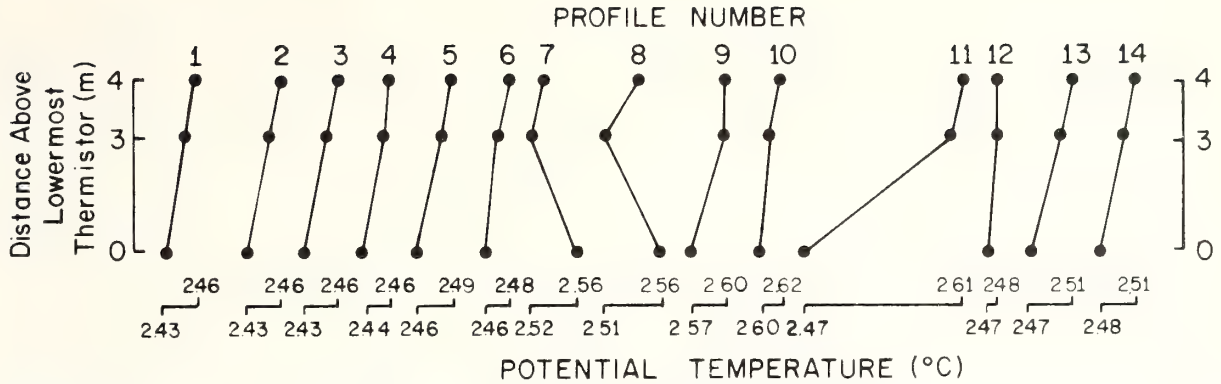


Fig. 2. A plot of the potential temperature vs. height above the lowest thermistor based on the data in Table 1 from Rona et al. [10].

The hydrothermal manganese oxide occurs both as crusts on basalt talus and as veins filling fractures in the talus along the inner margins of steps on the southeast wall of the rift valley. Bottom photographs [15] and narrow-beam bathymetry [16] reveal that the steps range from tens to hundreds of meters in width, are tens of meters in height, and kilometers to tens of kilometers in length. The steps are interpreted as fault scarps.

The manganese oxide is hypothesized to have been deposited by a sub-seafloor hydrothermal convection system involving the circulation of seawater through basalt [16], driven by intrusive heat sources beneath the rift valley. The discharge is thought to be focused by fractures in the rift valley wall which are overlain by a porous and permeable body of talus that may act to diffuse the fracture focused flow [16]. An abrupt temperature anomaly was measured in the water column over one of the steps on the southeast wall of the rift valley within the area of hydrothermal deposits, suggesting persistence of hydrothermal activity [9,10]. The temperature anomaly of  $+0.11^{\circ}\text{C}$  associated with an inverse gradient of  $1.5 \times 10^{-2} \text{ }^{\circ}\text{C}/\text{m}$  was measured within 20 m of the bottom, along a horizontal distance of 250 m, between water depths of 3000 and 2950 m using three thermistors mounted in a 4 m long towed vertical array (see Table 1 and Fig. 2). A second temperature profile made 5 km away on the southeast wall of the rift valley, showed no temperature anomaly [10] (see Fig. 1). The evidence for past and present activity led to designation of this area, the TAG hydrothermal field [14].

### 3. Thermal models

In order to simplify the interpretation of the water temperature data, we will assume that the temperature anomaly and superadiabatic gradient results from steady-state heat transfer to the seafloor. This is a reasonable assumption because the thickness of the hydrothermal deposits suggest a time scale for the discharge of  $2.5 \times 10^5$  years [8], which should be long enough for a steady state to be achieved [12]. Moreover, the existing data is insufficient to develop a meaningful time dependent model.

The water temperature data will be interpreted in two ways. First we will assume that the temperature anomaly is due to a steady, turbulent thermal plume discharging at the seafloor. The plume model will give an estimate of the heat transfer due to the assumed hydrothermal discharge. Secondly, we will estimate the heat transfer to the seafloor on the basis of a simple turbulent diffusion model. The heat transfer estimates based on these models provide useful information with regard to the hydrothermal circulation in the oceanic crust.

#### 3.1. Thermal plumes

We will first assume that the positive water temperature anomaly of  $0.11^{\circ}\text{C}$  measured over the southeast wall of the rift valley at the TAG area is due to hydrothermal discharge. Following Williams et al. [2], we will assume that this anomaly is due to a steady, turbulent, thermal plume rising by free convection in

a neutrally buoyant medium. We will assume that near-bottom currents are negligible. Expressions for the heat transfer in such a plume have been derived by Batchelor [18] based on the experimental data of Rouse et al. [19]. They may be written as  $Q = (\rho s/\alpha g)F$  where:

$$F = \left\{ \frac{z^{5/3} \alpha g (\Delta T)}{11} \exp(71r^2/z^2) \right\}^{3/2} \quad (1)$$

for a three-dimensional plume and:

$$F = \left\{ \frac{z \alpha g (\Delta T)}{2.6} \exp(41x^2/z^2) \right\}^{3/2} \quad (2)$$

for a two-dimensional plume. In the above equations  $\alpha$ ,  $\rho$ ,  $s$  and  $g$  represent the thermal expansion coefficient, the fluid density, specific heat and acceleration of gravity respectively.  $\Delta T$  represents the magnitude of the temperature anomaly at height  $z$  above the bottom, and at a distance from the axis of the plume given by  $r$  and  $x$  for the three-dimensional and two-dimensional plume respectively.

Since the temperature anomaly was measured with the lowest thermistor ranging from 2 to 20 m above the bottom, we will for convenience choose  $z = 10$  m. We will also let  $\rho = 10^3$  kg/m<sup>3</sup>,  $s = 4.2 \times 10^3$  J/kg °C,  $\alpha = 1.6 \times 10^{-4}$  /°C,  $g = 10$  m/s<sup>2</sup>. Lastly, we will assume that the temperature measurement was made at the axis of the plume. The results are:

$$Q = 5.3 \times 10^4 \text{ watts}$$

for a three-dimensional plume, and:

$$Q = 4.6 \times 10^4 \text{ watts/m}$$

for a two-dimensional plume. These results are approximately an order of magnitude greater than those given by Williams et al. [2] for a similar temperature anomaly at a similar height measured on the Galapagos spreading center. The reason for the difference is that Williams et al. [2] used eqs. 1 and 2 directly to obtain their estimate for the heat transfer. These equations must be multiplied by  $\rho s/\alpha g$  in order to be made dimensionally correct (see Batchelor [18]).

We must admit, here, that there is a significant difference between the rather narrow temperature anomalies observed over the Galapagos spreading center [2, fig. 8] and the anomaly observed over the TAG area. The anomaly feature over the TAG area is quite

broad (250 m at a height of approximately 10 m from the bottom). At a height of 10 m, however, the plume given by Batchelor [18] would be less than 10 m wide. On the plume model, it may be possible to partially explain the width of the temperature anomaly by means of (1) advection by currents, (2) plume discharge into a stably stratified surrounding medium, or (3) discharge from several vents along the profile and mixing of the plumes rising from each. Any or all of these mechanisms may be operating in the TAG area.

Bottom photographs were made concurrently with the thermistor profiles [15]. When the camera compass suspended 5 m below the camera hit pockets of sediment, sediment plumes rose vertically, indicating that currents were negligible at the time of the temperature measurements. The presence of ripple marks in the sediment indicated the existence of intermittent currents. Sizeable near-bottom currents (<25 cm/s) have been measured elsewhere in the median valley of the Mid-Atlantic Ridge [20]. Plumes discharging into a stable environment and forced plumes have not been as well investigated as the free plume model which has been used here. However, Morton et al. [21] have shown that plumes discharging in a stable environment reach a finite height and tend to spread laterally near the maximum height. An STD profile near the TAG field shows that the water column there is stable [10] and this may also be the case in the region of the thermistor profile. Since numerous faults were encountered along the thermistor profile, the temperature anomaly may in part be due to discharge from several vents with mixing of the individual plumes.

These are all ad hoc hypotheses, however, and there is no reliable data available to either substantiate or disprove them. Moreover, the width of the anomaly is of the same order of magnitude as the distance traversed by typical semi-diurnal tidal currents. Therefore we will examine an alternative model by which to interpret the water temperature anomaly. This model is based on the theory of turbulent diffusion.

### 3.2. Turbulent diffusion

Wimbush and Munk [22] have recently reviewed the structure of the ocean-bottom boundary layer. Only the essential points will be stated here.



(1) In nearly all cases the boundary layer is turbulent.

(2) There is a "constant stress layer" near the boundary such that a "friction" velocity may be defined by:

$$U^* = (\tau_0/\rho)^{1/2}$$

where  $\tau_0$  is the stress on the boundary.

(3) Within the constant stress layer there often exists a viscous sublayer in which heat is transferred by conduction. This layer has a thickness of the order of a few centimeters.

(4) Above the viscous sublayer, if it exists, there is a "logarithmic layer" in which the mean velocity and temperature increase as the natural logarithm of the height. This layer usually extends above the constant stress layer. Within the logarithmic layer we can define an "eddy diffusion" coefficient:

$$K = kU^*z \quad (3)$$

where  $k \approx 0.4$  is von Karmen's constant.

Thus we may write for the heat flux in this part of the boundary layer:

$$H = -\rho s K \frac{\partial T}{\partial z} \quad (4)$$

where  $\rho$  and  $s$  are the density and specific heat of seawater, respectively,  $H$  is the heat flux from the earth's interior, and  $\partial T/\partial z$  is the gradient of the potential temperature. For the TAG area we will assume  $\rho s = 4.2 \times 10^6 \text{ J/m}^3 \text{ }^\circ\text{C}$  and  $z = 10 \text{ m}$ . From Table 1, the gradient of the potential temperature is  $-1.5 \times 10^{-2} \text{ }^\circ\text{C/m}$ . The value  $U^*$  is uncertain, but observations in the ocean bottom boundary layer have yielded values from  $2 \times 10^{-4}$  to  $2 \times 10^{-3} \text{ m/s}$  [22]. Table 2 gives the heat flux per unit area, the heat flux per unit length of

the ridge axis assuming a width of 250 m for the TAG temperature anomaly, and the total heat output from the anomaly region, assuming lengths of 1 km and 10 km. The heat flux values in Table 2 appear to be rather large. This may partially be due to the fact that the logarithmic layer is expected to extend to a height of the order of 1 m above the seafloor, whereas the temperature gradient was measured at a height of the order of 10 m. Wimbush and Sclater [23] suggest that application of eqs. 3 and 4 at heights above the logarithmic layer may lead to overestimates of the heat flux. Nevertheless, for a "typical" value of  $U^* = 0.1 \text{ cm/s}$  [22], and a length of 10 km, the total heat output from the TAG anomaly area is of the same order of magnitude as for the Wairakei high-temperature area in New Zealand [24]. Furthermore, in high-temperature continental geothermal areas, the heat flow per unit area is often found to be of the order of several tens of watts per square meter [25,26]. It is possible that such heat transport could be achieved by hydrothermal circulation in the upper few kilometers of the oceanic crust. The absence of an observed temperature anomaly a few kilometers away (Fig. 1) suggests that the 1 km length may be more appropriate for the TAG area. Thus the results in Table 2 do not appear to be too unreasonable. In any case, it would appear that the heat flux in the region of the TAG anomaly is a significant fraction of the heat loss due to the creation of new lithosphere at the ridge axis.

#### 4. Conclusions

In order to estimate the heat flux through the ocean floor from temperature anomaly data, much

TABLE 2  
Heat transfer estimates based on turbulent diffusion

$U^*$ $\times 10^{-2}$ (m/s)	$H$ (W/m <sup>2</sup> )	Heat output per meter of ridge axis assuming 250 m anomaly width (kW/m)	Total heat out- put assuming 1 km length (MW)	Total heat out- put assuming 10 km length (MW)
0.02	5.0	1.26	1.26	12.6
0.05	12.6	3.15	3.15	31.5
0.1	25.2	6.30	6.30	63.
0.2	50.4	12.60	12.60	126.

better measurements are needed. Towed thermistor data can give only semi-quantitative results. Thermistors should be separated by no more than 1 m, and the array should be towed as close to the bottom as possible. Since it is generally not feasible to tow the thermistor array within the logarithmic layer ( $z < 1$  m) because of the irregular topography on ridge crests, we recommend that ocean floor heat flux measurements in the crestal zone be made by the techniques described by Wimbush and Sclater [23]. This would involve determination of the velocity and temperature spectra within the logarithmic layer by means of a bottom mounted device. Such measurements have not been made in regions of young oceanic crest, and they would be especially useful in regions where temperature anomalies have been measured with towed thermistors. Measurements of this type would show (1) whether the large superadiabatic temperature gradients measured by towed thermistors are real, (2) whether strongly unstable layers persist in the ocean-bottom boundary layer, at least on a time scale of a tidal cycle, and (3) whether the turbulence in the boundary layer is shear generated or buoyancy generated.

It may also be useful to measure temperatures in the upper 10–20 cm of sediment in regions of suspected hydrothermal activity. Dawson [26] has used soil temperatures to infer heat flow in convection dominated regions of the Wairakei area. The technological problems are, of course, somewhat more difficult for seafloor measurements. It may be difficult to correct for variations in sediment temperature due to periodic variations in bottom water temperature.

The two models which we have presented here for interpreting ocean-bottom water temperature anomalies have rather apparent limitations. This is especially true in view of the quality of the existing data. The results presented here, however, do suggest that small, localized near-bottom water temperature anomalies may be associated with a convective heat transfer through the seafloor of a significant magnitude. This suggests that water temperature anomalies may not be steady-state phenomena, but rather are indicative of transient cooling of very young oceanic crust by episodic hydrothermal circulation. Measurable water temperature anomalies may therefore be somewhat rare.

## Acknowledgements

We thank the reviewers for their valuable comments with regard to the original manuscript. In particular, we thank Dr. G. Bodvarsson for suggesting that the water temperature anomaly be interpreted on the basis of turbulent diffusion theory.

This work is part of the NOAA Trans-Atlantic Geotraverse (TAG) project. This work was supported by NOAA and the Oceanography Section of the National Science Foundation under NSF Grant DES 74-00513 A01.

## References

- 1 M. Talwani, C.C. Windisch and M.G. Langseth, Jr., Reykjanes Ridge Crest: a detailed geophysical study, *J. Geophys. Res.* 76 (1971) 473.
- 2 D.L. Williams, R.P. von Herzen, J.G. Sclater and R.N. Anderson, Galapagos spreading center: lithospheric cooling and hydrothermal circulation, *Geophys. J. R. Astron. Soc.* 38 (1974) 587.
- 3 C.R.B. Lister, On the thermal balance of a mid-ocean ridge, *Geophys. J. R. Astron. Soc.* 26 (1972) 515.
- 4 J.G. Sclater and J. Francheteau, The implications of terrestrial heat flow observations on current tectonic and geochemical models of the crust and upper mantle of the earth, *Geophys. J. R. Astron. Soc.* 20 (1970) 509.
- 5 R.L. Parker and D.W. Oldenburg, Thermal model of ocean ridges, *Nature* 242 (1973) 137.
- 6 F. Aumento, B.D. Loncarevic and D.I. Ross, Hudson geotraverse: geology of the Mid-Atlantic Ridge at 45°N, *Philos. Trans. R. Soc. Lond., Ser. A*, 268 (1971) 623.
- 7 J.B. Corliss, The origin of metal-bearing submarine hydrothermal solutions, *J. Geophys. Res.* 76 (1971) 8128.
- 8 M.R. Scott, R.B. Scott, P.A. Rona, L.W. Butler and A.J. Nalwalk, Rapidly accumulating manganese deposit from the median valley of the Mid-Atlantic Ridge, *Geophys. Res. Lett.* 1 (1974) 355.
- 9 P.A. Rona, B.A. McGregor, P.R. Betzer and D.C. Krause, Anomalous water temperatures over the Mid-Atlantic Ridge crest at 26°N, *EOS* 55 (1974) 293.
- 10 P.A. Rona, B.A. McGregor, P.R. Betzer, G.W. Bolger and D.C. Krause, Anomalous water temperatures over Mid-Atlantic Ridge crest at 26°N latitude, *Deep-Sea Res.* 22 (1975) 611.
- 11 E.R. Lapwood, Convection of a fluid in a porous medium, *Proc. Cambridge Philos. Soc.* 44 (1948) 508.
- 12 G. Bodvarsson and R.P. Lowell, Ocean-floor heat flow and the circulation of interstitial waters, *J. Geophys. Res.* 77 (1972) 4472.
- 13 R.P. Lowell, Circulation in fractures, hot springs and convective heat transport on mid-ocean ridge crests,

- Geophys. J. Astron. Soc. 40 (1975) 351.
- 14 R.B. Scott, P.A. Rona, B.A. McGregor and M.R. Scott, The TAG hydrothermal field, *Nature* 251 (1974) 301.
  - 15 B.A. McGregor and P.A. Rona, Crest of the Mid-Atlantic Ridge at 26°N, *J. Geophys. Res.* 80 (1975) 3307.
  - 16 P.A. Rona, R.H. Harbison, B.G. Bassinger, R.B. Scott and A.J. Nalwalk, Tectonic fabric and hydrothermal activity of Mid-Atlantic Ridge crest (26°N) *Geol. Soc. Am. Bull.* 87 (1976) 661.
  - 17 E.T.C. Spooner and W.S. Fyfe, Sub-sea-floor metamorphism heat and mass transfer, *Contrib. Mineral. Petrol.* 42 (1973) 287.
  - 18 G.K. Batchelor, Heat convection and buoyancy effects in fluids, *Q. J. R. Meteorol. Soc.* 80 (1954) 339.
  - 19 H. Rouse, C.-S. Yih and H.W. Humphreys, Gravitational convection from a boundary source, *Tellus* 4 (1952) 201.
  - 20 G.H. Keller, S.H. Anderson and J.W. Lavelle, Near-bottom currents in the Mid-Atlantic Ridge rift valley, *Can. J. Earth Sci.* 12 (1975) 703.
  - 21 B.R. Morton, Sir G. Taylor and J.S. Turner, Turbulent gravitational convection from maintained and instantaneous sources, *Proc. R. Soc. Lond., Ser. A*, 234 (1956) 1.
  - 22 M. Wimbush and W. Munk, The benthic boundary layer, in: *The Sea*, Vol. 4, A.E. Maxwell, ed. (Interscience, New York, N.Y., 1970) 731.
  - 23 M. Wimbush and J.G. Sclater, Geothermal heat flux evaluated from turbulent fluctuations above the sea floor, *J. Geophys. Res.* 76 (1971) 529.
  - 24 G.E.K. Thompson, C.J. Banwell, G.B. Dawson and D.J. Dickenson, Prospecting of hydrothermal areas by surface thermal survey, in: *Proceedings of United Nations 1961 Conference of New Sources of Energy, Geothermal Energy* 2, No. 1 (1964) 386.
  - 25 D.E. White, Rapid heat flow surveying of geothermal areas, utilizing individual snowfalls as calorimeters, *J. Geophys. Res.* 74 (1969) 5191.
  - 26 G.B. Dawson, The nature and assessment of heat flow from hydrothermal areas, *N.Z. J. Geol. Geophys.* 7 (1964) 155.

Reprinted from: *Sedimentology*, Vol. 23, No. 6, 867-872.  
*Sedimentology* (1976) 23, 867-872

## An automated rapid sediment analyser (ARSA)

TERRY A. NELSEN

*NOAA, Atlantic Oceanographic and Meteorological Laboratories,  
15 Rickenbacker Causeway, Miami, Florida 33149, U.S.A.*

### ABSTRACT

The automated rapid sediment analyser (ARSA) is a pressure-transducer grain-size analysis system. This basic Woods Hole-type fall tube was automated by the addition of a digital voltmeter, Hewlett-Packard 9810A calculator, and an x-y plotter. Eight min after sample introduction, the system automatically produces size distribution data in 0.25- $\phi$  intervals, distribution statistics, and a plotted frequency histogram.

### INTRODUCTION

As early as 1938, Emery (1938) turned to settling tubes as an alternative to traditional sieves for a more rapid method of sediment textural analysis. Since then others have modified the original sand accumulation vs. time technique (Emery, 1938; Poole, 1957) by measuring pressure changes in the water column with the transit of falling grains (Zeigler, Whitney & Hays, 1960; Schlee, 1966; Bascomb, 1968) or by weight accumulation on a balance pan (Felix, 1969) similar to earlier Dutch work.

Although the settling tubes achieve a significant time savings over sieving, the reduction of the analogue data produced still requires operator time for interpretation, statistical analysis, and graphic display. Only one early attempt at automated data acquisition from a settling tube is in the literature (Zeigler, Hayes & Webb, 1964), but it does not provide for real time data reduction, statistical analysis, and graphic display. For laboratories analysing hundreds of samples, it is desirable to have a rapid sediment analyser (RSA) which is as fast as those previously built and also yields highly accurate and precise data while eliminating the human element from the time of sample introduction to final statistical treatment of the data. Although the concept of the settling tube does not limit the analysis range to sand size particles, the long fall times required for silt and clay sized particles would negate the benefits of rapid

analysis gained by the settling tube. Hence the analysis of fines ( $< 62 \mu\text{m}$ ) is best undertaken by alternative methods (pipette or electronic particle counters), and the rapid sediment analyser is most efficiently employed for the textural analysis of sand.

The instrument described here was therefore developed for only the size analysis of sand. It is a computer based data acquisition system coupled to a Woods Hole type (Schlee, 1966) rapid sediment analyser and is hereafter referred to as an automated rapid sediment analyser (ARSA).

### ARSA COMPONENT HARDWARE

The fall tube used in this system is clear plastic and the inside diameter measures 10 cm by 200 cm in total length. Previous work (Gibbs, 1972) on the accuracy of particle-size analysis by settling tube indicated that tubes 7.5 cm and 12.7 cm in diameter were burdened with fall time inaccuracies of up to 34–8% respectively. It should be noted that these inaccuracies cited by Gibbs (1972) were the result of comparing the differences in fall velocities of a given size particle for a single sphere against samples of up to 4 g. Although the ARSA system described here is 10 cm in diameter, the calibration of the system was conducted relative to sieve analysis (Sanford & Swift, 1971), and the processes accounting for fall velocity errors were compensated for in the calibration technique.

Pressure ports are located at 0.5 and 133 cm below the water level in the tube. This separation is necessary to insure that all introduced particles are in the sensing zone after the time required to damp surface oscillations resulting from sample introduction. Pressure and pressure changes within the water column are detected by a Hewlett-Packard Model # 270 differential gas pressure transducer and are interpreted as voltage changes resulting from the displacement of the transducer diaphragm. The rate of change of pressure represents the size distribution of the sample being analysed. This analogue voltage signal is conditioned by a Sanborn (Hewlett-Packard) Model 350-1100C carrier preamplifier before it is sent to a Hewlett-Packard Model 3480B digital voltmeter (with Model 3482A DC range unit) where it is transformed into a digital voltage signal. A Hewlett-Packard 2570A coupler/controller with crystal clock provides a reference time base for the calculator's predetermined  $0.25\text{-}\phi$  fall times. Initial fall times were derived from Schlee's (1966) work and adjusted for the longer tube length of this system. The coupler/controller also provides electronic compatibility between the digital voltmeter and the calculator memory. The memory-calculation function of this system is provided by a Hewlett-Packard Model 9810A calculator. Final histogram display is generated on a Hewlett-Packard Model 9862A plotter. Total system compatibility dictated the exclusive use of a single electronics system. It should also be noted that line voltage fluctuations can introduce spurious transient signals into the system which cause erroneous voltmeter readings. Therefore it is necessary to supply power through a voltage regulator.

The ARSA system is pictured in Fig. 1. The fall tube is suspended from a wooden frame by metal turnbuckles with foam rubber separation pads. The entire system is shock mounted from the floor by additional foam pads. This minimizes vibration transmission to the tube mounted transducer. Spirit levels secured to the fall tube at right angles insure a perfectly vertical tube orientation through turnbuckle adjustments.



**Fig. 1.** View of the total ARSA system showing fall tube and associated electronics.

Approximately 150–200 samples can be run before accumulated sediment must be removed through the bottom drain valve and the tube refilled with deionized or distilled water.

Figure 2 shows the sample introduction device. A controlled electric motor mounted above the tube depresses a sediment coated screen onto the surface of the water column. The inverted sub-62 micron screen holds the sample in place (as seen in Fig. 2b) by water surface tension. Parallel contact of the sediment-laden screen and the water surface releases the particles and permits a gentle and simultaneous discharge of the grains. Sample sizes between 5–7 g are used for all ARSA analyses.

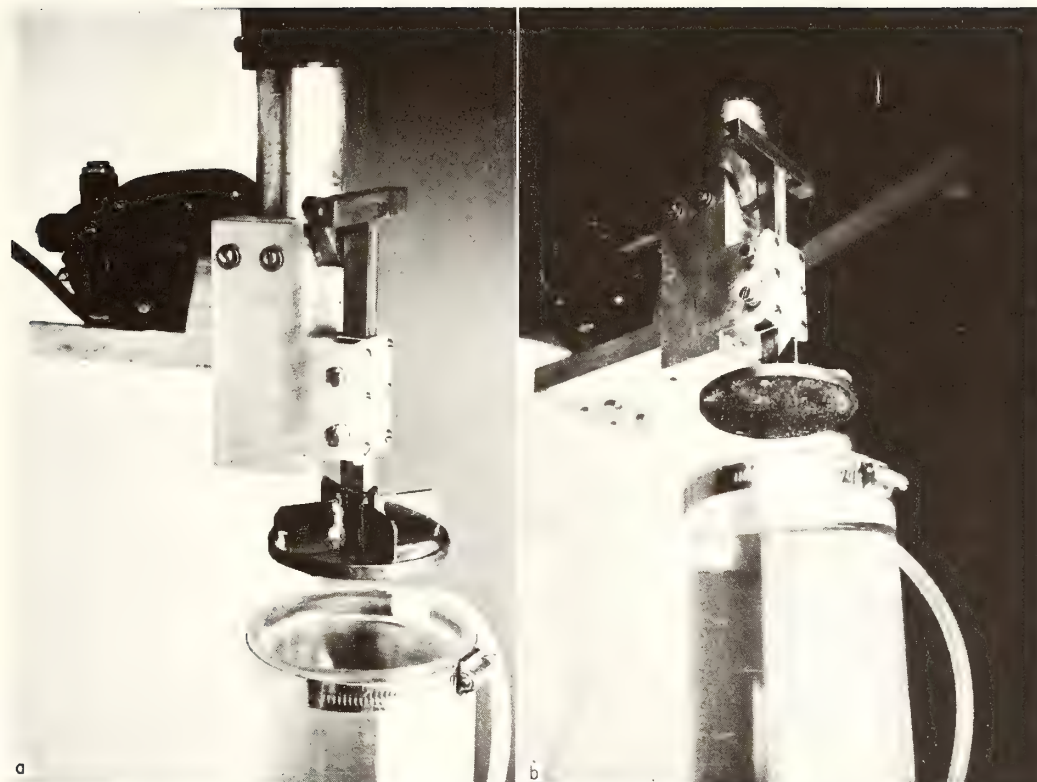


Fig. 2. (a) Showing variable speed sample introduction device, top of fall tube, and upper transducer pressure port. (b) Sample introduction device with sediment on screen ready for sample run.

### DATA ACQUISITION AND COMPUTATION PROGRAM

A Hewlett-Packard Model #9810A calculator provides the heart of this ARSA data acquisition system. The calculator program includes subroutines for data acquisition, storage, computation, and hard copy output.

Before sample introduction the transducer's output voltage is adjusted to an arbitrary small positive value which is simultaneously displayed on the digital voltmeter. Data acquisition starts when sample introduction causes a predetermined threshold millivoltage to be exceeded. The program then pauses for 5 s while surface oscillations caused by sample introduction damp. Following this, three voltage values are read in the next second and placed in memory. Later these values will be averaged and this average used in the computational subroutine as the 100% reference value. Based on fall-time values in the memory bank, the calculator then runs time comparison do-loops against the system's crystal clock. When the time value for each  $0.25\text{-}\phi$  interval of the sand range ( $-1.00\text{--}4.00\ \phi$ ) is satisfied, the calculator commands the digital voltmeter to read the transducer voltage and place this value in memory for future use in the data reduction subroutine. Successive voltage values decline in magnitude as grain fallout past the lower pressure port causes the transducer's diaphragm to return to the null (baseline) position. After gathering digital voltage values

for all the  $0.25\text{-}\phi$  intervals in the memory, the computational subroutine takes over. Since all samples analysed in the ARSA have been prescreened (wet and dry) at  $4.0\ \phi$  to remove sub- $62\mu$  material, the program assumes that no material remains in the water column and considers the final voltage reading as the zero baseline value. In reality, this is a valid assumption since the occasional trace amounts left in the water column are below the transducer's detection threshold.

Statistics computed are frequency distribution, cumulative distribution, phi mean, standard deviation, skewness, and kurtosis. All computations are based on the moment statistical methods described by Krumbein & Pettijohn (1938). These values are presented in hard copy by the calculator printer. The graphic display is a  $0.25\text{-}\phi$  frequency histogram on the x-y plotter. An example of this graphic display is shown in Fig. 3b. The entire process from sample introduction to printed statistics and plotted histogram takes 8 min.

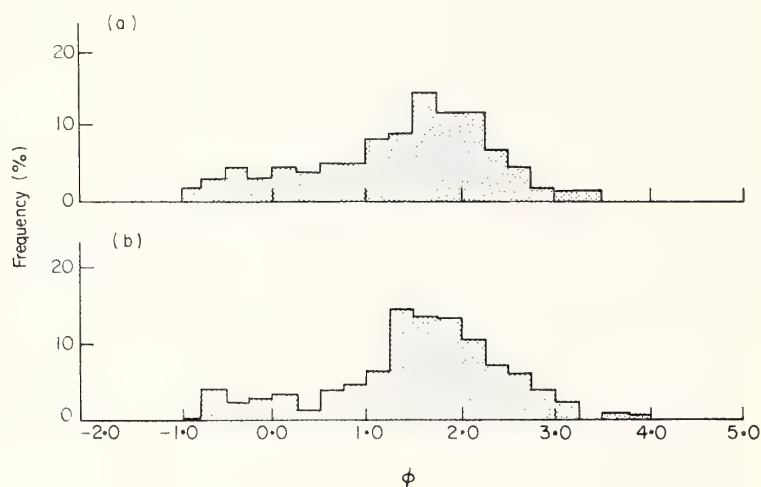


Fig. 3. Examples of the system's x-y plotter output (sample 10-0-A) for (a) manually imputed sieve data,  $\phi$  mean = 1.39, s.d. 0.91, and (b) an ARSA run data,  $\phi$  mean 1.40, s.d. 0.93.

### SYSTEM PERFORMANCE

Although the ARSA was developed as an instrument which gave phi means similar to sieve phi means (final correlation coefficient of 0.99), the final system also showed a remarkable similarity between ARSA frequency distributions and sieve frequency distribution data (Fig. 3) with an overall correlation coefficient for  $0.25\text{-}\phi$  intervals of 0.86.

### ACKNOWLEDGMENTS

Throughout the development of this system, Donald J. P. Swift, Patrick G. Hatcher, and Charles Lauter offered constructive criticism and sound advice which was greatly appreciated.



## REFERENCES

- BASCOMB, C.L. (1968) A new apparatus for recording particle size distribution. *J. sedim. Petrol.* **38**, 878–884.
- EMERY, K.O. (1938) Rapid method of mechanical analysis of sands. *J. sedim. Petrol.* **8**, 105–111.
- FELIX, D.W. (1969) An inexpensive recording settling tube for analysis of sands. *J. sedim. Petrol.* **39**, 777–780.
- GIBBS, R.J. (1972) The accuracy of particle-size analysis utilizing settling tubes. *J. sedim. Petrol.* **42**, 141–145.
- KRUMBEIN, W.C. & PETTJOHN, F.J. (1938) *Manual of Sedimentary Petrography*. Appleton-Century-Crofts, New York, U.S.A.
- POOLE, D.M. (1957) Size analysis of sand by a sedimentation technique. *J. sedim. Petrol.* **27**, 460–468.
- SANFORD, R.B. & SWIFT, D.J.P. (1971) Comparison of sieving and settling techniques for size analysis, using a Benthos rapid sediment analyser. *Sedimentology*, **17**, 257–264.
- SCHLEE, J. (1966) A modified Woods Hole rapid sediment analyser. *J. sedim. Petrol.* **36**, 403–413.
- ZEIGLER, J.M., WHITNEY, G.G. & HAYES, C.R. (1960) Woods Hole rapid sediment analyser. *J. sedim. Petrol.* **30**, 490–495.
- ZEIGLER, J.M., HAYES, C.R. & WEBB, D.C. (1964) Direct readout of sediment analysis by settling tube for computer processing. *Science*, **145**, 51.

(Manuscript received 21 January 1976; revision received 23 March 1976)

Reprinted from: *American Association of Petroleum Geologists Bulletin*, Vol. 60, No. 7, 1078-1106.

## Tectonics of Southwestern North Atlantic and Barbados Ridge Complex<sup>1</sup>

GEORGE PETER<sup>2</sup> and GRAHAM K. WESTBROOK<sup>3</sup>

Miami, Florida 33149, and Keele, Staffordshire, England

**Abstract** More than 40,000 km of bathymetric, magnetic, and gravity data and 2,000 km of seismic-reflection data were obtained in 1971 and 1972 aboard the NOAA ships *Researcher* and *Discoverer* over the Barbados Ridge complex and the adjacent southwestern North Atlantic. Most of the tracklines were oriented east-west and spaced closely (20 km) to attempt correlation between adjacent lines. About a dozen long, north-south-trending tracklines provided control on the structural variations in that direction.

From bathymetric and magnetic data it was established that from the Late Cretaceous to the present the development of the Mid-Atlantic Ridge in this area is essentially the same as in the rest of the North Atlantic.

Indications for relatively recent tectonic activity were found on some seismic records along several east-west faults, some of which were in alignment with offset zones of the magnetic-anomaly lineations. The implicit suggestion is that intraplate tectonic activity is common, and that the western extension or "dead traces" of transform faults may provide avenues where the accumulated tectonic energy within the oceanic plate is released.

The influence of many of the major east-west faults extends westward from the Atlantic basin across the Barbados Ridge complex to the platform of the Lesser Antilles volcanic arc. Major topographic changes, as well as changes in the character of the geophysical anomalies and in the chemistry of the volcanic rocks across the fault lines suggest that the faults have played a significant role in the evolution of this area. As these faults apparently have affected the structure west of the shallow earthquake belt and the axis of the gravity minima, this area appears ideal to study possible anomalies in the subduction process or, perhaps, the applicability of the concept itself.

### INTRODUCTION

The area from the Romanche fracture zone, near the equator, to the Barracuda Ridge, about 16°N, is one of the more complex geologic areas of the Atlantic Ocean floor. Whereas the general evolution of the North and South Atlantic Oceans, on the basis of magnetic-anomaly lineations, had been understood by 1970, this region remained a problem area because of the many fracture zones, the close proximity of the magnetic equator, and the lack of adequate survey coverage. Yet this area is in a key position for critical tests or refinements of the plate-tectonics hypothesis (Isacks et al, 1968; Le Pichon, 1968; Morgan, 1968). In addition to the still unresolved problem of the overlap of Central and South American Paleozoic rocks in the Bullard reconstruction of Pangea (Bullard et al, 1965), and the controversy

about the age and origin of the Barbados Ridge (Meyerhoff and Meyerhoff, 1972), the various tectonic concepts contained in the papers that discuss the evolution of this part of the Atlantic include north-south extension (Funnell and Smith, 1968), north-south extension and left-lateral shear (Ball and Harrison, 1969, 1970), and sea-floor spreading along east-west-trending mid-oceanic-ridge segments (Dietz and Holden, 1970; Freeland and Dietz, 1972).

To test some of these hypotheses, in 1971 and 1972 a systematic geophysical study of the sea floor was undertaken between the Lesser Antilles island arc and the Mid-Atlantic Ridge (Fig. 1). The northern and southern boundaries of the study area were approximately 18°N and 10°N, respectively. The specific scientific objectives were to: (1) investigate the possible presence of magnetic-anomaly lineations east of the Lesser Antilles island arc, establish their trend, and identify them; (2) define topographic and structural trends, and establish the development of the Mid-Atlantic Ridge and the associated fault zones in the area; (3) determine the east-west extent of the Barracuda fault zone and its role as a major

© Copyright 1976. The American Association of Petroleum Geologists. All rights reserved.

<sup>1</sup>Manuscript received, July 23, 1975; accepted, January 20, 1976.

<sup>2</sup>NOAA, AOML, MG&GL.

<sup>3</sup>The University.

The success of this work was due largely to the cooperation and dedication of the captains, officers, and crews of the NOAA ships *Researcher* and *Discoverer*.

We are grateful to Omar E. DeWald, George Merrill, and Sam A. Bush of the Atlantic Oceanographic and Meteorological Laboratories (AOML) of the NOAA for their significant contributions to the data-collection and processing phases of this work, and to the preparation of some of the bathymetric and magnetic maps.

We acknowledge George H. Keller and Bonnie C. McGregor for their critical reviews of the manuscript, and Claire Ulanoff for her cheerful editorial and typing work.

Data presented in this paper over the Barbados Ridge complex south of 14°N were provided before their publication by Graham K. Westbrook, University of Keele, England.

This work was supported by the Marine Geology and Geophysics Laboratory of AOML, NOAA, with contributions from NSF-IDOE Grant NO. AG-253 and AG-489.

Although the writers generally agree on the interpretation presented, the senior writer takes full responsibility for challenging some of the concepts of plate tectonics.

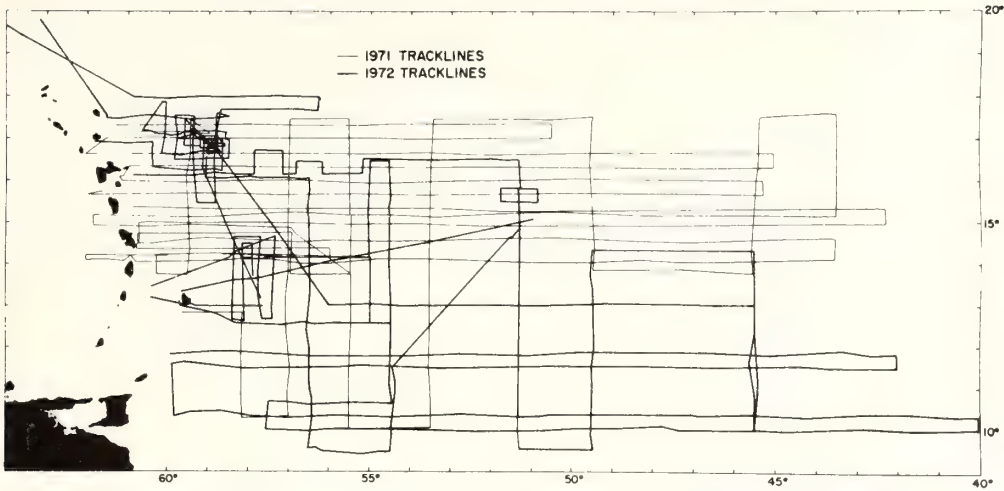


FIG. 1—Trackline coverage east of Lesser Antilles island arc (NOAA 1971, 1972).

transform fault or plate boundary; (4) describe in detail the southeast extension of the Puerto Rico Trench and the area of transition between it and the Barbados Ridge (of special interest was the determination of the role of the Barracuda and other fault zones as barriers to sediment deposition); and (5) determine the structure of the Barbados Ridge, and investigate subduction and underthrusting as possible mechanisms for its formation.

Data-collection techniques, instrumentation, and comments on data processing and accuracy were given by Peter et al (1973a, b) and Dorman et al (1973). In this paper the bathymetric, mag-

netic, gravimetric, and seismic-reflection results will be discussed in light of the basic objectives.

**MID-ATLANTIC RIDGE**

**Bathymetry**

Previous investigations have established that the overall trend of the Mid-Atlantic Ridge east of the Lesser Antilles island arc is north-south (Heezen and Tharp, 1961; Collette et al, 1969; van Andel et al, 1971; Collette and Rutten, 1972). Most of the NOAA tracklines (Fig. 2) were oriented perpendicular to this trend, and were expected to reveal the development of the Mid-Atlantic Ridge with little interference from

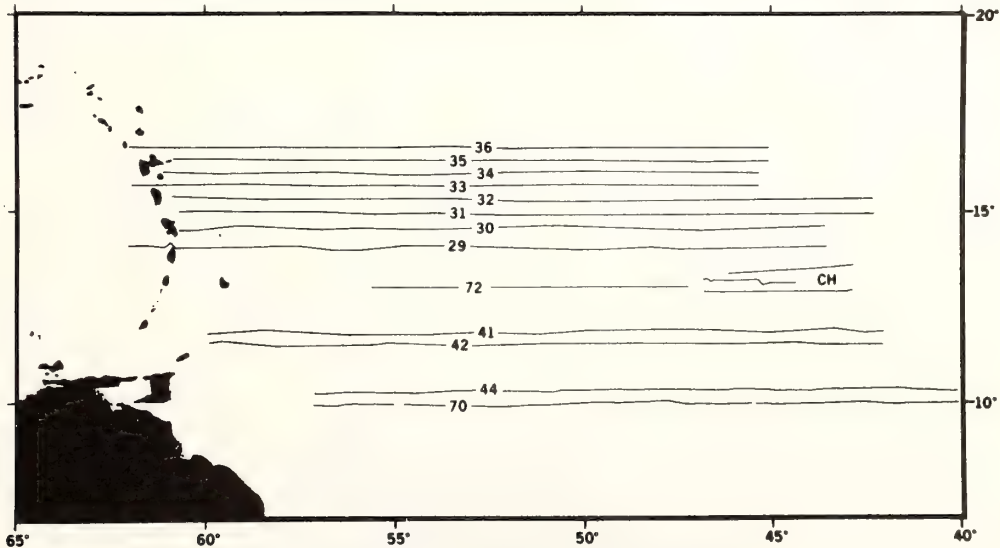


FIG. 2—Identification of selected east-west tracklines.

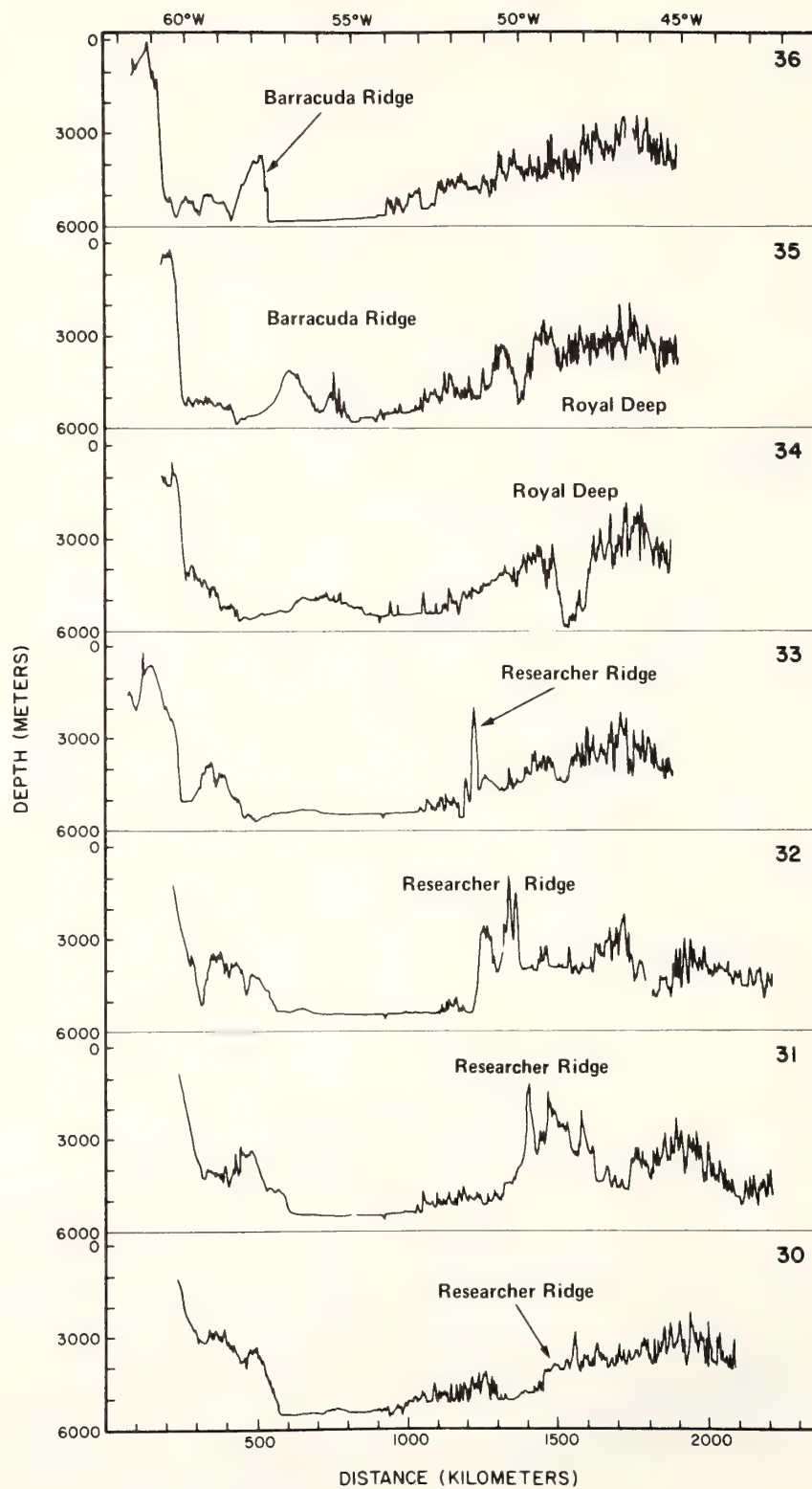


FIG. 3—Bathymetric profiles along northern half of east-west tracklines.

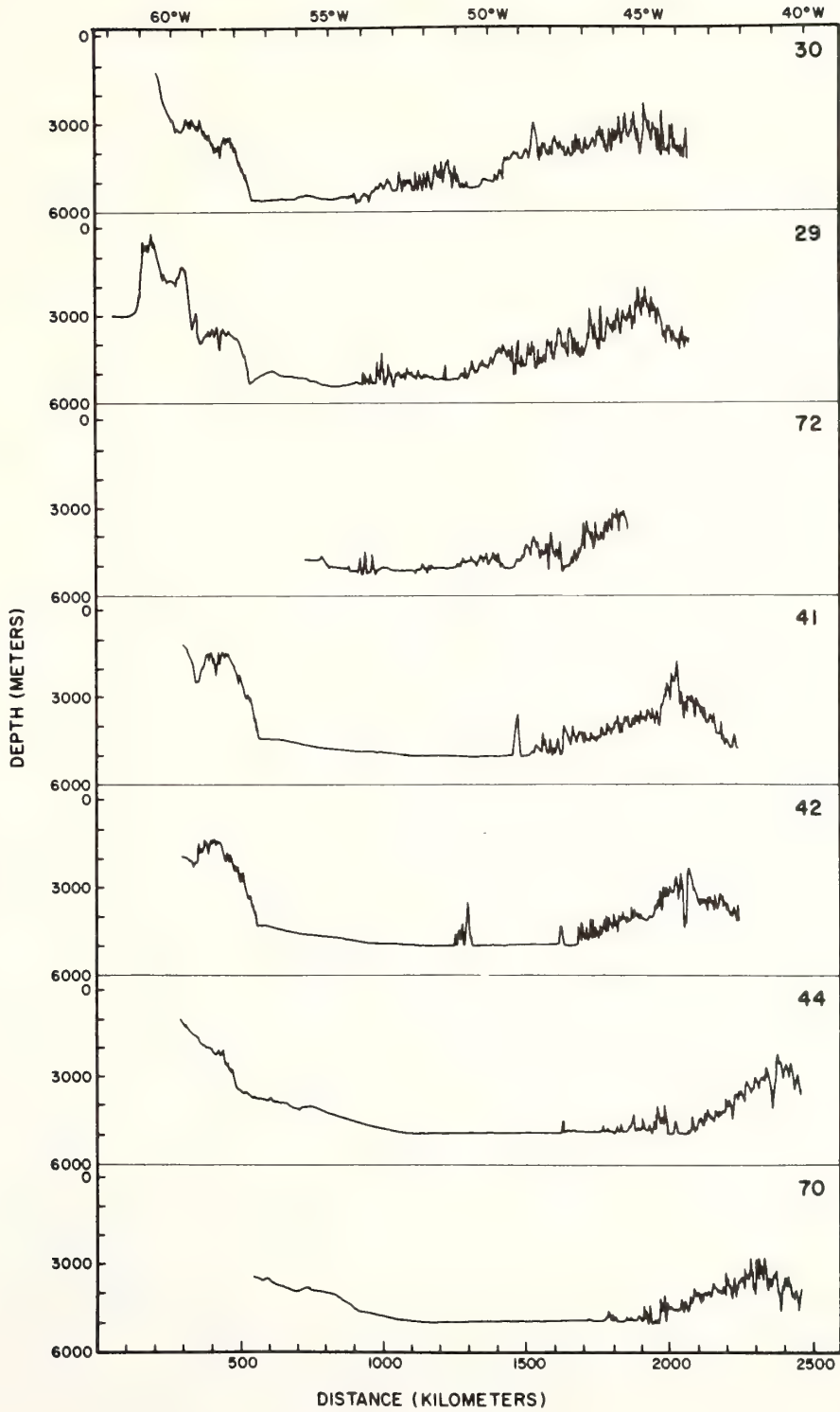


FIG. 4—Bathymetric profiles along southern half of east-west tracklines.

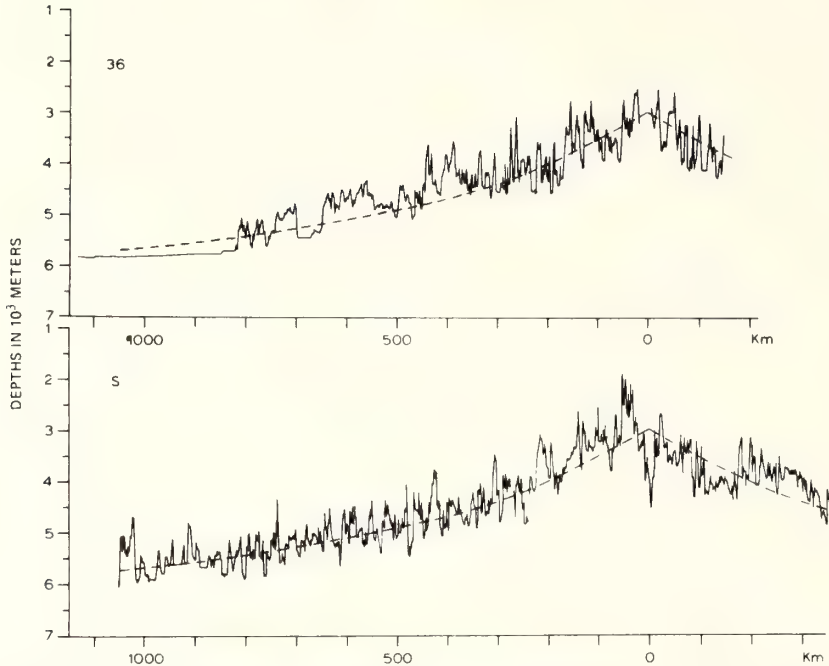


FIG. 5—"Standard" Mid-Atlantic Ridge profile *S* and comparison of its average elevation curve to bathymetric profile 36.

transform faulting. However, it was found that changes in the development of the ridge are significant even between relatively closely spaced lines (Figs. 3, 4). On most of the northern track-lines (Fig. 3) the crestal province is so rugged that it is hard to pick even the central rift valley or the axis of the ridge. On the southern lines the replacement of the central rift valley by a major axial mountain is illustrated on the adjacent profiles of 42 and 41, and 70 and 44 (Fig. 4). Other dramatic changes among adjacent profiles are due to fracture zones that cross the Mid-Atlantic Ridge obliquely. Profiles 35 and 34 cross the Royal deep (Collette et al, 1973), which reaches a depth of nearly 6,000 m only at a distance of 200 km from the axis of the ridge (after the southeast extension of the Puerto Rico Trench, this is the greatest depth east of the Lesser Antilles). Profiles 30 to 33 show the largest ridge and fracture zone of the area, the Researcher Ridge (Peter et al, 1973c), which appears to be a branch of (or an echelon with) the Fifteen-Twenty fracture zone (Collette and Rutten, 1972).

From the bathymetric sections in Figure 4, and from the sediment-thickness determinations of the area (Ewing et al, 1973) it is obvious that the flank of the Mid-Atlantic Ridge is buried by progressively more sediments as one approaches the

South American continent. When a "standard" Mid-Atlantic Ridge section from the North Atlantic is compared with ridge sections in this area (Figs. 5, 6), the average ridge-elevation curve matches all ridge segments well (Peter et al, 1973c). The identical height relations imply identical age (Sclater et al, 1971) and identical development; i.e., a continuity of the central half (from the axis toward the flank to about 1,000 km) of the Mid-Atlantic Ridge from the area of the "standard" section to the southern North Atlantic, adjacent to the Lesser Antilles island arc.

Two north-south profiles on Figures 7 and 8 illustrate the segmentation of the Mid-Atlantic Ridge due to transverse faulting. On profile 11-48 the deepest point is the Royal deep, the tallest peak is on the Researcher Ridge. The step-like deepening of the sea floor south of the Researcher Ridge is, of course, due to the eastward offset of the Mid-Atlantic Ridge at 15°N. Profile 13-46, north of 15°20'N, is over the eastern flank of the Mid-Atlantic Ridge; on the south the ridge offset at 15°20'N has shifted the ridge axis to the east of this profile, so the topography shown is the west flank of the ridge. Farther south along this profile are smaller offsets at approximately 13°30'N and 12°30'N, and the deepest valley at 11°N is part of the Vema fracture zone.

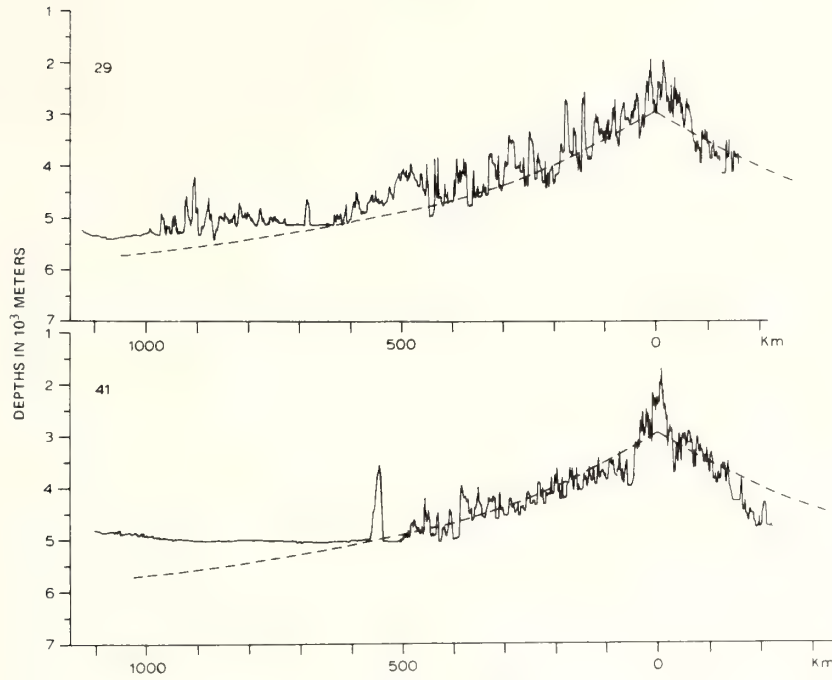


FIG. 6—Comparison of average elevation curve of “standard” Mid-Atlantic Ridge section S to bathymetric profiles 29 and 41.

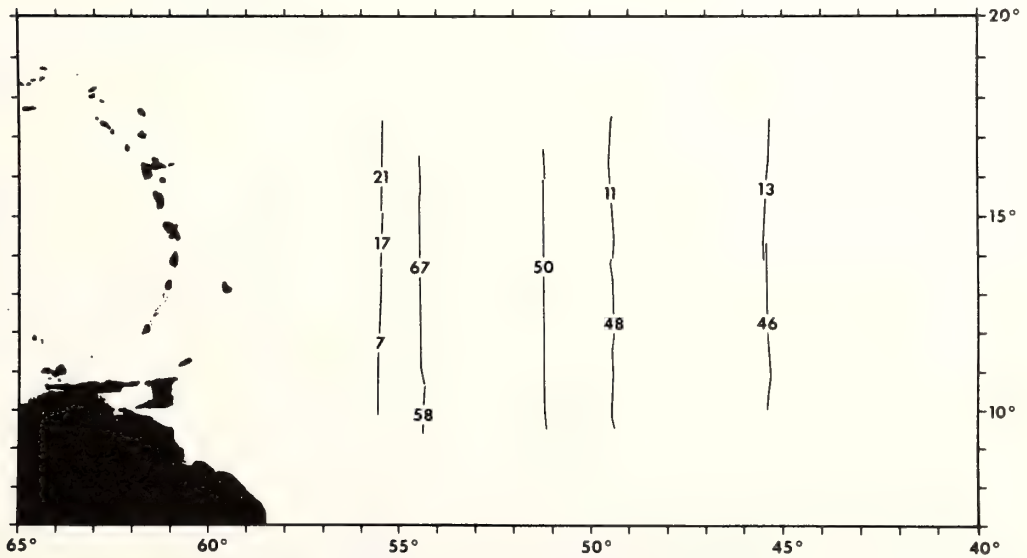


FIG. 7—Identification of selected north-south tracklines.

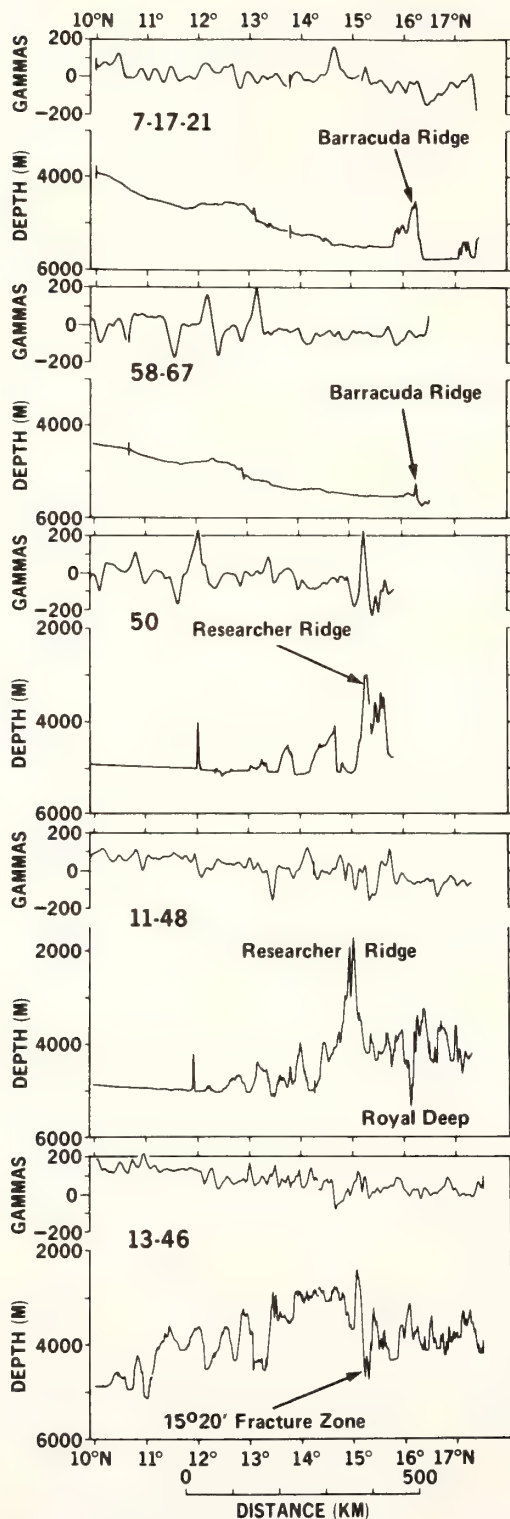


FIG. 8—Magnetic anomaly and bathymetric profiles along north-south tracklines.

Our interpretation of the fracture pattern of the Mid-Atlantic Ridge is somewhat different from that of Collette et al (1974). This difference essentially resulted from the orientation of the survey lines; theirs ran mostly north-south, ours mostly east-west. When the transform faults are close together, it is difficult to distinguish whether a major peak and trough sequence is part of a fracture zone or part of the north-south-trending ridge topography. To solve this minor discrepancy between the two interpretations, more east-west lines are needed between the Researcher and the Vema fracture zones, and more north-south lines west of 50°W.

Within the area of the more detailed survey coverage (between 14°N and 17°30'N) a change in the strike of the fracture zones was detected between 50°W and 53°W (Figs. 9, 10). The three major features on the map, the Royal trough, 15°20'N fracture zone, and the Researcher Ridge and fracture zone all strike west-northwest near the crest of the Mid-Atlantic Ridge. Trackline spacing was too wide to show clearly the ridge flank south of the 15°20'N fracture zone, but it is expected that the topography is just as rough there as north of the Royal trough. Due to the same problem, the transition from northwest to north-south trend south of the Researcher Ridge and northwest of the Royal trough is highly interpretive. What can be detected without doubt is that the Researcher Ridge terminates at 51°40'W, and that an east-west trending fault emerges from it at about 15°15'N (Fig. 9). The 15°20'N fracture zone and the Royal trough also seem to have their western limit around 51°20'W, and two east-west faults, one along 16°20'N and the other along 17°N, take their place.

#### Magnetics

Magnetic-anomaly lineations were identified, and a complete evolutionary history of the North Atlantic was given by Pitman and Talwani (1972). They noted that, compared to the Pacific Ocean, the identification and correlation of the magnetic anomalies are more difficult because of the much slower Atlantic-sea-floor-spreading rate and the more common transform fault zones. In the area east of the Lesser Antilles the reduced anomaly amplitudes due to the nearness of the magnetic equator, and the more common fracture zones, make the anomaly identifications and correlations even more of a problem. The technique and the set of criteria used to overcome these difficulties were described by Peter et al (1973c). Briefly, it involved the use of several "standard" North Atlantic profiles taken from Lattimore et al (1974) for comparison purposes (one is shown on Fig. 10), and the use of theoretical magnetic-



spreading models computed at different spreading rates. In addition, the relation between the ridge elevation and age of the oceanic crust, derived by Sclater et al (1971), was utilized by comparing both the magnetic and topographic profiles to the "standard" North Atlantic sections. The profiles obtained by Lattimore et al (1974) were used as "standard" because those were run parallel with and between the Atlantis and Kane fracture zones and, therefore, are not expected to be influenced by any other significant transform faults.

An amended version of the correlations of Peter et al (1973c) is shown in Figure 10. It is emphasized that several other identifications could have been made, depending on one's criteria. However, the differences among those would have changed only the identification of certain individual peaks without negating the overall pattern, or the existence of the late Mesozoic and Cenozoic magnetic lineations east of the Lesser Antilles island arc (Fig. 11). The lineation pattern shown in Figure 11 matches well the pattern derived by Pitman and Talwani (1972) north of 18°N, and several of the offsets correlate with fracture zones that also are present in the bathymetry.

Although the correlation of individual anomalies cannot be demonstrated convincingly by a single illustration alone, Figure 12 is offered to show that the overall character of the magnetic-anomaly profiles is the same on the north and south sides of the Vema fracture zone, between the 100- and 600-km marks.

The magnetic-anomaly profiles shown in Figure 8 dramatize the point made by Schouten (1974) about the large amplitude of the magnetic anomalies over the east-west-trending fracture zones in this area. Part of the correlation problems discussed before is the result of these large-amplitude anomalies, which because of the frequency of the east-west fracture zones mask the effect of those anomalies that are caused by the north-south-oriented, normally and reversely magnetized bands of crustal rocks associated with the Mid-Atlantic Ridge.

#### ATLANTIC BASIN

##### Bathymetry

The area between the western flank of the Mid-Atlantic Ridge and the eastern margin of the Barbados Ridge complex can be divided into several physiographic units. South of 14°30'N and west of 54°30'W, adjacent to the Barbados Ridge, the sea floor is cut into several regionally uplifted crustal blocks, characterized by gentle southern dips of the individual blocks, downdropped to the north along east-west-bounding faults (Figs. 8, 11,

13, profiles 7-17-21 and 58-67). Due to the northeasterly dip of the regional bathymetry, the eastern margin of these uplifted blocks is not obvious north of 13°N, but south of 13°N a clear boundary fault is present (Fig. 4, profile 72). However, south of 12°N the large accumulation of sediments of the South American continental rise obscures this boundary. The uplifted blocks are arched gently along a north-south axis. Their highest elevation is between 56°W and 57°W, and they gently dip away from this region toward the Barbados Ridge and the abyssal plain on the east (see Fig. 14).

With the exception of these regionally uplifted blocks, the area between the western flank of the Mid-Atlantic Ridge and the Barbados Ridge complex is occupied by the northwest extension of the Guiana basin, or the Demerara abyssal plain. As Embley et al (1970) have noted, the elevation of this abyssal plain is 350 m higher south of 13°N than between 14°30'N and the Barracuda Ridge. The change of elevation between 13°N and 14°30'N is controlled by the westward extension of the east-west faults described previously.

The northwest margin of the Demerara abyssal plain is a gentle topographic arch which connects the Barracuda Ridge and the foothills province of the Barbados Ridge complex (Fig. 13). East of this topographic high several small east-west-trending steps on the sea floor (see Fig. 15) indicate additional faulting; on the west, the sea floor is smooth and gently slopes westward to 58°30'W, where the northward continuation of the Barbados foothills province forms its limit.

The other two significant bathymetric features of this part of the Atlantic basin are the Barracuda Ridge and the Barracuda abyssal plain. The Barracuda Ridge extends approximately between 54°30'W and 59°W, and rises more than 1,600 m above the surrounding ocean floor (Paitson et al, 1964; Birch, 1970). Between 54°30'W and 57°W it forms part of the east-west structural fabric of the area: west of 57°W its overall strike is northwestward, but there are possible suggestions in the bathymetric (Fig. 13) and seismic data that the bulk of the ridge may be composed of smaller, en-echelon, east-west-trending ridge segments.

The Barracuda abyssal plain lies between the northern fault scarp of the Barracuda Ridge and another fault (possible transform fault shown on Fig. 11) along 17°N.

##### Magnetics

There is no clear pattern to the magnetic-anomaly distribution between the Barbados Frontal Hills zone and the western flank of the Mid-Atlantic Ridge (Fig. 16). Over the abyssal plains the magnetic anomalies reflect the com-

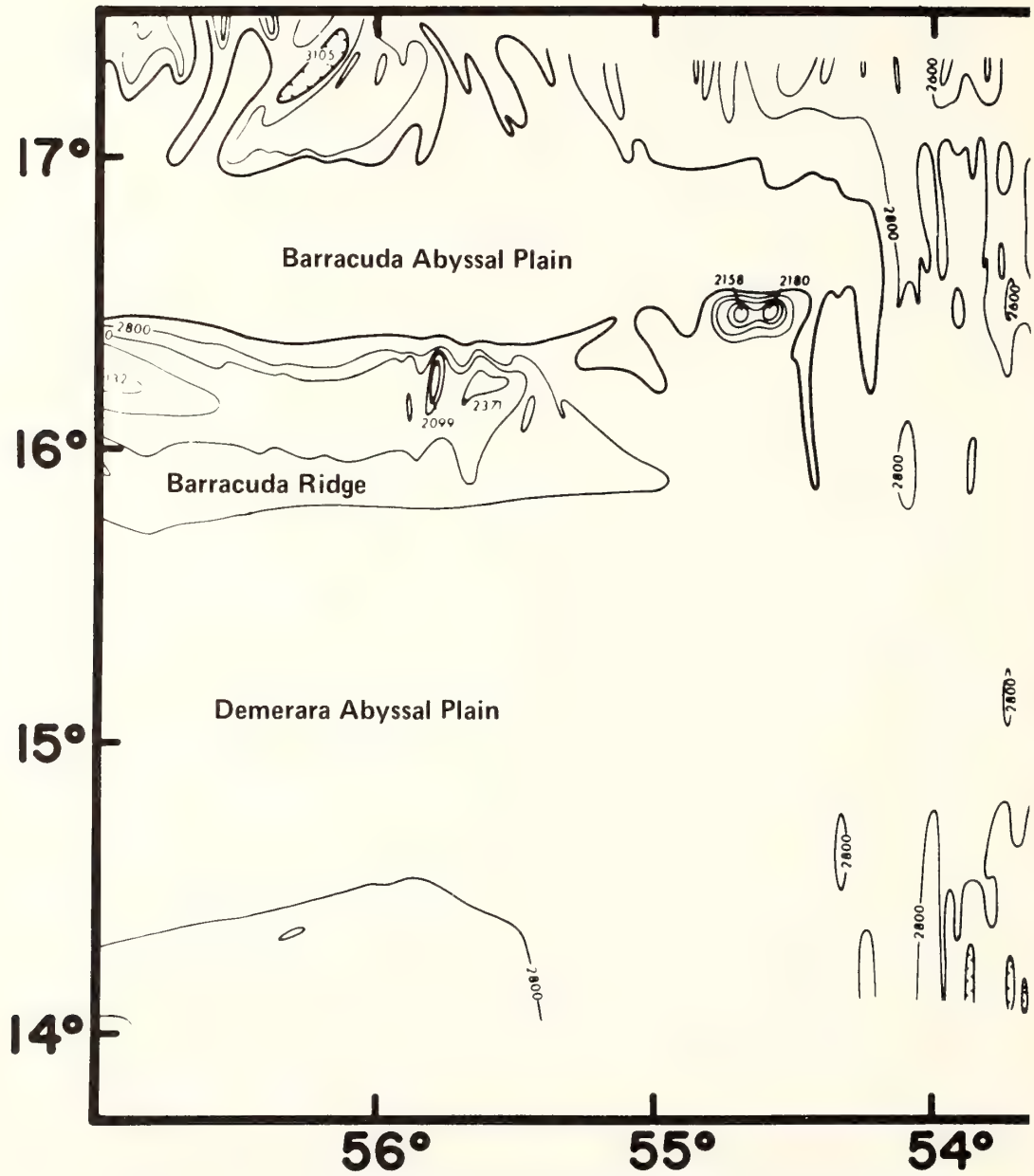
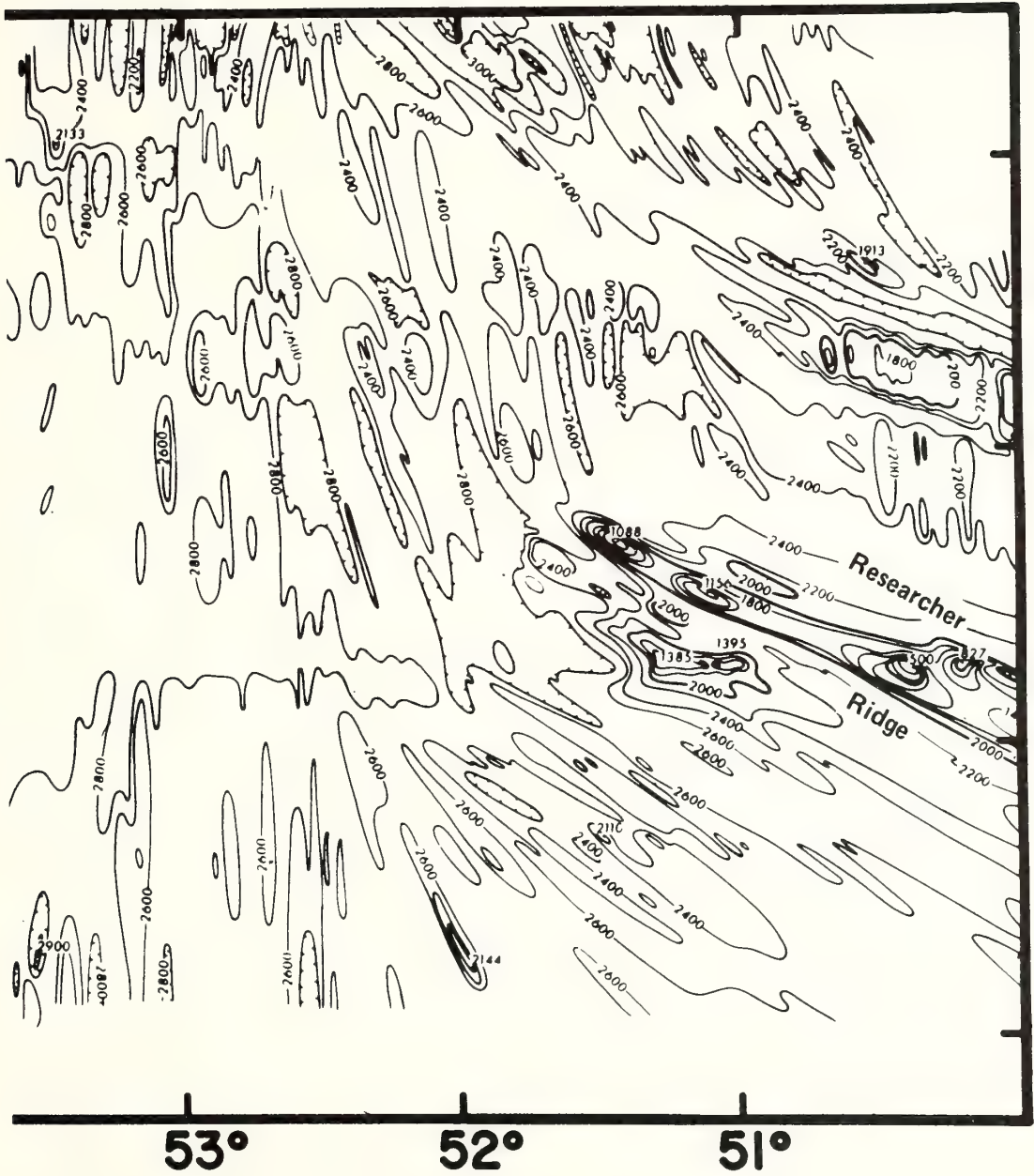


FIG. 9—Bathymetric map of western flank of Mid-Atlantic Ridge and adjacent abyssal plain between 14°N and 17°N. Contour interval 200 fm (fm = 1.83 m).





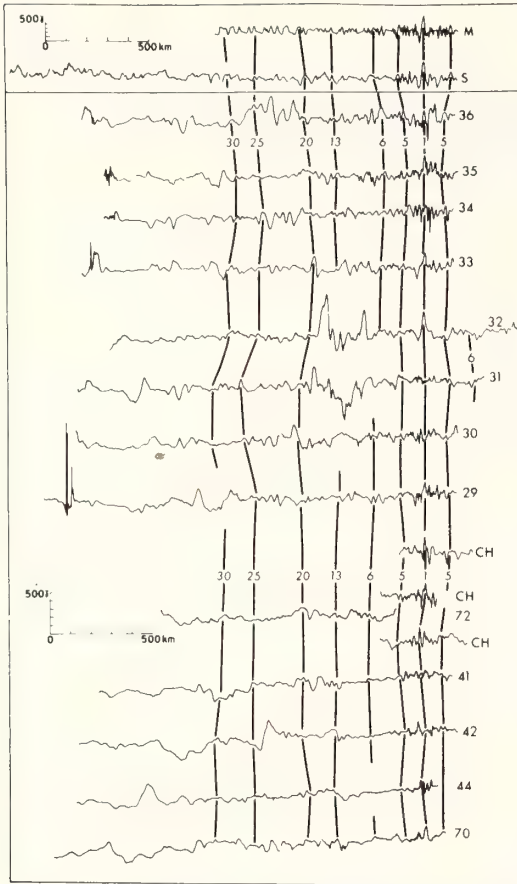


FIG. 10—Identification and correlation of magnetic anomalies along east-west tracklines. Anomaly numbers are after Pitman et al (1968).

bined effect of (1) possible vestiges of Late Cretaceous magnetic lineations; (2) segments of fracture zones; and (3) topographic features. Over the uplifted crustal blocks the anomalies are related to the east-west-trending faults.

In amplitude, the largest magnetic anomalies are associated with segments of the east-west fault zones (Fig. 8; Peter et al, 1973b; Collette et al, 1974). Within the area of closer control (between  $14^{\circ}\text{N}$  and  $17^{\circ}30'\text{N}$ ) many anomalies are aligned along  $15^{\circ}\text{N}$ , indicating the westward continuity of the fracture zone from the Researcher Ridge (Figs. 11, 16). The Barracuda Ridge does not have a large continuous sequence of magnetic anomalies associated with it. The only significant anomalies are at  $55^{\circ}43'\text{W}$  and at  $57^{\circ}\text{W}$ , but these anomalies may be parts of the north-south magnetic lineations, which appear to cross the Barracuda Ridge east of  $58^{\circ}\text{W}$ .

### Seismic-Reflection Data

The bathymetric map (Fig. 13) and the magnetic lineations map (Fig. 11) show a general east-west fault pattern in this area. The north-south seismic-reflection lines confirm this general pattern and reveal several smaller faults which in some cases permit estimations of timing of the tectonic events along these faults.

One of the seismic-reflection lines along  $54^{\circ}30'\text{W}$  (Fig. 17) is over the Demerara abyssal plain (north of  $14^{\circ}40'\text{N}$ ) and over the faulted and uplifted crustal blocks.

The sea floor of the northern area is flat except near  $16^{\circ}\text{N}$ , where the Barracuda Ridge, only a few tens of meters high, crosses the profile. South of the ridge, a sediment-filled trough, approximately 30 km wide and 1.8 km deep (assuming an average of 2 km/sec sediment velocity), lies along the entire southern margin of the ridge (Merrill et al, 1973) and is well developed even this far east.

The  $15^{\circ}20'\text{N}$  fault zone is represented by a narrow raised basement block, centered on  $15^{\circ}19'\text{N}$ , followed on the south by an 800-m drop of the basement (centered on  $15^{\circ}16'\text{N}$ ). Increasing displacement of the deeper reflectors along this fault, and along the fault at  $15^{\circ}04'\text{N}$ , suggests prolonged tectonic activity. The step on the sea floor above these faults indicates that this activity has been continuous to the present (seen better on original records).

Most of the prominent reflectors are traceable across the northern part of the Demerara abyssal plain from the Barracuda Ridge to about  $14^{\circ}38'\text{N}$ . The northward dip of the reflectors between the faults at  $15^{\circ}18'\text{N}$  and at  $14^{\circ}38'\text{N}$  is caused either by the concurrent displacement along the faults at  $15^{\circ}18'\text{N}$ ,  $15^{\circ}04'\text{N}$ , and  $14^{\circ}38'\text{N}$  with the deposition of the sediments, or it may be primary, and the result of the depositional environment north of the raised crustal block (south of  $14^{\circ}38'\text{N}$ ).

Several strong reflectors can be traced across most of the first uplifted block (south of  $14^{\circ}48'\text{N}$ ). These reflectors, and occasionally the sea floor as well, are offset by the larger faults, which again suggest tectonic activity that continued until the present. Many warps and small faults within the sedimentary strata, and small undulations of the sea floor over basement highs probably are related to differential compaction.

The sequence of sedimentary deposits overlying the basement starts with a transparent zone that mostly fills the basement depressions throughout the entire profile (Fig. 17). It has been suggested that the massively stratified sequence overlying the transparent zone represents late

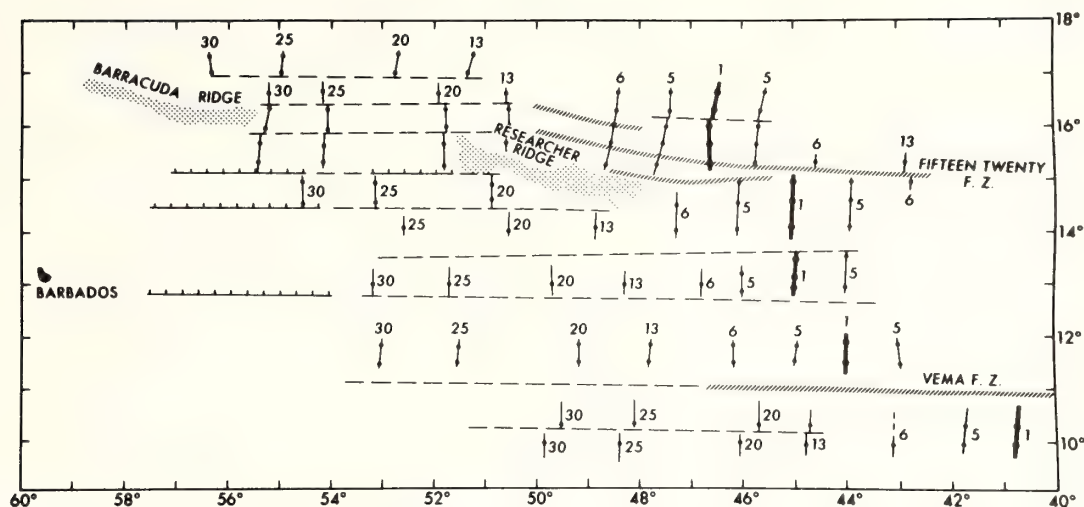


FIG. 11—Identification and offset pattern of magnetic-anomaly lineations east of Lesser Antilles arc. Anomaly numbers are after Pitman et al (1968). Anomaly no. 1 is over axis of Mid-Atlantic Ridge.

Tertiary, Quaternary turbidites (Damuth and Fairbridge, 1970; Embley et al, 1970). The block south of 12°54'N appears to be an exception, because here the transparent zone is overlain by a sedimentary unit approximately 1,000 m thick (intermediate turbidite unit) characterized by strong incoherent reflections and by three or four weak reflecting horizons, which locally fade into the incoherent zone. From 12°20'N southward this unit is overlain by strongly stratified sequence of late Tertiary-Quaternary turbidites.

Whereas normal, reverse, and thrust faults commonly can be recognized on seismic records run normal to the trends of these faults, strike-slip motion cannot be established on the basis of these records alone. The studies of Currey and Nason (1967) of the seaward extension of the San Andreas fault revealed that a zone of chaotic reflections, abruptly terminating coherent reflecting horizons, can be expected in a strike-slip fault zone. This zone also may involve complementary normal faulting. From these observations and the fact that some of the faults on Figure 17 lie at the

westward extension of magnetic-offset zones, the apparent normal faults centered on 15°15'N and 14°38'N, and the fault zones centered on 12°53'N and 11°05'N also may have had strike-slip displacements.

The importance of near-bottom currents in carrying and eroding the sediments is illustrated at 15°15'N (Fig. 17) where the trough left by the fault already is filled by transparent sediments, and at 11°40'N where there is a small erosion channel at the point where the dip of the sea floor changes from a southerly to a northerly direction.

Profile A (Figs. 13, 15) illustrates currently active faults south of the Barracuda Ridge. Their relative youth is indicated by the step-like displacements of the sea floor, and the increased displacement of the deeper reflectors also indicates activity along these faults in the geologic past. Most of the faults are associated with scarps or steep slopes of the basement, suggesting that the origin of the tectonic activity is within the oceanic crust. The northernmost fault at 15°39'N appears to be related to the relative uplift of the Barracuda Ridge, the troughs at 15°N and at 15°15'N are related to the east-west trending fault systems of this area.

**BARBADOS RIDGE COMPLEX**

**Bathymetry**

The Barbados Ridge complex is an outer sedimentary-island arc that consists of a system of the north-south and east-west-trending ridges, troughs, scarps, and topographic lineaments, whose respective development varies along the

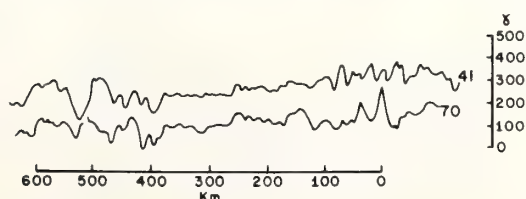


FIG. 12—Magnetic-anomaly profiles 41 and 70 showing correlation across Vema fracture zone.

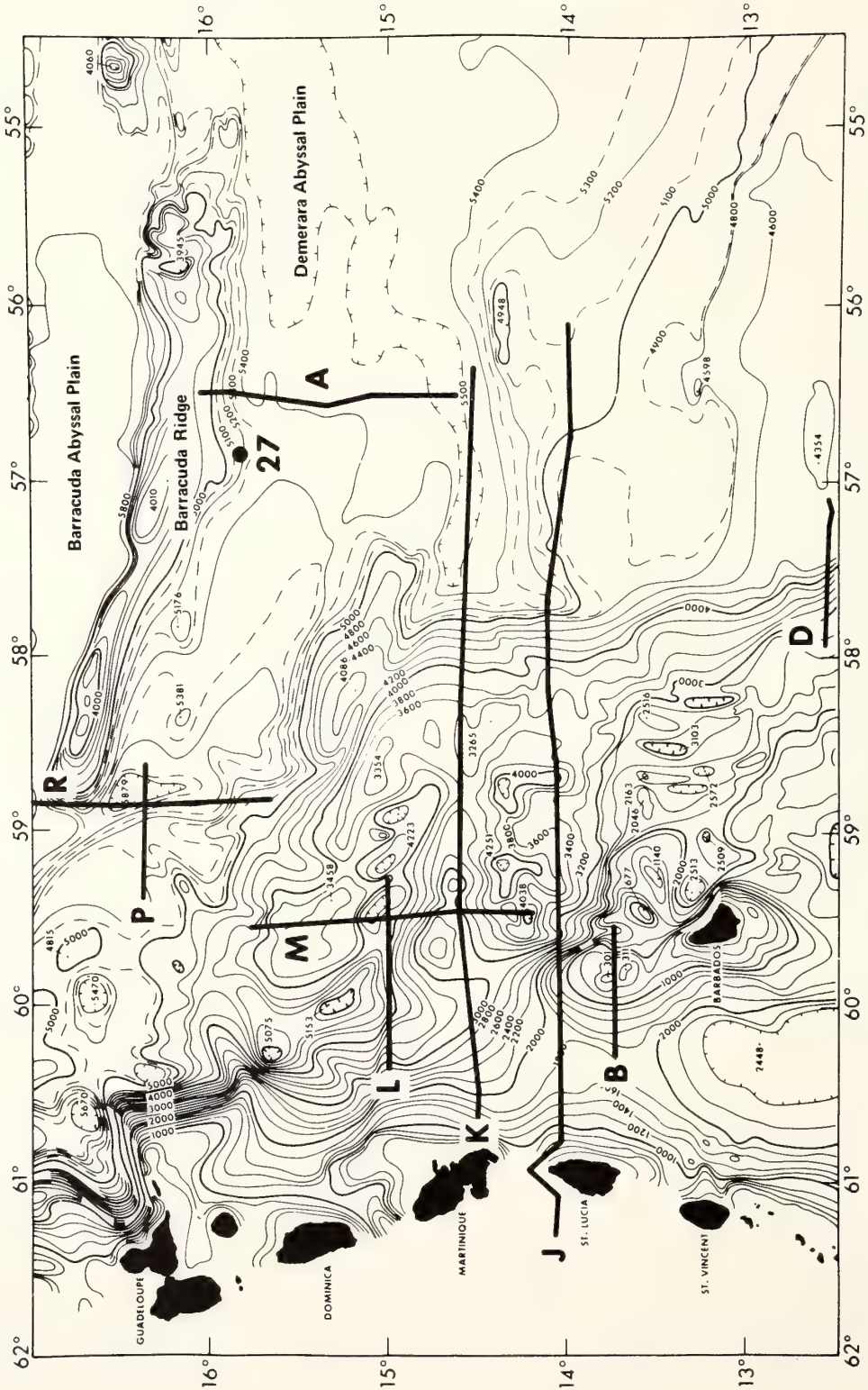


FIG. 13—Generalized bathymetric map of northern half of Barbados Ridge and adjacent Atlantic sea floor. Contour interval 200 m; 100 m below 5,000-m isobath.

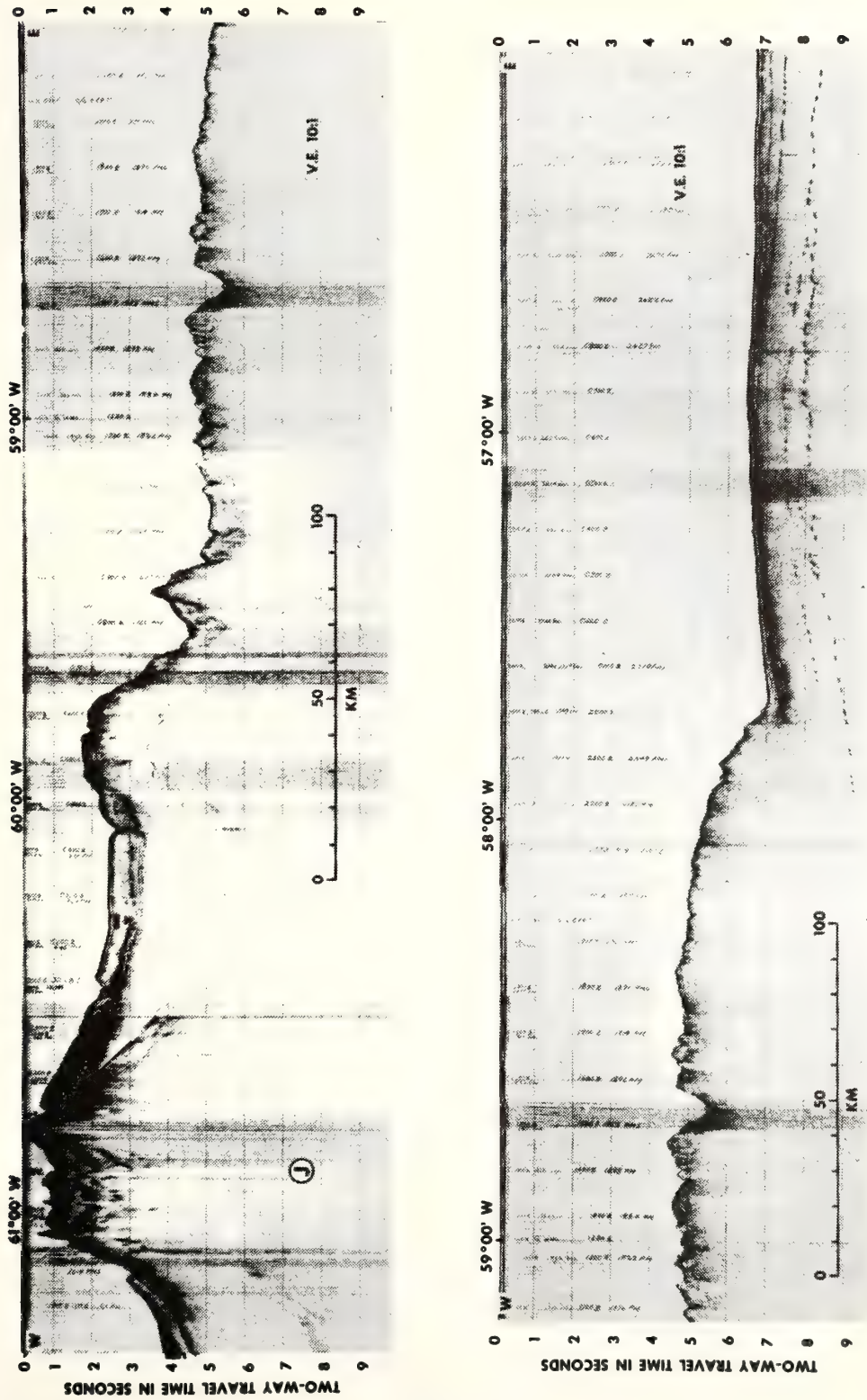


FIG. 14—Composite photograph of seismic section J (Fig. 13).

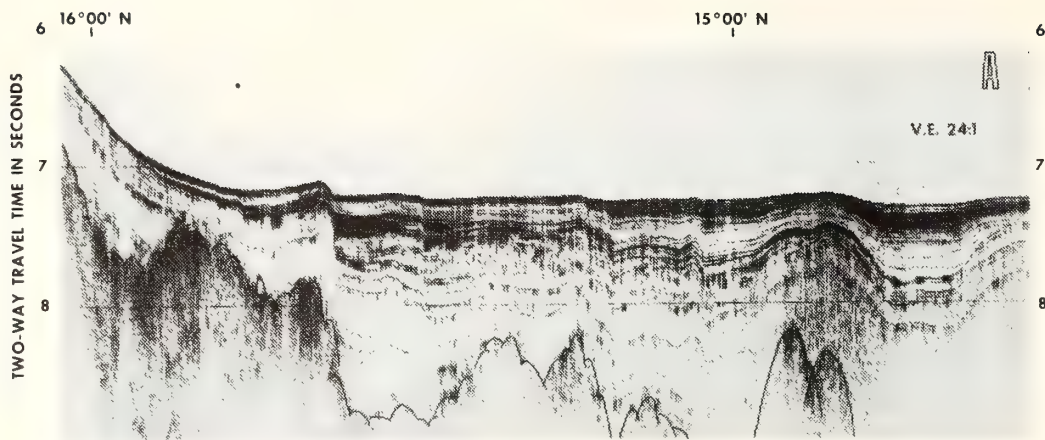


FIG. 15—Retouched photograph of north-south seismic-reflection line along  $56^{\circ}30'W$ , directly south of Barracuda Ridge.

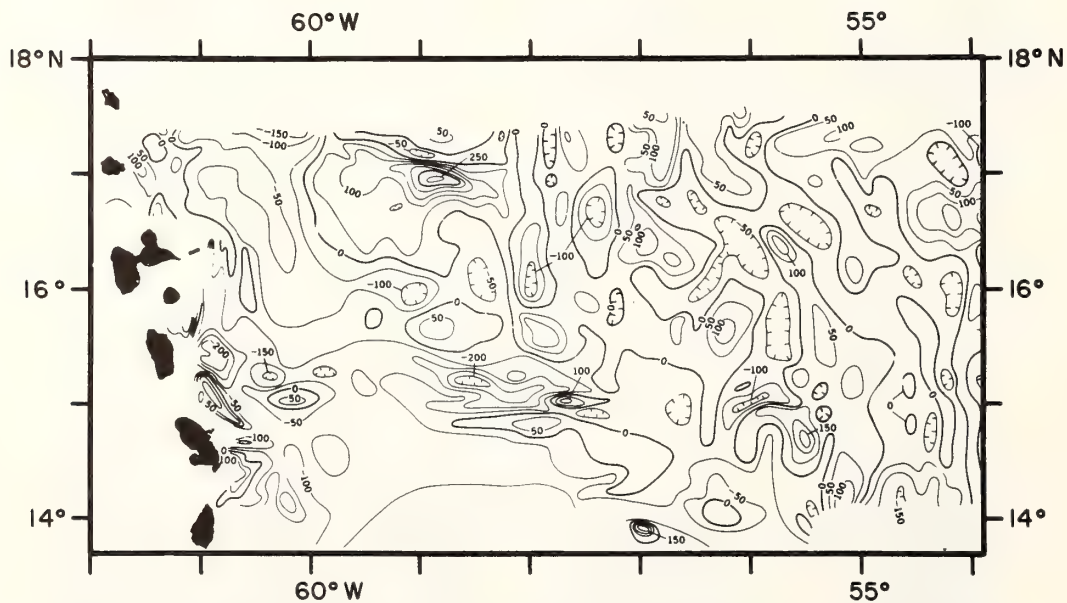


FIG. 16—Magnetic-anomaly map over northern half of Barbados Ridge and adjacent Atlantic sea floor.



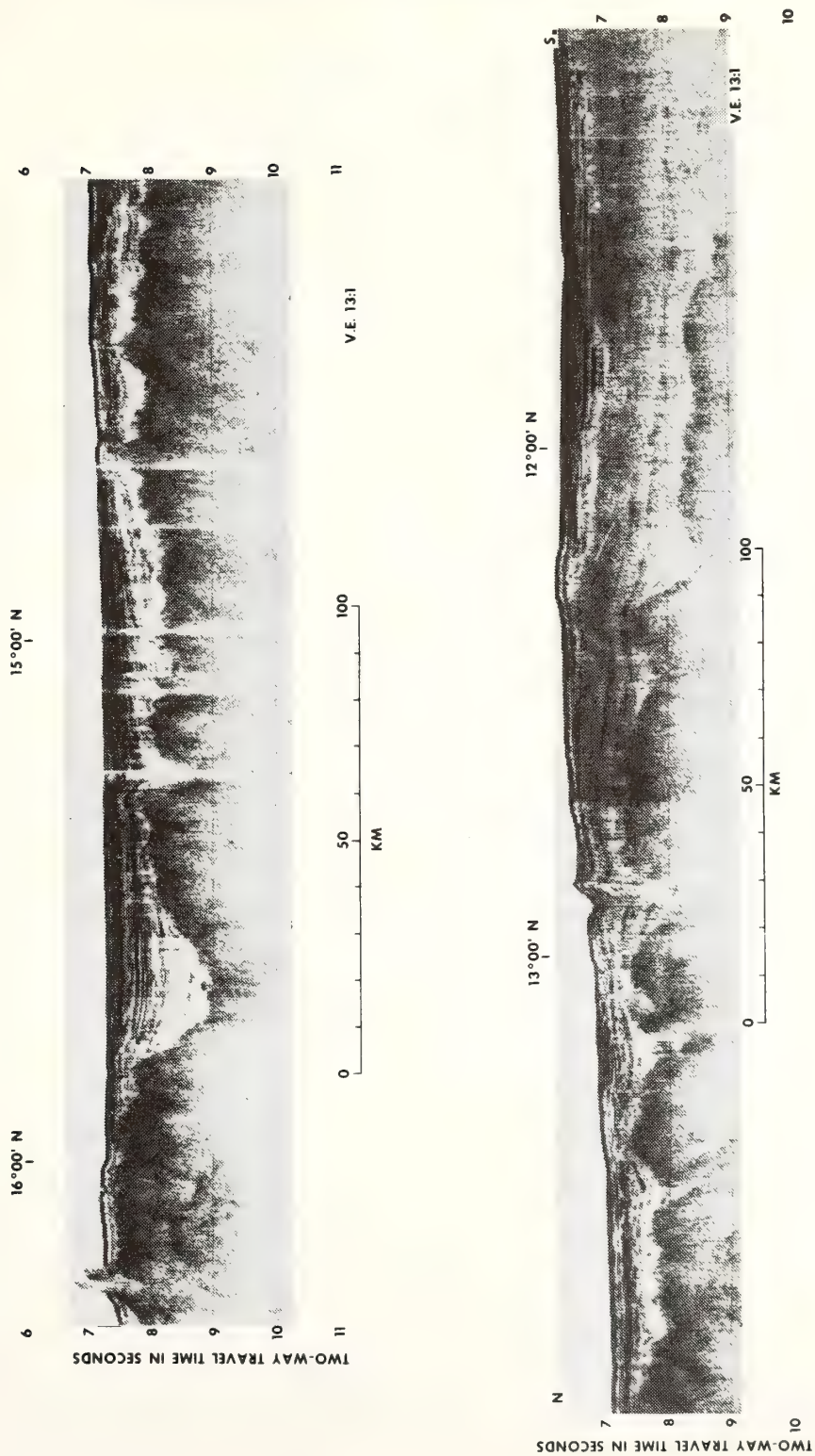


FIG. 17—North-south seismic-reflection profile along 54°30'W.

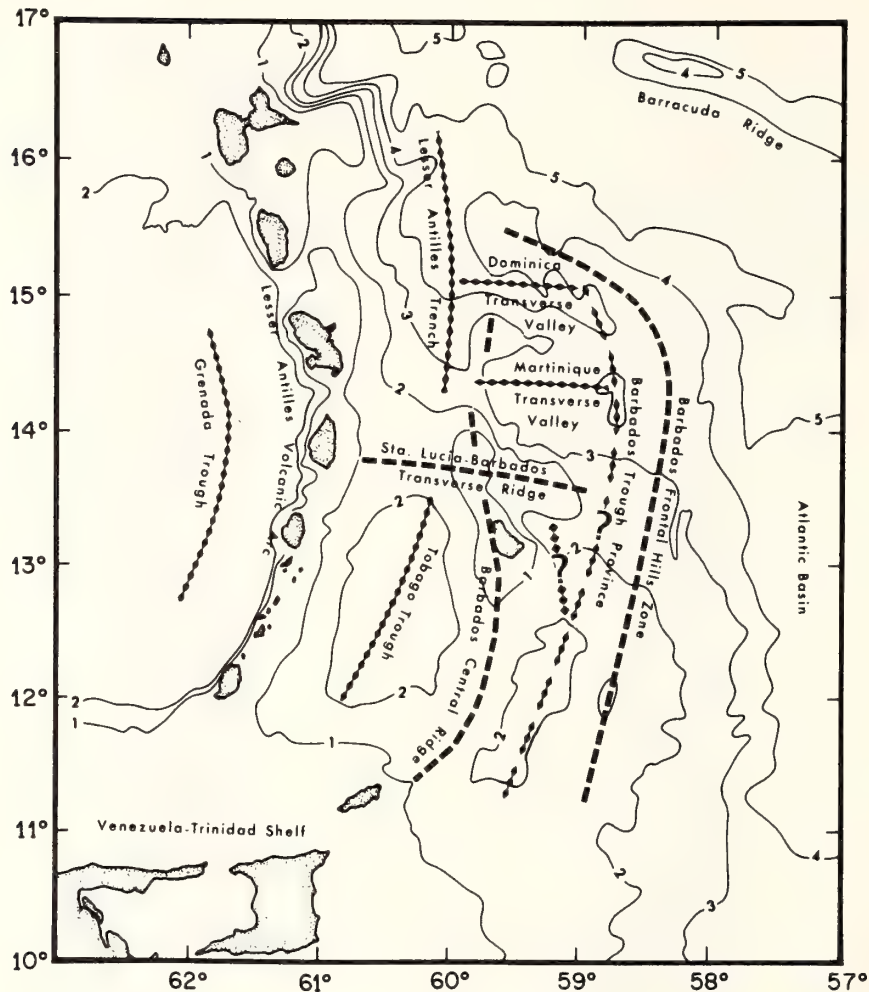


FIG. 18—Key physiographic elements of Lesser Antilles arc-Barbados Ridge complex. Contour interval 1 km.

arc. The north-south-trending topographic elements are part of the overall island-arc trends, the east-west elements are related to the fault systems of the adjacent Atlantic basin. These extend westward underneath the Barbados Ridge complex and have cut or modified the major north-south elements. The interaction of the north-south and east-west tectonic trends often produced locally complex structural and topographic patterns: compared to the trackline spacing, the wavelength of these features is too short and, therefore, these were not incorporated into the bathymetric presentation (Fig. 13).

Four major north-south-trending topographic elements may be distinguished within the Barba-

dos Ridge complex. These are: (1) the Tobago trough and Lesser Antilles Trench; (2) the Barbados Central Ridge province; (3) the Barbados Trough province; and (4) the Barbados Frontal Hills zone. The major east-west-trending topographic elements are: (1) the Dominica Transverse Valley system; (2) the Martinique Transverse Valley system; and (3) the Sta. Lucia-Barbados Transverse Ridge system (Fig. 18). The north-south topographic elements are prominent from the continental shelf of South America northward to about 13°N; there is a transition zone between 13°N and 14°N; and the east-west elements are more abundant north of 14°N. The 14°N parallel also cuts the Barbados Central

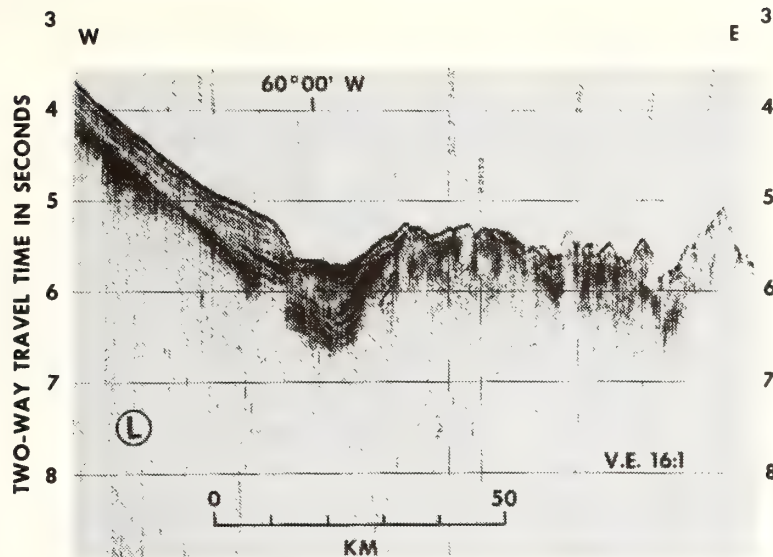


FIG. 19—Photograph of seismic section *L* (Fig. 13).

Ridge, and the average depth of the Barbados Ridge complex is more than 1,000 m greater north of here.

South of  $14^{\circ}\text{N}$ , the backbone of the Barbados Ridge complex is the Barbados Central Ridge, on which the island of Barbados is located. In addition to the change of strike at  $13^{\circ}\text{N}$ , the single Central Ridge also may have broken into a broader "ridge province," if one assumes that the isolated peaks north of Barbados are part of the Central Ridge. As an alternate interpretation, these peaks also could be related to the Sta. Lucia-Barbados Transverse Ridge system. The Barbados Central Ridge and the other elements of the Barbados Ridge complex are well developed south of  $13^{\circ}\text{N}$ .

North of  $14^{\circ}\text{N}$ , the topographic high between the Dominica and the Martinique Transverse Valley systems may represent the northernmost element of the Barbados Central Ridge province. The Lesser Antilles Trench separates it from the volcanic arc on the west, and a prominent, narrow depression at  $58^{\circ}45'\text{W}$  forms its eastern limit.

The Lesser Antilles Trench has the same overall width as the Tobago trough, but its northern half is "V" shaped with a graben 10 to 15 km wide in the center (Fig. 19).

It is difficult to trace the Barbados Trough province between  $13^{\circ}\text{N}$  and  $14^{\circ}\text{N}$  because, as stated before, there are several minor valleys and ridges there, occupying an area more than 100 km wide. North of  $14^{\circ}\text{N}$ , the valley at  $58^{\circ}45'\text{W}$  is a

feature that may be a structural equivalent or a northern extension of the Barbados Trough province. Its northern terminus is at  $15^{\circ}\text{N}$ , where it merges with the Dominica Transverse Valley system.

Among the major east-west-trending topographic elements the Dominica Transverse Valley system is the northernmost ( $15^{\circ}\text{N}$ ). Although there is a limited amount of data available, it appears that whereas the overall strike of the system is almost due east-west, it consists of four en-echelon, northwest-southeast-trending valleys, separated by narrow, sharp peaks. Its eastern terminus seems to be at  $58^{\circ}45'\text{W}$ . On the west it merges with the Lesser Antilles Trench, although the bench on the slope of the volcanic-arc platform also may be genetically related to it.

The Martinique Transverse Valley system is located between  $13^{\circ}55'\text{N}$  and  $14^{\circ}25'\text{N}$ . It is more than 50 km wide and has a definite east-west strike. In detail this valley system also is highly fragmented, but here by a combination of narrow troughs and ridges, striking both east-west and north-south.

The broad saddle between the Tobago trough and the Lesser Antilles Trench is the western third of the Sta. Lucia-Barbados Transverse Ridge system (Weeks et al, 1971; Bassinger and Keller, 1972). The east-west-trending axis of the system shifts southward to  $13^{\circ}35'\text{N}$  east of the Central Ridge, and the system becomes much narrower. It may extend from the Central Ridge

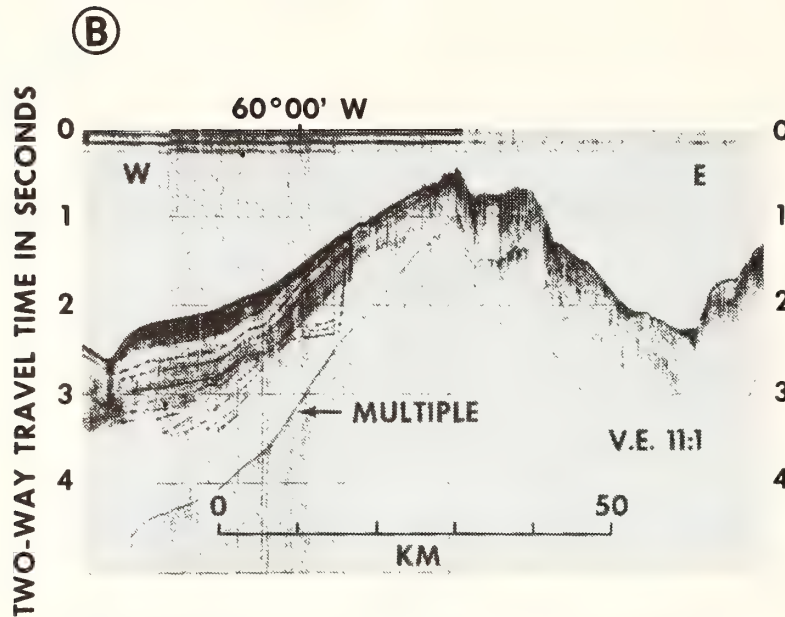


FIG. 20—Retouched photograph of western edge of the Barbados Central Ridge (sec. B, Fig. 13).

to the Frontal Hills zone in the form of irregular topographic highs. Data are inconclusive to decide whether the topographic highs between  $59^{\circ}\text{W}$  and  $59^{\circ}30'\text{W}$  are part of this Transverse Ridge system or part of a broader Central Ridge province.

North of the Barbados Frontal Hills zone, between about  $59^{\circ}\text{W}$  and the island platform of the volcanic arc, lies a generally hummocky topography that resembles in geologic and geophysical character the Frontal Hills zone. The area has a roughly triangular shape with the volcanic-arc platform, the Frontal Hills zone, and the topographic extension of the Puerto Rico Trench forming the sides of the triangle. The effect of both east-west and north-south faulting is indicated in the general bathymetric trends and in the basement configuration below the sediments (Schubert and Peter, 1973; Schubert, 1974).

#### Seismic-Reflection Data

Marine seismic-reflection data over several elements of the Barbados Ridge complex already have been discussed by Chase and Bunce (1969); Collette et al (1969); Bunce et al (1970); Westbrook (1973); and Peter et al (1974). Here only a few comments will be made about the NOAA 1971-1972 seismic-reflection data, as these illustrate the overall structural division of the Barba-

dos Ridge complex and the relative age of some of the tectonic events.

Line J (Fig. 14) is a continuous line from the Atlantic basin, across the Barbados Ridge complex, the volcanic arc, into the eastern margin of the Grenada trough. Because the east-west topographic elements are more significant north of  $14^{\circ}\text{N}$ , one can see from the topography (Fig. 13) that a 10-km north-south shift of the trackline would have highlighted different topographic elements. The line extends across the southern margin of the Lesser Antilles Trench and across the northern tip of the Barbados Central Ridge. On the west flank of the Central Ridge, subbottom reflectors of the Lesser Antilles Trench arch up and pinch out, or terminate at the sea floor over the Central Ridge. Only a thin layer of sediments covers the acoustic basement on the Central Ridge. This is shown well on line B (Fig. 20). Line J runs along the southern part of the Martinique Transverse Valley and, although good reflecting horizons are lacking, approximately  $\frac{1}{2}$  to 1 sec of penetration is indicated on the record. East of  $59^{\circ}\text{W}$ , the prominent valley on the record lies in the same structural province as the Barbados trough farther south; on the east lies the Frontal Hills zone. This zone is characterized by lack of reflectors and penetration along this line. The Atlantic basin on the east of this area (Fig. 13) is

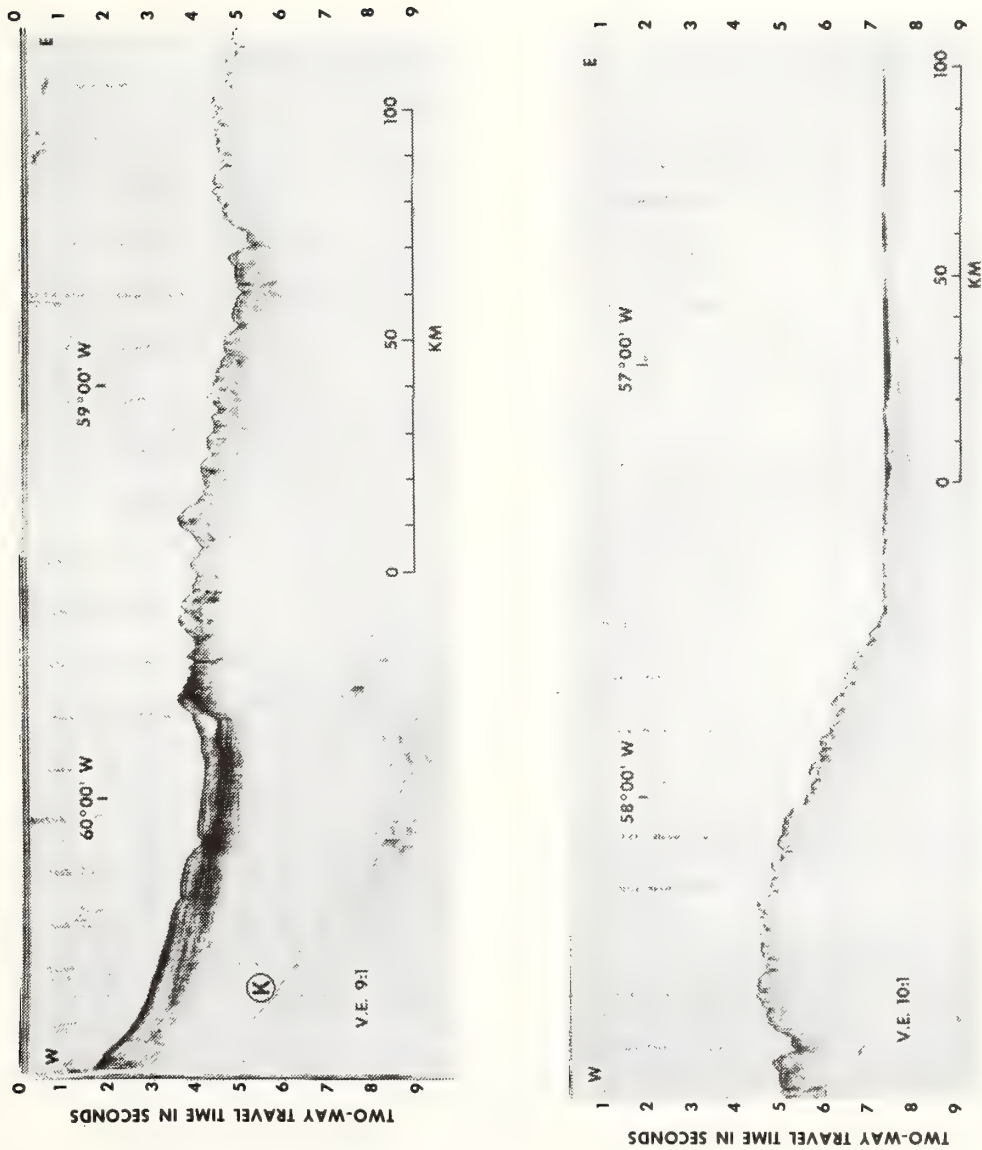
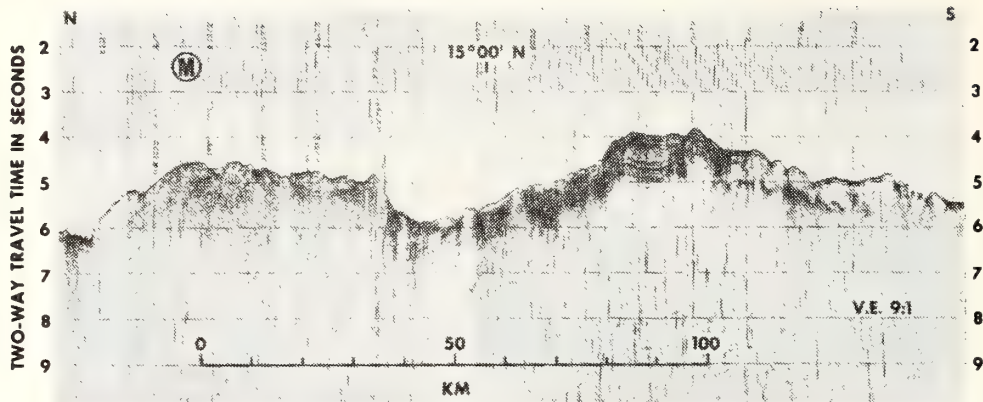


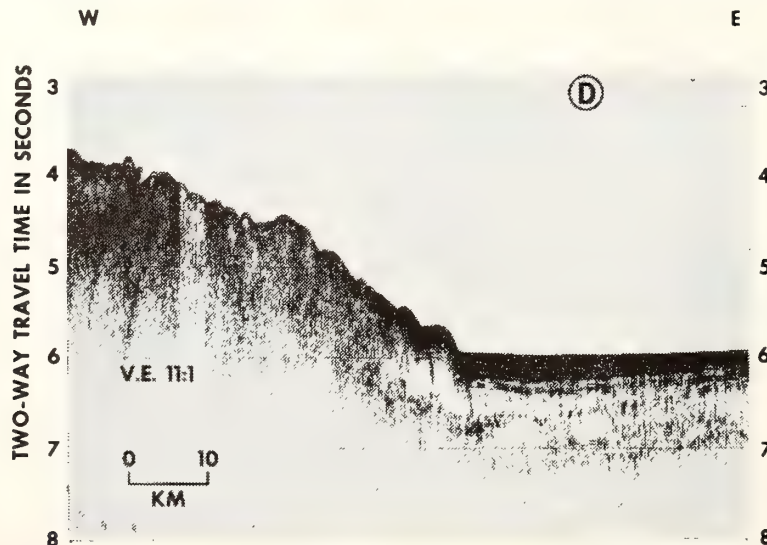
FIG. 21—Composite photograph of seismic section K (Fig. 13).

FIG. 22—Photograph of seismic section *M* (Fig. 13).

gently arched, and the sediments are dipping away from  $57^{\circ}\text{W}$ , both toward the Atlantic and toward the island arc. A good onlap sequence of sediments is present east of the arch at  $57^{\circ}\text{W}$  and there is an abrupt termination of a strong, shallow reflector under the toe of the Frontal Hills. It often is said that the lack of continuous reflectors and poor penetration under the toe of island arcs in general, and in this area in particular, is the result of very complex faulting (Chase and Bunce, 1969). Records will be presented here that show that when good reflectors are present, they can be detected even in cases of very intense faulting. The strong reflector that dips toward the Frontal Hills from the Atlantic basin does not show up on the Frontal Hills because it has not been deposited there. The termination point of that reflector

marks a former edge of the Atlantic basin and the toe of the Frontal Hills zone, which subsequently became covered by transparent sediments, extending the toe eastward.

Most of the reflectors of the Lesser Antilles Trench on line *K* (Fig. 21) are uplifted over that part of the Central Ridge that lies between the two transverse valleys. Despite intense faulting the reflectors are recognizable. Along line *M* (Fig. 22) this entire upper sequence is shown clearly, suggesting that the valleys and ridges are the product of tectonics rather than erosion. The Atlantic basin dips gently toward the west along line *K*, and it appears that the reflectors become less coherent toward the west. Some hints of weak reflectors suggest that this entire incoherent sequence of sediments is uplifted in the toe of the

FIG. 23—Photograph of seismic section *D* (Fig. 13).

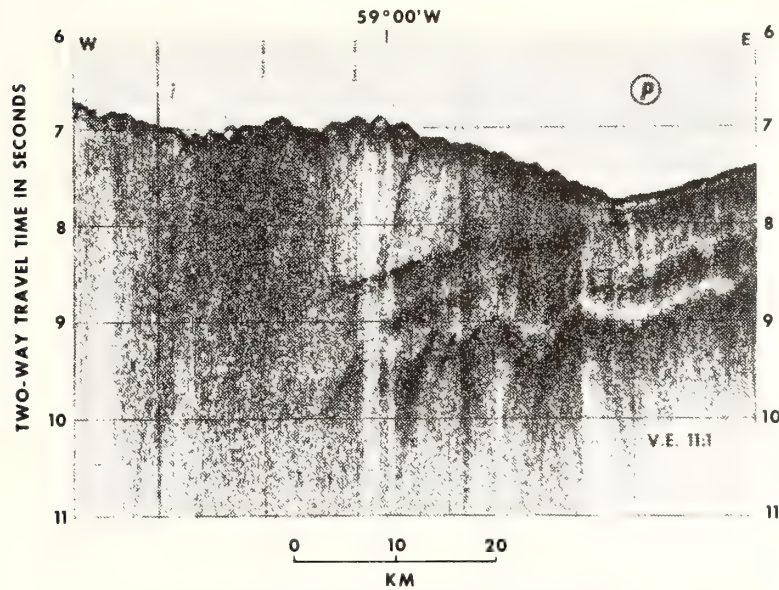


FIG. 24—Photograph of seismic section *P* (Fig. 13).

Frontal Hills. Farther south, line D (Fig. 23) shows the uplift of the Atlantic sediments quite clearly; the well-stratified beds are progressively thinner as they are uplifted successively along at least three faults to form the toe of the Frontal Hills. These faults are either high-angle reverse, or normal faults. Farther up on the slope the record shows an approximately 1-km thick zone of incoherent reflectors, which are similar to those shown in line K and on some other NOAA profiles (unpub.) that were run directly east of the Frontal Hills zone.

The uplifted sediments of the Atlantic basin on the Frontal Hills zone are in direct contrast with the gently westward-dipping (dip approx.  $2^\circ$ ) sediments of the Atlantic, north of the Barbados Ridge complex. On line P (Fig. 24) these sediments are overlain by a thick accumulation of an acoustically incoherent sediment pile and, as far as the instrumentation allowed them to be seen (3 sec penetration, 45 km from the edge of the overlying sediment pile), reflecting horizons within these sediments are undisturbed.

Line L (Fig. 19) illustrates the central graben and youthful tectonism of the Lesser Antilles Trench.

#### Gravity

Several aspects of the gravity anomalies of the Lesser Antilles island-arc system have been discussed by Talwani (1966), Bush and Bush (1969), and Bunce et al (1970). The NOAA and University of Durham investigations (Kearey, 1973; West-

brook, 1973, 1975; Peter, 1974; Peter and Westbrook, 1974a, b; Westbrook, 1974a, b; Kearey et al, 1975; Westbrook, 1975) allowed the mapping of the gravity field of this area in much greater detail than previously, and established the extension of certain structural trends from the Atlantic basin into the Barbados Ridge complex.

The most noticeable feature of the gravity field is the continuation of the negative free-air anomaly band of the Puerto Rico Trench, which turns away from the topographic axis as  $18^\circ\text{N}$ . As the anomaly band extends farther south, it reflects the east-west structural discontinuities similar to the topography. These effects manifest themselves as: (1) reduced amplitude of the gravity low ( $-192$  mgal) between  $19^\circ\text{N}$  and  $18^\circ\text{N}$  (from Schubert, 1974); (2) sharp increase of the amplitude at  $17^\circ20'\text{N}$  (from  $-220$  mgal to  $-276$  mgal, Schubert, 1974); (3) a 45-km sinistral offset of the axis of the low at  $16^\circ30'\text{N}$ , and another similar offset at  $15^\circ10'\text{N}$ ; (4) the interruption of the negative, north-south anomaly band by a positive, east-west-trending free-air anomaly band at  $13^\circ50'\text{N}$ ; and (5) the development of two approximately parallel negative free-air anomaly bands south of Barbados ( $13^\circ\text{N}$ ) with amplitudes about 100 mgal less than the amplitude of the single band on the north (Fig. 25).

The axis of the free-air anomaly minimum does not follow the Lesser Antilles Trench south of the Sta. Lucia-Barbados Transverse Ridge; the sinistral offset at  $15^\circ10'\text{N}$  places it east of the Barbados Central Ridge. South of Barbados, the axis of

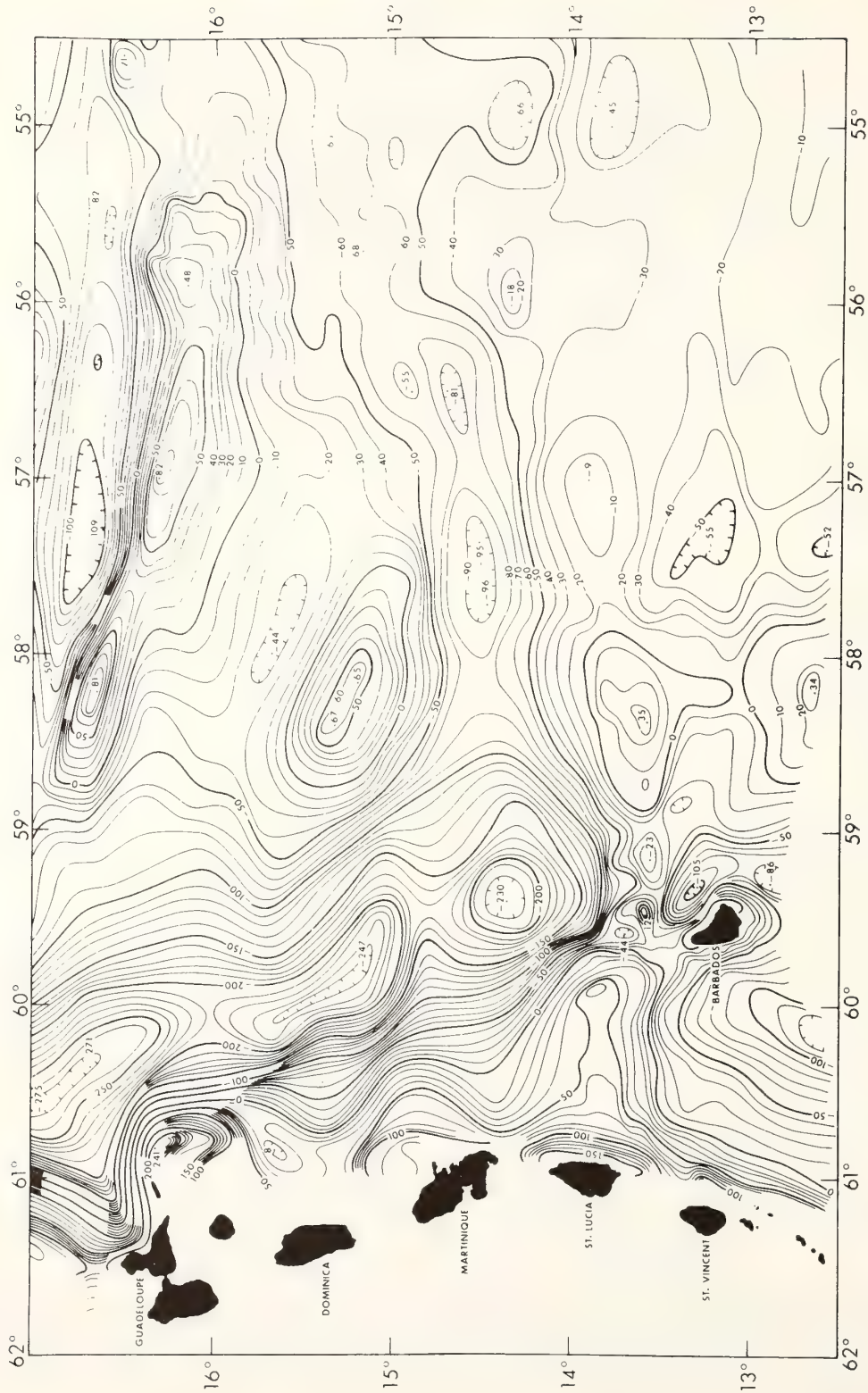


FIG. 25—Gravity free-air anomaly map over Barbados Ridge complex and adjacent Atlantic sea floor.



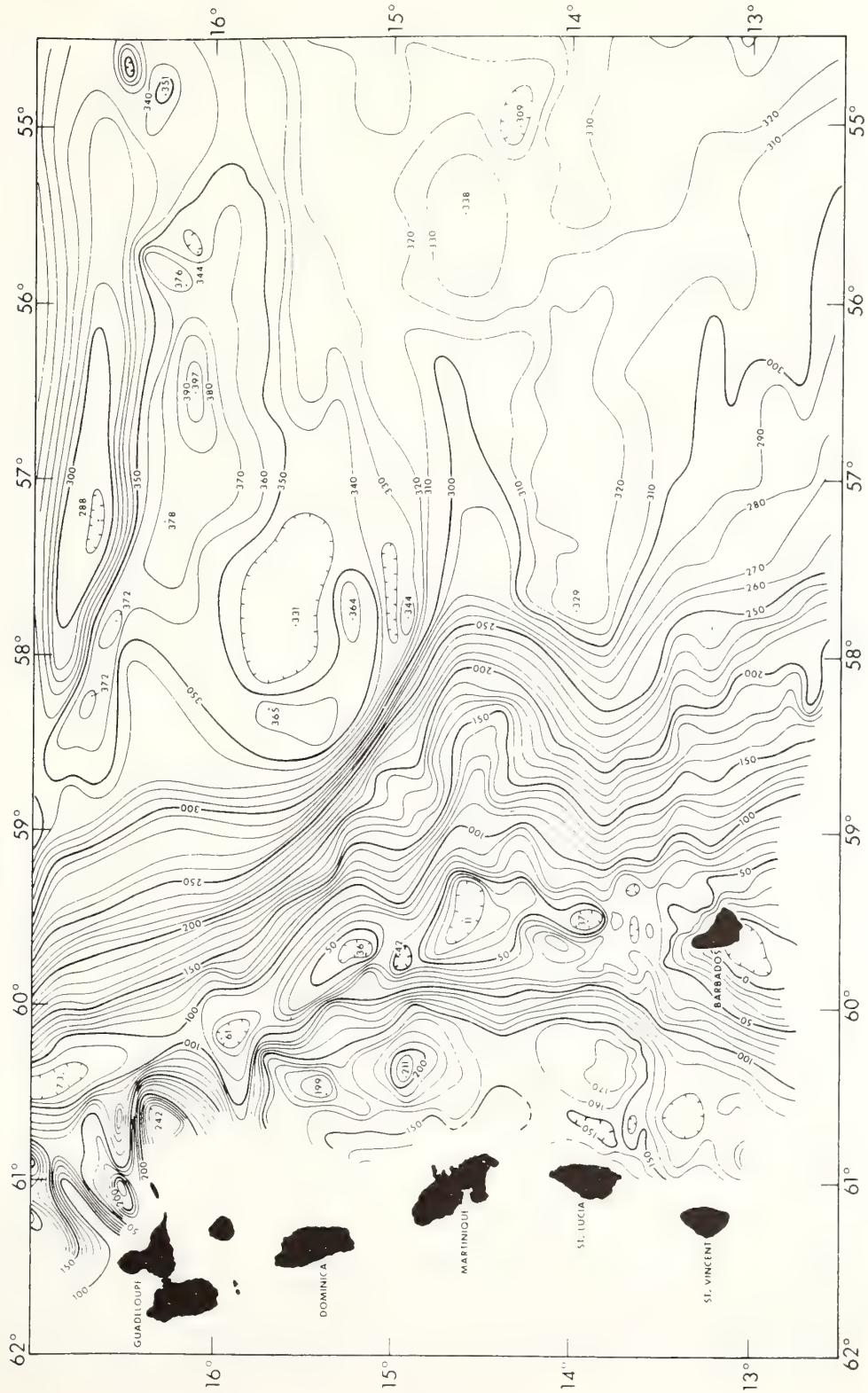


FIG. 26—Gravity Bouguer anomaly map over Barbados Ridge complex and adjacent Atlantic sea floor.

one of the negative anomaly bands is over the eastern edge of the Tobago trough, the axis of the other is over the Barbados trough. These two bands are parallel near Barbados, but separate at the latitude of Tobago ( $11^{\circ}15'N$ ), where the western band veers west-southwest onto the Paria shelf, and the eastern band continues south-southwest until about  $10^{\circ}30'N$ , where it sharply swings toward Trinidad.

The free-air anomaly contour lines trend essentially east-west over the Atlantic basin, east of the Barbados Ridge complex. There are two prominent east-west-trending anomaly bands; one is a positive band at about  $13^{\circ}50'N$ , the other is a negative band north of it. These two seem to extend from the volcanic platform to about  $56^{\circ}30'W$  in the Atlantic basin.

The Bouguer anomaly map of the area (Fig. 26) also is dominated by essentially north-south and east-west trends: the north-south trend follows the Barbados Ridge complex, and the east-west trend characterizes the Atlantic basin. When the regional gradient is removed from these data, some of the east-west-trending Bouguer anomalies also cross the complex, and extend to the island platform of the Lesser Antilles arc.

The north-south-trending Bouguer anomaly features include: (1) a gradient change under the Frontal Hills zone due to the dipping mantle; (2) a band of gravity lows over the greatest sediment accumulation, which on the south is over the Barbados Central Ridge (presumably this band marks the location of a former trench); and (3) a series of highs (170-240 mgal) that extend from the island platform east-southeast of Guadeloupe to the Sta. Lucia-Barbados Transverse Ridge over the lower slope of the island platform. Many of these highs are even larger than those reported over the volcanic islands themselves, which only reach 120-190 mgal (Kearey et al, 1975).

Bouguer anomalies also were used to study further the east-west structures of the Atlantic basin. Two-dimensional modeling of the crustal structure was performed using the Bouguer anomalies, NOAA seismic-reflection data (Peter and Westbrook, 1974b), and University of Durham and earlier seismic-refraction data (Ewing et al, 1957; Westbrook et al, 1973). An interesting result that emerged was the fact that when Bouguer anomalies were computed down to the acoustic basement with a realistic sediment density ( $2.0 \text{ g cm}^{-3}$ ), then many of the large anomalies were eliminated (Fig. 27). These results suggest that in this area the buried topography of the basement is responsible largely for the Bouguer anomalies, with only very minor contribution from changes of mantle elevation.

## DISCUSSION

One of the main objectives of this paper is to present a large body of new data over a previously little studied region of the southwestern North Atlantic, and the Barbados Ridge complex. Papers by Westbrook (1973, 1974a, 1975) discussed in detail how some of these data may be fitted into an overall plate-tectonics scheme. We intend only to highlight here the relation of these new data to (1) the scientific objectives outlined earlier; (2) some of the hypotheses advanced for the evolution of this area; and (3) some of the corollary assumptions of the plate-tectonics hypothesis.

At the time this project was initiated in 1971, the sea-floor-spreading history was not known east of the Lesser Antilles arc. Although the magnetic-anomaly lineation pattern presented (Fig. 11) is admittedly debatable in detail, the magnetic lineations and the east-west topographic profiles clearly establish that there is a well-developed Mid-Atlantic Ridge east of the Lesser Antilles, and that this segment of the ridge has evolved since the Late Cretaceous in the same way as in the rest of the North Atlantic. Two tracklines indicate similar development of the Mid-Atlantic Ridge even south of the Vema fracture zone. From geometric considerations of the original fit of the continents, we propose that the possible southern limit of this type of ridge development is the Doldrums fracture zone (approx.  $8^{\circ}N$ ). We found neither topographic nor magnetic evidence for major breaks in the continuity of the Mid-Atlantic Ridge, which would have supported a major north-south extension of this area during the Cenozoic (Funnell and Smith, 1968; Ball and Harrison, 1969, 1970). As the Late Cretaceous magnetic lineations also are trending north-south, there is no indication for the existence of a ridge-ridge triple junction at that time, which might have provided some indirect support for the interpretation and identification of the east-west-trending anomalies in the Colombia basin as being Late Cretaceous (Christofferson, 1973), if this part of the Caribbean were formed in an Atlantic spreading regime.

As part of the topographic and structural studies of the Mid-Atlantic Ridge, several major (transform) and minor faults were located. Data from the northern half of the study area indicate that the northwest-southeast trend of the faults near the ridge axis changes to east-west between magnetic anomalies 6 and 13. The eastern half of the Barracuda Ridge follows an east-west fault pattern, and there is no indication in the bathymetric data that it extends farther east and con-

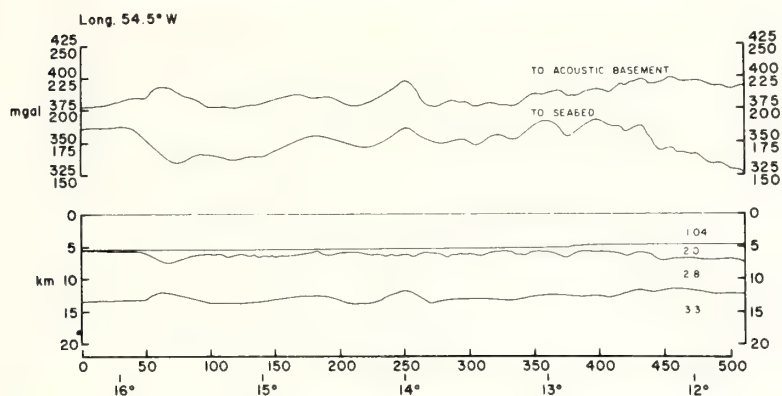


FIG. 27—Bouguer anomaly profiles and crustal structure along  $54^{\circ}30'W$ . Upper half: Bouguer anomaly profile to seabed, lower numbers on scale; Bouguer anomaly profile to acoustic basement, higher numbers on scale. Lower half: crustal section from sea surface to mantle. Density of 1.04 g/cc = sea water, 2.0 g/cc = sediment, 2.8 g/cc = average crust, and 3.3 g/cc = mantle. Top of 2.8-g/cc layer was taken from our seismic-reflection record, top of 3.3-g/cc layer was computed to fit "acoustic basement Bouguer profile," with nearby seismic-refraction data extrapolated as guide. Horizontal and vertical scales are in kilometers; for map location, latitude crossings also are shown.

nects with the Fifteen-Twenty or Researcher fracture zones. Clearly additional bathymetric and magnetic data are needed to define better the topography and structure of the flank of the Mid-Atlantic Ridge where changes in the trend of these faults take place, and where major ridges, like the Barracuda and Researcher, seemingly terminate.

One of the interesting results of our study was the discovery of relatively recent tectonic activity along many major and minor faults west of the exposed flank of the Mid-Atlantic Ridge. This activity was especially obvious in the bathymetric and seismic-reflection records from the Demarara abyssal plain directly south of the Barracuda Ridge (Fig. 15), and along the east-west faults on the 300-km-wide, uplifted crustal block adjacent to the Barbados Ridge complex. Our detailed surveys and the seismic records suggest that faulting and tectonic activity within an oceanic crustal plate may be common. The lack of any clear pattern of recorded earthquakes from these areas may indicate that (1) there are no very recent movements along these faults; (2) the displacements occur through creep; or (3) the magnitude of the earthquakes is so small that they cannot be recorded at far removed measuring stations.

Because of the east-west-trending offset zones of the magnetic lineations and the fact that the faults on the seismic records often coincide, one also may conclude that the offsets of magnetic-anomaly bands may not be due entirely to trans-

form faulting, or that the so-called "dead-traces" of transform faults remain zones of weakness where subsequent tectonic adjustments occur.

Relatively recent motions along these faults also may support one of the contentions of Ball and Harrison (1969, 1970) that most of the faults cutting the Mid-Atlantic Ridge in the equatorial region are very slow-moving transcurrent faults. They argued that if the transcurrent motion is slow compared to the combined spreading motion between the offset parts of the ridge crest, then the earthquake first-motion studies will show the "transform" movement but the transcurrent part may not be detected.

Bathymetric and seismic-reflection data show that the Barracuda Ridge becomes a subbottom feature west of  $58^{\circ}50'W$ , and extends westward along the same trend to the island platform of the Lesser Antilles arc (Schubert and Peter, 1973; Schubert, 1974). However, it is only one of the many east-west structural elements in this area, and does not appear to have had a controlling influence by itself on the transition, of the south-eastward extension of the Puerto Rico Trench.

As suggested by Peter et al (1974), the Puerto Rico Trench proper terminates at about  $18^{\circ}N$ ,  $60^{\circ}W$ , where the zones of the gravity minima and the shallow earthquakes separate from the topographic trough. If a definition of a trench as a structural feature accompanied by the zones of the gravity minima and shallow earthquakes is accepted, then the topographic trough extending

southeastward from the Puerto Rico Trench is not part of this trench. We believe that in this transition zone there is a buried trench, marked by the axis of the gravity minima and the co-located shallow earthquake zone, which connects with the Puerto Rico Trench on the north, and the Lesser Antilles Trench on the south.

The high acoustic reflectivity of the sea floor and the many incoherent subbottom reflectors make the structural analysis of this area very difficult. However, the roughly east-west bathymetric trends, and the abrupt changes in the amplitude of the gravity minima most likely reflect the westward extension of the fault systems that characterize the Atlantic basin east of the Lesser Antilles arc and the Barbados Ridge complex (Schubert, 1974). Some of these faults appear to have caused the offset of the axis of the buried trench in a left-lateral sense, and others probably are partly blocking it. Basically, however, it is not these faults, but the large amounts of sediments that have collected in the trenches and fault depressions east of the Lesser Antilles island arc that are responsible for the termination of the topographic expression of the Puerto Rico Trench.

The hummocky topography in the transition zone (between the Puerto Rico Trench and the Barbados Ridge complex) is most likely slump and current-derived sediment that has been trapped between the east-west faults. The sediments overlie the gently westward-dipping Atlantic sea floor (line P, Fig. 24), causing the topographic low that extends southeast from the Puerto Rico Trench. As an interpretation alternative to that proposed by plate tectonics, it is possible that the upper sedimentary horizon (strong upper reflector on line P) of the Atlantic sea floor is an unconformity, rather than a thrust surface. According to the subduction hypothesis the overlying sediment pile represents scrapings of sediments from the Atlantic sea floor. If such a process is possible, then in case of underthrusting not only the overlying sediment pile should be disturbed, but at least the upper, unconsolidated parts of the Atlantic sea-floor sediments as well. It is unlikely that the approximately 1-km-thick, mostly un lithified sediments covering the basement rocks of the Atlantic would underthrust a 2 to 3-km thick sediment pile to about 40 km, without undergoing any noticeable internal deformation.

The increasing width and height of the Barbados Ridge complex toward the south generally are attributed to the availability of more sediments closer to the South American source, and to the subsequent subduction of more sediments on the south (Chase and Bunce, 1969; Westbrook, 1973). Our north-south seismic-reflection profiles east of the Barbados Ridge complex show that the thickness of sediments over the basement

is essentially uniform between 13°N and 14°30'N; at about 15°30'N it increases rapidly toward the Barracuda Ridge, and at 12°20'N it increases substantially southward. West of the thickest sediments on the north, the Barbados Ridge complex terminates, and there are no changes in the Barbados Ridge complex south of 12°20'N either. These observations seem to indicate that there is no simple relation between the present sediment thickness of the Atlantic basin and the topography of the Barbados Ridge complex, and that other controlling factors should be considered. For this alternative we have suggested that the east-west faults of the Atlantic basin have extended across the trough now occupied by the Barbados Ridge complex, and that these have formed dams against the northward-advancing sediments within the trough (Peter, 1974; Peter and Westbrook, 1974a, b; Westbrook, 1974a, b, 1975). The influence of these fault zones also is manifested by the abrupt changes in the elevation of the Barbados Ridge complex, as they provided a sufficient discontinuity within the crust that uplifts of the sediment pile have occurred at different times and in different degrees between the various segments of these faults. The seismic records are especially clear in indicating a relatively recent (Pleistocene-Holocene) uplift of the Barbados Ridge complex north of 14°N (Fig. 19), but the uplift on the south has occurred earlier (Pliocene-Pleistocene?; Peter et al, 1974; Westbrook, 1975). In this context of decreasing age of the elements of the Barbados Ridge complex toward the north, the triangular-shaped hummocky region on the north—from its geophysical characteristics—is really the youngest member of this complex, that has not been subjected to significant uplift. If the major faults do define the boundaries of uplift, then it is reasonable to assume that the area between the Barracuda Ridge and the present edge of the complex (approximately 16°N) will be uplifted next.

The data presented here for the area of the Barbados Ridge complex show vertical uplift at the toe of the Frontal Hills zone (Fig. 2). Further, east-west fault zones, revealed by bathymetric, seismic, and gravity data, extend across the Barbados Ridge complex, the axis of the gravity minima, and the shallow-earthquake zone to the volcanic arc platform. At the largest of these fault zones, near 14°N, major changes occur both within the structure of the Barbados Ridge complex and the volcanic arc. These changes include: (1) the Barbados Ridge complex becomes 1,000 m deeper on the north; (2) the free-air gravity anomalies change character; (3) the positive Bouguer anomalies extending southward from Desirade over the lower slope of the island platform terminate; (4) the chemistry of the volcanic

rocks of the Lesser Antilles arc shows marked differences on the two sides of this fault (Stipp and Nagle, 1974; Wills, 1975); and (5) the trend of the volcanic arc changes.

These observations and changes may be explained by some anomaly in the subduction process (Westbrook, 1973, 1974a, b, 1975), and some of them may be only coincidences. In all certainty, however, these data are sufficient to question some of the current concepts of the subduction process as they are applied to this area, and suggest the need for serious, further investigations.

#### CONCLUSIONS

1. The Mid-Atlantic Ridge in the area east of the Lesser Antilles arc developed from about the Late Cretaceous to the Holocene much as in the rest of the North Atlantic. Thus, the Barracuda Ridge and fracture zone is not a major discontinuity between oceanic crusts of different spreading history.

2. Relatively recent tectonic activity along the western extension of some transform faults suggests that these "dead traces" actually may provide avenues for the release of tectonic energy in the oceanic plate.

3. Several east-west faults extend from the Atlantic basin to the island platform of the volcanic arc. These have cut the former trench east of the arc, have dammed the northward advance of sediments in the trough, and probably have caused the segmented differential uplift of the Barbados Ridge complex. Bathymetric and seismic-reflection records indicate that the area south of 14°N was uplifted before the area on the north; the area north of 16°N has geophysical characteristics similar to the Barbados Ridge complex and may be thought of as the youngest member of the complex that has not received substantial uplift.

4. The Puerto Rico Trench terminates at approximately 18°N, 60°W, where, because of sediment fill and the influence of east-west faults, the topographic trough veers sharply eastward of the shallow earthquake zone and the axis of the gravity minima. These, however, most likely mark the now buried part of the trench that connects southward with the Lesser Antilles Trench.

5. Because the east-west faults of the Atlantic basin cross the axis of the gravity minima and the shallow earthquake zone, and seemingly even influence the structure of the volcanic arc and the chemical composition of its rocks, a simple subduction model probably is not applicable for this area.

#### REFERENCES CITED

Ball, M. M., and C. G. A. Harrison, 1969, Origin of the Gulf and Caribbean and implications regarding

ocean ridge extension, migration, and shear: *Gulf Coast Assoc. Geol. Soc. Trans.*, v. 19, p. 287-294.

———, 1970, Crustal plates in the central Atlantic: *Science*, v. 167, p. 1128-1129.

Bassinger, B. G., and G. H. Keller, 1972, Marine geophysical observations across the Barbados Ridge-St. Lucia cross warp (abs.): 6th Caribbean Geol. Conf., Margarita, Venezuela, Trans., p. 379-380.

Birch, F. S., 1970, The Barracuda fault zone in the western North Atlantic: geological and geophysical studies: *Deep-Sea Research*, v. 17, p. 847-859.

Bullard, E. C., J. E. Everett, and A. G. Smith, 1965, The fit of the continents around the Atlantic: *Royal Soc. London Philos. Trans.*, ser. A, v. 258, p. 41-51.

Bunce, E. T., J. D. Phillips, R. L. Chase, and C. O. Bowin, 1970, The Lesser Antilles arc and the eastern margin of the Caribbean Sea, *in* The sea, v. 4: New York, Wiley-Intersci., p. 359-385.

Bush, S. A., and P. A. Bush, 1969, Isostatic gravity map of the eastern Caribbean region: *Gulf Coast Assoc. Geol. Soc. Trans.*, v. 19, p. 281-285.

Chase, R. L., and E. T. Bunce, 1969, Underthrusting of the eastern margin of the Antilles by the floor of the western North Atlantic Ocean, and origin of the Barbados Ridge: *Jour. Geophys. Research*, v. 74, p. 1413-1420.

Christofferson, E., 1973, Linear magnetic anomalies in the Colombia basin, central Caribbean Sea: *Geol. Soc. America Bull.*, v. 84, p. 3217-3230.

Collette, B. J., and K. W. Rutten, 1972, Crest and fracture zone geometry of the Mid-Atlantic Ridge between 10° and 16°N: *Nature, Phys. Sci.*, v. 237, p. 131-134.

———, H. Schouten, and K. Rutten, 1973, Fracture zones and flow trajectories in the southern North Atlantic (abs.): *Eos (Am. Geophys. Union Trans.)*, v. 54, p. 325.

———, J. I. Ewing, R. A. Lagaay, and M. Truchan, 1969, Sediment distribution in the oceans: the Atlantic between 10° and 19°N: *Marine Geology*, v. 7, p. 279-345.

———, H. Schouten, K. Rutten, and A. P. Slootweg, 1974, Structure of the Mid-Atlantic Ridge province between 12° and 18°N: *Marine Geophys. Researches*, v. 2, p. 143-179.

Curry, J. R., and R. D. Nason, 1967, San Andreas fault north of Point Arena, California: *Geol. Soc. America Bull.*, v. 78, p. 413-418.

Damuth, J. E., and R. W. Fairbridge, 1970, Equatorial Atlantic deep-sea sands and ice-age aridity in tropical South America: *Geol. Soc. America Bull.*, v. 81, p. 189-206.

Dietz, R. S., and J. C. Holden, 1970, Reconstruction of Pangea: Breakup and dispersion of continents, Permian to present: *Jour. Geophys. Research*, v. 75, p. 4939-4956.

Dorman, L. M., B. G. Bassinger, E. Bernard, et al, 1973, Caribbean Atlantic geotraverse, NOAA-IDOE 1971, Rept. 3, Gravity: NOAA Tech. Rept. ERL 277-AOML 11.

Embley, R. W., J. I. Ewing, and M. Ewing, 1970, The Vidal deep-sea channel and its relationship to the Demerara and Barracuda abyssal plains: *Deep-Sea Research*, v. 17, p. 539-552.

- Ewing, J. I., C. B. Officer, H. R. Johnson, and R. D. Edwards, 1957, Geophysical investigations in the eastern Caribbean: Trinidad shelf, Tobago trough, Barbados Ridge, Atlantic Ocean: *Geol. Soc. America Bull.*, v. 68, p. 897-912.
- Ewing, M., G. Carpenter, C. Windisch, and J. Ewing, 1973, Sediment distribution in the oceans: the Atlantic: *Geol. Soc. America Bull.*, v. 84, p. 71-88.
- Freeland, G. L., and R. S. Dietz, 1972, Plate tectonic evolution of the Caribbean-Gulf of Mexico region: 6th Caribbean Geol. Conf., Margarita, Venezuela, *Trans.*, p. 259-264.
- Funnell, B. M., and A. G. Smith, 1968, Opening of the Atlantic Ocean: *Nature*, v. 219, p. 1328-1333.
- Heezen, B. C., and M. Tharp, 1961, The physiographic diagram of the South Atlantic, the Caribbean, and the Scotia Sea, and the eastern margin of the South Pacific Ocean: *Geol. Soc. America*.
- Isacks, B., J. Oliver, and L. R. Sykes, 1968, Seismology and the new global tectonics: *Jour. Geophys. Research*, v. 73, p. 5855-5900.
- Kearey, P., 1973, Crustal structure of the eastern Caribbean in the region of the Lesser Antilles and Aves Ridge: PhD thesis, Univ. Durham, 182 p.
- G. Peter, and G. K. Westbrook, 1975, Geophysical maps of the eastern Caribbean: *Geol. Soc. London Jour.*, v. 131, p. 311-321.
- Lattimore, R. K., P. A. Rona, and O. E. DeWald, 1974, Magnetic anomaly sequence in the central North Atlantic: *Jour. Geophys. Research*, v. 79, p. 1207-1209.
- Le Pichon, X., 1968, Sea floor spreading and continental drift: *Jour. Geophys. Research*, v. 73, p. 3661-3697.
- Merrill, G., G. Peter, and W. Sproll, 1973, Seismic reconnaissance east of the Lesser Antilles arc (abs.): *Eos (Am. Geophys. Union Trans.)*, v. 54, p. 326.
- Meyerhoff, A. A., and H. A. Meyerhoff, 1972, Continental drift, IV: the Caribbean "plate": *Jour. Geology*, v. 80, p. 34-60.
- Morgan, J. W., 1968, Rises, trenches, great faults, and crustal blocks: *Jour. Geophys. Research*, v. 73, p. 1959-1982.
- Paitson, L., C. H. Savit, D. M. Blue, and W. A. Knox, 1964, Reflection survey at Barracuda fault: *Geophysics*, v. 29, p. 941-950.
- Peter, G., 1974, Tectonic evolution of the eastern margin of the Caribbean region (abs.): *Geol. Soc. America Abs. with Programs*, v. 6, p. 910.
- and G. K. Westbrook, 1974a, Tectonics of the Barbados Ridge and adjacent Atlantic basin (abs.): *Eos (Am. Geophys. Union Trans.)*, v. 55, p. 284.
- 1974b, Interconnection between the tectonic framework of Barbados Ridge and the adjacent Guiana basin (abs.): 7th Caribbean Geol. Conf. Abs., p. 50-51.
- O. E. DeWald, and B. G. Bassinger, 1973b, Caribbean Atlantic geotraverse, NOAA-IDOE 1971, Rept. 2, Magnetic data: NOAA Tech. Rept. ERL 288-AOML 12.
- G. Merrill, and S. Bush, 1973a, Caribbean Atlantic geotraverse, NOAA-IDOE 1971, Rept. 1, Project introduction—bathymetry: NOAA Tech. Rept. ERL 293-AOML 13, 29 p.
- C. Schubert, and G. K. Westbrook, 1974, NOAA-IDOE Caribbean Atlantic geotraverse: *Geotimes*, v. 19, p. 12-15.
- R. K. Lattimore, O. E. DeWald, and G. Merrill, 1973c, Development of the Mid-Atlantic Ridge east of the Lesser Antilles island arc: *Nature, Phys. Sci.*, v. 245, p. 129-131.
- Pitman, W. C., III, A. M. Herron, and J. R. Heirtzler, 1968, Magnetic anomalies in the Pacific and sea-floor spreading: *Jour. Geophys. Research*, v. 67, p. 2069-2985.
- and M. Talwani, 1972, Sea floor spreading in the North Atlantic: *Geol. Soc. America Bull.*, v. 83, p. 619-646.
- Schouten, H., 1974, Magnetic anomalies over fracture zones in the lower magnetic latitudes of the central North Atlantic (abs.): *Eos (Am. Geophys. Union Trans.)*, v. 55, p. 232.
- Schubert, C., 1974, Seafloor tectonics east of the northern Lesser Antilles (abs.): 7th Caribbean Geol. Conf. Abs., p. 62-63.
- and G. Peter, 1973, Sea floor tectonics west of the Barracuda Ridge (abs.): *Eos (Am. Geophys. Union Trans.)*, v. 54, p. 326.
- Slater, J. G., R. N. Anderson, and M. L. Bell, 1971, Evolution of ridges and evolution of the central Eastern Pacific: *Jour. Geophys. Research*, v. 76, p. 7898-7915.
- Stipp, J. J., and F. Nagle, 1974, A geochemical study of the Lesser Antilles island arc: regional distribution of Sr 87/86 initial ratios (abs.): 7th Caribbean Geol. Conf. Abs., p. 65.
- Talwani, M., 1966, Gravity anomaly belts in the Caribbean in continental margins and island arcs, in *Continental margins and island arcs: Canada Geol. Survey Paper 66-15*, p. 177.
- van Andel, Tj. H., R. P. Von Herzen, and J. D. Phillips, 1971, The Vema fracture zone and the tectonics of transverse shear zones in oceanic crustal plates: *Marine Geophys. Researches*, v. 1, p. 261-283.
- Weeks, L. A., R. K. Lattimore, R. N. Harbison, et al, 1971, Structural relations among Lesser Antilles, Venezuela, and Trinidad-Tobago: *AAPG Bull.*, v. 55, p. 1741-1752.
- Westbrook, G. K., 1973, Crust and upper mantle structure in the region of Barbados and the Lesser Antilles: PhD thesis, Univ. Durham, 228 p.
- 1974a, The structure of the Barbados Ridge and buried trench of the Lesser Antilles subduction zone (abs.): 7th Caribbean Geol. Conf. Abs., p. 71.
- 1974b, The structure of the Barbados Ridge: 7th Caribbean Geol. Conf. Trans. (in press).
- 1975, The structure of the crust and upper mantle in the region of Barbados and the Lesser Antilles: *Royal Astron. Soc. Geophys. Jour.*, v. 43, p. 1-42.
- M. H. P. Bott, and J. H. Peacock, 1973, The Lesser Antilles subduction zone in the region of Barbados: *Nature, Phys. Sci.*, v. 244, p. 18-20.
- Wills, K. J. A., 1975, The geologic history of southern Dominica and plutonic nodules from the Lesser Antilles: PhD thesis, Univ. Durham, 244 p.

## OPENING OF THE RED SEA WITH TWO POLES OF ROTATION \*

EVAN S. RICHARDSON<sup>1,2</sup> and C.G.A. HARRISON<sup>1</sup><sup>1</sup> *University of Miami, Rosenstiel School of Marine and Atmospheric Science, Miami, Fla. (USA)*<sup>2</sup> *NOAA - Atlantic Oceanographic and Meteorological Laboratories, Miami, Fla. (USA)*

Received August 12, 1975

Revised version received January 5, 1976

Previous studies have shown that the Red Sea was formed by two stages of sea-floor spreading, with a quiescent period in between. We suggest that these two phases have occurred in different directions. The shape of the central trough indicates that the present-day motion is almost E-W, whereas the total opening, deduced from the shape of the coastlines, is NE-SW. If the axial trough has opened in an E-W direction, the earlier stage of opening was in a direction which made the Dead Sea Rift fall along a small circle to the pole of early opening, and hence suggests that the Dead Sea Rift was a transform fault during this early stage. The later movement gives almost pure extension along the Dead Sea Rift, and this should be seen by normal faulting. Available first-motion studies are not precise enough to confirm or deny this hypothesis.

## 1. Introduction

It has been suggested that there have been two stages of sea-floor spreading in the Red Sea [1,2]. The latter stage was responsible for the narrow axial trough in the center of the Red Sea, which is approximately 50 miles wide and is believed to have been caused by spreading over the last 3.5 m.y. The earlier stage was responsible for the formation of the bulk of the Red Sea. Between the two stages of spreading there was a period of quiescence, which allowed thick salt deposits to be accumulated. These thick salt deposits indicate that the oceanic crust formed during the earlier stage of spreading is at a greater depth than the crust formed during the later stage. The axial trough is caused by the absence of salt accumulations over the younger crust. Bathymetric and magnetic evidence has been published to support this two-stage concept [2].

\* Contribution from the University of Miami's Rosenstiel School of Marine and Atmospheric Science, 4600 Rickenbacker Causeway, Miami, Florida 33149.

## 2. Coast to coast opening

Several poles of rotation for the opening of the Red Sea have been published in the past [1,3-6]. These

TABLE 1  
Poles of rotation for the Red Sea

Pole of rotation		Method of calculation	Reference
lat.	long.		
32.5° N	22.5° E	shear along Dead Sea Rift and Gulf of Aden data	[3]
29.0° N	32.0° E	fit of coastlines and rates of opening in Red Sea and Dead Sea Rift	[4]
36.5° N	18.0° E	fit of coastlines and Suez Rift	[5]
32.0° N	22.0° E	fit of lines 20-30 km seaward of coasts and fit of Danakil Horst	[6]
31.5° N	23.0° E	fit of lines 52 km seaward of coasts, Gulf of Suez	[1]

poles and the methods by which they were calculated are summarized in Table 1.

An important factor in obtaining a pole of rotation for the Red Sea is whether or not the sea opened from coast to coast. Davies and Tramontini [7] believe that much of the Red Sea is underlain by oceanic crust. They felt that the most important result to emerge from their work was the clear indication that the Red Sea is underlain by rocks whose seismic velocity is higher than the majority of velocities reported from the continents. They reported a layer with an approximate seismic velocity of 6.63 km/sec which is in good agreement with the oceanic layer 3 average of 6.69 km/sec. From where their refraction lines end to the shoreline, they were not prepared to generalize except to note that there is, apart from a superficial change in sediment reflection characteristics, no reason to suppose that the structure changes.

Magnetic anomalies in the axial trough are lineated parallel to the strike of the topography. The pattern fits the anomaly sequence expected from sea-floor spreading, and it seems absolutely certain that the axial trough has been formed by sea-floor spreading over the past few million years. Recently, Girdler and Styles [2] have shown that at one place outside the axial trough there are also lineated magnetic anomalies. They believe that these have also been caused by sea-floor spreading during an earlier episode, thus confirming the seismic evidence that almost all of the Red Sea is oceanic in nature.

Girdler and Styles proposed that there was a period of quiescence between the formation of the main portion of the Red Sea, which they thought was formed between 41 and 34 m.y. ago, based on the magnetic time scale of Heirtzler et al. [8], and the axial trough, which was formed during the past 3.5 m.y. Although the timing of the earlier stage of opening seems to be in doubt, the difference in structure and the change in character of the older magnetic anomalies, compared with the younger ones, suggesting a deeper source for the older ones, certainly is strongly indicative of two stages of spreading with quiescence in between.

### 3. Establishment of the later pole of rotation

The establishment of the pole of rotation for the total opening of the Red Sea by fitting together the

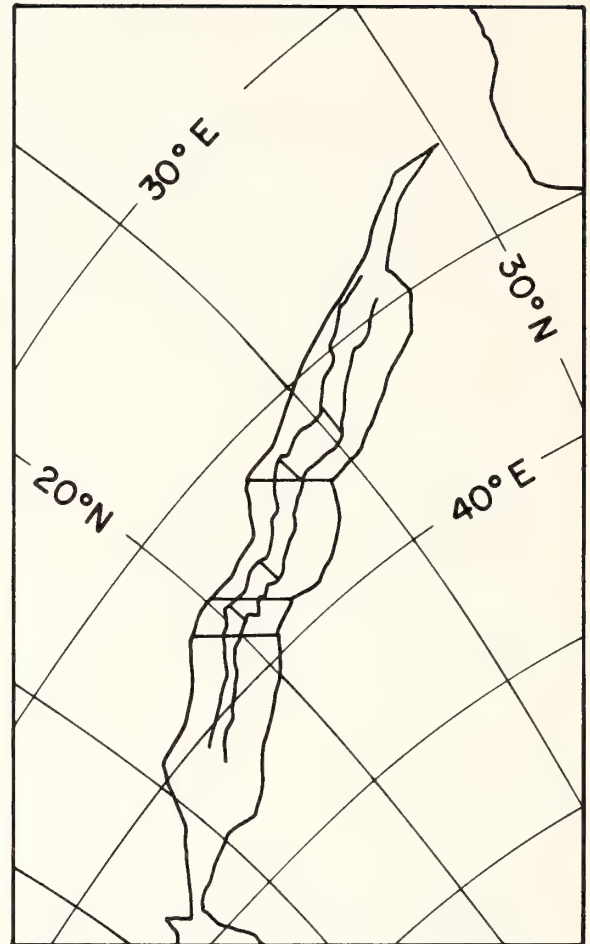


Fig. 1. Oblique Mercator projection of the Red Sea with projection pole at  $36.5^{\circ}\text{N}$ ,  $18.0^{\circ}\text{E}$ . This was the position of the pole of rotation used by McKenzie et al. [5] to describe the coastline fit on either side of the Red Sea. Lines connecting corresponding points on opposite coastlines are horizontal and represent small circles about the pole. The shorter lines connecting corresponding points across the axial valley are not horizontal.

coastlines gives a pole at  $36.5^{\circ}\text{N}$ ,  $18.0^{\circ}\text{E}$  [5]. Fig. 1 is an oblique Mercator projection of the Red Sea region using this point as the projection pole. It can be seen that lines connecting congruent points on each coastline are horizontal lines, representing small circles about the pole. But we noticed on a detailed chart of the Red Sea prepared by Laughton [9] that the axial trough appeared to have been formed by a more or less E–W separation. On this chart, the western bound-



ary of the axial trough, which is marked by the 500-fathom contour, can be superimposed on the same contour on the eastern boundary, by an eastward translation. We digitized the 500-fathom margins of the axial valley at 15' intervals of latitude. These margins are plotted on the transverse Mercator projection of Fig. 1. Congruent points on either side of the axial trough are connected by the short lines, and it can be seen that these lines are not horizontal. This suggests that the axial valley was not formed by relative motion about the pole used to plot Fig. 1, but about a different pole.

In order to establish a possible pole of rotation for the formation of the axial trough, we traced the western 500-fathom boundary of the axial trough from Laughton's map and slid it eastwards so that it matched the eastern boundary. Since the movement was almost exactly latitudinal, it is possible to do this because the

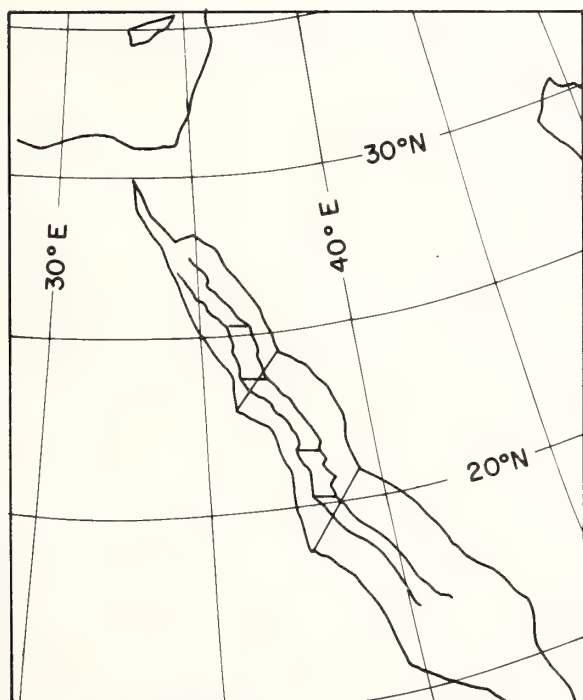


Fig. 2. Oblique Mercator projection of the Red Sea with projection pole at  $15.2^{\circ}\text{S}$ ,  $32.8^{\circ}\text{E}$ . This is the pole of rotation calculated for the later stage of opening. The lines connecting congruent points on either side of the axial trough (500-fathom isobath) are now horizontal, whereas the lines connecting the coastlines are not.

map of Laughton is plotted on a Mercator projection. We were able to measure a vector of opening for the northern end of the axial trough and one for the southern end. These two vectors enabled us to establish a pole of opening which was at  $15.2^{\circ}\text{S}$ ,  $32.8^{\circ}\text{E}$ , with a total opening angle of  $1.08^{\circ}$  about this pole. This is the pole for the clockwise rotation of Arabia from Nubia (or that part of Africa to the northwest of the East African rift valley). Using this rotation as the projection pole of an oblique Mercator projection (Fig. 2), we can see that now congruent points on either side of the axial valley are horizontal, and therefore lie on small circles about this pole.

One problem in establishing a pole for the later spreading episode is that there may have been flowage of salt deposits into the axial trough, which may therefore be narrower than the amount of sea floor created during the more recent episode of sea-floor spreading. Girdler and Darracott [1] have also suggested that the later opening may be about a pole different from that describing the early opening, but without going into details concerning what the difference might be. However, in a more recent paper, Girdler and Styles [2] make no mention of different poles of rotation. Girdler and Whitmarsh [10] have found evidence at two DSDP sites in the southern and central Red Sea (sites 227 and 228 in Fig. 3) that there has been lateral flow of salt deposits into the axial trough. At both sites Pliocene sediments and Miocene evaporites were found overlying oceanic crust which was predicted by magnetic anomaly evidence to be younger than 2.5 m.y. Coleman [11] has also mentioned the possibility of lateral flow of Red Sea evaporites. He suggested that the irregular bathymetry of the axial trough at  $16.67^{\circ}\text{N}$  may have resulted from salt flowage.

At present there is no evidence that there has been similar flowage in the northern Red Sea. Clearly the bathymetric shape of the axial valley is less smooth in the north. If there has been flowage of evaporites in the south but not in the north, this will cause an error in our calculation of the pole of opening of the axial trough. The error will be mainly in the determination of the latitude of the pole and not in the longitude. The true pole would lie further to the south than the position given above. If the axial valley in the south has been narrowed by 12 km due to flowage of salt, then the pole of opening should be shifted from a latitude of about  $15^{\circ}\text{S}$  to a latitude of about  $70^{\circ}\text{S}$ .

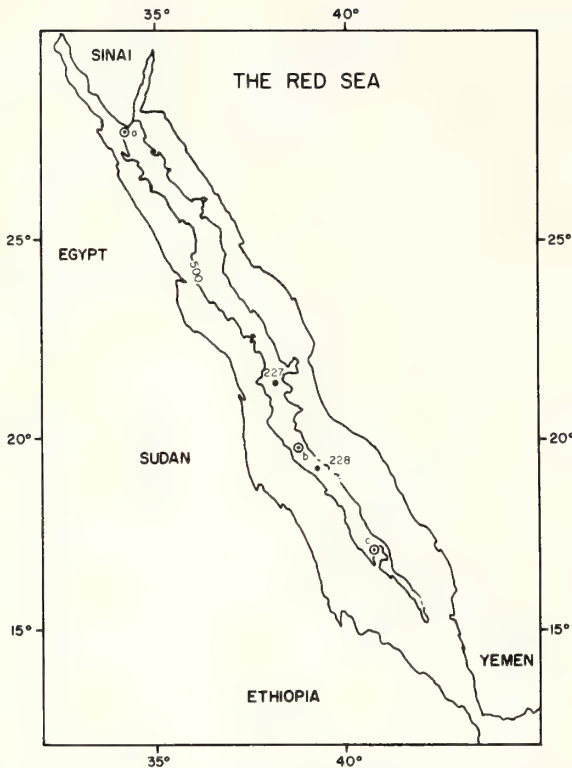


Fig. 3. Map of the Red Sea showing the location of three earthquakes (*a*, *b*, and *c*) [5,13,14] for which fault plane solutions have been obtained, and the locations of two DSDP sites (227 and 228) where it has been suggested that lateral flow of evaporites has occurred tending to smooth the boundaries of the axial trough [10].

However, since the amount of flowage is difficult to assess quantitatively, we shall assume that the pole at  $15.2^{\circ}\text{S}$ ,  $32.8^{\circ}\text{E}$  is correct, but will mention what the effect of moving it further south would be.

A better way of establishing the distance to a pole of rotation is to rotate magnetic anomalies on either side of the spreading center into coincidence, as done, for instance, by Pitman and Talwani [12]. Magnetic anomalies represent oceanic crust which is more precisely dated than the locus of the thick salt deposits outlined by the central valley described above. However, the development of magnetic anomalies is generally poor within the Red Sea. Estimates of spreading rate can only be obtained from a rather narrow latitudinal band from about  $17^{\circ}\text{N}$  to  $21^{\circ}\text{N}$  [13–15]. The uncertainty in observed spreading rates is so large that no

trend from south to north can be seen. All that these data tell us is that the pole of rotation lies sufficiently far away from the Red Sea such that a variation of spreading rate of 20% or more is not produced within this  $4^{\circ}$  band. This puts the pole of rotation further away than about  $20^{\circ}$ . Beyond that the magnetic data cannot go.

An alternative method of determining the direction of movement is to measure the strike of transform faults offsetting the axis of spreading. However, in the Red Sea we do not believe that there are any features which have been definitely identified as transform faults. Therefore this method of analysis is not available for this portion of the earth.

#### 4. Establishment of early pole

We accept the pole of McKenzie et al. ( $36.5^{\circ}\text{N}$ ,  $18.0^{\circ}\text{E}$ ) [5] as a good approximation of the mean pole of opening for the complete history of the Red Sea. However, if a two-stage model is accepted, this pole becomes a resultant of the first and second episodes of spreading. Therefore it is possible to obtain a pole of rotation for the early stage of spreading by vectorially subtracting the axial trough pole from the resultant or total pole of McKenzie et al. [5]. Employing this method, we have calculated the early pole at  $29.6^{\circ}\text{N}$ ,  $20.6^{\circ}\text{E}$ , some  $6^{\circ}$  south of the total pole opening. If there has been flowage of evaporites in the southern Red Sea, the later pole will be further south and this will tend to move the early pole to the north.

#### 5. Dead Sea Rift

One supposition of plate tectonics is that a transform fault always falls on a small circle to the relative pole of rotation of the two plates involved. The Dead Sea Rift has generally been accepted as such a boundary between the Arabian and Nubian plates. Fig. 4 shows the pole of McKenzie et al. [5] plotted on a map of the Mediterranean and Red Sea region. It is evident here that the Dead Sea Rift does not fall on a small circle to this pole. However, the Dead Sea Rift does fall quite close to a small circle about the early pole presented in this paper (Fig. 5). We feel that this is more than a fortuitous occurrence. In fact, depending



Fig. 4. Azimuthal equidistant projection of the Mediterranean and Red Sea region with projection pole at  $36.5^{\circ}$  N,  $18.0^{\circ}$  E marked with a cross. This is the position of the McKenzie et al. [5] pole. The Dead Sea Rift is marked with plus signs which are located from south to north as follows: south end of the Gulf of Aqaba, north end of the Gulf of Aqaba, south end of the Dead Sea, north end of the Dead Sea, Sea of Galilee. These points do not lie on a small circle with respect to the rotation pole.



Fig. 5. Same as Fig. 4, except that the projection pole is at  $29.6^{\circ}$  N,  $20.6^{\circ}$  E, which is the rotation pole calculated for the early stage of opening of the Red Sea. The points along the Dead Sea Rift now lie close to a small circle about the rotation pole.

on the amount of flowage of the evaporites from the main trough, the precise location of the early pole may be slightly north of its calculated position, therefore causing the Dead Sea Rift to fall even closer to a small circle about the pole.

By assuming a two-stage model for the development of the Red Sea we may therefore find a key to understanding the history of the Dead Sea Rift as a plate boundary. The strike of the fault was determined during the first stage of spreading in the Red Sea when most of the motion along the fault consisted of a left-lateral strike-slip component. Then when the second stage of spreading began, the fault took on a component of rifting. So, today the major source of earthquakes along the Dead Sea Rift should be caused by normal rather than strike-slip faulting. We suggest that this hypothesis be tested by first motion studies.

It should be noted that several authors have suggested that a significant amount of left-lateral shear has occurred along the Dead-Sea Rift during the Quaternary. Quennell [16] inferred a Pleistocene movement of 45 km from geomorphic features, the most prominent of which is the shape of the deep depression of the Dead Sea.

Zak and Freund [17] have recorded horizontal displacements (which are younger than the Lisan Marl – 23,000 years) of 150 m along the fault in the Dead Sea area. However, Freund et al. [18] do not hesitate to admit that a general agreement has not yet been reached concerning the Dead Sea Rift's lateral displacement. They refer to Neev and Emery [19] in discussing the geology of the Dead Sea as accepting the shear hypothesis, and Picard [20] as not accepting it.

We also refer to Bender [22] who lists several reasons why he does not accept the shear hypothesis. Along the entire east side of the rift, he notes that there is overwhelming evidence of dip-slip movement along hundreds of faults and fault zones with vertical throws of up to 1000 m. He reports that evidence of lateral displacement (horizontal slickensides, etc.) is very rare (observed at three places) and in the order of centimeters up to a few meters. Bender suggests that these minor lateral movements and some minor folding due to tangential compression can be explained as secondary structural phenomena.

Perhaps the confusion throughout the literature concerning movement on the Dead Sea Rift is because both strike-slip and normal faulting have occurred, but at

different times. We feel that our model of strike-slip and then normal faulting is not inconsistent with the observed data.

The Dead Sea Rift follows approximately a small circle about the early pole from its intersection with the Red Sea to as far north as the Huleh Depression in Lebanon. North of this, the Yamuneh Fault trends more or less northeasterly, clearly departing from the small circle. For this reason we postulate that the structural continuation of the Dead Sea transform fault follows the Roum Fault which trends north toward the Mediterranean near Beirut. Dubertret [23] also suggested a similar continuation, but for different reasons. He postulated that motion (strike-slip) be taken up along the Roum Fault rather than along the Yamuneh because the structures in Lebanon are far too gentle to accommodate the amount of shortening necessary to explain the displacement along the Dead Sea Rift to the south. Of course today the Roum Fault is not active, but was probably a continuation of the Dead Sea Rift as a transform fault during the first stage of spreading in the Red Sea.

One difficulty with our later pole is that, being south of the Red Sea, a much greater amount of extension would be expected across the Dead Sea Rift than is actually observed. The largest amount of extension appears to be less than 20 km in the Gulf of Aqaba. One possible solution to this problem is that again, depending on the amount of flowage of evaporites in the southern Red Sea, the later pole may be pushed far enough to the south so that its anti-pole may be north of, and not far from the Dead Sea Rift. In this case, a smaller amount of extension along the Dead Sea Rift than in the Red Sea's axial trough would be expected. However, it is also possible that some extension has been taken up in crustal thinning rather than faulting and could not be ascertained by field investigations alone.

## 6. Red Sea spreading rate

Girdler and Styles [2] published a spreading rate for the axial trough (recent episode) of 0.9 cm/yr. This rate was computed from a magnetic profile across the southern Red Sea trending N58°E. However, because we postulate a second-stage direction that is almost E-W, we calculate a new spreading rate. We use the

same profile used by Girdler and Styles but have obtained a spreading rate of 1.0 cm/yr.

## 7. Fault plane solutions

Fault plane solutions have been previously published for three earthquakes that have occurred in the Red Sea [5,24,25]. The locations of these earthquakes are shown in Fig. 3 and given in Table 2, and the solutions are shown in Fig. 6. The earthquake occurring in the northern Red Sea (*a* in Fig. 3, Fig. 6A and Table 2) occurred at the extreme northern boundary of the axial trough and was generated by a normal fault. Because of the relative paucity of data for this earthquake, it would be possible to draw the fault plane and the accessory plane so that they were striking approximately N-S, in agreement with what we would expect for a normal fault generated within an axial valley where the motion was E-W. We feel that first motion data from this earthquake are not inconsistent with the motion which we propose is happening in the Red Sea today.

Two of the earthquakes, one in the central and one in the southern Red Sea (*b* and *c* in Fig. 3, Fig. 6B and C, and Table 2), appear to have occurred on transform faults, although offsets of the axial trough are not evident. However, some disagreement exists between various solutions of these two earthquakes which have appeared in the literature. For the earthquake in the central Red Sea, Fairhead and Girdler [24] have obtained a focal plane with a strike of N53°E and dip 82°SE, whereas McKenzie et al. [5] published a solution for the same earthquake and obtained a focal plane with

TABLE 2  
First motion studies of earthquakes in the Red Sea

	Origin time	Lat.	Long.	Ref.
Northern Red Sea	31 Mar. 1969	27.5° N	33.8° E	[5,24]
Central Red Sea	13 Mar. 1967	19.7° N	38.9° E	[5,24]
Southern Red Sea	11 Nov. 1962	17.1° N	40.6° E	[5,24,25]

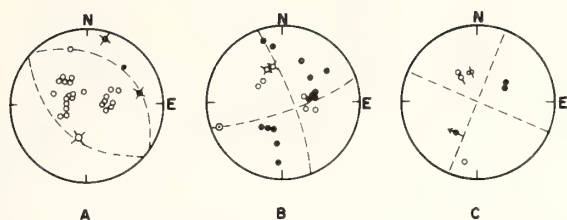


Fig. 6. Focal mechanism for three earthquakes in the Red Sea (see Table 2 and Fig. 3). The dashed focal planes are those that have been previously published. A. Solution for earthquake on March 31, 1969. B. March 13, 1967. C. November 11, 1962.

strike  $N68^{\circ}E$  and dip  $80^{\circ}SE$ , a difference of  $15^{\circ}$  in the strike. We have no means of knowing which solution is the more accurate, but point out that a slight modification to the solution of McKenzie et al. would give a motion close to the one which we predict.

The earthquake in the southern Red Sea has even less data (see Fig. 6), and a slight modification to the fault planes would give good agreement to our predicted motion. In this case, the fault would be a right-lateral fault along the approximately E–W plane, rather than the left-lateral motion along the approximately N–S plane, as proposed by McKenzie et al. [5].

We conclude that the first motion studies of these three earthquakes are sufficiently inaccurate that it is impossible to use them to decide whether our proposed E–W motion is more correct than the NE–SW motion derived from the total opening of the Red Sea. The first motion studies fit either hypothesis equally well.

## 8. Implications for the East Africa Rift

McKenzie et al. [5] and Girdler and Daracott [1] have both made use of three-dimensional vector addition to arrive at a pole and magnitude of rotation for the East Africa Rift system. This is possible because the rift is part of a three-plate spreading system; and by vectorially adding the poles and magnitudes of rotation for the Red Sea (Arabia–Nubia) and the Gulf of Aden (Arabia–Somalia), a pole and magnitude of rotation for the East Africa Rift (Nubia–Somalia) may be obtained.

Because we have obtained a new pole of rotation for the Red Sea, we can also calculate a new pole and

magnitude for the East Africa Rift. We use the same pole of rotation for the Gulf of Aden as presented by McKenzie et al. [5]. We find that this new pole for the East Africa Rift lies at  $51.7^{\circ}S$ ,  $3.5^{\circ}E$  and that the magnitude of rotation is  $2.65 \times 10^{-7}$  degree/year. This pole lies farther to the southwest than that presented by Girdler and Darracott [1] but lies in the same general direction with respect to the rift. They refer to seismological studies and gravity anomalies indicating a tensional stress field of approximately  $S30^{\circ}E$  across the rift. These geophysical data are as consistent with our pole as they are with theirs.

## 9. Summary

We have shown that the shape of the axial valley of the Red Sea suggests that recent spreading has been in an E–W direction, rather than the NE–SW direction of the earlier phase of spreading. If this is the case, then the Dead Sea Rift was a plate boundary with almost pure transform fault motion along it during the earlier phase of spreading. According to our model, present-day motion of the Dead Sea Rift is extensional, and should be marked by predominantly normal faulting. The available earthquake evidence is not capable of distinguishing between the E–W motion suggested in this paper and the motions suggested previously. The rotation pole position calculated for the later phase of spreading is probably not accurate, because of salt flowage. However, it can be taken as the northernmost limit of the true rotation pole.

## Acknowledgments

We thank M.M. Ball, R.S. Dietz and F. Nagle for constructive criticisms. The maps in Figs. 1, 2, 4 and 5 were drawn using FORTRAN program HYPERMAP, written by R.L. Parker, whom we thank. Research supported by NSF grant GA-42979 from the oceanography section and from NOAA.

## References

- 1 R. Girdler and B. Darracott, African poles of rotation, *Comments Earth Sci.: Geophys.* 2 (1972) 131–138.

- 2 R. Girdler and P. Styles, Two-stage Red Sea floor spreading, *Nature* 247 (1974) 7–11.
- 3 A. Laughton, The birth of an ocean, *New Sci.* 27 (1966) 218–220.
- 4 D. Roberts, Structural evolution of the rift zones in the Middle East, *Nature* 223 (1969) 55–57.
- 5 D. McKenzie, D. Davies and P. Molnar, Plate tectonics of the Red Sea and East Africa, *Nature* 226 (1970) 1–6.
- 6 R. Freund, Plate tectonics of the Red Sea and East Africa, *Nature* 228 (1970) 453.
- 7 D. Davies and C. Tramontini, The deep structure of the Red Sea, *Philos. Trans. R. Soc. Lond., Ser., A* 267 (1970) 181–189.
- 8 J.R. Heirtzler, G.O. Dickson, E.M. Herron, W.C. Pitman III and X. Le Pichon, Marine magnetic anomalies, geomagnetic field reversals, and motions of the ocean floor and continents, *J. Geophys. Res.* 73 (1968) 2119–2136.
- 9 A.S. Laughton, A new bathymetric chart of the Red Sea, *Philos. Trans. R. Soc. Lond., Ser. A* 267 (1970) 21–22.
- 10 R. Girdler and R. Whitmarsh, Miocene evaporites in Red Sea cores and their relevance to the problem of the width and age of oceanic crust beneath the Red Sea, in: *Initial Reports of the Deep Sea Drilling Project* 23 (1974) 913–921.
- 11 R. Coleman, Geologic background of the Red Sea, in: *Initial Reports of the Deep Sea Drilling Project* 23 (1974) 813–819.
- 12 W.C. Pitman III and M. Talwani, Sea-floor spreading in the North Atlantic, *Geol. Soc. Am. Bull.* 83 (1972) 619–646.
- 13 T.D. Allan, Magnetic and gravity fields over the Red Sea, *Philos. Trans. R. Soc. Lond., Ser. A* 267 (1970) 153–180.
- 14 J.D. Phillips, Magnetic anomalies in The Red Sea, *Philos. Trans. R. Soc. Lond., Ser. A* 267 (1970) 205–217.
- 15 F.J. Vine, Spreading of the ocean floor: new evidence, *Science* 154 (1966) 1405–1415.
- 16 A.M. Quennell, The structural and geomorphic evolution of the Dead Sea Rift, *Q.J. Geol. Soc. Lond.* 114 (1958).
- 17 I. Zak and R. Freund, Recent strike slip movements along the Dead Sea Rift, *Israel J. Earth Sci.* 15 (1966) 33–37.
- 18 R. Freund, Z. Garfunkel, I. Zak, M. Goldberg, T. Weissbrod and B. Denn, The shear along the Dead Sea Rift, *Philos. Trans. R. Soc. Lond., Ser. A* 267 (1970) 107–130.
- 19 D. Neev and K.O. Emery, The Dead Sea, depositional processes and environments of evaporites, *Bull. Geol. Surv. Israel* 41 (1967) 147.
- 20 L. Picard, Thoughts on the graben system in the Levant, *Geol. Surv. Can. Paper* 66–14 (1966) 22–32.
- 21 L. Picard, On the structure of the Rhinegraben with comparative notes on Levantgraben features, *Israel Acad. Sci. Hum.* 9 (1968) 34.
- 22 F. Bender, The shear along the Dead Sea Rift: discussion, *Philos. Trans. R. Soc. Lond., Ser. A* 167 (1970) 127–129.
- 23 L. Dubertret, Remarques sur le fosse de la Mer Morte et ses prolongements au nord jusqu'au Taurus, *Rev. Geogr. Phys. Geol. Dyn.* 9 (1967) 3–16.
- 24 D. Fairhead and R. Girdler, The seismicity of the Red Sea, Gulf of Aden and Afar Triangle, *Philos. Trans. R. Soc. Lond., Ser. A* 267 (1970) 49–74.
- 25 L. Sykes, Focal mechanism solutions for earthquakes along the world rift system, *Bull. Seis. Soc. Am.* 60 (1970) 1749–1752.

[4]

## OPENING OF THE RED SEA WITH TWO POLES OF ROTATION – REPLY

E.S. RICHARDSON<sup>1,2</sup> and C.G.A. HARRISON<sup>1</sup><sup>1</sup> *Rosenstiel School of Marine and Atmospheric Science, University of Miami, Miami, Fla. (USA)*<sup>2</sup> *NOAA – Atlantic Oceanographic and Meteorological Laboratories, Miami, Fla. (USA)*

Received August 2, 1976

We welcome the comments by Girdler and Styles [1] concerning our recent paper [2]. However, the reason for their first argument evades us.

Girdler and Styles state that the bathymetry of the Red Sea's axial trough is wider in the south than in the north, and that the extension in the Dead Sea Rift is even less than that in the Red Sea.

However, it is obvious that the axial trough from Laughton's bathymetric chart of the Red Sea [3] (defined by the 500-fm contour) is narrower in the southern Red Sea than in the north. (We have examined some of the seismic reflection profiles published in the literature [4,5] and have found that in the majority of profiles, the slope break on the walls of the axial trough occurs quite close to the 500-fm depth). With this in mind, we were not surprised to calculate a pole of rotation for the later stage of opening to the south of the Red Sea.

Two criteria, however, caused us to doubt the latitudinal accuracy of this pole:

(1) The Dead Sea rift has undergone a maximum amount of extension of less than 20 km (Gulf of Aqaba).

(2) Girdler and Whitmarsh [6] and Coleman [7] have reason to believe that lateral flow of evaporites into the axial trough has occurred in the southern Red Sea, causing the axial trough to be narrower than the amount of sea floor created during the later stage of spreading.

These two lines of evidence point to a pole of rotation to the north of the Dead Sea Rift. And we made note of this in our original paper, on page 140 (which Girdler and Styles obviously did not see).

We stated that depending on the amount of evapo-

rite flowage into the axial trough, the later pole may be pushed far enough to the south so that its anti-pole may be north of, and not far from, the Dead Sea Rift.

Our example was that, if the axial valley in the south has been narrowed by 12 km due to salt flowage, the rotation pole should be shifted from a latitude of about 15°S to a latitude of about 70°S. This is only an example, as Girdler and Whitmarsh [6] show evidence that the narrowing of the axial trough, in the south, is much more than 12 km. They note the presence of Miocene evaporites overlying oceanic crust with a magnetic age of 2.5 m.y. Assuming an average sea-floor spreading rate of 1.0 cm/yr, we estimate that the flowage of evaporites is close to 25 km (12 km on either side). This would push the pole of rotation so far south that its antipole would approach 55°N.

Girdler and Styles [1] object to our description of the motion of Arabia away from Nubia as clockwise. We wish simply to point out that an anticlockwise rotation about a pole requires a clockwise rotation about its anti-pole. Since the pole we describe is located south of the Red Sea, it would naturally require a clockwise rotation to move Arabia away from Nubia. The situation is illustrated in Fig. 1.

The other major point to which Girdler and Styles address themselves is that of northeast-southwest features within the axial trough. They go as far as to measure 67 azimuths from magnetic, gravity, bathymetry, and interpretation maps to prove their point of recent northeast-southwest motion. However, they note that due to the small width of the axial trough their measurements "are not very accurate" and "give rise to large errors". We agree with this conclusion. In addi-

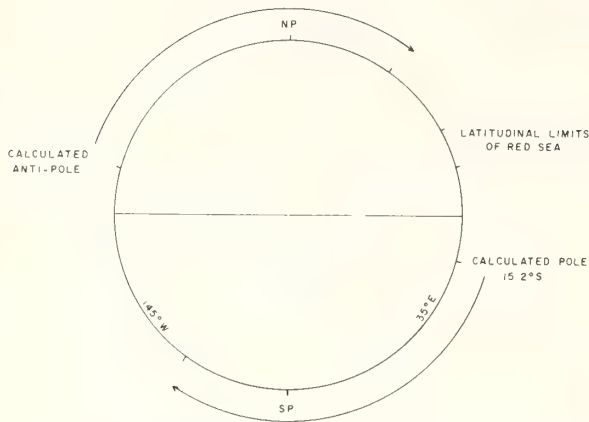


Fig. 1. Movement of pole of rotation to account for 25 km of salt flowage. Note that anti-pole moves to a position north of the Red Sea. Rotation of Arabia from Nubia is clockwise about the pole, when the motion is viewed from outside the earth, but anti-clockwise about the anti-pole.

tion, we note that none of the data referred to gives conclusive evidence of transform motion within the axial trough except the fault-plane solutions from Fairhead and Girdler [8]. Here, strike-slip motion is indicated. But because of scanty data, a precise azimuth of the nodal planes cannot be determined, as already discussed in our paper. We have checked carefully all the references used by Girdler and Styles [1] to make their measurements of azimuths, except that by Bäcker et al. [9]. To our surprise we found that in most cases the original authors made no suggestion that these features were transform faults. Searle and Ross [5] did suggest that the magnetic anomalies studied by them could be best explained by northeast-southwest motion, but other interpretations are also possible. Phillips [10] suggested three possible models for the magnetic anomalies he studied in the Red Sea. He was unable to choose between these models except on the basis of other evidence for directions of motion. This other evidence was the direction established from earthquake first-motion studies, which we have already discussed in our paper, and which we have suggested do not make great constraints on the actual motion because of the rather poor recording of earthquakes in this region. One of the models suggested by Phillips [10] was one in which there was east-west motion between Arabia and Nubia, in agreement with our model.

Several authors have made note of magnetic lineations striking  $N60^{\circ}E$  and  $N70^{\circ}E$  [5,10–12]. In fact, Allan [13] makes special mention of five earthquake epicenters which are aligned in an east-west direction and show remarkable coincidence with his postulated offsets in the axial trough. He states that this is convincing proof of a transform fault in this region.

Girdler and Styles [14] suggest that there was a cessation in spreading in the Red Sea of about 30 m.y. Even though the later stage of spreading took place at the same geographic location as the earlier stage (in the center of the Red Sea) it would be surprising indeed if the new *direction* of spreading were along exactly the same azimuth as the old direction, as the direction of spreading is controlled by processes underlying the lithosphere. If the processes ceased for 30 m.y., there is no reason to believe that the movements would regenerate in the same direction as before.

Our conclusions are that the shape of the axial trough suggests an east-west movement of Arabia away from Africa (as shown by super-position of the 500-fm contours). Problems of salt flowage, however, preclude the calculation of an accurate latitude for the pole of rotation, whereas the meridian of the rotation pole is much more accurately known.

Research supported by the National Science Foundation and by NOAA.

## References

- 1 R. Girdler and P. Styles, Opening of the Red Sea with two poles of rotation – some comments, *Earth Planet. Sci. Lett.* 33 (1976) 169–172.
- 2 E.S. Richardson and C.G.A. Harrison, Opening of the Red Sea with two poles of rotation, *Earth Planet. Sci. Lett.* 30 (1976) 135–142.
- 3 A.S. Laughton, A new bathymetric chart of the Red Sea, *Philos. Trans. R. Soc. Lond., Ser. A*, 267 (1970) 21–22.
- 4 J.D. Phillips and D.A. Ross, Continuous seismic reflexion profiles in the Red Sea, *Philos. Trans. R. Soc. Lond., Ser. A*, 267 (1970) 143–152.
- 5 R.C. Searle and D.A. Ross, A geophysical study of the Red Sea axial trough between  $20^{\circ}S$  and  $22^{\circ}N$ , *Geophys. J.R. Astron. Soc.* 43 (1975) 555–572.
- 6 R. Girdler and R. Whitmarsh, Miocene evaporites in Red Sea cores and their relevance to the problem of the width and age of oceanic crust beneath the Red Sea, in: *Initial Reports of the Deep Sea Drilling Project 23* (U.S. Government Printing Office, Washington, D.C., 1974) 913–921.



- 7 R. Coleman, Geologic background of the Red Sea, in: Initial Reports of the Deep Sea Drilling Project 23 (U.S. Government Printing Office, Washington, D.C., 1974) 813–819.
- 8 D. Fairhead and R. Girdler, The seismicity of the Red Sea, Gulf of Aden, and Afar Triangle, *Philos. Trans. R. Soc. Lond., Ser. A*, 267 (1970) 49–74.
- 9 H. Bäcker, K. Lange and H. Richter, Morphology of the Red Sea Central Graben (Valdivia Enzschlamme A & B, Preussag).
- 10 J.D. Phillips, Magnetic anomalies in the Red Sea, *Philos. Trans. R. Soc. Lond., Ser. A*, 267 (1970) 205–217.
- 11 J.D. Phillips, J. Woodside and C.O. Bowin, Magnetic and gravity anomalies in the Central Red Sea, in: *Hot Brines and Recent Heavy Metal Deposits in the Red Sea*, E.T. Degens and D.A. Ross, eds. (Springer-Verlag, New York, N.Y., 1969) 98–113.
- 12 F.K. Kabbani, Geophysical and structural aspects of the central Red Sea valley, *Philos. Trans. R. Soc. Lond., Ser. A*, 267 (1970) 89–97.
- 13 T.D. Allan, Magnetic and gravity fields over the Red Sea, *Philos. Trans. R. Soc. Lond., Ser. A*, 267 (1970) 153–180.
- 14 R.W. Girdler and P. Styles, Two-stage Red Sea floor spreading, *Nature* 247 (1974) 7–11.

[6]

## ASYMMETRIC FRACTURE ZONES AND SEA-FLOOR SPREADING

PETER A. RONA

*NOAA, Atlantic Oceanographic and Meteorological Laboratories, Miami, Fla. (USA)*

Received August 12, 1975

Revised version received January 29, 1976

An asymmetric pattern is observed in the orientation of minor fracture zones about the axis of the Mid-Atlantic Ridge at five sites where relatively detailed studies have been made between latitudes 22°N and 51°N. The minor fracture zones intersect the axis of the Mid-Atlantic Ridge in an asymmetric V-shaped configuration. The V's point south north of the Azores triple junction (38°N latitude) and point north south of that junction.

The rates and directions of sea-floor spreading are related to the asymmetric pattern of minor fracture zones at the sites studied. Half-rates of sea-floor spreading averaged between about 0 and 10 m.y. are unequal measured perpendicular to the ridge axis. The unequal half-rates of spreading are faster to the west north of the Azores triple junction and faster to the east south of that junction. The half-rates of sea-floor spreading calculated in the directions of the asymmetric minor fracture zones are equal about the ridge axis within the uncertainty of the direction determinations.

A discrepancy exists between minor fracture zones that form an asymmetric V about the axis of the Mid-Atlantic Ridge, and major fracture zones that follow small circles symmetric about the ridge axis. To reconcile this discrepancy it is proposed that minor fracture zones are preferentially reoriented under the influence of a stress field related to interplate and intraplate motions. Major fracture zones remain symmetric about the Mid-Atlantic Ridge under the same stress field due to differential stability between minor and major structures in oceanic lithosphere. This interpretation is supported by the systematic variation in the orientation of minor fracture zones and the equality of sea-floor spreading half-rates observed about lithospheric plate boundaries.

**1. Introduction**

A discrepancy is becoming apparent between the overall symmetry of the Atlantic ocean basin and asymmetry of both topography and sea-floor spreading about the Mid-Atlantic Ridge. The overall symmetry of the Atlantic (Fig. 1) was first recognized from bathymetric profiles along widely spaced tracklines that revealed the nearly median position of the Mid-Atlantic Ridge [1], the nearly mirror image distribution of physiographic provinces about the ridge axis [1], the trajectories of major fracture zones which follow small circles symmetric about the axis of the Mid-Atlantic Ridge [2,3], and the sequences of remanent magnetic anomalies attributed to polarity reversals that indicate a grossly similar history of sea-floor spreading in the eastern and western basins [4,5].

Recent work summarized in Table 1 reveals asymmetry of both topographic features (Fig. 1) and half-rates of sea-floor spreading about the axis of the Mid-Atlantic Ridge at sites where relatively detailed investigations have been made between major fracture zones. A problem exists in reconciling the overall symmetry of the Atlantic ocean basin with the asymmetry revealed by the recent work.

**2. Asymmetric topography of the oceanic ridge crest**

Valleys with intervening ridges oriented transverse to the rift valley have been delineated where relatively detailed bathymetric surveys have been made at sites along the crest of the Mid-Atlantic Ridge (Fig. 1). The spacing between the transverse valleys ranges between

TABLE 1

Relation between topography and sea-floor spreading on the Mid-Atlantic Ridge

Reference	Topography			Azimuth of transverse valleys and ridges		Average spacing between transverse valleys (km)	Sense of offset of axis of MAR at transverse valleys
	bounding lithospheric plates	latitude on MAR	azimuth of axis of MAR	Side of MAR			
				W	E		
[33]	America and Eurasia	61–62°N	033°	280°	—	30	left lateral
		61–62°N	033°	280°	—	30	left lateral
		61–62°N	033°	280°	—	30	left lateral
[30]	America and Eurasia	47–51°N	335 and 360°	280–295°	080–090°	30	left lateral
		47–51°N	335 and 360°	280–295°	080–090°	30	left lateral
[10,23,30]	America and Eurasia	45–46°N	019°	285 ± 10°	087 ± 10°	30	left lateral
		45–46°N	019°	285 ± 10°	087 ± 10°	30	left lateral
<i>Azores triple junction</i>							
[8,9,11, 24,25]	America and Africa	36–37°N	018°	270 ± 10°	108°	50	right lateral
		36–37°N	018°	270 ± 10°	108°	50	right lateral
		36–37°N	018°	270 ± 10°	108°	50	right lateral
[6,7,26,27]	America and Africa	25–27°N	025°	265°	115°	55	right lateral
		25–27°N	025°	265°	115°	55	right lateral
		25–27°N	025°	265°	115°	55	right lateral
[12]	America and Africa	22–23°N	020°	260 ± 10°	110 ± 10°	50	left lateral
		22–23°N	020°	260 ± 10°	110 ± 10°	50	left lateral
		22–23°N	020°	260 ± 10°	110 ± 10°	50	left lateral
[28,34]	America and Africa	6–8°S	350°	231 ± 10°	080°	—	left lateral
		6–8°S	350°	231 ± 10°	080°	—	left lateral
		6–8°S	350°	215 ± 10°	080°	—	left lateral
		6–8°S	350°	215 ± 10°	080°	—	left lateral

MAR = Mid-Atlantic Ridge; — indicates no data. Italicized values are computed values (this paper).

30 and 55 km at the various sites (Table 1). The transverse valleys and intervening ridges are distinctly delineated by those surveys that include tracklines at spacings closer than 20 km oriented parallel to the axis of the Mid-Atlantic Ridge, such as the surveys at 26°N (Fig. 2) [6,7], and at 36°N [8]. The transverse features are less distinctly delineated by surveys based only on tracklines oriented perpendicular to the axis of the Mid-Atlantic Ridge, as at the other sites (Table 1).

Where distinctly delineated at 26°N (Fig. 2) [6,7] and at 36°N [8,9], the transverse valleys exhibit the

characteristics of minor fracture zones associated with small ridge-ridge transform faults. These characteristics include ridge-ridge offset of the rift valley up to about 20 km, the association of earthquake epicenters with the zone of offset, the presence of a basin several hundred meters deep at the intersection of the zone of offset with the rift valley, and relief of hundreds of meters between the floors of the transverse valleys and the crests of the intervening ridges. It is inferred by analogy with their characteristics at 26°N and 36°N that the transverse valleys and intervening ridges at the

Amount of offset of axis of MAR at transverse valleys (km)	Age of crust (m.y. B.P.)	Sea-floor spreading			Azimuth of spreading direction (relation to axis of MAR)
		average half- rate of spread- ing (cm/yr)	averaging interval (m.y.)	side of MAR	
<10	3-7	1.0	0-10	W	303° (normal)
<10	3-7	1.1	0-10	W	280° (oblique)
<10	3-7	-	0-10	E	123° (normal)
<10	0-10	1.10	0-10	E	070° (normal)
<10	0-10	-	0-10	W	250° (normal)
<10	0-10	1.10	0-10	E	109° (normal)
<10	0-10	1.28	0-10	W	289° (normal)
<10		1.19 ± 0.10	0-10	E	087 ± 10° (oblique)
20	0-10	1.3	0-10	E	108° (normal)
20	0-10	1.0 ± 0.1	0-10	W	288° (normal)
20	0-10	1.1 ± 0.2	0-10	W	270 ± 10° (oblique)
<10	0-10	1.3	0-10	E	115° (normal)
<10	0-10	1.1	0-10	W	295° (normal)
<10	0-10	1.3	0-10	W	265° (oblique)
≤10	0-10	1.5 ± 0.1	0-10	E	110° (normal)
≤10	0-10	1.4	0-10	W	280° (nearly normal)
≤10	0-10	1.5 ± 0.1	0-10	W	260 ± 10° (oblique)
-	0-4.5	2.16 ± 0.24	0-4.5	E	080° (normal)
-	0-4.5	1.89 ± 0.04	0-4.5	W	260° (normal)
-	4.5-10	1.59 ± 0.24	4.5-10	E	080° (normal)
-	4.5-10	1.12 ± 0.08	4.5-10	W	260° (normal)

other sites described (Table 1) are also minor fracture zones associated with small ridge-ridge transform faults.

The transverse valleys and intervening ridges at each site intersect the east and west sides of the rift valley in an asymmetric V-shaped configuration (Fig. 1; Table 1). The two sides of the rift valley are parallel. North of the Azores triple junction between 45°N and 46°N the angle of intersection of the transverse valleys and intervening ridges with the rift valley is oblique on the east side and nearly normal on the west side [10]. Between 47°N and 51°N the transverse valleys

and intervening ridges appear to retain the same orientation as between 45°N and 46°N, but the azimuth of the axis of the Mid-Atlantic Ridge changes from northeast to northwest resulting in oblique intersections on both sides of the rift valley. At both sites north of the Azores triple junction the V formed by the intersection of the transverse valleys and intervening ridges with the two sides of the rift valley points southward (Fig. 1). South of the Azores triple junction at 36°N (Table 1) [8,9,11], at 26°N (Fig. 1; Table 1) [6,7], and at 22°N [12], the angle of intersection of the transverse valleys

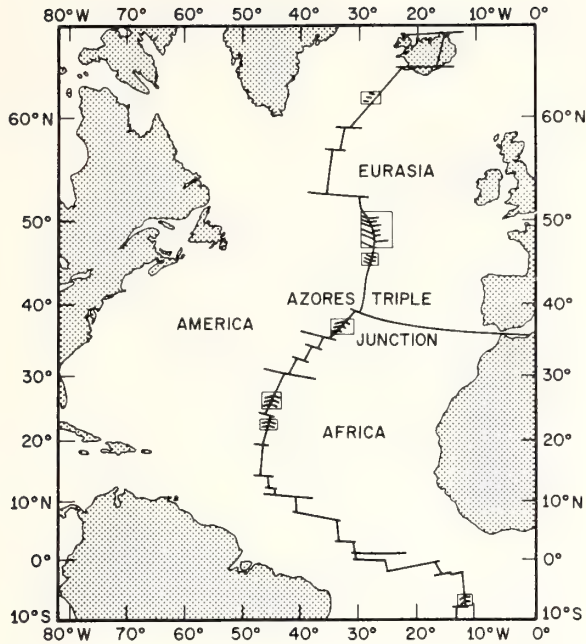


Fig. 1. Map of the Atlantic ocean basin showing principal lithospheric plates, axis of the Mid-Atlantic Ridge, major fracture zones that form small circles symmetric about the ridge axis, minor fracture zones that form V-shaped configurations asymmetric about the ridge axis delineated in areas of relatively detailed investigations (boxes). The configuration of inferred minor fracture zones in the area at 6°S is predicted rather than observed, as discussed in the text.

and intervening ridges with the rift valley reverses becoming nearly normal on the east side and oblique on the west side. The V formed by the intersection of the transverse ridges and intervening valleys at the sites south of the Azores triple junction points northward (Fig. 1).

The characteristics of the minor fracture zones described are distinct in several respects from major fracture zones. Major fracture zones of the Atlantic like the Gibbs (latitude 52°N) [13], the Oceanographer (latitude 35°N) [14], the Atlantis (latitude 30°N) [15], the Kane (latitude 24°N) [16], and the Vema (latitude 10°N) [17], follow families of small circles symmetric about the axis of the Mid-Atlantic Ridge, generally exhibit ridge-ridge offsets of at least 100 km, and are spaced hundreds of kilometers apart along the ridge axis.

### 3. Apparent and true relative rates of sea-floor spreading

Determination of rate and direction of sea-floor spreading are related in that the apparent and true relative rates of spreading are a function of direction. The principle method to determine spreading rate is based on the Vine and Matthews hypothesis [18]. Strips of crustal material that are alternately magnetized during spreading about an oceanic ridge are identified in the magnetic polarity reversal time scale. Relative half-rates of sea-floor spreading may be derived from the distance between the axis of the oceanic ridge and the identified magnetic anomaly. The distance measured perpendicular to the axis of the oceanic ridge yields an apparent relative half-rate of spreading. The distance measured parallel to transform faults and their continuation as fracture zones that may be oblique to the axis of the oceanic ridge, yields a true relative half-rate of spreading, because these features indicate the true direction of relative motion between diverging lithospheric plates [3,19–21]. In the case that the direction of a fracture zone is perpendicular to the axis of an oceanic ridge the apparent and true relative half-rates of spreading are equal.

The apparent relative half-rates of sea-floor spreading determined perpendicular to the axis of the Mid-Atlantic Ridge at the sites studied are unequal (Table 1). To facilitate comparison between sites and to suppress shorter period variations [22] the spreading rates are averaged over the period 0–10 m.y. B.P. The average apparent relative half-rates of spreading are faster to the west of the Mid-Atlantic Ridge axis at latitude 45°N north of the Azores triple junction [23], and are faster to the east at latitudes 36°N, 26°N, and 6°S south of that junction [24–28].

The average true relative half-rates of sea-floor spreading in the directions of the minor fracture zones were calculated from the average apparent relative half-rates perpendicular to the ridge axis using simple trigonometric relations (Fig. 3). At latitude 26°N where the azimuths of the minor fracture zones are accurately known (Fig. 2: Table 1), the average true relative half-spreading rates are equal about the ridge axis. At the other sites at latitudes 45°N, 36°N, and 22°N, where the azimuths of the minor fracture zones are less accurately known (Table 1), the average true relative half-spreading rates are equal about the ridge axis

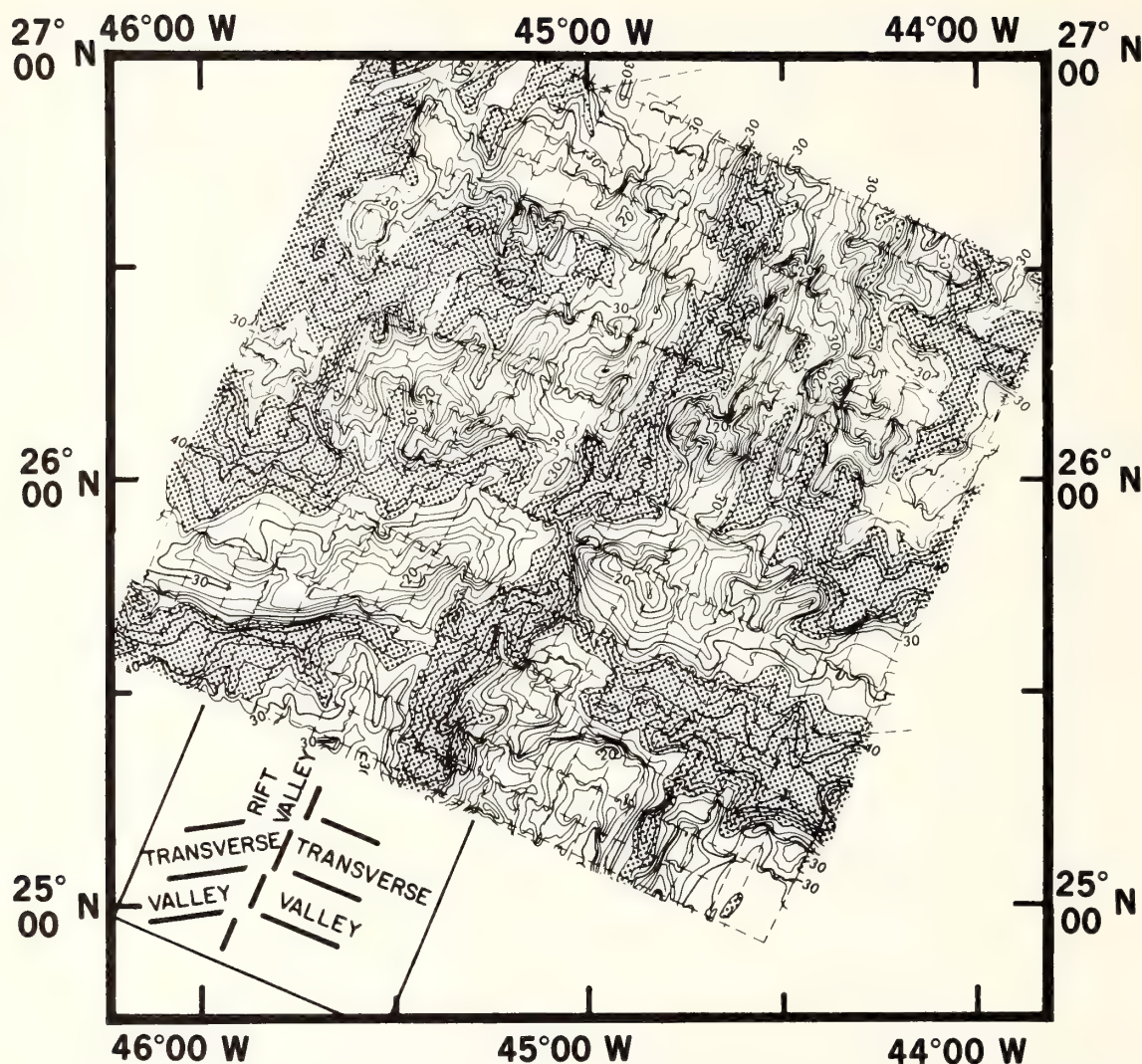


Fig. 2. Bathymetric map [7] contoured in hundreds of meters of a 180-km square on the Mid-Atlantic Ridge crest at 26°N latitude (Fig. 1; Table 1). Sounding tracks are dashed. Depths exceeding 3400 m are shaded to delineate the rift valley and transverse valleys that trend normal to the east side and oblique to the west side of the rift valley, as sketched in the inset.

within the uncertainty of the azimuth determinations.

The five sites described are the only sites known in sufficient detail to reveal the systematic variation in orientation of minor fracture zones and the equality of average true relative half-rates of sea-floor spreading about the Mid-Atlantic Ridge. If the relations observed between the orientation of minor fracture zones and half-rates of spreading are consistent, then the orienta-

tions of minor fracture zones may be computed from half-rates of spreading. For example, at the Mid-Atlantic crest between latitudes 6° and 8°S the apparent relative half-rates of spreading are known [28], and orientations of minor fracture zones are unknown. The predicted orientations of the minor fracture zones are computed from the apparent relative half-rates of spreading (Table 1). Detailed studies (line spacing closer than

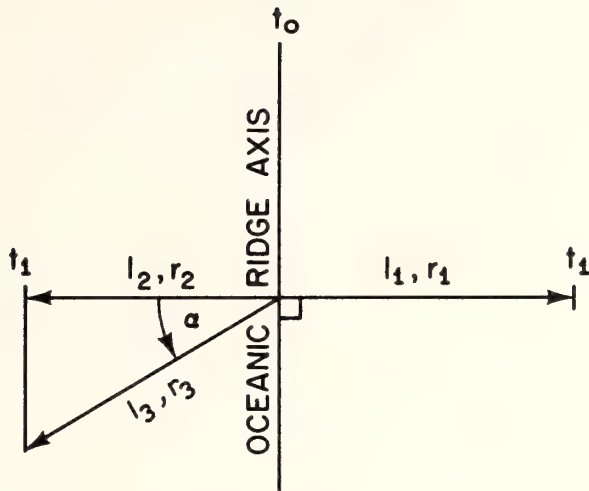


Fig. 3. Geometry of spreading normal and oblique to the axis of an oceanic ridge.  $t_0$  = zero isochron;  $t_1$  = isochron at unit time;  $l_1$  and  $l_2$  = lengths of crust generated in  $t_1$ , normal to the axis of an oceanic ridge;  $r_1$  and  $r_2$  = half-rates of spreading corresponding to  $l_1$  and  $l_2$ ;  $l_3$  = length of crust generated in  $t_1$  along a direction defined by angle  $\alpha$  oblique to the axis of the ridge;  $r_3$  = half-rate of spreading corresponding to  $l_3$ . An angle  $\alpha$  exists such that:  $l_3 = l_2/\cos \alpha = l_1$  and  $r_3 = r_2/\cos \alpha = r_1$ .

20 km both perpendicular and parallel to the ridge axis) are needed at more sites along the Mid-Atlantic Ridge to test these relations.

#### 4. Discussion

Hypotheses to explain the observations presented of fracture zones and sea-floor spreading must consider the various characteristics described. In particular, the asymmetric V-shaped intersection of the inferred minor fracture zones with the axis of the Mid-Atlantic Ridge, the inversion of the V north and south of the Azores triple junction, the inequality of apparent relative spreading half-rates determined perpendicular to the ridge axis, the equality of true relative spreading half-rates determined parallel to minor fracture zones normal and oblique to the ridge axis, and the existence of asymmetric features within the symmetric framework of the Atlantic ocean basin.

Two alternative hypotheses are considered to account for the observed relations between topography and sea-floor spreading, as follows:

(1) *Original orientation.* The asymmetric orientation of minor fracture zones about the axis of an oceanic ridge is produced by asymmetric processes of development of the oceanic lithosphere. According to this hypothesis the relative motions of the lithospheric plates follow the directions of the asymmetric minor fracture zones. This hypothesis poses problems in reconciling asymmetric with symmetric features of the ocean basin because asymmetric plate motions at minor fracture zones would be incompatible with symmetric plate motions at major fracture zones.

(2) *Reorientation.* The processes of development of oceanic lithosphere are essentially symmetric and produce both symmetric minor and major fracture zones associated with symmetric sea-floor spreading. The minor fracture zones are continuously reoriented while the major fracture zones maintain their original orientations. As a consequence of this reorientation apparent relative half-rates of spreading determined perpendicular to the axis of an oceanic ridge are unequal. True relative half-rates of spreading determined in the directions of the reoriented minor fracture zones normal and oblique to the axis of an oceanic ridge are equal. This hypothesis is supported by the relations between spreading directions and rates determined at sites along the Mid-Atlantic Ridge (Table 1), and offers promise of reconciling the discrepancy between asymmetric and symmetric features of the Atlantic ocean basin.

The continuous reorientation of minor fracture zones according to hypothesis 2 may be caused by the application of an external stress field deriving from different sources, as follows:

(1) *Forces related to magmatic processes.* These forces are related to vertical and horizontal magmatic movements associated with the axial region of an oceanic ridge. A type of regional magmatic movement proposed by Vogt [29] and applied by Johnson and Vogt [30] to account for V-shaped topography about the axis of an oceanic ridge depends on the principle of a geopotential gradient to drive asthenospheric flow from topographic highs over inferred mantle plumes such as at Iceland and the Azores. According to their hypothesis, the V should point in the direction of flow away from the high as the result of asthenospheric flow along and sea-floor spreading about an oceanic ridge. The Vogt-Johnson hypothesis does not account for the orientation of the V-shaped topography

described to the north and south of the Azores because the V points toward rather than away from the Azores (Fig. 1). Forces related to magmatic processes undoubtedly contribute to the stress field, but are considered secondary rather than primary components.

(2) *Forces related to tectonic processes.* These forces are related to interplate and intraplate motions and may be primary components of the stress field inferred to be reorienting the direction of minor fracture zones and sea-floor spreading along the Mid-Atlantic Ridge. The role of interplate and intraplate forces as primary components of the stress field is supported by the observation that the orientation of the minor fracture zones and of sea-floor spreading systematically changes about lithospheric plate boundaries. The orientation of minor fracture zones and of sea-floor spreading is different on the two sides of the rift valley of the Mid-Atlantic Ridge, a divergent plate boundary, and differs between the America and Eurasia plates north of the Azores triple junction and the America and Africa plates south of that junction (Fig. 1; Table 1). The Azores triple junction has been a major influence in the development of the Atlantic at least since the early Mesozoic opening of the central North Atlantic [31].

### 5. Differential stability of symmetric and asymmetric structures in oceanic lithosphere

The reorientation hypothesis allows the simultaneous development of small asymmetric structures and large symmetric structures in oceanic lithosphere. Minor fracture zones associated with small transform faults (offset <30 km) behave in an unstable manner at the relatively slow average half-rates of spreading ( $\leq 2$  cm/yr) prevalent at the Mid-Atlantic Ridge. The minor fracture zones are continuously reoriented under the influence of an external stress field as they are generated by sea-floor spreading about the small transform faults. Major fracture zones associated with large transform faults (offset >50 km) behave in a stable manner at relatively slow average half-rates of spreading ( $\leq 2$  cm/yr). The major fracture zones maintain their orientation under the influence of the same external stress field as they are generated by sea-floor spreading about the large transform faults. Thickness of lithosphere related to distribution of isotherms at a transform fault

may be a determinant of the stability of fracture zones [32]. Asymmetric small structures may then develop within the overall symmetry of the Atlantic ocean basin as a consequence of the differential stability between minor and major fracture zones of the oceanic lithosphere.

### Acknowledgement

I thank Walter C. Pitman, III, for a helpful review.

### References

- 1 B.C. Heezen, M. Tharp and M. Ewing, The floors of the oceans, I. The North Atlantic, *Geol. Soc. Am. Spec. Paper* 65 (1959) 122 pp.
- 2 B.C. Heezen and M. Tharp, Physiographic diagram of the North Atlantic Ocean, *Geol. Soc. Am. Spec. Paper* 65 (1968) revised.
- 3 W.J. Morgan, Rises, trenches, great faults and crustal blocks, *J. Geophys. Res.* 73 (1968) 1959.
- 4 W.C. Pitman, III and M. Talwani, Sea-floor spreading in the North Atlantic, *Geol. Soc. Am. Bull.* 83 (1972) 619.
- 5 G.O. Dickson, W.C. Pitman, III and J.R. Heirtzler, Magnetic anomalies in the South Atlantic and ocean-floor spreading, *J. Geophys. Res.* 73 (1968) 2087.
- 6 P.A. Rona, R.N. Harbison, B.G. Bassinger and R.B. Scott, Asymmetrical bathymetry of the Mid-Atlantic Ridge at 26°N latitude (abstract), *EOS Trans. Am. Geophys. Union* 54 (1973) 243.
- 7 P.A. Rona, R.H. Harbison, B.G. Bassinger, R.B. Scott and A.J. Nalwalk, Tectonic fabric and hydrothermal activity of Mid-Atlantic Ridge crest (26°N), *Geol. Soc. Am. Bull.* (1976) in press.
- 8 R.S. Detrick, J.D. Mudie, B.P. Luyendyk and K.C. Macdonald, Near-bottom observations of an active transform fault (Mid-Atlantic Ridge at 37°N), *Nature* 246 (1973) 59.
- 9 I. Reid and K. Macdonald, Microearthquake study of the Mid-Atlantic Ridge near 37°N, using sonobuoys, *Nature* 246 (1973) 88.
- 10 P.J. Bhattacharyya and D.I. Ross, Mid-Atlantic Ridge near 45°N, computer interpolation and contouring of bathymetry and magnetics, Marine Sciences Directorate, Dep. of Environment, Ottawa, *Mar. Sci. Paper* 11 (1972) 9 pp.
- 11 H. Fleming, Naval Research Laboratory, personal communication.
- 12 T.H. van Andel and C.O. Bowin, Mid-Atlantic Ridge between 22° and 23° north latitude and the tectonics of mid-ocean rises, *J. Geophys. Res.* 73 (1968) 1279.
- 13 H.S. Fleming, N.Z. Cherkis and J.R. Heirtzler, The Gibbs fracture zone: a double fracture zone at 52°30'N in the Atlantic Ocean, *Mar. Geophys. Res.* 1 (1970) 37.



- 14 P.J. Fox, A. Lowrie, Jr. and B.C. Heezen, Oceanographer Fracture Zone, *Deep-Sea Res.* 16 (1969) 59.
- 15 J.D. Phillips, B.P. Luyendyk and D.W. Forsyth, Central North Atlantic plate motions, *Science* 174 (1971) 846.
- 16 P.J. Fox, W.C. Pitman, III and F. Shephard, Crustal plates in the Central Atlantic: evidence for at least two poles of rotation, *Science* 165 (1969) 487.
- 17 T.H. van Andel, J.B. Corliss and V.T. Bowen, The intersection between the Vema Fracture Zone and the Mid-Atlantic Ridge in the North Atlantic, *J. Mar. Res.* 25 (1967) 343.
- 18 F.J. Vine and D.H. Matthews, Magnetic anomalies over oceanic ridges, *Nature* 199 (1963) 947.
- 19 B.C. Heezen and M. Tharp, Tectonic fabric of the Atlantic and Indian oceans and continental drift, *Philos. Trans. R. Soc. London, Ser. A* 258 (1965) 90.
- 20 D.P. McKenzie and R.L. Parker, The North Pacific: an example of tectonics on a sphere, *Nature* 216 (1967) 1276.
- 21 X. LePichon, Sea-floor spreading and continental drift, *J. Geophys. Res.* 73 (1968) 3661.
- 22 D.L. Anderson, Accelerated plate tectonics, *Science* 187 (1975) 1077.
- 23 B.D. Loncarevic and R.L. Parker, The Mid-Atlantic Ridge near 45°N, XVII. Magnetic anomalies and ocean-floor spreading, *Can. J. Earth Sci.* 8 (1971) 883.
- 24 H.D. Needham and J. Francheteau, Some characteristics of the Rift Valley in the Atlantic Ocean near 36°48' North, *Earth Planetary Sci. Lett.* 22 (1974) 29.
- 25 D. Greenewalt and P.T. Taylor, Deep-tow magnetic measurements across the axial valley of the Mid-Atlantic Ridge, *J. Geophys. Res.* 79 (1974) 4401.
- 26 R.K. Lattimore, P.A. Rona and O.F. DeWald, Magnetic anomaly sequence in the Central North Atlantic, *J. Geophys. Res.* 79 (1974) 1207.
- 27 B.A. McGregor, C.G.A. Harrison, J.W. Lavelle and P.A. Rona, Magnetic anomaly pattern on Mid-Atlantic Ridge crest at 26°N, *J. Geophys. Res.* (1976) in press.
- 28 T.H. van Andel and T.C. Moore, Magnetic anomalies and sea-floor spreading rates in the northern South Atlantic, *Nature* 226 (1970) 328.
- 29 P.R. Vogt, Asthenosphere motion recorded by the ocean floor south of Iceland, *Earth Planetary Sci. Lett.* 13 (1971) 155.
- 30 G.L. Johnson and P.R. Vogt, Mid-Atlantic Ridge from 47° to 51° north, *Geol. Soc. Am. Bull.* 84 (1973) 3443.
- 31 P.A. Rona and H.S. Fleming, Mesozoic plate motions in the eastern central North Atlantic, *Mar. Geol.* 14 (1973) 239.
- 32 P.R. Vogt, O.E. Avery, E.D. Schneider, C.N. Anderson and D.R. Bracey, Discontinuities in sea-floor spreading, *Tectonophysics* 8 (1969) 285.
- 33 P.R. Vogt and G.L. Johnson, Seismic reflection survey of an oblique aseismic basement trend on the Reykjanes Ridge, *Earth Planet. Sci. Lett.* 15 (1972) 248.
- 34 T.H. van Andel and G.R. Heath, Tectonics of the Mid-Atlantic Ridge, 6–8° south latitude, *Mar. Geophys. Res.* 1 (1970) 5.

## PLATE TECTONICS AND OIL

Alfred G. Fischer and Sheldon Judson (Editors), 1975. *Petroleum and Global Tectonics*. Princeton University Press, Princeton, N.J., 322 pp., US. \$16.50.

*Petroleum and Global Tectonics* is a collection of nine papers discussing geological processes relevant to the occurrence of oil from the point of view of plate tectonics. The papers, by scientists from universities and the petroleum industry, were presented at a symposium held at Princeton University in 1972 to honor Hollis D. Hedberg.

The papers are meaningfully arranged and introduced by the editors. In an overview of plate tectonics, Sir Edward Bullard points out that while petroleum exploration is largely concerned with vertical crustal movements which allow the accumulation of sediments, plate tectonics is primarily concerned with horizontal movements. Five successive papers demonstrate how both vertical and horizontal movements determine the evolution of sedimentary basins as the sites of petroleum generation, accumulation and storage.

W. Jason Morgan contributes theoretical background on the relation between heat flow and vertical movements of the oceanic lithosphere, one of the most thoroughly understood of the phenomena producing vertical crustal displacements. A.G. Fischer demonstrates that the vertical movements of oceanic lithosphere, combined with horizontal movements of plates, provide a plausible mechanism for basins that develop on continental margins; basins developed on continental interiors remain problematic. Those basins that originated by rifting contain the largest volume of prospective sediment. D.J.J. Kinsman explains their development by initial uplift and post-rifting subsidence related to subcrustal temperature and density distributions. J.D. Lowell, G.J. Genik, T.H. Nelson, and P.M. Tucker consider the evolution of the southern Red Sea as an example of how structural arching, rifting, subsidence, and breaching of continental lithosphere act to control the occurrence of petroleum. J.R. Curray synthesizes different assemblages of marine sedimentary facies that constitute basins and shows that orogenic histories of these sedimentary assemblages follow almost infinite variations in plate tectonic settings, rather than an invariant geotectonic cycle.

The generation of petroleum is treated by J.G. Erdman who reviews the processes by which an organic fraction of sediment may be transformed into hydrocarbons by inorganic processes related to temperature, degree of oxidation, and the mineral matrix. H.D. Klemme assembles substantial data to examine relations between hydrocarbon occurrence and both the tectonics and thermal regime of productive basins. His evidence indicates that basins associated with significantly higher heat flow located along continental margins and rift zones provide optional conditions for the generation, migration, and accumulation of petroleum.

The papers of this symposium demonstrate that plate tectonics provides insight to problems relevant to the occurrence of petroleum including the origin of basins, sources of sediment, open basins, restricted marine circulation, basin geometry, basin relations on opposite continental margins, and thermal regimes within basins. Most of the 198 known giant oil fields discussed by J.D. Moody in the concluding paper were found prior to the advent of plate tectonics, but plate tectonics will play a significant role in finding the estimated 200 to 300 remaining giant fields. This book exemplifies the kind of creative interplay between academe and industry that results in intellectual and material advances. It is worthwhile reading both for scientists and informed laymen.

Peter A. Rona, Miami, Fla.

Reprinted from: *Geological Society of America, Microform Publication, Vol. 5,*  
490 p.

Mid-Atlantic Ridge: Selected

Reprints and Bibliography

Edited by

Peter A. Rona

## INTRODUCTION

The following articles from publications of the Geological Society of America are assembled in chronological order and provide perspective of the development of geological knowledge of the Mid-Atlantic Ridge spanning a quarter century of research from early studies to the present frontier.

Early bathymetric reconnaissance gradually revealed the regional morphology of the Mid-Atlantic Ridge (Tolstoy and Ewing, 1949; Tolstoy, 1951). Cross-sections of the deep crustal structure underlying the Mid-Atlantic Ridge determined by the two-ship seismic refraction method (Ewing and Ewing, 1959) are only now being refined by new methods. Groundwork on the regional distribution of sediment type by coring (Ericson and others, 1961) and of sediment thickness by seismic reflection profiling (Ewing and others, 1964) preceded studies of sedimentary processes at representative sites on the Mid-Atlantic Ridge (van Andel and Komar, 1969; Ruddiman, 1972). Sampling of rocks from emerged (Le Maitre, 1962) and from submerged (Quon and Ehlers, 1963; Engel and others, 1965; Switzer and others, 1970; Melson and Thompson, 1973) portions of the Mid-Atlantic Ridge has contributed to recognition of the distinctive petrology of oceanic rocks, and has stimulated their comparison with ophiolites (Thayer, 1969; Green, 1970).

The designation of the Mid-Atlantic Ridge as a divergent plate boundary in the theory of plate tectonics has focused research on processes at the axial region of the ridge. Advances in magnetic interpretation made it possible to determine the history of generation about the ridge crest of Atlantic oceanic lithosphere (Pitman and Talwani, 1972). Studies of the thermal regime of the Mid-Atlantic Ridge are related both to its characteristic profile (Sclater and Detrick, 1973) and to the petrologic effects of hydrothermal activity (Anderson, 1972).

Increasing realization of the complexity of axial processes has led to the concentration of studies at representative areas of the Mid-Atlantic Ridge crest (Ward, 1971; Johnson and Vogt, 1973; van Andel and others, 1973; Phillips and others, 1975). Interdisciplinary, cooperative investigations have been adopted as an effective research approach. These investigations of the crestal region of the Mid-Atlantic Ridge include work near lat 36°N by project FAMOUS (French-American Mid-Ocean Undersea Study; Heirtzler and Le Pichon, 1974), near lat 45°N by Canadian scientist (Loncarevic, this publication), and near lat 26°N by the Trans-Atlantic Geotraverse (TAG) project of the National Oceanic and Atmospheric Administration (Rona and others, 1976). No longer an enigmatic geographic feature, the Mid-Atlantic Ridge is being studied as the locus of processes that affect the entire Earth.

Reprinted from: *Marine Geology*, Vol. 21, No. 4, M59-M66.

*Marine Geology*, 21 (1976) M59-M66

M59

© Elsevier Scientific Publishing Company, Amsterdam — Printed in The Netherlands

## Letter Section

### PATTERN OF HYDROTHERMAL MINERAL DEPOSITION: MID-ATLANTIC RIDGE CREST AT LATITUDE 26° N

PETER A. RONA

*National Oceanic and Atmospheric Administration, Atlantic Oceanographic and Meteorological Laboratories, Miami, Fla. 33149 (U.S.A.)*

(Received February 25, 1976; revised and accepted May 20, 1976)

#### ABSTRACT

Rona, P.A., 1976. Pattern of hydrothermal mineral deposition: Mid-Atlantic Ridge crest at latitude 26° N. *Mar. Geol.*, 21: M59-M66.

Interdisciplinary studies of the TAG Hydrothermal Field on the Mid-Atlantic Ridge crest at latitude 26° N reveal two principal depositional patterns of hydrothermal minerals:

(1) A pattern of deposition controlled by physical and chemical processes within the hydrothermal field. A major process in determining depositional pattern within the hydrothermal field is inferred to be sealing of talus by deposition of hydrothermal minerals from solutions discharged through underlying faults at and adjacent to the wall of the rift valley. The sealing of a given volume of talus is inferred to occur during a period of the order of  $1 \cdot 10^5$  yr, causing successive migrations of the zone of discharge. The resulting pattern of hydrothermal mineral deposition within the hydrothermal field would be expected to be a mosaic of deposits overlapping in time and space with a predominantly fault-controlled trend parallel to the axis of the rift valley.

(2) A pattern of deposition controlled by sea-floor spreading encompassing the entire hydrothermal field. A linear zone of hydrothermal deposits will extend from an active depositional locality at a rift valley along the direction of sea-floor spreading depending both on the continuity of sea-floor spreading and the persistence in time of the special structural and thermal conditions that concentrate the hydrothermal activity. The special structural and thermal conditions that have concentrated hydrothermal activity at the TAG Hydrothermal Field have persisted during sea-floor spreading for at least  $1.4 \cdot 10^6$  yr.

#### INTRODUCTION

Concentrated hydrothermal mineral deposits are known from several localities along divergent plate boundaries, including the Red Sea (Degens and Ross, 1969), the Galapagos spreading axis (Moore and Vogt, 1976), and the Mid-Atlantic Ridge at latitudes 36° N (ARCYANA, 1975), 26° N (M.R. Scott et al., 1974), and 23° N (Thompson et al., 1975). The minerals are deposited by sub-sea floor hydrothermal convection systems inferred to involve the circulation of seawater through oceanic crust driven by intrusive heat sources at sea-floor spreading centers (Spooner and Fyfe, 1973). Knowledge of the

depositional pattern of hydrothermal minerals in time and space at localities along divergent plate boundaries would help to elucidate the nature of sub-sea floor hydrothermal convection systems and metallogenesis in oceanic crust (Rona, 1973; Bonatti, 1975). Interdisciplinary studies by the NOAA Trans-Atlantic Geotraverse (TAG) project of concentrated hydrothermal mineral deposits on the Mid-Atlantic Ridge at latitude  $26^{\circ}\text{N}$  provide the basis for a preliminary interpretation of their pattern of deposition (Rona et al., 1976). Evidence for past and present concentration of hydrothermal activity including at least a  $10\text{-km}^2$  area at the southeast side of the rift valley has led to designation of this locality as the TAG Hydrothermal Field (Fig.1; R.B. Scott et al., 1974).

#### OBSERVATIONS

The bathymetric setting of the TAG Hydrothermal Field is a ridge that

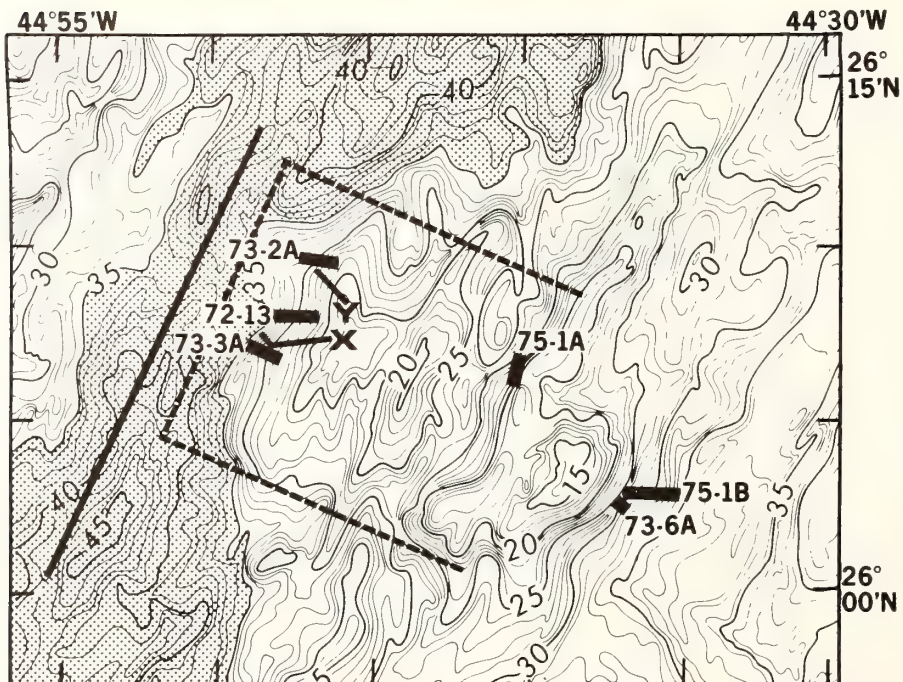


Fig.1. Bathymetric map (McGregor and Rona, 1975) contoured in hundreds of meters showing axis (solid line) of rift valley (shaded) of the Mid-Atlantic Ridge at latitude  $26^{\circ}\text{N}$ , two profiles (X, Y) along which temperature measurements and bottom photographs were made concurrently, and dredge stations at the southeast wall of the rift valley (TAG 1972-13 [72-13], TAG 1973-2A [73-2A] TAG 1973-3A [73-3A] and along a ridge (unshaded) trending orthogonal to the axis of the rift valley (TO-75AK61-1A [75-1A], TO-75AK59-1B [75-1B], TAG 1973-6A [73-6A]). The approximate known area of the TAG Hydrothermal Field is indicated (dashed line).

trends orthogonal to the rift valley (Fig.1). The west end of the ridge forms the southeast wall of the rift valley. Abundant manganese oxide crusts were recovered from three dredge stations where the orthogonal ridge forms the southeast wall of the rift valley (Fig.1; dredge stations TAG 1972-13, TAG 1973-2A, TAG 1973-3A). The hydrothermal origin of the manganese oxide crusts is evidenced by their rapid rates of accumulation (200 mm per  $10^6$  yr) determined radiogenically, and by their extreme purity of composition (40% Mn), with only trace quantities of metals other than manganese (M.R. Scott et al., 1974), occupying the Mn-rich end member of Bonatti's hydrothermal classification (Bonatti, 1975). Manganese oxide crusts were also present at one station situated along the crest of the orthogonal ridge (Fig.1; dredge station TO-75AK61-1A). Manganese oxide crusts were absent at two other dredge stations along the crest of the orthogonal ridge (Fig.1; dredge stations TAG 1973-6A, TO-75AK59-1B), where ropy-textured, apparently fresh basalt with high  $K_2O$  content (0.3%) characteristic of off-axial extrusion was recovered (R.B. Scott et al., 1976).

The hydrothermal manganese oxide occurs as a crust on talus of basalt fragments (Fig.2), as veins in the basalt fragments, and as a crust on and matrix in breccia of altered basalt fragments (Fig.3). The talus and breccia occur along the inner margins of steps on the southeast wall of the rift valley revealed by narrow-beam bathymetry and bottom photographs (McGregor and Rona, 1975). The steps are interpreted as the topographic expression of faults that may act as conduits for hydrothermal solutions.

Two profiles combining water temperature measurements and bottom photographs were made over steps on the southeast wall of the rift valley between depths of about 2500 and 3500 m (Rona et al., 1975). A temperature anomaly about 300 m wide consisting of an increase in ambient temperature ( $+0.1^\circ\text{C}$ ) and an inversion of potential temperature gradient ( $0.015^\circ\text{C}$  per m warming downwards), was measured within 20 m of the sea floor over a talus-covered step at a depth of about 3000 m on one of the two profiles (Fig.1; profile X; Rona et al., 1975). The character and geologic setting of this temperature anomaly favor its interpretation as due to convective transfer of heat by discharge of hydrothermal solutions focussed by faults in the wall of the rift valley and diffused by a porous and permeable layer of talus overlying the faults. A temperature anomaly was absent at the second profile (Fig.1; profile Y) situated 5 km along the step on the wall of the rift valley where the temperature anomaly was measured on profile A. Bottom photographs revealed that breccia and pillow lavas are the predominant rock types present along profile B (McGregor and Rona, 1975, their fig.6).

## DISCUSSION

The duration and position of deposition of the manganese oxide crusts observed at the TAG Hydrothermal Field may be deduced from their rates of accumulation and the local half-rate of sea-floor spreading (1.3 cm per yr;



Fig.2. Bottom photographs (field of view approximately  $4 \times 6$  m) showing talus of basalt fragments at 3000-m depth along profile X (Fig.1) on the southeast wall of the rift valley where a water temperature anomaly was measured (Rona et al., 1975). The camera water current compass (length 34 cm) is visible suspended 5 m below the camera.

Lattimore et al., 1974). The manganese oxide crust sampled attains a thickness of 42 mm at the southeast wall of the rift valley, 5 km from the axis of the rift valley (Fig.1; dredge station TAG 1972-13). U-Th dating of the manganese crust shows it to have accumulated at a rate of about 200 mm per  $10^6$  yr, with cessation of accumulation about  $15 \cdot 10^3$  yr ago (M.R. Scott et al., 1974, their table 1b, fig.3). Assuming a constant rate, the manganese oxide crust at dredge station TAG 1972-13 began to accumulate about  $2 \cdot 10^5$  yr ago at a position 2 km from the axis of the rift valley and continued to accumulate during sea-floor spreading nearly up to its present position at the wall of the rift valley.

The manganese oxide crust at dredge station TO-75AK61-1A, situated 17 km from the axis of the rift valley (Fig.1), consists of two layers. An underlying layer of hydrothermal manganese up to 10 mm thick accumulated at a rate of about 35 mm per  $10^6$  yr (R.B. Scott et al., 1976), during a period of  $3 \cdot 10^5$  yr, at distances between 8 and 12 km from the axis of the rift valley. The deposition of hydrothermal manganese oxide ceased 12 km from the axis of the rift valley when the underlying basalt was about  $1 \cdot 10^6$  yr old. Then a layer of hydrogenous ferromanganese oxide up to 3 mm thick accumulated at a rate of about 8 mm per  $10^6$  yr on the hydrothermal manganese (R.B. Scott et al., 1976) during a period of about  $4 \cdot 10^5$  yr, at distances between 12 and 17 km from the axis of the rift valley. The reconstructed





Fig. 3. Bottom photograph (field of view approximately  $4 \times 6$  m) showing hydrothermal manganese oxide crust (upper left and central portion of photograph) on breccia of basalt fragments at 2600-m depth along profile Y (Fig. 1). The camera water current compass (length 34 cm) is visible suspended 5 m below the camera.

sequence of events indicates that hydrothermal deposits began to accumulate on the floor of the rift valley and continued to accumulate through uplift of the floor to form the walls and adjacent orthogonal ridge during a period of about  $8 \cdot 10^5$  yr.

The duration of deposition of the hydrothermal manganese crusts is of the same order of magnitude at dredge stations TAG 1972-13 ( $2 \cdot 10^5$  yr) and TO-75AK61-1A ( $3 \cdot 10^5$  yr), in spite of the different distances from the axis of the rift valley at which the accumulation occurred. The similar duration of accumulation implies the operation of a process that may limit hydrothermal discharge at a given site adjacent to the rift valley to a period of the order of  $1 \cdot 10^5$  yr. It has been suggested that development of an impermeable sediment cover may suppress hydrothermal discharge on an oceanic ridge (Lister, 1972). However, our studies indicate that sediment cover is negligible in the area of the TAG Hydrothermal Field (Rona et al., 1976).

The observations presented of near-bottom water temperature, bottom photographs, and petrology, support the hypothesis that hydrothermal dis-

charge becomes suppressed at sites within the hydrothermal field when deposition of hydrothermal minerals seals off a portion of the discharge zone. Self-sealing by mineral precipitation is a mechanism that has been recognized to operate in certain geothermal systems on continents (Elder, 1966; Facca and Tonani, 1967; Helgeson, 1968; Elders and Bird, 1974; Batzle and Simmons, 1976). The temperature anomaly attributed to convective transfer of heat occurs where the wall of the rift valley is covered by talus, a porous and permeable material through which hydrothermal discharge from underlying faults can flow (Figs.1,2; profile X). Hydrothermal manganese oxide recovered near profile X occurs as a crust on basalt talus (Fig.1; dredge stations TAG 1972-13 and TAG 1973-3A; Rona et al., 1976, their table 3). A temperature anomaly was absent along profile Y (Fig.1), where a high proportion of breccia and pillow lava was photographed (Fig.2), materials which are impermeable to hydrothermal flow. Hydrothermal manganese oxide occurs as a crust on and matrix in breccia recovered near profile Y (Fig.1; dredge station TAG 1973-2A; Rona et al., 1976, their table 3). According to this interpretation, the breccia may form by alteration and cementation of the talus by concentrated hydrothermal activity.

#### CONCLUSIONS

A preliminary pattern of deposition of hydrothermal minerals at a locality along a divergent plate boundary is emerging from interdisciplinary studies of the TAG Hydrothermal Field. Two principal patterns may be discerned, that will require testing by more detailed studies at this and other localities:

(1) A pattern of deposition controlled by physical and chemical processes within a hydrothermal field. A major process is inferred to be sealing of interstices in talus by deposition of hydrothermal minerals from solutions discharged through underlying faults at and adjacent to the wall of the rift valley. The duration of accumulation of hydrothermal manganese oxide crusts determined at two sites (Fig.1; dredge stations TAG 1972-13, TO-75AK61-1A), indicates that the sealing process, inferred to involve the conversion of talus to breccia, occurs during a period of the order of  $1 \cdot 10^5$  yr. As the talus overlying fracture-focussed hydrothermal discharge becomes sealed, the zone of discharge gradually migrates to areas of unsealed talus. The migration of the hydrothermal discharge zone is probably controlled by the characteristics of the fracture system that focusses the flow. Consequently, the migration will follow the direction of faults at and near to the wall of the rift valley, which are primarily aligned parallel to the axis of the rift valley. Once sealed, the breccia may be fractured by tectonic forces opening the possibility of another generation of hydrothermal deposition; however, the fractured breccia probably would not regain the original porosity and permeability of the talus. An additional process that may suppress hydrothermal activity within the area of a hydrothermal field is off-axis intrusive and extrusive volcanism (Rona et al., 1976). The resulting pattern of hydrothermal mineral deposition within

the hydrothermal field would be expected to be a mosaic of hydrothermal deposits overlapping in time and space, partially covered by extrusive volcanic rocks, with a predominant fault-controlled trend parallel to the axis of the rift valley.

(2) A pattern of deposition of hydrothermal minerals controlled by sea-floor spreading encompassing an entire hydrothermal field. It was previously proposed (Rona, 1973; Rona et al., 1976) that a linear zone of relict hydrothermal deposits will extend along the direction of sea-floor spreading from an active depositional locality at a rift valley. The length of the linear zone would depend both on the continuity of sea-floor spreading and the persistence in time of the special structural and thermal conditions that concentrate the hydrothermal activity. The width of the linear zone of relict hydrothermal deposits would equal the width of the associated hydrothermal field, which is 10 km in the case of the TAG Hydrothermal Field. The relict hydrothermal manganese crust recovered 17 km in the direction of sea-floor spreading from the axis of the rift valley (Fig.1; dredge station TO-75AK61-1A), indicates that the special structural and thermal conditions that have concentrated hydrothermal activity at the TAG Hydrothermal Field have persisted during sea-floor spreading for at least  $1.4 \cdot 10^6$  yr. Off-axis extrusive volcanism, such as that evidenced at dredge stations TAG 1973-6A and TO-75AK59-1B (Fig.1), may cover linear zones of hydrothermal deposits that may extend along flow lines of sea-floor spreading.

#### REFERENCES

- ARCYANA, 1975. Transform fault and rift valley from bathyscaph and diving saucer. *Science*, 190: 108–116.
- Batzle, M.L. and Simmons, G., 1976. Microfractures in rocks from two geothermal areas. *Earth Planet. Sci. Lett.*, 30: 71–93.
- Bonatti, E., 1975. Metallogensis at oceanic spreading centers. *Annu. Rev. Earth Planet. Sci.*, 3: 401–431.
- Degens, E.T. and Ross, D.A. (Editors), 1969. *Hot Brines and Recent Heavy Metal Deposits in the Red Sea — A Geochemical and Geophysical Account*. Springer, New York, N.Y., 571 pp.
- Elder, J.W., 1966. Heat and mass transfer in the Earth: hydrothermal systems. *N.Z.D.S.I.R., Bull.*, 169: 115 pp.
- Elders, W.A. and Bird, D.K., 1974. Investigations of the Dunes geothermal anomaly, Imperial Valley, California, II. Petrological studies, presented at the International Symposium on Water–Rock Interaction of the International Union of Geochemistry and Cosmochemistry, Prague, 14 pp.
- Facca, G. and Tonani, F., 1967. The self-sealing geothermal field. *Bull. Volcanol.*, 30: 271.
- Helgeson, H.C., 1968. Geologic and thermodynamic characteristics of the Salton Sea geothermal system. *Am. J. Sci.*, 266: 129.
- Lattimore, R.K., Rona, P.A. and DeWald, O.E., 1974. Magnetic anomaly sequence in the central North Atlantic. *J. Geophys. Res.*, 79: 1207–1209.
- Lister, C.R.B., 1972. On the thermal balance of a mid-ocean ridge. *Geophys. J. R. Astron. Soc.*, 26: 515–535.
- McGregor, B.A. and Rona, P.A., 1975. Crest of Mid-Atlantic Ridge at 26°N. *J. Geophys. Res.*, 80: 3307–3314.

- Moore, W.S. and Vogt, P.G., 1976. Hydrothermal manganese crusts from two sites near the Galapagos spreading axis. *Earth Planet. Sci. Lett.*, 29: 349—356.
- Rona, P.A., 1973. Plate tectonics and mineral resources. *Sci. Am.*, 229 (1): 86—95.
- Rona, P.A., McGregor, B.A., Betzer, P.R. and Krause, D.C., 1975. Anomalous water temperatures over Mid-Atlantic Ridge crest at 26° north latitude. *Deep-Sea Res.*, 22: 611—618.
- Rona, P.A., Harbison, R.N., Bassinger, B.G., Scott, R.B. and Nalwalk, A.J., 1976. Tectonic fabric and hydrothermal activity of Mid-Atlantic Ridge crest (lat. 26°N). *Geol. Soc. Am. Bull.*, 87: 661—674.
- Scott, M.R., Scott, R.B., Rona, P.A., Butler, L.W. and Nalwalk, A.J., 1974. Rapidly accumulating manganese deposit from the median valley of the Mid-Atlantic Ridge. *Geophys. Res. Lett.*, 1: 355—358.
- Scott, R.B., Rona, P.A., McGregor, B.A. and Scott, M.R., 1974. The TAG hydrothermal field. *Nature*, 251: 301—302.
- Scott, R.B., Malpas, J., Rona, P.A. and Udintsev, G., 1976. Duration of hydrothermal activity at an oceanic spreading center, Mid-Atlantic Ridge (lat. 26°N). *Geology*, 4: 233—236.
- Spooner, E.T.C. and Fyfe, W.S., 1973. Sub-sea floor metamorphism, heat and mass transfer. *Contrib. Mineral. Petrol.*, 42: 287—304.
- Thompson, G., Woo, C.C. and Sung, W., 1975. Metalliferous deposits on the Mid-Atlantic Ridge. *Geol. Soc. Am. Abstr. Progr.*, 7: 1297—1298.

Reprinted from: Proc. of NOAA Marine Minerals Workshop, March 1976, 111-119.

Resource Research and Assessment of Marine Phosphorite  
and Hard Rock Minerals

Peter A. Rona  
National Oceanic and Atmospheric Administration  
Atlantic Oceanographic and Meteorological Laboratories

## INTRODUCTION

The National Oceanic and Atmospheric Administration (NOAA) is involved in six projects related to assessment of marine phosphorite and hard rock minerals (Table 1). NOAA involvement constitutes support through the Sea Grant Program of four of the projects (S-3, S-9, S-28, S-32), and actual implementation of two of the projects (M-4 and S-37, NOAA Metallogenesis). Brief summaries and a list of publications are presented for each of the six projects.

## PROJECT SUMMARIES

Evaluation and Economic Analysis of Southern California Phosphorites and Sand-Gravel Deposits (S-3).

The Principal Investigators of this project are Peter J. Fischer of California State University, Northridge, and Walter Mead of the University of California, Santa Barbara (Table 1). The project objective is to make a geological evaluation, integrated with economic and socio-economic assessment, of offshore and onshore sand and gravel and phosphorite deposits.

The assessment of the sand and gravel resource potential of the southern California shelf is nearing completion. The study extends from the Mexican border north to Point Conception, a distance of 460 km. Based upon preliminary estimates, the volume of unconsolidated shelf sediments is 26.5 km<sup>3</sup>. Economic studies are in progress to determine which, if any, of these deposits are viable resources.

With regard to phosphorite, a set of maps of the southern California continental borderland has been completed showing all available phosphorite resource data.

Undersea Mineral Survey of the Georgia Continental Shelf (S-9).

The Principal Investigator of this project is John Noakes of the University of Georgia. The project was completed in 1975, accomplishing the following:

1. The technique of neutron activation analysis using a Californium 252 neutron source has been applied to both

shipboard and in situ identification of elements in seafloor minerals.

2. Field tests have demonstrated the potential of using a mobile sled equipped with radiation detection equipment to locate and differentiate between thorium associated with heavy mineral deposits and uranium associated with phosphorites.

3. Over 300 miles of Georgia coastal area have been covered by reconnaissance surveys.

#### Lake Superior Copper Survey (S-28).

R. P. Meyer of the University of Wisconsin is the Principal Investigator of this project which was completed in 1975. Accomplishments of the project include the following:

1. Five areas adjacent to the copper producing area of the Keweenaw Peninsula were investigated and were identified as possible target areas for future development.

2. Bottom-towed and surface-towed resistivity arrays were successfully applied to the location of known copper-bearing veins and sand deposits with high heavy mineral content.

3. An active-source audiomagnetotelluric system with towed receivers successfully detected conductivity anomalies associated with known copper-bearing veins.

4. A first-order analytical method was developed to distinguish resistivity anomalies related to bottom topography from those due to changes in conductivity.

#### Marine Lode Minerals Exploration (S-32)

The Principal Investigator of this project is J. R. Moore of the Marine Research Laboratory of the University of Wisconsin. The project objective is to provide basic chemical, mineral, and textural exploration clues that will indicate the presence of sub-seafloor lode bodies, particularly ores of copper, lead, zinc, nickel, and barite. The project has already received cooperative assistance from Chromalloy Corp. and ASV Corp. for surveys at industry mining sites at Castle Island (barite) and Ellamar (copper), Alaska.

#### Coronado Bank Phosphorite Deposit (M-4)

The Principal Investigator of this project is B. B. Barnes of the former Marine Minerals Technology Center. The project was completed

in 1971, accomplishing the following:

1. A typical marine phosphorite deposit on Coronado Bank offshore southern California, was investigated to test equipment and techniques for phosphorite deposit delineation. The investigation included bathymetry, seismic reflection profiling, bottom photography, and dredging.
2. Areas of Coronado Bank that yielded the highest percentage of  $P_2O_5$  (nodules) were related to zones of deep weathering, fractures in the sea floor, and organic activity.

#### Metallogenesis at Dynamic Plate Boundaries (A-1)

In 1972 the NOAA Trans-Atlantic Geotraverse (TAG) project (P. A. Rona, Chief Scientist) of the Atlantic Oceanographic and Meteorological Laboratories (AOML), dredged hydrothermal manganese oxide crusts from the wall of the rift valley of the Mid-Atlantic Ridge at latitude 26° N. Subsequent multidisciplinary investigations including narrow-beam bathymetry, gravity, magnetics, bottom photography, near-bottom water temperature and chemistry measurements, dredging and coring revealed both active and relict hydrothermal manganese oxide deposits covering at least a 15 km square area, in and adjacent to the rift valley, that has been designated the TAG Hydrothermal Field.

The TAG Hydrothermal Field is hypothesized to be the discharge zone of a voluminous sub-seafloor hydrothermal convection system involving the circulation of seawater through oceanic crust driven by intrusive heat sources beneath the rift valley. From geochemical considerations and analogy with ophiolites, such as the Troodos Massif of Cyprus, massive copper - iron stratabound sulfide bodies, are inferred to underlie the hydrothermal manganese oxide crusts, although only disseminated sulfides have been sampled to date.

A new NOAA project, Metallogenesis at Dynamic Plate Boundaries (see A-1) is being proposed to increase understanding of the hydrothermal process of metal concentration in oceanic crust, to develop exploration criteria for both active and relict hydrothermal deposits in oceanic crust in situ and in ophiolites, and to determine the distribution of hydrothermal deposits in oceanic crust. The Principal Investigator of this project is P. A. Rona (AOML, Miami). Ophiolites, slices of oceanic crust formed about an oceanic ridge and incorporated into certain islands and continents are presently accessible to exploitation, and are being mined for base and precious metals at certain localities such as Cyprus.

TABLE 1.

NOAA Activities in Assessment of Marine  
Phosphorite and Hard Rock Minerals

<u>Project Identification*</u>	<u>Principal Investigator(s)</u>	<u>Title</u>	<u>Term</u>
S-3	P. J. Fischer and W. Mead	Evaluation and economic analysis of southern California's phosphorite and sand-gravel deposits	1975-76
S-9	J. Noakes	Undersea mineral survey of the Georgia continental shelf	1970-75
S-28	R. P. Meyer	Lake Superior copper survey	1971-75
S-32	J. R. Moore	Marine lode minerals exploration	1975-78
M-4	B. B. Barnes	Coronado Bank phosphorite deposit	1968-71
A-1	P. A. Rona	Metallogenesis at Dynamic Plate Boundaries	1976 (pursuant to work initia- in 1972) - 198

\* S - Sea Grant Program

\* M - Marine Minerals Technology Center

\* A - Atlantic Oceanographic and Meteorological Labs, NOAA



REFERENCES BY PROJECT (TABLE 1)

Evaluation and Economic Analysis of Southern California's  
Phosphorite and Sand-Gravel Deposits (S-3)

- Ashley, R., Berry, R., and Fischer, P.J., 1975, Geology of the northern continental shelf of the Santa Barbara Channel from Gaviota to El Capitan: in, Studies on the Geology of Camp Pendleton and Western San Diego County, California, p. 77-79.
- Ashley, R., Berry, R., and Fischer, P.J., 1976, Geology of the northern continental shelf of the Santa Barbara Channel from Gaviota to El Capitan: Journ. of Sedimentary Petrology, in press.
- Byrd, R., Berry, R., and Fischer, P.J., 1975, Quarternary geology of the San Diego - La Jolla Underwater Park: in, Studies on the geology of Camp Pendleton and Western San Diego County, California, p. 77-79 and p. 300.
- Drake, D., Kolpack, R., and Fischer, P.J., 1972, Sediment transport on the Santa Barbara - Oxnard shelf, Santa Barbara Channel, California: in, Swift, D.J.P., and others, editors, Shelf sediment transport: Dowden, Hutchinson and Ross, Inc., p. 307-331.
- Mead, W. J., 1969, and Sorensen, P.E., 1969, A new economic appraisal of marine phosphorite deposits: Marine Technology Society, The Decade Ahead.
- Mead, W. J., and Sorensen, P. E., 1970, The principal external costs and benefits of marine mineral recovery: Offshore Technology Conference, Proceedings, V. 1.
- Wilcox, S., Mead, W., and Sorensen, P.E., 1972, A preliminary estimate of the economic potential of marine placer mining: Marine Technology Society, Proceedings.

Undersea Mineral Survey of the Georgia Continental Shelf (S-9)

- Noakes, J. E. and Harding, J. L., 1971, New techniques on seafloor mineral exploration: Marine Technology Society, V. 5, No. 6, p. 41.
- Noakes, J. E., Harding, J.L., and Spaulding, J.D., 1974, Locating offshore mineral deposits by natural radioactive measurements: Marine Technology Society, V. 8, No. 5, p. 36-39.
- Noakes, J. E., Harding, J. L., Spaulding, J. D. and Fridge, D. S., Surveillance system for sub-sea survey and mineral exploration: Offshore Technology Conference, Paper 2239, p. 909-914.
- Noakes, J. E., Harding, J. L., Spaulding, J. D., and Hill, J., Radioactive monitoring of offshore nuclear power stations: Offshore Technology Conference, Paper OTC 1988, p. 501-506.
- Noakes, J. E., Smithwick, G., Harding, J. and Kirst, A., 1971, Undersea mineral analysis with Californium-252: Proceedings Am Nuclear Society Meeting, April.

Lake Superior Copper Survey (S-28)

- Brzozowy, C. P., 1973, Magnetic and seismic reflections surveys of Lake Superior: University of Wisconsin, Sea Grant College Technical Report WIS-SG-74-220, 40 pp.
- Goodden, J. J. P., 1973, Surveying the lake floor in search of underwater copper reserves to revive an ancient mining district, Keweenaw Peninsula, Northern Michigan: University of Wisconsin - Madison Marine Research Laboratory, Sea Grant Underwater Minerals Program, 7 pp.
- Goodden, J. J. P., 1974, Sedimentological aspects of underwater copper exploration in Lake Superior: University of Wisconsin - Madison, Master's Thesis.
- Meyer, R. P., Moore, J. R. and Nebrya, E., 1975, Underwater copper explorations in Lake Superior II: Specific targets charted in 1974: Offshore Technology Conference, Paper OTC 2291, 16 pp.

- Moore, J. R., Meyer, R. P., and Wold, R. J., 1972, Underwater copper exploration in Lake Superior - prospects mapped in 1971: Offshore Technology Conference, Paper OTC 1648, p. II - 307-322.
- Nebrija, E., Young, C., Meyer, R., and Moore, J. R., 1976, Electrical prospecting for copper veins in shallow water: Offshore Technology Conference, in press.
- Smith, P. A., and Moore, J. R., 1972, The distribution of trace metals in the surficial sediments surrounding Keweenaw Point, Upper Michigan: International Assoc. Great Lakes Res., Proc. 15th Conf. Great Lakes Res., p. 383-393; The University of Wisconsin Sea Grant College Reprint WIS-SG-73-341.
- Thornton, S. E., A shipboard geochemical prospecting technique for determining copper in Lake Superior sediments: University of Wisconsin, Sea Grant Underwater Minerals Program, 7 pp.
- Tuerkheimer, F. M., 1974, Copper mining from under Lake Superior: The legal aspects: Natural Resources Lawyer, Winter issue, p. 137-155, University of Wisconsin, Sea Grant College Reprint WIS-SG-74-354.

#### Marine Lode Minerals Exploration (S-32)

- Moore, J. R., and Welkie, C. W., 1975, Metal-bearing sediments of economic interest, coastal Bering Sea: Anchorage, Proc. Conference of the Alaska Geological Society, April.
- Moore, J. R., and Van Tassel, J., 1976, Exploration research for marine gold placers: Grantley Harbor - Tuksuk Channel region, Seward Peninsula, Alaska: Sea Grant Technical Report, in preparation.
- Panel on Operational Safety in Marine Mining, Moore, T. R., Chairman, 1975, Mining in the outer continental shelf and in the deep ocean: Washington, D.C., National Academy of Sciences, 119 pp.

- Otjen, R. P., 1975, Texture and composition of surficial sediments between Cape Horn and Rocky Point, Alaska: University of Wisconsin - Madison, M.S. Report, 89 pp.
- Owen, R. M., 1975, Sources and depositions of sediments in Chagvan Bay, Alaska: University of Wisconsin - Madison, Ph. D. Thesis, 201 pp.
- Welkie, C. J., 1976, Noble metals placer formation: An offshore processing conduit: University of Wisconsin - Madison, M.S. Thesis, in preparation.

#### Coronado Bank Phosphorite Deposit (M-4)

- Barnes, B. B., 1970, Marine phosphorite deposit delineation techniques tested on the Coronado Bank, Southern California: Offshore Technology Conference, Paper OTC 1259, p. II - 315-347.

#### Metallogenesis at Dynamic Plate Boundaries (A-1)

- Betzer, P. R., Bolger, G. W., McGregor, B. A., and Rona, P. A., 1974, The Mid-Atlantic Ridge and its effect on the composition of particulate matter in the deep ocean: EOS (Am. Geophys. Union Trans.), V. 55, No. 4, p. 293.
- McGregor, B. A. and Rona, P. A., 1975, Crest of Mid-Atlantic Ridge at 26° N: Jour. Geophys. Research, V. 80, p. 3307-3314.
- Rona, P. A., 1973, Plate tectonics and mineral resources: Scientific American, V. 229, #1, pp. 86-95.
- Rona, P. A., Harbison, R. H., Bassinger, B. G., Scott, R. B., and Nalwalk, A. J., 1976, Tectonic fabric and hydrothermal activity of Mid-Atlantic Ridge Crest (lat. 26° N): Geol. Soc. Am. Bull., V. 87, 661-674.

Rona, P. A., McGregor, B. A., Betzer, P. R., and Krause, D. C., 1975, Anomalous water temperatures over Mid-Atlantic Ridge Crest at 26° North latitude: Deep-Sea Research, V. 22, p. 611-618.

Scott, M. R., Scott, R. B., Rona, P. A., Butler, L.W., and Nalwalk, A. J., 1974, Rapidly accumulating manganese deposit from the median valley of the Mid-Atlantic Ridge: Geophysical Research Letters, V. 1, p. 355-358.

Scott, R. B., Rona, P. A., McGregor, B. A., Scott, M. R., 1974, the TAG hydrothermal field: Nature, V. 251, p. 301-302.

Reprinted from: *Special Volume of 'Annals of the Brazilian Academy of Sciences.'* *Anais Acad. Brasil Ciencias (Suplemento)*, Vol. 48, 256-274.

## SALT DEPOSITS OF THE ATLANTIC

PETER A. RONA

National Oceanic and Atmospheric Administration  
Atlantic Oceanographic and Meteorological Laboratories  
15 Rickenbacker Causeway, Miami, Florida 33149 U.S.A.

### ABSTRACT

The distribution in space and time of salt deposits beneath Atlantic continental margins and the adjacent ocean basin is presented in a map and synthesized in a table. Criteria for detecting the salt deposits are defined. The major features of the distribution of the salt deposits are summarized. The distribution of the salt deposits corresponds to the independently determined history of opening of the North Atlantic and South Atlantic.

### INTRODUCTION

The present paper reviews the occurrence of salt deposits beneath continental margins and the adjacent ocean basin around the Atlantic (Fig. 1). Major features of the distribution in space and time of Atlantic salt deposits are deduced from this review.

### DISTRIBUTION OF ATLANTIC SALT DEPOSITS

The distribution of salt deposits of the Atlantic is illustrated in Figure 1 and synthesized in Table 1. The location of each salt deposit and the association of salts present are listed in Table 1. Only those salt deposits that include halite (rock salt) are listed.

The mode of occurrence of the salt is specified in Table 1 as either diapirs or strata. Strata refers to beds of salt that may be undeformed or partially deformed. The thickness of salt

present is given where known from physical evidence (drilling, outcrop, seismic reflection and/or refraction). The thickness given is that of stratified deposits and not of diapirs. Theoretical computations are not used as evidence for thickness of a salt deposit. However, it is useful to recall that theoretical studies indicate that salt thicknesses of the order of hundreds of meters beneath a sedimentary overburden of at least 600 m are generally necessary to produce diapirism (Nettleton, 1934; Parker and McDowell, 1955).

Evidence for the occurrence of the salt deposits described in Table 1 derives from the distinctive physical and chemical properties of salt given in Table 2. Drilling and outcrops furnish direct evidence of the presence of salt deposits. Indirect evidence of the presence of salt deposits is furnished by the following methods:

1. Seismic reflection and refraction measurements based on density-velocity contrasts between salt and surrounding sediment.
2. Magnetic measurements based on the amagnetic properties of salt relative to surrounding sediment.
3. Gravity measurements based on the density differential between the salt and surrounding sediment. In practice, the density of salt deposits varies widely depending on the mass of associated caprock and other factors.

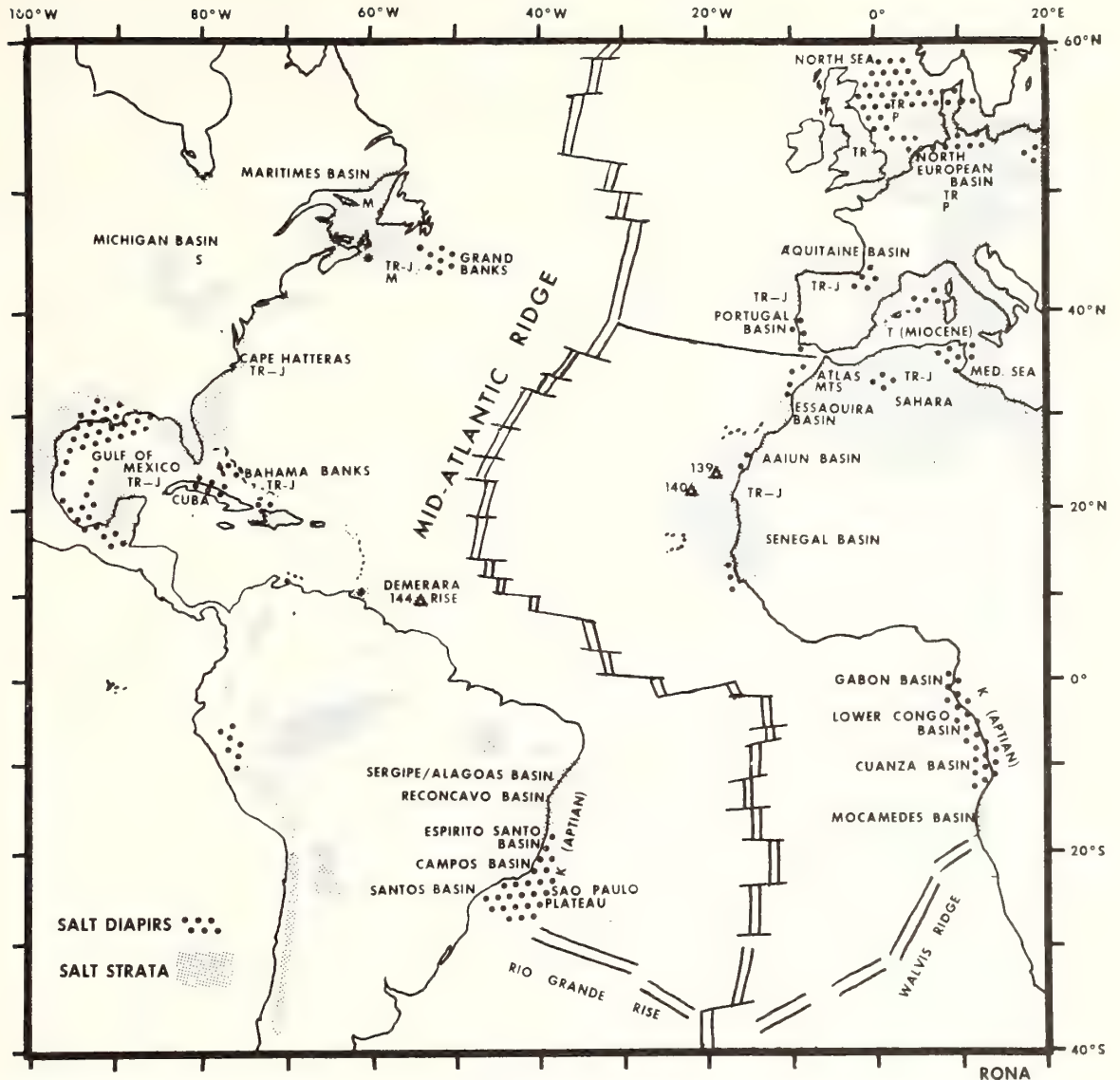


Fig. 1 — Distribution of Atlantic salt deposits. T: Tertiary period; K: Cretaceous period; J: Jurassic period; TR: Triassic period; M: Mississippian (Carboniferous) period; S: Silurian period; DSDP 139, 140, 144: Deep Sea Drilling Project sites

4. Thermal gradient measurements based on the high conductivity of salt relative to surrounding sediment.
5. Salinity and chlorinity gradient measurements of interstitial water in unconsolidated sediment over salt deposits based on the high solubility of certain salts, especially halite, in water. The measured salinity gradients are given in Table 1 in parts per thousand (ppt).

Seismic, magnetic, and gravity measurements alone may be inadequate to unambiguously dis-

tinguish diapirs of salt from diapirs of mud or igneous rock. Thermal gradient and salinity measurements used in conjunction with the other geophysical methods can distinguish salt diapirs from those of other materials.

Salinity gradients in interstitial water of unconsolidated sediment have been effectively used by the Deep Sea Drilling Project to indicate the presence of both salt diapirs and strata beneath the seabed (Manheim et al., 1973). As a consequence of the solubility of halite and rapid rates of ionic diffusion, vertical salinity

TABLE 1. SALT DEPOSITS OF THE ATLANTIC (FIG. 1).

LOCATION	SALT	OCCURRENCE	ESTIMATED THICKNESS	EVIDENCE	AGE	CRITERIA	REFERENCES
Maritimes basin	Halite, anhydrite, minor sylvite, carnallite	Diapirs and strata	270 m (minimum)	Drilling; outcrop; seismic	Mississippian (Windsor)	Stratigraphic relations	Gussow, 1953; Bell, 1958; Howie and Cumming, 1963; Belt, 1965; Evans, 1967; Bliggood, 1969; Evans, 1970.
Scotian Shelf	Halite, anhydrite	Diapirs and strata	760 m (Argo)	Drilling; seismic	Mississippian (Windsor); Late Triassic and Jurassic (Argo)	Regional geology, stratigraphic relations	King and McLean, 1970; Keen, 1970; Pamerter, 1971; McIver, 1972; Webb, 1973.
Grand Banks	Halite, anhydrite	Diapirs and strata	350 m (Windsor)	Drilling; seismic	Mississippian (Windsor); Late Triassic and Jurassic	Palynology of caprock	Watson and Johnson, 1970; Bartlett and Smith, 1971; Offshore Exploration Staffs, 1974.
Michigan basin	Halite, anhydrite	Strata	500 m (maximum)	Drilling; seismic	Late Silurian (Salina formation)	Stratigraphic relations	Landes, 1945; Landes, <i>et al.</i> , 1945.
Atlantic Continental Margin, USA	Halite, anhydrite, gypsum	Strata and possible diapirs	Unknown	Stratigraphy; seismic; salinity gradients	Late Triassic and Jurassic	Regional geology	Manheim and Horn, 1968; Rona, 1970; Emery <i>et al.</i> , 1970; Maher and Appin, 1971; Sheridan, 1974; Matlick <i>et al.</i> , 1974; Olson, 1974.
Gulf of Mexico	Halite, minor gypsum, anhydrite	Diapirs and strata	3 km	Drilling; salinity gradients seismic	Late Triassic through Middle Jurassic	Palynology of salt and caprock; stratigraphic relations.	Jux, 1961; Murray, 1968; Bunk <i>et al.</i> , 1969; Manheim and Sayles, 1970; Kirkland and Gerhard, 1971; Antoine <i>et al.</i> , 1974.
Cuba	Halite, anhydrite, gypsum	Diapirs	2 to 5 km	Drilling; seismic	Late Triassic (Rhaetic) to Late Jurassic (Callovian)	Palynology of interbedded shale	Meyerhoff and Hatten, 1958.
Baham Banks	Halite, anhydrite, gypsum	Diapirs and probable strata	Unknown	Seismic	Late Triassic and Jurassic	Regional Geology	Ball <i>et al.</i> , 1971, 1974.
Demerara Rise	Halite	Strata	Unknown	Salinity gradient (DSDP Site 144; 36.8 to 41.8 ppt)	Unknown		Waterman <i>et al.</i> , 1972.



LOCATION	SALT	OCCURRENCE	ESTIMATED THICKNESS	EVIDENCE	AGE	CRITERIA	REFERENCES
Sergipe-Alagoas, Recôncavo, Espírito Santo, Campos, and Santos basins	Halite, gypsum, anhydrite	Diapirs and strata	500 m	Drilling; seismic	Aptian	Ostracod fauna in associated strata	Krömmelbein and Wenger, 1966; Viana, 1966, 1971; Fonseca, 1966; Campos <i>et al.</i> , 1974.
São Paulo Plateau	Halite,	Diapirs	Unknown	Thermal and salinity (34 to 50 ppt) gradients; seismic	Aptian	Regional geology	Butler, 1970; Leyden <i>et al.</i> , 1975.
Mocâmedes basin	Gypsum, anhydrite	Strata	100 m	Drilling; seismic	Aptian	Stratigraphic relations	Reyre, 1966 a, b.
Cuanza, Lower Congo, and Gabon basin; onshore portions	Halite, carnallite, sylvinite, anhydrite, gypsum	Diapirs and strata	Cuanza: 500 to 750 m Lower Congo: 700 to 1000 m Gabon: 200 to 2000 m	Drilling; seismic	Aptian	Ostracod fauna in associated strata	Belmonte <i>et al.</i> , 1965; Reyre, 1966 a, b; Brognon and Verrier, 1966; Krömmelbein and Wenger, 1966.
Cuanza, Lower Congo, and Gabon basins; offshore portions	Halite	Diapirs	2 to 3 km	Thermal and salinity (DSDP sites 364; 365; 35-122 ppt) gradients; seismic	Aptian	Regional geology; stratigraphic relations	Baumgartner and van Andel, 1971; Von Herzen <i>et al.</i> , 1972; Leyden <i>et al.</i> , 1972; Pautot <i>et al.</i> , 1973; Scientific Party, 1975.
Senegal basin	Halite, minor anhydrite, gypsum	Diapirs	1.5 to 3 km	Drilling; seismic	Late Triassic (Keuper) and early Jurassic (Lias)	Palynology of salt	Aymé, 1965; Templeton, 1971.
Aaiun basin	Halite	Diapirs and strata	700 m	Drilling; seismic	Late Triassic and possibly early Jurassic	Stratigraphic relations	Querol, 1966; Reyre, 1966 a, b.
Offshore Northwest Africa	Halite	Strata and possible diapirs	Unknown	Salinity gradients (DSDP sites 139; 140)	Late Triassic and early Jurassic	Regional geology	Rona, 1969, 1970; Schneider and Johnson, 1970; Waterman <i>et al.</i> , 1972.

LOCATION	SALT	OCCURRENCE	ESTIMATED THICKNESS	EVIDENCE	AGE	CRITERIA	REFERENCES
Essaouira basin	Halite	Diapirs and strata	1200 m (maximum)	Drilling; seismic	Late Triassic and early Jurassic	Stratigraphic relations	Société Chérienne des Pétroles, 1966; Reyre, 1966 a, b.
Atlas Mountains of North Africa	Halite, gypsum	Diapirs and strata	Unknown	Outcrop	Triassic	Stratigraphic relations	La Coste, 1934.
Algerian Sahara	Halite, anhydrite	Diapirs and strata	800 to 1600 m	Drilling; outcrop; seismic	Late Triassic (Keuper) and early Jurassic (Lias)	Associated stratigraphic; brachiopod fauna in carbonates interbedded with salt.	Eurolet and Dumestre, 1952; De-maison, 1965.
Western Mediterranean	Halite, anhydrite	Diapirs and strata	1200 m (maximum) halite overlain by 600 m anhydrite, gypsum, marl	Drilling (DSDP); seismic	Upper Miocene (Messinian)	Stratigraphic relations; nannofossils and microfossils in strata overlying and interbedded with anhydrite and gypsum	Auzende <i>et al.</i> , 1971; Mauffret <i>et al.</i> , 1973; Ryan <i>et al.</i> , 1973; Biju-Duval <i>et al.</i> , 1974.
Portugal basin	Halite	Diapirs and strata	Unknown	Drilling; seismic	Triassic and early Jurassic	Stratigraphic relations	Montadert <i>et al.</i> , 1974.
Pyrenees, Cantabrian, Andalusian mountains of Spain	Halite, gypsum, anhydrite	Diapirs	500 m	Drilling; seismic	Late Triassic (Keuper)	Stratigraphic relations	Brinkmann and Lögters, 1968.
Aquitaine basin	Halite, anhydrite	Diapirs and strata	800 m	Drilling; seismic	Late Triassic (Keuper) and early Jurassic (lower Lias)	Stratigraphic relations	Dupouy-Carnet, 1953; Bonnard <i>et al.</i> , 1958; Winnock, 1973.

LOCATION	SALT	OCCURRENCE	ESTIMATED THICKNESS	EVIDENCE	AGE	CRITERIA	REFERENCES
North European basin	Halite, potash salts	Diapirs and strata	800 to 1000 m (Zechstein)	Drilling; seismic	Late Permian (Zechstein); Late Triassic (Keuper)	Stratigraphic relations	Beitz, 1958; Sannemann, 1968.
North Sea	Halite, anhydrite, gypsum	Diapirs and strata	100 to 1500 m (Zechstein)	Drilling; seismic	Late Permian (Zechstein); Late Triassic (Keuper)	Stratigraphic relations	Kent, 1969; Ziegler, 1975.
British Isles	Halite, anhydrite, gypsum	Strata and possible diapirs	50 to 1000 m	Drilling; seismic	Late Triassic (Keuper)	Stratigraphic relations	Audley-Charles, 1970.

COMPOSITION	DENSITY gm per cc	Vp km/sec	THERMAL CONDUCTIVITY 10 <sup>-3</sup> cal per cm sec °C	SOLUBILITY gm per 100 ml of cold water	MAGNETIC SUSCEPTIBILITY cgs emu per cm <sup>3</sup>
Halite	2.16	4.3-4.4	12-17	35.7	0
Anhydrite	2.9	4.1-5.0	12-13	0.209	0
Gypsum	2.32	2.0-3.5	3	0.241	0
Sylvite	1.99	4.4-6.5	—	34.7	0
Carnallite	1.61	4.4-6.5	—	64.5	0
Unconsolidated sediment (wet)	1.5	1.5-2.0	1.9-2.7	insoluble	10-5-1

TABLE 2. PROPERTIES OF SALT (HODGEMAN ET AL., 1963; CLARK, 1966)

gradients may develop over halite deposits through several kilometers of water-saturated unconsolidated sediment overburden (Manheim, 1970). The horizontal salinity gradients that develop are approximately equal to the vertical salinity gradients, so that the distribution of vertical salinity gradients delineates the horizontal extent of an underlying salt deposit (Manheim and Bischoff, 1969).

The ages of the salt deposits listed in Table 1 are based on various criteria, in order of increasing reliability:

1. Stratigraphic relations: The stratigraphic position of salt strata or the base of salt diapirs in a known stratigraphic sequence.
2. Associated strata: Paleontologic or radiogenic dating of strata associated with stratified salt or incorporated in salt diapirs.
3. Caprock: Palynologic dating of the caprock of a salt diapir.
4. Salt: Palynologic dating of the salt of diapirs or strata.

#### MAJOR FEATURES OF THE DISTRIBUTION OF ATLANTIC SALT DEPOSITS

The information presented in Figure 1 and Table 1 on the distribution of Atlantic salt deposits is probably incomplete. Salt deposits are generally detected in their most spectacular manifestation as diapirs. Extensive areas of relatively thick salt strata may remain undetected beneath Atlantic continental margins and the adjacent ocean basin. For example, layers of competent materials such as carbonates and basalt flows and sills may suppress diapirism and mask underlying salt beds. However, major features of the distribution of Atlantic salt deposits may be deduced from Figure 1 and Table 1, as follows:

- I. Salt deposits are present along those rifted portions of the continental margins of North America, South America, Africa, and Eurasia that trend nearly perpendicular to fracture zones of the Atlantic ocean basin.
- II. Salt deposits are absent along those sheared portions of the equatorial continental margins of South America and Africa that trend nearly parallel to fracture zones of the Atlantic ocean basin.
- III. Salt deposits are absent in the South Atlantic south of the Rio Grande Rise and the Walvis Ridge.
- IV. The salt deposits of the rifted continental margins appear to extend continuously in basins opening seaward from the continents to the deep ocean basin.
- V. The farthest seaward known extent of salt deposits in the Atlantic is beneath the lower continental rise off northwest Africa at least 450 km from the coast, as predicted from geophysical measurements (Rona, 1969, 1970) and confirmed by measurement of salinity gradients (DSDP sites 139, 140; Waterman et al., 1972). Salt deposits beneath the São Paulo Plateau extend 700 km seaward from the coast. According to continental drift reconstructions of the Mesozoic opening of the Atlantic (Dietz and Holden, 1970), the extent of salt deposits off northwest Africa represents a half-width of opening. The extent of salt deposits of the São Paulo Plateau represents a full-width of opening.
- VI. Atlantic salt deposits exhibit a systematic distribution in time and space, as follows:
  1. Late Silurian period: Eastern North America including the Michigan basin.
  2. Mississippian period: Northwestern Atlantic including the Maritimes basin, Scotian shelf, and Grand Banks.
  3. Late Permian period: Northeastern Atlantic including the North European basin and the North Sea.
  4. Late Triassic and Jurassic periods:
    - a. North Atlantic including the Grand Banks, Scotian shelf, Atlantic continental margin of North America, Cuba, Bahama Banks, Senegal basin, Aaiun basin, offshore northwestern Africa, Essaouira basin, Portugal basin, Aquitaine basin, North European basin, North Sea, and British Isles.
    - b. Gulf of Mexico.
    - c. Mediterranean region including the Atlas Mountains and the Algerian Sahara.
  5. Aptian stage of the Cretaceous period: South Atlantic including the southeastern continental margin of South America (Sergipe/Alagoas, Recôncavo, Espirito Santo, Campos, and Santos basins), and the southwestern continental margin of Africa (Moçâmedes, Cuanza, Lower Congo, and Gabon basins).

6. Miocene epoch of the Tertiary period: Western Mediterranean Sea.
  7. The age and geographic relations of inferred salt deposits beneath the Demerara Rise off the northeastern continental margin of South America remain problematic.
- VII. Salt deposits of two different ages separated by intervals of nonsaliferous sediments are superposed in at least two regions of the North Atlantic:
1. Mississippian and Late Triassic through Jurassic salt deposits are superposed in the Scotian shelf-Grand Banks region.
  2. Late Permian and Late Triassic salts are superposed in the North European basin — North Sea region.
- VIII. The distribution of Atlantic salt deposits in space and time (Fig. 1; Table 1) is genetically related to the independently

determined history of opening of the North Atlantic in the Late Triassic and Jurassic (Rona, 1969, 1970; Schneider and Johnson, 1970; Pautot et al., 1970; Olson and Leyden, 1973), and the opening of the South Atlantic in the Early Cretaceous (Belmonte et al., 1965; Campos et al., 1974).

#### ACKNOWLEDGEMENTS

I thank Professor F. F. M. de Almeida, other members of the Organizing Committee, Professor H. Martin, and the Brazilian Academy of Sciences for the opportunity to participate in the International Symposium on Continental Margins of Atlantic Type. The research was supported by the National Oceanic and Atmospheric Administration (NOAA) as part of the Trans-Atlantic Geotraverse (TAG) project.

#### REFERENCES

- ANTOINE, J. W., MARTIN, R., PYLE, T., and BRYANT, W. R. — 1974 — Continental margins of the Gulf of Mexico, in Burk, C. A., and Drake, C. L., *Geology of continental margins*. New York, Springer Verlag, 1009 pp., pp. 683-694.
- AUDLEY-CHARLES, M. G. — 1970 — Triassic paleogeography of the British Isles. *Geol. Soc. London Quart. Jour.*, v. 126, pp. 49-90.
- AUZENDE, J. M., BONNIN, J., OLIVET, J. O., PAUTOT, G., and MAUFFRET, A. — 1971 — Upper Miocene salt layer in the Western Mediterranean basin. *Nature Phys. Sci.*, v. 230, pp. 82-84.
- AYME, J. M. — 1965 — The Senegal salt basin, in *Salt Basins Around Africa*, London, Institute of Petroleum, 112, pp., pp. 83-90.
- BALL, M. M., BOCK, W., HARRISON, C. G. A., NAGLE, F., JR., and WILLIAMS, G. J. — 1974 — Diapirs of the Old Bahama Channel. *EOS, Amer. Geophys. Union Trans.*, v. 55, pp. 284.
- BALL, M. M., DASH, B. P., HARRISON, C. G. A., and AHMED, K. O. — 1971 — Refraction seismic measurements in the northeastern Bahamas (abs.). *EOS, Trans. Amer. Geophys. Union*, v. 52, n. 4, pp. 252.
- BARTLETT, G. A., and SMITH, L. — 1971 — Mesozoic and Cenozoic history of the Grand Banks of Newfoundland. *Canadian Jour. Earth Sci.*, v. 8, n. 1, pp. 65-84.
- BAUMGARTNER, T. R., and VAN ANDEL, T. H. — 1971 — Diapirs of the continental margin of Angola, Africa. *Geol. Soc. America Bull.*, v. 82, pp. 793-802.
- BELL, W. A. — 1958 — Possibilities for occurrences of petroleum reservoirs in Nova Scotia Dept. Mines, 277 pp.
- BELMONTE, Y., HIRTZ, P., and WENGER, R. — 1965 — The salt basins of the Gabon and the Congo (Brazzaville). A tentative paleogeographic interpretation, in *Salt Basins Around Africa*. London, Institute of Petroleum, 112 pp., pp. 55-74.
- BELT, E. S. — 1965 — Stratigraphy and paleogeography of Mabou Group and related Middle Carboniferous facies, Nova Scotia, Canada. *Geol. Soc. America Bull.*, v. 76, pp. 777-802.
- BIDGOOD, D. E. T. — 1969 — The distribution and diapiric nature of some Nova Scotia evaporites — a geophysical evaluation, 3rd Symp. on Salt, Cleveland, Ohio.
- BENZ, A. — 1958 — Relations between oil fields and sedimentary troughs in Northwest German Basin, in Weeks, L. D., editor, *Habitat of Oil*. Tulsa, Amer. Assoc. Petroleum Geologists, 1384 pp., pp. 1054-1066.
- BIJU-DUVAL, B., LETOUZEY, J., MONTADERT, L., COURRIER, P., MUGNIOT, J. F., and SANCHO, J. — 1974 — Geology of the Mediterranean Sea basins, in Burk, C. A., and Drake, C. L. editors, *The geology of continental margins*. New York, Springer-Verlag, 1009 pp., pp. 695-721.
- BONNARD, E., DEBOURLE, A., HLAUSCHEK, H., MICHEL, P., PEREBASKINE, V., SCHOEFFLER, J., SERONIE-VIVIEN, R., and VIGNEAUX, M. — 1958 — The Aquitanian basin, southwest France, in Weeks, L. G., editor, *Habitat of Oil*. Tulsa, Amer. Assoc. Petroleum Geologists, 1384 p., pp. 1091-1122.
- BRINKMANN, R., and LÖGTERS, H. — 1968 — Diapirs in Western Pyrenees and foreland Spain, in Brauns-teiw, J., and O'Brien, G. D., *Diapirism and diapirs.. a symposium*. Tulsa, Amer. Assoc. Petroleum Geologists, Memoir 8, 444p., pp. 275-292.
- BROGNON, G. P., and VERRIER, G. R. — 1966 — Oil and geology in Cuanza basin of Angola, Amer. Assoc. Petroleum Geologists Bull., v. 50, pp. 108-158.
- BURK, C. A., EWING, M., WORZEL, J. L., BEALL, A. O., JR., BERGGREN, W. A., BUKRY, D., FISCHER, A. G., and PESSAGNO, E. A., JR. —

- 1969 — Deep-sea drilling into the Challenger Knoll, central Gulf of Mexico. *Amer. Assoc. Petroleum Geologists Bull.*, v. 53, pp. 1338-1347.
- BUROLLET, P., and DUMESTRE, A. — 1952 — Le diapir du Djebel Rhoëuis. Algeria, 19th International Geological Congress, S.2, p. 6.
- BUTLER, L. W. — 1970 — Shallow structure of the continental margin, southern Brazil and Uruguay. *Geol. Soc. America Bull.*, v. 81, pp. 1079-1096.
- CAMPOS, C. W. M., PONTE, F. C., MIURA, K. — 1974 — Geology of the Brazilian continental margin, in Burk, C. A., and Drake, C. L., editors, *The geology of continental margins*. New York, Springer-Verlag, 1009 pp., pp. 447-461.
- CLARK, S. O., JR., editor — 1966 — *Handbook of physical constants*: Geol. Soc. America, Memoir 97, 587 pp.
- DEMAISON, G. J. — 1965 — The Triassic Salt in the Algerian Sahara, in *Salt basins around Africa*. London, Institute of Petroleum, 122 pp., pp. 91-100.
- DIETZ, R. S. and HOLDEN, J. C. — 1970 — Reconstruction of Pangaea. Breakup and dispersion of continents, Permian to present. *Jour. Geophys. Res.*, v. 75, pp. 4939-4956.
- DUPOUY-CAMET, J. — 1953 — Triassic diapiric salt structures, southwestern Aquitaine basin, France. *Amer. Assoc. Petroleum Geologists Bull.*, v. 37, pp. 2348-2388.
- EMERY, K. O., UCHUPI, S., PHILLIPS, J. D., BOWEN, C. O., BUNCE, E. T., and KNOTT, S. T. — 1970 — Continental rise off eastern North America. *Amer. Assoc. Petroleum Geologists*, v. 54, pp. 44-108.
- EVANS, R. — 1970 — Sedimentation of the Mississippian evaporites of the Maritimes: an alternative model. *Canadian Jour. Earth Sci.*, v. 7, pp. 1349-1352.
- FONSECA, J. I. — 1966 — Geological outline of the Lower Cretaceous Bahia supergroup, in Van Hinte, J. E., ed., *Proc. 2nd West African Micropaleontological Colloquium*, Ibadan, pp. 49-71.
- GUSSOW, W. C. — Carboniferous stratigraphy and structural geology of New Brunswick, Canada. *Amer. Assoc. Petroleum Geologists Bull.*, v. 37, pp. 1713-1816.
- HODGMAN, C. D., WEAST, R. C., SHANKLAND, R. S., and SELBY, S. M., editors — 1963 — *Handbook of chemistry and physics*. Cleveland, Ohio, The Chemical Rubber Pub. Co., 3604 pp.
- HOWIE, R. O., and CUMMING, L. M. — 1963 — Basement features of the Canadian Appalachians. *Geol. Surv. Canada, Bull.* n. 89, 18 pp.
- JUX, V., 1961 — The palynologic age of diapiric and bedded salt in the Gulf coastal province. *Louisiana Geol. Survey, Geol. Bull.* 38, 46 pp.
- KEEN, M. J. — 1970 — A possible diapir in the Laurentian Channel. *Canadian Jour. Earth Sci.*, v. 7, pp. 1561-1564.
- KENT, P. E. — 1969 — The geological framework of petroleum exploration in Europe and North Africa and the implications of continental drift hypotheses, in Hepple, P., editor, *The exploration for petroleum in Europe and North Africa*. London, Institute of Petroleum, pp. 3-17.
- KING, L. H., and MAC LEAN, B. — 1970 — A diapiric structure near Sable Island-Scotian shelf. *Maritime Sediments*, v. 6, pp. 1-4.
- KIRKLAND, D. C., and GERHARD, J. E. — 1971 — Jurassic salt, central Gulf of Mexico, and its temporal relation to circum-Gulf evaporites. *Amer. Assoc. Petroleum Geologists Bull.*, v. 55, pp. 680-686.
- KRÖMMELBEIN, K., and WENGER, R. — 1966 — Sur quelques analogies remarquables dans les microfaunes crétacées du Gabon et du Brésil Oriental (Bahia et Sergipe), in Reyre, D., editor, *Sedimentary basins of the African coasts, Part 1, Atlantic Coast*. Paris, Association of African Geological Surveys, 304 pp., pp. 193-196.
- LACOSTE, J. — 1934 — Études géologiques dans le Rif Meridional. Protectorat Repub. Française au Maroc, Serv. Mines, Notes et Mem. 31 and 32, v vols., 660 pp.
- LANDES, K. K., EHLERS, G. M., and STANLEY, G. M. — 1945 — Geology of the MacKinac Straits Region. *Michigan Geol. Survey, Pub.* 44, *Geol. Ser.* 37, pp. 192.
- LANDES, K. K. — 1945 — Preliminary map n° 40, The Salina and Bass Island rocks in the Michigan basin. U. S. Geol. Survey, Oil and Gas Inv.
- LEYDON, R., BRYAN, G., and EWING, M. — 1972 — Geophysical reconnaissance on African shelf: 2. Margin sediments from Gulf of Guinea to Walvis Ridge. *Amer. Assoc. Petroleum Geologists Bull.*, v. 56, pp. 682-693.
- LEYDEN, R., DAMUTH, J. E., ONGLEY, L. K., KOSTECKI, J., and VAN STEVENICK, W. — 1975 — Salt diapirs on the São Paulo Plateau, Brazilian continental margin. *Geol. Soc. America, Abstracts with programs*, v. 7, n. 7, 1350 pp., pp. 1168-1169.
- MAHER, J. C., and APPLIN, E. R. — 1971 — Geologic framework and petroleum potential of the Atlantic coastal plain and continental shelf. U. S. Geol. Survey Prof. Paper 659, 98 pp.
- MANHEIM, F. T., and BISHOFF, J. L. — 1969 — Geochemistry of pore waters from Shell Oil Company drill holes in the continental slope of the northern Gulf of Mexico. *Chemical Geol.*, v. 4, pp. 63.
- MANHEIM, F. T., SAYLES, F. L., and WATERMAN, L. S. — 1973 — Interstitial water studies on small core samples, Deep-Sea Drilling Project: Leg 10, in Worzel, J. L., Bryant, W., et al., *Initial Reports of the Deep Sea Drilling Project*, v. 10. Washington, D. C., U. S. Government Printing Office, 748, pp. 615-623.
- MANHEIM, F. T., and HORN, M. K. — 1968 — Composition of deeper subsurface waters along the Atlantic continental margin. *Southeastern Geology*, v. 9, pp. 215-236.
- MATTICK, R. E., FOOTE, R. Q., WEAVER, N. L., and GRIM, M. S. — 1974 — Structural framework of United States Atlantic outer continental shelf north of Cape Hatteras. *Amer. Assoc. Petroleum Geologists Bull.*, v. 58, Part II of II, pp. 1179-1190.
- MAUFFRET, A., FAIL, J. P., MONTADERT, L., SANCHO, J., and WINNOCK, E. — 1973 — Northwestern Mediterranean sedimentary basin from seismic reflection profile. *Amer. Assoc. Petroleum Geologists Bull.*, v. 57, pp. 2245-2262.
- MC IVER, N. L. — 1972 — Cenozoic and Mesozoic stratigraphy of the Nova Scotia shelf. *Canadian Jour. Earth Sci.*, v. 9, pp. 54-70.

- MEYERHOFF, A. A., and HATTEN, C. W. — 1968 — Diapiric structures in central Cuba, in Braunstein, J., and O'Brien, G. D., editors, Diapirism and diapirs, a symposium. Tulsa, Amer. Assoc. Petroleum Geologists, Memoir 8, 444 pp., pp. 315-357.
- MONTADERT, L., WINNOCK, E., DELTEIL, J. R., and GRAU, G. — 1974 — Continental margins of Galicia-Portugal and Bay of Biscay, in Burk, C. A., and Drake, C. L., editors, The geology of continental margins. New York, Springer-Verlag, 1009 pp., pp. 323-342.
- MURRAY, G. E. — 1968 — Salt structures of Gulf of Mexico basin — a review, in Braunstein, J., and O'Brien, G. D., editors, Diapirism and diapirs, a symposium. Tulsa, Amer. Assoc. Petroleum Geologists, Memoir 8, 444 pp., pp. 99-121.
- NETTLETON, L. L. — 1934 — Fluid mechanics of salt domes. Amer. Assoc. Petroleum Geologists Bull., v. 18, pp. 1175-1204.
- OFFSHORE EXPLORATION STAFFS, AMOCO CANADA PETROLEUM COMPANY LTD., AND IMPERIAL OIL LTD. — 1974 — Regional geology of Grand Banks. Amer. Assoc. Petroleum Geologists, v. 58, Pt. II of II, pp. 1109-1123.
- OLSON, W. S., and LEYDEN, R. J. — 1973 — North Atlantic rifting in relation to Permian-Triassic salt deposition; in Logan, A., and Mills, L. V. editors, The Permian and Triassic systems and their mutual boundary. Canadian Soc. Petroleum Geologists, Memoir 2, 766, pp., 720-732.
- OLSON, W. S. — 1974 — Structural history and oil potential of offshore area from Cape Hatteras to Bahamas. Amer. Assoc. Petroleum Geologists Bull., v. 58, Part II of II, pp. 1191-1200.
- PARKER, T. J., and MC DOWELL, A. N. — 1955 — Model studies of salt-dome tectonics. Amer. Assoc. Petroleum Geologists Bull., v. 39, pp. 2384-2470.
- PAMENTER, B. — 1971 — Sands aplenty in Onondaga well. Oilweek, 22 November, pp. 22-24.
- PAUTOT, G., AUZENDE, J. M., and LE PICHON, X. — 1970 — Continuous deep salt layer along North Atlantic margins related to early phase of rifting. Nature, v. 227, pp. 351-354.
- QUEROL, R. — 1966 — Regional geology of the Spanish Sahara, in Reyre, D., editor, Sedimentary basins of the African coasts, Part I, Atlantic coast. Paris, Association of African Geological Surveys, 304 pp., pp. 27-38.
- REYRE, D. — 1966 a — Particularités géologiques des Bassines de l'Ouest African (essai de recapitulation), in Reyre, D., editor, Sedimentary basins of the African coasts, Part I, Atlantic coast. Paris, Association of African Geological Surveys, 304 pp., pp. 253-304.
- REYRE, D. — 1966 b — Récapitulation générale: Les formations permienues, Triassiques, Jurassiques et Crétacées dans les bassins côtiers Ouest-Africains, in Reyre, D., editor, Sedimentary basins of the African coasts, Part I, Atlantic coast. Paris, Association of African Geological Surveys, 304 pp., 3 tables.
- RONA, P. A. — 1969 — Possible salt domes in the deep Atlantic off North-west Africa. Nature, v. 224, pp. 141-143.
- RONA, P. A. — 1970 — Comparison of continental margins of eastern North America at Cape Hatteras and northwestern Africa at Cap Blanc. Amer. Assoc. Petroleum Geologists Bull., v. 54, pp. 129-157.
- RYAN, W. B. F., HSU, K. J., *et al.* — 1973 — Initial reports of the Deep Sea Drilling Project, v. XIII, Parts 1 and 2. Washington, D. C., U. S. Gov't Printing Office, 1447 pp.
- SANNEMANN, D. — 1968 — Salt-stock families in northwestern Germany, in Braunstein, J., and O'Brien, G. D., editors, Diapirism and diapirs, a symposium. Tulsa, Amer. Assoc. Petroleum Geologists, Memoir 8, 444 pp., pp. 261-270.
- SCHNEIDER, E. D., and JOHNSON, G. L. — 1970 — Deep-ocean diapir occurrences. Amer. Assoc. Petroleum Geologists, v. 54, pp. 2151-2169.
- SCIENTIFIC PARTY — 1975 — Basins and margins of the eastern South Atlantic, Leg 40 of the Deep Sea Drilling Project. Geotimes, v. 20, n. 6, pp. 22-24.
- SHERIDAN, R. E. — 1974 — Atlantic continental margin of North America in Burk, C. A., and Drake, C. L., editors, The geology of continental margins. New York, Springer-Verlag, 1009 pp., pp. 391-407.
- SOCIÉTÉ CHÉRIFIENNE DES PETROLES — 1966 — Le bassin du sud-ouest Marocain, in Reyre, D., editor, Sedimentary basins of the African coasts, Part I, Atlantic coast. Paris, Association of African Geological Surveys, 304 pp., pp. 5-12.
- SWAIN, F. M. — 1952 — Ostracoda from wells in North Carolina. 2. Mesozoic ostracoda. U. S. Geol. Survey, Prof. Paper 234-B, pp. 59-192.
- TEMPLETON, R. S. M. — 1971 — The geology of the continental margin between Dakar and Cape Palmas, in Delany, F. M., editor, ICSU/SCOR Working Party 31 Symposium. Cambridge 1970. The geology of the East Atlantic continental margin. 2. Africa. Rép. N° 70/16, Inst. Geol. Sci., 209 pp., pp. 44-60.
- VIANA, C. F. — 1971 — Revisão estratigráfica da Bacia do Recôncavo-Tucano. Bol. Tec. Petrobrás, Rio de Janeiro, v. 14, n. 3/4, pp. 157-192.
- VIANA, C. F. — 1966 — Stratigraphic distribution of ostracoda in the Bahia supergroup (Brazil), in Van Hinte, J. E., ed., Proc. 2nd West African Micropaleontological Colloquium, Ibadan, pp. 240-256.
- VON HERZEN, R. P., HOSKINS, H., and VAN ANDEL, T. H. — 1972 — Geophysical studies in the Angola diapirs field. Geol. Soc. America Bull., v. 83, pp. 1901-1910.
- WATERMAN, L. S., SAYLES, F. L., and MANHEIM, F. T. — 1972 — Interstitial water studies on small core samples, Leg 13, in Hayes, D. E., Pimm, A. C., *et al.*, Initial reports of the Deep Sea Drilling Project, v. XIV. Washington, U. S. Government Printing Office, 975 pp., pp. 753-762.
- WATSON, J. A., and JOHNSON, G. L. — 1970 — Seismic studies in the region adjacent to the Grand Banks of Newfoundland. Canadian Jour. Earth Sci., v. 7, pp. 306-316.
- WEBB, G. W. — 1973 — Salt structures east of Nova Scotia. Earth Science Symposium on Offshore Eastern Canada, Geol. Survey Canada, Paper 71-23, pp. 197-218.
- WINNOCK, E. — 1973 — Exposé succinct de l'évolution paléogéologique de l'Aquitainé. Bull. Soc. Géol. France, 7eSerie, v. XV, pp. 5-12.
- ZIEGLER, P. A. — 1975 — Geologic evolution of the North Sea and its tectonic framework. Amer. Petroleum Geologists, v. 59, pp. 1073-1097.

Reprinted from: *Journal of Ocean Management*, Vol. 3, 57-78.

*Ocean Management*, 3 (1976) 57-78

© Elsevier Scientific Publishing Company, Amsterdam — Printed in The Netherlands

## Energy and Mineral Resources of the Pacific Region in Light of Plate Tectonics

Peter A. Rona \* and Lawrence D. Neuman \*\*

---

### ABSTRACT

The Pacific is a closing ocean basin that is diminishing in size as it is consumed at convergent plate boundaries around three-fourths of its perimeter. Geothermal energy sites, areas of offshore petroleum potential, deposits of precious, base, iron and ferroalloy metals are distributed along the convergent plate boundaries of the Pacific including the surrounding continents. The energy and mineral resources of the Pacific region are concentrated by geologic processes at the convergent plate boundaries.

---

### INTRODUCTION

The Pacific is a region of geologic diversity. The Pacific region encompasses the largest ocean basin on earth, extensive chains of volcanic islands that follow arcuate trends around the western margin of the Pacific Ocean, and seas occupying marginal basins between the island arcs and eastern Asia (Fig. 1). The theory of plate tectonics has gained wide scientific acceptance during the past five years, and offers a conceptual framework to unify the diverse geological phenomena of the Pacific region. The conceptual framework of plate tectonics is leading to a new understanding of the relation between the geology and the distribution of energy and mineral resources of the Pacific region.

An earlier paper treated principles of the relation between plate tectonics and mineral resources (Rona, 1973). This paper aims to apply these principles to develop a basic understanding of the distribution of energy and min-

---

\* National Oceanic and Atmospheric Administration (NOAA), Atlantic Oceanographic and Meteorological Laboratories, Miami, Fla. 33149, U.S.A.

\*\* Office for Ocean Economics and Technology, United Nations, New York, N.Y. 10017, U.S.A.

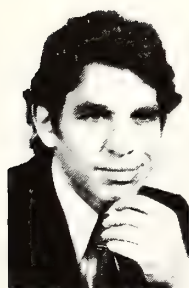


eral resources of the Pacific region. The approach taken is first to present salient features of the geology of the Pacific region from the point of view of plate tectonics (Figs. 1–3). Then to view the distribution of selected energy and mineral resources of the Pacific region with respect to the geology in a series of maps (Figs. 4–9) compiled from various sources (Van Royan and Bowles, 1952; ECAFE, 1962, 1963, 1970; McKelvey and Wang, 1969;



Dr. Peter A. Rona is presently Senior Research Geophysicist with the NOAA, Atlantic Oceanographic and Meteorological Laboratories in Miami, Florida and Adjunct Professor of Marine Geology and Geophysics at the University of Miami. He is Chief Scientist of the Trans-Atlantic Geotraverse (TAG), an international cooperative project to investigate the Earth's crust along a corridor across the Atlantic between southeastern North America and northwestern Africa to gain an understanding of continental drift, sea-floor spreading, and the occurrence of seabed minerals. He generally spends several months of the year at sea leading explorations of the seabed.

Prior to joining NOAA in 1969 he was Exploration Geologist with Standard Oil Company (N.J.) between 1957 and 1959. From 1960 to 1969 he was with Columbia University, Hudson Laboratories where he developed and became Head of Marine Geophysics. He received the degree of Ph.D. in 1967 from the Department of Geology and Geophysics at Yale University. He has published about 50 scientific papers and is a member of 12 professional societies.



Lawrence D. Neuman joined the Ocean Economics and Technology Office as Scientific Affairs Officer in 1973, specializing in the economic potential of the sea and the economic development of coastal areas. A native New Yorker, he received his bachelor's degree in physics at Columbia College and his doctorate in geology and marine geophysics at Columbia University's Lamont-Doherty Geological Observatory.

---

Anon., 1972; DEMR, 1972; Jones, 1972; Eimon, 1974). Finally, to attempt to understand the distribution of the energy and mineral resources in terms of geologic processes (Fig. 10). Attention is focused on those energy and mineral resources associated with present plate boundaries of the Pacific region. Other deposits may then be interpreted in terms of past plate boundaries following the uniformitarian principle of geology that the present is the key to the past.

## GEOLOGY OF THE PACIFIC

### Lithospheric plates

The conceptual framework of plate tectonics, developed by many workers, views the earth as comprised of a rigid outer shell about 100 km (60 miles) thick, the lithosphere, that behaves as if it were floating on an underlying plastic layer, the asthenosphere (Fig. 2). The upper, more brittle part of the lithosphere is termed crust, of which there are two major types, the granitic continental crust (about 30 km thick) and the basaltic oceanic crust

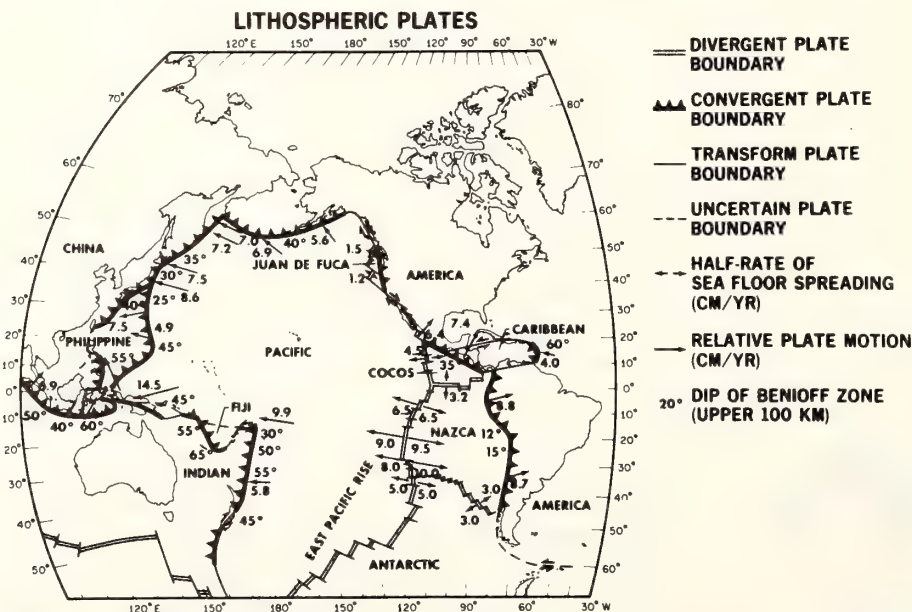


Fig. 1. Lithospheric plates of the Pacific region showing directions (arrows) and half-rates of sea-floor spreading about divergent plate boundaries in the eastern Pacific, directions (arrows) and rates of convergence at convergent plate boundaries bordering the Pacific ocean basin, and angles of inclination (in degrees from horizontal) of Benioff zones beneath the convergent plate boundaries (Fig. 2). (Le Pichon et al., 1973)

(about 10 km thick). The lithosphere is segmented into a number of major plates, each of which may encompass a continent and part of an ocean basin, and numerous minor plates. The Pacific region includes portions of the Pacific, China, America, and Antarctic major plates, and several minor plates (Fig. 2).

## PLATE BOUNDARIES

The boundaries of lithospheric plates are delineated by narrow earthquake zones where the plates are moving with respect to each other. Two types of boundaries are considered (Fig. 2). At the first type, a divergent plate boundary, two adjacent plates move apart as new lithosphere is added to each plate by the process of sea-floor spreading. Divergent plate boundaries extend around the globe through all the major ocean basins as part of a 65,000 km- (40,000 mile-) long undersea mountain chain. Divergent plate boundaries of the Pacific region including the East Pacific Rise are located in the eastern Pacific ocean basin off South America, Central America, and North America (Fig. 1). The sea floor is spreading about different segments of the East Pacific Rise at rates ranging between about 1 and 10 cm per year (Fig. 1).

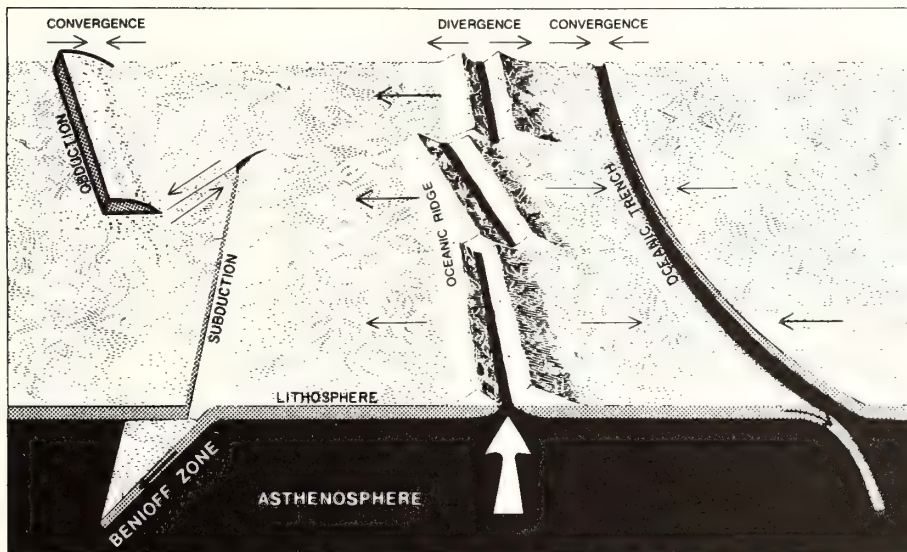


Fig. 2. Diagram showing plate motions at divergent and convergent plate boundaries. Lithospheric plates move like conveyor belts from a divergent plate boundary (oceanic ridge) to a convergent plate boundary where they either descend along a Benioff zone at an oceanic trench (subduction) or they override the adjacent plate (obduction).

At the second type of boundary, a convergent plate boundary, two adjacent plates come together. In the general case, one plate descends under another plate along an inclined plane (Benioff zone) and is resorbed into the asthenosphere (subduction; Fig. 2). In the special case, one plate may temporarily override the other plate (obduction) until the situation reverts to subduction. The Pacific is bounded on three sides by convergent plate boundaries marked by oceanic trenches where lithosphere descends along Benioff zones at rates comparable to the rates of sea floor spreading. As a consequence of the crustal consumption at the convergent plate boundaries bounding the Pacific, the Pacific is a closing ocean basin that is diminishing in size, in contrast to the Atlantic which is an opening ocean basin that is growing larger. The coexistence of divergent plate boundaries where lithosphere is created, and convergent plate boundaries where lithosphere is destroyed, implies that the diameter of the earth is not radically changing.

The inclination of Benioff zones at convergent plate boundaries plays an important role in the development of basins marginal to continents and the generation of volcanism. The inclination of a Benioff zone is inversely proportional to the rate of convergence of adjacent plates at a convergent plate boundary (Luyendyk, 1970). Marginal basins are present in the western Pacific where the rates of plate convergence are relatively slow and the inclination of the Benioff zone exceeds about  $35^\circ$  (Fig. 1; Karig, 1971; Oxburgh and Turcott, 1971; Sleep and Toksóz, 1971; Bracey and Ogden, 1972). Marginal basins are absent in the eastern Pacific where the rates of plate convergence are relatively fast and the inclination of the Benioff zone is less than about  $35^\circ$ . As will be shown, the presence or absence of marginal basins affects offshore petroleum potential. The inclination of Benioff zones also affects the composition of igneous rocks (rocks solidified from molten material) and associated metal deposits.

## AGE OF SEA FLOOR AND OF CONTINENTS

The range and distribution of ages differs markedly between the Pacific Ocean basin and the surrounding continents (Fig. 3). The age of the Pacific sea floor, determined by dating of rock samples recovered by the Deep Sea Drilling Project (Fischer et al., 1971) and by the magnetic polarity reversal time scale (Pitman et al., 1974), ranges between about 150,000,000 years (Late Jurassic period) and the present. The distribution of the ages about the divergent plate boundaries in the eastern Pacific is regular, the sea floor being youngest adjacent to the boundaries and becoming progressively older away from the boundaries as a consequence of sea-floor spreading. The distribution of ages at the convergent plate boundaries around the Pacific is irregu-

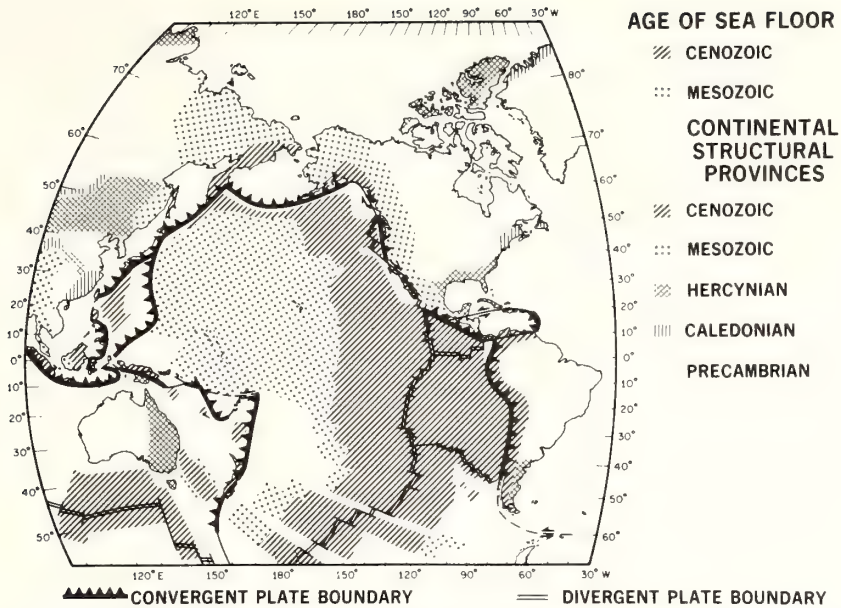


Fig. 3. Age of the Pacific sea floor and of continental structural provinces. Lithospheric plate boundaries are shown.

lar, the age of the sea floor varying along the boundaries as a consequence of subduction.

The circum-Pacific continents are divided into structural provinces according to the time of their most recent deformation during mountain building episodes (Fig. 3). Structural provinces are predominantly Cenozoic (0–70,000,000 years) in western South America, and Mesozoic (70,000,000–200,000,000 years) in western North America. The island arcs of the western Pacific are Cenozoic (0–70,000,000 years). Structural provinces of eastern Asia and Australia exhibit a more complex distribution spanning nearly the entire age range of the earth. The ages of most circum-Pacific metal deposits range from Mesozoic through Cenozoic (0–200,000,000 years ago), corresponding to the known history of lithospheric plate motions in the Pacific Ocean basin.

## DISTRIBUTION OF SELECTED ENERGY RESOURCES

### Geothermal Energy

Geothermal phenomena including active volcanos, thermal springs, fumaroles, geysers, and high values of heat flow are distributed along convergent

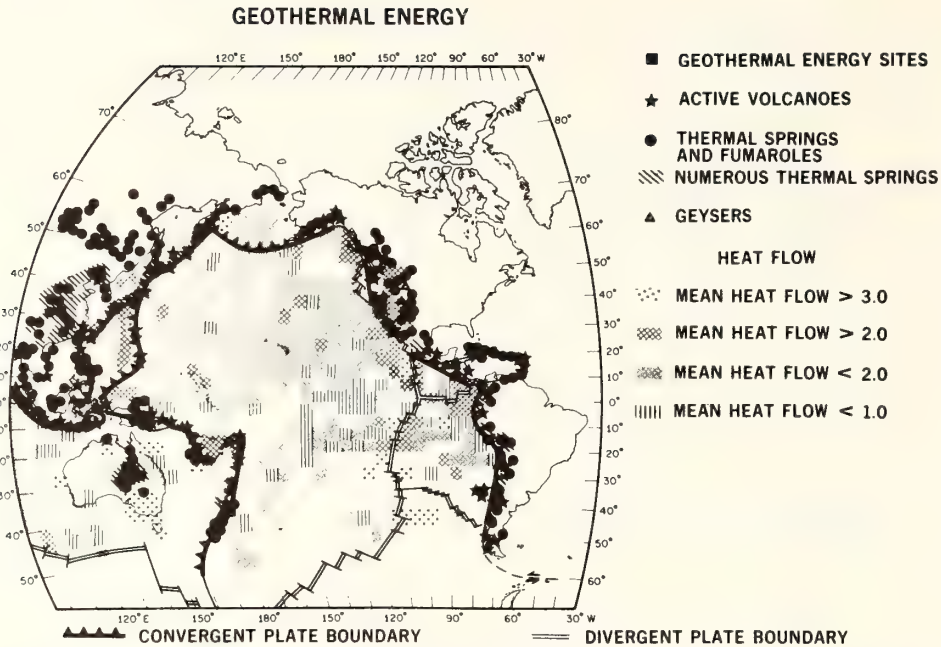


Fig. 4. Map of geothermal energy of the Pacific region. Lithospheric plate boundaries are shown.

plate boundaries around the Pacific (Fig. 4; Kennedy and Richey, 1947; Waring, 1965; Karig, 1971; Snead, 1972). These geothermal phenomena result from heating due to mechanical factors (friction), chemical reactions (dehydration), and to the internal heat of the earth, as the lithospheric plates descend into the asthenosphere at convergent plate boundaries. Similar geothermal phenomena are inferred to occur along the East Pacific Rise and the divergent plate boundaries of the Pacific region where heat flow is high, as a consequence of the upwelling of magma during sea-floor spreading (Langseth, 1969; Sclater, 1972).

Geothermal energy is being tapped at sites in the western United States, Japan, and New Zealand. In addition to its direct utilization, geothermal energy drives hydrothermal processes involving the circulation of hot solutions through the lithosphere which act to concentrate metals both at divergent and convergent plate boundaries, as will be discussed. Hydrothermal mineral deposits, that is, mineral deposits precipitated from hot aqueous solutions, constitute a major part of useful metallic ores on continents and may be important in ocean basins.

## Organic energy: petroleum

Areas of offshore petroleum potential conform with convergent plate boundaries around the Pacific (Fig. 5; McKelvey and Wang, 1969). Both the circum-Pacific trenches and the island arcs of the western Pacific create a habitat that is favorable for the accumulation of petroleum in several respects. The trenches and island arcs act as barriers that catch sediment and organic matter from the continent and ocean basin. Deep-sea sediment with variable content of organic matter is continuously transported into the trenches on a conveyor belt of spreading sea floor (Sorokhtin et al., 1974). The island arcs divide the ocean basin into marginal basins such as the South China Sea, the East China Sea, the Yellow Sea, the Sea of Japan, the Sea of Okhotsk, and the Bering Sea. The shape of the trenches and marginal basins acts to restrict the circulation of the ocean, so that oxygen is not replenished in the seawater and the organic matter is preserved. Geothermal heat in the trenches and marginal basins may facilitate the conversion of organic matter to petroleum (Fig. 4; Tarling, 1973; La Plante, 1974). Finally, geological structures that develop as a result of deformation of the sediment in the trenches and marginal basins by tectonic forces form traps that favor the accumulation of petroleum. In contrast to the areas of offshore petroleum

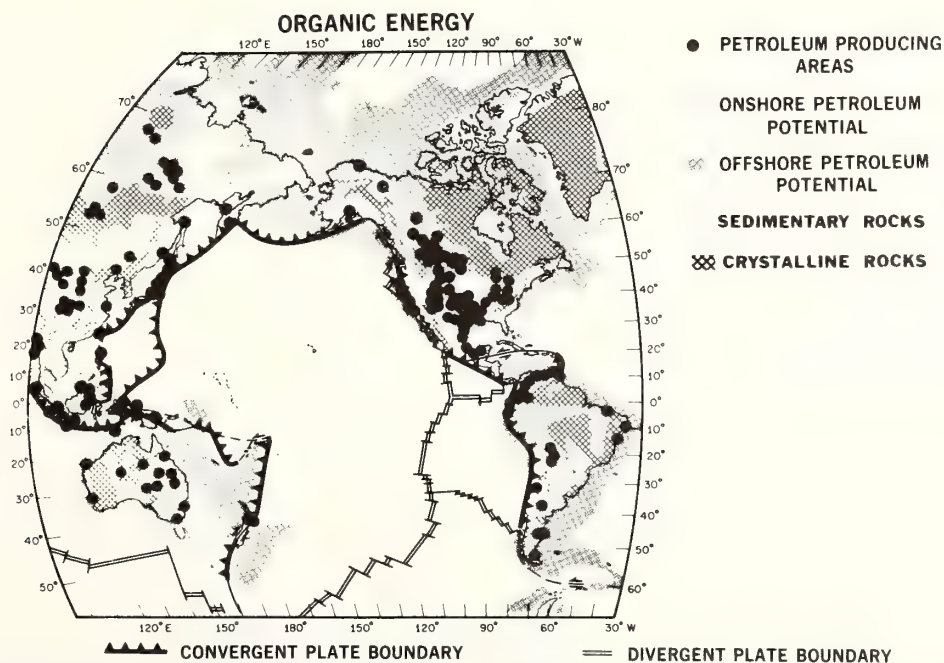


Fig. 5. Areas of petroleum potential and production of the Pacific region (adapted from Rona and Neuman, 1974, 1975; after McKelvey and Wang, 1969).

potential, the sedimentary basins from which petroleum is produced on continents around the Pacific exhibit no apparent spatial relation to plate boundaries (Fig. 5; Irving et al., 1974; Rona and Neuman, 1974).

## DISTRIBUTION OF SELECTED MINERAL RESOURCES

### Metal deposits at divergent plate boundaries

Knowledge of the distribution of metal deposits with respect to divergent plate boundaries is limited because, as submerged oceanic ridges, these boundaries are less accessible to observation than convergent plate boundaries. This knowledge is necessary to evaluate the metallic mineral potential of oceanic lithosphere. All oceanic lithosphere is generated by sea-floor spreading about oceanic ridges and underlies all ocean basins which cover two-thirds of the earth. The Red Sea and the Atlantic Ocean provide evidence of the nature of processes that may be concentrating metals in oceanic lithosphere of the Pacific.

Evidence from the Red Sea and the Mid-Atlantic Ridge indicates that hydrothermal processes are concentrating metals in oceanic crust at divergent plate boundaries. The Red Sea represents the earliest stage in the growth of an ocean basin, the stage when a divergent plate boundary rifts a continent in two. About five years ago the richest known submarine metallic sulfide deposits were found in basins along the center of the Red Sea at a depth of about 2,000 m (6,600 ft.) below sea level (Degens and Ross, 1969). The sulfide minerals, in which various metals are combined with elemental sulfur, are disseminated in sediments that fill the basins to a thickness estimated between 20 m (66 ft.) and 100 m (330 ft.). The top 10 m (33 ft.) of sediment, which has been explored by coring the largest of the basins, has a total dry weight of about 80 million tons, with average metal contents of 29% iron, 3.4% zinc, 1.3% copper, 0.1% lead, 0.005% silver, and 0.00005% gold (Bischoff and Manheim, 1969). The deposits are saturated with (and overlain by) salty brines carrying the same metals in solution as those present in the sulfide deposits. The salty brines are considered to be the hydrothermal solutions from which the sulfide minerals are precipitated.

The most advanced growth stage of a divergent plate boundary is the oceanic ridge system including the Mid-Atlantic Ridge and the East Pacific Rise. An active area of submarine hydrothermal mineral deposits, the TAG Hydrothermal Field, was recently discovered at the crest of the Mid-Atlantic Ridge (26°N) by the Trans-Atlantic Geotraverse (TAG) project of the National Oceanic and Atmospheric Administration (NOAA). As the first of its kind discovered, the distribution of such hydrothermal fields along oceanic



ridges is unknown, but it is suspected that the TAG Hydrothermal Field may represent an important class of features.

The TAG Hydrothermal Field includes both active and relict areas (Rona et al., 1976). The active area (15 × 15 km), including the east wall of the rift valley between depths of 2000 and 3500 m, is covered by a discontinuous layer of manganese oxide at least 5 cm (2 in.) thick (R. Scott et al., 1974; McGregor and Rona, 1975), that is being deposited by hydrothermal solutions enriched in various metals (Betzer et al., 1974). The hydrothermal solutions emanate as hot springs from fractures in the ocean bottom (Rona et al., 1975). The relict area comprises hydrothermal material that was deposited in the active area adjacent to the rift valley and transported at least tens of kilometers away from the ridge crest on a conveyor belt of spreading sea floor (Rona, 1973). A hydrothermal origin for the metallic oxide present is indicated by its chemical purity (40% manganese with only trace quantities of iron and copper compared with manganese nodules which generally contain about 10% manganese and appreciable quantities of iron and copper), and rapid rate of accumulation (about 200 mm per 1,000,000 yr. which is about one hundred times faster than manganese nodules) (M. Scott et al., 1974). The TAG Hydrothermal Field not only confirms that metals are concentrated in normal oceanic crust by hydrothermal processes, but indicates that such processes may occur at a divergent plate boundary more-or-less continuously from early (Red Sea) to advanced (Mid-Atlantic Ridge) stages of growth.

Sediment samples directly overlaying the basalt that forms the foundation of the Pacific and other ocean basins recovered by the Deep Sea Drilling Project both at and away from oceanic ridges, reveal widespread enrichment by certain precious, base, iron and ferro-alloy metals (Böstrom and Peterson, 1969; Dymond et al., 1970; Von der Borch and Rea, 1970; Von der Borch et al., 1971; Cook, 1972; Piper, 1973; Sayles and Bischoff, 1973; Dasch, 1974). The observation that the enrichment is limited to sediment in the basal layer directly overlying basalt indicates that it occurred soon after the generation of the underlying basalt by sea-floor spreading about an oceanic ridge. The metal enrichment is ascribed to hydrothermal processes similar to those that produced the metalliferous sediments in the Red Sea and the metallic oxides at the TAG Hydrothermal Field. The concentration of metals in the widespread enriched sediments of the Pacific is only a fraction of that observed in the Red Sea, but higher concentrations may exist locally.

#### **Processes of metal concentration at divergent plate boundaries**

A model of metallogenesis at divergent plate boundaries, based on various lines of evidence (Spooner and Fyfe, 1973), considers that certain precious,

base, iron and ferro-alloy metals may be concentrated as deposits by sub-sea floor hydrothermal convection systems involving the circulation of seawater as a hydrothermal solution through rocks to a depth of about 5 km (Hart, 1973) beneath the ocean bottom. The development of such hydrothermal convection systems is favored by the supply of seawater, heat, and the intensely fractured basaltic rocks at divergent plate boundaries. According to the model, cold, dense seawater descends through fractures in the basalt of an oceanic ridge and is heated by contact with hot, intrusive bodies of magma (molten rock material) and rock that upwell to form new lithosphere at the ridge crest. The warm, less dense seawater rises through the features and leaches metals disseminated in the basalt that are then transported in solution as complexes with chlorides in the seawater. A fraction of the metals in solution combines with sulfur in the seawater and precipitates to form massive statiform bodies of metallic sulfide including copper and iron, possibly associated with gold. It is suspected that such copper-iron sulfide bodies may underlie the TAG Hydrothermal Field, but it is technically infeasible at present to drill into the ocean bottom to test this idea (Rona, 1973; R. Scott et al., 1974; Rona et al., 1976). Metallic oxides, like the manganese oxide at the TAG Hydrothermal Field, precipitate under oxidizing conditions as the hydrothermal solutions discharge from the ocean bottom in hot springs. Amorphous particles of ferric hydroxide precipitate from the hydrothermal solutions in the overlying seawater. The ferric hydroxide scavenges the remaining metals from solution and settles to deposit a layer of metalliferous sediment on basalt of the ocean bottom, like the metalliferous sediments observed in the Red Sea and the Pacific Ocean.

### **Metal deposits at convergent plate boundaries**

Precious-metal deposits including gold, silver, and platinum are distributed along convergent plate boundaries around the Pacific Ocean (Fig. 6). In the eastern Pacific precious-metal deposits occur landward of convergent plate boundaries along the western margins of North America and South America. In the western Pacific, precious-metal deposits occur on island arcs situated along convergent plate boundaries including Japan, the Philippines, and Indonesia. Deposits are also present in eastern Asia and Australia, where they are separated by a gap from the active convergent plate boundaries.

The distribution of light-metal deposits including aluminum, beryllium, lithium, and titanium appears unrelated to plate boundaries of the Pacific (Fig. 7). These metals are associated with granitic rocks of the continents that are compositionally different from the basaltic rocks of the ocean basin. The distribution of light-metal deposits on the circum-Pacific continents is

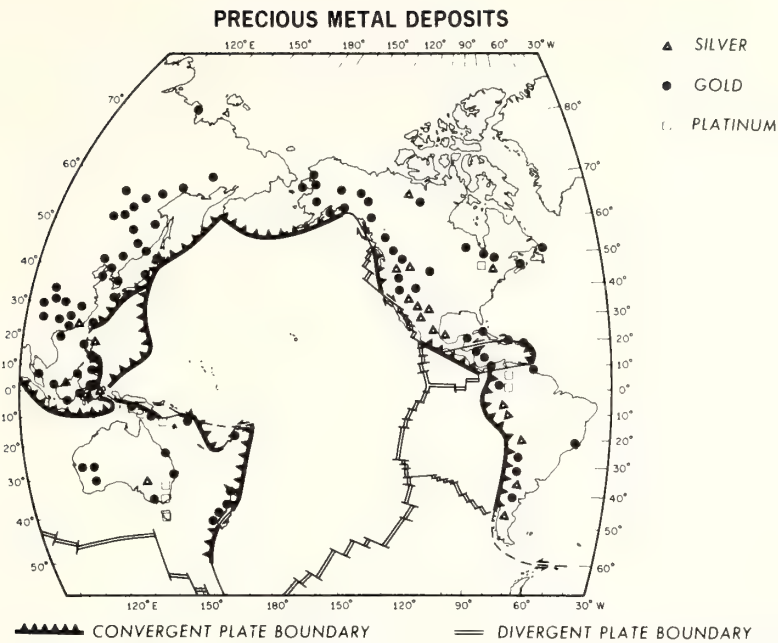


Fig. 6. Map of precious-metal deposits of the Pacific region (adapted from Rona and Neuman, 1974, 1975). Lithospheric plate boundaries are shown.

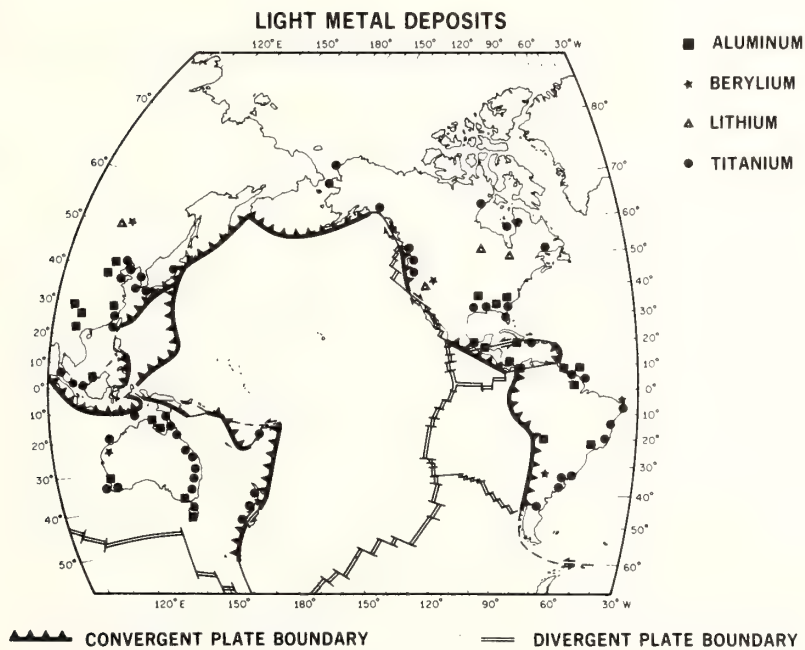


Fig. 7. Map of light-metal deposits of the Pacific region. Lithospheric plate boundaries are shown.

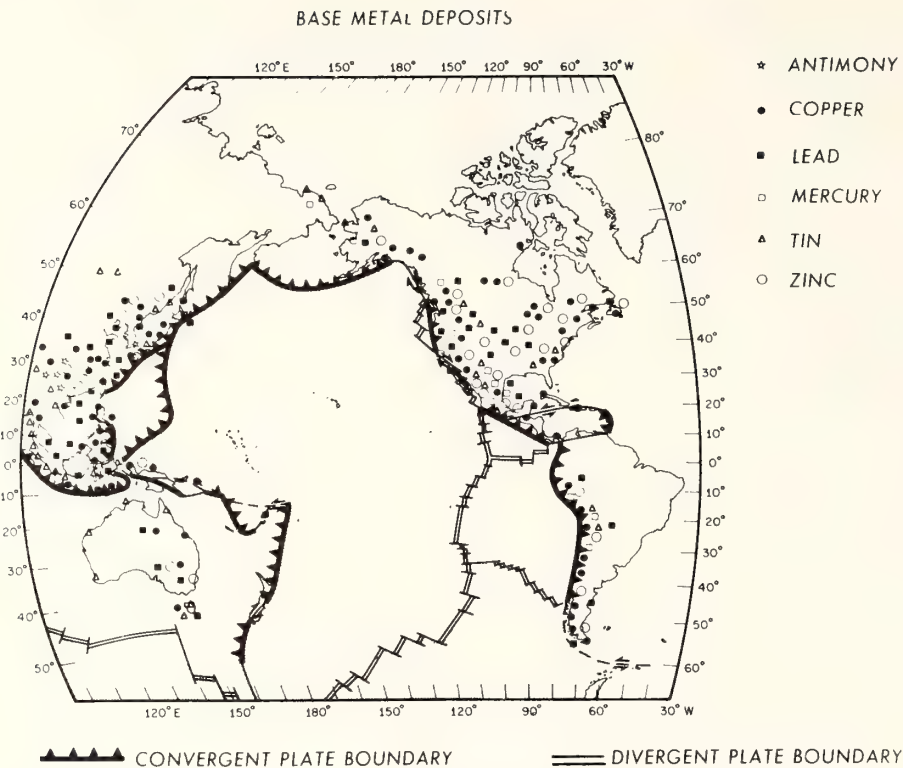


Fig. 8. Map of base-metal deposits of the Pacific region (adapted from Rona and Neuman, 1974, 1975). Lithospheric plate boundaries are shown.

related to the occurrence of particular minerals in granitic rocks and to the concentration of these minerals by processes of subaerial weathering.

Base-metal deposits including antimony, copper, lead, mercury, tin, and zinc are distributed along convergent plate boundaries around the Pacific Ocean (Fig. 8), similar to the distribution of precious metal deposits (Fig. 6). The base-metal deposits occur landward of convergent plate boundaries along the western margins of the Americas in the eastern Pacific, and on island arcs along convergent plate boundaries of the western Pacific. In southeast Asia deposits of tin associated with tungsten, fluorite, bismuth, and molybdenum occur in belts of granites of predominantly Mesozoic age (70,000,000–200,000,000 years ago). Base-metal deposits also occur in eastern Asia and Australia where they are separated by a gap from active convergent plate boundaries.

The copper occurs associated with other metals along convergent plate boundaries of the Pacific region in two economically important classes of ore deposits — massive stratiform sulfide bodies and porphyry ore bodies.

Massive statiform sulfide bodies, deposits confined to layers within bedded sequences of volcanic or sedimentary rocks, are present in western North America, Japan, and the Philippines (Eimon, 1974) where they range in age from Paleozoic through Cenozoic (0–500,000,000 years old). Porphyry ore bodies, disseminated deposits of copper-sulfide minerals associated with volcanic rocks, constitute over one-half of the world's copper production. The majority of porphyry copper deposits lie in two belts of the Pacific region (Eimon, 1974): 1) the western Americas belt extending from Chile to Alaska where the deposits are Mesozoic and Cenozoic in age (0–200,000,000 years old), 2) the southwest Pacific belt including Taiwan, the Philippines, Borneo, West Siam, New Guinea (Papua), and the Solomon Islands, where the deposits are Cenozoic in age (0–70,000,000 years old).

Iron and ferro-alloy metal deposits including chromium, cobalt, manganese, molybdenum, nickel, tungsten, and vanadium are distributed along convergent plate boundaries around the Pacific (Fig. 9), similar to the distribution of precious (Fig. 6) and base (Fig. 8) metals. Iron and ferro-alloy metal deposits occur landward of convergent plate boundaries along the western margins of the Americas in the eastern Pacific, and on island arcs

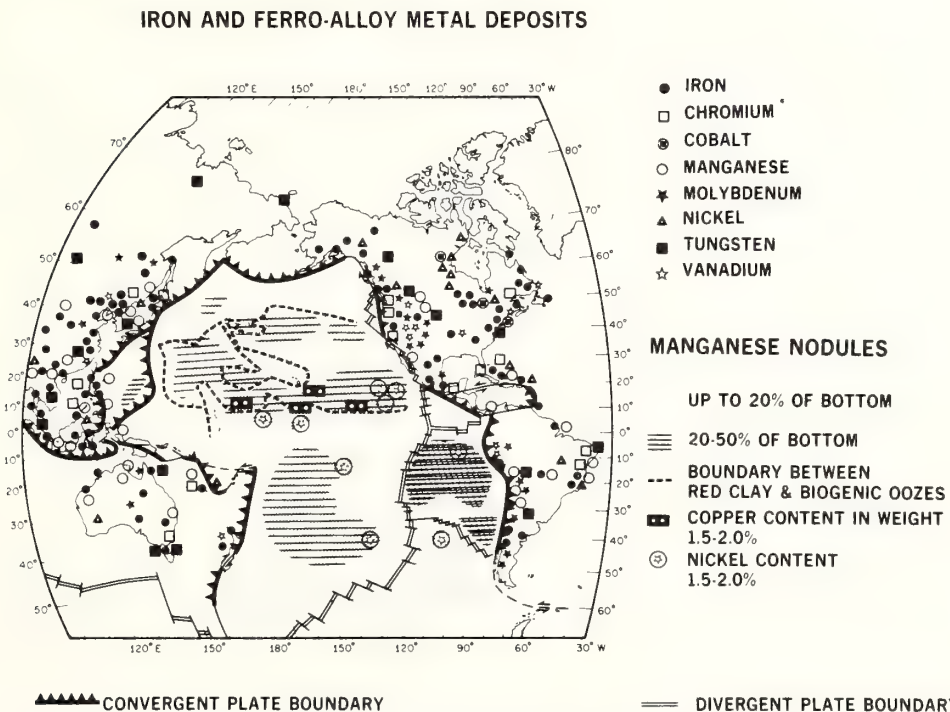


Fig. 9. Map of iron and ferro-alloy metal deposits including manganese nodules of the Pacific region (adapted from Rona and Neuman, 1974, 1975). Lithospheric plate boundaries are shown.

along convergent plate boundaries of the western Pacific. These deposits also occur in eastern Asia and Australia where the deposits are separated by a gap from active convergent plate boundaries.

Nodules containing variable percentages of manganese, copper, nickel, and cobalt are present on about two-thirds of the Pacific sea floor (Fig. 9; Strakhov et al., 1968; Horn et al., 1972; Skornyakova and Andrushchenko, 1974). A zone of nodules of anomalously high copper and nickel content (1.5–2.0%) and areal density (20–50% of sea floor) extends east-west across the central Pacific between latitudes 5° and 20°N coinciding with a region of high biological productivity and may be related to additional concentration of these metals from seawater by organisms (R.M. Garrels, pers. comm.). No apparent relation exists between the positions of the plate boundaries and either the overall distribution of the enriched zone of nodules in the Pacific Ocean basin. The nodules are formed by hydrogenous processes in which the metals are precipitated both from seawater and from interstitial water of underlying sediments. The metals are at least partially derived from hydrothermal sources.

In the special case of obduction, the upper layer of oceanic lithosphere is thrust up and overrides an adjacent plate at a convergent plate boundary (Fig. 2). The slice of oceanic lithosphere, up to several tens of kilometers thick, may contain the various types of precious, base, iron and ferro-alloy deposits that were described to form at oceanic ridges (divergent plate boundaries). Areas of obduction in the southwest Pacific are Papua, New Guinea (Davies and Smith, 1971), where gold and copper prospects exist (Eimon, 1974; Grainger and Grainger, 1974), and the island of New Caledonia (Arias, 1967), where nickel and chromium deposits are mined. The island arcs of the western Pacific, the Kamchatka Peninsula, and western North America from Alaska to Baja California are areas of former obduction which incorporate slices of oceanic lithosphere (Coleman, 1971, fig. 4).

#### **Processes of metal concentration at convergent plate boundaries**

The observation that precious, base, iron and ferro-alloy metal deposits are associated with convergent plate boundaries of the Pacific region (Figs. 6–9) has led to the interpretation of these deposits as genetically related to plate convergence. Models are being developed to gain an understanding of the sources of the various metals and the processes that concentrate the metal deposits.

Prior to the theory of plate tectonics, the source for metals was generally considered to be anomalous metal concentrations in continental crust and mantle underlying the deposits (Krauskopf, 1967; Noble, 1970). Plate tec-

tonics has turned attention to the oceanic lithosphere as a source for a significant fraction of the metals in deposits at convergent plate boundaries of the Pacific. Early models stressed metals concentrated by hydrothermal processes in particulate phases (metalliferous sediments) and in solid phases (oxides and sulfides) in oceanic crust as primary sources (Sawkins, 1972; Sillitoe, 1972a). However, the amounts of those precious, base, iron and ferroalloy metals disseminated in oceanic crust by magmatic processes more than suffice to quantitatively account for the majority of deposits of these metals observed along convergent plate boundaries (see NOTES, p. 75).

Adequate sources and supplies of various metals exist to account for the metal of ore deposits (Krauskopf, 1967). The principal problems in metallogenesis are extraction of metals from the sources, transport of the metals, their concentration and deposition. In simplest form, models of metallogenesis at convergent plate boundaries envisage the extraction of metals from sea water-saturated oceanic crust as it undergoes partial melting under conditions of increasing temperature and pressure during descent of the oceanic lithosphere along a Benioff zone (Fig. 10; Sawkins, 1972; Sillitoe, 1972a). The metals ascend as components of magmas, are concentrated in fluids released from the magmas, and are deposited.

The models are becoming increasingly complex to account for the actual characteristics of metal deposits at convergent plate boundaries of the Pacific region (Mitchell and Bell, 1973; Ridge, 1972). The distribution of metal deposits parallel to convergent plate boundaries in metal provinces of the western Americas (Fig. 10) may be related to progressive increase in temperature and pressure and change in chemical environment down the inclined plane of the Benioff zone which together act to separate different components of the oceanic lithosphere during partial melting (Sillitoe, 1972b). Different associations of metals and igneous rocks may be related to variation in composition of magmas controlled by changes in the inclination of Benioff zones resulting from changes in rates of lithospheric plate convergence and sea floor spreading through time (Mitchell, 1973). The actual inclinations of Benioff zones are not constant as shown in models (Fig. 10), but vary with depth.

Metals other than those present in oceanic crust such as tin, as well as additional quantities of metals and sulfur present in oceanic crust, may be derived from the asthenosphere and continental lithosphere overlying Benioff zones (Fig. 10). The proportion of metals and sulfur derived from the various potential sources is unknown and is the subject of studies using sulfur, lead, and strontium isotopes as tracers (Corliss, 1974; Dasch, 1974). Volatile components such as hydrogen fluoride and carbon dioxide liberated from dry oceanic lithosphere at depths exceeding 200 km along a Benioff zone may lower melting points, assist in transporting metals, and liberate tin

and associated metals (tungsten, bismuth, fluoride, and molybdenum) from granite in overlying continental crust (Mitchell and Garson, 1972; Stern and Wylie, 1973; Oyarzun and Frutos, 1974). The tin and associated metals in eastern Asia and the various metal deposits in eastern Australia may have been deposited above former Benioff zones of shallow inclination adjacent to the continental margins related to relatively fast plate convergence. Subsequent increase in inclination of the Benioff zones related to relatively slow plate convergence has resulted in the seaward migration of the Benioff zones as a consequence of the growth of marginal basins (Fig. 10), leaving the observed gap between the deposits of the continental margins and active convergent plate boundaries of the western Pacific (Mitchell, 1973).

Convergent plate boundaries are the loci of a multiplicity of interacting geologic processes that are difficult to differentiate. The models incorporate different processes to explain the factors that control the locations of ore deposits along the convergent plate boundaries of the Pacific region: (1) deep processes: variations in sources of metals, physico-chemical mechanisms, magmatic processes, seismic activity, rate and inclination of lithospheric descent, and geologic structure associated with subduction along Benioff zones (Krauskopf, 1967; James, 1971; Sawkins, 1972; Sillitoe, 1972a, 1974; Mitchell, 1973); (2) shallow processes: regional and local volcanism, magmatic processes, hydrothermal activity, geologic deformation and structure of circum-Pacific mountain belts and island arcs (Minato et al., 1965; Hollister, 1973; Solomon, 1974). The models of metallogenesis at convergent plate boundaries are becoming more complex as factors are added to successively approximate the actual deposits. The models are still interpretive in that they explain the distribution of known deposits. With further development these models may predict the locations of new deposits.

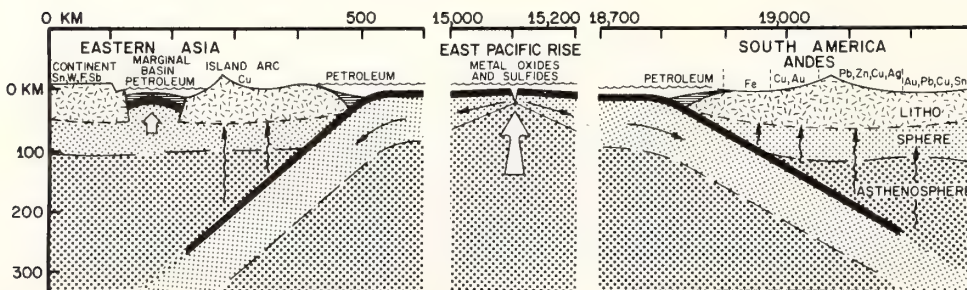


Fig. 10. A diagrammatic east-west section across the central Pacific region shows the relation of petroleum and metal deposits to divergent (East Pacific Rise) and convergent (Pacific margins) plate boundaries, as discussed in the text. Metals are disseminated in the rocks and concentrated as oxides and sulfides in oceanic crust represented by the black layer at the top of the oceanic lithosphere.



## SUMMARY

Despite the geologic diversity of the Pacific region, the distribution of selected energy and mineral resources follows a pattern with respect to lithospheric plate boundaries (Fig. 1), as follows:

(1) Hydrothermal processes acting at divergent plate boundaries (oceanic ridges) concentrate metals in the upper layers of oceanic lithosphere as metalliferous sediments, metallic oxide deposits, and possibly as massive stratabound copper-iron sulfide deposits. Because all of the oceanic lithosphere is generated by sea-floor spreading about oceanic ridges (Figs. 1, 2), the processes of metal concentration at divergent plate boundaries affect the oceanic lithosphere underlying two-thirds of the earth including the entire Pacific ocean basin (Fig. 10).

(2) Oceanic trenches along convergent plate boundaries of the eastern, northern, and western Pacific, and marginal basins formed between island arcs and eastern Asia are areas of offshore petroleum potential (Figs. 5, 10).

(3) Deposits of precious, base, iron and ferro-alloy metals occur along the landward side of convergent plate boundaries on continents and island arcs of the Pacific region (Figs. 6-9).

(4) Models suggest that the observed distribution of petroleum and metal deposits of the Pacific region are genetically related to geologic processes acting at the circum-Pacific convergent plate boundaries (Fig. 10). The development of oceanic trenches and marginal basins create conditions that favor the accumulation of sediment and organic matter, the conversion of the organic matter to petroleum, and the trapping of the petroleum. Metals undergo multiple stages of concentration from various sources in two principal regions (Fig. 10):

(a) Divergent plate boundaries: certain precious, base, iron and ferro-alloy metals are disseminated in oceanic lithosphere by magmatic processes and concentrated by hydrothermal processes.

(b) Convergent plate boundaries: metals are concentrated from oceanic lithosphere descending along Benioff zones and from the overlying asthenosphere and continental lithosphere by various physical and chemical processes. The deposits at convergent plate boundaries are products of complex histories that are only beginning to be understood.

In conclusion, the conceptual framework of plate tectonics may be applied to predict areas hundreds to thousands of kilometers in extent of the Pacific region where certain types of energy and mineral resources are likely to occur. Conventional geological, geochemical, and geophysical methods must then be employed to locate the deposits that may be only tens to thousands of meters in extent within the areas of potential occurrence identified from plate-tectonic considerations. The resolution of plate tectonics in pre-

dicting the locations of deposits will improve as models of geologic processes at plate boundaries are refined, but conventional exploration methods will continue to complement plate tectonics.

### ACKNOWLEDGMENTS

We thank V. Baum, Chief of the Resources and Transport Division, and J.P. Levy, Chief of the Office for Ocean Economics and Technology of the United Nations for their important encouragement. The United Nations and the National Oceanic and Atmospheric Administration supported this work.

### NOTES

The amount of many precious, base, iron and ferro-alloy metals disseminated in oceanic crust (basalt) is considerably greater than in continental crust (granite). For example, the copper content of basalt (about 100 ppm) is approximately five times that of granite (Turekian and Wedepohl, 1961; Vinogradov, 1962). An orebody containing 1,000,000 tons of copper is equivalent to only about 4% of the copper disseminated in a 100-km<sup>3</sup> volume of oceanic basalt (1 ppm = 10<sup>4</sup> tons per mile<sup>3</sup> or 25 · 10<sup>2</sup> tons per km<sup>3</sup>). Sulfur is also present both in oceanic crust (100–400 ppm; Vinogradov, 1962) and in seawater (1 g/l) in sufficient quantities to form the various sulfide ores. A continuous supply of metals and sulfur is provided by the conveyor belt of seawater-saturated oceanic crust that is generated at divergent plate boundaries, moves across the ocean basin, and is consumed at the convergent plate boundaries. An estimated volume of 100,000–250,000 km<sup>3</sup> of oceanic crust has been overridden for every kilometer of leading edge along the western Americas (Gilluly, 1973). Four percent of the copper disseminated in this volume of oceanic crust is equivalent to between 1,000,000,000 and 2,500,000,000 tons, only a fraction of which is known to be concentrated in massive stratabound and porphyry copper deposits along the western margins of North and South America.

### REFERENCES

- Anon., 1972. *The Times Atlas of the World*. Bartholomew, Times Newspapers Ltd., Edinburgh, 4th rev. ed., 272 pp.
- Avias, J., 1967. Overthrust structure of the main ultrabasic New Caledonian massives. *Tectonophysics*, 4: 531–541.
- Betzer, P.R., Bolger, G.W., McGregor, B.A. and Rona, P.A., 1974, The Mid-Atlantic Ridge and its effect on the composition of particulate matter in the deep ocean. *Am. Geophys. Union Trans.*, 55: 293.

- Bischoff, J.L. and Manheim, F.T., 1969. Economic potential of the Red Sea heavy metal deposits. In: E.T. Degens and D.A. Ross (Editors), *Hot Brines and Recent Heavy Metal Deposits in the Red Sea*. Springer, New York, N.Y., 600 pp.
- Böstrom, K. and Peterson, M.N.A., 1969. The origin of aluminum-poor ferromanganous sediments in areas of high heat flow on the East Pacific Rise. *Mar. Geol.*, 7: 427-447.
- Bracey, D.R. and Ogden, T.A., 1972. Southern Mariana Arc: geophysical observations and hypothesis of evolution. *Geol. Soc. Am. Bull.*, 83: 1509-1522.
- Coleman, R.G., 1971. Plate tectonic emplacement of upper mantle peridotites along continental edges. *J. Geophys. Res.*, 76: 1212-1222.
- Cook, H.E., 1972. Stratigraphy and sedimentation. In: J.D. Hayes et al. (Editors), *Initial Reports of the Deep Sea Drilling Project, IX*. U.S. Govt. Printing Office, Washington, D.C., 1205 pp., pp. 933-943.
- Corliss, J.B., Dasch, E.J., Dymond, J.D., Field, C.W., Heath, G.R., Senechal, R.G. and Veeh, H.H., 1974. Metallogenesis in southeast Pacific Ocean: Nazca Plate Project. *Am. Assoc. Pet. Geol. Bull.*, 58: 1434 (abstract).
- Dasch, E.J., 1974. Metallogenesis in the southeastern Pacific: a progress report on the IDOE Nazca Plate Project. *Phys. Earth Planet. Inter.*, 9: 249-258.
- Davies, H.L. and Smith, I.E., 1971. Geology of Eastern Papua. *Geol. Soc. Am. Bull.*, 82: 3299-3312.
- DEMRC, 1972. Principal mineral areas of Canada, scale 1 : 7,600,200. Dept. Energy, Mines and Resour., Min. Resour. Branch and Geol. Surv. of Canada, Map 900A, 22nd ed.
- Dymond, J., Corliss, J.B., Heath, G.R., Field, C.W., Dasch, E.J. and Veeh, H.H., 1973. Origin of metalliferous sediments from the Pacific Ocean. *Geol. Soc. Am. Bull.*, 84: 3355-3372.
- ECAFE, 1962. Oil and natural gas map of Asia and the Far East, scale 1 : 5,000,000. UN Econ. Comm. for Asia and the Far East (ECAFE), No. 16351, UN Publ. Sales No. 62-1-16, 4 sheets.
- ECAFE, 1963. Mineral distribution map of Asia and the Far East, scale 1 : 5,000,000. UN Econ. Comm. for Asia and the Far East (ECAFE). No. 63-15714, UN Publ. Sales No. 63-1-18, 4 sheets.
- ECAFE, 1970. Energy atlas of Asia and the Far East. UN Econ. Comm. for Asia and the Far East (ECAFE). UN Publ. Sales No. E.70.1.11, E/CN.11/900, 25 pp.
- Eimon, P.I., 1974. World copper resources. Mineral Res. Company, Salt Lake City, Utah, map in 3 sheets.
- Fischer, A.G., Heezen, B.C., Boyce, R.E., Bukry, D., Douglas, R.G., Garrison, R.E., Kling, S.A., Krasheninnikov, V., Lisitsin, A.P. and Pimm, A.C., 1971. Initial Reports of the Deep Sea Drilling Project, VI. U.S. Govt. Printing Office, Washington, D.C., 1329 pp.
- Gilluly, J., 1973. Steady plate motion and episodic orogeny and magmatism. *Geol. Soc. Am. Bull.*, 84: 499-514.
- Grainger, D.J. and Grainger, R.L., 1974. The minerals deposits map of Papua New Guinea, 1 : 2,500,000. *Aust. Bur. Miner. Resour., Geol. Geophys., Bull.*, 148, PNG 8, 171 pp.
- Hart, R.A., 1973. A model for chemical exchange in the basalt-seawater system of oceanic layer II. *Canadian J. of Earth Sci.*, 10: 799-816.
- Hollister, V.F., 1973. Regional characteristics of porphyry copper deposits of South America. *Soc. of Mining Engineers Preprint No. 73-I-2*.
- Horn, D.R., Horn, B.M. and Delach, M.N., 1972. Metal content of ferromanganese deposits of the oceans. Lamont-Doherty IDOE/NSF GX33616 Tech. Rep. 3. Office for Int. Decade of Ocean Exploration, Natl. Sci. Found., Washington, D.C., 51 pp.
- Irving, E., North, F.K. and Couillard, R., 1974. Oil, climate, and tectonics. *Can. J. Earth Sci.*, 11: 1-17.
- Isacks, B., Oliver, J. and Sykes, L.R., 1968. Seismology and the new global tectonics. *J. Geophys. Res.*, 73: 5855-5899.
- James, D.E., 1971. Plate tectonic model for the evolution of the Central Andes. *Geol. Soc. Am. Bull.*, 82: 3325-3346.

- Jones, D.B. (Advisory Editor), 1972. Oxford Economic Atlas of the World. Oxford University Press, 4th ed., 239 pp.
- Karig, D.E., 1971. Origin and development of marginal basins in the western Pacific. *J. Geophys. Res.*, 76: 2542-2561.
- Kennedy, W.Q. and Richey, J.E., 1947. Catalog of the active volcanoes of the world. *Bull. Volcanol. Suppl. Ser. II, VII*: 1-11.
- Krauskopf, K.B., 1967. Source rocks for metal-bearing fluids. In: H.L. Barnes (Editor), *Geochemistry of Hydrothermal Ore Deposits*. Holt, Rinehart and Winston, New York, N.Y., pp. 1-33.
- Langseth, M.G., Jr., 1969. The flow of heat from the Earth and the global distribution at the surface. *Am. Inst. Aeronaut. Astronaut.*, Pap, 69-589: 1-10.
- La Plante, R.E., 1974. Hydrocarbon generation in Gulf Coast Tertiary sediments. *Am. Assoc. Pet. Geol. Bull.*, 58: 1281-1289.
- Le Pichon, X., 1968. Sea floor spreading and continental drift. *J. Geophys. Res.*, 73: 3661-3697.
- Le Pichon, X., Francheteau, J. and Bonnin, J., 1973. *Plate Tectonics*. Elsevier, Amsterdam, 300 pp.
- Luyendyk, B.P., 1970. Dips of downgoing lithospheric plates beneath island arcs. *Geol. Soc. Am. Bull.*, 81: 3411-3416.
- McGregor, B.A. and Rona, P.A., 1975. Crest of the Mid-Atlantic Ridge at 26°N. *J. Geophys. Res.*, 80: 3307-3314.
- McKelvey, V.E. and Wang, F.F.H., 1969. World subsea mineral resources. *U.S. Geol. Surv., Misc. Geol. Invest.*, Map I-632.
- Minato, M., Gorai, M. and Hunabashi, M., 1965. *The Geological Development of Japanese Islands*. Tokyo, Tsukiji Shoka.
- Mitchell, A.H.G., 1973. Metallogenic belts and angle of dip of Benioff zones. *Nature Phys. Sci.*, 245: 49-52.
- Mitchell, A.H. and Bell, J.D., 1973. Island-arc evolution and related mineral deposits. *J. Geol.*, 81: 381-405.
- Mitchell, A.H.G. and Garson, M.S., 1972. Relationship of porphyry copper and circum-Pacific tin deposits to palaeo-Benioff zones. *Inst. Min. Metall., Trans., Sec. B*, 81: B10-B25.
- Oxburgh, E.R. and Turcotte, D.L., 1971. Origin of paired metamorphic belts and crustal dilation in island arc regions. *J. Geophys. Res.*, 76: 1315-1327.
- Oyarzun, J.M. and Frutos, J.J., 1974. Porphyry copper and tin-bearing porphyries: a discussion of genetic models. *Phys. Earth Planet. Inter.*, 9: 259-263.
- Piper, D.Z., 1973. Origin of metalliferous sediments from the East Pacific Rise. *Earth Planet. Sci. Lett.*, 19: 75-82.
- Pitman, W.C. III, Larson, R.L. and Herron, E.M., 1974. Age of the ocean basins determined from magnetic anomaly lineations. *Geol. Soc. Am.*, map.
- Ridge, J.D., 1972. Annotated bibliographies of mineral deposits in the western hemisphere. *Geol. Soc. Am. Mem.*, 131: 681 pp.
- Rona, P.A., 1973. New evidence for seabed resources from global tectonics. *Ocean Management*, 1: 145-159.
- Rona, P.A. and Neuman, L.D., 1974. Plate tectonics and mineral resources of the Pacific (abstract). *Am. Assoc. Pet. Geol. Bull.*, 58: 1456.
- Rona, P.A. and Neuman, L.D., 1975. Plate tectonics and mineral resources of the circum-Pacific. *Circum-Pacific Energy and Mineral Resources* — *Am. Assoc. Pet. Geol., Mem.* 25, in press.
- Rona, P.A., McGregor, B.A., Betzer, P.R. and Krause, D.C., 1975. Anomalous water temperatures over Mid-Atlantic Ridge crest at 26°N. *Deep-Sea Res.*, 22: 611-618.
- Rona, P.A., Harbison, R.N., Bassinger, B.G., Scott, R.B. and Nalwalk, A.J., 1976. Tectonic fabric and hydrothermal activity of Mid-Atlantic Ridge crest (26°N). *Geol. Soc. Am. Bull.*, in press.

- Sawkins, F.J., 1972. Sulfide ore deposits in relation to plate tectonics. *J. Geol.*, 80: 377–397.
- Sayles, F.L. and Bischoff, J.L., 1973. Ferromanganous sediments in the equatorial East Pacific. *Earth Planet. Sci. Lett.*, 19: 330–336.
- Slater, J.G., 1972. Heat flow and elevation of the marginal basins of the western Pacific. *J. Geophys. Res.*, 77: 5705–5709.
- Scott, M.R., Scott, R.B., Rona, P.A., Butler, L.W. and Nalwalk, A.J., 1974. Rapidly accumulating manganese deposit from the median valley of the Mid-Atlantic Ridge. *Geophys. Res. Lett.*, 1: 355–358.
- Scott, R.B., Rona, P.A., McGregor, B.A. and Scott, M.R., 1974. The TAG hydrothermal field. *Nature*, 251: 301–302.
- Sillitoe, R.H., 1972a. A plate tectonic model for the origin of porphyry copper deposits. *Econ. Geol.*, 67: 184–197.
- Sillitoe, R.H., 1972b. Relation of metal provinces in western America to subduction of oceanic lithosphere. *Geol. Soc. Am. Bull.*, 83: 813–818.
- Sillitoe, R.H., 1974. Tectonic segmentation of the Andes: implications for magmatism and metallogeny. *Nature*, 250: 542–545.
- Skornyakova, N.S. and Andrushchenko, P.F., 1974. Iron-manganese concretions in the Pacific Ocean. *Int. Geol. Rev.*, 16: 863–919.
- Sleep, N.H. and Toksöz, M.N., 1971. Evolution of marginal basins. *Nature*, 233: 548–550.
- Snead, R.E., 1972. *Atlas of World Physical Features*. Wiley, New York, N.Y., 158 pp.
- Solomon, M., 1974. Massive sulfides and plate tectonics. *Nature*, 249: 821–822.
- Sorokhtin, O.G., Ushakov, S.A. and Fedynskiy, V.V., 1974. Dynamics of crustal plates and origin of petroleum deposits. *Akad. Nauk SSSR, Doklady*, 214: 1407–1410.
- Spooner, E.T.C. and Fyfe, W.S., 1973. Sub-sea floor metamorphism, heat and mass transfer. *Contrib. Miner. Pet.*, 42: 287–304.
- Stern, C.R. and Wylie, P.J., 1973. Water-saturated and undersaturated melting relations of a granite to 35 kilobars. *Earth Planet. Sci. Lett.*, 18: 163–167.
- Strakhov, N.M., Shterenberg, L.E., Kalinenko, V.V. and Tikhomirova, E.S., 1968. Geochemistry of a sedimentary manganese ore-forming process. *Akad. Nauk. SSSR Geol. Inst., Trans.*, 185: 495 pp.
- Tarling, D.H., 1973. Continental drift and reserves of oil and natural gas. *Nature*, 243: 277–279.
- Turekian, K.K. and Wedepohl, K.H., 1961. Distribution of the elements in some major units of the Earth's crust. *Geol. Soc. Am. Bull.*, 72: 175–192.
- Van Royan, W. and Bowles, O., 1952. *The mineral resources of the world. V. II, Atlas of the World's Resources*. Prentice-Hall, New York, N.Y., 181 pp.
- Vinogradov, A.P., 1962. Average contents of chemical elements in the principal types of igneous rocks of the earth's crust. *Geokhimiya*, 7: 555–571.
- Von der Borch, C.C., Nesteroff, W.D. and Galehouse, J.S., 1971. Iron-rich sediments cored during Leg 8 of the Deep Sea Drilling Project. In: J.I. Tracey, Jr. et al. (Editors), *Initial Reports of the Deep Sea Drilling Project, VIII*. U.S. Govt. Printing Office, Washington, D.C., 1037 pp., pp. 725–819.
- Von der Borch, C.C. and Rex, R.W., 1970. Amorphous iron oxide precipitates in sediments cored during Leg 5, Deep Sea Drilling Project. In: D.A. McManus et al. (Editors), *Initial Reports of the Deep Sea Drilling Project, V*. U.S. Govt. Printing Office, Washington, D.C., pp. 541–544.
- Waring, G.A., 1965. Thermal springs of the United States and other countries of the world: a summary. *U.S. Geol. Surv., Prof. Pap.*, 492.

Reprinted from: Papers from Circum-Pacific Energy and Mineral Resources Conference, Honolulu, Hawaii, August 26-30, 1974, publ. by Amer. Assoc. of Petroleum Geologists, Memoir 25, 48-57.

## Plate Tectonics and Mineral Resources of Circum-Pacific Region<sup>1</sup>

PETER A. RONA<sup>2</sup> and LAWRENCE D. NEUMAN<sup>3</sup>

**Abstract** Distribution of selected energy (petroleum and geothermal) and mineral (precious, base, iron, and ferro-alloy metals) resources of the Pacific Ocean basin and Circum-Pacific continents appears to be related to lithospheric plate boundaries. Divergent plate boundaries (oceanic ridges) are related in time to the development of stratigraphic traps in sedimentary basins of the continents, and in space to metalliferous deep-sea sediments and the possible occurrence of massive stratabound metallic sulfide deposits in oceanic crust. Convergent plate boundaries are related in space to areas of offshore petroleum potential and to onshore deposits of precious, base, iron, and ferro-alloy metals. Models suggest genetic relations between the observed distribution of deposits and geologic processes at plate boundaries, and may lead to the discovery of new resources.

### INTRODUCTION

The Pacific Ocean basin and surrounding continents provide a natural laboratory to develop and test ideas on the relation between plate tectonics and mineral resources. Our approach is as follows:

1. Outline the geologic framework of the Pacific with particular attention to boundaries of the lithospheric plates.
2. Determine the spatial distribution of various mineral resources with respect to the plate boundaries (Figs. 1-4).
3. Consider models of mineral-concentrating processes related to plate boundaries that may explain the observed distribution of mineral resources (Fig. 5).

The boundaries of lithospheric plates are delineated by narrow earthquake zones where the plates are moving with respect to each other. The theory of plate tectonics recognizes three types of plate boundaries (Isacks et al, 1968). One type, a convergent plate boundary, is where two adjacent plates move together and collide or where one plate descends under the other plate along a Benioff seismic zone and is subducted into the upper mantle. The second type, a divergent plate boundary, is where two adjacent plates move apart because new lithosphere is added to each plate by the process of seafloor spreading. The third type is the transform plate boundary, where two adjacent plates slide past one another.

A series of resource maps (Figs. 1-4), using the same base map (Van der Grinten projection) as that used by McKelvey and Wang (1969), was compiled from numerous sources (Van Royan

and Bowles, 1952; Roberts and Irving, 1957; Anon., 1962, 1963, 1970, 1972a, b; Lafitte and Rouveyrol, 1965; McKelvey and Wang, 1969; Bonine et al, 1970; Dengo and Levy, 1970; Jones, 1972).

### PACIFIC GEOLOGIC FRAMEWORK

#### Lithospheric Plate Boundaries

Divergent plate boundaries expressed as oceanic ridges divide the Pacific into several lithospheric plates (Fig. 1). The oceanic ridge system of the Pacific is not midoceanic but is located in the eastern Pacific off Central America and South America and northwestern North America. The average half-rates of seafloor spreading about the oceanic ridges of the Pacific, determined from the geomagnetic polarity-reversal time scale, range from 1.2 cm/yr at the Gorda Rise off the northwestern United States to about 10 cm/yr off Chile and Peru (Table 1).

The Pacific is a closing ocean basin surrounded on three sides by convergent plate boundaries expressed as oceanic trenches (Fig. 1). In the global crustal budget, the Circum-Pacific convergent plate boundaries account for the major portion of crustal consumption. Linear rates of crustal consumption around the Pacific, assumed to be equal to rates of plate convergence, range between about 1 and 15 cm/yr (Table 2).

The dip of the Benioff zone at convergent plate boundaries (Table 3) is inversely proportional to the relative rate of convergence of the adjacent plates (Luyendyk, 1970). For example, the dip of the Benioff zone in the upper 100 km is about 12° beneath Peru, where the relative rate of plate convergence is 8.8 cm/yr (Table 2), and the half-rate of seafloor spreading about the corresponding section of the East Pacific Rise is 9.5 cm/yr (Table 1). The dip of the Benioff zone increases to about 55° beneath the Kermadec Islands (Table 3), where the relative rate of convergence decreases to 5.8 cm/yr, and the half-rate of seafloor

<sup>1</sup>Manuscript received, December 26, 1974.

<sup>2</sup>National Oceanic and Atmospheric Administration, Atlantic Oceanographic and Meteorological Laboratories, 15 Rickenbacker Causeway, Miami, Florida 33149.

<sup>3</sup>Office for Ocean Economics and Technology, United Nations, New York, New York 10017.

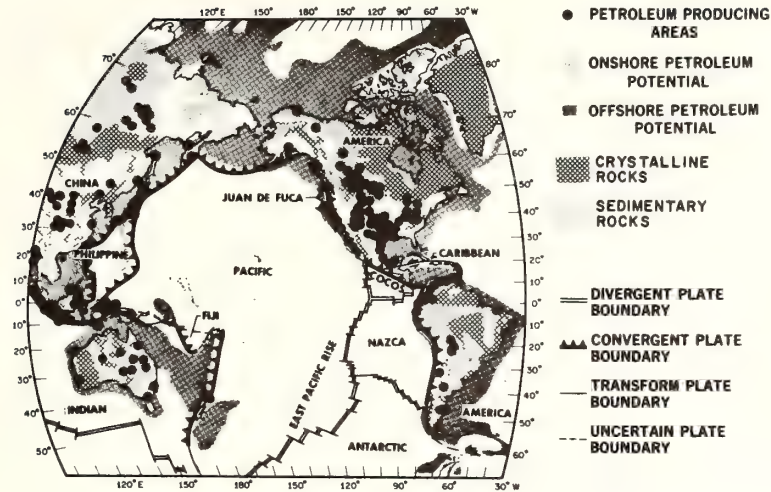


FIG. 1—Areas of petroleum production and potential of Pacific region. Lithospheric plates and plate boundaries are shown.

spreading about the East Pacific Rise decreases to about 5.5 cm/yr.

Oceanic and continental crust are juxtaposed at convergent plate boundaries in the eastern Pacific (Fig. 1). Marginal basins generally underlain by oceanic crust intervene between convergent

plate boundaries and continental crust in the western Pacific. The development of marginal basins may be related to the dip of Benioff zones (Oxburgh and Turcotte, 1971; Karig, 1971; Sleep and Toksöz, 1971; Bracey and Ogden, 1972). Where the marginal basins are present in the western Pacific, the dip of the Benioff zone exceeds about 35°; where marginal basins are absent in the eastern Pacific, the dip is less than about 35° (Table 3).

Table 1. Seafloor-Spreading Half-Rates about Pacific Oceanic Ridges

Latitude (+North, -South)	Longitude (+East, - West)	Half-spreading rate (cm/yr)	Location
46.5	-129	1.5	Juan de Fuca Ridge <sup>1</sup>
41.3	-127.5	1.2	Gorda Rise <sup>2</sup>
12.5	-103.5	4.5	East Pacific Rise <sup>3</sup>
3.2	-102	6.4	East Pacific Rise <sup>3</sup>
3.0	- 83.5	3.2	Galapagos rift zone <sup>3</sup>
2.0	- 97.5	3.2	Galapagos rift zone <sup>3</sup>
0.75	- 87.6	3.2	Galapagos rift zone <sup>3</sup>
- 5.6	-106.8	6.5	East Pacific Rise <sup>3</sup>
- 9.2	-110.3	7.5	East Pacific Rise <sup>3</sup>
-19	-113	9-9.5	East Pacific Rise <sup>3</sup>
-28	-112	8-10	East Pacific Rise <sup>3</sup>
-35.6	-110.9	5.0	East Pacific Rise <sup>3</sup>
-43.2	- 82.5	3.0	Chile Ridge <sup>3</sup>

<sup>1</sup> Vine and Wilson, 1965.

<sup>2</sup> Atwater and Mudie, 1973.

<sup>3</sup> Herron, 1972.

Ages of Seafloor and Continents

The age of the Pacific seafloor, as determined by dating of remanent magnetic anomalies in the geomagnetic polarity-reversal time scale (Pitman et al, 1974) and dating of rock samples recovered by the Deep Sea Drilling Project (Fischer et al, 1971), ranges between Late Jurassic (about 150 m.y. ago) and recent. The distribution of ages about divergent plate boundaries is regular, and the seafloor becomes progressively older with distance from these boundaries. The distribution of ages at convergent plate boundaries is irregular, and the seafloor is of various ages at these boundaries. The distribution of ages on continents is delineated by structural provinces that reflect the youngest deformational event, as distinguished from the ages of the seafloor, which reflect the origin of the constituent rocks. Structural provinces of the eastern Pacific are predominantly Cenozoic along western South America and Mesozoic along western North America. In the western Pacific, structural provinces of eastern Asia and Australia exhibit a complex distribution and

Table 2. Rate of Plate Convergence at Convergent Plate Boundaries of the Pacific<sup>1</sup>

<i>Latitude</i> (+ North, - South)	<i>Longitude</i> (+ East, - West)	<i>Rate</i> (cm/yr)	<i>Azimuth</i>	<i>Location</i>
51	160	7.2	114	Kurile Trench
43	148	7.5	107	Kurile Trench
35	142	8.6	101	Japan Trench
27	143	7.5	265	Japan Trench
19	148	4.9	282	Mariana Trench
11	142	2.3	243	Mariana Trench
- 3	142	14.5	78	New Guinea
- 13	- 172	9.9	97	N. Tonga Trench
- 34	- 178	5.8	95	S. Kermadec Trench
- 45	169	3.5	72	S. New Zealand
- 55	159	2.6	29	Macquarie Island
- 50	- 75	3.1	240	Cape Horn
- 35	- 74	8.7	74	S. Chile Trench
- 4	- 82	8.8	77	N. Peru Trench
7	- 79	8.3	75	Panama Gulf
20	- 106	6.4	39	N. Middle America Trench
57	- 150	5.6	144	E. Aleutian Trench
50	- 178	6.9	126	W. Aleutian Trench
54	162	7.0	115	W. Aleutian Trench

<sup>1</sup>From Le Pichon et al, 1973, Table V.

range in age from Precambrian through Cenozoic.

#### DISTRIBUTION OF GEOTHERMAL PHENOMENA

The distribution of geothermal phenomena, including heat flow, active volcanoes, thermal springs, fumaroles, and geysers, is spatially related to lithospheric plate boundaries. Values of heat flow in the Pacific Ocean basin (Langseth, 1969; Sclater, 1972) are relatively high (>2 HFU) at divergent plate boundaries and decrease basinward away from these boundaries. Values of heat flow at convergent plate boundaries and in marginal basins (Karig, 1971) around the Pacific are variable. The distribution of heat-flow values on the Circum-Pacific continents is complex. Relatively high values (>2 HFU) are present in limited areas of eastern Australia, eastern Asia, and western North America. Active volcanoes, thermal springs, and fumaroles are aligned along the landward side of convergent plate boundaries on continents and island arcs around the Pacific (Kennedy and Richey, 1947; Waring, 1965; Snead, 1972). These features are not evenly spaced but are grouped (Kelleher, 1972).

It is apparent from the distribution of heat-flow values and thermal springs on islands and continents around the Pacific that numerous potential sites exist for the development of geothermal energy. Geothermal energy is being utilized at sites in New Zealand, Japan, and the western United States.

#### DISTRIBUTION OF PETROLEUM RESOURCES

Areas of offshore petroleum potential conform with convergent plate boundaries around the Pacific (Fig 1; McKelvey and Wang, 1969). Areas of petroleum potential in the eastern Pacific comprise thick sedimentary accumulations underlying the continental margins of western North America and South America and partially filling oceanic trenches seaward of the margins of Central America and South America along convergent plate boundaries. In the western Pacific, island arcs directly landward of convergent plate boundaries divide the ocean basin into marginal basins partially enclosed between the islands and eastern Asia—for example, the South China Sea, the East China Sea, the Yellow Sea, the Sea of Japan, the Sea of Okhotsk, and the Bering Sea.



Table 3. Dip of Benioff Zone (upper 100 km)<sup>1</sup>

Dip (degrees)	Location (counter-clockwise around Pacific)
45	New Zealand
55	Kermadec
50	Tonga (south)
30	Tonga (north)
65	New Hebrides (south)
55	New Hebrides (north)
65	Solomons
45	New Britain
40	Sunda: Flores Sea
60	Sunda: Java
50	Sumatra
50	Burma
55	Mindanao
45	Marianas
25	Izu-Bonin
40	Ryukus
35	Kurile
30	Honshu
40	Aleutians
35	Middle America
12	Peru
15	Chile (north)

<sup>1</sup>Isacks and Molnar, 1971; Oliver et al, 1973.

Areas of petroleum potential in the western Pacific comprise sedimentary accumulations in the marginal basins as well as in oceanic trenches along convergent plate boundaries.

The oceanic trenches along the eastern and western sides of the Pacific Ocean basin receive deep-sea sediments that presumably are transported into the trenches on a "conveyor belt" of spreading seafloor during subduction of the oceanic lithosphere. The content of organic matter in the deep-sea sediments that are transported into the trenches varies in space and in time; for example, a zone of high organic productivity extending across the equatorial Pacific affects the composition of the sediments deposited in that region. Both the amount of organic matter delivered to the oceanic trenches and the petroleum potential are expected to vary accordingly. Temperature and pressure conditions beneath the trenches and the marginal basins may facilitate the conversion of organic matter in the sediments to petroleum (Tarling, 1973; Sorokhtin et al, 1974).

Areas of onshore petroleum production are sedimentary basins on continents with no apparent spatial relation either to divergent or convergent plate boundaries of the Pacific (Fig. 1). However, the development of the sedimentary sequences in the basins may be related to divergent plate boundaries in time, if not in space, through the influence on global sea level of reversible volume changes of oceanic ridges (Rona, 1973b; Rona and Wise, 1974). The volume of the world oceanic ridge system is not constant but appears to vary directly with rates of seafloor spreading. A volume increase in the world oceanic ridge system reduces the cubic capacity of ocean basins, resulting in transgression of the sea onto all the continents and deposition of a sedimentary sequence that may contain organic source material and reservoir rocks. Conversely, a volume decrease in the oceanic ridge system increases the cubic capacity of ocean basins, resulting in regression of the sea from all the continents and the development of widespread unconformities that may be associated with traps for the accumulation of petroleum. Reversible volume changes of the worldwide oceanic ridge system have operated on a time scale of tens of millions of years, as evidenced by the presence of six sedimentary sequences separated by surfaces of unconformity in the Phanerozoic stratigraphy of North America (Sloss, 1963). The inferred relations of the volume of oceanic ridges to sedimentary sequences and unconformities may prove useful in exploration for stratigraphic traps.

#### DISTRIBUTION OF SELECTED MINERAL RESOURCES

##### Light Metal Deposits

Deposits of light metals, including aluminum, beryllium, lithium, and titanium, exhibit no apparent relation to plate boundaries of the Pacific. These metals are associated with granitic rocks of the continents as opposed to basaltic rocks of the ocean basins. The distribution of aluminum, beryllium, lithium, and titanium on continents is related to the occurrence of particular minerals in granitic rocks and to conditions of weathering.

##### Metal Deposits at or Near Convergent Plate Boundaries

*Precious metal deposits*—Deposits of precious metals, including gold, silver, and platinum, exhibit a spatial relation to convergent plate boundaries (Fig. 2). In the eastern Pacific, precious metal deposits are found along the western margins of North America and South America. Additional deposits are present in eastern North America

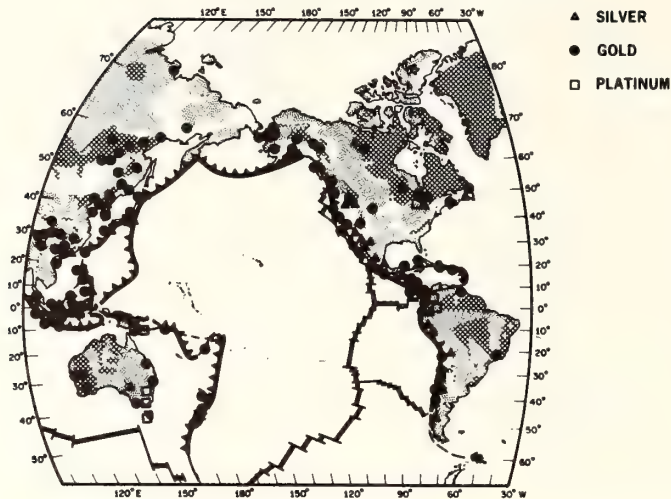


FIG. 2—Map of precious metal deposits of Pacific region. Lithospheric plate boundaries are shown.

in the area of the Canadian shield and in eastern South America in the area of the Guianian and Brazilian shields. In the western Pacific, precious metal deposits occur on island arcs (including Japan, the Philippines, and Indonesia) situated along convergent plate boundaries. Deposits also occur in eastern Asia and Australia, where they are separated by a gap from active convergent plate boundaries. Precious metal deposits have not been found along those sections of convergent plate boundaries where oceanic lithosphere is juxtaposed and island arcs are absent (e.g., the eastern side of the Philippine Sea and the section between New Zealand and Samoa).

*Base metal deposits*—Deposits of base metals exhibit a spatial relation to convergent plate boundaries (Fig. 3). Their distribution is grossly similar to that of precious metal deposits (Fig. 2). In the eastern Pacific, base metal deposits are present along the western margins of North America and South America. In the Peruvian Andes, porphyry copper and vein-type mineralization are associated with Neogene silicic volcanic rocks (Mitchell, 1973). Additional base metals occur in central and eastern North America including the area of the Canadian shield.

In the western Pacific, base metal deposits are found on island arcs along convergent plate boundaries. Deposits of tin, tungsten, and fluorite with minor bismuth and molybdenum occur in belts of predominantly Mesozoic granites and acidic eruptive rocks along the southern margin of Alaska and the eastern margin of Asia (Mitchell, 1973). Base metal deposits also occur in eastern Asia and Australia, which are separated

by a gap from active convergent plate boundaries. As in the case of precious metals, base metal deposits have not been found along those sections of convergent plate boundaries where oceanic lithosphere is juxtaposed and island arcs are absent.

Sediment samples recovered by coring near the crest of oceanic ridges and by deep-sea drilling away from the crest reveal widespread enrichment by base metals of those strata directly overlying basalt of the Pacific Ocean basin (Boström and Petersen, 1969; von der Borch et al, 1971; Cook, 1972; Cronan et al, 1972; Dymond et al, 1973; Sayles and Bischoff, 1973; Piper, 1973). The base metals include antimony, copper, lead, mercury, and zinc, but no tin. The observation that the base metal enrichment is limited to the basal sedimentary layer overlying basalt implies that the enrichment occurred soon after the generation of the underlying basalt by seafloor spreading about an oceanic ridge at a divergent plate boundary.

*Iron and ferro-alloy metal deposits*—Deposits of iron and ferro-alloy metals exhibit a spatial relation to convergent plate boundaries around the Pacific (Fig. 4). Their distribution is grossly similar to that of precious and base metals. In the eastern Pacific, iron and ferro-alloy metal deposits occur along the western margins of North America and South America. Additional deposits occur in central and eastern North America, including the Canadian shield, and in the Guianian and Brazilian shields of South America. In the western Pacific, iron and ferro-alloy deposits occur on island arcs along convergent plate bound-

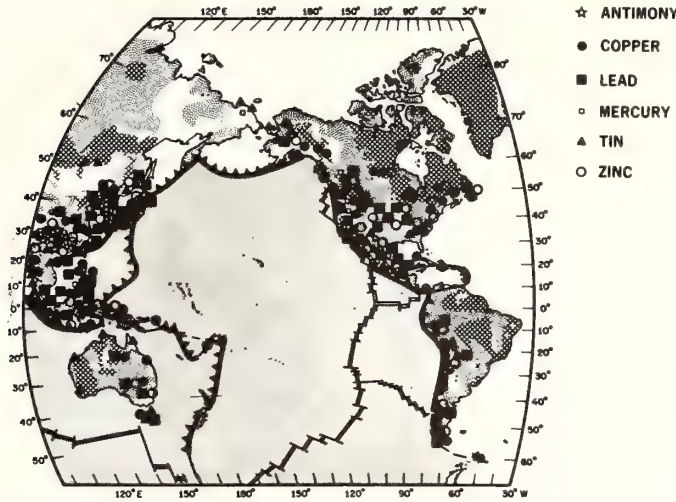


FIG. 3—Map of base metal deposits of Pacific region. Lithospheric plate boundaries are shown. Sediments enriched in base metals (shaded) overlie basalts of ocean basin.

aries and in eastern Asia and Australia, where they are separated by a gap from active convergent plate boundaries. Iron and ferro-alloy metal deposits have not been found along those sections of convergent plate boundaries where oceanic lithosphere is juxtaposed and island arcs are absent. Sedimentary strata directly overlying basalt of the Pacific Ocean basin are enriched in iron and ferro-alloy metals, in addition to base metals.

Nodules containing variable percentages of manganese, copper, nickel, and cobalt are present on about two thirds of the Pacific seafloor (Fig. 4;

Strakhov et al, 1968). A zone of nodules of anomalously high copper and nickel content (1.5–2.0%) and areal density (20–50% of seafloor) extends east-west across the Pacific between latitudes 5° and 20°N. No apparent spatial relation exists between plate boundaries and either the overall distribution or the enriched zone of nodules in the Pacific Ocean basin.

**Metal Deposits at Divergent Plate Boundaries**

Knowledge of the distribution of metal deposits with respect to divergent plate boundaries is

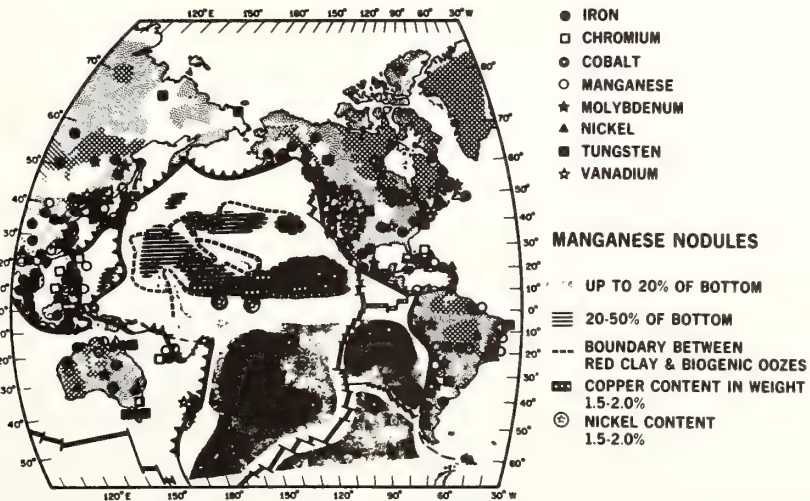


FIG. 4—Map of iron and ferro-alloy metal deposits, including manganese nodules, of Pacific. Lithospheric plate boundaries are shown.

limited because, as submerged oceanic ridges, these boundaries are less accessible to observation than are convergent plate boundaries. Sediments deposited about divergent plate boundaries in the Pacific Ocean basin are enriched in certain base, iron, and ferro-alloy metals. The recently discovered TAG hydrothermal field (R. Scott et al, 1974; Rona et al, in press), named after the Trans-Atlantic Geotraverse (TAG) of the National Oceanic and Atmospheric Administration, represents a type of metal deposit present in oceanic crust and may provide insights to processes of metal concentration at divergent plate boundaries, including those of the Pacific.

The TAG hydrothermal field occupies an area at least 15 km by 15 km including the east wall of the rift valley of the Mid-Atlantic Ridge at 26°N. Manganese oxide was recovered consistently by dredging from deposits concentrated along steps in the wall that are interpreted as faults which have acted as conduits for hydrothermal fluids. Concentration of the manganese oxide by hydrothermal processes capable of extreme chemical fractionation is evidenced by an exceptionally rapid rate of accumulation, about 200 mm per million years, and extreme purity, about 40% manganese with only trace quantities of iron and copper (M. Scott et al, 1974). Present activity is indicated by a positive temperature anomaly with an inverted temperature gradient (Rona et al, 1975) and by metal enrichment of suspended particulate matter (Betzer et al, 1974) in the seawater overlying the TAG hydrothermal field.

#### MODEL OF METAL DEPOSITS AT DIVERGENT PLATE BOUNDARIES

A model based on various lines of evidence (Spooner and Fyfe, 1973) considers that certain precious, base, iron, and ferro-alloy metals may be concentrated as deposits by sub-seafloor hydrothermal convection systems that may develop at crests of oceanic ridges. According to the model, cold dense seawater enters fractures in the basalt of an oceanic ridge. The seawater is heated as it encounters hot material intruded at the divergent plate boundary. The warm, less dense seawater rises through fractures in the basalt and leaches metals that are transported in solution as complexes with chloride in the seawater. A fraction of the metals then combines with sulfur in the seawater and precipitates as a massive stratabound sulfide body under reducing conditions beneath the basalt-seawater interface. Manganese oxide precipitates under oxidizing conditions at the basalt-seawater interface as the hydrothermal solutions discharge from the seafloor. Colloidal

ferric hydroxide precipitates from the hydrothermal solutions in the overlying seawater. The ferric hydroxide scavenges the remaining metals from solution by colloidal absorption and settles to deposit a layer of metalliferous sediments on basalt of the adjacent seafloor.

An example of an economic mineral deposit interpreted as the product of a sub-seafloor hydrothermal convection system occurs in the Troodos massif of Cyprus. The Troodos massif is interpreted as an obducted slice of oceanic crust generated at a divergent plate boundary (Gass and Masson-Smith, 1963; Moores and Vine, 1971). An "umber" of metallic oxides overlies massive stratabound copper sulfide ore bodies in basaltic rocks of the Troodos massif. The manganese oxide of the TAG hydrothermal field chemically resembles the umber and may be underlain by massive copper sulfide bodies (Rona, 1973a; R. Scott et al, 1974; Rona et al, in press). Relict metallic oxide and sulfide deposits may be expected to extend in belts along flow lines of seafloor spreading transverse to the axis of an oceanic ridge; the extent of the belts would depend on the continuity of seafloor spreading and the persistence of the sub-seafloor hydrothermal convection system which concentrates the deposits (Rona, 1973a). The metal deposits may be buried by off-axis volcanism.

#### MODEL OF METAL DEPOSITS AT CONVERGENT PLATE BOUNDARIES

A model to interpret the observed association of precious, base, iron, and ferro-alloy metal deposits with the convergent plate boundaries of the Pacific is based on the following concepts:

1. The dip of Benioff zones is inversely proportional to the rate of plate convergence (Tables 1-3; Luyendyk, 1970).
2. Marginal basins develop where the dip of Benioff zones exceeds about 35°.
3. Calc-alkalic andesitic volcanic rocks and tonalitic plutons occur above steeply dipping Benioff zones (Mitchell, 1973).
4. Silicic volcanic rocks and granitic plutons occur above shallow-dipping Benioff zones (Mitchell, 1973).
5. Metals in deposits along convergent plate boundaries are primarily derived from oceanic crust descending along the associated Benioff zone (Sawkins, 1972; Sillitoe, 1972) and from continental crust. The role of the mantle as a source of material remains to be evaluated.
6. The nature and volume of volatile matter expelled from oceanic crust descending along Benioff zones influence the extraction, transport,

concentration, and deposition of metals (Rub, 1972).

The model presents two regimes to account for the past and present distribution of metals along convergent plate boundaries of the western and eastern Pacific, as follows:

1. Relatively fast seafloor spreading and plate convergence are associated with a shallow Benioff zone and the generation of silicic volcanic rocks and granitic plutons (Fig. 5a, b). High-level porphyry copper deposits occur in the silicic volcanic rocks, and deep-level tin, tungsten, bismuth, fluorite, and molybdenum occur in the granites. The copper is primarily derived from metalliferous sediments and massive stratabound metallic sulfide deposits of the oceanic crust that descends along the underlying Benioff zone. The tin and associated metals, along with a portion of the granite (Stern and Wyllie, 1973), are derived from continental crust and their segregation is aided by the rise of volatile matter expelled from the descending oceanic crust. This regime is exemplified by western South America at present and by eastern Asia in late Mesozoic time.

2. Relatively slow seafloor spreading and plate convergence are associated with a steep Benioff zone, the development of marginal basins, and the generation of calc-alkalic andesitic volcanic rocks and tonalitic plutons with associated porphyry copper deposits (Fig. 5c, d). The calc-alkalic volcanic rocks and the copper are primarily derived from the oceanic crust (Jakes and White, 1972) that descends along the underlying Benioff zone; this crust includes metalliferous strata and

massive strata-bound metallic sulfide deposits. The tonalitic plutons and some copper may be derived from the base of continental or island-arc crust (Jakes and White, 1971; Brown, 1973). Granitic plutons emplaced during the first regime (Fig. 5b) are unroofed by erosion to expose deposits of tin and associated metals (Fig. 5d). The development of marginal basins (Fig. 5c, d) results in the separation of island arcs from the continent, producing a gap such as that observed between the metal deposits of eastern Asia and Australia and the active convergent plate boundaries of the western Pacific (Figs. 2-4). This regime is exemplified by eastern Asia at the end of the Mesozoic and at present.

#### SUMMARY

Consideration of the distribution of selected energy and material resources with respect to lithospheric plate boundaries of the Pacific (Figs. 1-4) leads to the following conclusions:

1. Divergent plate boundaries (oceanic ridges) are inferred to be related in time to the development of stratigraphic traps for petroleum in sedimentary basins on continents through the control of eustatic sea level by reversible volume changes of oceanic ridges.

2. Divergent plate boundaries are related in space to metalliferous deep-sea sediments and to the possible occurrence of massive strata-bound metallic sulfide deposits in oceanic crust.

3. Convergent plate boundaries are related in space to areas of offshore petroleum potential

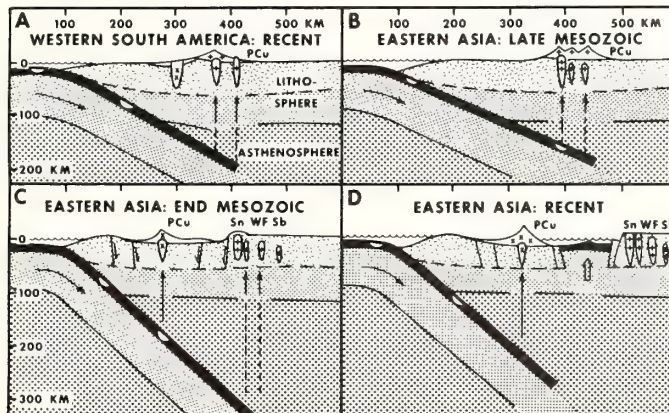


FIG. 5—Model of metallogensis at convergent plate boundaries of Pacific (modified from Mitchell, 1973). Diagrammatic cross sections through convergent plate boundaries show Benioff zone, oceanic crust (black) incorporating metalliferous sediments and massive strata-bound metallic sulfide bodies (white semicircles in oceanic crust), rising magma (solid vertical arrows), rising volatile matter (dashed vertical arrows), silicic volcanic rocks and granitic plutons (+), andesitic volcanic rocks and tonalitic plutons (x), and known deposits of porphyry copper (PCu), tin (Sn), tungsten (W), fluorite (F), and antimony (Sb). For explanation, see text.

and to onshore deposits of precious, base, iron and ferro-alloy metals.

4. Certain precious, base, iron, and ferro-alloy metal deposits that are present in Precambrian shields and old orogenic belts distant from present plate boundaries may be related to former plate boundaries.

5. Models suggest genetic relations between the observed distribution of metal deposits and geologic processes at plate boundaries. The models are interpretative in that they attempt to explain the observed distribution of deposits. With further development these models may predict the locations of undiscovered metal deposits.

#### REFERENCES CITED

- Anonymous, 1962, Oil and natural gas map of Asia and the Far East, scale 1:5,000,000: U.N. ECAFE, no. 16351, U.N. Pub. Sales No. 62-1-16, 4 sheets.
- 1963, Mineral distribution map of Asia and the Far East, scale 1:5,000,000: U.N. ECAFE, no. 63-157 14, U.N. Pub. Sales No. 63-1-18, 4 sheets.
- 1970, Energy atlas of Asia and the Far East: U.N. ECAFE, U.N. Pub. Sales No. E-70-1-11, E/CN-11/900, 25 p.
- 1972a, Principal mineral areas of Canada, scale 1:7,600,200, 22nd ed.: Canada Dept. Energy, Mines and Resources, Mineral Resources Br., and Canada Geol. Survey, Map 900A.
- 1972b, The Times atlas of the world, 4th ed. (revised): Edinburgh, John Bartholomew and Son Ltd., Times Newspapers Ltd., 272 p.
- Atwater, T., and J. D. Mudie, 1973, Detailed near-bottom geophysical study of the Gorda Rise: Jour. Geophys. Research, v. 78, p. 8665-8686.
- Betzer, P. R., et al, 1974, The Mid-Atlantic Ridge and its effect on the composition of particulate matter in the deep ocean: Eos (Am. Geophys. Union Trans.), v. 55, no. 4, p. 293.
- Bonine, M. E., et al, 1970, Atlas of Mexico: Univ. Texas at Austin, Bur. Business Research, 138 p.
- Boström, K., and M. N. A. Petersen, 1969, The origin of aluminum-poor ferromanganous sediments in areas of high heat flow on the East Pacific Rise: Marine Geology, v. 7, p. 427-447.
- Bracey, D. R., and T. A. Ogden, 1972, Southern Mariana arc; geophysical observations and hypothesis of evolution: Geol. Soc. America Bull., v. 83, p. 1509-1522.
- Brown, G. C., 1973, Evolution of granite magmas at destructive plate margins: Nature; Phys. Sci., v. 241, p. 26-28.
- Cook, H. E., 1972, Stratigraphy and sedimentation, p. 933-943 in J. D. Hays et al, eds., Initial reports of the Deep Sea Drilling Project, v. IX: Washington, U.S. Govt. Printing Office, 1205 p.
- Cronan, D. S., et al, 1972, Iron-rich basal sediments from the eastern equatorial Pacific; Leg 16, Deep Sea Drilling Project: Science, v. 175, no. 4017, p. 61-63.
- Dengo, G., and E. Levy, 1970, Estudios et mapa metalogénicos de América Central: Inst. Centroamericano Inv. y Tecnologia Indus., Pub. Geol. No. 3, 57 p., scale 1:200,000.
- Dymond, J., et al, 1973, Origin of metalliferous sediments from the Pacific Ocean: Geol. Soc. America Bull., v. 84, p. 3355-3372.
- Fischer, A. G., et al, 1971, Initial Reports of the Deep Sea Drilling Project, v. VI: Washington, U.S. Govt. Printing Office, 1329 p.
- Gass, I. G., and D. Masson-Smith, 1963, The geology and gravity anomalies of the Troodos Massif, Cyprus: Royal Soc. London Philos. Trans., Ser. A, v. 255, p. 417-467.
- Herron, E. M., 1972, Sea-floor spreading and the Cenozoic history of the east-central Pacific: Geol. Soc. America Bull., v. 83, p. 1671-1692.
- Isacks, B., J. Oliver, and L. R. Sykes, 1968, Seismology and the new global tectonics: Jour. Geophys. Research, v. 73, p. 5855-5899.
- and P. Molnar, 1971, Distribution of stresses in the descending lithosphere from a global survey of focal mechanism solutions of mantle earthquakes: Rev. Geophys. and Space Physics, no. 9, 103 p.
- Jakes, P., and A. J. R. White, 1971, Composition of island arcs and continental growth: Earth and Planetary Sci. Letters, v. 12, p. 224-230.
- and ——— 1972, Major and trace element abundances in volcanic rocks of orogenic areas: Geol. Soc. America Bull., v. 83, p. 29-39.
- Jones, D. B., advisory ed., 1972, Oxford economic atlas of the world, 4th ed.: London, Oxford Univ. Press, 239 p.
- Karig, D. E., 1971, Origin and development of marginal basins in the western Pacific: Jour. Geophys. Research, v. 76, p. 2542-2561.
- Kelleher, J. A., 1972, Rupture zones of large South American earthquakes and some predictions: Jour. Geophys. Research, v. 77, p. 2087-2103.
- Kennedy, W. Q., and J. E. Richey, 1947, Catalogue of the active volcanoes of the world: Bull. Volcanol., Supp. Ser. 2, v. 7, 11 p.
- Lafitte, P., and P. Rouveyrol, 1965, Carte minière du globe sur fond tectonique au 1:20,000,000 (projection équiareale): Paris, Bur. Recherches Géol. et Minières, 74, ed. provisoire, pt. 2.
- Langseth, M. G., Jr., 1969, The flow of heat from the Earth and the global distribution at the surface: Am. Inst. Aeronautics and Astronautics, Paper No. 69-589, 10 p.
- Le Pichon, X., J. Francheteau, and J. Bonnin, 1973, Plate tectonics: New York, Elsevier, 300 p.
- Luyendyk, B. P., 1970, Dips of downgoing lithospheric plates beneath island arcs: Geol. Soc. America Bull., v. 81, p. 3411-3416.
- McKelvey, V. E., and F. F. H. Wang, 1969, World sub-sea mineral resources: U.S. Geol. Survey Misc. Geol. Inv. Map I-632.
- Mitchell, A. H. G., 1973, Metallogenic belts and angle of dip of Benioff zones: Nature; Phys. Sci., v. 245, p. 49-52.
- Moores, E. M., and F. J. Vine, 1971, The Troodos Massif, Cyprus, and other ophiolites as oceanic crust; evaluation and implications: Royal Soc. London Philos. Trans., Ser. A, v. 268, p. 443-466.

- Oliver, J., et al, 1973, Dynamics of the downgoing lithosphere: *Tectonophysics*, v. 19, p. 133-147.
- Oxburgh, E. R., and D. L. Turcotte, 1971, Origin of paired metamorphic belts and crustal dilation in island arc regions: *Jour. Geophys. Research*, v. 76, p. 1315-1327.
- Piper, D. Z., 1973, Origin of metalliferous sediments from the East Pacific Rise: *Earth and Planetary Sci. Letters*, v. 19, p. 75-82.
- Pitman, W. C. III, R. L. Larson, and E. M. Herron, 1974, Age of the ocean basins determined from magnetic anomaly lineations: *Geol. Soc. America*, map.
- Roberts, R. J., and E. M. Irving, 1957, Mineral deposits of Central America: *U.S. Geol. Survey Bull.* 1034, 205 p.
- Rona, P. A., 1973a, Plate tectonics and mineral resources: *Sci. American*, v. 229, no. 1, p. 86-95.
- 1973b, Relations between rates of sediment accumulation on continental shelves, sea-floor spreading, and eustasy inferred from the central North Atlantic: *Geol. Soc. America Bull.*, v. 84, p. 2851-2872.
- and D. U. Wise, 1974, Symposium: global sea level and plate tectonics through time: *Geology*, v. 2, no. 3, p. 133-134.
- et al, 1975, Anomalous water temperatures over Mid-Atlantic Ridge crest at 26° North latitude: *Deep Sea Research*, v. 22, p. 611-618.
- et al, in press, Tectonic fabric and hydrothermal activity of Mid-Atlantic Ridge crest (lat. 26°N): *Geol. Soc. America Bull.*
- Rub, M. G., 1972, The role of the gaseous phase during the formation of ore bearing magmatic complexes: *Chem. Geology*, v. 10, p. 89-98.
- Sawkins, F. J., 1972, Sulfide ore deposits in relation to plate tectonics: *Jour. Geology*, v. 80, p. 377-397.
- Sayles, F. L., and J. L. Bischoff, 1973, Ferromanganous sediments in the equatorial East Pacific: *Earth and Planetary Sci. Letters*, v. 19, p. 330-336.
- Sclater, J. G., 1972, Heat flow and elevation of the marginal basins of the western Pacific: *Jour. Geophys. Research*, v. 77, p. 5705-5709.
- Scott, M. R., et al, 1974, Rapidly accumulating manganese deposit from the median valley of the Mid-Atlantic Ridge: *Geophys. Research Letters*, v. 1, p. 355-358.
- Scott, R. B., et al, 1974, The TAG Hydrothermal Field: *Nature*, v. 251, p. 301-302.
- Sillitoe, R. H., 1972, A plate tectonic model for the origin of porphyry copper deposits: *Econ. Geology*, v. 67, p. 184-197.
- Sleep, N. H., and M. N. Toksöz, 1971, Evolution of marginal basins: *Nature*, v. 233, p. 548-550.
- Sloss, L. L., 1963, Sequences in the cratonic interior of North America: *Geol. Soc. America Bull.*, v. 74, p. 93-114.
- Snead, R. E., 1972, Atlas of world physical features: New York, Wiley, 158 p.
- Sorokhtin, O. G., S. A. Ushakov, and V. V. Fedynskiy, 1974, Dynamics of crustal plates and origin of petroleum deposits: *Akad. Nauk SSSR Doklady*, v. 214, p. 1407-1410.
- Spooner, E. T. C., and W. S. Fyfe, 1973, Sub-sea floor metamorphism, heat and mass transfer: *Contr. Mineralogy and Petrology*, Springer-Verlag, p. 287-304.
- Stern, C. R., and P. J. Wylie, 1973, Water-saturated and undersaturated melting relations of a granite to 35 kilobars: *Earth and Planetary Sci. Letters*, v. 18, p. 163-167.
- Strakhov, N. M., et al, 1968, Geochemistry of a sedimentary manganese ore-forming process: *Akad. Nauk SSSR Geol. Inst. Trans.*, v. 185, 495 p.
- Tarling, D. H., 1973, Continental drift and reserves of oil and natural gas: *Nature*, v. 243, p. 277-279.
- Van Royan, W., and O. Bowles, 1952, The mineral resources of the world, in *Atlas of the world's resources*, v. II: New York, Prentice-Hall, 181 p.
- Vine, F. J., and J. T. Wilson, 1965, Magnetic anomalies over a young oceanic ridge off Vancouver Island: *Science*, v. 150, no. 3695, p. 485-489.
- von der Borch, C. C., W. D. Nesteroff, and J. S. Galehouse, 1971, Iron-rich sediments cored during Leg 8 of the Deep Sea Drilling Project, in J. I. Tracey, Jr., et al, eds., *Initial reports of the Deep Sea Drilling Project*, v. VIII: Washington, U.S. Govt. Printing Office, p. 725-819.
- Waring, G. A., 1965, Thermal springs of the United States and other countries of the world: a summary: *U.S. Geol. Survey Prof. Paper* 492, 383 p.

# Tectonic fabric and hydrothermal activity of Mid-Atlantic Ridge crest (lat 26°N)

PETER A. RONA  
REGINALD N. HARBISON\*  
BOBBY G. BASSINGER†

National Oceanic and Atmospheric Administration, Atlantic Oceanographic and Meteorological Laboratories, 15 Rickenbacker Causeway, Miami, Florida 33149

ROBERT B. SCOTT *Department of Geology, Texas A&M University, College Station, Texas 77843*  
ANDREW J. NALWALK† *Marine Sciences Institute, University of Connecticut, Groton, Connecticut 06340*

## ABSTRACT

An asymmetric tectonic fabric was delineated by narrow-beam bathymetric profiles in a 180-km<sup>2</sup> area of the Mid-Atlantic Ridge crest at lat 26°N. Features of the tectonic fabric are a continuous rift valley offset by small (<10-km) transform faults and minor fracture zones expressed as valleys with intervening ridges that trend normal and oblique to the two sides of the rift valley. The discharge zone of a postulated sub-sea-floor hydrothermal convection system is focused by faults on the southeast wall of the rift valley and driven by intrusive heat sources beneath the rift valley.

The rift valley has a double structure consisting of linear segments, bounded by ridges, and basins at the intersections of the minor fracture zones. The double structure of the rift valley acts like a template that programs the reproduction of the tectonic fabric. The minor fracture zones form an asymmetric V about the rift valley at variance with the symmetric small circles formed by major fracture zones. To reconcile the asymmetry of minor fracture zones with the symmetry of major fracture zones, it is proposed that the minor fracture zones have been preferentially reoriented by an external stress field attributed to interplate and intraplate motions. Major fracture zones remain symmetric under the same stress field owing to differential stability between minor and major structures of oceanic lithosphere. *Key words:* oceanic ridges, Mid-Atlantic Ridge, tectonic fabric, fracture zones, transform faults, rift valley, hydrothermal activity, hydrothermal min-

eral deposits, sub-sea-floor hydrothermal convection system.

## INTRODUCTION

The crest of the Mid-Atlantic Ridge at lat 26°N in the corridor of the Trans-Atlantic Geotraverse (TAG) of the National Oceanic and Atmospheric Administration (NOAA) was selected for study because the oceanic crust in this region is believed to have undergone a long history of relatively normal development isolated from mantle plumes and multiple plate boundaries (Fig. 1; Rona, 1973a). The tectonic fabric of the ridge crest at lat 26°N should be useful as a standard of crust produced from a slow-spreading ridge (Menard, 1967).

An interdisciplinary study of the Mid-Atlantic Ridge crest at lat 26°N performed as part of the TAG project in 1972 and 1973 included narrow-beam bathymetric, gravimetric, and magnetic profiling, dredging, coring, measurements of the thermal structure and chemistry of the water column, and ocean-bottom photography. The study resulted in the discovery of the TAG Hydrothermal Field, an area of at least 15 km<sup>2</sup>, including the southeast wall of the rift valley, where manganese oxide of hydrothermal origin is present (Fig. 2; Scott, R. B., and others, 1974) and hydrothermal solutions may be discharging from the sea floor (Rona and others, 1975). Previous evidence of the concentration of metals by hydrothermal processes in ocean basins has come from widespread metal enrichment in sediment immediately overlying basalt generated by sea-floor spreading about divergent plate boundaries (Degens and Ross, 1969; Böstrom and Peterson, 1966; Böstrom and others, 1972; von der Borch and Rex, 1971; von der Borch and others, 1971; Hollister and others, 1972; Dymond

and others, 1973; Sayles and Bischoff, 1973; Piper, 1973).

This report describes the regional tectonic fabric of a 180-km square of the Mid-Atlantic Ridge crest at lat 26°N centered on the TAG Hydrothermal Field and considers the relation of the tectonic fabric to hydrothermal activity. The tectonic fabric was delineated by a rectilinear grid of narrow-beam bathymetric, gravimetric, and magnetic profiles spaced about 10 km apart parallel to and 20 km apart perpendicular to the axis of the rift valley (Figs. 3 through 8). Directions of features are given in the azimuth system (0° to 360° clockwise

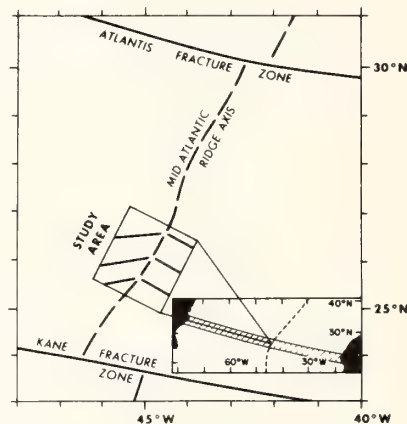


Figure 1. Inset shows location of study area on the crest of the Mid-Atlantic Ridge in the corridor (striped) of the NOAA Trans-Atlantic Geotraverse (TAG) in the central North Atlantic Ocean between southeastern North America and northwestern Africa. Locations and trends of transverse valleys (minor fracture zones) delineated within the study area are shown by solid lines. The axis of the Mid-Atlantic Ridge is dashed. The locations of major fracture zones (Atlantis and Kane) are shown.

\* Present address: U.S. Geological Survey, P.O. Box 7944, Metairie, Louisiana 70011.

† Deceased.





Figure 2. Photograph of first specimen of hydrothermal manganese oxide, 15.0 cm in diameter and 4.2 cm thick, recovered from the site of the TAG Hydrothermal Field in 1972 (Table 2, Station TAG 1972-13, see footnote 1; photograph by Wayne Stevens).

from north). Primary position control was by a satellite navigational system with estimated accuracy of  $\pm 1.0$  km.

## BATHYMETRY

### Rift Valley

Features of the tectonic fabric in the study area are the rift valley of the Mid-Atlantic Ridge, three valleys with intervening ridges transverse to the rift valley, and valleys that transect the transverse ridges (Figs. 3, 4). The rift valley trends northeast and consists of two structural elements that alternate along its axis. Linear segments of the rift valley, 20 to 40 km in length, alternate with irregularly shaped areas 15 to 25 km in length. The azimuth of the linear segments is  $25^\circ$ . The width of the linear segments at the 3,400-m isobath, which continuously delineates the floor of the rift valley, ranges between 5 and 15 km; the width of the irregularly shaped areas ranges between 15 and 25 km. The irregularly shaped areas between the linear segments are occupied by topographic depressions that form basins between 200 and 500 m below the 3,800-m isobath. The linear segments of the rift valley are successively offset in a right-lateral sense by as much as 10 km at the irregularly shaped areas.

### Transverse Valleys and Intervening Ridges

The transverse valleys and intervening ridges on the southeast side of the rift valley trend about  $115^\circ$ , nearly perpendicular to the rift valley axis (Figs. 3, 4). Those on the northwest side trend about  $265^\circ$ , oblique (about  $60^\circ$ ) to the axis of the rift valley

(Rona and others, 1973). The trend of the transverse valleys and intervening ridges appears to change near the northwestern margin of the study area.

Intersections of the transverse valleys and intervening ridges with the rift valley are topographically complex (Fig. 3). Certain of the transverse valleys are continuous with the rift valley (the southernmost transverse valley and the western half of the central transverse valley). Other transverse valleys are blocked by topographic highs within 25 km of the rift valley (the northernmost transverse valley and the eastern half of the central transverse valley). The actual or projected juncture of each transverse valley with the rift valley occurs at one of the irregularly shaped areas where the linear segments of the rift valley are offset. All transverse ridges continue up to the rift valley, where they form the walls along the linear segments.

Narrow-beam bathymetric profiles (effective total beam width about  $20^\circ$ ) across the three transverse valleys and intervening ridges are shown in Figure 5. The normal and oblique orientations of the transverse valleys and ridges with respect to the axis of the rift valley are apparent from the alignment of the transverse valleys. Width of the transverse valleys at their floors is about 10 km, and the average spacing between adjacent valley floors is 55 km. Relief of the intervening ridges measured from the valley floors ranges between 1,000 and 2,000 m. The transverse valleys appear linear and continuous along their axis on the basis of the bathymetric profiles (Fig. 5) and isobaths (Fig. 3), with the exception of the topographic complexities noted at certain junctures with the rift valley. The floor of each transverse valley progressively deepens

away from the rift valley, and the mean depth successively increases from northeast to southwest (Fig. 5).

Narrow-beam bathymetric profiles that cross the study area transverse to the axis of the rift valley (Fig. 6; also see McGregor and Rona, 1975, Fig. 5) reveal four things: (1) Echo returns are predominantly diffractions, as distinguished from specular reflections (Hoffman, 1957), indicating that the rock surface is irregular relative to the 12.5-cm wavelength of the projected acoustic pulse. (2) The floor of the rift valley is irregular and has relief up to several hundred metres that is related to the presence of discontinuous linear topographic prominences that project from either wall (Fig. 6, profiles C, D, E, H, J) or stand near the center of the rift valley (Fig. 6, profiles B through G), subparallel with the axis. (3) Steplike topographic levels with relief of hundreds of metres and widths of kilometres are present on both walls of the rift valley; the steplike levels may be correlated along either wall for distances corresponding to at least the width of each transverse ridge (about 30 km; Fig. 6, profiles B through G). (4) The mean inclination of the two walls of the rift valley ranges between about  $5^\circ$  and  $35^\circ$ , with no systematic difference apparent between the walls.

### Branches of the Rift Valley

The rift valley has branches that extend from either side (Figs. 3, 4). Branches extending from the southeast side trend nearly parallel to the rift valley ( $25^\circ$ ). Some branches that extend from the northwest side trend nearly parallel ( $25^\circ$ ), and others trend oblique ( $355^\circ$ ) to the rift valley.

Valleys parallel to the branches of the rift valley transect the transverse ridges at irregular intervals, with a minimum spacing of 5 km. These valleys generally extend only partly across the transverse ridges, although some valleys extend across the ridges. The valleys that transect the transverse ridges on the southeast side of the rift valley trend nearly parallel to the rift valley ( $25^\circ$ ) and perpendicular to the transverse ridges. The valleys that transect the transverse ridges on the northwest side of the rift valley have two trends corresponding to the two trends of the branches on the northwest side of the rift valley: (1) a trend ( $355^\circ$ ) oblique to the axis of the rift valley and nearly perpendicular to the transverse ridges, and (2) a trend ( $25^\circ$ ) parallel to the rift valley and oblique to the transverse ridges. The two trends appear to intersect.

### TAG Hydrothermal Field

The TAG Hydrothermal Field occupies a salient of the southeast wall that projects into the rift valley between depths of about 3,500 and 2,000 m (Fig. 3). The salient is

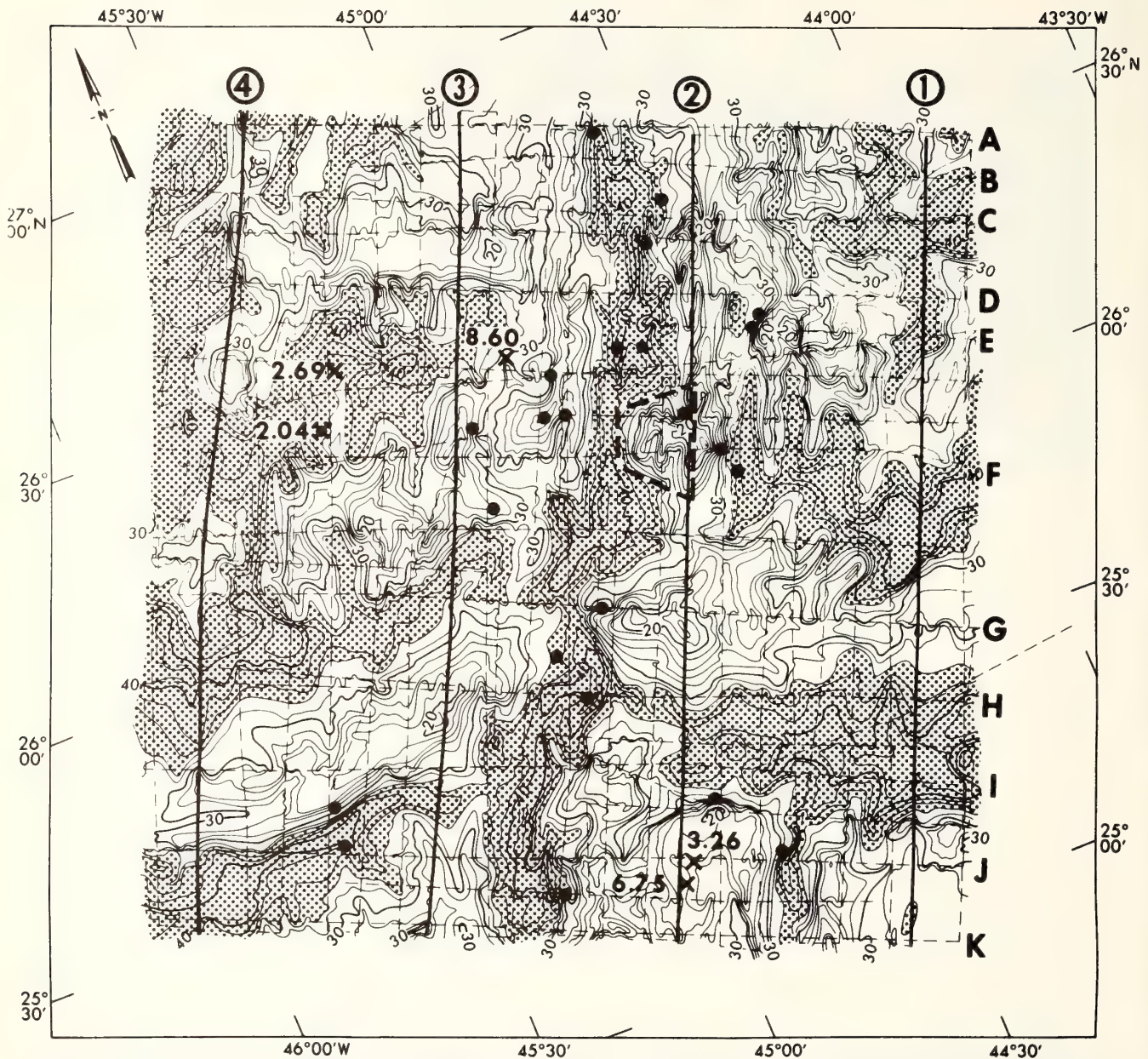


Figure 3. Isobath map of the study area (Fig. 1) contoured in hundreds of metres corrected for ship's draft and vertical sounding velocity (Matthews, 1939). Depths exceeding 3,400 m are shaded. Sounding tracks are dashed. The known portion of the TAG Hydrothermal Field on the southeast wall of the rift valley is outlined (trapezoid). Dredge and core stations are marked with dots (Table 2). Dots are omitted for three dredge stations within the TAG Hydrothermal Field (Table 2, stations TAG 1972-13, TAG 1973-2A, TAG 1973-3A). Values of heat flow in heat-flow units are shown at five stations marked with crosses (Langseth and others, 1972). The northeast-trending sounding tracks of bathymetric profiles 1 through 4 shown in Figure 5 are labeled (solid lines). The northwest-trending sounding tracks of bathymetric profiles A through K shown in Figure 6 are labeled. Note the north arrow in the upper left corner. Contour interval 200 m.

the end of a transverse ridge and forms the wall along a linear segment of the rift valley just north of the intersection with the central transverse valley. This transverse ridge is transected by more valleys perpendicular to its axis than any other ridge in the study area.

The southeast wall of the rift valley at the TAG Hydrothermal Field has steplike

topographic levels several kilometres wide at depths of about 3,200 and 2,500 m (Fig. 6, profile F). Two stereophotograph transects of this area resolve steps on the wall that are 100 to 300 m wide with 75-m average relief between depths of 3,400 and 3,100 m, 30 to 400 m wide with 40-m average relief between depths of 2,800 and 2,400 m, and smaller steps between depths

of 2,500 and 2,400 m, indicating that steps in the wall range in scale from metres to kilometres (McGregor and Rona, 1975).

#### GRAVITY

Measurements of gravity were made with a shipborne Graf-Askania gravimeter to an estimated accuracy of  $\pm 5$  mgal. The free-air

gravity anomalies of the study area range between  $-40$  and  $+80$  mgal (Fig. 7). Negative free-air gravity anomalies coincide with the rift valley and the transverse valleys. Positive free-air anomalies coincide with the transverse ridges, and largest values are on the highest parts of the transverse ridges adjacent to the rift valley. The TAG Hydrothermal Field occurs adjacent to such an anomaly. The values of gravity agree in magnitude with a rough calculation of the terrain effect. These observations suggest that the free-air anomalies are primarily due to topography.

### MAGNETIC MEASUREMENTS

Linear magnetic anomalies parallel the rift valley (Fig. 8). The linear anomalies are offset at transverse valleys in direction and amount corresponding to the offset of the linear segments of the rift valley. Low to negative values of residual magnetic intensity are associated with the transverse valleys. The linear magnetic anomalies are interpreted to have been generated during the Brunhes (axial anomaly), Matuyama, Gauss, and Gilbert magnetic polarity epochs between 0 and 5.8 m.y. B.P. The positive axial anomaly does not coincide with the axis of the rift valley but is centered over the southeast wall 5 km from the axis. About 2 km of the 5-km offset may be attributed to shift in the magnetic field owing to superposition of the sea floor and regional magnetic fields. The polarity of the residual magnetic field is indistinct between the end of the Gilbert epoch and anomaly 5 (10 m.y. B.P.) of the magnetic polarity reversal time scale (Heirtzler and others, 1968) identified about 120 km to either side of the rift valley. Half rates of sea-floor spreading measured perpendicular to the axis of the rift valley and averaged over various intervals to 10 m.y. B.P. are asymmetric, being faster to the southeast than to the northwest (Table 1).

The TAG Hydrothermal Field is situated within the positive axial anomaly and is associated with irregularities in the shape of that anomaly (Fig. 8). A more detailed magnetic survey reveals a pronounced low in the axial anomaly that coincides with the TAG Hydrothermal Field (Fig. 9; McGregor and Rona, 1975). Magnetic modeling indicates that the magnetic low is due to reduction in intensity of remanent magnetization (McGregor and others, 1976) that may be attributed to alteration of the magnetic mineral component in basalt by hydrothermal solutions (Luyendyk and Melson, 1967; Watkins and Paster, 1971; Ade-Hall and others, 1971). Hydrothermal alteration of basalt is evidenced by the presence of greenstone at

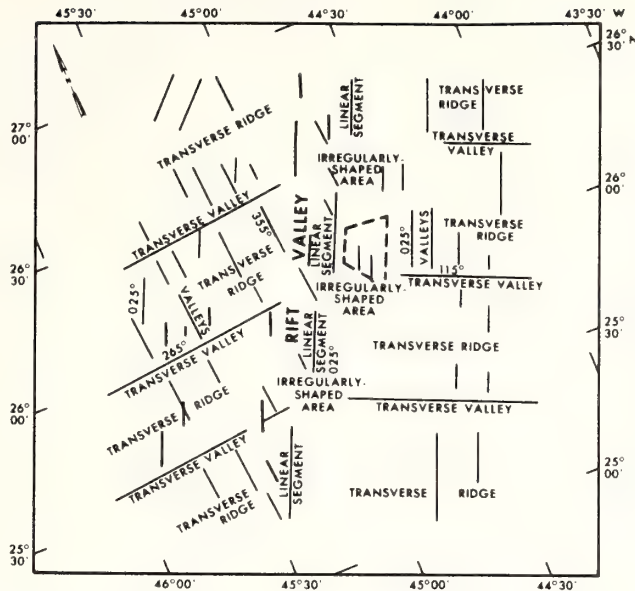


Figure 4. Diagrammatic representation of the tectonic fabric of the study area outlined from Figure 3. Azimuths of the major trends are noted. The TAG Hydrothermal Field is outlined (trapezoid). Note the north arrow in the upper left corner.

several sites along transverse ridges (Table 2; stations TAG 1972-8, TAG 1972-15).

### HEAT FLOW

Five measurements of conductive transfer of heat through the sea floor were made by Langseth and others (1972). The heat-flow measurements show higher heat flow through the transverse ridges (3.26 to 8.60 HFU) than through the intervening transverse valleys (2.04 to 2.69 HFU; Fig. 3). From the limited number of measurements, it is ambiguous whether this distribution of values is related to topography or to distance from the rift valley. A large variation in heat flow occurs over a horizontal distance of 5 km on one of the transverse ridges (6.75 and 3.26 HFU).

A water-temperature profile parallel to the ocean bottom over the southeastern wall of the rift valley at the TAG Hydrothermal Field was made with a 4-m-long vertical array of three thermistors mounted on a towed deep-sea camera (Rona and others, 1975). The profile revealed an abrupt anomaly of  $+0.11^{\circ}\text{C}$  associated with a gradient of  $0.008^{\circ}\text{C}/\text{m}$ , warming downward within 20 m of the bottom along a horizontal distance of about 350 m between depths of 3,030 and 2,950 at a step-like level on the southeast wall (Fig. 6, profile F), where hydrothermal material

<sup>1</sup> Table 3, "Rocks recovered from the Study Area of the NOAA Trans-Atlantic Geotraverse (TAG) of the Mid-Atlantic Ridge Crest at lat.  $26^{\circ}\text{N}$ ," GSA supplementary material 76-4, may be ordered from Documents Secretary, Geological Society of America, 3300 Penrose Place, Boulder, Colorado 80301.

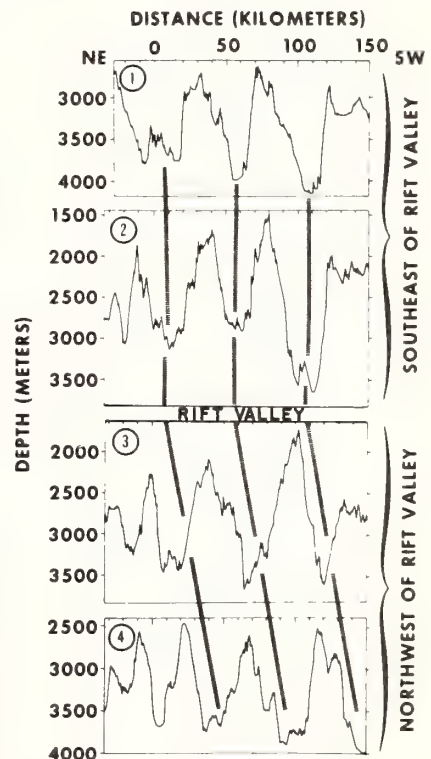


Figure 5. Digitized reproductions of narrow-beam bathymetric profiles 1 through 4 recorded along sounding tracks parallel to the rift valley located in Figure 3. The three transverse valleys correlate (dashed lines) as continuous features on either side of the rift valley, consistent with the isobath map (Fig. 3). Vertical exaggeration is about  $\times 60$ .

was dredged (Table 2, dredge station TAG 1973-3A). The source of the water-temperature anomaly may be either discharge of hydrothermal solutions or conductive transfer of heat from the ocean bottom. The abrupt, narrow character of the anomaly, inverted gradient, and associated geological and geochemical evidence favor a hydrothermal source.

## PETROLOGY

Rocks recovered by dredging and coring from the different features of the tectonic fabric in the study area are described in Table 2 (see footnote 1); sampling sites are marked in Figure 3. Fresh pillow basalt was recovered from the topographic prominences on the floor of the rift valley (Table 2, stations TAG 1972-17, TAG 1973-4C, TAG 1973-4G). Fresh basalt was also recovered from the walls of the rift valley. A varied suite of altered and metamorphosed rocks and limestone in addition to basalt was recovered from the transverse ridges. A

coarse-grained cumulate gabbro exposed in the wall of a valley that transects one of the transverse ridges may be a magma chamber formed in layer 3 of oceanic crust (Table 2, stations TAG 1973-7A, TAG 1973-7B, TO 75AK60-2A).

Manganese oxide was consistently dredged from the southeast wall of the rift valley within the area of the TAG Hydrothermal Field (Fig. 3; Table 2, stations TAG 1972-13, TAG 1973-2A, TAG 1973-3A). The manganese oxide occurs as a crust up to 42 mm thick on basalt talus, as veins in the talus fragments, and as a crust on and matrix in a breccia of basalt fragments. Stereophotograph transects of the rift valley wall show that the manganese oxide is associated with sediment-free talus and breccia-covered inner portions of the steps observed on the southeast wall between depths of 3,100 and 2,500 m (McGregor and Rona, 1975). The accumulation rate of the manganese oxide measured from the growth rate of Th<sup>230</sup> and Pa<sup>231</sup> toward secular equilibrium with their uranium parents

is about 200 mm/10<sup>6</sup> yr, two orders of magnitude faster than deep-sea hydrogenous ferromanganese nodules and crusts (Scott, M. R., and others, 1974). Atomic absorption spectrophotometry of the manganese indicates that the Mn content is 40 percent, Fe less than 0.1 percent, Al 0.1 percent, Zn 100 ppm, Cr 15 ppm, Ni 300 ppm, Co 20 ppm, and Cu 30 ppm; deep-sea hydrogenous ferromanganese nodules and crusts contain less Mn (10 to 20 percent) and considerably more of the other elements (Scott, M. R., and others, 1974). The relatively rapid rate of accumulation and the pure composition of the manganese oxide indicate concentration by a hydrothermal mechanism capable of extreme chemical fractionation. A crust consisting of an upper layer of hydrogenous manganese oxide up to 2 mm thick underlain by a lower layer of hydrothermal manganese oxide up to 10 mm thick was recovered from a site 12 km southeast of the sites at the southeast wall of the rift valley on the same transverse ridge (Fig. 3; Table 2, sta-

TABLE 1. HALF RATES OF SEA-FLOOR SPREADING ABOUT THE MID-ATLANTIC RIDGE

Reference	Latitude on Mid-Atlantic Ridge	Orientation	Averaging interval	Average half rate (cm/yr)	Direction
van Andel and Moore (1970)	6° to 8°S	Perpendicular to axis of rift valley	Axis of rift valley (0 m.y. B.P.) to anomaly 3 (4.5 m.y. B.P.)	2.16 ± 0.24 1.89 ± 0.04	E W
			Anomaly 3 (4.5 m.y. B.P.) to anomaly 5 (10 m.y. B.P.)	1.59 ± 0.24 1.12 ± 0.08	E W
Lattimore and others (1974)	26°N	Perpendicular to axis of rift valley	Axial anomaly to anomaly 5 (10 m.y. B.P.)	1.3 1.1	SE NW
McGregor and others (1976)	26°N	Perpendicular to axis of rift valley	Axis of rift valley (0 m.y. B.P.) to Brunhes-Matuyama boundary (0.69 m.y. B.P.)	1.7 0.7	SE NW
McGregor and others (1976)	26°N	Perpendicular to axis of rift valley	Matuyama epoch (0.69 to 2.43 m.y. B.P.)	1.3 1.1	SE NW
Present paper	26°N	Normal (115°) and oblique (265°) to axis of rift valley (25°)	Axis of rift valley (0 m.y. B.P.) to anomaly 5 (10 m.y. B.P.)	1.3 1.3	SE NW
Needham and Francheteau (1974)	36°N	Perpendicular to axis of rift valley	Axis of rift valley (0 m.y. B.P.) to Brunhes-Matuyama boundary (0.69 m.y. B.P.)	1.5 0.7	E W
			Matuyama epoch (0.69 to 2.43 m.y. B.P.)	1.3 0.9	E W
Greenewalt and Taylor (1974)	36°N	Perpendicular to axis of rift valley	Axis of rift valley (0 m.y. B.P.) to Brunhes-Matuyama boundary (0.69 m.y. B.P.)	1.3 1.0	E W
Macdonald and others (1975b)	36°N	Perpendicular to axis of rift valley	Axis of rift valley (0 m.y. B.P.) to anomaly 2 (1.8 m.y. B.P.)	1.33 0.70	E W
Macdonald and others (1975b)	36°N	Perpendicular to axis of rift valley	Anomaly 2 (1.8 m.y. B.P.) approximately to anomaly 4 (8 m.y. B.P.)	0.95 1.35	E W
Loncarevic and Parker (1971)	45°N	Perpendicular to axis of rift valley	Center of Brunhes (0 m.y. B.P.) to anomaly 5 (10 m.y. B.P.)	1.10 1.28	E W

tion TO 75AK61-1A; Scott and others, 1975). Seven attempts to dredge the northwest wall of the rift valley opposite the TAG Hydrothermal Field to determine whether hydrothermal deposits were symmetrically disposed about the rift valley recovered only a few fragments of basalt (Table 2, station TAG 1973-5C). The hydrothermal material is sufficiently friable that samples would probably have been recovered if present on the northwest wall.

## DISCUSSION

### Comparison of Tectonic Fabric

The continuous rift valley at lat 26°N consisting of linear segments and basins (Figs. 3, 4) is similar to that observed along the Mid-Atlantic Ridge between lat 22°N and 23°N (van Andel and Bowin, 1968), at lat 36°N (Needham and Francheteau, 1974), at lat 45°N (Aumento and others, 1971), and between lat 47°N and 51°N (Johnson and Vogt, 1973). The topographic prominences on the floor of the rift valley at lat 26°N, from which fresh basalt was recovered, appear similar to the discontinuous medial ridge as much as 250 m high by 1 km wide and as much as 4 km long described from the rift valley at lat 36°N (Bellaiche and others, 1974; Needham and Francheteau, 1974; Moore and others, 1974; Macdonald and others, 1975a), interpreted as a locus of crustal emplacement and basalt eruption.

Steplike levels and steps in the walls of the rift valley on scales ranging from metres to kilometres similar to those at lat 26°N have been observed in walls of the rift valley at lat 36°N (Needham and Francheteau, 1974) and at the Gorda Rise, where the steps are interpreted as fault blocks (Atwater and Mudie, 1973). Block faulting involving uplift is evidenced in the study area by the exposure of the cumulate gabbro from a deeper crustal level in an inferred fault scarp 1.2 km high (Table 2, stations TAG 1973-7A, TAG 1973-7B, TO 75AK60-2A) and by the exposure of greenstone in the walls of transverse ridges. Transverse ridges with intervening valleys that intersect and offset the rift valley at lat 26°N at a spacing of 55 km occur at an average spacing of 65 km along the Mid-Atlantic Ridge between lat 10°N and 40°N (Perry and Feden, 1974) and are present at lat 36°N (Detrick and others, 1973). The portions of the transverse valley that transect the rift valley are the loci of earthquake epicenters at lat 26°N (McGregor and Rona, 1975) and at lat 37°N (Reid and Macdonald, 1973).

The asymmetry in tectonic fabric, rates of sea-floor spreading, and position of the axial magnetic anomaly at lat 26°N is observed at other intensively studied sites along the Mid-Atlantic Ridge. Transverse

valleys and intervening ridges that trend normal and oblique to the southeast and northwest sides of the rift valley, respectively, at lat 26°N are also present at lat 36°N (Detrick and others, 1973; H. Fleming, 1975, personal commun.), and at lat 36°N, where the normal and oblique sides reverse (Bhattacharyya and Ross, 1972). Between lat 47°N and 51°N, the azimuths of linear segments of the rift valley alternate north and northwest; transverse ridges

occur adjacent to the former and intervening transverse valleys occur adjacent to the latter, forming a V-shaped pattern that is asymmetric about the rift valley (Johnson and Vogt, 1973, Fig. 7).

Half rates of sea-floor spreading measured perpendicular to the axis of the rift valley of the Mid-Atlantic Ridge and averaged over corresponding time intervals are faster to the east than to the west at lat 36°N, similar to the half rates at lat 26°N

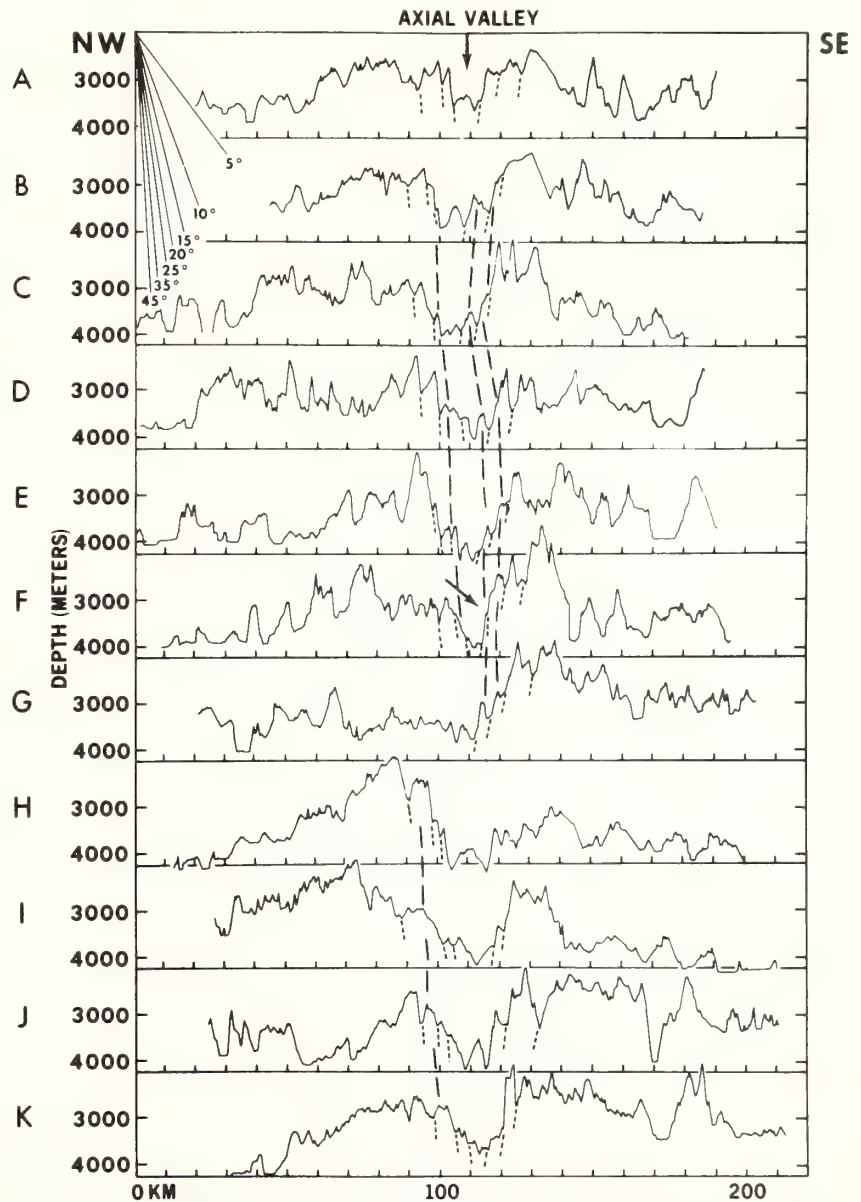


Figure 6. Digitized reproductions of narrow-beam bathymetric profiles recorded along sounding tracks A through K transverse to the rift valley located in Figure 3. The rift valley and the TAG Hydrothermal Field (arrow on profile F) are noted. Steplike topographic levels on the rift valley walls are tentatively correlated by dashed lines between the profiles. Faults inferred between fault blocks are indicated by dashed lines on profiles. Vertical exaggeration is about  $\times 15$ .

(Table 1). Conversely, average half rates of spreading at lat 45°N are faster to the west than to the east (Table 1). The axial anomaly is centered over the southeast wall offset about 5 km from the axis of the rift valley at lat 36°N (Needham and Francheteau, 1974) and at lat 22°N (van Andel and Bowin, 1968, Fig. 13), similar to the position of the axial anomaly at lat 26°N (Fig. 8). Earthquake epicenters along the linear segments of the rift valley may favor the southeastern side at lat 26°N (McGregor and Rona, 1975) and lat 36°N (Spindel and others, 1974) and the west side between lat 47°N and 51°N (Johnson and Vogt, 1973).

#### Tectonic Fabric and Hydrothermal Activity

The concentration of a hydrothermal mineral deposit in the Earth's crust requires special physical and chemical conditions. The emplacement of igneous rocks and the propagation of fractures and faults at divergent plate boundaries are conducive to the development of sub-sea-floor hydrothermal convection systems (Spooner and Fyfe, 1973; Hutchinson, 1973; Sillitoe, 1973; Rona, 1973b; Lister, 1974b; Lowell, 1975; Bonatti, 1975). Dense, cold sea water may penetrate down fractures and acquire heat at depth, and less dense hydrothermal

water may ascend and discharge as submarine springs through fracture systems. The circulating sea water may remove elements including heavy metals from the oceanic crust through which it circulates by high-temperature leaching and mass transfer (Krauskopf, 1956; Holland, 1967; Helgeson, 1964; Corliss, 1971; Hart, 1973). Metals including Fe, Mn, Cu, and Ni have been experimentally leached by sea water from basalt at 200° to 500°C and 0.5 to 1 kb (Mottl and others, 1974; Bischoff and Dickson, 1975). The convection of sea water as a hydrothermal solution through rocks emplaced at divergent plate boundaries is indicated by several lines of evidence. (1) Low values of heat flow from oceanic ridge crests imply that heat must be removed by water circulation (Palmason, 1967; Deffeyes, 1970; Talwani and others, 1971; Lister, 1972; Anderson, 1972; Williams and others, 1974; Sclater and others, 1974). (2) Hydrous metamorphosed oceanic crust and oceanic serpentine require a voluminous source of water (Miyashiro and others, 1971; Christensen, 1972). (3) Isotopic compositions of the hydrated rocks require a low  $\delta O^{18}$  isotopic source such as sea water (Muelenbachs and Clayton, 1972; Spooner and others, 1974). The TAG Hydrothermal Field is hypoth-

esized to be the zone where a voluminous sub-sea-floor hydrothermal convection system discharges through faults between steps of the southeast wall of the rift valley that act as conduits for the hydrothermal solutions (Figs. 9, 10). The system may be charged with sea water through fractures that underlie both the adjacent transverse valleys and the many valleys that transect the adjacent transverse ridge. Experimental (Elder, 1965) and theoretical (Donaldson, 1962; Elder, 1967) modeling shows that hydrothermal discharge is localized, and recharge is delocalized. Discharge is confined to vertically rising narrow jets (Wooding, 1963) and fracture-focused streams (Elder, 1965). Recharge occurs over large areas and involves downward water flow at rates that are fast enough to reduce the upward conductive heat flux (Wooding, 1963). Heat-flow measurements from the study area and from other areas on oceanic ridges are consistent with downwelling of sea water at valleys and upwelling at ridges (Lister, 1972), a circulation pattern favored by a geometric forcing effect of the topography (Lister, 1974a, 1974b). Such hydrothermal circulation can account for the low-intensity hydration and metamorphism under the influence of geothermal gradients that are higher than background value in certain rocks recovered from the transverse ridges (Table 2).

The southeast wall of the rift valley at the TAG Hydrothermal Field projects over the locus of crustal emplacement beneath the rift valley, the source of heat that vigorously drives the ascending limb of the hypothetical hydrothermal convection system. As hydrothermal solutions enriched in heavy metals complexed with sea-water chlorides ascend through the rocks, metals may combine with sulfur in the sea water and precipitate sulfides under reducing conditions within the basalt (Meyer and Hemley, 1967). Chalcopyrite, pyrrhotite, and marcasite have been experimentally grown from sea water during reaction with oceanic tholeiite at 500°C and 0.8 kb (Hajash, 1974). Metallic oxides may form under oxidizing conditions at the basalt-sea-water interface. Amorphous ferric hydroxide may precipitate as a colloid in the overlying sea water (Zelenov, 1964) and scavenge the metals remaining in solution or in admixed sea water by absorption (Krauskopf, 1956). Manganese oxide of hydrothermal origin has been sampled from the basalt-sea-water interface (Scott, M. R., and others, 1974), a positive temperature anomaly (0.11°C) and inversion of the gradient have been measured in near-bottom water (Rona and others, 1975), and amorphous particulate matter enriched in iron and manganese has been sampled from the water column overlying the TAG Hydrothermal Field (Betzer and others, 1974).

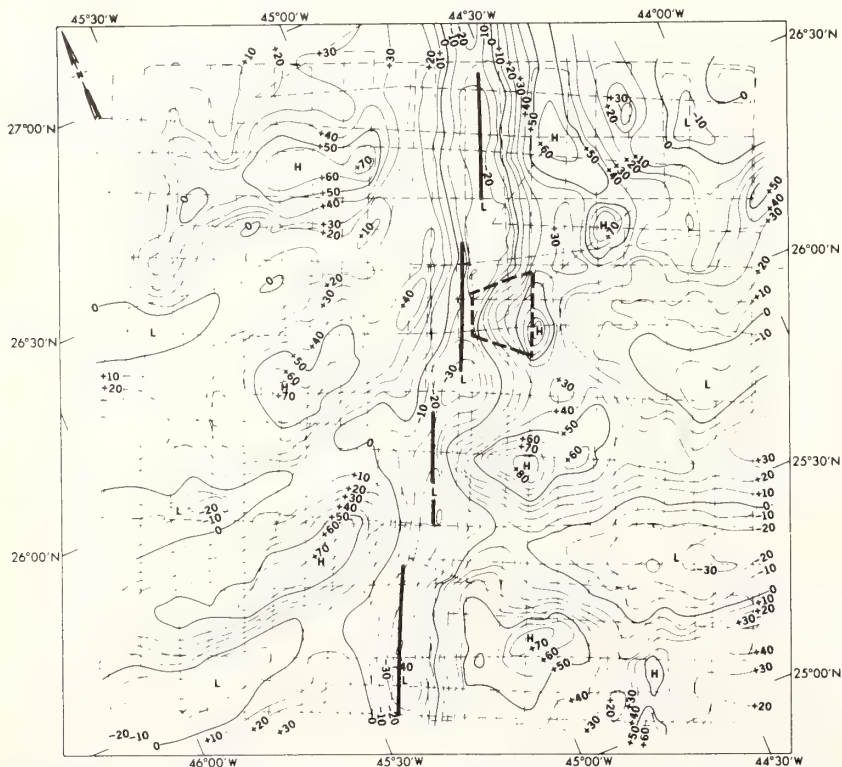


Figure 7. Map of free-air gravity contoured in milligals. Gravity highs (H) and lows (L) are indicated. The ship's tracklines are dashed. The TAG Hydrothermal Field is outlined (trapezoid). The axis of the rift valley along the linear segments is shown. Note the north arrow in the upper left corner.

Metallic sulfides have not been sampled from the TAG Hydrothermal Field, but their presence is suspected from geochemical considerations and analogy with ophiolites. Disseminated pyrite occurs in greenstone dredged from a transverse ridge in the study area (Table 2, station TAG 1972-15), and metallic sulfides are common in altered oceanic rocks (Dmitriev and others, 1970; Bonatti, 1975). Certain ophiolites, including those of Newfoundland (Upadhyay and Strong, 1973) and the Troodos Massif of Cyprus (Constantinou and Govett, 1973; Hutchinson, 1973; Robertson and Hudson, 1973), exhibit an association of cupreous pyrite bodies, altered pillow lava, and overlying manganese sulfide bodies attributed to hydrothermal processes similar to those inferred to be operating on the Mid-Atlantic Ridge at lat 26°N. Troodos-type massive stratiform cupreous sulfide bodies may be forming in pillow lava under the manganese oxide deposits at the TAG Hydrothermal Field (Fig. 10; Rona, 1973b; Scott, R. B., and others, 1974). It is infeasible to test this hypothesis by deep-sea drilling at this time because techniques constrain drilling to areas of sediment accumulation that, as topographic lows, are the inferred inflow areas of sub-sea-floor hydrothermal convection systems, and hydrothermal deposits would be absent. The massive stratiform sulfides would be expected to underlie hydrothermal discharge areas at topographic highs expressed as transverse ridges.

#### Development of Tectonic Fabric

Why is a crustal layer of uniform thickness not generated about the rift valley instead of a layer of varying thickness that forms topographic highs (transverse ridges) and lows (intervening transverse valleys)? Why is the tectonic fabric not symmetric about the rift valley? How can the asymmetry of the tectonic fabric be explained? How is hydrothermal activity related to tectonic fabric? These questions pinpoint problems addressed in a model that describes the development of the tectonic fabric of the study area (Fig. 11).

In the initial configuration of the model, the sea floor spreads symmetrically at equal half rates ( $r_1$ ) perpendicular to either side of the axis of a rift valley (Fig. 11a). The rift valley consists of alternating linear segments and irregularly shaped areas. The irregularly shaped areas are transected by minor fracture zones that successively offset the linear segments in a right-lateral sense. These minor fracture zones are considered to originate as small ridge-ridge transform faults on the basis of their characteristics in the study area, including offset of the linear segments of the rift valley and linear remnant magnetic anomalies, presence of topographic depressions, and seismicity.

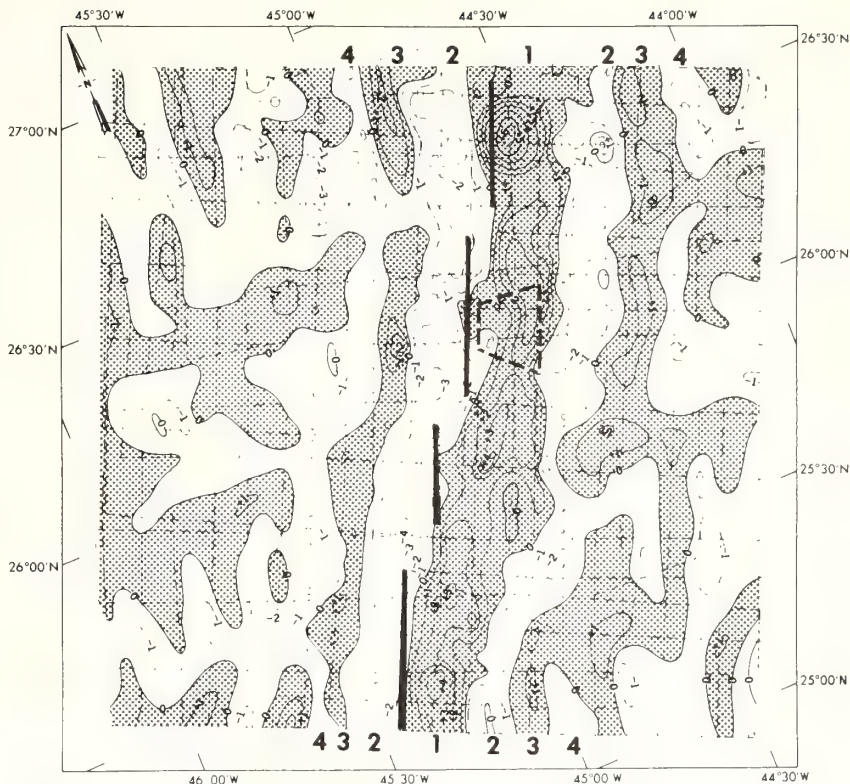


Figure 8. Map of residual magnetic intensity contoured in hundreds of gammas. The regional field was removed (IAGA, 1969), and a constant 300  $\gamma$  was added to the resultant field to balance the distribution of positive and negative values. The TAG Hydrothermal Field is outlined (trapezoid). The axis of the rift valley along the linear segments is shown. Note the north arrow in the upper left corner. The sequence of normal (shaded) and reversed (unshaded) magnetic polarity epochs is labeled as follows (Talwani and others, 1971, Fig. 11): 1. Brunhes, 0 to 0.69 m.y.; 2. Matuyama, 0.69 to 2.43 m.y.; 3. Gauss, 2.43 to 3.32 m.y.; 4. Gilbert, 3.32 to 5.18 m.y.

Spacing between the small transform faults and sense of offset may be related to the geometry of the rift between the continental margins of Africa and North America (Wilson, 1965), as demonstrated for the margins of the Red Sea rift (McKenzie and

others, 1970). The propagation of the fracture zones may be related to thermal contraction of the lithosphere (Turcotte, 1974; Collette, 1974).

Crustal material is emplaced by a dike-injection mechanism beneath the rift valley,

TABLE 2. PARTIAL LIST OF POSITIONS OF ROCKS RECOVERED FROM THE STUDY AREA

Station	Latitude	Longitude	Depth (corrected m)
TAG 1972-2A	26°09.7'N	44°47.4'W	3,240
TAG 1972-3A	26°07.3'N	44°48.8'W	3,170
TAG 1972-8	25°22.5'N	44°54.8'W	2,820
TAG 1972-13	26°08.0'N	44°45.0'W	3,080
TAG 1972-15	26°33.9'N	44°30.0'W	3,400
TAG 1972-17	26°44.5'N	44°37.2'W	3,590
TAG 1973-2A	26°09.7'N	44°47.4'W	3,240
TAG 1973-3A	26°07.3'N	44°48.8'W	3,170
TAG 1973-4C	26°18.2'N	44°42.1'W	4,262
TAG 1973-4G	26°19.2'N	44°44.1'W	4,060
TAG 1973-5C	26°13.8'N	44°57.0'W	3,010
TAG 1973-7A	26°15.3'N	44°27.0'W	3,390 to 2,410
TAG 1973-7B	26°15.3'N	44°27.0'W	3,390 to 2,410
TO 75AK60-2A	26°17.8'N	44°24.0'W	2,520 to 1,920
TO 75AK61-1A	26°07.6'N	44°40.5'W	2,600 to 2,000

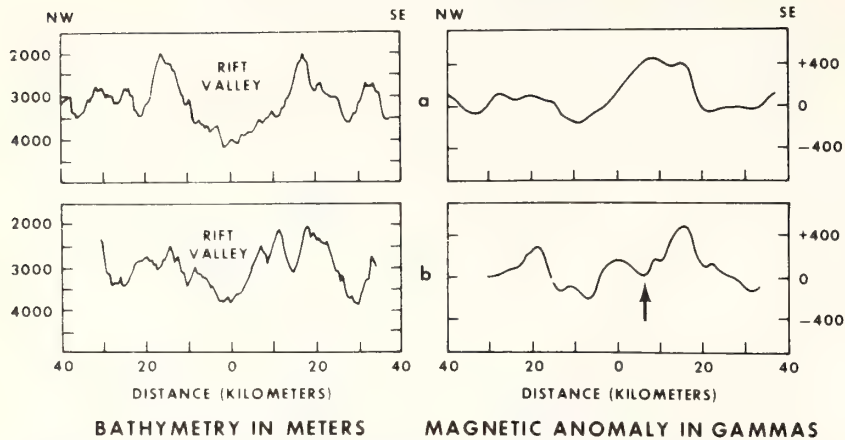


Figure 9. Bathymetric and residual magnetic profiles across rift valley of Mid-Atlantic Ridge near lat 26°N (McGregor and Rona, 1975). a. Profiles 12 km north of TAG Hydrothermal Field; this magnetic profile has large axial (Brunhes) positive anomaly over rift valley typical of profiles outside TAG Hydrothermal Field. b. Profiles across TAG Hydrothermal Field. Arrow on magnetic profile points to magnetic low in positive axial (Brunhes) anomaly. Reduction in magnetic intensity may provide a useful criterion in exploration for active or relict submarine hydrothermal mineral deposits.

which is a zone of extension (Heezen and others, 1959; Matthews and Bath, 1967; Harrison, 1968; Cann, 1970). The dikes and the sides of the rift valley are parallel. The crustal material remains near its level of emplacement in the form of relative topographic lows at the irregularly shaped areas because the cold walls at the intersection of the rift valley with the transverse fractures may cause upwelling material to solidify below its isostatic equilibrium level (Sleep and Biehler, 1970).

The crust is at least 1.5 km thinner at the transverse fractures than at the intervening transverse ridges inferred from the difference of topographic relief. Crustal material also solidifies below its eventual isostatic equilibrium level beneath linear segments of the rift valley (Sleep, 1969), where the material is isostatically uplifted in fault blocks as a result of processes of crustal thickening and extension (Deffeyes, 1970; Osmaston, 1971; Lachenbruch, 1973; Parker and Oldenburg, 1973; Neebham and Francheteau, 1974).

Sea-floor spreading at equal rates perpendicular to either side of the rift valley results in the generation of transverse valleys about the topographic lows at the irregularly shaped areas of the rift valley and intervening transverse ridges about the topographic highs at the linear segments. The transverse ridges are constructed of fault blocks that are uplifted from the floor and accrete at the walls of the rift valley; each fault block is several kilometres wide, and its long axis lies parallel to the rift valley.

The transverse ridges are transected perpendicular to their axes by valleys. The valleys originate as branches nearly parallel to the rift valley that remain near the level of

the rift valley floor during differential uplift of the adjacent fault blocks. The branches are inactive compared with the rift valley, which is active because it is coincident with the locus of crustal emplacement. The rift zones of Iceland (Kjartansson, 1960, 1962, 1965, 1968, 1969) and the Afar region (Lowell and Genik, 1972) also exhibit branches subparallel to the active rift. As the sea floor spreads, the branches split off from the rift valley and form the valleys that transect the transverse ridges. Lengths of crust  $l_1$  and  $l_2$  are generated per unit time perpendicular to the axis of the rift valley, such that  $l_1 = l_2$ .

The second configuration of the model (Fig. 11b) introduces apparent asymmetric directions and half rates of sea-floor spreading. The half rate of spreading  $r$  perpendicular to the rift valley decreases 15 percent to the left ( $r_2$ ) relative to the right side ( $r_1$ ), corresponding to half rates of 1.1 and 1.3 cm/yr averaged over an interval of 10 m.y. in the study area (Table 1); the corresponding lengths of crust generated per unit time are  $l_2$  and  $l_1$ , such that  $l_2 < l_1$ . The direction of spreading remains perpendicular to the axis of the rift valley to the right and reorients 30° to the left, corresponding to the trends of the transverse valleys on either side of the rift valley in the study area (Figs. 3, 4). Solving for the half rate of spreading in the reoriented direction to the left ( $r_3$ ) using values from the study area,  $r_3 = r_2 / \cos 30^\circ = 1.3$  cm/yr. The crustal length generated at spreading half rate  $r_3$  per unit time is  $l_3$ . Using values from the study area,  $r_1 = r_3$  and  $l_1 = l_3$ .

The asymmetric directions and equal half rates ( $r_1, r_3$ ) of spreading introduced in the second configuration of the model (Fig. 11b) continue for 6.5 m.y. to produce the

third configuration (Fig. 11c). Transverse valleys and intervening ridges are generated about topographic highs and lows, as previously described (Fig. 11a). However, these features are oriented normal (right side) and oblique (left side) to the rift valley, that is, aligned with the true relative directions of spreading. In spite of the reorientation of spreading direction, the long axes of the fault blocks uplifted from the rift valley floor remain parallel to the axis of the rift valley. This parallelism accounts for the parallelism of the walls observed along linear segments of the rift valley. Do the long axes of the fault blocks remain parallel to the axis of the rift valley during oblique spreading, or do the blocks rotate until the long axes become perpendicular to the re-oriented spreading direction? If the fault blocks rotated during spreading, then a delta-shaped gap would be expected to form between the unrotated blocks adjacent to the rift valley and the rotated blocks away from the rift valley on the side of oblique spreading. The apparent absence of such gaps in the study area (Fig. 3) makes such rotation unlikely. Rather, the long axes of the fault blocks probably remain nearly parallel to the axis of the rift valley during both symmetric and asymmetric spreading, as shown in the model (Fig. 11).

Two sets of branches of the rift valley form, corresponding to the two sets observed in the study area (Figs. 3, 4). One set is parallel to the rift valley and the long axes of the fault blocks. This set controls the structural development of the valleys that transect the transverse ridges perpendicular to their axes on the normal spreading (right) side of the model and controls development of a secondary trend that transects the transverse ridges on the oblique spreading (left) side of the model. The second set of branches is oblique to the rift valley and to the long axes of the fault blocks. This second set appears only on the oblique spreading (left) side, where it controls the structural development of the valleys that transect the transverse ridges perpendicular to their axes. The actual bathymetric features transecting the transverse ridges on the northwest side of the rift valley in the study area appear to be a composite of at least these two trends (Fig. 3).

The central ridge on the right side of the rift valley is transected by several closely spaced valleys that originated as branches of the rift valley (Fig. 11c). These valleys facilitate the inflow of sea water to charge a sub-sea-floor hydrothermal convection system. Hydrothermal deposits shown in black in Figure 11c form at and adjacent to the wall of the rift valley. Relict deposits extend along the transverse ridge as a consequence of sea-floor spreading (Rona, 1973b). The relict hydrothermal manganese recovered 12 km along flow lines of



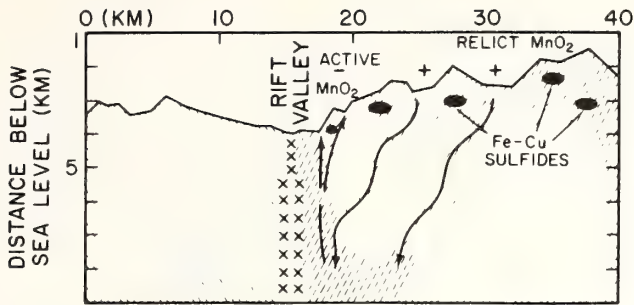


Figure 10. Diagrammatic sketch of a sub-sea-floor hydrothermal convection system like that hypothesized to exist at the TAG Hydrothermal Field (drawn from profile F, Fig. 6; vertical exaggeration is about  $\times 2$ ). Arrows indicate directions of hydrothermal flow. Slant lines indicate directions of maximum permeability controlled by structural grain, including fractures, faults, and dikes. Hydrothermal deposits are forming adjacent to the rift valley, and relict deposits are present away from the rift valley as a consequence of sea-floor spreading. Actually, relict deposits may be covered by off-axis volcanism. Symbols: +, zone of recharge; -, zone of discharge; x, zone of igneous intrusion.

sea-floor spreading southeast of the active site at the wall of the rift valley (Table 2; station TO 75AK61-1A) indicates the persistence of the special structural and thermal conditions that maintain sub-sea-floor hydrothermal convection for at least 1 m.y. Off-axis extrusive volcanism may act both to suppress hydrothermal activity and to cover hydrothermal deposits. Consequently, the actual extent of hydrothermal deposits along flow lines of sea-floor spreading may be difficult to determine.

Relative to magnetic measurements, the model (Fig. 11) is consistent with the ob-

served general parallelism between remanent magnetic lineations and the rift valley (Fig. 8). Because remanent magnetization resides in the rocks of the fault blocks, the inferred parallelism between the long axes of these blocks and the rift valley ensures that the gross pattern of linear residual anomalies remains parallel to the axis of the rift valley in spite of the asymmetric tectonic fabric. The 3-km southeastward offset of the center of the axial (Brunhes) magnetic anomaly from the rift valley that remains after removal of the magnetic field effect may be alternatively interpreted as fol-

lows: (1) if it is possible for the locus of crustal emplacement to shift from the rift valley to one of its branches, then a north-westward shift to the present rift valley could account for the off-center position of the axial anomaly, or (2) asymmetric half rates of sea-floor spreading perpendicular to the rift valley would produce a wider magnetic anomaly on the faster spreading side, resulting in a displacement of the geometric center of the anomaly in the direction of faster spreading while the locus of spreading remained at the rift valley. The second interpretation is supported by the

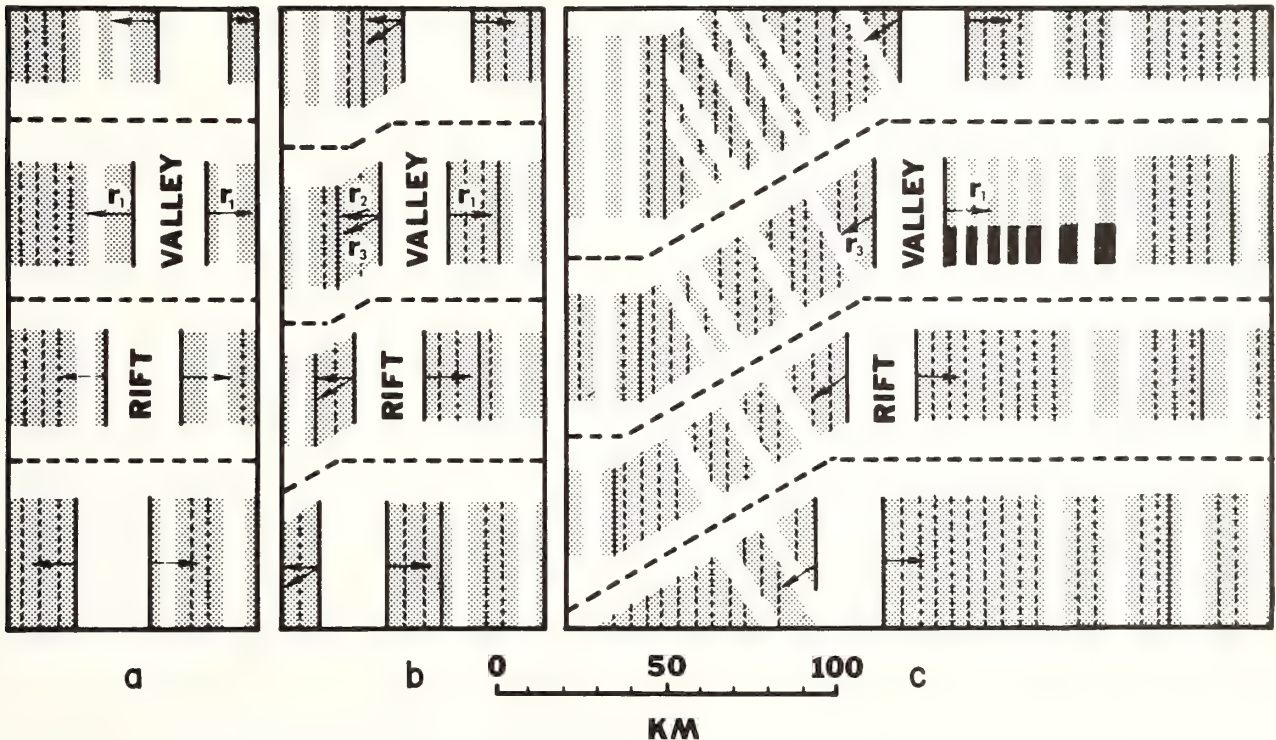


Figure 11. Diagrammatic model for development of tectonic fabric and hydrothermal activity observed on Mid-Atlantic Ridge crest at lat  $26^{\circ}\text{N}$  (Figs. 3, 4). Axis and two sides of rift valley (heavy solid vertical lines) are parallel. Arrows indicate apparent directions of sea-floor spreading at apparent half rates  $r_1$ ,  $r_2$ , and  $r_3$  about rift valley. Transverse ridges (shaded) and intervening transverse valleys (open) are shown. Transverse ridges are transected by valleys perpendicular to their axes (open). Most of valleys only partly transect transverse ridges, and valleys to left of rift valley exhibit composite trends (Fig. 3). Transverse ridges are constructed of fault blocks with long axes (light vertical dashed lines) parallel to rift valley. Lengths of crust generated per unit time are bracketed between sides of the rift valley (heavy solid vertical lines) and solid vertical lines on transverse ridges to either side of the rift valley (b, c). Sites of active and relict hydrothermal mineralization (black) are shown along one of transverse ridges (c). Successive configurations of model (a, b, c) are explained in text. Distinct tectonic fabric of model is obscured in ocean basin by off-axis volcanism.

asymmetric spreading rates in the study area (Table 1) and poses fewer mechanical problems than the first interpretation.

### Symmetric and Asymmetric Processes of Oceanic Ridges

The asymmetric tectonic fabric of the study area occurs within the overall symmetric framework of the central North Atlantic, as indicated by the nearly median position of the Mid-Atlantic Ridge; the nearly mirror-image distribution of physiographic provinces about the ridge axis (Heezen and others, 1959); the trajectories of major fracture zones such as the Atlantis and Kane (Fig. 1), which follow small circles symmetric about the axis of the Mid-Atlantic Ridge (Morgan, 1968); and the sequences of remanent magnetic anomalies that indicate a grossly similar history of sea-floor spreading in the eastern and western Atlantic (Pitman and Talwani, 1972) since the time of the magnetic quiet zone boundary (Rona and others, 1970). Two alternative hypotheses are considered to reconcile the development of the observed asymmetric tectonic fabric within a symmetric framework:

1. Original orientation. The asymmetric orientation of minor fracture zones about the axis of an oceanic ridge, such as the normal and oblique orientation of the minor fracture zones of the study area, is produced by asymmetric processes of development of oceanic lithosphere. This hypothesis poses problems in reconciling asymmetric with symmetric fractures of the ocean basin, because asymmetric plate motions at minor fracture zones would be incompatible with symmetric plate motions at major fracture zones.

2. Reorientation. The processes of development of oceanic lithosphere are essentially symmetric and produce both symmetric minor and major fracture zones associated with symmetric sea-floor spreading. The minor fracture zones are continuously reoriented, whereas the major fracture zones maintain their original orientations. As a consequence of reorientation, apparent<sup>2</sup> half rates of spreading determined perpendicular to the axis of an oceanic ridge are asymmetric. True<sup>2</sup> half rates of spreading determined in the directions of the reoriented minor fracture zones normal and oblique to the axis of an oceanic ridge are equal. This hypothesis is supported by the relations between spreading directions and rates determined in the study area and may reconcile the discrepancy between asymmetric and symmetric features of the ocean basin.

The continuous reorientation of minor fracture zones according to hypothesis 2

may be caused by the application of an external stress field deriving from different sources, as follows:

1. Forces related to magmatic processes. These forces are related to magmatic movements associated with the axial region of an oceanic ridge. A type of regional magmatic movement proposed by Vogt (1971) and applied by Johnson and Vogt (1973) and Vogt and Johnson (1975) to account for V-shaped topography about the axis of an oceanic ridge depends on the principle of a geopotential gradient to drive asthenospheric flow along the axis of the ridge from topographic highs over inferred mantle plumes, for example, the Azores about 1,000 km north of the study area. According to their hypothesis, the V should point in the direction of flow away from the high as the vector resulting from asthenospheric flow along and sea-floor spreading about an oceanic ridge. The Vogt-Johnson hypothesis does not account for the V-shaped configuration of the minor fracture zones about the Mid-Atlantic Ridge in the study area because the V points toward rather than away from the Azores (Fig. 1). Forces related to magmatic processes undoubtedly contribute to the stress field, but they are considered secondary rather than primary components.

2. Forces related to tectonic processes. These forces are related to interplate and intraplate motions and may be primary components of the stress field that we infer to be reorienting the direction of minor fracture zones and sea-floor spreading along the Mid-Atlantic Ridge. The role of interplate and intraplate forces as primary components of the stress field is supported by the observation that the orientation of minor fracture zones and of sea-floor spreading differs about lithospheric plate boundaries. The orientation of minor fracture zones and of sea-floor spreading is different on the two sides of the rift valley of the Mid-Atlantic Ridge and differs between the American and Eurasian plates north of the Azores triple junction and the American and African plates south of that junction (Table 1).

The reorientation hypothesis allows the simultaneous development of small-scale asymmetric structures and large-scale symmetric structures in oceanic lithosphere. Minor fracture zones associated with small transform faults (offset  $\leq 30$  km) like those in the study area (Fig. 1) behave in an unstable manner at the relatively slow average half rates of spreading ( $\leq 2$  cm/yr) prevalent at the Mid-Atlantic Ridge. The minor fracture zones are continuously reoriented under the influence of an external stress field as they are generated by sea-floor spreading about the small transform faults. Major fracture zones like the Atlantis and Kane associated with large transform faults

behave in a stable manner at relatively slow average half rates of spreading. The major fracture zones maintain their orientation under the influence of the same external stress field as they are generated by sea-floor spreading about the large transform faults. Thickness of lithosphere related to distribution of isotherms at a transform fault may be a determinant of the stability of fracture zones (Vogt and others, 1969). Asymmetric small-scale structures may then develop within the large-scale symmetry of the Atlantic Ocean basin as a consequence of the differential stability between minor and major fracture zones (Rona, 1976).

### CONCLUSIONS

The tectonic fabric of oceanic crust that is slowly spreading about an oceanic ridge develops according to a definite geometry, which has been deduced from analysis of the asymmetric tectonic fabric of the Mid-Atlantic Ridge crest at lat 26°N within the overall symmetric framework of the central North Atlantic Ocean basin (Figs. 3, 4, 11), as follows: (1) The double structure of the rift valley consisting of linear segments between transform faults, alternating with basins at transform faults, acts as a template that programs the reproduction of tectonic fabric through control of the formation of topographic highs and lows. (2) The transverse ridges are constructed of fault blocks that are uplifted from the floor and accrete at the walls along the linear segments of the rift valley. (3) The transverse valleys are minor fracture zones aligned with the direction of sea-floor spreading about the topographic lows. (4) Branches of the rift valley extend to either side oriented parallel to the rift valley and perpendicular to the axis of the transverse ridges; the branches split off from the rift valley as a consequence of sea-floor spreading and form valleys that transect the transverse ridges. (5) Minor fracture zones expressed as transverse valleys between ridges may be asymmetric about the axis of a rift valley, tending to remain normal to one side and to reorient oblique to the other side of the rift valley. (6) Where tectonic fabric is asymmetric about the rift valley, apparent half rates of spreading measured perpendicular to the rift valley are also asymmetric, with faster half rates on the normal side and slower half rates on the oblique side. (7) The half rates of spreading measured in the directions of the minor fracture zones normal and oblique to the rift valley tend toward equality over averaging intervals of millions of years. (8) The observed tectonic fabric may be explained by preferential asymmetric reorientation of minor fracture zones relative to symmetric major fracture zones, resulting from differential structural stabil-

<sup>2</sup> relative.

ity under the influence of an external stress field.

Structural and thermal conditions at divergent plate boundaries are conducive to hydrothermal activity. The concentration of sub-sea-floor hydrothermal systems is favored by special conditions in the tectonic fabric of an oceanic ridge crest, such as close spacing of valleys and proximity to intrusive heat sources that promote vigorous circulation (Fig. 10). The distribution of hydrothermal convection systems along divergent plate boundaries, like the inferred system at the TAG Hydrothermal Field, can only be conjectured from the known distribution of 17 active hydrothermal systems over a distance of 250 km in the neovolcanic zone of Iceland on the Mid-Atlantic Ridge (Bödvarsson, 1961) and at least 14 systems over a distance of 900 km in the Red Sea (Degens and Ross, 1969; Backer and Schoell, 1972). Because all of the oceanic crust that covers two-thirds of the Earth has been generated about divergent plate boundaries, the relation between tectonic fabric and hydrothermal activity on the Mid-Atlantic Ridge crest at lat 26°N is relevant to the metallic mineral potential of ocean basins and regions where oceanic crust has been incorporated into islands and continents.

#### ACKNOWLEDGMENTS

We lament the early death of our colleague and friend, Andrew J. Nalwalk, who generously contributed his prowess at sea to this work.

We thank Louis W. Butler of the National Oceanic and Atmospheric Administration (NOAA) for his help in all phases of the work and Bonnie A. McGregor of NOAA for recontouring the bathymetric map. We are grateful to Bruce C. Heezen for encouraging us to determine the characteristics of normal oceanic crust.

We thank Gleb B. Udintsev and others onboard the R/V *Akademik Kurchatov* for obtaining the AK series of dredge samples (Table 2, see footnote 1) on a cooperative TAG cruise in 1975 as part of the U.S.-USSR Agreement on Cooperation in Studies of the World Ocean.

We acknowledge the excellent cooperation of Captain Floyd J. Tucker, Jr., Captain Lavon L. Posey, Cdr. Richard H. Allbritton, Cdr. Walter S. Simmons, Lt. Paul M. Duernberger, and the other officers and crews of NOAA Ship *Discoverer* and NOAA Ship *Researcher* during the 1972 and 1973 TAG cruises.

#### REFERENCES CITED

- Ade-Hall, J. M., Palmer, H. C., and Hubbard, T. P., 1971, The magnetic and opaque petrological response of basalts to regional hydrothermal alteration: *Royal Astron. Soc. Geophys. Jour.*, v. 24, p. 137-174.
- Anderson, R. N., 1972, Petrologic significance of low heat flow on the flanks of slow-spreading mid-ocean ridges: *Geol. Soc. America Bull.*, v. 83, p. 2947-2956.
- Atwater, T., and Mudie, J. D., 1973, Detailed near-bottom geophysical study of the Gorda Rise: *Jour. Geophys. Research*, v. 78, p. 8665-8686.
- Aumento, F., Loncarevic, B. D., and Ross, D. I., 1971, IV. Regional studies; Hudson geotransverse: *Geology of the Mid-Atlantic Ridge at 45°N*: *Royal Soc. London Philos. Trans.*, ser. A, v. 268, p. 623-650.
- Backer, H., and Schoell, M., 1972, New deeps with brines and metalliferous sediments in the Red Sea: *Nature Phys. Sci.*, v. 240, p. 153-158.
- Bellaiche, G., Cheminee, J. L., Francheteau, J., Hekinian, R., Le Pichon, X., Needham, H. D., and Ballard, R. D., 1974, Inner floor of the rift valley: First submersible study: *Nature*, v. 250, p. 558-560.
- Betzer, P. R., Bolger, G. W., McGregor, B. A., and Rona, P. A., 1974, The Mid-Atlantic Ridge and its effect on the composition of particulate matter in the deep ocean: *EOS (Am. Geophys. Union Trans.)*, v. 55, p. 293.
- Bhattacharyya, P. J., and Ross, D. I., 1972, Mid-Atlantic Ridge near 45°N, computer interpolation and contouring of bathymetry and magnetics: *Canada Dept. Environment, Marine Sci. Directorate, Marine Sci. Paper* 11, 9 p.
- Bischoff, J. L., and Dickson, F. W., 1975, Seawater-basalt interaction at 200°C and 500 bars: Implications for origin of sea-floor heavy mineral deposits and regulation of seawater chemistry: *Earth and Planetary Sci. Letters*, v. 25, p. 385-397.
- Bödvarsson, G., 1961, Physical characteristics of natural heat resources in Iceland: *Jökull*, v. 11, p. 29-38.
- Bonatti, E., 1975, Metallogensis at oceanic spreading centers, in *Annual Reviews of Earth and Planetary Sciences*, Vol. 3: Palo Alto, Calif., Annual Reviews, Inc. p. 401-431.
- Böstrom, K., and Peterson, M.N.A., 1966, Precipitates from hydrothermal exhalations on the East Pacific Rise: *Econ. Geology*, v. 61, p. 1258-1265.
- Böstrom, K., Farquarson, B., and Eyl, W., 1972, Submarine hot springs as a source of active ridge sediments: *Chem. Geology*, v. 10, p. 189-203.
- Cann, J. R., 1970, New model for the structure of the ocean crust: *Nature*, v. 226, p. 928-930.
- Christensen, N. I., 1972, The abundance of serpentinites in the oceanic crust: *Jour. Geology*, v. 80, p. 709-719.
- Collette, B. J., 1974, Thermal contraction joints in a spreading seafloor as origin of fracture zones: *Nature*, v. 251, p. 299-300.
- Constantinou, G., and Govett, G.J.S., 1973, *Geology, geochemistry, and genesis of Cyprus sulfide deposits*: *Econ. Geology*, v. 68, p. 843-858.
- Corliss, J. B., 1971, The origin of metal-bearing submarine hydrothermal solutions: *Jour. Geophys. Research*, v. 76, p. 8128-8138.
- Deffeyes, K. S., 1970, The axial valley: A steady-state feature of the terrain, in Johnson, H., and Smith, B. L., eds., *The megatectonics of continents and oceans*: Camden, N.J., Rutgers Univ. Press, p. 194-222.
- Degens, E. T., and Ross, D. A., eds., 1969, *Hot brines and recent heavy metal deposits in the Red Sea*: New York, Springer, 600 p.
- Detrick, R. S., Mudie, J. D., Luyendyk, B. P., and Macdonald, K. C., 1973, Near-bottom observations of an active transform fault (Mid-Atlantic Ridge at 37°N): *Nature Phys. Sci.*, v. 246, p. 59-61.
- Dmitriev, L. V., Barsukov, V. L., and Udintsev, G. B., 1970, Rift zone of the oceans and the problem of ore formation: *Geokhimiya*, v. 4, p. 937.
- Donaldson, I. D., 1962, Temperature gradients in the upper layers of the Earth's crust due to convective water flows: *Jour. Geophys. Research*, v. 67, p. 3449-3459.
- Dymond, J., Corliss, J. B., Heath, J. R., Field, C. W., Dash, E. J., and Veeh, H. H., 1973, Origin of metalliferous sediments from the Pacific Ocean: *Geol. Soc. America Bull.*, v. 84, p. 3355-3372.
- Elder, J. W., 1965, Physical processes in geothermal areas, in *Terrestrial heat flow*: *Am. Geophys. Union Geophys. Mon.* 8, p. 211-239.
- 1967, Steady free convection in a porous medium heated from below: *Jour. Fluid Mechanics*, v. 27, p. 29-48.
- Greenewalt, D., and Taylor, P. T., 1974, Deep-tow magnetic measurements across the axial valley of the Mid-Atlantic Ridge: *Jour. Geophys. Research*, v. 79, p. 4401-4405.
- Hajash, A., 1974, An experimental investigation of high temperature seawater-basalt interactions: *Geol. Soc. America Abs. with Programs*, v. 6, p. 771.
- Harrison, C.G.A., 1968, Formation of magnetic anomaly pattern by dyke injection: *Jour. Geophys. Research*, v. 73, p. 2137-2142.
- Hart, R. A., 1973, A model for chemical exchange in the basalt-seawater system of oceanic layer II: *Canadian Jour. Earth Sci.*, v. 10, p. 799-816.
- Heezen, B. C., Tharp, M., and Ewing, M., 1959, The floors of the oceans. I. The North Atlantic: *Geol. Soc. America Spec. Paper* 65, 122 p.
- Heirtzler, J. R., Dickson, G. O., Herron, E. M., Pitman, W. C. III, and Le Pichon, X., 1968, Marine magnetic anomalies, geomagnetic field reversals, and motions of the sea floor and continents: *Jour. Geophys. Research*, v. 73, p. 2119-2136.
- Helgeson, H. C., 1964, *Complexing and hydrothermal ore deposition*: New York, Pergamon Press.
- Hoffman, J., 1957, Hyperbolic curves applied to echo sounding: *Internat. Hydrog. Rev.*, v. 34, p. 45-55.
- Holland, H. D., 1967, Gangue minerals in hydrothermal systems, in Barnes, H. L., ed., *Geochemistry of hydrothermal ore deposits*: New York, Holt, Rinehart & Winston, p. 382-436.

- Hollister, C. D., Fwing, J. I., Habib, D., Hathaway, J. C., Lancelot, Y., Luterbacher, H., Paulus, F. J., Poag, C. W., Wilcoxon, J. C., and Worstell, P., 1972, Initial reports of the Deep Sea Drilling Project, Vol. II: Washington, D.C., U.S. Govt. Printing Office, 1077 p.
- Hutchinson, R. W., 1973, Volcanogenic sulfide deposits and their metallogenic significance: *Econ. Geology*, v. 68, p. 1223-1246.
- IAGA Commission 2, Working Group 4, 1969, International geomagnetic reference field 1965.0: *Jour. Geophys. Research*, v. 74, p. 4407-4408.
- Johnson, G. L., and Vogt, P. R., 1973, Mid-Atlantic Ridge from 47° to 51° North: *Geol. Soc. America Bull.*, v. 84, p. 3443-3462.
- Kjartansson, G., 1960, 1962, 1965, 1968, 1969, Geological map of Iceland, sheets 1, 2, 3, 5, 6: Reykjavik, Mus. Nat. History.
- Krauskopf, K. B., 1956, Factors controlling the concentrations of thirteen rare metals in seawater: *Geochim. et Cosmochim. Acta*, v. 9, p. 1-32B.
- Lachenbruch, A. H., 1973, A simple mechanical model for oceanic spreading centers: *Jour. Geophys. Research*, v. 78, p. 3395-3417.
- Langseth, M. G., Jr., Malone, I. F., and Bookman, C. A., 1972, Sea floor geothermal measurements from Vema Cruise 25: Palisades, N.Y., Lamont-Doherty Geol. Observatory Tech. Rept. 4, CU-4-72; Tech. Rept. 2, CU-2-72, 159 p.
- Lattimore, R. K., Rona, P. A., DeWald, O. E., 1974, Magnetic anomaly sequence in the central North Atlantic: *Jour. Geophys. Research*, v. 79, p. 1207-1209.
- Lister, C.R.B., 1972, On the thermal balance of a mid-ocean ridge: *Royal Astron. Soc. Geophys. Jour.*, v. 26, p. 515-535.
- 1974a, Water percolation in the oceanic crust: *EOS (Am. Geophys. Union Trans.)*, v. 55, p. 740-742.
- 1974b, On the penetration of water into hot rock: *Royal Astron. Soc. Geophys. Jour.*, v. 39, p. 465-509.
- Loncarenic, B. D., and Parker, R. L., 1971, The Mid-Atlantic Ridge near 45°N. XVII. Magnetic anomalies and sea floor spreading: *Canadian Jour. Earth Sci.*, v. 8, p. 883-898.
- Lowell, J. D., and Genik, J. D., 1972, Sea-floor spreading and structural evolution of southern Red Sea: *Am. Assoc. Petroleum Geologists Bull.*, v. 56, p. 247-259.
- Lowell, R. P., 1975, Circulation in fractures, hot springs, and convective heat transport on mid-ocean ridge crests: *Royal Astron. Soc. Geophys. Jour.*, v. 40, p. 351-365.
- Luyendyk, B. P., and Melson, W. G., 1967, Magnetic properties and petrology of rocks near the crest of the Mid-Atlantic Ridge: *Nature*, v. 215, p. 147-149.
- Macdonald, K., Luyendyk, B. P., Mudie, J. D., and Spiess, F. N., 1975a, Near-bottom geophysical study of the Mid-Atlantic Ridge median valley near lat 37°N: Preliminary observations: *Geology*, v. 3, p. 211-215.
- 1975b, Near-bottom magnetic measurements, asymmetric spreading, oblique spreading, and the zone of intrusion in the FAMOUS area of the Mid-Atlantic Ridge (37°N): *FOS (Am. Geophys. Union Trans.)*, v. 56, p. 375.
- Matthews, D. H., and Bath, J., 1967, Formation of magnetic anomaly pattern of Mid-Atlantic Ridge: *Royal Astron. Soc. Geophys. Jour.*, v. 13, p. 349-357.
- Matthews, D. J., 1939, Tables of the velocity of sound in pure water and sea water for use in echo-sounding and sound ranging (2nd ed.): London, Admiralty, Hydrographic Dept. Pub. 282, 52 p.
- McGregor, B. A., and Rona, P. A., 1975, Crest of Mid-Atlantic Ridge at 26°N: *Jour. Geophys. Research*, v. 80, p. 3307-3314.
- McGregor, B. A., Harrison, C.G.A., Lavelle, J. W., and Rona, P. A., 1976, Magnetic anomaly pattern on Mid-Atlantic Ridge crest at 26°N: *Jour. Geophys. Research*, v. 81 (in press).
- McKenzie, D. P., Davis, D., and Molnar, P., 1970, Plate tectonics of the Red Sea and East Africa: *Nature*, v. 226, p. 243-248.
- Menard, H. W., 1967, Sea floor spreading, topography, and the second layer: *Science*, v. 157, p. 923-924.
- Meyer, C., and Hemley, J. J., 1967, Wall rock alteration, in Barnes, H. L., ed., *Geochemistry of hydrothermal ore deposits*: New York, Holt, Rinehart & Winston, p. 166-235.
- Miyashiro, A., Shido, F., and Ewing, M., 1971, Metamorphism in the Mid-Atlantic Ridge near 24°N and 30°N: *Royal Soc. London Philos. Trans.*, ser. A, v. 268, p. 589-603.
- Moore, J. G., Fleming, H. S., and Phillips, J. D., 1974, Preliminary model for extrusion and rifting at the axis of the Mid-Atlantic Ridge, 36°48'N: *Geology*, v. 2, p. 437-440.
- Morgan, W. J., 1968, Rises, trenches, great faults and crustal blocks: *Jour. Geophys. Research*, v. 73, p. 1959-1982.
- Mottl, M. J., Corr, R. F., and Holland, H. D., 1974, Chemical exchange between sea water and mid-ocean ridge basalt during hydrothermal alteration: An experimental study: *Geol. Soc. America Abs. with Programs*, v. 6, p. 879-880.
- Muehlenbachs, K., and Clayton, R. N., 1972, Oxygen isotope geochemistry of submarine greenstones: *Canadian Jour. Earth Sci.*, v. 9, p. 471-478.
- Needham, H. D., and Francheteau, J., 1974, Some characteristics of the rift valley in the Atlantic Ocean near 36°48' North: *Earth and Planetary Sci. Letters*, v. 22, p. 29-43.
- Osmaston, M. F., 1971, Genesis of ocean ridge median valleys and continental rift valleys: *Tectonophysics*, v. 11, p. 387-405.
- Palmason, G., 1967, On heat flow in Iceland in relation to the Mid-Atlantic Ridge, in Björnsson, S., ed., *Iceland and mid-oceanic ridges*: *Soc. Sci. Islandica*, v. 38, p. 111-127.
- Parker, R. L., and Oldenburg, D. W., 1973, Thermal model of ocean ridges: *Nature Phys. Sci.*, v. 242, p. 137-139.
- Perry, R. K., and Feden, R. H., 1974, Bathymetry of the Mid-Atlantic Ridge from 10°N to 40°N latitudes: *Geol. Soc. America Abs. with Programs*, v. 6, p. 909.
- Piper, D. Z., 1973, Origin of metalliferous sediments from the East Pacific Rise: *Earth and Planetary Sci. Letters*, v. 19, p. 75-82.
- Pitman, W. C. III, and Talwani, M., 1972, Sea-floor spreading in the North Atlantic: *Geol. Soc. America Bull.*, v. 83, p. 619-649.
- Reid, I., and Macdonald, K., 1973, Microearthquake study of the Mid-Atlantic Ridge near 37°N, using sonobuoys: *Nature*, v. 246, p. 88-90.
- Robertson, A.H.F., and Hudson, J. D., 1973, Chemical precipitates on a Tethyan ocean ridge: *Earth and Planetary Sci. Letters*, v. 18, p. 93-106.
- Rona, P. A., 1973a, Marine geology, in *McGraw-Hill yearbook of science and technology*: New York, McGraw-Hill Book Co., p. 252-256.
- 1973b, Plate tectonics and mineral resources: *Sci. American*, v. 229, no. 1, p. 86-95.
- 1976, Asymmetric fracture zones and sea-floor spreading: *Earth and Planetary Sci. Letters* (in press).
- Rona, P. A., Brakl, J., and Heitzler, J. R., 1970, Magnetic anomalies in the northeast Atlantic between the Canary and Cape Verde Islands: *Jour. Geophys. Research*, v. 75, p. 7412-7420.
- Rona, P. A., Harbison, R. N., Bassinger, B. G., Butler, L. W., and Scott, R. B., 1973, Asymmetrical bathymetry of the Mid-Atlantic Ridge at 26°N latitude: *EOS (Am. Geophys. Union Trans.)*, v. 54, p. 243.
- Rona, P. A., McGregor, B. A., Betzer, P. R., Bolger, G. W., and Krause, D. C., 1975, Anomalous water temperatures over Mid-Atlantic Ridge crest at 26° North latitude: *Deep-Sea Research*, v. 22, p. 611-618.
- Sayles, F. L., and Bischoff, J. L., 1973, Ferromanganese sediments in the equatorial East Pacific: *Earth and Planetary Sci. Letters*, v. 19, p. 330-336.
- Slater, J. G., Von Herzen, R. P., Williams, D. L., Anderson, R. N., and Klitgord, K., 1974, The Galapagos spreading center: Heat flow low on the north flank: *Royal Astron. Soc. Geophys. Jour.*, v. 38, p. 609-626.
- Scott, M. R., Scott, R. B., Rona, P. A., Butler, L. W., and Nalwalk, A. J., 1974, Rapidly accumulating manganese deposit from the median valley of the Mid-Atlantic Ridge: *Geophys. Research Letters*, v. 1, p. 355-358.
- Scott, R. B., Rona, P. A., McGregor, B. A., and Scott, M. R., 1974, The TAG Hydrothermal Field: *Nature*, v. 251, p. 301-302.
- Scott, R. B., Mialpas, J., Udintsev, G., and Rona, P. A., 1975, Submarine hydrothermal activity and sea-floor spreading at 26°N, MAR: *Geol. Soc. America Abs. with Programs*, v. 7, p. 1263.
- Sillitoe, R. H., 1973, Environments of formation of volcanogenic massive sulfide deposits: *Econ. Geology*, v. 68, p. 1321-1336.
- Sleep, N. H., 1969, Sensitivity of heat flow and gravity to the mechanism of sea-floor spreading: *Jour. Geophys. Research*, v. 74, p. 542-549.
- Sleep, N. H., and Biehler, S., 1970, Topography and tectonics at the intersections of fracture zones with central rifts: *Jour. Geophys. Research*, v. 75, p. 2748-2752.
- Spindel, R. C., Davis, S. B., Macdonald, K. C., Porter, R. P., and Phillips, J. D., 1974, Mi-

- croearthquake survey of median valley of the Mid-Atlantic Ridge at 36°30'N: *Nature*, v. 248, p. 577-579.
- Spooner, E.T.C., and Fyfe, W. S., 1973, Sub-sea floor metamorphism, heat and mass transfer: *Contr. Mineralogy and Petrology*, v. 42, p. 287-304.
- Spooner, E.T.C., Beckinsale, R. D., Fyfe, W. S., and Smewing, J. D., 1974, O<sup>18</sup> enriched ophiolitic metabasic rocks from E. Liguria (Italy), Pindos (Greece), and Troodos (Cyprus): *Contr. Mineralogy and Petrology*, v. 47, p. 41-74.
- Talwani, M., Windish, C. C., and Langseth, M. G., Jr., 1971, Reykjanes Ridge crest: A detailed geophysical study: *Jour. Geophys. Research*, v. 76, p. 473-517.
- Turcotte, D. L., 1974, Are transform faults thermal contraction cracks?: *Jour. Geophys. Research*, v. 79, p. 2573-2577.
- Upadhyay, H. D., and Strong, D. F., 1973, Geological setting of the Betts Cove copper deposits, Newfoundland: An example of ophiolite sulfide mineralization: *Econ. Geology*, v. 68, p. 161-167.
- van Andel, T. H., and Bowin, C. O., 1968, Mid-Atlantic Ridge between 22° and 23° North latitude and the tectonics of mid-ocean rises: *Jour. Geophys. Research*, v. 73, p. 1279-1298.
- van Andel, T. H., and Moore, T. C., 1970, Magnetic anomalies and sea floor spreading rates in the northern South Atlantic: *Nature*, v. 226, p. 328-330.
- Vogt, P. R., 1971, Asthenosphere motion recorded by the ocean floor south of Iceland: *Earth and Planetary Sci. Letters*, v. 13, p. 155-160.
- Vogt, P. R., and Johnson, G. L., 1975, Transform faults and longitudinal flow beneath the midoceanic ridge: *Jour. Geophys. Research*, v. 80, p. 1399-1428.
- Vogt, P. R., Avery, O. E., Schneider, E. D., Anderson, C. N., and Bracey, D. R., 1969, Discontinuities in sea-floor spreading: *Tectonophysics*, v. 8, p. 285-317.
- von der Borch, C. C., and Rex, R. W., 1971, Amorphous iron oxide precipitates in sediments cored during Leg 5, Deep Sea Drilling Project, *m* Initial reports of the Deep Sea Drilling Project, Vol. 5: Washington, D.C., U.S. Govt. Printing Office, p. 541-544.
- von der Borch, C. C., Nesteroff, W. D., and Galehouse, J. S., 1971, Iron-rich sediments cored during Leg 8 of the Deep Sea Drilling Project, *m* Initial reports of the Deep Sea Drilling Project, Vol. 8: Washington, D.C., U.S. Govt. Printing Office, p. 829-833.
- Warkins, N. D., and Paster, T. P., 1971, The magnetic properties of igneous rocks from the ocean floor: *Royal Soc. London Philos. Trans., ser. A*, v. 268, p. 507-550.
- Williams, D. L., Von Herzen, R. P., Sclater, J. G., and Anderson, R. N., 1974, The Galapagos spreading center: Lithospheric cooling and hydrothermal circulation: *Royal Astron. Soc. Geophys. Jour.*, v. 38, p. 587-608.
- Wilson, J. T., 1965, A new class of faults and their bearing on continental drift: *Nature*, v. 207, p. 343-347.
- Wooding, R. A., 1963, Convection in a saturated porous medium at large Rayleigh numbers and Peclet number: *Jour. Fluid Mechanics*, v. 15, p. 527-544.
- Zelenov, K. K., 1964, Iron and manganese in exhalations from the submarine volcano Bano Wuhu (Indonesia): *Akad. Nauk SSSR Doklady*, v. 155, p. 1315-1320.

MANUSCRIPT RECEIVED BY THE SOCIETY AUGUST 21, 1974

REVISED MANUSCRIPT RECEIVED JULY 24, 1975

MANUSCRIPT ACCEPTED AUGUST 20, 1975

# Duration of hydrothermal activity at an oceanic spreading center, Mid-Atlantic Ridge (lat 26°N)

Robert B. Scott

Department of Geology, Texas A&M University, College Station, Texas 77843

John Malpas

Department of Geology, Memorial University, St. Johns, Newfoundland,  
Canada A1C5S7

Peter A. Rona

National Oceanic and Atmospheric Administration—Atlantic Oceanographic and  
Meteorological Laboratories, 15 Rickenbacker Causeway, Miami, Florida 33149

Gleb Udintsev

Institute of Oceanology, USSR Academy of Sciences, Moscow, USSR

## ABSTRACT

Hydrothermal manganese oxide coats talus on the Mid-Atlantic Ridge at lat 26°N until spreading moves the rock past the thermally and structurally active rift-valley wall. Hydrothermal activity is replaced by hydrogenous ferromanganese oxide precipitation on ocean crust older than 0.7 m.y. on the ridge-crest highlands.

## INTRODUCTION

Abundant hydrothermal manganese oxide crusts were found coating basalt talus on the rift-valley wall at the Mid-Atlantic Ridge at lat 26°N during the Trans-Atlantic Geotraverse project of the National Oceanic and Atmospheric Administration in 1972 and 1973 (Scott, R. B., and others, 1974; Scott, M. R., and others, 1974). These crusts are almost pure manganese oxide with only a trace of Fe,

Co, Cu, and Ni and compositionally fall into the Mn-rich end member of Bonatti's hydrothermal classification (Bonatti, 1975).

Very rapid growth of the manganese deposits is required because they are as great as 50 mm thick only 5 km from the rift axis. U-Th dating of the outermost layers of these manganese crusts shows them to be accumulating at 200 mm/m.y., nearly two orders of magnitude faster than typical hydrogenous ferromanganese crusts or nodules (Scott, M. R., and others, 1974). Bottom photographs of the hydrothermally active portion of the rift wall (McGregor and Rona, 1975) show the presence of similar coatings over talus. Betzer and others (1974) found abnormally high concentrations of weak-acid-soluble Fe- and Mn-bearing particulate matter suspended over the Mid-Atlantic Ridge at lat 26°N. A region of low magnetic intensity within the Brunhes normal in the hydrothermal area may be related to the destruction of magnetic domains during hydrothermal alteration of basalt (McGregor and Rona,

1975). From these data, R. B. Scott and others (1974) concluded that cold, dense sea water flows down fracture systems (Lister, 1974), reacts with hot rocks or magma under the ridge crest, produces less dense hydrothermal fluids enriched in Ca, Si, Fe, Mn, and H<sub>2</sub>S and depleted in Mg (Hajash, 1975; Mottl and others, 1974; Bischoff and Dickson, 1975), and then is emitted as submarine springs, where oxygenated sea water causes precipitation of manganese oxides on talus overlying fractured fault scarps.

However, the distribution of dredge sites did not define the limits of this hydrothermal activity in time or space. Definition of the limits of activity at lat 26°N became one of the objectives of participation of the NOAA Trans-Atlantic Geotraverse project in the U.S.-U.S.S.R. Agreement for Cooperative Studies of the World Ocean. The hydrothermal region at lat 26°N was dredged during the spring of 1975 aboard the R/V *Akademik Kurchatov* by Soviet and American scientists.

## DREDGED ROCKS

Manganese oxide crusts and associated veins in basalt talus were recovered from site 75-1A, 18 km from the rift axis (Fig. 1). Unlike the hydrothermal crusts found at sites 72-13, 73-2A, and 73-3A, the crusts at site 75-1A have two distinct layers. The basal layers on the altered basalt have the same physical appearance as the hydrothermal crusts dredged in 1972 and 1973. The basal layers have a smooth, slightly botryoidal surface over an undulating laminated interior, a uniform brownish-black to submetallic gray color, and a thickness as great as 10 mm. The slightly undulating botryoids are about 1 mm in diameter. In contrast, the upper layers are most similar to hydrogenous crusts; these upper layers have highly irregular micro-botryoidal surfaces. Small columnlike botryoids are less than 0.1 mm in diameter and vary from a shiny grayish-black to an earthy, dark yellowish orange color. Organism tests are trapped between botryoid columns. The upper crusts are less than 2 mm thick. The two crust types were carefully separated for chemical, mineralogical, and scanning electron microscope (SEM) studies.

The basalts have been altered from nearly fresh basalt to extremely friable grayish yellow green material. Numerous veins of manganese oxides similar to the lower crusts fill fractures that cut the talus of basaltic breccia. One vein of free-growing zeolite crystals (75-1A28) as much as 5 mm in diameter was found coating altered basaltic glass; a thin (<0.1 mm thick) irregularly botryoidal manganiferous crust coated these zeolites.

## RESULTS OF CHEMICAL, MINERALOGICAL, AND SEM INVESTIGATIONS

The lower crusts (sample 75-1A24) only have x-ray diffraction patterns of birnessite (7.1, 3.5, and 2.46 Å d-spacings). The upper crust (75-1A24) is apparently amorphous to x-rays. The zeolite (75-1A28) is obviously an analcite from powder camera patterns, and chemically it is a potassic Na analcite (10 percent Na<sub>2</sub>O, 1 percent K<sub>2</sub>O, and trace of CaO). Atomic absorption spectrophotometry shows the lower crusts to contain 40 percent Mn, less than 0.1 percent Fe, and 0.15 percent Cu+Co+Ni; in contrast, the upper crusts contain more than 16 percent Fe and 0.4 percent Cu+Ni+Co (Fig. 2). The low Cu+Ni+Co contents and low Fe contents of the basal crust are similar to hydrothermal crusts found in 1972 and 1973.

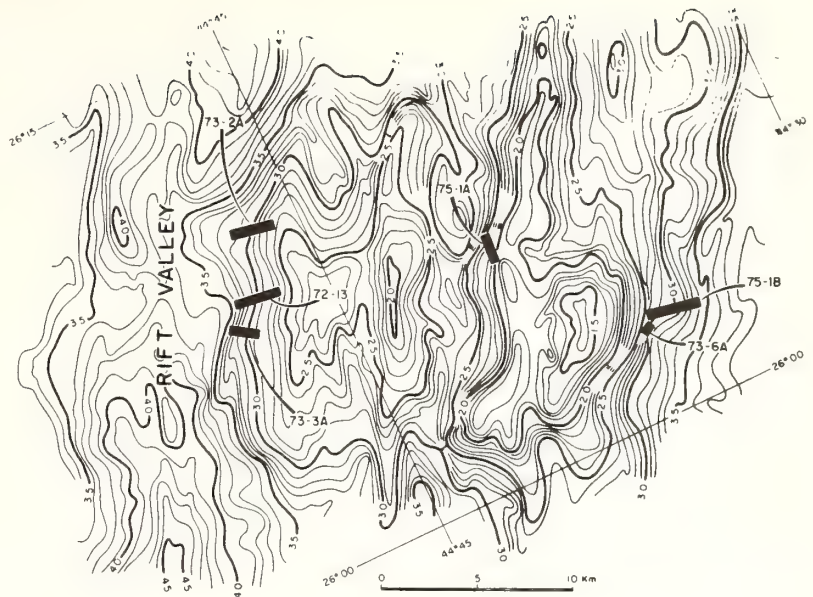


Figure 1. Hydrothermal field at lat 26°N. The 4-km-deep rift valley is on left; year and dredge number are used to identify dredge sites; contour intervals are 0.1 km. Hydrothermal sites 72-13, 73-2A, 73-3A, and 75-1A lie along an irregular ridge that trends southeast perpendicular to rift valley. This ridge seems to be cut into blocks by northeast-trending depressions parallel to rift that may represent normal faults. Bathymetry from McGregor and Rona (1975).

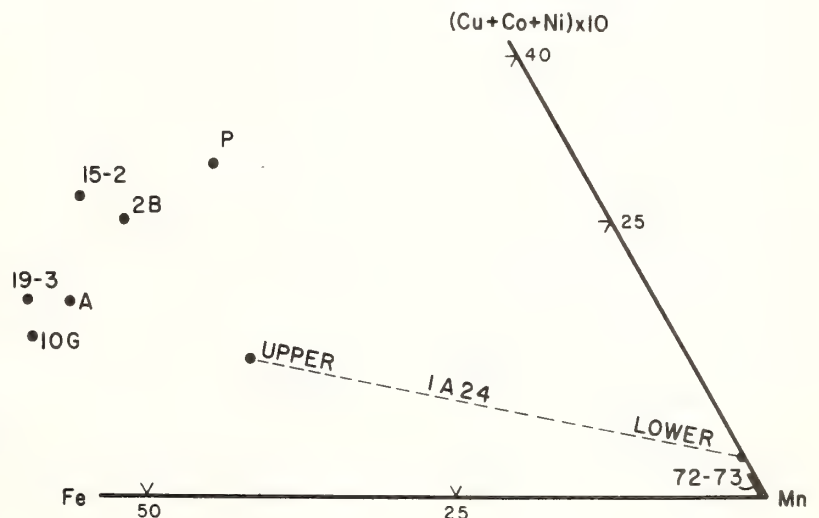


Figure 2. Composition of hydrothermal and hydrogenous Mn deposits plotted on Mn portion of the Mn-Fe-(Cu+Co+Ni)10 ternary diagram. Average composition of three analyses of upper and lower crust of sample 75-1A24 are attached by dashed line. At Mn apex, 1972 and 1973 analyses of hydrothermal crust are shown. Hydrogenous materials are represented by points on left: P = average Pacific and A = average Atlantic nodule; 10G and 2B are Mn crusts from the Atlantis Fracture Zone; 19-3 and 15-2 are Mn crusts from pillow lavas close to hydrothermal field at lat 26°N (Scott, M. R., and others, 1974). By atomic absorption spectrophotometry; precision expressed as percent of value determined: Fe±2 percent, Mn±1 percent, Cu±1 percent, Ni±5 percent, Co±5 percent.

The coating on the zeolites (Fig. 3d) with a 0.3 percent Co+Cu+Ni content is transitional between hydrothermal and hydrogenous crust compositions; the high Fe content in this coating (18 percent) may be indicative of a hydrogenous origin. Even though no Fe-rich hydrothermal manganese deposits have been identified at lat 26°N, Bonatti (1975) showed their existence elsewhere. SEM photographs show the lower crust to have the texture of well-crystallized birnessite (Fig. 3a); this boxwork of plates is very similar to the texture found in birnessite from widely differing environments (Swanson, 1975; Brown and others, 1971; Fewkes, 1973). In contrast, the upper crust at the same scale (Fig. 3b) shows a smooth featureless surface with no textural indication of crystallinity. The smaller scale view in Figure 3c shows the overall microbotryoidal form of the lower crust that is similar to columnar zones described by Sorem and Foster (1972) in hydrogenous ferromanganese.

#### DISCUSSION

Clearly, from the chemical and physical description and SEM observations, the manganese oxide lower crust 75-1A24 appears to be most similar to other hydrothermal manganese crusts; the ferro-

manganese oxide upper crust 75-1A24 has strong affinities to hydrogenous ferromanganese crusts and nodules. A comparison of the compositions shown in Figure 2 with those of Bonatti (1975, Fig. 4) support these conclusions. The dramatic differences in iron and Cu+Co+Ni contents between the upper and lower crust samples taken only a few millimetres from one another suggest drastically different mechanisms of formation or different sources of fluids.

Several authors (Bonatti and others, 1972; M. R. Scott and others, 1974) have noted an inverse relation between the rate of manganese crust accumulation and the content of trace metals. If data given by M. R. Scott and others (1974, Table 2, Figs. 2, 3) are representative of this relationship, then the approximate growth rate in millimetres/10<sup>6</sup>yr =  $e^{14.85 - 1.54 \ln \text{Cu+Co+Ni ppm}}$ .

The Cu+Co+Ni for the lower crust equals 1,520 ppm and for the upper crust equals 3,910 ppm. Growth rates for the lower and upper crusts are calculated to be 35 and 8 mm/10<sup>6</sup>yr, respectively. The maximum thickness of the upper crust is about 3 mm, and the underlying hydrothermal layer is as great as 10 mm thick; this implies that the hydrothermal activity may have continued to affect the talus for 0.3 m.y. before hydrogenous activity began.

The magnetic anomaly age of the ocean crust under site 75-1A is approximately 1.4 m.y. (McGregor and Rona, 1975). With this spacial relationship (Fig. 1), the half-spreading rate of about 1.3 cm/yr, and estimated growth rates of crusts, a sequence of events can be postulated. When site 75-1A rocks spread from the rift axis to the rift wall position of modern hydrothermal activity, they were 0.4 m.y. old. Hydrothermal activity continued until this site was 0.7 m.y. old and had moved beyond the influence of hydrothermal activity. Hydrogenous growths of manganese then ensued for 0.4 m.y. The total age of the site to account for this sequence of events would be 1.1 m.y., close to the magnetic anomaly age of 1.4 m.y. Thus, it seems that the most active hydrothermal region is on the rift wall near both high geothermal gradients in the rift and active faults scarps on the rift wall. A trip of hydrothermally altered oceanic crust results.

A ropy-textured, seemingly fresh, thin basalt flow was dredged at site 73-6A and at 75-1B; chemical analysis of basalt 73-6A2 shows an abnormally high K<sub>2</sub>O content of 0.3 percent, whereas fresh typical rift-valley tholeiites in this region have only 0.05 to 0.10 percent K<sub>2</sub>O (Scott and others, 1973). Samples 6A and 1B may be

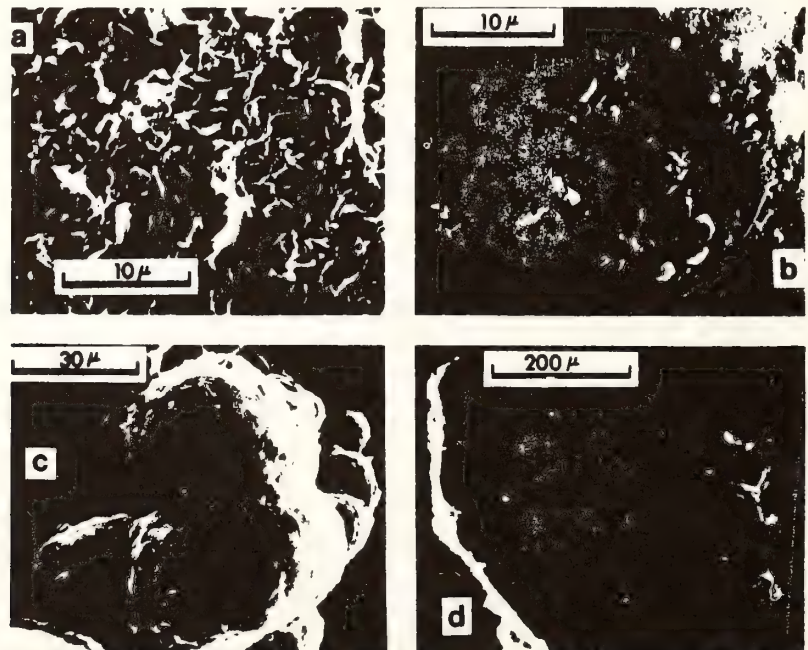


Figure 3. SEM photographs of manganese crust. (a) Lower crust 75-1A24 showing crystal plates of birnessite. (b) and (c) Botryoids of upper crust 75-1A24 showing the absence of crystallinity. (d) Smooth interior of a ferromanganese crust that caps analcite crystals of a vein 75-1A28.



slightly alkalic younger off-axis basalts (Strong, 1974) that may have covered older hydrothermal areas. The  $\text{La}_{e.f.}/\text{Sm}_{e.f.}$  ratio (0.6) and the rare-earth element abundances fit intraplate or ridge-crest criteria (Schilling and Bonatti, 1975). However, the possibility of simple low-temperature addition of K during weathering cannot be discounted (Scott and Hajash, 1975). Thus, no definite limit to the size of the hydrothermal field can be established.

Three other localities of hydrothermal manganese have recently been located; one is close to the Galapagos spreading axis, and it has nearly identical physical, chemical, isotopic, and growth rate characteristics to the lat 26°N deposits (Moore and Vogt, 1975). Another occurs at lat 23°N on the Mid-Atlantic Ridge (Thompson and others, 1975). French scientists have also found a hydrothermal manganese deposit in a transform fault in the FAMOUS area (ARCYANA, 1975). Recognition of such occurrences immediately following publication of findings at lat 26°N suggests that these deposits may be common and were overlooked in the past.

The most common hydrothermal deposit in oceanic spreading centers and related structures besides manganese crusts are sulfides precipitated as veins within the crust (Dmitriev and others, 1970; Bonatti, 1975). It is probable that these two phenomena are both part of the same complex hydrothermal process operating in the ocean crust. The association is strengthened by Hajash's (1975) observation of experimental chalcopyrite and pyrrhotite precipitation in Fe- and Mn-rich sea water resulting from reaction with basalt at 400° to 500°C. Some mechanisms may even exist to precipitate sulfides at the water-rock interface from chloride-rich brines (Sillitoe, 1972; Constantinou and Govett, 1972; Searle, 1972; Upadhyay and Strong, 1973; Sato, 1973). Thus far, no massive sulfides have been observed in rocks dredged from open-ocean centers either within or on the rock-water interface. Obviously, both hydrothermal manganese and sulfides will have to be studied to understand the total chemical effects of cycling sea water through cooling oceanic crust.

## REFERENCES CITED

- ARCYANA, 1975, Transform fault and rift valley from bathyscaph and diving saucer: *Science*, v. 190, p. 108-116.
- Betzer, P. R., Bolger, G. W., McGregor, B. A., and Rona, P. A., 1974, The Mid-Atlantic Ridge and its effect on the composition of particulate matter in the deep ocean: *EOS (Am. Geophys. Union Trans.)*, v. 55, p. 193.
- Bischoff, J. L., and Dickson, F. W., 1975, Seawater-basalt interaction at 200°C and 500 bars: Implications for origin of seafloor heavy-metal deposits and regulation of seawater chemistry: *Earth and Planetary Sci. Letters*, v. 25, p. 385-397.
- Bonatti, E., 1975, Metallogenesis at oceanic spreading centers, in *Annual review of Earth and planetary sciences*: Palo Alto, Calif., Annual Reviews, Inc., p. 401-431.
- Bonatti, E., Kramer, T., and Rydell, H. S., 1972, Classification and genesis of submarine iron-manganese deposits, in *Ferromanganese deposits on the ocean floor*: Palisades, N.Y., Lamont-Doherty Geol. Obs., Columbia Univ., p. 146-166.
- Brown, F. H., Pabst, A., and Sawyer, D. L., 1971, Birnessite on colemanite at Boron, California: *Am. Mineralogist*, v. 56, p. 1057-1064.
- Constantinou, G., and Govett, G.T.S., 1972, Genesis of sulphide deposits, ochre and amber of Cyprus: *Inst. Mining and Metallurgy Trans.*, v. 81, p. B33-B46.
- Dmitriev, L. V., Barsukov, V. L., and Udintsev, G. B., 1970, Rift zones of the ocean and the problem of ore formation: *Geokhimiya*, v. 4, p. 937-944.
- Fewkes, R. H., 1973, External and internal features of marine manganese nodules as seen with the SEM and their implications in nodule origin, in *Morganstein, M., ed., The origin and distribution of manganese nodules in the Pacific and prospects for exploration*: Honolulu, Hawaii Inst. Geophysics, Univ. Hawaii, p. 21-29.
- Hajash, A., 1975, Hydrothermal processes along mid-ocean ridges: An experimental investigation: *Contr. Mineralogy and Petrology (in press)*.
- Lister, C.R.B., 1974, Water percolation in the ocean crust: *EOS (Am. Geophys. Union Trans.)*, v. 55, p. 740-742.
- McGregor, B. A., and Rona, P. A., 1975, Crest of Mid-Atlantic Ridge at 26°N: *Jour. Geophys. Research*, v. 80, p. 3307-3314.
- Moore, W. S., and Vogt, P. R., 1975, Hydrothermal manganese crusts from two sites near the Galapagos spreading axis: *Earth and Planetary Sci. Letters (in press)*.
- Mottl, M. J., Corr, R. F., and Holland, H. D., 1974, Chemical exchange between sea water and mid-ocean ridge basalt during hydrothermal alteration: An experimental study: *Geol. Soc. America Abs. with Programs*, v. 6, p. 879-880.
- Sato, T., 1973, A chloride complex model for Kuroko mineralization: *Geochem. Jour.*, v. 7, p. 245-270.
- Schilling, J. G., and Bonatti, E., 1975, East Pacific Ridge (2°S-10°S) versus Nazca intraplate volcanism: Rare-earth evidence: *Earth and Planetary Sci. Letters*, v. 25, p. 93-102.
- Scott, M. R., Scott, R. B., Rona, P. A., Butler, L. W., and Nalwalk, A. J., 1974, Rapidly accumulating manganese deposit from the median valley of the Mid-Atlantic Ridge: *Geophys. Research Letters*, v. 1, p. 355-358.
- Scott, R. B., and Hajash, A., 1975, Initial submarine alteration of basaltic pillow lavas: A microprobe study: *Am. Jour. Sci. (in press)*.
- Scott, R. B., Hajash, A., Kuykendall, W. E., Rona, P. A., Butler, L. W., and Nalwalk, A. J., 1973, Petrological and structural significance of the Mid-Atlantic Ridge between 25°N and 30°N: *EOS (Am. Geophys. Union Trans.)*, v. 54, p. 249.
- Scott, R. B., Rona, P. A., McGregor, B. A., and Scott, M. R., 1974, The TAG hydrothermal field: *Nature*, v. 251, p. 301-302.
- Searle, D. L., 1972, Mode of occurrence of the cupriferous pyrite deposits of Cyprus: *Inst. Mining and Metallurgy Trans.*, v. 81, p. B189-B197.
- Sillitoe, R. H., 1972, Formation of certain massive sulphide deposits at sites of seafloor spreading: *Inst. Mining and Metallurgy Trans.*, v. 81, p. B141-B148.
- Sorem, R. K., and Foster, A. R., 1972, Marine manganese nodules: Importance of structural analysis: *Internat. Geol. Cong., 24th, Montreal 1972, sec. 8*, p. 192-200.
- Strong, D. F., 1974, An "off-axis" alkali volcanic suite associated with the Bay of Islands ophiolites, Newfoundland: *Earth and Planetary Sci. Letters*, v. 21, p. 301-309.
- Swanson, S. B., 1975, Two examples of secondary alteration associated with mid-ocean ridges [Master's thesis]: College Station, Texas A&M Univ.
- Thompson, G., Woo, C. C., and Sung, W., 1975, Metalliferous deposits on the Mid-Atlantic Ridge: *Geol. Soc. America Abs. with Programs*, v. 7, p. 1297-1298.
- Upadhyay, H. D., and Strong, D. F., 1973, Geological setting of the Betts Cove copper deposits, Newfoundland: An example of ophiolite sulfide mineralization: *Econ. Geology*, v. 68, p. 161-167.

## ACKNOWLEDGMENTS

Reviewed by Enrico Bonatti and Ronald Sorem.

Research supported by the Institute of Oceanology of the USSR Academy of Sciences, the National Oceanic and Atmospheric Administration, and National Science Foundation Grant DES 74-18567.

We are indebted to the scientific colleagues and crew aboard the R/V *Akademik Kurchatov*. Mark DiStefano and Steve Swanson of Texas A&M University significantly aided our SEM and x-ray research.

MANUSCRIPT RECEIVED DEC. 4, 1975

MANUSCRIPT ACCEPTED JAN. 13, 1976

Reprinted from: *Marine Geology*, Vol. 20, No 4, 315-334.

*Marine Geology*, 20(1976) 315-334

© Elsevier Scientific Publishing Company, Amsterdam — Printed in The Netherlands

## RIDGE DEVELOPMENT AS REVEALED BY SUB-BOTTOM PROFILES ON THE CENTRAL NEW JERSEY SHELF

W. L. STUBBLEFIELD and D. J. P. SWIFT

*National Oceanic and Atmospheric Administration, Atlantic Oceanographic and Meteorological Laboratories, Miami, Fla., (U.S.A.)*

(Received December 12, 1974; accepted August 4, 1975)

### ABSTRACT

Stubblefield, W. L. and Swift, D. J. P., 1976. Ridge development as revealed by sub-bottom profiles on the central New Jersey shelf. *Mar. Geol.*, 20: 315-334.

Closely-spaced 3.5 kHz seismic profiles were collected over the north-easterly trending ridge and swale system 50 km east-southeast of Atlantic City, New Jersey. They yield information on the Late Quaternary depositional history of the area, and on the origin of the ridge system. Four of the sub-bottom reflectors identified were sufficiently persistent to warrant investigation and interpretation. These reflectors, which have been cored, lithologically identified, and radiocarbon dated, are stratigraphically higher than the reflectors dealt with by the majority of previous studies. The upper three reflectors are definitely mid- and post-Wisconsin in age and present a record of the most recent glacial cycle. The upper three units associated with the observed reflectors appear to exert a pronounced influence on the bathymetry. The gently corrugated ridge system of Holocene sand is formed over the regionally flat-lying upper unit, an Early Holocene lagoonal silty clay. The characteristically flat, broad depressions of the area are floored by this lagoonal material. Locally, however, marine scour has cut through the silty clay into an underlying unit of unconsolidated fine Pleistocene sand. Several stages of trough development appear to be represented. After penetrating the lagoonal clay, troughs are initially narrow, but when incised through the sand into a lower, Pleistocene, silty-clay unit, the troughs become notably wider. As downcutting is inhibited by the lower clay, the upper clay is undercut as the trough widens in a fashion similar to a desert blowout.

The sub-bottom reflectors indicate that ridge development on the central shelf has involved aggradation as well as erosion. Some ridges seem to have grown by vertical and lateral accretion from small cores. The internal structure of other ridges suggests that they formed by the coalescence of several small ridges. Others appear to have undergone appreciable lateral migration.

The ridges appear to be in a state of continuing adjustment to the hydraulic regime of the deepening post-Pleistocene water column.

### INTRODUCTION

A prominent system of northeasterly trending ridges and depressions exists on the shelf floor 50 km east-southeast of Atlantic City, New Jersey. Examination of a 1:125,000 scale ESSA bathymetric map contoured by Stearns (1967) suggests that the ridges comprise two basic populations in

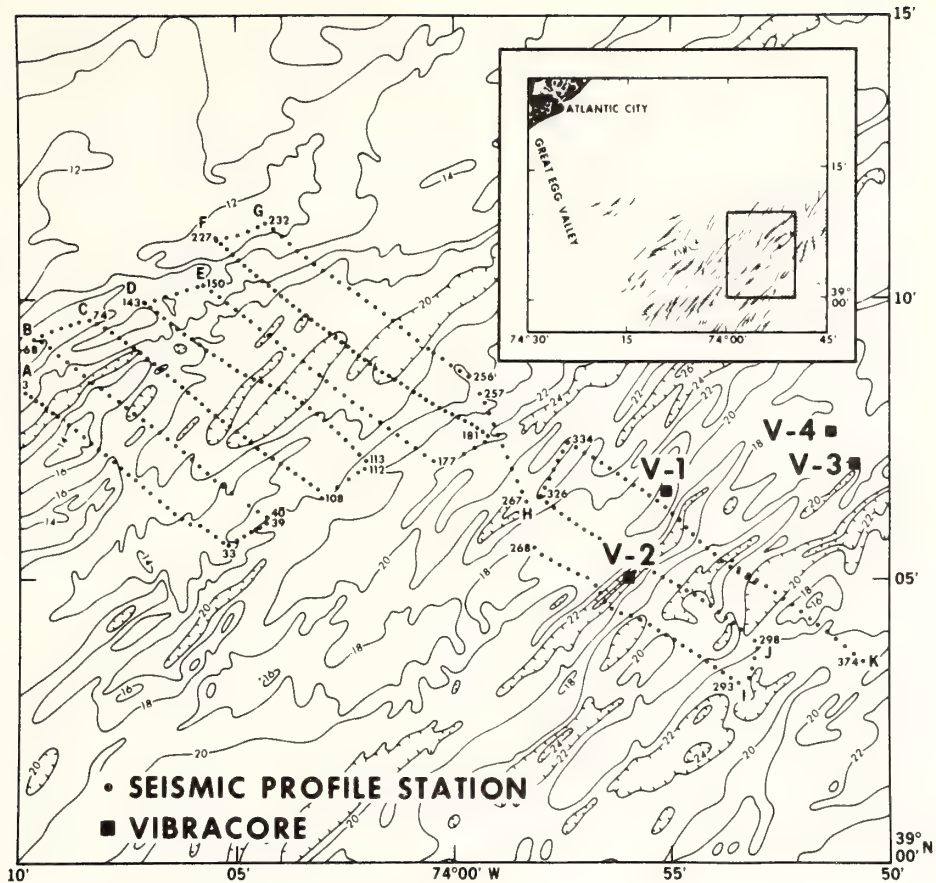


Fig.1. Index map of the study area with the New Jersey coastline inset for regional setting. The bathymetric contour lines are in fathoms.

terms of spacing and height (Fig.1). A small-scale ridge system is superimposed on a large system. The latter appears to be impressed onto a broad shoal-retreat massif, a constructional feature resulting from the retreat of a littoral drift depositional center associated with a retreating estuary mouth (Swift, 1973). The ridge spacing of the larger ridge system averages 3.1 km with a mean flank dip of  $0.4^\circ$ . In addition to the two basic populations a third, smaller system of contrasting sediment bands of negligible relief, has been observed from side-scan records, bottom photographs, and submersible dives (McKinney et al., 1974).

Genesis of the ridge topography of the surficial sand sheet on the inner and central continental shelf has remained an enigma to workers since the pioneer work of Veatch and Smith (1939). A historical school of thought suggests that the pronounced undulations of the sandsheet are fluvial or littoral features formed during the lower sea-level stands of the Pleistocene (Veatch and Smith, 1939; Shepard, 1963; Kraft, 1971; McKinney and

Friedman, 1970). Others questioned the feasibility of these structures surviving a marine transgression and suggest instead a post-transgressive response to the Holocene hydraulic regime (Uchupi, 1968; Swift et al., 1972; Stubblefield et al., 1975). Uchupi (1970) subsequently abandoned the hypothesis of recent reworking of the Holocene sands and proposed a mechanism of terraces and barrier beaches overstepped by a transgressive Holocene sea.

In order to resolve the controversy surrounding the origin of the ridges, a dense network of high-resolution, shallow-penetration seismic-reflection profiles was collected in a 400 km<sup>2</sup> area (Fig.1). The investigation was directed toward the internal structure of the sand sheet and the role which the sub-bottom reflectors contribute to the existing bathymetry. In addition, some of the reflectors were correlated with data of previous workers in an effort to establish geological continuity with other sections of the New Jersey continental shelf.

## METHODS

### *Field methods*

The seismic reflection data were collected from the NOAA ship "Peirce" during August 1973 using a 3.5 kHz transducer. The transducer, with a 0.2 m/sec pulse length was towed 5–6 m beneath the surface at ship's speeds varying from 3.5 to 4.0 knots. The seismic record was recorded at a 250 m/sec scan rate.

The seismic lines were run normal to the ridged features in an area previously vibracored (Fig.1). This approach ensured maximum delineation of the sand sheet's structure and permitted correlation between the core record and seismic reflectors.

Raydist navigation provided an accuracy of  $\pm 10$  m.

### *Laboratory methods*

The 115 km of seismic records were scanned for bottom and sub-bottom reflectors and "hand-smoothed" to compensate for sea surface waves. Each reflector was converted to X–Y values, placed on computer data cards by means of a X–Y digitizer unit, and subsequently plotted by a Univac 1108 computer. With this method, the horizontal scale was reduced by a 1:10 ratio and the vertical by 1:2 resulting in a vertical exaggeration of 5. This exaggeration, together with that resulting from the speed of the vessel, yields a composite vertical exaggeration of 12:1. Such a degree of vertical exaggeration enables delineation of subtle features in the original record.

A travel time of 1.65 km/sec was used through both the water and unconsolidated sediment. The negligible error induced by a slightly fast travel time through the water (1.65 km/sec as opposed to 1.50 km/sec) is not in conflict with the purpose of the study.

## LATE-QUATERNARY STRATIGRAPHY

The seismic profiles reveal changes in acoustic impedance (reflectors) which, in turn, can be correlated with the lithology sampled by vibracores. As many as eleven reflectors were observed in the seismic records but only four were of sufficient consistency throughout the area to warrant discussion. The four reflectors of interest have been lithologically identified, stratigraphically dated from vibracores (Stubblefield et al., 1975) and described (Fig.2). Radiocarbon dates were obtained from analysis of shell material in

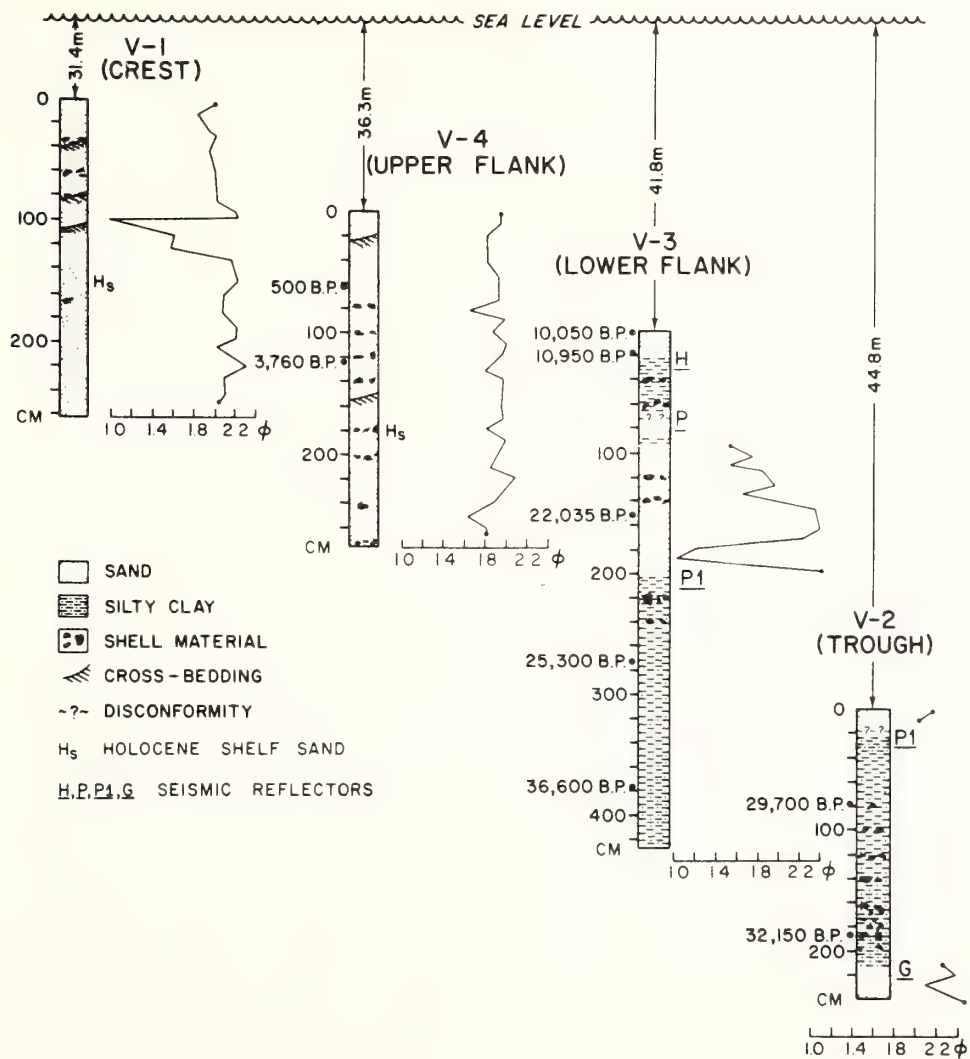


Fig.2. Lithic log of four vibracores and mean grain size in quarter phi ( $\phi$ ) units within the sand horizons. (Modified from Stubblefield et al., 1975).

TABLE I

## Description of the sub-bottom units

Unit	Age	Lithology	Thickness (m)	Glacial stage	Suggested depositional environment	Possible correlation
G	36,600	clean, fine-grained sand	?	commencement of Plum Point Interstadial (Late Altonian)	nearshore	
P1	<25,300 >36,600	medium gray silty clay	1-7	Plum Point Interstadial (Late Altonian—Early Farmdalian)	offshore in advance of a prograding shoreline	P2 (McMaster and Ashraf, 1973) Pleistocene unconformity (Garrison, 1970)
P	<22,035 <25,300	clean, fine to medium sand	1-8	Late Farmdalian—Early Woodfordian	prograding shoreline	
H	10,950 <22,035	medium gray silty clay	0-6	Woodfordian	lagoon associated with landward passage of the shoreline	H1 (Sheridan et al., 1974)

the vibracores. To avoid the often confusing situation of reflector labeling versus stratigraphic-horizon labeling, each unit in Fig. 2 is denoted by the same label as its upper boundary reflector; e.g., reflector H marks the upper boundary of unit H. H denotes Holocene deposits, P the Pleistocene material, and sediment of questionable age is marked as G. Various observed features of the four seismic reflectors are summarized in Table I.

#### QUATERNARY STRATIGRAPHY

##### *Unit G*

Unit G is the lowest unit in the section. It has been penetrated by vibracoring only in its uppermost 10 cm (core V2, Fig. 2), where it appears as a clean, fine-grained, shell-free sand. Its textural character and its minimum constraining age of  $>36,000$  B.P., suggests that this unit was deposited in a near-shore environment, perhaps during a period of an advancing sea marking the commencement of the Plum Point Interstadial (mid-Wisconsin). This inference is supported by the apparent absence of an unconformity between this supposed basal sand and the overlying offshore silty-clay deposit. Stratigraphically, however, this unit appears to correlate with the unit underlying Garrison's (1970) Pleistocene unconformity, which he suggests as Late Tertiary in age. Garrison's work was over a broad area of the continental shelf south of New England and to the northeast of our work area. The small size of the study area relative to Garrison's work may have resulted in the lack of detection of an unconformity. Until a more detailed coring program is completed, the age of unit G and thus an interpretation of its depositional environment remains uncertain.

##### *Unit P1*

This medium gray, silty clay is perhaps the most widespread of the Late-Quaternary sequence, as indicated by the persistency of its reflective surface, reflector P1 (pp. 324–325). This unit is of Pleistocene age, with dates ranging from  $25,300 \pm 1040$  B.P. to  $>36,000$  B.P. The younger section of this unit was probably an offshore deposit formed in advance of the prograding shoreline represented by unit P. However, the older part of unit P1, approximately 36,000 B.P. in age, may reflect the maximum glacial retreat during the Plum Point Interstadial as described by Goldthwait et al. (1965) and Milliman and Emery (1968).

The age of unit P1, mid-Wisconsin including the Farmdalian substage, is comparable to that proposed by McMaster and Ashraf (1973) for their reflector, P2. They made a tentative correlation of their reflector with Garrison's (1970) Pleistocene unconformity. McMaster and Ashraf's work was to the east of this study on the eastern fringe of Long Island extending south to the shelf break. They traced their P2 reflector across most of the shelf at sub-bottom depths of 17–34 m, but fail to mention the amount of

regional dip of their P2 other than that it parallels the present shelf surface. In the present study area of this study the regional dip of P1 was calculated to be  $0.04^\circ$  to the S61°E. If  $0.04^\circ$  dip is assumed, an approximation of 17m/97 km (17 m/ $1^\circ$  latitude) depth compensation may be applied. By projecting McMaster and Ashraf's reflector for an additional 80–90 km in a plane normal to the strike of the eastern Long Island coastline, a depth comparable to that of our reflector P1 results.

### Unit P

The uppermost Pleistocene sand, dated at  $22,035 \pm 665$  B.P., possesses a slightly irregular reflective surface and ranges in thickness from 1 to 8 m. Throughout most of the sample area, however, the thickness varies from 2 to 4 m. The maximum thickness of unit P is in the southeast sector.

The upper reflective boundary of this unit, reflector P, has a dip of  $0.02^\circ$  and a strike of S38°E. The dip angle and strike direction were calculated using the reflector's depth throughout the study area. The strike direction is within  $5^\circ$  of the present beach orientation in the vicinity of Little Egg Inlet, New Jersey (Fig.1).

Unit P is a clean, medium-grained upward-coarsening sand (Fig.2). This characteristic and its date of 22,035 B.P. suggest a deposition environment of a prograding shoreline. If this inference is valid, the advance of the Holocene seas was controlled by the regional gradient established during periods of lower sea level, since the coast-concordant strike indicates only a slight reorientation of the beach during the last 20 millenia.

After the Plum Point Interstadial, the ice sheets readvanced, the marginal seas withdrew, and the Pleistocene sand of this unit was exposed to subaerial processes. Fig.3 suggests that the Pleistocene sand, which is 40–50 m below

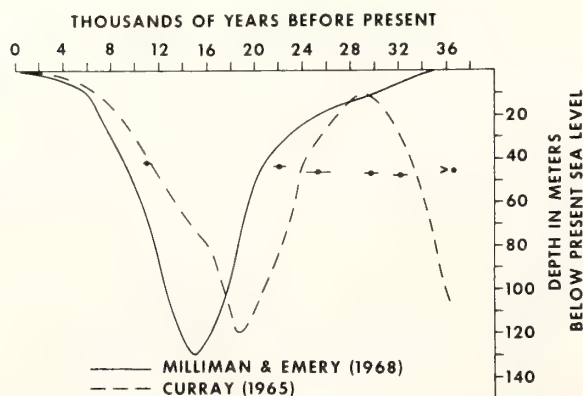


Fig.3. Comparison of data from the vibracores with sea level curves of Milliman and Emery (1968) and Curray (1965). The sample ages are represented by dots and the range in age by error bars. (From Stubblefield et al., 1975)



present sea level, was a positive area from 12,000 to 20,000 B.P. Radio-carbon dates from the four vibracores are in general agreement with the sea-level curves of Milliman and Emery (1968) and Curray (1965). Visual evidence in Core V-3 (Fig.2) indicates a possible disconformity at the top of the clean sand (unit P). Sheridan et al. (1974) report an extensive erosion surface on their upper Pleistocene unit, which probably correlates with P. Core V-2 (Fig.2) demonstrates further evidence for erosion, in that the Holocene lagoonal deposit and the bulk of the Pleistocene sand are both absent. However, much of the missing section in Core V-2 is thought to have been removed by the modern marine erosion as explained in a later discussion, rather than by subaerial erosion during Early Holocene times.

### *Unit H*

The upper unit in Core V-3 (Fig.2) is a medium gray silty clay with a locally irregular and discontinuous upper boundary (reflector H). The reflector appears as an undulating surface with the deepest part found under a topographic high in the eastern sector of the study area. The depth of reflector H, below present sea level, ranges from 36 to 52 m and the thickness of unit H varies from 0 to 6 m. Unit H thickens to the southeast in the direction of its regional slope.

The absence of this upper silty clay at various places throughout the study area is probably the result of both erosion and non-deposition. Examination of the bathymetry in Fig.1 fails to suggest recent downcutting in those places where the upper silty clay is missing within the substrate, suggesting that its absence may be due to a positive area during deposition, rather than subsequent erosion. However, where unit H intersects the surface, particularly as an outcrop in the deep topographical troughs (McKinney et al., 1974), and in those places where an underlying unit is surficially exposed (profile A, Fig.4a; profile K, Fig.4b) erosion of unit H is obviously occurring.

The depositional environment of the upper silty clay is inferred from radiometric ages, lithology, depth of unit, and fragmented shell material. The silty clay is underlain by medium to fine sand (unit P) which is dated at  $22,035 \pm 665$  B.P., and is overlain by coarse sand with shell material dated at  $10,950 \pm 360$  B.P. These limiting ages indicate that the unit was deposited during a period in which landward passage of the shoreline occurred. The lithology of cored sections of this unit is similar to that described by Sheridan et al. (1974) as a Holocene lagoonal deposit, near the Delaware coast. In addition, the average depth of reflector H is approximately 42 m below present sea level which places the unit in that portion of the Emery et al. (1967, fig.4) diagram described as lagoonal. The geographic limits of the Emery et al. (1967) study is sufficiently close to this work to allow application of its interpretations to our data. Shell material, too small to radiocarbon date, has been identified by Don Moore, University of Miami, as organisms capable of living in shallow, brackish environments (*Crassostrea virginica* and *Mercenaria mercenaria*), a conclusion which supports our inference of lagoonal deposition.

Holocene lagoonal deposits tend to occur during glacial retreat and marine transgression. The bracketing dates for unit H (>10,950 <22,035 B.P.) include the time of maximum glacial advance which occurred 18,000 to 22,000 B.P. during the Woodfordian glacial cycle (Goldthwait et al., 1965; Schafer and Hartshorn, 1965). If this unit does in fact reflect deposition during glacial retreat subsequent to maximum Late Wisconsin ice advance, and if a date of approximately 16,000 years B.P. is accepted for the Pleistocene—Holocene boundary (Emery and Uchupi, 1972) a date of post-Pleistocene may confidently be applied to this silty clay.

These four units, their related seismic reflectors, and their time-stratigraphic framework provide a record of a complete glacial cycle on the central New Jersey shelf. The retreat of the ice sheet, accompanied by the advance of the ocean is indicated by the lower unit G. P1 possibly represents maximum glacial retreat and marine transgression during late mid-Wisconsin time. Unit P is then representative of the subsequent ice advance and retreat of the ocean. Unit H was deposited by the advancing Holocene lagoonal belt.

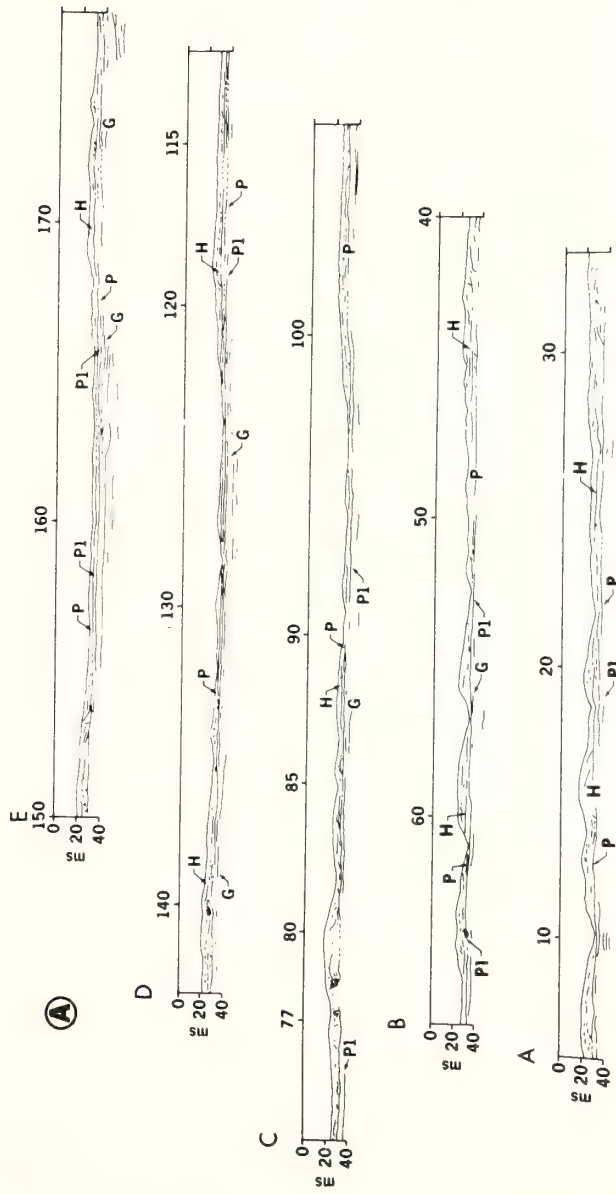
#### SURFICIAL SAND SHEET

##### *Topography and internal structure*

The surficial sand sheet above reflector H is complexly structured. Large-scale ridges (shaded pattern of inset, Fig.1) appear as half-cylinders of sand resting on a relatively level reflector H (Fig.4a, b). In some cases, internal structure may be observed. This may take the shape of apparent ridge "cores", formed by internal strata which parallel the ridge flanks (station 86, profile C, Fig.4a; record A, Fig.5). Elsewhere, multiple "cores" within a ridge suggest coalescence of several nuclei during growth (station 77 to 80, record C, Fig.4a). Internal reflectors with consistent direction of dip occur in some ridges (station 251 to 255, record G, Fig.4b) suggesting lateral ridge migration. Internal patterns are locally very complex; in record B, Fig.5, truncated reflectors suggest that a former ridge on the northwest side of the record has been leveled and the adjacent trough filled in; a new ridge has appeared to the southeast.

Large-scale troughs (stations 120—140, profile D, Fig.4a) appear to bottom in reflector H which is thinly mantled with a few centimeters of coarse, shelly or pebbly sand locally grading upward into centimeters of finer sand. This fine sand thickens towards the ridge flanks (Stubblefield et al., 1975). Locally, reflector H is without this surficial coating. Small-scale ridges (linear pattern of inset, Fig.1) likewise appear to be half cylinders of sand resting on reflector H. In the few cases where internal structure have been resolved, it appears to be similar to that of the large-scale ridges.

Small-scale troughs, unlike large-scale troughs, locally penetrate through reflectors H and P, into unit P1 (Fig.6). Two variants of such apparently erosional troughs appear. Small-scale troughs which penetrate into the sand of unit P tend to be "V" shaped in cross-section (station 60 to 62, profile B, Fig.4a; record A, Fig.6). Other small-scale troughs extend completely through



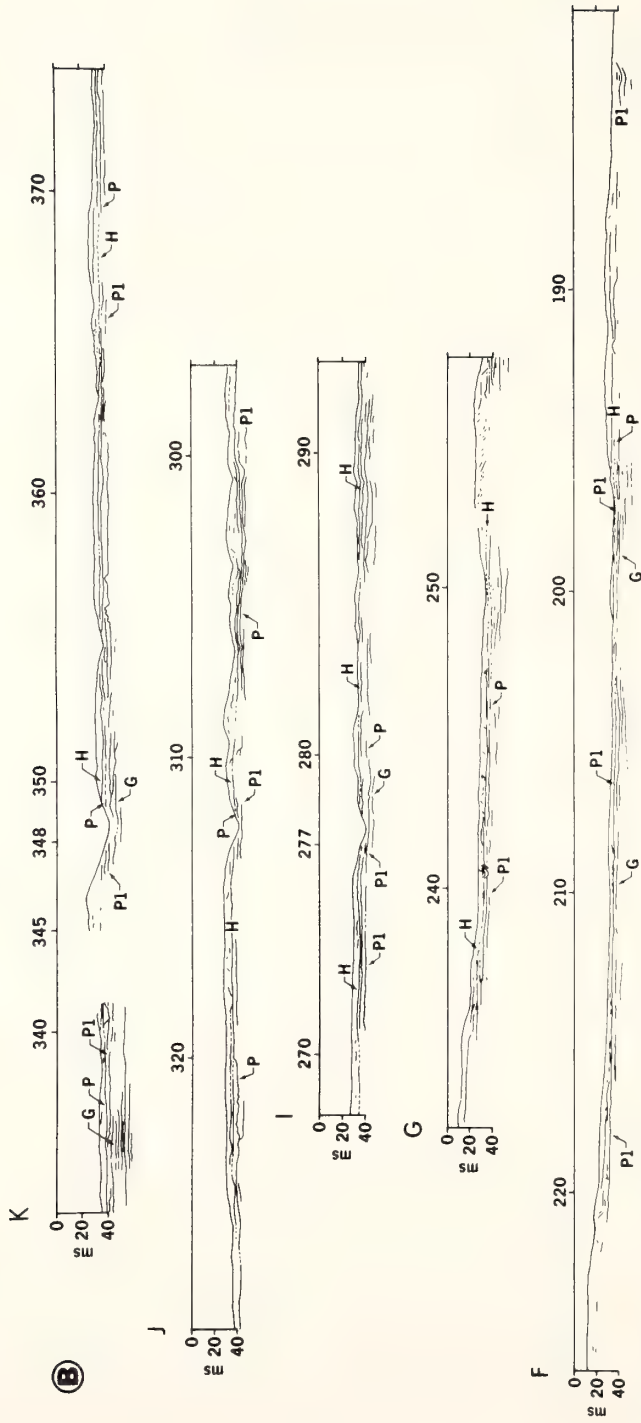


Fig. 4. Seismic profile lines hand reduced from the original records. The 0 ms datum is 13.1 m below present sea level. A travel time of 1.65 km/sec for sound velocity was used. See Fig. 1 for the geographic relationship of each profile to the study area and to bathymetry.

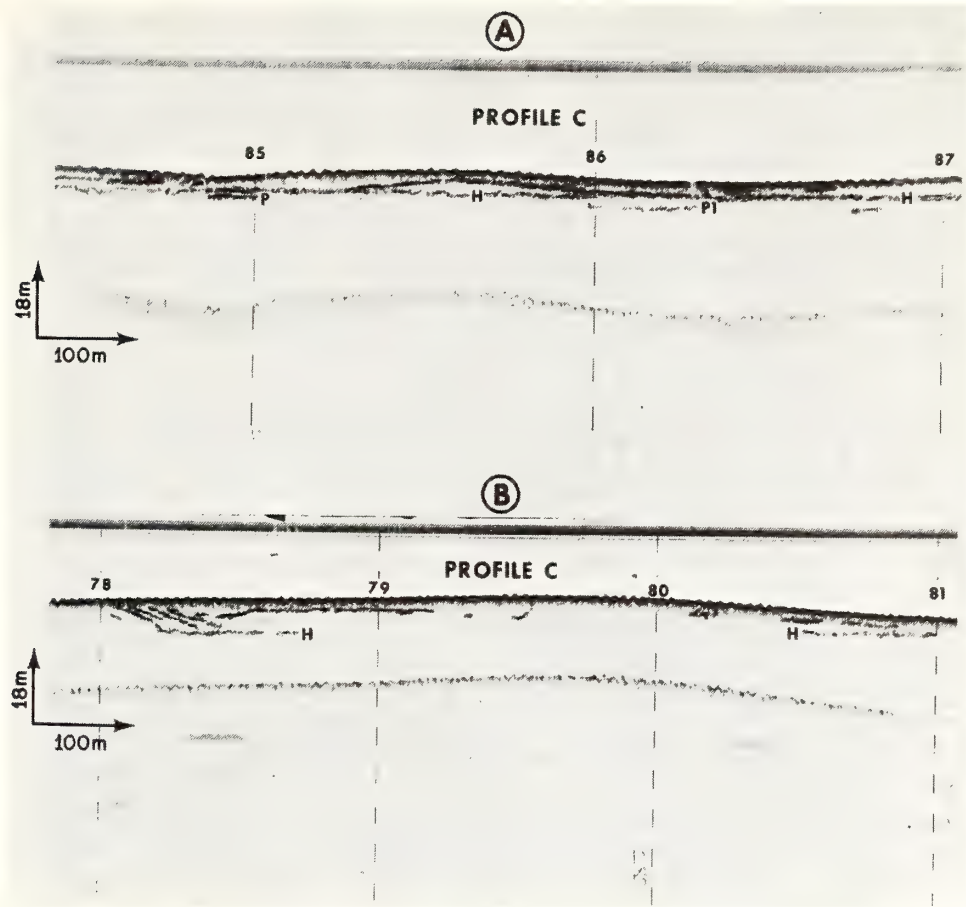


Fig. 5. Hand-enhanced, high-resolution seismic-reflection profiles. A. Ridge with internal "core", suggesting upward ridge growth by the addition of conformable beds. B. Zone of discontinuous ridge growth. Ridge at right was formed subsequent to filling of trough at left by the progradation of incline strata. See Fig. 1 for location.

the unconsolidated Pleistocene sand and are floored by the silty clay of unit P1 and assume a more nearly parabolic cross-section, with a rounded bottom and more gently inclined flanks.

#### *Evolution of the ridge topography*

Large-scale ridges are locally broken into segments by small-scale troughs which cross them at a low angle, suggesting that small-scale troughs formed after large-scale troughs (McKinney et al., 1974). The varieties of ridges and their internal structure suggest the following model for ridge evolution (Fig. 7). Large-scale ridges, hereafter called primary ridges, were initiated immediately after the passage of the shoreline, at about 10,000 B.P. (Fig. 7a). They formed in the leading edge of the shelf sand sheet (Duane et al., 1972), which

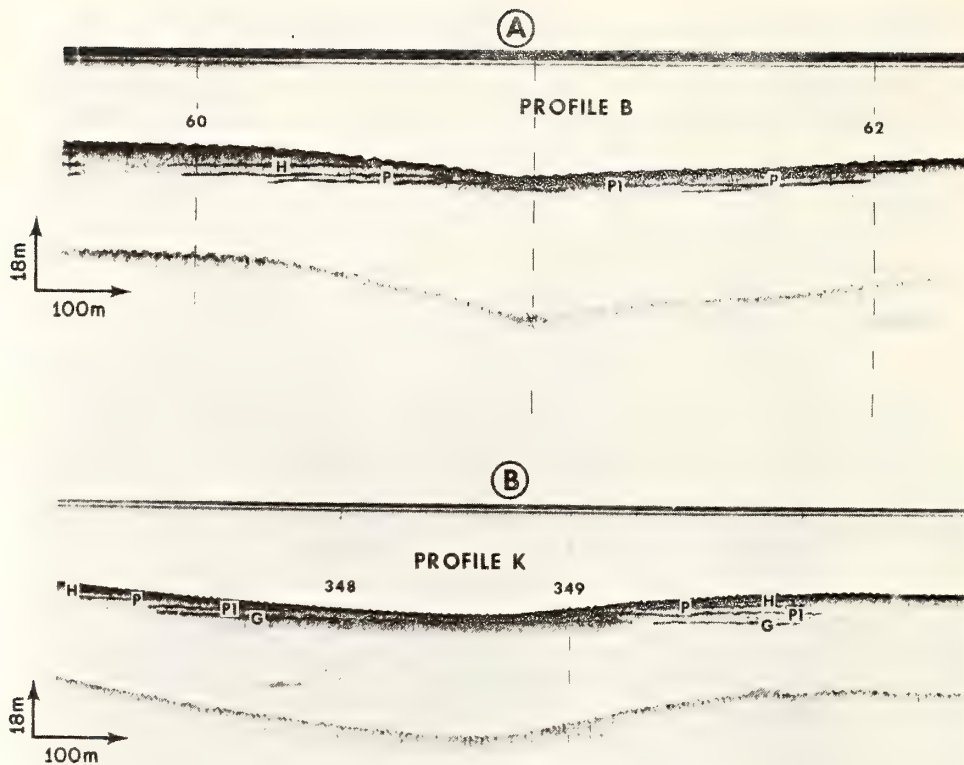


Fig. 6. Hand-enhanced, high-resolution seismic-reflection profiles. A. Immature, small-scale trough with a V-shaped profile. B. Mature trough with a parabolic profile with a broad axis and gentle side slopes. Note that the flat-lying strata abut against sides of troughs. The upper datum is approximately 5 m beneath the sea surface.

advanced as the shoreface underwent erosional retreat (Stahl et al., 1974). Primary troughs formed concomitantly with primary ridges, by non-deposition between ridges, or by the movement of sand off reflector H onto the ridges.

As the Holocene transgression continued and the water column deepened, the ridge topography underwent progressive modification. Ridge spacing, a function of flow depth (Allen, 1968), increased. Internal ridge structure suggests that this was accomplished by lateral ridge migration, or by coalescence of several smaller ridges. Ridge width appears to have increased as a result of more intense sedimentation on ridge flanks than on ridge crests, so that the ridges expanded laterally, rather than building upwards. As a result internal reflectors are generally steeper than present ridge flanks.

Scour of the trough floors has locally breached reflector H. Where this has

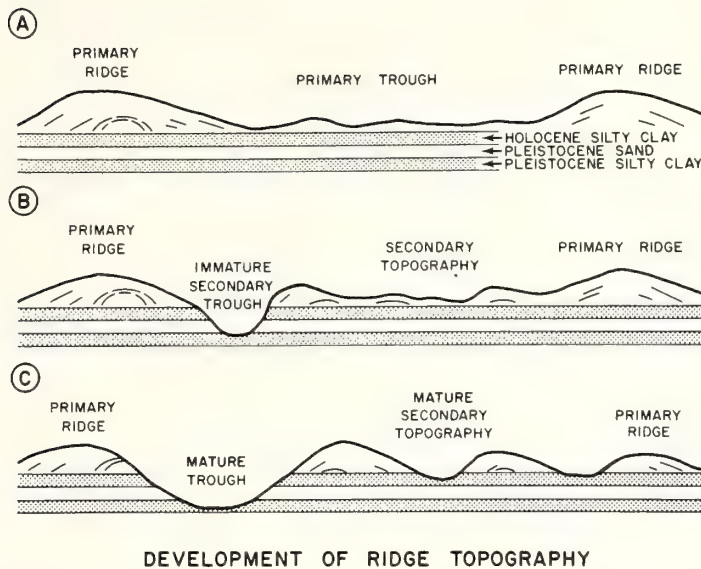


Fig. 7. Hypothetical model for ridge development. A. Large-scale ridges are initiated in the nearshore environment. The ridges grow by vertical and lateral aggradation, resulting in "concentric" stratification. Large-scale troughs are zones of non-deposition. B. Small-scale, secondary trough is incised into older substrate. Profile is initially V-shaped. C. Secondary trough widens; the Pleistocene sand is readily eroded and the Holocene clay is subject to undercutting. Aggradation of secondary ridges is fed in part by sand released during trough erosion.

occurred, rapid downcutting and removal of the noncohesive sand of underlying unit P appears to have resulted in a relatively steep-walled small-scale trough, hereafter called a secondary trough (Fig. 7B). At the same time, secondary ridges began to appear in the primary troughs. Some ridges seem to bear a levee-like relation to the secondary troughs (Fig. 7B), as though excavation of the former supplied material to the latter. Where secondary troughs have penetrated as far as the silty-clay surface of reflector P1 (Fig. 7C) the troughs are broader, as though the clay inhibited further downcutting, and encouraged lateral erosion and trough widening, after the fashion of a desert blow-out.

This model for ridge formation may be compared with the inshore portion of the study area, traversed by profiles A-G (Fig. 1). Here a broad primary trough between two primary ridges develops a secondary topography as it is traced southwest (profiles A-G, Fig. 4). In Fig. 8, bathymetry of transects A, B and C are matched with a common datum, approximately 13 m below sea level (computed with a travel speed of 1.5 km/sec through water), and adjusted laterally so that successive crests of the landward primary ridge (position 1) coincide. Since the secondary topography (positions 2-5) becomes increasingly better developed through profiles C, B and A to the south, this series may be approximately equivalent to a time series, and as such may be compared with Fig. 7.

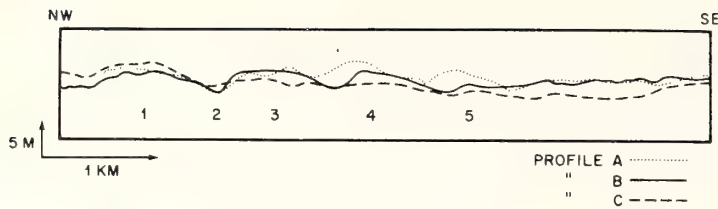


Fig.8. Overlay of bathymetry from transects A, B, and C. See Fig.1 for relative geographic positions. The five labeled positions are explained in the text.

#### *Possible relation of ridge topography to hydraulic regime*

The progressive evolution of the ridge topography appears to reflect an attempt on the part of the sea floor to maintain an equilibrium response to the slowly changing hydraulic regime during the period of water column deepening and shoreline retreat associated with the Holocene transgression. While a morphologic progression may be inferred on the basis of seismic reflection and related data, the character of the hydraulic forcing mechanism must remain speculative until the nature of the flow field on the New Jersey shelf is adequately documented. Our present, rather unsatisfactory state of knowledge may be summarized as follows. Beardsley and Butman (1974) have noted that sustained, high-velocity currents in the Middle Atlantic Bight occur primarily during those winter storms whose trajectories, relative to the shelf, permit a prolonged period of northerly winds. Such winds cause an Ekman transport of surface water to the coast, and result in coastal setup on the order of 40–60 cm (Beardsley and Butman, 1974). When this occurs, a shelf-wide southward geostrophic flow ensues. Studies conducted by Csanady and Scott (1974) under somewhat different circumstances suggest that the coastal margin of such geostrophic flow may assume a jet-like character, with velocities greater than those of the main flow. Limited data from the North Carolina coast (Swift, 1975) suggests that during periods of peak flow such accelerated coastal flows may experience downwelling and that inner shelf ridges may in fact be initiated by such flow, with the downwelling jet localized between the ridge and the shoreface.

Ridges left behind on the shelf floor by the retreating shoreface continue to be maintained by the flow field. Pre-recent substrate continues to be exposed in the troughs, and as noted above, secondary patterns of ridges may appear. Continued ridge maintenance requires that the storm flow field be structured; a homogeneous flow field would serve to degrade ridge crests and fill in troughs. Such structure has not been observed, but it is predicted by theoretical and experimental work of Ekman (1905), Faller (1963, 1971), Faller and Kaylor (1966), Lilly (1966), Hanna (1969) and Brown (1971). Ekman (1905) has shown that wind-driven shelf flows would tend to have a three-layered structure. An upper boundary layer consists of wind-driven water, whose speed is in excess of the geostrophic value induced by regional set-up. The upper boundary layer is characterized by an Ekman spiral in



which wind-driven surface water moves at  $45^\circ$  to the right of the wind (in the northern hemisphere). With increasing depth, velocity vectors shift progressively to the right, and speed decreases to the geostrophic value. Depth-averaged flow in the upper boundary layer is  $90^\circ$  to the right of the wind direction. Beneath the upper boundary layer, the core flow is geostrophic in nature, moving approximately parallel to the coast in response to the pressure field induced by wind set-up. Below the core flow, water is sheared against the stationary sea floor, causing a lower boundary layer that is characterized by a reverse Ekman spiral. As the bottom is approached, flow is diverted progressively toward the left (in the northern hemisphere), and the speed is progressively reduced.

The thickness of the boundary layers is a function of velocity at the top of each layer, and the characteristic eddy viscosity of the layer. Very little is known about the values that these parameters attain on the Atlantic shelf during storms. However, it seems probable that during storm flows, the boundary layers would expand at the expense of the core flow and would partially or completely overlap (Leetmaa, 1975).

Above a critical Reynolds number the internal character of the boundary layers, as well as their thickness, must change markedly. The boundary layers become unstable. However, since the flows are still subject to the Coriolis effect, the instability is not randomized but ordered (Faller and Kaylor, 1966; Faller, 1971). The flow divides into relatively sharply defined zones of downwelling, high-velocity surface water, alternating with more diffuse zones of upwelling lower-velocity bottom water (Faller, 1971). The result is a series of helical vortices, with alternate cells rotating with the opposite sense.

The extent to which this scheme applies to storm flows on the Atlantic shelf is not known. However, if such a cellular flow structure should couple with the cohesiveless substrate of the Atlantic shelf during periods of peak flow, sand ridges might be expected to localize, and be localized at, zones of bottom-current convergence; and troughs at zones of bottom-current divergence. According to this model the ridges would be classic bedforms, in the sense of morphologic responses to secondary flow patterns within a sheared flow (Wilson, 1973).

The nature of such coupling is problematic. The flow cells, if they indeed occur, are very flat. In the study area the ratio of ridge height to crest-to-crest distances averages 1:12 for the secondary ridges and 1:120 for the larger primary ridges. The ratio for the secondary ridges is similar to flow-cell spacing described by Faller and Kaylor (1966) for rotating tank experiments. They noted a spacing of  $11D$  for "small scale" cells where  $D$  is equal to the thickness of the Ekman layer. The spacing is "much greater" for large-scale cells. The sharply defined nature of the secondary troughs corresponds with the sharply defined nature of downwelling zones. Large-scale, primary troughs, however, are broad and flat. If they are responses to zones of downwelling, then the focus of downwelling must shift across the trough during the storm event in order to produce substrate mobility over large areas.

Faller and Kaylor note that small-scale cells are aligned to the left of the

mean flow, while the large-scale cells are aligned to the right of the smaller cells. Large-scale, primary ridges, in fact, tend to be aligned to the right of small-scale, secondary ridges. By this criterion, primary and secondary ridges may be of synchronous origin. However, morphologic relationships suggest that primary ridges formed prior to secondary ridges. The sequence of primary ridges can be traced landward on the northern flank of the Great Egg Shelf Valley (Swift, et al., 1972) where they appear to be presently forming on the shoreface. The offshore primary ridges tend to be J-shaped, hooking landward into the Great Egg Shelf Valley, as though affected by the tidal flow of the shelf valley when it was an active estuary mouth (McKinney et al., 1974). Secondary ridges only occur in this offshore zone. Their associated troughs pass through primary ridges, as though they were a later overprinting. If this is the case, then the secondary ridges may be a response to a change in the hydraulic regime initiated by a critical alteration in the shoreline configuration and bathymetry during the course of the Holocene transgression.

#### *Source of the Holocene sand sheet*

The seismic reflection observations presented above, including published data, place some constraints on possible sources for the Holocene sand sheet of the central New Jersey shelf. As noted by Meade (1969), Atlantic coastal estuaries are not sources of fluvial sand, but instead serve as sinks for both fluvial and littoral sands. Thus sands overlying the Holocene lagoonal carpet must be of other than fluvial origin. Possible sources are: (1) erosional retreat of the barrier face; (2) in-situ origin by breaching of the lagoonal carpet and erosion of the underlying sand; and (3) southerly transport on the shelf surface during storms.

The first possibility is difficult to evaluate. Since the Late Holocene reduction in the rate of sea-level rise, New Jersey coastal barriers appear to be at least locally growing upwards in place, being nourished by the inner shelf sand sheet, rather than vice versa (McMaster, 1954). The reverse may have been true during the earlier period of rapid sea-level rise, with the sand sheet forming as a debris blanket resulting from erosional shoreface retreat (Stahl et al., 1974). Since the barriers themselves rest on the lagoonal carpet deposited landward of them, *their* source of sand during this period must have been from updrift, from eroding headlands, or from zones where the shoreface was incised through the lagoonal carpet (unit H) into the underlying Pleistocene sand (unit P). This hypothesis is in accord with the regional ridge pattern (Fig.1) in which the sequence of ridges extending from the study area back to the New Jersey coast appears to form a shoal-retreat massif, marking the retreat path of the littoral drift depositional center on the north side of the ancestral Great Egg Estuary (Swift et al., 1972).

The second potential source, from the excavation of secondary troughs into the pre-recent substrate, is by itself inadequate to account for the Holocene sand sheet. Examination of Fig.4 indicates that of the 115 km of

seismic record, less than 9 km reveal erosion through the silty clay of unit H into the loose sand of unit P beneath. Furthermore, the surficial sand sheet is 2–12 m thick, but the Pleistocene sand, where still capped by unit H, is 1–8 m thick; its volume is inadequate to serve as a sole source.

We note, however, that northeast of the study area, the ridge topography of the massif gives way to a nearly flat surface with broad shallow hollows (Uchupi, 1970, pl.1). Deflation of this surface by shelf flows may also have contributed to ridge growth in the study area.

#### SUMMARY

The ridges occur in a belt trending across the shelf normal to the shore (Fig.1). The axis of individual ridges extend across the ridged zone, parallel or sub-parallel to the shore. The ridge sequence is inferred to be a shoal-retreat massif, the retreat path of the littoral-drift convergence localized on the northeast side of the ancestral Great Egg Estuary. Nearshore members of this sequence appear to be forming as shoreface-connected ridges in response to coastal storm flows (Duane et al., 1972). A little further seaward, similar ridges may have been detached from and abandoned by the shoreface during Holocene sea-level rise. Yet further seaward, in the study area described by this paper, larger ridges are spaced further apart. This may be an innate characteristic, due to the more intense nature of tidal flows associated with the Great Egg Estuary when it still received the drainage of the ancestral Schuylkill River (Swift et al., 1972), or it may reflect an adjustment of the ridge topography to the increasing depth of the flow. The character of internal reflectors suggests that this response took the form of a dominance of flank over crestal aggradation, so that narrow, steep-sided ridges became broader with more gently inclined flanks, and that lateral migration of ridges also occurred.

The large-scale, offshore ridges appear to have undergone a second stage of evolution, in that a pattern of small-scale, more southerly trending ridges have been imprinted over the first pattern. Secondary troughs have locally been incised into the Early Holocene silty clay that underlies the surficial sand sheet. These are relatively steep-walled features. However, where they have penetrated to the underlying Pleistocene sand, undercutting and lateral erosion have resulted in broader, more gently rounded features. Secondary ridges may have been nourished in part by material released during the formation of secondary troughs.

#### ACKNOWLEDGEMENTS

We are indebted to the officers and crew of NOAA ship "Peirce" for their professional abilities and cooperative attitude. We thank Sue O'Brien and Dave Senn for drafting, Thomas Clarke of the University of Virginia for computer programming, and Drs. G. H. Keller and H. B. Stewart, Jr. for critical review. Radiocarbon dates were provided by facilities at the Department of Geology, University of Miami, Florida.

This study is part of the National Oceanic and Atmospheric Administration's Marine Ecosystem Analysis (MESA) program.

#### REFERENCES

- Allen, J. R. L., 1968. The nature and origin of bed-form hierarchies. *Sedimentology*, 10: 161-182.
- Beardsley, R. C. and Butman, B., 1974. Circulation on the New England Continental shelf: Response to strong winter storms. *Geophys. Res. Lett.*, 1: 181-184.
- Brown, R. A., 1971. A secondary flow model for the planetary boundary layer. *J. Atmos. Sci.*, 27: 742-757.
- Csanady, G. T. and Scott, J. T., 1974. Baroclinic coastal jets in Lake Ontario during IFYGL. *J. Phys. Oceanogr.*, 4: 524-541.
- Curray, J. R., 1965. Late Quaternary history continental shelves of the United States. In: H. E. Wright, Jr. and I. G. Frey, (Editors), *The Quaternary of the United States*. Princeton Univ. Press, Princeton, N. J., pp.723-735.
- Duane, D. B., Field, M. E., Meisburger, E. P., Swift, D. J. P. and Williams, S. J., 1972. Linear shoals on the Atlantic inner continental shelf, Florida to Long Island. In: D. J. P. Swift, D. B. Duane and O. H. Pilkey, (Editors), *Shelf Sediment Transport: Process and Pattern*. Dowden, Hutchinson and Ross, Stroudsburg, Pa., pp.499-575.
- Ekman, V. W., 1905. On the influence of the earth's rotation on ocean currents. *Ark. Mat. Astron. Fys.*, 2: 1-53.
- Emery, K. O. and Uchupi, E., 1972. Western North Atlantic Ocean; Topography, rocks, structure; water, life, and sediments. *Am. Assoc. Pet. Geol. Bull.*, Memoir 17: p.532.
- Emery, K. O., Wigley, R. L., Bartlett, A. S., Rubin, M. and Barghoorn, E. S., 1967. Fresh water peat on the continental shelf. *Science*, 158: 1301-1307.
- Faller, A. J., 1963. An experimental study of the instability of the laminar Ekman boundary layer. *J. Fluid Mech.*, 15: 560-576.
- Faller, A. J., 1971. Oceanic turbulence and the Langmuir Circulations. *Ann. Review Ecology and Systematics*, 2: 201-233.
- Faller, A. J. and Kaylor, R. E., 1966. A numerical study of the instability of the laminar Ekman boundary layer. *J. Atmos. Sci.*, 23: 466-480.
- Garrison, L. E., 1970. Development of continental shelf south of New England. *Am. Assoc. Pet. Geol. Bull.*, 54: 109-124.
- Goldthwait, R. P., Dreimanis, A., Forsyth, J., Karrow, P. F. and White, G. W., 1965. Pleistocene deposits of the Erie Lake. In: H. E. Wright, Jr. and J. G. Frey (Editors), *The Quaternary of the United States*. Princeton Univ. Press, Princeton, N. J., pp.85-97.
- Hanna, S., 1969. The formation of longitudinal sand dunes by large helical eddies in the atmosphere. *J. Appl. Meteorol.*, 8: 874-883.
- Kraft, J. C., 1971. Sedimentary facies patterns and geologic history of a Holocene transgression. *Geol. Soc. Am. Bull.*, 82: 2131-2158.
- Leetma, A., 1975. Some simple mechanisms for steady shelf circulation. In: D. J. Stanley and D. J. P. Swift, (Editors), *Marine Sediment Transport and Environmental Management*. Wiley Interscience, New York, N. Y., in press.
- Lilly, D. K., 1966. On the instability of Ekman boundary flow. *J. Atmos. Sci.*, 23: 481-494.
- McKinney, T. F. and Friedman, G. M., 1970. Continental shelf sediments off Long Island, New York. *J. Sediment Petrol.*, 40: 213-248.
- McKinney, T. F., Stubblefield, W. L. and Swift, D. J. P., 1974. Large-scale current lineations on the central New Jersey shelf: investigation by side-scan sonar. *Mar. Geol.*, 17: 79-102.
- McMaster, R. L., 1954. Petrography and genesis of New Jersey beach sands. *State of New Jersey Dept., Conservation and Econ. Development, Geol. Surv. Bull.*, 63: 239 pp.

- McMaster, R. L. and Ashraf, A., 1973. Drowned and buried valleys on the southern New England continental shelf. *Mar. Geol.*, 17: 79—103.
- Meade, R. H., 1969. Landward transport of bottom sediments in the estuaries of the Atlantic Coastal Plain. *J. Sediment. Petrol.*, 39: 222—234.
- Milliman, J. I. and Emery, K. O., 1968. Sea levels during the past 35,000 years. *Science*, 162: 1121—1123.
- Schafer, J. P. and Hartshorn, J. H., 1965. The Quaternary of New England. In: H. E. Wright, Jr. and J. G. Frey (Editors), *The Quaternary of the United States*, Princeton Univ. Press, Princeton, N. J., pp. 113—127.
- Shepard, F. P., 1963. *Submarine Geology*. Harper and Row, New York, N. Y., 557 pp.
- Sheridan, R. E., Dill, C. E. and Kraft, J. C., 1974. Holocene sedimentary environment of the Atlantic inner shelf off Delaware. *Geol. Soc. Am. Bull.*, 85: 1319—1328.
- Stahl, L., Koczan, J. and Swift, D. J. P., 1974. Anatomy of a shoreface connected sand ridge on a New Jersey shelf: Implications for the genesis of the shelf surficial sand sheet. *Geology*, 2: 117—120.
- Stearns, F., 1967. Bathymetric Maps of the New York Bight, Atlantic Continental Shelf of the United States, Scale 1:125,000. National Ocean Survey, National Oceanic and Atmospheric Administration, Rockville, Md.
- Stubblefield, W. L., Lavelle, J. W., McKinney, T. F. and Swift, D. J. P., 1975. Sediment response to the present hydraulic regime on the Central New Jersey shelf. *J. Sediment. Petrol.*, 45: 337—358.
- Swift, D. J. P., 1973. Delaware Shelf Valley: Estuary retreat path, not drowned river valley. *Geol. Soc. Am. Bull.*, 84: 2743—2748.
- Swift, D. J. P., 1975. Coastal sedimentation. In: D. J. Stanley and D. J. P. Swift (Editors), *Marine Sediment Transport and Environmental Management*. Wiley Interscience, New York, N. Y., in press.
- Swift, D. J. P., Kofoed, J. W., Saulsbury, F. P. and Sears, P., 1972. Holocene evolution of the shelf surface, central and southern Atlantic shelf of North America. In: D. J. P. Swift, D. B. Duane and O. N. Pilkey (Editors), *Shelf Sediment Transport, Process and Pattern*. Dowden, Hutchinson and Ross, Stroudsburg, Pa., pp.499—575.
- Uchupi, E., 1968. Atlantic continental shelf and slope of the United States — Physiography. *U. S. Geol. Surv. Prof. Pap.*, 529-C: 30 pp.
- Uchupi, E., 1970. Atlantic continental shelf and slope of the United States — shallow structure. *U. S. Geol. Surv. Prof. Pap.*, 529-I, 44 pp.
- Veatch, A. C. and Smith, P. A., 1939. Atlantic submarine valleys of the United States: The Congo submarine valley. *Geol. Soc. Am. Spec. Pap.*, No. 7: 101 pp.
- Wilson, I. G., 1973. Equilibrium cross-section of braided and meandering rivers. *Nature*, 241: 393—394.

## Coastal Sedimentation

DONALD J. P. SWIFT

*Atlantic Oceanographic and Meteorological Laboratories, Miami, Florida*

The preceding chapters have discussed sedimentation in the intracoastal zone of lagoons and estuaries which lie seaward of the main shoreline, and on the open beach and associated surf zone. This chapter looks at sedimentation in the coastal zone as a whole, from the shoreline out to an indeterminate distance on the order of 5 km, where shelf flows are no longer affected by proximity to shore. From this perspective, the system of longshore sand transport beneath the zone of shoaling and breaking waves can be examined together with a deeper system of longshore sediment transport driven by intermittent wind or tidal flows. Time and space patterns of sediment input into this double system, the character of sediment transport, zones of temporary storage or permanent deposition, and the bypassing of sediment onto the shelf surface are analyzed. More complex patterns of sediment transport are also described, which result when coastal flows associated with straight coastal compartments interact with circulation in the erosional reentrants of rocky coasts or constructional inlets of lagoons and river mouths.

### ONSHORE-OFFSHORE SEDIMENT TRANSPORT

In considering coastal sediment transport, it is convenient to divide the movement of sediment into an onshore-offshore component and a coast-parallel component, and to consider these separately before examining the coastal sediment budget as a whole. Coast-parallel transport is many times more intensive than onshore-offshore trans-

port, but it is the latter that determines morphologic changes at given coastal transects. Hence this chapter begins by examining the coast in profile.

### Hydraulic Zones and Morphologic Provinces

When examined in cross section, the inner shelf is seen to consist of a regular succession of morphologic provinces, each associated with a distinctive zone of hydraulic activity (Fig. 1).

Subaerial environments of open coasts are most highly developed on barrier islands, where a zone of storm washover and eolian activity results in *washover flats* and *dune belts*, respectively. The intertidal swash zone builds the *beach foreshore*. The foreshore progrades seaward during fair weather by the addition of successive inclined sand strata to form the *beach prism*, a body of stored sand. The upper surface of the beach prism is the *beach backshore*. The zone of breaking waves may be divided into the breaker line, which tends to maintain a *breakpoint bar*, and a surf zone, in which a wave-driven littoral current flowing parallel to the beach is overridden by the bores of breaking waves. The littoral current tends to scour a *longshore trough*.

On unconsolidated coasts capable of relatively short-term response to the hydraulic regime, the inner shelf seaward of the breakpoint bar tends to exhibit two morphologic elements. A more steeply dipping *shoreface* extends to depths of 12 to 20 m. Its upper slope may be as steep as 1:10; its seaward extremity, at 2 to 20 km from shore, may slope as gently as 1:200. Beyond it lies

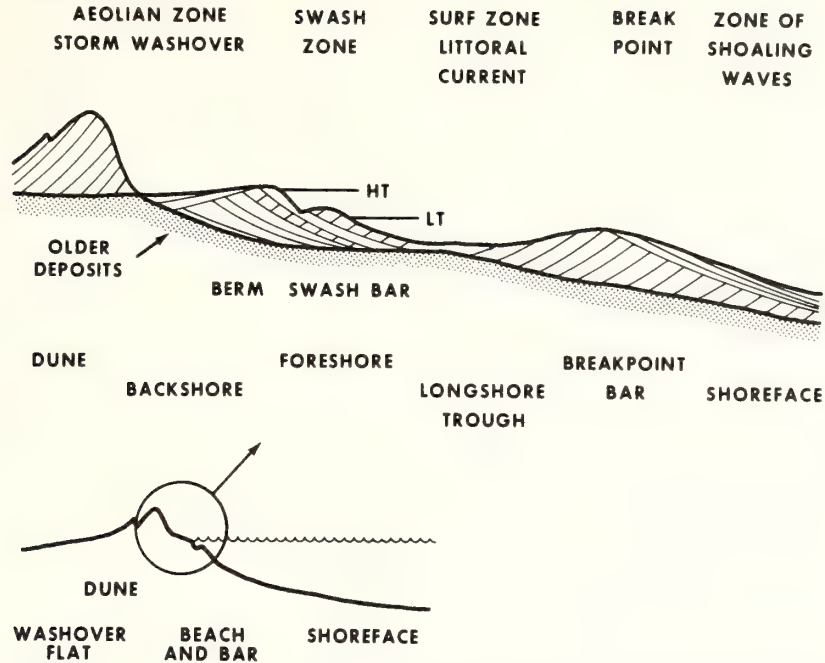


FIGURE 1. *Morphologic elements of the open coast and corresponding hydraulic provinces.*

the flatter *inner shelf floor* proper; the transition may be abrupt or very gentle. The upper shoreface, to a depth of perhaps 10 m, corresponds to the hydraulic zone of shoaling waves. The lower shoreface and inner shelf flow also experience the surge of shoaling waves, but their slopes, textures, and bed forms are equally a response to unidirectional shelf flows.

### The Beach Profile

Circulation in the surf zone and the morphologic response of the substrate are described in Chapter 13. This section deals with the net effect of such hydraulic process and substrate response on the onshore-offshore sediment budget.

As a consequence of the enormous and nearly continuous expenditure of energy in the beach and surf zones, the topographic features of cohesionless sand found there may only exist as equilibrium or near-equilibrium responses to the circulation patterns described in the preceding chapter. The equilibrium is not a static one, however, as the characteristics of the wave regime that force the response are constantly changing, often more rapidly than the morphologic response can accommodate. As a consequence, the nearshore beach and surf zone topography is endlessly destroyed and rebuilt according to a complex cycle, as the nearshore wave regime and circulation pattern alternate between fair-

weather and storm configurations, and on a larger scale between the summer season of infrequent storms and the winter season of frequent storms (Davis and Fox, 1972); see Fig. 2.

**FAIRWEATHER PHASE: BEACH AND BAR BUILDING.** The cycle is controlled by two mechanisms: the wave regime and the net circulation pattern driven by it. During fair weather, waves tend to be far-traveled swells, of low amplitude and long period. The asymmetry of associated bottom wave surge is marked, with the landward stroke beneath the wave crest being significantly more prolonged and more intense than the seaward stroke beneath the trough (Chapter 8, Fig. 8). Peak orbital velocities may be separated by periods of 8 seconds or on windward coasts, markedly longer. These same fair-weather swells tend to result in a relatively weak nearshore circulation pattern. Momentum flux, which is a function of wave height, is relatively low during fair weather both seaward and landward of the breaker, hence discharge through the littoral circulation cells is relatively low.

During fair weather, these two mechanisms, bottom wave surge and the littoral circulation pattern, cooperate to store sand in the beach prism. The wave regime appears to serve as a fractionating mill, dividing the available sand into a fraction undergoing mainly bed load transport, and a fraction undergoing mainly suspensive

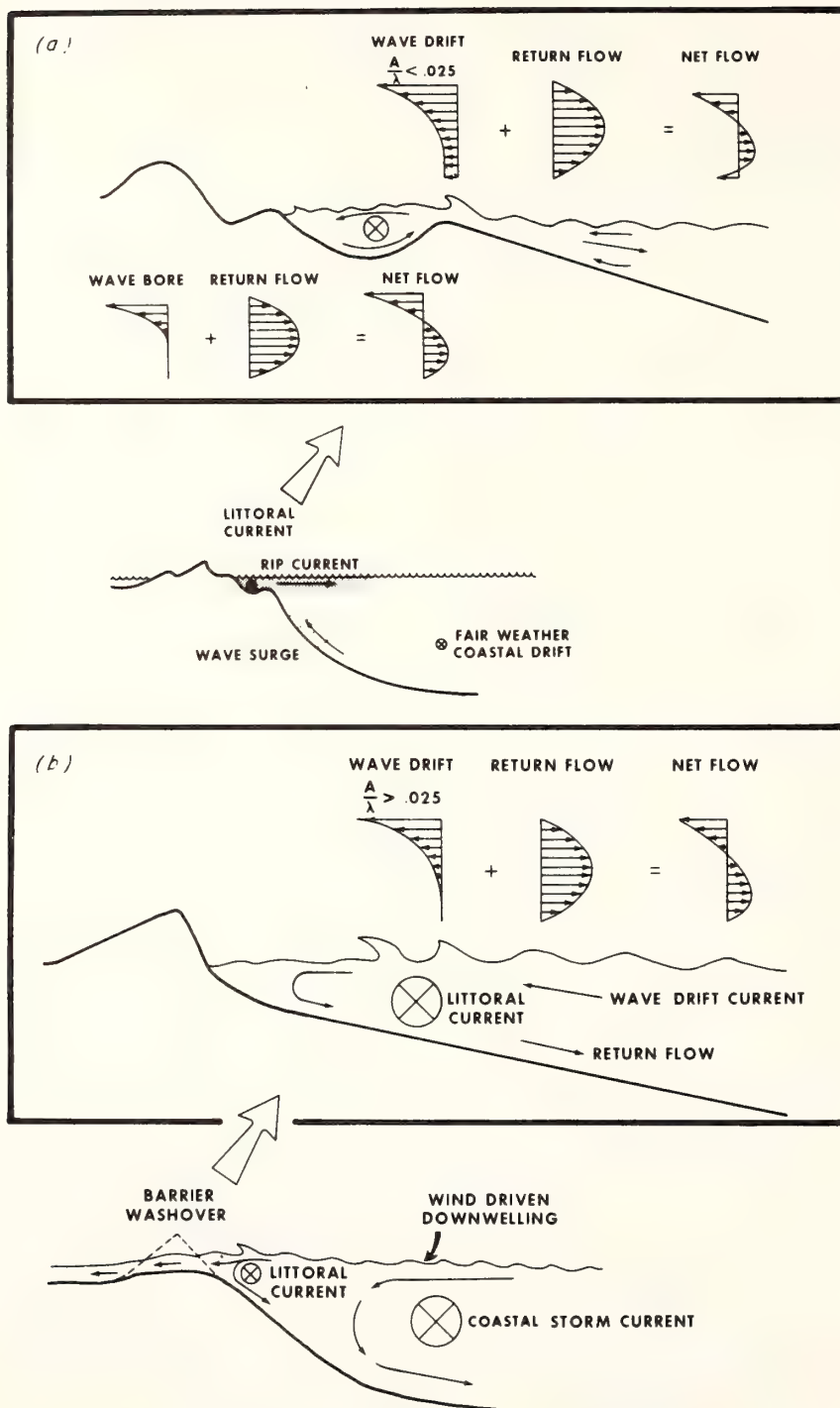


FIGURE 2. Comparison of (a) fair-weather and (b) storm hydraulic regimes. Based on Longuet-Higgins (1953), Schiffman (1965), and Ingle (1966).



transport. Sand coarser than a critical size threshold will be driven landward as bed load, by the landward asymmetry of bottom wave surge, toward the breakpoint. Longuet-Higgins (1953) and Russell and Osorio (1958) have undertaken calculations and experiments to determine the shore-normal components of flow averaged over a wave cycle, in the nearshore zone of shoaling waves. Their results indicate an increase in net landward flow with increasing height off the bottom, as a result of the failure of wave orbitals to close. Superimposed on this is a mid-depth return flow resulting in a three-layer flow system (Fig. 2). It is not entirely clear, however, if the latter component of flow would exist in nature as a response to wave setup, or if it was merely a wave tank artifact, induced by the continuity requirements of a closed system.

At the breakpoint, much of the energy heretofore available to drive sand landward over the bottom is lost to turbulence, and sand tends to accumulate as a breakpoint bar. Waves of oscillation turn into waves of translation (bores), in which water moves forward as a mass, and there is some evidence to indicate that landward of the breakpoint the velocity cross section averaged over the wave cycle changes to a two-layer system (Schiffman, 1965); see Fig. 2. An upper layer moves landward as a series of bores, and tends to be compensated by a basal return flow. This two-layer system is of course superimposed on the generally much stronger coast-parallel flow characteristic of the longshore trough. To the extent that the two-layer flow prevails, the bar crest is a zone of flow convergence, and its sand storage capability is readily understood. The bar builds upward until the rate of deposition of sand at the conclusion of wave breaking is equaled by resuspension during wave breaking. Depth of water over the bar at equilibrium is generally a third of the water depth prior to formation of the bar (Shepard, 1950).

Breakpoint bars tend to orient themselves normal to wave orthogonals. When deep-water orthogonals make a high angle to the shore, wave refraction does not fully eliminate this angle near the beach. Under these conditions, the bar tends to consist of series of *en echelon* segments, each aligned obliquely with respect to the beach, and alternating with rip current channels (Sonu et al., 1967).

Bar position is very sensitive to wave height, as this determines breakpoint position (Keulegan, 1948). If the tide range is appreciable, bar position will shift detectably through the tidal cycle. New bars tend to form during the peak or waning phases of a storm and to be slowly driven onshore as waves diminish during the ensuing fair-weather period, although an abrupt decrease in wave height may cause a second bar to form landward

of the first. During the period of landward migration of the bar, coarser bed load sand may bypass the bar and move onto the beach, if the waves are sufficiently long in period to re-form after breaking (King and Williams, 1949). Such bypassed sand will tend to accumulate as a swash bar (intertidal bar), or the plunge point bar itself will tend to migrate landward to the point where it is captured by intertidal processes, and becomes a swash bar (Fig. 3). As noted by King (1972), a swash bar may only form when the beach slope is lower than the maximum potential slope permitted by the grain size of the available sand; swash bars thus comprise attempts by the regime of wave swash and backwash to build to this ideal beach profile. Unlike plunge-point bars which are formed at a bottom current convergence, swash bars are formed by an abrupt bottom current deceleration. Their seaward slopes are swash current graded, but the landward slopes are lower than the angle of repose, and have the same net landward sense of sand transport.

Swash bars are the dominant bar on fine, flat beaches such as those of the central Gulf of Mexico, where the wave climate is mild and the supply of fine sand is abundant. They also tend to form on beaches with a high tidal range, where the bar is exposed to swash and backwash throughout much of the tidal cycle (ridge and runnel systems).

The landward movement of coarser fine sand during fair weather on open beaches may thus proceed as a sheet flow bypassing the bar, or migration of the bar up the beach, or more commonly as both. The result of this landward flux of sand is the formation of the beach prism of gently inclined sand strata, differentiated into the backshore beach (constructional upper surface subject to eolian action) and foreshore beach (swash-graded forward surface) separated by the berm (Fig. 1). If swash bar migration is the dominant mode of beach aggradation, then the berm will prograde seaward mainly by the welding to it of successive swash bars, and the internal structure of the beach prism will consist of seaward-dipping cross-strata sets, whose internal structures dip more steeply landward (Davis et al., 1972).

The ease with which breakpoint and swash bars can be constructed in wave tanks strongly suggests that these are indeed basic genetic types of bars. These two relatively simple types belong to a broad class of bed forms that arise in response to the mutual interaction of flow with the substrate. However, it has recently become apparent that much more elaborate patterns of bars may form more or less passively, in response to an innate pattern within the velocity field. Crescentic bars that form in response to standing edge wave patterns have been described in Chapter 13. On gently inclined shore-faces, shore-parallel bars may form in arrays of up to 30

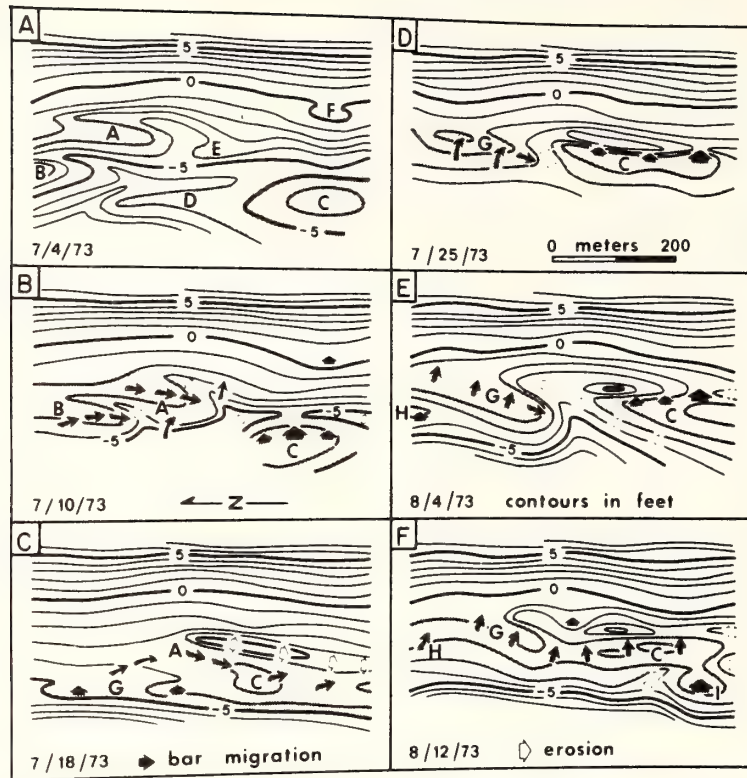


FIGURE 3. Sequence of maps showing bar migration and erosion at South Beach, Oregon. Bars form below mean sea level and advance up beach at rate of 1 to 5 m/day. Under the influence of strong, southward-flowing currents they migrate southward at 10 to 15 m/day. When they reach midtide level, they become stationary, or welded to the beach. From Fox and Davis (1974).

units. Bowen (personal communication) has suggested that such multiple bar systems may form in response to standing waves generated by the partial reflection of low-amplitude, long-period (1–2 minutes) incident waves. Such complex bar patterns clearly amplify the fair-weather storage capacity of the surf zone.

As noted above, the fair-weather littoral hydraulic regime is a fractionating mill, which splits the available sand into bed load and suspended fractions. The behavior of the bed load fraction has been traced above. Sand thrown into suspension at the breakpoint and fine enough to stay in suspension in the turbulent surf zone will tend to be fluxed alongshore by the longshore flow in the surf zone, and out through a rip channel to rain out on the shoreface (Cook, 1962).

**STORM PHASE: BEACH AND BAR DESTRUCTION.** During a storm, the wave regime and the littoral circulation patterns cooperate to withdraw littoral sand stored during the preceding fair-weather period. Wave steepness (ratio of wave height to wavelength) increases beyond a critical value (Johnson, 1949), at which point bottom

wave surge asymmetry is no longer efficient in driving coarser sand landward as bed load. Waves during storms are locally generated, and they tend to be shorter in period and higher (more energetic) with higher maximum orbital velocities. More sand is thrown into suspension and the critical grain-size threshold between suspensive and tractive sand fractions is shifted to favor suspension. Suspension is more nearly continuous. At the same time, discharge through the littoral circulation cells is increased manyfold.

During the advent of a severe storm the sudden seaward shift in breaker position, plus the great intensification of seaward sand transport, may be sufficient to destroy the bar and beach prism altogether. Some sand is driven across the back beach and over the dunes in the form of a washover fan (if this area is low enough to be so flooded), but most is transported seaward through rip channels and in rip current plumes. Toward the end of the storm, fallout from rip currents accumulates as a series of coalescing aprons of sand on the shoreface. Lagoons that are flooded during the period of rising storm surge may cut new inlets and break out

through their barrier islands. The associated sand-laden jets may greatly add to this shoreface fallout (Hayes, 1967). As the storm wanes, the bar re-forms, and the cycle begins anew.

The cyclic nature of sand storage on beaches has been quantitatively assessed by Sonu and Van Beek (1971) in a study of northern North Carolina beaches (Fig. 4).

They observed a sequence wherein a storm-degraded concave beach profile, representing minimum storage, passed by means of swash bar accretion to a convex profile of maximum storage, during a four-month period. They noted that the sense of sedimentation (erosion or accretion) was more strongly correlated with the direction of wave approach (and hence with wind direc-

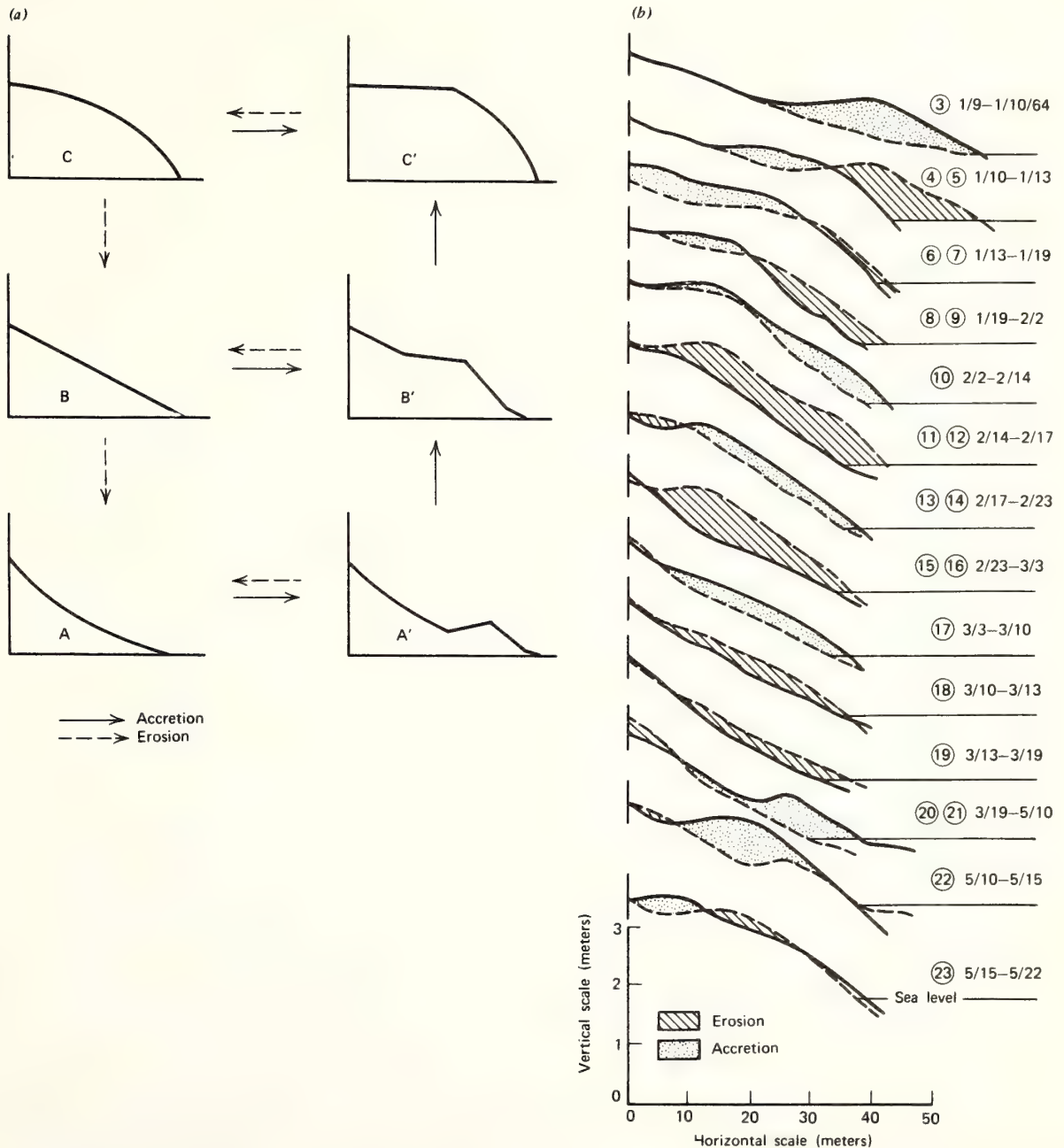


FIGURE 4. (a) Characteristic sequences of beach profile change. (b) Observed sequences. (c) Observed sequences as a function of sediment storage (Q) and beach width (S).

(d) Time history of sand storage. From Sonu and Van Beek (1971).

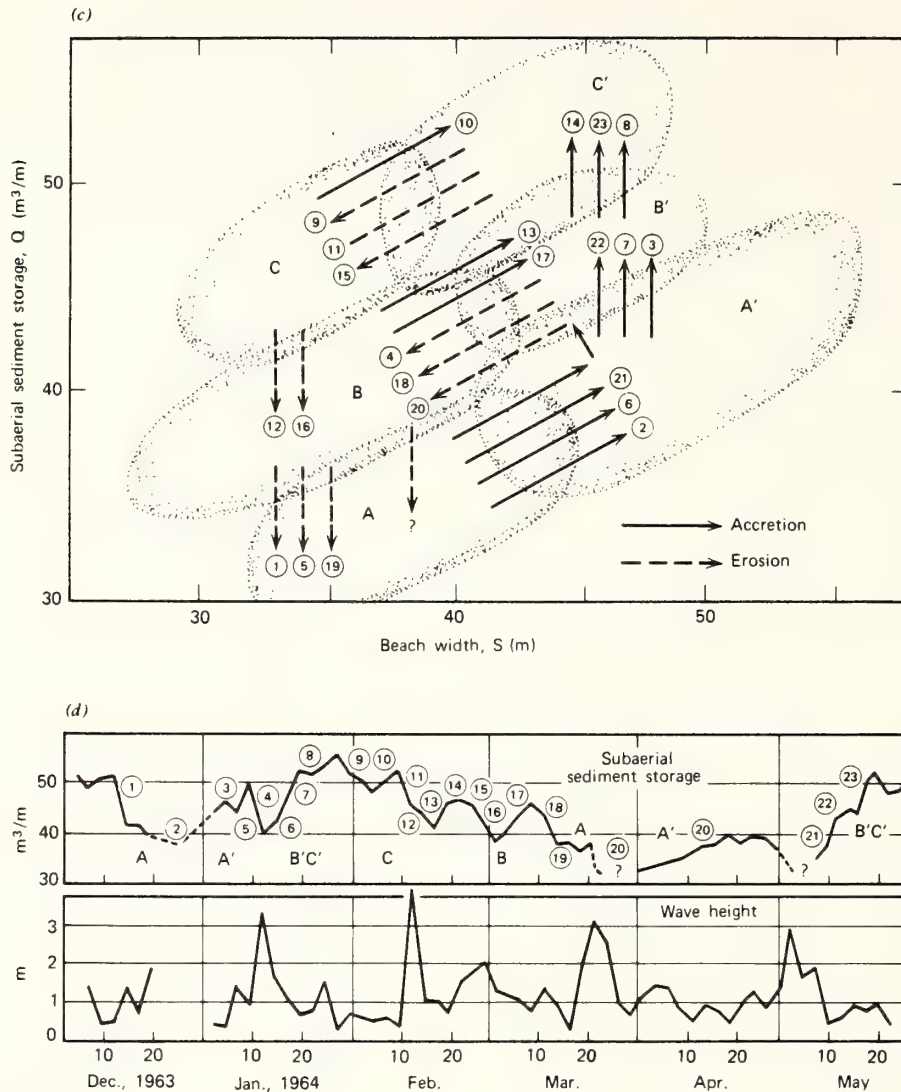


FIGURE 4. (continued)

tion) than with the wave steepness. Waves arriving from the northeast tended to cause erosion. These were associated with strong onshore winds and probably a wind-driven bottom return flow. It appears that during periods of strong alongshore or onshore winds, the system of littoral sand transport is no longer a closed system but discharges its sand into the wind-driven flow of the adjacent shelf floor. This deeper, intermittent system of transport is described in the following sections.

## THE SHOREFACE PROFILE

### Hydraulic Climate of the Shoreface

Far less is known about the circulation patterns of the shoreface and inner shelf than is known about the cir-

ulation patterns of the surf zone. Classical coastal workers, long preoccupied by the surf, have been indifferent to this topic, as have been physical oceanographers, whose habit has long been to hurry in their ships across the inner shelf, to the intellectual challenges of the large-scale planetary flows of the deep ocean basins. This situation is being rapidly reversed in view of rising public concern over the coastal environment (see Chapter 2), but old mental sets still linger.

The shoreface and inner shelf are a zone of transition, where the wave climate is still a major factor in shaping the seafloor, but where the shelf flow field is becoming of increasing significance in a seaward direction. There is some justice in the indifference of classical coastal workers to this hydraulic province. During periods of fair weather, the shelf flow on most coasts may be many

times less intense than littoral drift (Fig. 2.4). Its velocities, on the order of 1 to 10 cm/sec, are capable of moving whatever fines happen to be in suspension, but are not significant transporters of sand, although sand is repeatedly suspended by bottom wave surge at the crests of wave-generated ripples. Fair-weather flows, however, may be relatively complex in pattern, with nearshore reversals of the open shelf flow, induced by coastal promontories and by interaction with the tidal streams of inlets and estuary mouths.

Two kinds of inner shelf flows are quite significant in transporting sand and in molding coastal topography. On coasts with high tidal ranges, midtide current veloci-

ties associated with the passage of the coastal tidal wave may exceed 2 knots and locally attain 4 knots a few hundred meters seaward of the surf. Enormous volumes of sand are shifted on each tidal cycle, with significant net transport in the direction of the residual tidal current. Coastal tidal flows are poorly understood and tend to be rather complex because of strong interactions between tide-built topography and the tidal flow. Some examples are discussed in later sections (see pp. 294-295).

Intense coastal flows may also develop during storms (see Chapter 4). Such flows are far more infrequent than semidiurnal tidal currents, but unlike the latter, they occur on every coast, whether or not strong tidal cur-

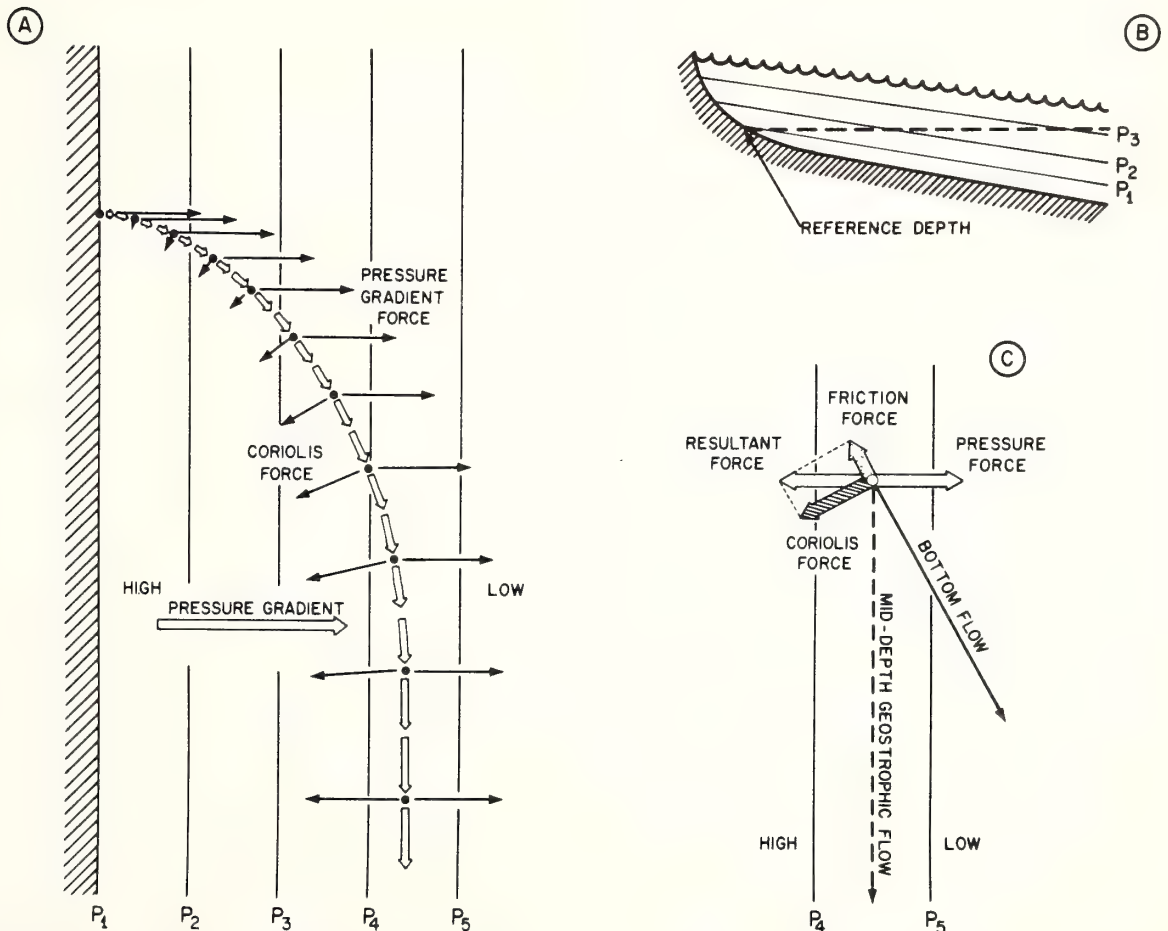


FIGURE 5. Geostrophic flow on the continental shelf. (A) Parcel of water at a reference depth moves seaward in response to pressure gradient force. As it accelerates, it experiences a Coriolis force impelling it to the right of its trajectory. Eventually trajectory parallels isobars, and pressure force and Coriolis force balance. (B) Cross section of hypothetical shelf experiencing geostrophic flow: illustrating

relationship of sea surface slope, isobaric surfaces, and reference depth. (C) Relationship between geostrophic flow and flow in bottom boundary layer. In latter case, a friction term enters the equation of motion, and the balance of forces occurs among a friction term, a pressure term, and a Coriolis term. Modified from Strabler (1963).

rents occur. They, too, are significant transporters of sand. Without these storm-driven flows, the coasts of our planet would have a markedly different appearance.

Storms, whether of tropical or extratropical origin, are rapidly moving counterclockwise wind systems that may be a thousand or more kilometers in lateral extent. Winds intensify rapidly toward the storm center, and in hurricanes, by definition, exceed 74 mph. The extent to which the shelf water column will couple with storm winds depends on the trajectory of the storm with respect to the geometry of the shelf. Sustained regional coupling of water flow with wind flow appears to occur when the winds blow equatorward along the length of eastward-facing coasts (Beardsley and Butman, 1974) or blow poleward along the length of westward-facing coasts (Smith and Hopkins, 1972). Under such conditions, water in the surface layer will be transported landward as a consequence of the Coriolis effect. Coastal sea level will rise until the coastal pressure head balances bottom friction, and bottom water can flow seaward as rapidly as surface water flows landward. Beardsley and Butman report up to 100 cm of coastal setup under such conditions. Since the sea surface is inclined against the coast, there is a gradient of seaward-decreasing pressure at any reference depth. A parcel of water, accelerated by the pressure force, has its trajectory steadily deflected to the right by the Coriolis "force," until finally, it is flowing along the isobars and the pressure and Coriolis terms balance (Fig. 5).

**INNER SHELF VELOCITY FIELD.** The complex velocity structure of the coastal zone is best approached in terms of the interaction of three major flow strata (Ekman, 1905; see Neumann and Pierson, 1966, p. 202). These are an upper boundary layer, a core flow, and a lower boundary layer (Fig. 6). The reader is advised to review Chapters 3 and 4 for a better understanding of this section.

The upper velocity boundary layer experiences strong wave orbital motion and, much of the time, a vertical velocity gradient imposed on it by wind stress. When the surface boundary layer is fully developed, surface water tends to move at  $45^\circ$  to the right of surface wind as a consequence of the Coriolis effect. Each successive lower layer moves at slower speed than the one above it, and is deviated successively further to the right (Ekman spiral). Net flow averaged over the depth of the layer trends  $90^\circ$  to the right of the surface wind. Above a critical Reynolds number this Ekman velocity structure becomes unstable, and is overprinted by a more complex structure, in which zones of upwelling and downwelling alternate, forming a pattern of horizontal helical vortices aligned parallel to or at a small angle to the

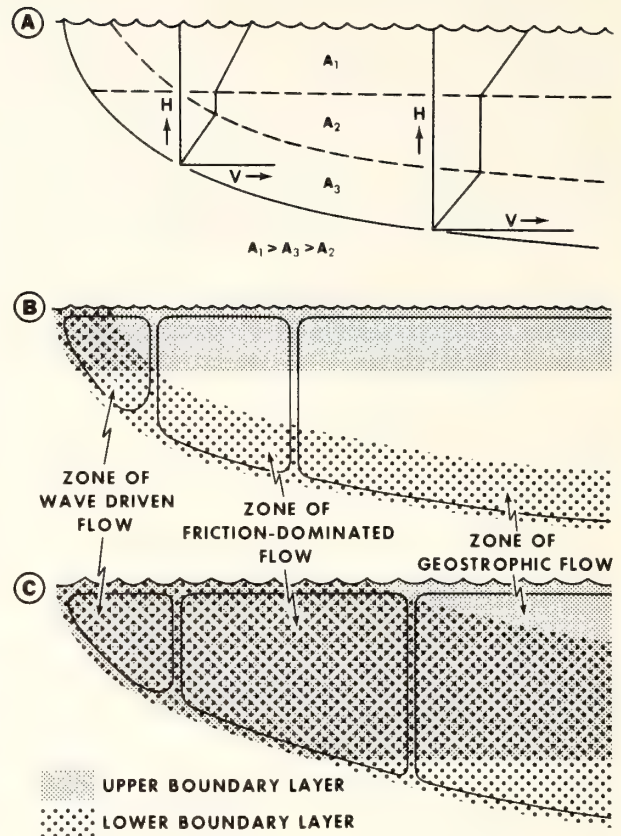


FIGURE 6. *Velocity structure of the shoreface and inner shelf. (A) General form of velocity profiles through the upper boundary layer, core flow, and lower boundary layer, and relative values of eddy viscosity. (B) Velocity structure during a period of relatively mild flow. (C) Velocity structure during peak flow.*

mean flow direction (Langmuir circulation: Langmuir, 1925). The transition tends to occur at surface wind speeds of 10 km (Assaf et al., 1971). The coefficient of eddy diffusion  $A_v$  is relatively large in the surface layer as a consequence of wave-generated turbulence (Fig. 6); it must undergo an abrupt increase at the onset of Langmuir circulation.

Below the base of the layer, core flow extends, unmodified, down to the bottom boundary layer. In the core, water flows in slablike fashion, with little vertical shear. Core flows are generally geostrophic in the sense that in the equation of motion, the pressure term is primarily balanced by the Coriolis term (Fig. 5). However, a steady state geostrophic balance is rarely maintained for any length of time. The shelf pressure field is in a state of continual change, in response to the passage of the diurnal tidal wave and to the passage of weather systems. As the pressure field builds up and then decays, the flow must accelerate and decelerate in sympathy,

constantly changing direction so that the pressure and Coriolis terms may balance. Such time-dependent flows are referred to as rotary tidal currents if mainly tide-forced, or inertial currents if mainly wind-forced.

The character of the bottom velocity boundary layer differs fundamentally from its surface analog. The surface boundary layer is externally forced, by the wind. Its velocity gradient, wave surge, and secondary flow patterns are overprinted on the core flow, and are carried along with it. The bottom velocity boundary layer is caused by frictional retardation of the core flow as it shears over the motionless substrate. Its lowermost meter exhibits a logarithmic velocity profile (Chapter 7), but the lower boundary layer as a whole is a thicker stratum, characterized by a velocity profile that is a reverse Ekman spiral. Frictional retardation of flow results in a deviation of boundary flow direction to the left of core flow, so that Coriolis and frictional terms may together balance the pressure term (Fig. 5C). The lowest layers, experiencing the greatest retardation, are deviated the furthest. Theoretical studies (Faller, 1963; Faller and Kaylor, 1966) suggest that this layer is also subject to helical flow structure above a critical Reynolds number. However, no field studies of this phenomenon have been undertaken. Such innate flow stabilities, and also turbulence induced by bottom roughness elements, would lead to an eddy coefficient larger than that of the core flow (Fig. 6A).

Three hydraulic provinces may be defined on the inner shelf on the basis of flow structure (Figs. 6B, C). Near the beach, the two boundary layers of the shelf flow field must completely overlap. In this zone the effects of the regional pressure gradient on water behavior are largely damped out as a consequence of frictional retardation. Oscillatory wave surge is the dominant water motion, giving rise to the complex nearshore circulation pattern described in the preceding chapter. A little farther seaward, the two boundary layers are more or less separate, but still occupy most of the water column. Flow is frictionally dominated; in the equation of motion the wind stress is largely balanced by friction. The effect of the Coriolis term is negligible in shallow water and there is little or no deviation of boundary flow with respect to core flow. The flow is Couette-like, in that there is a more or less linear velocity gradient from top to bottom. Still further seaward, the two boundary layers diverge significantly. The geostrophic core flow dominates the water column.

This pattern of coastal flow zonation must vary with the intensity of the regional and local wind fields. An intensified regional wind will accelerate core flow and increase the thickness of the bottom boundary layer. Intensification of the local wind field will cause the upper boundary layer to thicken, though not necessarily

at the same rate. The intensification of local wind may either lead or lag the intensification of wind on the adjacent shelf, depending on the trajectory of the weather system.

The net effect of a storm is to expand the width of the coastal flow zones and to displace the outer two zones seaward. There are few data available for such situations (see Chapter 4). From theoretical considerations, it appears that the upper and lower boundary layers may overlap far out on the shelf. Zonation becomes primarily a function of depth (Fig. 5C). In the zone of friction-dominated flow, the water accelerates in response to direct wind stress until the stress is balanced entirely by friction; the Coriolis term is not significant, and flow in this zone may take on the dimensions of a coastal jet (Csanady and Scott, 1974). The zone of friction-dominated flow will be a downwelling zone if local winds have an onshore component, or if regional coast-parallel winds result in onshore surface transport. It will be an upwelling zone if the reverse situation prevails (Cook and Gorsline, 1972).

The deeper, offshore flow may retain a primarily geostrophic balance of forces during a storm, although the friction term is necessarily more prominent. If overlap of the boundary layers extends through this zone, it is theoretically possible (Faller, 1971) that there be top to bottom overturn as a consequence of Ekman instability, with high-velocity, wind-driven surface water delivered to the seafloor in zones of downwelling.

The velocity structure of the shelf water mass follows a seasonal cycle that is coupled to the cycle of density stratification. During the summer, this upper velocity boundary layer is the same as the upper mixed layer. Wave turbulence and Langmuir circulation maintain the layer's mixed character, while the pycnocline tends to decouple upper boundary flow from core flow. During the fall, the thermal contrast is weakened by surface cooling. The increasing frequency and severity of storms cause steady erosion of the lower, stratified portion of the water column by Langmuir circulation (Faller, 1971) and the upper mixed layer thickens at the expense of the stratified water below. Meanwhile, a lower mixed layer may be induced by intensified turbulence in the bottom boundary layer, and may thicken until the density structure has simplified to a two-layer system (Charnell and Hansen, 1974). Further vigorous storm action will drive the weakening pycnocline down to the seafloor, so that there is no further impediment to top-to-bottom overturn by secondary flow components.

### Sedimentation on the Upper Shoreface

The shoreface slope, with its gradient of seaward-decreasing grain size, occurs primarily in the zone of wave-

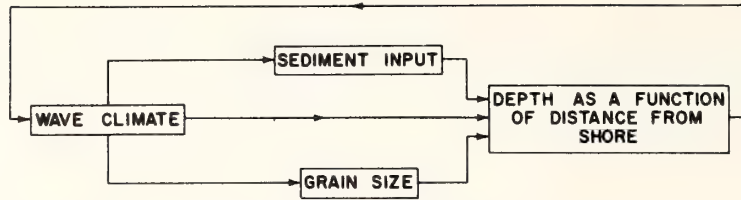


FIGURE 7. *Relationships of variables controlling slope of the shoreface.*

driven flow (Fig. 6) although its lower portion tends to extend into and be modified by the zone of friction-dominated flow. The slope and grain-size gradient of the shoreface have been generally considered to comprise a response to the regime of shoaling waves seaward of the breakpoint, in which depth as a function of distance from shore is itself a function of littoral wave power, sediment discharge, and grain size (Fenneman, 1902; Johnson, 1919, p. 211; Johnson and Eagleson, 1966; Price, 1954; Wright and Coleman, 1972; see Fig. 7. Johnson (1919, p. 211) has described this equilibrium relationship as follows:

The subaqueous profile is steepest near land where the debris is coarsest and most abundant; and progressively more gentle further seaward where the debris has been ground finer and reduced in volume by the removal of the part in suspension. At every point, the slope is precisely of the steepness required to enable the amount of wave energy there developed to dispose of the volume and size of debris there in transit.

The main line of inquiry into the forces maintaining the shoreface profile has led to the null-line hypothesis, evaluated in Chapter 8. The hypothesis has been expressed in its most complete form by Johnson and Eagleson (1966). It envisages shoreface dynamics in terms of a Newtonian balance of forces experienced by a sand particle on the shoreface, in which the downslope component of gravitation is opposed by the net fluid force averaged over a wave cycle. Since in shallow water, bottom orbital velocities are asymmetrical, with stronger landward surge (Chapter 8, Fig. 8), fluid forces are directed upslope. The gravitational force becomes more intense as the shoreline is approached and the slope increases. However, the fluid force increases yet more rapidly. As a consequence, for a given grain size there should be a null isobath, seaward of which particles of the critical size tend to move downslope, and landward of which they tend to move upslope. The equilibrium grain size should decrease with increasing depth. Hence, the shoreface sand sheet should tend to become finer downslope, as indeed it does. The shoreface slope at each point should be uniquely determined by the grain size of substrate and the intensity of bottom wave surge.

However, attempts to utilize null theory in the field have met with ambiguous or negative results (Miller

and Zeigler, 1958, 1964; Harrison and Alamo, 1964). Objections include: (1) slopes are not sufficiently steep over much of the shoreface (Zenkovitch, 1967, p. 120), and (2) slope sorting by waves tends to be overwhelmed by other processes, which as the authors of the theory admit, are not accounted for in null theory. No account, for instance, has been taken of the process of ripple sorting as described in Chapter 8 (p. 117). Wells (1967) has shown that divergence of onshore-offshore transport of a given grain size from its null isobath should occur as an innate response to higher order wave interactions, without regard to the gravitational force acting on the grains.

A perhaps more telling criticism of null-line theory is that a significant portion of shoreface sand travels not as bed load, but in suspension. Murray (1967) has performed tracer studies that indicate that on the upper shoreface, the dispersal of sand corresponds to the prediction of diffusion theory. Field observations by Cook and Gorsline (1972) have led them to conclude that the seaward-fining grain-size gradients of the shoreface are more likely to be caused by rip current fallout rather than by the null-line mechanism.

It may be more fruitful to approach the problem of shoreface maintenance from the point of view of energetics, rather than from the point of view of a balance of forces. Such an approach would view the depth at each point of a shoreface profile as a function of wave power at that point. The ideal wave-graded profile would be one that experiences at each point a maximum bottom orbital velocity equivalent to the threshold velocity of the size class of available sand. It should be possible to construct an algorithm for calculating water depth as a function of wave characteristics and bottom sediment grain size, based on the equations for bottom orbital velocity, for friction energy loss to the bottom, and for the shoaling transformations of waveform that have been presented in Chapter 6.

#### **Lower Shoreface Sedimentation: Onshore-Offshore Sand Budget**

It seems doubtful that such a model for maintenance of the shoreface profile by the wave regime would be sufficient to fully account for the distribution of slopes and



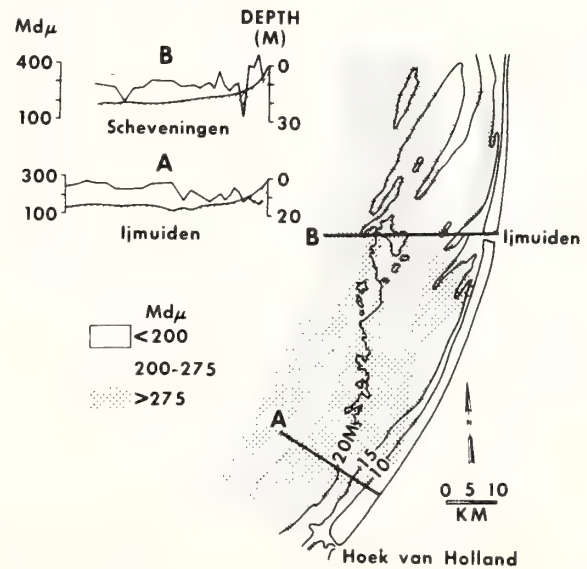
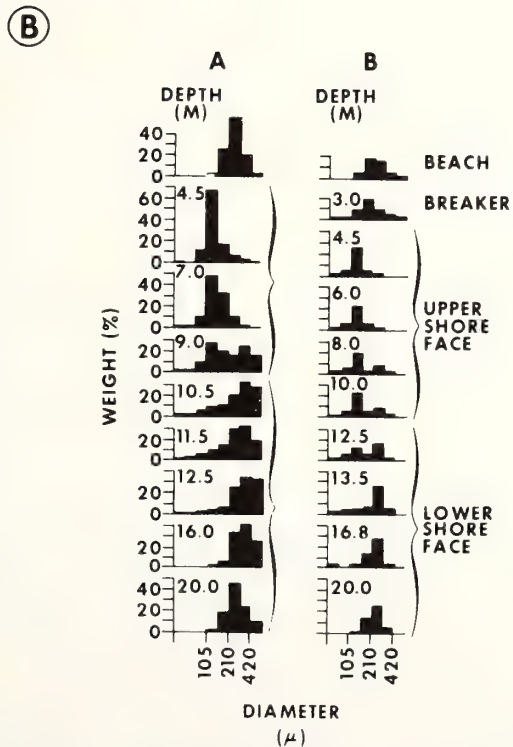
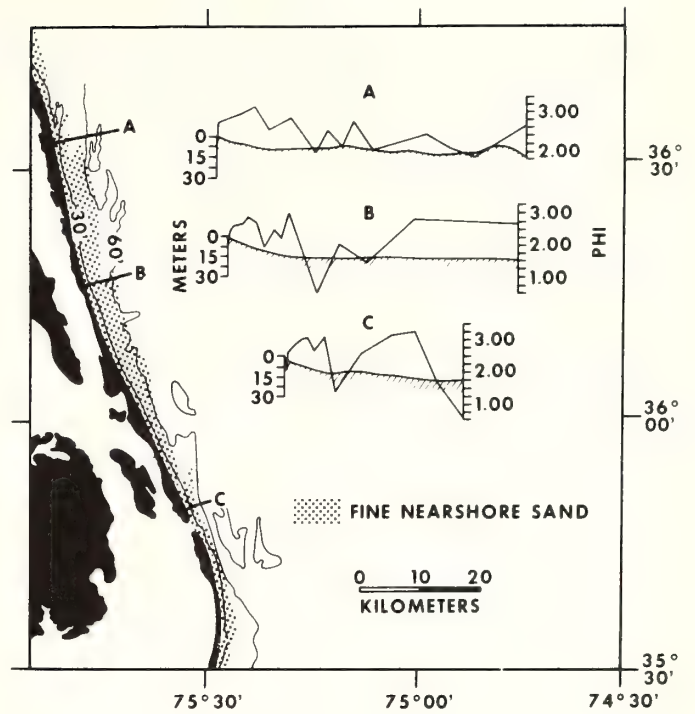
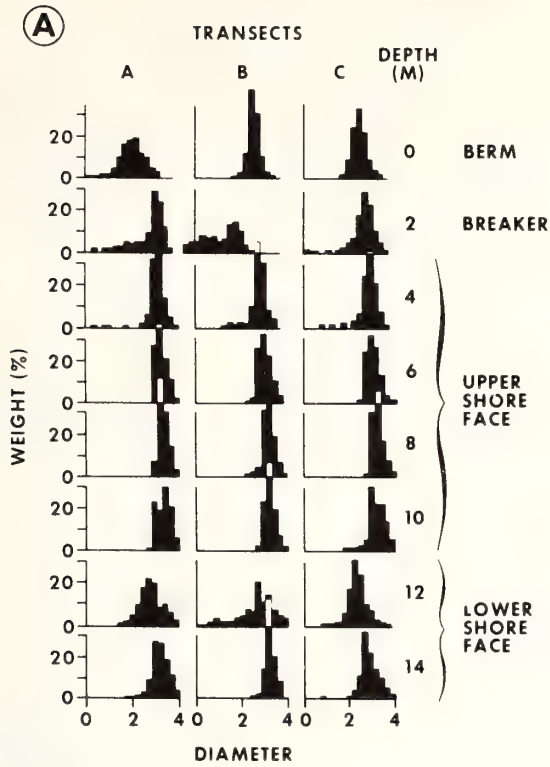


FIGURE 8. Distribution of grain sizes on retrograding coasts. (A) The storm-dominated coast of Virginia-northern North

Carolina. Data from Swift et al. (1971). (B) Dutch coast. Data from Van Straaten (1965).

grain sizes associated with observed shoreface profiles. For instance, modern coasts whose historical records indicate that they are undergoing erosional retreat tend to consist of two distinctive grain provinces. From the breaker to a depth of about 10 m, the upper shoreface consists of fine, seaward-fining sand (Fig. 8). Seaward of 10 m, grain size on the lower shoreface and adjacent shelf floor is far more variable and generally markedly coarser.

We may account for the fine, upper shoreface sand province as a mantle of rip current fallout, whose slope is adjusted by the regime of shoaling waves (Cook, 1969). However, the lower shoreface province of coarse variable sand does not fit the model for wave maintenance of the shoreface. We may consider the hypothesis that it is instead a response to the deeper, intermittent high-intensity flows of the zone of friction-dominated flow (Figs. 2B and 6B, C).

Observations by Moody (1964, pp. 142-154) on the erosional retreat of the Delaware coast lend some support to this hypothesis (Fig. 9). In this area, the shoreface steepens over a period of years toward the ideal wave-graded profile, during which time the shoreline remains relatively stable. The steepening is both a depositional and erosional process. Moody notes that steepening was accelerated after 1934 because a groin system initiated then "presumably trapped sand, causing the upper part of the barrier between mean low water and -3 m to build seaward" (Moody, 1964, p. 142). However, erosion continued offshore at depths of 6 or 7 m below mean low water. The steepening process is not continuous, but varies with the frequency of storms and duration of intervening fair-weather periods. The slope of the barrier steepened from 1:40 to 1:25 between 1929 and 1954, but erosion on the upper barrier face between 1954 and 1961 regraded the slope to 1:40.

The steepening process is terminated by a major storm, during which time the gradient is reduced and a significant landward translation of the shoreline occurs. Moody (1964, p. 199) describes the Great Ash Wednesday Storm of 1962, bracketed within his time series, as having stalled for 72 hours off the central Atlantic coast. Its storm surge raised the surf into the dunes for six successive high tides. The shoreline receded 18 to 75 m during the storm. While much of the sand was transported over the barrier to build washover fans over 1 m thick, much more was swept back onto the seafloor by large rip currents and by the storm-driven seaward-trending bottom flow of the shoreface (Moody, 1964, p. 114); see Fig. 2B.

Moody's observations allow us to present a general model of shoreface maintenance, in terms of the on-shore-offshore sediment budget. There seems to be little

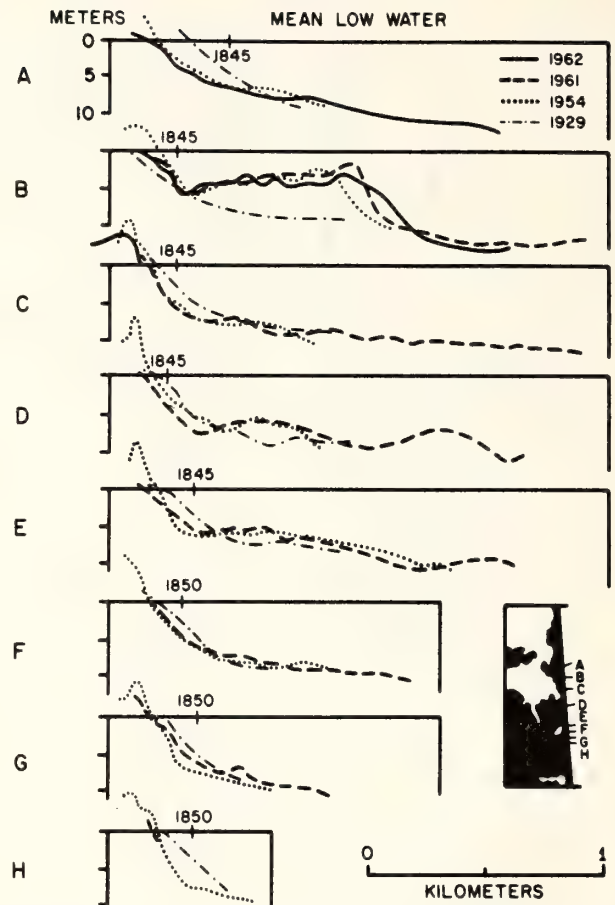


FIGURE 9. Retreat of the Delaware coast, based on U.S. Coast and Geodetic Survey records and a survey by Moody. From Moody (1964).

reason to doubt the applicability of the conventional wave-grading model to the upper shoreface, even if we cannot yet present this model in a quantitative manner. Upper shoreface textures and slopes are time-averaged responses to two opposing mechanisms, the seaward flux of suspended sand in rip currents on one hand, and the landward creep of bottom sand in response to the net landward sense of bottom wave surge on the other hand. The upper shoreface profile varies in cyclic fashion, with storage of sand mainly on the beach during the fair-weather summer season, and storage of sand mainly on the upper shoreface during the winter. For long periods of time, the upper shoreface profile may oscillate about the ideal wave-graded configuration.

During major storms, however, the upper shoreface system of wave-driven longshore sand flux interacts with coastal boundary of the storm flow field. Sand eroded from the beach and bar by storm waves passes seaward

in intensified rip currents to the zone of friction-dominated flow (Fig. 2B), which during storms may take the form of a downwelling coastal jet. When this occurs, bottom flow on the lower shoreface will have a seaward component of flow, and the coastal sand transport system is transformed from a closed system of net sand storage to an open system of net sand loss. Sand raining out of rip currents will not come to rest, but will be transported obliquely seaward. If the storm is severe enough, the mantle of rip current fallout that accumulated during the preceding fair-weather period will be stripped off, and the underlying strata will be exposed to erosion.

This hypothetical scheme has not yet been adequately tested by field observations. However, as a hypothesis, it has a number of advantages. It provides a rationale for the Bruun model of erosional shoreface retreat (Fig. 10). Bruun (1962; see also Schwartz, 1965, 1967, 1968) noted the characteristic exponential curve of the inner shelf profile, and accepted the hypothesis that it constituted an equilibrium response to the hydraulic climate. With this premise adopted, it follows that a rise in sea level must result in a landward and upward translation of the profile, as long as coastwise imports of sand into the coastal sector under study are equaled by coastwise exports. The translation necessitates shoreface erosion and provides a sink for the debris thus generated beneath the rising seaward limb of the profile.

Moody's time series shows that over a 32 year period, shoreface erosion on the Delmarva coast was in fact nearly compensated by aggradation on the seafloor in accordance with the Bruun principle (Table 1). The small deficit is probably attributable to loss to washover fans, and through littoral drift to nearby Cape Henlopen spit.

Moody's studies provide us with insight into the processes governing the Bruun model. His observations indicate that the process of erosional retreat of the shoreface is not continuous. It is cyclic in a manner analogous to the annual cycle of the upper shoreface profile, but the period is related to the frequency of exceptional storms, and is on the order of years.

The model also provides a more detailed and satisfactory explanation for the origin of the surficial sands of shelves undergoing transgression than does the relict-Recent sediment model of Emery (1968). The surficial sand sheet of the shelf is a lag deposit created during the process of erosional shoreface retreat by the seaward transfer of sand during storms and its deposition on the adjacent shelf floor (Fig. 10A). The nearshore modern sands of the upper shoreface are a transient veneer of rip current fallout. Both textural provinces are "modern" in the sense of being adjusted to the prevailing hydraulic regime; both are "relict" in the sense of being derived

TABLE 1. Sediment Budget from the Delmarva Coast

Sediment Source	Period	Average Volumetric Change* (m <sup>3</sup> /year)
Barrier (mean low water to toe of sand barrier)	1929-1961	-148,000
Sand dunes (mean low water to top of sand dunes)	1954-1961	-100,000 (estimated)
Offshore erosion (principally on north- west side of ridges)	1919-1961	-100,000
Erosion from bay inside Indian River Inlet	—	-69,000
	Total erosion	-417,000
<u>Site of Deposition</u>		
Tidal delta	1939-1961	+120,000
Barrier south of Indian River Inlet	1939-1961	+5,700
Offshore accretion	1919-1961	+256,000
	Total accretion	+381,700
Total erosion		-417,000
Total accretion		+318,700
Net erosion		-98,300 m <sup>3</sup> /year

Source. From Moody (1964).

\* "+" indicates accretion; "-" indicates erosion.

from the underlying substrate. The role of shoreface retreat in generating shelf sediments is explored further in Chapter 15.

### Deposits of the Coastal Profile: Textures and Bed Forms

**TEXTURES OF THE SHOREFACE.** The patterns of onshore and offshore sediment transport described in the preceding sections give rise to systematic distributions of sediment types and bed forms over the beach and shoreface. The beach and surf zones consist of alternating belts of finer and coarser sand, the absolute grain-size values depending on grain sizes available to the coast and on the hydraulic climate of the coast (Bascom, 1951). The coarsest grain sizes are found on the crest of the berm, in the axis of the longshore trough during the erosional phase of the beach cycle, and on the crest of the plunge point bar.

The distribution of grain sizes on retrograding shorefaces has already been described (Fig. 8). Upper shoreface sands tend to be fine grained to very fine grained, and become finer in a seaward direction. The grain-size

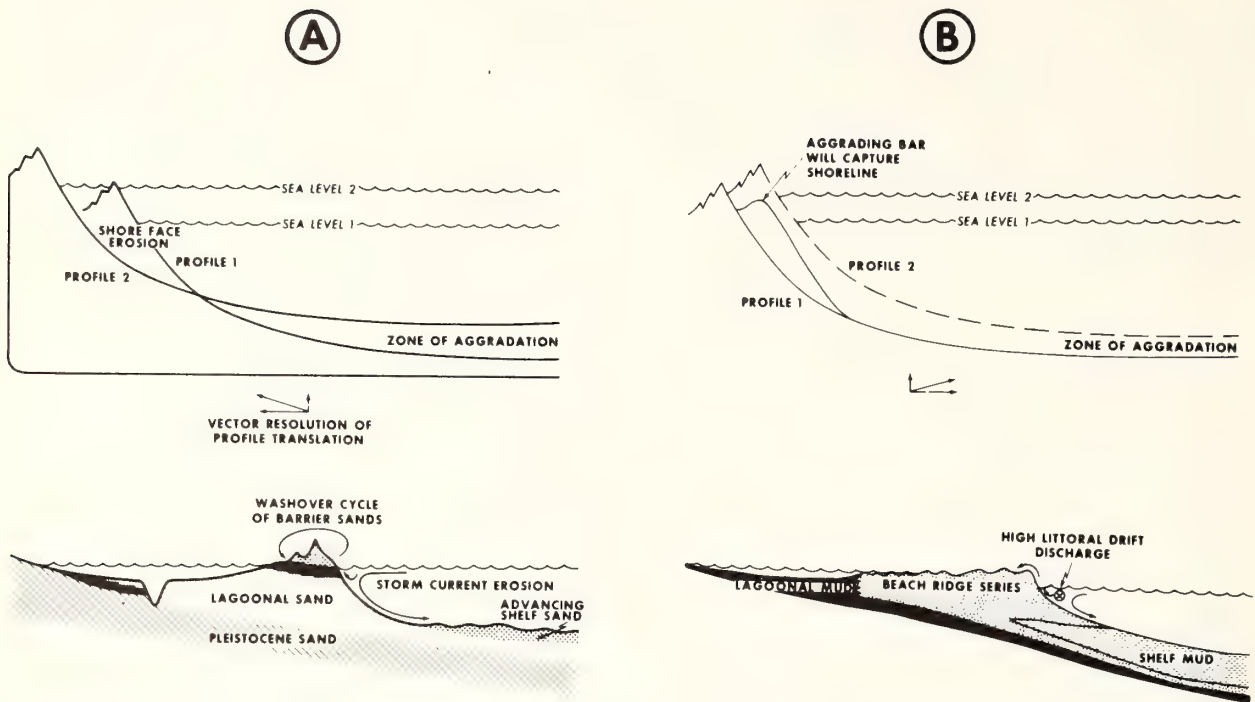


FIGURE 10. *Dynamic and stratigraphic models for (A) a retrograding and (B) a prograding coast during a rise in sea level. If coastwise sand imports are balanced by or are less than coastwise sand exports, the hydraulically maintained coastal profile must translate upward and landward by a process of*

*shoreface erosion and concomitant aggradation of the adjacent seafloor (Brunn, 1962). If coastwise sand imports exceed exports, as is the case for deltaic coasts, then the profile must translate seaward and upward. Based on Curray et al. (1969).*

gradient is perhaps originally the result of progressive sorting (see p. 162) operating on the suspended sand load of rip current plumes; the underlying deposit becomes finer down the transport direction in the manner of loess or volcanic ash deposits. It is perhaps secondarily the result of adjustment to the landward increase in bottom orbital velocity, and to the mechanism of ripple sorting (p. 117).

On retrograding coasts such as the North Carolina and Dutch coasts (Fig. 8), the lower shoreface consists of variable but generally coarser sand. It is texturally adjusted to the coastal boundary currents associated with peak flow events. This material is of negligible thickness and constitutes a residuum mantling the eroding surface of the underlying older deposits. Its final resting place appears to be the adjacent seafloor, where it forms a discontinuous layer up to 10 m thick (Stahl et al., 1974).

Bimodal sands tend to occur at the contact between the two provinces, where the rip current fallout blanket thins to a feather edge. This contact advances down-slope during fair-weather periods of upper shoreface aggradation, and retreats upslope during periods of storm erosion of the entire shoreface.

On prograding coasts, such as the western Gulf of Mexico (Bernard and Le Blanc, 1965) or the Costa de Nayarit (Curray et al., 1969), more sand is delivered by littoral drift during fair weather than can be removed by storms. The fine, seaward-fining sand of the upper shoreface extends down to the break in slope where it may become as fine as mud, and continues across the shelf floor (Fig. 10B).

Visher (1969) has observed size frequency distributions in the surf zone and on the shoreface (see Fig. 11). Moss' theory may be applied to his observations (see p. 162), but caution must be used, as Moss' theory relates to quasi-steady flows, while in the coastal marine environment a high-frequency flow oscillation due to wave surge tends to be superimposed on a steady flow component. Peak wave surge regularly induces the upper flow regime (Moss' rheologic regime), while the intervening flow may consist of one of the less intense stages.

In Fig. 12, the supercritical flows of swash and backwash in the intertidal zone have resulted in complex subpopulation assemblage (lower foreshore, 1.5 ft samples). The contact (C) population, consisting primarily of shell debris, comprises up to 10% of the total distri-

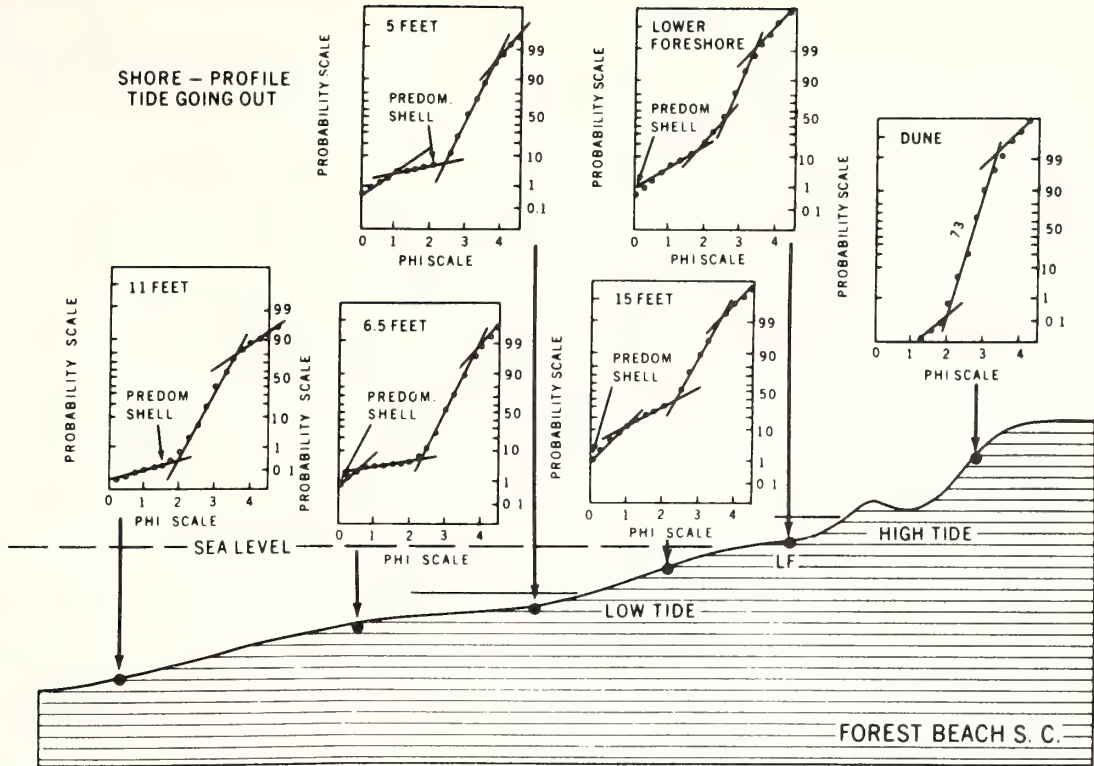


FIGURE 11. Representative size frequency distributions of the shoreface. From Visser (1969).

bution. A large C population is characteristic of Moss' rheologic regime; the B population, however, is less than 1%. While the hydraulic microclimate of rheologic flow is conducive to the incorporation of a large B population into the bed, such a response is presumably inhibited by the gross hydraulic structure of the surf zone; suspended fines are steadily flushed seaward through rip channels. Two framework (A) populations are locally present, reflecting perhaps discrete responses to swash and the slightly higher backwash velocities. Subtidal surf zone populations (5 and 6.5 ft) are similar, but the framework population is better sorted (corresponding segment of the cumulative curve is steeper). This sorting is further improved in the upper foreshore sample (11 ft sample). This sample has a reduced contact (C) population and an enriched interstitial (B) population. B population enrichment reflects the heavy rip current fallout of fine suspended sand experienced at this depth, and perhaps also the presence of Moss's fine ripple regime.

**BED FORMS OF THE SHOREFACE.** Clifton et al. (1971) have noted that the high-energy shoreface of southern Oregon is characterized by zones of primary structures that reflect the hydrodynamic subenvironment (Fig. 12). An "inner planar facies" occurs beneath the reversing supercritical flows of the swash zone; the associated

structure within the deposit consists of thin beds and laminae of gently inclined sand. The rhomboid ripple marks and antidunes that form in each backwash are rarely preserved.

Beneath the surf zone of gently sloping beaches lies an "inner rough facies" of shore-parallel ridges and troughs 1 to 2 m across and 10 to 50 cm deep. The flat-topped ridges tend to be steepest on the seaward side, and the ridges migrate seaward. During periods of strong littoral currents, troughs are more nearly perpendicular to land, and migrate downcurrent and offshore. The internal structure of this facies consists of medium-scale (units 4–100 cm thick) seaward-dipping trough cross-bedding.

Beneath the breakpoint lies an "outer planar facies." No bar existed here during the period of Clifton's study. Small ripples may form during the initiation of trough or crest surge, but the flow becomes supercritical during maximum surge, and the ripples are destroyed. The internal structure is horizontal lamination.

Clifton et al. describe the upper shoreface of the Oregon coast as the "outer rough facies." The characteristic bed forms are lunate megaripples, 30 to 100 cm high, and with spans (terminology of Allen, 1968a, pp. 60–62) between 1 and 4 m. Concave slopes face landward, and the ripples migrate landward at rates of 30 cm/hr.

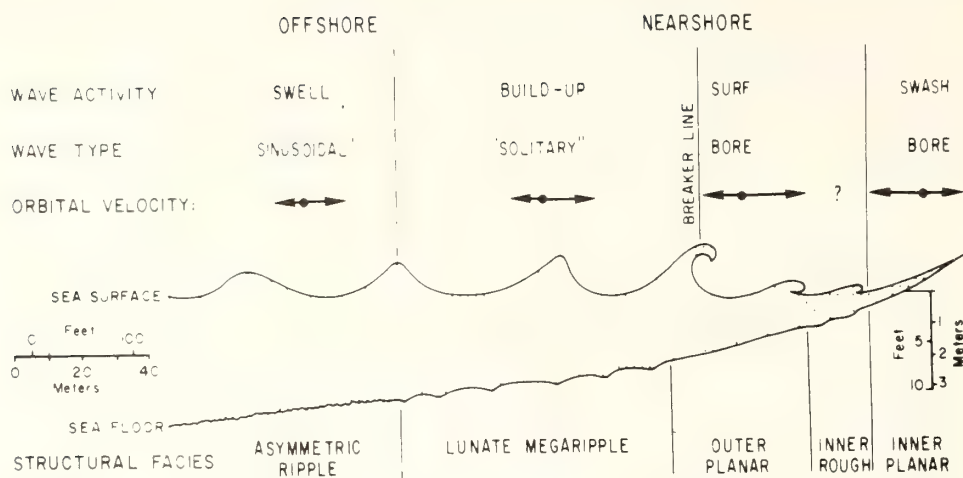


FIGURE 12. Relationship of depositional structures to wave type and activity. From Clifton et al. (1971).

Crestal sands are notably coarser than trough sands. The resulting internal structure is a medium-scale cross-stratification with foresets dipping steeply landward.

The lower portion of the upper shoreface of the Oregon coast has an "asymmetrical ripple facies" of short-crested wave ripples 3 to 5 cm high with chord lengths (Allen, 1968a, pp. 60–62) of 10 to 20 cm. They may reverse asymmetry with each passing crest and trough, or reveal a persistent landward asymmetry. Crests become lower, longer, and straighter as the pattern is traced seaward. Interfering sets are common, weaker sets tending to occur as ladderlike rungs in the troughs of the stronger set. The angle between the two sets is bisected by the wave surge direction. The internal structure of this facies tends to consist of small-scale (less than 4 cm) shoreward-inclined ripple cross-lamination, interfingering with gently dipping, medium-scale scour and fill units.

A similar sequence of bed forms and textural provinces has been reported from the Georgia coast by Howard and Reineck (1972). The Georgia coast has a milder wave climate than those described above, although it is also characterized by strong tidal flows. The equilibrium configuration of the shoreface is rather different here (Fig. 13): the slope is much gentler, and the break between the fine sand of the upper shoreface and the coarse sand of the lower shoreface occurs as far seaward as 14 km from the beach.

An inner planar zone of laminated sand is equivalent to that of Clifton et al.'s (1971) but is markedly wider, extending from 0 to -1 m, 200 m from the beach. An inner rough facies (1–2 m depth) is equivalent to that of Clifton et al.'s, but is expressed as rippled, laminated sand, rather than megaripples. An outer planar facies (5–10 m depth) consists of laminae and thin beds with sharp, erosional lower contacts, grading upward into

bioturbate texture. Howard and Reineck (1972) suggest deposition during storm intervals, alternating with periods of fair weather and bioturbation. An upper shoreface facies of fully bioturbated, muddy fine sand has no parallel in Clifton's study of the high-energy Oregon coast, and is a consequence of the high input of fine sand and reduced wave energy.

Seaward of 10 m, the muddy, gently sloping shoreface becomes markedly coarser, then gives way to a flatter seafloor of medium to coarse sand, characterized by heart urchin bioturbation and trough cross-stratification. Clifton and co-workers did not extend their study sufficiently far seaward to detect such a coarse lower shoreface and seafloor facies. However, an equivalent facies does appear on retreating coasts of both North Carolina and Holland (Fig. 8).

Reineck and Singh (1971) have described shoreface and inner shelf deposits from the low wave energy, high mud input, prograding coast of the Gulf of Gaeta, Italy. The inner facies are rather similar to those of the Georgia coast. Ripple bedding is the main sedimentary structure out to 2 m. Below 2 m, laminated bedding becomes the main structure, and bioturbation becomes prominent, increasing seaward. Laminae are inferred to be deposited from graded suspensions after storms. At 6 m, sand gives way to silty mud, heavily bioturbated by *Echnocardium cordatum*. There is no equivalent of the coarse offshore facies of retreating coasts.

## LONGSHORE SEDIMENT TRANSPORT

The seasonal cycle of onshore and offshore sand migration in the surf is superimposed on a much more intensive flux of sand parallel to the beach, under the impetus of the wave-driven littoral current. The mechanisms driving

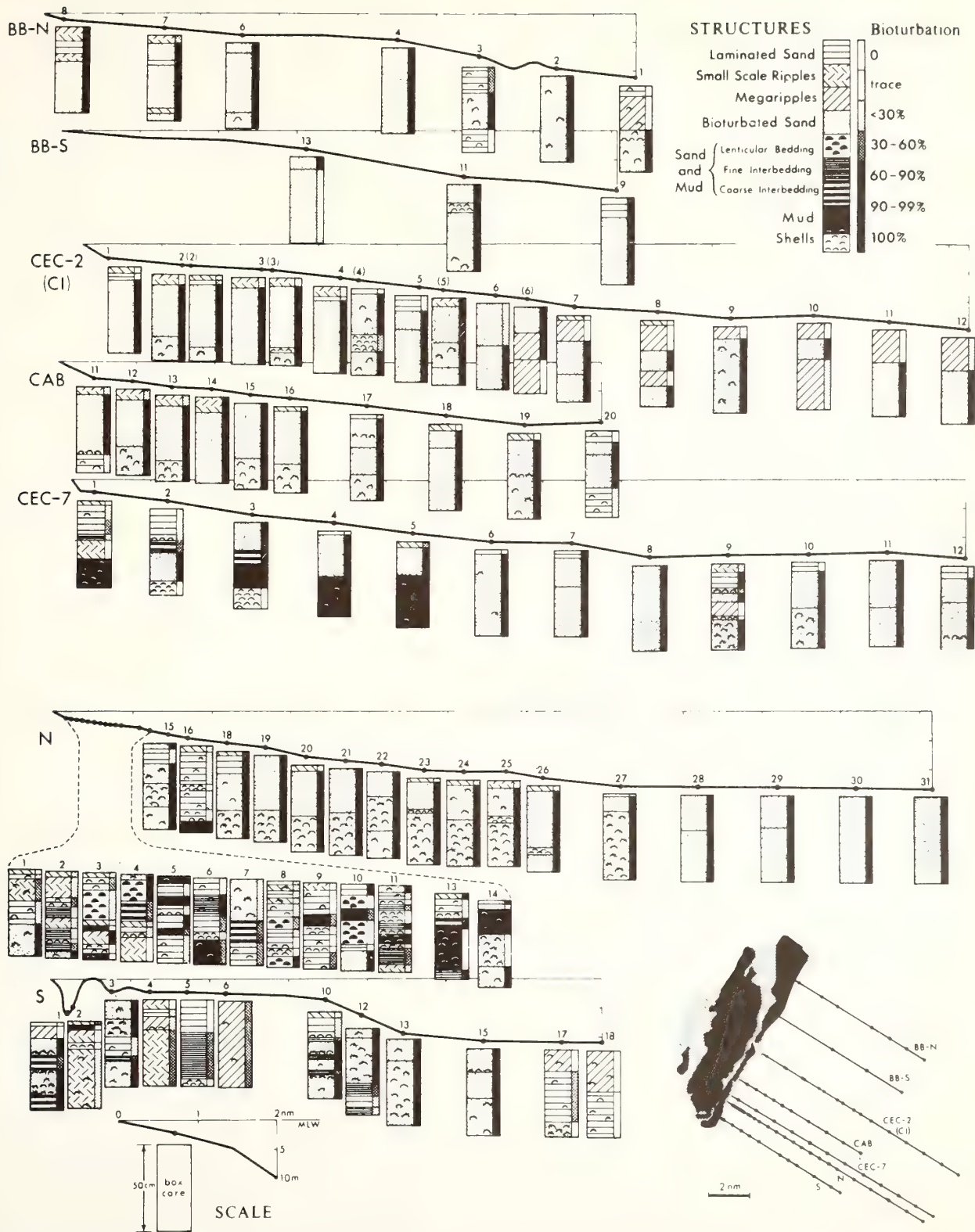


FIGURE 13. Primary structures of the Georgia shoreface, as revealed by box cores. Complexity of lines N and S are due to

their traversing the north flank of an estuary mouth shoal. From Howard and Reineck (1972).

this littoral drift and equations for determining its transport rate are described in Chapter 13.

The propensity of this coastwise sand flux to aggrade or erode the shoreline can be understood by reference to a convenient graphical model presented by May and Tanner (1973). As a consequence of refraction of waves about a coastal headland, such a headland will tend to concentrate the wave rays on it and hence wave energy (see p. 76). As a consequence, the wave energy density (proportional to the spacing of wave rays) decreases steadily from point *a* on the headland to point *e* in the bay. These relationships are shown in highly schematic fashion in Fig. 14.

The longshore component of wave power  $P_L$  is a function of both the wave energy density and the breaker angle (see Equation 2, Chapter 13). It must therefore pass through a maximum between the point of greatest wave energy density *a*, and the point of greatest breaker

angle at *c*. The maximum is attained, however, closer to point *c*, as the gradient of wave energy density on this subdued model coast is relatively flat.

Both the sand transport rate  $I_L$  (see p. 247) and the discharge of sand ( $q$ ) are proportional to  $P_L$  and vary with it. Therefore, the longshore discharge gradient  $\partial q/\partial x$  varies as the derivative of  $P_L$  (Fig. 14). The sediment continuity equation (p. 190) states that the time rate of change of seafloor elevation along a streamline in the littoral current is proportional to the littoral discharge gradient under conditions of steady flow. In other words, if more sand is moving into a given section of shoreface than is moving out (negative  $\partial q/\partial x$ ), then the seafloor of that section must aggrade. If, on the other hand, more sand is being exported than imported (positive  $\partial q/\partial x$ ), the seafloor of that sector must erode (see the discussion on p. 190). In general, erosion occurs along a positive discharge gradient, and deposition occurs along a negative discharge gradient.

In the model of Fig. 14, this relationship means that the shoulder of the headland, from *a* to *c*, should erode, with the material being transported into the bay, to fill sections *c* through *e*. The same sort of process should occur on the other side of the bay (not shown) and the other side of the headland (not shown). If the direction of wave approach were held constant and normal to the regional trend of the coast, then a very peculiar coastline should eventually result. It would straighten out to a nearly east-west line running through *c*, but with a needlelike projection at *a*, the point of littoral drift divergence, and a similarly narrow indentation at *e*, the point of littoral drift convergence. On real coasts, however, the direction of wave approach is not constant, but fluctuates about the mean value, with changes occurring on a scale of hours to days. As the direction of wave approach fluctuates, so do the positions of points *a* and *e*, and the development of coastal reentrants and projections is suppressed.

If waves tend to approach at an angle instead of approaching normal to shore, and if coastal relief is more deeply embayed (Fig. 15), then a rather different distribution of longshore wave power will result. The locus of maximum deposition will be shifted from the bay head toward the tip of the adjacent headland where the gradients of wave energy density and breaker angle are the steepest. During a storm when the intensity of littoral drift discharge is the greatest, deposition at this point may be so intense that a discontinuity in the shoreface may occur, in the form of a spit that builds out across the bay as an extension of the headland shoreface. As the shoreline matures, headland retreat, spit extension, and bay head beach progradation occur simultaneously and in this model also, the final coastline is again straight.

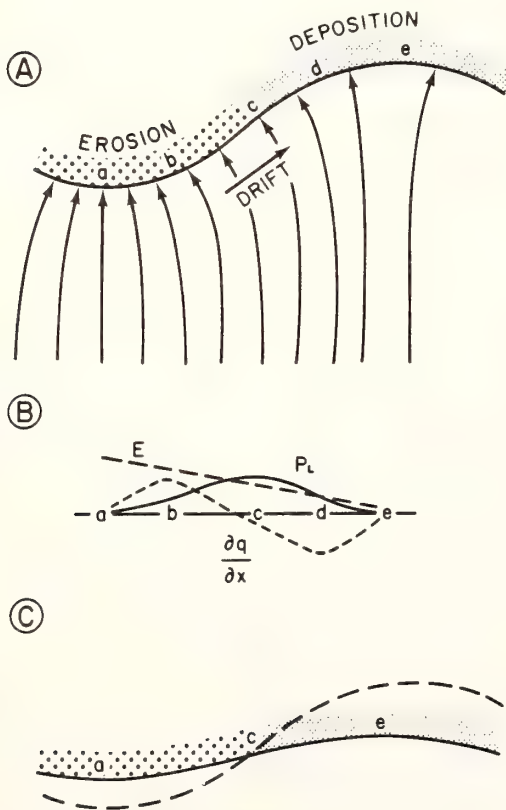


FIGURE 14. Model for littoral sediment transport. (A) Wave refraction pattern, with wave approach normal to coast. (B) Resulting curves for energy density at the breaker  $E$  (dimensions  $MT^{-2}$ ); longshore component of littoral wave power  $P_L$  (dimensions  $MLT^{-3}$ ); and the littoral discharge gradient  $\partial q/\partial x$  (dimensions  $L^2T^{-1}$ ). (C) Advanced state of coastal evolution. After May and Tanner (1973).



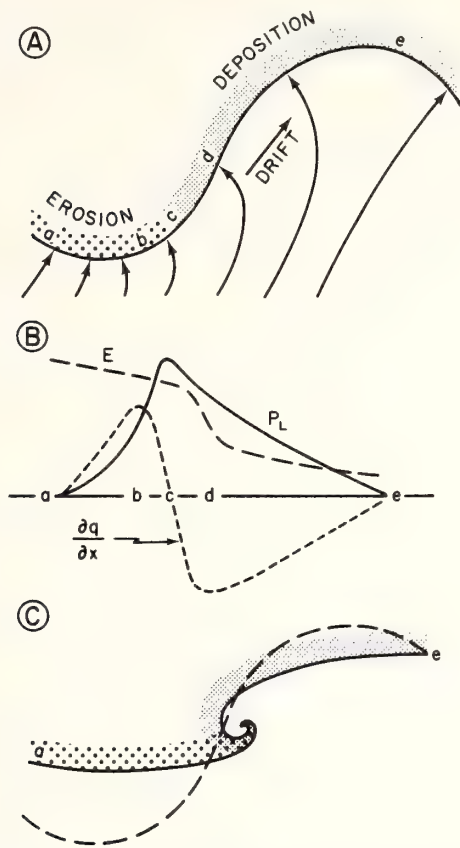


FIGURE 15. Variant of the littoral transport model with a more deeply embayed coast and an oblique direction of wave approach. Conventions as in Fig. 14.

Thus, as a consequence of the submarine refraction of waves about the shoals off headlands, the shoreface tends toward an equilibrium plan view as well as an equilibrium profile. Headlands tend to be suppressed and bays filled, because their existence leads to longshore wave power gradients that transfer sand from headland to bay head.

A similar smoothing process operates at deeper levels on the shoreface, where sand transport occurs in response to tide- and wind-driven currents. Such flows accelerate past the projecting headlands which impede them, and expand and decelerate off the bays. The result is a positive discharge gradient on the upcurrent sides of the headlands, and a negative discharge gradient on the downcurrent side. This pattern reverses when the currents themselves reverse, so that the lower shoreface off headlands experiences net erosion, while the lower shoreface off bays experiences aggradation. Thus the equilibrium plan view of a coast tends to be straight, to the extent that variations in the homogeneity of the sub-

strate and the rate of sand supply to the surf zone will permit.

A second characteristic of equilibrium coastal configuration is the adjustment of the trend of the coast to the angle of wave approach as mediated by the rates and locations that sand is put into and taken out of a littoral drift cell. A perfectly straight and infinitely long coast could ideally maintain any angle to wave approach, if the only source of sand were its own shoreface erosion. In fact, however, such an ideal straight coast is rarely attained. Sea level is rising or has been until very recently, and the straightening process must operate continuously as successive portions of the irregular subaerial surface are inundated. Depending on the degree of induration of the coast, an effective equilibrium is attained with less than the "climax" degree of coastal straightness; some irregularity usually persists, with at least subdued headlands serving as sand sources, and embayments serving as sand sinks. Locally, river mouths may serve as point sources of sand with high sand input rates. These result in deltas and an effective coastal equilibrium at less than climax straightness.

Komar (Chapter 13, Figs. 12, 13) has provided two examples of the adjustment of coastal trend to the angle of wave approach, and to the location of sources and sinks. His river mouth (Fig. 12) injects sand at a point in the littoral drift system at a rate greater than the system can initially accommodate, and the coastline progrades. As it does so, orientation of the coast at each point adjusts so that the river mouth protrudes as a delta. Eventually, an equilibrium configuration is attained so that each point along the shoreline maintains an incident wave angle sufficient to bypass the same amount of sand at every other point.

Komar's beach (Fig. 13) has no point source of sand. He starts with a straight beach and a landward-convex waveform, a form that might arise from offshore refraction over the rocky headlands enclosing a pocket beach. The center of the beach becomes a source and the ends become sinks; the shoreface adjusts to the wave refraction profile.

Komar's two examples correspond to two basic categories of coastlines. In the *swash alignment* (Davies, 1973, p. 123), each point on the coast tends to be oriented normal to the direction of wave approach, either as an initial condition or because the configuration of the shoreface and the wave refraction pattern have interacted until this is the case. Such an adjustment is only possible if there is a projecting headland in the down-drift direction as in the case of Komar's beach, or another reason to cause a sand sink and allow coastal progradation. *Drift alignments* (Davies, 1973, p. 123) are more nearly like Komar's delta model. These coasts are

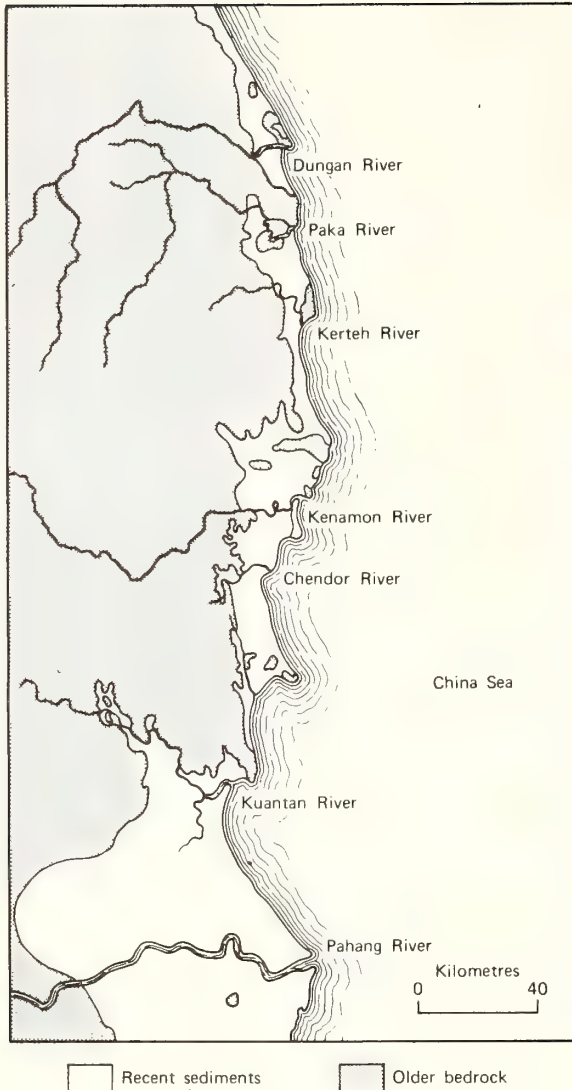


FIGURE 16. Zetaform bays on the offset coast of eastern Malaya. Major wave approach direction is from the northeast. From Davies (1973).

stabilized by competition between two opposing trends for control of the littoral transport system. As a coastal compartment becomes more nearly normal to wave orthogonals, littoral energy density increases; however, the longshore component of wave energy decreases. Maximum discharge tends to occur when the orthogonals of prevailing wave trains make an angle of 40 to 50° with the coast. A coast captured in this alignment will tend to be stable, as it is the alignment of maximum transport.

Coasts with closely spaced barriers to littoral drift, in the form of river mouths or projecting headlands, may form offset coasts consisting of successive zetaform bays (Halligan, 1906). These fishhook beaches have a curved

swash-aligned beach in the shadow zone immediately downdrift from the barrier, and a straight drift-aligned beach extending downdrift from the swash segment to the next headland (Fig. 16). If the variance of the direction of wave approach is high, then the shadow zone behind the barrier will be exposed to the direct approach of waves for a significant part of the time and will intermittently operate as a drift-aligned beach of reverse drift. The apex of the barrier will become a zone of net drift convergence, and hence a self-sustaining constructional feature.

The dynamics of zetaform bays have been discussed in detail, with summaries of earlier observations, by Silvester (1974, pp. 71-90).

### TRANSLATION OF THE SHOREFACE

The preceding evaluation of the alongshore and onshore-offshore components of sediment transport permits us to take a more general look at the coastal sediment budget and its effect on the shoreface stability.

It is clear from the preceding discussion that the shoreface profile will translate either landward or seaward (the coast will retreat or prograde) depending on whether the effects of the fair-weather regime, which tends to aggrade the shoreface, or the storm (or tidal) regime, which tends to erode it, are dominant. The sense of coastal profile translation further depends on coastwise gradient of sand discharge (whether sand imports and exports for the sector under consideration sum to a surplus or deficit). As a consequence of the onshore-offshore cycle of sand exchange, the nature of coastal translation will finally depend on which shoreface province, if any, is actually subjected to a sand surplus. The coastal transport system may be visualized as two coast-parallel pipes, corresponding to the wave-driven littoral drift near the beach and the intermittent storm- or tide-driven sand flux that occurs on the shoreface and inner shelf seaward of the breaker. These two pipes are connected by valves, corresponding to the onshore-offshore cycle of sand exchange. The factors listed above determine what valves are open, for how long, and the net sense of flow through the valves. We do not have the measurements of onshore-offshore sand transport that would allow us to document the manner in which this system actually works. Until we do, we must be satisfied with an exploration of possible limiting cases, by means of deductive reasoning (Fig. 17).

Four basic cases may be distinguished. On modern coasts, undergoing relatively rapid sea-level rise, the gradient of littoral drift discharge ( $\partial q/\partial x$ ) is either positive or is so slightly negative that the resulting sand surplus is not sufficient to balance offshore transport

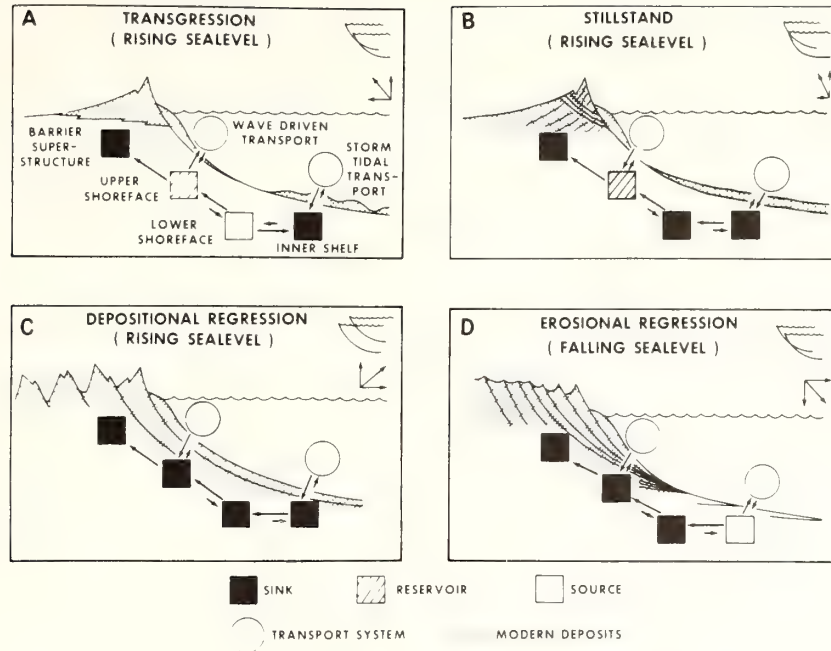


FIGURE 17. Schematic models for the shore face sand budget. (A) Retrograding coastal sector with rising sea level and balance or deficit in coastwise sand flux. (B) Near-stillstand coastal sector with effect of rising sea level compensated by sand surplus associated with coastwise sand flux. (C) Prograding coastal sector with effect of rising sea level and reversed by sand surplus associated with coastwise sand flux. (D) Prograding coastal sector with falling sea level and balance in or sand deficit resulting from coastwise sand throughput.

during storms. Under these conditions Bruun coastal retreat must prevail (Fig. 17A). Storm erosion must predominate over fair-weather aggradation on the shoreface as it translates landward and upward in response to sea-level rise. During fair weather, sand may be temporarily stored on the upper shoreface and beach (see Fig. 4A). The barrier superstructure becomes a long-term reservoir, receiving sand from the eroding shoreface by storm washover, storing it, and finally releasing it to the eroding shoreface. The inner shelf floor tends to become a sand sink, retaining the coarser sand transmitted to it by seaward bottom flow during storms, and releasing the finer fraction to the coastwise shelf flows. The coast of northern New Jersey appears to be undergoing such a retreat (Stahl et al., 1974).

Locally, however, the sand discharge gradient associated with the deeper storm-driven shelf flows may be steeply negative (Fig. 17B), resulting in a sand surplus. The surplus tends to be absorbed by inner shelf and lower shoreface aggradation and also by storm washover on the barrier. The upper shoreface, however, is relatively unaffected. The trajectory of the shoreface profile appears to be nearly parallel to the upper shoreface slope, resulting in stillstand of the shoreline. The

barrier system of coastal North Carolina immediately north of Cape Hatteras appears to be undergoing such a depositional stillstand, resulting in the opening of an anomalously wide lagoon behind it as sea level continues to rise (Swift, 1975).

If the littoral drift transport system has a strongly negative discharge gradient, as is the case downdrift from river mouths with a high sand discharge, the saturation of the upper shoreface with sand causes the flooding of all other inner shelf provinces as well, and the shoreface progrades by the successive capture of upper shoreface bars as beach ridges (Figs. 10B and 17C). The analysis of the Holocene history of the Costa de Nayarit by Curray et al. (1969) provides an excellent case history of such a coast.

Finally, we must consider the case of falling sea level. If, under such conditions, the net littoral drift input is negligible, not all portions of the shoreface will prograde. The shoreface must translate seaward down the gradient of the shelf in a reversal of the Bruun process. Under these conditions, successive beach-upper shoreface sand prisms undergo subaerial capture, and the lower shoreface and inner shelf undergo erosion as sea level drops (Fig. 17D). However, should the sand surplus due to

littoral throughput increase, the sand budget must approach that of the subsiding prograding coast and a more rapid shoreline regression must result. Modern examples of such falling sea-level budgets are confined to regions of glacial rebound or tectonic uplift, but the surfaces of the world's coastal plains were molded by it during the withdrawal of the Sangamon (Riss-Würm) Sea (Oaks and Coch, 1963; Colquhoun, 1969).

A word on the factors controlling the steepness and curvature of the shoreface profile is in order at this point. Grain size is the most obvious control (Bascom, 1951); the coarser the sediment supplied to the coast, the steeper are the shoreface profiles. Shorefaces built of shingle may attain 30° slopes near the beach; shorefaces of sand are rarely more than 10° at their steepest, while shorefaces on muddy coasts are so flat as to be virtually indistinguishable from the inner shelf. Sediment input and the wave climate also affect the shape of the profile. In general, inner shelves experiencing a higher influx of sediment and a lower wave energy flux per unit area of the bottom are flatter, whereas inner shelves with a lower influx of sediment and a higher wave energy flux per unit area of the bottom are steeper (Wright and Coleman, 1972). Because of the complex interdependence of the process variables, cause and effect are difficult to ascertain; on a steeper shelf, for instance, grain size is coarser because the steeper slope results in more energy being released per unit area of the bottom; more energy is released because the coarser grain size results in a higher effective angle of repose. Or a reduced input of sand will allow the profile to attain the maximum steepness permissible under the prevailing wave climate, with a resultant higher rate of energy expenditure on the shoreface, and a consequent coarsening of its surface (Langford-Smith and Thom, 1969).

The relationship between the rate of sea-level displacement and the shape of the profile requires some thought. A number of workers have assumed that rapidly translating coasts are in a state of disequilibrium, and that equilibrium can only be realized on very slowly translating or stillstand coasts. This view results from an inadequate appreciation of the equilibrium concept and is tantamount to stating that only chemical reactions that have gone to completion are equilibrium reactions.

It is important to clearly distinguish between the concept of coastal maturity on one hand, and the concept of coastal equilibrium on the other. Davis (in Johnson, 1919) has assembled a spectrum of coastal types that suggest that the coastal profile passes through stages of "youth, maturity, and old age" in which the profile becomes increasingly flatter, until a final profile of static equilibrium is reached—ultimate wave base, in which

the continental platform has been shaved off to a level below which further marine erosion occurs so slowly as to be negligible. The scheme is unrealistic in that it fails to recognize the continuous nature and mutual dependence of the process variables of an equilibrium system. Some of these stages will occur as transient states after the sudden rejuvenation of a tectonic coast. But as the profile becomes increasingly mature, its rate of change decreases, until it attains the equilibrium configuration required by existing rates of such other process variables as sediment input and eustatic sea-level change. At this point the profile must continue to translate according to the Bruun (1962) model of parallel shoreface retreat, until the rate of one or another variable changes again. This equilibrium, of course, is only apparent if the coastal profile is examined over a sufficiently long period of time—on the order of decades. Shorter periods of observation will resolve the apparent "equilibrium" into a series of partial adjustments to periods of fair weather and periods of storms.

Only in cases of relatively rapid tectonism may hysteresis, or lagged response, occur, and strictly speaking, the term "disequilibrium" should be applied only to such cases. Slower changes in a process variable will allow continuous and compensating adjustment of profile, and while its shape changes, the profile is at all times in equilibrium. Coastal disequilibrium tends to be more apparent on rocky coasts, because of the greater response time of the indurated substrate, and because such coasts are more likely to be subject to tectonism.

Consequently, the effect of the rate of sea-level displacement in the equilibrium profile must depend on the initial slope of the substrate. On low coasts, where the initial slope is flatter than the maximum potential slope of the equilibrium profile, then the more rapid the sea-level displacement, the flatter is the resulting equilibrium profile (e.g., see Van Straaten, 1965). This relationship may be viewed as a function of work done on a substrate to build the optimum shoreface. As a coast advances more rapidly, successive shorelines experience the erosive effect of shoaling waves for shorter periods of time and the resulting profile is flat (immature). If, however, a coast undergoes stillstand, the climax or fully mature configuration can develop, which is the steepest profile possible for the available grain size of sand, rate of sediment influx, and hydraulic climate.

On high, rocky coasts, however, the initial slope of the substrate may be steeper than the mean, or even the maximum slope of the steepest profile permitted by these variables. Under such circumstances, the more rapidly transiting shorelines, since these have the least work done on them, have the least modified and hence steepest (most immature) profiles, while the most slowly moving

shorelines are the most modified and hence flattest profiles.

As noted above, existing measurements of the coastal hydraulic climate and resulting sand transport are generally inadequate to define the coastal sand budget. It is possible, however, to extend the inferential models presented in Fig. 17 so as to take into account the effect of these variables on shoreface slope and curvature (Fig. 18).

COASTAL ENVIRONMENTS

The preceding sections of this chapter have described the onshore-offshore component of sediment transport, and also the flow of sediment parallel to the coast. Modes of shoreface displacement in response to rising and falling sea level have been considered. These insights are prerequisites to an examination of specific patterns of coastal sedimentation. But before we proceed to such an

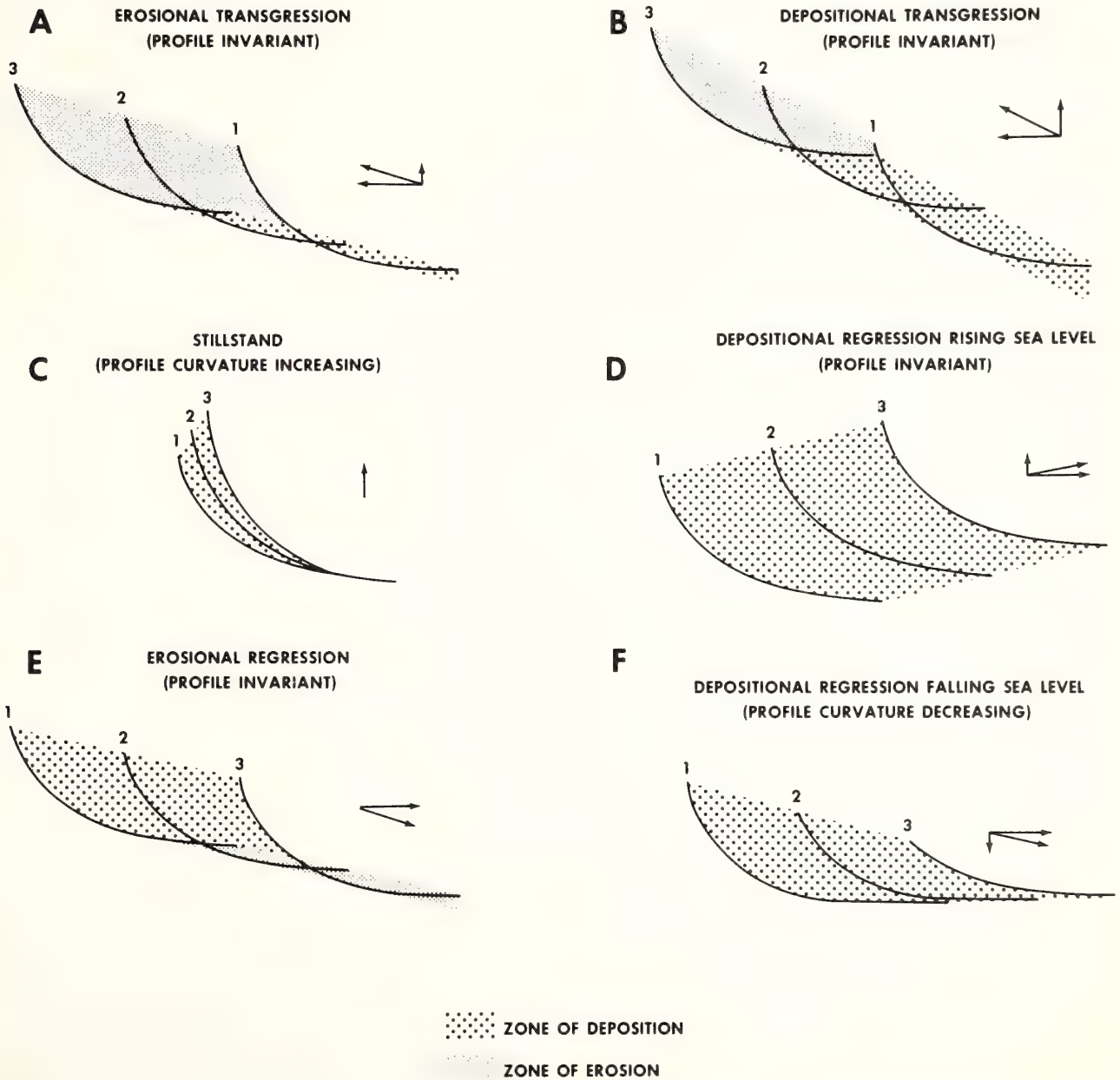


FIGURE 18. Modes of shoreface translation as a function of curvature. Envelopes of erosion and aggradation are shown. (1) direction of profile translation and (2) change in profile curvature. Terms from Curray (1964).

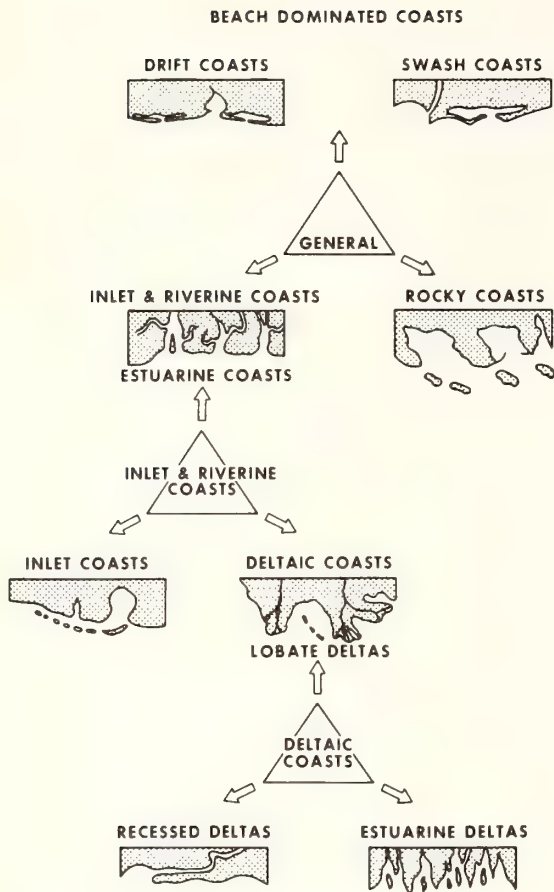


FIGURE 19. Descriptive taxonomy of coasts.

analysis, we should consider a scheme for classifying the coastal settings in which the transport patterns occur.

A study of maps of the world's coastlines suggests that the apparently unlimited variety of coastal configurations falls into a relatively small number of repeating patterns. Considerable thought has gone into coastal classification, and the reader is referred to the excellent summary of existing classifications presented by C. A. M. King (1972; also Chapter 15). The operational classification that is used in this text is presented in Table 2 and Fig. 19.

The most basic practicable division appears to be into coasts with substrates of crystalline or lithified sedimentary rock versus coasts bordering coastal plains, with substrates of unlithified sediment. Both lithified and unlithified coasts may adjust their configurations in response to the coastal wave climates but they do so at different rates, and in response to somewhat different mechanisms. Patterns of sedimentation may be relatively simple on straight rocky coasts, but coasts of structured rock may be so deeply embayed as to greatly complicate the pattern (crenulate rocky coasts).

Unconsolidated coasts are floored by easily eroded and flat-lying strata, and the surficial sediment tends to be both abundant in quantity and continuous in extent. On such coasts, wave-driven currents in the littoral zone and wind- or tide-driven currents farther offshore tend to build straight coastal segments of the sediment available to them. A basic second-order division in the morphology of unconsolidated coasts depends on the relative importance of straight coastal segments versus inlets that alternate with them.

TABLE 2. A Coastal Taxonomy

Criterion	Coastal Type
Substrate indurated	Rocky coasts
Coast-parallel anisotropy	Straight rocky coasts
Coast-transverse anisotropy	Crenulate rocky coasts
Substrate unconsolidated	Unconsolidated coasts
Littoral drift dominant	Beach and barrier coasts
Low drift angle	Drift coasts (straight)
High drift angle	Swash coasts (cusped)
Transverse drainage dominant	Inlet and riverine coasts
Fluvial drainage dominant	Deltaic coasts
Mild wave climate	Lobate deltas
Moderate wave climate	Arcuate deltas
Moderate-strong wave climate	Cusped deltas
Strong wave climate	Recessed deltas
Tide modified	Estuarine deltas
Tidal drainage dominant	Estuarine coasts
Wave-modified tidal drainage	Inlet coasts

Inlets occur at river mouths, where they may be maintained by river and tidal flow or by purely tidal flow, where there is a tidal exchange between lagoons and the sea. A dense subaerial drainage net or a high tide range may cause inlets with their coast-normal flow to occupy over 50% of the shoreline, resulting in deltaic, estuarine, or tidal inlet coasts. Open coasts with rigorous wave climates and frequent strong wind-driven currents tend to have fewer inlets than coasts not so affected, resulting in mainland beach-barrier beach coasts.

This chapter has so far dealt mainly with the sedimentary regime of such simple, two-dimensional coasts. The succeeding sections examine in greater detail the modes of sand storage on beach-barrier island coasts, and also the modes of sediment storage on more complex coasts. The following chapter on shelf sedimentation stresses the role of varying coastal configurations in bypassing sediment to the continental shelf, and thus modulating the shelf sedimentary regime.

## SAND STORAGE IN THE SHOREFACE

### Storage in Low Retreating Shorefaces: Barrier Spits and Islands

**BARRIER FORMATION.** On most retreating coasts, the most important form of sand storage is within the shoreface itself, in the form of barrier spits and barrier islands. It would seem that along many coastal sectors, the coastal sedimentary regime rejects the primary shoreline formed by the intersection of the subaerial continental surface with the sea surface, and instead builds a secondary "barrier" shoreline seaward of the primary one. A characteristic of the equilibrium shoreface surface that as much as any mechanism is the basic "cause" of barrier islands and spits is its innate tendency toward two-dimensionality, its tendency to be defined by a series of nearly identical profiles in the downdrift direction. The equilibrium shoreface does not "want" a lateral boundary, since the wave and current field to which it responds does not generally have one. The initial conditions during a period of coastal sedimentation may, however, include such discontinuities, as in the case of a coast of appreciable relief (bay-headland coast) beginning transgression.

On such a coast shoreface surfaces will tend to be incised into the seaward margins of headlands exposed to oceanic waves, and will propagate by constructional means in the downdrift direction as long as material is available with which to build, and a foundation is available to build on. The basic mechanism is that described by May and Tanner (1973); see Fig. 14. Where the

shoreline curves landward into a bay, the longshore component of littoral wave power decreases, and the alongshore gradient of sediment discharge ( $\partial q/\partial x$ ) is negative. The shoreface at that point must aggrade until the gradient approaches zero at that point, and the zone of negative gradient has moved downdrift. We give the lateral propagation of the shoreface into coastal voids the descriptive term "spit building by coastwise progradation" (Gilbert, 1890; Fisher, 1968).

However, the tendency of the shoreface to maintain lateral continuity also acts to prevent discontinuities as well as to seal them off after they have formed. In order to illustrate this, we may consider another set of initial conditions—a low coastal plain with wide, shallow valleys after a prolonged stillstand during which processes of coastal straightening by headland truncation and spit building have gone to completion. As this coastline submerges, the water, seeking its own level, will invade valleys more rapidly than headlands can be cut back. The oceanic shoreline, however, cannot follow, for if it should start to bulge into the flooding stream valleys, the bulge would become a zone of negative discharge gradient; hence the rate of sedimentation would increase to compensate for any incipient bulge. The shoreface would translate more nearly vertically than landward at this sector, until continuity along the coast was restored (Fig. 17E). Thus a straight or nearly straight oceanic shoreline must detach from an irregular inner shoreline, and be separated from it by a lagoon of varying width. This process of mainland beach detachment was first proposed by McGee (1890), and later described in detail by Hoyt (1967); see Fig. 20.

**COASTWISE SPIT PROGRADATION VERSUS MAINLAND BEACH DETACHMENT.** Much of the debate concerning origin of barriers deals with the relative importance of spit building versus mainland beach detachment (Fisher, 1968; Hoyt, 1967, 1970; Otvos, 1970a,b); see Chapter 12 (p. 223). The problem can be fully answered only by careful study of the field evidence, and as noted by several authors (Otvos, 1970a,b; Pierce and Colquhoun,

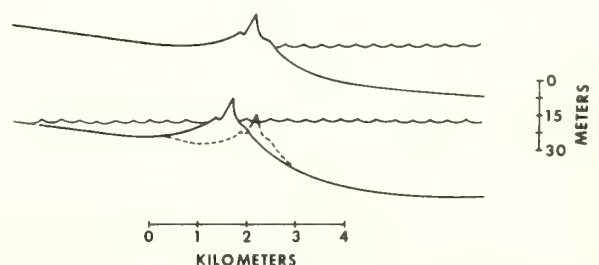


FIGURE 20. Barrier island formation by mainland beach detachment. Modified from Hoyt (1967).

1970) the evidence has frequently been destroyed by landward migration of the barriers. However, it is possible, in the time-honored deductive fashion of coastal morphologists, to consider the conditions most favorable to these two modes of barrier formation. Spits are certainly characteristic of coasts of high relief undergoing rapid transgression as described above [see the papers in Schwartz (1973)]. It seems probable that under such conditions mainly beach detachment would be severely inhibited. Even allowing for ideal initial conditions with a classic coast of old age (Fig. 21), where alluvial fans are flush with truncated headlands, detached mainland beaches would have a limited capability for survival. With significant relief, the submarine valley floors adjacent to retreating headlands must lie in increasingly deeper water after the onset of transgression. As the barrier grows into the bay, its submarine surface area must increase, and the capacity of littoral drift to nourish it may eventually be exceeded. As this point is approached, the combination of storm washover and shoreface erosion will cause the barrier to retreat until equilibrium is restored, a position which may be well inland from the tips of headlands. Both littoral wave power and sediment supply may be deficient in these inland positions, further jeopardizing the survival of

the barrier. As the loop of the barrier into the bay becomes extreme, sediment supply from headlands is liable to capture by secondary spits formed during storms. These may prograde out toward the drowned valley thalweg until capacity is again exceeded and their tips are stabilized, further movement being limited to retreat coupled with that of the headland to which they are attached.

Finally the survival of primary barriers on such a coast would be limited by the tendency of submerging headlands to form islands. A spit tied to a promontory that becomes an island can retreat no further if a drowned tributary valley lies landward of it, but must instead be overstepped. The few unequivocal examples of transgressed barriers on the shelf floor appear to be overstepped, rock-tied spits (Neveeskii, 1969; McMaster and Garrison, 1967).

On the other hand, transgression of a coast of very subdued relief, such as is the case for most coastal plains, would tend to promote mainland beach detachment at the expense of spit formation, given initial conditions of a straight coast (Fig. 22). The depth of water in which detached bay mouth barriers would be built would be less, because the relief would be less. The upper, erosional zone of the shoreface (Fig. 10A) would be more likely to extend down into the pre-Recent substrate (Fig. 23A); hence erosion of the inner shelf floor would become as important a source of sand for the barrier as the erosion of adjacent headlands. With a rise in sea level, valley-front dune lines would grow upward. River mouths, initially deltaic, would flood as estuaries, while lagoons would creep behind the beaches toward the headlands on either side. Barriers would retreat in cyclic, tank-trend fashion by means of storm washover, burial, and reemergence of the buried sand at the shoreface (Fig. 10A). Coastal discontinuities sufficient to induce coastwise spit progradation would occur only locally. Thus, on a low, initially straight coast, barrier spits and barrier islands would preferentially form by mainland beach detachment rather than by coastwise progradation.

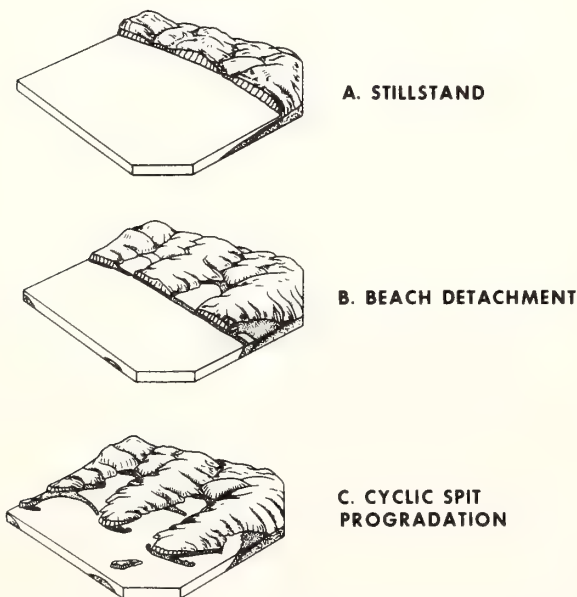


FIGURE 21. Barrier formation with spit-building dominant. As a rugged coast passes from stillstand to transgression, a mature configuration is replaced by a transient state of mainland beach detachment, then by a quasi-steady state regime of cyclic spit building. This diagram also illustrates the relationship between the concepts of coastal equilibrium and coastal climax, since it consists of Johnson's (1919) stages of coastal maturity—portrayed in reverse sequence!

### Storage in Prograding Shorefaces

The preceding discussion has identified barrier islands and spits as forms of sand storage on retreating coastlines. On prograding coastlines, sand storage occurs in beach ridges and cheniers; the two forms differ in that beach ridges are separated by sand flats, whereas cheniers are separated by, and rest on, mud deposits.

Sequences of beach ridges 15 to 200 m apart may form subaerial strand plains tens of kilometers wide. These are smaller scale features than the barriers, which



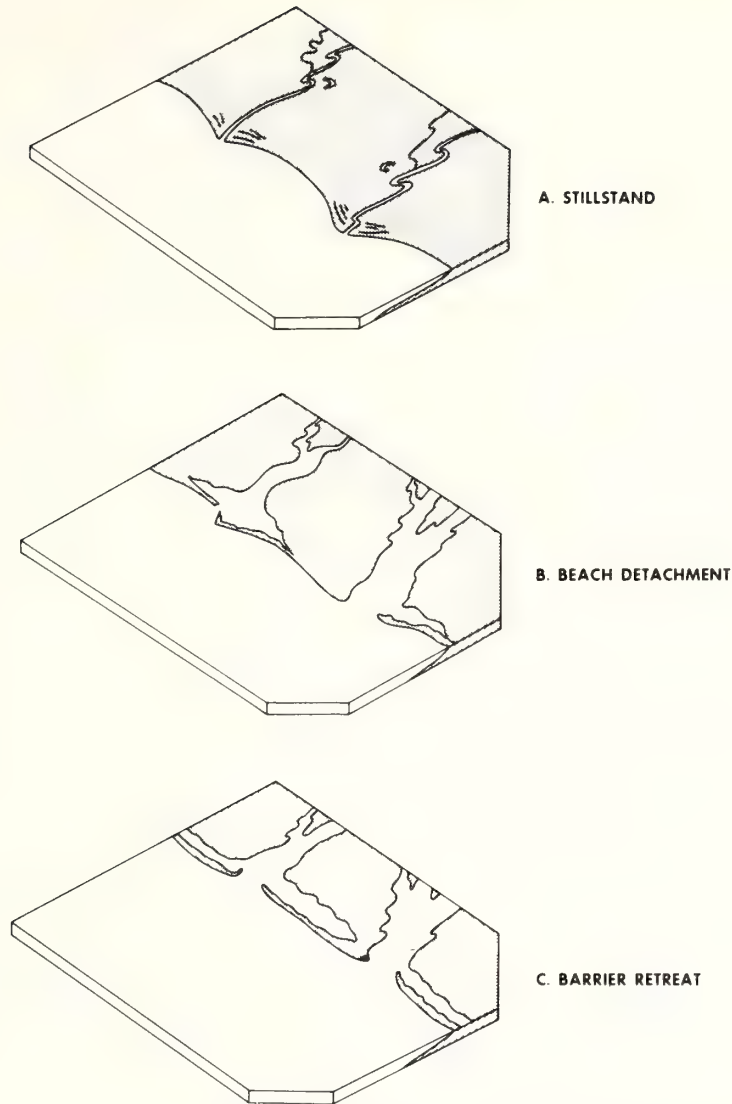


FIGURE 22. *Barrier formation with mainland beach detachment as the dominant process. A mature low coast passes via main land beach detachment into a steady state regime of barrier retreat.*

characterize retreating and stillstand coasts; and barriers may, in fact, be locally comprised of beach ridge fields, as a consequence of minor frontal progradation or more extensive distal, coast-parallel migration (Hoyt and Henry, 1967). Curray et al. (1969) have presented a detailed study of what has been recognized as a classic strand plain coast, the Costa de Nayarit (Fig. 24). They postulate that each ridge forms as a plunge point bar, which in the presence of an oversupply of littoral sand, builds up close to mean low water. During a period of constant low swells, the bar may grow above this level as tides rise to the spring tide value (0.98–1.25 m);

the bar becomes a subaerial feature during the subsequent neap phase, and continues to grow by eolian activity (Fig. 10B).

Chenier plains form on coasts with a high suspended sediment input. In the classic chenier plain of the Louisiana coast west of the Mississippi Delta, the sand ridges support stands of live oaks (French, *chêne*), hence the name (Price, 1955). The formation of chenier plains has been ascribed to rapid progradation of mud flats during periods of high suspended sediment discharge from nearby rivers or delta distributaries. When distributaries crevasse and the subdeltas are abandoned, the

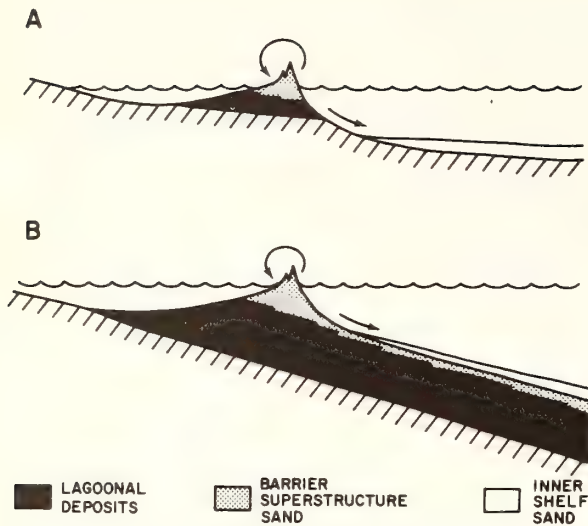


FIGURE 23. *Contrasting sand budgets of a barrier built (A) on a gentle submarine gradient as in Fig. 22, and (B) on a steep submarine gradient as in Fig. 21. In (A), zone of shoreface erosion penetrates to Pre-Recent substrate, which becomes "income" for barrier nourishment. In (B) the barrier may only "borrow" from its own "capital" through shoreface erosion, and the heavy expenditure involved in paving the shelf with sand during barrier retreat may "bankrupt" the retreating barrier, which must either accelerate its retreat or be overstepped. In either case shoreface continuity is liable to be broken, resulting in cyclic spit building.*

downdrift coast becomes sediment starved. The mud flat erodes back and a beach ridge formed of the coarse sediment is thrown up by storm high tide. Todd (1968) has stressed the role of estuary mouths and inlets in the localization of chenier plains. He notes that littoral currents updrift of the inlet tend to decelerate during ebb tide because of a reduction of the coastwise pressure gradient by the ebb jet, resulting in sediment deposition. Littoral currents in the same locality are accelerated by proximity of the inlet during flood tide, but fine sediment deposited requires a greater velocity for erosion than for deposition, and in any case has already compacted. Hence chenier plains tend to be localized on the muddy, updrift sides of tidal inlets. Downdrift of the inlet, the coast may instead be starved for fines as a result of seaward transport or "dynamic diversion" of the littoral current by the ebb jet, and the littoral sand deposits have more nearly the character of a beach ridge sequence.

Otvos (1969) recognizes the role of inlets in localizing deposition, but notes that chenier deposition goes on for long distances beyond inlets. He cites new chronologic evidence from the Mississippi chenier plains to indicate that chenier ridge formation cannot be closely correlated with the abandonment of a subdelta mouth, and suggests that the intermittent shielding effect of nearby sub-

delta growth on the wave climate plays a greater role in cyclic chenier plain growth.

Beall (1968) has examined in detail sediment distribution and stratigraphy in the present shoreface of the western Louisiana shoreline (Fig. 25). He distinguishes between three main stratigraphic patterns. *Mud flats* are defined on their seaward margins by a break point bar zone of very fine sand. Midtidal and upper tidal flats are distinguished by progressively finer sand and increasing percentages of silt and clay. A thin sand storm beach may rest on eroded marsh sediments. The stratigraphy is complex. Apparently a period of increasing littoral sediment discharge results in progressive flattening of a shoreface, until the bar zone is triggered and becomes the maximum locus of sedimentation, prograding both landward and shoreward. A (submarine) mud flat zone is thereby initiated in the sheltered longshore trough, and progrades toward the bar and landward.

*Transitional beaches* have largely erosional profiles, with thin bar, beach, and washover sands overlying the erosional surface near the high-water line. The sequence is typical of that of erosional transgression, where the thin sand cap is a transient fair-weather veneer. However, Beall interprets these transitional beaches as progradational, with rates of progradation intermediate between those of mud flats and those of "normal beaches."

*Normal beaches* consist of up to 1.7 m of seaward-fining fine sand, prograding seaward over an outer shoreface facies. Washover fans of normal beaches are thicker than those of transitional beaches. The three types of beaches described by Beall would appear to illustrate a temporal as well as a spatial sequence. Periods of rapid mud flat progradation are presumably followed by erosion, then the formation of transitional beaches, which prograde to become cheniers, then prograde more rapidly as mud flats.

## SAND STORAGE OFF CAPES

South of the Middle Atlantic Bight of North America, the generally southwest-trending coastline has been molded into a series of large-scale cusped forelands (Fig. 26). They are the response of the shoreface regime to a moderate to intense wave climate and a high variance in the direction of wave approach (Swift and Sears, 1974). Storm waves approach from the northeast, as is the case in the Middle Atlantic Bight, but the coast is also exposed to waves from more distant storms in the southeastern Atlantic. As a result, the cusped forelands have been self-maintaining features throughout the postglacial period of sea-level rise and erosional shoreface retreat. Each foreland apex is a zone of littoral drift convergence.

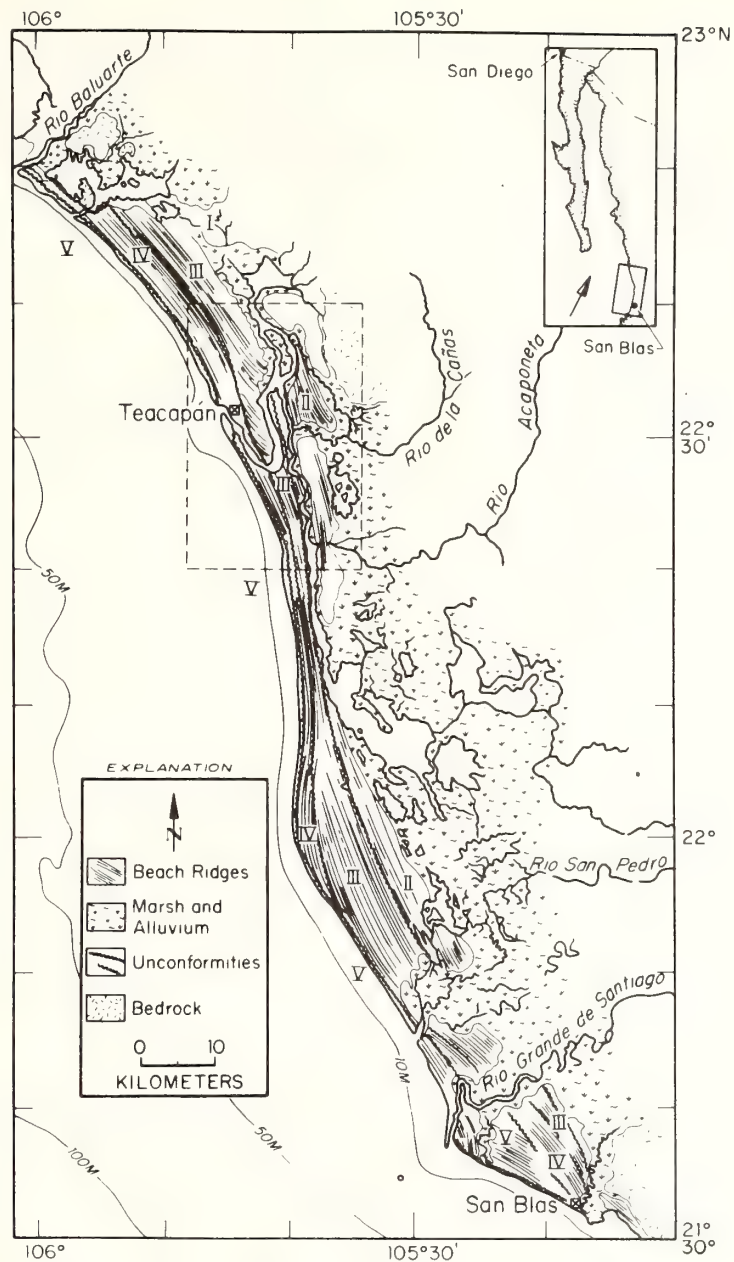


FIGURE 24. The strand plain of the Costa de Nayarit, showing beach ridge sequences. Rio de la Cañas meanders through interlocking spits, indicating reversal of drift directions. From Curray et al. (1969).

The resulting surplus of sand at the apex creates a coastal shoal. The shoal in turn maintains a pattern of wave refraction that drives littoral drift convergence (Swift and Sears, 1974); see Fig. 27.

The question arises as to how such a closely coupled feedback system begins. The answer is that in a sense, it does not matter. It is a truism that as process variables

approach the instability threshold, any singularity in a water-substrate system will excite the feedback of the process and response that lends to the formation of bed forms. In the case of the cusped Carolina coast, the initial conditions were probably the sequence of shelf-edge deltas during the Late Wisconsinan low stand, corresponding to the Peedee, Cape Fear, Neuse, and Pam-

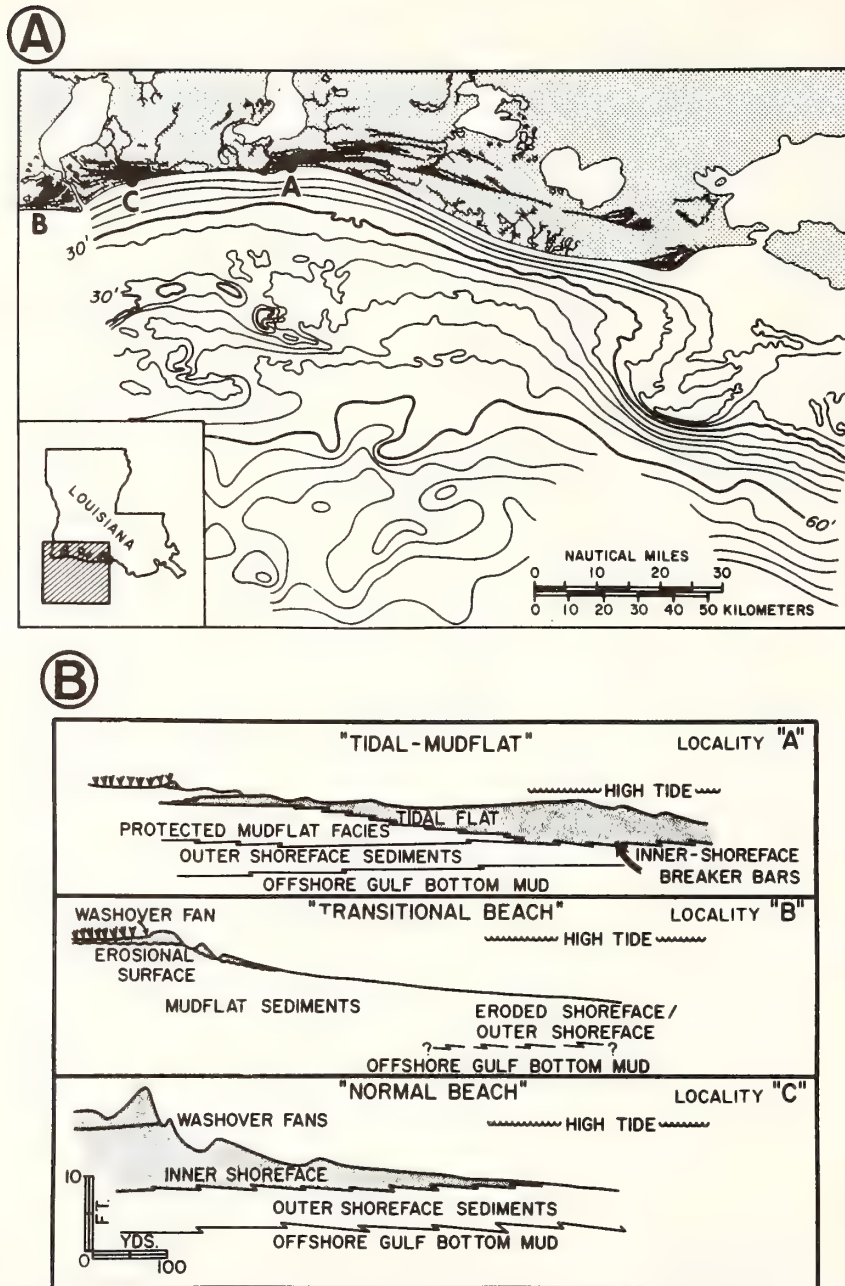


FIGURE 25. (A) *The chenier plan of southeastern Louisiana.* (B) *Characteristic beach configurations.* See text for explanation. From Beall (1968).

lico rivers (note river system of Fig. 26 and compare Fig. 27). The Appalachian cusped foreland of the Florida Panhandle is particularly suspect as having been formed by this mechanism (Swift, 1973). Other cape-associated shoals may occur as a consequence of the reduction in intensity of littoral drift around a rock-defended cape with consequent reduction in the compe-

tence of littoral drift (Tanner, 1961; Tanner et al., 1963). On offset coasts (forelands separated by zetaform bays; p. 275), the forelands may be triggered by cape extension shoals, either river mouths or rocky promontories (Davies, 1958). Forelands and cape-associated shoals also occur on swash-aligned coasts. These coasts tend to be inherently unstable, breaking into short "arcs

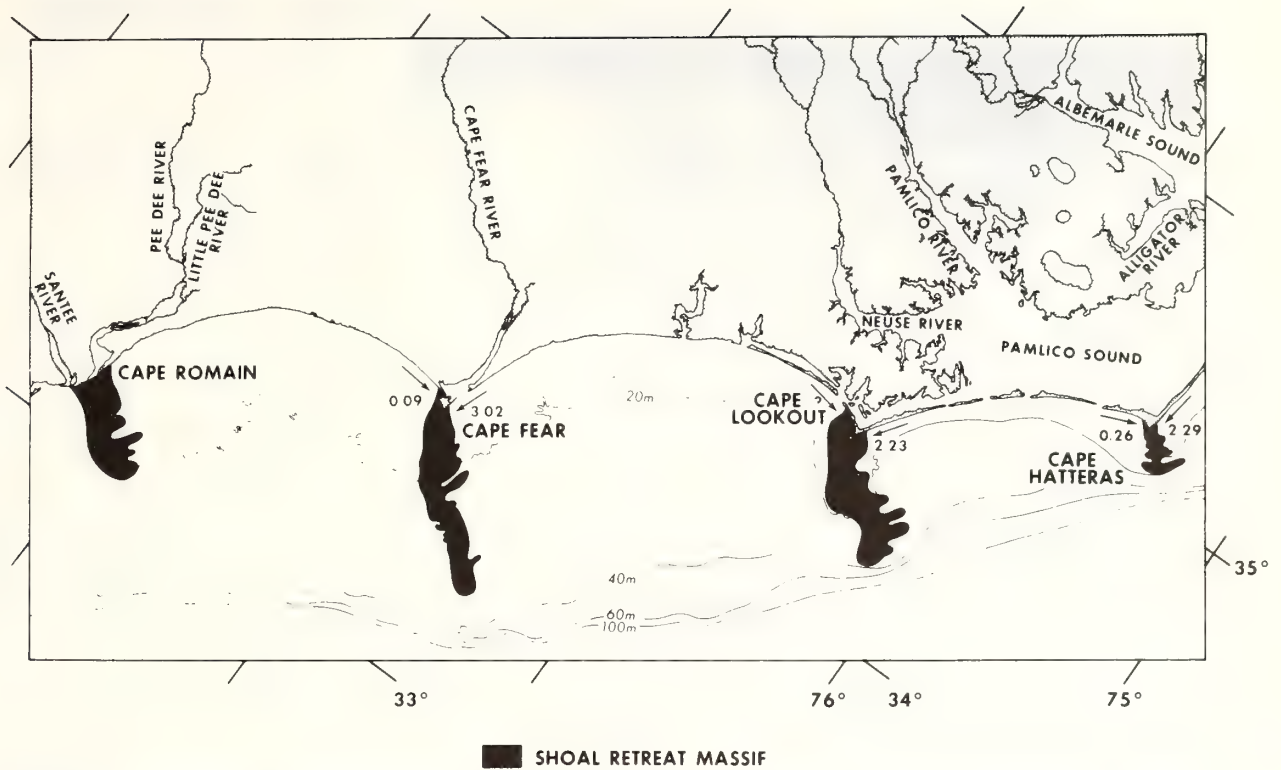


FIGURE 26. Cuspate coast of the Carolinas. Values for littoral drift are in  $\text{yd}/\text{year} \times 10^{-3}$ . From Langfelder et al. (1968).

of equilibrium," terminating in cuspate forelands with neither rivers nor outcrops required for cusp formation. Tidal inlets may evolve into cuspate forelands with associated shoals. Chincoteague Shoals, on the Delmarva coast, is an example of a barrier-overlap inlet that has become a cuspate spit with associated shoal (Fig. 36). Shoals developing over cuspate forelands may extend seaward the width of the shelf. Such cape extension shoals do not result from the seaward transport of sand, but rather from the landward translation of the cuspate foreland in response to rising postglacial sea level, together with the retreat of the associated littoral drift convergence. The seaward-trending shoal marks the retreat path of this convergence. Its response to the shelf regime is discussed in the next chapter.

## SAND STORAGE IN INNER SHELF RIDGE FIELDS

### Storm-Induced, Shoreface-Connected Ridges

A major category of inner shelf sand storage found on low retreating coasts is storage in shoreface-connected ridges (Fig. 28) and in associated inner shelf ridge fields. These features are up to 10 m high, 2 to 5 km apart, and

their crestlines may extend for tens of kilometers. Side slopes are rarely more than a degree. They typically converge with the shoreface at angles of 25 to 35° (Duane et al., 1972) and may merge with it at depths as shoal as 3 m. The best known development is on the coast of the Middle Atlantic Bight of North America, but they may be found on coastal charts as far south on the Atlantic coast as Florida, and around the Gulf coast littoral as far as Alabama. They also appear locally on the Texas coast. Allersma (1972) has reported them on the muddy coast of Venezuela, where they are dominantly composed of mud. They have been detected by ERTS satellite imagery on the Mozambique coast (John McHone, personal communication), and also appear on the southern littoral of the North Sea. With the exception of the Venezuelan coast, most settings are that of a low, unconsolidated coast undergoing Bruun erosional retreat (Fig. 10.4) in response to a moderate to strong wave climate and periodic intense storm or tidal flows.

Where best studied, on the Virginia-northern North Carolina coast (McHone, 1972), the ridges appear to have some of the response characteristics of wave-built bars at their inner ends where they merge with the shoreface. Like wave-built bars, their landward ends are asymmetrical, with steep landward flanks, although the



FIGURE 27. Model for the transformation of a stillstand delta into a retreating cusped foreland. From Swift and Sears (1974).

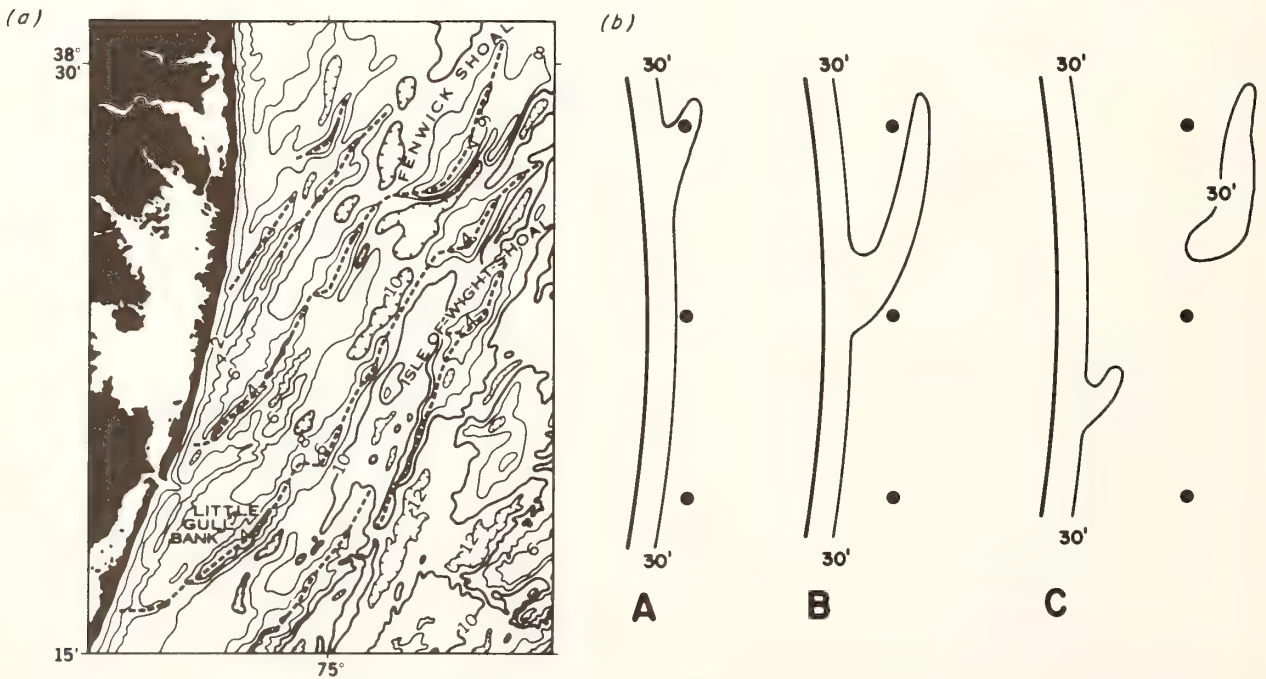


FIGURE 28. (a) Shoreface-connected ridges of the Delmarva inner shelf, contoured at 2 fathom intervals. From ESSA bathymetric map 0807N-57. Ridges are in varying stages of detachment. (b) Schematic diagram of detachment sequence as inferred

from (a). Dots represent hypothetical fixed points during a period of shoreface retreat and downcoast ridge migration. See text for explanation. From Swift et al. (1974).

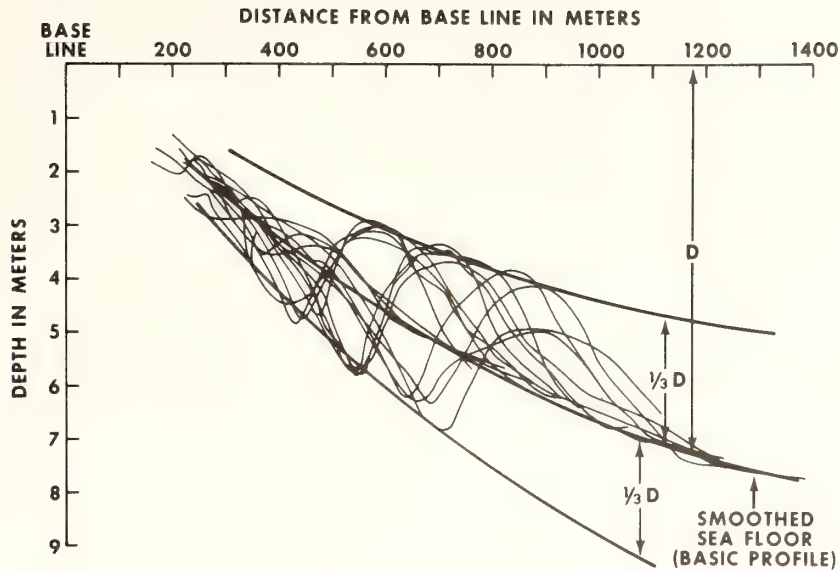


FIGURE 29. Superimposed profiles of the inner shoreface-connected ridge at False Cape, Virginia. From McHone (1972).

reverse asymmetry tends to prevail further seaward. Envelopes of profiles indicate that, as in the case of their small-scale break-point counterparts, ridges built to a height of approximately one-third water depth, at which point wave agitation is sufficiently intense to preclude further growth. The troughs between the ridges and the shoreface are similarly excavated to one-third of water depth below the smoothed profile (McHone, 1972); see Fig. 29. At the False Cape Ridge Field, Virginia (McHone, 1972; Swift et al., in press), analysis of the wave climate suggests that waves are capable of breaking on some part of the inner ridge crest about 10% of the time. As a consequence of their oblique orientation and varying crestal depth, such ridges may utilize energy from a relatively broad spectrum of wavelengths.

As wave-built bars, however, the low-angle ridges are anomalous. They are much larger than surf zone bars and their oblique orientation is more nearly parallel to the direction of wave approach than normal to it. The ridges may be primarily a response to a downwelling coastal jet that comprises the coastal margin of the storm flow field (see p. 275), although storm wave action is clearly a complementary mechanism. At False Cape, Virginia, a 28 hour current-meter station revealed a steady southward and offshore flow on the order of 15 cm/sec at a distance of 8 cm off the bottom, subsequent to the passage of a cold front with winds in excess of 25 knots (Fig. 30). During this period, however, the anchored observation vessel maintained a wake trending southward and shoreward. The inferred structure of the coastal flow field during the observation period is pre-

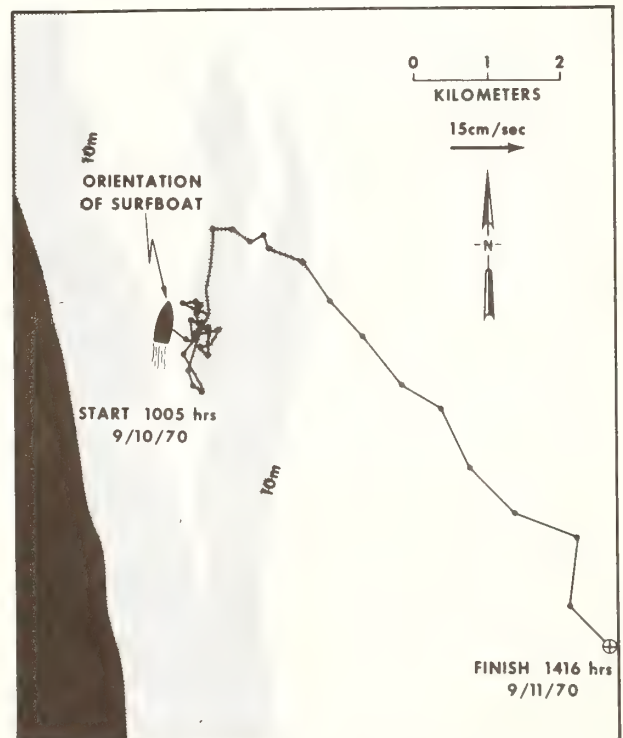


FIGURE 30. Progressive vector diagram of storm bottom flow at the innermost ridge at False Cape, Virginia. Vectors represent velocities taken for 3 minute intervals every 30 minutes by two orthogonal Bendix Q-18 meters mounted in a plane parallel to the seafloor, 16 cm off the bottom. After passage of a cold front, bottom flow trended southeast obliquely seaward over ridge crest at velocities up to 18 cm/sec, while wake of anchored observation vessel streamed southeast, toward shore. Based on Holliday (1971).

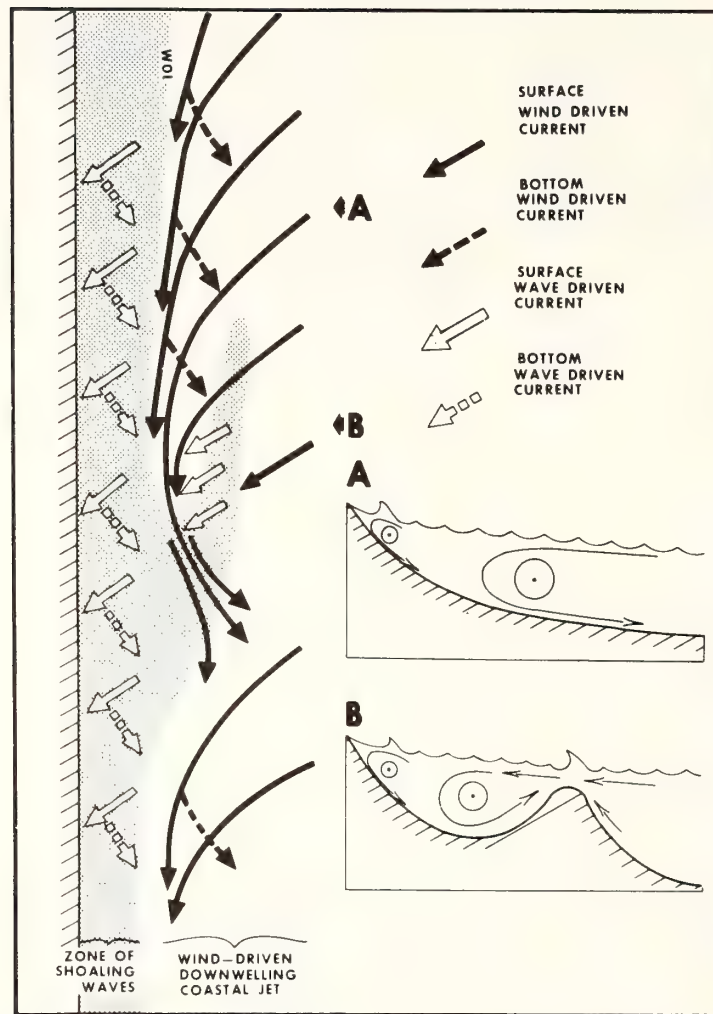


FIGURE 31. Hypothetical structure of the coastal boundary of the storm flow field, based on Figs. 2 and 30.

sented in Fig. 31. The observed pattern is interpreted as downwelling coastal flow intensified by constriction of the trough toward its southern end, and also by the setup of waves breaking on the inshore end of the trough. Mapping of the junction of this ridge with the shoreface on four successive occasions has revealed the presence of a shifting saddle, where storm flows presumably break out over the ridge base (McHone, 1972).

A grain-size profile over the ridge is extremely asymmetric (Fig. 32). Sands are coarsest in the landward trough and become steadily finer up the landward flank, are of relatively constant grain size across the crest, and become finer again down the seaward flank. Sorting is variable on the landward flank and crest but increases steadily down the seaward flank.

The profile is characteristic of a flow-transverse sand wave, and suggests that the ridges are responding as would a sand wave to the cross-shoal component of flow. As described in Chapter 10 (p. 166), bed shear stress increases up the upcurrent flank of a sand wave, attaining a maximum at the crest or just forward of it, then decreases down the downcurrent flank. Grain size would tend to decrease monotonically across such a shear stress maximum as a consequence of the progressive sorting mechanism; as sand is eroded out of the trough, the coarser grains are more likely to be trapped out in the initial portion of the transport path (Chapter 10, p. 162). On this particular ridge, however, size characteristics do undergo a reversal on the landward side of the crest, where maximum shear stress is to be expected.



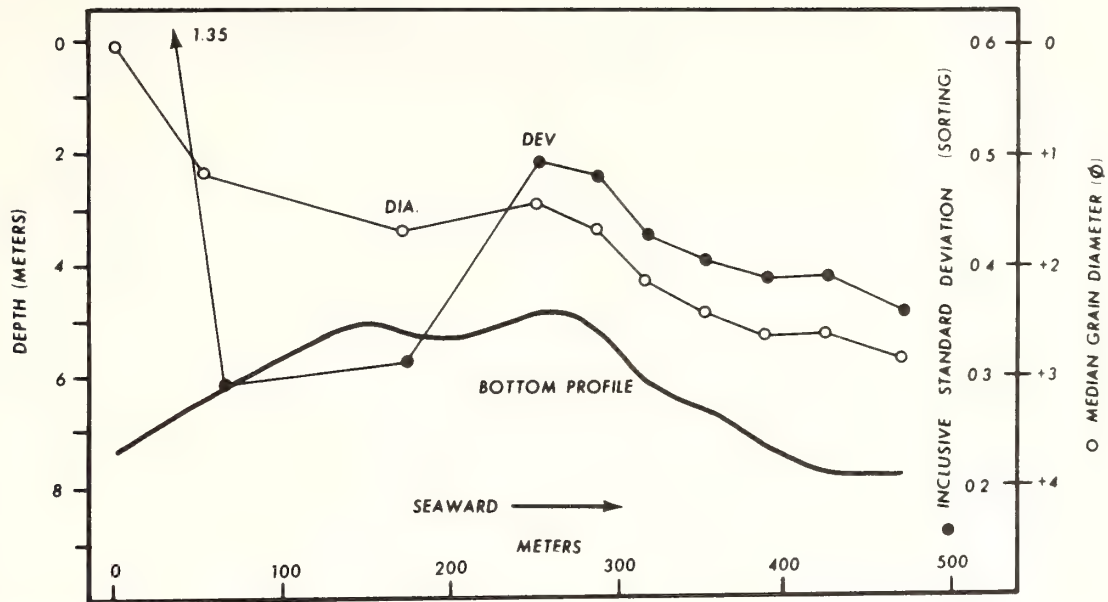


FIGURE 32. Grain-size profile across the inner ridge at False Cape, Virginia (by Leonard Nero).

Shoreface ridges are not simply giant sand waves, however, because flow crosses them at an oblique angle. The model presented in Fig. 31 suggests that they partake of the characteristics of both flow-transverse sand waves (Chapter 10, p. 166) and flow-parallel sand ridges (Chapter 10, p. 172).

Thus the ridges appear to represent the attempt of an intensified coastal flow to build an outer bank with materials scoured from the high-velocity axis of downwelling. The topography presented in Fig. 30 presents a clue to the historical development. The initial perturbation required to trigger these large-scale instabilities of the shoreface might be something on the order of the migrating "sand humps" of the surf zone described by Bruun (1954) and Dolan (1971). As the ridge and trough take form in response to the interaction of storm waves with the coastal storm flow, they would tend to be self-propagating. Enlargement of the trough by headward erosion and downward scour of the trough, and aggradation of the ridge crest by peak flow events would create a morphology that would amplify successive trough flows. Thus during a period of general shoreface retreat due to storm erosion, ridges would be carved out of the shoreface partly because the shoreface would retreat away from them, and partly because they themselves would tend to migrate obliquely offshore, extending their crestlines to maintain contact with the shoreface as they do so (Fig. 28). The sinuous pattern of crestlines on the inner shelf floor of the Delmarva peninsula suggests that ridge formation may be an episodic affair; troughs en-

large and trough flows amplify until the flow is intense enough to cut through the ridge base, whereupon the process is repeated farther down the shoreline. Shoreface-connected ridges are seen in all stages of detachment in Fig. 28. It is doubtful, however, if this is a full or adequate explanation of ridge genesis even in a qualitative sense. Any more comprehensive analysis must undertake to explain the relative orientations of peak bottom flow, the ridge crest, and the shoreline. As noted, neither the breakpoint bar nor the sand wave models meet this requirement.

The ridges are generally oriented along a trend that is intermediate between the dominant direction of storm wave approach and the coast-parallel trend of storm currents (narrow-angle ridges), perhaps as a consequence of the dual role of these elements in ridge genesis. Locally, however, they may be aligned along the direction of storm wave approach (wide-angle ridges: Duane et al., 1972); see Fig. 33. Such ridges would resemble the "finger bars" of Niedoroda and Tanner (1970), rather than break-point bars. While breaking waves tend to drive sand across break-point bars, the bottom surge of refracting waves tends to drive sand obliquely crestward and landward, up both sides of a finger bar. Wide-angle ridges exhibit the same textural and morphologic asymmetry as do narrow-angle ridges, indicating that they too are shaped by storm flow as well as by wave surge. But they presumably react to storm flow more nearly as a flow-transverse bed form than as a flow-parallel bed form, as in the case of narrow-angle

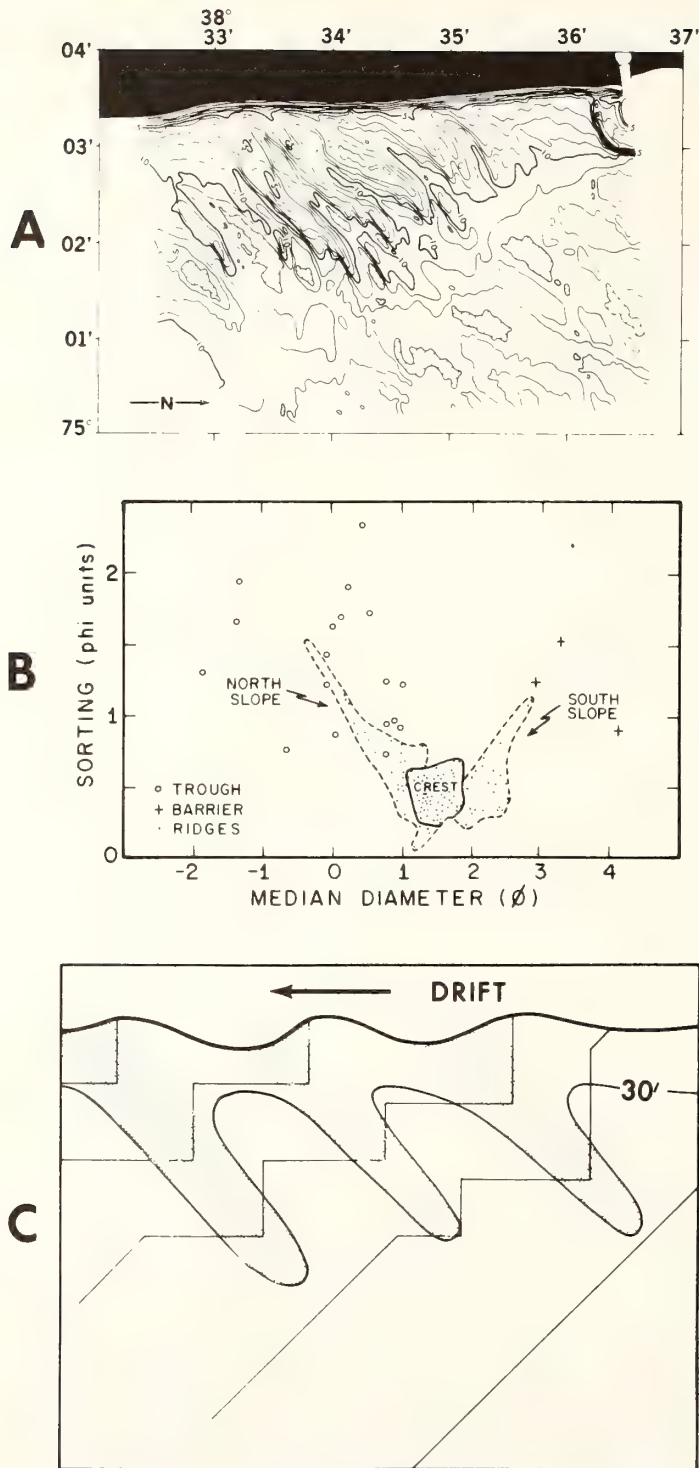


FIGURE 33. Substrate response and hydraulic process for a wide-angle, shoreface-connected ridge system, Bethany Beach, Delaware. (A) Bathymetry. From Moody (1964). (B) Median diameter versus inclusive graphic standard deviation for sand samples. From Moody (1964). (C) Schematic model for the generation and maintenance of wide-angle ridges. Refracted waves converge toward ridge crests. Breaker angle is most intense at heads of trough. Storm flow is coast parallel and to the south.

ridges. A full understanding of the genesis of these coastal sand bodies must await more detailed field measurements of the responsible flows.

### Storm-Induced Inner Shelf Ridge Fields

Ridge fields on the inner shelf floor continue their morphologic identity and their characteristic pattern of grain-size distribution (Fig. 34). Relief continues at 10 m, and slopes for isolated inner shelf ridges are very similar to those of shoreface-connected ridges. Scour continues in troughs; the erosional surface cut by shoreface translation extends beneath the ridges and is locally exposed in trough axes (Swift et al., 1972a,b). Generally, however, it is veneered with a few decimeters of coarse, pebbly sand, overlaid by finer sand. The coarser sand is commonly exposed in elongate windows through the finer sand veneer. Sidescan sonar records suggest that the finer sand is moving as ribbonlike streamers over a coarser lag substrate. Ridge crests consist of medium to fine, well-sorted sand, with cross-stratified horizons (Swift et al., 1972a; Stubblefield et al., 1975). Flanks consist of fine to very fine sand and are distinctly asymmetrical in their textural pattern; seaward flanks are notably finer, and are locally steeper than landward flanks. Crestal sands, however, may be distinctly coarser than

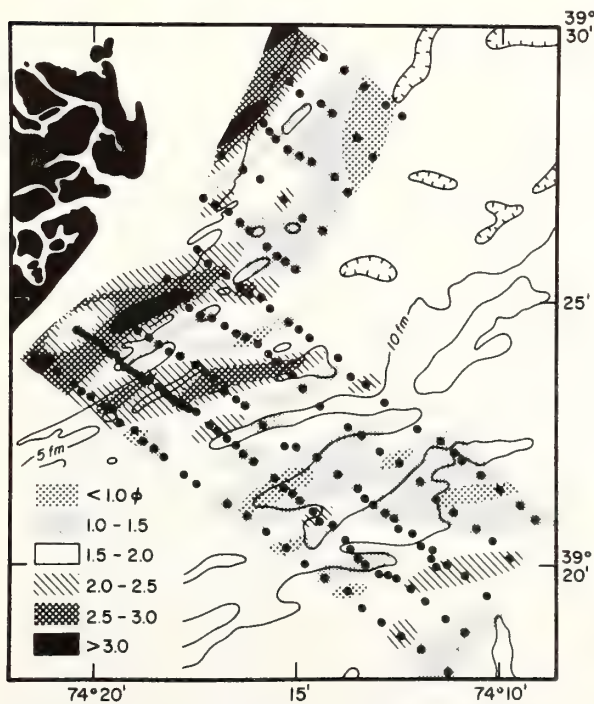


FIGURE 34. Grain size distribution in the Brigantine inner shelf ridge field, New Jersey. Data of M. Dicken.

the flank sands of either side, probably a response to winnowing by wave surge.

The inner shelf ridges themselves appear to be in a state of slow transit, wherever there is a bathymetric time series adequate to test this hypothesis (Figs. 35 and 36). The pattern of movement is a fairly consistent one, in which both shoreface-connected and isolated inner shelf ridges move along similar trajectories. Where the angle of convergence of the ridge crest with the shoreline is fairly large, the ridges are moving downcoast and offshore, extending their crestlines so as to maintain contact with the shoreface as they do so. Where the ridges are nearly coast-parallel, they are extending these crestlines downcoast, and may move either inshore or offshore, but more commonly offshore.

The considerations just discussed strongly suggest that inner shelf ridges continue to interact with the shelf flow field after detachment, in such a way as to maintain their morphologic and textural characteristics. In fact, ridged inner shelf topography occurs on sectors of the North American inner shelf where it cannot have

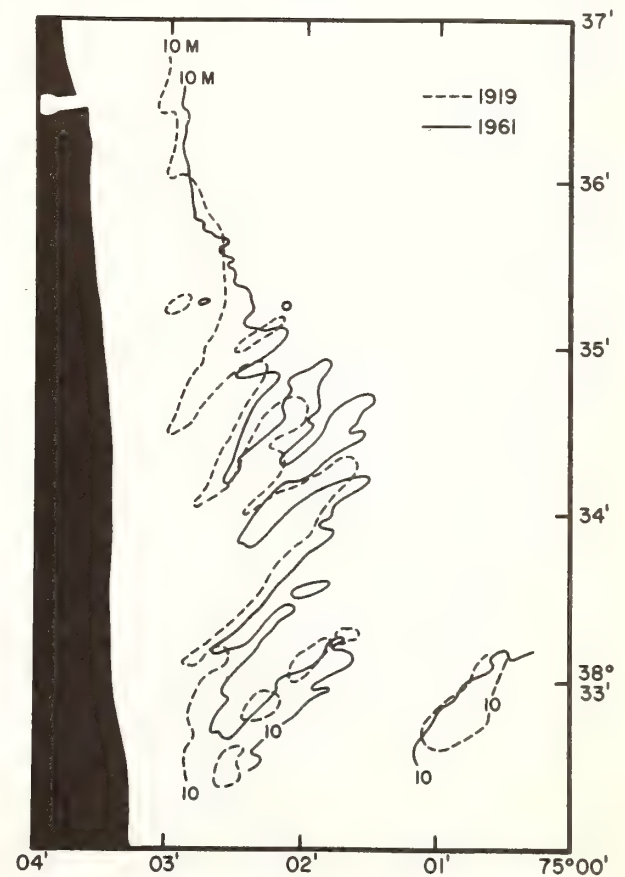


FIGURE 35. Bathymetric time series from the Bethany Beach ridge field, Delaware, between 1919 and 1961. From Moody (1964).



FIGURE 36. Bathymetric time series of Chincoteague shoals, Delmarva (Delaware-Maryland-Virginia) coastal compartment. Ridges have migrated slightly offshore, and have extended their crestlines markedly to the south between the Coast and Geodetic surveys of 1881 (dashed line) and 1934 (solid line). From Duane et al. (1972).

been formed by shoreface ridge detachment (Swift et al., 1974); see Chapter 15. It appears that the shelf hydraulic regime will adopt ridges from the retreating shoreline or mold them afresh in the substrate if the hydraulic regime is conducive to a ridged substrate. A possible mechanism for ridge maintenance involving helical flow structure in the storm flow field is presented in Chapter 10 (p. 173).

There is in addition a smaller scale bed form pattern on the inner shelf whose patterns of distribution are compatible with this hypothesis. These are the sand ribbons on the inner shelf of the Middle Atlantic Bight of North America, revealed by sidescan sonar. They tend to be 5 to 50 m wide, are of negligible relief, and tend to make angles of 10 to 45° with the shore. They are most commonly observed as dark streaks on sidescan sonar, which means that they are not true sand ribbons (streamers of finer sand over an immobile substrate of coarser sand or gravel) but are instead erosional windows in which a coarser substrate is locally exposed through a discontinuous sand sheet (Chapter 10, p. 170). Locally, however, the pattern anastomoses so as to create a true sand ribbon pattern (Fig. 37). The dark streaks in many areas are distinctly asymmetrical, with sharper landward boundaries (Chapter 10, Fig. 17). The streaky patterns occur on the smooth inner shelf or in ridge fields. In the latter case they are largely confined to troughs, where they tend either to parallel the trough axes or make a somewhat larger angle with the shoreline.

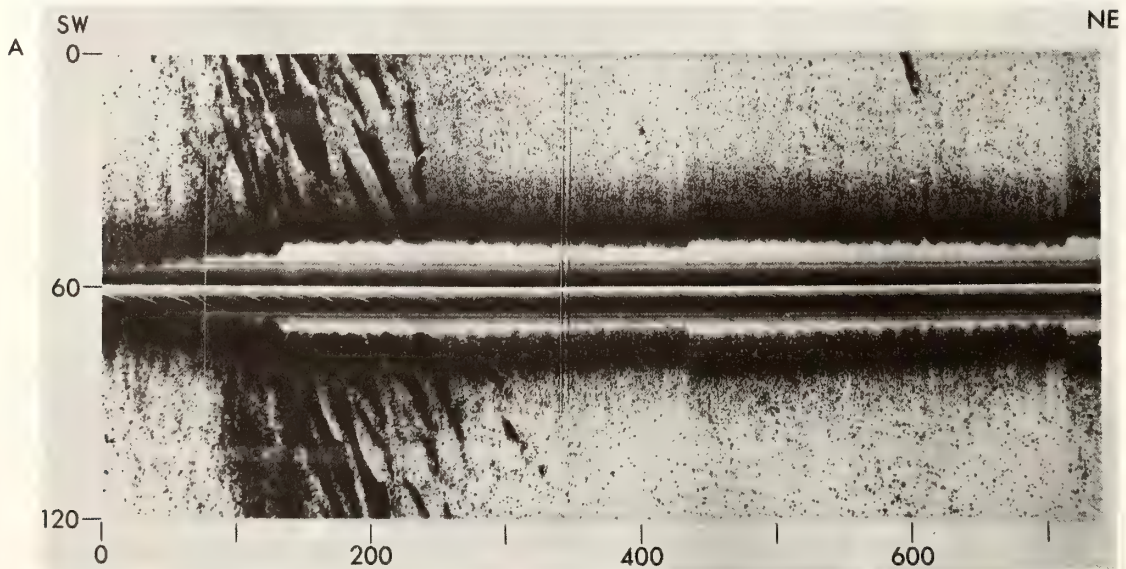


FIGURE 37. Sidescan sonar record of sand ribbon pattern in the trough of a central shelf ridge. From McKinney et al. (1974). Dark band is a window of coarse sand. Lighter band is a window of fine sand.

As noted in Chapter 10, the larger ridges are probably responses to repeated flow events, whereas the smaller sand ribbons and erosional windows may be formed during a single flow event. The similar orientations and asymmetries of the sand ribbons and ridges suggest that both may be responses to a geostrophic flow regime in which secondary flow cells occur at several spatial scales. With fully developed secondary flow, the tendency for regional landward transport of surface water and regional seaward transport of bottom water (solid arrows, Fig. 38) would be suppressed in order to maintain continuity. Instead, cells rotating with the sense of regional shore-normal flow component would be enhanced, and cells rotating with the opposite sense would be suppressed. Detailed measurements of the velocity field in the vicinity of such offshore ridges during peak flow events would serve to test this model, and perhaps lead to alternative models.

#### Tide-Induced Inner Shelf Ridge Fields

Tide-dominated coasts such as the Anglian coast of England also tend to store sand in shoreface-connected

and inner shelf ridges. The forcing mechanism for ridge formation must be in part the storm-augmented shelf flow field as in the case of such storm-dominated coasts as the Middle Atlantic Bight of North America, since the Anglian coast is also subjected to severe storms (Valentin, 1954). However, this coast experiences in addition the progressive tidal edge wave associated with the amphidromic tidal system of the North Sea (see Chapter 5, p. 60) on a twice daily basis; midtide coastal tidal velocities regularly exceed 2 knots.

As a consequence of the greater rate of energy expenditure in tidal flow than in wave- and wind-current-generated flow, storage of sand in the subaerial zone as barrier superstructure, or in the surf zone as a beach and surf prism, is greatly inhibited at the expense of submarine storage in tide-maintained sand bodies. The efficiency of this storage is greatly strengthened by the tendency of the coastal tidal wave to interact with a loose substrate by the formation of interdigitating ebb and flood channels separated by sand shoals which form effective sand traps (Robinson, 1966); see the discussion on page 177. As in the case of the Middle Atlantic

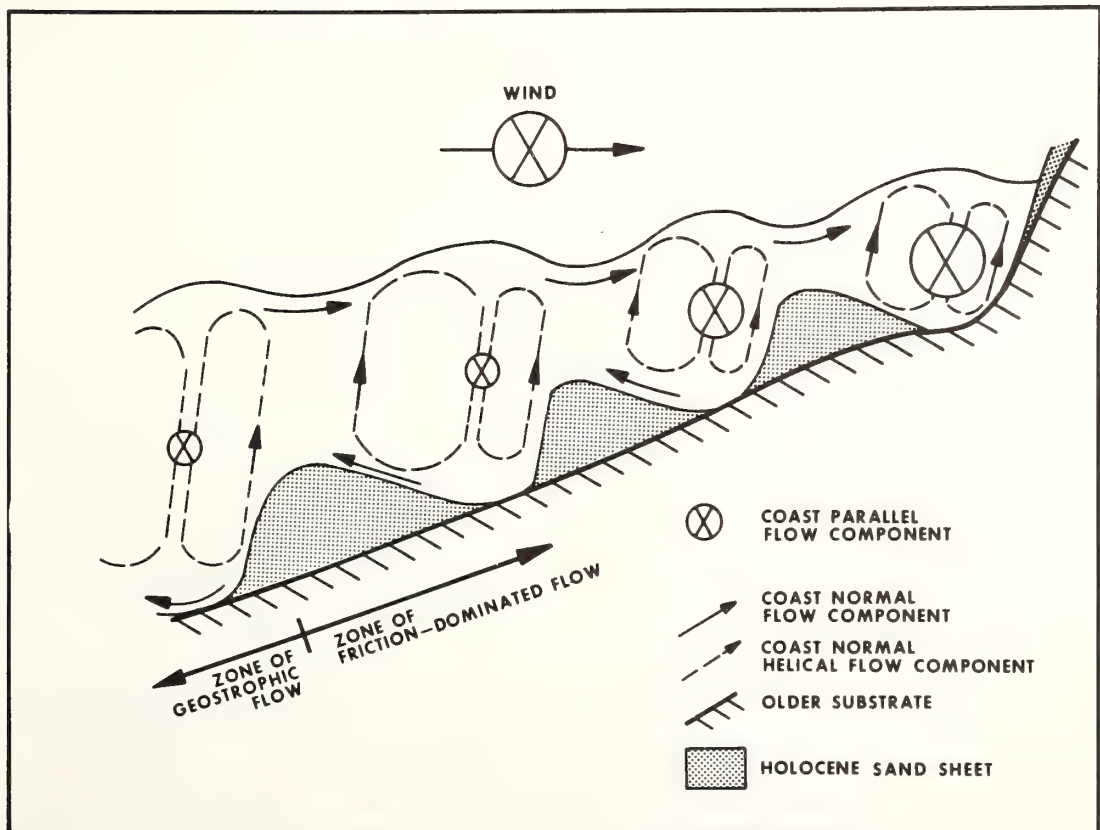


FIGURE 38. Hypothetical scheme showing a possible mode of coupling between Ekman flow cells and a mobile inner shelf substrate during a period of strong downcoast winds. See text for explanation.

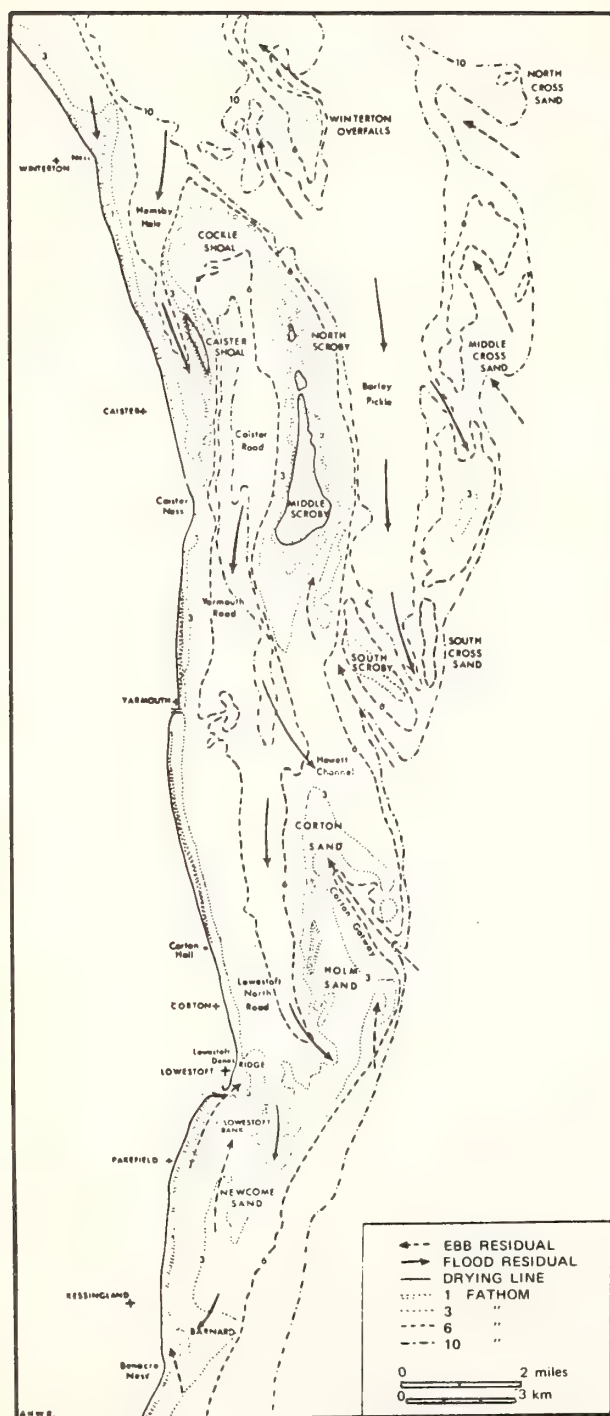


FIGURE 39. Tide-maintained ridge topography on the inner Anglian shelf. Shoreface-connected ridges separate ebb- and flood-dominated channels. Ridges tend to migrate southward with time, and to detach from retreating shoreface. Ridges are nourished at the expense of shoreface, hence constitute cases of downdrift by-

passing. Offshore ridges are probably being nourished at expense of nearshore ridges; if so, sand is moving seaward more rapidly than are the ridge forms. From Robinson (1966).

Bight, the nearshore zone of sand storage is not a stationary one but is translating landward in response to postglacial sea-level rise and erosional shoreface retreat. The primary element of storage is again a shoreface-connected sand ridge (Fig. 39). The angle between these ridges and the coast opens northward, into the direction of the advancing coastal tidal wave, and therefore the trough opens into the flood-dominated residual tidal flow. Downwelling may also occur during the flood tide, since the high velocity axis of trough flow will tend to converge with the rising trough axis. The outside of the ridge is shielded from the flood tide, and therefore experiences a greater ebb discharge. This diversion of flow might be expected to result in a sand circulation cell, with sand moving obliquely up the inner flank and over the crest during the flood tide, to be returned along the seaward flank during the ebb tide. As in the case of storm-maintained shoreface-connected ridges, probably any initial perturbation of the shoreface would result in such a self-maintaining system.

As in the case of the Middle Atlantic Bight, the ridges tend to migrate offshore and downcoast, in the direction of the residual tidal flow (Robinson, 1966), and tend to become detached and isolated on the inner shelf floor. However, unlike storm-maintained ridges, tidal ridges on the inner shelf floor tend to be unstable. Variations in the rate of offshore migration along the length of the ridges tend to result in self-propagating modifications of ridge morphology (Caston, 1972; Chapter 10, Fig. 21), whereby the ridge deforms into a sigmoidal pattern, because of the growth of secondary ebb- and flood-dominated channels, and may eventually split into three ridges.

As in the case of the Middle Atlantic Bight, isolated inner shelf ridges continue to be maintained, but the character of interaction between the flow field and substrate changes as the water column deepens. Ridge spacing increases as a function of flow depth (Allen, 1968b) as sand is partitioned between fewer, wider ridges. As channels widen, they cease to become wholly ebb- or flood-dominated, but are themselves partitioned into ebb-dominant and flood-dominant sides (Caston and Stride, 1970); see Chapter 10, Fig. 20). All channels have the same sense of shear. Thus the offshore ridges are sand circulation cells, but the sense of circulation is the same from ridge to ridge, instead of alternating between clockwise and counterclockwise as on the shoreface.

## SAND STORAGE AT COASTAL INLETS

### Categories of Coastal Inlets

In addition to the coastal flow discontinuities found at capes and cusped forelands and on ridged shorefaces, discontinuities also occur at coastal inlets, which likewise result in sand storage systems. The term coastal inlet is here used in its broadest sense, for a variety of coastal reentrants, defined by the ratio of salt- to fresh-water discharge in their two-layer circulation systems, and in the extent to which their channel cross sections have equilibrated with the discharge (Table 3).

TABLE 3. Categories of Coastal Inlet

	Constructional form (equilibrium channel)	→	Erosional form (inherited river valley)
Saline/freshwater discharge ratio ↓	Delta distributary		
	Tidal delta distributary or equilibrium estuary		
		Disequilibrium estuary	
		Tidal channel-mud flat complex	
	Tidal inlet		Bay

The main sequence of coastal inlet morphologies trends diagonally across Table 3, from delta distributaries entering tideless seas, through tidal distributary mouths and trumpet-shaped equilibrium estuaries to funnel-shaped disequilibrium estuaries, to tidal channel-tidal flat complexes and open bays. Tidal inlets are hybrid cases, in which an equilibrium channel has been fitted to a lagoon. Special effects such as mirror-image ebb, flood "tidal deltas," and offset barrier coasts result. Tidal inlet morphologies are continuous with equilibrium estuary morphologies and grade into them through intermediate cases in which a central channel meanders through a marsh-filled lagoon.

### Equilibrium River Mouths

Delta distributaries (prograding river mouths) and equilibrium estuaries (retrograding river mouths) belong to a general class of river mouths. The cross-sectional area of river channels is a power function of river discharge (Leopold et al., 1964, p. 215). Where rivers enter the sea, a salt wedge intrudes beneath the fluvial jet, whose discharge is amplified by a two-layer (estuarine) circu-

lation (see p. 24). Most rivers enter tidal seas, and river mouth discharge is further amplified by the discharge associated with the semidiurnal tidal cycle, which propagates for some distance upstream. Thus a river mouth whose channel is in equilibrium with total discharge must expand rapidly through the tide-influenced zone toward the sea, resulting in a trumpet-shaped plan configuration.

At the river mouth proper, a variety of processes conspire to construct an arcuate, seaward-convex sand shoal (Fig. 40). The most fundamental factor is the hydrodynamic continuity relationship: Expansion of the fluvial jet results in rapid deceleration and loss of competence, and river sand is deposited in the form of a shoal. Estuarine circulation also plays a role; river mouth morphology and the circulation interact, so that the crest of the shoal becomes the leading edge of the salt wedge during flood stage (Fig. 41), or, if the tidal component of river mouth discharge is very large, the spring ebb tide terminus of the salt wedge, or both (Wright and Coleman, 1974; Moore, 1970; Farmer, 1971). The crest of the shoal thus becomes a bottom current convergence during periods of maximum sediment transport, and hence a reservoir for sand storage. A second major source of sand maintaining the river mouth shoal is littoral drift, which is diverted seaward along the shoal crest.

Sediment storage in tidal river mouths is mediated by the behavior of the tidal wave as it passes over the shoal crest. Here, as on open tidal coasts, tidal wave and substrate tend to interact to form interdigitating ebb- and flood-dominated channels separated by shoals that are efficient sand traps. The tide within the estuary is retarded by friction and is out of phase with the shelf tide; it continues to ebb after the shelf tide has already begun to flood. The two water masses tend to interpenetrate, with the main ebb jet passing out over the center of the shoal and the oceanic tide flooding on either side of it. The response of the shoal surface to this periodic flow pattern is an interdigitation of ebb- and flood-dominated channels, separated by a discontinuous, zigzag system of sandbanks (Ludwick, in press); see the discussion on page 177.

A further process modifying the surface of the shoal and enhancing its capacity for sand storage is the interaction between the tide-generated pattern of channels and sand ridges and incident wave patterns. The arcuate pattern of the shoal as a whole serves to focus wave energy on it. Sand ridges between ebb and flood channels tend to build toward the level of mean high tide. As their upper surfaces emerge into the intertidal zone they become swash platforms, on which intersecting patterns of wave trains tend to drive sand in the resultant, landward direction (Oertel, 1972); see Fig. 40.

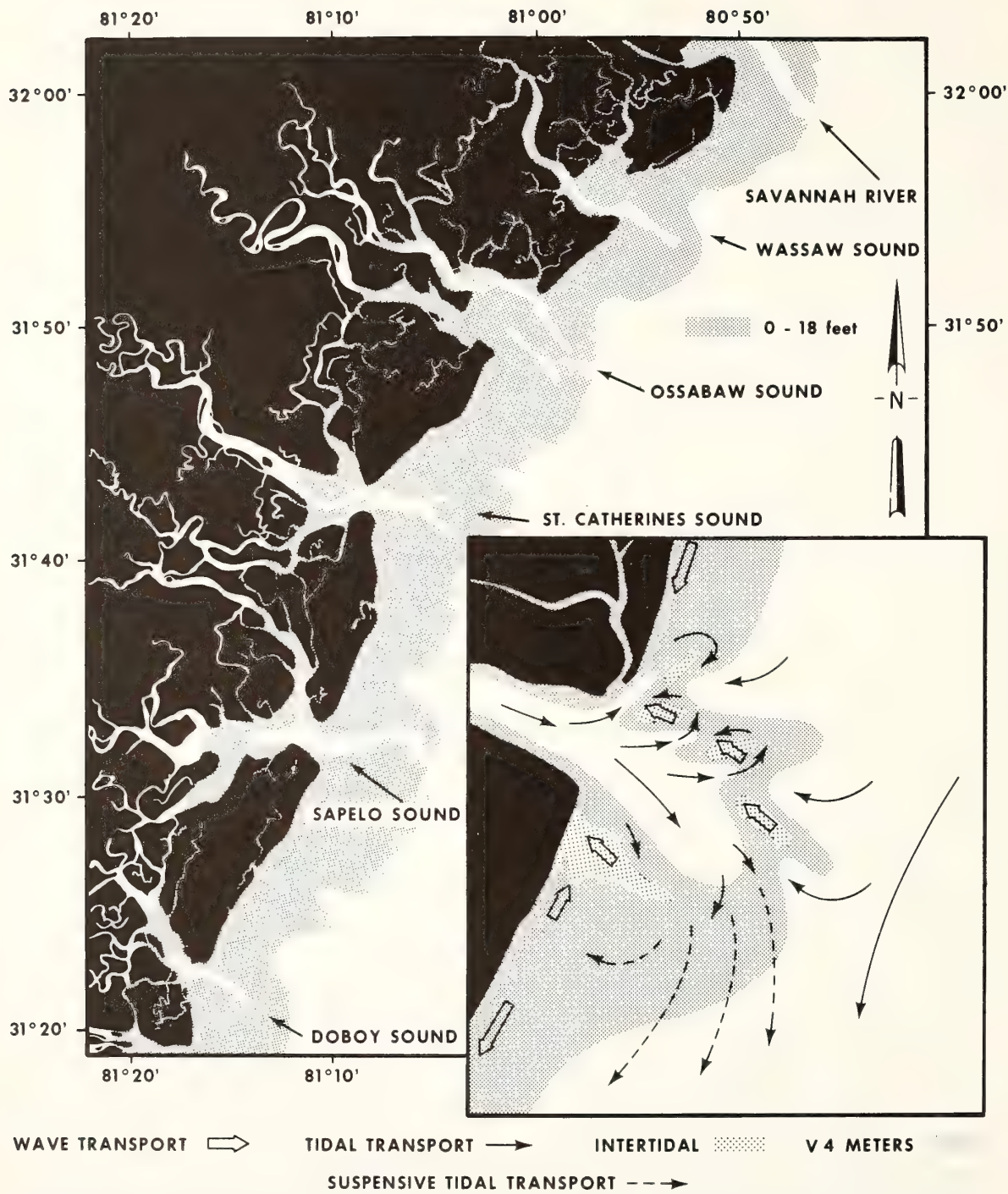


FIGURE 40. Sedimentation patterns at the mouths of Georgia estuaries as inferred from Oertel (1972) and Oertel and Howard (1972).



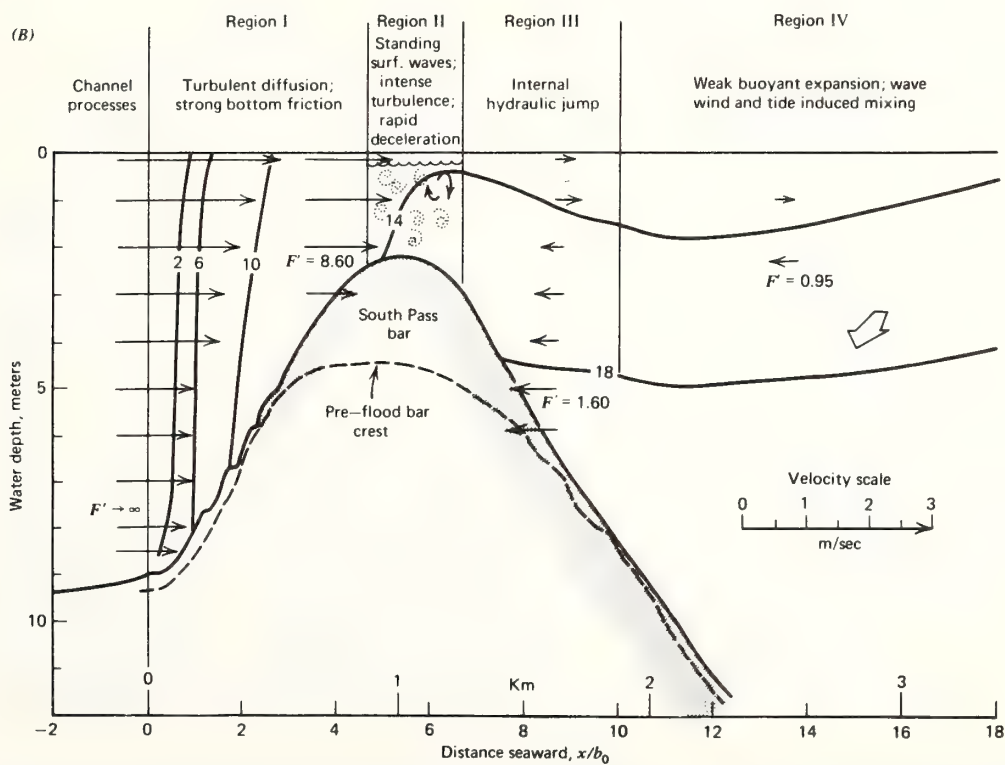
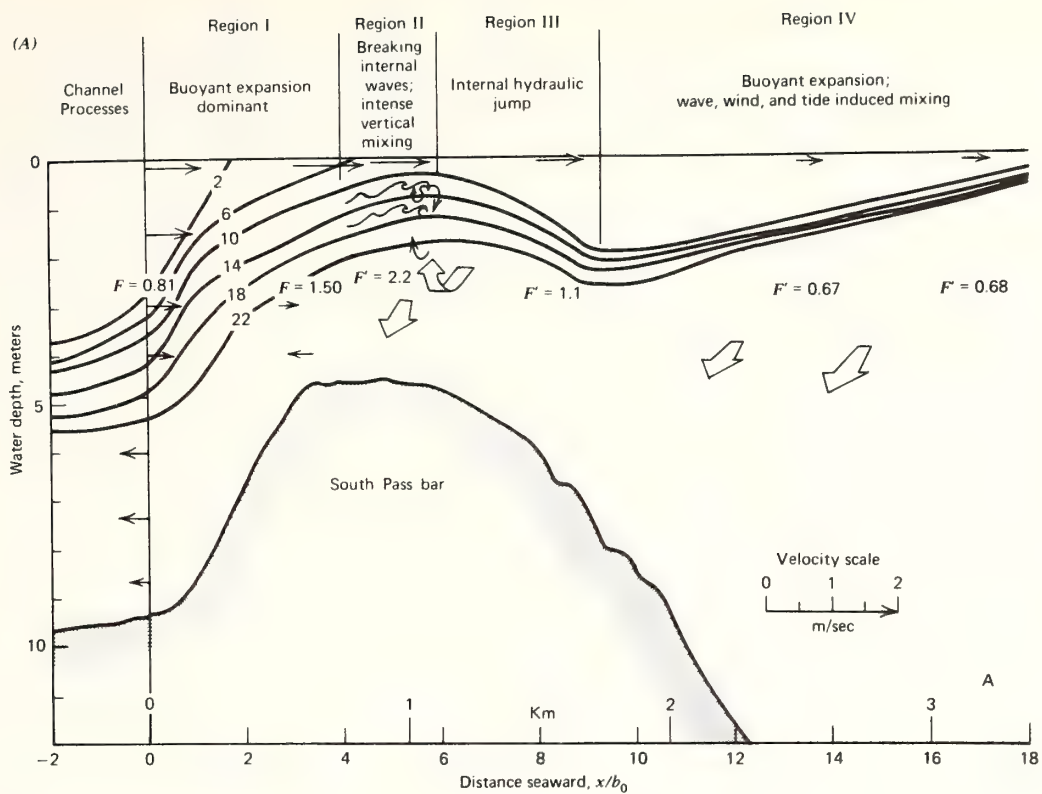


FIGURE 41. (A) Cross section of density and flow during flood stage (April 5, 1973). Both sections taken during flood tide. From Wright and Coleman (1974). (B) Cross section of density and flow during low river stage (October 25, 1969) and

Despite the relatively rapid postglacial rise in sea level, some river mouths have been able to maintain equilibrium channels in which cross-sectional area is adjusted to discharge, as deltas (prograding river mouths) or as equilibrium estuaries (slowly retrograding river mouths; see Figs. 42A,B). Most, however, have not. Disequilibrium estuaries have resulted whenever aggradation of the estuary floor in millimeters per year has been less than the rate of sea-level rise, so that before any given segment of channel could close down to the required cross-sectional area, the main shoreline had passed it by.

Such "drowned" or disequilibrium estuaries are generally nearly funnel-shaped, rather than trumpet-shaped, as are the equilibrium forms. As a consequence of their higher ratio of saltwater to fluvial discharge, their river mouth shoals are retracted into the throat of the estuary and the interpenetration of ebb and flood channels becomes marked (Fig. 42C).

With a yet further increase of tidal over fluvial discharge such a coastal indentation may no longer be appropriately called an estuary, but simply a bay. Large bays experiencing high tidal ranges may build a tide

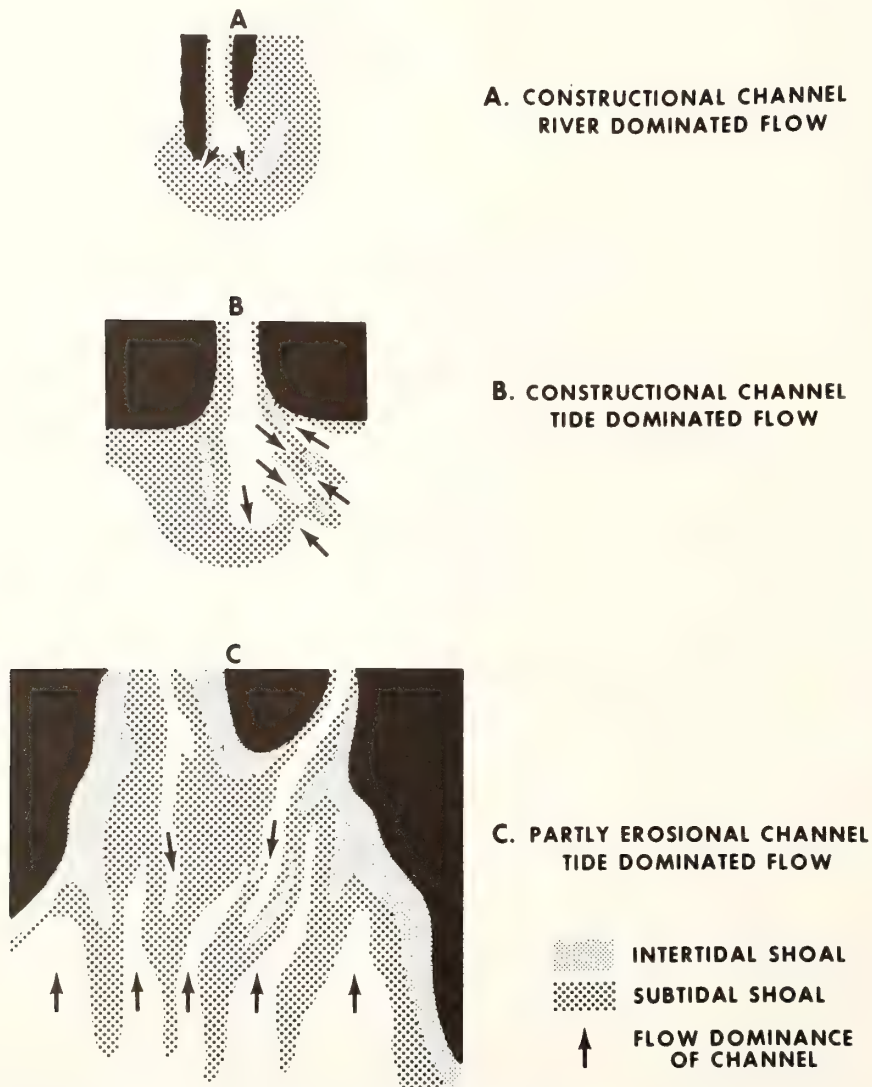


FIGURE 42. *Varieties of river mouths. (A) Prograding delta distributary entering tideless sea (based on Mississippi River Delta). (B) Equilibrium (discharge adjusted) tidal estuary mouth (based on Georgia coast estuaries). (C) Disequilibrium estuary mouth (based on Thames estuary). From Swift (1975b).*

flat-tidal channel complex at their heads as a consequence of net landward sediment transport by the shoaling tidal wave. These deposits are the functional equivalent of the tide-molded deposits of a disequilibrium estuary.

The patterns of sand storage in estuary mouths may be extremely elaborate. These dynamic topographies are of major concern to port authorities concerned with the maintenance of deep-water approaches. As in the case of the systems of open coasts, estuary mouth sand storage systems are in a state of continuous reorganization in response to the postglacial rise in sea level.

Kraft et al. (1974) have attempted to trace the transgressive history of the mouth of Delaware Bay by equating a series of transects across the modern bay with the time series of profiles that would be expected at a single point during transgression (Fig. 43). Here ridges first appear as subaqueous tidal levees on the edge of tidal flats marginal to tidal channels. Unlike the tidal sand ridges of open shelf seas, these ridges migrate away from their steep sides (Weil et al., 1974). As transgression proceeds, the channels service a larger and larger tidal prism and tend to widen. The effect on the levees is erosion on the steep, channel-facing side, and aggradation on the gently sloping side facing away from the channel. Weil et al. (1974) have attributed the submarine levees of Delaware Bay tidal channels to density-driven

secondary flow associated with the tidal cycle (Chapter 10, Fig. 26).

Inner estuary channels tend to be ebb-dominated perhaps because the upper estuary water mass tends to flood as a sheet, but tends to preferentially ebb through the channel system under the impetus of gravity discharge. Further down the estuary, as levees begin to build, the interfludes tend to become flood-dominated channels in their own right, although the dominance of channel and interfludes may locally be reversed. As previously noted, retardation of the tidal wave in the estuary results in a phase lag across the estuary mouth shoal, causing an interdigitation of ebb and flood channels, separated by partition ridges, across the crest of the shoal. Thus ridges initiated in the upper estuary may undergo a complex evolution as successive estuary environments and associated flow regimes pass over them. Individual ridges may maintain their integrity through this process or be replaced by related forms maintained by somewhat different mechanisms.

Modification of ridge morphology intensifies as the regional shoreline passes, and the lower estuarine regime is replaced by an open shelf regime. If the wave climate is intense, then the outer surface of the estuary mouth shoal is pushed back by erosional shoreface retreat in a fashion similar to that transpiring on the adjacent main-

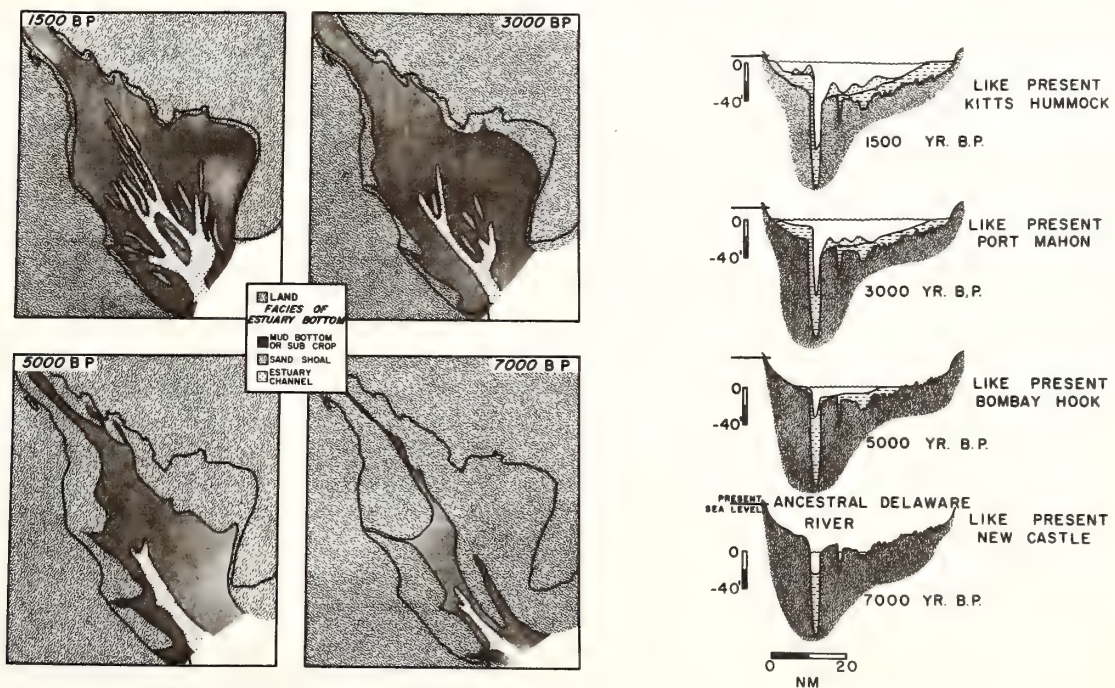


FIGURE 43. Late Holocene evolution of the mouth of Delaware Bay, as inferred from cross sections across the modern bay. Apron of sand extending into bay mouth is assumed to have prograded up the bay concurrently with the landward movements of the shoreline on either side. From Kraft et al. (1974).

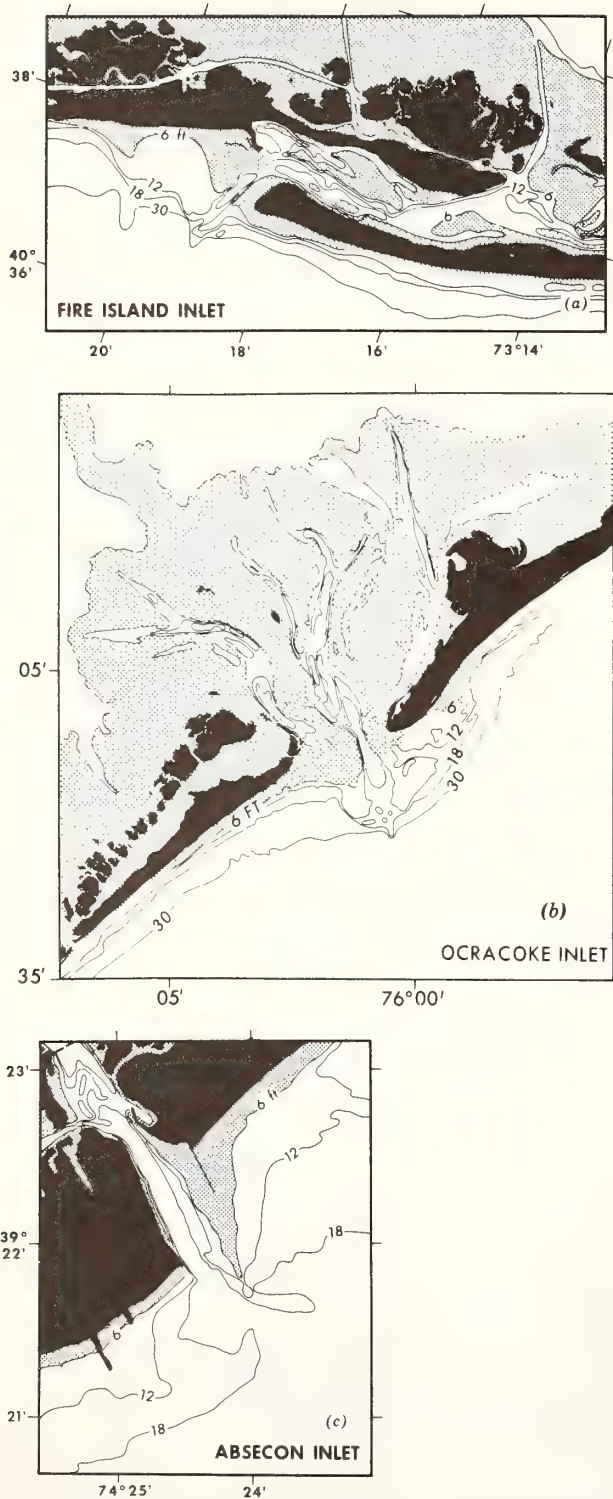


FIGURE 44. Representative examples of inlet morphology. (a) Fire Island Inlet, Long Island, a barrier-overlap inlet on a drift-aligned coast. Littoral drift dominates the ebb tidal jet. (b) Ocracoke Inlet, North Carolina. Nearly symmetrical inlet

land coast. Frequently, however, the retreat path of the estuary is visible in the form of a cross-shelf channel and a ridge on the updrift side of the channel. On the Delaware inner shelf, such a ridge can be seen to mark the retreat path of the shoal on the north side of the estuary mouth, while the associated channel has formed by the retreat of the main flood channel of the estuary mouth (see Fig. 12, Chapter 15).

### Coastal Inlets and Littoral Drift

The morphology of narrow estuary mouths and their analogs, coastal inlets, depends on the relative strengths of the river mouth or inlet jet, the wave-driven littoral current, and the tidal- and wind-driven components of the shelf flow field. Distributary mouths, subject to periodic flooding and entering relatively tideless, wave-sheltered seas, consist of subaerial levees capped by a lunate distributary mouth shoal (Fig. 42A). As a consequence of the Coriolis effect, flow is more intense on the right-hand side of the channel looking downstream, and as a consequence, the right-hand levee tends to extend itself farther seaward as in the case of Mississippi distributary mouths. If the inlet faces an open or tidal sea, then the wave- and tide-driven coastal flow is diverted seaward around the ebb tidal jet (Todd, 1968) and the shoal assumes a half-teardrop shape (Fig. 42B).

On barrier coasts, the pattern of sand storage at tidal inlets tends toward one of three basic patterns: overlap, symmetrical, or offset inlets (Fig. 44). While these patterns have long been recognized, the responsible transport systems and sand budgets are imperfectly understood (Hayes et al., 1970; Byrne et al., in press; Goldsmith et al., in press). As noted by Byrne (personal communication), the patterns appear to reflect the relative intensities of gross littoral drift (both up and down the coast) and net drift (the difference between mean annual upcoast discharge and mean annual downcoast discharge). If both the gross rates of drift and the net rate are high, a disproportionately high volume of sand storage may occur in the updrift barrier segment, and an overlap barrier may result (Fig. 44A). Where moderate gross rates of drift are associated with a strong net rate of drift, the situation favors a barrier offset inlet, in which the storage of sand on the downdrift side of the exterior shoal is favored (Fig. 44C). In one of the best studied barrier offset inlets, Wachapreague Inlet on the

*flow on a wash-aligned coast has resulted in sand storage in the wave-protected interior (flood delta) shoal. Ebb tidal jet dominates over littoral drift. (c) Absecon Inlet, New Jersey. Ebb-dominated flow has resulted in sand storage on the downdrift side of the inlet and an offset of the flanking barrier islands.*

Delmarva coast, the role of the lagoonal reservoir in modifying the hydraulic characteristics of the inlet is of paramount importance (Byrne et al., in press a). In lagoon-inlet systems where the ratio of the intertidal water prism to the subtidal volume is very large, a strong time-velocity asymmetry develops (see Postma, 1967). The strongest currents occur just before high tide, when the tidal channels have filled and the vast marsh surface is beginning to flood, and just after high tide, when the marshes are draining. Flows around low tide are weaker, as they are associated with the much slower discharge and recharge of the tidal creek system.

In addition, flood and ebb durations are dissimilar, with a greater ebb duration. This phenomenon is a consequence of the lagoonal basin's morphology and frictional characteristics (Byrne et al., in press a), and has been predicted by shallow water tidal theory for storage systems with sloping banks (Mota-Oliveira, 1970; King, 1974). In physical terms, the hydraulic head generated across the inlet by the flood tide is imposed on the deepest part of the lagoon relatively early in the tidal cycle. Here frictional retardation of flow is least efficient, and the resulting sea surface slope propagates rapidly across the lagoon, resulting in rapid water influx. The greatest potential drop across the lagoon surface during the ebb half-cycle occurs when the marsh surface is still uncovering. Frictional retardation of flow is more effective in the thin landward portions of the lagoonal water column, and the ebb is prolonged.

As a result of these modifications of the tidal cycle, the inlet operates in a bypassing mode. Sand is swept into the inlet from the updrift side, but does not penetrate very far before it is swept out again, and the prolonged ebb carries it into the storage area on the down-drift side of the external shoal. Here sand storage is enhanced by the refraction pattern of shoaling waves (Goldsmith et al., in press).

Symmetrical inlets are favored by swash-aligned coasts, where the ratio of the littoral component of wave power to tidal power is relatively low (Fig. 44*B*). Symmetrical inlets, particularly those backed by lagoons with relatively small intertidal prisms and relatively large subtidal volumes, tend to store sand primarily in the interior shoal within the lagoon.

### SAND STORAGE ON ROCKY COASTS

Rocky coasts display the greatest complexity in three dimensions. Rocky hinterlands in a mature state of dissection result in embayed coasts with deep reentrants between rocky salients. If the substrate consists of folded metamorphic rocks, then it may have a well-defined

anisotropy of its own and truly baroque patterns may result (Fig. 45). The fields of wave refraction developed over the seaward extensions of headlands result in frequent reversals of the sense of littoral drift cells and closely spaced alteration of zones of littoral drift divergence and convergence. Because of the relative steepness of the regional seaward slope and the resistant nature of the substrate, wave energy is concentrated along a very narrow intertidal zone. Waves breaking against vertical surfaces can generate enormous instantaneous forces of tens of metric tons per square meter (Zenkovitch, 1967, p. 139). Rocky shores yield along planes of weakness to become mantled with boulders under this assault (Fig. 46) and the intertidal and subtidal talus slopes become grinding mills where attrition produces finer debris and continues to grind it finer until, at about the grade of medium sand, the immersed weight of grains is no longer adequate to result in significant chipping or cracking—as long as the particles are able to escape the proximity and nutcracker behavior of coarser particles. The interaction of intertidal and shallow subtidal wave forces with the three-dimensional complexity of rocky coasts results in such erosional forms as stacks, arches, and sea caves, and the constructional forms of looped, fringing, recurved, and cusped spits, and tombolos that have long been the delight of coastal morphologists (Fig. 47). The constructional forms constitute localized depositional regressions and are usually comprised of sets and subsets of beach ridges reflecting stages in the feature's growth. If the net rate of sedimentation is sufficiently high relative to the rate of sea-level rise, these forms tend to grow and coalesce, and will ultimately form a continuous shoreface.

Rocky coasts are more nearly likely to be tectonically active than low, unindurated coasts, other things being equal, and the resistant character of their substrate may result in delays in the adjustment of the incised equilibrium profile to the crustal movement, if this adjustment is indeed attained. Comparison of rocky coasts from different parts of the world has revealed a continuum of adjustment from coasts as irregular as the margins of newly dammed reservoirs, to coasts whose adjustment has been complete, so that, by a combination of headland truncation and the filling in of bays, the coastline has been straightened in plan view and the shoreface has received the characteristic exponential curvature.

This continuum led Davis (1909) and Johnson (1919) to the concept of a cycle of coastal evolution in which, after an initial relative movement of sea level, the shoreline is straightened and the equilibrium profile passes through a cycle of youth, maturity, and old age. Zenkovitch (1967) has objected to the simplified assumptions of the model and suggests that three types of em-

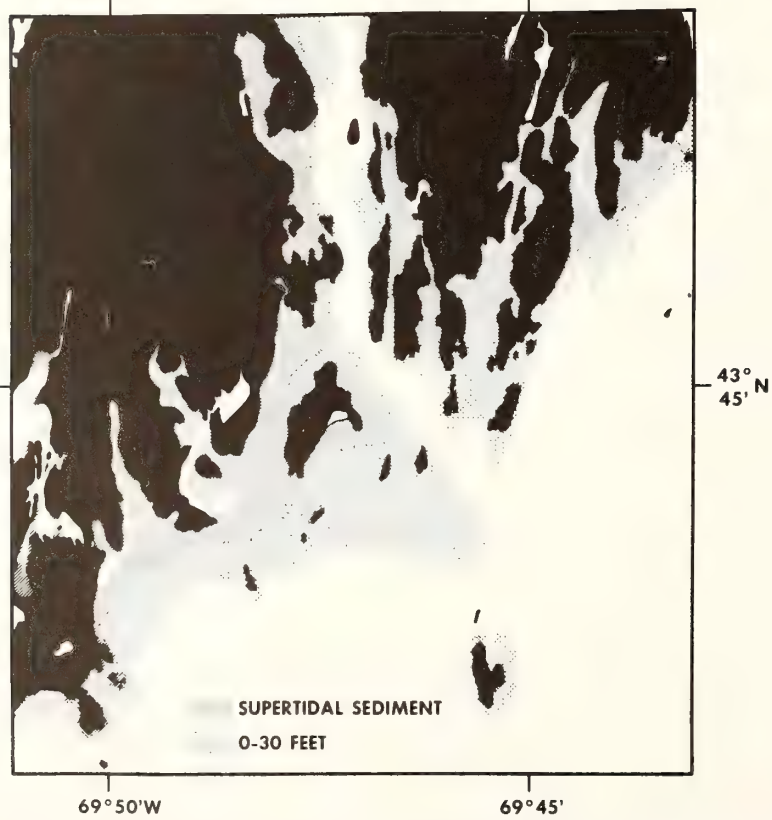
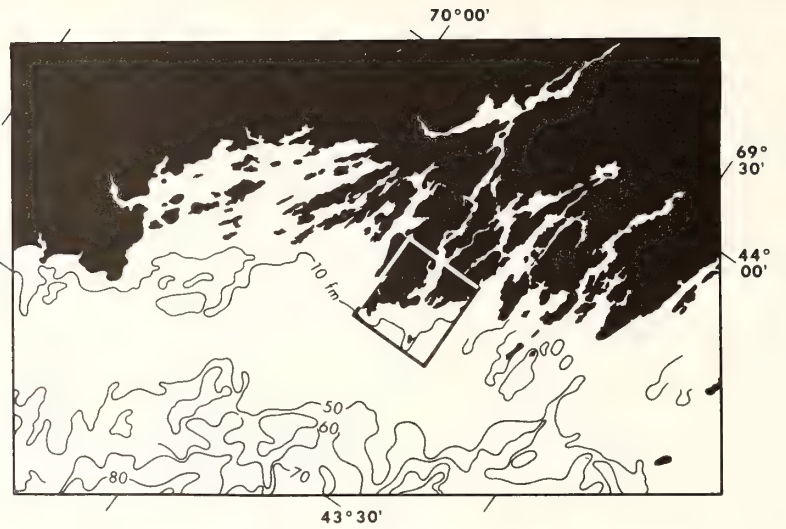


FIGURE 45. *Upper: A portion of the coast of southern Maine. Bedrock is isoclinally folded schist and gneiss. Lower: Beginning of formation of constructional shoreface and estuary mouth shoal at mouth of Kennebec River; see the upper diagram for location.*

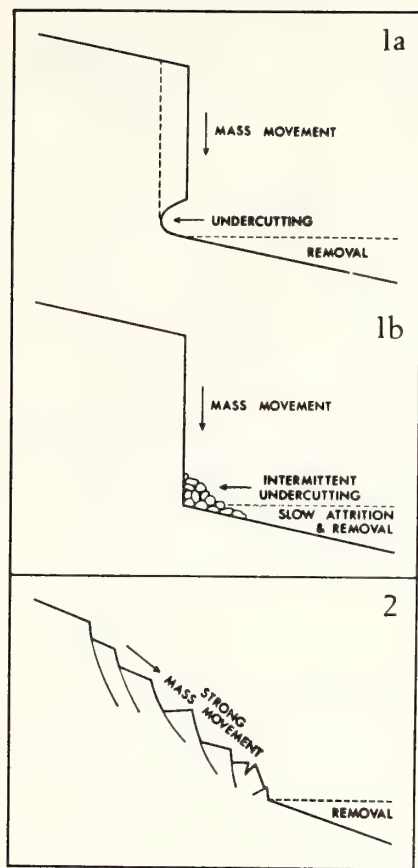


FIGURE 46. Diagrammatic representation of major processes of cliff retreat and evolution. (1a) Undercutting and rapid removal of collapsed material. (1b) Undercutting and slow removal of collapsed material. (2) Mass movement and removal at various rates. From Davies (1973).

bayed coasts may be distinguished on the basis of the relationship between the submarine slope and the equilibrium profile generated on it, as follows: (1) deep-water coasts where the submarine bottom passes immediately below the equilibrium profiles; (2) coasts with deep-water capes, where this is true only off capes, and (3) shallow-water coasts, where the submarine slope is everywhere above the equilibrium profile. The term "effective wave base" is probably best substituted for equilibrium profile here, for Zenkovitch concludes that sectors of coasts "above the profile of equilibrium" are those sectors that develop forms of accumulation (sandy beaches, barriers, spits, and tombolos; Fig. 47), and that shallow water coasts develop the most complex array of these features. Zenkovitch further traces subcycles of coastal evolution caused by feedback between evolving accumulation forms and the rocky substrate, or between two forms, whereby the growth of some spits into wave shadows behind headlands may distort their sub-

sequent pattern, and the growth of other spits may shield and starve younger spits, or induce yet others where none existed.

These subcycles are probably more common than the Davis-Johnson cycle, which requires an isostatic crustal movement or eustatic sea-level jump for rejuvenation. They may be observed on all stable rocky coasts undergoing transgression by postglacial sea-level rise. Such coasts probably do not evolve at all in the Davis-Johnson sense, but undergo steady state subsidence in a state of perpetual youth, maturity, or old age, depending on the degree of induration of the substrate and the amplitude of the inherited relief.

The relationship between the rate of sea-level rise and the relief and induration of the substrate also determines the geometry of sediment storage (Fig. 48). Cores off transgressed crystalline coasts of high relief might be expected to reveal a residual rubble overlain by fine-grained bay deposits. Overlying sand deposits of complex shape would reflect the passage of the outer shoreline with its array of accumulation forms. The upper surface of the sand horizon will have been beveled at least locally by shoreward profile translation, and offshore sands or muds may locally have accumulated over the surface of marine erosion. Off high crystalline coasts, the full sequence will rarely develop and will be completely missing off capes, where surf-rounded boulders may litter bare rock surfaces for kilometers offshore. Pocket beaches and spits may locally survive the transgressive process relatively intact; a rock-tied spit cannot retrograde with the ease of a low coast barrier.

On steep coasts transgressive deposits may be minimal. On steep coasts with very narrow shelves, submarine canyons may penetrate almost to the shoreface, to tap the littoral drift, through such gravity processes as sand creep. On steep deep-water coasts, prisms of beach shingle intermittently cascade to bathyal depths down steep rock slopes that may be erosion-modified fault scarps; sediment passes through the coastal zone by gravity bypassing (Fig. 49). As the coast is lower and softer, so will the sequence more nearly resemble the uniform sequence typical of the low coast transgression. Bay muds will more nearly resemble lagoonal muds, capped perhaps by nearly uniform sheets of backbarrier and shelf sands instead of lenticular remnants of spits and tombolos.

Regressive deposits occur on some rocky coasts, as a consequence of the Late Holocene reduction in the rate of sea-level rise, where sediment input is sufficient to reverse the sense of shoreline migration. In extreme cases, alluvial gravel cones may build out across the transgressive deposits. Boulderly topset beds may pass into foreset sands and then into bottomset sands within a few hun-

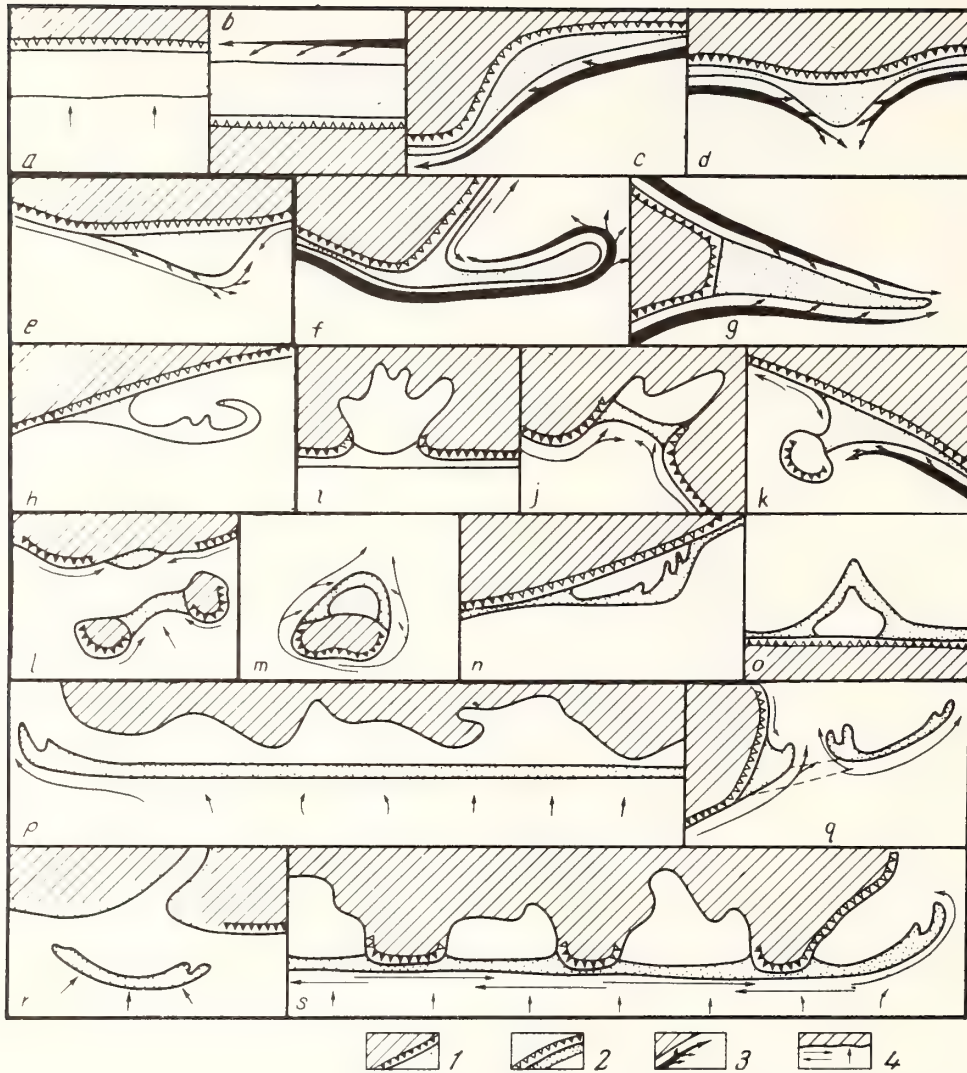


FIGURE 47. Types of coastal accumulation forms, according to Zenkovitch (1967). Fringing: a, beach nourished from offshore; b, beach nourished from alongshore; c, beach filling an indentation; d, cusped beach with bilateral nourishment; e, asymmetrical, cusped beach with bilateral nourishment, attached at one end; f, spit with unilateral nourishment; g, arrow (spit with bilateral nourishment); h, spit on smooth coast; i, bay mouth barrier; j, midbay barrier; k,

tombolo; l, interisland tombolo, doubly attached; m, looped spit with bilateral nourishment; n, looped spit with unilateral nourishment; o, cusped spit, detached; p, barrier island; q, barrier island resulting from cutting of inlet; r, estuary mouth swash bar; s, barrier sequence. Symbols: (1) mainland and active cliff; (2) dead cliff and coast with beach; (3, 4) major and minor transport directions.

dred meters. On steep, unstable coasts, such masses may periodically slump down the submarine slopes to the basin floor.

## SUMMARY

In considering coastal sediment transport, it is convenient to divide the movement of sand into an onshore-

offshore component and a coast-parallel component. Onshore-offshore transport occurs in two provinces. In the nearshore province of beach, longshore trough, plunge point bar, and upper shoreface, onshore-offshore transport is controlled by the regime of shoaling and breaking waves. Breakpoint bars are initiated during the waning phases of storms. During the ensuing fair-weather period they tend to migrate onshore, and weld



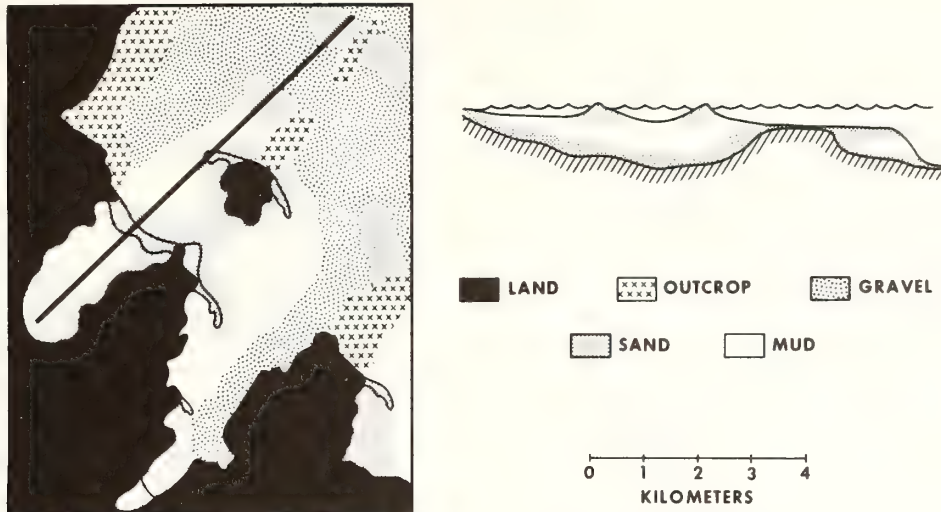


FIGURE 48. *Hypothetical stratigraphy of a rocky coast undergoing transgression.*

to the berm. The high, steep waves of storms tend to strip sand from the beach and transport it out to the surf zone, and the cycle begins anew. The cycle tends to be linked to the cycle of seasons in that offshore transport dominates during the period of winter storms, while onshore transport tends to dominate during the summer season of fair weather. The lower shoreface is a second province subject to onshore-offshore transport. The corresponding hydraulic regime is the zone of friction-dominated unidirectional flow that constitutes the coastal boundary of the shelf flow field. During storms (or peak tidal flows) velocity in this zone may be more intense than in the zone of quasi-geostrophic flow further offshore. Downwelling and a seaward component of bottom flow may occur in this zone during some storm flows, at the same time that sand is moving seaward in the surf zone, so that sand is transported off the shoreface altogether.

The interrelated behavior patterns of the zone of shoaling and breaking waves and zone of friction-dominated flows give rise on many coasts to a long-term cyclic pattern of advance or retreat of the coastal profile. The upper shoreface undergoes net aggradation and progradation over a period of years tending toward the ideal wave-graded profile. A major storm or period of severe storms will result in large-scale seaward transport of sand, causing flattening and significant landward translation of the profile. On coasts experiencing a net littoral drift surplus, fair-weather progradation is more effective than storm erosion, and the profile translates seaward and (in compensation for postglacial sea-level rise) upward. On coasts experiencing a net littoral drift deficit,

the storm regime controls the offshore-onshore sand budget, and the coastal profile undergoes landward and upward translation through a process of erosional shoreface retreat. The debris resulting from this process nourishes the leading edge of the surficial sand sheet that mantles the shelf.

The cycle of onshore-offshore transport is superimposed on a much more intensive flux of sand parallel to the beach, under the impetus of the wave-driven littoral flows, and wind- and tide-driven coastal currents. As a result, there is an innate tendency toward two-dimensionality of the shoreface, in that successive downcoast profiles tend to be very similar. Headlands experience a greater littoral wave energy density, greater breaker angles, and decreasing littoral sand discharge along the beach toward the adjoining bay. A pattern of transport away from headlands toward bays is superimposed on a regional direction of littoral sand transport determined by the prevailing direction of deep-water wave approach. The resulting alternation of littoral drift divergences and convergences may impose a three-dimensionality on an unconsolidated coast in the form of alternate cusped forelands and zetaform bays. Three-dimensionality may also be inherited from the relief of a rocky surface undergoing transgression, or may be induced on an unconsolidated coast in the form of constructional river mouths and tidal inlets.

The beach and shoreface comprise major reservoirs of sand in the coastal sediment transport system. During a transgression, the superimposition of a straight, wave-maintained upper shoreface on an irregular surface results in the formation of two shorelines. An inner, la-

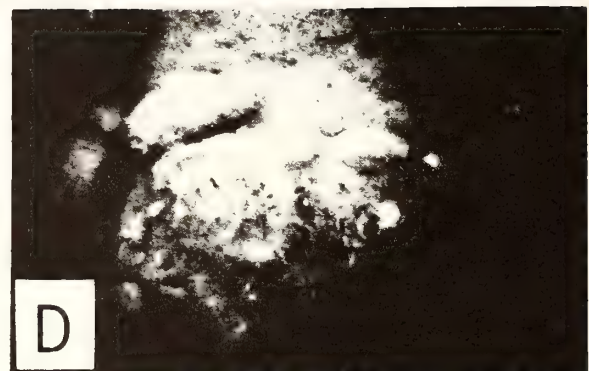
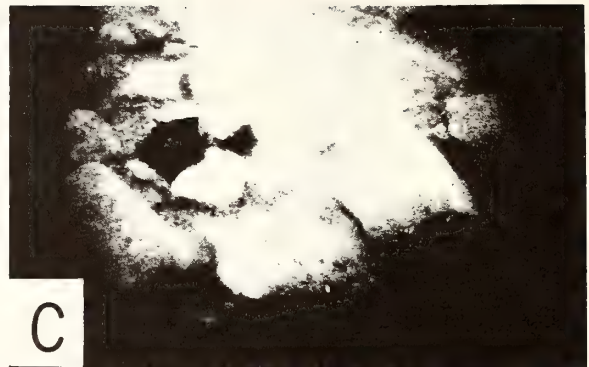
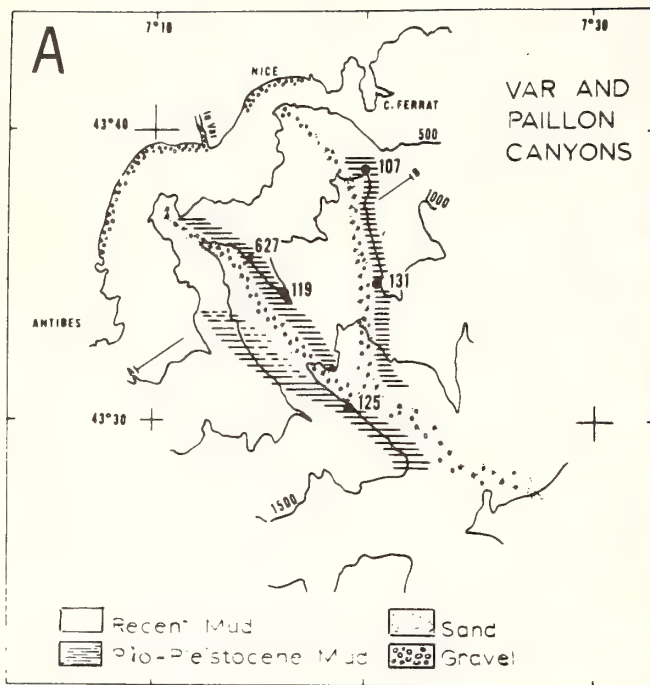


FIGURE 49. Gravity bypassing on a recently formed continental margin, Provençal coast of France. (A) Axial facies of the Var and Paillon canyons. (B) Paillon River mouth (left) and pebble beach, Baie des Anges, Nice. (C, D) Boulder (up to 50 cm) mud

admixture at diving locality shown in (B); depth 25 m. (E) Large blocks of Jurassic limestone overgrown with *Poseidonia* near Cap Ferrat. From Stanley (1969).

goonal shoreline approximates the intersection of still water level with the dissected subaerial surface undergoing erosion. An outer, oceanic shoreline of barrier spits and islands results from (1) the detachment of drift-nourished, wave-maintained beaches from the mainland as the rising sea floods the swales behind them, and (2) the lateral propagation of the shoreface from headlands across the mouths of adjoining bays. Sand is also stored in shoals that form at littoral drift convergences,

and in oblique-tending, shoreface-connected sand ridges that form at the foot of the shoreface in response to the storm wave regime and storm coastal currents. Where the littoral drift system intersects with the river- and tide-driven jets of river mouths and inlets, sand is stored in arcuate, seaward-convex shoals whose crests bear complex patterns of interdigitating ebb and flood channels, separated by sand ridges that build into the intertidal zone as swash platforms.

## REFERENCES

- Allen, J. R. L. (1968a). *Current Ripples*. Amsterdam: North-Holland, 433 pp.
- Allen, J. R. L. (1968b). The nature and origin of bedform hierarchies. *Sedimentology*, **10**: 161-182.
- Allersma, E. (1972). Mud on the oceanic shelf off Guiana. In *Symposium on Investigations and Resources of the Caribbean Sea and Adjacent Regions*. UNESCO, Paris (Unipub, N.Y.), pp. 193-203.
- Assaf, G., R. Gerard, and A. L. Gordon (1971). Some mechanisms of oceanic mixing revealed in aerial photographs. *J. Geophys. Res.*, **76**(27): 6550-6572.
- Bascom, W. N. (1951). The relationship between sand size and beach slope. *Trans. Am. Geophys. Union*, **32**: 866-874.
- Beall, A. O. (1968). Sedimentary processes operative along the western Louisiana shoreline. *J. Sediment. Petrol.*, **38**: 869-877.
- Beardsley, R. C. and B. Butman (1974). Circulation on the New England continental shelf: Response to strong winter storms. *Geol. Res. Lett.*, **1**: 181-184.
- Bernard, H. A. and R. J. Leblanc (1965). Resume of the Quaternary geology of the Northwest Gulf of Mexico Province. In H. E. Wright, Jr. and D. J. Frey, eds., *The Quaternary of the United States*. Princeton: Princeton Univ. Press, pp. 137-185.
- Bruun, P. (1954). Migrating sand waves and sand humps, with special reference to investigations carried on in the Danish North Sea coast. *Conf. Coastal Eng., 5th Proc.*, 460-468.
- Bruun, P. (1962). Sea level rise as a cause of shore erosion. *Proc. ASCE J. Waterw. Harbors Div.*, **88**: 117-130.
- Byrne, R. J., P. Bullock, and D. G. Tyler (in press a). Response characteristics of a tidal inlet: A case study. In M. O. Hayes, ed., *Second International Estuarine Conference Proc., Myrtle Beach, S.C., Oct. 15-18, 1973*: New York, Academic Press.
- Byrne, R. J., J. T. De Alteris, and P. A. Bullock (in press b). Channel stability in tidal inlets. *14th Conf. Coastal Eng. Proc., Copenhagen, 1974*.
- Caston, V. N. D. (1972). Linear sand banks in the southern North Sea. *Sedimentology*, **18**: 63-78.
- Caston, V. N. D. and A. H. Stride (1970). Tidal sand movement between some linear sand banks in the North Sea off northeast Norfolk. *Mar. Geol.*, **9**: M38-M42.
- Charnell, R. L. and D. V. Hansen (1974). *Summary and Analysis of Physical Oceanography Data from the New York Bight Apex Collected During 1969-70*. MESA Rept. 74-3, National Oceanic and Atmospheric Administration, Washington, D.C.: U.S. Govt. Printing Office, 44 pp.
- Clifton, H. E., R. E. Hunter, and R. L. Phillips (1971). Depositional structures and processes in the non-barred, high energy nearshore. *J. Sediment. Petrol.*, **41**: 651-670.
- Colquhoun, D. J. (1969). *Geomorphology of the Lower Coastal Plain of South Carolina*. MS-15, South Carolina Development Board, Div. Geol., 36 pp.
- Cook, D. O. (1969). Occurrence and geologic work of rip-currents in southern California. *J. Sediment. Petrol.*, **39**: 781-786.
- Cook, D. O. and D. S. Gorsline (1972). Field observations of sand transport by shoaling waves. *Mar. Geol.*, **13**: 31-55.
- Csanady, G. T. and J. T. Scott (1974). Baroclinic coastal jets in Lake Ontario during IFYGL. *J. Phys. Oceanogr.*, **4**: 524-541.
- Curry, J. R. (1964). Transgressions and regressions. In R. L. Miller, ed., *Papers in Marine Geology—Shepard Commemorative Volume*. New York: Macmillan, pp. 175-203.
- Curry, J. R., F. J. Emmel, and P. J. S. Crampton (1969). Lagunas costeras, un simposio. In *Mem. Simp. Int. Lagunas Costeras. UNAM-UNESCO, Nov. 28-30, 1967, Mexico, D.F.*, pp. 63-100.
- Davies, J. L. (1958). Wave refraction and the evolution of curved shorelines. *Geogr. Stud.*, **5**: 1-14.
- Davies, J. L. (1973). *Geographical Variation in Coastal Development*. New York: Hafner, 204 pp.
- Davis, R. A. and W. T. Fox (1972). Coastal process and near-shore sand bars. *J. Sediment. Petrol.*, **42**: 401-412.
- Davis, R. A., W. T. Fox, M. O. Hayes, and J. C. Boothroyd (1972). Comparison of ridge and runnel systems in tidal and non-tidal environments. *J. Sediment. Petrol.*, **32**: 413-421.
- Davis, W. M. (1909). *Geographical Essays*, 1954 Dover edition. New York: Dover Publications, 777 pp.
- Dolan, R. (1971). Coastal landforms: Crescentic and rhythmic. *Geol. Soc. Am. Bull.*, **82**: 177-180.
- Duane, D. B., M. E. Field, E. P. Meisburger, D. J. P. Swift, and S. J. Williams (1972). Linear shoals on the Atlantic inner continental shelf, Florida to Long Island. In D. J. P. Swift, D. B. Duane, and O. H. Pilkey, eds., *Shelf Sediment Transport: Process and Pattern*. Stroudsburg, Pa.: Dowden, Hutchinson & Ross, pp. 447-499.
- Ekman, V. W. (1905). On the influence of the earth's rotation on ocean currents. *Ark. J. Mat., Astron. Phys.*, **2**: 1-53.
- Emery, K. O. (1968). Relict sediments on continental shelves of world. *Am. Assoc. Pet. Geol. Bull.*, **52**: 445-464.
- Faller, A. J. (1963). An experimental study of the instability of the laminar Ekman boundary layer. *J. Fluid Mech.*, **15**: 560-576.
- Faller, A. J. (1971). Oceanic turbulence and the Langmuir circulations. *Ann. Rev. Ecol. System.*, **2**: 201-233.
- Faller, A. J. and R. B. Kaylor (1966). A numerical study of the instability of the laminar Ekman boundary layer. *J. Atmos. Sci.*, **23**: 466-480.
- Farmer, D. G. (1971). A computer simulation model of sedimentation in a salt wedge estuary. *Mar. Geol.*, **10**: 133-143.
- Fenneman, N. M. (1902). Development of the profile of equilibrium of the subaqueous shore terrace. *J. Geol.*, **10**: 1-32.
- Fisher, J. J. (1968). Barrier island formation: Discussion. *Geol. Soc. Am. Bull.*, **79**: 1421-1426.
- Fox, W. T. and R. A. Davis (1974). *Beach Processes on the Oregon Coast, July 1973*. Tech. Rep. 12, Office of Naval Research, Washington, D.C., 85 pp.
- Gilbert, G. K. (1890). *Lake Bonneville*. U.S. Geol. Surv. Mono. 1, 438 pp.
- Goldsmith, U., R. J. Byrne, A. H. Sallenger, and R. Driecker (in press). The influence of waves on the origin and development of the offset coastal inlets of the southern Delmarva Peninsula, Virginia. In M. O. Hayes, ed., *Second International Estuarine Conference Proceedings, Myrtle Beach, South Carolina, Oct. 15-18, 1973*. New York: Academic Press.
- Halligan, G. H. (1906). Sand movement on the New South Wales coast. *Proc. Limnol. Soc. NSW*, **31**: 619-640.
- Harrison, W. and R. M. Alamo (1964). *Dynamic Properties of Immersed Sand at Virginia Beach, Virginia*. Coastal Eng. Res. Cent., Tech. Memo. 9, pp. 1-52.
- Hayes, M. O. (1967). *Hurricanes as Geological Agents: Case Studies of Hurricanes Carla, 1961, and Cindy, 1963*. Texas Bureau of Economic Geology, Report of Investigation 61, 54 pp.

- Hayes, M. O., U. Goldsmith, and C. H. Hobbs (1970). Offset coastal inlets. In *12th Conference Coastal Engineering Proceedings*, pp. 1187-1200.
- Holliday, B. W. (1971). Observations on the hydraulic regime of the ridge and swale topography of the inner Virginia shelf. Masters Thesis, Old Dominion University, Inst. of Oceanography, Norfolk, Va.
- Howard, J. D. and H. E. Reineck (1972). Physical and biogenic sedimentary structures of the nearshore shelf. *Senckenbergiana Marit.*, 4: 81-124.
- Hoyt, J. H. (1967). Barrier island formation. *Geol. Soc. Am. Bull.*, 78: 1125-1136.
- Hoyt, J. H. (1970). Development and migration of barrier islands, northern Gulf of Mexico, discussion. *Geol. Soc. Am. Bull.*, 81: 3779-3782.
- Hoyt, J. H. and V. J. Henry (1967). Influence of island migration on barrier island sedimentation. *Geol. Soc. Am. Bull.*, 78: 77-86.
- Ingle, J. C. (1966). *The Movement of Beach Sand*. New York: American Elsevier, 221 pp.
- Johnson, D. W. (1919). *Shore Processes and Shoreline Development*. New York: Hafner (1965 facsimile), 584 pp.
- Johnson, J. W. (1949). Scale effects in hydraulic models involving wave motion. *Trans. Am. Geophys. Union*, 30: 517-527.
- Johnson, J. W. and P. S. Eagleson (1966). In A. J. Ippen, ed., *Estuary and Coastline Hydrodynamics*. New York: McGraw-Hill, pp. 404-492.
- Keulegan, G. H. (1948). *An Experimental Study of Submarine Sand Bars*. Beach Erosion Board Tech. Rep. 3, 42 pp.
- King, C. A. M. (1972). *Beaches and Coasts*. New York: St. Martins Press, 570 pp.
- King, C. A. M. and W. W. Williams (1949). The formation and movement of sand bars by wave action. *Geogr. J.*, 113: 70-85.
- King, D. B., Jr. (1974). *The Dynamics of Inlets and Bays*. Tech. Rep. 22, College of Engineering, University of Florida, Gainesville, 82 pp.
- Kraft, J. C., R. E. Sheridan, R. D. Moose, R. N. Strom, and C. B. Weil (1974). Middle-Late Holocene evolution of the morphology of a drowned estuary system—the Delaware Bay. In *International Symposium on Interrelationships of Estuarine and Continental Shelf Sedimentation*. Inst. Géol. du Bassin d'Aquitaine, July 9-14, 1973, pp. 297-306.
- Langfelder, J., D. Stafford, and M. Amein (1968). *A Reconnaissance of Coastal Erosion in North Carolina*. Dept. Civil Eng., North Carolina State University, Raleigh, N.C., 127 pp.
- Langford-Smith, T. and B. G. Thom (1969). New South Wales coastal morphology. *J. Geol. Soc. Aust.*, 16: 572-580.
- Langmuir, I. (1925). Surface motion of water induced by the wind. *Science*, 87: 119-123.
- Leopold, L. B., M. G. Wolman, and J. P. Miller (1964). *Fluvial Processes in Geomorphology*. San Francisco: Freeman, 522 pp.
- Longuet-Higgins, M. S. (1953). Mass transport in water waves. *Phil. Trans. Roy. Soc. London*, 245: 535-581.
- Ludwick, J. C. (in press). Tidal currents, sediment transport, and sandbanks in Chesapeake Bay entrance, Virginia. In M. O. Hayes, ed., *Second International Estuarine Conf. Proc. Myrtle Beach, S.C., Oct. 15-18, 1973*: New York, Academic Press.
- McGee, W. D. (1890). Encroachments of the sea. *The Forum*, 9: 437-449.
- McHone, J. F., Jr. (1972). Morphologic time series from a submarine sand ridge on the south Virginia coast. Masters Thesis, Old Dominion University, Norfolk, Va., 59 pp.
- McKinney, T. F., W. L. Stubblefield, and D. J. P. Swift (1974). Large scale current lineations on the Great Egg shoal retreat massif: Investigations by sidescan sonar. *Mar. Geol.*, 17: 79-102.
- McMaster, R. L. and L. E. Garrison (1967). A submerged Holocene shoreline near Block Island, Rhode Island. *Mar. Geol.*, 75: 335-340.
- May, J. P. and W. F. Tanner (1973). The littoral power gradient and shoreline changes. In D. R. Coates, ed., *Publications in Geomorphology*. Binghamton: State University of New York, 404 pp.
- Miller, R. L. and J. M. Zeigler (1958). A model relating dynamics and sediment pattern in equilibrium in the region of shoaling waves, breaker zone, and foreshore. *J. Geol.*, 66: 417-441.
- Miller, R. L. and J. M. Zeigler (1964). A study of sediment distribution in the zone of shoaling waves. In R. L. Miller, ed., *Papers in Marine Geology—Shepard Commemorative Volume*. New York: MacMillan, pp. 133-153.
- Moody, D. W. (1964). Coastal morphology and processes in relation to the development of submarine sand ridges off Bethany Beach, Delaware. Ph.D. Thesis, Johns Hopkins University, Baltimore, 167 pp.
- Moore, G. T. (1970). Role of salt wedge in bar finger sand and delta development. *Am. Assoc. Pet. Geol. Bull.*, 54: 326-333.
- Mota-Oliveira, I. B. (1970). Natural flushing ability in tidal inlets. *Proc. 12th Coastal Eng. Conf., Washington, D.C.*, pp. 1827-1845.
- Murray, S. P. (1967). Control of grain dispersion by particle size and wave state. *J. Geol.*, 75: 612-634.
- Murray, S. P. (1970). Bottom currents near the coast during Hurricane Camille. *J. Geophys. Res.*, 75: 4579-4582.
- Neumann, G. and W. J. Pierson, Jr. (1966). *Principles of Physical Oceanography*. Englewood Cliffs, N.J.: Prentice Hall, 545 pp.
- Neveskii, E. N. (1969). Some data on the postglacial evolution of Karkinit Bay and the accumulation of bottom sediments within it. In V. V. Longinov, ed., *Dynamics and Morphology of Seacoasts*. Akademiya Nauk SSSR Trudy Instituta Okeanologii, Vol. 48, 371 pp., translated from Russian by Israel Program for Scientific Translations; reproduced by the Clearinghouse for Federal Scientific and Technical Information, Springfield, Va., pp. 92-110.
- Niedoroda, A. W. and W. F. Tanner (1970). Preliminary study of transverse bars. *Mar. Geol.*, 9: 41-62.
- Oaks, R. Q., Jr. and N. K. Coch (1963). Pleistocene sealevels, southeastern Virginia. *Science*, 140: 979-983.
- Oertel, G. F. (1972). Sediment transport of estuary entrance shoals and the formation of swash platforms. *J. Sediment. Petrol.*, 42: 858-863.
- Oertel, G. F. and J. D. Howard (1972). Water circulation and sedimentation at estuary entrances on the Georgia coast. In D. J. P. Swift, D. B. Duane, and O. H. Pilkey, eds., *Shelf Sediment Transport: Process and Pattern*. Stroudsburg, Pa.: Dowden, Hutchinson & Ross, pp. 411-427.
- Otvos, E. G. (1969). A sub-recent beach ridge complex in southern Louisiana. *Geol. Soc. Am. Bull.*, 80: 2353-2358.
- Otvos, E. G. (1970a). Development and migration of barrier islands, northern Gulf of Mexico. *Geol. Soc. Am. Bull.*, 81: 241-246.
- Otvos, E. G. (1970b). Development and migration of barrier islands, northern Gulf of Mexico: Reply. *Geol. Soc. Am. Bull.*, 81: 3783-3788.
- Pierce, J. W. and D. J. Colquhoun (1970). Holocene evolution of

- a portion of the North Carolina coast. *Geol. Soc. Am. Bull.*, **81**: 3697-3714.
- Postma, H. (1967). Sediment transport and sedimentation in the marine environment. In G. H. Lauff, ed., *Estuaries*. Washington, D.C.: Am. Assoc. Adv. Sci., pp. 158-180.
- Price, W. A. (1954). Dynamic environments: Reconnaissance mapping, geologic and geomorphic, of continental shelf of Gulf of Mexico. *Trans. Gulf Coast Assoc. Geol. Soc.*, **4**: 75-107.
- Price, W. A. (1955). *Correlation of Shoreline Type with Offshore Bottom Conditions*. Dept. of Oceanography, Texas A&M University, Project 65: 75-107.
- Reineck, H. E. and I. B. Singh (1971). Der Golf von Gaeta (Tyrrhenisches Meer). III. Die gefuge von vorstrand—und schelfsedimenten. *Senckenbergiana Marit.*, **3**: 135-183.
- Robinson, A. H. W. (1966). Residual currents in relation to shoreline evolution of the East Anglian coast. *Mar. Geol.*, **4**: 57-84.
- Russell, R. C. H. and J. D. C. Osorio (1958). An experimental investigation of drift profiles in a closed channel. *Proc. 6th Conf. Coastal Eng.*, pp. 171-183.
- Schiffman, A. (1965). Energy measurements in the swash-surf zone. *Limnol. Oceanogr.*, **10**: 255-260.
- Schwartz, M. L. (1965). Laboratory study of sea level rise as a cause of shore erosion. *J. Geol.*, **73**: 528-534.
- Schwartz, M. L. (1967). The Bruun theory of sea level rise as a cause of shore erosion. *J. Geol.*, **75**: 76-92.
- Schwartz, M. L. (1968). The scale of shore erosion. *J. Geol.*, **76**: 508-517.
- Schwartz, M. L. (1973). *Barrier Islands*. Stroudsburg, Pa.: Dowden, Hutchinson & Ross, 451 pp.
- Shepard, F. P. (1950). *Longshore-Bars and Longshore-Troughs*. Beach Erosion Board Tech. Memo. 15, 32 pp.
- Silvester, R. (1974). *Coastal Engineering II*. New York: American Elsevier, 338 pp.
- Smith, J. D. and T. S. Hopkins (1972). Sediment transport on the continental shelf off of Washington and Oregon in the light of recent current meter measurements. In D. J. P. Swift, D. B. Duane, and O. H. Pilkey, eds., *Shelf Sediment Transport: Process and Pattern*. Stroudsburg, Pa.: Dowden, Hutchinson & Ross, pp. 143-180.
- Sonu, C. J. and J. L. van Beek (1971). Systematic beach changes in the outer banks, North Carolina. *J. Geol.*, **74**: 416-425.
- Sonu, C. J., J. M. McCloy, and D. S. McArthur (1967). Longshore currents and nearshore topographies. *Proc. 10th Conf. Coastal Eng.*, pp. 55-549.
- Stahl, L., J. Koczan, and D. Swift (1974). Anatomy of a shoreface-connected ridge system on the New Jersey shelf: Implications for genesis of the shelf surficial sand sheet. *Geology*, **2**: 117-120.
- Stanley, D. J. (1969). Submarine channel deposits and their fossil analogs (fluxoturbidites). In D. J. Stanley, ed., *The New Concepts of Continental Margin Sedimentation*. Washington, D.C.: Am. Geol. Inst., pp. DJS-9-1 to DJS-9-17.
- Strahler, A. (1963). *The Earth Sciences*. New York: Harper and Row, 681 pp.
- Stubblefield, W. L., J. W. Lavelle, T. F. McKinney, and D. J. P. Swift (1975). Sediment response to the hydraulic regime on the central New Jersey shelf. *J. Sediment Petrol.*, **45**: 337-358.
- Swift, D. J. P. (1973). Delaware Shelf Valley: Estuary retreat path, not drowned river valley. *Geol. Soc. Am. Bull.*, **84**: 2743-2748.
- Swift, D. J. P. (1975a). Barrier island genesis: Evidence from the Middle Atlantic Shelf of North America. *Sediment. Geol.*, **14**: 1-43.
- Swift, D. J. P. (1975b). Tidal sand ridges and shoal retreat massifs. *Mar. Geol.*, **18**: 105-134.
- Swift, D. J. P., D. B. Duane, and T. McKinney (1974). Ridge and swale topography of the Middle Atlantic Bight: Secular response to Holocene hydraulic regime. *Mar. Geol.*, **15**: 227-247.
- Swift, D. J. P., B. W. Holliday, N. F. Avignone, and G. Shideler (1972a). Anatomy of a shoreface ridge system, False Cape, Virginia. *Mar. Geol.*, **12**: 59-84.
- Swift, D. J. P., J. W. Kofoed, F. P. Saulsbury, and P. Sears (1972b). Holocene evolution of the shelf surface, central and southern Atlantic coast of North America. In D. J. P. Swift, D. B. Duane, and O. H. Pilkey, eds., *Shelf Sediment Transport: Process and Pattern*. Stroudsburg, Pa.: Dowden, Hutchinson & Ross, pp. 499-574.
- Swift, D. J. P., R. B. Sanford, C. E. Dill, Jr., and N. F. Avignone (1971). Textural differentiation on the shoreface during erosional retreat of an unconsolidated coast, Cape Henry to Cape Hatteras, North Carolina. *Sedimentology*, **16**: 221-250.
- Swift, D. J. P. and P. Sears (1974). Estuarine and littoral depositional patterns in the surficial sand sheet, central and southern Atlantic shelf of North America. In *International Symposium on Interrelationships of Estuarine and Continental Shelf Sedimentation*. Inst. Géol. du Bassin d'Aquitaine, Bordeaux, Mém. 7, pp. 171-189.
- Tanner, W. F. (1961). Offshore shoals in an area of energy deficit. *J. Sediment. Petrol.*, **31**: 87-95.
- Tanner, W. F., R. G. Evans, and C. W. Holmes (1963). Low energy coast near Cape Romano, Florida. *J. Petrol.*, **33**: 713-722.
- Todd, T. W. (1968). Dynamic diversion: Influence of longshore current-tidal flow interaction on chenier and barrier island plains. *J. Sediment. Petrol.*, **38**: 734-746.
- Valentin, H. (1954). Der landverlust in Holderness, Ostengland von 1852 bis 1952. *Die Erde*, **6**: 296-315. See also, Land loss at Holderness, 1852-1952. In J. D. Steers, ed., *Applied Coastal Morphology*. Cambridge, Mass.: MIT Press, 1971, pp. 116-137.
- Van Straaten, L. M. J. U. (1965). Coastal barrier deposits in south and north Holland—in particular in the area around Scheveningen and Ijmuden. *Meded. Geol. Sticht.*, NS **17**: 41-75.
- Visher, G. S. (1969). Grain size distribution and depositional processes. *J. Sediment. Petrol.*, **34**: 1074-1106.
- Weil, C. B., R. D. Moose, and R. E. Sheridan (1974). A model for the evolution of linear tidal built sand ridges in Delaware Bay, U.S.A. In G. Allen, ed., *Estuary and Shelf Sedimentation: A Symposium*. University of Bordeaux, July 1973.
- Wells, D. R. (1967). Beach equilibrium and second order wave theory. *J. Geophys. Res.*, **72**: 497-509.
- Wright, L. D. and J. M. Coleman (1972). River delta morphology: Wave climate and the role of the subaqueous profile. *Science*, **176**: 282-284.
- Wright, L. D. and J. M. Coleman (1974). Mississippi River mouth processes: Effluent dynamics and morphologic development. *J. Geol.*, **82**: 751-778.
- Zenkovitch, V. P. (1967). *Processes of Coastal Development*. New York: Wiley, 738 pp.

Offprints from:

*Marine Sediment Transport and Environmental Management*

Edited by D. J. Stanley and D. J. P. Swift

Copyright 1976 by John Wiley & Sons, Inc.

## Continental Shelf Sedimentation

DONALD J. P. SWIFT

*Atlantic Oceanographic and Meteorological Laboratories, Miami, Florida*

The preceding chapter considered in detail the nature of hydraulic process and substrate response along the coast. This chapter examines patterns of sedimentation on the shelf as a whole. It reexamines the coastal boundary of the shelf as a source of sediment for the rest of the shelf, and as a zone which thus regulates the rate and character of sedimentation on the shelf surface. Chapter 14 described a "littoral energy fence" imposed upon coastal sedimentation by the landward-directed asymmetry of wave surge in shoaling water, which causes sediment to be retained on the shoreface. This chapter concerns itself with the mechanisms by which this dynamic barrier is penetrated, along the shoreface or at river mouths, and by which sediment is injected into the shelf dispersal system. The relative efficiencies of shoreface and river mouth bypassing during periods of transgression on one hand, and during periods of regression on the other are described. These varying efficiencies lead to two distinct shelf regimes: a passive regime in which the shelf sand sheet is generated by erosional shoreface retreat (autochthonous sedimentation) and a more active regime in which river mouth bypassing causes deposition across the shelf surface (allochthonous sedimentation). The chapter analyzes the transport patterns associated with these two regimes, and the resulting patterns of morphology, stratigraphy, and grain-size distribution. Portions of the material in this chapter have been presented elsewhere (Swift, 1974).

### MODELS OF SHELF SEDIMENTATION

One of the first comprehensive models for the genesis of clastic sediments on continental shelves was a by-product of Douglas Johnson's (1919, p. 211) attempt to apply Davis' geomorphic cycle of youth, maturity, and old age to the continental shelf (see p. 277). Johnson saw the shelf water column and the shelf floor as a system in dynamic equilibrium, in which the slope and grain size of the sedimentary substrate at each point control, and are controlled by, the flux of wave energy into the bottom. He described the resulting surface as an exponential curve in profile, concave up, with the steeper segment being the shoreface. Grain size was considered to decrease as a function of increasing depth with distance from shore, as a consequence of the diminishing input of wave energy into the seafloor. The model derived its sediment from coastal erosion rather than from river input, a more broadly applicable interpretation than many subsequent textbooks have realized.

Despite its qualitative expression and limited applicability, the model was in advance of its time in its dynamical systems approach. However, this model could not withstand in its initial form the subsequent flood of data on the characteristic of shelf sediments. Shepard (1932) was the first to challenge it, noting that nautical charts of the world's shelves bore notations indicating that most shelves were veneered with a

complex mosaic of sediment types, rather than a simple seaward-fining sheet. He suggested that these patches were deposited during Pleistocene low stands of the sea, rather than during Recent time. Emery (1952, 1968) raised this concept to the status of a new conceptual model. He classified shelf sediments on a genetic basis, as *authigenic* (glauconite or phosphorite), *organic* (foraminifera, shells), *residual* (weathered from underlying rock), *relict* (remnant from a different earlier environment such as a now submerged beach or dune), and *detrital*, which includes material now being supplied by rivers, coastal erosion, and colian or glacial activity. On most shelves, a thin nearshore band of modern detrital sediment is supposed to give way seaward to a relict sand sheet veneering the shelf surface.

A third, more generalized model for shelf sedimentation has been primarily concerned with the resulting stratigraphy. It incorporates elements of both the Johnson and Emery models. Like the Johnson model, it views the shelf surface as a dynamic system in a state of equilibrium with a set of process variables. The rate of sea-level change, however, is one of these variables; hence the effects of post-Pleistocene sea-level rise, as noted by Shepard and Emery, may be accounted for. The model may be referred to as the transgression-regression model, since it is generally expressed in these terms, or the coastal model, since it focuses on the behavior of this dynamic zone. It was first explicitly formulated by Grabau (1913), and more recently by Curray (1964) and Swift et al. (1972). In this model, the rate of sediment input to the continental shelf  $S$ , the character of the sediment  $G$  (grain size and mineralogy), the rate of energy input  $E$ , the sense and rate of relative sea-level change  $R$ , and slope  $L$  are seen as variables that govern the sense of shoreline movement (transgression or regression) and ultimately the character of shelf deposits.

The relationship may be expressed in quasi-quantitative form as

$$\frac{SG}{E} - \frac{R}{L} \propto T$$

The processes controlling shelf sedimentation are much too complex to be adequately described by this equation and there is no way to evaluate its variables adequately. The expression is useful, however, in helping to sort out relationships. The first term,  $SG/E$ , might be called the effective rate of coastal deposition. It increases with increasing  $S$ , the rate at which sediment is delivered to the shore. It increases with increasing grain size  $G$ , since coarser sediments are less easily bypassed across the shelf. It decreases with increasing  $E$ , the rate of wind and tidal energy input, since a more

rigorous hydraulic climate causes more sediment to be bypassed across the shelf.

The second term,  $R/L$ , might be called the effective rate of sea-level movement. It increases with increasing  $R$ , the absolute rate of sea-level movement (eustatic or tectonic), but decreases with increasing slope,  $L$ , of the coast. The steeper the slope, the greater the fall of sea level must be in order for the coast to advance a given distance. Also, with a greater slope, a greater volume of sediment must be delivered to the shoreline in order for the shoreline to prograde a given distance shoreward.

The equation tells us that the rate and sense of shoreline movement,  $T$ , whether landward (negative) or seaward (positive), depends on the relationship between these two terms. Basic elements of the relationship are presented graphically in Fig. 1, according to a scheme of Curray (1964). In Fig. 2, the history of the Nayarit coast of Mexico has been plotted.

### The Coastal Boundary as a Filter: Shelf Sedimentary Regimes

The fundamental determinants of shelf sedimentation are the areal extent of the adjacent continent undergoing denudation, and its relief, climate, and drainage pattern. These factors control the quantity of sediment delivered to the shoreline, and its textural and mineralogical composition. However, the rate and sense of shoreline movement, as determined by the parameters described above, have a modulating effect on the shelf sedimentary regime.

It is helpful to think of the coastline as a "littoral energy fence" (Allen, 1970b, p. 169) in which the net landward flow associated with bottom wave surge tends

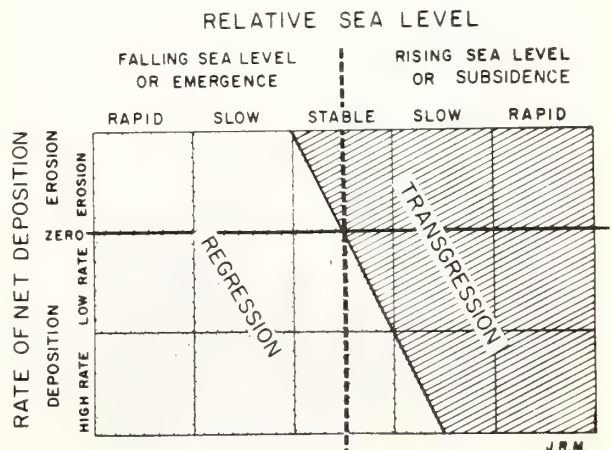


FIGURE 1. Diagram of the effects of sea-level movement and the rate of coastal deposition on lateral migration of the shoreline. See text for explanation. From Curray (1964).

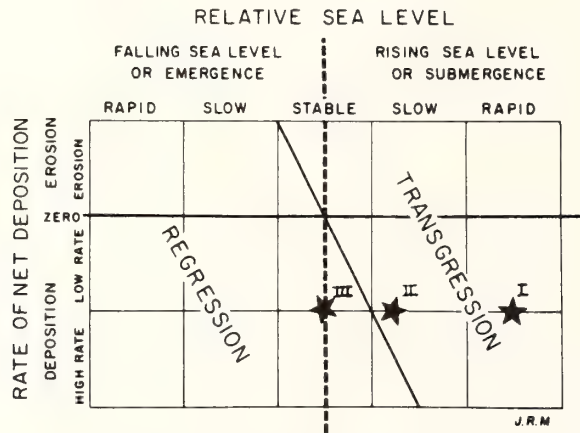
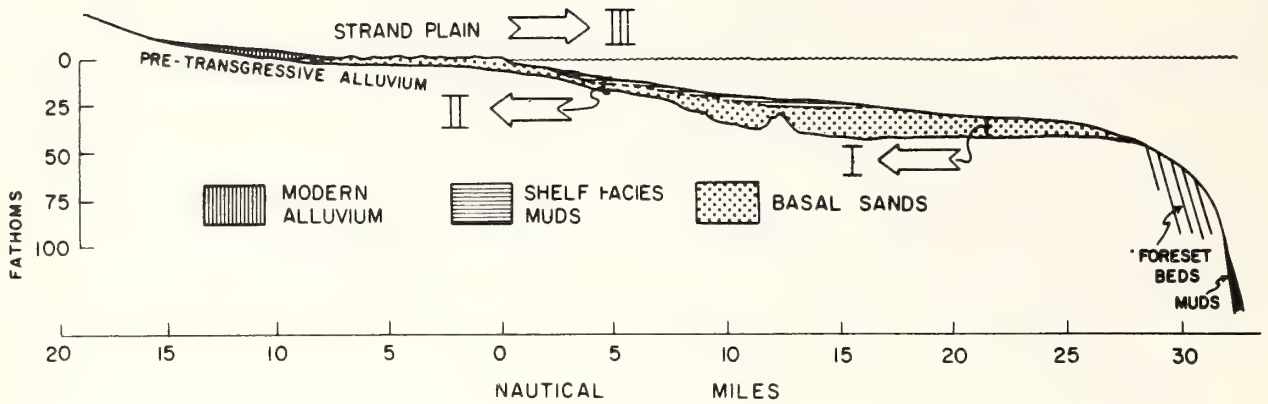


FIGURE 2. Above: Diagrammatic section off the Costa de Nayarit, Mexico. See Fig. 10A, Chapter 14 for details of coastal strati-

graphy. Below: Schematic representation of shoreline migration. From Curray (1964).

to push sediment toward the shore. There are two basic categories of “valve” which regulate the passage of sediment through this dynamic coastal barrier into the transport system of the shelf surface. The shoreface may serve as a zone of sediment bypassing. The erosional retreat of the shoreface during a marine transgression bevels the subaerial surface being transgressed (Fig. 10A, Chapter 14), and spreads the resultant debris as a thin sheet over the shelf floor. The process by which the sediment is so transferred is described in the accompanying text. The process is a passive and indirect one; the sediment that is released has undergone long-term storage as flood plain, lagoonal, or estuarine deposits, or has been derived from an earlier cycle of sedimentation.

A second, more active route by which sediment may pass through the littoral energy fence is via the ebb tidal jet or flood stage jet of a river mouth. Patterns of river mouth bypassing are illustrated in Chapter 14 (Fig. 42). River mouth bypassing is more direct than shoreface by-

passing, but sediment must still undergo storage. Sand is stored in the throat of the river mouth, and fines are stored in marginal marshes and mud flats until the period of maximum river discharge, when the salt wedge moves to the shoal crest, and stored sediment is bypassed to the shoreface of the shoal front (Wright and Coleman, 1974); see Chapter 14, Fig. 41. It may undergo a second period of storage on the shoreface and inner shelf until the period of maximum storm energy (Wright and Coleman, 1973).

The mode of operation of these valves is dependent on basic parameters of coastal sedimentation. The spacing of river mouths is the fundamental determinant of the relative roles of shoreface versus river mouth bypassing. The character of the hydraulic climate is also important; an intense tidal regime increases the efficiency of river mouth bypassing, whereas an intense wave climate increases the efficiency of shoreface bypassing.

The rate and sense of coastal translation as described in the preceding section strongly affect the relative



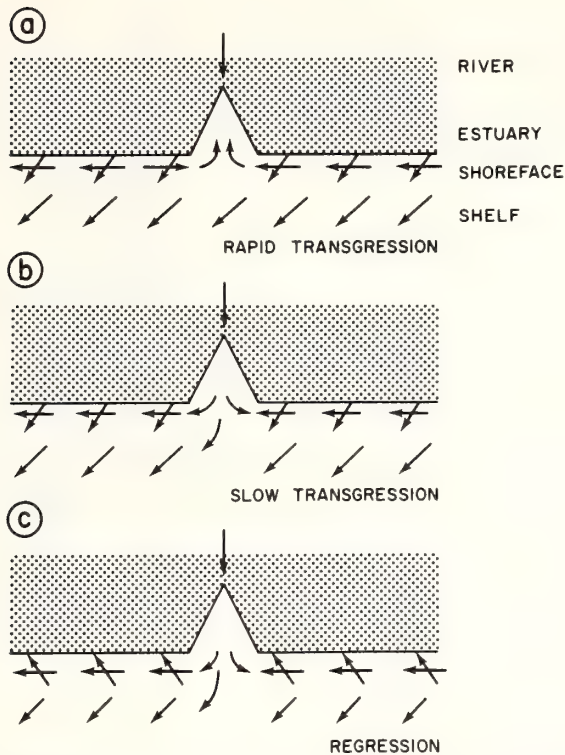


FIGURE 3. Sense of net sediment transport for (a) rapid transgression, (b) slow transgression, and (c) regression. Offshore component of transport is exaggerated for continuity. See text for explanation.

roles of river mouth and shoreface bypassing (Fig. 3). Rapid transgression results in disequilibrium estuaries which become sediment sinks (see Chapter 14, Fig. 42 and associated text), and shoreface bypassing must dominate (Fig. 3a). The resulting deposits consist of a transient veneer of surf fallout on the upper shoreface, and the residual sand sheet of the lower shoreface and adjacent shelf (see Chapter 14, Fig. 8 and discussion, p. 265). These two deposits correspond to the nearshore modern sand and shelf relict sand, respectively, of Emery (1968). Both deposits are relict in the sense that they have been eroded from a local, pre-Recent substrate, and both are modern in the sense that they have been redeposited under the present hydraulic regime. They are, in fact, palimpsest sediments (Swift et al., 1971) since they have petrographic attributes resulting from both the present and the earlier depositional environment. The term relict is best reserved for those specific textural attributes reflecting the earlier regime. Perhaps the most effective term for describing the relationship of these materials to the present depositional cycle is autochthonous (of local origin: Naumann, 1858), and a shelf sedimentary regime characterized by rapid transgression and by-

passing via shoreface erosion is described in this chapter as a regime of autochthonous shelf sedimentation.

With a slower rate of translation (Fig. 3b), estuaries can equilibrate to their tidal prisms (see Chapter 14, Fig. 42 and associated text). River mouth as well as shoreface bypassing becomes a significant source of sediment. More subtle, but equally important, is the effect of a slow transgression on the grain size of bypassed sediment. With a slower rate of shoreline translation the intra-coastal zone of estuaries and lagoons can aggrade nearly to mean sea level. The resulting surface of salt marshes (or in low latitudes, mangrove swamps), threaded by high-energy channels, tends to serve as a low-pass, or bandpass filter, in the sense that the finer fraction of the sediment load is preferentially bypassed, while the coarsest fraction (and in the bandpass case, the finest fraction as well) is preferentially trapped out. In this process, migrating channels tend to select coarse materials for permanent burial in their axes. The surfaces of the tidal interflues receive the finest material for prolonged storage or permanent burial. However, fine sands and silts are deposited as overbank levees and tend to be reentrained by the migrating channels; hence they have the highest probability of being bypassed to the shelf surface. This material is sufficiently fine to travel in suspension for long distances.

The estuaries of the Georgia coast have built a gently sloping shoreface of fine to very fine sand up to 20 km wide (Pilkey and Frankenberg, 1964; Henry and Hoyt, 1968); see Chapter 14, Fig. 13. This unusually wide and broad shoreface may be built by the combined contributions of shoreface and river mouth bypassing. Recent studies (Visher and Howard, 1974) suggest that the reversing tidal flows within the estuary constitute an efficient mechanism for the sorting of sands into size fractions, the spatial segregation of these fractions, and the bypassing of the finest sand out onto the shoreface.

There is clearly a contribution of sand from shoreface erosion; however, shoreface sands, like the adjacent shelf sands, contain trace amounts of phosphorite (Pilkey and Field, 1972), indicating erosion of the Miocene strata which underlie the shoreface between the closely spaced estuaries, and which floor the deep scour channels of the estuary mouths (Barby and Hoyt, 1964).

As the sense of coastal translation passes through stillstand to progradation (Fig. 3c), the shoreface becomes a sink rather than a mechanism for bypassing. Distributary mouths must further partition their pre-filtered load between sand sufficiently coarse to be captured by the littoral drift and buried on the shoreface, and sand fine enough to escape in suspension in the ebb

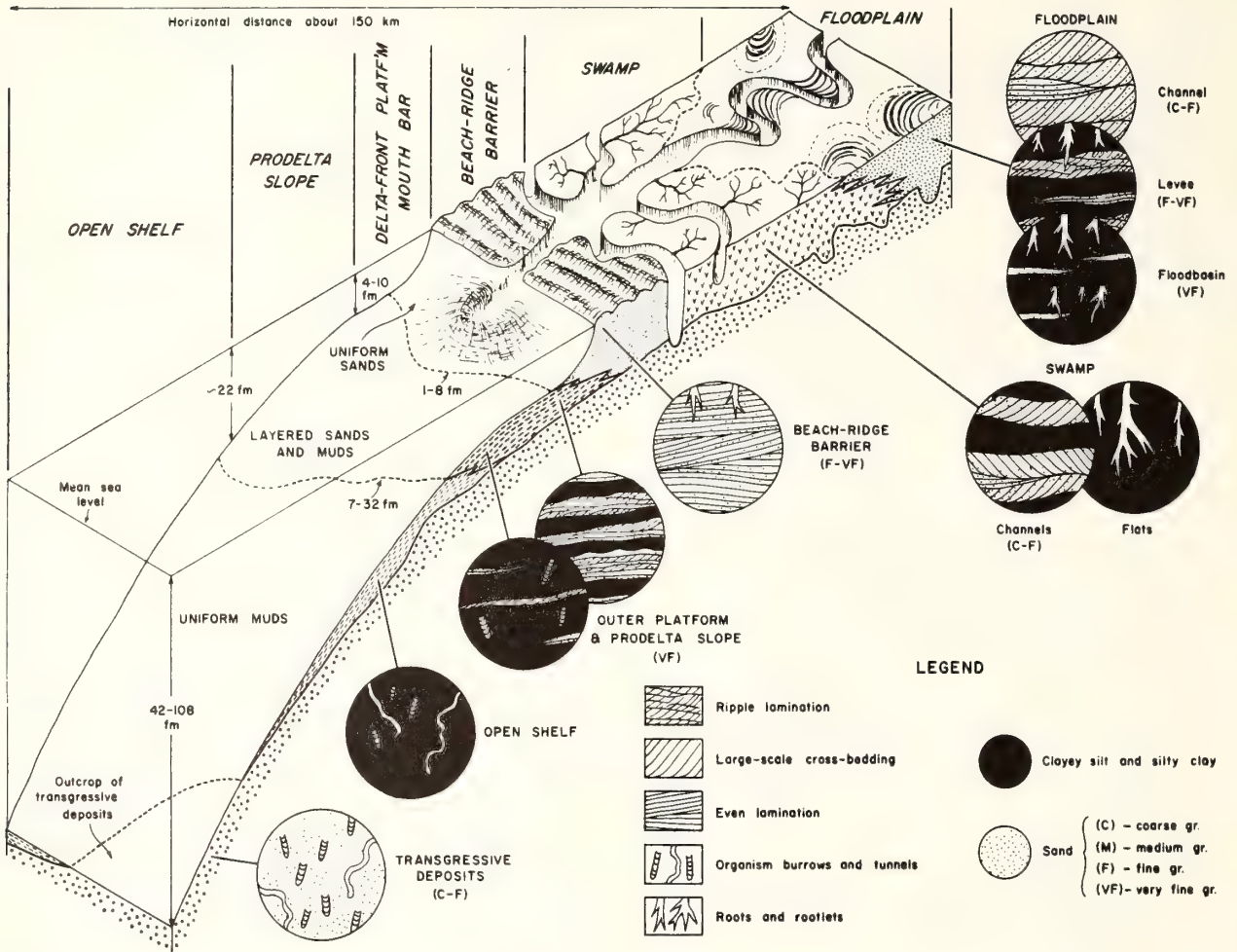


FIGURE 4. Schematic illustration of the depositional environments and sedimentary facies of the Niger Delta and Niger shelf. Progressive size sorting of sediment results in a decrease in grain

size through successive depositional environments in a seaward direction. From Allen (1970a).

tidal jet, and be entrained into the shelf dispersal system. The shoreface behaves more nearly as a sediment trap, and bypassing occurs primarily through river mouths.

The Niger-Benue delta system is one of the best studied examples of differential sediment bypassing through a prograding, deltaic environment (Allen, 1964, 1970a). The Niger-Benue river system delivers about  $0.9 \times 10^6 \text{ m}^3$  of bed load sediment and about  $16 \times 10^6 \text{ m}^3$  of suspended sediment (Allen, 1964) to its delta each year. During peak discharge from September to May, average flow velocities range from 50 to 135 cm/sec, and gravel as well as sand is in violent transport. During low stages, flow velocities decrease to 37 to 82 cm/sec, enough to transport sand and silt. In the higher part of the flood plain, the Niger is

braided; in the rest the Niger shows large meanders (Fig. 4). During high stages, levees are overtopped, crevasse develops, and bottom lands are flooded. Gravel and coarse sand are deposited as a substratum of braid bars and meander point bars, respectively, and are veneered with a top stratum of overbank clays. Silt undergoes temporary deposition in levees in the lower flood plain but these tend to be undermined, so that their deposits reenter the transport system.

Thus the flood plain environment serves as a skewed bandpass filter, with preferential bypassing of the medium and finer grades, preferential entrapment of the finest material over bank, and much coarse material being deposited in channel axes. This process continues through the tidal swamp environment, where the entrapment of fines dominates. Reversing tidal flows

generate velocities of 40 to 180 cm/sec in tidal creeks, enough to move sand and gravel. Entrapment of fines overbank in the mangrove swamps is enhanced by the phenomena of slack high water and the prolonged period of reduced velocity associated with it. Fines then deposited begin to compact, and require greater velocities to erode them than served to permit their deposition.

Major channels, which pass through the intertidal environment to the sea, must store their coarser sediment during low water stages at the foot of the salt wedge, where the landward-inclined surface of zero net motion intersects the channel floor. During high water stages, stored bottom sediment must be rhythmically flushed out of the estuary mouth by the tidal cycle. Sand coarser than the effective suspension threshold of 230  $\mu$  (Bagnold, 1966) will be deposited on the arcuate estuary mouth shoals, where, after a prolonged period of residence in the sand circulation cells of the shoal (see Chapter 10, p. 177), it leaks into the downcoast littoral drift system. Finer sand is entrained into suspension by large-scale top-to-bottom turbulence in the high-velocity estuary throat (Wright and Coleman, 1974) and will be swept seaward with the ebb tidal jet, to rain out on the inner shelf (Todd, 1968) where it is accessible to distribution by the shelf hydraulic regime.

Shelves undergoing slow transgression or regression (Figs. 3*b,c*) thus experience a contrasting regime of allochthonous shelf sedimentation (Naumann, 1858) characterized by significant river mouth bypassing. In this regime there is a massive influx of river sediment whose grain size has been modified by passage through the coastal zone. Sheets of mobile fine sand and mud stretch from the coast toward the shelf edge. Shorefaces are broad and gentle and merge imperceptibly with a shallow inner shelf.

Sedimentation on tectonic continental margins is a special case of allochthonous shelf sedimentation so distinctive as to warrant designation as a third and equal category. Shelves subject to such a regime are narrow and steep, if developed at all. River mouth bypassing and fractionation of the sediment load occur here also. Rubble subaerial fans may pass over short distances into sandy marine deltas with bottomset mud beds. Gravity dispersal becomes a significant coastal bypassing mechanism. Submarine canyons may cut completely across narrow shelves to tap the littoral drift (Shepard, 1973, p. 140) and divert sand seaward by slow or rapid mass movements. Where shelves are altogether lacking, coarse littoral prisms cascade intermittently down slopes that are nearly tectonic surfaces, to bathyal depths (Stanley, 1969). Tectonic regimes on incipient shelves are beyond the scope of this chapter, partly because they are more appropriately discussed in

the chapter on slope sedimentation, and partly because of our ignorance, as this category is one of the last to be better known in the rock record (Stanley, 1969) than in modern environments.

## AUTOCHTHONOUS PATTERNS OF SEDIMENTATION

### Morphologic-Stratigraphic Patterns

Shelves undergoing autochthonous sedimentation characteristically have a varied and systematic pattern of relief. The pattern tends to be correlated with both the distribution of surficial sediment and the internal structure of the surficial sediment mantle, and hence is a morphologic-stratigraphic pattern. On shelves of high relief, the pre-Holocene surface is exposed at the surface over wide areas, and constitutes an additional control of the pattern.

### Survival of Subaerial Patterns

On high-latitude shelves, relief may exceed 200 m. Much of this relief may be the consequence of pre-Holocene fluvial and glacial erosion of a crystalline substrate (Holtedahl, 1940, 1958), and of the dissection of flat-lying or gently inclined Cenozoic strata into cuestas and plateaulike remnants. On the North American Atlantic shelf, the Fall Line, where turbulent piedmont streams pass onto the coastal plain strata, intersects the shoreline at New Jersey (Fig. 5). To the north, the Fall Line cuesta, of gently inclined coastal plain strata, forms first islands (Long Island, Nantucket), then offshore banks (Georges Banks, the Nova Scotian Banks). Basins landward of the drowned Fall Line (Long Island Sound, the Gulf of Maine, the Nova Scotian basins) have inner margins of crystalline rock thinly veneered with coarse detritus. The basin centers have a lower stratum of glacial lake deposits overlain by Holocene marine mud.

Shelves of lower relief tend to be divided into broad, flat, plateaulike compartments by shelf valleys excavated during Quaternary low stands of the sea (Figs. 6 and 7). The outer margins of such shelves tend to consist of low-stand deltas, whose fronts are seaward-bulging shelf-edge scarps and whose landward margins may be marked by V-shaped, seaward-facing scarps that rise to the level of the inner shelf.

Subaerial morphologic elements smaller in scale than cuestas, basins, and shelf valleys seem in general to have been destroyed by erosional retreat of the shoreface, and the larger scale elements have often been subtly but pervasively modified by this process. This point can usually be demonstrated by a comparison of

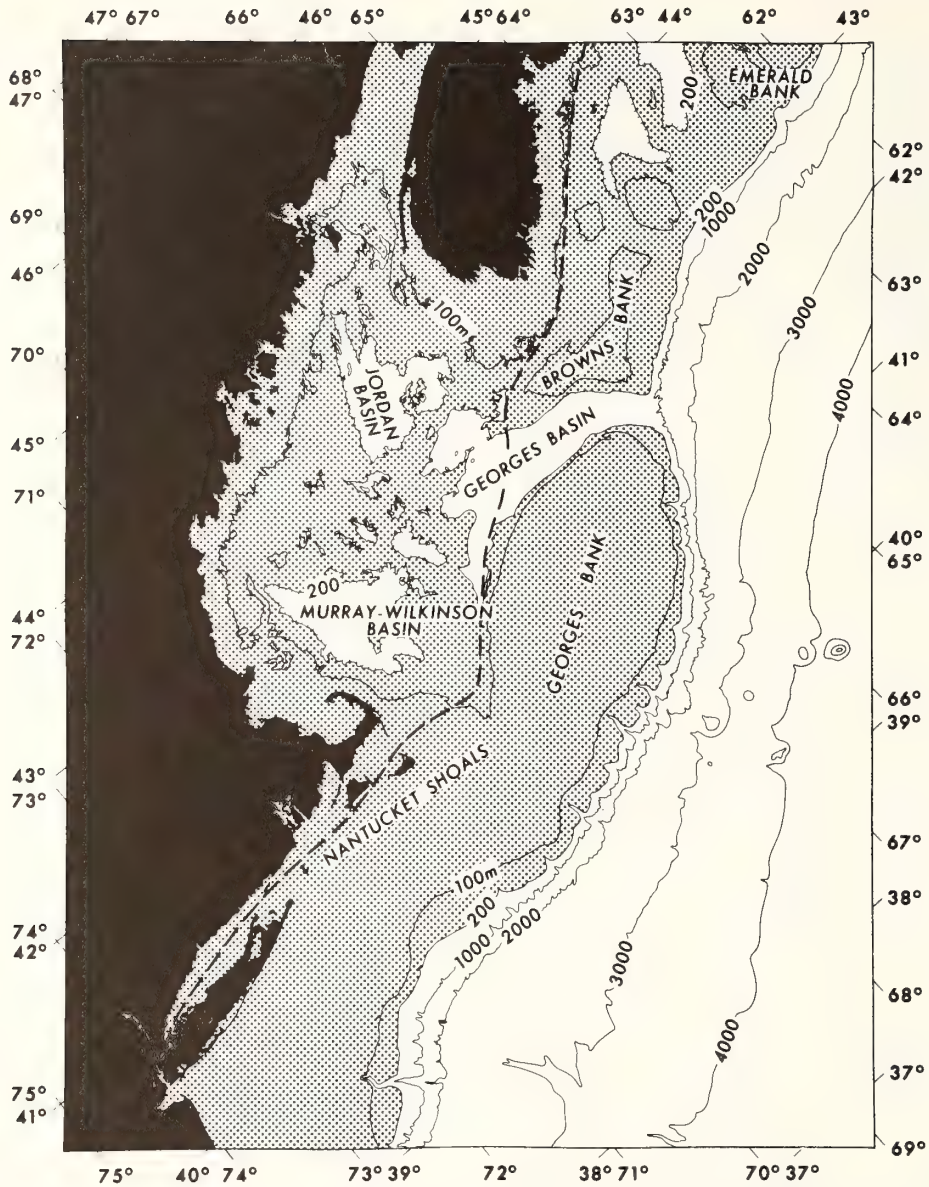


FIGURE 5. Bathymetry of the Gulf of Maine and Nova Scotian shelf. Dashed line is submerged extension of the Fall Line, separating gently dipping coastal strata from the crystalline substrate of the Appalachian orogenic belt. From Uchupi (1968).

shelf morphology with the morphology of the associated subaerial surface. The coastal plains of the world bear a delicate fabric of high-stand scarps, separated by terraces overprinted with beach ridge fields, commonly dating from the last interglacial, or a high stand during the Würm-Wisconsin glacial epoch (see, e.g., Colquhoun, 1969; Oaks and Coch, 1963; Bernard and Le Blanc, 1965). However, most submarine shelves are relatively featureless (the Aquitaine shelf: Caralp et al., 1972) or bear complex patterns of sand ridges that are the conse-

quence of marine systems of sediment transport initiated after the passage of the shoreline (ridge and swale topography of Fig. 6).

Major exceptions to this rule are the littoral bed forms of carbonate coasts; fringing reefs, beach rock, and calcarenite dunes cement as they form, and are far more resistant to the destruction during the passage of the shoreline. Carbonate littoral and sublittoral features have been reported from many shelves (Kaye, 1959; Ginsburg and James, 1974; Van Andel and Veevers,

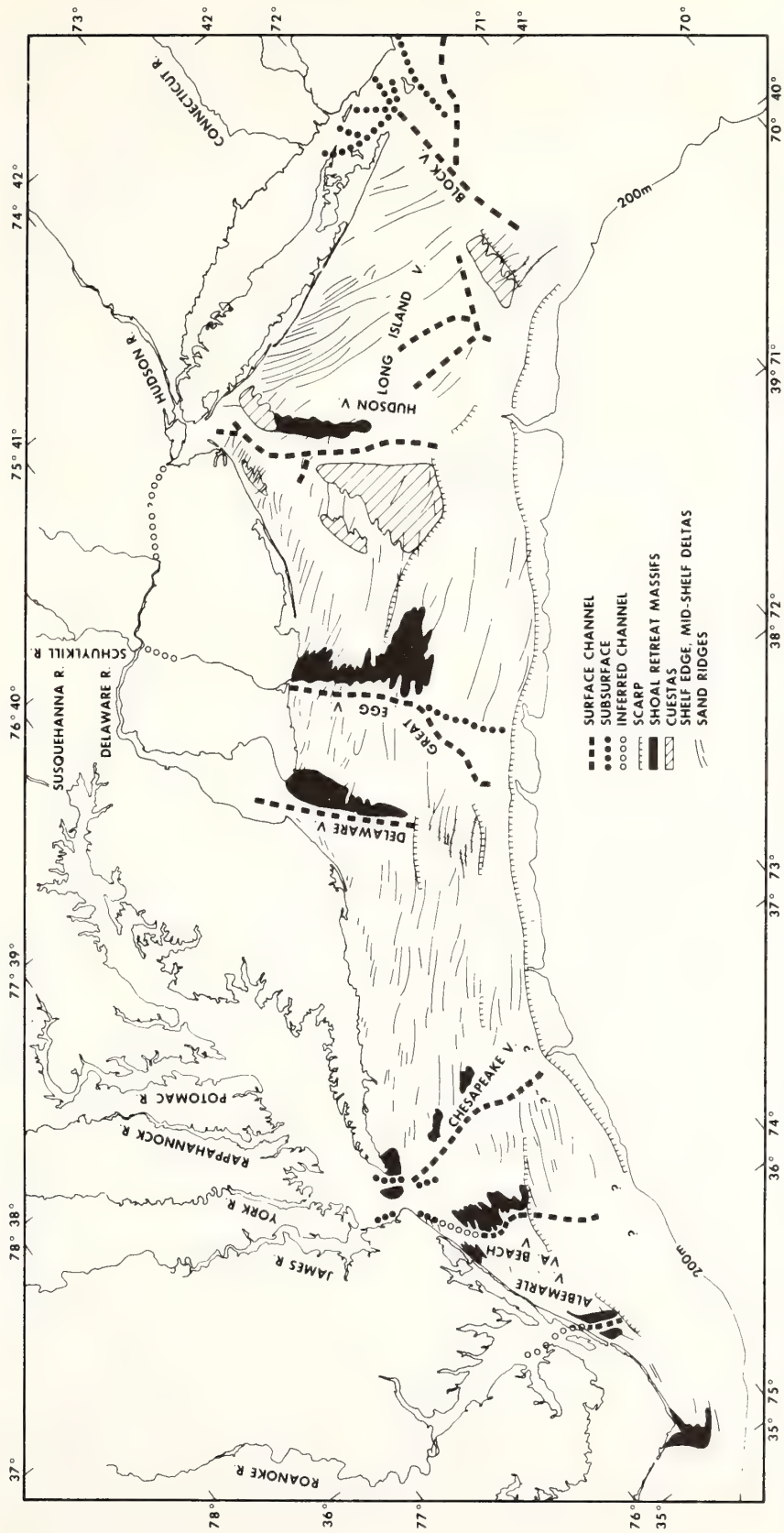


FIGURE 6. Morphologic elements of the Middle Atlantic Bight, North America. Based on ESSA 1:120,000 bathymetric map with a 1 fathom contour interval and Uchupi (1970) endpaper map with a 4 m contour interval. From Swift (1975).

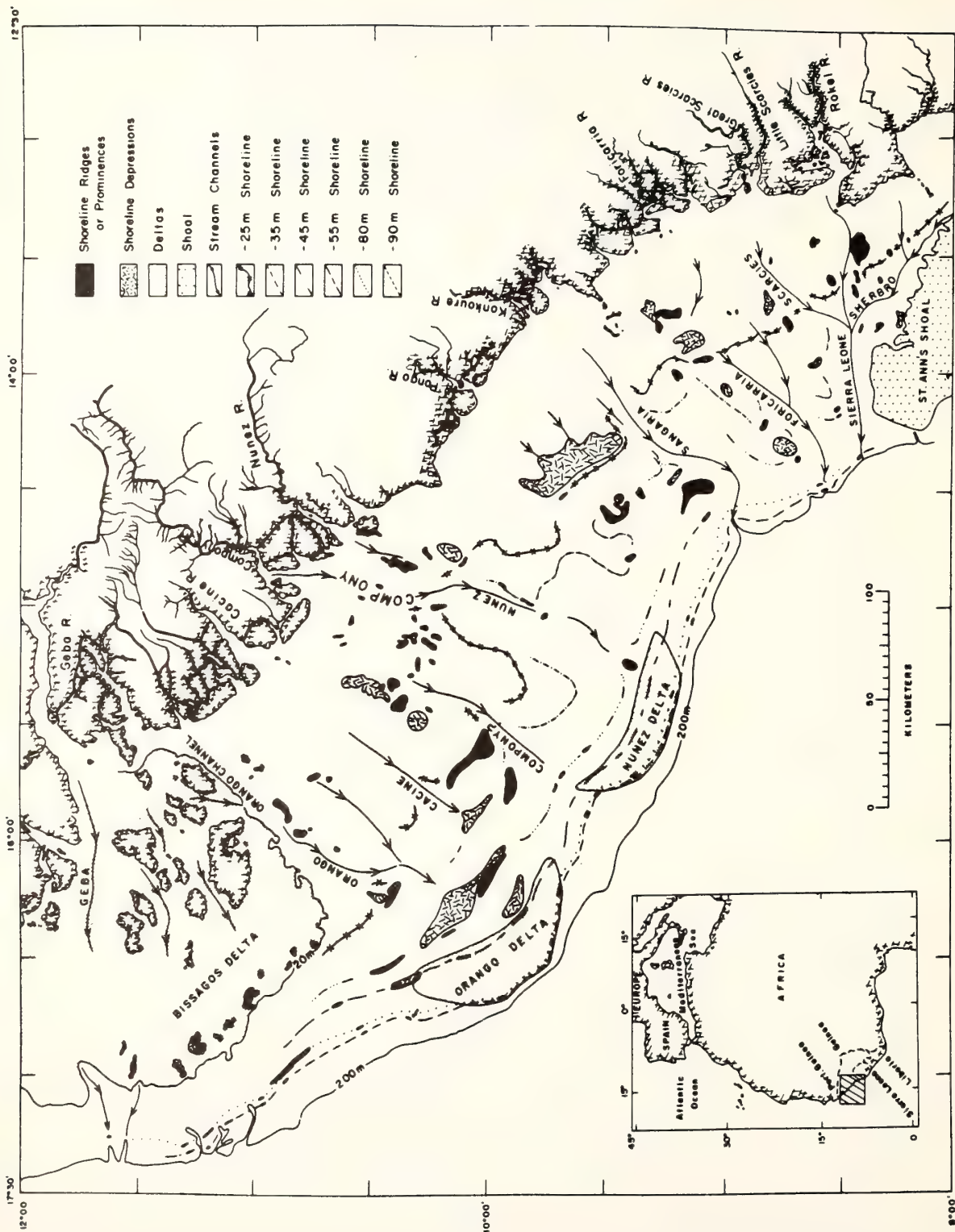


FIGURE 7. Morphologic elements of the continental shelf of Portuguese Guinea, Guinea, and Sierra Leone. Based on a map with a 5 m contour interval. Subtler morphologic elements may not be resolved. From McMaster et al. (1970).

1967; Stanley et al., 1968; Sarnthein, 1972). Other exceptions are the "perilittoral" deltas of terrigenous sand which seem to have survived transgression in the Gulf of Mexico (Curry, 1964, p. 299). The latter are large river-fed spits that grow in the direction of littoral drift, causing the river to flow parallel to the coast before it breaks out to the sea. End moraines have survived on the New England-Canadian shelf (King et al., 1972), but they were apparently emplaced seaward of the shoreline by grounded ice; King notes the vulnerability of glacial deposits on the present shoreline to glacial attack. The rinnenaler of the North Sea (subicestream channels) may likewise have been formed by an ice sheet seaward of the shoreline (Brouwer, 1964).

### Survival of Nearshore Marine Patterns

**THE SURFICIAL SAND SHEET.** The most characteristic aspect of shelves undergoing autochthonous sedimentation is the discontinuous surficial sand sheet 0 to 10 m thick, deposited during the erosional retreat of the

shoreface during the Holocene transgression (Fig. 8). On flat-lying constructional shelves such as the Middle Atlantic Bight of North America, relief elements on the surface of this sheet formed as the zones of nearshore sand storage (estuary mouth and cape extension shoals; shoreface-connected sand ridges: Swift et al., 1972), and both the surface morphology and the internal structure of the sand sheet bear little relation to the surface morphology and the internal structure of the older strata beneath (McClennen and McMaster, 1971). On shelves of greater relief, the surficial sediment blanket occurs as a thin drape over topographic highs, broken by substrate outcrops. In the adjoining basins, marginal sands, shed by highs, pass laterally into deposits of mud (Fig. 9).

The stratigraphy of the surficial deposits of the shelf is twofold. On shelves bordering low coasts a lower unit of fine sands and mud was deposited in the belt of lagoons and estuaries in advance of the main shoreline (Fig. 10). Its lower surface is ribbed with estuarine channel fillings that fill the buried drainage pattern of the pre-Recent substrate (Sheridan et al., 1974; Emery, 1968). Meandering of these channels in response to

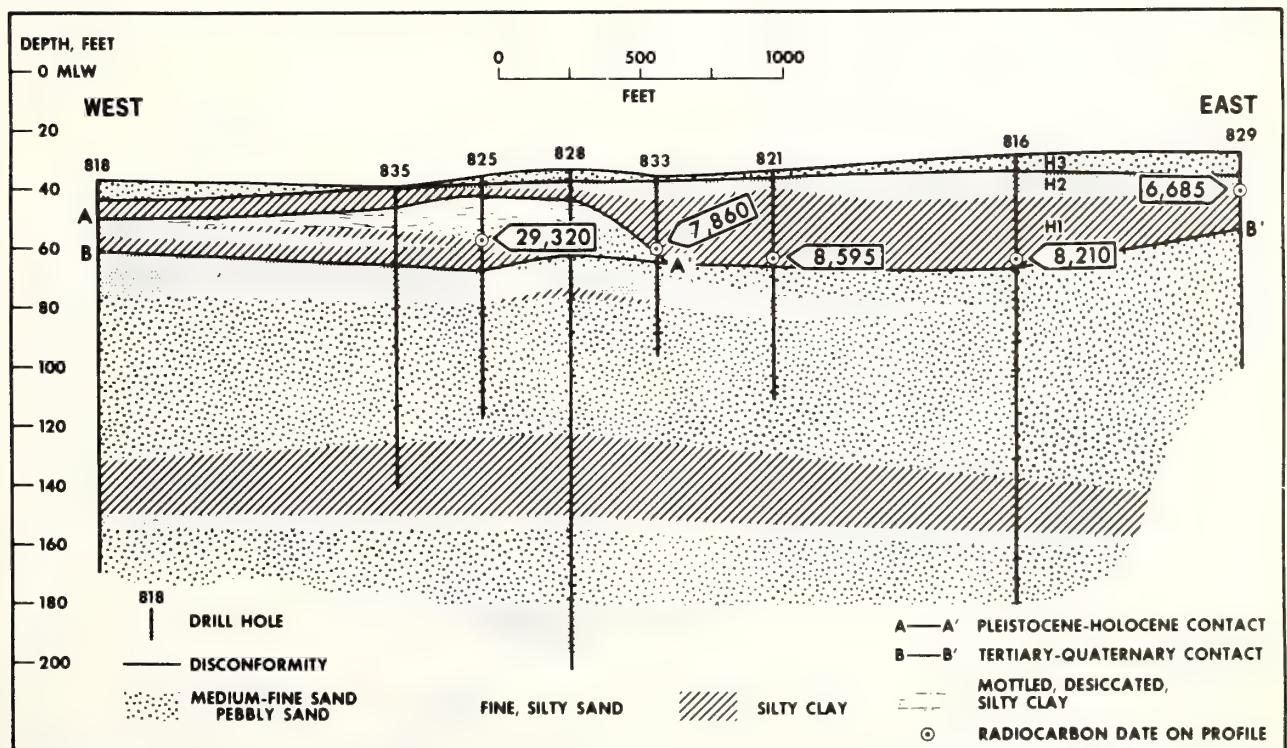


FIGURE 8. Surficial sand of the inner New Jersey shelf. Stratum H3 is a shelf sand. Stratum H2 is a backbarrier sand. Stratum H1 is a lagoonal mud. Thick zone in H1 is inferred to be a filled tidal scour channel whose axis is normal to the plane of the diagram. The sequence was produced by coastal retreat during the Holocene trans-

gression. The barrier superstructure is represented in this sequence by an unconformity; its forward face underwent continuous erosional retreat (Chapter 14, Fig. 10A) and the resulting debris accumulated seaward of the shoreface as the leading edge of H2. From Stabl et al. (1974).

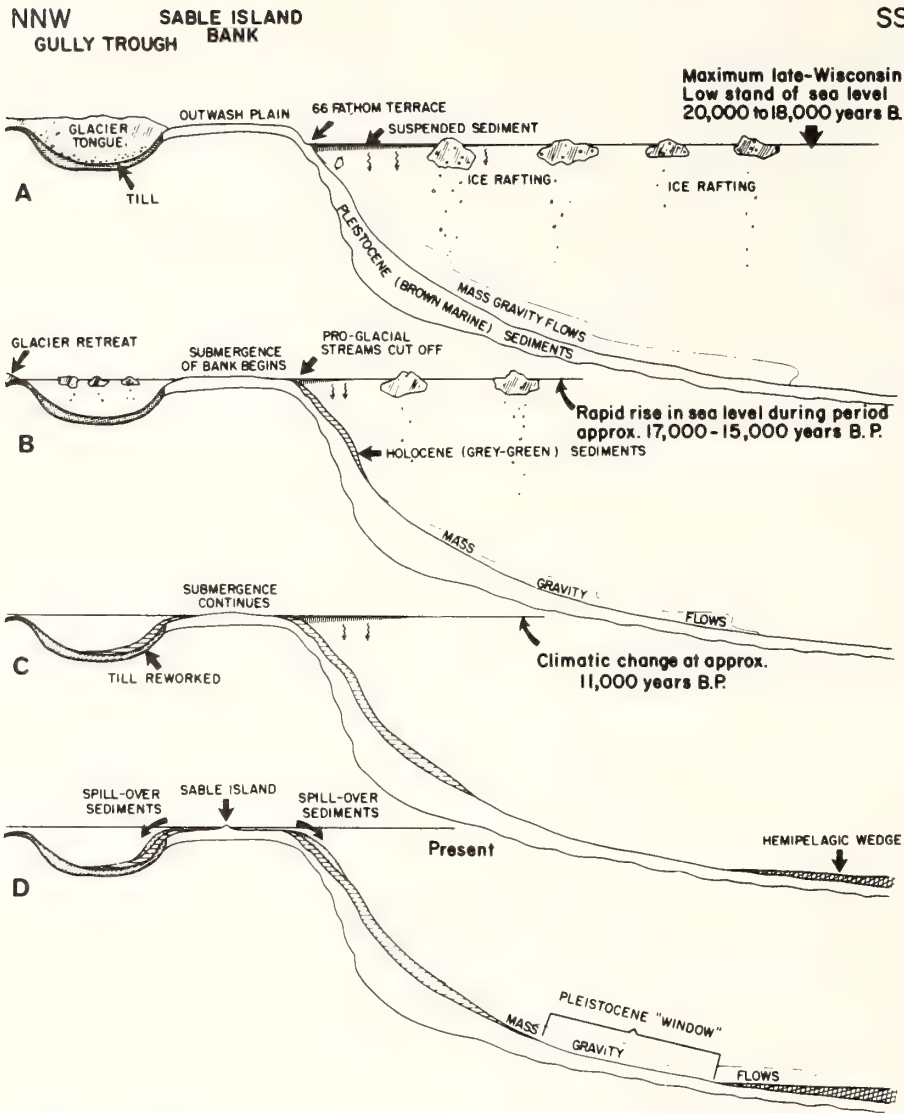


FIGURE 9. Evolution of the surficial sand shelf on a glaciated shelf of appreciable relief (Nova Scotia shelf; compare with Fig. 5). From Stanley (1969).

tidal flow has served to reduce the relief of the buried subaerial surface. Tidal inlets scour trenches into the lagoonal stratum, then backfill these trenches as they migrate downdrift (Hoyt and Henry, 1967; Kumar and Sanders, 1970). The lagoonal carpet is itself discontinuous; Pleistocene beach ridges and other topographic highs protrude through the lagoonal deposits as peninsulas or islands during their formation and are sheared off by shoreface retreat during passage of the main shoreline (Sheridan et al., 1974). On rocky coasts, lagoonal and estuarine deposits are confined to shelf valleys.

Passage of the main shoreline results in destruction of the barrier and the upper part of the lagoonal sequence,

and in the deposition of a second major stratum, a sheet of residual sand. This sand sheet overlies a surface of marine erosion whose areal geology is a patchwork of remnant lagoonal deposits and older substrate. On shelf sectors where the lagoonal carpet is well developed, this sand must travel from eroding headlands along the shoreface of retreating barriers, before being spread over the lagoonal carpet; or it is released as the retreating shoreface cuts into tidal inlet fills, or into estuarine channel sands scoured out of the pre-Recent substrate (Andrews et al., 1973). On shelves with poorly developed lagoonal strata, the retreating shoreface may be incised all the way through the lagoonal deposits and into



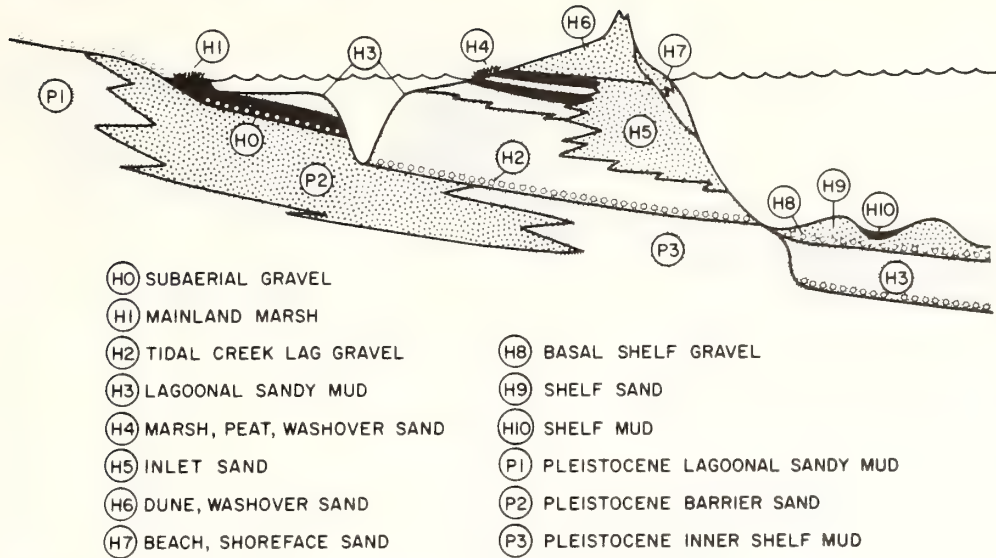


FIGURE 10. Stratigraphic model for a low coast undergoing erosional shoreface retreat.

Pleistocene sands, whose erosion provides material for the surficial sand sheet.

The basal layer of the surficial sand sheet is a thin, discontinuous gravel (Powers and Kinsman, 1953; Belderson and Stride, 1966; Veenstra, 1969; Norris, 1972) or shell hash rich in backbarrier and beach

species (Fischer, 1961; Merrill et al., 1965; Milliman and Emery, 1968; Field, 1974). More exotic clasts are clay pebbles eroded from Early Holocene lagoonal deposits, elephant teeth (Whitmore et al., 1967), and concretions from Tertiary strata (Stanley et al., 1967). The basal gravel is rarely more than a meter thick. It is

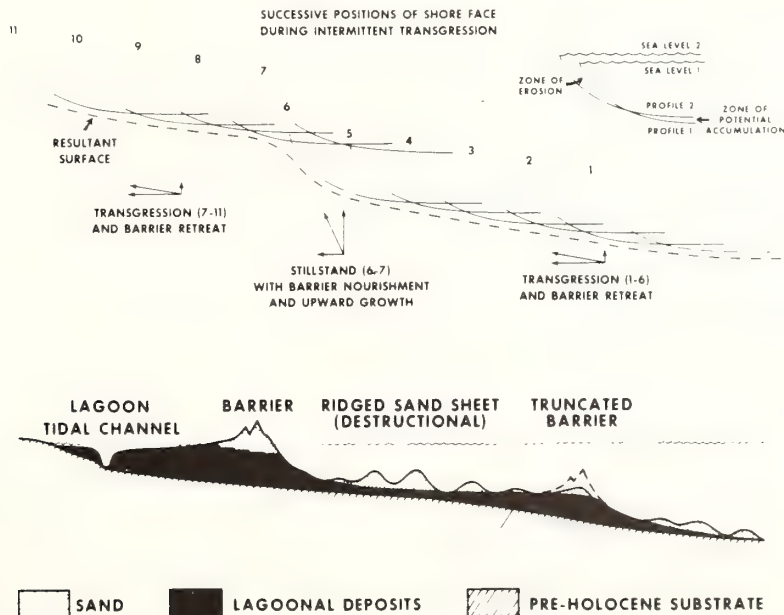


FIGURE 11. Above: Schematic illustration of intermittent shoreface retreat. As shoreface profile translates primarily landward in response to rising sea level, material eroded from shoreface accumulates on adjacent shelf as ridged sand sheet. Periods of primarily vertical translation of profile followed by periods of resumed landward translation result in truncated scarp. Below: Resulting stratigraphy. From Swift et al. (1973).

commonly overlain by 1 to 10 m of sand, with a sublittoral molluscan fauna (Shideler et al., 1972).

**TERRACES AND SCARPS.** Most continental shelves are terraced, with terraces separated by scarps 10 m or more in height (Fig. 6). Their counterparts on the adjacent subaerial coastal plains mark Quaternary (or earlier) high stands of the sea. Shelf scarps appear to have resulted primarily from stillstands of the returning Holocene sea, although they may in some cases be reoccupied Pleistocene shorelines. On the Georgia coast, for example, the modern barrier island system is perched on the forward face of a Pleistocene shoreline, and the modern tidal inlets are reoccupied Pleistocene inlets (Hoyt and Hails, 1967).

Shelf scarps are drowned shorelines only in the broadest sense; more specifically, they are relict lower shorefaces. To form such a scarp would require a period of near stillstand during a general transgression. The shoreface profile will translate more nearly upward than landward (Fig. 11) during this period, by means of upper shoreface and barrier surface aggradation. At the resumption of rapid transgression, the superstructure of the stillstand barrier will resume its landward migration through the process of shoreface erosion and storm washover, leaving behind a truncated lower shoreface. If both the lower and upper shoreface undergo aggradation during the stillstand period, so that the ideal profile is realized at all times, then there will be no surface expression of the stillstand shoreline, although seismic profiles may reveal a buried scarp (Stanley et al., 1968).

**SHELF VALLEY COMPLEXES AND SHOAL RETREAT MASSIFS.** A second nearshore marine pattern of relief and sediment distribution that may survive from the nearshore environment during a marine transgression is a shelf valley complex. This term refers to the groups of morphologic elements that occur along the paths of retreat of estuary mouths on autochthonous shelves. Shelf valley complexes are composed of deltas, shelf valleys, and shoal retreat massifs (Figs. 6 and 12). A shoal retreat massif is a broad, shelf-transverse sand ridge of subdued relief that marks the retreat path of a zone of littoral drift convergence (Swift et al., 1972). It may be dissected by subsequent storm or tidal flows into a cross-shelf sequence of smaller coast-parallel ridges, and the term massif is used in the sense of a composite topographic high, itself consisting of smaller highs.

Such complexes are locally well developed on low-relief shelves such as the Middle Atlantic Bight of North America. Here they are largely constructional features molded into the Holocene sand sheet. The sand

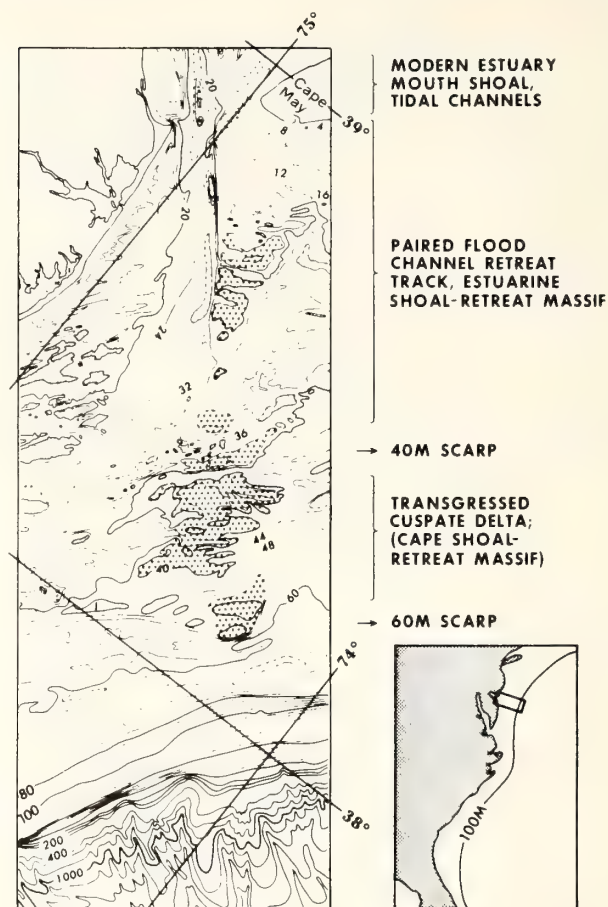


**FIGURE 12.** *The Delaware shelf valley complex, Delaware shelf of North America. Southward littoral drift of New Jersey coastal compartment is injected into reversing tidal stream of mouth of Chesapeake Bay. The resulting shoal is stabilized as a system of interdigitating ebb and flood channels, north of the main couplet of a mutually evasive ebb and flood channel. The shelf valley complex seaward of the bay mouth is the retreat path of the bay mouth sedimentary regime through Holocene time. Retreat of the main flood channel has excavated the Delaware shelf valley; retreat of the bay mouth shoal has left a seaward-trending shoal retreat massif on the shelf valley's north flank. From Swift (1973).*

sheet tends to completely fill the former subaerial valley cut by the river into the Pleistocene strata, and the shelf valley complex and the buried river channel may not everywhere coincide (Fig. 13).

Shelf valley complexes are built in serial fashion by the retreating shoreline. It is important to remember that the last high-energy depositional environment experienced by any given segment was the nearshore zone. As a consequence of remodeling of preexisting deposits in this zone, elements of shelf valley complexes are not always what they seem. For instance, in Fig. 12, the topographic characteristics of the Delaware midshelf

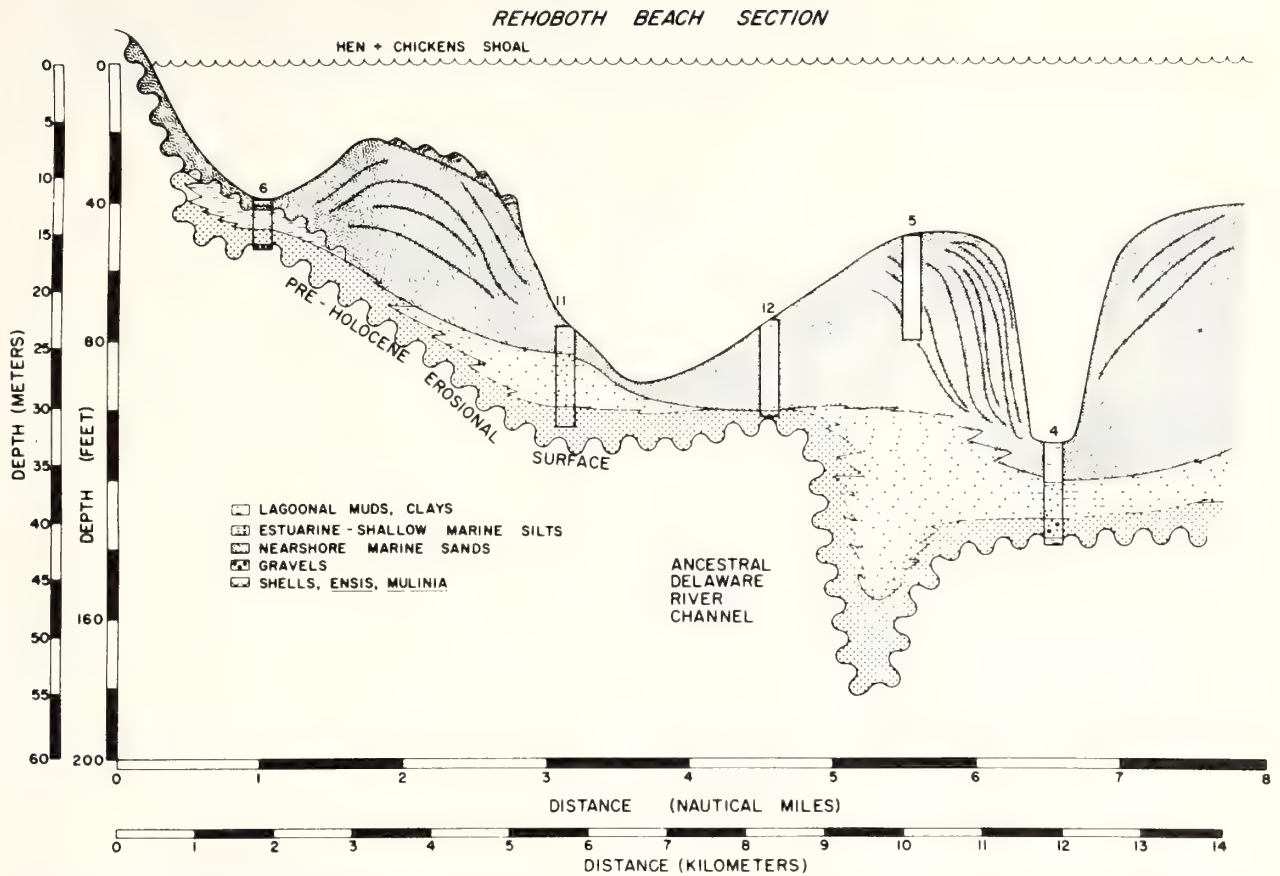


FIGURE 13. Section across the head of the Delaware shelf valley complex based on vibracores and a 3.5 kHz seismic profile. Marine sand sheet with constructional tidal topography rests on Holocene

lagoonal and older Pleistocene deposits. Delaware shelf valley occurs entirely within Pleistocene sands. Note offset between shelf valley and buried river channel. From Sheridan et al. (1974).

delta suggest that the surface of this stillstand feature was successively remodeled at the resumption of transgression, first as a retreating cusped foreland, then as cape shoal retreat massif, as illustrated in Chapter 14, Fig. 22. After a further period of stillstand indicated by a 60 m scarp, the coastal regime again changed, and the Delaware River mouth resumed retreat, this time as an estuary. The retreat path of this estuary mouth consists of a sharply defined submarine channel (shelf valley) flanked by a shoal retreat massif. The origins of these two features are easily deduced from uniformitarian reasoning. The shoal retreat massif may be traced into the modern north side shoal of the Delaware estuary mouth. This shoal is a sink for the littoral drift of the New Jersey coastal compartment, and is stabilized by a system of interdigitating ebb and flood channels. The shelf valley may be traced into the flood channel of a large ebb channel-flood channel couplet on the south side of the estuary mouth that accommodates most of the tidal discharge.

On the central and southern Atlantic shelf of North America, four basic morphologic provinces may be described on the basis of constructional morphologic elements inherited from the retreating shoreline (Fig. 14). In the Middle Atlantic Bight (Fig. 6), widely spaced master streams have resulted in widely spaced shelf valley complexes. The plateaulike interfluvial ridges between the shelf valley complexes bear ridge fields that were also generated by shoreface retreat (see Chapter 14, Fig. 28).

The more intense wave climate experienced by the Carolina salient has elicited a different response from the retreating river mouths. Capes Romain, Fear, Lookout, and Hatteras may have originally been cusped deltas, associated with the Pee Dee, Cape Fear, Neuse, and Pamlico rivers (Chapter 14, Fig. 26). Retreat of these forelands has left large widely spaced shoal retreat massifs. South of Cape Romain the retreat of small, closely spaced cusped forelands has generated a blanket of coalescing shoal retreat massifs on the adjacent shelf

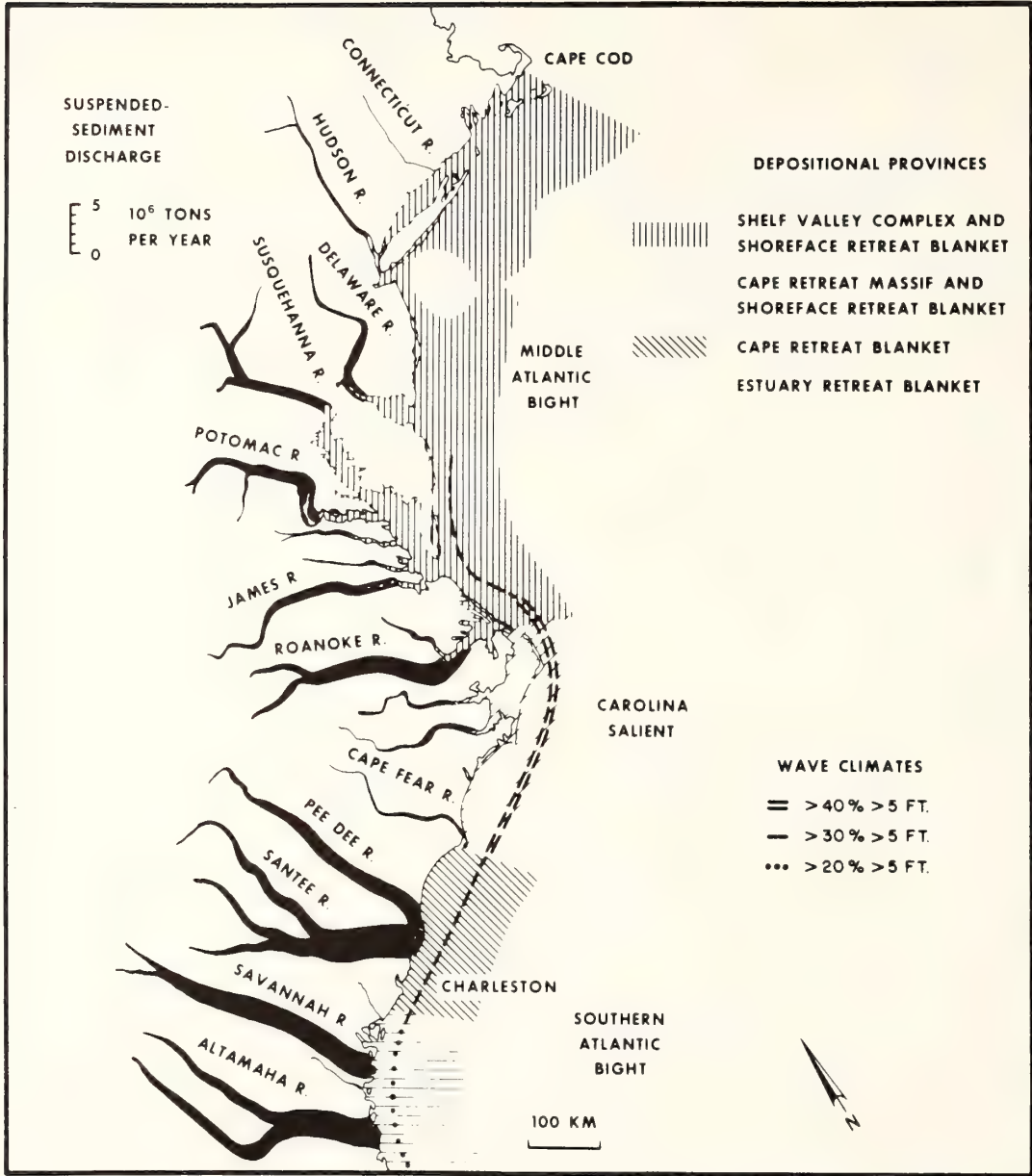


FIGURE 14. Coastal sediment discharge (Meade, 1969) and wave climate of the Middle Atlantic Bight (Dolan et al., 1973) and resulting depositional provinces. From Swift and Sears (1974).

(Fig. 15). Yet further south, the Georgia Bight experiences a high tide range, a milder wave climate, and the closely spaced river mouths are estuarine in configuration. Their retreat has generated a blanket of coalescing shelf valley complexes (Fig. 16).

**Initiation of Modern Patterns**

TEXTURAL AND MORPHOLOGIC PATTERNS ON A STORM-DOMINATED SHELF. On two of the best studied autoch-

thonous shelves, the Middle Atlantic Bight of North America and the shelf around the British Isles, the hydraulic climate is sufficiently intense to overprint older subaerial and nearshore marine patterns of the surficial sand sheet with a modern textural and morphologic pattern.

In the Middle Atlantic Bight fair-weather flows are driven by the geostrophic response of the stratified shelf water column to freshwater runoff and to winds (McClenen, 1973; Bumpus, 1973); see Fig. 17. How-



FIGURE 15. Cusped forelands and cape shoal-retreat massifs (stippled) of the South Carolina shelf. Note overprinting by ridge and swale topography. Contours in fathoms. From Swift et al. (1972).

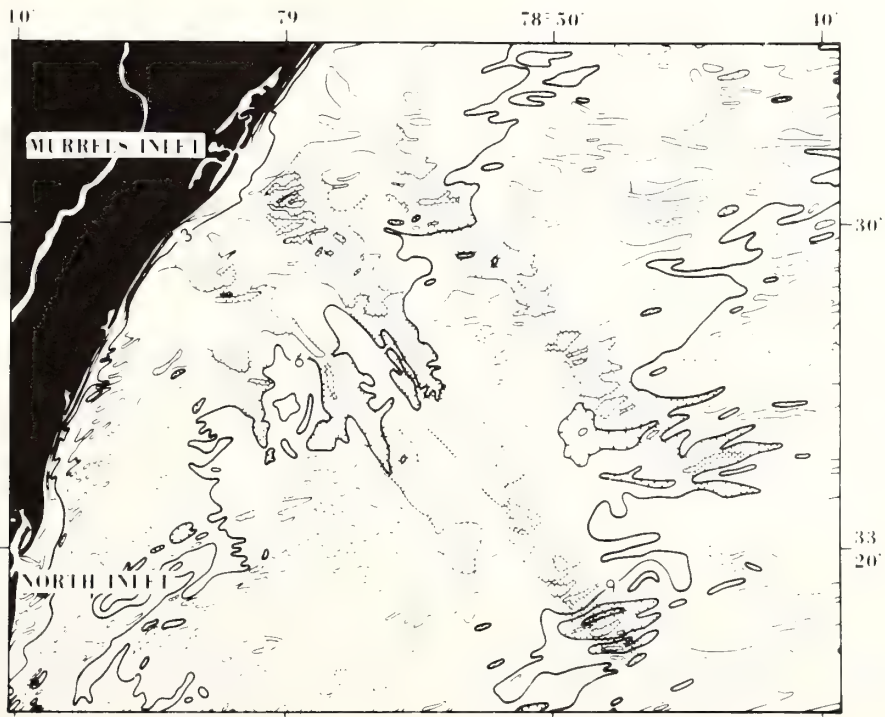


FIGURE 16. Morphologic pattern of estuarine shoal retreat blanket, overprinted by ridge and swale topography. South Carolina coast. Highs are stippled. Contours in fathoms. From Swift and Sears (1974).

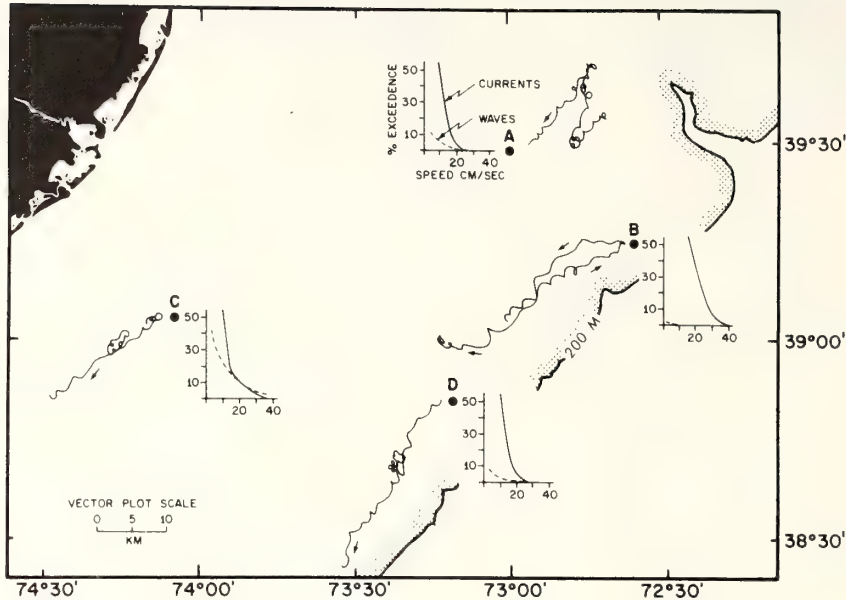


FIGURE 17. Fair-weather hydraulic regime of the New Jersey shelf as indicated by Savonius rotor current meters mounted 1.5 to 2.0 m above the seafloor at four stations on the New Jersey shelf, for periods of 9 to 11 days in late spring. Progressive vector diagrams indicate a general southerly water drift, partly correlatable with wind directions (McClenen, 1973). Loops, spikes, and bulges on progressive vector diagrams are modulation by the semidiurnal tide. In percent exceedence diagrams, current velocities are compared with bottom wave surge calculated from wave climate data. All data from McClenen (1973).

ever, neither these unidirectional flow components nor the superimposed wave oscillations (McClenen, 1973) and tidal oscillations (Redfield, 1956) are strong enough to result in significant bed load transport over broad areas. During the winter period of frequent storms, the water column is not stratified, and air-water coupling is more efficient (see discussion, pp. 263-264). The geometry of the Middle Atlantic Bight is especially conducive to strong flows during this period. When low-pressure systems pass over the bight, so that the isobars of atmospheric pressure parallel the isobaths of the shelf surface, the resulting winds blow southward down the length of the Middle Atlantic Bight, paralleling the curve of the shoreline, and induce a uniform setup of the shelf water mass against the coast of 40 to 60 cm. High-velocity "slablike" flows of remarkable longshore coherence result (Beardsley and Butman, 1974; Boicourt, personal communication).

The coastal boundary of these storm flows appears to initiate ridge topography at the foot of the shoreface (Duane et al., 1972); see Chapter 14, Figs. 28 and 31. However, it is clearly an oversimplification to describe the ridge topography of the Middle Atlantic Bight as a purely inherited topographic pattern. The ridges maintain their characteristic 10 m relief and textural patterns across the central shelf (Swift et al., 1974);

see Fig. 18. Troughs retain erosional windows in which Early Holocene lagoonal clays are thinly veneered with a lag deposit of pebbly sand. Calculations based on current-meter records suggest that the unidirectional components of storm flows are sufficient to mobilize the sandy bottom (Fig. 19), and to slowly level the ridge topography, if the topography were not in fact a continuing response of the seafloor to the modern hydraulic climate.

In several areas on the Middle Atlantic shelf, there is evidence to suggest that ridge topography may be initiated on the central shelf, if not already present as a survival from the nearshore environment. Off South Carolina, shoal retreat massifs are overprinted by a ridge topography even though the modern nearshore zone is not apparently forming ridges (Fig. 15). Elsewhere, the ridge pattern appears to have changed as the water column deepened and the shoreline receded during the course of the Holocene transgression. The estuary mouth shoal that is the landward end of the Delaware Massif (Fig. 12) has impressed into it a tide-maintained ridge pattern that trends normal to the shoreline and parallel to the sides of the estuary mouth. As the crest of the massif is traced seaward, the trend of the ridges and troughs superimposed on it shifts toward a shore-parallel orientation. The bay

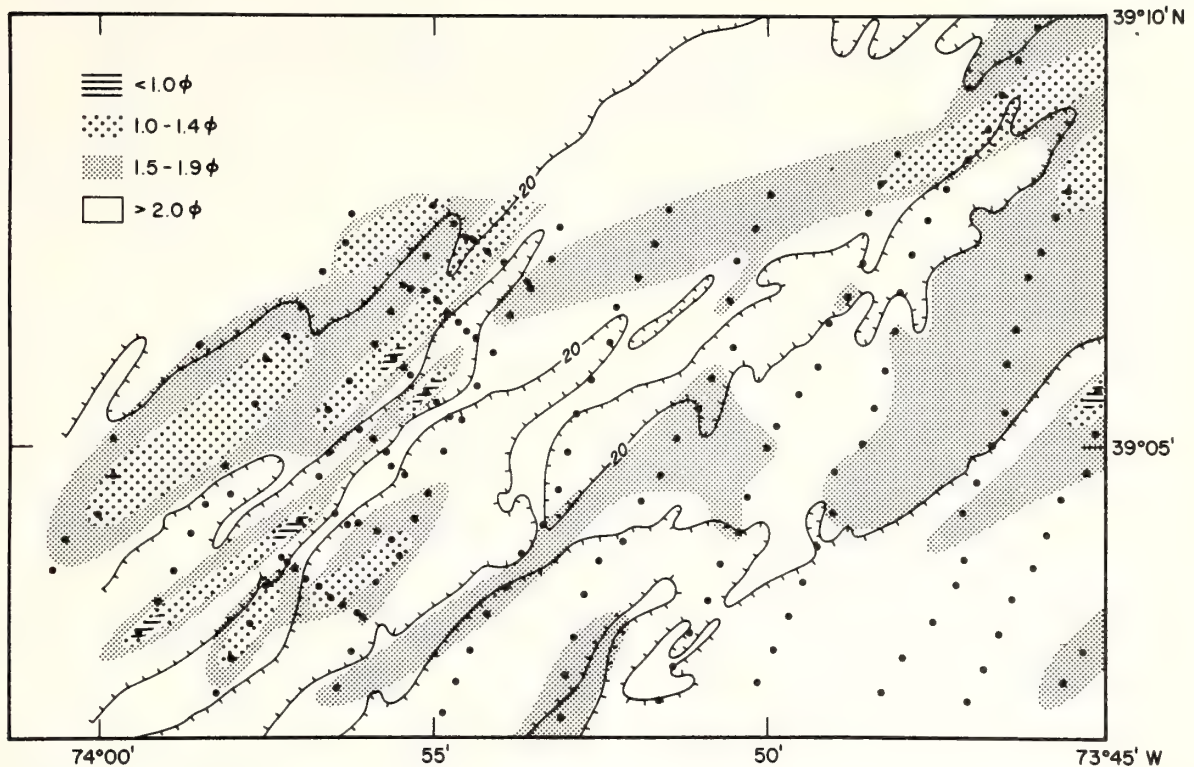


FIGURE 18. Distribution of grain sizes on the central New Jersey shelf. Medium to fine sands occur on ridge crests. Fine to very fine sands occur on ridge flanks and in troughs. Locally, erosional contours in troughs expose a thin lag of coarse, shelly, pebbly sand over lagoonal clay. From Stubblefield et al. (in press).

mouth ridges are oriented parallel to the reversing tidal flows of the bay mouth; the offshore ridges appear to parallel instead the geostrophic storm flows of the open shelf.

The Great Egg Massif, associated with the former course of the Schuylkill River across the shelf, has been heavily dissected into a transverse ridge pattern. Seaward of a scarp whose toe lies at 90 m, a second, small-scale ridge pattern with a somewhat different trend has been superimposed on the first (Fig. 20). Stubblefield and Swift (1975) have presented a model for the evaluation of the compound ridge pattern based on vibracores, and 3.5 kHz seismic profiles collected in the area (Fig. 21). Radiocarbon dates indicate that the large-scale ridges appear to have formed immediately subsequent to the passage of the shoreline at approximately 11,000 BP (Fig. 21A). Internal stratification indicates that large-scale ridges grow by the accretion of conformable beds. Wide, large-scale troughs appear as zones of bare Pleistocene substrate, where the surficial sand sheet was never formed, or where its material was swept away to nourish the growth of adjacent ridges.

With continuing transgression and deepening of the water column, the ridges appear to have increased

their spacing by means of lateral migration or the coalescence of adjacent ridges. Internal strata tend to dip more steeply than present ridge flanks, suggesting that toward the latter part of their history, ridge growth was mainly the consequence of lateral rather than vertical accretion

Small-scale troughs transect large-scale ridges, and tend to break large-scale ridges up into *en echelon* segments (Fig. 20). Where small-scale troughs cross large-scale troughs they are incised into the flat-lying Early Holocene and Pleistocene strata that floor the large-scale troughs. Small-scale troughs are commonly narrow features that do not penetrate through the Early Holocene lagoonal clay (Fig. 21B). Where this clay is in fact breached, so that the small-scale troughs penetrate the underlying sand, the troughs are noticeably wider, as though they had expanded by undercutting of the clay in a fashion analogous to the growth of a blowout on a grass-covered eolian flat (Fig. 21C).

The ridge topography of the Middle Atlantic Bight is accompanied by mesoscale bed form patterns, whose relationship to the ridge pattern is not clearly understood. The most ubiquitous mesoscale bed forms are the current lineations, which occur as sand ribbons or more

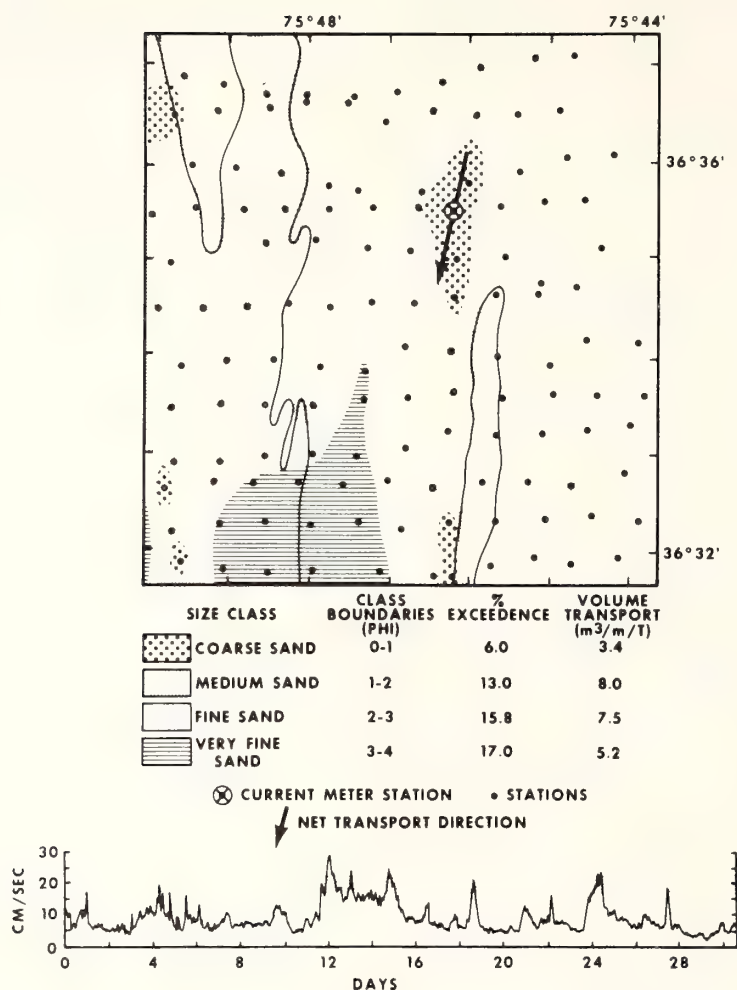


FIGURE 19. Sediment transport in response to the unidirectional component of flow during the month of November 1972, in an inner shelf ridge field, False Cape, Virginia. Estimates based on Shield's threshold criterion, a drag coefficient of  $3 \times 10^{-3}$ , and Laursen's (1958) total load equation. Values expressed as cubic meters of quartz per meter transverse to transport direction for time elapsed. Solid line is the 10 m isobath.

commonly as linear erosional furrows. They may trend parallel to the trend of the ridge topography, or may cut across it, so as to make a larger acute angle with the shoreline (Fig. 22). Toward the southern end of the Middle Atlantic Bight, the shelf surface shoals, narrows and curves to the east. Sand wave fields appear, perhaps indicative of the acceleration of storm flows in response to the decreasing cross-sectional area of the shelf water column.

Ridges molded into the Albermarle shoal retreat massif bear sand waves on their crests (Fig. 23). Sand waves locally attain 2 m heights and angle of repose slopes. Sand wave crestlines are not quite normal to shore, suggesting that the ridge crests on which they are

found experience a seaward component of flow during storms. At Diamond Shoals, the southern extremity of the Middle Atlantic Bight, sand waves up to 7 m high occur between sand ridges, forming a reticulate pattern (see Fig. 27, Chapter 16).

Grain-size patterns in the Middle Atlantic Bight suggest that the storm flows that interact with the ridge topography and the mesoscale bed forms are capable of transporting at least the finer grades of sand for appreciable distances. The inner shelf sectors before the seaward-convex coastal compartments of the Middle Atlantic Bight exhibit a repeating pattern of grain-size distribution (Fig. 24). The northern half of each of these inner shelf sectors, where south-trending storm flows must



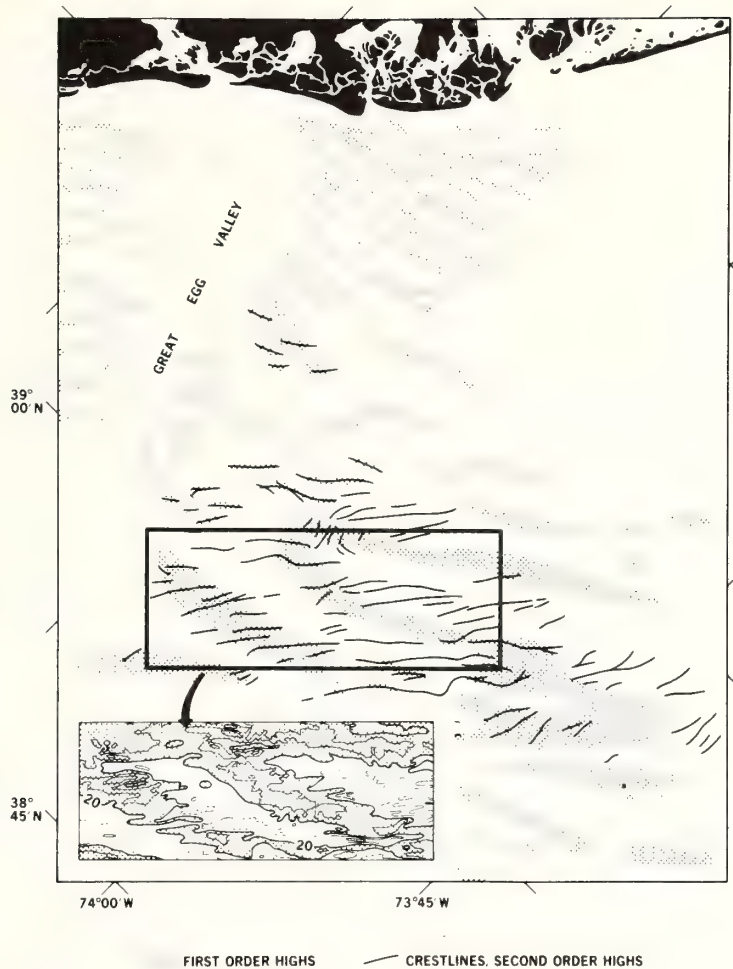
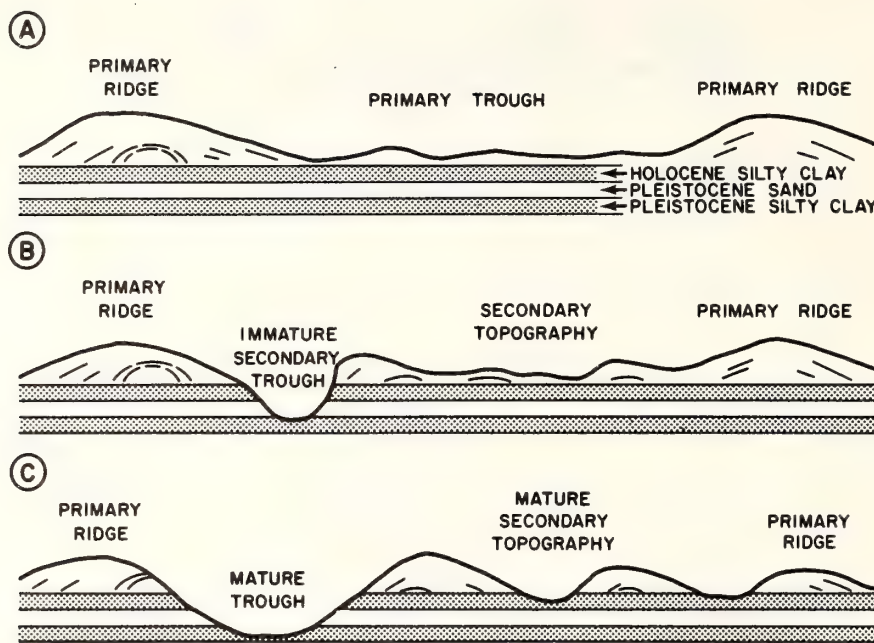


FIGURE 20. Great Egg shelf valley and shoal retreat massif. Large-scale ridges in inset may date from a period when the ancestral Great Egg estuary was active. Nearshore large-scale ridges were probably formed by shoreface detachment during erosional retreat of the shoreface, after capture of the ancestral Schuylkill River by the Delaware River, and consequent reduction in discharge of the Great Egg estuary. See Fig. 6 for relationships of Schuylkill, Delaware, and Great Egg rivers. From Stubblefield and Swift (*in press*).

presumably converge with the shoreline, tend to be floored with primarily medium- and coarse-grained sands, molded into a well-defined ridge topography. On the southern halves of the coastal compartment, where the shoreline tends to curve to the west, storm flows might be expected to expand and decelerate. Here the fine sand blanket of the shoreface extends across the inner shelf floor, as though nourished by material swept out of the ridge topography to the north. The schematic flow pattern in the lowest panel of Fig. 24 is not based on detailed observations. It is intended to indicate that current flowing generally southwest parallel to the long dimension of the shelf will tend to converge

with the northeastern portion of the shoreline and diverge from the southwestern portion of the shoreline.

A somewhat closer relationship appears to exist between flow geometry and sediment distribution in the vicinity of the shoal retreat massifs (Fig. 25). The ridge topography attains its maximum relief where it has been molded onto the crests of the massifs. The massifs do not exhibit bilateral symmetry; troughs are deepest and widest on the northern sides. As a trough axis is traced across the massif, erosional windows exposing the basal pebbly sand or the underlying clayey substrate become less frequent. The fine sands of the trough flanks tend to bridge across the trough floor.



**DEVELOPMENT OF RIDGE TOPOGRAPHY**

FIGURE 21. Ridge evolution on the central New Jersey shelf. (A) Ridge nuclei are formed during the process of ridge detachment and shoreface retreat, or by other means in the nearshore zone. Sand continues to be swept out of troughs onto ridges as water column deepens during the course of the Holocene transgression. (B) Seafloor scour during storms locally penetrates the Early Holocene lagoonal clay carpet, and a secondary trough forms, initially by downcutting. (C) Downcutting in the secondary trough decreases and lateral erosion increases as second silty clay layer is exposed. Secondary trough widens by undercutting of upper clay in "blowout" fashion. Sand from similar excavations upcurrent forms secondary ridges. From Stubblefield and Swift (in press).

The trough axis tends to climb toward a low sill on the southern side of the massif; beyond this the seafloor drops off rapidly to the adjacent shelf valley. The valley floor commonly consists of fine to very fine featureless sand. The topography and grain-size pattern suggest that south-trending flows converge with the rising seafloor and accelerate up the northern flanks of the massifs. Fine sand swept out of the troughs is deposited in the zone of flow expansion and deceleration over the shelf valley south of the massif.

TEXTURAL AND MORPHOLOGIC PATTERNS ON A TIDE-DOMINATED SHELF. The tide-swept shelf around the British Isles (Stride, 1963) provides an interesting contrast with the storm-induced sedimentation of the Middle Atlantic Bight. Surges are at least as frequent here as in the Middle Atlantic Bight (Steers, 1971). However, much more work is done on the seafloor by the semidiurnal tidal currents associated with the amphidromic edge waves that sweep the margins of mar-

ginal shelf seas of western Europe (see Chapter 5, Fig. 4 and discussion, p. 60). The rotary tidal currents associated with these tidal waves are in fact analogous in some respects to the inertial wind-driven currents generated by storms. Midtide surface velocities in excess of 50 cm/sec (1 knot) are sustained over vast areas, and locally exceed 200 cm/sec. Ebb-flood discharge differentials result in currents residual to the tidal cycle, whose velocities may be as great as a tenth of the midtide value.

As a consequence of the higher rate of expenditure of energy on the seafloor, morphologic and textural patterns inherited from the retreating nearshore zone have been largely erased. Erosional shoreface retreat has resulted in a surficial sediment sheet that is comparable in many respects to that of the Middle Atlantic Bight (see Belderson and Stride, 1966). However, the poorly resolved sand transport patterns of the Middle Atlantic Bight are replaced by well-defined transport paths, with sand streams that diverge from beneath

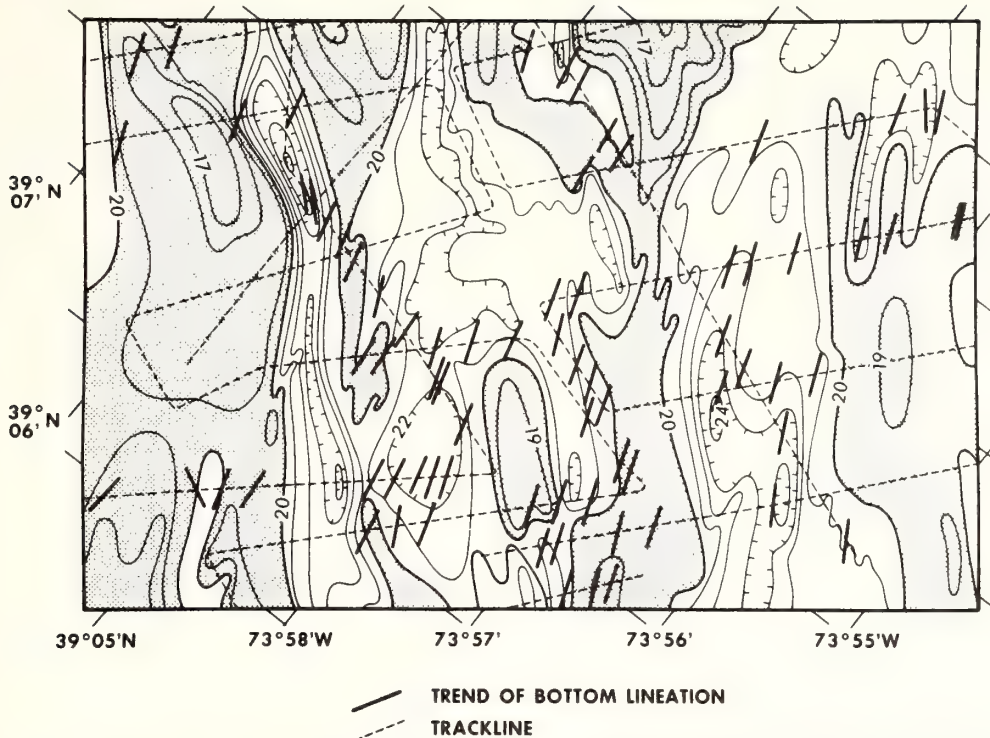


FIGURE 22. Current lineation patterns on the central New Jersey shelf. Bars indicating lineations are over 10 times as long as features that they represent. They locally represent sets of lineations. High areas are stippled. Contours in fathoms. From McKinney et al. (1974).

tide-induced "bed load partings" and flow down the gradient of maximum tidal current velocities until either the shelf edge or a zone of "bed load convergence" and sand accumulation is reached (Stride, 1963; Kenyon and Stride, 1970; Belderson et al., 1970); see Fig. 26.

Each stream tends to consist of a sequence of more or less well-defined zones of characteristic bottom morphology and sediment texture (Fig. 27). Streams may begin in high-velocity zones [midtide surface velocities in excess of 3 knots (150 cm/sec)]. Here rocky floors are locally veneered with thin (centimeters thick) lag deposits of gravel and shell. Where slightly thicker, the gravel may display "longitudinal furrows" parallel to the tidal current (Stride et al., 1972), a bed form related to sand ribbons (see Chapter 10, p. 170).

Between approximately 2.5 and 3.0 knots (125–150 cm/sec) sand ribbons are the dominant bed form (Kenyon, 1970). These features are up to 15 km long and 200 m wide, and usually less than a meter deep. Their materials are in transit over a lag deposit of shell and gravel. Kenyon has distinguished four basic patterns that seem to correlate with maximum tidal current

velocity and with the availability of sand (Chapter 10, Fig. 15).

Further down the velocity gradient, where midtide surface velocities range from 1 to 2 knots (50–100 cm/sec), sand waves are the dominant bed form. Where the gradient of decreasing tidal velocity is steep or transport convergence occurs, this may be the sector of maximum deposition on the transport path. Over 20 m of sediment has accumulated at the shelf-edge convergence of the Celtic Sea, although it is not certain that this sediment pile is entirely a response to modern conditions.

The Hook of Holland sand wave field off the Dutch coast is one of the largest (15,000 km<sup>2</sup>) and the best known (McCave, 1971). The sand body is anomalous in that it sits astride a bed load parting; the sand patch as a whole may be a Pleistocene delta or other relict feature. Sand waves with megaripples on their backs grow to equilibrium heights of 7 m with wavelengths of 200 to 500 m in water deeper than 18 m; in shallower water, wave surge inhibits or suppresses them. Elongate tidal ellipses favor transverse sand wave formation, and the sand waves tend to be destroyed by midtide cross

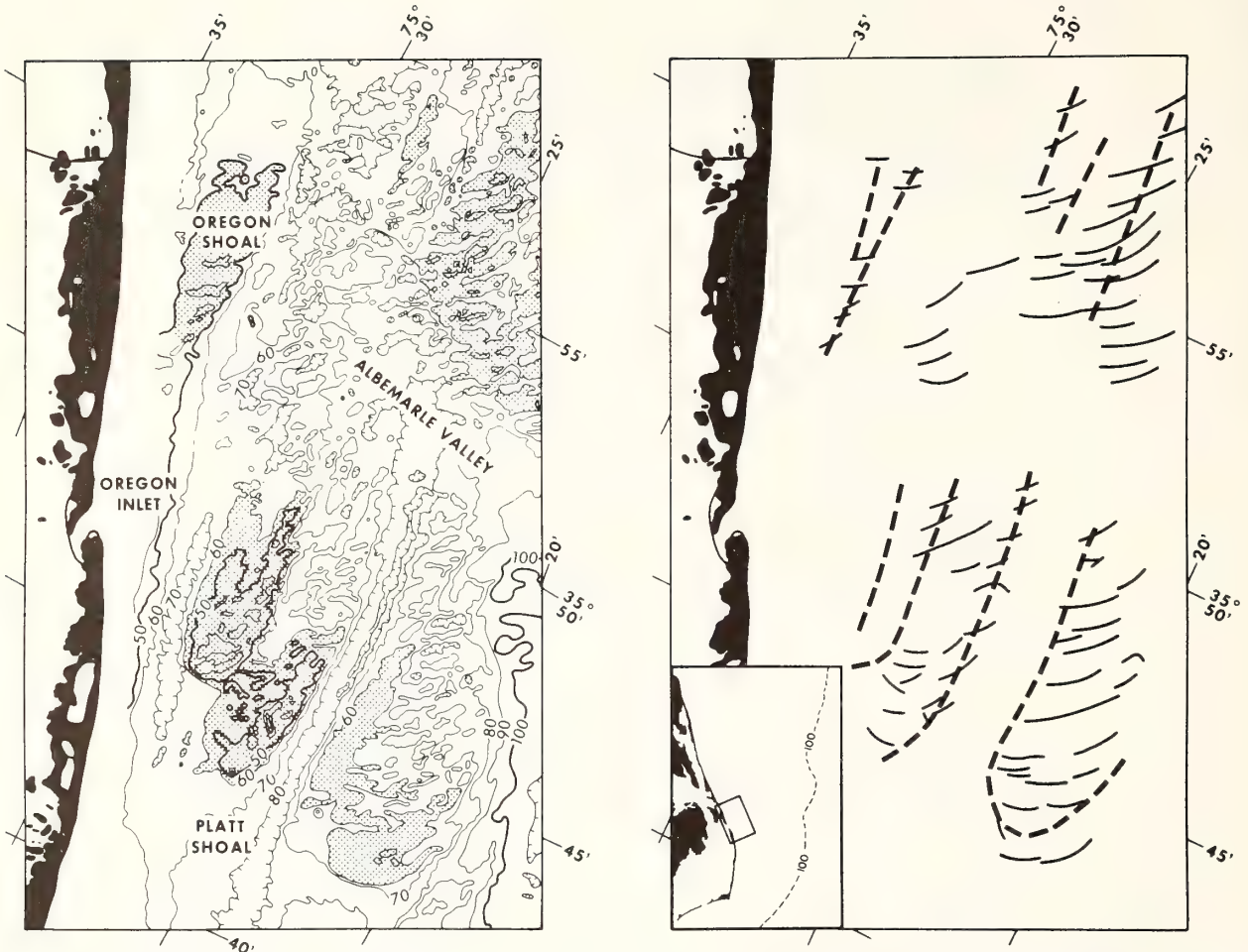


FIGURE 23. Sand ridges with superimposed sand waves on the northern North Carolina inner shelf. Topographic highs are stippled. Contours in feet. From Swift et al. (1973).

flow when the ellipse is less symmetrical. Under the latter condition, linear sand ridges may be the preferred bed form, as midtide cross flow would tend to nourish rather than degrade them (Smith, 1969). The triangular sand wave field is limited by a lack of sand on the northwest, by shoaling of the bottom and increasing wave surge on the coast to the south, and by fining of sand to the point that suspensive transport is dominant to the north (McCave, 1971).

Further down the velocity gradient, beyond the zones of obvious sand transport, there are sheets of fine sand and muddy fine sand and in local basins, mud. They lack bed forms other than ripples, and appear to be the product of primarily suspensive transport (McCave, 1971) of material that has outrun the bed load stream (see discussion, Chapter 10, p. 160). These deposits may be as thick as 10 m (Belderson and Stride, 1966), but

where they do not continue into mud, they break up into irregular, current-parallel or current-transverse patches of fine sand less than 2 m thick, resting on the gravelly substrate.

The complex pattern and mobile character of the shelf floor around the British Isles have led British workers to reject the relict model for the shelf sediments (Belderson et al., 1970). They note that it correctly draws attention to the autochthonous origin of the sediment, but that it fails to allow for its subsequent dynamic evolution. They propose instead a dynamic classification:

1. Lower sea-level and transgressive deposits, patchy in exposure, but probably more or less continuous beneath later material; largely the equivalent of a blanket (basal) conglomerate.

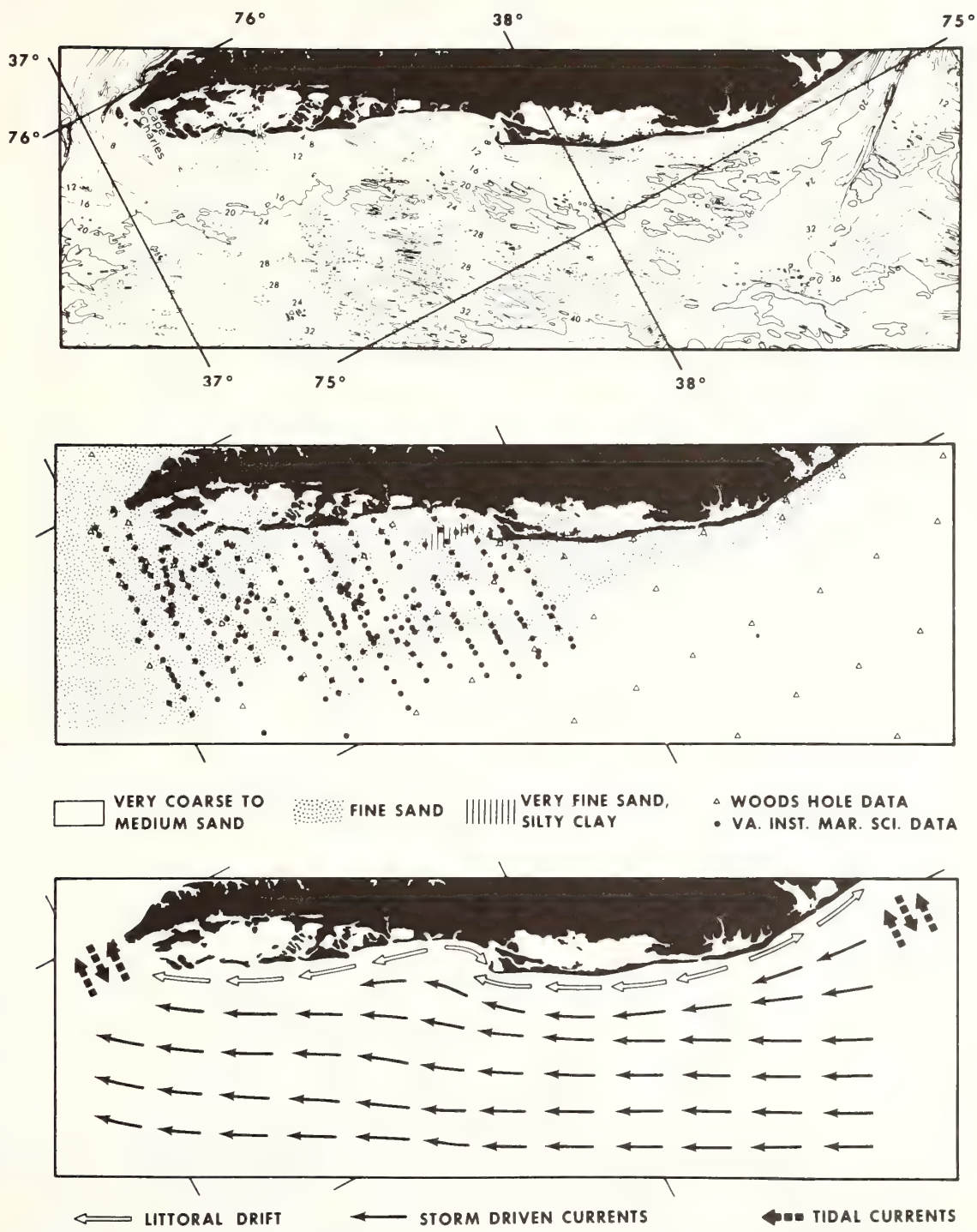


FIGURE 24. Above: Bathymetry of the Delmarva inner shelf. From Uchupi (1970). Center: Distribution of sediment. From Hathaway (1971) and Nichols (1972). Below: Inferred direction of currents responsible for bed load sediment transport. Reproduced from Swift (1975).

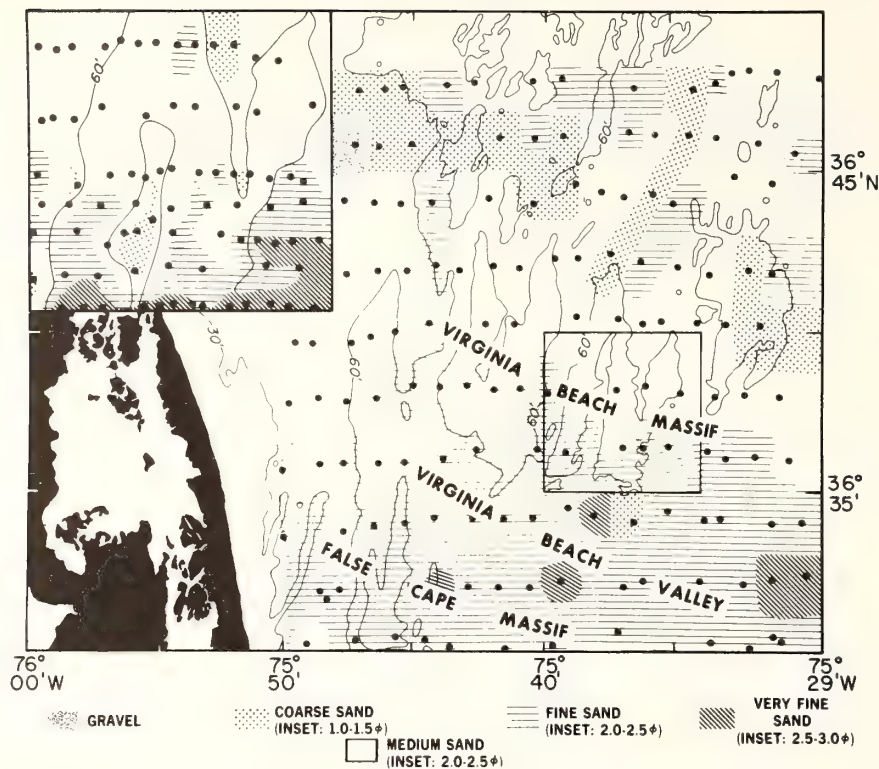


FIGURE 25. Grain-size distribution on a portion of the Virginia Beach massif, and adjacent shelf valley.

2. Material moving as bed load (over the coarser basal deposits) mainly well sorted sand and in places first-cycle calcareous sand.

3. Present sea-level deposits (category 2 sediment having come to permanent rest) consisting of large sheets to small patches, which range from gravel and shell gravel to sand and calcareous sands, muddy sands, and mud.

The implication is that of a shelf surface moving toward a state of equilibrium with its tidal regime. The degree of adjustment appears to be greater than in the case of the North American Atlantic Shelf, in that there is less preservation of nearshore depositional patterns. As a consequence of the intensity of the hydraulic climate, there is less on shelf storage (category 3) and more material in transit.

Locally, sand ridges similar to those of the Middle Atlantic Bight do occur. Like those of the Middle Atlantic Bight, they tend to be grouped in discrete fields. In some cases, it is possible to infer that these ridge fields are in fact shoal retreat massifs, generated by the retreat of a near shore depositional center during the course of the Holocene transgression (Swift, 1975). The clearest case may be made for the Norfolk Banks

(Houbolt, 1968; Caston and Stride, 1970; Caston, 1972); see Fig. 28. Here a series of offshore sand ridges may be traced into a modern nearshore generating zone (Robinson, 1966; see Chapter 14, Fig. 39) where sand is packaged by the specialized tidal regime of the shoreface into shapes hydrodynamically suited for survival on the open shelf (see discussion, p. 180). The Nantucket Shoals sector of the North American Atlantic shelf appears to constitute a similar evolutionary sequence of ridges (see Chapter 10, Fig. 30).

The Norfolk Banks are analogous to the cape shoal retreat massifs of the Carolina coast of North America, in that the generating zone is a coastal salient that serves as a sink for the nearshore sand flux. Other, more poorly defined ridge fields in the southern bight of the North Sea (Fig. 28) may be analogous to the estuarine shoal retreat massifs of the Middle Atlantic Bight in that they may have been generated by the retreat of the ancestral Rhine and Thames estuaries.

#### ALLOCHTHONOUS PATTERNS OF SEDIMENTATION

Shelves undergoing allochthonous sedimentation differ from autochthonous shelves in a variety of character-



FIGURE 26. Generalized sand transport paths around the British Isles and France, based on the velocity asymmetry of the tidal ellipse and the orientation and asymmetry of bed forms. From Kenyon and Stride (1970).

istics. The most obvious is that allochthonous shelves tend to be floored by fine sands, fine muddy sands, or muds that have escaped from adjacent river mouths: autochthonous shelves in contrast are generally covered by coarser grained sand of local origin. Although surfaces of allochthonous shelves are constructional in nature, they tend to be smooth and featureless; their fine materials have traveled primarily in suspension, and the effective underwater angles of repose of the sediment may be too low to result in such large-scale bed forms as sand waves or sand ridges. However, such features are not totally unknown. Allersma (1972) has reported "mud waves" from the Venezuelan shelf that appear to be very similar to the shoreface-connected ridges of the Middle Atlantic Bight.

**Transport on Allochthonous Shelves**

Mechanisms of sediment transport on allochthonous shelves have been generally described by Drake in Chapter 9. Since this chapter stresses regional transport patterns, it seems worthwhile to summarize Drake et al.'s (1972) study of river-dominated sedimentation on the southern California shelf. This carefully documented, real time study of the dispersal of flood sediment is probably the most detailed report on the nature of allochthonous sediment dispersal available at the time of writing.

In January and February of 1969, southern California experienced two intense rainstorms which resulted in a record flood discharge. The freshly eroded sediment was a distinctive red-brown in contrast to the drab hue of

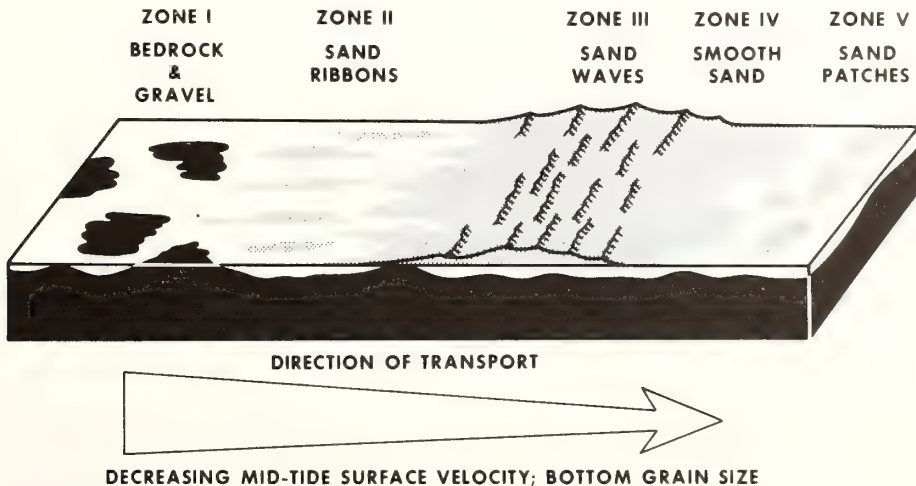


FIGURE 27. Succession of morphologic provinces along a tidal transport path. Based on Belderson et al. (1970).

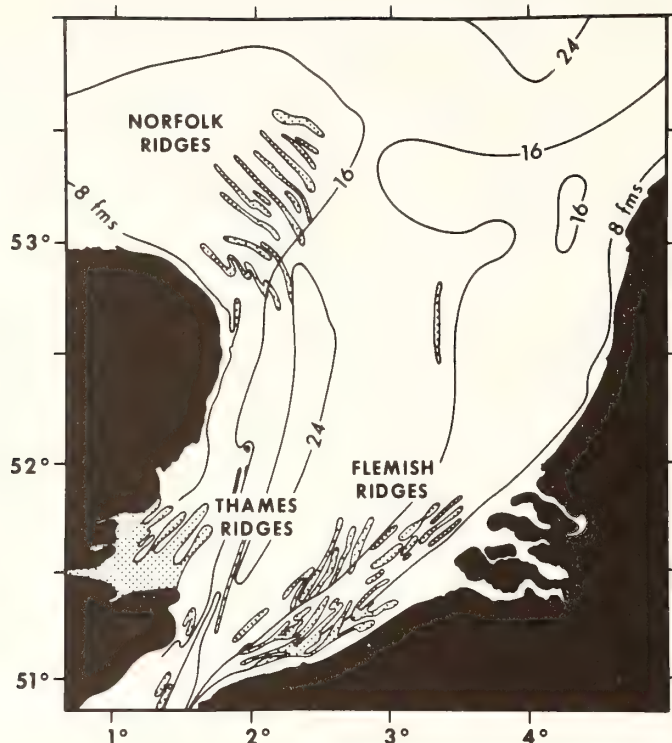


FIGURE 28. Tidal ridge fields of the southern bight of the North Sea. Northernmost ridge field appears to constitute a shoal retreat massif, marking the retreat path of the nearshore tidal regime of the Norfolk coast. Ridge fields in the approach to the English Channel may have been initiated in an earlier, more nearly estuarine environment. From Houbolt (1968).

the reduced shelf sediments. The flood deposit on the shelf could therefore be repeatedly cored and isopached, and its shifting center of mass traced seaward through time.

USGS stream records show that  $33$  to  $45 \times 10^6$  metric tons of suspended silt and clay and  $12$  to  $20 \times 10^6$  metric tons of suspended sand were introduced by the Santa Clara and Ventura rivers. By the end of April 1969, more than 70% of this material was still on the shelf in the form of a submarine sand shoal extending 7 km seaward, and a westward-thinning and -fining blanket of fine sand, silt, and clay existed seaward of that (Fig. 29A).

By the end of the summer of 1969, the layer extended further seaward, had thinned by 20%, and had developed a secondary lobe beneath the Anacapa current to the south (Fig. 29B). Eighteen months after the floods, the surface layer was still readily detectable. Considerable bioturbation, scour, and redistribution had occurred south of Ventura, but the deposit was more stable to the north (Fig. 29C).

A concurrent study of suspended sediment distribution in the water column revealed the pattern of sediment transport (Fig. 29D). Vertical transparency profiles, after four days of flooding, showed that most of the suspended matter was contained in the brackish surface layer, 10 to 20 m thick. Profiles in April and May revealed a layer 15 m thick, with concentrations in excess of 2 mg l, and a total load of  $10$  to  $20 \times 10^4$  metric tons. Since this load was equal to river discharge for the entire month of April, it must have represented lateral transport of sediment resuspended in the nearshore zone. Vertical profiles over the middle and outer shelf for the rest of the year were characterized by sharply bounded turbidity maxima, each marking a thermal discontinuity. These also were nourished by lateral transport from the nearshore sector where the discontinuities impinged on the sloping bottom. The near-bottom nepheloid layer was the most turbid zone in the inner shelf. This nepheloid layer was invariably the coolest, and was invariably isothermal, indicating that its turbidity was the result of turbulence generated



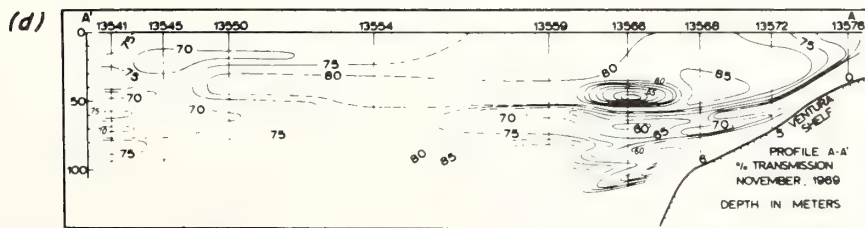
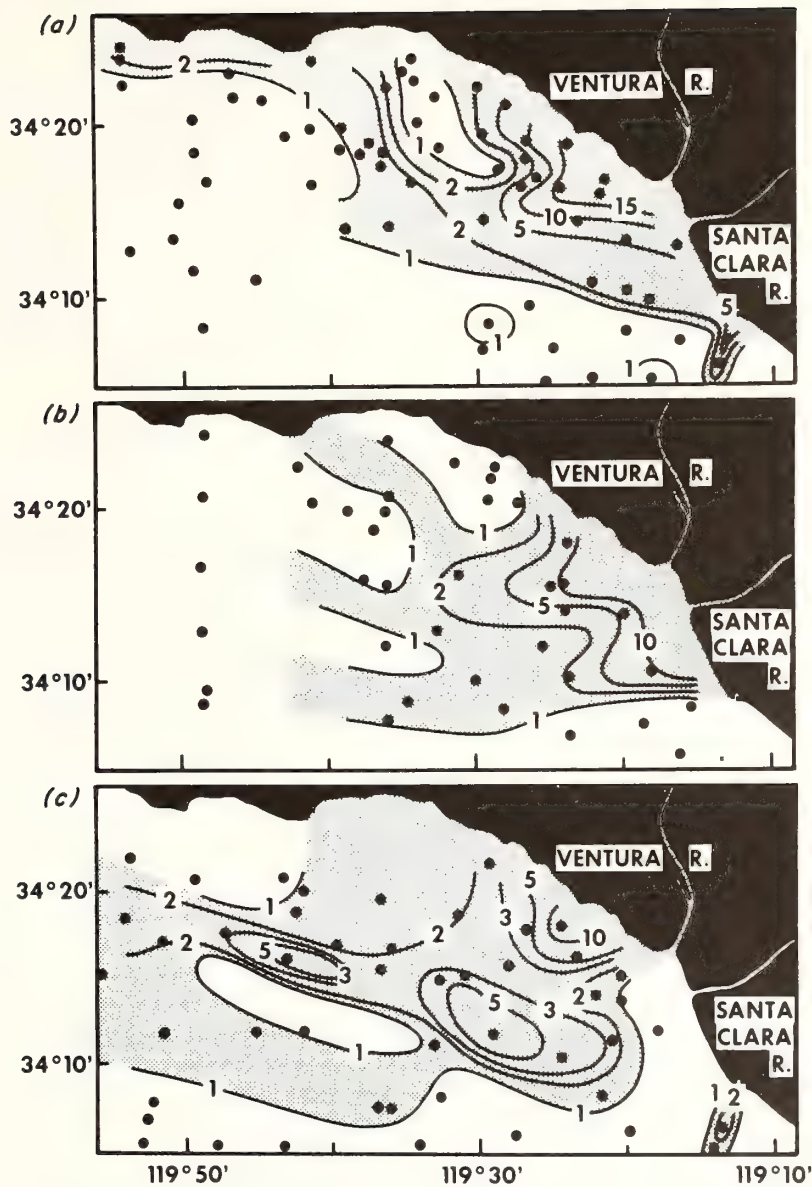


FIGURE 29. Thickness of flood sediment (centimeters) on the Santa Barbara-Oxnard shelf in (a) March-April 1969; (b) May-August 1969; and (c) February-June 1970, based on cores. (d) East-west cross section showing vertical distribution of light-attenuating substances over Santa Barbara-Oxnard shelf. For clarity, the bottom 20 m of the water column is not contoured, but the percent transmission value at the bottom is noted. From Drake et al. (1972).

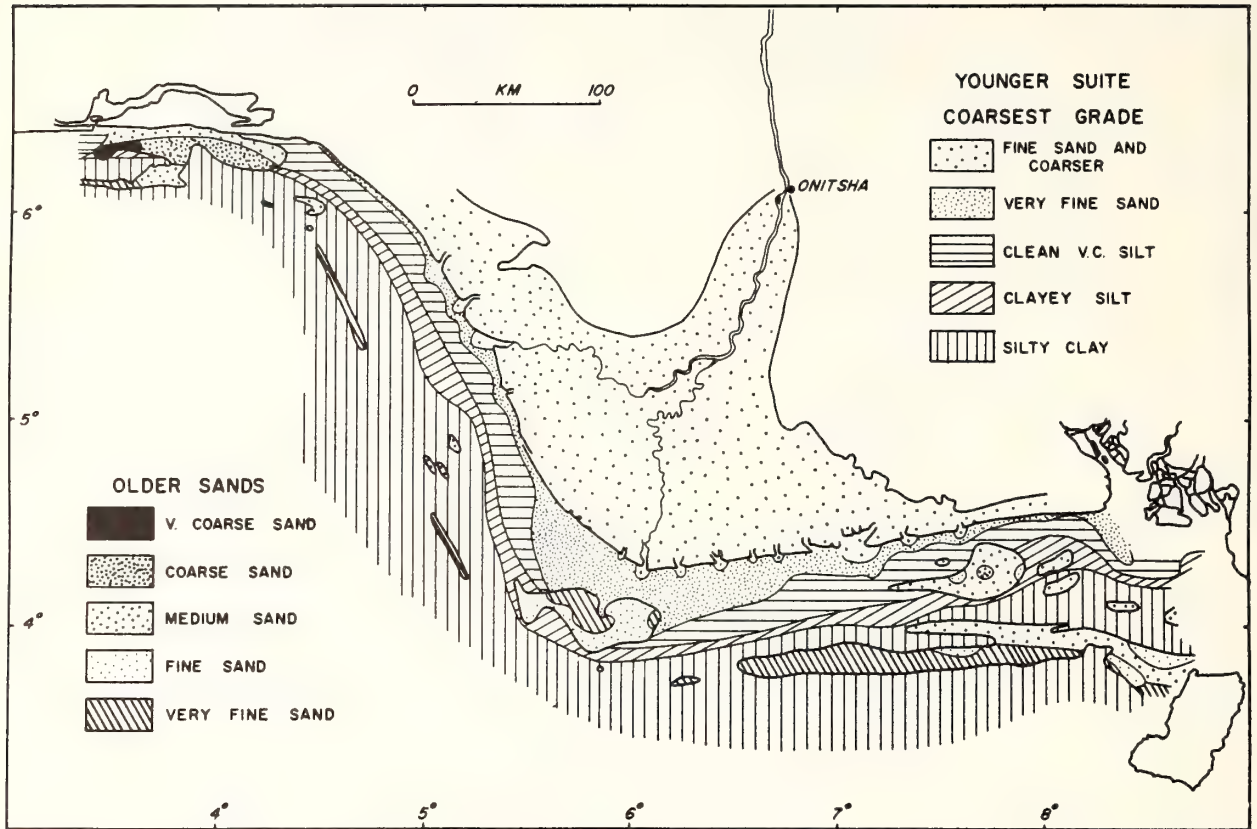


FIGURE 30. Distribution of sediments on the Niger shelf. Young suite is of allochthonous origin; older suite of autochthonous sand is exposed in nondepositional windows. From Allen (1964).

by bottom wave surge. Bottom turbidities ranged from 50 mg l during the flood to 4 to 6 mg l during the next winter, but were at no time dense enough to drive density currents.

Drake et al.'s study suggests that the transport of suspended sediment across shelves undergoing allochthonous sediment action starts with introduction by a river jet, and continues with deposition, resuspension, and intervals of diffusion and advection by coastal currents in a near-bottom nepheloid layer.

#### Depositional Patterns on Allochthonous Shelves

Fine sediments deposited on allochthonous shelves may occur as a seaward-thinning sheet (Fig. 30), or as a series of strips of fine sand or mud oriented generally parallel to the shoreline; see Figs. 31 and 32 (see also Venkatarathnam, 1968; McMaster and Lachance, 1969; and Niino and Emery, 1966). On shelves of equant or irregular dimensions, shelf sectors surfaced by far-traveled, fine-grained sediment may be more irregular in shape (Niino and Emery, 1966; McManus et al.,

1969; Knebel and Creager, 1973). Such allochthonous deposits tend to be separated by, or to enclose, nondepositional "windows" in which relatively coarse autochthonous sands are exposed. The disposition of these strips and sheets of allochthonous sediment is generally meaningful in terms of what is known of regional circulation patterns. Locally, the strips may underlie turbid, brackish water plumes that extend from river mouths under the impetus of buoyant expansion and inertial flow (Chapter 14, Fig. 41). Where such flows of high-turbidity water extend for long distances parallel to the coast or seaward across the shelf at promontories, they have been described by McCave (1972) as "advective mud streams" (Fig. 33). He cites Jerlov (1958) as describing such a mud stream running south from the Po Delta, over the mud bed shown in Fig. 34.

However, the presence of windows of older sand does not necessarily mean that the sediment pattern is a transient one, which must be eventually followed by a total masking of the old surface of transgression by fine sediment. Instead, the pattern may be a steady state one,

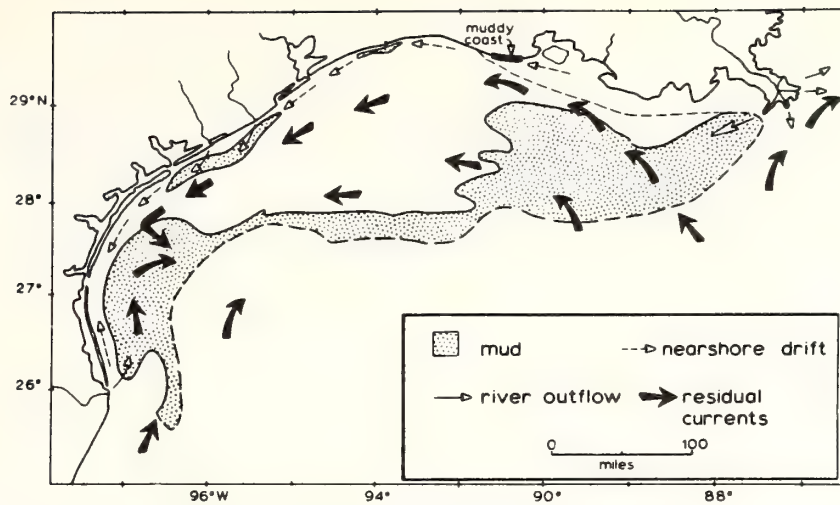


FIGURE 31. Distribution of mud and generalized transport pattern on the western Gulf shelf of North America. From McCave (1972), after Van Andel and Curaray (1960).

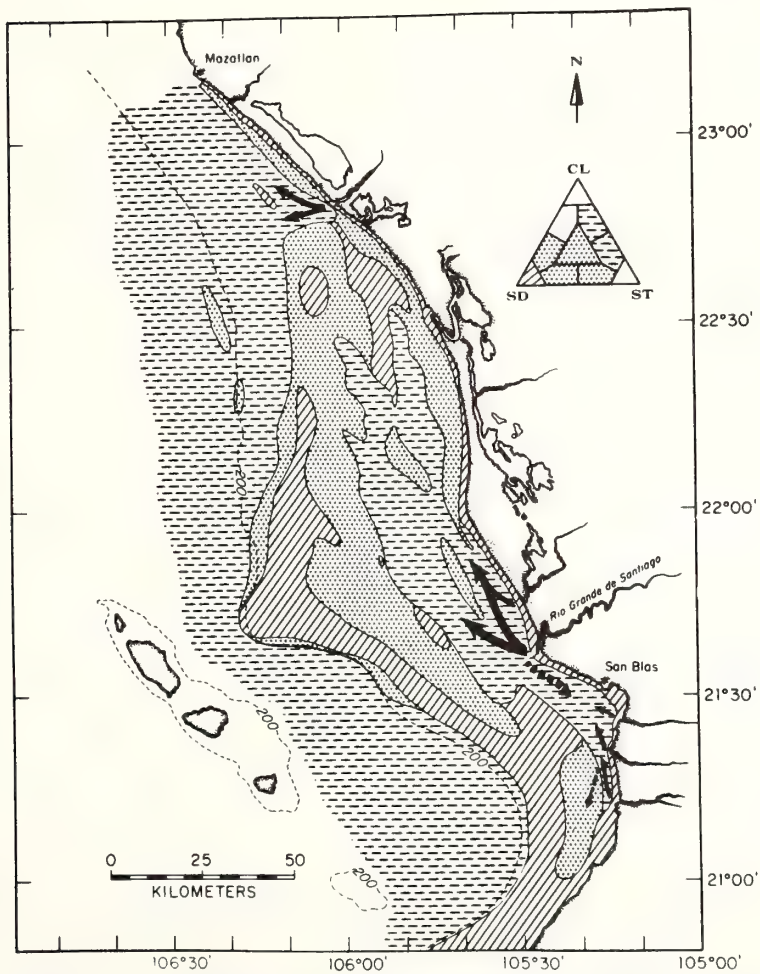


FIGURE 32. Distribution of sediment and generalized transport pattern off the Nayarit coast, Pacific side of Mexico. Autochthonous sands occur in non-depositional windows. From Curaray (1969).

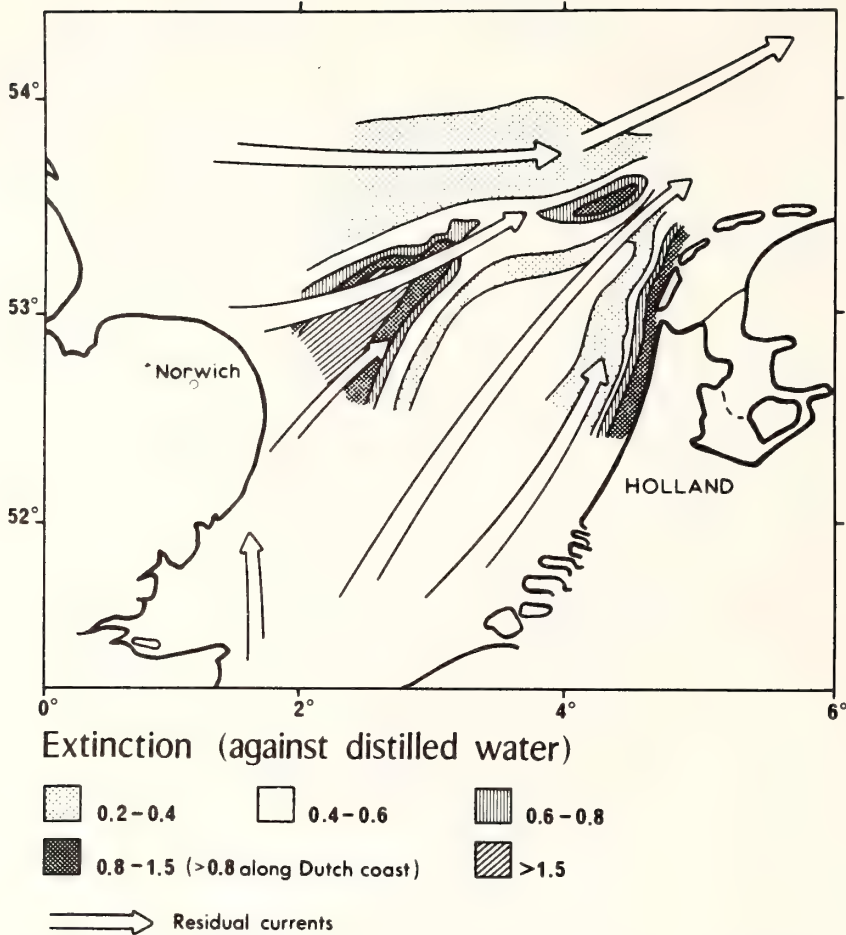


FIGURE 33. Turbidity (light extinction) given by Joseph (1953) with the residual current pattern in the southern North Sea. Two advective mud streams are illustrated, one crossing from the English to the Dutch side of the area, the other running up the Dutch coast from the mouths of the Plime River. Actual sediment concentrations are higher in the latter. From McCave (1972).

determined by the local relationship between the hydraulic activity (primarily wave surge) on the bottom and the near-bottom concentration of suspended sediment (Fig. 35), as well as by the regional transport pattern.

On autochthonous shelves, sand transport is primarily advective in nature, occurring during short, intense episodes of wind-driven or tidal flow, and textural gradients tend to reflect the direction of sand transport, with transport becoming finer down the transport path (see Figs. 25 and 27). The transport of fine sand and mud on shelves undergoing allochthonous sedimentation is also primarily advective in nature, in that the turbid water tends to flow as a mass in response to the regional circulation pattern. However, because of the greater role of reversing tidal currents and wave surge in dis-

tributing fine sediment it is convenient to think of fine sediment transport on allochthonous shelves as consisting of a dominant advective component, driven by the regional circulation pattern, and an important but subordinate diffusive component, driven by reversing tidal flows and wave surge.

The diffusive component of transport not only influences the regional pattern of fine sediment deposition as noted in Fig. 35 and Chapter 9, Fig. 15, but may also result in textural gradients within allochthonous sediment sheets that trend at an angle across the advective transport direction. On the Niger shelf, for instance, the dominant, advective transport direction is from east to west, under the impetus of the Guinea current (Allen, 1964). However, bottom sediments tend to become finer in a seaward (north to south) direction (Fig. 36). Sharma et al.

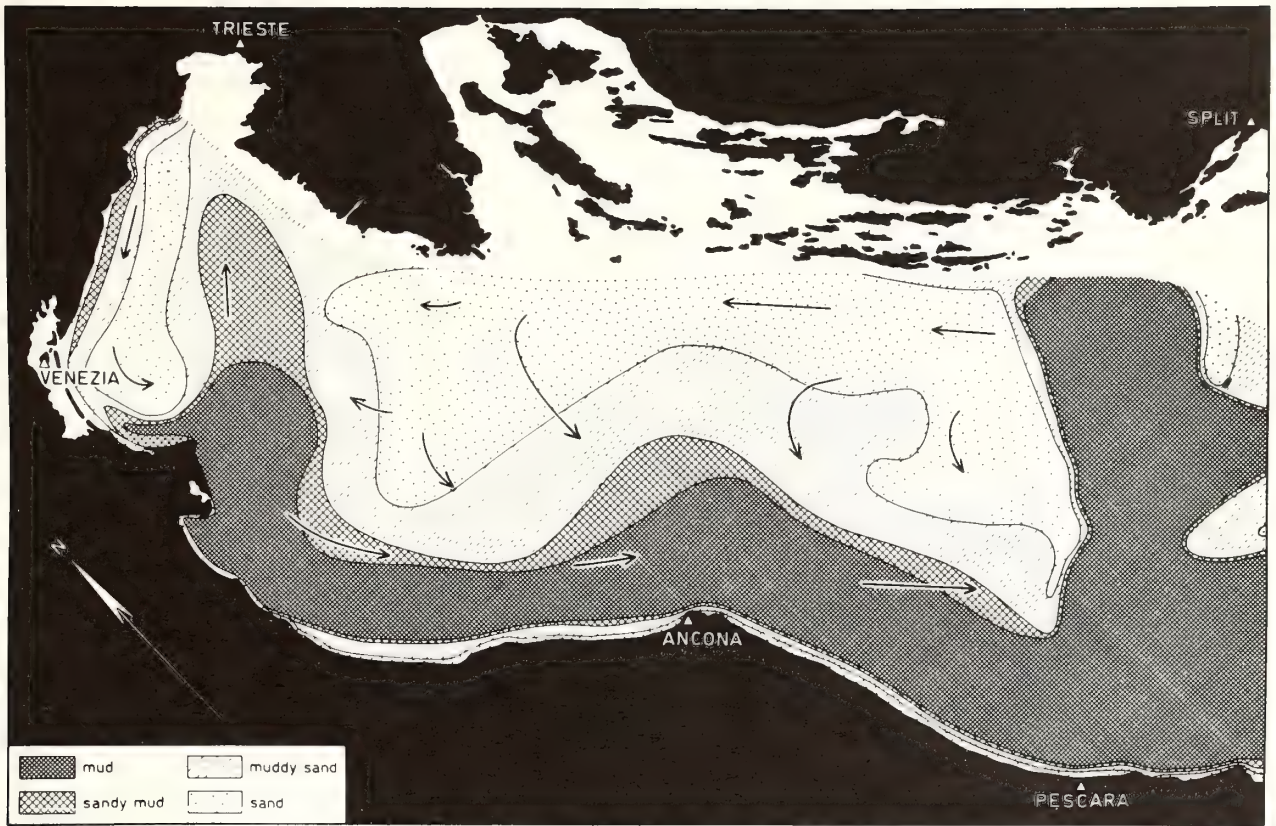


FIGURE 34. *Distribution of sediment in the northern Adriatic Sea. From Van Straaten (1965).*

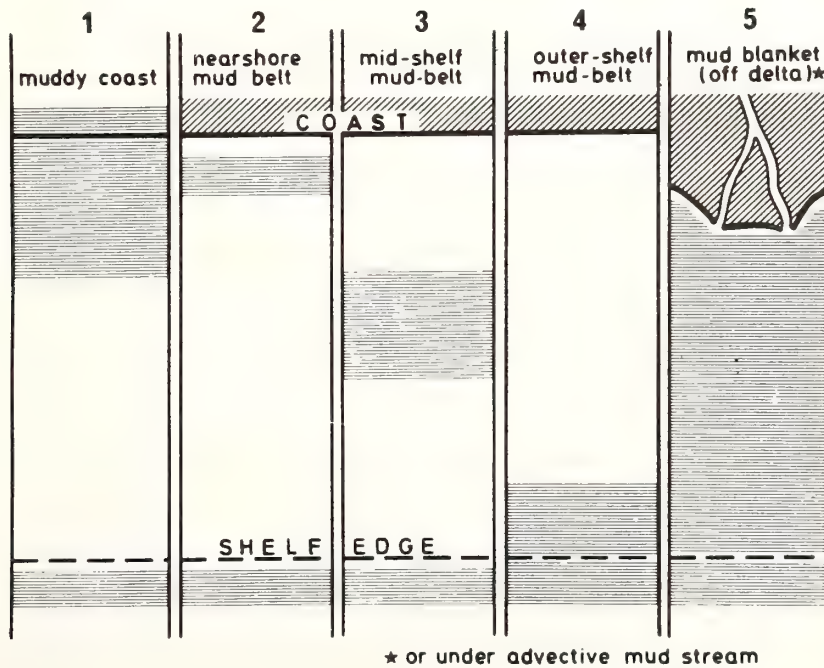


FIGURE 35. *Schematic representation of five cases of sites of shelf mud accumulation. Compare with Fig. 15 in Chapter 9. From McCave (1972).*

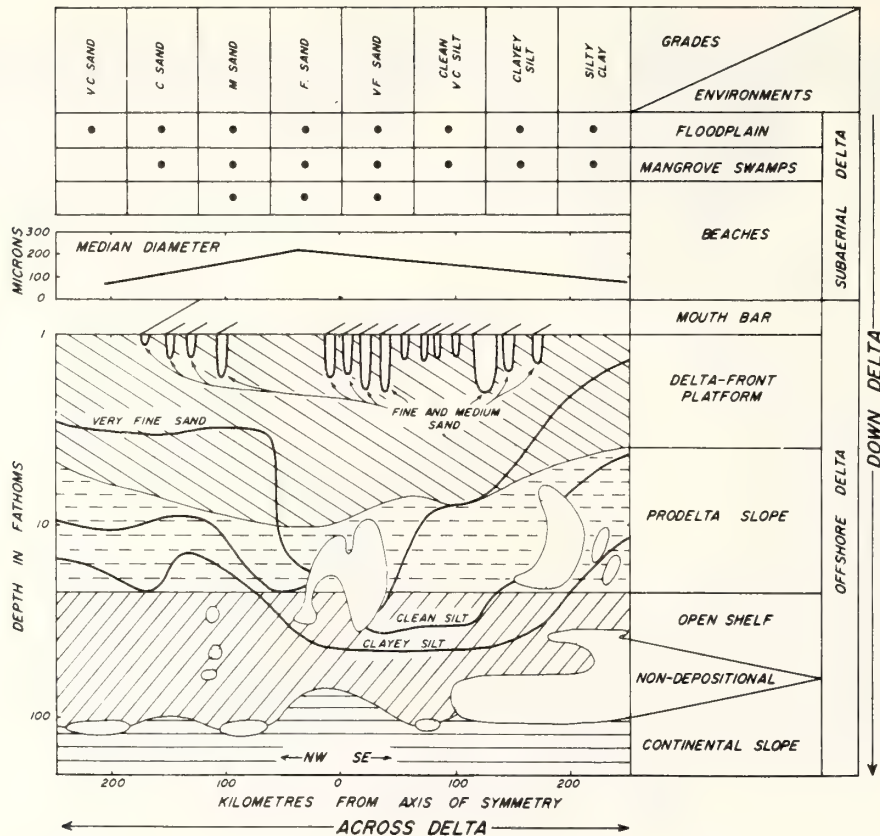


FIGURE 36. Grain size in relation to sedimentary environments in Niger Delta area. In subaerial delta, all grades present are shown. In offshore part of delta, coarsest grade in near-surface layers is projected onto vertical plane perpendicular to axis of delta symmetry. From Allen (1964).

(1972) have described grain-size gradients in Briston Bay of the Bering Sea that are more nearly related to the isobaths than to the prevailing currents. They consider the textural gradients to be the consequence of wave surge diffusion (Fig. 37). The operative mechanism would be progressive sorting during the seaward diffusion of sediment. In this process, sediment that drifts seaward into deeper water during a transport event is likely to leave its coarsest fraction behind when reentrained, because of the weaker nature of deep-water wave surge (see discussion of progressive sorting, Chapter 10, p. 162).

### Stratigraphy of Allochthonous Shelves

The tenfold reduction in the rate of eustatic sea-level rise experienced between 4000 and 7000 years ago (Milliman and Emery, 1968) has resulted in a shift from autochthonous to allochthonous regimes in a number of shelf sectors (Curry, 1964). River mouths servicing such shelves have equilibrated with their tidal prisms,

and have begun to bypass fine sediment in quantities sufficient to result in deposition on the shelf surface. Two characteristic stratigraphies have resulted, which may be correlated with the transport schemes illustrated in Figs. 3a and 3c. Where the shift in the balance between the rate of sedimentation and the rate of sea-level rise has not been adequate to cause coastal progradation, the coast has continued to undergo erosional shoreface retreat, or has approached stillstand conditions (see discussion of equation, p. 312). Patches and sheets of fine-grained sediments have accumulated more or less simultaneously over the sand sheet produced during the earlier period of erosional shoreface retreat (Fig. 38). Elsewhere, where the Late Holocene balance between sedimentation and sea-level rise has resulted in coastal progradation, the transgressive sand sheet passes landward beneath a veneer of mud some few meters thick into a thick littoral sand body deposited during stillstand, and a second, subaerial, sand sheet extends seaward over the inner portion of the mud veneer (see Chapter 14, Fig. 10B).

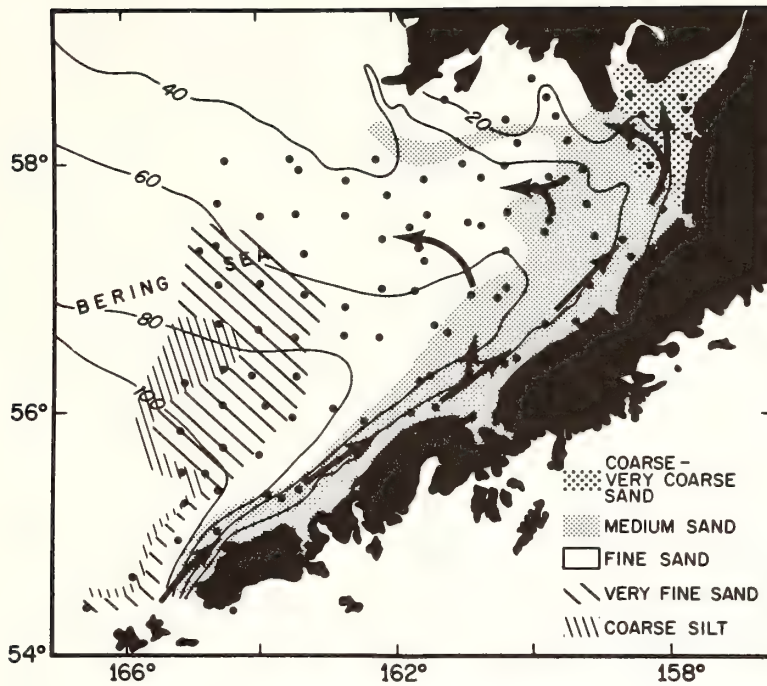


FIGURE 37. The distribution of grain sizes in Bristol Bay. See text for analysis. From Sharma et al. (1972).

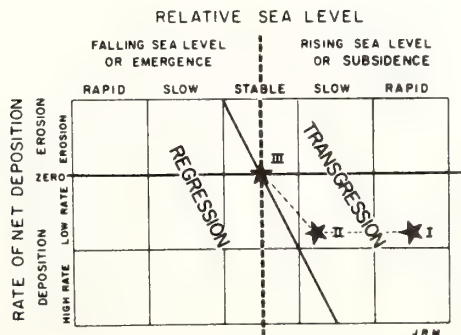
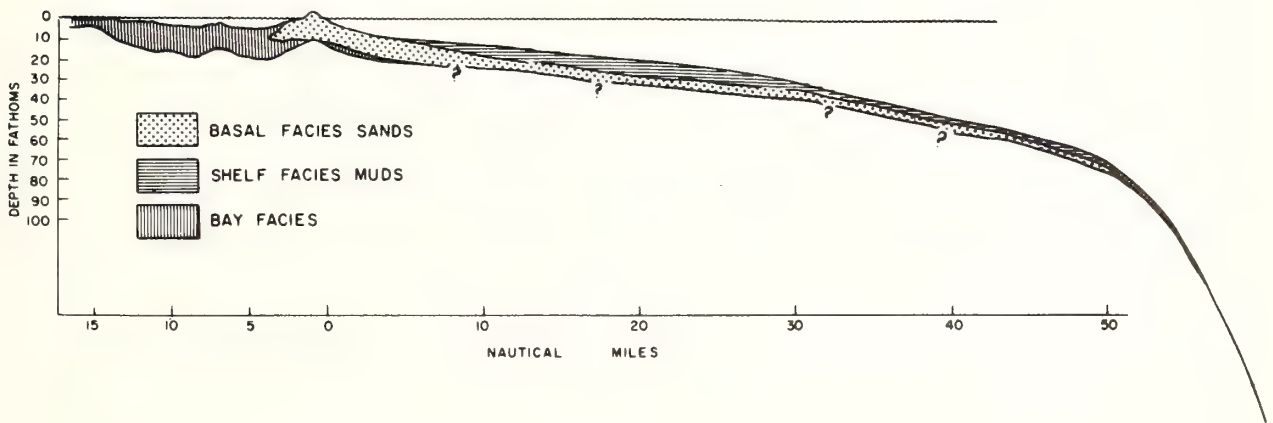


FIGURE 38. Above: Generalized cross section of Late Quaternary sediments in a line perpendicular to the coast near Rockport,

Texas. Below: Schematic representation of shoreline migration. From Curry (1964).

The abrupt nature of the transition from Early Holocene autochthonous regimes and the recent nature of this transition have prevented us from observing on modern continental margins a third characteristic stratigraphy, which is widespread in the rock record, namely "marine onlap" (Grabau, 1913, Fig. 144). In this model, a prolonged period of relatively slow sea-level rise is accomplished by the transport scheme shown in Fig. 3*b*, where both shoreface and river mouth bypassing occur in a regime of transgressive allochthonous sedimentation. Subaerial and submarine depositional environments are linked by a unified pattern of sediment transport, and their landward displacement results in a threefold sequence of fluvial, marine marginal, and open shelf lithosomes beneath the shelf surface.

During the slow eustatic transgression of the Cretaceous, such a sequence was deposited on the North American shelf off North and South Carolina (Fig. 39). The present erosional surface approximates a time plane, and seaward decrease in grain size across this environment suggests progressive sorting through fluvial, estuarine, and marine environments (Swift and Heron, 1969). Shoreface erosion was an important source of sediment, as indicated by the internal unconformity that largely replaces the littoral sand facies. River mouth injection may also have been an important mechanism of coastal bypassing, since the fine-grained, open marine facies thickens seaward.

The Amazon shelf off Brazil, South America may represent a modern analog of such a transgressive autochthonous sequence (Milliman et al., in press). Milliman et al. describe the mud deposits of the Amazon shelf as a landward-thickening wedge, whose offshore portions were deposited during lower stands of sea level, by the predecessor of the coastal mud stream which presently trends northwest, from the mouth of the Amazon toward the Guyana coast (Fig. 40). Milliman and his associates suggest that the offshore surface of this mud deposit is at present experiencing an autochthonous sedimentary regime. They suggest that the net fine sediment budget of the offshore shelf is negative, with more fine material being lost to erosion than is replaced by diffusion from the coastal source, so that a silty lag is accumulating over its surface. More detailed investigations may indicate that this type of transgressive allochthonous regime is more common than now supposed.

## SUMMARY

The rate and sense of shoreline movement have an important modulating effect on the shelf sedimentary regime. It is helpful to think of the coastline as a "littoral

energy fence" in which the landward-oriented net surge of shoaling waves tends to push sediment back toward the beach. There are two basic categories of "valves" that serve to regulate the passage of sediment through this barrier into the shelf dispersal system: river mouths and the intervening expanses of shoreface.

During rapid transgressions, river mouths generally cannot adjust to their combined river and tidal discharges as fast as required by the rise of sea level, and they become sediment sinks. Sediment is bypassed through the coastal zone by the basically passive process of erosional shoreface retreat, which leaves the shelf surface veneered with a sandy residue.

During slow transgressions, estuarine channels are more likely to equilibrate to their discharge. Such channels are capable of bypassing sand as well as finer sediment, and sediment is supplied by both shoreface and river mouth bypassing.

During regressions, river mouth bypassing is dominant. Shorefaces become sand sinks, which advance seaward by means of the successive growth of beach ridges.

Rapid transgressions result in autochthonous shelf regimes, in which the surficial sediments are of in situ origin. Slow transgressions result in allochthonous shelf regimes. The sediment load is filtered during passage through a broad intracoastal zone of estuaries and lagoons, so that the fraction reaching the shelf is fine-grained and mobile, and may be dispersed for long distances across the shelf surface.

On autochthonous shelves, only such large-scale subaerial features as cuestas and river valleys seem able to survive transgression, and even these are strongly modified by passage of the shoreline. On shelves of low relief, most morphologic elements have formed at the foot of the retreating shoreface. Shelf valley complexes consist of shelf valleys, shoal retreat massifs, and deltas. In many cases shelf valleys are the retreat paths of estuary mouth scour channels, and do not always overlie the buried subaerial river channels. They tend to be paired with estuarine shoal-retreat massifs, the retreat paths of estuary mouth shoals. Littoral drift convergences at capes and headlands may also result in shoal retreat massifs. Scarps on autochthonous shelves do not seem to be drowned shorelines in the strict sense, but instead are truncated lower shorefaces formed during postglacial stillstands.

In the Middle Atlantic Bight of North America, both morphology and grain-size distribution patterns can be shown to be in part of post-transgressional origin, forming in response to storm flows. The shelf surface is characterized by a pervasive ridge and swale topography. It is locally forming at the foot of the retreating shoreface,



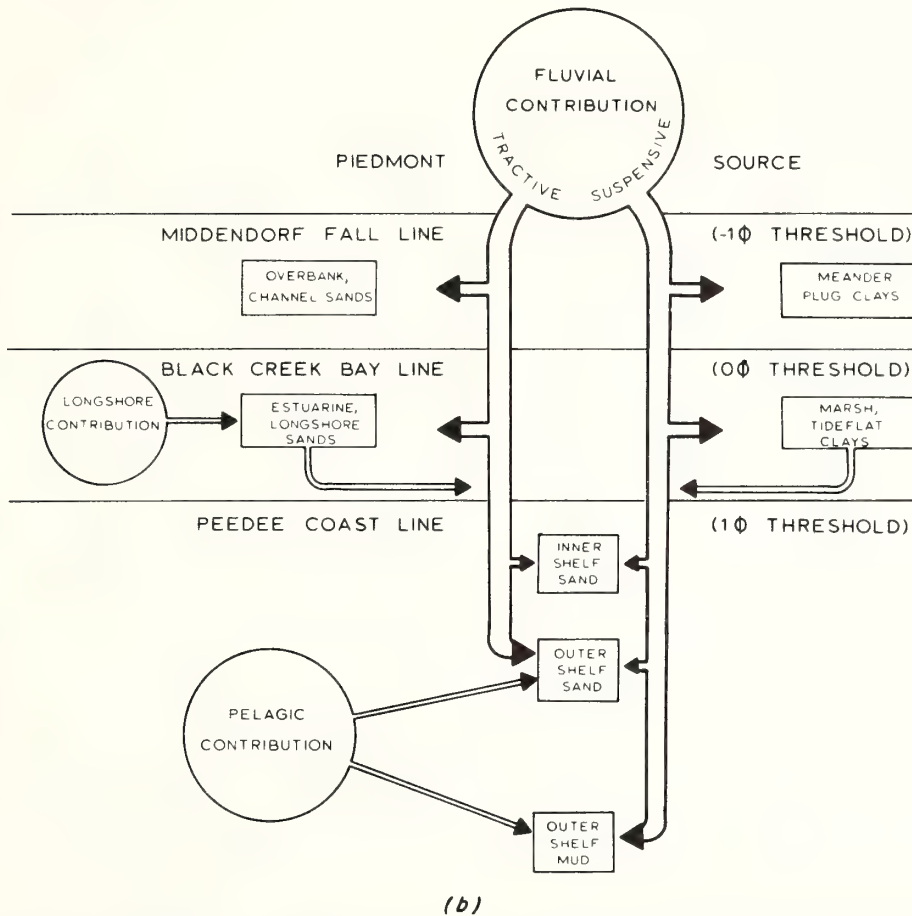
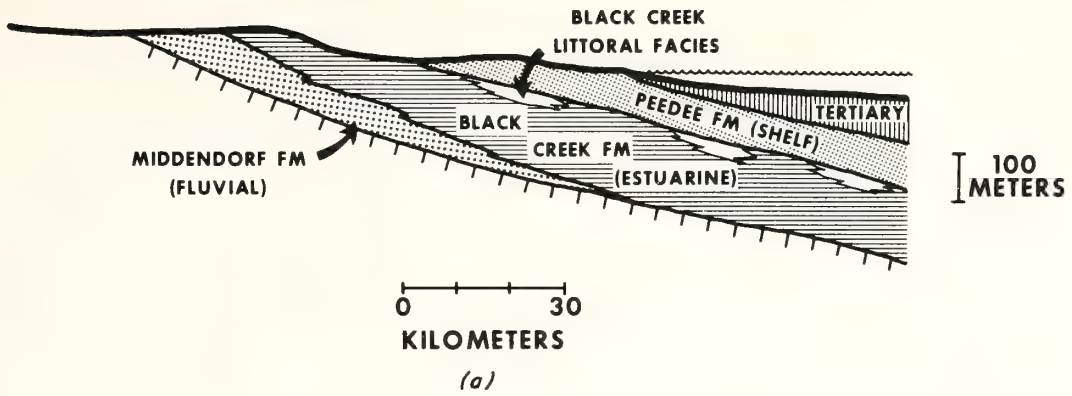


FIGURE 39. (a) Schematic section through the Cretaceous Lumbee Group of North and South Carolina. The Middendorf, Black Creek, and Pee Dee Formations are deposits of landward-displacing fluvial, estuarine-

lagoonal, and shelf environments, respectively. (b) Pattern of sediment transport as reconstructed from grain-size gradients and primary structures in outcrops. From Swift and Heron (1969).

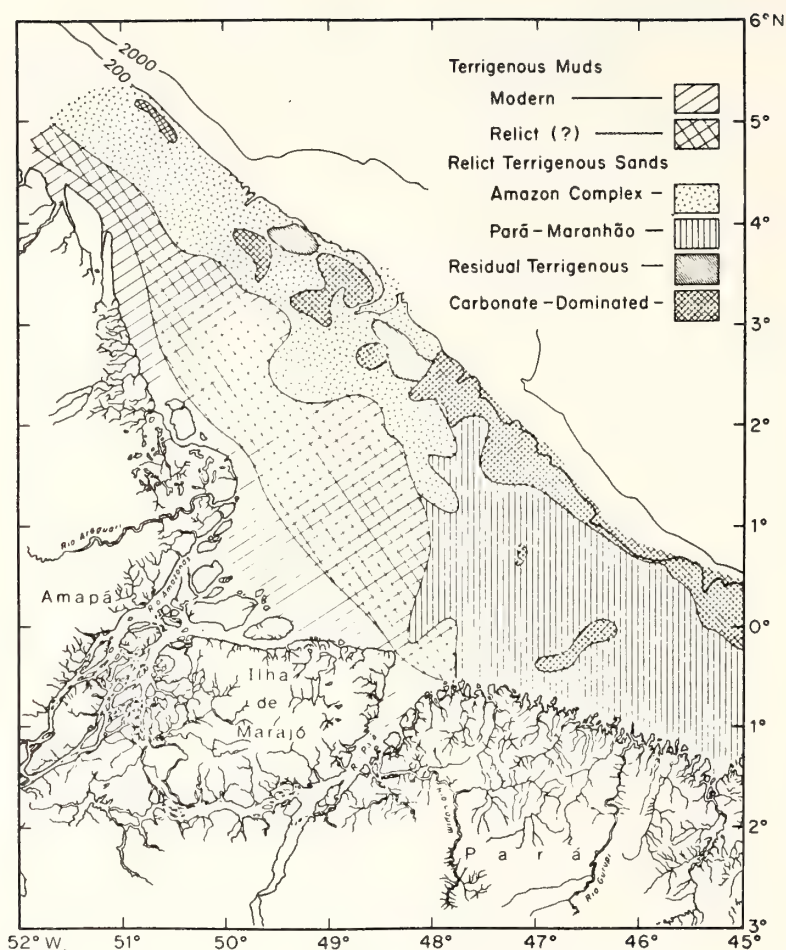


FIGURE 40. *Sediment distribution of the Amazon shelf. Modern terrigenous muds are deposited beneath a north-trending coastal mud stream. "Relict" muds are believed to have been deposited by the same mud stream during lower stands of sea level. From Milliman et al. (in press).*

in response to coastal boundary flow, but elsewhere appears to have developed more or less spontaneously further out on the shelf surface. Current lineations (sand ribbons and erosional furrows) are abundant. Coarse sand lags occur on highs, finer sands occur on their downcurrent slopes and in adjacent lows.

The shelf around the British Isles is an example of an autochthonous shelf that has reacted in a more vigorous fashion, in response to a high-intensity tidal regime. A well-organized pattern of sand dispersal consists of sand streams that extend from bed load partings to bed load convergences, or to the shelf edge. Nearshore morphologic elements have largely been obliterated. However, well-defined fields of tide-maintained sand ridges are probably analogous to the shoal retreat massifs of the Middle Atlantic Bight.

Allochthonous shelves occur adjacent to large rivers with sediment loads sufficiently large to locally slow or reverse the sense of the postglacial transgression. Transport is dominantly by water column advection (mud streams) but diffusion in response to bottom wave surge is important. Allochthonous deposits of fine sand and mud are commonly not continuous, but tend to leave "windows" in which autochthonous sands are exposed. Such windows are not necessarily transient phenomena, but may reflect areas in which the concentration of suspended sediment in the bottom nepheloid layer is counteracted by a relatively high level of "hydraulic activity." Textural gradients in autochthonous deposits may more nearly reflect the seaward, diffusive component of transport, rather than the coast-parallel advective component.

## ACKNOWLEDGMENTS

I thank Paul E. Potter and Orrin H. Pilkey for their helpful criticisms of this chapter.

## REFERENCES

- Allen, J. R. L. (1964). Late Quaternary Niger Delta, and adjacent areas: Sedimentary environments and lithofacies. *Am. Assoc. Pet. Geol. Bull.*, **19**: 547-600.
- Allen, J. R. L. (1970a). Sediments of the modern Niger delta: A summary and review. In J. P. Morgan, ed., *Deltaic Sedimentation, Modern and Ancient*. Soc. Econ. Paleontologists and Mineralogists Spec. Publ. 15, Tulsa, Okla., pp. 138-151.
- Allen, J. R. L. (1970b). *Physical Processes of Sedimentation*. New York: American Elsevier, 248 pp.
- Allersina, E. (1972). Mud on the oceanic shelf off Guiana. In *Symposium on Investigations and Resources of the Caribbean Sea and Adjacent Regions*. UNESCO, Paris (Unipub, N.Y.), pp. 193-203.
- Andrews, E., D. G. Stephens, and D. J. Colquhoun (1973). Scouring of buried Pleistocene barrier complexes as a source of channel sand in tidal creeks, North Island Quadrangle, South Carolina. *Geol. Soc. Am. Bull.*, **84**: 3659-3662.
- Bagnold, R. A. (1966). An approach to the sediment transport problem from general physics. *U.S. Geol. Surv. Prof. Pap.* 422-1, 37 pp.
- Barby, D. G. and J. H. Hoyt (1964). An upper Miocene dredged fauna from tidal channels of coastal Georgia. *J. Paleontol.*, **38**: 67-73.
- Beardsley, R. C. and B. Butman (1974). Circulation on the New England continental shelf: Response to strong winter storms. *Geol. Res. Lett.*, **1**: 181-184.
- Belderson, R. H. and A. H. Stride (1966). Tidal current fashioning of a basal bed. *Mar. Geol.*, **4**: 237-257.
- Belderson, R. H., N. H. Kenyon, and A. H. Stride (1970). *Holocene Sediments on the Continental Shelf West of the British Isles*. Inst. Geol. Sci. Rep. No. 70, pp. 157-170.
- Bernard, H. A. and R. J. Le Blanc (1965). Resume of the Quaternary geology of the northwest Gulf of Mexico province. In H. E. Wright, Jr., and D. J. Frey, eds., *The Quaternary of the United States*. Princeton, N.J.: Princeton University Press, pp. 137-185.
- Brouwer, J. E. (1964). The North Sea. In L. D. Stamp, ed., *The North Sea and the Law of the Continental Shelf*. Bude, Cornwall, England, Geographical Publications Ltd., World Land Use Survey Occ. Papers 5, pp. 3-14.
- Bumpus, D. F. (1973). A description of circulation on the continental shelf of the east coast of the United States. *Prog. Oceanogr.*, **6**: 117-157.
- Caralp, M., A. Klingebiel, C. Latouche, J. Moyes, and R. Prud'homme (1972). *Bilan Cartographique sur le Plateau Continental d'Aquitaine*. Bull. Inst. Géol. Bassin d'Aquitaine, Numéro Spécial. 351 Cours de la Libération, 33 Talence, France, 25 pp.
- Carter, L. (1973). Surficial sediments of Barkley Sound and the adjacent continental shelf, West Vancouver Island. *Can. J. Earth Sci.*, **10**: 441-459.
- Caston, V. N. D. (1972). Linear sand banks in the southern North Sea. *Sedimentology*, **18**: 63-78.
- Caston, V. N. D. and A. H. Stride (1970). Tidal sand movement between some linear sand banks in the North Sea off north-eastern Norfolk. *Mar. Geol.*, **9**: M38-M42.
- Colquhoun, D. J. (1969). *Geomorphology of the Lower Coastal Plain of South Carolina*. Geological Notes, Division of Geology, Columbia, South Carolina State Development Board, 36 pp.
- Curry, J. R. (1964). Transgressions and regressions. In R. L. Mills, ed., *Papers in Marine Geology: Shepard Commemorative Volume*. New York: MacMillan, pp. 175-203.
- Curry, J. R. (1969). History of continental shelves. In *The New Concepts of Continental Margin Sedimentation*. Washington, D.C.: Am. Geol. Inst., pp. JC-6-1 to JC-6-18.
- Dolan, R., B. Hayden, G. Hoenenbergh, J. Zeeman, and M. Vincent (1973). Classification of the coastal environments of the world, Part 1. *The Americas*. Tech. Rep. 1, Office of Naval Research, Washington, D.C., 163 pp.
- Drake, D. E., R. L. Kolpack, and P. J. Fischer (1972). Sediment transport on the Santa Barbara-Oxnard shelf, Santa Barbara channel, California. In D. J. P. Swift, D. B. Duane, and O. H. Pilkey, eds., *Shelf Sediment Transport: Process and Pattern*. Stroudsburg, Pa.: Dowden, Hutchinson & Ross, pp. 301-332.
- Duane, D. B., M. E. Field, E. P. Meisburger, D. J. P. Swift, and S. J. Williams (1972). Linear shoals on the Atlantic inner continental shelf, Florida to Long Island. In D. J. P. Swift, D. B. Duane, and O. H. Pilkey, eds., *Shelf Sediment Transport: Process and Pattern*. Stroudsburg, Pa.: Dowden, Hutchinson & Ross, pp. 447-499.
- Emery, K. O. (1952). Continental shelf sediments of southern California. *Geol. Soc. Am. Bull.*, **63**: 1105-1108.
- Emery, K. O. (1968). Relict sediments on continental shelves of the world. *Am. Assoc. Pet. Geol. Bull.*, **52**: 445-464.
- Field, M. E. (1974). Buried strandline deposits on the central Florida inner shelf. *Geol. Soc. Am. Bull.*, **85**: 57-60.
- Fischer, A. G. (1961). Stratigraphic record of transgressing seas in the light of sedimentation Atlantic coast of New Jersey. *Am. Assoc. Pet. Geol. Bull.*, **15**: 1656-1666.
- Ginsburg, R. N. and N. P. James (1974). Holocene carbonate sediments of continental shelves. In C. A. Burk and C. C. Drake, eds., *The Geology of Continental Margins*. Berlin and New York: Springer-Verlag, pp. 137-156.
- Grabau, A. W. (1913). *Principles of Stratigraphy*, 1960 facsimile edition of 1924 revision. New York: Dover, 1185 pp.
- Hathaway, J. C. (1971). *Data File, Continental Margin Program, Atlantic Coast of the United States, Vol. 2, Samples Collection and Analytical Data*. Woods Hole Oceanographic Institution Ref. 71-15, U.S. Geol. Surv., Woods Hole, Mass., 446 pp.
- Henry, V. J., Jr. and J. H. Hoyt (1968). Quaternary paralic shelf sediments of Georgia. *Southeast. Geol.*, **9**: 195-214.
- Holtedahl, H. (1958). Some remarks on the geomorphology of the continental shelves off Norway, Labrador, and southeast Alaska. *J. Geol.*, **66**: 461-471.
- Holtedahl, O. (1940). *The Submarine Relief off the Norwegian Coast*. Oslo: Norske Videnskaps-Akade, 43 pp.
- Houbolt, J. J. H. C. (1968). Recent sediments in the southern bight of the North Sea. *Geol. Mijnbouw*, **47**: 245-273.
- Hoyt, J. H. and J. R. Hails (1967). Pleistocene shoreline sediments in coastal Georgia: Deposition and modification. *Science*, **155**: 1541-1543.
- Hoyt, J. H. and V. J. Henry, Jr. (1967). Influence of island migration on barrier island sedimentation. *Geol. Soc. Am. Bull.*, **78**: 77-86.

- Jerlov, N. G. (1958). Distribution of suspended material in the Adriatic Sea. *Arch. Oceanogr. Limnol.*, **11**: 227-250.
- Johnson, D. (1919). *Shore Processes and Shoreline Development*. New York: Wiley, 585 pp. (2nd ed., 1938).
- Joseph, J. (1953). Die Trubangsverhältnisse in der Südwestlichen Nordsee Während der "Gauss Fahrt" im Februar/März, 1952. *Ber. Dtsch. Wiss. Komm. f. Meeresforsch.* **13**: 93-103.
- Kaye, C. A. (1959). Shoreline features and quaternary shoreline changes, Puerto Rico. *U.S. Geol. Surv. Prof. Pap.*, 317-B, 140 pp.
- Kenyon, N. H. (1970). Sand ribbons of European tidal seas. *Mar. Geol.*, **9**: 25-39.
- Kenyon, N. H. and A. H. Stride (1970). The tide-swept continental shelf sediments between the Shetland Isles and France. *Sedimentology*, **14**: 159-175.
- King, L. H., B. Maclean, and G. Drapeau (1972). The Scotian shelf submarine end moraine complex. In *24th Int. Geol. Congr., Montreal*, pp. 237-239.
- Knebel, H. J. and J. S. Creager (1973). Sedimentary environments of the east-central Bering Sea continental shelf. *Mar. Geol.*, **15**: 25-47.
- Kumar, N. and J. E. Sanders (1970). Are basal transgressive sands chiefly inlet filling sands? *Marit. Sediments*, **6**: 12-14.
- Laursen, E. M. (1958). The total sediment load of streams. *Proc. Am. Soc. Civil Eng.*, **84**(HV1): 1530.
- McCave, I. N. (1971). Sand waves in the North Sea off the coast of Holland. *Mar. Geol.*, **10**: 149-227.
- McCave, I. N. (1972). Transport and escape of fine-grained sediment from shelf areas. In D. J. P. Swift, D. B. Duane, and O. H. Pilkey, eds., *Shelf Sediment Transport: Process and Pattern*. Stroudsburg, Pa.: Dowden, Hutchinson & Ross, pp. 225-248.
- McClennen, C. F. (1973). New Jersey continental shelf near bottom current meter records and recent sediment activity. *J. Sediment. Petrol.*, **43**: 371-380.
- McClennen, C. E. and R. L. McMaster (1971). Probable Holocene transgressive effects on geomorphic features of the continental shelf off New Jersey, United States. *Marit. Sediments*, **7**: 69-72.
- McKinney, T. F. (1974). Large-scale current lineations on the Great Egg shoal retreat massif, New Jersey shelf. Investigation by side-scan sonar. *J. Sediment. Petrol.*, **17**: 79-102.
- McKinney, T. F., W. L. Stubblefield, and D. J. P. Swift (1974). Large-scale current lineations on the central New Jersey shelf: Investigations by side scan sonar. *Mar. Geol.*, **17**: 79-102.
- McManus, D. A., J. C. Kelley, and J. S. Creager (1969). Continental shelf sedimentation in an arctic environment. *Geol. Soc. Am. Bull.*, **80**: 1961-1984.
- McMaster, R. L. and T. P. Lachance (1969). Northwestern African continental shelf sediments. *Mar. Geol.*, **7**: 57-67.
- McMaster, R. L., T. P. Lachance, and A. Ashraf (1970). Continental shelf geomorphic features off Portuguese Guinea, Guinea, and Sierra Leone (West Africa). *Mar. Geol.*, **9**: 203-213.
- Meade, R. H. (1969). Landward transport of bottom sediments in the estuaries of the Atlantic coastal plain. *J. Sediment. Petrol.*, **39**: 229-234.
- Merrill, A. S., K. O. Emery, and M. Rubin (1965). Oyster shells on the American continental shelf. *Science*, **147**: 395-400.
- Milliman, J. D. and K. O. Emery (1968). Sea levels during the past 35,000 years. *Science*, **162**: 1121-1123.
- Milliman, J. D., C. P. Summerhayes, and H. T. Barretto (in press). Quaternary sedimentation on the Amazon continental margin: A model. *Geol. Soc. Am. Bull.*
- Naumann, C. T. (1858). *Lehrbuch der Geognosie*, Bd. 1, 2nd ed. Leipzig: Wilhelm Engelmann, 1000 pp.
- Nichols, M. M. (1972). *Inner Shelf Sediments off Chesapeake Bay. I. General Lithology and Composition*. Spec. Sci. Rep. 64, Virginia Institute of Marine Science, Gloucester Point, Va., 20 pp.
- Niino, H. and K. O. Emery (1966). Continental shelf off north-eastern Asia. *J. Sediment. Petrol.*, **36**: 152-161.
- Norris, R. M. (1972). Shell and gravel layers, western continental shelf, New Zealand. *N.Z. J. Geol. Geophys.*, **15**: 572-589.
- Oaks, R. Q., Jr. and N. K. Coch (1963). Pleistocene sea levels, southeastern Virginia. *Science*, **140**: 979-983.
- Pilkey, O. H. and M. E. Field (1972). Onshore transportation of continental shelf sediment: Atlantic southeastern United States. In *Shelf Sediment Transport: Process and Pattern*. Stroudsburg, Pa.: Dowden, Hutchinson & Ross, pp. 424-446.
- Pilkey, O. H. and J. Frankenberg (1964). The relict-Recent sediment boundary on the Georgia continental shelf. *Georgia Acad. Sci. Bull.*, **22**: 1-4.
- Powers, M. C. and B. Kinsman (1953). Shell accumulations in underwater sediments and the thickness of the traction zone. *J. Sediment. Petrol.*, **23**: 229-234.
- Redfield, A. C. (1956). The influence of the continental shelf on the tides of the Atlantic coast of the United States. *J. Mar. Res.*, **17**: 432-448.
- Robinson, A. H. W. (1966). Residual currents in relation to shoreline evolution of the East Anglian coast. *Mar. Geol.*, **4**: 57-84.
- Sarnthein, M. (1972). Sediments and history of the postglacial transgression in the Persian Gulf and Northwest Gulf of Oman. *Mar. Geol.*, **12**: 245-266.
- Sharma, G. D., A. S. Naidu, and D. W. Hood (1972). Bristol Bay: Model contemporary graded shelf. *Am. Assoc. Pet. Geol. Bull.*, **56**: 2000-2012.
- Shepard, F. P. (1932). Sediments on continental shelves. *Geol. Soc. Am. Bull.*, **43**: 1017-1034.
- Shepard, F. P. (1973). *Submarine Geology*. 3rd Edition. New York: Harper & Row, 517 pp.
- Sheridan, R. E., C. E. Dill, Jr., and J. C. Kraft (1974). Holocene sedimentary environment of the Atlantic inner shelf off Delaware. *Geol. Soc. Am. Bull.*, **85**: 1319-1328.
- Shideler, G. L., D. J. P. Swift, G. H. Johnson, and B. W. Holliday (1972). Late Quaternary stratigraphy of the inner Virginia continental shelf: A proposed standard section. *Geol. Soc. Am. Bull.*, **83**: 1787-1804.
- Smith, J. D. (1969). Geomorphology of a sand ridge. *J. Geol.*, **77**: 39-55.
- Stahl, L., J. Koczan, and D. Swift (1974). Anatomy of a shore-face-connected ridge system on the New Jersey shelf: Implications for genesis of the shelf surficial sand sheet. *Geology*, **2**: 117-120.
- Stanley, D. J. (1969). Submarine channel deposits and their fossil analogs (fluxoturbidites). In D. J. Stanley, ed., *The New Concepts of Continental Margin Sedimentation*. Washington, D.C.: Am. Geol. Inst., pp. DJS-9-1 to DJS-9-17.
- Stanley, D. J., G. Drapeau, and A. E. Cok (1968). Submerged terraces on the Nova Scotian shelf. *Z. Geomorphol., Suppl.*, **7**: 85-94.

- Stanley, D. J., D. J. P. Swift, and H. G. Richards (1967). Fossiliferous concretions on Georges Bank. *J. Sediment. Petrol.*, **37**: 1070-1083.
- Stanley, D. J., D. J. P. Swift, N. Silverberg, N. P. James, and R. G. Sutton (1972). *Late Quaternary progradation and sand spill-over on the outer continental margin off Nova Scotia, Southeast Canada*. Smithsonian Contr. Earth Sciences, **8**: 88 pp.
- Steers, J. A. (1971). The East Coast floods, 31 January-1 February, 1953. In J. A. Steers, ed., *Applied Coastal Geomorphology*. Cambridge, Mass.: MIT Press, pp. 198-224, 227 pp. (reprinted).
- Stride, A. H. (1963). Current-swept sea floors near the southern half of Great Britain. *Q. J. Geol. Soc. London*, **119**: 175-199.
- Stride, A. H., R. H. Belderson, and N. H. Kenyon (1972). *Longitudinal Furrows and Depositional Sand Bodies of the English Channel*. Mém. Bur. Rech. Géol. Min. No. 79, pp. 233-244.
- Stubblefield, W. L., J. W. Lavelle, T. F. McKinney, and D. J. P. Swift (1975). Sediment response to the present hydraulic regime on the Central New Jersey shelf. *J. sediment. Petrol.*, **45**: 337-358.
- Stubblefield, W. L. and D. J. P. Swift (in press). Ridge development as revealed by sub-bottom profiles on the central New Jersey shelf. Submitted to *Mar. Geol.*
- Swift, D. J. P. (1973). Delaware shelf valley: Estuary retreat path, not drowned river valley. *Geol. Soc. Am. Bull.*, **84**: 2743-2748.
- Swift, D. J. P. (1974). Continental shelf sedimentation. In C. A. Burke and C. L. Drake, eds., *The Geology of Continental Margins*. Berlin and New York: Springer-Verlag, pp. 117-133.
- Swift, D. J. P. (1975). Tidal sand ridges and shoal retreat massifs. *Mar. Geol.*, **18**: 105-134.
- Swift, D. J. P. (in press). Continental shelf sedimentation. In R. Fairbridge, ed., *Encyclopedia of Sedimentology*. Princeton, N.J.: Van-Nostrand-Reinhold.
- Swift, D. J. P., D. B. Duane, and T. F. McKinney (1973). Ridge and swale topography of the Middle Atlantic Bight, North America: Secular response to the Holocene hydraulic regime. *Mar. Geol.*, **15**: 227-247.
- Swift, D. J. P. and S. D. Heron, Jr. (1969). Stratigraphy of the Carolina Cretaceous. *Southeast. Geol.*, **10**: 201-245.
- Swift, D. J. P., J. W. Kofoed, F. P. Saulsbury, and P. Sears (1972). Holocene evolution of the shelf surface, central and southern Atlantic coast of North America. In D. J. P. Swift, D. B. Duane, and O. H. Pilkey, eds., *Shelf Sediment Transport: Process and Pattern*. Stroudsburg, Dowden, Hutchinson & Ross, pp. 499-574.
- Swift, D. J. P. and P. Sears (1974). Estuarine and littoral depositional patterns in the surficial sand sheet, central and southern Atlantic shelf of North America. In *International Symposium on Interrelationship of Estuarine and Continental Shelf Sedimentation*. Inst. Géol. du Bassin d'Aquitaine, Mém. 7, pp. 171-189.
- Swift, D. J. P., D. J. Stanley, and J. R. Curray (1971). Relict sediments, a reconsideration. *J. Geol.*, **79**: 322-346.
- Todd, T. W. (1968). Dynamic diversion: influence of longshore current-tidal floor interaction on Chenier and barrier island plains. *J. Sediment. Petrol.*, **38**: 734-746.
- Uchupi, E. (1968). Atlantic continental shelf and slope of the United States—Physiography. *U.S. Geol. Surv. Prof. Pap.* 529-C, 30 pp.
- Uchupi, E. (1970). Atlantic continental shelf and slope of the United States: Shallow structure. *U.S. Geol. Surv. Prof. Pap.* 524-7, 44 pp.
- Van Andel, Tj. H. and J. R. Curray (1960). Regional aspects of modern sedimentation in the northern Gulf of Mexico and similar basins, and Paleogeographic significance. In F. P. Shepard, F. B. Phegler and T. H. Van Andel, eds., *Recent sediments, northwest Gulf of Mexico*. Tulsa: Am. Assoc. Pet. Geol., pp. 345-364.
- Van Andel, Tj. H. and J. J. Veevers (1967). *Morphology and Sediments of the Timor Sea*. Commonwealth of Australia, Bureau of Mineral Resources, Geology and Geophysics, Bull. 83, 172 pp.
- Van Straaten, L. M. J. V. (1965). Sedimentation in the north-western part of the Adriatic Sea. In W. F. Whitland and R. Bradshaw, eds., *Submarine Geology and Geophysics*. London: Butterworths, pp. 143-162.
- Veenstra, H. J. (1969). Gravels of the southern North Sea. *Mar. Geol.*, **7**: 449-464.
- Venkatarathnam, K. (1968). Studies on the sediments of the continental shelf off the regions Visakhapatnam-Pudimadaka and Pulicat Lake-Penner River confluence along the east coast of India. *Natl. Inst. Sci. India Bull.*, **38**: 472-482.
- Visher, G. S. and J. D. Howard (1974). Dynamic relationship between hydraulic and sedimentation in the Altamaha estuary. *J. Sediment. Petrol.*, **44**: 502-521.
- Whitmore, F. C., Jr., K. O. Emery, H. B. S. Cooke, and D. J. P. Swift (1967). Elephant teeth from the Atlantic continental shelf. *Science*, **156**: 1477-1481.
- Wright, L. D. and J. M. Coleman (1973). Variations in morphology of major river deltas as functions of ocean wave and river discharge regimes. *Am. Assoc. Pet. Geol. Bull.*, **57**: 320-348.
- Wright, L. D. and J. M. Coleman (1974). Mississippi River mouth processes: Effluent dynamics and morphological development. *J. Geol.*, **82**: 751-778.

## Substrate Response to Hydraulic Process: Grain-Size Frequency Distributions and Bed Forms

DONALD J. P. SWIFT

*Atlantic Oceanographic and Meteorological Laboratories, Miami, Florida*

JOHN C. LUDWICK

*Institute of Oceanography, Old Dominion University, Norfolk, Virginia*

Chapters 8 and 9 dealt with the entrainment of sand and mud, respectively, on the continental shelf. In addition, Chapter 8 discussed the most ubiquitous shelf bed form, the sand ripple formed by bottom wave surge, since it plays a critical role in the entrainment and transport of sand on the continental shelf.

This chapter explores further the response of the shelf floor to the hydraulic climate. Two key responses that are used to infer regional patterns of sediment transport are grain-size frequency distributions and substrate bed forms. The chapter also describes a numerical model for estimating sediment transport and areas and rates of erosion and deposition.

### GRAIN-SIZE FREQUENCY DISTRIBUTIONS

Krumbein (1934) was the first to bring to popular attention the concept that the size frequency distribution of sand samples tends to be log-normally distributed. It has become a tenet of conventional wisdom that this distribution, as defined by its mean and standard distribution, is the signature of the depositional event, and that deviations from log normality, as measured in terms of

standard deviation, skewness, and kurtosis, reflect both the provenance and subsequent hydraulic history of the sediment (see Inman, 1949; Friedman, 1961; Visher, 1969).

### Genesis of the Normal Curve

Recent theoretical studies (Middleton, 1968; Swift et al., 1972b) have attempted to present this hypothesis in a more rigorous manner by consideration of probability theory. The reader is referred to these papers for the mathematical foundation of the following discussion.

The probability model for the genesis of a log-normally distributed grain population considers a flow over a sand substrate in which the total load is adjusted to flow conditions. If deposition is to occur, there must be a decrease in bottom shear stress ( $-\partial\tau_0/\partial x$ ) and discharge ( $-\partial q/\partial x$ ) down the transport path. The distribution of grain sizes in the load undergoing transport down this shear stress gradient and the absolute value of the gradient is such that for each grain-size class, an upstream portion of the path is experiencing supercritical stress, and a downstream portion is experiencing subcritical stress. We are concerned with the central portion

of the transport path, where a series of transition points for critical shear stress occur, with each successive downstream transition point being associated with a successively finer grain-size class. The grains are assumed to travel down the transport path in a series of discrete hops as a consequence of the turbulent structure of the flow, and as a consequence of a larger scale cycle of flow events separated by periods of quiescence. The model is thus a stochastic model, with an inherently random aspect to its behavior, and the problem may be dealt with in terms of probability theory.

Under these conditions, it is conceptually possible to define the grain-size frequency distribution at each point as the product of two probability vectors, an admittance vector and a retention vector (Fig. 1). The admittance vector is the sequence of probabilities of entrance of the size classes present, ordered in sequence of decreasing grain size. The retention vector is similarly the sequence of probabilities of retention of successively finer grain sizes.

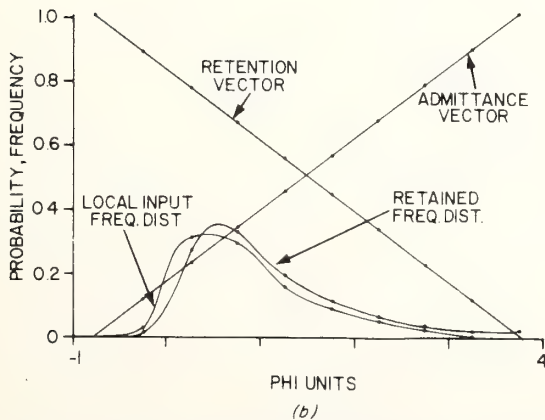
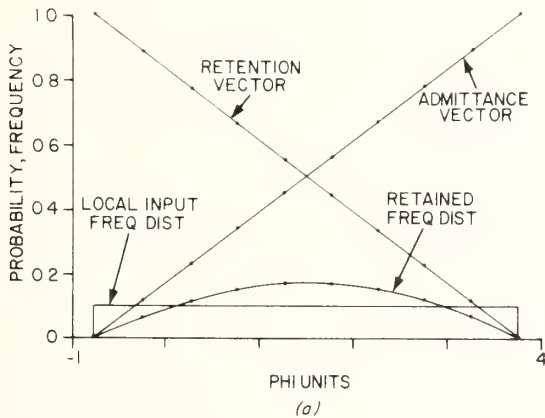


FIGURE 1. Grain-size frequency distributions as a product of a retention vector and an admittance vector. See text for explanation. From Swift et al. (1972b).

If  $P_{jn}$  is an element in an admittance vector, where  $j$  denotes the  $j$ th station in the transport path and  $n$  denotes one of  $n$  grain-size classes, and if  $P'_{jn}$  is a corresponding element in a retention vector for the same station, then the product of the two probabilities,  $P_{jn}(1 - P'_{jn})$  gives the probability that the particle in the local input enters but does not leave the station. The product of the input vector with all corresponding elements in the admittance and retention vectors for a station gives the frequency distribution for that station (Fig. 1). This is a restatement, in probabilistic terms, of the intuitively apparent fact that the modal diameter of a deposit is that grain size most likely to arrive and least likely to be carried away from the place of deposition under prevailing flow conditions; progressively coarser sizes are progressively less frequent because they are less likely to arrive, and progressively finer sizes are progressively less frequent because they are more likely to be carried away.

In Fig. 1a, the two linear numerical filters (admittance and retention vectors) are applied to a local input frequency distribution that is uniform in nature and a symmetrical retained frequency distribution results. If, however, the local input has a skewed distribution (Fig. 1b), then the retained distribution is still skewed, although it has been modified by the station probabilities. If the filters are not linear, then further modification of the input vector occurs.

In Fig. 2, various hypothetical input distributions are subjected to sorting down the stations of a hypothetical transport path according to the probabilistic algorithm described above. In column A, an initially rectangular distribution is seen to evolve into a distribution with a distinct mode, and the mode is seen to shift toward the finer end of the distribution at successive stations. The coarse flank of the mode becomes visibly sigmoid (S-shaped) as is characteristic of the side of the normal distribution frequency curve. The increasingly sigmoid shape is the consequence of the multiplication of successive admittance vectors in order to obtain the coarse admixture of the local input frequency distribution. For instance, if the admittance vector has the form

$$0.100, 0.200, 0.300, 0.400, 0.500, 0.600, \\ 0.700, 0.800, 0.900, 1.00$$

and retains this form from station to station, then at the third station the size frequency distribution of the coarse admixture will be determined primarily by the third power of the admittance vector,

$$0.001, 0.008, 0.027, 0.064, 0.125, 0.216, \\ 0.343, 0.512, 0.729, 1.00$$

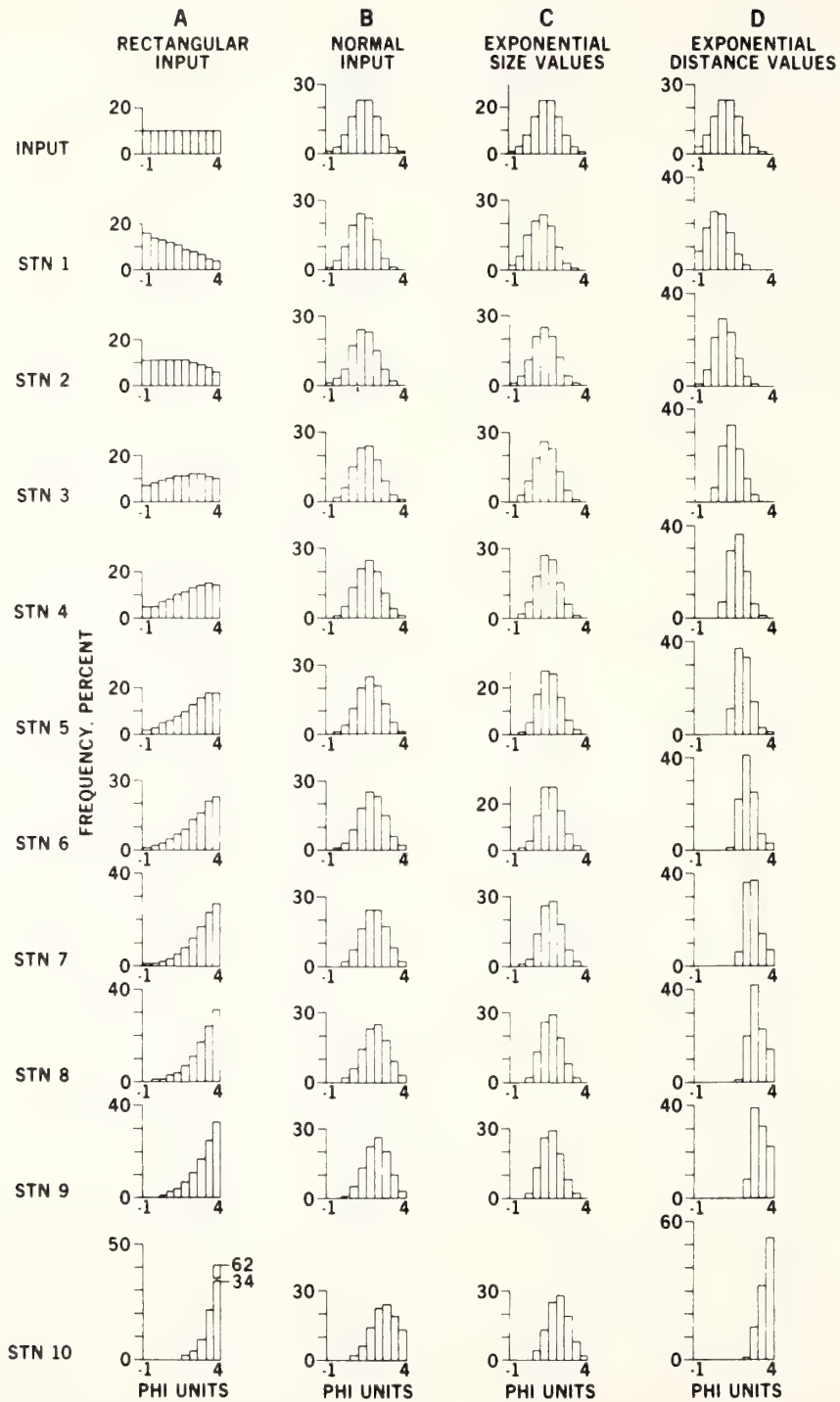


FIGURE 2. Grain-size frequency distributions along sediment transport paths under different conditions. See text for explanation. From Swift et al. (1972b).



The initially small probabilities have decreased more than the initially large ones, and the resulting curve of frequency against size class will be exponential in form.

The modal shift is the phenomenon of *progressive sorting* (Russell, 1939) whereby the deposit becomes finer down the transport path, as a consequence of the steady depletion of the transported material in coarser particles. In physical terms, this means that the coarsest particles tend to get left behind whenever the bottom is eroded by a flow event that is weaker than the one that preceded it.

If it is assumed that the input distribution is normal to begin with (Fig. 2, column *B*), and if it is assumed that the probabilities of admittance and retention vary linearly with grain size, then the mode shifts toward the fine end of the distribution as the sediment is traced down the transport path with no change in the shape of the normal curve. However, in a more realistic case, the probabilities of admittance and retention are assumed to vary exponentially with grain size; in other words, the transport rate varies exponentially with grain size. As a consequence, vector multiplication acts on the two sides of the frequency curve in a dissimilar fashion (column *C*). The greater range of transport probabilities assigned to the coarser sands results in greater efficiency of sorting on that side of the curve, and progressive steepening of that side, as the sediment is traced down the transport path. The sediment becomes increasingly enriched in the fine admixture at the expense of the coarse admixture (becomes fine-skewed), as well as becoming finer down the transport path. This effect is particularly marked where the intensity of the flow field is made to decrease down the transport path (column *D*).

### Size Frequency Subpopulations and Flow Regimes

Thus there are at least theoretical reasons supporting the concept that the size frequency distribution of fluid-deposited sands constitutes hydraulic signatures of the flow process. Attempts to interpret these signatures have in general generated more heat than light (Emery and Uchupi, 1972, p. 375). However, the analysis of the subpopulations constituting sand samples has proved more fruitful. The basic work has been undertaken by Moss (1962, 1963, 1972). He notes that most grain-size frequency distributions of sand deposited from fluid flow do not plot as a straight line on probability paper as they should if they are normally distributed. Instead the curves are Z-shaped (Fig. 3). He has demonstrated that these Z-shaped curves are composite distributions and are the consequence of the presence of three or more log-normally distributed subpopulations, and that these subpopulations are an outcome of the manner in which

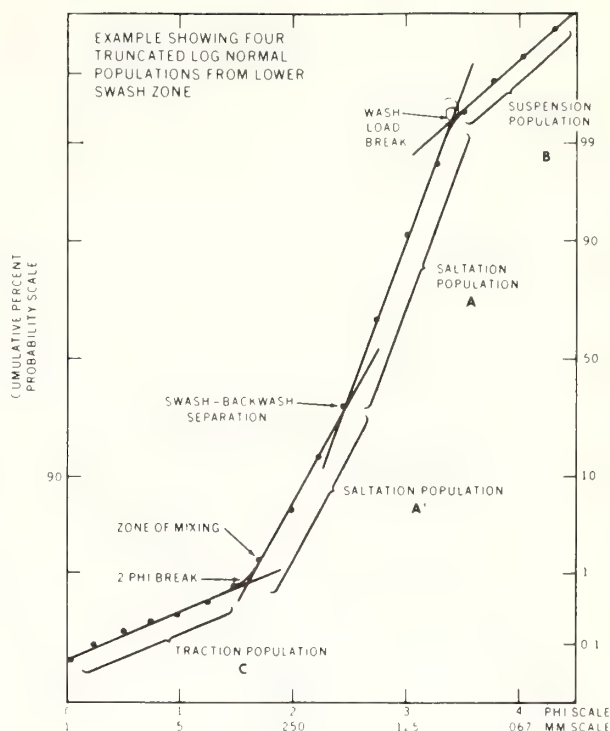


FIGURE 3. Cumulative curve of a swash zone sample. In Moss' terminology, *A* is framework population, *B* is interstitial population, and *C* is contact population. From Visser (1969).

the bed is built (Fig. 4). A *framework population* (*A* population) constitutes the bulk of the sample. Its modal diameter is a function of the average dimensions of the relatively large spaces between grains on the aggrading surface. There is a strong feedback in this system between deposit grain size and bed load grain size; the dimensions of grains selected from bed load for deposition in such holes depend on the dimensions of grains already deposited, which in turn depend on the dimensions of available grains in the bed load, and ultimately on the dimensions of the hydraulic parameters of the flow.

A fine *interstitial subpopulation* (*B* population: fine tail of the size frequency distribution curve) consists of grains that are small enough to filter into the interstices of the grain framework of the deposit. Their average diameter is not that of the bowl-shaped openings on the bed surface but the smaller average diameter of the interstices within the deposit.

A coarse *contact subpopulation* (*C* population: coarse tail of the frequency curve) consists of grains that are too coarse to fit into or through the surface openings as do the grains of the *A* and *B* populations. Instead they accumulate as slowly moving to stationary clogs of mutually interfering coarse grains on the bed surface. When a critical area of these rejected coarse particles has ac-

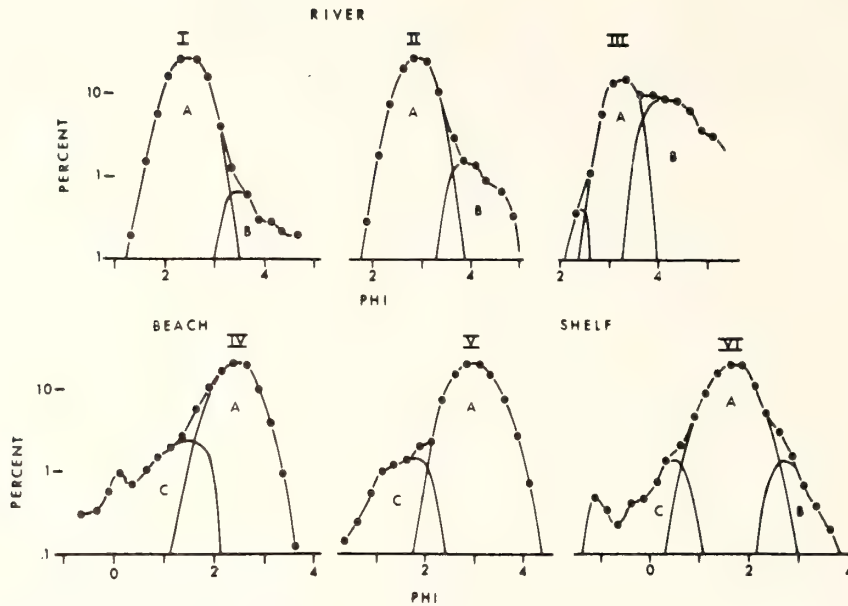


FIGURE 4. Size-frequency curves of sands from various environments. Curves have been dissected to indicate subpopulations. From McKinney and Friedman (1970).

cumulated, it will be buried beneath further layers of A population grains.

It is important to assess the relationship between Moss' rather sophisticated theory of subpopulation genesis, and the prevailing equation of transport modes with subpopulation characteristics. It has been generally assumed [see the review by Visser (1969)] that the contact population represents particles moved by dragging or rolling, the framework population represents particles moving by saltation, and the interstitial population represents particles traveling in suspension. There is a correlation between these differing modes of transport and the per-

centage of respective subpopulations in the deposit, because each of these modes is most likely to carry the appropriate size of material for the subpopulations with which they have been correlated. The relative percentages of subpopulations, however, are a *direct* consequence of mechanisms of bed construction, and only indirectly reflect modes of transport. Moss has shown, for instance, that both B and A subpopulations may be generated from saltative transport alone.

The percentages of these three populations in a given deposit will vary, within limits set by grain geometry and grain interaction processes, according to the regional

TABLE 1. Nomenclature and Grain-Size Characteristics of Sediment Flow Regimes

Moss (1972)	Southard and Boguchwal (1973)	Population			Mean Diameter (Moss, 1972)
		A	B	C	
Fine ripple stage	Ripples	Dominant	Abundant	Scarce	0.07-0.25 mm (3.75-2.00 $\phi$ )
Coarse ripple stage	Ripples	Dominant	Scarce	Scarce	0.25-0.92 mm (2.00-0.25 $\phi$ )
Dune stage	Dunes	Dominant	Scarce	Scarce	0.25-2.2 mm (2.0 to -1.1 $\phi$ )
Rheologic stage	Transition Upper flat bed Antidunes	Dominant	Abundant	Abundant	0.17-4.8 mm (2.6 to -2.3 $\phi$ )

availability of the three populations, and also according to the hydraulic microclimate of the bed. Moss (1972), on the basis of flume studies and studies of river deposits, has described five bed regimes. These may be correlated with the flow regimes described by Southard and Boguchwal (1973, Fig. 23). Each tends to form a characteristic admixture of subpopulations (Table 1). Moss (1972) notes that in the *fine ripple* stage, grains do not protrude through the laminar sublayer of the bottom boundary layer of the flow and microturbulence is absent from the bed surface. Fine particles can become concentrated near the bed, and can pass copiously into the interstices. Hence the fine ripple regime is characterized by an abundant B population.

In the *coarse ripple stage* and *dune stage*, grains protrude through the lamina sublayer. Fluid dynamic lift and bed grain turbulence operate to keep fine particles from being concentrated near the bed, and the interstitial (B) population is normally a minor bed constituent.

In the *rheologic stage*, flow is supercritical, and bed load particle behavior is dominated by the dispersive pressure associated with grain collisions (Bagnold, 1954). These pressures force the particles against and into the bed. This effect is evidently dominant over the lift forces which act at the bed, and the interstitial B population again passes copiously into the bed. The rheologic stage is furthermore the only stage in which Moss observed an abundant contact (C) population.

Moss' theory may thus be used to infer flow regime from the grain-size distribution. It must be applied with caution, however, as it was developed for quasi-steady flows, and the continental margin environment tends to be subjected to an additional oscillatory flow component because of wave surge. Grain-size distributions consequently tend to indicate more intense unidirectional flows than actually exist (Stubblefield et al., 1975).

## BED FORMS

In this section, it is necessary to deal with more varied and larger bed forms than the wave ripples described in Chapter 7. Sand wave fields and sand ridge fields may generate bed form spacings of a kilometer or more, and bed form amplitudes of up to 30 m. Such large-scale bed form arrays become significant storage elements in continental margin sediment budgets, and such budgets cannot be understood without an awareness of bed form mechanics. Furthermore, large-scale bed forms impact directly on human usage of the continental margin. Large tankers navigate the Thames estuary channels (Langhorne, 1973) with scant meters of clearance over sand wave crests. Sewage outfalls and nuclear power

plants are planned or are being constructed in the inner shelf ridge fields of the Atlantic shelf. Seafloor well heads are subject to burial by migrating bed forms.

**CONCEPTS.** A bed form is an irregularity in the particulate substrate of a fluid flow. This definition includes the subaqueous sand wave and sand ridge fields of the earth's shelves, the subaerial dune fields of the earth's deserts and those photographed on Mars, and the bed forms of the base surge deposits surrounding the lunar craters, sedimented out of a transient fluid of gas, dust, and debris generated by the impact of meteors. Bed forms are not independent phenomena; they are equilibrium configurations of the interface between a mobile, usually cohesionless substrate, and an overlying flow field, and tend to occur in repetitious arrays rather than alone. They are the product of feedback between flow structure and substrate structure. The three-dimensional pattern of flow does not "cause" the bed form to arise, nor does the bed form "cause" the deformation of the boundary layer of the flow field; instead, strictly speaking, these two elements of a flow-substrate system interact to cause each other.

Wilson (1972, p. 204) notes that when a fluid is sheared, either against another fluid, against itself, or against a rigid boundary, there are many situations in which secondary flows develop. Secondary flows are regularly repeated patterns of velocity variation superimposed on the mean flow. The primary flows satisfy the three continuity laws (of mass, energy, and momentum), but in such a way that any small disturbance is initially self-aggravating; in other words, the flow is an unstable system. In sheared flows, this usually involves the development of any combination of such secondary flows as transverse internal waves, or transverse or flow-parallel vortices. Such secondary flows may occur simultaneously at several scales.

Wilson further notes that sheared fluids may become unstable in response to almost any sort of strong gradient in velocity, pressure, viscosity, temperature, or density in the direction normal to the shear force. These may arise over completely plane beds. Eventually, however, as the perturbed flow and the bed deform in response to each other, a new stable state is attained.

The theory of fluid instability has been outlined by Lin (1955), Chandrasekhar (1961), Rosenhead (1963), and Yih (1965), and these authors have discussed many cases to which it has been applied. Allen (1968a, p. 50) has summarized their computational approach. The algorithm requires that equations of motion be set up to describe the fluid motion of interest. These equations are solved to discover whether a small sinusoidal disturbance of one variable will be damped or amplified

under the chosen limits for other variables. The motion is stable if the disturbance is damped, but unstable if it is amplified. In nature the unstable disturbance is amplified until the other variables of the system set some limiting condition on the amplification and a new state of quasi equilibrium is attained. Stability analysis has been successfully applied to the problem of ripple and sand wave formation (e.g., Smith, 1969) and it seems likely that all bed forms will ultimately prove susceptible to this mode of attack.

**BASIC MODES OF BED FORM BEHAVIOR.** Most bed forms fall into two basic categories: those that are oriented across the flow direction, such as sand waves and ripples, and those that are oriented parallel to the flow direction, such as sand ribbons. These two basic patterns must correspond to two basic patterns within the flow field itself, a transverse pattern in which zones of scour and aggradation alternate down the flow path, and one in which zones of scour and deposition alternate across the flow path (Figs. 5 and 6). There is considerable evidence to indicate that this is the case, although the basic mechanisms are far from clear.

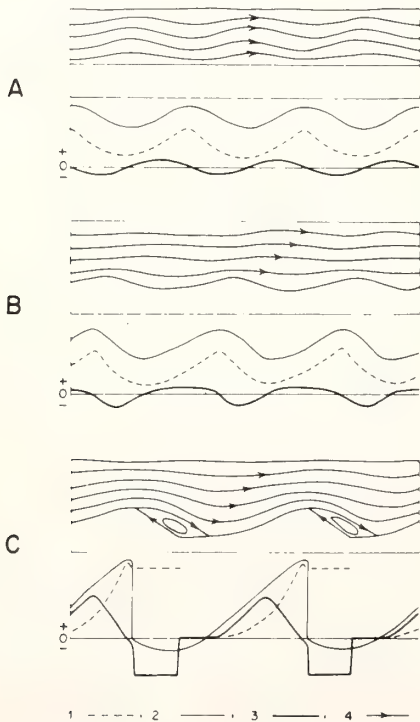


FIGURE 5. The development of a transverse bed form. (A) Initiation; (B) growth; (C) equilibrium. (1) Sand transport rate; (2) shear velocity at bed; (3) erosion rate; (4) streamlines. From Wilson (1972).

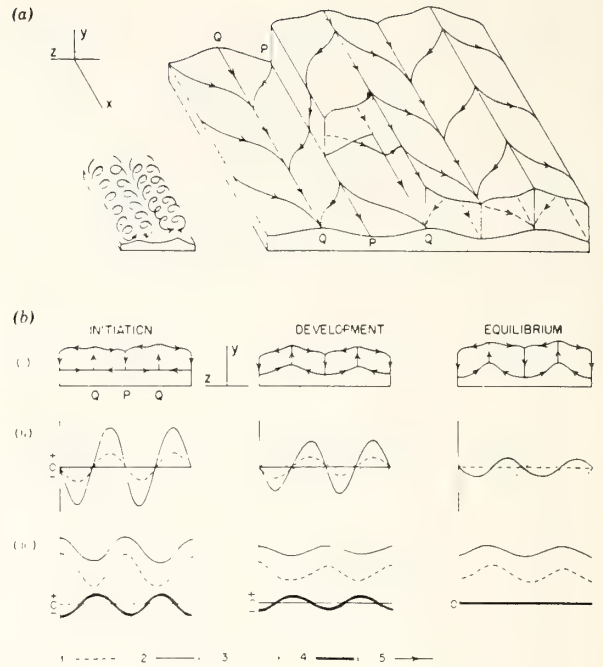


FIGURE 6. The development of a longitudinal bed form. (a) The pattern of secondary flow over longitudinal bed elements: PP, flow attachment lines along ridge trough; QQ, flow separation lines along crests. (b) Development of longitudinal elements in vertical cross section perpendicular to mean flow direction. (i) Form and flow components; (ii) components in z direction; (iii) components in x direction. Numbers as in Fig. 4. Note alternate notation of coordinate axes. From Wilson (1972).

**Transverse Bed Forms**

**MODE OF FORMATION.** As noted by Wilson (1972), most transverse bed forms are probably caused by transverse wave perturbations in the flow. The problem is a complex one, and the solutions offered to date have not been altogether satisfactory. Summaries are presented by Allen (1968a, pp. 130-149), Kennedy (1969, p. 151), and Smith (1970, p. 5928).

Smith points out that many of these studies are unnecessarily restrictive; they assume an eddy viscous mean flow but neglect the inertial terms in the equation of motion (Exner, 1925, in Raudkivi, 1967) or assume inviscid irrotational flow (Kennedy, 1969). These assumptions require an a priori phase shift in the velocity field relative to the interface disturbance in order for instability to occur. Smith (1970) has undertaken a stability analysis employing inertial terms in the equations of motion. His results indicate that the interface is unstable with respect to infinitesimal perturbations of wavelength greater than the wavelength for which the inertia of the grains is important (wavelengths less than 10 times mean

grain diameter). Smith utilizes the sediment continuity equation, which may be presented in its simplest two-dimensional form as

$$\frac{\partial \eta}{\partial t} = -\kappa \frac{\partial q}{\partial x} \tag{1}$$

where  $\eta$  is height of the interface above a datum,  $t$  is time,  $\kappa$  is a constant,  $q$  is sediment discharge at a level near the bed, and  $x$  is horizontal distance. In physical terms, the time rate of change of the height of the interface at a point above the datum is proportional to the horizontal discharge gradient at that point, assuming saturation of the boundary flow with sediment; a decrease in discharge across the point ( $-\partial q/\partial x$ ) must result in aggradation, while an increase ( $\partial q/\partial x$ ) must result in erosion. Smith has rewritten the equation in terms of boundary shear stress and discharge:

$$\frac{\partial \eta}{\partial t} = - \left( \frac{1}{c_0} \frac{\partial q}{\partial \tau_0} \right) \frac{\partial \tau_0}{\partial x} \tag{2}$$

where  $c_0$  is the boundary concentration of sediment,  $q$  is the mean volume flux of sediment per unit width, and  $\tau_0$  is the local mean shear stress on the bed.

Smith's analysis divides the nonuniform horizontal velocity along the waveform interface into an in-phase component and an out-of-phase component. The in-phase component consists of accelerating flow over crests with maximum shear stress at those points, as required by flow continuity. Since boundary erosion varies directly with  $\partial \tau_0/\partial x$ , this in-phase component simply causes upstream erosion of the interface perturbation and downstream deposition; the perturbation moves downstream with neither growth nor decay. However, the inertia of the high-velocity water of the upper part of the water column causes it to converge with the rising bed on the upstream side of an interface perturbation, and there is as a consequence an out-of-phase component

of velocity and bottom shear stress which attains its maximum value at this zone. This maximum persists when the components are added; hence, since deposition is proportional to  $-\partial \tau_0/\partial x$ , some sand must always be deposited on the crest of the perturbation.

Smith (1970) cites Exner's (1925) earlier stability analysis as qualitatively correct, despite neglect of the inertial terms in the momentum equations. Exner had shown that when downcurrent spacing is wide, the crests of perturbations move faster than the troughs between them, resulting in oversteeping of the downcurrent slope to the angle of repose ( $30^\circ$  underwater), and consequently, in the formation of a horizontal roller eddy (wake, flow separation bubble) downstream of the crest. The perturbation is now a mature ripple or sand wave.

The generation of a wake behind a growing bed form results in propagation of interface instability in the downstream direction. Smith (1970) cites Schlichting (1962, p. 200) who has studied the development of a turbulent wake. Behind a negative step such as the avalanche slope of a growing transverse bed form, flow accelerates downstream of the attachment line (Fig. 7) and at the same time a boundary layer is initiated that grows in height downstream. Shear increases downstream because of flow acceleration, then decreases as the effects of boundary layer growth dominate over the effects of flow acceleration. Here, in a zone where  $\partial \tau_0/\partial x < 0$ , sand is deposited and a new ripple grows, which in turn deforms, develops a wake, and triggers a third. Smith's stability analysis does not specify wavelength for growing bed form perturbations, and it is apparent that this parameter must be defined by spatial adjustments in the turbulent velocity field. As downstream ripples grow in height and their separation bubbles in width, they must grow in length, which is accomplished by the smaller ripples moving faster, and stretching out the ripple field.

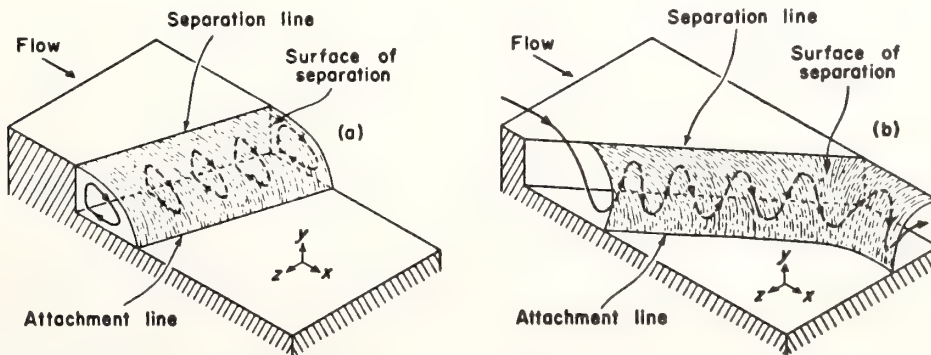


FIGURE 7. Three-dimensional separated flows. (a) Roller; (b) vortex. Note alternative notation of coordinate axes. From Allen (1970).

Smith's scheme of transverse bed form formation by the spontaneous deformation of the interface into a moundlike perturbation, its increasing asymmetry, the formation of a separation bubble, and the downstream propagation of the instability, has been strikingly confirmed in experimental work by Southard and Dingler (1971). Their work suggests that if the critical flow threshold is approached slowly, preexisting bed irregularities may trigger downstream ripples in the interval of metastability before the threshold is attained. However, if the threshold is passed rapidly, or if marked preexisting irregularities do not occur, mounds will spontaneously appear and transform themselves into regular ripples.

Other schemes for the formation of transverse bed forms have been proposed, in which the wavelike perturbation of flow precedes bed deformation, rather than arising from interaction with the bed. Cartwright (1959) has proposed that the shelf-edge sandwave field of La Chapelle Bank in the Celtic Sea are responses to stationary internal waves (tidal lee waves) in the stratified water column. Furnes (1974) has analyzed the formation of sand waves in response to internal waves of a fluid whose density stratification is a consequence of its suspended load. While compatible with the field evidence, these models for sand wave formation remain unconfirmed. They are important contributions, however, if only in that they reduce the bias toward the results of experimental laboratory work. The space and time scales and the internal structure of shelf flows are qualitatively different than those of laboratory flumes and there is no reason to assume that such further modes of sand wave formation do not exist in nature.

**TYPES OF TRANSVERSE BED FORMS.** Field and laboratory observations show that there tend to be two overlapping populations of transverse bed forms: *ripples*, with wavelengths up to 0.6 m, and *sand waves*, with wavelengths in excess of 0.6 m (Fig. 8). Sand waves commonly bear ripples on their backs. The two populations appear to be responses to two distinct genetic mechanisms. As small forms grow up through the velocity gradient of the boundary layer, the zone of maximum stress on the upcurrent flank shifts to the crest, at which point the entire upcurrent slope is erosional and the lee slope depositional; upward growth is stopped, and the ripple migrates at constant speed (Wilson, 1972, p. 200). Transverse bed forms of larger wavelengths are insensitive to the boundary layer velocity gradient and their upflank zone of maximum shear stress shifts to the crest only when the whole flow is significantly deformed by their upward growth. As a consequence, the equilibrium height of sand waves in shallow flows is proportional to flow depth, while the equilibrium height of ripples is

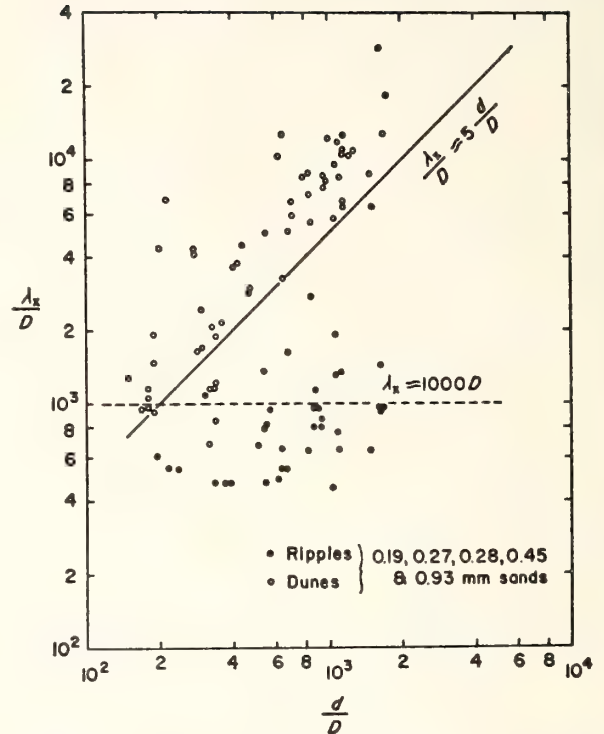


FIGURE 8. Wavelength parallel to flow of experimental ripples and sand waves in relation to flow depth. Data of Guy et al. (1966). From Allen (1970).

depth independent for all flow depths (Allen, 1967); see Fig. 8. Expressions for the equilibrium heights of ripples and sand waves have been considered by Kennedy and used by McCave (1971).

Stride (1970) has plotted measurements of height versus depth for sand wave fields of the North Sea at depths of 90 to 60 m, and found no correlation. Large bed forms grow slowly, and equilibrium heights may be rarely obtained in such shallow tidal seas subject to strong periodic storm surges. Deep-sea sand waves (Lonsdale and Malfait, 1974) can obviously never equilibrate with total water depth, although the significant flow depth may be only a small fraction of total depth, because of density stratification.

The distinction between small- and large-scale bed forms may be due to more than interaction of wavelength with the velocity gradient. Kennedy (1964) has suggested that small transverse bed forms represent perturbations of the traction and saltation loads that move very near to or on the bed, and hence must react quickly to changes of flow speed. Larger transverse bed forms, on the other hand, could reflect a perturbation of the suspended load, which will tend to respond slowly, and therefore over a large distance to a change in flow speed.

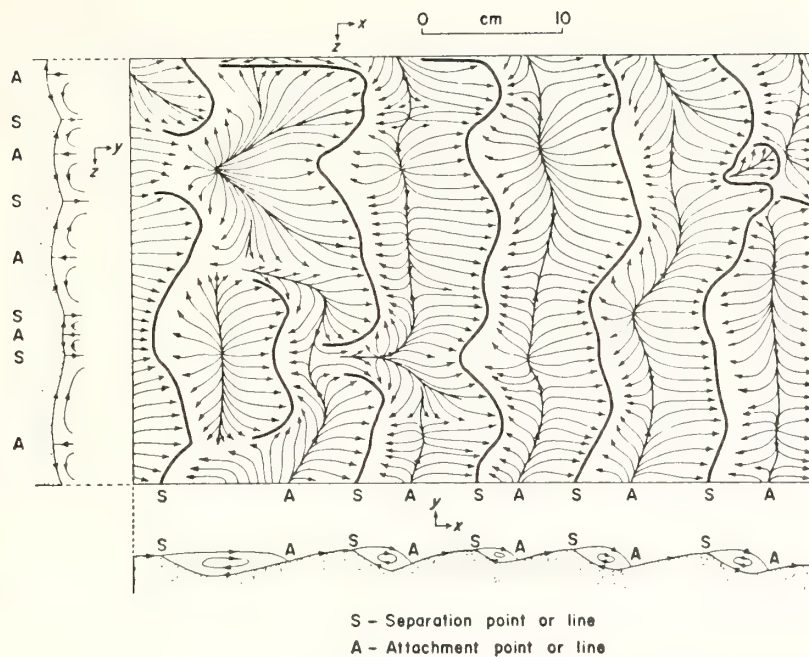


FIGURE 9. Skin friction lines and streamlines associated with a portion of a bed of experimental ripples in fine-grained quartz sand. Mean flow velocity 22 cm/sec from left to right. Mean flow depth 4.5 cm. Note alternative notation of coordinate axes. From Allen (1970).

In continental margin sand wave fields, there are often three orders of transverse bed forms: current ripples, sand waves, and larger sand waves. McCave (1971) suggests that the two classes of sand waves may be the consequence of Kennedy's two categories of substrate response.

Because of the turbulent diffusion of sand normal to the flow direction, an initially equant interface perturbation will tend to extend itself normal to flow, hence the quasi-two-dimensional nature of ripples and sand waves (ripple profile does not change down the length of the ripple crest). However, at increasing values of mean velocity, and therefore of turbulent instantaneous velocity component, transverse bed forms tend to become three-dimensional (Znamenskaya, 1965). As crests become locally inclined to the mean flow direction, the horizontal "roller eddy" of the separation bubble becomes a horizontal helical vortex (Fig. 7) and irregular patterns of skin flow result (Fig. 9). Under yet more intense flows, the irregularities may take on ordered patterns (Fig. 10). Bagnold (1956) attributes one particularly common pattern, that of the lingoid ripple, to "... the partial diversion of grain flow ... and its funneling into channels between existing ripples; deposition (of a new lingoid ripple) would take place immediately downstream of such a funnel." A diagonal or diamond-like pattern of lingoid ripples results.

TRANSVERSE BED FORMS AND FLOW REGIMES. It has long been known that as a shallow flow over a noncohesive substrate intensifies, a sequence of bed configurations transpires (Simons et al., 1961; Simons and Richardson, 1963; Guy et al., 1966). The flow variables governing this sequence are  $h$ , depth of flow;  $\bar{u}$ , mean velocity of flow;  $\rho$ , density of fluid;  $\rho_s$ , density of sediment;  $\mu$ , viscosity of fluid; and  $D$ , mean diameter of sediment.

The critical parameters are fluid power (proportional to  $\bar{u}^3$ ; see Chapter 8) and grain size (Fig. 11). Grain density is variable to the extent that heavy minerals may be present; and fluid density and viscosity vary somewhat with temperature and salinity. Flow depth determines whether or not the flow is subcritical or supercritical as expressed by the dimensionless Froude number  $F = \bar{u}/(gh)^{1/2}$ , where  $(gh)^{1/2}$  is the celerity of a shallow water wave. In supercritical flows ( $F > 1$ ), surface waves couple with substrate perturbations (antidunes) that tend to migrate upcurrent. On the continental margin supercritical flows are confined to the swash and breakpoint zones of the surf, and to tidal flats; and the antidunes and rhomboid ripples that form in these zones are ephemeral.

Southard (1971) and Southard and Boguchwal (1973) have argued that bed configuration diagrams such as Fig. 11 should be presented in terms of dimensionless depth, velocity, and grain size to eliminate the overlap-

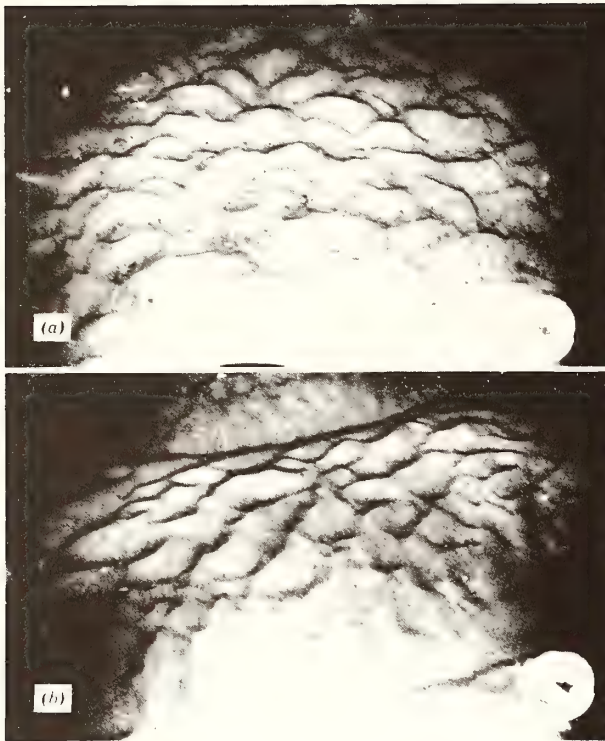


FIGURE 10. (a) *Lingoid ripple pattern on shelf floor off Cape Hatteras, North Carolina.* (b) *Lingoid ripples on back of sand wave, straight ripples in trough, same area.*

ping of fields that occurs in diagrams utilizing fluid power or bed shear stress.

Figure 11 shows that dunes (sand waves) occur at higher values of fluid power than do ripples by themselves. This fact is consonant with Kennedy's suggestion that sand wave formation involves suspended load transport, which requires higher values of fluid power than does bed load transport.

**TRANSVERSE BED FORMS AND TIDAL FLOWS.** Tidal flows, which reverse every 6 hours, generate transverse bed forms in a cohesionless substrate. Tidal current ripples are no different than ripples generated by unidirectional currents, except that their sense of asymmetry is reversed as the tide changes. Small sand waves (height of 1 m or less) may have their asymmetries partly or wholly reversed by strong reversing tidal currents (Klein, 1970). Larger sand waves tend to display a time-integrated response to reversing tidal flows, maintaining an ebb or flood asymmetry in accord with the dominant flow component residual to the semidiurnal cycle. "Cat-backed" sand waves are large sand waves that have a sloping upcurrent side, a flat top, and (in profile) an "ear" perched on the edge of the downcurrent slope (Van Veen,

1936). The ear is a response to the subordinate portion of the tidal cycle. Tide-formed sand waves in areas of equal ebb and flood flow are commonly symmetrical.

As distance from shore increases, the tidal current is no longer reversing but rotary (Chapter 5). The advent of midtide cross flow tends to inhibit the formation of sand waves large enough to survive through the tidal cycle (McCave, 1971). Under such circumstances longitudinal bed forms are favored (Smith, 1969).

### Longitudinal Bed Forms

Wilson (1972) comments that practically all longitudinal bed form elements, whether formed in wind or water, are initiated by regular helical vortices with axes parallel to flow. His reasons for his admittedly sweeping assertion are as follows:

1. Longitudinal helical flow cells occur in many different kinds of situations. They are the only kind of flow perturbations known to fluid mechanics whose wavelength is measured normal to the mean flow direction.
2. With the exception of alternating parallel lanes of fast and slow flow, the double helical pattern is the only one that meets the theoretical requirements, namely bilateral symmetry parallel to flow, regular repetition normal to flow, and conformity with the law of continuity.
3. Many investigations of flow over longitudinal bed forms resulted in some evidence for the occurrence of helical flow over the longitudinal elements, for instance, model ripples and dunes (Allen, 1968a); in river channels (Gibson, 1909); over tidal sand ridges (Houbolt, 1968); and over desert dunes (Hanna, 1969).

The theory of longitudinal flow perturbation is less well developed than the theory of transverse flow perturbation. Such perturbations are not as obvious in laboratory flumes as transverse (streamwise) flow perturbations, and many occur at scales far beyond those of laboratory flumes. As in the case of transverse bed forms, longitudinal bed forms appear to be able to form in response to perturbations of boundary flow, or in response to perturbations of the whole flow field. As in the case of transverse bed forms, they appear to form during the course of flow-substrate interaction, and also in response to the preexisting internal structure of a sheared flow.

Preexisting flow structures appear to be more important than in the case of transverse perturbations. Perhaps the most general statement that can be made is that in a sheared flow that is wide relative to its depth, a significant portion of flow energy must be diverted to an ordered secondary flow component, in order to maintain lateral flow continuity. At least three basic varieties of such secondary flow structure exist.



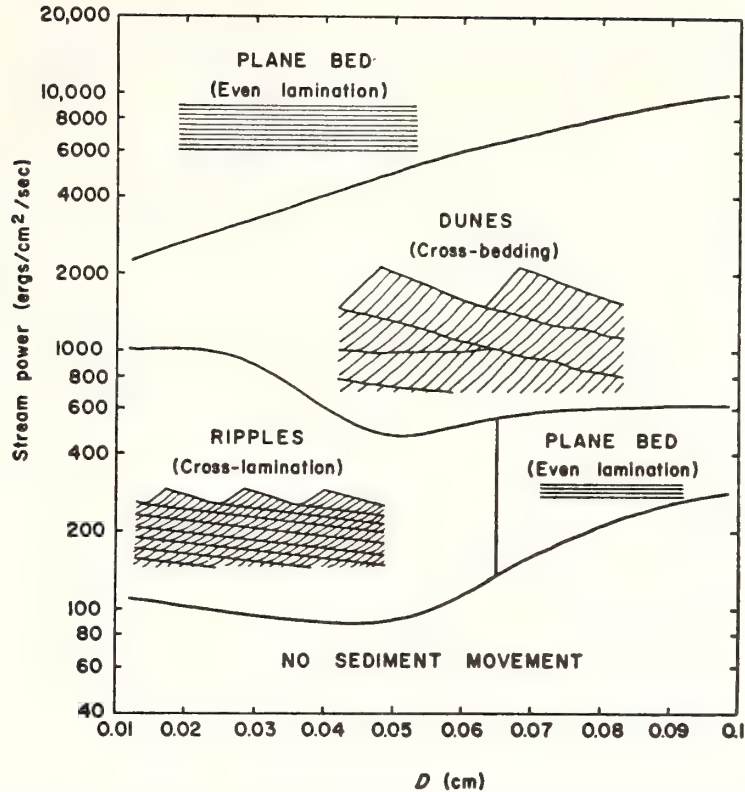


FIGURE 11. *Bed forms in relation to stream power and grain size. Data of G. P. Williams, H. P. Guy, D. B. Simons, and E. V. Richardson. From Allen (1970).*

MICROSCALE LONGITUDINAL BED FORMS (PARTING LINEATION). It has been repeatedly suggested that the logarithmic boundary layer tends to be so patterned, although an adequate analytic model has not yet been devised (Schlichting, 1962, pp. 500-509). Kline (1967) and Kline et al. (1967) have conducted dye experiments in flumes which suggest that the laminar sublayer and the lower part of the buffer sublayer of the turbulent boundary layer have a structure characterized by vigorous transverse components of flow (see discussion, p. 94). Dye introduced into the boundary layer forms into bands that are more slowly moving than those in the intervening water zones. Although the streaks are randomly generated, they have a mean transverse spacing of  $\lambda_z = 100\nu/u_*$  in which  $\nu$  is the kinematic viscosity and  $u_*$  is the shear velocity (Kline, 1967). The response to helically structured boundary flow over a cohesionless particulate substrate is, however, well known; it is the ubiquitous parting lineation (Sorby, 1859), so named for the tendency of flagstones (silty sandstones with strong bedding fissility) to exhibit lineations on bedding planes. Closer examination reveals a waveform bedding surface whose undulations parallel flow direction; ridges are a few grain diameters high and are up to several

centimeters apart (Allen, 1964; 1968a, pp. 31-32); see Fig. 12. There is clear evidence for the divergence and convergence of bottom flow in that the azimuths of long grains are bimodal, although this evidence does not resolve the secondary flow pattern. A similar structure has been reported from mud beds (Allen, 1969). Here the notches are frequently narrower than the ridges.

Coupling probably occurs between bed and flow structure, in that the grain ridges localize flow cells. Also, the sand of the ridges is coarser (Allen, 1964) and the resulting roughness would tend to slow crestal flow. This feature would cause downstream growth in the retarded wake of the grain ridges, and would perhaps induce upward ridge growth until ridge crests reach a level whose flow is rapid enough to counteract growth.

MESOSCALE LONGITUDINAL BED FORMS (CURRENT LINEATIONS). "Current lineations" (McKinney et al. 1974) is a generic term for low-amplitude strips of sand resting on a coarser substrate (sand ribbons) and for strips of coarse sand or gravel flooring and elongate depression of slight depth (longitudinal furrows). Current lineations are a larger scale of longitudinal bed form, with spacings ranging from a few meters to many hun-

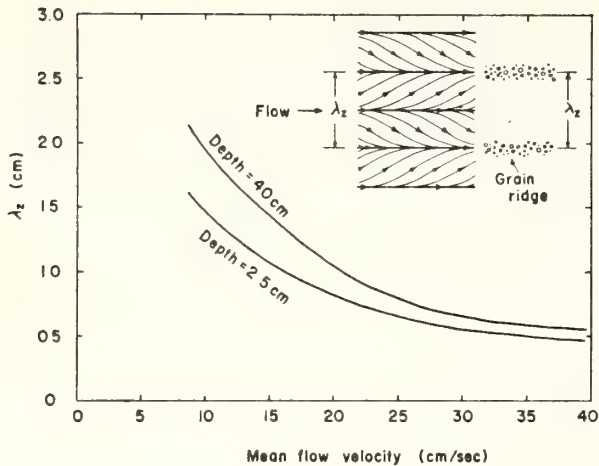


FIGURE 12. *The mean transverse spacing of parting lines as a function of mean flow velocity and flow depth. From Allen (1970).*

dreds of meters (Allen, 1968a). They are best observed by means of sidescan sonar (Figs. 13 and 14). The large-scale patterns are characteristic of shelves with strong tidal flows (Kenyon, 1970); see Fig. 15. Sand ribbons and longitudinal furrows are probably the most common mesoscale bed form on the continental shelf, being widely distributed on both shelves dominated by tidal flows (Kenyon, 1970; Belderson et al., 1972) and storm-dominated shelves (Newton et al., 1973; McKinney et al., 1974); see Fig. 14. Unpublished data of the Atlantic Oceanographic and Meteorological Laboratories, Miami, Florida, show them to be characteristic of large sectors of the Middle Atlantic Bight. Relief is negligible relative to width. Kenyon would restrict the term "sand ribbon" to features having length-to-width ratios of 1:40 and refers to shorter, broader features as elongate sand patches, but the distinction seems arbitrary. Unlike parting lineation ridges, sand ribbons tend to consist of streamers of finer sand in transit over a coarser substrate which may, in fact, be a gravel. A continuum may exist between a sand ribbon pattern of sand and gravel streets of equal width, to a "longitudinal furrow" pattern (Stride et al., 1972; Newton et al., 1973) in which widely spaced, elongate erosional windows in a thin sand sheet reveal a coarser substrate. Ribbon width relative to the width of the interribbon zone does not appear to be simply a function of the height of a sinusoidal surface of sand layer over a coarser substrate, since the windows in profile are notchlike affairs separated by flat plateaulike zones (Fig. 16). Furthermore, the ribbons are commonly rather asymmetrical, as though the sand sheet occurs at minimum thickness on one side, and increases very slowly to maximum thickness on the other side. Such asymmetrical ribbons could be interpreted as

degraded sand waves, but the sharpness of the contacts plus the lack of relief suggests instead asymmetrical helical flow cells (Fig. 17).

Small sand ribbons may be large-scale analogs of the responses described in the preceding section that involve the entire logarithmic boundary layer. However, most shelf sand ribbon patterns have spacings of tens or hundreds of meters, and as noted by Allen (1970, p. 69), can only be responses to the entire depth of flow.

Theoretical studies (Faller, 1971; Faller and Kaylor, 1966; Brown, 1971; Lilly, 1966) and experimental studies (Faller, 1963) show that there is a mechanism by which a helical flow pattern may be induced in the large-scale flows of the continental margin. When such flows are in geostrophic balance (pressure term balanced by Coriolis term in the equation of motion; see p. 25). The lower portion of the flow is an Ekman boundary layer (see p. 97). The basal meter behaves as a logarithmic boundary layer in that flow speed decreases rapidly to a zero value or nearly so at the seafloor. Flow direction (in the northern hemisphere) is to the left of the free-stream direction, however, since the Coriolis term is reduced along with mean velocity; the equation of motion more nearly constitutes a balance between friction and pressure terms. With increasing height off the bottom, flow is more nearly geostrophic and its direction is more nearly parallel to the isobars, until free stream conditions are reached. Thus velocity vectors at successively higher levels constitute a left-handed spiral. On the continental shelf, this lower Ekman boundary layer may extend to the base of the mixed layer, if it exists, or to the surface, where it is overprinted with a right-handed Ekman spiral (upper Ekman boundary layer) because of direct wind stress (Ekman, 1905, Plate 1).

Above a critical Reynolds number, this Ekman layer is unstable. However, because the instability transpires in an Ekman field subject to the Coriolis effect, the instability does not result in random turbulence, but instead in a regular pattern of secondary flow (Faller, 1971, pp. 223-225). In this pattern zones of surface convergence, downwelling, and bottom divergence alternate with zones of surface divergence, upwelling, and bottom convergence. The resulting flow structure consists of horizontal helical cells with alternating right- and left-hand senses of rotation (Fig. 6). Angles of convergence and divergence (pitch) are generally a few degrees; in other words, the secondary component of flow is weak, relative to the main geostrophic component. The flow cells may occur at several scales (Faller and Kaylor, 1966). In laboratory studies (Faller, 1963), smaller scale cells have a spacing of approximately  $11D$ , where  $D$  is a characteristic depth of the Ekman layer, and tend to be oriented up to  $14^\circ$  to the left of the mean flow. They occur at Reynolds numbers above 125. Larger

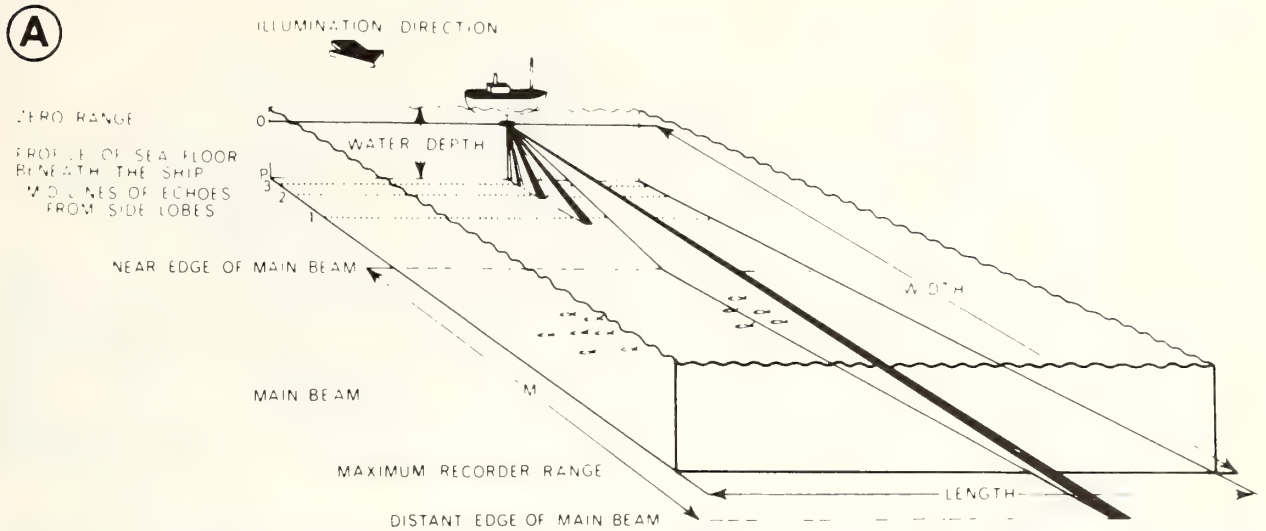


FIGURE 13. (A) Sidescan sonar. (B) The resulting record. A, Bottom of seafloor; B, turbulence in water column due to ship's wake; C, zigzag pattern is due to refraction of sound in density-

stratified water; D, main lobe (see above); E, side lobe. From Belderson et al. (1972).

scale cells have wavelengths much greater than  $11D$  and are oriented to the right of geostrophic flow. They occur at much lower Reynolds numbers.

Helical flow structure may occur in the upper Ekman layer where its wind-driven stirring creates the mixed layer above the thermocline (Faller, 1971), or may occur in the lower layer (Faller, 1963). In surface helical flow the downwelling zones that collect the high-velocity wind-driven surface water are more sharply defined than the upwelling zones (Langmuir, 1925). In bottom helical flow, downwelling zones deliver higher velocity water to the seafloor, and may also be more sharply defined than the upwelling zones. During intense flows, when stratification breaks down and the layers partly or completely overlap, a compound top-to-bottom helical flow structure might be expected.

Observational and theoretical studies required to link this scheme to the observed shelf sand ribbon patterns have not been undertaken; however, there are obvious points of compatibility. The ribbons tend to be parallel, or oriented at a small angle to the regional trend of shelf contours, and presumably to the mean geostrophic flow direction. The greater intensity of downwelling zones would explain the dissimilar width of ribbons and intervening erosional windows. The Reynolds numbers required are not excessive for either tide- or wind-driven shelf flows.

**LONGITUDINAL SAND RIDGES.** Large-scale longitudinal bed forms of the continental margin, with relief of up to

10 m and spacings measured in kilometers, are called sand ridges (Off, 1963; Swift et al., 1974); see Fig. 18. They are comparable in scale to the seif dunes, and the yet larger "draas" of the sand seas of the world's deserts (Wilson, 1972), except that as befits submarine sand bodies, their side slopes are much lower, usually being measured in fractions of a degree.

Sand ridges appear to form in two basic types of situations. They are characteristic of the reversing flows of tidal estuaries and bays, where they tend to form in complex arrays parallel to the estuary axis (Figs. 18A,B). They also appear on inner shelves of coasts undergoing erosional retreat (Figs. 18C,D), where they appear to be specific responses to the coastal boundary of the shelf flow field (Duane et al., 1972; Robinson, 1966; Swift et al., 1972a); the mechanism is discussed in detail in Chapter 14. On the inner shelf, either tidal or storm flows may be the forcing mechanism (Duane et al., 1972; Swift, in press). The ridges tend to extend obliquely seaward from the shoreface. Like sand ribbon patterns, the generally larger scale sand ridge fields tend to comprise discontinuous sheets of finer sand over a coarser substrate. However, where sand ridges build up into the wave-agitated zone on open coasts, their crests tend to be coarser than their flanks although generally not as coarse as the substrate exposed in trough axes (Houbolt, 1968; Swift et al., 1972b; Stubblefield et al., 1975).

**SAND RIDGES AS RESPONSES TO WIND-DRIVEN FLOWS.** Sand ridges are found on continental shelves seaward

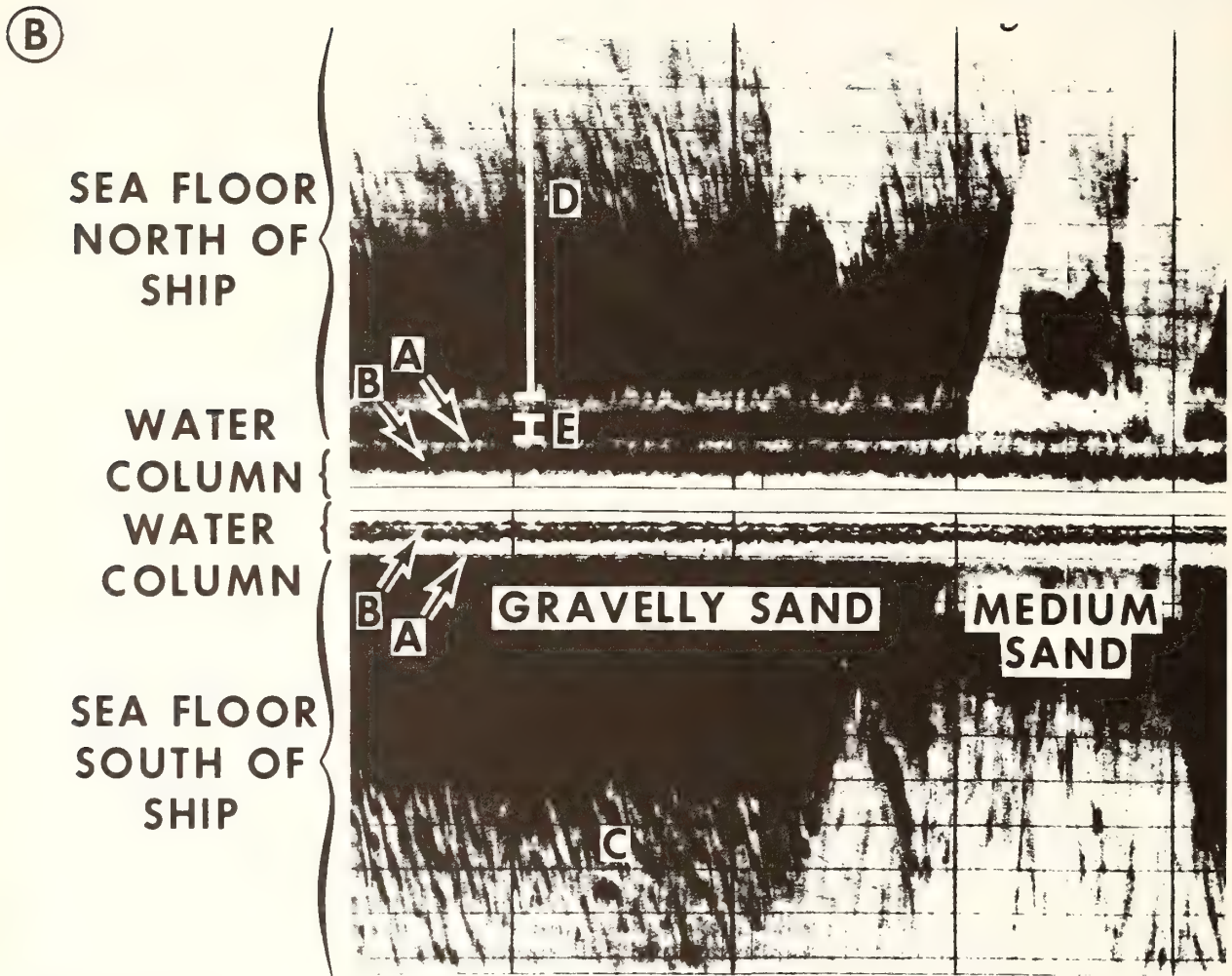


FIGURE 13—Continued.

of active inner shelf-generating zones, and occur as well on some shelves whose inner margins are not actively forming them (Swift et al., 1974). It appears that shelf flow fields can continue to maintain these ridges of coastal origin after the retreating shoreline has abandoned them, and can even locally generate them afresh (see discussion in Chapter 14). Without a maintaining mechanism, shelf flows might be expected to degrade sand ridges by leveling crests and filling in troughs. In fact, however, the ridges of the Atlantic continental shelf tend to expose compact clays or lag gravels in their troughs, indicating continuing trough scour (Swift et al., 1972a; McKinney et al., 1974).

There are a variety of competing hydraulic mechanisms that may serve to explain the formation and maintenance of large-scale sand ridges on the continental margin, none of which is clearly understood. On the

open shelf, cellular flow structure in storm flows, as described in the preceding section, may couple with the shelf floor. Such cellular flow structure might generate ridges along the coastal boundary (see discussion in Chapter 14) where wind-driven flows are frequent and intense and there is an abundant supply of sand. As these ridges have been left behind by the retreating shoreline during the Holocene transgression, the same cellular flow structure may be continuing to maintain them on the outer shelf.

If this analysis is correct, then sand ribbons and sand ridges may differ in that sand ribbons represent responses to one flow event or a flow season while sand ridges represent time-averaged responses to repeated flow events, whose emerging relief tends to localize the position of large-scale flow cells. Events capable of forming such large-scale flow cells would presumably be peak storm

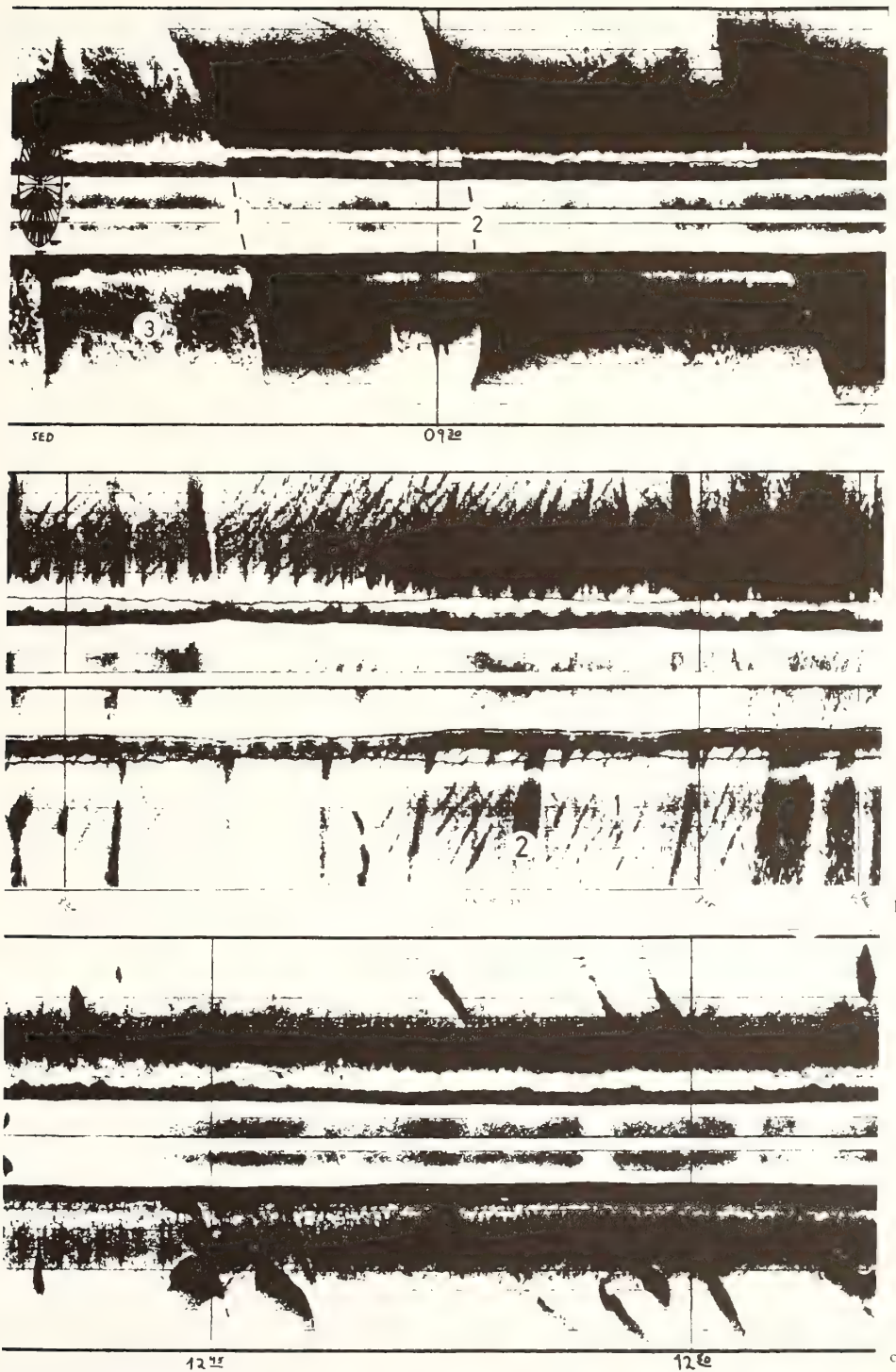


FIGURE 14. Sand ribbon patterns from the Spanish Sahara shelf. Light is sand; dark is ridges of asymmetrical ribbons; 3: pinna (pelecypod) bed. (b) 1: Symmetrical ribbon; 2: sand coarser sand and gravel. Distortion ellipse with scales on first record. (a) 1, 2: Sharply defined sand waves. From Newton et al. (1973).

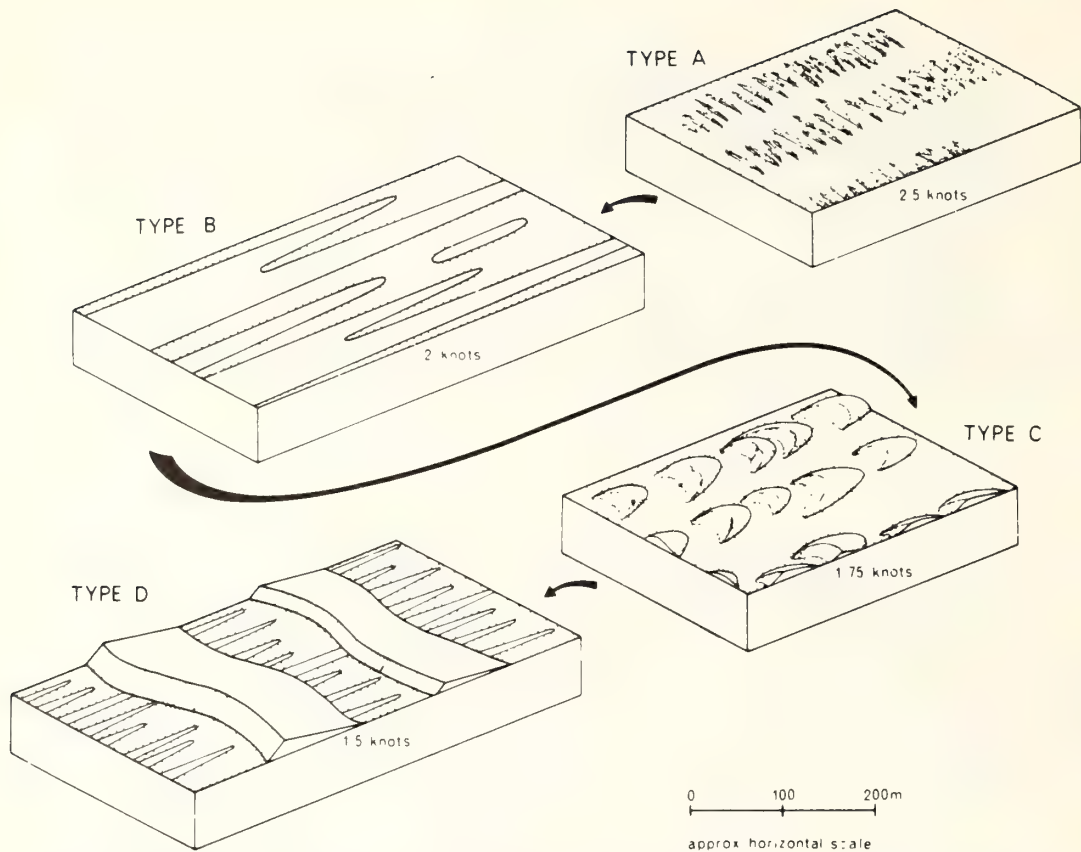


FIGURE 15. Categories of sand ribbon from the shelf around the British Isles, and associated current velocities. From Kenyon (1970).

or tidal flows, in which secondary circulation involves the entire water column.

The most problematic aspect of shelf ridge fields is the depth-to-width ratios of the troughs, which range from 1:10 to 1:150. The smaller ratios are compatible with the "type I" flow cells of Faller's (1963) experimental work, whereas the large ratios may derive from Faller's "type II" cells which have "much greater" di-

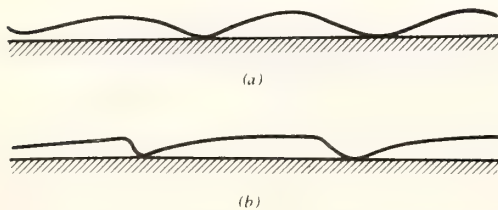


FIGURE 16. (a) Wide sand ribbons alternating with narrow streets of coarse sand (erosional windows) due to intersection of sinusoidal surface of sand sheet with horizontal substrate. (b) Same pattern due to notchlike incision of erosional windows. The latter pattern is a common one.

mensions. It is perhaps easier to conceive of such flattened cells if it is remembered that the central downwelling zone is the only sharply defined portion of a double helical flow cell; the marginal zones of diffuse upwelling may take up much of the "stretch," serving to complete flow continuity in a fashion analogous to the role of "ground" in electrical circuitry.

The advent of appreciable relief in a growing system of sand ridges may bring other hydraulic mechanisms into play. Secondary flow cells appear to be an innate response to channeled flow. It has long been known (Gibson, 1909; Jeffreys, 1929; Einstein and Li, 1958; Leopold et al., 1964, pp. 251-284; Wilson, 1972) that driftwood or ice in a river tends to move toward the center, whose surface is elevated slightly above that of the margins, and that the thread of maximum velocity tends to be depressed below the surface. The result is a double helical flow cell, in which bottom water spreads, rises along the margins, converges over the center, and sinks there. Flume and theoretical work (Kennedy and Fulton, 1961; Gessner, 1973) indicates that in flumes of

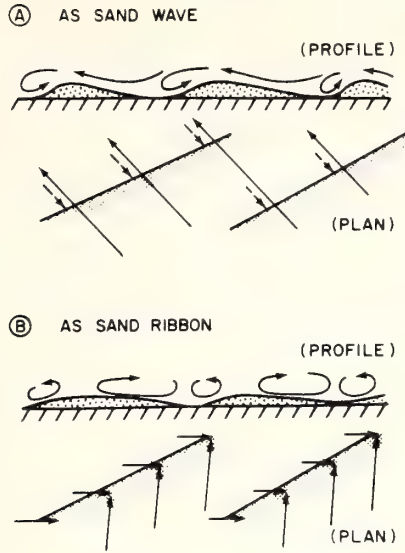


FIGURE 17. Interpretation of asymmetrical sand ribbons; B is more probable.

square cross section the unequal distribution of turbulent (Reynolds) stresses will result in secondary flow from the center toward the corners. The resulting multiple flow cells do not form the double helical pattern postulated for natural channels, however, and their applicability to the natural situation is uncertain. Bagnold (1966, pp. 112-115) offers an independent explanation. He suggests that there is asymmetrical exchange of momentum between the bottom boundary layer of a river and the overlying flow in that tongues of boundary water abruptly penetrate the overlying flow, to be compensated by a general sinking of the latter (see Chapter 7, p. 98). This results in elevation of the water surface over the channel axis where this exchange is most intense. The ensuing pressure head, he suggests, drives the secondary component of flow.

The preceding discussion has dwelt on double helical flow cells as mechanism for generating a large-scale sand ridge topography. An attempt has been made to match

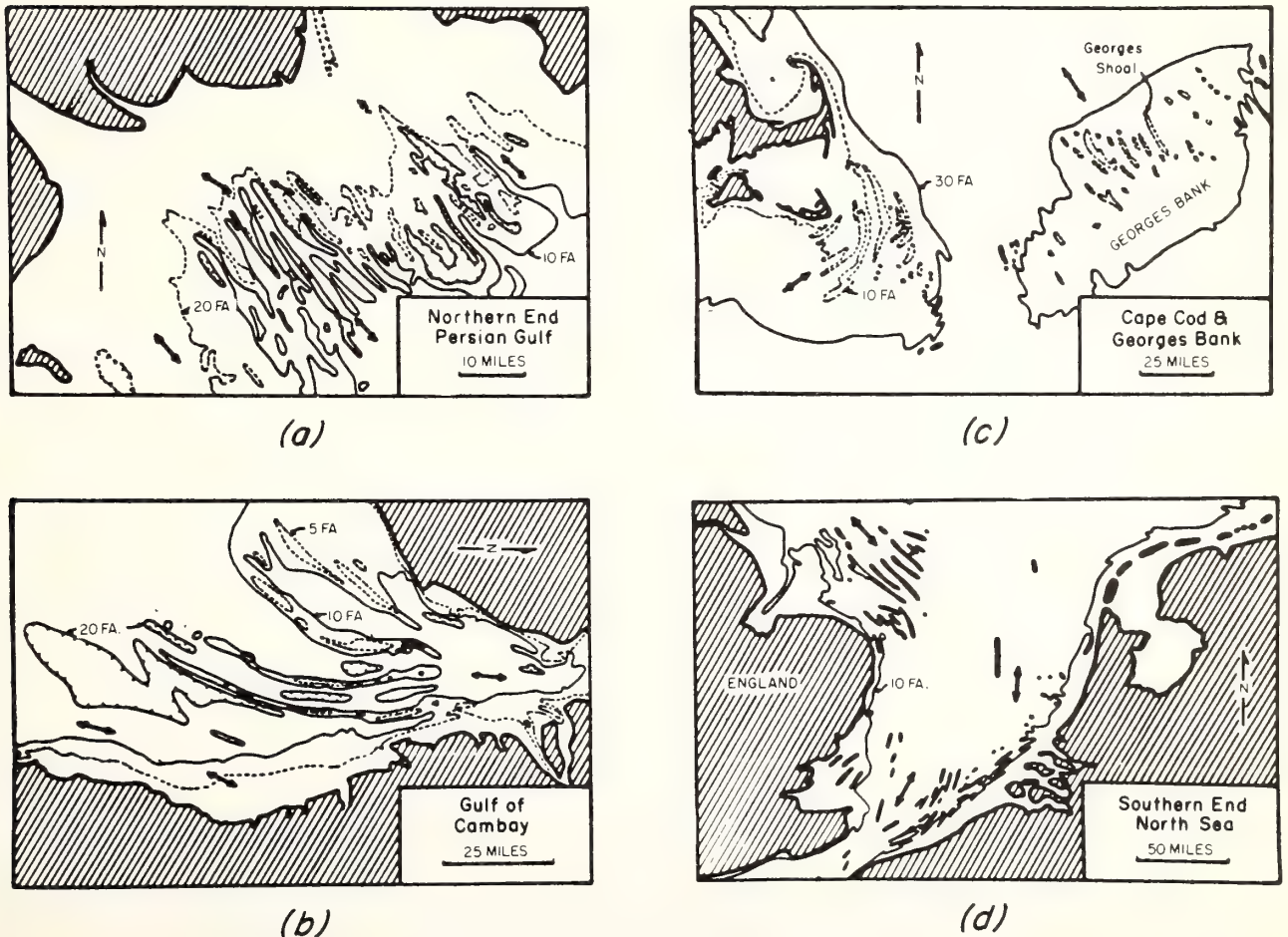


FIGURE 18. Patterns of sand ridges on tide-dominated shelves. From Off (1963).

theoretical and experimental studies with characteristics of shelf ridge fields. However, such large-scale coupling of flow with substrate has not yet been observed in the field. It is worth noting that there is an independent mechanism that is theoretically capable of maintaining a ridge topography, either by itself or in conjunction with other mechanisms. The mechanism described by Smith (1969) requires that ridges be aligned with mean flow direction and that the variance in flow direction be high, either because the flow is a rotary tidal flow; or because it is storm-driven, and the direction of flow varies during a storm and also among storms (see Chapter 4). As a consequence, most flows intense enough to entrain sand will be aligned at an oblique angle with the ridges during most of their duration. Flow across the ridge can be treated two-dimensionally according to slender body theory (Smith, 1969) and the stability analysis of Smith (1970) applies (see the preceding section). First one flank then the other flank of the ridge will be eroded, with sand transferred to the crest and far flank each time.

**SAND RIDGES IN RESPONSE TO TIDAL FLOWS.** The reversing nature of nearshore tidal flows adds another mechanism capable of maintaining a ridged topography. The velocity of the tidal wave is a function of water depth, and flow over a step or across a sill in a cohesionless substrate will result in a phase discontinuity between the behavior of the tidal wave on either side of the sill

(Fig. 19). Thus, when the tide is in the last stages of ebb on one side, it may be already beginning to flood on the other, so that there is an opposing sense of flow over the crest of the sill. If the flow is broad relative to its depth, and if the sill is a relatively large-scale feature, then this is an inherently unstable situation. Slight irregularities in the seafloor on either side of the sill will result in inequalities in the rate of propagation of the tidal wave, and during the brief period of opposing flow the two water masses on either side of the sill will tend to interpenetrate along a zigzag front. The tongues of flow on either side of the sill crest will tend to scour its channels until the crestline of the sill has also become zigzag (Fig. 19). A channel that is on the side of the sill facing the oncoming tidal wave and opens in that direction is called a *flood sinus* (Ludwick, 1973). It experiences an excess of flood over ebb discharge (is flood-dominated). A channel on the other side of the sill is called an *ebb sinus*, and is ebb dominated.

Scour in the interdigitating channels of such an ebb-flood channel complex is matched by aggradation of the interchannel shoals. This transfer is perhaps aided by the secondary circulation mechanisms described in the preceding section. As a consequence of the residual current pattern, net vectors of bottom flow integrated over the tidal cycle meet obliquely head-on over crests (Fig. 20), with the result that each ridge becomes a sand circulation cell, or closed loop in the sand transport pattern. Mean  $\partial\tau_0/\partial x$  is negative along these vectors toward the

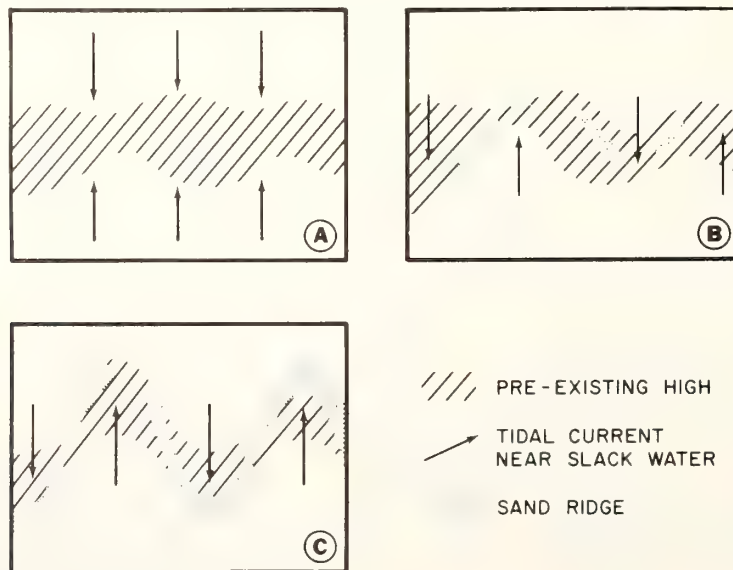


FIGURE 19. Hypothetical scheme of development of an ebb-flood channel topography as a consequence of the phase lag experienced by the tidal wave in its passage across a submarine sill.



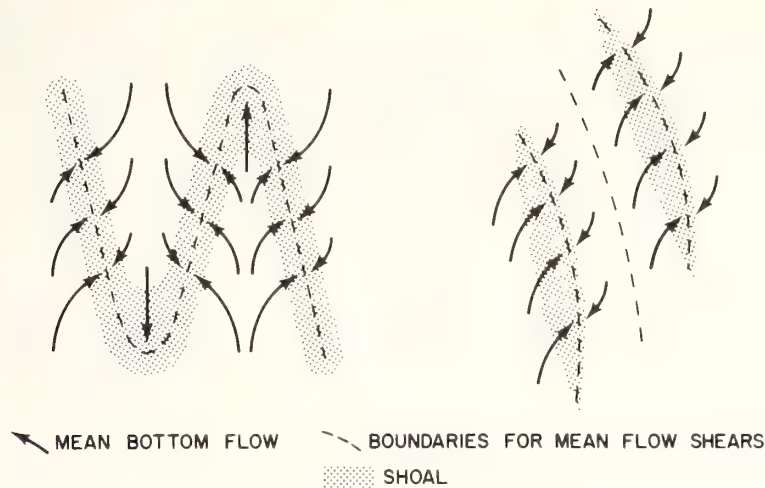


FIGURE 20. *Nearshore and offshore patterns of tidal flow about sand ridges. Based on Ludwick (1970b) and Caston and Stride (1970).*

zone of residual current shear at the ridge crest. The ridges therefore tend to aggrade toward the intertidal zone where they become "drying shoals" or swash platforms dominated by wave processes (Oertel, 1972). On open coasts, however, wave surge erosion may balance tidal current construction when the crests are still subtidal.

Tidal sand ridges that partition ebb- and flood-dominated flows usually experience a stronger residual current on one side than on the other, and tend to migrate away from that side (Fig. 21). In such cases, where the cross-ridge component of flow is strong, a ridge may itself deform into a sigmoid pattern, and eventually into two or three separate ridges (Caston, 1972); see Fig. 21.

Sills with interdigitating ebb and flood channel systems occur at the mouths of most tidal estuaries (Fig. 22), as a consequence of frictional retardation of the tidal wave within the estuary, and the resultant phase lag. On the Bahama Banks, they occur on the inner sides of islands, where the two wings of the tidal wave meet as they refract around the island (Fig. 23). The evolution of such a system portrayed in Fig. 19 probably rarely occurs in nature; the channel systems form simultaneously with such sills, not afterward. For instance, the ebb-flood channel system of the Chesapeake Bay mouth shoal appears to have formed during the Late Holocene reduction in the rate of sea-level rise (Ludwick, 1973). It can be inferred from the present morphology that the sill prograded south across the bay mouth, fed by the littoral drift discharge of the Delmarva coastal compartment. The ridges would have developed in zig-zag fashion, alternately and progressively segregating the flow into ebb-dominated and flood-dominated channels (Fig. 24).

Tidal flows often occur in the presence of salinity stratification so intense as to persist for part or all of the tidal cycle despite the powerful mixing effect of flow turbulence. Flow structure may be yet more complicated as a result. In Fig. 25, the residual circulation over the Hudson estuary mouth shoal (New York Harbor entrance) is seen to be a resultant response to flow interdigitation due to the phase lag effect (Fig. 25C) and to estuarine (two-layer) circulation (Fig. 25B).

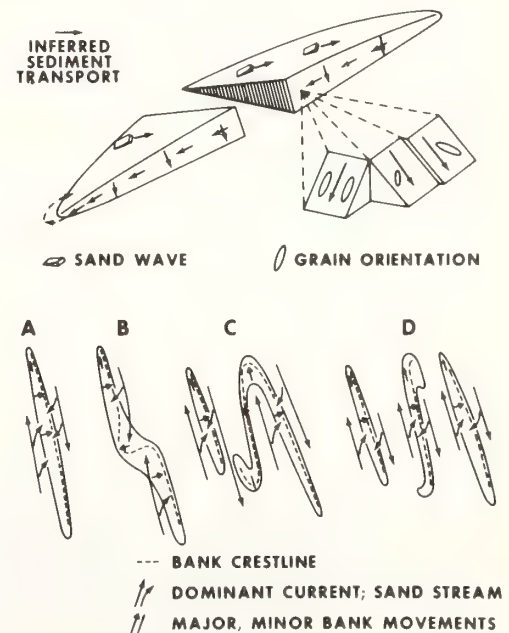


FIGURE 21. *Above: Anatomy of a tidal sand ridge. From Houbolt (1968). Below: Evolution of a tidal sand ridge. From Caston (1972).*

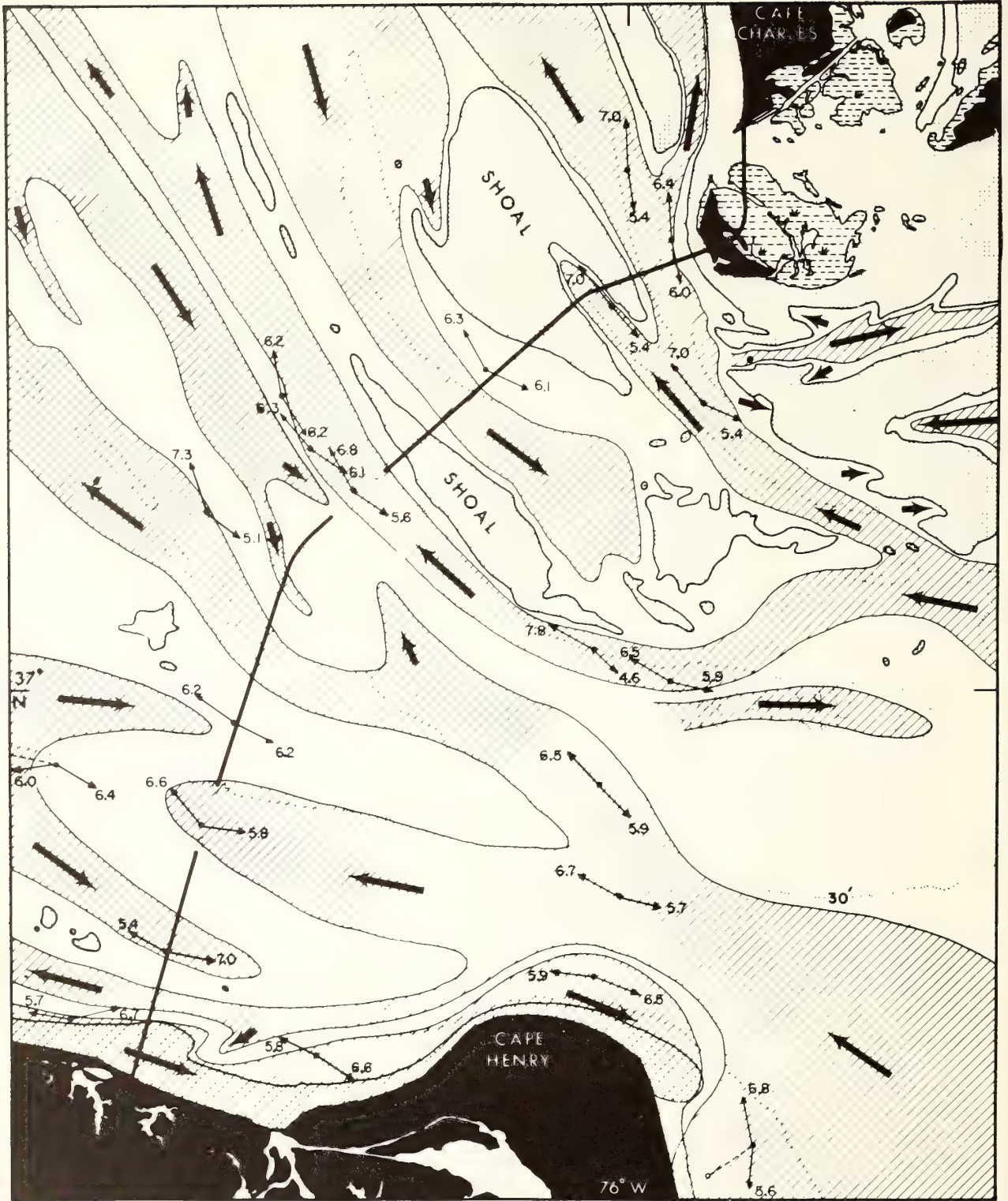


FIGURE 22. A hydraulic and geomorphic interpretation of the net nontidal (residual) flow pattern at the bottom in the entrance to Chesapeake Bay. Numbers are measured flood and ebb durations at the bottom in hours; small arrows show measured direction of

near-bottom currents. Stippled areas are shoaler than 18 ft. Ruled areas show where there is an ebb or a flood flow predominance. From Ludwick (1970a).



FIGURE 23. *Ebb-flood channel pattern on the Great Bahama Bank. Altitude 3000 ft. Photo: Charles True.*

Stratification may also play a role in the formation of ridge topography within the estuary. Weil et al. (in press) describe the formation of subtidal levees in Delaware Bay as the consequence of the penetration of subsurface saline tongues up the channels during flood tide, resulting in an internal pressure head that can drive channel axis downwelling (Fig. 26), and as a consequence of the overriding of the tongues by fresher water during the ebb tide, with similar effects. One of us (Ludwick, in press) has mapped near-bottom convergences and divergences of flow in the Chesapeake Bay mouth during flood tide. These are absent during the more thoroughly stratified ebb. Here stratification appears to inhibit channel axis downwelling and bottom current divergence (see Fig. 31). Velocity profiles of Chesapeake Bay mouth tidal flows tend to be parabolic but with markedly sigmoidal perturbations (Ludwick, 1973), and may imply the presence of standing internal waves or wakes from shoals.

Tidal flows in confined estuary mouths thus tend to develop an interdigitating pattern of ebb- and flood-dominated channels, whose sequence of partitioning ridges tends to alternate between clockwise and counterclockwise current flows (Fig. 20). On the offshore shelf,

however, the tide becomes rotary rather than reversing and a different pattern tends to appear (Caston and Stride, 1970). Ridges appear in free-standing sets rather than in continuous zigzag arrays. Residual current shears occur in channel axes as well as on ridge crests, and successive ridges experience residual flows with the same sense of rotation.

Huthnance (1972) attributes this open shelf flow pattern to interaction of the ridges with the shelf tide. His model considers a rectilinear reversing tide whose flow directions make an oblique angle with the ridge axis. The cross-ridge component of flow must accelerate over the ridge crest for continuity reasons. The ridge-parallel component of flow must decrease up the upcurrent flank as the water column shoals, and influence of friction becomes proportionately greater. However, because high-velocity fluid is being transported into the shoal region, the decrease in the ridge-parallel flow component lags behind the decrease in depth. On the downcurrent flank, the restoration of the ridge-parallel flow to ambient velocity is similarly lagged. When the tide changes, upcurrent and downcurrent flanks reverse roles. When flow is averaged over the tidal cycle, a clockwise pattern of residual flow around the ridge results (or counter-

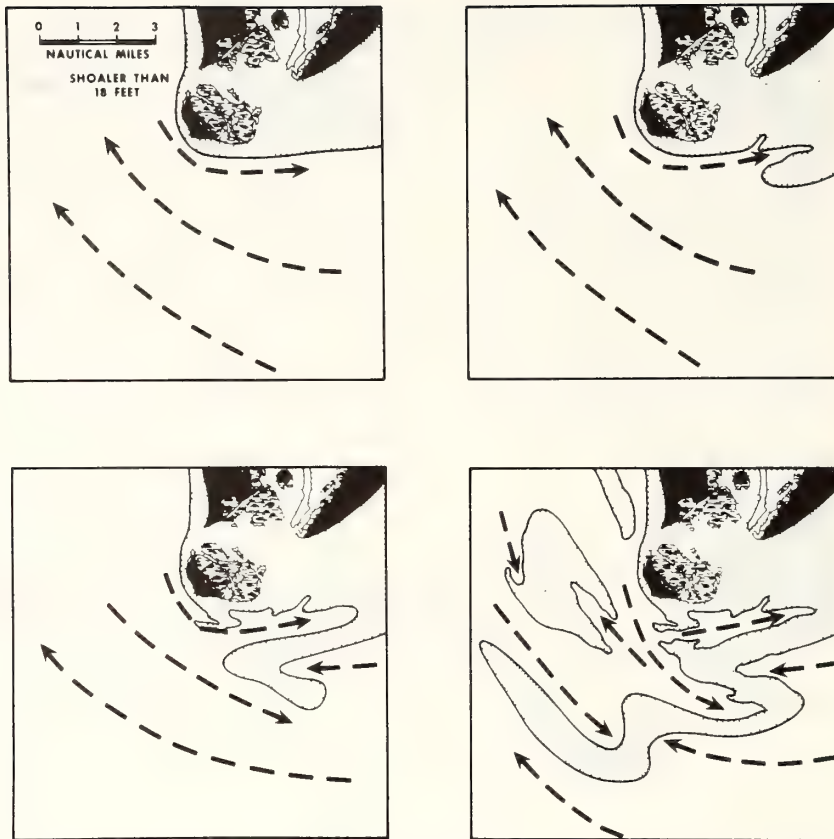


FIGURE 24. Evolution of "submarine zigzag spit" across Chesapeake Bay mouth. Based on Ludwick (1972).

clockwise, depending on whether the oblique, reversing tidal stream is sinistral or dextral with respect to the ridge). Huthnance proposes a second mechanism whereby in the northern hemisphere, Coriolis force also results in clockwise circulation.

Huthnance's mechanisms are interesting, but the requirement that there be a significant angle between the axis of the tidal stream and that of the ridge presents a problem. The ridges are a response element within the flow field-substrate system, not an independent forcing element. It seems doubtful that ridges of cohesionless sand could maintain a significant angle with the tidal stream for any length of time, unless it were somehow an equilibrium response to flow. Smith (1969) notes that tidal sand ridges might be expected to orient themselves parallel to the long axis of the tidal ellipse, as the sand body would then be at a small angle of attack throughout most of the high-velocity part of the tidal cycle. According to slender body theory the cross-shoal component of flow during this period can be considered to

be two-dimensional and driven by the cross-shoal pressure gradient. It would thus sweep sand first up one side and then up the other as the tide rotated.

Possibly the dilemma is resolved by the lag effect cited by Postma (1967) and Stride (1974); see Fig. 27. Because of a lag in the entrainment of sand, the period of maximum sand transport is believed to lag behind maximum flood flow, and again behind maximum ebb flow. The result should be to align the response element (sand ridge) obliquely across the major axis of the tidal ellipse. It also seems likely that the large-scale, unbounded tidal flow field of the open shelf might at least locally generate Ekman flow structure during midtide, and couple with inner shelf ridge fields in the fashion that has been suggested for wind-driven flows.

#### Limiting Conditions of Bed Form Formation on the Continental Margin

In attempting to apply the elements of bed form theory presented on the preceding pages to analyses of conti-

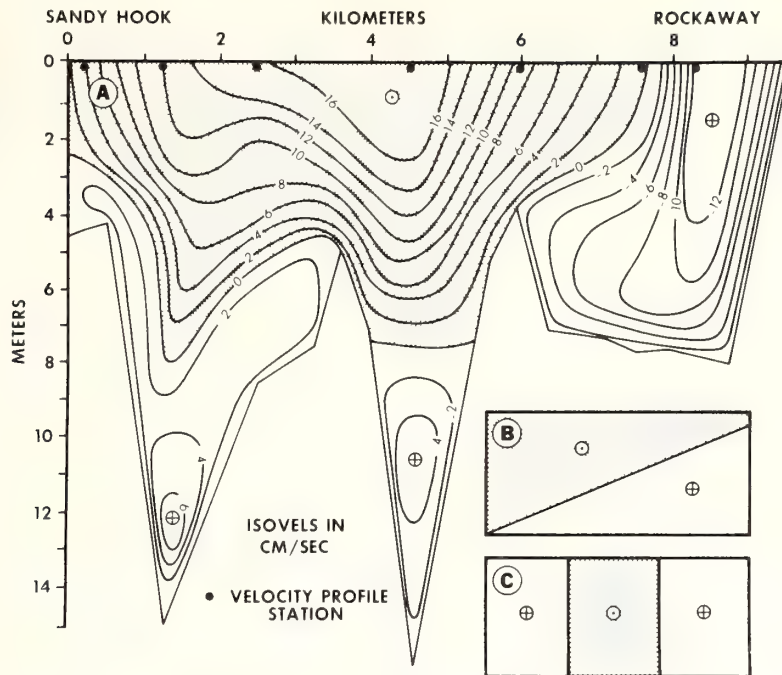


FIGURE 25. (A) Profile across the Hudson estuary mouth (mouth of New York Harbor) contoured for velocity residual to the tidal cycle. The flow pattern is a resultant response to component flow patterns shown in (B) and (C). (B) Schematic diagram of two-layered, estuarine flow pattern. (C) Schematic diagram of component of flow pattern resulting from phase lag of tidal wave. From Duedall et al. (in press), after Kao (1975).

mental margin sedimentation patterns, it is useful to keep in mind some generalizations presented by Allen (1966; 1968a, pp. 50–53; 1968b). Allen, following Bagnold (1956), notes that the grain-fluid system is a decidedly multivariate one, and that we should expect to find co-existing instabilities of several different modes and scales. Flows that experience both transverse and streamwise perturbations may develop *bed form associations* consisting of two different bed form types, for instance a reticulate pattern with sand waves overprinted on sand ridges. Likewise, flows tend to experience one or more instability modes at several different spatial scales, resulting in a *bed form hierarchy* as, for instance, in the case of the Diamond Shoals sand wave field (Hunt et al., in press), where photos show that current ripples are superimposed on sand waves (Fig. 10) and sidescan sonar records show in turn that sand waves are superimposed on giant sand waves (Fig. 28). Elaborate hierarchical associations of bed forms occur over vast areas of the earth's surface, in subaerial sand seas (Wilson, 1972), and also in widely disparate environments on the continental margin (compare Fig. 29 with Fig. 30).

The physical scale at which bed forms occur affects their response characteristics, and in turn the flow fre-

quency to which they are tuned. For instance, on the crests of the drying sand ridges of the Minas Basin, current ripples reflect radial drainage at the last stages of ebb, sand waves are oriented with slip faces seaward as responses to peak ebb flow, while larger dunes locally are landward facing, reflecting a stronger flood than ebb flow (Swift and McMullen, 1968; Klein, 1970; Dalrymple, 1973).

The largest scale transverse and longitudinal bed forms have had to readjust to continuous environmental change associated with Holocene deglaciation and the accompanying transgression of the continental margins. In some cases, they appear to have taken nearly the duration of the Holocene to form. Sand ridges on the central New Jersey shelf have basal strata containing 11,000-year-old shells (Stubblefield et al., 1975). These features and many other shelf ridge fields appear to have been formed by shoreface ridge formation and detachment (Swift, in press) during the Holocene transgression; see Fig. 28, Chapter 14. Plan geometry and internal structure of Atlantic Shelf ridge fields suggest that ridge spacing has increased by ridge migration or coalescence as the water column deepened (Swift et al., 1974).

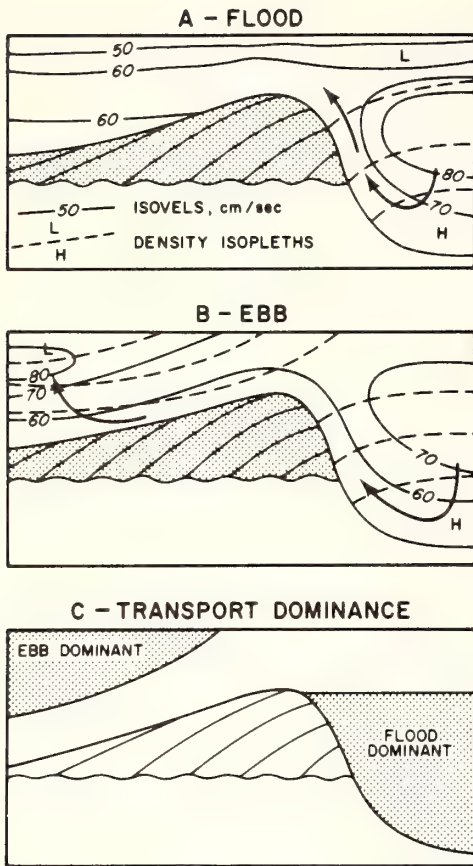


FIGURE 26. Tidal sand ridge as a submarine levee, formed in response to stratified flow. From Weil et al. (in press).

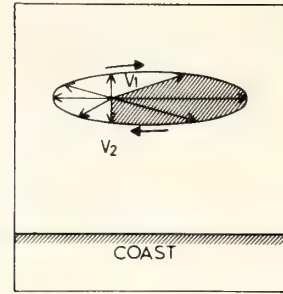


FIGURE 27. Lag effects in a rotating tide. Radial arrows are vectors of tidal current velocity at intervals through the tidal cycle. Sand entrainment starts at velocity  $V_1$  and continues to velocity  $V_2$ . Net sand transport is to right and onshore. From Postma (1967).

The response of larger bed forms tends to lag beyond the peak flow event or may comprise an average response to repeated events. Allen (1973) notes that maximum sand wave height in the Fraser River and Gironde estuary is lagged behind peak tidal flow by as much as a quarter of the tidal period. Ludwick (1972) notes that tidal sand waves are symmetrical over portions of the Chesapeake Bay mouth where the tidal cycle is symmetrical, but are asymmetrical when there is flood or ebb asymmetry in the tidal cycle. Thus their response to reversing tidal flow is time-averaged in a manner entirely analogous to the response of oscillation ripples to wave surge (Chapter 8). Tidal sand waves in Chesapeake Bay mouth attain their greatest height and slopes during the summer months when wave activity is

FIGURE 28. Sidescan sonar record of sand waves on the back of giant sand waves, Cape Hatteras, North Carolina. Sand waves are larger in coarse sand of trough than on finer sand of giant waves. Giant sand waves are 120 m apart, 7 m high. Unpublished data of Swift and Hunt.

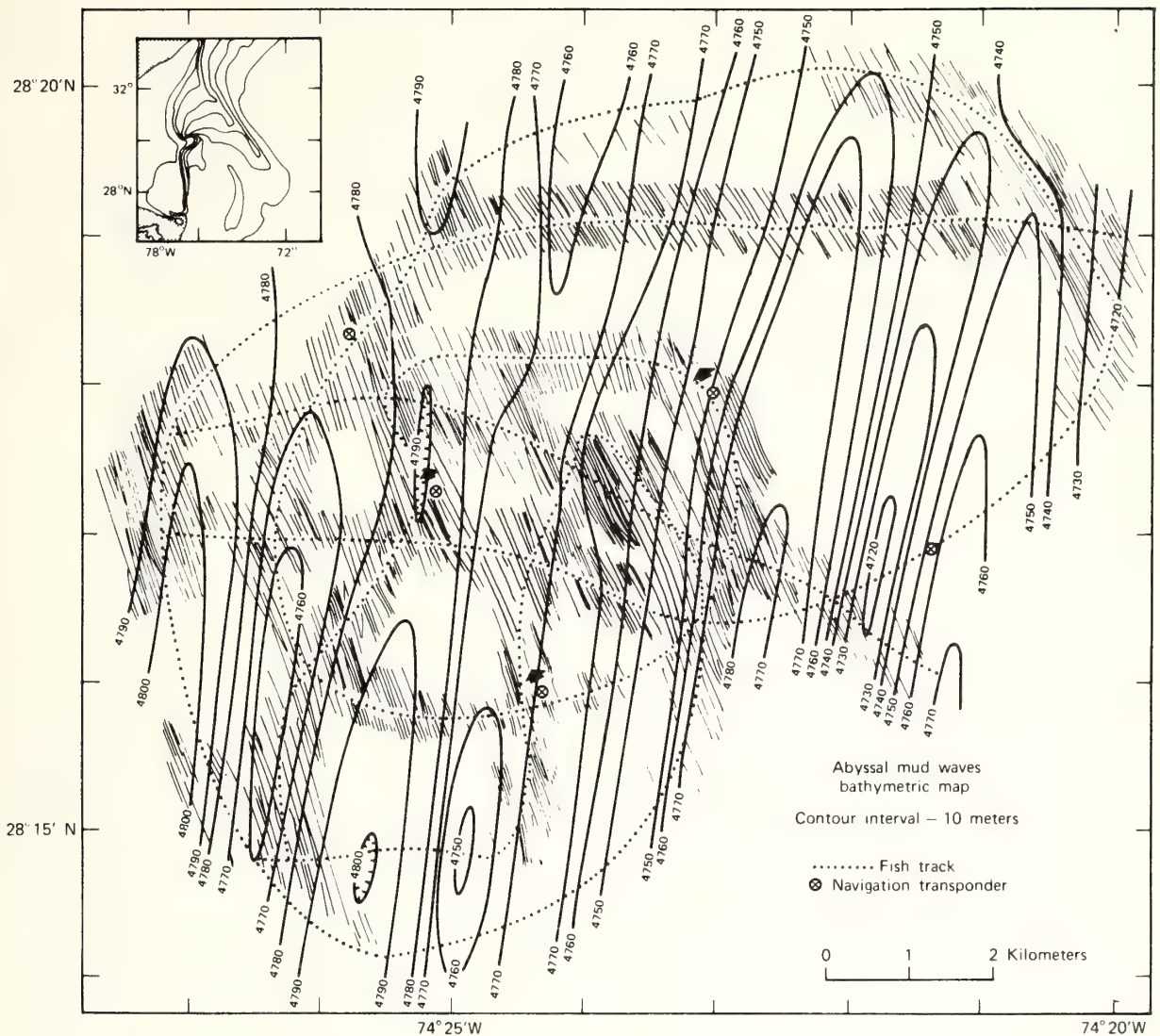


FIGURE 29. *Erosional furrows and large-scale silt ridges on the Blake-Bahamas outer ridge, 4700 m depth. From Hollister et al. (1974).*

at a minimum; they are degraded by the more intense wave activity of winter months (Ludwick, 1970a,b, 1972). The Platt Shoals sand wave field on the open Virginia shelf appears to be induced by storm flows, hence it may have the opposite behavior pattern; sand waves would be highest in the winter months and would tend to be degraded by fair-weather wave surge and burrowing organisms during the summer (Swift et al., 1974).

## ESTIMATES ON SEDIMENT TRANSPORT

### A Numerical Model

port systems, and to determine the rates of erosion, transport, and sedimentation associated with these elements. Much of the material in the following chapters is devoted to available information of sediment sources, pathways, and sinks on the continental margin. However, there have been very few attempts to estimate rates of sediment transport. It should be possible to measure the time history of a marine flow by means of a current-meter array, then employ the empirical relationships developed by hydraulic engineers to estimate the time history of sediment transport. The difficulties however, are formidable. In situ recording current meters are expensive and difficult to maintain. Data processing is com-

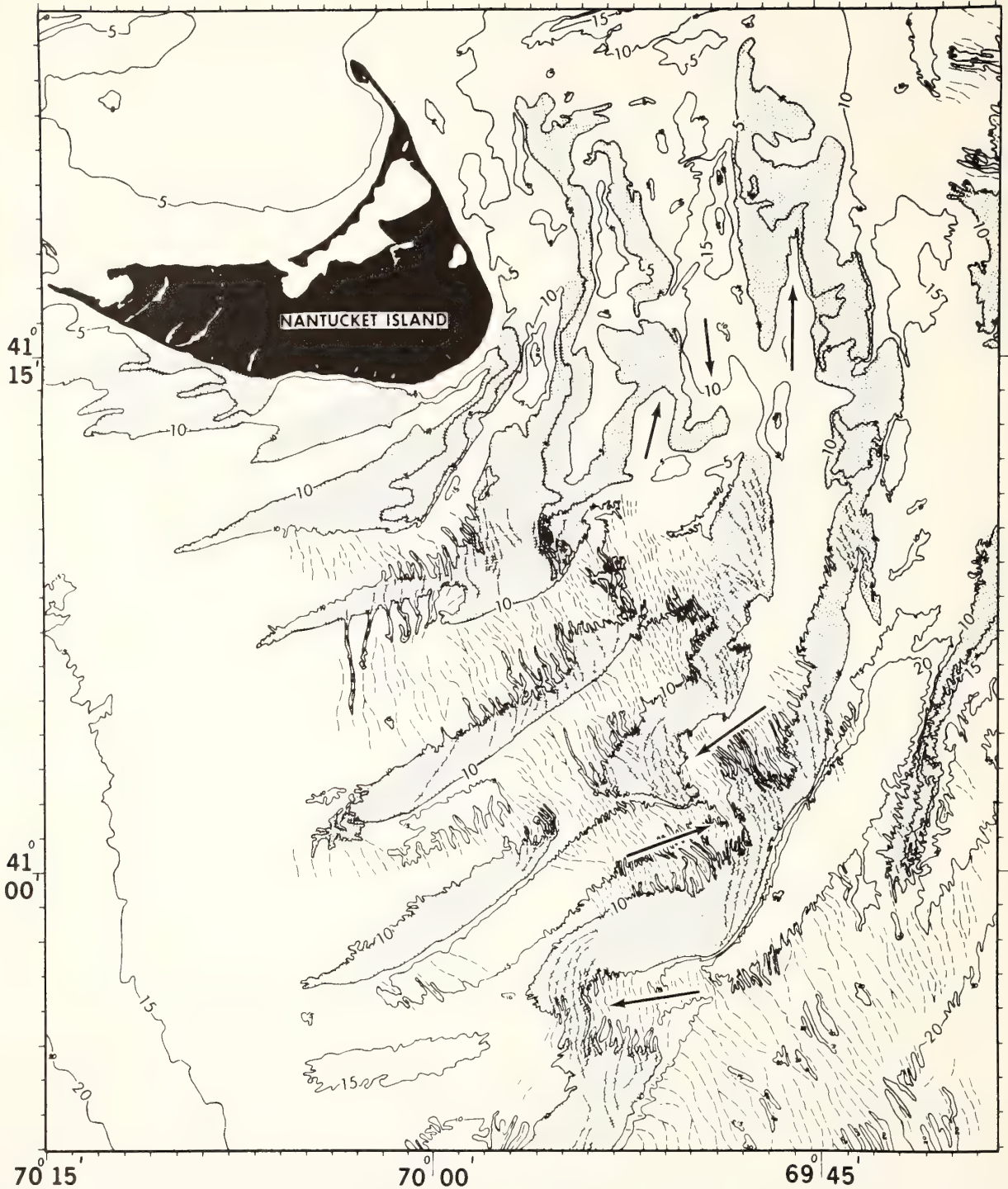


FIGURE 30. Pattern of sand waves (dark lines) and sand ridges at Nantucket Shoals. Significant highs are stippled and ebb-flood channel couplets are indicated by arrows. Ebb and flood sinuses as inferred from morphology, are indicated by arrows. The ridges

appear to have initially formed as shoreface-connected ridges similar to those attached to the shoreface of modern Nantucket Island, and to have been stranded on the shelf floor as the shoreface underwent erosional retreat. From Swift (1975).



wave surge. There is no general agreement on the most satisfactory transport equation, or on the applicability of equations developed under laboratory conditions to the complex deep-water flow fields of the continental margin.

A simple numerical model for estimating rates and patterns of sediment transport in areas of tidal flow has been devised by one of us (Ludwick, in press). It is summarized below.

**STRUCTURE OF THE MODEL.** The model requires determination of the distribution across the study area of a sediment transport index  $\tau_0 u_{100}$  over a tidal cycle. The index is derived from Bagnold's (1956) work (see p. 113), in which sediment discharge  $q$  is set proportional to fluid power  $\omega$  defined as

$$\omega = \tau_0 \bar{u}$$

so that

$$q = K \tau_0 \bar{u}$$

where  $\tau_0$  is bottom shear stress and  $\bar{u}$  is the depth-averaged flow velocity. For convenience of measurement, Ludwick substitutes  $u_{100}$ , the velocity measured 100 cm off the bottom. With this information, it is possible to use the sediment continuity equation (p. 166) to determine the distribution and relative rates of aggradation and erosion along streamlines of sediment transport.

**DETERMINATION OF  $\tau_0$ .** In order to determine the distribution of  $\tau_0$ , current velocities were measured over 27 hour intervals at 24 stations in the mouth of Chesapeake Bay. A Kelvin Hughes direct reading current meter was employed from an anchored ship. At each station the current meter was used successively through 11 different depth levels. Hourly profiles with 4 minute observation periods were obtained at each level.

These speed values were then reduced to pseudo-synoptic data sets for standard times and depths at each station (see Ludwick, in press). Each data set was fitted to Hama's (1954) parabolic velocity defect law (see the discussion in Chapter 7, p. 96). This empirical function pertains to outer boundary flow, at distances greater than  $0.15h$ , where  $h$  is the thickness of a turbulent boundary layer, or water depth in the case of fully developed flow in a uniform channel. The equation is

$$\frac{\bar{u}_\infty - u}{u_*} = 9.6 \left(1 - \frac{z}{h}\right)^2$$

where  $\bar{u}_\infty$  is the free stream velocity,  $u$  is velocity at distance  $z$  above the bed, and  $u_*$  is the friction or shear velocity.

An estimate of  $u_*$  on the bottom is then obtained by least squares curve fitting. The value can be converted to an estimate of  $\tau_0$ , the boundary shear stress, through the relationship  $u_* = (\tau_0 / \rho)^{1/2}$ , where  $\rho$  is fluid density.

This measurement, obtained by observation of the entire water column, provides a far more reliable estimate for  $\tau_0 u_{100}$ , the fluid power, than does  $\tau_0$  determined simply from the product  $C_{100} \rho (u_{100})^2$ , due to uncertainties in determining  $C_{100}$  (see Chapter 7, p. 99).

**MAPS OF BED SEDIMENT TRANSPORT.** Values of the sediment transport index obtained for 24 stations must be converted to maps of near-bottom streamlines of sediment transport. The values are adjusted to the mean tidal range, a process described by Ludwick (1973). They are further corrected by subtracting  $150 \text{ dyne} \cdot \text{cm} / \text{sec cm}^2$ , a threshold value for the initiation of sediment movement (Fig. 31). The value at each station is integrated separately over each flood and each ebb half-cycle, and the results are averaged for ebb and flood. After averaging and integrating, the units of the sediment transport index are  $\text{dyne} \cdot \text{cm} / \text{cm}^2$  per average ebb (or flood) half-cycle.

The values obtained at points on the field grid of 24 irregularly placed stations must then be redistributed over a systematic grid. This is a problem in vector interpolation. The first step is to prepare separate maps of the north-south and east-west components of  $\tau_0 u_{100}$  for the flood cycle. Each map is contoured. The flood component maps are superimposed. Resultant vectors may now be calculated at any point, if the contour interval is sufficiently small. The density of resultant vectors may be increased in areas of complex flow. Finally, streamline maps may be prepared by drawing lines that are everywhere tangent to the vectors (Fig. 32A). The process is repeated for the ebb half-cycle and the vector sum of ebb and flood (Figs. 33A and 34A).

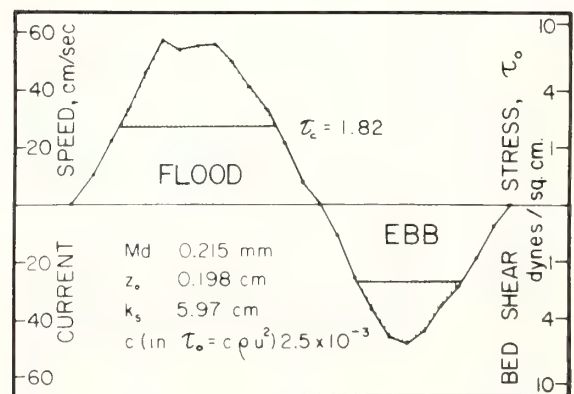


FIGURE 31. Tidal current speed and bottom shear stress at a flood channel station, Chesapeake Bay mouth. Speed values are for a distance of 18.5 ft off the bottom. Total depth, 56 ft. Observed speeds were corrected from mean tidal range and averaged over six cycles.  $z_0$  is the roughness length estimated from vertical velocity profiles,  $k_s$  is the height of bottom roughness elements, and  $\tau_c$  is the critical shear stress, calculated from the Shields entrainment diagram. From Ludwick (1970a).

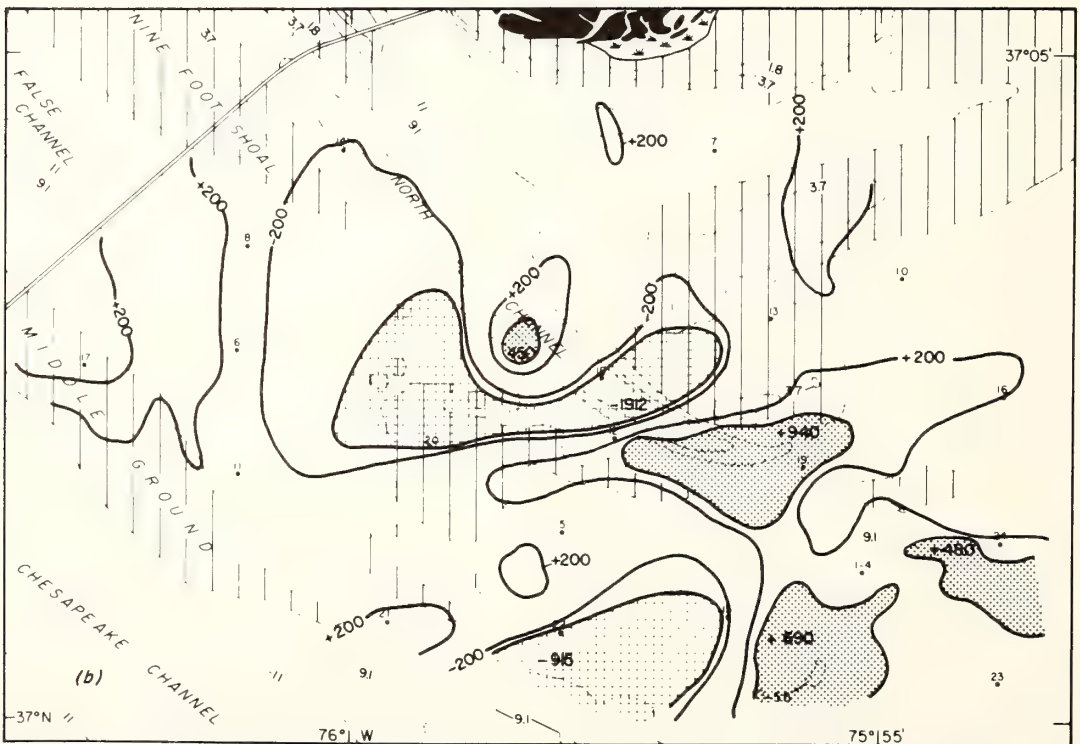
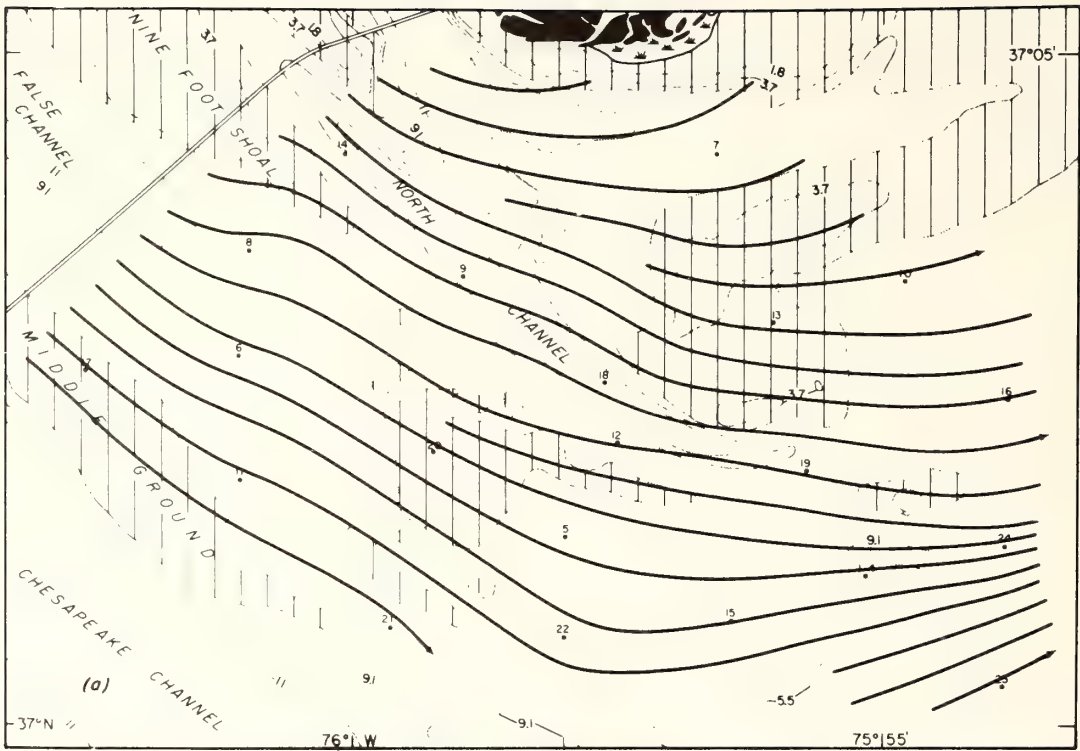


FIGURE 32. Ebb-directed sediment transport at the bed. (a) Streamlines of the sediment transport vector  $\tau_{00.100}$ ; depths are in meters; vertically ruled areas are shoaler than 5.5 m. (b) Erosion-deposition chart on which erosion is positive (+) and deposition is negative

(-); units are  $\text{dyne-cm/cm}^2$  per ebb half-tidal cycle per 463 m of transport  $\times 10^{-4}$ ; cross-hatched areas indicate erosion intensity greater than -400 units; stippled areas indicate deposition intensity greater than +400 units. From Ludwick (in press).



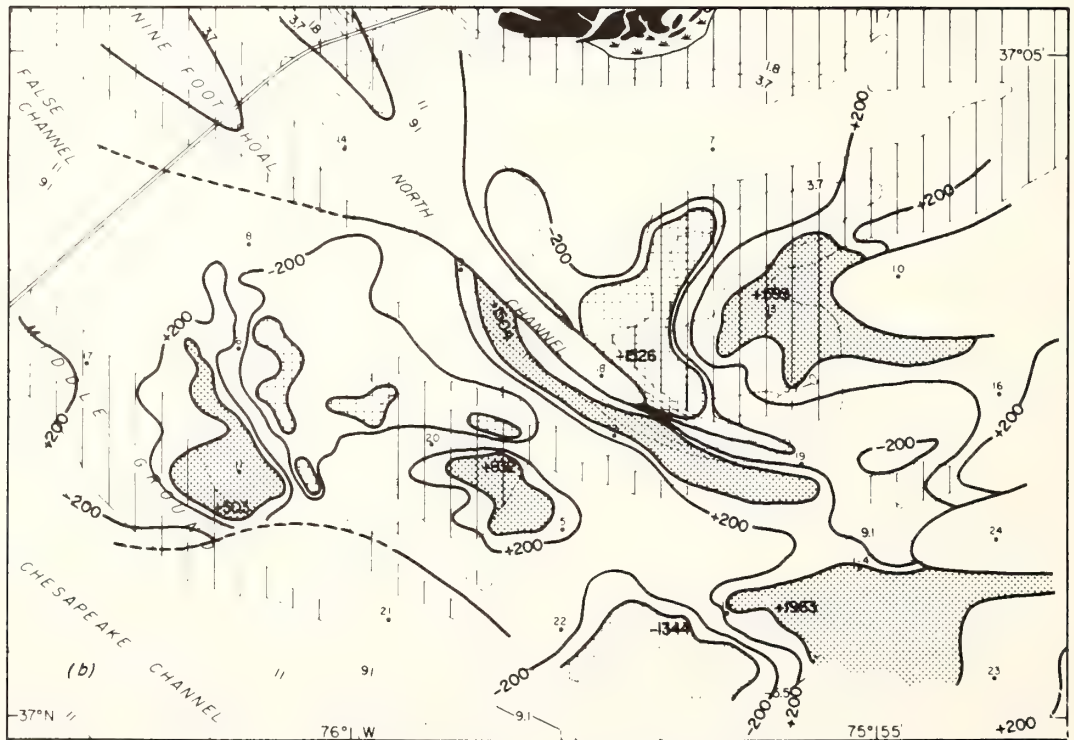
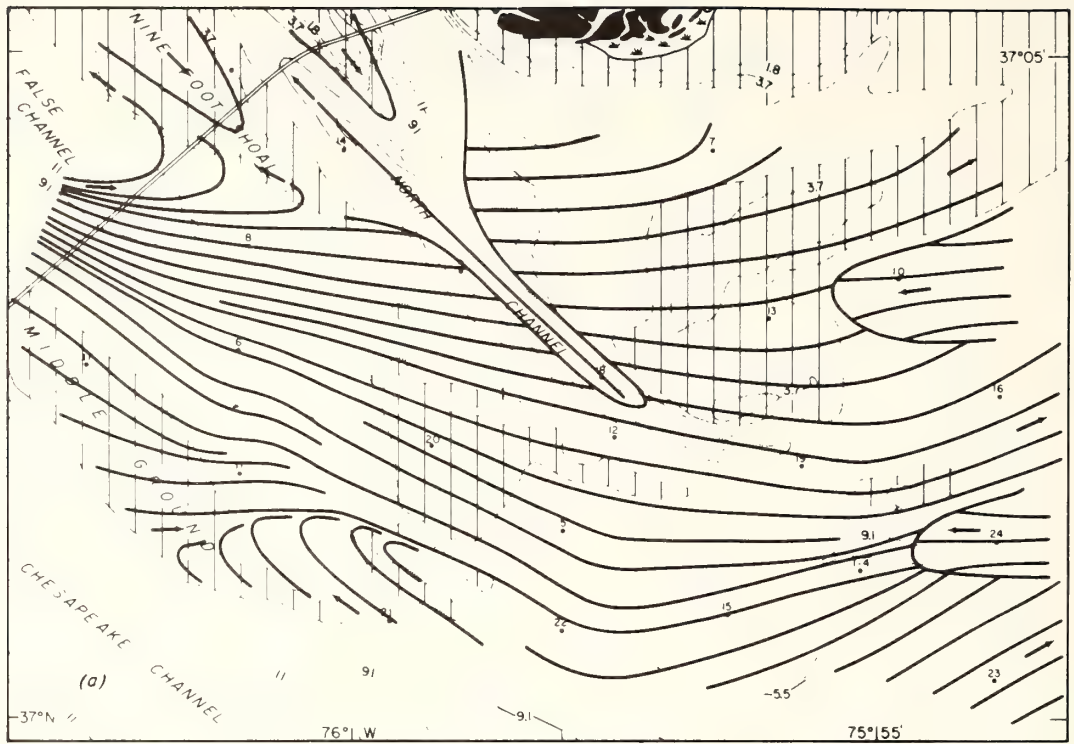


FIGURE 34. Vector sum of ebb and flood sediment transport at the bed. (a) Streamlines of the resultant sediment transport vector  $\tau_{0u100}$ ; depths are in meters; vertically ruled areas are shoaler than 5.5 m. (b) Erosion-deposition chart on which erosion is positive (+)

and deposition is negative (-); units are  $\text{dyne-cm/cm}^2$  per tidal cycle per 463 m of resultant transport  $\times 10^{-4}$ ; cross-hatched areas indicate erosion intensity greater than -400 units; stippled areas indicate deposition intensity greater than +400 units. From Ludwick (in press).

It is important to realize the limitations of the streamlines of bottom sediment transport so determined. The redistribution of information has not in any way increased the accuracy or resolution of the original data. Sediment input in a stream tube does not necessarily equal sediment output, since deposition or erosion may occur. There is no underlying stream function in the method, and the spacing of the streamlines is not a measure of transport rates. It is assumed, however, that transport is confined to a path of unit width that conforms to the bathymetry of the seafloor, and that the streamline is the center line of this path. It is further assumed that conditions are steady and nonuniform for the entire pattern.

**NET SEDIMENTATION MAPS.** As a separate and ensuing procedure, it is possible to estimate the extent of areas of erosion and deposition, and also the rates at which these processes occur. The estimate utilizes the sediment continuity equation written in terms of discharge:

$$\frac{\partial \eta}{\partial t} = -\epsilon \frac{\partial q}{\partial x}$$

where  $\eta$  is bed elevation relative to a datum plane,  $t$  is time,  $\epsilon$  is a dimensional constant related to sediment porosity,  $q$  is the weight rate of bed sediment transport per unit width of streamline path, and  $x$  is distance along the streamline.

Discharge ( $q$ ) may be taken as proportional to  $\tau_0 u_{100}$  and the right-hand partial derivative may be approximated by a finite difference:

$$\frac{\partial q}{\partial x} \approx \frac{\Delta q}{\Delta x} = K \frac{(\tau_0 u_{100})_2 - (\tau_0 u_{100})_1}{x_2 - x_1}$$

The term  $x_2 - x_1$  is held constant arbitrarily at a value of 465 m, hence

$$\frac{\partial \eta}{\partial t} \propto -\Delta \tau_0 u_{100}$$

Thus a decrease in transport rate along a transport pathway induces deposition; an increase causes erosion.

The resultant vector map for a half-cycle is superimposed on the equivalent streamline map. The magnitude of  $\tau_0 u_{100}$  is determined at equispaced points along each streamline;  $\Delta \tau_0 u_{100}$  is determined as a positive or negative value, and mapped over the area of study as an estimate of relative erosion and deposition intensity. In Figs. 32B, 33B, and 34B, net sedimentation maps have been prepared for the ebb and flood half-cycles and for the vector sum of ebb and flood.

**UTILITY OF THE MODEL.** Such a manipulation of the data from 24 current-meter stations extracts a surprising

amount of information from them. Streamlines of bed sediment transport associated with the ebb tidal jet are seen to pass over the bay mouth shoal in parallel fashion. Flood streamlines, however, form a pattern in which flow divergence and flow convergence alternate across the flow in sympathy with the topographic pattern of interdigitating ebb and flood channels.

The vector sum map shows a complex pattern of flow dominance that is also correlated with bottom morphology. Patterns of net sedimentation do not correlate as closely with the topography, probably because they do not indicate the areas of maximum relief, but instead areas undergoing maximum change. In particular, the parabolic shoals that envelop each ebb or flood sinus are seen to be subject to a systematic pattern of sedimentation. The sides of shoal segments that face the dominant flow, however obliquely, are eroding. The crest and downcurrent sides, however, are undergoing aggradation. Thus, the processes that Smith (1970) has inferred to cause sand waves (see p. 165) appear also to be applicable to ebb-flood channel topography.

The model can be generalized for portions of the shelf dominated by storm flows if each flow event is treated in the same fashion as Ludwick treated a tidal half-cycle, or sediment transport can be integrated over an arbitrary period of observation.

### Transport Estimates from Tracer Dispersal Studies

One of the main stumbling blocks in divising quantitative estimates of sediment transport has been the limited applicability of empirical relationships based on laboratory observations to the complex flows of the marine environment. The model partially circumvents this problem by recourse to the sediment transport index, based on Bagnold's generalized evaluation of fluid power (Chapter 8, p. 113). In doing so, it provides only a relative answer. Sediment transport is proportional to fluid power, and the proportionality constant remains unevaluated. Despite this sacrifice, the model has not resolved the problem of adequately treating the complex time and space scales of marine flows. In particular, it fails to deal with the vexing problem of the role of bottom wave surge in "lubricating" bottom sediment transport by reducing the effective transport threshold for a unidirectional flow component (see discussion, Chapter 8, p. 115). This wave surge factor becomes part of the proportionality constant. Wave-surge-amplified transport is not that critical a problem in the analysis of a primarily tide-built topography. It becomes critical, however, in open shelf transport, where wind-driven unidirectional flows attain their maximum intensities just as the wave regime does.

It is clear that the best resolution of a marine sediment transport system will be obtained when a model such as the one presented above is employed together with an independent method for evaluating the proportionality constant. The most promising method to date is the deployment of radioisotope tracers. Fluorescent tracers have been widely used (see Ingle and Gorsline, 1973; Inman and Chamberlain, 1959). However, since counting of labeled particles must be done in the laboratory, the analysis is tedious, and it is generally not possible to watch the development of dispersal patterns in real time. Furthermore, fluorescent tracers have a very limited applicability seaward of the surf, as a consequence of the limited sensitivity of the method and the difficulties of hand sampling. Tracer dispersal can usually be observed in an area 50 m in diameter or less, under fair-weather conditions. After a storm, when a major displacement of sediment has occurred, the tracer grains are liable not to be there at all.

Radioisotope tracers avoid much of this difficulty. The RIST (Radio Isotope Sand Tracer) system, developed by Oak Ridge National Laboratories and the Coastal Engineering Research Center (Duane, 1970) detects radioisotope-labeled tracers by means of a towed scintillometer. The data logging system provides for real time readout, which greatly aids mapping of the dispersal pattern. A relatively long-lived isotope such as ruthenium-103, with a half-life of 40 days, permits effective tracing for three times that duration, or an entire storm season.

A numerical estimate of sediment transport may be fine-tuned by quantitative analysis of radioisotope tracer dispersal patterns. The procedure requires not only the mapping of successive outlines of the tracer pattern but the ability to account for all of the labeled particles at each stage. In order to establish such a mass balance, it is necessary to know the depth of reworking, which is the depth to which labeled particles have penetrated during dispersal. This depth can be calculated from the known ability of the sediment to absorb radiation, if it is assumed that the tagged particles are mixed into the reworked layer in a homogeneous fashion. If tracer particles can be accounted for through successive mappings of the dispersal pattern, then the rate of sediment transport as indicated by dispersal of tracers may be checked against the rate of transport as estimated from current-meter records in one of two ways. Transport rates may be determined directly from the dispersal pattern and compared with estimates based on current-meter records. Or current-meter records may be used to simulate tracer dispersal patterns, and these ideal patterns may be compared with observed dispersal patterns.

Figure 35 shows a series of radioisotope dispersal patterns from an experiment conducted by J. W. Lavelle and his associates, Atlantic Oceanographic and Meteorological Laboratories, Miami, Florida. Water-soluble bags of labeled sand were released along a line in 20 m of water on the south shore of Long Island during April and May of 1974. Over a period of 69 days, a typical fair-weather dispersal pattern formed (panels B-F). The data in these panels have been corrected for decay, but in the last panel, the corrected values on the margins of the pattern are so much weaker than background, that they were lost when smoothed background values were subtracted. The mild summer storms during this period only briefly generated flows strong enough to transport sand, and much of the labeled sand remained in close proximity to the drop line, where it was not readily resolved by the towed scintillometer. It will be necessary to apply a statistical smoothing function to the data, in order to undertake a mass balance calculation for the dispersed tracer sand. If continued experimentation leads to improved field techniques and data processing, then radioisotope tracers should prove a fruitful method for calibrating numerical models of sediment transport.

## SUMMARY

The size frequency distribution of marine sand samples tends to be log-normally distributed. This distribution, as defined by its mean and standard deviation, is the "signature" of the depositional event, and deviations from log normality, as measured in terms of skewness and kurtosis, may be taken to reflect both the provenance and the hydraulic history of the sediment.

The modal diameter of a sand deposit is that grain size most likely to arrive and least likely to be carried away from the place of deposition; progressively coarser sizes are progressively less frequent because they are progressively less likely to arrive, and progressively finer grain sizes are progressively less frequent because they are more likely to be carried away. This intuitively apparent concept can be explained in terms of probability theory.

As sand progresses down a transport path by intermittent hops, it tends to leave its coarser grains behind, and the deposits are progressively finer in the direction of transport (have undergone progressive sorting). They also will tend to be fine-skewed, particularly if the intensity of hydraulic activity also declines down the transport path.

Moss has shown that the size distributions of marine sands tend to be made up of three log-normal popula-

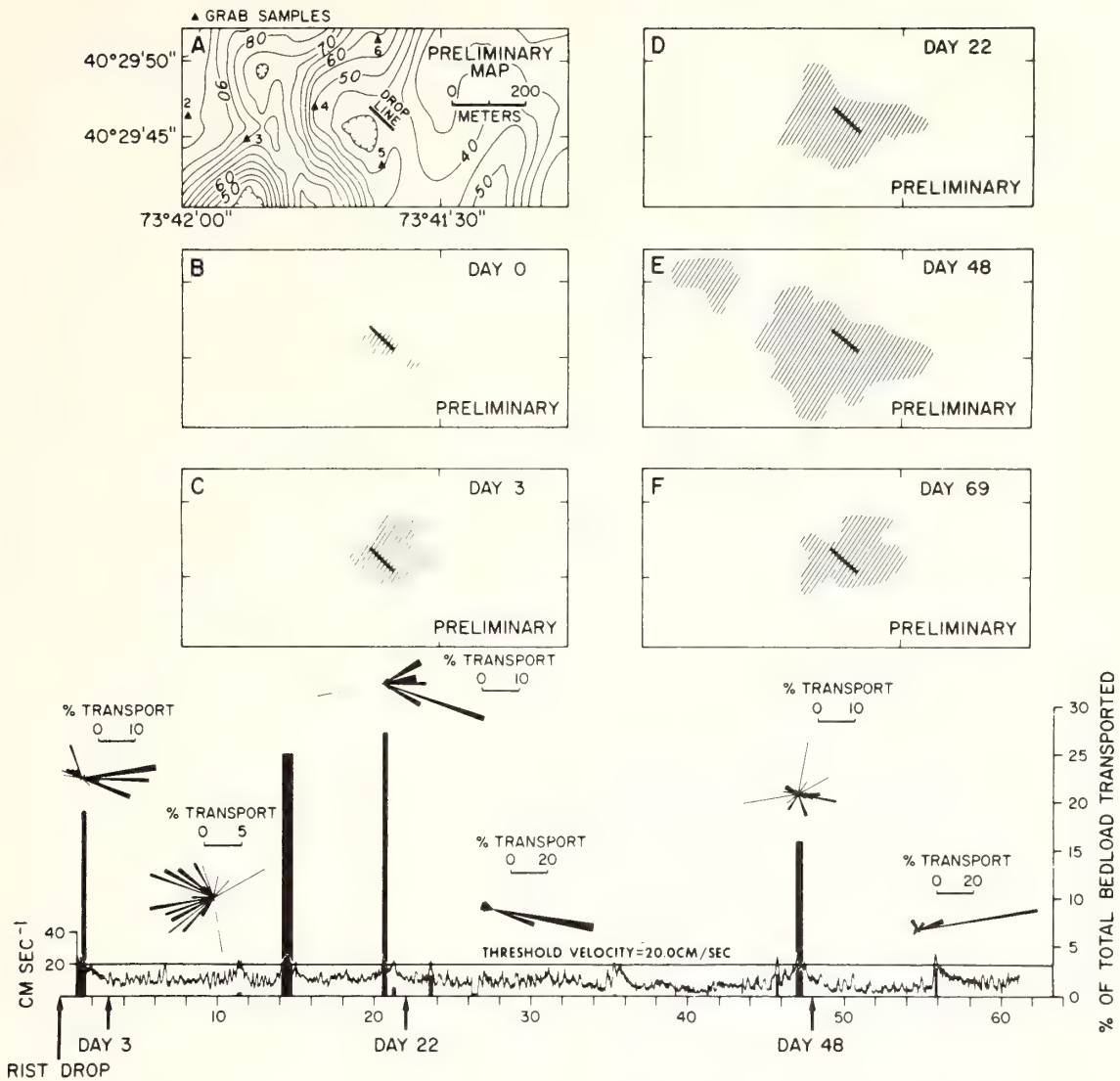


FIGURE 35. Time sequence of dispersal of radioisotope-labeled sand, south shore of Long Island, April 22–July 2, 1974. (A) Background radioactivity in arbitrary units. Heavy black line is line of emplacement of sand labeled with ruthenium-103. (B–F) Maximum extent of detectable signal after removal of background on successive mapping days. Data have been corrected for decay. Bottom panel: time-velocity record (jagged line). Height of vertical bars indicates percentage of total bed load transported, as

determined from a normalized sediment transport index,  $V_{100} - V_c$ . Width of vertical bars indicates duration of transport event. Rose diagrams indicate direction of transport. Length of radial bar indicates percentage of transport during that event; width is proportional to direction and intensity. Velocity was sampled every 10 minutes. Unpublished data of Lavelle et al., Atlantic Oceanographic and Meteorologic Laboratories, Miami, Florida.

tions as a consequence of the fashion in which the bed is built; the main subpopulation (A population) comprises the framework of the deposit. A fine B population is interstitial; a coarse C population is the consequence of “traction clogs.” The A:B:C ratio varies with the flow regime.

Bed forms are irregularities in the particulate substrate of a fluid flow. Sheared flow is innately unstable, and tends to develop repeated patterns of velocity variation, either parallel or normal to the flow direction. Such instabilities tend to interact with the bed so as to cause rhythmic variations in elevation. Flow and bed

perturbation amplify each other until equilibrium is attained.

Bed forms occur in *associations* (more than one genetic type present), in *hierarchies* (successive scales of bed forms of similar genesis), and in hierarchical associations. *Transverse bed forms* interact with wavelike perturbations of flow transverse to the flow direction. *Current ripples* are small-scale transverse bed forms that appear to result from boundary layer instability; their wavelength is independent of depth. *Sand waves* result from perturbations of the whole flow field, or a density-homogeneous portion of it. Several scales of sand waves may occur together; the smaller scale may perhaps be a response to primarily tractive transport, whereas the larger scale may be a response to primarily suspensive transport.

*Longitudinal bed forms* are caused by velocity perturbations parallel to flow. In some cases, the perturbation takes the form of horizontal, flow-parallel vortices whose sense of rotation is alternately right and left handed, and this may be true for all cases. *Parting lineations* are small-scale longitudinal bed forms. They are sand ridges a few grain diameters high and a few centimeters apart. *Current lineations* have wavelengths ranging from a few meters to hundreds of meters; their heights are negligible relative to width.

In a characteristic pattern, *sand ribbons* occur on a gravel substrate. In *longitudinal furrow* patterns, the lows are more sharply defined than the intervening highs.

*Sand ridges* may have wavelengths of hundreds of meters to several kilometers, and amplitudes of 10 m or more. They are induced by tidal flows at estuary mouths, by tidal or wind-driven flows on the shelf, and perhaps by boundary undercurrents on the continental rise. They appear to be time-averaged responses to intermittent flow, and in many cases have survived successive environmental transitions associated with the Holocene transgression.

A simple numerical model for estimating bed load transport on the continental margin requires as input current-meter measurements. Streamlines of bottom sediment transport may be based on the sediment transport index. The index is derived from Bagnold's energetics, in which sediment discharge is set proportional to fluid power, equal to bottom shear stress times the depth-averaged velocity. The sediment continuity equation is used to predict areas and relative intensities of erosion and deposition. In this equation, the discharge gradient along a streamline is related to the time rate of change of bottom height above a datum by a dimensional constant.

It may be possible to evaluate Bagnold's proportionality constant for sediment transport by means of mass balance assessments of radioisotope dispersal patterns.

However, improvements in field tracer techniques and data processing are required before such an evaluation is possible.

#### ACKNOWLEDGMENTS

We thank J. R. L. Allen and R. L. Miller for critical review of the manuscript.

#### SYMBOLS

$C_{100}$	drag coefficient determined from measurements 100 cm above the bottom
$D$	grain diameter
$h$	water depth
$K$	a constant
$k_s$	height of bottom roughness elements
$q$	sediment discharge
$t$	time
$u$	velocity
$\bar{u}$	depth-averaged velocity
$\bar{u}_\infty$	time-averaged free stream velocity
$u_{100}$	velocity 100 cm off the bottom
$u_*$	shear velocity; shear stress with velocity units
$x$	distance downstream
$y$	distance above the bed
$z$	distance transverse to flow
$z_0$	roughness length
$\epsilon$	dimensional constant related to sediment porosity
$\lambda$	wavelength
$\rho$	fluid density
$\rho_s$	sediment density
$\eta$	elevation of a surface above a datum
$\tau$	shear stress
$\tau_0$	shear stress at the bed
$\tau_c$	critical bed shear stress
$\nu$	kinematic viscosity
$\omega$	fluid power

#### REFERENCES

- Allen, J. R. L. (1964). Primary current lineation in the lower old red sandstone (Devonian) Anglo-Welsh Basin. *Sedimentology*, **3**: 89-108.
- Allen, J. R. L. (1966). On bedforms and paleocurrents. *Sedimentology*, **6**: 153-190.



- Allen, J. R. L. (1967). Depth indicators of clastic sequences. *Mar. Geol.*, **5**: 429-446.
- Allen, J. R. L. (1968a). *Current Ripples*. Amsterdam: North-Holland Publ., 433 pp.
- Allen, J. R. L. (1968b). The nature and origin of bedload hierarchies. *Sedimentology*, **10**: 161-182.
- Allen, J. R. L. (1969). Erosional current markings of weakly cohesive mud beds. *J. Sediment. Petrol.*, **34**: 607-623.
- Allen, J. R. L. (1970). *Physical Processes of Sedimentation*. New York: American Elsevier, 248 pp.
- Allen, J. R. L. (1973). Phase difference between bed and flow in natural environments and their geologic relevance. *Sedimentology*, **20**: 323-329.
- Bagnold, R. A. (1954). Experiments on a gravity-free dispersion of large solid in a Newtonian fluid under shear. *Proc. Roy. Soc. London*, **A225**: 49-63.
- Bagnold, R. A. (1956). The flow of cohesionless grains in fluids. *Proc. Roy. Soc. London*, **A249**: 235-250.
- Bagnold, R. A. (1966). An approach to the sediment transport problem from general physics. *U.S. Geol. Surv. Prof. Paper 422-1*, 37 pp.
- Belderson, K. H., N. A. Kenyon, A. H. Stride, and A. R. Stubbs (1972). *Sonographs of the Sea Floor*. Amsterdam: Elsevier, 185 pp.
- Brown, R. A. (1971). A secondary flow model for the planetary boundary layer. *J. Atmos. Sci.*, **27**: 742-757.
- Cartwright, D. E. (1959). On submarine sand waves and tidal lee waves. *Proc. Roy. Soc. London*, **A253**: 218-241.
- Caston, V. N. D. (1972). Linear sand banks in the southern North Sea. *Sedimentology*, **18**: 63-78.
- Caston, V. N. D. and A. H. Stride (1970). Tidal sand movement between some linear sand banks in the North Sea off north-east Norfolk. *Mar. Geol.*, **9**: M38-M42.
- Chandrasekhar, B. (1961). *Hydrodynamic and Hydromagnetic Stability*. New York and London: Clarendon Press, 654 pp.
- Dalrymple, R. W. (1973). Preliminary investigations of an intertidal sand body, Cobequid Bay, Bay of Fundy. *Marit. Sediments*, **4**: 21-28.
- Duane, D. B. (1970). Synoptic observations of sand movement. *Proc. 12th Coastal Eng. Conf., Washington, D.C.*, 799-813.
- Duane, D. B., M. E. Field, E. P. Meisburger, D. J. P. Swift, and S. J. Williams (1972). Linear shoals on the Atlantic inner shelf, Florida to Long Island. In D. J. P. Swift, D. B. Duane, and O. H. Pilkey, eds., *Shelf Sediment Transport: Process and Pattern*. Stroudsburg, Pa.: Dowden, Hutchinson & Ross, pp. 447-498.
- Duedall, I., H. B. O'Connors, J. B. Parker, R. Wilson, W. Miloski, and G. Hulse (in press). The seasonal and tidal variation of nutrients and chlorophyll in the New York Bight Apex. Marine Sciences Research Center, State University of New York.
- Einstein, H. A., and H. Li (1958). Secondary currents in straight channels. *Trans. Am. Geophys. Union*, **39**: 1085-1088.
- Ekman, U. W. (1905). On the influence of the earth's rotation on ocean currents. *Ark. Mat. Astron. Fysik*, **2**: 1-53.
- Emery, K. O. and E. Uchupi (1972). Western North Atlantic Ocean: topography, rocks, structure, water, life, and sediments. *Am. Assoc. Pet. Geol. Mem.*, **17**: 532.
- Exner, F. M. (1925). Über die wechselwirkung zwischen wasser und geschiebe in flüssen. *Setzungsberichte der Academie der Wissenschaften*. Vienna Heft 3-4. pp. 165-180.
- Faller, A. J. (1963). An experimental study of the instability of the laminar Ekman boundary layer. *J. Fluid Mech.*, **15**: 560-576.
- Faller, A. J. (1971). Oceanic turbulence and the Langmuir circulations. *Ann. Rev. Ecol. System.*, **2**: 201-233.
- Faller, A. J. and R. B. Kaylor (1966). A numerical study of the instability of the laminar Ekman boundary layer. *J. Atmos. Sci.*, **23**: 466-480.
- Friedman, G. M. (1961). Distinction between dune, beach, and river sands from their textural characteristics. *J. Sediment. Petrol.*, **31**: 514-529.
- Furnes, G. K. (1974). Formation of sand waves on unconsolidated sediments. *Mar. Geol.*, **16**: 145-160.
- Gessner, F. B. (1973). The origin of turbulent secondary flow along a corner. *J. Fluid Mech.*, **58**: 1-25.
- Gibson, A. H. (1909). On the depression of the filament of maximum velocity in a stream flowing through an open channel. *Proc. Roy. Soc. London*, **A82**: 149-159.
- Guy, H. P., D. B. Simons, and E. V. Richardson (1966). Summary of alluvial channel data from flume experiments 1956-1961. *U.S. Geol. Surv. Prof. Paper 462-J*, 96 pp.
- Hama, F. R. (1954). Boundary characteristics for smooth and rough surfaces. *Trans. Soc. Naval Architects and Marine Engineers*, **62**: 333-358.
- Hanna, S. R. (1969). The formation of longitudinal sand dunes by large helical eddies in the atmosphere. *J. Appl. Meteorol.*, **88**: 874-883.
- Hollister, C. D., R. D. Flood, D. A. Johnson, P. Lonsdale, and J. B. Southard (1974). Abyssal furrows and hyperbolic echo traces on the Bahama outer ridge. *Geology*, **2**: 395-400.
- Houbolt, J. J. H. C. (1968). Recent sediments in the southern bight of the North Sea. *Geol. Mijnbouw*, **47**: 245-273.
- Huthnance, J. M. (1972). Tidal current asymmetries over the Norfolk sandbanks. *Estuarine Coastal Mar. Sci.*, **1**: 89-99.
- Ingle, J. C. and D. S. Gorsline (1973). Use of fluorescent tracers in the nearshore environment. In *Tracer Techniques in Sediment Transport*. Vienna: Int. At. Energy Agency, pp. 125-148.
- Inman, D. L. (1949). Sorting of sediments in the light of fluid dynamics. *J. Sediment. Petrol.*, **19**: 51-70.
- Inman, D. L. and T. K. Chamberlain (1959). Tracing beach sand movement with irradiated quartz. *J. Geophys. Res.*, **64**: 41-47.
- Jeffreys, H. (1929). On the transverse circulation in streams. *Proc. Cambridge Phil. Soc.*, **25**: 20-25.
- Kao, A. (1975). A study of the current structure in the Sandy Hook-Rockaway Point transect. M.S. Research Paper, Marine Sciences Research Center, State University of New York, Stony Brook.
- Kennedy, J. F. (1964). The formation of sediment ripples in closed rectangular conduits and in the desert. *J. Geophys. Res.*, **69**: 1517-1524.
- Kennedy, J. F. (1969). The formation of sediment ripples, dunes and antidunes. *Ann. Rev. Fluid Mech.*, **1**: 147-168.
- Kennedy, R. J. and J. F. Fulton (1961). The effect of secondary currents upon the capacity of a straight open channel. *Trans. EIC*, **5**: 12-18.
- Kenyon, N. H. (1970). Sand ribbons of European tidal seas. *Mar. Geol.*, **9**: 25-39.

- Klein, G. D. (1970). Depositional and dispersal dynamics of intertidal sand bars. *J. Sediment. Petrol.*, **40**: 1095-1127.
- Kline, S. J. (1967). Observed structure features in turbulent and transitional boundary layers. In G. Sovran, ed., *Fluid Mechanics of Internal Flow*. Amsterdam: Elsevier, pp. 27-68.
- Kline, S. J., W. C. Reynolds, F. A. Schraub, and P. W. Runstler (1967). The structure of turbulent boundary layers. *J. Fluid Mech.*, **30**: 741-773.
- Krumbein, W. C. (1934). Size-frequency distributions of sediments. *J. Sediment. Petrol.*, **4**: 65-77.
- Langhorne, D. N. (1973). A sandwave field in the outer Thames estuary. *Mar. Geol.*, **14**: 129-143.
- Langmuir, I. (1925). Surface motion of water induced by the wind. *Science*, **87**: 119-123.
- Leopold, L. B., M. G. Wolman, and J. P. Miller (1964). *Fluvial Processes in Geomorphology*. San Francisco: Freeman, 522 pp.
- Lilly, D. K. (1966). On the instability of Ekman boundary flow. *J. Atmos. Sci.*, **23**: 481-494.
- Lin, C. C. (1955). *The Theory of Hydrodynamic Stability*. London and New York: Cambridge University Press, 155 pp.
- Lonsdale, P. and B. Malfait (1974). Abyssal dunes of foraminiferal sand on the Carnegie Ridge. *Geol. Soc. Am. Bull.*, **85**: 1697-1712.
- Ludwick, J. C. (1970a). Sand waves in the tidal entrance to Chesapeake Bay: Preliminary observations. *Chesapeake Sci.*, **11**: 98-110.
- Ludwick, J. C. (1970b). *Sandwaves and Tidal Channels in the Entrance to Chesapeake Bay*. Technical Report 1, Inst. of Oceanography, Old Dominion University, Norfolk, Va., 7 pp.
- Ludwick, J. C. (1972). Migration of tidal sandwaves in Chesapeake Bay entrance. In D. J. P. Swift, D. B. Duane, and O. H. Pilkey, eds., *Shelf Sediment Transport: Process and Pattern*. Stroudsburg, Pa.: Dowden, Hutchinson & Ross, pp. 377-410.
- Ludwick, J. C. (1973). *Tidal Currents and Zig-Zag Sand Shoals in a Wide Estuary Entrance*. Technical Report 7, Inst. of Oceanography, Old Dominion University, Norfolk, Va., 23 pp.
- Ludwick, J. C. (in press). Tidal currents, sediment transport, and sand banks in Chesapeake Bay entrance, Virginia. In M. O. Hayes, ed., *Second International Estuarine Conf. Proc. Myrtle Beach, South Carolina, Oct. 15-18, 1973*.
- McCave, I. N. (1971). Sandwaves in the North Sea off the coast of Holland. *Mar. Geol.*, **16**: 199-225.
- McKinney, T. F. and G. M. Friedman (1970). Continental shelf sediments of Long Island, New York. *J. Sediment. Petrol.*, **40**: 213-248.
- McKinney, T. F., W. L. Stubblefield, and D. J. P. Swift (1974). Large scale current lineations on the central New Jersey shelf: Investigations by sidescan sonar. *Mar. Geol.*, **17**: 79-102.
- Middleton, G. V. (1968). The generation of log normal size frequency distributions in sediments. In *Problems of Mathematical Geology*. Leningrad: Science Press, pp. 37-46.
- Moss, A. J. (1962). The physical nature of common sandy and pebbly deposits (Part I). *Am. J. Sci.*, **260**: 337-373.
- Moss, A. J. (1963). The physical nature of common sandy and pebbly deposits (Part II). *Am. J. Sci.*, **261**: 297-343.
- Moss, A. J. (1972). Bedload sediments. *Sedimentology*, **18**: 159-219.
- Newton, R. S., E. Seibold, and F. Werner (1973). Facies distribution patterns on the Spanish Sahara continental shelf mapped with sidescan sonar. *Meteor. Forsch. Ergebnisse*, **15**: 55-77.
- Oertel, G. F. (1972). Sediment transport of estuary entrance shoals and the formation of swash platforms. *J. Sediment. Petrol.*, **42**: 857-863.
- Off, T. (1963). Rhythmic linear sand bodies caused by tidal currents. *Am. Assoc. Pet. Geol. Bull.*, **47**: 324-341.
- Postma, H. (1967). Sediment transport and sedimentation in the marine environment. In G. H. Lauff, ed., *Estuaries*. Washington, D.C.: Am. Assoc. Adv. Sci., pp. 158-180.
- Raudkivi, A. J. (1967). *Loose Boundary Hydrodynamics*. Oxford: Pergamon, 331 pp.
- Robinson, A. H. W. (1966). Residual currents in relation to shoreline evolution of the East Anglian coast. *Mar. Geol.*, **4**: 57-84.
- Rosenhead, L. (1963). *Laminar Boundary Layers*. London and New York: Oxford University Press (Clarendon), 687 pp.
- Russell, R. D. (1939). Effects of transportation on sedimentary particles. In P. P. Trask, ed., *Recent Marine Sediments*. London: Thomas Murphy, pp. 32-47.
- Schlichting, H. (1962). *Boundary Layer Theory*. New York: McGraw-Hill, 647 pp.
- Simons, D. B. and E. V. Richardson (1963). Forms of bed roughness in alluvial channels. *ASCE Trans.*, **128**: 284-302.
- Simons, D. B., E. V. Richardson, and M. L. Albertson (1961). Flume studies using medium sand (0.45 mm). *U.S. Geol. Surv. Water Supply Pap.* 1498A, 76 pp.
- Smith, J. D. (1969). Geomorphology of a sand ridge. *J. Geol.*, **77**: 39-55.
- Smith, J. D. (1970). Stability of a sand bed subjected to a shear flow of low Froude number. *J. Geophys. Res.*, **30**: 5928-5940.
- Sorby, H. C. (1859). On the structures produced by the current present during the deposition of stratified rocks. *Geologist*, **2**: 137-147.
- Southard, J. B. (1971). Representation of bed configurations in depth-velocity-size diagram. *J. Sediment. Petrol.*, **41**: 903-915.
- Southard, J. B. and L. A. Boguchwal (1973). Flume experiments on the transition from ripples to lower flat bed with increasing grain size. *J. Sediment. Petrol.*, **43**: 1114-1121.
- Southard, J. B. and J. R. Dingler (1971). Flume study of ripple propagation behind mounds on flat sand beds. *Sedimentology*, **16**: 257-263.
- Stride, A. H. (1970). Shape and size trends for sand waves in a depositional zone of the North Sea. *Geol. Mag.*, **469**-477.
- Stride, A. H. (1973). Interchange of sand between coast and shelf in European tidal seas (abstract). In *Abstracts Symposium on Estuarine and Shelf Sedimentation, Bordeaux, France, July 1972*, p. 97.
- Stride, A. H. (1974). Indication of long term tidal control of net sand loss or gain by European coasts. *Estuarine Coastal Mar. Sci.*, **2**: 27-36.
- Stride, A. H., R. H. Belderson, and N. H. Kenyon (1972). *Longitudinal Furrows and Depositional Sand Bodies of the English Channel*. Mémoire Bureau Recherches Géologique et Minières, No. 79, pp. 233-244.
- Stubblefield, W. L., J. W. Lavelle, T. F. McKinney, and D. J. P. Swift (1975). Sediment response to the present hydraulic regime on the central New Jersey shelf. *J. Sediment. Petrol.*, **15**: 227-247.

- Swift, D. J. P. (1975). Tidal sand ridges and shoal retreat masses. *Mar. Geol.*, **18**: 105-133.
- Swift, D. J. P., D. B. Duane, and T. F. McKinney (1974). Ridge and swale topography of the Middle Atlantic Bight, North America: Secular response to the Holocene hydraulic regime. *Mar. Geol.*
- Swift, D. J. P., B. Holliday, N. Avignone, and G. Shideler (1972a). Anatomy of a shoreface ridge system, False Cape, Virginia. *Mar. Geol.*, **12**: 59-84.
- Swift, D. J. P., J. C. Ludwick, and W. R. Boehmer (1972b). Shelf sediment transport: A probability model. In D. J. P. Swift, D. B. Duane, and O. H. Pilkey, eds., *Shelf Sediment Transport: Process and Pattern*. Stroudsburg, Pa.: Dowden, Hutchinson & Ross, pp. 195-223.
- Swift, D. J. P. and R. M. McMullen (1968). Preliminary studies of intertidal sand bodies in the Minas Basin, Bay of Fundy, Nova Scotia. *Can. J. Earth Sci.*, **5**: 175-183.
- Van Veen, J. (1936). *Underzoekingen in der Hookden*. The Hague: Algemene Landsdrukkerij, 252 pp.
- Visher, G. S. (1969). Grain size distribution and depositional processes. *J. Sediment. Petrol.*, **39**: 1074-1106.
- Weil, C. B., R. D. Moose, and R. E. Sheridan (in press). A model for the evolution of linear tidal built sand ridges in Delaware Bay, U.S.A. In G. Allen and A. Klingbiel, eds., *Symposium International: Relations Sédimentaires entre estuaires et plateaux continentaux*, University of Bordeaux, July 9-14, 1973.
- Wilson, I. G. (1972). Aeolian bedforms—their development and origins. *Sedimentology*, **19**: 173-210.
- Wilson, I. G. (1973). Equilibrium cross-section of braided and meandering rivers. *Nature*, **241**: 393-394.
- Yih, C. S. (1965). *Dynamics of Non-homogeneous Fluids*. New York: MacMillan, 235 pp.
- Znamenskaya, N. S. (1965). The use of the laws of sediment dune formation in computing channel formation. *Soviet Hydrology Selected Papers (Am. Geophys. Union 1966)*, **5**: 415-432.

Section 3

## Geological processes

### Morphologic evolution and coastal sand transport, New York–New Jersey shelf<sup>1</sup>

*Donald J. P. Swift, George L. Freeland, Peter E. Gadd, Gregory Han,  
J. William Lavelle, and William L. Stubblefield*

Atlantic Oceanographic and Meteorological Laboratories, NOAA, Virginia Key, Miami, Florida

*Abstract*

The surface of the New York–New Jersey shelf has been extensively modified by landward passage of nearshore sedimentary environments during the postglacial rise of sea level. The retreat of estuary mouths across the shelf surface has resulted in shelf valley complexes. Constituent elements include shelf valleys largely molded by estuary mouth scour, shoal retreat massifs left by the retreat of estuary mouth shoals, and midshelf or shelf-edge deltas.

The erosional retreat of the straight coast between estuary mouths has left a discontinuous sheet of clean sand 0–10 m thick. During the retreat process, a sequence of oblique-trending, shoreface-connected sand ridges formed at the foot of the shoreface. As a consequence, the surficial sand sheet of the shelf floor bears a ridge and swale topography of sand ridges up to 10 m high and 2–4 m apart.

The mechanics of sedimentation in these two nearshore environments (estuary mouth and interestuarine coast) are now being investigated for purposes of environmental management as well as for further understanding of shelf history. In late fall and winter 1974, current meters were deployed on the Long Island coast and a radioisotope tracer dispersal pattern was traced over an 11-week period. Eastward or westward pulses of water were generated during this period of successive weather systems. Flows in excess of the computed threshold velocity of substrate materials were sustained for hours or days and were separated by days and weeks of subthreshold velocities, and the sand tracer pattern expanded accordingly. A single intense westward flow transported more sand than all the other events combined. The storm was anomalous with respect to the short term observation period, but it may in fact have been representative of the type of peak flow event that shapes the inner shelf surface.

Systematic observations of sedimentation in New York Harbor mouth have not yet been initiated. However, reconnaissance data reveal a complex pattern of ebb- and flood-dominated zones that control the pattern of sand storage.

We review in this paper our knowledge of the surface of the continental shelf off New York and New Jersey by considering two distinct topics: the geological history of this surface and the nature of sand transport across it. Our knowledge of the New York–

New Jersey shelf surface is primarily the result of a decade of work by K. O. Emery and his colleagues at the Woods Hole Oceanographic Institution. A summary of this information and much more has recently been provided by Emery and Uchupi (1972). As the work of the Woods Hole group drew to a close, we attempted to consider in greater detail some aspects of the morphologic evolution of the Middle At-

<sup>1</sup> Contribution of the New York Bight Project of the NOAA Marine EcoSystems Analysis (MESA) Program.

lantic Bight surface (Swift et al. 1972, 1974; Swift 1973; Swift and Sears 1974; Stubblefield et al. 1974). A summary of this work constitutes the first section of this paper.

As participants in NOAA's MESA (Marine EcoSystems Analysis) program, we have been asked not only to evaluate the geological history of the New York Bight, but also to provide quantitative estimates of sediment transport that will be of direct use to environmental managers. It turns out that these two goals are closely related. Our surveys of the shelf surface have led us to infer that it has been shaped by the landward retreat of two basic sedimentary regimes during the Holocene transgression: tide-dominated sedimentation at estuary mouths, and the sand transport pattern of the adjacent shoreface and adjacent inner shelf. Environmental engineers and managers must deal with these same regimes.

To satisfy their needs, we have initiated real-time studies of fluid motion and substrate response. State-of-the-art techniques for such studies are inadequate and progress has been slow. We report in the second portion of this paper fragments of our studies

of sand transport to encourage colleagues engaged in similar studies. Our own initial experiments have raised more questions than they have answered.

#### *Evolution of the continental shelf surface*

*Evolution of shelf valley complexes*—The New York Bight is a pentagonal sector of the North American Atlantic shelf, extending 800 km from Cape May, New Jersey, to Montauk Point, Long Island. Off New York, the shelf is 180 km wide (Fig. 1).

The sandy shelf floor is divided into compartments by shelf valley complexes extending from the shoreline toward shelf edge canyons (Fig. 1). The most obvious elements of these complexes are the shelf valleys themselves which may appear as narrow, well defined channels (Delaware Shelf Valley; Hudson Shelf Valley) or as broad, shallow depressions which barely perturb the isobaths defining the shelf surface (Block Shelf Valley, Long Island Shelf Valley, North New Jersey Shelf Valley, Great Egg Shelf Valley). Shelf valley complexes generally contain other morphologic elements. The north rims of the shelf valleys

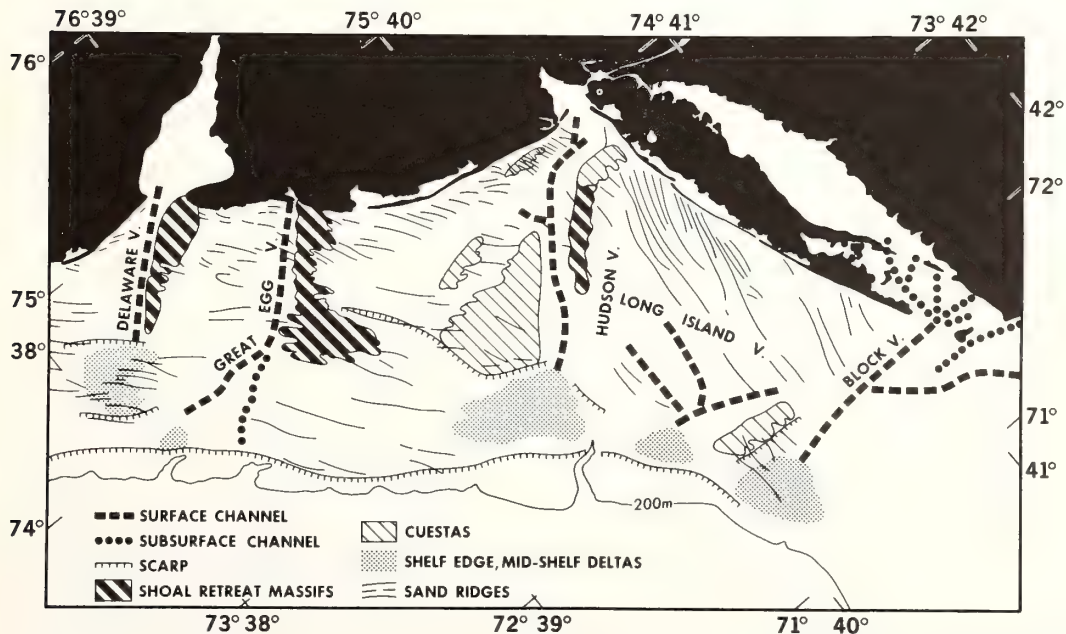


Fig. 1. Morphologic framework of the New York–New Jersey shelf. (Modified from Swift et al. 1972.)

tend to be elevated like levees above the adjacent shelf. Seaward ends of shelf valleys often terminate in delta terraces. Shelf valley complexes tend to be broken into segments by coast-parallel scarps, which may have been formed by temporary stillstands of the returning Holocene sea.

The origin of the shelf valley complexes is best inferred from the configuration of the Delaware Shelf Valley (Fig. 2), which can be traced without interruption into its modern estuary. The Delaware estuary mouth has a sill of sand nourished by littoral drift from the New Jersey coast (Swift 1973). The sill is stabilized by an interdigitating system of ebb- and flood-dominated channels, whose discharge inequalities are a consequence of the phase lag of the tidal wave in its passage across the sill (Swift and Ludwick in press). The Delaware Shelf Valley may be traced directly into the flood channel of the main ebb channel–flood channel couplet. Its leveelike north rim may be traced directly into the complex of smaller ebb channels, flood channels, and sand banks on the north side of the estuary mouth. This shoal area serves as the depositional center for the littoral sand discharge of the New Jersey coast.

The shelf valley complex, then, is not a drowned river valley, but is rather the track left by the retreat of the Delaware estuary mouth across the shelf during the Holocene sea-level rise. The shelf valley is the retreat path of a flood channel. The north flank levee is the retreat path of the estuary mouth shoal or is a shoal retreat massif—massif in the sense of a compound topographic high consisting of smaller scale highs (Swift 1973). The surface channel does not directly overlie the buried river-cut channel but is offset to the south (Sheridan et al. 1974). As the estuary retreated up the river valley, it not only tended to fill the river valley but in the final, estuary-mouth stage decoupled from it altogether by migrating to the south.

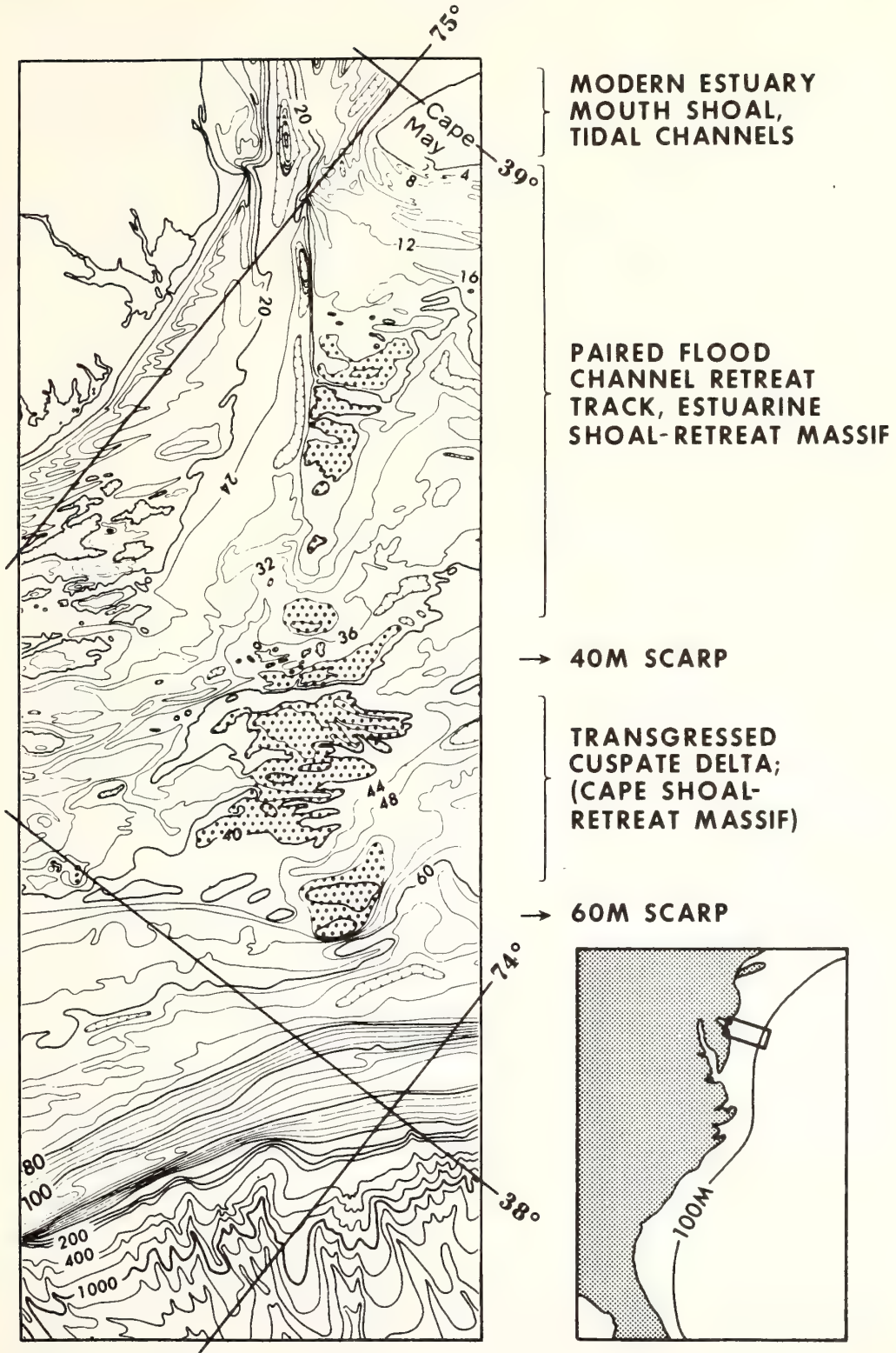
The largely constructional nature of the Delaware Shelf Valley complex is also characteristic of the Great Egg Shelf Valley complex (Fig. 1), although the associated massif has been heavily dissected by the

posttransgressional regime of southerly storm flows. To the north, however, the Hudson and Block Shelf Valleys occur on a terrain of innately greater relief. There are cuestaslike highs, and the estuarine deposits only partly fill the shelf valleys. The deeply incised nature of the Hudson Shelf Valley may reflect the era when it received Great Lakes meltwater (Veatch and Smith 1939).

*Evolution of interfluves*—Plateaulike interfluves between the shelf valleys have likewise been intensively modified by passage of the shoreline. Interfluve surfaces range from exceedingly flat plains (slopes of 1:2,000) to irregularly undulating sand ridge topography (Fig. 3). Sand ridges exhibit up to 10 m of relief, are spaced 2 to 4 km apart, and their crestlines may be traced for tens of kilometers. Side slopes are generally less than a degree. Crestlines are not quite parallel to the regional trend of the isobaths but tend to converge to the southwest with the shoreline (Fig. 1). Ridges attain their maximum development on the northeast sides of shoal retreat massifs.

The ridges are molded into a surficial sheet of relatively homogeneous, well sorted sand, 0–10 m thick. In trough axes the sheet thins to a basal shelly, gravelly sand several decimeters or less thick, and a more heterogeneous older substrate is locally exposed (Donahue et al. 1966; Stubblefield et al. 1974). This is commonly a muddy sand or mud deposited behind the retreating Holocene barrier system (Stahl et al. 1974; Sheridan et al. 1974), but it is locally absent due to erosion or nondeposition, so that the Holocene sands rest directly on older Pleistocene sands.

To understand the genesis of this postglacial stratigraphy, it is necessary to consider the dynamics of a transgressing shoreline. We are indebted in this regard to Bruun (1962) and Fischer (1961) who appear to have independently appreciated the role of the landward translation of the wave- and current-maintained coastal profile in generating transgressive stratigraphy. In the New York Bight, as along most low, unconsolidated coasts, the coastal profile consists of a steeply sloping nearshore sector (the shoreface) and a gently dipping in-



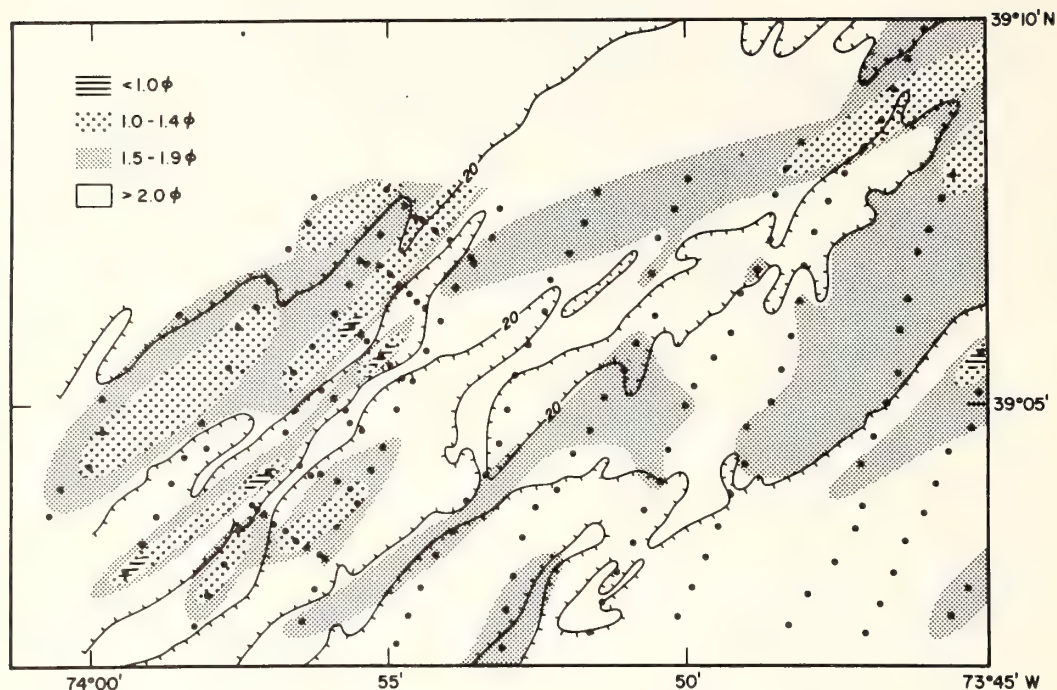


Fig. 3. Simplified bathymetry and distribution of grain sizes on a portion of the central New Jersey shelf. Medium to fine sand occurs on ridge crests. Fine to very fine sand occurs on ridge flanks and in troughs. Locally, erosion in troughs has exposed a thin lag of coarse, shelly, pebbly sand over lagoonal clay. (Reprinted from Stubblefield et al. 1974 by permission of the *Journal of Sedimentary Petrology*.)

ner shelf floor. The break in slope, which may be well defined or gently rounded, generally occurs at depths of 12 to 18 m, some few kilometers from the shoreline.

Bruun (1962) pointed out that if this profile is in fact an equilibrium response of the seafloor to the coastal hydraulic climate, then a rise in sea level must result in a landward and upward translation of the profile (Fig. 4A). Such a translation necessitates erosion of the shoreface. Much of the resulting debris will presumably be entrained in the littoral current and move downcoast, but during periods of onshore storm winds, the littoral drift may leak sea-

ward, due to an offshore component of bottom flow, to be deposited beneath the rising seaward limb of the equilibrium profile on the adjacent inner shelf floor.

Evidence for such seaward bottom transport is varied. Murray (1975) described periods of offshore bottom flow on the gulf coast, when winds are onshore and the water column is not stratified. Sonu and Van Beek (1971) noted that sand loss from North Carolina beaches correlates poorly with periods of high waves but correlates well with high waves generated by onshore northeast winds. On the Long Island inner shelf, we used sidescan sonar to map inner

←

Fig. 2. Delaware Shelf Valley complex. Southward littoral drift along the New Jersey coast is injected into the reversing tidal stream of Delaware Bay mouth. The resulting sand shoal is stabilized as a system of interdigitating ebb- and flood-dominated channels. The shelf valley complex seaward of the bay mouth was formed by the retreat of the coastal sedimentary regime through Holocene time. Retreat of the main flood channel has excavated the Delaware Shelf Valley; retreat of the bay mouth shoal has left a levee-like high on the shelf valley's north flank. (Reprinted from Swift 1973 by permission of the *Geological Society of America Bulletin*.)



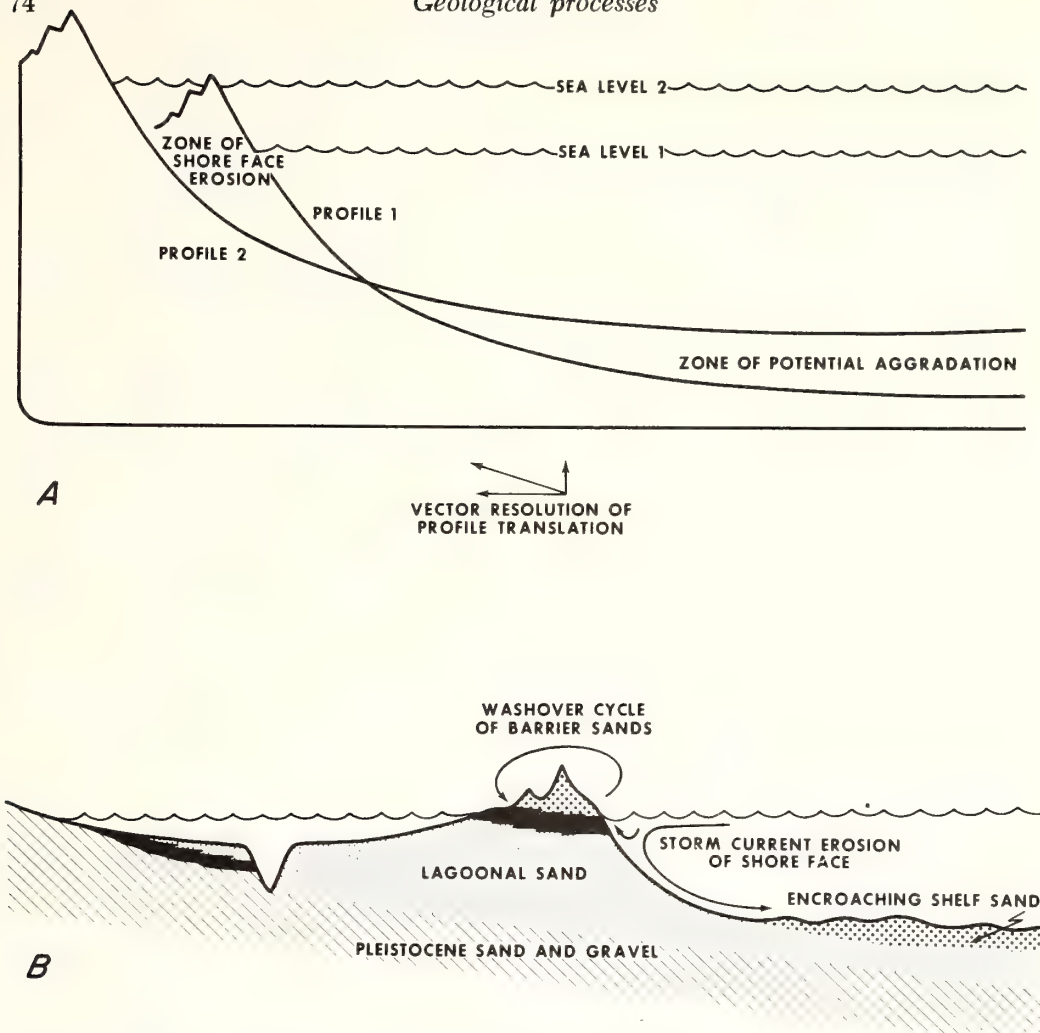


Fig. 4. Models for a coast undergoing erosional shoreface retreat during a rise in sea level. A—Rise in sea level results in landward and upward translation of coastal profile (Bruun 1962). B—Translation is accomplished. Wind and storm washover transport on the barrier surface and erosion of the shoreface and seaward transport of the resulting debris (Fischer 1961).

shelf current lineations that form an eastward-opening angle with the beach (Fig. 5). A poorly defined asymmetry is apparent: the western sides of the lineations are gradational, whereas the eastern sides are sharply defined. The origin of this pattern is not clear. The dark bands are strips of coarse or gravelly sand that may either be troughs between low amplitude, current-transverse sand waves or troughs between current-parallel sand ribbons. However, considering the angle that the lineations make with the beach, sand ribbons seem unlikely for reasons of flow continuity. If

sand waves, the lineations are responses to strong bottom flows trending westerly and offshore.

Fischer (1961), Stahl et al. (1974), and Sanders and Kumar (1975) described the stratigraphic consequences of erosional shoreface retreat, based on their observations of the New Jersey and New York coasts. The barrier superstructure will retreat over the lagoonal deposits by a cyclic process of storm washover, burial, and re-emergence at the shoreface (Fig. 4B). Lower shoreface sands will tend to be transported seaward to accumulate over the

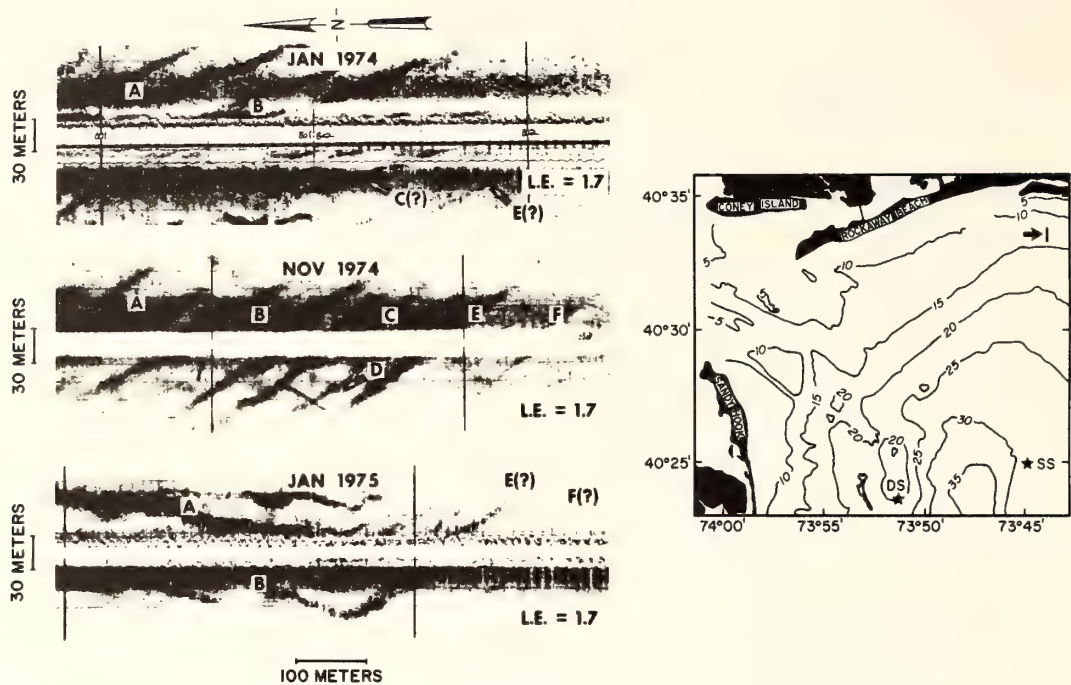


Fig. 5. Sidescan sonar records of current lineations on the Long Island coast, collected at three different periods. Positioning by Raydist. Current lineation pattern (bands A–F) expands to south during observation period. Apparent change in orientation in last panel is due to ship maneuvering. (From Stubblefield et al. in prep.)

eroded surface of the lagoonal deposits as the leading edge of a marine sand sheet. Bruun's hypothesis is compatible with the stratigraphic evidence and with our limited knowledge of coastal hydraulics. A more rigorous test requires bathymetric time series to document changes in the coastal profile. Limited data of this sort are becoming available. Harris (1954) undertook a study of the Long Branch, New Jersey, dredge spoil dumpsite to determine if dumping was nourishing the beach (Fig. 6). In fact, during a 4-year period, the shoreface underwent between 5 and 26 cm of erosion, while an irregular pattern of deposition prevailed on the inner shelf floor. A somewhat longer time series has been prepared by Kim and Gardner (Woodward-Clyde Assoc.) during study of proposed sewage outfall routes for the Ocean County, New Jersey, sewerage authority (Fig. 7). Two out of three profiles taken indicate 1.5–2.0 m of erosion over 20 years. The third profile is immediately south of a shoreface-connected sand ridge; here

comparable aggradation has occurred as a consequence of southward ridge migration.

*Growth of ridges*—Erosional shoreface retreat on the Atlantic cannot be adequately described by a two-dimensional model such as Fig. 4 because the shoreface appears to be the formative zone for sand ridge topography as well as for the sand sheet into which it is impressed. Clusters of shoreface-sand ridges occur on the New Jersey coast between Brigantine and Barnegat Inlets, on the north New Jersey coast between Manasquan and Sea Bright, and on the Long Island coast from Long Beach to the shoreface of eastern Fire Island.

The shoreface-connected ridges are named for their oblique, fingerlike extensions of the shoreface, causing seaward deflections of isobaths as shoal as 5 m. The ridges tend to be asymmetric in cross-section, with steep seaward flanks, although this relationship may be reversed at the base of the ridge where it joins the shoreface. Seaward flanks tend to be notably

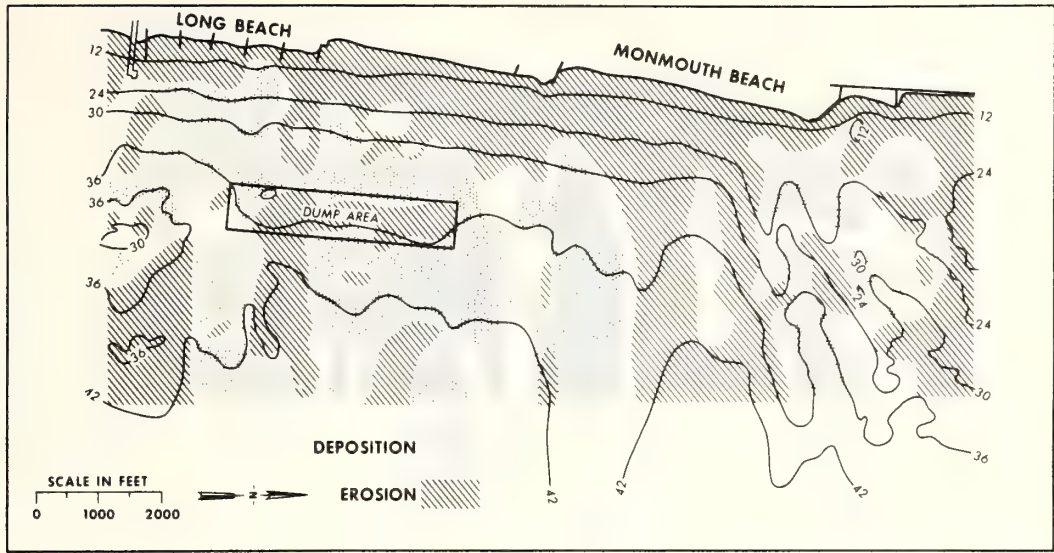


Fig. 6. Erosion and deposition near Long Branch, New Jersey, dredge spoil dumpsite during a 4-yr period. Recorded changes are 0.4–1.4 ft. Shoreface has undergone erosion; adjacent seafloor primarily has undergone aggradation. (From Harris 1954.)

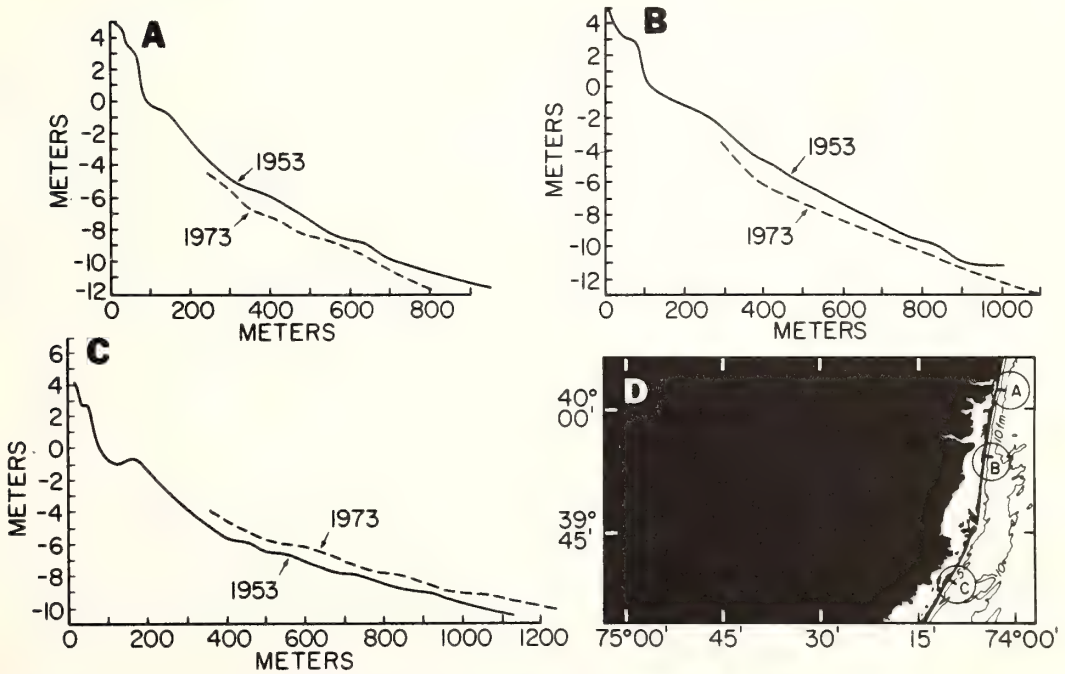


Fig. 7. Profiles of proposed sewage outfall sites on the New Jersey coast. Sites A and B have eroded over a 20-yr period. Site C, immediately downcoast of a shoreface-connected sand ridge, has aggraded. (Reprinted from Kim and Gardner 1974 with permission of Woodward-Clyde Assoc.)

finer than landward flanks. Off Brigantine Inlet and off the New Jersey coast, shore-face-connected ridges are associated with free-standing inner shelf ridges that can be traced seaward for tens of kilometers in apparent genetic sequence. The ridges form on the shoreface in response to south-trending coastal storm currents (Duane et al. 1972) and become detached from the shoreface as it retreats. They tend to migrate downcoast (to the south or west) and offshore, extending their crestlines so as to maintain contact with the shoreline (Fig. 8). Eventually, however, contact is broken, and they are stranded on the deepening shelf floor. Downcoast ridge migration is part of a general pattern of southwesterly sand transport on the Atlantic shelf. In the offshore ridge topography, this pattern is indicated by the tendency of both ridge crests and trough talwegs to rise toward the southwest. Locally, it is indicated by patterns of erosion and deposition near wrecks (Fig. 9).

*Sand transport on the inner shelf*

The preceding description of the morphologic evolution of the New York shelf surface is based primarily on the interpretation of bathymetric maps, aided by local substrate inventories in which the bottom is

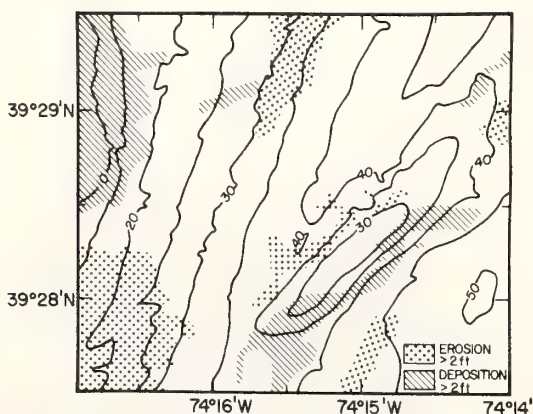


Fig. 8. Patterns of erosion and deposition on Beach Haven Ridge, New Jersey, between 1935 and 1954, superimposed on 1954 bathymetry. Pattern of north flank erosion and south flank deposition indicates downcoast migration of ridge. (From DeAlteris et al. in press.)

examined by grab sampling, photography, Vibracoring, and seismic profiling. The conclusions are qualitative but nonetheless valid. However, fuller understanding of the behavior of the shelf surface requires a different approach.

We must directly measure fluid and sediment transports involved in the two basic mechanisms that have shaped the shelf surface: tidal flow and sand storage at estuary mouths, and erosional retreat of the shoreface between estuary mouths. Environmental managers who must make decisions about dredged channels, sewage outfalls, sewage and dredge spoil dumpsites, deep-water tanker terminals, and offshore power plants need to understand these processes before they can evaluate the stability of the inner shelf surface.

The nature of coastal sand transport during storms is the first major problem we will consider. Fluid motions in the surf zone have been studied for decades, and the role of longshore currents driven by shoaling and breaking waves has been described (e.g. Bowen 1969). In the New York area,

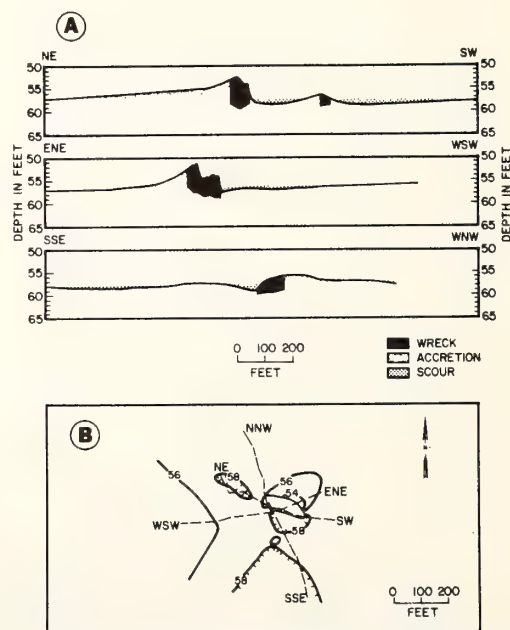


Fig. 9. Accretion and scour by a wreck near Beach Haven Ridge, New Jersey. (From DeAlteris et al. in press.)

massive discharges of sand in the surf zones of the Long Island and New Jersey coasts move toward the New York harbor mouth; these discharges have built Sandy Hook and Rockaway spits within subhistoric to historic times. However, we know almost nothing about fluid motions over the adjacent inner shelf, although the geologic data presented above show that currents seaward of the surf play a major role in the coastal sand budget. We must specifically ask what time and space scales of inner shelf flows are intense enough to entrain sand? Is their velocity field so structured that there are periods of significant offshore bottom flow and sand transport?

Equally important is the problem of the inner shelf sand ridges, which seem to occur wherever a sewage outfall or power plant is to be located. If we wish to predict the probable behavior of these features through the design life of the structure, we must understand their genesis and how they are maintained by flow. It is a truism of loose boundary hydraulics that sheared boundary flows are innately unstable, and that these instabilities tend to interact with the substrate to generate sand ripples, sand ribbons, sand waves, and sand dunes. The circumstantial evidence that inner shelf sand ridges are similarly responses to flow is strong. How are they formed and maintained?

As a first attempt to investigate these questions, Lavelle et al. (in press) placed 40 Aandaraa current meters at 19 stations over the Tobay Beach sand ridges of the Long Island inner shelf (Figs. 10 and 11). The meters were in place for 6 weeks during late November and December 1974; a single meter recorded for an additional 5 weeks. All meters averaged speed over 10 min and took an instantaneous direction reading during each sampling period.

During the observation period, a series of moderate storms induced easterly and westerly flows parallel to the coast. A final storm on 1-4 December was very intense, causing more beach erosion than any storm since the Ash Wednesday storm of 1962 (C. Galvin personal communication).

In Fig. 12, vector averages for all near-bottom, middepth, and near-surface meters

are presented for periods of both westward and eastward flows. A wind-controlled pattern of coastal flow emerges. There is a top to bottom speed shear as well as a directional shear. Prevailing fall and winter winds blow out of the northwest, across the east-west Long Island shoreline; the result is a tendency toward coastal upwelling. Surface flows have an offshore component for both eastward and westward flow directions. The response is less symmetrical at depth; westward bottom flows parallel the isobaths, whereas eastward bottom flows have an onshore component. Net water transport during the observation period was eastward.

During the early December storm there was a small offshore component to the water flow near the bottom. Figure 13 shows the winds during the storm and the associated current velocities from a near-bottom current meter, which have been filtered with a 40-h and a 3-h low-pass filter. The 40-h low-pass filtered record, which is a segment

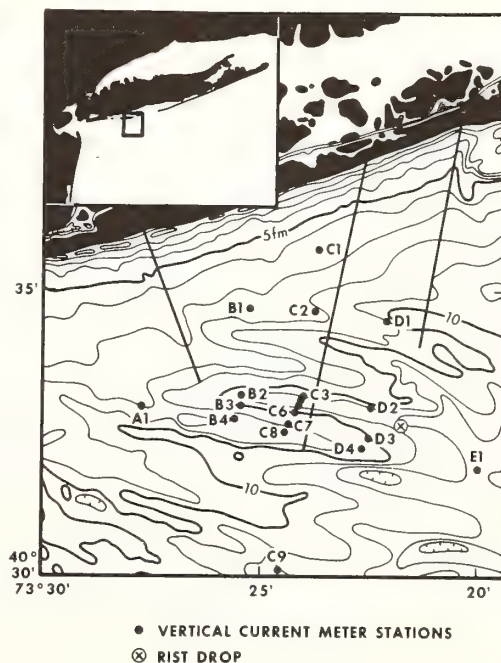


Fig. 10. Bathymetry, current meter stations, and tracer release point (RIST drop) for the Long Island nearshore (LINS) experiment. (From Lavelle et al. in press.)

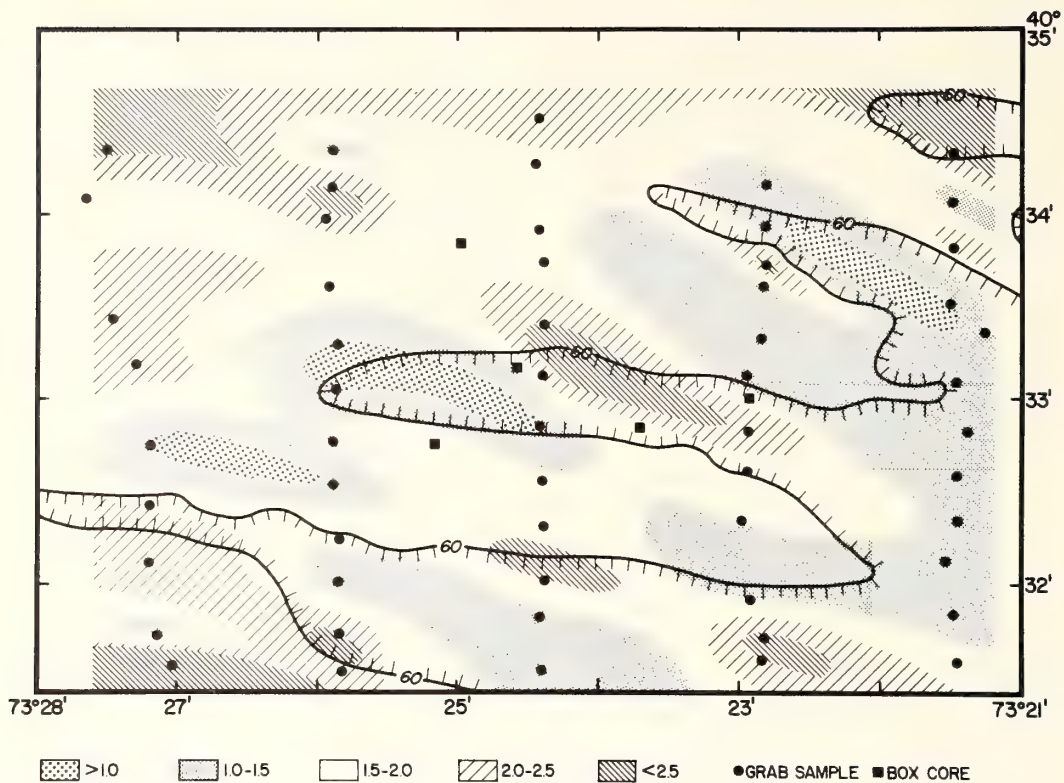


Fig. 11. Distribution of grain sizes over the Tobay Beach ridges, LINS area. Size classes in phi units.

taken from Fig. 12, obscures the brief time-scale flow associated with the storm. The 3-h low-pass record, which is only slightly smoothed and still contains the tidal signal, shows a period of offshore flow more clearly. These results must be viewed cautiously. The Aandaraa current meters which were used have large direction and speed errors when used in shallow water with surface wave amplitudes as large as were present during the event described here.

During the November–December experiment on the Long Island inner shelf, estimates of sand transport were made from calculations from current meter records (Lavelle et al. in press) and also from radioisotope tracer dispersal patterns (Lavelle et al. unpublished data). To generate the patterns, about 500 cm<sup>3</sup> of indigenous fine to very fine sand was surface-coated with 10 Ci of <sup>103</sup>Ru (half-life, 39.6 d). On 12 November, equal portions of tagged sand were released in water soluble bags at three

points at the east end of the main trough (Fig. 14). The injection points formed an equilateral triangle with sides roughly 100 m long. The developing dispersal pattern of labeled sand was surveyed at intervals by scintillation detectors mounted in a cylinder towed across the bottom. Navigation was by a Raydist system with 10-m resolution. Four postinjection surveys were made during the 11-week tracer experiment. Dispersal patterns mapped 2 and 8 weeks after injection are shown in Fig. 14. After 2 weeks (25 November) roughly ellipsoidal smears trended east from each of the three injection points (Fig. 14A). Each smear could be traced for about 200 m before the signal was lost in the background radiation. After 8 weeks (10 January) the three eastward smears had been replaced by a single, more extensive pattern extending 700 m to the west (Fig. 14B). Partially processed data from an intermediate survey (17–19 December) indicate that the reversal in fact had

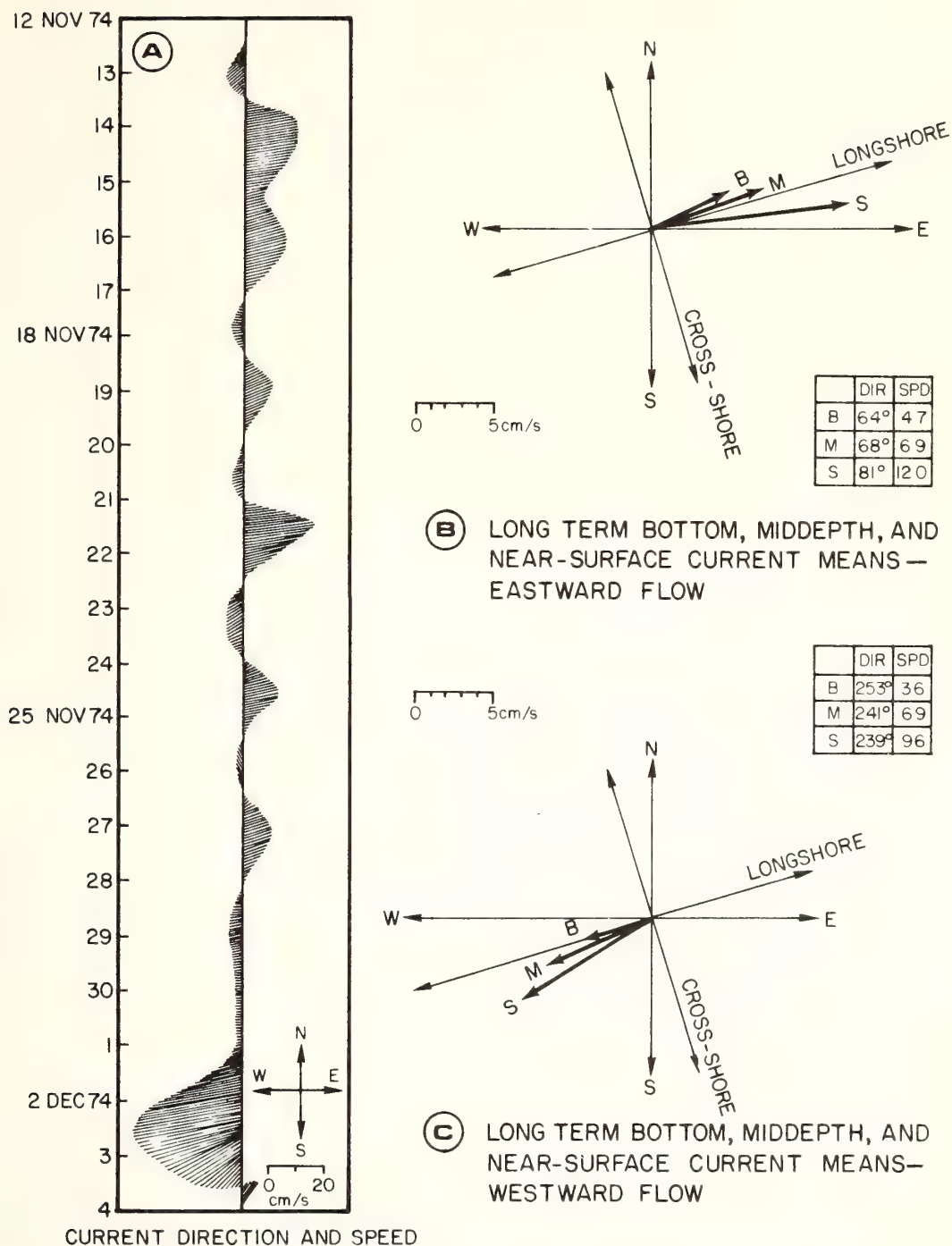


Fig. 12. Summary of flow data for the LINS experiment. A—Vector time series of representative near-bottom flow. Data have been subjected to a 40-h low-pass filter. B, C—Long term velocity averages of eastward and westward flow for meters grouped by depth in water column. Bottom, middepth, and near-surface groupings are labeled B, M, and S. (From Lavelle et al. in press.)

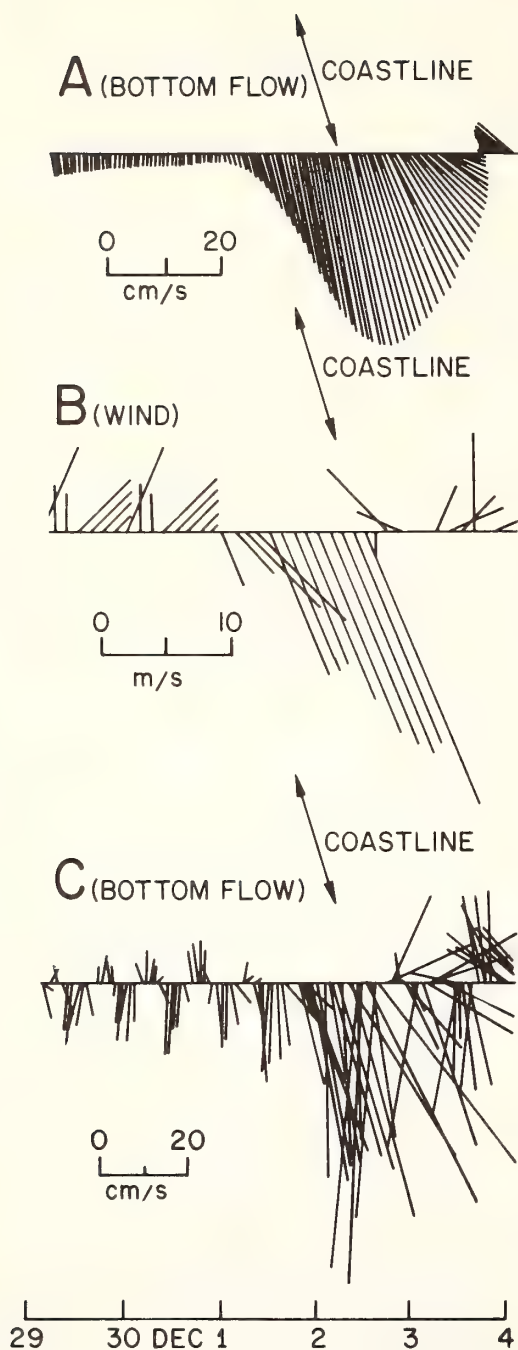


Fig. 13. Vector time series for bottom current and wind velocities during the 1–4 December storm. A—40-h low-pass filtered record (Lanczos filter with response,  $-6$  db at 36 h and  $-20$  db at 40 h). B—Wind record from Ambrose Tower. C—3-h low-pass filtered record (Lanczos filter with response,  $-6$  db at 2.5 h and  $-20$  db at 3 h).

occurred before this and that it initially had been at least 1,200 m long.

The temporal pattern of sediment transport over 60 days may be inferred from Fig. 14C. Current speed, measured 1.5 m from the bed, is plotted against time. The horizontal line at 18 cm/s is an estimated threshold for the fine to very fine sand (mean diameter,  $3.0 \phi$ ) found at the site. It is based on the work of Shields and subsequent workers (Graf 1971: p. 90) and on a choice of  $3.0 \times 10^{-3}$  for the drag coefficient (Sternberg 1972). This choice of threshold velocity was supported by empirical evidence obtained during the course of the experiment (Lavelle et al. in press). Estimates have been prepared for the relative role each transport event played in the overall transport record, based on the concept of frictional energy expenditure proportional to the transport volume (Bagnold 1963). For each event where velocities exceeding threshold were recorded, a transport volume was calculated:

$$Q_i = \alpha \int_i (|u| - |u_{th}|)^3 dt,$$

where  $|u|$  is measured current speed,  $|u_{th}|$  is threshold speed,  $\alpha$  is a constant of proportionality, and  $t_i$  is the duration of the transport event (Lavelle et al. in press).

Expression of sand transport as a power of the difference of measured and threshold velocity is supported by Kennedy's (1969) analysis of stream transport data. Without assigning a value to  $\alpha$ , we can calculate the rate of transport of one flow event relative to the next or in relation to the sand discharge that occurred over the entire duration of the current meter record. The second of these options has been used in Fig. 14C, where relative sand transport as percent of total transport has been represented as solid bars superimposed on the current meter record. Bar height is a measure of volume percent of transport; bar width is a measure of duration of the transport event. Despite the exceedence of the sediment transport threshold at many points in the record, only the solid bars centered on 2 and 16–17 December are visible in the figure. Thus sand transport during observation



consisted of periods of quiescence separated by brief, intense transport events. Furthermore, since discharge is calculated as a power function of excess velocity, intense storms are far more efficient transporters of sand than mild ones. Although the transport index calculated for the 1-4 December storm may be biased by the choice of threshold speed as well as by the functional dependence on velocity, it seems probable that any reasonable parameterization would lead to the same general conclusion: the storm event of 1-4 December moved more sand at 20-m water depth than the combination of all other transport events.

Attempts have also been made to calculate sediment transport indices over longer

periods of time in the New York Bight apex. The following computation is based on 30-80-day Aandaraa current meter records (Fig. 15). Data in each current meter record consist of an average speed,  $u$ , and an instantaneous direction,  $\theta$ , taken for each 10-min sampling interval. For each interval in which an assigned threshold speed,  $|u_{th}|$ , is exceeded, a sediment transport index,  $Q$ , has been computed, as follows:

$$Q = (|u| - |u_{th}|)^3, (|u| - |u_{th}|) > 0.$$

For each current meter, the set of vectors of flow direction,  $\theta$  ( $0^\circ \leq \theta \leq 359^\circ$ ), and of sediment transport index,  $Q$ , is sorted into 10-degree classes. The results are plotted as

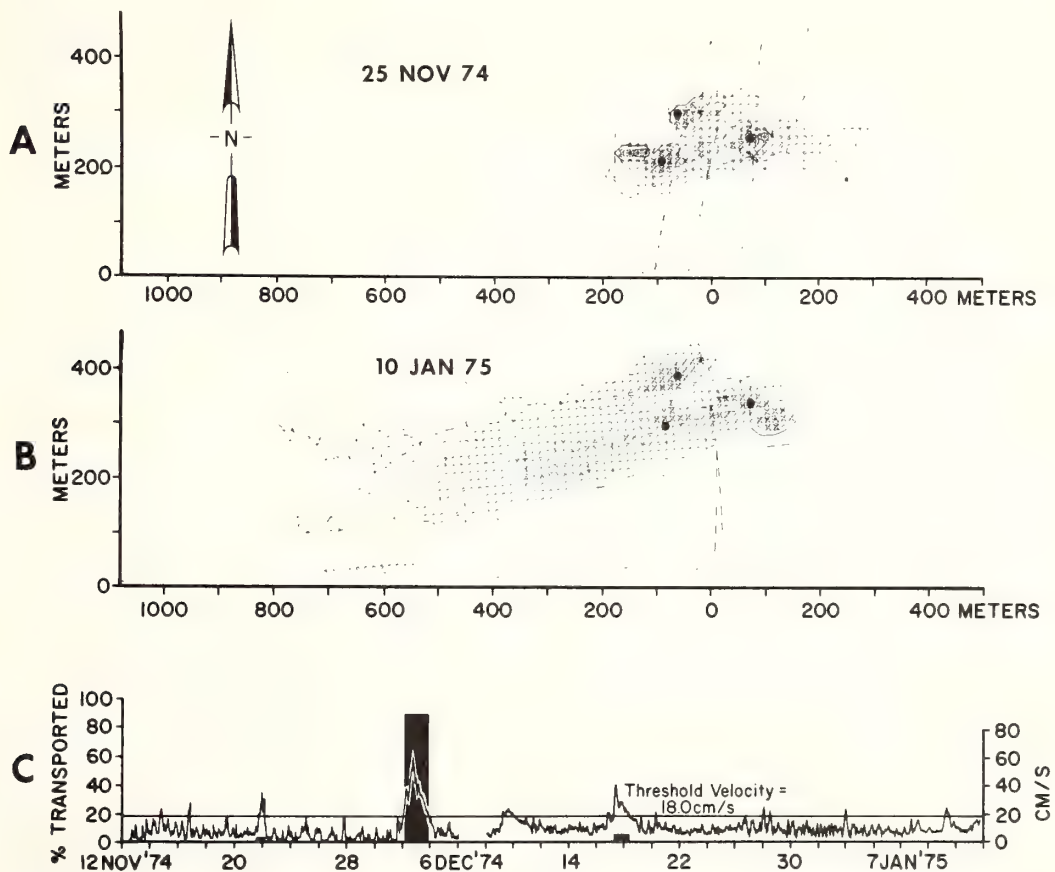


Fig. 14. Sand transport data. A, B—Dispersion patterns measured 13 and 59 days after injection of tagged sand. Point sources are represented by dots. Broken line is the survey trackline. Dots, coarse dots, and Xs indicate increasing intensity of radiation. C—Near-bottom current speed record over the duration of the experiment and calculated sediment transport information. (From Lavelle et al. in press.)

APRIL - JUNE 1974

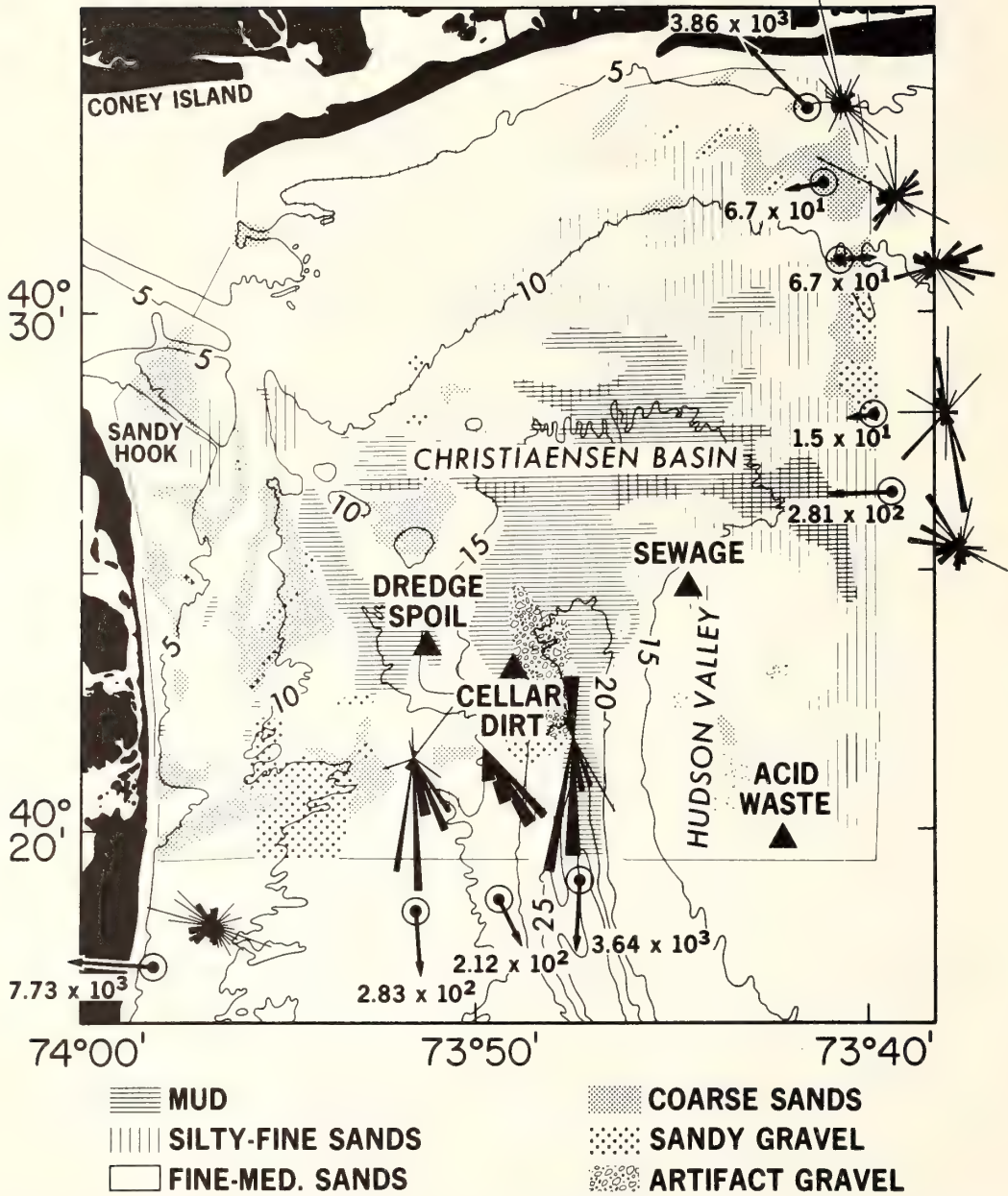


Fig. 15. Bathymetry, bottom sediment character, and calculated patterns of sediment transport for April-June 1974 in the New York Bight apex (*see text*). Depth in fathoms.

rose diagrams in Fig. 15. The length of each radial bar is proportional to the mean sediment transport index, while the width is proportional to the duration of flow above threshold, hence the bars may overlap.

For each current meter station in Fig. 15, the normalized resultant of all sediment transport vectors is indicated by a single arrow. The resulting magnitude has been divided by the total number of days that the

current meter was in operation ( $T_p$ ) to derive a daily average,  $\bar{Q}_D$ :

$$\bar{Q}_D = \frac{1}{T_p} \int_0^T (|u| - |u_{th}|)^3 \mathbf{u} dt,$$

where  $\mathbf{u}$  is a unit vector with direction  $\theta$ , and  $T$  is the total number of days. The integrand is zero when the velocity is less than threshold.

Figure 15 suggests that during April–June 1974, sand transport was westward off the Long Island shore and southward off the New Jersey shore. Nearshore stations reveal a strong onshore component of the sand transport index, perhaps because of wind-induced upwelling or because of the landward directed asymmetry of bottom wave surge, or both. The magnitude of the sand transport index generally decreases seaward but is anomalously large within the Hudson Shelf Valley. The easterly transport revealed by a single station off the Long Island coast is probably due to instrument problems.

#### *Some unsolved problems*

*The inner shelf sand budget*—Our studies of sand transport on the New York inner shelf have resolved some questions but raised others. It is clear that sand transport occurs seaward of the surf zone. Transport is episodic in nature. Sand is entrained and transported by brief, intense, wind-driven coast-parallel flows lasting for hours or days and separated by days or weeks of quiescence. Our measurements suggest that inner shelf bottom flows are more likely to transport shelf sands shoreward than seaward. This appears to be due to intermittent coastal upwelling induced by northwesterly winds and perhaps also to the landward-oriented asymmetry of near-bottom wave surge. Baylor (1973) has also noted this pattern of wind-induced coastal upwelling off Long Island, and R. Scarlet (EG&G, Waltham, Mass., unpublished) reported a similar regime of coastal upwelling for the Beach Haven Ridge site (Fig. 16).

However, our observations indicate that the 1–4 December storm was the only event

that caused massive sand transport. It stands out within our two periods of current monitoring not only in its duration, intensity, and westward direction of net transport but in the offshore component of bottom flow. We must consider the hypothesis that the 1–4 December storm, anomalous within the context of our short term winter observation period, is in fact the kind of peak flow event that shapes the inner shelf surface and controls its sand budget. We have noted that Atlantic shelf stratigraphy is best explained by erosional shoreface retreat and seaward transport of the eroded material. We have described the southwest migration of shoreface-connected ridges off New Jersey and have cited evidence for the net southwest transport of sand (Fig. 8). We note that the Tobay Beach ridges (Fig. 11) are, like other Atlantic Bight ridge fields, asymmetrical in both grain-size distribution and morphology; the seaward-facing southwest slopes are steeper and finer grained, implying that westward flows scour the upcurrent flanks and deposit fine sand on the seaward-facing downcurrent flanks.

Recent studies by physical oceanographers also suggest that southwestward currents generated by “northeaster” storms have the greatest potential for shaping the shelf surface. Beardsley and Butman (1974) have described a scale-matching phenomenon, in which the Middle Atlantic Bight tends to interact with “northeasters” of the appropriate size and trajectory so that intensive southwestward flows result (Fig. 17). Their observations indicate that if low pressure cells cross the bight on a trajectory such that the isobars of atmospheric pressure cross the isobaths of the shelf surface at a high angle, then oscillations of the water column may result, but there is little net displacement of water. However, when the trajectory and scale of the storm are such that for a period it rests in the Middle Atlantic Bight so that the isobars parallel the isobaths, then strong sustained coupling of wind and water flow results. The winds blow along the isobars, down the arc of the Middle Atlantic Bight. Landward Ekman transport of surface water causes 40 to 60 cm of coastal setup and results in a south-

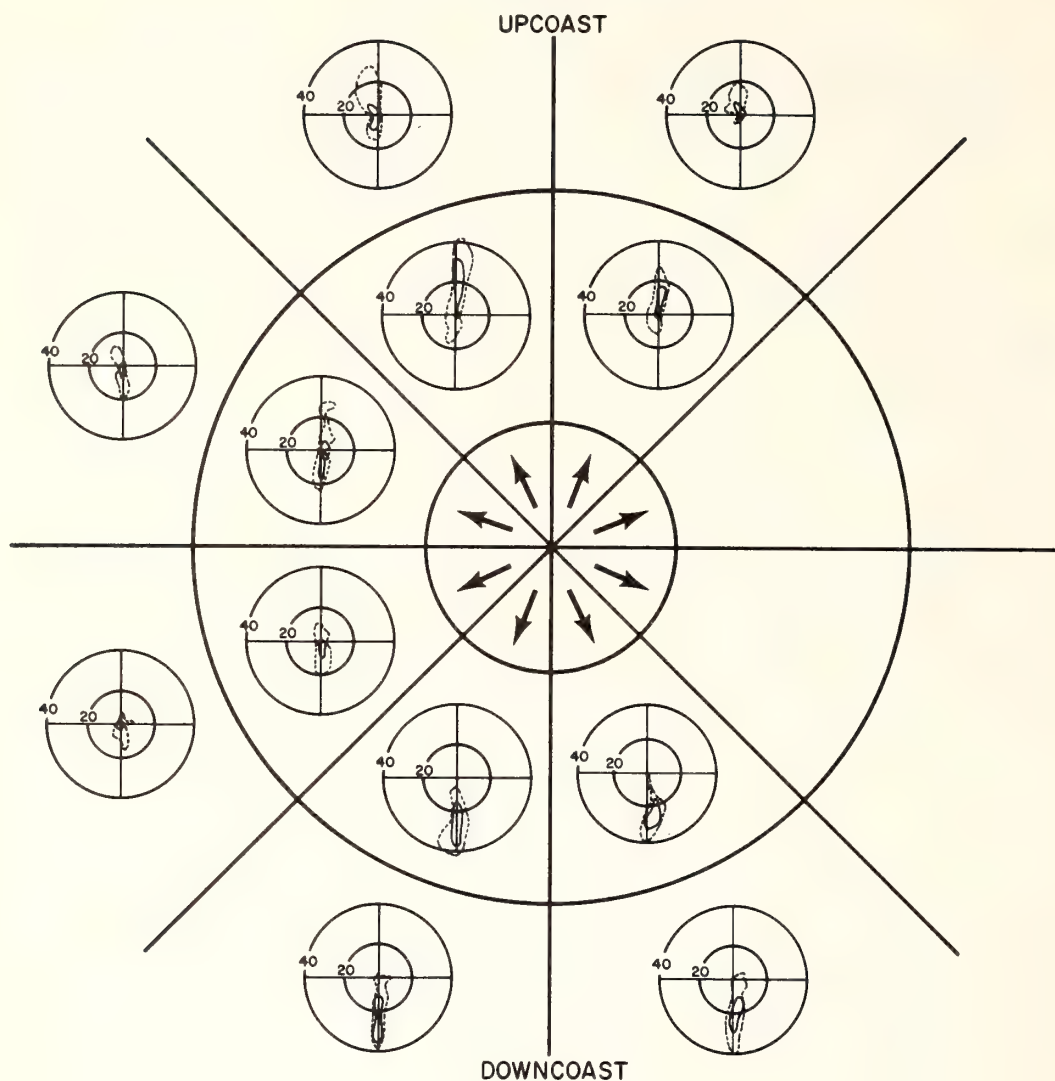


Fig. 16. Polar histograms of hourly averaged, de-tided summer currents in cm/s in the vicinity of Beach Haven Ridge, New Jersey. Only flows associated with winds over 5 m/s are shown. Prevailing wind is indicated by location of histogram on page with wind direction shown in center. Inner ring of histograms is for near-surface measurements, outer ring is for near-bottom measurements. Directions of winds and currents are indicated with top of page representing upcoast motion ( $036^\circ$  true). Histograms are omitted if fewer than 35 h of data were found for specified wind condition. Solid contours enclose 50% and dashed contours enclose 90% of data. (Adapted from EG&G Environ. Consult. 1975.)

ward geostrophic transport of the shelf water column that is coherent and slablike. Boicourt and Hacker (1976) described a similar period of southward storm flow on the Virginia coast with sustained middepth velocities of 30–50 cm/s. Both sets of investigators noted a marked asymmetry in the hydraulic climate, whereby southwest storm

flows tend to be noticeably more intense than northeast flows.

It is clear from the preceding discussion that the role of storm-driven currents in mediating the coastal sand budget requires additional study. We need to know more about the frequency of southwestward storm flows and their velocity structure. We

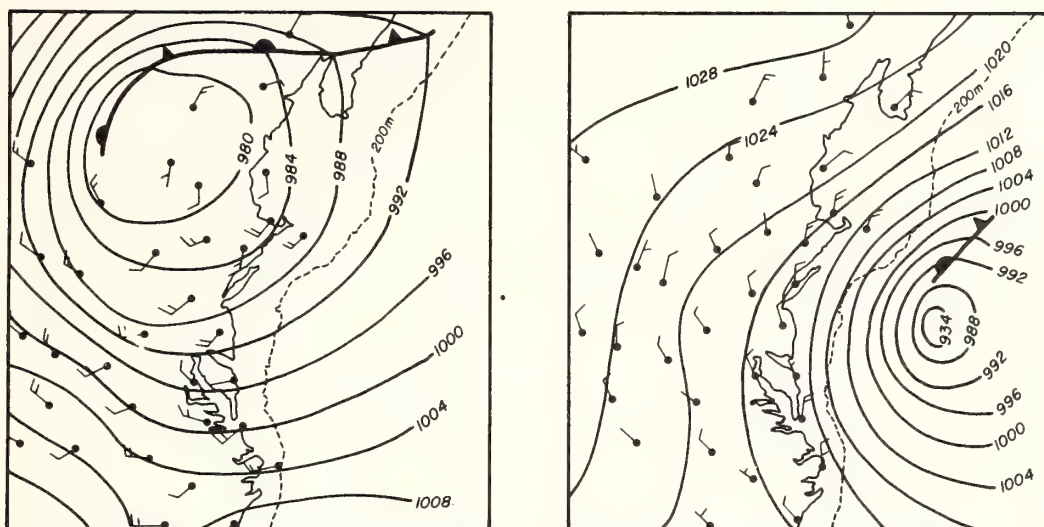


Fig. 17. Surface weather maps for 18 and 22 March 1974. Only the second storm produced sustained coupling between wind and water flow. (From Beardsley and Butman 1974.)

must also learn to design experiments that will resolve perturbations of flow that build and maintain ridge systems.

*Sand transport and storage at New York Harbor mouth*—Major sections of the New York–New Jersey shelf have been shaped by the tidal regimes associated with estuary mouths during the postglacial rise of sea level. Sand budgets of estuary mouths are also of great interest to environmental managers; the Atlantic coast estuaries are the approaches to the major coast ports and require repeated costly dredging. At present, the only estuary mouth subjected to systematic study is that of Chesapeake Bay (Ludwick 1972, 1974, in press). However, reconnaissance data are available for the Hudson estuary mouth, which suggest directions for further study.

New York Harbor mouth is clearly a sink for the littoral drift of the Long Island and New Jersey coasts. Within the past century, much of the deposition has occurred on the ends of Rockaway and Sandy Hook spits; these features have grown rapidly, nearly closing off the harbor mouth within historic times (Shepard and Wanless 1971). However, it appears that much sand has bypassed the spits; a complex system of sand banks separated by interdigitating ebb

and flood channels lies between them (Fig. 18). A profile of velocity residual to the semidiurnal tidal cycle gives some indication of the flow structure responsible for

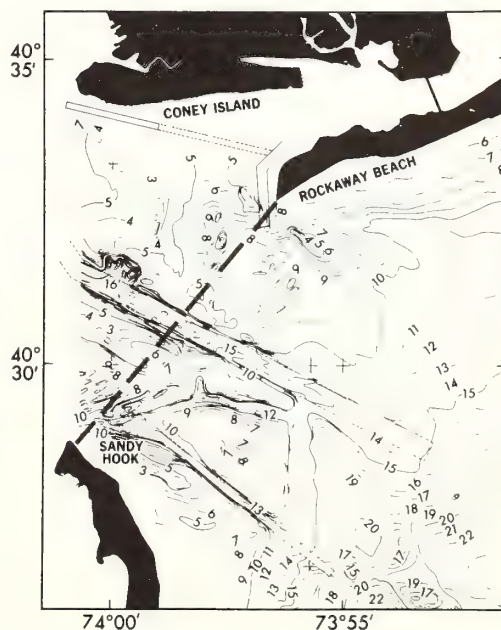


Fig. 18. Bathymetry of the New York Harbor mouth, from a 1973 NOAA/AOML survey. Depth in meters. Dashed line indicates profile of Fig. 19.

bank-channel topography (Fig. 19). The characteristic estuarine two-layer flow is present as indicated schematically in Fig. 19B. The less saline upper water has a residual seaward flow, and the more saline lower water has a residual landward flow. As a consequence of the Coriolis effect, the interface is tilted so that the east side of the harbor mouth is flood dominated while the upper level of the west side is ebb dominated. The distribution of isovels in Fig. 19A suggests that this basic pattern has been modified by the frictional retardation of the tidal wave in the shallow estuary and the resulting phase lag (Swift and Ludwick

in press). Because of retardation, there is a brief period during the tidal cycle when the estuary tide is still ebbing through the central channel while the shelf tide has already turned and is flooding on either side of the ebb tidal jet. This flow pattern, integrated over the tidal cycle, results in greater ebb than flood discharge in the central channel (ebb dominance) and greater flood than ebb discharge in the marginal zones (flood dominance; Fig. 19C). It is probably because of this lag-induced flow interpenetration that the Sandy Hook Channel is not completely ebb dominated as required by the two-layer,

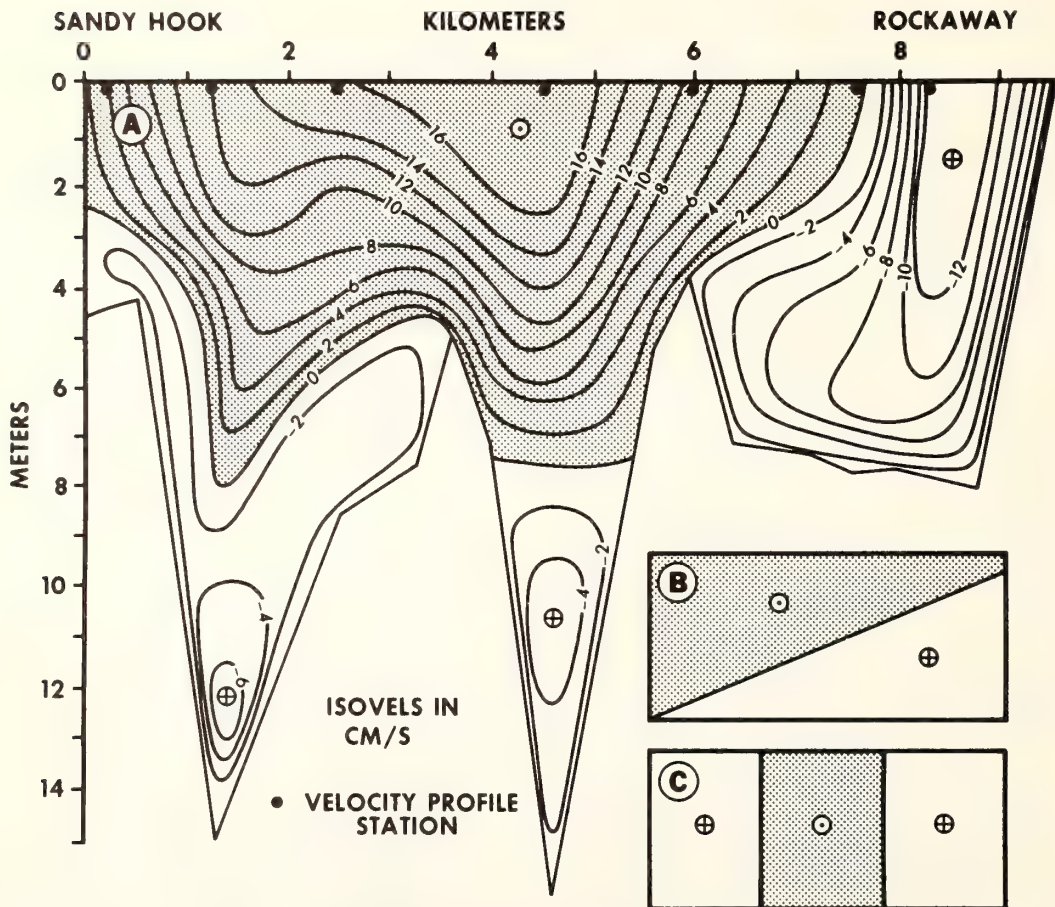


Fig. 19. A—Profile across the Hudson estuary mouth (mouth of New York Harbor), contoured for velocity residual to the semidiurnal cycle. Pattern is interpreted as a resultant response to component patterns shown in B and C. B—Schematic diagram of two-layered, density-driven estuary flow. C—Schematic diagram of pattern resulting from phase lag of the tidal wave. (Modified from data of Kao 1975; reprinted from Duedall et al. in press by permission of *Estuarine and Coastal Marine Science*.)

estuarine component of flow but is flood dominated near the channel floor (Fig. 19A). The two sand ridges that separate the three channels are presumably built by this pattern of flow dominance. Residual flow on the opposite sides of a given sand ridge will have the opposite sense; each ridge is therefore a sand circulation cell or closed loop in the sand transport pattern.

Here perhaps are the ultimate sinks in the littoral sand transport pattern of the New York Bight. Efficient maintenance of the dredged shipping channels demands verification of this inferred pattern of flow dominance and careful analysis of the resulting sand budget.

### References

- BAGNOLD, R. A. 1963. Mechanism of marine sedimentation, p. 507-528. *In* M. N. Hill [ed.], *The sea*, v. 3. Interscience.
- BAYLOR, E. R. 1973. Final report of the oceanographic and biological study for Southwest Sewer District No. 3, Suffolk County, New York. Rep. for Bowe Walsh Assoc. by Mar. Sci. Res. Center. SUNY, Stony Brook.
- BEARDSLEY, R. C., AND B. BUTMAN. 1974. Circulation on the New England continental shelf: Response to strong winter storms. *Geophys. Res. Lett.* 1: 181-184.
- BOICOURT, W. C., AND P. W. HACKER. 1976. Circulation on the Atlantic continental shelf of the United States, Cape May to Cape Hatteras. *Mem. Soc. R. Sci. Liege Ser. 6* 10: 187-200.
- BOWEN, A. J. 1969. The generation of longshore currents on a plane beach. *J. Mar. Res.* 27: 206-215.
- BRUUN, P. 1962. Sealevel rise as a cause of shore erosion. *J. Waterways Harbors Div. Am. Soc. Civ. Eng. Proc.* 88: 117-130.
- DEALTERIS, J. T., J. R. RONEY, L. E. STAHL, AND C. CARR. *In press*. A sediment transport study, offshore New Jersey. *Am. Soc. Civ. Eng. Spec. Conf.*, Jun 1975.
- DONAHUE, J. G., R. C. ALLEN, AND B. C. HEEZEN. 1966. Sediment size distribution profile on the continental shelf off New Jersey. *Sedimentology* 7: 155-159.
- DUANE, D. B., M. E. FIELD, E. P. MIESBERGER, D. J. SWIFT, AND S. J. WILLIAMS. 1972. Linear shoals on the Atlantic continental shelf, Florida to Long Island, p. 447-498. *In* D. J. Swift et al. [eds.], *Shelf sediment transport: Process and pattern*. Dowden, Hutchinson & Ross.
- DUEDALL, I., H. B. O'CONNORS, J. B. PARKER, R. WILSON, W. MILOSKI, AND G. HULSE. *In press*. The abundance, distribution, and flux of nutrients and chlorophyll *a* in the New York Bight apex. *Estuarine Coastal Mar. Sci.*
- EG&G ENVIRONMENTAL CONSULTANTS. 1975. Forecasting power plant effects on the coastal zone. EG&G, Waltham, Mass. 335 p.
- EMERY, K. O., AND E. UCHUPI. 1972. Western North Atlantic Ocean: Topography, rocks, structure, water, life, and sediments. *Am. Assoc. Pet. Geol. Mem.* 17.
- FISCHER, A. G. 1961. Stratigraphic record of transgressing seas in the light of sedimentation on the Atlantic coast of New Jersey. *Am. Assoc. Pet. Geol. Bull.* 45: 1656-1660.
- GRAF, W. H. 1971. *Hydraulics of sediment transport*. McGraw-Hill.
- HARRIS, R. L. 1954. Restudy of test shore nourishment by offshore deposition of sand, Long Branch, New Jersey. Beach Erosion Board Tech. Memo. 62.
- KAO, A. 1975. A study of the current structure in the Sandy Hook-Rockaway Point transect. M.S. Res. Pap., Mar. Sci. Res. Center. SUNY, Stony Brook.
- KENNEDY, J. F. 1969. The formation of sediment ripples, dunes, and antidunes. *Annu. Rev. Fluid Mech.* 1: 147-168.
- KIM, J. H., AND W. S. GARDNER. 1974. Geomarine investigation. Final design study wastewater ocean outfalls. Ocean Co. Sewerage Authority, Ocean Co., N.J.
- LAVELLE, J. W., AND OTHERS. *In press*. Preliminary results of coincident current meter and sediment transport observations for wintertime conditions on the Long Island inner shelf. *Geophys. Res. Lett.*
- LUDWICK, J. C. 1972. Migration of tidal sandwaves in Chesapeake Bay entrance, p. 377-410. *In* D. J. Swift et al. [eds.], *Shelf sediment transport: Process and pattern*. Dowden, Hutchinson & Ross.
- . 1974. Tidal currents and zig-zag sand shoals in a wide estuary entrance. *Geol. Soc. Am. Bull.* 85: 717-726.
- . *In press*. Tidal currents, sediment transport, and sandbanks in Chesapeake Bay entrance, Virginia. *Proc. Int. Estuarine Conf.*, 2nd, Myrtle Beach, S.C., Oct 1973.
- MURRAY, S. P. 1975. Trajectories and speeds of wind-driven currents near the coast. *J. Phys. Oceanogr.* 5: 347-360.
- SANDERS, J. E., AND N. KUMAR. 1975. Evidence of shoreface retreat and in-place "drowning" during Holocene submergence of barriers, shelf off Fire Island, New York. *Geol. Soc. Am. Bull.* 86: 65-76.
- SHEPARD, F. P., AND H. R. WANLESS. 1971. *Our changing shorelines*. McGraw-Hill.
- SHERIDAN, R. E., C. E. DILL, JR., AND J. C. KRAFT. 1974. Holocene sedimentary environment of the Atlantic inner shelf off Delaware. *Geol. Soc. Am. Bull.* 85: 1319-1328.
- SONU, C. J., AND J. L. VAN BEEK. 1971. System-

- atic beach changes on the Outer Banks, North Carolina. *J. Geol.* **79**: 416–425.
- STAHL, L., J. KOCZAN, AND D. J. SWIFT. 1974. Anatomy of a shoreface-connected sand ridge on the New Jersey shelf: Implications for the genesis of the shelf surficial sand sheet. *Geology* **2**: 117–120.
- STERNBERG, R. W. 1972. Predicting initial motion and bedload transport of sediment in the marine environment, p. 61–82. *In* D. J. Swift et al. [eds.], *Shelf sediment transport: Process and pattern*. Dowden, Hutchinson & Ross.
- STUBBLEFIELD, W. L., J. W. LAVELLE, T. F. MCKINNEY, AND D. J. SWIFT. 1974. Sediment response to the present hydraulic regime on the central New Jersey shelf. *J. Sediment. Petrol.* **45**: 337–358.
- SWIFT, D. J. 1973. Delaware Shelf Valley: Estuary retreat path, not drowned river valley. *Geol. Soc. Am. Bull.* **84**: 2743–2748.
- , D. B. DUANE, AND T. F. MCKINNEY. 1974. Ridge and swale topography of the Middle Atlantic Bight: Secular response to Holocene hydraulic regime. *Mar. Geol.* **15**: 227–247.
- , J. W. KOFOED, F. P. SAULSBURY, AND P. SEARS. 1972. Holocene evolution of the shelf surface, central and southern shelf of North America, p. 499–574. *In* D. J. Swift et al. [eds.], *Shelf sediment transport: Process and pattern*. Dowden, Hutchinson & Ross.
- , AND J. C. LUDWICK. *In press*. Substrate response to hydraulic process: Grain size frequency distributions and bedforms. *In* D. J. Stanley and D. J. Swift [eds.], *Marine sediment transport and environmental management*. Wiley-Interscience.
- , AND P. SEARS. 1974. Estuarine and littoral depositional patterns in the surficial sand sheet, central and southern Atlantic shelf of North America. *Inst. Geol. Bassin Aquitaine Mem.* **7**, p. 171–189.
- VEATCH, A. G., AND P. A. SMITH. 1939. Atlantic submarine valleys of the United States and the Congo submarine valley. *Geol. Soc. Am. Spec. Pap.* **7**. 101 p.









PENN STATE UNIVERSITY LIBRARIES



A000072832721